FEL2022

40th International Free-Electron Laser Conference

Trieste, Italy | August 22-26 2022

www.fel2022.org

Proceedings

Hosting Organization

Elettra Sincrotrone Trieste

FEL2022

40th International Free Electron Laser Conference
Trieste, Italy | August 22-26, 2022

PROCEEDINGS

www.fel2022.org

Table of contents

FEL2022

Preface

We present the proceedings of FEL2022, the 40th International Free-Electron Laser Conference held from August 22nd to August 26th in Trieste, a multi-cultural city, well renowned for its writers, artists and food, a city well-worth discovering, as did famous James Joyce and several other distinguished writers a century ago. The conference was organized by Elettra-Sincrotrone Trieste, the international, multidisciplinary research center specialized in the generation of synchrotron and free-electron laser radiation together with their applications in material and life sciences.

Considering the prevailing circumstances, the conference achieved a remarkable level of participation. We were aware of the challenging global pandemic situation, which resulted in the exclusion of some countries and significantly limited the involvement of others. Despite these challenges, the exceptional work carried out by the Scientific Program Committee (SPC) ensured the quality of the oral presentations, engaging discussions, and the consistent involvement of attendees in all sessions. This dedication undoubtedly contributed to the success of the event.

The conference brought together approximately 260 individuals, including exhibitors and the dedicated support team from Elettra-Sincrotrone Trieste. Throughout the event, we witnessed 66 outstanding oral presentations (including 6 delivered remotely), featured 30 exhibitors, sponsored 14 students, showcased 180 posters during the dedicated poster sessions, and hosted the LEAPS-INNOV Workshop, which attracted 11 participants.

We wish to extend our sincere appreciation to the industrial companies that demonstrated great interest in the conference by presenting their exhibitions and providing vital support. Their contributions were instrumental in creating a venue with ample spaces and a high level of professionalism, enriching the overall conference experience. Furthermore, we would like to express our gratitude to the institutions that generously offered a number of student fellowships. These fellowships played a crucial role in enabling young scientists to attend the conference, providing them with valuable opportunities to learn, network, and contribute to the scientific community. Their presence and active participation added a dynamic and vibrant dimension to the event.

The conference offered participants a unique opportunity to explore the remarkable facilities of Elettra and FERMI. The organized visit, which attracted approximately 150 attendees divided into five groups, allowed participants to gain firsthand experience and insights into the fascinating world of these advanced scientific installations.

In addition to the visit, another significant highlight of the conference was the memorable social dinner held at the Stazione Marittima of Trieste. This evening brought together participants in an atmosphere of camaraderie, fostering networking opportunities and celebrating the outstanding accomplishments within the field of Free-Electron Lasers. The event provided a platform for attendees to connect, exchange ideas, and strengthen professional relationships, contributing to the vibrant and collaborative spirit of the conference. During this special occasion, we had the privilege of awarding the prestigious FEL prize to Brian W. J. McNeil and Ying K. Wu for their exceptional achievements and significant contributions to the advancement of Free-Electron Lasers. Their groundbreaking work has propelled the field forward, inspiring researchers and shaping the future of FEL technologies. In addition, we were thrilled to present the Young Scientist Award to Svitozar Serkev, Yawei Jan, and Zen Zhang to acknowledge their outstanding achievements at an early stage of their careers, highlighting their potential and promising contributions to the field.

We hope that these proceedings capture the spirit of FEL2022, serving as a valuable resource for all attendees and the broader scientific community.

Sincerely,

Luca Giannessi and Michele Svandrlik,

Conference Chairs

Conference Organization

Local Organizing Committee

Chairs
Luca Giannessi and Michele Svandrlik

Editor in Chief
Ivan Andrian

LOC Coordinators
Giuseppe Penco and Annamaria Accettulli

International Executive Committee

Stephen Benson (TJNAF)
Marie-Emmanuelle Couprie (Synchrotron SOLEIL)
Aharon Friedman (Ariel University)
John N. Galayda (Princeton, PPPL)
Luca Giannessi (INFN & Elettra Sincrotrone Trieste)
Ryoichi Hajima (QST)
Hiroyuki Hama (Tohoku University)
Zhirong Huang (SLAC)
Heung-Sik Kang (PAL/POSTECH)
Vladimir N. Litvinienko (Stony Brook University & BNL)
Brian McNeil (Strathclyde University)
Dinh C. Nguyen (SLAC)
Britta Redlich (Radboud University)
Sven Reiche (PSI)
Joerg Rossbach (DESY& Hamburg University)
Oleg A. Shevchenko (BINP)
Hitoshi Tanaka (RIKENSPring-8 Center)
Richard P. Walker (Diamond Light Source)
Ying K. Wu (Duke University)
Zhentang Zhao (SARI)

Scientific Programme Committee

Giovanni De Ninno and Simone Di Mitri (Chairs)

Laura Badano (Elettra)
Stephen Benson (TJNAF)
Simona Bettoni (PSI)
Martin Beye (DESY)
Sandra Biedron (UNM)
Sebastien Boutet (SLAC)
Carlo Callegari (Elettra)
Flavio Capotondi (Elettra)
Bruce Carlsten (LANL)
Daniele Cocco (LBNL)
Yuantao Ding (SLAC)
David Dunning (STFC)
Chao Feng (SINAP)
Massimo Ferrario (INFN-LNF)
Gianluca Geloni (EU-XFEL)
Avi Gover (Tel-Aviv Univ.)
Jan Gruenert (EU-XFEL)
Ryochi Hajima (QST)
Erik Hamsing (SLAC)
Jang-Hui Han (PAL)
Toru Hara (RIKENSpring-8)
Rasmus Ischebeck (PSI)
Young Jeong (KAERI)
Huaidong Jiang (SINAP)
Heung-Sik Kang (PAL)
Marie Labat (SOLEIL)
Vladimir Litvinenko (BNL)
Alex Lumpkin (FNAL)
Alberto Lutman (SLAC)
Agostino Marinelli (SLAC)
Claudio Masciovecchio (Elettra)
Atoosa Meseck (HZB)
Hideoki Ohgaki (IAE)
Eduard Prat (PSI)
Jia Qika (USTC)
Eléonore Roussel (CNRS)
Steven Russell (LANL)
Fernando Sannibale (LBNL)
Oleg Schevchenko (BINP)
Evgeny Schneidmiller (DESY)
Roseanne J. Sension (Un. of Michigan)
Svitozer Serkez (EU-XFEL)
Frank Stephan (DESY)
Takashi Tanaka (RIKENSpring-8)
Sara Thorin (MAX IV)
Kiyoshi Ueda (Tohoku Un.)
Mathias Vögt (DESY)
Dong Wang (SINAP)
Sverker Werin (MAX-IV)
Juhao Wu (SLAC)
Ying K. Wu (DUKE)
Alexander Zholents (ANL)

FEL Prize Committee

Zhirong Huang (SLAC), Chair
Bruce Carlsten (LANL)
Mikhail Yurkov (DESY)
Marie-Emmanuelle Couprie (Soleil)
Hiroyuki Hama (Tohoku Un.)

Student Grant Committee

Agostino Marinelli (SLAC)
Giuseppe Penco (Elettra, Chair)
Joerg Rossbach (DESY& Hamburg University)
Zhentang Zhao (SARI)

JACoW Editorial Team

Ivan Andrian (Elettra-Sincrotrone Trieste, Italy, Editor-in-Chief)
Stefano Deiuri (Elettra-Sincrotrone Trieste, Italy)
Wojciech Grabowski (NCBJ,Polland)
Massimiliano Gualtiero Iungo (INFN,Italy)
Giovanni Perosa (Elettra-Sincrotrone Trieste, Italy)
Christine Petit Jean Genaz (CERN,Switzerland)
Giada Petringa (INFN, Italy)
Cristiana Roberti (Elettra-Sincrotrone Trieste, Italy)
Volker Schaa (GSI, Germany)
Filippo Sottocorona (Elettra-Sincrotrone Trieste, Italy

Organizing Secretariat

the office
www.theoffice.it

FEL2022

Conference Sponsors

KYMA

saes

CINEL

saes RIAL VACUUM

Kashiyama Vacuum Solutions

CPI Communications & Power Industries

Cycle

phytron a step ahead

INSTRUMENTATION TECHNOLOGIES

PFEIFFER VACUUM

FARADAY MOTION CONTROLS

IRELEC ALCEN

R&K

CAENels Gear For Science

T.E.E.S.

ScandiNova

XP Power | fug HIGH PRECISION POWER ELECTRONICS

AMPEGON

OCEM POWER ELECTRONICS

VACUUM FAB MOTION CONTROL & OPTICS

Student grants supporting institutes

DESY. PAUL SCHERRER INSTITUT PSI MAX IV

INFN Istituto Nazionale di Fisica Nucleare Laboratori Nazionali di Frascati SACLA SLAC Elettra Sincrotrone Trieste

Conference Photos

Group photo

Conference location: Trieste Convention Center

Photo by Massimo Goina & Luca Giannessi

Group photo

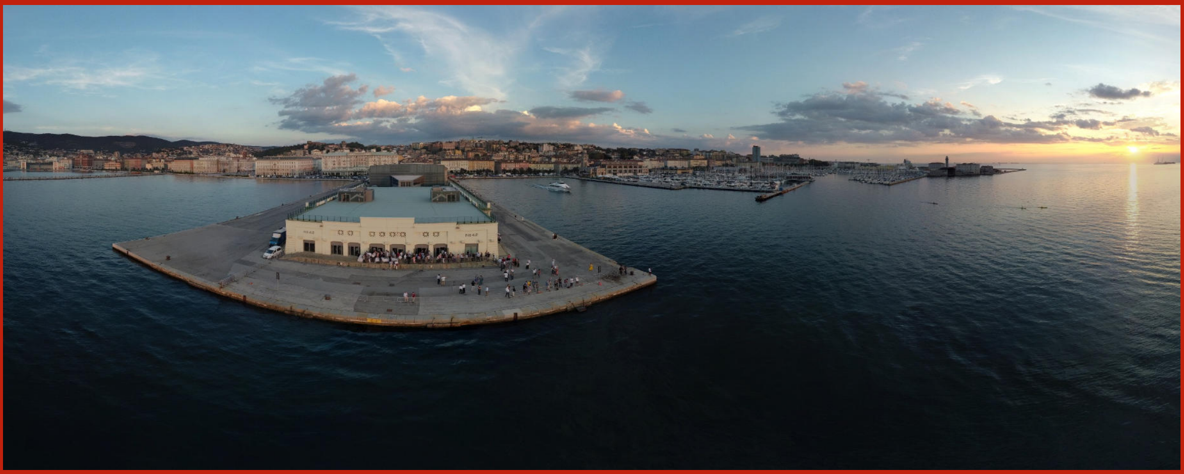
Stazione Marittima


Conference dinner at Stazione Marittima

Photo by Massimo Goina & Luca Giannessi

2022 FEL Prize

The prestigious FEL prize was awarded to Brian W. J. McNeil and Ying K. Wu for their exceptional achievements and significant contributions to the advancement of Free-Electron Lasers.

Brian W. J. McNeil receives the 2022 FEL Prize from Zhirong Huang, Chair of the FEL Prize Committee.

Ying K. Wu receives the 2022 FEL Prize from Zhirong Huang, Chair of the FEL Prize Committee.

Photo by Massimo Goina

2022 FEL Young Scientist Awards

Svitozar Serkev receives the 2022 FEL Young Scientist Award from Zhirong Huang, Chair of the FEL Prize

Yawei Jan receives the 2022 FEL Young Scientist Award from Zhirong Huang

Zen Zhang receives the 2022 FEL Young Scientist Award from Zhirong Huang

Photo by Massimo Goina

Photo by Massimo Goina

Past FEL Prize Winners at the 2022 FEL Prize Ceremony

Photo by Massimo Goina

Young Scientist Award Winners at the 2022 FEL Prize Ceremony

FEL2022

40th International Free Electron Laser Conference
Trieste, Italy | August 22-26

www.fel2022.org

ISBN: 978-3-95450-220-2 ISSN: 2673-5474 doi: 10.18429/JACoW-FEL2022

Table of Contents

ISBN: 978-3-95450-220-2 ISSN: 2673-5474 doi: 10.18429/JACoW-FEL2022

ISBN: 978-3-95450-220-2 ISSN: 2673-5474 doi: 10.18429/JACoW-FEL2022

ISBN: 978-3-95450-220-2 ISSN: 2673-5474 doi: 10.18429/JACoW-FEL2022-MOA03

ATTOSECONDS AT HARMONICS AT THE EUROPEAN XFEL: FIRST RESULTS AT SASE3

A. Trebushinin*, G. Geloni†, S. Serkez, G. Mercurio, N. Gerasimova
European XFEL, Schenefeld, Germany
M. Guetg, and E. Schneidmiller‡, DESY, Hamburg, Germany

Abstract

We report on the observation of a substantial amount of single-spike spectra collected at the SASE3 beamline of European XFEL using a two-stage scheme (3 - 11 % with respect to all events). The undulators at the first stage were set to the resonance at the "fundamental", and the undulators at the second stage operated at the "harmonic" of the fundamental, in this case, it was the 4th harmonic. In the experiments, we expected radiation generation in the second stage to start from the high level of bunching created in the first stage. Moreover, the nonlinear characteristic of harmonic bunching growth rate at the first stage leads to the most rapid growth of the most prominent spikes. After being amplified at the second stage this provides occasional single spike pulses in the time domain. With that, we expect these single spike events in the spectrum correspond to single spike events in the time domain. We estimated *the minimal possible* pulse duration for these pulses using Fourier transform of the experimental spectra amplitude where we assume a flat phase across a pulse spectrum. The typical duration was at the level of several hundreds of attoseconds (300-500 as). Considering the appearance frequency of single spike events, this method may be attractive for high repetition-rate free electron lasers for generating sub-femtosecond radiation pulses.

INTRODUCTION

High bunching at harmonics driven by the fundamental has drawn the attention of researchers in the past and described in numerous publications, e.g. [1–3]. Underling effect consists in the fact that, the longitudinal phase space of the electron beam buckets "rotates" from nearly sin-like shape at the beginning of linear regime to a set of "strokes" in deep linear regime. This enhances the content of higher harmonics. The growth of bunching at harmonics is rapid and it reaches very shortly a sufficient level. This process is non-linear and is characterized by a power law dependence with respect to the fundamental ($b_n(t) \sim b_1^n(t)$), Fig. 1, where b_n denotes the bunching at the corresponding n-th harmonic.

Due to this power law dependence, spikes of bunching along the electron beam length are effectively being filtered: suppression of low value of bunching, increase of contrast, and reduction of the width of the spike follow, as depicted in Fig. 2.

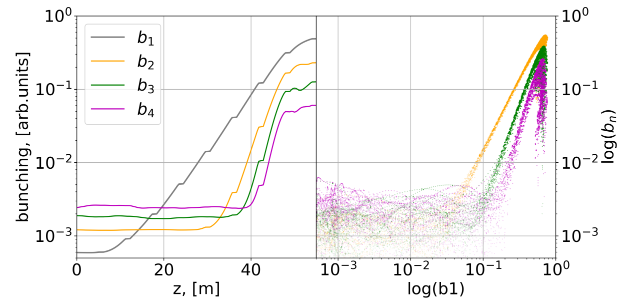

Figure 1: Simulation of the growth of the harmonics bunging with GENESIS 1.3 code, [4]. Left: evolution of the bunching factor for the fundamental (1st), 2nd, 3rd, and 4rd harmonic. Right: dependence of the harmonics bunching factor on bunching factor at fundamental in log-log scale. The long plateau on the left corresponds to a negligible level of the higher harmonics content, followed by a linear dependence $b_n(t) \sim b_1^n(t)$, the slopes of the lines is $2, 3, 4$ for the corresponding harmonics, which corresponds to linear regime, on the right a hook-like dependence represents saturation.

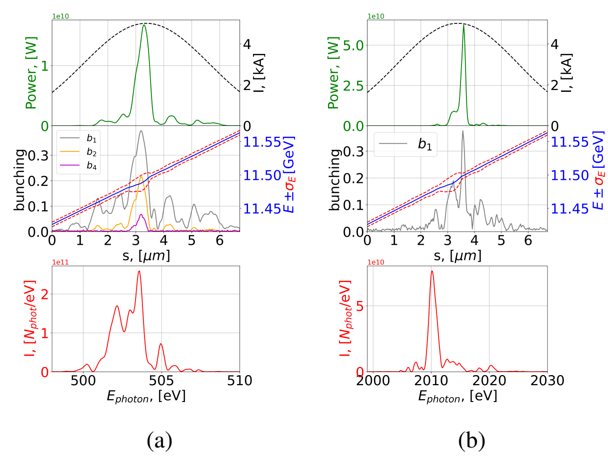

(a) (b)

Figure 2: A first part of the FEL is tuned at the fundamental harmonic (a), while a second part lases at the fourth harmonic with respect to the first stage (b). The spikes of the harmonics were effectively filtered when compared to the bunching distribution of the fundamental harmonic. One may observe suppression of low values of bunching, increase in contrast, and reduction of the width of the spike.

The authors of [5] proposed to use this effect for generating sub-femtosecond pulses with two (or *multi*) stage

* andrei.trebushinin@xfel.eu
† gianluca.aldo.geloni@xfel.eu
‡ evgeny.schneidmiller@desy.de

ISBN: 978-3-95450-220-2 ISSN: 2673-5474 doi: 10.18429/JACoW-FEL2022-MOA03

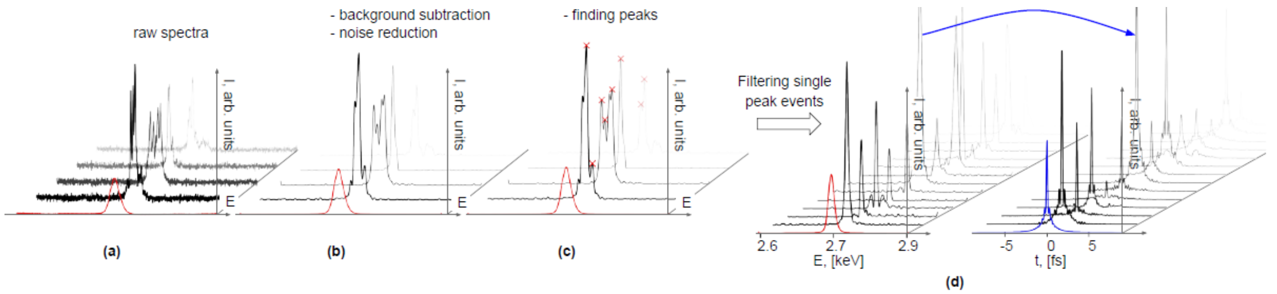

Figure 3: Data analysis procedure. (a) raw spectra extracted from the SASE3 spectrometer, (b) background subtracted, noise reduced, (c) spectrum peaks mapped, (d) single peak events chosen, Fourier transform performed to estimate *minimal possible* pulse duration.

undulator scheme. We shall call "attoseconds at harmonics" scheme. In the first stage, one creates high bunching at harmonics of the fundamental λ. The following stages are tuned to a fundamental wavelength corresponding to harmonics of the first stage to the harmonics of the first stage (λ/n). In this way, lasing starts up from the substantial level of bunching at harmonics created at the previous stage. The idea behind this scheme is to statistically filter out the events with only one prominent spike in the time domain and then amplify this harmonic at the second stage. This allows for the generation of the single spike sub-femtosecond pulses with appearance frequency at the level of several percent with respect to all events. The method may be attractive for high repetition rate machines.

EXPERIMENTS AT EUROPEAN XFEL

We performed two experiments in September 2021 and October 2020 at the SASE3 beamline [6], of the European XFEL facility using a two stage setup. The second stage was set to the 4th harmonic. In Table 1 we present the relevant electron beam energy E_{ebeam} and and photon resonance energy E_γ.

Table 1: Experiments parameters

Experiment	E_{ebeam} [GeV]	E_γ [eV]	4E_γ [eV]
Sep 2021	11.5	503	2012
Oct 2020	14	675	2700

SPECTRA ANALYSIS

During the experiments, we collected raw spectra from the spectrometer [7]. In this data, we look for single-spike events only. Here we assumed that, on a statistical basis, a single spike event in a spectrum often corresponds to a single spike event in the time domain. At first, we extracted raw data from the SASE3 spectrometer, Fig. 3, (a), subtracted the background and proceeded with the application of a noise reduction algorithm, Fig. 3, (b). The latest step was needed to ease the mapping of the number of peaks in the spectrum Fig. 3, (c). After this, the only information on the pulse duration that we could actually extract was an estimation of the duration of the time-bandwidth limited pulse

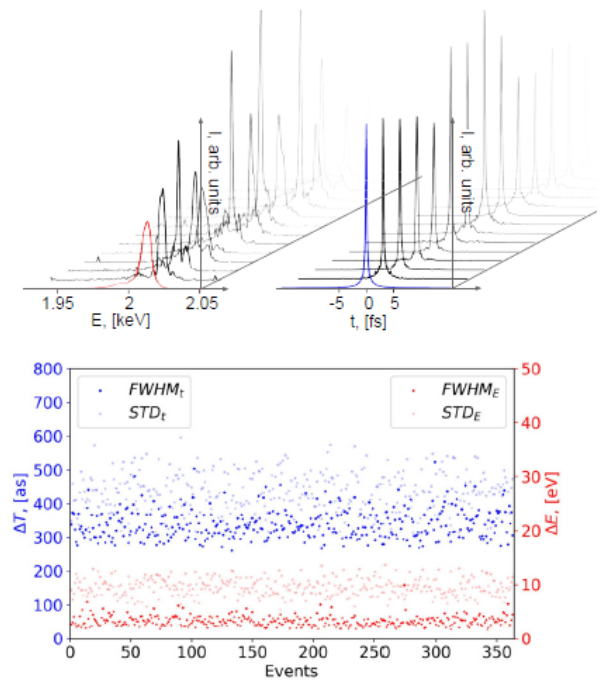

Figure 4: Experiment from September 2021. On the top left plot we show filtered single spike events and – on the top left plot – their power distributions in the time domain obtained by Fourier transformation (assuming a flat spectral phase). On the bottom plot, we present the width of the peaks (standard deviation ($STD_{E,t}$) and full width at half maximum ($FWHM_{E,t}$)); power distributions that correspond to time domain are presented in blue, spectral width in eV are presented in red.

that corresponds to the filtered spectrum. To evaluate it we performed the Fourier transform of the spectrum amplitude, in other words, we estimated a flat phase across the spectrum. With this estimation, we only say the *minimal possible* pulse duration.

ESTIMATED PULSE DURATION

The filtered event and the corresponding values for the pulse duration are presented in Figs. 4 and 5. The estimated pulses duration was at the level of 300 – 500 as. The ap-

ISBN: 978-3-95450-220-2 ISSN: 2673-5474 doi: 10.18429/JACoW-FEL2022-MOA03

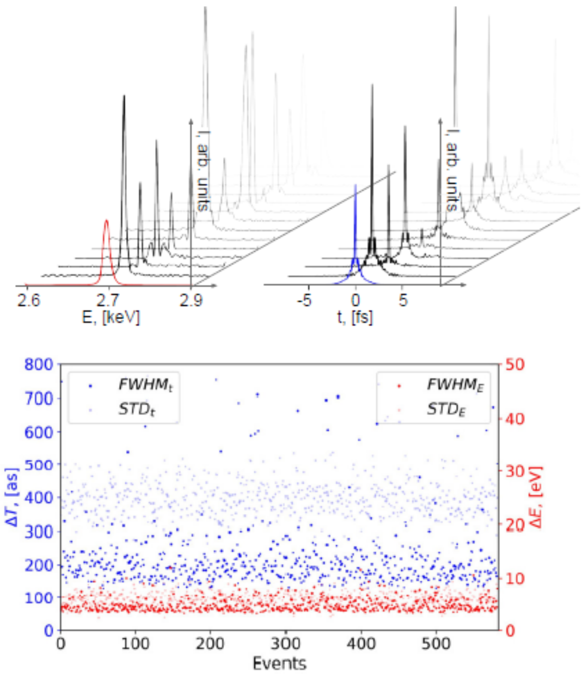

Figure 5: Experiment from October 2020. The notation for the plot is the same as for Fig. 4.

pearance frequency in the percent of single spike events was at the level of 3 % for September 2021 run and 11 % for October 2020 run. Our simulation results (not shown here) indicate that our previous assumption of Fourier-limited pulses (flat phase) seems approximatively correct. However, the actual time domain power distribution is unknown in these experiments. We plan to conduct measurements with the angular streaking technique, [8], to measure actual temporal duration.

CONCLUSION

In this contribution, we show first experimental results concerning the generation of attosecond-level FEL pulses with the "attoseconds at harmonics" method. We show the presence of single spike spectra in the experimental results that as we expect correspond to single spike in the time domain. We estimated that the *minimal possible* pulse duration for these events were of several hundreds attoseconds (300 – 500 as). This work is propaedeutic to direct time-domain measurements with angular streaking technique at European XFEL.

ACKNOWLEDGEMENTS

We thank Serguei Molodtsov for his interest in this work.

REFERENCES

[1] R.Bonifacio *et al.*, "Large harmonic bunching in a high-gain free-electron laser", *Nucl. Instrum. Methods Phys. Res., Sect. A*, vol. 293, no. 3, pp. 627–629, Aug. 1990, doi:10.1016/0168-9002(90)90334-3

[2] Z. Huang and K. J. Kim, "Three-dimensional analysis of harmonic generation in high-gain free-electron lasers", *Phys. Rev. E*, vol. 62, p. 5, pp. 7295–7308, 2000. doi:10.1103/PhysRevE.62.7295

[3] Z. Huang and K. J. Kim, "Nonlinear harmonic generation of coherent amplification and self-amplified spontaneous emission", *Nucl. Instrum. Methods Phys. Res., Sect. A*, vol. 475, pp. 112–117, 2001. doi:10.1016/S0168-9002(01)01553-4

[4] S. Reiche, "Numerical studies for a single pass high gain free-electron laser", Ph.D. thesis, Phys. Dept., Hamburg university, Hamburg, Germany, 2022

[5] E. L. Saldin *et al.*, "Scheme for attophysics experiments at a X-ray SASE FEL", *Optics Communications*, vol. 212, issues 4–6, pp. 377-390, 2002. doi:10.1016/S0030-4018(02)02008-4

[6] D. L. Civita *et al.*, "SASE3: soft x-ray beamline at European XFEL", in *Proc. X-Ray Free-Electron Lasers: Beam Diagnostics, Beamline Instrumentation, and Applications II*, San Diego, California, United States, Oct. 2014, vol. 9210. doi:10.1117/12.2061693

[7] N. Gerasimova, "Diffraction Orders of the SASE3 Monochromator", *XFEL.EU. Technical Report*, 2014 doi:10.3204/XFEL.EU/TR-2014-003

[8] N. Hartmann *et al.*, "Attosecond time–energy structure of X-ray free-electron laser pulses", *Nat. Photonics*, vol. 12, p. 4, 2018. doi:10.1038/s41566-018-0107-6

ISBN: 978-3-95450-220-2 ISSN: 2673-5474 doi: 10.18429/JACoW-FEL2022-MOA08

FIRST LASING OF THE THz SASE FEL AT PITZ*

M. Krasilnikov †, Z. Aboulbanine, G. Adhikari, N. Aftab, P. Boonpornprasert, R. General, G. Georgiev, J. Good, M. Gross, L. Heuchling, A. Hoffmann, M. Homann, L. Jachmann, D. Kalantaryan, W. Köhler, G. Koss, X.-K. Li, A. Lueangaramwong, S. Maschmann, D. Melkumyan, F. Müller, R. Netzel, R. Niemczyk, A. Oppelt, B. Petrosyan, S. Philipp, M. Pohl, H. Qian, C. Richard, C. Rüger, A. Sandmann-Lemm, M. Schade, E. Schmal, J. Schultze, F. Stephan, G. Vashchenko, T. Weilbach, S. Weisse, DESY, Zeuthen, Germany
B. Krause, E. Schneidmiller, M. Tischer, P. Vagin, M. Yurkov, DESY, Hamburg, Germany
W. Hillert, Univ. Hamburg, Institut fuer Experimentalphysik, Hamburg, Germany
A. Brachmann, N. Holtkamp, H.-D. Nuhn, SLAC, Menlo Park, CA, USA

Abstract

The Photo Injector Test Facility at DESY in Zeuthen (PITZ) develops a prototype of an accelerator-based high-power tunable THz source for pump-probe experiments at the European XFEL. The PITZ injector is also the site for the development and preparation of the high-brightness electron source for the main linac of the European XFEL and has the same pulse train structure as the X-ray photon source of the XFEL. For the proof-of-principle experiments on high-power THz generation an LCLS- I undulator (on loan from SLAC) is installed in the tunnel annex downstream of the existing accelerator. The extension of the beam line consists of a bunch compressor and a collimation system in the main PITZ tunnel, as well as a matching section, the undulator and the THz diagnostic setup in the tunnel annex. A Self-Amplified Spontaneous Emission (SASE) FEL is used to generate the THz pulses. High radiation power can be achieved by utilizing high charge (up to several nC) electron bunches from the PITZ photo injector. A beam energy of ~17 MeV is used to generate THz radiation with a centre wavelength of 100 µm. The transport of this space charge dominated electron beam and its thorough matching into the planar LCLS-I undulator with a strong vertical focusing is one of the project challenges. The installation of the first THz beamline setup was finished in summer 2022 and commissioning with electron beam started. A specially developed procedure for a high charge beam matching into the undulator was successfully tested resulting in a first THz pulse generation. The start-up THz diagnostics is based on pyrodetectors. First measurements of the THz generation from 1 nC, 2 nC and 3 nC bunches have been taken, the statistics properties analysis corresponds to the expected SASE performance. The gain curve for the 3 nC case reflects the onset of saturation regime.

INTRODUCTION

The Photo Injector Test Facility at DESY in Zeuthen (PITZ) currently develops a prototype for a high-power tunable accelerator-based THz source for pump-probe experiments at the European XFEL [1]. A promising concept to provide THz pulses with a pulse repetition rate identical to that of the X-ray pulses is to generate them using the PITZ photo injector. Because PITZ develops the high-brightness electron source for the European XFEL, properties of the photo injector are fully compatible with the XFEL one, especially both injectors maintain the same pulse train structure. To generate a high-power THz pulses a SASE FEL is considered as a main mechanism. One of the key parameters for the THz SASE FEL high performance is a high beam peak current of up to 200 A. The PITZ RF-gun with a Cs_2Te photocathodes is capable of generating electron bunches with charges of up to several nC (up to 5nC), making it suitable for the proof-of-principle experiments on the high-gain THz SASE FEL. The THz beamline has been designed and implemented as an extension of the existing PITZ linac in the tunnel annex [2]. A planar LCLS-I undulator (on-loan from SLAC) is used to generate the THz radiation. The undulator parameters (period of 3 cm and undulator parameter of ~3.5) demand an electron beam energy of ~17 MeV for the centre radiation wavelength of ~100 µm. The strong magnetic field with a horizontal gradient requires a thorough beam matching. Another challenge is the narrow vacuum chamber (height 5 mm, width 11 mm, and length ~3.5 m), which makes matching and transport of the space charge dominated electron beams a complicated task.

The THz beamline was successfully commissioned [3] with 100 pC beams, then high-charge transport and matching started. A special procedure was developed and experimentally tested before at the existing part of the PITZ linac [4] and then successfully applied at the newly installed THz beamline. The first THz SASE FEL lasing was first detected with 1 nC bunch charge, then the bunch charge was stepwise increased to 3 nC. The gain curves were measured for 1 nC, 2 nC, and 3 nC.

THz BEAMLINE

The previously existing PITZ beamline was extended by a bunch compressor and a collimator system in the first tunnel and a matching system, the LCLS-I undulator and THz diagnostics in the second tunnel annex (second PITZ tunnel) downstream of the existing accelerator [2]. The current THz beamline in the tunnel annex is shown in Fig. 1. The THz radiation is measured using pyrodetectors at two stations after the undulator [3]. To measure gain

*The project is supported by the R&D program of the European XFEL.
† mikhail.krasilnikov@desy.de

ISBN: 978-3-95450-220-2 ISSN: 2673-5474 doi: 10.18429/JACoW-FEL2022-MOA08

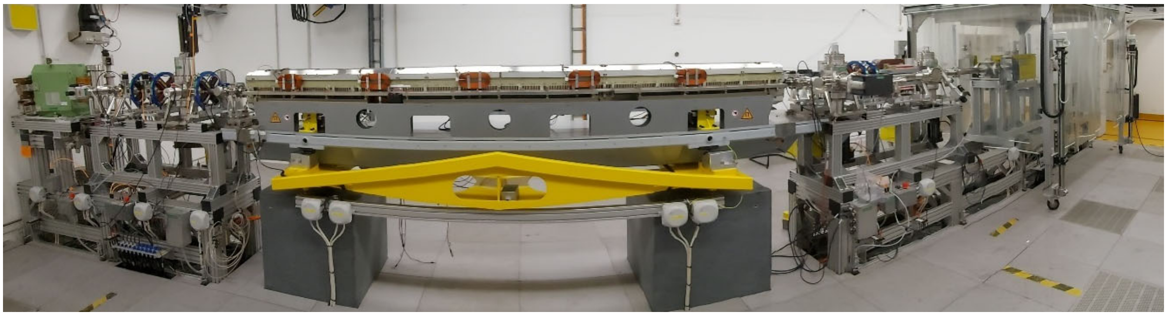

Figure 1: PITZ tunnel annex with installed THz beamline. The electron beam direction is from left to right. Five steering coils are distributed along the undulator to enable gain curve measurements.

curves a set of air coils evenly distributed along the undulator (Fig. 1) is used. They allow to kick an electron bunch away from the nominal trajectory in the undulator to measure the THz pulse energy radiated until the kick location (active undulator length).

ELECTRON BEAM MATCHING

A high-charge electron beam is generated at the PITZ gun (prototype Gun5.1 [5]), the gun gradient is tuned to yield a beam mean momentum of ~6.3 MeV/c at the phase of maximum acceleration. The bunch charge of 1, 2, and 3 nC was obtained by adjustment of the laser spot size at the cathode and the photocathode laser pulse energy. The final beam momentum of 16.5-17 MeV/c was achieved by tuning the gradient and the phase of the CDS booster. The booster phase was chosen to be ~20 deg off-crest, which roughly corresponds to the minimum projected energy spread at the undulator entrance. Main linac and electron beam parameters are summarized in [3].

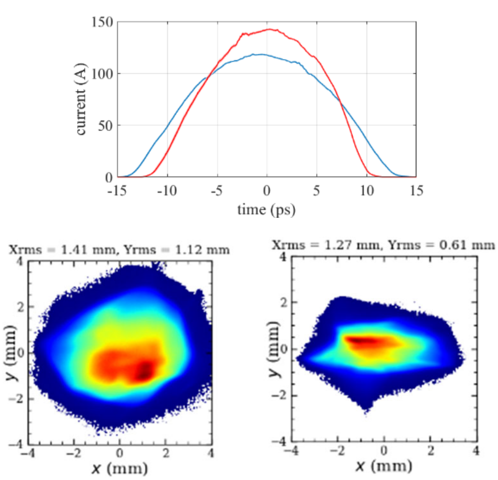

Figure 2: Top: electron bunch current profile, measured by TDS, two curves correspond to two various slopes of the deflecting RF field used for measurements. Bottom: electron beam transverse distribution at the YAG screen before (left) and after (right) undulator for 2 nC bunch.

For the space charge dominated beam transport through the PITZ linac was realized by use of two quadrupole triplets. The third quadrupole triplet is located in the tunnel annex and was utilized for thorough matching of the electron beam into the undulator. The beam current profile was measured by making use of the transverse deflecting system (TDS), the measured beam current profile for 2 nC bunches is shown in Fig. 2 (top plot). The beam matching was realized by subsequent transverse distribution measurements at YAG screens along the beamline. An example of beam characterization is shown in Fig. 2 (bottom plots). The charge was measured with Faraday Cup and integrating current transformer (Bergoz ICT), the charge jitter is estimated to be lower that 1.8% and at larger extent is due to the electronic noise.

THz MEASUREMENTS

The THz radiation is measured by pyroelectric detectors located on the top of dedicated screen stations HIGH3.Scr2 and HIGH3.Scr3. Cylindrical adapters with a conic internal surface for the radiation collection are mounted on the top of a flange with a diamond window. This setup is shown in Fig. 3 (left). Station HIGH3.Scr2 is equipped with a movable THz toroidal mirror with a 5 mm diameter hole for further electron beam transport, and station HIGH3.Scr3 is a solid mirror without a hole for transport of the complete THz radiation to the detector. Losses from the HIGH3.Scr2 mirror due to the hole are roughly estimated to be at least 30%. Typical waveform of the pyroelectric detector signal is shown in Fig. 3 (right).

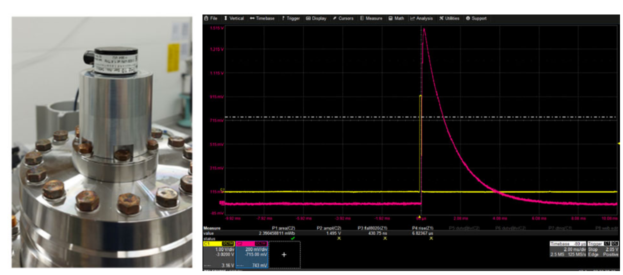

Figure 3: Left: pyroelectric detector on top of conic adapter. Right: typical scope signal from the pyroelectric detector (pink curve).

GAIN CURVES AND SASE STATISTICS

After optimizing the THz radiation signal by making use of many shots averaging and setting the correct electron beam transport, the corresponding gain curve is supposed to be measured. The gain curve measurements procedure is based on application of the short steering coils (see 5 coils on the side of the undulator in Fig. 1). Starting with the last

ISBN: 978-3-95450-220-2 ISSN: 2673-5474 doi: 10.18429/JACoW-FEL2022-MOA08

coil, all coils one after another are set to a current of +3 A which is supposed to kick the beam from the lasing trajectory (in fact, the beam is dumped on the wall of the vacuum chamber). The measured THz pulse energy using 500-shots statistics along the undulator is shown in Fig. 4 for three values of the bunch charge. The last (rightmost) two points of each curve represent measurements of a single pulse, and the error bars reflect rms fluctuations of the detector signal amplitude. Other points use more pulses in a 1 MHz pulse train, so the pyrodetector shows a better signal-to-noise ratio. The backward propagation of the exponential range of the gain curves leads to an initial signal of a pJ level, which is in basic agreement with expectation for the shot noise at this wavelength. The estimated FEL gain of ~10^6 indicates a high gain THz SASE FEL, which is a quite remarkable result for this radiation wavelength range.

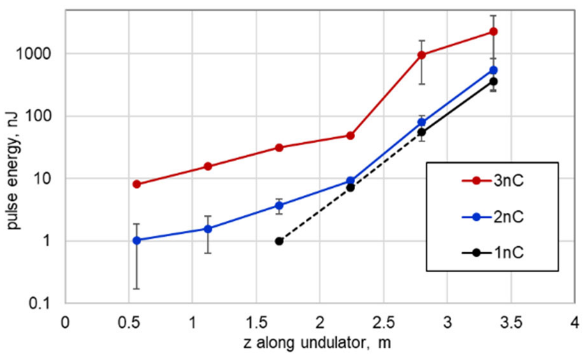

Figure 4: Gain curves for 1, 2 and 3 nC.

Probability distribution of the radiation pulse energy from SASE FEL operating in the high gain linear regime follows gamma distribution [6]:

$$\rho(W) \propto \frac{M^M}{\Gamma(M)}\left(\frac{W}{\langle W\rangle}\right)^{M-1}\frac{1}{\langle W\rangle}\exp\left[-M\frac{W}{\langle W\rangle}\right], \quad (1)$$

where $M = \frac{\langle W\rangle^2}{\sigma_W^2}$ is number of modes in the radiation pulse. Relevant probability distributions for second-to-last point for the 3 nC gain curve is presented in Fig. 5. It can be seen that the probability distribution of the radiation pulse energy indeed follows that of the high gain SASE-FEL in linear regime. A reduction of the gain curve slope indicates the onset of the saturation regime.

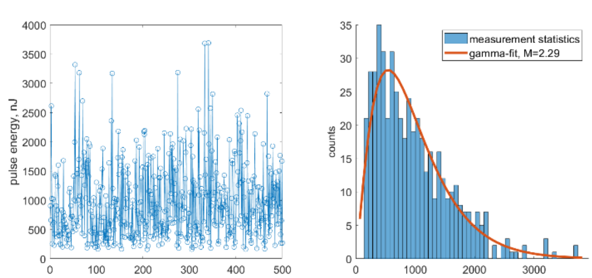

Figure 5: Single pulse radiation measurements (left) and probability distribution of the radiation pulse energy (right). Bunch charge is 3 nC, active undulator length is 2.8 m, average pulse energy is $\langle W\rangle = 0.96$ μJ, the rms spread $\sigma_W = 0.64$ μJ. Red curve is gamma distribution with M=2.29.

CONCLUSION AND OUTLOOK

The first lasing of the high-gain THz SASE FEL at the Photo Injector Test facility at DESY in Zeuthen has been achieved. This is an important milestone in the development on an accelerator-based high-power tunable THz source for pump-probe experiments at the European XFEL. Gain curves for the THz SASE FEL at the wavelength of 100 μm for a bunch charge of up to 3 nC were measured. Statistical properties of the pulse energy fluctuations demonstrate features of the high-gain SASE FEL linear regime. The onset of THz pulse energy saturation has been observed for the 3 nC case. Detailed studies of the properties of the generated THz pulses, as well as steps to optimize the high-power THz source performance are in progress.

ACKNOWLEDGEMENTS

The work is supported by the European XFEL research and development program.

REFERENCES

[1] E.A. Schneidmiller, M.V. Yurkov, M. Krasilnikov, and F. Stephan, “Tunable IR/THz source for pump probe experiments at the European XFEL”, in *Proc. 34th Int. Free Electron Laser Conf. (FEL'12)*, Nara, Japan, August 2012, paper WEPD55, pp. 503-505.

[2] T. Weilbach *et al.*, "Status of the THz@PITZ Project – The proof-of-principle experiment on a THz SASE FEL at the PITZ facility", in *Proc. 13th Int. Particle Accelerator Conf. (IPAC'22)*, Bangkok, Thailand, Jun. 2022, pp. 1033-1036. doi:10.18429/JACoW-IPAC2022-TUPOPT016

[3] P. Boonpornprasert et al., “First commissioning of the proof-of-principle experiment on a THz SASE FEL at the PITZ facility”, presented at FEL'22, Trieste, Italy, August 2022, paper MOP19, this conference.

[4] X. Li *et al.*, “Matching of a Space-Charge Dominated Beam into the Undulator of the THz SASE FEL at PITZ”, in *Proc. IPAC'21*, Campinas, Brazil, May 2021, pp. 3244-3247. doi:10.18429/JACoW-IPAC2021-WEPAB257

[5] M. Krasilnikov *et al.,* “RF Performance of a new generation L-band RF gun at PITZ”, presented at FEL'22, Trieste, Italy, August 2022, paper TUP03, this conference.

[6] E.L. Saldin, E.A. Schneidmiller, and M.V. Yurkov, “Statistical properties of radiation from VUV and X-ray free electron laser”, *Opt. Commun.*, vol. 148, p. 383, March 1998. doi:10.1016/S0030-4018(97)00670-6

ISBN: 978-3-95450-220-2 ISSN: 2673-5474 doi: 10.18429/JACoW-FEL2022-MOBI3

MICROBUNCHING OF RELATIVISTIC ELECTRON BEAMS*

Alex H. Lumpkin†, Argonne Associate, Argonne National Laboratory, Lemont, IL USA

Abstract

Microbunching in relativistic electron beams provides the opportunity for generation of coherent radiation at the wavelengths that characterize that periodic longitudinal modulation. Since microbunching is an inherent process in the free-electron laser (FEL) mechanism for both single-pass and oscillator configurations, studies of these properties can elucidate the fundamental interactions. Diagnostics of these microbunched electron beams can be performed using coherent optical transition radiation (COTR) imaging techniques. Four COTR-based experiments from SASE FELs to recent laser wakefield accelerated beams will be presented.

INTRODUCTION

Imagine that a relativistic charged-particle beam transiting the vacuum to a metal interface generates a burst of light in a few fs that is linear with the charge distribution. The unique angular distribution pattern with opening lobes of $1/\gamma$, where γ is the Lorentz factor, carries energy and divergence information, and the near-field image provides the beam transverse profiles. This works for a total charge of 100s of pC and sub-mm beam sizes. This is the description of optical transition radiation (OTR) [1,2]. Now imagine that the light is 5-6 orders of magnitude times brighter due to microbunching in the beam and the concomitant coherent enhancements at specific wavelengths. It's an experimentalist's dream realized.

One of the fundamental facets of microbunching in relativistic electron beams is the potential for generation of coherent radiation at the wavelengths that characterize that periodic longitudinal modulation. This microbunching is an inherent process in the free-electron laser (FEL) mechanism for both single-pass [3] and oscillator configurations. Besides the FEL output, diagnostics of these microbunched electron beams can be performed using coherent optical transition radiation (COTR) and imaging techniques in the former case. In these cases, the COTR from the microbunched portion of the beam in 6-D space generally dominates the images. We note that other mechanisms include the longitudinal-space-charge-induced microbunching in ultra-bright beams and laser-induced microbunching such as observed in laser wakefield accelerator (LWFA) beams. More recently, we consider the diagnostics of the TESSA FEL concepts where a seed laser copropagating with the electron beam through a short modulator and chicane may result in bunching fractions of >10 % leading to COTR enhancements of >22 million. Examples of these past, present, and future investigations will be discussed.

* Work supported by the U.S. Department of Energy, Office of Science, Office of Basic Energy Sciences, under Contract No. DE-AC02-06CH11357.
† lumpkin@anl.gov

MICROBUNCHING MECHANISMS

Microbunching of an electron beam, or a z-dependent density modulation with a period λ, can be generated by several mechanisms:

In self-amplified spontaneous emission (SASE) induced microbunching (SIM) the electron beam is also bunched at the resonant wavelength and harmonics. This is narrow band.

The longitudinal space-charge-induced microbunching (LSCIM) starts from noise fluctuations in the charge distribution which causes an energy modulation that converts to density modulation following a dispersive section. This is a broadband case: e.g., LCLS-1 and APS linacs.

The laser-induced microbunching (LIM) occurs at the laser resonant wavelength (and harmonics) as the e-beam co-propagates through the wiggler with the 1-GW laser beam followed by a dispersive section. This is narrow-band. (TESSA prebuncher)

With very high-power lasers in the >100-TW regime, the laser wakefield accelerator (LWFA) beams have been shown to be microbunched at 1-10 % at visible wavelengths [4,5].

To help the reader visualize the phenomenon, we consider one of the first time-domain observations reported by Ricci and Smith (2000) using off-phase rf acceleration at the end of their infrared FELO beamline [6]. Basically, at the phase of 90 degrees off crest for the accelerating structure, the electrons acquired different energies for their different arrival times. The downstream electron spectrometer then displayed the effective temporal information of the pulse with about 100-fs resolution in the focal plane. This was sufficient to display the longitudinal modulation at the FEL resonant wavelengths of 60 and 51 μm. Other FELOs of that generation did not have this configuration to display the longitudinal modulation. The indirect result was of course the FEL's optical power increased with the number of passes up to saturation of the process. However, for single-pass SASE or seeded FELs one can get access to the laser power and the electron microbunching after each undulator, in principle. In practice, this was done at ANL in 2000-2004, initially at visible wavelengths.

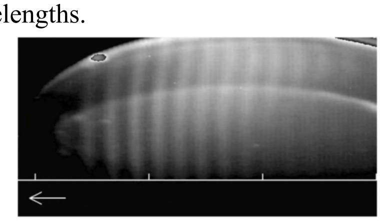

Figure 1: Early time-domain grey-scale image of electron beam microbunching at 60 μm from an FELO process and using an off-phase acceleration technique and

ISBN: 978-3-95450-220-2 ISSN: 2673-5474 doi: 10.18429/JACoW-FEL2022-MOBI3

spectrometer. The horizontal scale is 1 ps per tic mark and beam travel is with the arrow [6].

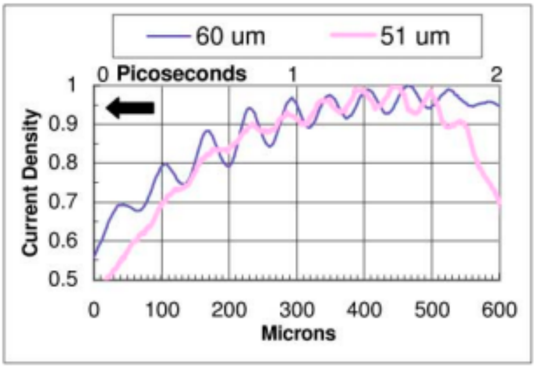

Figure 2: Normalized beam current density for microbunching at two cases, 60 and 51 μm at the Stanford FELO experiment. These data were averaged from slices through images like Fig. 1. There is a modulation amplitude variation along the bunch. The arrow indicates the direction of beam travel [6].

COTR FORMALISM

A microbunched beam will radiate coherently as an FEL or by interaction at a vacuum to metal screen interface as COTR. The complete description of the formalism has been given previously [4] and in these proceedings [7]. The simple view is that radiation is generated as a charged-particle beam both enters and leaves a metal foil in vacuum as schematically shown in Fig. 3 for forward and backward OTR, respectively. The cone angle is at 1/γ, and the modulation of the pattern is divergence sensitive. One can see that if one has a two-foil configuration, the forward OTR will arrive at the second foil with the electron beam and interference effects could occur. The backward OTR is emitted around the angle of specular reflection so for a 45-degree angle the radiation is centered around 90 degrees to the beam for diagnostic purposes. In Fig. 4 we show the optics for near-field (NF) and far-field (FF) imaging that provide the beam spatial distribution image and the angular distribution pattern that has energy and divergence dependencies.

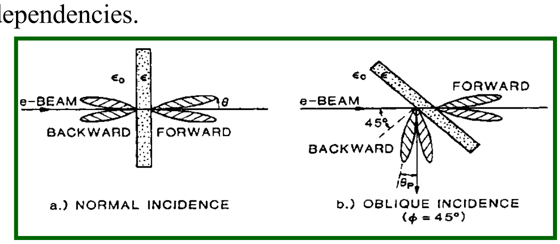

Figure 3: Schematic of the generation of OTR for (a) normal incidence (b) oblique incidence at the screen.

In a shortened discussion, the OTR/COTR equations are summarized below without details of the constants which are provided elsewhere in these proceedings [7]. The equation set includes: (1) the single-electron spectral angular distribution, (2) COTRI formalism, (3) two-foil interference term with separation L, interference function *I(k), (4)* coherence function *J(k),* and (5) the charge form factor *H(k)*. These were initially developed for the ANL SASE FEL case [8] and revised as noted below for LWFA experiments at HZDR [4].

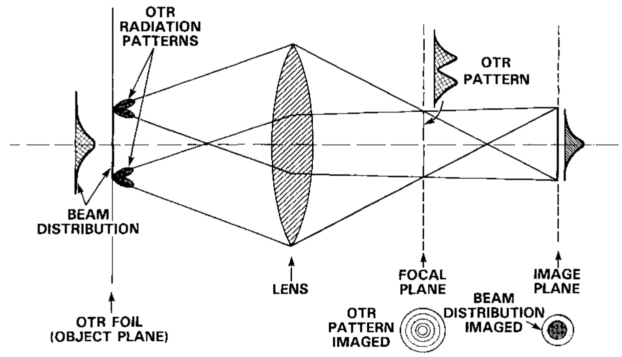

Figure 4: Aschematic of the NF and FF imaging of OTR with the sensor at the image plane or the focal plane, respectively.

$$\frac{d^2W_1}{d\omega d\Omega} = \frac{e^2}{\hbar c}\frac{1}{\pi^2\omega}\frac{(\theta_x^2+\theta_y^2)}{(\gamma^{-2}+\theta_x^2+\theta_y^2)^2} \qquad (1)$$

$$\frac{d^2W}{d\omega d\Omega} = |r_{\parallel,\perp}|^2\frac{d^2W_1}{d\omega d\Omega}\boldsymbol{I}(\boldsymbol{k})\boldsymbol{J}(\boldsymbol{k}) \qquad (2)$$

$$\boldsymbol{I}(\boldsymbol{k}) = 4\sin^2[\tfrac{kL}{4}(\gamma^{-2}+\theta_x^2+\theta_y^2)] \qquad (3)$$

$$\boldsymbol{J}(\boldsymbol{k}) = N + N_B(N_B-1)|H(\boldsymbol{k})|^2 \qquad (4)$$

$$H(\boldsymbol{k}) = \frac{\rho(\boldsymbol{k})}{Q} = g_x(k_x)\,g_y(k_y)\,F_z(k_z) \qquad (5)$$

The coherence function was defined previously for the beam sizes assuming Gaussian spatial distributions at each source point with a drift between them [4]. At the larger beam sizes (100 μm) and small divergences, the potential transverse size growth in the drift is a negligible effect. However, for the microbunched beams with few-micron transverse size in the LWFA with the drift between foils, a formalism was developed that accounted for the change of beam size at the two source points [4]. The coherence function can be defined as

$$\boldsymbol{J}(\boldsymbol{k}) = \left[H_1(\boldsymbol{k}) - H_2(\boldsymbol{k})\right]^2 + H_1(\boldsymbol{k})H_2(\boldsymbol{k})\boldsymbol{I}(\boldsymbol{k}) \qquad (6)$$

where $H_j(\boldsymbol{k}) = \rho_j(\boldsymbol{k})/Q = g_j(k_x)g_j(k_y)F(k_z)$ for an *e*-bunch of charge distribution $\rho_j(\boldsymbol{x})$ and total charge Q, with j = 1, 2. Here we have introduced two microbunch form factors, H_1 and H_2, to account for the increase in bunch radius from the first to the second interferometer foil due to beam divergence. Each $H_j(\boldsymbol{k})$ is a product of Fourier transforms $g_i(k_i) = exp(-\sigma_i^2k_i^2/2)$ of transverse $(i = x,y)$ charge form factors (with $k_i \approx k\theta_i$), and of longitudinal form factor $F_z(k_z) = \exp(-\sigma_z^2k_z^2/2)$, with $k_z \sim k$ and $\theta << 1$, assuming the Fourier transform $\rho_j(\boldsymbol{k})$ of $\rho_j(\boldsymbol{x})$ is separable. If $\boldsymbol{J}(\boldsymbol{k}) << 1$ or $N_B \to 0$, only the incoherent OTR term (~N) remains in Eq. (2).

ISBN: 978-3-95450-220-2 ISSN: 2673-5474 doi: 10.18429/JACoW-FEL2022-MOBI3

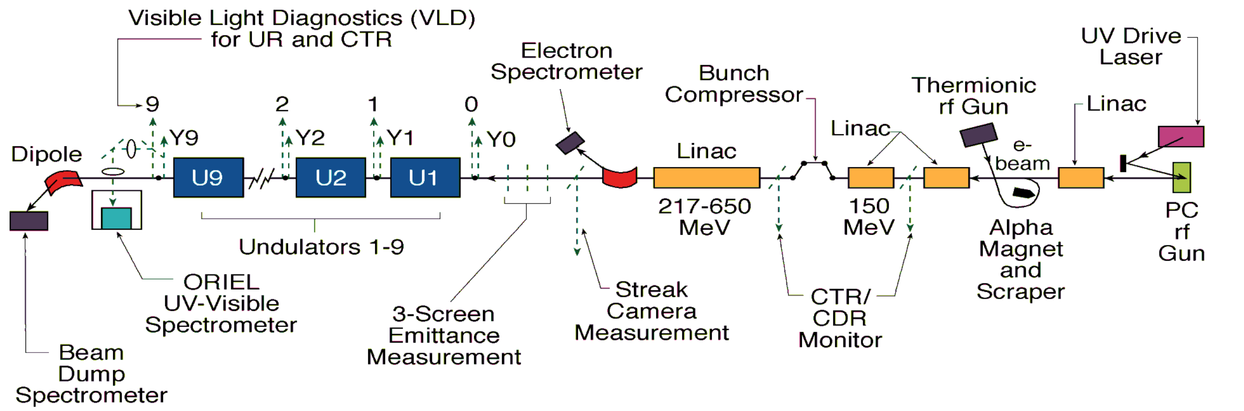

Figure 5: A schematic of the Argonne SASE FEL circa 2000 showing the PC rf gun, linac, bunch compressor, undulators, and visible light diagnostic station locations after each undulator [9].

MICROBUNCHING EXAMPLES

SASE FEL at ~530 nm at ANL

Although the microbunching signature at 16 μm at the end of a single pass IR FEL at Los Alamos was reported by Hogan et al. [10], the first z-dependent measurements in a SASE FEL reaching saturation were done at Argonne [9,11] using the facility configuration shown in Fig. 5. The photocathode (PC) rf gun, S-band linac, nine 2.4-m long undulators, and the diagnostics are indicated. The intra-undulator visible light diagnostics (VLDs) allowed the measurement of optical power or COTR strength after each undulator to provide the tracking of the FEL signal evolution. A schematic of a VLD station is shown in Fig. 6 between two undulators. One camera was on a translation stage to move the sensor to the image plane or focal plane. It was designed for the larger optical modes, so the calibrations were about 100 μm/pixel and 110 μrad/pixel, respectively. A retractable mirror is shown that directed the light to an optical spectrometer to obtain z-dependent spectra. The initial resonant wavelength was ~530 nm so standard cameras and lenses could be used to image the NF and FF FEL radiation and COTR. The latter was enabled by adding a thin (6-μm) Al foil into the first screen holder that could be inserted to block the laser light, but it also generated the forward COTR for COTRI with the spacing between the foils, *L*=6.3 cm. We will show evidence that the microbunched portion of the beam could be at the 25-μm level, so we relied on the COTRI to assess this smaller feature indirectly. Initially, the GENESIS code assumed the start up from a noise seed.

The experiments were based on taking 100 images at both NF and FF optical setups and for FEL light and the COTR at all nine stations. The image intensities were processed within a region of interest and averaged. The z-dependent gain curve was then plotted for the nine stations as shown in Fig. 7 (L) with a comparison of the UR, COTR and the GENESIS predictions. The two runs at 530 nm and 539 nm are shown and the spectral evolution is shown for both UR and COTR in the Fig. 7 (R). Note the narrowband COTR at the resonant wavelength in VLD 5 which then becomes complex with saturation and side-band development in VLD 7 and 9.

The COTRI patterns are dependent on the microbunched beam's transverse size through the coherence function. As an example, Fig. 8a shows the outer fringes are suppressed in intensity as the beam size increases from 25 to 50 to 100 μm. The actual COTRI image then shows that for θ_x only the inner lobes are seen while in θ_y we see 3 peaks for positive and negative angles.

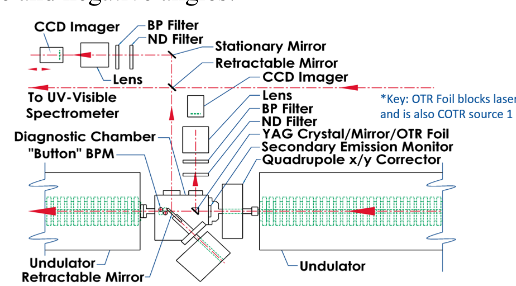

Figure 6: Schematic of the intra-undulator VLD features with options for NF imaging, FF imaging, and the path to the UV-visible spectrometer [9].

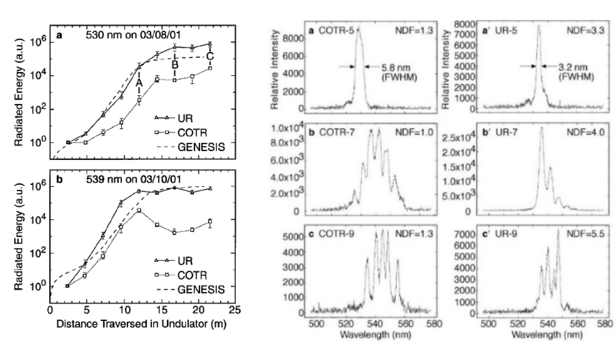

Figure 7: Observations of the radiated energy sampled after each undulator showing the exponential gain and saturation for two runs at 530 and 539 nm (Left). Examples of the COTR and FEL spectra at stations 5,7, and 9 showing the onset of spectral sidebands (Right) [9].

ISBN: 978-3-95450-220-2 ISSN: 2673-5474 doi: 10.18429/JACoW-FEL2022-MOBI3

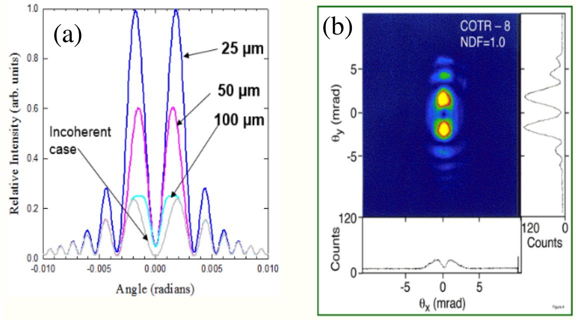

Figure 8: (a) Model predictions of the enhanced COTRI patterns for three beam sizes of the microbunching and (b) an actual COTRI-8 image showing the θ_x-θ_y asymmetry due to the asymmetry in the spatial size of the microbunched portion of the beam at VLD-8.

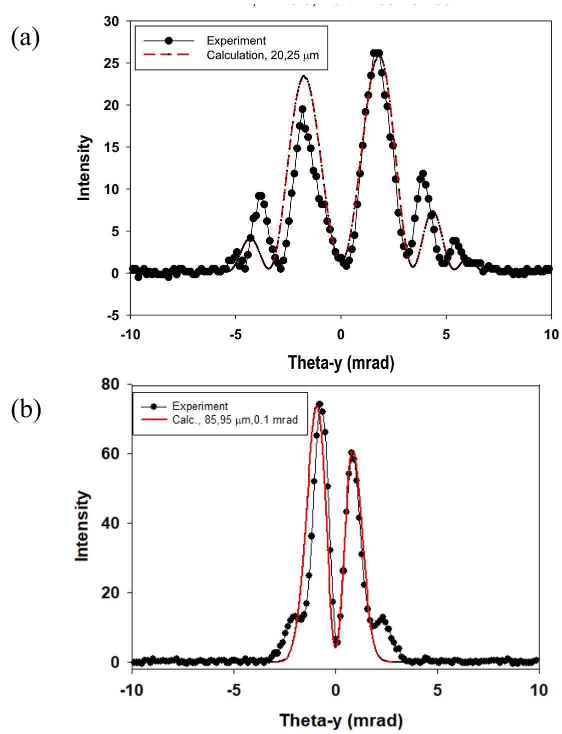

Figure 9: Z-dependent COTRI theta-y images at (a) VLD2 and (b) VLD4 which show that the vertical size of the microbunched beam evolves from ~20 to ~90 µm as well as changes to the bunching fraction.

I have revisited the data to explore the evolution of the microbunched portion of the beam. The nominal match into the undulators gives e-beam sizes of σ_x =200 µm and σ_y = 100 µm while the optical mode is larger in both planes.

As can be seen in Figs. 9a and 9b the observed fringe pattern for *vertical* angles changes dramatically as the microbunched beam size goes from a modeled 20-25 µm split Gaussian at VLD2 to 85 – 95 µm at VLD4 as indicated in the legends of the panels. The deduced 20-25 µm beam size at VLD8 after debunching is indicated in Fig. 8. The split Gaussian of the spatial distribution then approximates the peak intensity asymmetry via the coherence function. Physically, if the e-beam angle and FEL mode are not the same, some asymmetries result in the COTR patterns. The microbunching fraction increases from VLD2-VLD4 as indicated by the increase in the ND filter from 0.5 to 3.0. The vertical plane does have focusing from the planar undulator.

In the x-plane or wiggle plane, we observed larger beam sizes in the microbunched portion of the beam at VLD 2 of ~100 µm where the two inner peaks appear and then varied in relative intensity after each undulator up to saturation in VLD5 where the ND value increased to 4. We note that the post-saturation evolution is also different since Fig. 8b shows the Theta-x pattern with the inner lobes which was matched by the model using a 75-µm beam size, 3 times larger than the inferred vertical size at VLD8. It would be interesting to see if GENESIS simulations show this effect for microbunching trends in and out of the wiggle plane.

We would expect that the initial microbunching would occur at the peak of the charge distribution and the FEL optical fields so the transverse size of the microbunched portion would be smaller than the total ensemble of the electron distribution. Spatially localized microbunching due to LSCIM also can play a role.

LSCIM at visible wavelengths at ANL

It was noted that additional signal fluctuations were occurring in OTR images of bright beams at LCLS-1 [12]. This was identified as LSCIM, and the COTR from localized transverse locations that resulted obscured the incoherent OTR and the actual beam sizes. An example of the effect at the APS linac is shown in Fig. 10a where the image has spatially localized intensity spikes ~20x brighter than the normal intensity. On the diagnostic side we could mitigate the problem by imaging at 400 nm with a LYSO scintillator with a bandpass filter rejecting most of the red-end LSCIM COTR while passing the purple scintillator light. Figure 10b shows this true beam shape. It was subsequently shown that this microbunching had some content at the resonant wavelength and seeded the 530 nm SASE FEL at APS so it started up faster than from noise. There were spatially localized regions that spiked in intensity compared to the rest of the distribution.

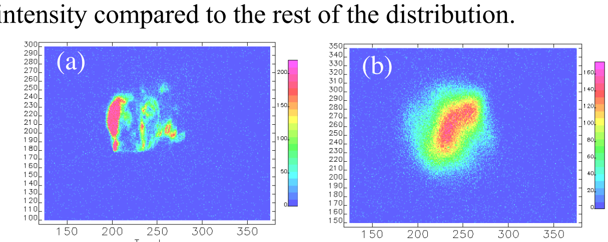

Figure 10: (a) Image of the 2-mm sized beam with the OTR screen with significant, localized intensity spikes from COTR. (b) image of the beam with the LYSO scintillator.

LWFA and Microbunching in Beams at Visible Wavelengths

In the LWFA application [4], we used the DRACO 100-TW drive laser at HZDR operating at 800 nm and focused to 25 µm at the gas-jet location as shown in Fig. 11. The challenge is to survive this high-power laser pulse and still acquire the COTR images cleanly in the cameras. We chose an Al blocking foil followed by an Aluminized Kapton foil

ISBN: 978-3-95450-220-2 ISSN: 2673-5474 doi: 10.18429/JACoW-FEL2022-MOBI3

that were changed after each laser pulse with a 75-position wheel. Downstream we used a polished Si mirror oriented at 45 degrees to the beam direction at a separation of 18.5 mm from the first foil. The first optical objective provided a high-resolution NF image at the downstream Al side of the Kapton foil, and the signal was passed through a linear polarizer. The NF image in Fig. 11c is dominated by the COTR annular point-spread function (PSF). A second path with an additional lens provided the FF imaging for the COTRI as in Fig 11d. The comparison of the azimuthally-averaged profile is shown in Fig. 12a with a 0.33-mrad divergence determined. A coherent PSF model was used to reconstruct the beam profile at 2.75 µm with the comparison of model and data given in Fig. 12b. We observed COTR throughout the visible region with a blue-shifting effect in the LWFA process. Further 3-D reconstructions are reported at this conference by LaBerge *et al*. [5].

TESSA at Visible Wavelengths

Tapering Enhanced Super-radiant Stimulated Amplification (TESSA) experiments depend on inducing strong microbunching by copropagating a pulsed laser with the electron beam though a modulator magnet array followed by a dispersive section followed by four tapered undulators for gain. Such an experiment is currently underway at FNAL in a collaboration of UCLA, RadiaBeam, RadiaSoft, FNAL, and ANL [13]. It is proposed to demonstrate TESSA at 515 nm using a beam energy of 220 MeV. A schematic of the seed laser injection, prebuncher, COTR diagnostics location, and 4 tapered undulators is shown in Fig. 2 of ref. [7]. One microbunching diagnostics chamber has been loaned to FNAL for the single-shot diagnostics.

The next image in Fig. 13 is reminiscent of the COTR NF image for very small beams or an FF image with some asymmetry. However, I was struck by the different scale of 40-billion km involved in this reconstructed image of the gas clouds swirling around the black hole "shadow" at the center of our galaxy. This is from the Event Horizon Telescope report released in May 2022 [14].

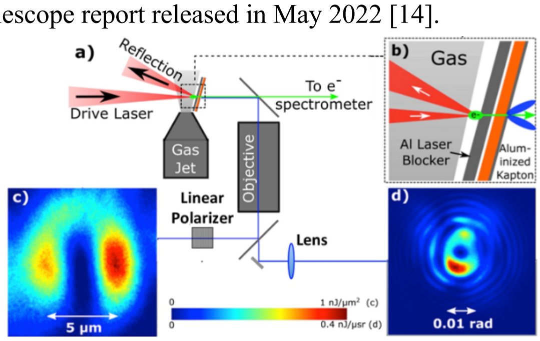

Figure 11: (a) Schematic of the LPA experiment at HZDR (b) inset showing the laser blocking Al foil and the Aluminized Kapton (c) the linearly polarized NF image of a few-µm beam (d) the FF image showing the COTRI fringe pattern [4].

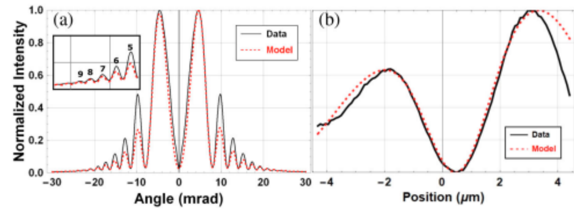

Figure 12: (a) Azimuthally averaged fringe pattern from Fig. 10 (black) with comparison to the COTRI model (red) for $\sigma_\theta = 0.33$ mrad and (b) Profile through the NF image in Fig. 10 and the match to the model for $\sigma_x = 2.75$ µm [4].

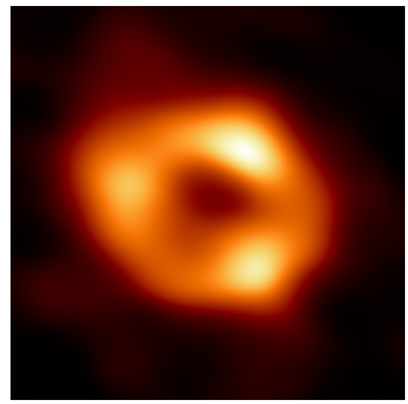

Figure 13: First image of the black hole Sagittarius A* at the center of our Galaxy as captured by the Event Horizon Telescope (EHT) [14]. (This is not a COTR image.)

SUMMARY

In summary, the inherent relativistic, microbunched beams in FELs, bright beams, LWFAs, and TESSA schemes will continue to be on our horizons to investigate. I look forward to one's seeing the COTR signal after the FEL undulator at HZDR and after the prebuncher at TESSA-515 in the coming year and the studies that will follow.

ACKNOWLEDGEMENTS

The author acknowledges the support of N. Sereno, K.-J. Kim, and J. Byrd at ASD/APS/ANL. He acknowledges the COTR modeling over two decades by D.W. Rule.

He also acknowledges his FEL collaborators through the years at Los Alamos, Boeing, Duke, and Argonne.

Finally, I dedicate this talk *in memoriam* to my parents, Dr. William W. Lumpkin and Mrs. Dallas H. Lumpkin.

REFERENCES

[1] V. L. Ginzburg and I. M. Frank, "Radiation of a uniformly moving electron arising from its going from one medium into another", *Sov. Phys. JETP* 16, p.15, 1946.

[2] L. Wartski, S. Roland, J. Lasalle, M. Bolore, and G. Fillippi, "Interference phenomenon in optical transition radiation and its application to particle beam diagnostics and multiple-scattering measurements", *J. Appl. Phys.*, vol. 46, p. 3644, 1975. doi:10.1063/1.322092

[3] K.-J. Kim, "Three-Dimensional Analysis of coherent amplification and self-amplified spontaneous emission in

ISBN: 978-3-95450-220-2 ISSN: 2673-5474 doi: 10.18429/JACoW-FEL2022-MOBI3

free-electron lasers", *Phys. Rev. Lett*, vol. 57, p. 1871, 1986. doi:10.1103/PhysRevLett.57.1871

[4] A. H. Lumpkin *et al*., "Coherent Optical Signatures of Electron Microbunching in Laser-Driven Plasma Accelerators", *Phys. Rev. Lett.*, vol. 125, pp. 014801, 2020. doi: 10.1103/PhysRevLett.125.014801.

[5] M. LaBerge *et al*., "Coherent 3D Microstructure of Laser-Wakefield-Accelerated Electron Bunches", presented at FEL'22, Trieste, Italy, Aug. 2022, paper THOI2, this conference.

[6] K. N. Ricci and T. I. Smith, "Longitudinal electron beam and free electron laser microbunch measurements using off-phase rf acceleration", *Phys. Rev. ST Accel. Beams*, vol. 3, p. 032801, 2000. doi:PhysRevSTAB.3.032801.

[7] A. H. Lumpkin, D. W. Rule, A. Murokh, and P. Musumeci, "Feasibility of Single-Shot Microbunching Diagnostics for a Pre-bunched Beam for TESSA at 515 nm", presented at FEL'22, Trieste, Italy, Aug. 2022, paper WEP17, this conference.

[8] D. W. Rule and A. H. Lumpkin, "Analysis of Coherent Optical Transition Radiation Interference Patterns Produced by SASE-Induced Microbunches", in *Proc. PAC'01*, vol. 2. Piscataway, NJ, USA, paper TPAH029, pp. 1288-1290.

[9] A.H. Lumpkin *et al*., "Evidence for Microbunching "Sidebands" in a Saturated Free-Electron Laser Using Coherent Optical Transition Radiation", *Phys. Rev. Lett.*, vol. 88, p. 234801, 2002. doi: 10.1103/PhysRevLett.88.234801

[10] M. Hogan *et a*l., "Measurements of High Gain and Intensity Fluctuations in a Self-Amplified, Spontaneous-Emission Free-Electron Laser", *Phys. Rev. Lett.*, vol. 80, p. 289, 1998. doi:10.1103/PhysRevLett.80.289

[11] S.V. Milton *et al*., "Exponential Gain and Saturation of a Self-Amplified Spontaneous Emission Free-Electron Laser", *Science*, vol 292, p. 2037, 2001. doi:10.1126/science.1059955

[12] D. H. Dowell *et al.*, "LCLS Injector Commissioning Results", presented at FEL'07, Novosibirsk, Russia. https://accelconf.web.cern.ch/f07/TALKS/WEAAU01_TALK.PDF

[13] P. Musumeci *et al.*, "FAST-GREENS: A High-Efficiency FEL Driven by a Superconducting rf Accelerator", presented at FEL'22, Trieste, Italy, Aug. 2022, paper TUP33, this conference.

[14] IOP Publishing, https://physicsworld.com/a/first-ever-image-of-the-black-hole-shadow-at-the-heart-of-the-milky-way-revealed-by-the-event-horizon-telescope/

ISBN: 978-3-95450-220-2 ISSN: 2673-5474 doi: 10.18429/JACoW-FEL2022-MOCO3

PROPOSAL FOR A QUANTUM FREE ELECTRON LASER DRIVEN BY ULTRACOLD ELECTRONS

B. H. Schaap*, S. Schouwenaars, O.J. Luiten
Eindhoven University of Technology, Eindhoven, Netherlands

Abstract

Operation of a Quantum Free-Electron Laser (QFEL) could provide fully coherent X- and gamma-rays in a compact setup. Imperative to experimental realization is allowing for decoherence of either spontaneous emission or space-charge to take place, having opposing constraints. Here, we discuss a comprehensive QFEL model that takes into account both decoherence effects. Then, we use this model to investigate the ultracold electron source (UCES) as a potential QFEL electron injector. The UCES, based on near-threshold photoionization of laser-cooled and trapped atomic gas, has the unique property of allowing highly charged electron bunches to be extracted while maintaining ultralow transverse emittance. We find that the ultracold electron bunches meet the stringent requirement for potential QFEL operation with commercially available laser systems

INTRODUCTION

Free-electron lasers (FELs) offer tunable and coherent X-ray pulses required for spatiotemporal imaging on the atomic and molecular scale. However, these machines are only available at specialized, costly, large-scale facilities and produce pulses with poor longitudinal coherence and pulse-to-pulse stability. One can scale down a FEL by the use of a laser undulator, which has significantly smaller wavelength than its magnetostatic counterpart, therefore requiring much lower electron beam energy. The resonant wavelength in a laser undulator of wavelength λ_0 is given by

$$\lambda_r = \frac{\lambda_0}{4\gamma_r^2}\left(1 + a_0^2 + X\right) \tag{1}$$

where γ_r is the resonant Lorentz factor of the electron beam, $a_0 = eE_0\lambda_0/(2\pi m_e c^2)$ is the laser strength parameter and $X = 4\gamma_r\lambda_c/\lambda_0$ is the recoil parameter with e the elementary charge, m_e the mass of an electron, c the speed of light, E_0 the laser electric field amplitude and $\lambda_c \simeq 2.42$ pm the Compton wavelength. Besides red-shifting of the resonant wavelength, recoil parameter X is a measure for the relative momentum loss of an electron due to the emission of a X-ray photon. For the low electron beam energy required to reach the X-ray regime with a laser undulator, the recoil momentum $X\gamma_r mc$ can be larger than the FEL-induced momentum modulation $\rho\gamma_r mc$, where $\rho = (a_0\lambda_0\omega_p/(8\pi c)^{2/3}/\gamma_r$ the Pierce parameter and $\omega_p = (e^2 n_e/(m_e\epsilon_0))^{1/2}$ the plasma frequency with n_e the electron density. If this is the case $\bar{\rho} = \rho/X < 1$, the quantum mechanical momentum transitions play a dominant role in operation of the FEL. The dynamics of such a quantum free-electron laser (QFEL) can result in longitudinal spectral coherence similar to solid-state lasers even from self amplified spontaneous emission. [1].

However, detrimental effects of spontaneous emission [2] and space-charge [3] limit the quantum dynamics. Moreover, these effects have opposite constraints [4], making it impossible to operate in a regime where both effects are neglible. The opposite contraints become clear by rewriting the Pierce parameter to

$$\rho = \frac{\frac{1}{4}\sigma\beta}{\beta + \frac{\alpha_f}{6\pi X}} \tag{2}$$

with $\sigma = 4(\lambda_0\omega_p/(8\pi a_0 c)^{2/3}(1 + a_0^2)/\gamma_r$ is the universally scaled space charge parameter and $\beta = \alpha_f a_0^2/(6\pi X)$ the scaled spontaneous emission rate and α_f the fine structure constant. In this work, we investigate the interplay between spontaneous emission and space charge in steady state QFEL dynamics using a comprehensive discrete Wigner model. Then, based on the results, we propose the ultracold electron source as potential QFEL driver.

THEORETICAL MODEL

Here, we combine the QFEL models that include microscopic space charge [3] and spontaneous emission [2]. These models describe the evolution of the periodic quasi-phase space distribution (discrete Wigner function) W_m of the electron beam during steady state FEL operation. The discrete Wigner function for a pure quantum state is given by [5]

$$\begin{aligned} W_m =& \frac{1}{\pi}\int_{-\pi/2}^{+\pi/2} \mathrm{d}\vartheta' e^{-2im\vartheta'}\Psi^*(\vartheta - \vartheta')\Psi(\vartheta + \vartheta') \\ =& \frac{1}{2\pi}\sum_{n=-\infty}^{+\infty}\left[w_m^n + \sum_{m'=-\infty}^{+\infty}\frac{(-1)^{m-m'-1}}{(m-m'-\frac{1}{2})\pi}w^n_{m'+\frac{1}{2}}\right]e^{in\vartheta} \end{aligned} \tag{3}$$

where a periodic wave function $\Psi(\vartheta) = \sum_m c_m e^{im\vartheta}/\sqrt{2\pi}$ was assumed with ϑ the ponderomotive phase. The Fourier components of the wave function c_m are related to the Fourier components of the Wigner function w_m^n in the following way: $w_m^{2n} = c^*_{m+n}c_{m-n}$ and $w^{2n+1}_{m+1/2} = c^*_{m+n+1}c_{m-n}$. In particular, $w_m^0 = |c_m|^2$ is the occupation probability of the m-th momentum state ($p = m\hbar k$) *i.e.* the projection of the Wigner function, Eq. (3) on the momentum axis $\int_{-\pi}^{+\pi} d\vartheta W_m = |c_m|^2$. The projection on the position axis gives the probability density distribution $\sum_m W_m = |\Psi(\vartheta)|^2$.

* b.h.schaap@tue.nl

ISBN: 978-3-95450-220-2 ISSN: 2673-5474 doi: 10.18429/JACoW-FEL2022-MOCO3

The 1D QFEL equations describing the steady state dynamics of the Wigner Fourier components are

$$\frac{\mathrm{d}w_s^n}{\mathrm{d}\bar{z}} = -in\frac{s}{\bar{\rho}}w_s^n + \frac{\beta}{\bar{\rho}}\left[w_{s+1}^n - w_s^n\right] + \bar{\rho}\left[(A+i\sigma b)\left(w_{s+\frac{1}{2}}^{n-1} - w_{s-\frac{1}{2}}^{n-1}\right) + (A^* - i\sigma b^*)\left(w_{s+\frac{1}{2}}^{n+1} - w_{s-\frac{1}{2}}^{n+1}\right)\right], \tag{4a}$$

$$\frac{\mathrm{d}A}{\mathrm{d}\bar{z}} = b + i\delta A, \tag{4b}$$

where $s = m$ or $s = m + 1/2$ with m an integer, $\bar{z} = z/L_g$ the distance along the laser undulator and b the bunching factor given by

$$b = \sum_{m=-\infty}^{\infty} w_{m+\frac{1}{2}}^1 \tag{5}$$

The first term of Eq. (4a) describes the kinetic part of the electronic dynamics. The second term takes into account the loss of momentum due to spontaneous emission of rate β. Last, the term between square brackets denotes the coupling with the radiation field $A = \sqrt{\epsilon_0/n_e\hbar\omega\bar{\rho}}E$ and space charge field, where ϵ_0 is the vacuum permittivity, n_e the electron density and E the electric field of the generated radiation. Equation (4b) describes the evolution of the classical radiation field, which is normalized such that $\bar{\rho}|A|^2$ is the average number of photons emitted per electron.

QFEL INCLUDING SPACE CHARGE AND SPONTANEOUS EMISSION

In the following we investigate the interplay between space charge and spontaneous emission and the detrimental effect on QFEL operation by numerical integration of Eqs. (4a) and (4b). Unless stated otherwise the initial conditions for the simulations are $\bar{\rho} = 0.2$, $A(0) = 0$, $b(0) = \epsilon\sqrt{1-\epsilon^2}$, $|c_0|^2 = 1 - \epsilon^2$ and $|c_{-1}|^2 = \epsilon^2$ with $\epsilon = 10^{-4}$. The detuning for maximal gain $\delta = \sqrt{1/(4\bar{\rho}^2) + \sigma}$ is chosen [3].

Two State Dynamics

In Figure 1 the occupation probability of the $m = 0$ and $m = 1$ state under QFEL operation is shown for several regimes. First, in Fig. 1(a) The evolution of the states in the Quantum Compton regime without spontaneous emission is given. We find that the electron wave-function completely de-excites around $\bar{z} = 26$. Saturation of the field is found at this point, which is further downstream with respect to the classical Compton regime having a saturation distance of about ten gain lengths for the chosen initial conditions.

Second, in Fig. 1(b) Compton QFEL operation is shown with spontaneous emission rate $\beta = 10^{-3}$. Here, decoherence is clearly demonstrated by the loss of the sum of probabilities $|c_0|^2 + |c_-1|^2$. Due to spontaneous emission the $m = -1$ momentum state never is fully occupied. Furthermore, the maximum of occupation probability of the de-excited state is found even later than the quantum Compton regime.

Next, in Fig. 1(c) momentum state evolution is shown in the Raman regime for $\sigma = 3$. Due to the space charge field, the transition to the $m = -1$ state is attenuated leading to longer gain length. However, in the Raman regime no decoherence occurs $|c_0|^2 + |c_-1|^2 = 1$, so that the ground state gets reoccupied completely after saturation.

Last, in Fig. 1(d) the occupation probability under influence of spontaneous emission and space charge along the laser undulator is plotted. One can identify the signature of decoherence by spontaneous emission and attenuated transition by space charge to take place, simultaneously. Consequently, the maximum field amplitude, scaling with $|c_1|^2$ is also limited. The effect on the field amplitude will be discussed in the next section.

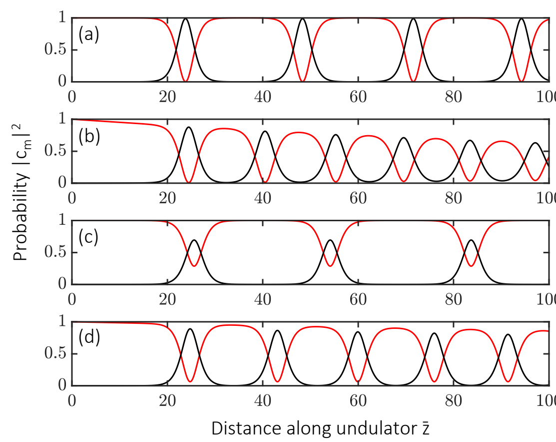

Figure 1: Evolution of the $m = 0$ (red) and $m = -1$ (black) momentum state for $\rho = 10^{-4}$, $\bar{\rho} = 0.2$ and (a) $\sigma = \beta = 0$, (b) $\beta = 10^{-3}$, $\sigma = 0$, (c) $\beta = 0$, $\sigma = 3$ and (d) $\beta = 3 \times 10^{-4}$, $\sigma = 1$.

Radiation Efficiency

Spontaneous emission and space charge have opposing constraints. We use our definition of the Pierce parameter ρ to investigate how these constraints affect the radiation efficiency, *i.e.* the number of photons per electron $\bar{\rho}|A|^2$. The black dots in Fig. 2 present the radiation efficiency for different values of space charge parameter σ and corresponding spontaneous emission rate β for a Pierce parameter $\rho = 10^{-4}$ and QFEL parameter $\bar{\rho} = 0.2$. The left side of the graph (white background) is the spontaneous emission dominated part. In this regime, the decoherence due to spontaneous emission reduces the photon yield significantly, which is shown clearly by the blue line denoting space charge free results. The optimal radiation efficiency is found around $\sigma = 1$ on right side of the graph (grey background) which denotes the space charge dominated part. Therefore, in the quantum regime, antibunching by the space charge field influences

ISBN: 978-3-95450-220-2 ISSN: 2673-5474 doi: 10.18429/JACoW-FEL2022-MOCO3

the yield less dominantly than decoherence by spontaneous emission. Furthermore, we find that for lower $\bar{\rho}$ (deeper quantum), the optimum shifts even more towards the Raman regime (not shown in the graph).

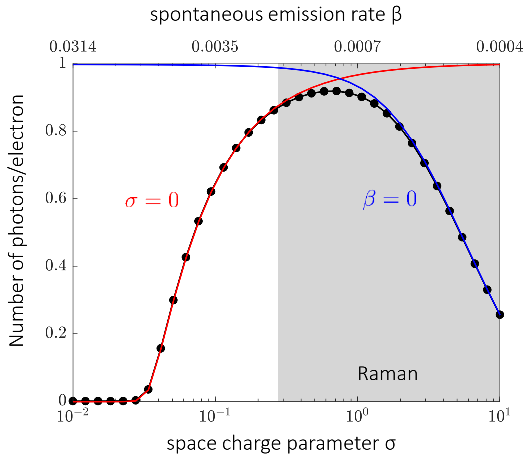

Figure 2: Radiation efficiency for $\rho = 10^{-4}$ and $\bar{\rho} = 0.2$ for different values of the space charge parameter and spontaneous emission rate.

ULTRACOLD ELECTRON SOURCE

Besides allowing for either spontaneous emission or space charge to take place in a QFEL, the electron and laser beam parameters have to satisfy strict conditions. To reach the stringent electron beam requirements, we propose to use the ultracold electron source (UCES) as a potential QFEL driver. This electron source has the unique property of allowing high charge electron bunches to be extracted while maintaining ultralow transverse emittance, by minimization of the space charge forces due to the large ionization volume. The UCES is based on near-threshold photo-ionization of a laser-cooled atomic gas in a magneto-optical trap (MOT). The electron temperatures after ionization are as low as 10 K [6–8].

It is clear that the UCES allows much smaller normalized emittances than are possible with conventional photoemission sources. For example, for an rms transverse source size $\sigma_s = 25\,\mu\text{m}$ and 10 K electron temperature, the normalized emittance $\epsilon_n = 1$ nm rad, a value that is routinely achieved with the UCES. The size of the trapped gas cloud and thus the longitudinal size of the ionization volume is typically 1 mm and the atom densities can be as high as a few 10^{18} m^{-3}, implying that $N_e = 10^6 - 10^7$ electrons can be created with $\epsilon_n = 1$ nm rad.

For efficient QFEL operation, the electrons emit their radiation in phase. Consequently, the relative energy spread must be below the gain bandwidth $\Gamma = \rho\sqrt{\bar{\rho}}(1 + 4\sigma\bar{\rho}^2)^{-1/4}$ [3]. Similarly, for emission into a discrete frequency band, the angular spread σ_θ should be below $\sqrt{2\Gamma}/\gamma$.

Furthermore, for optimized overlap between the beams the transverse emittance of the electron beam should also satisfy $\epsilon_n^\perp \leq \gamma\sigma_e^2/L_{\text{int}}$, where σ_e the rms electron beam width and L_{int} the interaction distance. For the same reason, the Rayleigh length of the laser is not allowed to exceed $L_{\text{int}}/2$. Other, less stringent conditions come from laser intensity (a_0^2) variations and non-planar laser wavefronts. For an elaborate discussion on the experimental requirements see ref. [4].

Given these constraints and based on the simulations discussed in previous sections, we now propose a 1.5 nm Quantum SASE FEL driven by ultracold electrons. In Table 1 a summary is given of the proposed Quantum FEL parameters. The charge of the electron bunch is set to 100 fC, assuming a MOT of density 2.5×10^{18}m^{-3} and a spherical ionization volume of rms radius $\sigma_s = 25\,\mu$m, which corresponds to transverse and longitudinal emittance of 1 nm-rad.

To reach $\lambda_r = 1.5$ nm from head-on collision with a laser pulse of wavelength $\lambda = 1\,\mu$m, the electron beam must have a kinetic energy of 6.1 MeV, which can be achieved using table-top accelerator structures. Consequently, this sets the recoil parameter to $X = 1.25\times10^{-4}$. we choose a QFEL parameter $\bar{\rho} = 0.4$, such that the Pierce parameter is $\rho = 5 \times 10^{-5}$. For the value of ρ, we find the optimal space charge parameter $\sigma = 0.75$ and spontaneous emission rate $\beta = 8 \times 10^{-4}$ by performing 1D QFEL simulations.

The results of the steady-state simulations using the optimal parameters for which the experimental constraints hold are shown in Fig. 3. The two-state dynamics, presented in Fig. 3(b), show minor signs of decoherence by spontaneous emission and attenuated transition by space charge. The electron beam occupies the $m = -1$ state almost completely around $L_{\text{int}} = 3$ cm. As a result, the number of X-ray photons also saturates around this point as seen in Fig. 3(a).

If we assume that the Rayleigh length of the laser pulse is equal to $L_{\text{int}}/2$, then the required laser pulse energy is 5.5 J and the pulse length is $\sigma_t = 2L_{\text{int}}/c = 200$ ps for the laser strength corresponding to the deduced spontaneous emission rate. These laser pulse parameters are well within the range of commercially available technology.

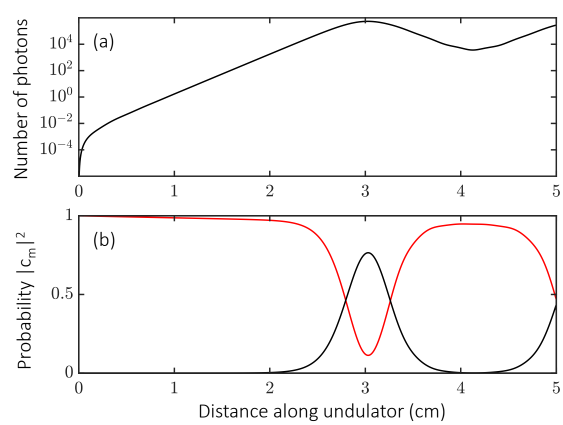

Figure 3: Radiation and momentum state dynamics for the proposed QFEL parameters.

ISBN: 978-3-95450-220-2 ISSN: 2673-5474 doi: 10.18429/JACoW-FEL2022-MOCO3

Table 1: Summary of the Quantum FEL Parameters

QFEL Parameters	
QFEL parameter $\bar{\rho}$	0.4
Pierce paramter ρ	5×10^{-4}
Gain length L_g	1.6 mm
Saturation length L_{int}	3 cm
Electron Beam Parameters	
Kinetic Energy $(\gamma_r - 1)mc^2$	6.1 MeV
Bunch charge Q	100 fC
Trans. norm emittance $\epsilon_n^{\perp}$	1 nm-rad
Long. norm emittance $\epsilon_n^{\parallel}$	1 nm-rad
Peak current I	5.4 A
Electron density n_e	1.8×10^{22} m^{-3}
Laser Undulator Parameters	
Wavelength λ_0	1000 nm
Pulse length σ_t	200 ps
Pulse Energy U_l	5.5 J
Rayleigh length z_R	2.5 cm
X-ray Parameters	
Radiation wavelength λ_r	1.5 nm
Number of photons N_{ph}	5.5×10^5
Rel. bandwidth $\Delta\lambda/\lambda$	2.7×10^{-4}

CONCLUSION

We discussed how spontaneous emission and microscopic space charge affect QFEL dynamics using a comprehensive model. The specific signatures of spontaneous emission and space charge were shown. Furthermore, we show that a FEL operating in the quantum regime, radiates optimally when space charge effects are significant.

Based on the 1D QFEL simulations, we proposed the ultracold electron source as driver for a compact $\lambda_r = 1.5$ nm QFEL. We find that the ultracold electron bunches meet the stringent requirement for potential QFEL operation with commercially available laser systems

ACKNOWLEDGEMENTS

This research was funded by the Ministry of Economic Affairs in the Netherlands through a TKI-grant.

REFERENCES

[1] R. Bonifacio, N. Piovella,G. R. M. Robb, and A. Schiavi, "Quantum regime of free electron lasers starting from noise", *Phys. Rev. Accel. Beams*, vol. 9, p. 090701, 2006. doi:PhysRevSTAB.9.090701

[2] H. Fares, N. Piovella, and G. R. M. Robb, "The detrimental effect of spontaneous emission in quantum free electron lasers: A discrete Wigner model", *Phys. Plasmas*, vol. 25, p. 013111, 2018. doi:10.1063/1.5003913

[3] B. H. Schaap, S. Schouwenaars, O. J. Luiten, 2022 "A Raman Quantum Free Electron Laser Model", under review

[4] A. Debus, K. Steiniger, P. Kling, C. M. Carmesin, and R. Sauerbrey, "Realizing quantum free-electron lasers: a critical analysis of experimental challenges and theoretical limits", *Phys. Scr.*, vol. 94, p. 074001, 2019. doi:10.1088/1402-4896/aaf951

[5] N. Piovella, M. M. Cola, L. Volpe, R. Gaiba, A. Schiavi and R. Bonifacio, "A Wigner function model for free electron lasersl", *Opt. Commun.*, vol. 274, pp. 347-353, 2007. doi:10.1016/j.optcom.2007.02.061

[6] A. J. McCulloch, D. V. Sheludko, M. Junker, and R. E. Scholten, "High-coherence picosecond electron bunches from cold atomsl", *Nat. Commun.*, vol. 4, pp. 1-6, 2013. doi:10.1038/ncomms5489

[7] W. j. Engelen, M. A. Van Der Heijden, J. D. Bakker, E. J. D. Vredenbregt, and O. J. Luiten, "High-coherence electron bunches produced by femtosecond photoionization", *Nat. Commun.*, vol. 4, no. 1, pp. 1–5, 2013. doi:10.1038/ncomms2700

[8] J. G. H. Franssen, T. C. H. De Raadt, M. A. W. Van Ninhuijs and O. J. Luiten, "Compact ultracold electron source based on a grating magneto-optical trapl", *Phys. Rev. Accel. Beams*, vol. 22, p. 023401, 2019. doi:10.1103/PhysRevAccelBeams.22.023401

ISBN: 978-3-95450-220-2 ISSN: 2673-5474 doi: 10.18429/JACoW-FEL2022-MOCO4

QUANTUM DIFFUSION DUE TO COHERENT RADIATION *

Gennady Stupakov
SLAC National Accelerator Laboratory, Menlo Park, CA, USA

Abstract

Quantum diffusion caused by synchrotron radiation plays an important role in circular electron and positron accelerators. It is, however, cannot be applied to FELs, because the original derivation of the quantum diffusion [1] assumes incoherent radiation. In this paper, we overcome this limitation and develop the theory of quantum diffusion for coherent radiation. We also give a new interpretation of the quantum diffusion as due to quantum fluctuations of the vacuum electromagnetic field.

INTRODUCTION

Quantum diffusion due synchrotron radiation in circular accelerators defines such important characteristics of the beam as its energy spread, the bunch length and the beam horizontal emittance [2]. The mechanism of the diffusion is usually interpreted in the following way: an emission of a photon of frequency ω causes a discontinuous jump $\hbar\omega$ in the energy of the particle; the stochastic component of these jumps leads to the particle's energy diffusion and the averaged smooth part of the accumulated jumps acts as a radiation reaction force. Based on this interpretation, the quantum diffusion coefficient can be expressed through the spectrum of the synchrotron radiation of a single particle [1–3]; in particular, the energy variance of an electron in the beam due to this diffusion is given by the following formula,

$$(\Delta W)^2 = \int \hbar\omega \frac{d\mathcal{W}_{\mathrm{rad}}}{d\omega d\Omega} d\omega\, d\Omega, \tag{1}$$

where $d\mathcal{W}_{\mathrm{rad}}/d\omega d\Omega$ is the energy radiated by an electron into a unit frequency interval $d\omega$ and a unit solid angle $d\Omega$. The energy variance Eq. (1) is not correlated between different electrons in the beam.

Fundamental in the existing derivation of quantum diffusion is an assumption of incoherent radiation. This means that it cannot be applied to FELs. On the other hand, the number of photons that a beam radiates during the passage of an undulator in an FEL can be many orders of magnitude larger than in a ring synchrotron. A natural question arises: how large is the quantum diffusion caused by the coherent radiation in an FEL? In this paper, we will give an answer to this question.

An attempt to generalize the original derivation of the quantum excitation [2] for the case of coherent radiation encounters the following problem: how the recoil momentum of a single photon is distributed between the group of electrons that are involved in coherent radiation of this photon (these are electrons located within the coherence volume for a given type of radiation)? To overcome this problem, we have to return to quantum description of the electromagnetic field in terms of the creation and annihilation operators. At the same time we treat the beam as a classical current because the quantum effects in relativistic electron beams are negligible [4]. Such a combined treatment is well known in the literature [5, 6] and is relatively easy to apply to the problem at hand.

* Work supported by the Department of Energy, contract DE-AC03-76SF00515.

QUANTUM RADIATION OF A CLASSICAL CURRENT

The electromagnetic field of radiation is represented by the operator $\hat{\boldsymbol{E}}(\boldsymbol{r},t)$ that is expressed through the Heisenberg photon annihilation and creation operators, $\hat{a}_{\boldsymbol{k}\nu}(t)$ and $\hat{a}^\dagger_{\boldsymbol{k}\nu}(t)$,

$$\hat{\boldsymbol{E}}(\boldsymbol{r},t) = i\sum_{\boldsymbol{k}\nu} c_k \left[\hat{a}_{\boldsymbol{k}\nu}(t)e^{i\boldsymbol{k}\cdot\boldsymbol{r}} - \hat{a}^\dagger_{\boldsymbol{k}\nu}(t)e^{-i\boldsymbol{k}\cdot\boldsymbol{r}}\right]. \tag{2}$$

Here $\boldsymbol{k}$ is the wavenumber of the mode, $\nu = 1,2$ denotes its polarization with the unit polarization vectors $\boldsymbol{e}_{\boldsymbol{k}\nu}$ that are perpendicular to $\boldsymbol{k}$, $\boldsymbol{e}_{\boldsymbol{k}\nu}\cdot\boldsymbol{k} = 0$, and $c_k = (2\pi\hbar\omega_{\boldsymbol{k}}/V)^{1/2}$ with $\omega_{\boldsymbol{k}} = ck$ and V the quantization volume. If radiation is emitted by a classical current $\boldsymbol{j}(\boldsymbol{r},t)$, the time dependence of the Heisenberg operator $\hat{a}_{\boldsymbol{k}\nu}(t)$ is given by the following equation [6]:

$$\hat{a}_{\boldsymbol{k}\nu}(t) = \hat{a}_{\boldsymbol{k}\nu}(0)e^{-i\omega_{\boldsymbol{k}}t} + \alpha_{\boldsymbol{k}\nu}(t), \tag{3}$$

where the amplitude $\alpha_{\boldsymbol{k}\nu}(t)$ is

$$\alpha_{\boldsymbol{k}\nu}(t) = \frac{2\pi i}{c_k}\int_{-\infty}^{t} dt' e^{-i\omega_{\boldsymbol{k}}(t-t')} j_{\perp\boldsymbol{k}\nu}(t'), \tag{4}$$

and $j_{\perp\boldsymbol{k}\nu}(t)$ is the transverse component of the current projected onto the polarization vector $\boldsymbol{e}_{\boldsymbol{k}\nu}$,

$$j_{\perp\boldsymbol{k}\nu}(t) = \int \frac{d^3r}{V}\boldsymbol{e}_{\boldsymbol{k}\nu}\cdot\boldsymbol{j}(\boldsymbol{r},t)e^{-i\boldsymbol{k}\cdot\boldsymbol{r}}.$$

In Eq. (3) we assumed that at $t=0$ the field is in vacuum state (zero photons) and in Eq. (4) we integrate over time from $-\infty$ instead of 0 assuming that the current is zero for $t<0$.

Let us now consider a bunch with the charge distribution $\rho(\boldsymbol{r})$ moving as a rigid body along the orbit given by the vector function $\boldsymbol{r}_0(t)$,

$$\boldsymbol{j}(\boldsymbol{r},t) = \boldsymbol{v}(t)\rho(\boldsymbol{r}-\boldsymbol{r}_0(t)), \tag{5}$$

with $\boldsymbol{v}(t) = d\boldsymbol{r}_0(t)/dt$. Consider an electron located at coordinate $\boldsymbol{a}$ relative to the center of the bunch which we associate with coordinate $\boldsymbol{r} = \boldsymbol{r}_0(t)$ and let us define its

ISBN: 978-3-95450-220-2 ISSN: 2673-5474 doi: 10.18429/JACoW-FEL2022-MOCO4

energy change $\Delta\hat{W}(\boldsymbol{a})$ due to the radiation process. This enery change can be calculated as the work done by the radiation field $\hat{\boldsymbol{E}}$ on the particle,

$$\Delta\hat{W}(\boldsymbol{a}) = e\int_{-\infty}^{\infty} dt\, \hat{\boldsymbol{E}}(\boldsymbol{r}_0(t)+\boldsymbol{a},t)\cdot\boldsymbol{v}(t). \tag{6}$$

Note that together with $\hat{\boldsymbol{E}}$, $\Delta\hat{W}(\boldsymbol{a})$ is an operator. The expectation value of this operator, $\langle\Delta\hat{W}(\boldsymbol{a})\rangle = \langle 0|\Delta\hat{W}(\boldsymbol{a})|0\rangle$, gives the average value of the energy change. Using the relations that follow from Eq. (3),

$$\langle 0|\hat{a}_{\boldsymbol{k}\nu}(t)|0\rangle = \alpha_{\boldsymbol{k}\nu}, \qquad \langle 0|\hat{a}^{\dagger}_{\boldsymbol{k}\nu}(t)|0\rangle = \alpha^{*}_{\boldsymbol{k}\nu}, \tag{7}$$

we find

$$\langle\Delta\hat{W}(\boldsymbol{a})\rangle = 2e\sum_{\boldsymbol{k}\nu} \times\int_{-\infty}^{\infty} dt\, \mathrm{Re}\left[ic_k\alpha_{\boldsymbol{k}\nu}(t)e^{i\boldsymbol{k}\cdot(\boldsymbol{r}_0(t)+\boldsymbol{a})}\boldsymbol{e}_{\boldsymbol{k}\nu}\cdot\boldsymbol{v}(t)\right]. \tag{8}$$

This expression does not involve the Planck constant $\hbar$ and hence is classical in nature. It can also be obtained from the classical electromagnetic theory of radiation[1].

To characterize the quantum diffusion we now calculate the quantity $C(\boldsymbol{a},\boldsymbol{a}')$,

$$C(\boldsymbol{a},\boldsymbol{a}') = \frac{1}{2}\langle\Delta\hat{W}(\boldsymbol{a})\Delta\hat{W}(\boldsymbol{a}')+\Delta\hat{W}(\boldsymbol{a}')\Delta\hat{W}(\boldsymbol{a})\rangle - \langle\Delta\hat{W}(\boldsymbol{a})\rangle\langle\Delta\hat{W}(\boldsymbol{a}')\rangle. \tag{9}$$

This quantity describes the correlation of energy fluctuations at two different positions in the bunch, $\boldsymbol{a}$ and $\boldsymbol{a}'$. For $\boldsymbol{a}=\boldsymbol{a}'$ it gives the variance of the energy spread of an electron located at coordinate $\boldsymbol{a}$. Note that we symmetrized the product $\Delta\hat{W}(\boldsymbol{a})\Delta\hat{W}(\boldsymbol{a}')$ because even though the operators $\Delta\hat{W}(\boldsymbol{a})$ and $\Delta\hat{W}(\boldsymbol{a}')$ are Hermitian they do not commute and hence their product is not self-adjoint while the symmetrized combination is Hermitian and corresponds to an observable quantity. For the product $\Delta\hat{W}(\boldsymbol{a})\Delta\hat{W}(\boldsymbol{a}')$ we have

$$\begin{aligned}\Delta\hat{W}(\boldsymbol{a})\Delta\hat{W}(\boldsymbol{a}') &= -e^2\int_{-\infty}^{\infty} dt\, v_\alpha(t)\sum_{\boldsymbol{k}\nu} c_k e_{\boldsymbol{k}\nu,\alpha}\\ &\times\left[\hat{a}_{\boldsymbol{k}\nu}(t)e^{i\boldsymbol{k}\cdot(\boldsymbol{r}_0(t)+\boldsymbol{a})} - \hat{a}^{\dagger}_{\boldsymbol{k}\nu}(t)e^{-i\boldsymbol{k}\cdot(\boldsymbol{r}_0(t)+\boldsymbol{a})}\right]\\ &\times\int_{-\infty}^{\infty} dt'\, v_\beta(t')\sum_{\boldsymbol{k}'\nu'} c_{k'} e_{\boldsymbol{k}'\nu',\beta}\\ &\times\left[\hat{a}_{\boldsymbol{k}'\nu'}(t')e^{i\boldsymbol{k}'\cdot(\boldsymbol{r}_0(t)+\boldsymbol{a}')} - \hat{a}^{\dagger}_{\boldsymbol{k}'\nu'}(t')e^{-i\boldsymbol{k}'\cdot(\boldsymbol{r}_0(t)+\boldsymbol{a}')}\right].\end{aligned} \tag{10}$$

We now substitute Eq. (3) for the operator $\hat{a}_{\boldsymbol{k}\nu}(t)$ into this expression and take the matrix element $\langle 0|\ldots|0\rangle$ of the symmetrized product Eq. (10). The first thing we notice is that due to the vanishing matrix elements $\langle 0|\hat{a}_{\boldsymbol{k}\nu}(0)|0\rangle = \langle 0|\hat{a}^{\dagger}_{\boldsymbol{k}\nu}(0)|0\rangle = 0$ the only non-zero contribution to the $C(\boldsymbol{a},\boldsymbol{a}')$ comes from the terms in which $\hat{a}_{\boldsymbol{k}\nu}(t)$ is replaced by the first term on the right-hand side of Eq. (3), that is $\hat{a}_{\boldsymbol{k}\nu}(0)e^{-i\omega_k t}$. Using the equation

$$\langle 0|\hat{a}_{\boldsymbol{k}\nu}(0)\hat{a}^{\dagger}_{\boldsymbol{k}'\nu'}(0)|0\rangle = \delta_{\boldsymbol{k}\nu,\boldsymbol{k}'\nu'}, \tag{11}$$

we arrive at the following result:

$$\begin{aligned}C(\boldsymbol{a},\boldsymbol{a}') &= \frac{1}{2}e^2\sum_{\boldsymbol{k}\nu}\frac{2\pi\hbar\omega_k}{V}\\ &\times\left(\int_{-\infty}^{\infty} dt\, \boldsymbol{v}(t)\cdot\boldsymbol{e}_{\boldsymbol{k}\nu}e^{-i\omega_k t+i\boldsymbol{k}\cdot(\boldsymbol{r}_0(t)+\boldsymbol{a})}\right.\\ &\times\left.\int_{-\infty}^{\infty} dt'\, \boldsymbol{v}(t')\cdot\boldsymbol{e}_{\boldsymbol{k}\nu}e^{i\omega_k t'-i\boldsymbol{k}\cdot(\boldsymbol{r}_0(t')+\boldsymbol{a}')} + \boldsymbol{a}\leftrightarrow\boldsymbol{a}'\right),\end{aligned} \tag{12}$$

where the abbreviation $\boldsymbol{a}\leftrightarrow\boldsymbol{a}'$ indicates the first term in the brackets with $\boldsymbol{a}$ and $\boldsymbol{a}'$ interchanged. Replacing the sum over $\boldsymbol{k}$ by the integral

$$\sum_{\boldsymbol{k}} \to \frac{V}{(2\pi)^3}\int k^2\, dk\, d\Omega, \tag{13}$$

we obtain

$$\begin{aligned}C(\boldsymbol{a},\boldsymbol{a}') &= e^2\sum_{\nu}\frac{\hbar c}{(2\pi)^2}\int k^3 dk\, d\Omega\, \cos\left[\boldsymbol{k}\cdot(\boldsymbol{a}'-\boldsymbol{a})\right]\\ &\times\left|\int_{-\infty}^{\infty} dt\, \boldsymbol{v}(t)\cdot\boldsymbol{e}_{\boldsymbol{k}\nu}e^{-i\omega_k t}e^{i\boldsymbol{k}\cdot\boldsymbol{r}_0(t)}\right|^2.\end{aligned} \tag{14}$$

The right-hand side of Eq. (12) can be expressed through the spectrum of radiation of a single partile $d\mathcal{W}_{\mathrm{rad}}/d\omega d\Omega$ which is given by the following formula

$$\frac{d\mathcal{W}_{\mathrm{rad}}}{d\omega d\Omega} = \frac{q^2\omega^2}{4\pi^2c^3}\left|\int_{-\infty}^{\infty} dt e^{i\omega t-i\boldsymbol{k}\cdot\boldsymbol{r}_0(t)}\boldsymbol{e}_{\boldsymbol{k}\lambda}\cdot\boldsymbol{v}(t)\right|^2. \tag{15}$$

We then obtain

$$C(\boldsymbol{l}) = \int \hbar\omega\, d\omega\, d\Omega\, \frac{d\mathcal{W}_{\mathrm{rad}}}{d\omega d\Omega}\cos(\boldsymbol{k}\cdot\boldsymbol{l}), \tag{16}$$

where $\boldsymbol{l} = \boldsymbol{a}-\boldsymbol{a}'$. Note that for $\boldsymbol{l}=0$ we recover the incoherent radiation result Eq. (1). Hence, we come to the conclusion that the variance of the energy spread for one electron is the same as for incoherent radiation. The new element that the coherence introduces is the correlation in the energy diffusion between different electrons.

The fact that in calculation of $C(\boldsymbol{l})$ we discarded the terms $\alpha_{\boldsymbol{k}\nu}(t)$ in Eq. (3) (and $\alpha^{*}_{\boldsymbol{k}\nu}(t)$ in the correspondent expression for $\alpha^{\dagger}_{\boldsymbol{k}\nu}(t)$) because they did not contribute to the final result has an important physical meaning: the radiated electromagnetic field of the beam does not contribute to the energy fluctuations caused by quantum diffusion. The only contribution to $C(\boldsymbol{l})$ came from the terms involving $\hat{a}_{\boldsymbol{k}\nu}(0)$ and $\hat{a}^{\dagger}_{\boldsymbol{k}\nu}(0)$, that is the vacuum field that existed before the radiation was generated. This brings up an important interpretation of the quantum diffusion as due to the vacuum quantum fluctuations of the electromagnetic field, in contrast to the original interpretation as a recoil effect in the emission of photons. The new interpretation puts quantum diffusion into same category of such QED effects as the Casimir force and the Lamb shift (see, e.g., [7]).

[1] It is worth pointing out that Eq. (8) provides a new method for calculation of the CSR wake fields.

ISBN: 978-3-95450-220-2 ISSN: 2673-5474 doi: 10.18429/JACoW-FEL2022-MOCO4

THE HELICAL UNDULATOR

To illustrate the usage of Eq. (16) here we will calculate the function $C(\boldsymbol{l})$ for the wiggler radiation. For a long helical wiggler the radiated energy of a relativistic particle is given by the following equation [8]

$$\frac{d\mathcal{W}_{\rm rad}}{d\omega d\Omega} = A\omega^2 \sum_{n=1}^{\infty} \left[J_n'^2(x) + \left(\frac{\gamma\theta}{K} - \frac{n}{x} \right)^2 J_n^2(x) \right] \times \delta\left(\frac{\omega}{\omega_1} - n \right), \tag{17}$$

where A is a constant which is not important for our analysis, J_n and J_n' are the Bessel function of n-th order and its derivative, θ is the polar angle measured from the wiggler axis, $x = K\omega\theta/\gamma\omega_0$, $\omega_0 = k_u v_z$ with $k_u = 2\pi/\lambda_u$ and λ_u the wiggler period, and

$$\omega_1 = \frac{2\gamma^2\omega_0}{1+K^2+\gamma^2\theta^2} = \omega_{10}\frac{1+K^2}{1+K^2+\gamma^2\theta^2}, \tag{18}$$

where $\omega_{10} = 2\gamma^2\omega_0/(1+K^2)$ is the frequency radiated in the forward direction. We assume that the angles of the radiation are small, $\theta \ll 1$. We represent the vector $\boldsymbol{l}$ as a sum of the longitudinal and transverse components, $\boldsymbol{l} = l_\parallel \hat{z} + \boldsymbol{l}_\perp$, where $\hat{z}$ is the unit vector along the axis of the wiggler. Introducing the normalized quantities $\tilde{l}_\parallel = l_\parallel\omega_{10}/c$ and $\tilde{l}_\perp = l_\perp\omega_{10}/c\gamma$ after some calculations we obtain,

$$C(\tilde{l}_\perp, \tilde{l}_\parallel) \propto \int_0^\infty \xi d\xi \sum_{n=1}^{\infty} \frac{n^3}{(1+K^2+\xi^2)^4} \times J_0\left[n\xi\tilde{l}_\perp \frac{1+K^2}{1+K^2+\xi^2} \right] \cos\left[n\tilde{l}_\parallel \frac{1+K^2}{1+K^2+\xi^2} \right] \times \left[J_n'^2(x_n) + \left(\frac{\xi}{K} - \frac{n}{x_n} \right)^2 J_n^2(x_n) \right]. \tag{19}$$

where

$$x_n = \frac{2Kn\xi}{1+K^2+\xi^2}. \tag{20}$$

The plot of this function for $K = 1$ calculated with $n_{\rm max} = 20$ harmonics in the sum of Eq. (19) is shown in Fig. 1. The function is normalized so that $C = 1$ at the origin. Note that the correlations are localized in the region $\tilde{l}_\perp \sim \tilde{l}_\parallel \sim 1$. The product $c\gamma/\omega_{10} \times c\gamma/\omega_{10} \times c/\omega_{10}$ in dimensional units defines the coherent volume for the undulator radiation.

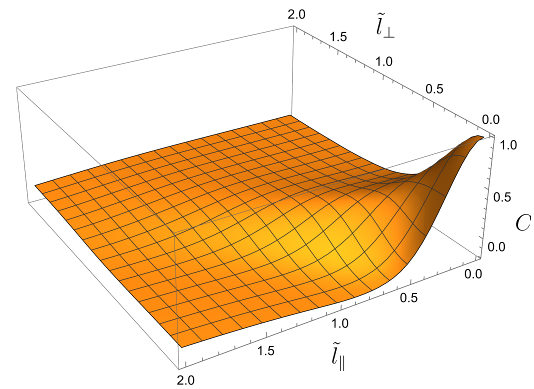

Figure 1: Plot of function $C(\tilde{l}_\perp, \tilde{l}_\parallel)$ for wiggler radiation with $K = 1$.

DISCUSSION

A somewhat surprising result of this work that the quantum diffusion in coherent radiation for a given electron is the same as for incoherent radiation can be clarified by the following thought experiment. Let us consider N electrons tightly packed into a small volume so that they radiate coherently. Together, they can be considered as one "heavy" particle with the charge equal to Ne. The radiation of this particle is N^2 larger than that of an electron with charge e, and according to Eq. (1) its rms energy spread will be N times larger than the rms energy spread of one electron moving along the same orbit. However, the N times increased energy spread of the composite particle is equally divided between the constituent electrons because of their proximity to each other. As a result, the energy diffusion of each electron is the same, and is equal to the energy diffusion of a single electron radiated incoherently. The only difference is that all N electrons will diffuse in a correlated manner, that is the random variations of their energy will follow each other.

The quantum diffusion studied in this paper usually does not play a big role in FELs because these machines are based on linear accelerators and the beam is dumped after only one passage through the system. In contrast, the importance of quantum diffusion in circular accelerators is due to the fact that its effect accumulates over many revolutions in the ring, but as already was mentioned in the Introduction, this diffusion is incoherent. This situation may change in the current upgrades APS-U [9] and ALS-U light sources that are moving toward the regimes where the radiation becomes more transversely coherent. Another example of the machine where the coherent quantum diffusion can play a role is the SSMB concept proposed in Ref. [10] which relies on coherent radiation of a microbunched beam in a circular accelerator.

Finally, we mention here that description of beam dynamics with account of coherent quantum diffusion requires a modification of the Vlasov equation. The incoherent diffusion is included in this equation as a diffusion operator on the right-hand side, and is often referred to as the Vlasov-Fokker-

ISBN: 978-3-95450-220-2 ISSN: 2673-5474 doi: 10.18429/JACoW-FEL2022-MOCO4

Planck equation. The coherent diffusion should be added to this equation as a stochastic force with the correlation propertied derived in this paper.

ACKNOWLEDGMENTS

I would like to thank P. Milonni for illuminating discussions on the subject of this work.

REFERENCES

[1] M. Sands, "Synchrotron oscillations induced by radiation fluctuations," *Phys. Rev.*, vol. 97, pp. 470–473, 1955. doi:10.1103/PhysRev.97.470

[2] M. Sands, "The Physics of Electron Storage Rings: An Introduction," *Conf. Proc. C*, vol. 6906161, pp. 257–411, 1969.

[3] E. Saldin, E. Schneidmiller, and M. Yurkov, "Calculation of energy diffusion in an electron beam due to quantum fluctuations of undulator radiation," *Nuclear Instruments and Methods in Physics Research Section A: Accelerators, Spectrometers, Detectors and Associated Equipment*, vol. 381, no. 2, pp. 545–547, 1996. doi:10.1016/S0168-9002(96)00708-5

[4] V. N. Baier, V. M. Katkov, and V. S. Fadin, *Radiation from relativistic electrons*. Atomizdat, Moscow, 1973.

[5] C. Itzykson and J. Zuber, *Quantum Field Theory*. Dover Publications, 2012.

[6] D. Klyshko, *Physical Foundations of Quantum Electronics*, M. Chekhova and S. Kulik, Eds. World Scientific, 2011. doi:10.1142/7930

[7] P. Milonni, *The Quantum Vacuum: An Introduction to Quantum Electrodynamics*. Elsevier Science, 1994. https://books.google.com/books?id=P83vAAAAMAAJ

[8] B. M. Kincaid, "A short-period helical wiggler as an improved source of synchrotron radiation," *Journal of Applied Physics*, vol. 48, no. 7, pp. 2684–2691, 1977. doi:10.1063/1.324138

[9] T. E. Fornek, "Advanced photon source upgrade project final design report," Argonne National Lab. (ANL), Argonne, IL (United States), Tech. Rep. APSU-2.01-RPT-003 153666, 2019.

[10] D. F. Ratner and A. W. Chao, "Steady-state microbunching in a storage ring for generating coherent radiation," *Phys. Rev. Lett.*, vol. 105, p. 154 801, 2010. doi:10.1103/PhysRevLett.105.154801

ISBN: 978-3-95450-220-2 ISSN: 2673-5474 doi: 10.18429/JACoW-FEL2022-MOP01

EVOLUTION OF MICROBUNCHING IN DRIFT SECTIONS

S. Khan*†, Center for Synchrotron Radiation, TU Dortmund University, Dortmund, Germany
G. Perosa[1], F. Sottocorona[1], E. Allaria, A. Brynes, G. Penco, P. R. Ribič, S. Spampinati, C. Spezzani, M. Trovò, L. Giannessi[2], G. De Ninno[3], Elettra-Sincrotrone Trieste SCpA, Basovizza, Italia
E. Ferrari, E. Schneidmiller, DESY, Hamburg, Germany
[1] also at Università degli Studi di Trieste, Trieste, Italy
[2] also at Laboratori Nazionali di Frascati, INFN, Frascati, Italy
[3] also at University of Nova Gorica, Nova Gorica, Slovenia

Abstract

The typical layout adopted in a seeded harmonic generation free-electron laser (FEL) is based on radiator undulators immediately following the dispersive section, in which the microbunching is created. With the advent of new and more complex seeding schemes, this solution cannot always be implemented and cases, where the bunched beam needs to be propagated in free space before entering the radiator, should be investigated. The evolution of the density modulation in a drift space may also play a role in long intra-undulator sections of short-wavelength FELs. The paper reports on recent studies aimed at investigating the impact of the bunching evolution in a drift space on coherent harmonic emission. Experimental results collected at the FERMI free-electron laser are compared with numerical predictions.

INTRODUCTION

The FERMI user facility [1] at the Elettra laboratory located near Trieste, Italy, provides powerful radiation in the spectral range from 100 to 4 nm with two free-electron laser (FEL) lines, FEL-1 and FEL-2. Both rely on the use of an external seed laser to initiate the process of FEL amplification and coherent emission in order to provide a high degree of longitudinal and transverse coherence enabling experiments not possible with other radiation sources. Until recently, FEL-1 [2] was based on high-gain harmonic generation (HGHG) [3, 4] with a single undulator (modulator) for seeding, a dispersive section to convert the laser-induced energy modulation into microbunching, and six undulators (radiators) for the FEL process. In order to extend its spectral range, FEL-1 is presently being upgraded to implement the echo-enabled harmonic generation (EEHG) [5–7] scheme employing two modulators and two dispersive sections to generate microbunching with higher harmonic content [8]. FEL-2 [9], on the other hand, is based on two successive modulator-radiator stages employing a fresh-bunch scheme (HGHG-FB) [10], and studies for a future upgrade have started [11].

In an externally seeded FEL, a dispersive section transforms a laser-induced energy modulation of the electrons into microbunches with a strongly increased charge density giving rise to longitudinal space charge (LSC) effects. In a single-stage HGHG scheme, the radiator is usually placed immediately after the dispersive section and the FEL process starts before LSC effects become significant. With the recent advent of more complex seeding schemes, such as HGHG-FB and EEHG mentioned above, the need may arise to transport the microbunched electrons through drift sections before entering the radiator. Here, LSC increases the energy spread within the microbunches causing a longitudinal elongation (debunching). On the other hand, the correlated energy spread between the microbunches can be reduced which was proposed as a way to improve the output of HGHG FELs at high harmonics [12].

* shaukat.khan@tu-dortmund.de
† Work supported by Heinrich-Hertz-Stiftung, MKW NRW, Düsseldorf.

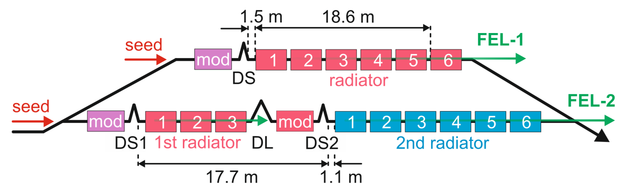

Figure 1: Schematic view of the seeded FEL lines of FERMI with modulators (mod), radiators, dispersive sections (DS), and a delay line (DL) for two-staged HGHG. Also indicated is the shortest drift from the respective DS to the radiator and the range of drift lengths used in the present study (not to scale, see also Table 1).

In order to investigate these effects, measurements were performed at both FEL lines of FERMI, and experimental results are presented below together with preliminary numerical predictions.

EXPERIMENTAL SETUP

In contrast to other experimental studies (e.g. [13]), the layout of FERMI shown in Fig. 1 allows to study the evolution of microbunching under variation of the drift length before entering the radiator.

Experiments were performed in three different configurations: (i) a single undulator as radiator at FEL-1 preceded by zero to five undulators with open magnetic gap acting as a variable drift space, (ii) a four-undulator FEL at FEL-1 preceded by zero to two undulators with open gap, and (iii) the full six-undulator FEL of the second HGHG stage of FEL-2 with microbuncing in the dispersive section of the first or the second stage. The experimental parameters are summarized in Table 1.

The FEL pulse intensity generated by different harmonics of the laser wavelength was recorded using an intensity mon-

ISBN: 978-3-95450-220-2 ISSN: 2673-5474 doi: 10.18429/JACoW-FEL2022-MOP01

itor (I_0M) based on the photo-ionization of a low-density rare gas [14] and a spectrometer (PRESTO) comprising a dispersive grating and a CCD detector [15]. The measurements were performed under variation of the matrix element R_{56} representing the strength of the respective dispersive section and repeated for different electron density by tuning a magnetic bunch compressor (BC1) accordingly.

Table 1: Summary of Experimental Parameters

Parameter	Value
beam energy E	1300 and 900 MeV
relative energy spread σ_η	$4 \cdot 10^{-5}$
peak current I	350 to 1400 A
normalized emittance $\varepsilon_{x,y}$	$1 \cdot 10^{-6}$ m rad
average beta function $\beta_{x,y}$	10 m
seed wavelength λ_L	230 to 260 nm
seed pulse energy E_L	15 to 25 µJ
longitudinal dispersion R_{56}	0 to 100 µm
drift length s in FEL-1	1.5 to 20.1 m (6 steps)
drift length s in FEL-2	1.1 to 18.8 m (2 steps)

THEORY

A laser-induced sinusoidal modulation of the electron energy followed by a dispersive section with appropriate R_{56} value leads to microbunches, i.e., sharp maxima of the longitudinal electron density spaced at the laser wavelength λ_L. Given a tilted sinusoidal phase space distribution, electrons preceding a microbunch have a negative, trailing electrons a positive energy offset. As shown in Fig. 2, the repulsive LSC forces of the microbunches reduce the energy offset of electrons between them, while the energy spread within the microbunches increases. A one-dimensional model already provides good insight into this process.

Following the notation of Ref. [12], the coupled equations

$$\frac{dp_i}{d\tau} = \frac{2}{\alpha} \sum_{h=1}^{\infty} b_h \frac{\sin h\theta_i}{h} \quad \text{and} \quad \frac{d\theta_i}{d\tau} = \alpha\, p_i \tag{1}$$

are iterated for macroparticles ($i = 1, \ldots n$) in small steps of plasma phase advance τ, which translates into longitudinal position s via $\tau = k_P\, s$, where $k_P = \sqrt{e^2 n_0 / m_e c^2 \varepsilon_0 \gamma^3}$ is the plasma wavenumber with the electron charge $-e$ and mass m_e, the electron density n_0, the dielectric constant ε_0, and the Lorentz factor γ. The phase space coordinates are $p_i(\tau) = \eta_i/\sigma_\eta$ and $\theta_i = k_L z_i$ with $\eta_i \equiv \Delta\gamma_i/\gamma$, $k_L = 2\pi/\lambda_L$ and z being the longitudinal coordinate in a co-moving frame. Furthermore, $b_h = (1/n) \sum_i \exp(ih\theta_i)$ is the bunching factor at laser harmonic h, which is updated at every iteration, and the parameter $\alpha \equiv (k_L/k_P)\, \sigma_\eta/\gamma^2$ normalizes the frequency of the plasma oscillaton given by Eq. (1).

The first of the coupled equations describes the change of energy due to a longitudinal electric field caused by a gradient of the charge distribution, which is here assumed to be a periodic function and given by a Fourier sum over harmonics h. The second equation can be rewritten as $dz_i/ds = \eta_i/\gamma^2$ meaning that relativistic particles with an energy offset change their longitudinal position due to a (small) velocity mismatch. The LSC-induced energy spread within the microbunches is sufficient to cause significant debunching over a drift length of a few meters.

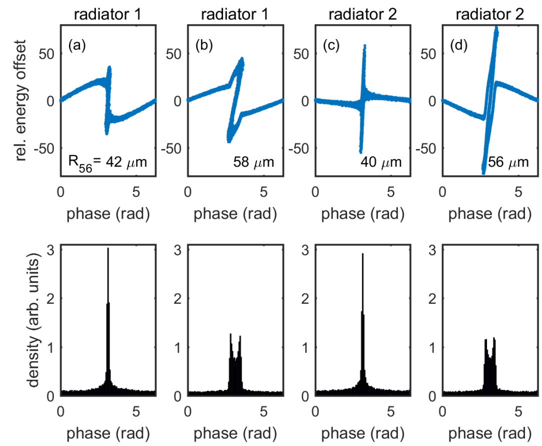

Figure 2: Phase space evolution (top) and projected electron density (bottom) after a drift length of 1.5 m (radiator 1) and 5.2 m (radiator 2) for two cases: (a,c) R_{56} value for the largest bunching factor at the 10th seed harmonic; (b,d) At larger R_{56}, a double peak of the electron density with a spacing of $\lambda_L/10$ ($\pi/5$ in phase) results in a second maximum of the bunching factor. While the energy spread within the microbunch increases, the energy offset of the other electrons is first reduced and then overshooting (d).

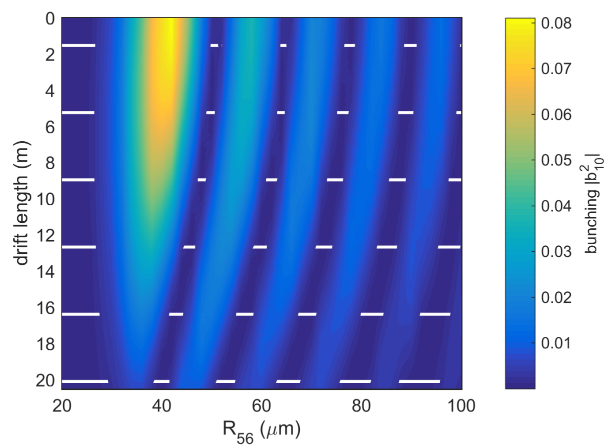

Figure 3: Squared bunching factor of the 10th seed harmonic as function of R_{56} and drift length. The white lines correspond to the drift between dispersive section and the undulators of the FEL-1 radiator. See text for further details.

Figure 3 shows an example with a moderate peak current of 700 A before microbunching. The bunching factor for the 10th harmonic of the seed wavelength λ_L decreases strongly over a drift length of 20 m. Along the R_{56} axis, the first maximum occurs for optimum microbunching, and the nth maximum results from a microbunch with two peaks which are $(n-1)\,\lambda_L/10$ apart, as shown in Fig. 2 (b) and (d). The

ISBN: 978-3-95450-220-2 ISSN: 2673-5474 doi: 10.18429/JACoW-FEL2022-MOP01

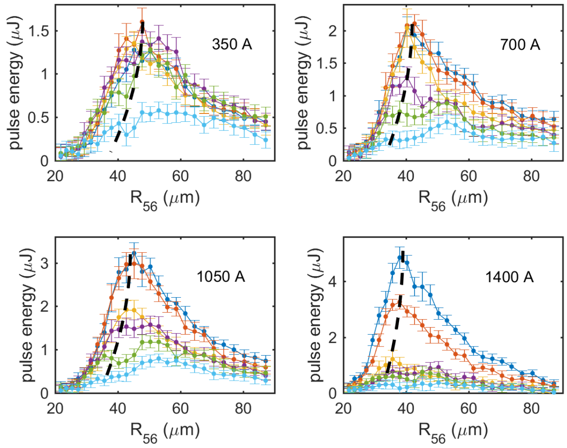

Figure 4: Measured single-undulator pulse energy as function of R_{56} for drift lengths from 1.5 to 20.1 m (sequence: blue, red, orange, purple, green, cyan) and estimated peak currents ranging from 350 to 1400 A. The dashed lines qualitatively indicate the shift of the first maximum towards lower R_{56} with increasing drift length.

LSC-induced evolution along the drift space is different for each maximum, causing their relative height to change. Furthermore, the maxima are slightly shifted to lower R_{56} with increasing drift length because the LSC effect provides additional longitudinal dispersion.

RESULTS FROM FEL-1

The following discussion of results from FEL-1 concentrates on measurements of the pulse energy from single undulators with a 6-fold variation of drift distance. Given an undulator length of 2.4 m, the effect of FEL dynamics will be small and the pulse energies can be assumed to correspond to the squared bunching factors from the simulation. The signal from a single undulator is too low for the PRESTO spectrometer and was therefore recorded by the I_0M device.

As an example, Fig. 4 shows the pulse energy of the 10th harmonic of the seed while scanning the R_{56} value of the dispersive section. The scans were repeated under variation of drift length (color code given in the figure caption) and compressor setting with the estimated peak current given in each panel. Background radiation from the dispersive section magnets, which shows up with a characteristic R_{56} dependence in the I_0M, was subtracted.

The peak structure shown in the simulation with uniform energy modulation is recognizable but strongly washed out in the data, which can be attributed to the intensity distribution along the seed pulse leading to a spread of R_{56} values for optimum bunching. The effect of debunching, i.e., the reduction of pulse energy with drift length, depends strongly on the peak current, confirming its collective nature. Also visible is the dependence of the maxima on drift length as observed in the simulation. While the maxima shift towards lower R_{56}, the debunching effect on the first maximum is stronger than on the second, which causes the centroid of the distribution to shift towards higher R_{56} values.

Except for high electron density (peak current 1400 A), the signal after 5.2 m (red curve in Fig. 4) seems to be comparable or even slightly larger than after the shortest drift of 1.5 m (blue curve). Similar observations were made in the four-undulator experiments at FEL-1 and may indicate an onset of FEL amplification enhanced by a reduced energy spread between the microbunches, as suggested in [12]. Definite conclusions, however, are subject to further analysis.

RESULTS FROM FEL-2

Taking advantage of the layout of FEL-2 (Fig. 1), it has been possible to investigate the LSC effect for an electron beam already bunched (as for FEL-1) after an energy modulation induced by the seed laser. Operating FEL-2 with a reduced electron beam energy of 0.9 GeV allowed to tune the second-stage undulators to the 12th harmonic of the seed where significant bunching can be produced in a single HGHG stage. With the magnetic delay line (DL), normally used for the two-stage fresh-bunch technique, switched off and with the first-stage radiators fully open, the bunching could be performed after the seed-induced energy modulation either using the first dispersive section (DS1) or the

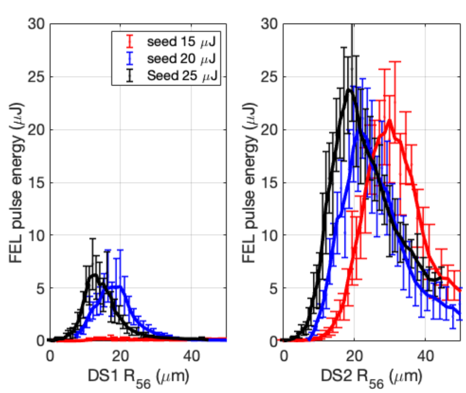

Figure 5: FEL pulse energy as function of R_{56} for different seed pulse energy using only the first (left) or the second (right) dispersive section of FEL-2.

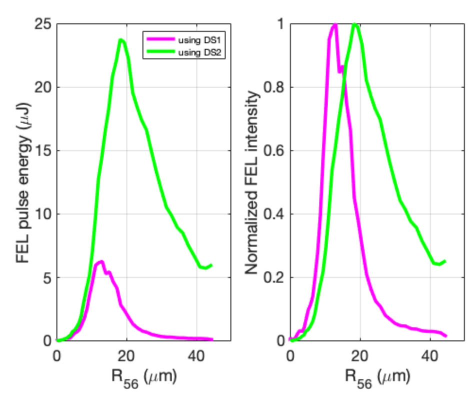

Figure 6: FEL pulse energy (left) and normalized curves (right) as function of R_{56} for configurations using dispersive section DS1 or DS2 with a seed pulse energy of 25 μJ.

ISBN: 978-3-95450-220-2 ISSN: 2673-5474 doi: 10.18429/JACoW-FEL2022-MOP01

second one (DS2). In the first case, a bunched beam with current spikes will propagate in a 18.8 m long drift space before starting emission in the radiator. In the second case instead, an energy modulated beam will go through the long drift without density modulation and current spikes will be produced only 1.1 m before the radiator.

For both cases, the pulse energy and the spectral properties of the FEL for three values of the seed pulse energy were measured. Figure 5 shows the FEL intensity measured with a calibrated ionization monitor as function of the strength R_{56} of the dispersive section. The red, blue and black curves refer to different seed pulse energies. The left panel of Fig. 5 reports the data for the case where the DS1 is used and the second dispersive section is switched off. The right panel shows the results for bunching produced right before the radiator using DS2.

The results in Fig. 5 clearly show the impact of space charge forces that affect a bunched beam when propagating in a drift section. Instead, propagation of a beam that is only energy-modulated is not a problem and good HGHG performance can be obtained if the bunching is produced right before the radiator.

A comparison of the R_{56} scans performed on DS1 or DS2 (Fig. 6) shows a clearly different behavior for the two cases. In the range of $R_{56} < 10$ µm, the space charge forces are small due to the low degree of bunching and the two configurations have comparable FEL intensity. As soon as R_{56} is large enough to produce sufficient electron density (above 10 µm), space charge forces spoil the bunching in the configuration using DS1. In this case, the maximum occurs at a lower value of R_{56} and drops faster (Fig. 6, right panel).

CONCLUSIONS

For microbunched electron beams in seeded FELs, the peak current is high enough to cause LSC-induced debunching over a few meters in a drift section. Measurements at FERMI under variation of drift length, longitudinal dispersion, and electron density are in good qualitative agreement with numerical predictions. As a general conclusion, long drift spaces between dispersive section and radiator should be avoided in the design of FELs with complex seeding schemes whereas the propagation of an unbunched beam is not critical. Further analysis of the data will reveal whether and to what degree the predicted energy spread reduction between the microbunches in a dedicated short drift space could be beneficial for coherent harmonic emission.

ACKNOWLEDGEMENTS

S.K. would like to thank the TU Dortmund University and its Physics Department for granting a sabbatical term. The kind hospitality for the FERMI team and the support during the measurements and data analysis is gratefully acknowledged. The research visit was supported by the Heinrich-Hertz-Stiftung of the German state NRW.

REFERENCES

[1] E. Allaria *et al.*, "The FERMI free-electron lasers", *J. Synchrotron Radiat.*, vol. 22, pp. 485-491, 2015. doi:10.1107/S1600577515005366

[2] E. Allaria *et al.*, "Highly coherent and stable pulses from the FERMI seeded free-electron laser in the extreme ultraviolet", *Nat. Photonics*, vol. 6, pp. 699-704, 2012. doi:10.1038/nphoton.2012.233

[3] I. Boscolo and V. Stagno, "The converter and the transverse optical klystron", *Nuovo Cimento B*, vol. 58, pp. 267-285, 1980. doi:10.1007/BF02874012

[4] L. H. Yu, "Generation of intense uv radiation by subharmonically seeded single-pass free-electron lasers", *Phys. Rev. A*, vol. 44, pp. 5178-5193, 1991. doi:10.1103/PhysRevA.44.5178

[5] G. Stupakov, "Using the beam-echo effect for generation of short-wavelength radiation", *Phys. Rev. Lett.*, vol. 102, p. 74801, 2009. doi:10.1103/PhysRevLett.102.074801

[6] D. Xiang and G. Stupakov, "Echo-enabled harmonic generation free electron laser", *Phys. Rev. ST Accel. Beams*, vol. 12, p. 030702, 2009. doi:10.1103/PhysRevSTAB.12.030702

[7] P. Rebernik Ribic *et al.*, "Coherent soft X-ray pulses from an echo-enabled harmonic generation free-electron laser", *Nat. Photonics*, vol. 13, pp. 555-561, 2019. doi:10.1038/s41566-019-0427-1

[8] C. Spezzani *et al.*, "FEL-1 Upgrade to EEHG", presented at the 40th International Free Electron Laser Conference (FEL'22), Trieste, Italy, Aug. 2022, paper TUP59, this conference.

[9] E. Allaria *et al.*, "Two-stage seeded soft-X-ray free-electron laser", *Nat. Photonics*, vol. 7, pp. 913-918, 2013. doi:10.1038/nphoton.2013.277

[10] L.-H. Yu, I. Ben-Zvi, "High-gain harmonic generation of soft X-rays with the "fresh bunch" technique", *Nucl. Instrum. Methods Phys. Res. A*, vol. 393, pp. 96-99, 1997. doi:10.1016/S0168-9002(97)00435-X

[11] L. Giannessi *et al.*, "Future Upgrade Strategy for the FERMI Seeded FEL Facility", presented at the 40th International Free Electron Laser Conference (FEL'22), Trieste, Italy, Aug. 2022, paper TUP53, this conference.

[12] E. Hemsing *et al.*, "Correlated Energy-Spread Removal with Space Charge for High-Harmonic Generation", *Phys. Rev. Letters*, vol. 113, p. 134802, 2014. doi:10.1103/PhysRevLett.113.134802

[13] K. Hacker et al., "Measurements and simulations of seeded electron microbunches with collective effects" *Phys. Rev. ST Accel. Beams*, vol. 18, p. 090704, 2015. doi:10.1103/PhysRevSTAB.18.090704

[14] M. Zangrando *et al.*, "The photon analysis, delivery, and reduction system at the FERMI@Elettra free electron laser user facility", *Rev. Sc. Instrum.*, vol. 80, p. 113110, 2009. doi:10.1063/1.3262502

[15] C. Svetina *et al.*, "PRESTO, the on-line photon energy spectrometer at FERMI: design, features and commissioning results", *J. Synchrotron Radiat.*, vol. 23, pp. 35-42, 2016. doi:10.1107/S1600577515021116

ISBN: 978-3-95450-220-2 ISSN: 2673-5474 doi: 10.18429/JACoW-FEL2022-MOP03

GAUSSIAN RANDOM FIELD GENERATOR SERVAL: A NOVEL ALGORITHM TO SIMULATE PARTIALLY COHERENT UNDULATOR RADIATION

A. Trebushinin*, G. Geloni, and S. Serkez†
European XFEL, Schenefeld, Germany

Abstract

Wavefront propagation codes play pivotal roles in the design of optics at synchrotron radiation sources. However, they usually do not account for the stochastic behavior of the radiation field originating from shot noise in the electron beam. We propose a computationally efficient algorithm to calculate a single statistical realization of partially coherent undulator radiation fields at a given frequency under the approximation of quasi-homogeneity of the source. The proposed algorithm relies on a method for simulating Gaussian random fields. This algorithm is consistent with other well-established approaches, and, in addition, it possesses an advantage in terms of computational efficiency. It can be extended to other types of sources that follow Gaussian statistics. Finally, the demonstration of the algorithm is well suited for educational purposes.

INTRODUCTION

The wave optics approach allows to straightforwardly account for the effects related to fully coherent radiation. Nevertheless, the case of partially coherent radiation remains a sophisticated problem. The characteristics of synchrotron radiation heavily depend on the presence of the shot noise in an electron beam. Because of it, amplitudes and phases of the radiation exhibit stochastic fluctuations. In other words, radiation fields distributions change from realization to realization, and in order to obtain statistically meaningful intensities and correlation functions one needs to average over a statistical ensemble, so that the framework of statistical optics becomes quite natural.

Approaches for simulating partially coherent undulator radiation are proposed in several codes and in plenty of publications. Based on the framework of statistical optics, one can consider propagating the cross-spectral density function of the electric field by exploiting coherent mode decomposition methods, e.g. [1]. An alternative type of methods is based on Monte-Carlo-like simulations. One of the most well-known wave-optics simulation toolkits, Synchrotron Radiation Workshop (SRW) [2, 3] where the intensities are being summed up to form an intensity of the synchrotron radiation.

The algorithm we propose here relies on the generation of instances of the stochastic process, instead of dealing with ensemble-averaged quantities like correlation functions or averaged intensities. The method we propose is based on Gaussian random field generator. In practice, we restrict complex Gaussian noise by the effective size and divergence of the radiation field. Introducing Gaussian noise, we effectively emulate the contribution of the shot noise accounting for all electrons at once. As a result the algorithm provides complex amplitude of a multimode field of the undulator radiation, suitable for propagation through a beamline. We call this method SERVAL (**S**ynchrotron **E**mittion **R**apid e**VAL**uator)[1]. The results reported in this contribution were published in [4].

THEORETICAL BACKGROUND ON UNDULATOR RADIATION STATISTICAL PROPERTIES

Undulator radiation has an intrinsic stochastic structure caused by random distribution of electrons in a volume of 6D phase space. This distribution follows the shot noise statistics as the number of electrons located in the finite volume of the electron beam phase space is *discrete* and *random*. This shot noise is imprinted in the radiation structure. It manifests itself as longitudinal and transverse spikes in the radiation pulse as illustrated in Fig. 1. By its nature, those fields follow the same statistics as *thermal light*: both are described in terms of Gaussian random processes [5].

However in contrast with thermal sources, which are fully incoherent and whose coherent spot-size at the source is about the radiation wavelength, undulator sources are partially coherent, and they exhibit a coherent spot size equal to the single-electron diffraction size.

For the case of the thermal light, the relation of the spiky structure in the far zone with the source size is described by Van Cittert-Zernike theorem [6, 7]. This theorem relates the cross-spectral density in the far zone with the intensity distribution at the source via Fourier transform. For undulator radiation this theorem is only applied to the special case of quasi-homogeneous sources. Applicability of Van Cittert-Zernike theorem to undulator radiation was thoroughly reviewed in [8]. To assess the coherence properties of the source one should compare the natural size and divergence of the radiation from a single electron with the size and divergence of the electron beam.

Field Correlation

The electron beam length $c\sigma_T$ (c is the speed of light and σ_T is the electron beam duration) is almost always much

* andrei.trebushinin@xfel.eu
† svitozar.serkez@xfel.eu

[1] This is a backronym. From the beginning we came up with this name SERVAL and only then decided that it stands for **S**ynchrotron **E**mittion **R**apid e**VAL**uator.

ISBN: 978-3-95450-220-2 ISSN: 2673-5474 doi: 10.18429/JACoW-FEL2022-MOP03

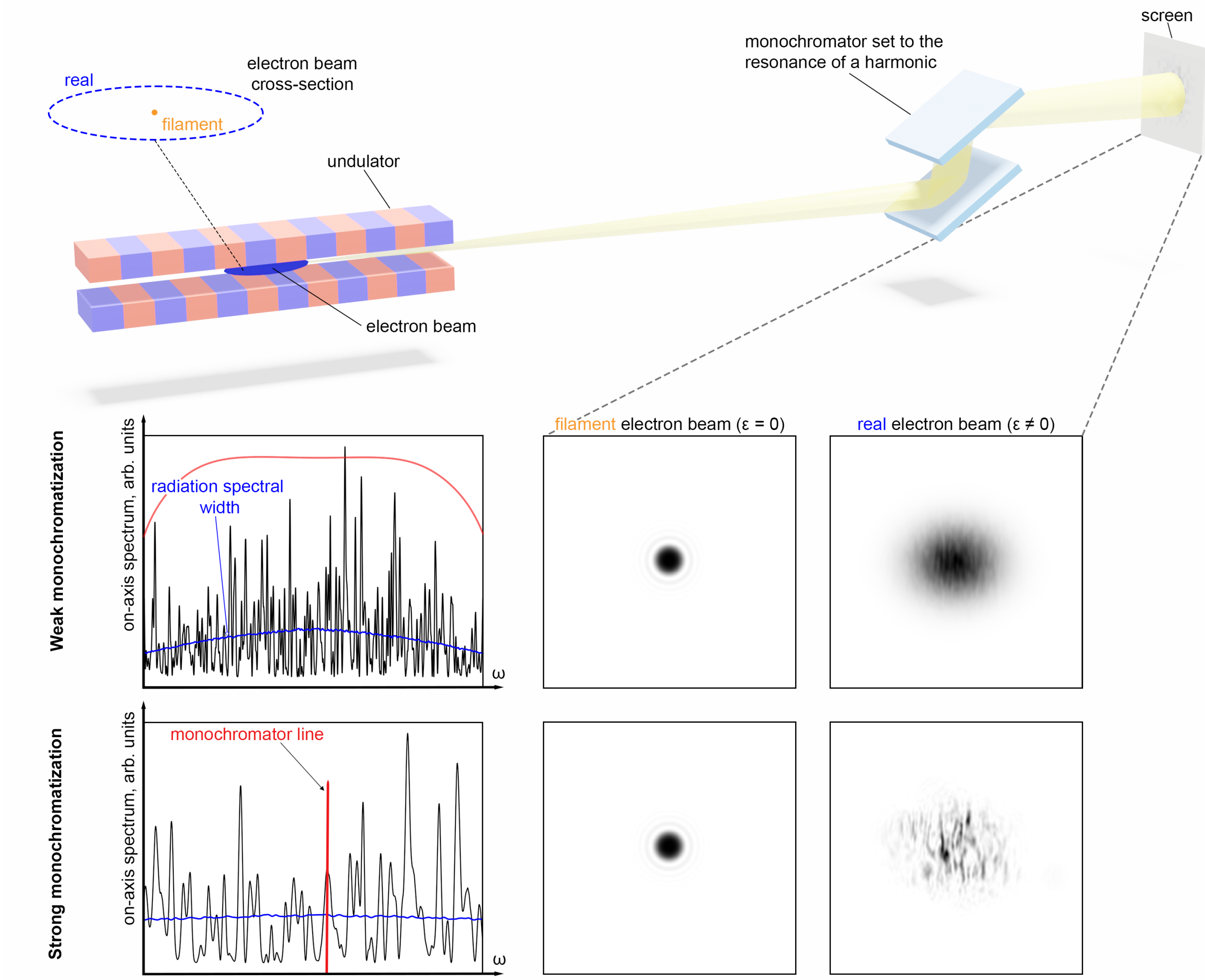

Figure 1: Spiky structure of synchrotron radiation. We compare radiation from a filament electron beam and from an electron beam with non-zero emittance. Figures on the left contain a single realization of spectrum (black lines) and ensemble-averaged spectrum (blue lines). Red lines represent the resolving power of monochromators. The plot on the top row illustrates a typical monochromatization incapable of resolving spectral spikes. To obtain the intensity observed at a detector (after a single passage of the electron beam) one needs to average over these frequencies/realizations. This is justified as the different spikes in the spectrum are not correlated both in time and, correspondingly, in the frequency domain The bottom plot represents the resolving power of a monochromator that allows to resolve a single spectral spike of undulator radiation revealing its transverse spiky structure. Four figures on the right represent transverse intensity distribution upon monochromatization.

larger than the radiation wavelength ($\omega\sigma_T \gg 1$), this we call "long" electron beam approximation, and under this assumption we can express the spatial correlation separately from the longitudinal correlation, via the *cross-spectral density function* G at fixed frequency ω (see e.g. Eq. (12) in [8]):

$$G(z, \vec{r}_1, \vec{r}_2, \omega) \equiv \left\langle \bar{E}(\vec{\eta}, \vec{l}, z, \vec{r}_1, \omega) \bar{E}^*(\vec{\eta}, \vec{l}, z, \vec{r}_2, \omega) \right\rangle, \quad (1)$$

where $\langle \ldots \rangle$ denotes averaging over the ensemble of fields $\bar{E}(\vec{\eta}_k, \vec{l}_k, z, \vec{r}, \omega)$ emitted by electrons with the deflections $\vec{\eta}_{1,\ldots,N_e}$ and offset $\vec{l}_{1,\ldots,N_e}$ at fixed frequency ω. We represent the field of undulator radiation in the $\omega\vec{r}$-domain by a function $\bar{E}(z, \vec{r}, \omega)$, where the radiation field is considered at a given frequency ω. $\bar{E}(z, \vec{r}, \omega)$ is related with the field $E(z, \vec{r}, t)$ in the $t\vec{r}$-domain by an inverse Fourier transform. Then, it is customary to define a normalized version of G, the *spectral the degree of coherence* $g(z, \vec{r}_1, \vec{r}_2)$, as:

$$g(z, \vec{r}_1, \vec{r}_2) = \frac{G(z, \vec{r}_1, \vec{r}_2)}{\sqrt{\langle |\bar{E}(\vec{\eta}, \vec{l}, z, \vec{r}_1)|^2 \rangle \langle |\bar{E}(\vec{\eta}, \vec{l}, z, \vec{r}_2)|^2 \rangle}}. \quad (2)$$

Starting from here we will omit ω in the equations for brevity of the notation.

Quasi-homogeneous Sources

Quasi-homogeneity is the transverse equivalent of quasi-stationarity. It means that at different transverse positions

ISBN: 978-3-95450-220-2 ISSN: 2673-5474 doi: 10.18429/JACoW-FEL2022-MOP03

across the radiation beam intensity $\bar{I}(z,\vec{\bar{r}})$ transverse modes have the same "shape". It allows us to factorize cross-spectral density of the virtual source (located at $z = 0$):

$$G(0,\vec{\bar{r}},\Delta\vec{r}) = \bar{I}(0,\vec{\bar{r}})g(0,\Delta\vec{r}), \quad (3)$$

here we introduced two new variables: $\vec{\bar{r}} = (\vec{r}_1 + \vec{r}_2)/2$ and $\Delta\vec{r} = (\vec{r}_1 - \vec{r}_2)$.

Quasi-homogeneous sources are characterized by a special relation[2], which is strictly related to the van Cittert-Zernike theorem [6,7] between source-intensity distribution $\bar{I}(0,\vec{\bar{r}})$ and spectral[3] degree of coherence in the far zone $g(z_0,\Delta\theta)$, where z_0 denotes position in the far zone. Namely, these two quantities form a Fourier pair. Note that the factorization presented in Eq. (3) is possible if:

(i) intensity of the radiation at the source varies slowly at the scale of coherence length (i.e. large number of transverse modes)

(ii) transverse coherence length does not depend on the transverse position (i.e. similar shape of transverse modes)

SERVAL ALGORITHM

We shape the transverse distribution of the field from an undulator as a Gaussian Random Field (GRF) in a manner similar to those mathematically described in [9], explained in simple words in [10], and exploited in imitating spectra and power distributions of free-electron laser in the linear regime [11,12]

The SERVAL field at the center of undulator ($z = 0$) can be written in the following form:

$$\phi(\vec{r}) = \mathcal{F}^{-1}\left\{\sqrt{\hat{I}(\vec{\theta})}\mathcal{F}\left\{\sqrt{\bar{I}(\vec{r'})}\mathcal{W}(\vec{r'})\right\}(\vec{\theta})\right\}(\vec{r}), \quad (4)$$

where $\mathcal{F}\{\cdot\}(\vec{\theta})$ and $\mathcal{F}^{-1}\{\cdot\}(\vec{r})$ are direct and inverse Fourier transforms, $\mathcal{W}(\vec{r}) = X(\vec{r}) + iY(\vec{r})$ is a complex Gaussian white noise where $X(\vec{r}), Y(\vec{r})$ follow the normal distribution with a mean is equal to zero and a variance is equal to unity. Finally,

$$\bar{I}(\vec{r}) = |\bar{E}_b(0,\vec{r})|^2 = \int_{\mathbb{R}^2} f_l(\vec{l})|\bar{E}(\vec{\eta},\vec{l},0,\vec{r})|^2 d\vec{l}, \quad (5)$$

$$\hat{I}(\vec{\theta}) = |\hat{E}_b(0,\vec{\theta})|^2 = \int_{\mathbb{R}^2} f_\eta(\vec{\eta})|\hat{E}(\vec{\eta},\vec{l},0,\vec{\theta})|^2 d\vec{\eta}, \quad (6)$$

are the intensity distributions of the radiation from the whole electron beam in $\vec{r}$-domain and inverse-spatial $\vec{\theta}$-domain domains, correspondingly. The fields $\bar{E}(\vec{\eta},\vec{l},0,\vec{r})$ and $\hat{E}(\vec{\eta},\vec{l},0,\vec{\theta})$ are calculated with a help of Eq. (39) and Eq. (40) from [13]. $f_l(\vec{l})$ and $f_\eta(\vec{\eta})$ represents (smooth) distribution functions of offsets and deflections of transverse electron beam phase space. The physical idea behind Eq. (4) is that the resulting field $\phi(\vec{r})$ should follow Gaussian statistics and obey the correct first order cross-spectral density function $g(0,\vec{r}_1,\vec{r}_2)$ under the quasi-homogeneous approximation, as we show in Appendix A of the original publication [4]. Following Eq. (4), the proposed algorithm consists of four steps: (i) creating complex Gaussian white noise, (ii) constraining it by the radiation distribution in the spatial domain at the source location, (iii) Fourier transform to inverse-spatial domain, and (iv) constraining the resulting field in the inverse-spatial domain. $\vec{r}$ and $\vec{\theta}$ are assumed to be uncorrelated. Here we discuss these steps in more details:

(i) Creating complex Gaussian white noise $\mathcal{W}(\vec{r}) = X(\vec{r}) + iY(\vec{r})$ in spatial domain.

(ii) Constraining the complex Gaussian white noise by multiplication of the effective distribution of the radiation at the source expressed by Eq. (5). The result of this step is depicted at Fig. 2b.

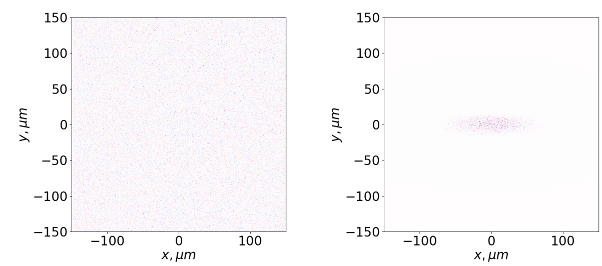

(a) (b)

Figure 2: Intensity of the complex Gaussian white noise in spatial domain before (a) and after constraining (b) by the effective field size.

(iii) Fourier transforming to the inverse-spatial domain (Fig. 3a). At this stage, we have a fully incoherent light source bounded in space akin to a *thermal light source*.

(iv) Constraining the inverse-spatial distribution at Fig. 3a by multiplication with the effective radiation divergence following Eq. (6). This field is ready for propagation through free space, as the free space propagator works in the inverse-space domain.

After an inverse Fourier transform of the field in Fig. 3b back to real space one obtains the intensity distribution at the source, presented in Fig. 4.
As a result Fig. 4 and 3b depict a single realization of undulator radiation distribution at the source (in the center of the undulator cell), seen through a monochromator capable of resolving beyond the width of a single spike in the frequency domain.

[2] Following the reasoning from [8].
[3] Despite the word “spectral”, this degree of coherence determines coherence properties in *real* or *inverse* space domain at given frequency ω, which is implied.

ISBN: 978-3-95450-220-2 ISSN: 2673-5474 doi: 10.18429/JACoW-FEL2022-MOP03

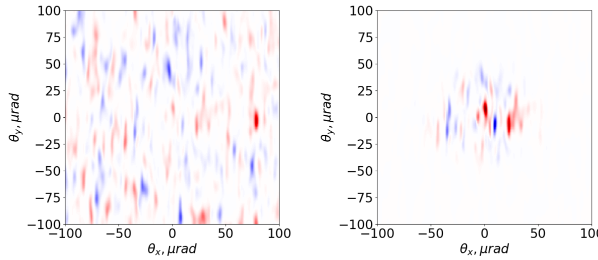

(a) (b)

Figure 3: Angular intensity distribution of the field before (a) and after applying radiation divergence constraints (b).

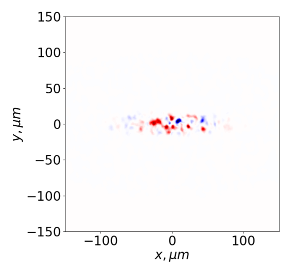

Figure 4: Radiation distribution at the source in real space.

Underlining Assumptions and Approximations

As it was said in the present section and demonstrated in Appendix A of the original publication [4], SERVAL is mathematically well-founded for quasi-homogeneous sources, where the cross-spectral density at the source factorizes Eq. (3). This is a strong restriction. In the Appendix A we show to which extent we can apply SERVAL when quasi-homogeneity (large number of spikes) does not hold. However, we found numerically that our method is satisfactorily applicable if a source is not strictly quasi-homogeneous.

When using SERVAL we consider single-cell undulators: the single source must have only one waist. This basically implies no quadrupoles, phase shifters, etc. in the magnetic structure of the insertion device. For the magnetic structure with imperfections, one can calculate the intensity distributions from a filament beam (Eq. (5) and (6)) numerically for a given magnetic structure and then convolve them with the electron beam phase space. If we simulate the radiation with SERVAL the effects of the electron beam emittance (along with energy spread) are accounted for in $\bar{I}(\vec{r})$ and $\hat{I}(\vec{\theta})$, Eq. (4).

Under these assumptions SERVAL accurately calculates sychrotron radiation pulses with computational advantages over Monte-Carlo-like methods. The SERVAL algorithm is not exclusively restricted to undulators sources, as $\bar{I}(\vec{r})$ and $\hat{I}(\vec{\theta})$ do not impose any additional restrictions except quasi-homogeneity. Thus, this Gaussian random field generator can be used to simulate the stochastic properties of other types of radiation sources.

CONCLUSION

In this contribution, we propose a novel computationally efficient algorithm, SERVAL, for simulating partially coherent synchrotron radiation emitted by an undulator at a specific harmonic. The proposed method is based on generating a Gaussian random field followed by application of constraints in real and inverse space domains. The result exhibits multimode structure which qualitatively corresponds to a radiation "slice" along the radiation pulse or which could be observed experimentally upon extreme monochromatization.

The algorithm yields a radiation field at the source position, which is usually in the middle of the undulator. One can propagate this field through an optical beamline to the sample location by conventional methods and codes for coherent radiation propagation. The proposed algorithm may be exploited for educational purposes when explaining basics of coherence. For more details, see the original publication [4].

ACKNOWLEDGEMENTS

We thank Evgeny Saldin for the initial discussions on the realization of the proposed method and his guiding support. We thank Serguei Molodtsov for his interest in this work.

REFERENCES

[1] A. Singer and I. A. Vartanyants, “Modelling of partially coherent radiation based on the coherent mode decomposition”, in *Advances in Computational Methods for X-Ray Optics II*, Sep. 2011, vol. 8141, p. 814106. `doi:10.1117/12.893618`

[2] O. Chubar, Available: `https://github.com/ochubar/SRW`

[3] O. Chubar and P. Elleaume, “Accurate and efficient computation of synchrotron radiation in the near field region”, in proc. of the *EPAC98 Conference*, 1998, pp. 1177–1179.

[4] A. Trebushinin *et al.*, “Gaussian random field generator for simulating partially coherent undulator radiation”, *Optica*, vol. 9, no. 8, pp. 842–852, Aug. 2022, `https://doi.org/10.1364/OPTICA.460902`

[5] J. W. Goodman, “Statistical Optics”. Wiley, 2015.

[6] P. H. van Cittert, “Die Wahrscheinliche Schwingungsverteilung in Einer von Einer Lichtquelle Direkt Oder Mittels Einer Linse Beleuchteten Ebene”, *Physica*, vol. 1, no. 1, pp. 201–210, Jan. 1934, `doi:10.1016/S0031-8914(34)90026-4`

[7] F. Zernike, “The concept of degree of coherence and its application to optical problems”, *Physica*, vol. 5, no. 8, pp. 785–795, Aug. 1938, `doi:10.1016/S0031-8914(38)80203-2`

[8] G. Geloni, *et al.*, “Transverse coherence properties of X-ray beams in third-generation synchrotron radiation sources”, *Nucl. Instrum. Methods Phys. Res., Sect. A*, vol. 588, no. 3, pp. 463–493, Apr. 2008, `doi:10.1016/j.nima.2008.01.089`

[9] A. Lang, “Simulation of stochastic partial differential equations and stochastic active contours”, Ph.D. Thesis (Universität Mannheim, 2007) `http://ub-madoc.bib.uni-mannheim.de/1770`

ISBN: 978-3-95450-220-2 ISSN: 2673-5474 doi: 10.18429/JACoW-FEL2022-MOP03

[10] G. Goon, "Cosmic Microwave Background simulations", Available: https://github.com/garrett361/cmbpy

[11] T. Pfeifer *et al.*, "Partial-coherence method to model experimental free-electron laser pulse statistics", *Opt. Lett.*, OL, vol. 35, no. 20, pp. 3441–3443, Oct. 2010, doi:10.1364/OL.35.003441.

[12] OCELOT collaboration, Available: https://github.com/ocelot-collab/ocelot

[13] G. Geloni *et al.*, "Fourier treatment of near-field synchrotron radiation theory", *Optics Commun.*, vol. 276, no. 1, pp. 167–179, Aug. 2007, doi:10.1016/j.optcom.2007.03.051.

ISBN: 978-3-95450-220-2 ISSN: 2673-5474 doi: 10.18429/JACoW-FEL2022-MOP06

BRINGING GENESIS TO THE CLOUD WITH SIREPO

C. C. Hall, P. Moeller, J. P. Edelen, E. Carlin, M. Keilman,
G. Khalsa, R. Naglar, R. O'Rouke, RadiaSoft LLC, CO, USA

Abstract

Genesis is widely used in the free electron laser community as a simulation tool for studying both simple and complex FEL systems. Until now, this has necessitated learning the command line interface, which can be challenging for new users. `Sirepo` Genesis provides an intuitive graphic interface for building Genesis simulations in the browser that can then be run using our cloud computing services. Our interface also provides the ability to export simulations for command line use, simulation post-processing with publication quality graphics and the power to share their results with the click of a button to anyone, anywhere, in the world. This poster describes our new GUI and highlights the notable features that have been developed.

INTRODUCTION

RadiaSoft has built a computer aided engineering (CAE) gateway called `Sirepo` [1], using our open source cloud computing framework of the same name [2–4]. `Sirepo` supports over 1,500 (and growing) free users, of whom approximately 200 are active in a given month. `Sirepo` is also available through a series of subscription programs. `Sirepo Premium` provides users enhanced support, greater access to compute cores, and scientific consulting from RadiaSoft scientists and engineers. The US Particle Accelerator School[1] is our first `Sirepo Education` customer and the NSLS-II is our first `Sirepo Private` customer. RadiaSoft supports a few university programs and workshops each year as a service to the community. Recent beneficiaries include Stanford University and the SAGE-S 2021 Summer Camp[2]

`Sirepo` is designed to bring scientific, engineering and educational softwares to the cloud, with a rich browser-based interface that works in any modern browser on any computing device. The number of supported codes is continuing to grow, with more features for code coupling and benchmarking. For particle accelerator modeling, we support: MAD-X, `elegant`, OPAL, Synergia, Zgoubi, Warp PBA (plasma-based accelerators with a cylindrical mesh and azimuthal modes), and JSPEC (electron cooling and intra-beam scattering in rings). For X-ray beamlines, synchrotron radiation and X-ray optics, we support: Shadow for ray tracing and the Synchrotron Radiation Workshop (SRW) for full physical optics. Other interesting apps include: Warp VND (using the Warp code as a 2D and 3D electrostatic PIC engine) to simulate thermionic converters and other vacuum nanoelectronic devices, and the Radia code for magnet design.

More recently, `Sirepo` is supporting our own app, called `Activait`,for the use of machine learning techniques to analyze data. The newest app, called `Controls`, enables users to explore control system algorithms, using MAD-X as a virtual particle accelerator.

Some codes `Sirepo` supports are proprietary, e.g. FLASH for hydrodynamic and MHD plasma simulations. Proprietary codes are enabled through `Sirepo`'s role-based authorization system. Authentication of users is secured through password-less logins via email using short-lived one-time tokens. For some codes, `Sirepo` also gives users the option to launch simulations on the Cori supercomputer at NERSC, if they have access to a NERSC repository. `Sirepo` supports the two-factor authentication mandated by NERSC.

`Sirepo` provides single sign-on access to an integrated Jupyter[3] server, enabling interactive cloud computing with Python and other languages. All of the `Sirepo`-supported codes and associated dependencies are pre-installed, together with standard machine learning tools and libraries. Our Juptyer configuration supports a variety of graphics and numeric libraries including Matplotlib, Pandas, Plotly, Seaborn, and yt.

GENESIS IN SIREPO

We have recently added Genesis to the family of codes supported in `Sirepo`. Due to the uniqueness of Genesis the code the interface does not follow the same convention as many of our other particle accelerator design tools. When users enter the `Sirepo` Genesis app they have access to a sandbox with an array of examples from notable free electron lasers. Figure 1 shows a screenshot of the examples folder in the Genesis application. Note that users can start a simulation from scratch, import an existing simulation, or build off of one of the provided examples.

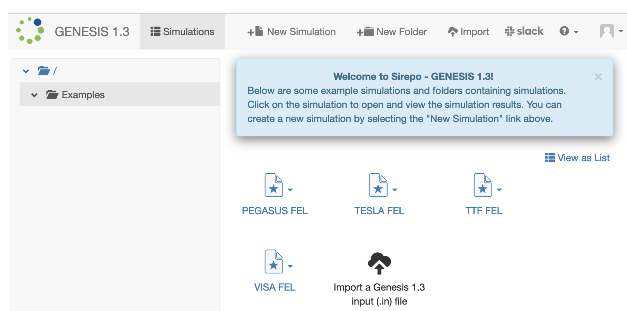

Figure 1: Screenshot of the examples folder for `Sirepo Genesis`.

The app allows users to configure and execute time-independent simulations. Users can adjust all parameters specified in the `Genesis` input file related to time-independent simulations. The full set of `Genesis` inputs are

[1] https://uspas.fnal.gov/
[2] https://conf.slac.stanford.edu/sage/
[3] https://jupyter.org

ISBN: 978-3-95450-220-2 ISSN: 2673-5474 doi: 10.18429/JACoW-FEL2022-MOP06

available to the user. They are broken down based on which aspect of the simulation is being modified, (e.g. the electron beam, the undulator, the simulation parameters such as the resolution, the diagnostic output, etc.). Figure 2 shows a screenshot of the simulation configuration tab. Note that when a user enters the source tab they are only presented with parameters that are directly manipulated as opposed to computed parameters. Computed parameters can be viewed on subsequent pages.

Once the simulation is set up, users are able to execute the simulation and visualize the results in the Visualization tab. The outputs are broken into three reports: Parameter, Particle Distribution, and Field Distribution, Fig. 3. The Parameter report provides information about, for example, the laser power, electron beam bunching, rms parameters, average beam energy, and other aggregate parameters produced by `Genesis`. The Particle Distribution and Field Distribution reports show more fine grain details about the electron beam phase space, as well as the radiation field intensity and phase. Users are able to toggle the output parameters and the appearance of the plots, as well as download PNGs of the reports or the raw data used to produce them if further post-processing is required. We show the beam distribution, the photon distribution, and the beam optics functions as they evolve through the undulator. Figure 3 shows a screenshot of this interface.

FUTURE WORK

We have plans to extend our interface capabilities which will allow users to build undulaors using the familiar drag-and-drop model. We will develop the ability to specify tapering period-by-period, or by using a set of mathematical functions that will automatically compute the tapering from a user-specified function. Users will be able to specify the initial distribution in a Source tab using either the output of a simulation, an external file, or by specifying the relevant bunch parameters such as an initial bunching factor and energy modulation. Finally, we will implement plots of relevant information such as the radiation power, bunching factor, and electron beam phase space, among the other relevant FEL diagnostics, through the `Sirepo` Visualization tab.

We will allow users to specify initial radiation by uploading a supported file format, or by exporting radiation field information from the `SHADOW` and `SRW` simulations. We will also make the exported radiation field from `Genesis` readable by the synchrotron radiation codes for full inter-operability. This will require some extensions to the `Switchyard` class we developed above for exchanging particle data between tracking codes. In the end, we will be able to read in initial particle distributions from any of the accelerator tracking codes, export that particle distribution to a tracking code for modeling the longitudinal phase space diagnostic, and read in radiation fields from a synchrotron radiation code and read out the fields from `Genesis` into those codes.

We also have plans to extend the `Sirepo` framework to handle building multi-code end-to-end simulations of a free electron laser. This includes the photoinjector, LINAC sections, beamline sections, undulators, and diagnostics. The basic back-end code for handing off simulations and controlling the flow in Python exists and is utilized within the RSOpt library. We plan to integrate these features fully into `Sirepo` providing a more integrated development environment for end-to-end modeling.

REFERENCES

[1] "The Sirepo scientific gateway." (2021), `https://sirepo.com`
[2] D. L. Bruhwiler *et al.*, "Knowledge Exchange Within the Particle Accelerator Community via Cloud Computing," in *Proc. IPAC'19*, Melbourne, Australia, May 2019, pp. 3548–3551, `doi:10.18429/JACoW-IPAC2019-THPMP046`
[3] M. S. Rakitin *et al.*, "Sirepo: An open-source cloud-based software interface for x-ray source and optics simulations," *Journal of Synchrotron Radiation*, vol. 25, no. 6, pp. 1877–1892, 2018, `doi:10.1107/S1600577518010986`
[4] "The Sirepo framework for scientific cloud computing." (2021), `https://github.com/radiasoft/sirepo`

ISBN: 978-3-95450-220-2 ISSN: 2673-5474 doi: 10.18429/JACoW-FEL2022-MOP06

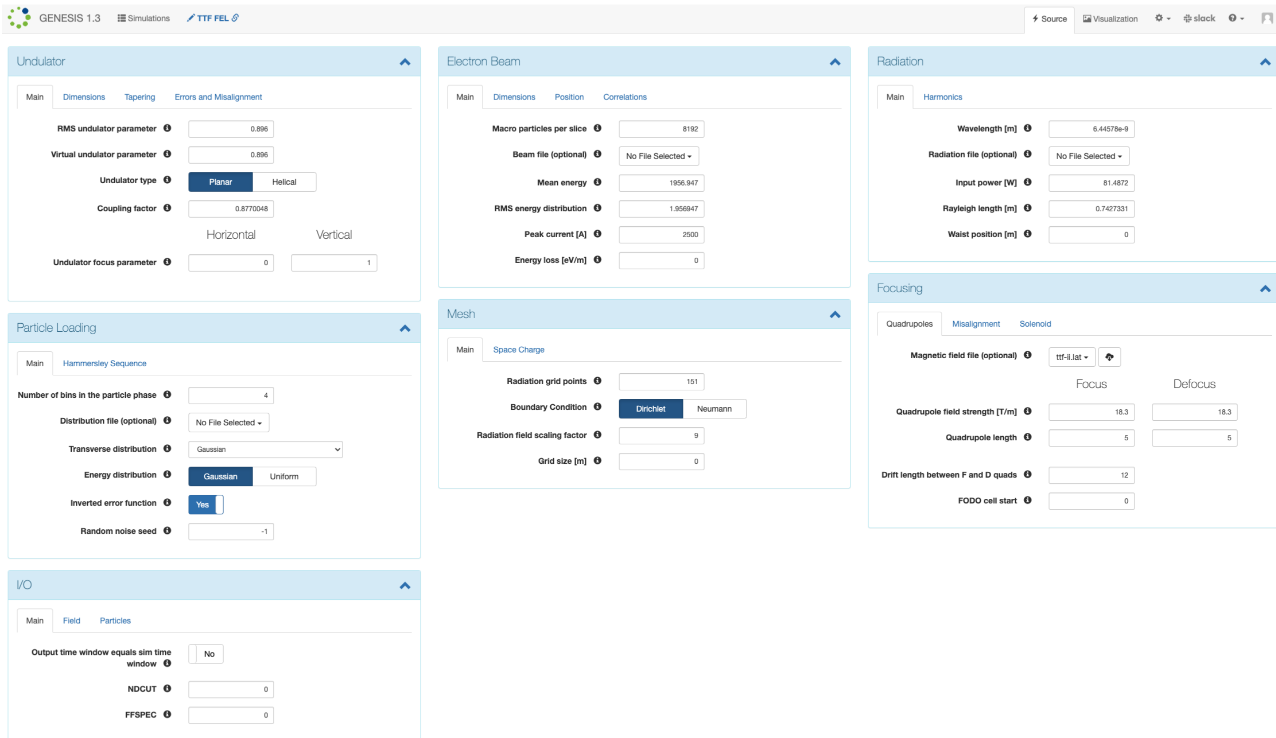

Figure 2: Screenshot of the input tab for building a `Genesis` simulation in `Sirepo`. Note, the user configuration tab is more reminiscent of our JSPEIC tools.

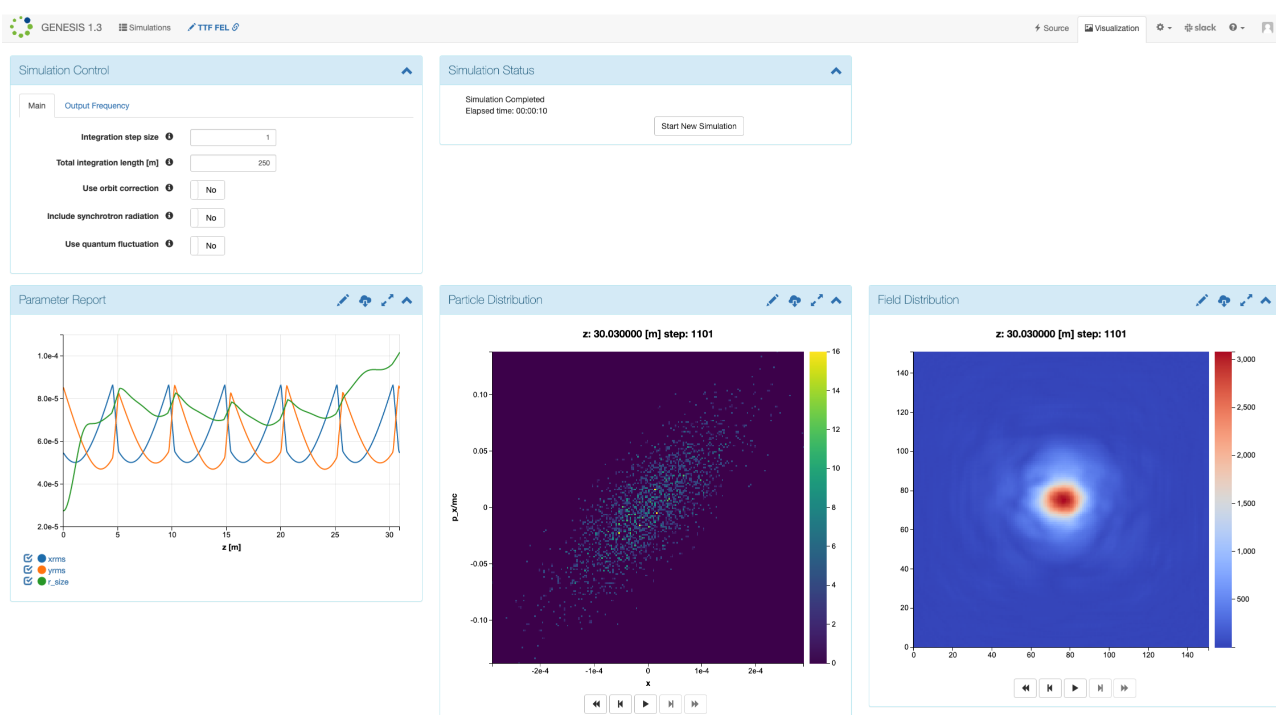

Figure 3: Visualizations of time-independent `Genesis` output.

ISBN: 978-3-95450-220-2 ISSN: 2673-5474 doi: 10.18429/JACoW-FEL2022-MOP07

SPECTROMETER-BASED X-RAY FREE-ELECTRON LASER PULSE DURATION MEASUREMENTS OF CHIRPED BEAMS

R. Robles[1]*, A. Halavanau, A. Lutman, D. Cesar, G. Stupakov,
SLAC National Accelerator Laboratory, Menlo Park, USA
[1]also at Stanford University, Stanford, USA

Abstract

Accurate measurements of the X-ray pulse duration produced by X-ray free-electron lasers (XFELs) typically rely on longitudinal electron beam phase space diagnostics, e.g. in a transverse deflecting cavity or TCAV, or from measurements of spectral correlations. All of the known spectral methods share the weakness that they will underestimate the pulse length in the case that the FEL spectrum is broadened due to the electron beam having an energy chirp. We present a statistical analysis of FEL radiation in the presence of a linear electron beam energy chirp which extends previous results by including an accurate description of the FEL gain process. In doing so, we show that with measurements of the spectral intensity correlations and the average spectrum, one can reconstruct the X-ray pulse length, e-beam chirp, and spectrometer resolution. Our approach is validated by comparison with 1D FEL simulations.

INTRODUCTION

Several methods exist to measure the pulse duration produced by XFELs. One can directly infer something about the XFEL pulse shape and duration if a longitudinal phase space diagnostic is available for the electron beam, such as a transverse deflecting cavity (TCAV) [1]. In practice, however, TCAVs can be difficult to operate and have a limited temporal resolution, about 2-4 fs, particularly at higher beam energies, and thus other methods which do not rely on knowledge of the e-beam phase space pose interest. It has been known for decades that the fluctuations of spectral intensity of the radiation emitted by electron beams stores information about the bunch length [2–5]. A technique applied to the XFEL by Lutman *et al* in [6, 7], showed that by evaluating the spectral intensity correlations, one can reconstruct not only the pulse duration but also the resolution of the spectrometer used to measure the XFEL spectra. A similar approach was recently taken in [8] to unveil slightly more information about the time-frequency correlations of the XFEL pulses. Both of these approaches, as well as other approaches based on studying intensity correlations, are inaccurate if the electron beam has a time-energy correlation or chirp. The presence of the e-beam chirp broadens the FEL spectrum and results in these measurements underestimating the pulse duration [9]. This inability stems from the assumption, in those models, that each electron emits radiation centered around the same central frequency ω_0 defined by the FEL resonance condition.

The behavior of the FEL gain process in the presence of a linear e-beam energy chirp is well-understood, however, and an appropriate Green's function was derived by Krinsky and Huang in [9]. These spectral correlation-based measurements should be extendable to include the chirp. We present a revised analysis of FEL intensity fluctuations in the presence of a linear energy chirp and non-zero spectrometer resolution. By fitting to both the spectral intensity correlation function and the average spectrum, we are able to extract all three parameters - the X-ray pulse length, the electron beam chirp, and the spectrometer resolution. There is inherent uncertainty in this method which stems from ambiguity in the value of the SASE bandwidth, however, we demonstrate that the impact of that uncertainty is negligible on practical measurements. We validate our approach by using it to reconstruct the beam parameters of 1D FEL simulations.

CALCULATION OF SPECTRAL INTENSITY CORRELATION

In an experiment, one typically has access to spectral intensity measurements of the FEL field via spectrometer. The measurement is a convolution of the true intensity spectrum with a spectrometer resolution function:

$$\tilde{S}(\omega) \equiv \int \frac{d\omega}{2\pi} e^{-\frac{(\omega-\omega_0)^2}{2\sigma_m^2}} \left|\tilde{E}(\omega)\right|^2 \quad (1)$$

where σ_m is the spectrometer resolution. The measured spectral intensity correlation is then defined as

$$G_2(\delta\omega) \equiv \frac{\left\langle \tilde{S}(\omega - \frac{\delta\omega}{2})\tilde{S}(\omega + \frac{\delta\omega}{2})\right\rangle}{\left\langle \tilde{S}(\omega - \frac{\delta\omega}{2})\right\rangle \left\langle \tilde{S}(\omega + \frac{\delta\omega}{2})\right\rangle} - 1 \quad (2)$$

We utilize an integral form of this equation given by Eq. (A5), in [6], omitted here for brevity. We now compute two quantities: the spectral field correlation $\left\langle \tilde{E}(\omega - \frac{\delta\omega}{2})E^*(\omega + \frac{\delta\omega}{2})\right\rangle$ and the spectral intensity correlation $\left\langle \left|\tilde{E}(\omega - \frac{\delta\omega}{2})\right|^2 \left|E^*(\omega + \frac{\delta\omega}{2})\right|^2\right\rangle$. We will do this within the framework of [9], which treated a 1D FEL in the high-gain regime including the effects of a linear energy chirp. In this model, the SASE electric field takes the form

$$E(t) = \sum_j e^{i\omega_j\left(\frac{z}{c}-(t-t_j)\right)} g(t-t_j) h_{td}(t_j) \quad (3)$$

where $\omega_j = \omega_0 + ut_j$ is the frequency of light emitted by the j-th electron which is the central frequency ω_0 offset by a

* This work was supported by the Department of Energy, Laboratory Directed Research and Development program at SLAC National Accelerator Laboratory, under contract DE-AC02-76SF00515.

ISBN: 978-3-95450-220-2 ISSN: 2673-5474 doi: 10.18429/JACoW-FEL2022-MOP07

term proportional to the electron beam chirp u. Furthermore,

$$g(t) \propto \exp\left[-b\left(t-\frac{z}{v_g}\right)^2 - \frac{iu}{2}\left(t-\frac{z}{v_0}\right)\left(t-\frac{z}{c}\right)\right] \quad (4)$$

is the time-independent gain function. The parameter $b = \frac{3}{4}\left(1+\frac{i}{\sqrt{3}}\right)\sigma_\omega^2$ where $\sigma_\omega^2 = \frac{3\sqrt{3}\rho}{k_w z}\omega_0^2$ is the SASE bandwidth. Furthermore, $v_g = \omega_0/(k_r + \frac{2}{3}k_u)$ and $v_0 = \omega_0/(k_r + k_u)$ with $k_r = 2\pi/\lambda_r$ the radiation wavenumber, $k_u = 2\pi/\lambda_u$ the undulator wavenumber, and ω_0 the central resonant FEL frequency. We note here that this model is valid only for small chirps where $u \ll \sigma_\omega^2$. The function $h_{td}(t_j)$ is a stand-in for any time-dependent effect in the gain process, and can thus account for variations in the e-beam current profile, in principle, undulator taper, etc. With these definitions, the frequency domain field is defined by the Fourier transform

$$\tilde{E}(\omega) \equiv \int e^{i\omega t}E(t)dt = \sum_j e^{i\left(\frac{\omega_j}{c}z+\omega t_j\right)}\tilde{g}(\omega-\omega_j)h_{td}(t_j) \quad (5)$$

where $\tilde{g}(\omega) \equiv \int e^{i\omega t}g(t)dt$. The spectral field correlation is then evaluated as a double sum, however, under the assumption that the beam particle arrival times are independent we can reduce it to a single sum. Similarly, the intensity correlation is a four-way sum which can be reduced to two. The process is similar to that found in [6, 10], and we omit the details here. The resulting correlations are

$$\left\langle \tilde{E}\left(\omega-\frac{\delta\omega}{2}\right)\tilde{E}^*\left(\omega+\frac{\delta\omega}{2}\right)\right\rangle = \tilde{F}(\omega,\delta\omega) \quad (6)$$

$$\left\langle \left|\tilde{E}\left(\omega-\frac{\delta\omega}{2}\right)\right|^2\left|\tilde{E}^*\left(\omega+\frac{\delta\omega}{2}\right)\right|^2\right\rangle = \quad (7)$$

$$\tilde{F}\left(\omega-\frac{\delta\omega}{2},0\right)\tilde{F}\left(\omega+\frac{\delta\omega}{2},0\right)+\left|\tilde{F}(\omega,\delta\omega)\right|^2,$$

where $\tilde{F}(\omega,\delta\omega)$ is defined as:

$$\tilde{F}(\omega,\delta\omega) \equiv \left\langle \sum_j e^{-i\delta\omega t_j}\tilde{g}\left(\omega-\omega_j-\frac{\delta\omega}{2}\right)\times \right. \quad (8)$$

$$\left. \times\tilde{g}^*\left(\omega-\omega_j+\frac{\delta\omega}{2}\right)|h_{td}(t_j)|^2\right\rangle$$

With this definition we can write G_2 as

$$G_2(\delta\omega) = \left[\int d\Delta d\Omega e^{-\frac{\Delta^2}{4\sigma_m^2}-\frac{\Omega^2}{\sigma_m^2}}\left|\tilde{F}(\omega+\Omega,\delta\omega+\Delta)\right|^2\right] / \quad (9)$$

$$\left[\int d\Delta d\Omega e^{-\frac{\Delta^2}{4\sigma_m^2}-\frac{\Omega^2}{\sigma_m^2}}\times\right.$$

$$\left.\times\tilde{F}\left(\omega+\Omega+\frac{\Delta+\delta\omega}{2},0\right)\tilde{F}\left(\omega+\Omega-\frac{\Delta+\delta\omega}{2},0\right)\right]$$

Our expression for $\tilde{F}$ can be simplified further by replacing the ensemble average of the sum with an integral over the beam current distribution $f(t)$, as

$$\tilde{F}(\omega,\delta\omega) = \int dt_j f(t_j)|h_{td}(t_j)|^2 e^{-i\delta\omega t_j}\times \quad (10)$$

$$\times\tilde{g}\left(\omega-\omega_j-\frac{\delta\omega}{2}\right)\tilde{g}^*\left(\omega-\omega_j+\frac{\delta\omega}{2}\right)$$

So far we have left h_{td} inexplicit, which is problematic for future applications. To resolve this, we may connect it to the average X-ray intensity profile $\chi(t)$ by first writing

$$\chi(t) \equiv \left\langle|E(t)|^2\right\rangle = \int dt_j f(t_j)|h_{td}(t_j)|^2|g(t-t_j)|^2 \quad (11)$$

In the limit that the bunch is long compared to the inverse of the SASE bandwidth, $\sigma_t\sigma_\omega \gg 1$, the SASE Green's function $g(t)$ is much narrower than the product $f(t)|h_{td}(t)|^2$, and thus behaves much like a delta function, allowing us to write the proportionality

$$\chi(t) \propto f(t)|h_{td}(t)|^2 \quad (12)$$

Thus, up to some multiplicative factor that will drop out of G_2 in the end, we may write

$$\tilde{F}(\omega,\delta\omega) = \int dt_j\chi(t_j)e^{-i\delta\omega t_j}\times \quad (13)$$

$$\times\tilde{g}\left(\omega-\omega_j-\frac{\delta\omega}{2}\right)\tilde{g}^*\left(\omega-\omega_j+\frac{\delta\omega}{2}\right)$$

One can easily carry out these calculations for the Green's function described by Eq. (4) for a gaussian X-ray intensity profile, $\chi(t) = e^{-t^2/2\sigma_t^2}$, which yields G_2 in the form

$$G_2(\delta\omega) = \frac{1}{\sqrt{1+2\sigma^2\sigma_t^2}}\exp\left[-\frac{\delta\omega^2\sigma_t^2\xi_0^2}{1+2\sigma^2\sigma_t^2}\right] \quad (14)$$

where to make an explicit connection to [6] we define

$$\sigma = \frac{\sqrt{2}\sigma_m\sigma_\omega}{\sqrt{\sigma_m^2+(1+\delta_u^2)\sigma_\omega^2}} \qquad \xi_0 = \frac{\sigma_\omega^2\sqrt{1+\delta_u^2}}{\sigma_m^2+(1+\delta_u^2)\sigma_\omega^2} \quad (15)$$

where $\delta_u^2 = \tilde{u}+\tilde{u}^2\left(1+3\sigma_t^2\sigma_\omega^2\right)$ with $\tilde{u} \equiv u/\sqrt{3}\sigma_\omega^2$. If the bunch is long enough that $\frac{u\sigma_t}{\sigma_\omega}$ is of order one, then $\delta_u \simeq u\sigma_t/\sigma_\omega$. Finally, we also note that the average spectral intensity can be written as

$$F(\omega,0) \propto \exp\left[-\frac{(\omega-\omega_0)^2}{2(\sigma_m^2+\sigma_\omega^2(1+\delta_u^2))}\right] \quad (16)$$

Taking Eqs. (14) and (16) together, we have a total of four unknown parameters σ_m, σ_t, σ_ω, and u. By fitting to the measured spectrum and the measured G_2 we can extract three parameters in the form of the amplitude of G_2, the width of G_2, and the width of the spectrum. Assuming we can estimate the SASE bandwidth reasonably well, we can then solve for the three remaining parameters to extract the bunch length, beam chirp, and spectrometer resolution.

ISBN: 978-3-95450-220-2 ISSN: 2673-5474 doi: 10.18429/JACoW-FEL2022-MOP07

VALIDATION WITH 1D FEL SIMULATIONS

To verify the equations derived in the previous section, we performed simulations using a one-dimensional FEL code. The parameters common to all simulations are shown in Table 1. We scanned the chirp of the electron beam over a wide range of values, performing 1000 statistically independent simulations at each working point in order to generate sufficient statistics for calculating G_2 and the average spectral intensity. The undulator length of 30 m was chosen such that the simulation ends during the exponential gain regime where the equations explicitly apply. To mimic a true experimental measurement, we computed the spectral intensity $\left|\tilde{E}(\omega)\right|^2$ and convolved it with a gaussian of width 0.2 eV, as in Eq. (1). As stated in the previous section, the method demands some prior knowledge of the SASE bandwidth, which we can estimate as $\sigma_\omega = \sqrt{\frac{3\sqrt{3}\rho}{k_w z}\omega_0^2} = 4.55$ eV.

Table 1: 1D FEL Simulation Parameters

Parameter	Unit	Value
Beam energy	GeV	12.1
Beam energy spread	MeV	0.726
Norm. emittance	µm rad	0.6
Peak current	kA	3
β function	m	25
Undulator period	cm	3
Undulator K		3.5
Radiation wavelength	nm	0.19061
Bunch shape		Gaussian
RMS bunch length	µm	2
Undulator length	m	30

The results of the reconstruction are shown in Fig. 1. In it we see that, in spite of the varying chirp and therefore varying bandwidth and G_2, our model can successfully extract the correct pulse length. A naive application of the model of [6] would on the other hand predict a successively smaller pulse length as the chirp was increased. In addition to that, the chirp itself is effectively reconstructed, as is the spectrometer resolution.

SENSITIVITY TO THE KNOWLEDGE OF SASE BANDWIDTH

Since the method we have laid out leaves the SASE bandwidth unspecified, it is worth considering how sensitive the predictions are to the estimated value of σ_ω. To understand this we should look explicitly at the fitted solutions. In particular, suppose from our measurements we extract $G_2(\delta\omega) = A_G e^{-\delta\omega^2/2\sigma_G^2}$ and $\tilde{F}(\omega, 0) \propto e^{-(\omega-\omega_0)^2/2\sigma_{BW}^2}$. Equating these with Eqs. (14) and (16) allows us to solve explicitly for σ_m, σ_t, and u. In doing so we find that

$$\sigma_m = \frac{\sigma_G \sigma_{BW}\sqrt{1-A_G^2}}{\sqrt{2\sigma_{BW}^2 + (1-A_G^2)\sigma_G^2}} \tag{17}$$

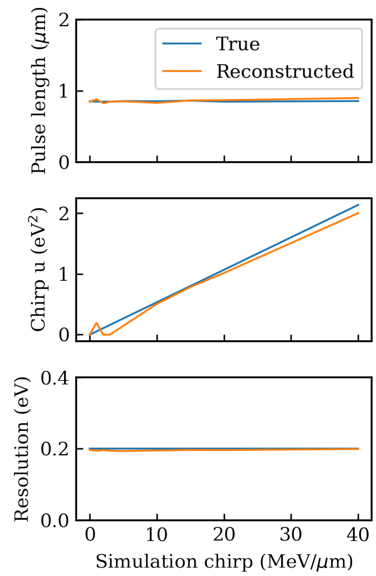

Figure 1: Reconstruction of X-ray pulse length, e-beam chirp, and spectrometer resolution from 1D simulations.

The spectrometer resolution prediction is thus independent of the SASE bandwidth estimate. The pulse length, on the other hand, is

$$\sigma_t = \frac{\sqrt{2\sigma_{BW}^2 + (1-A_G^2)\sigma_G^2}}{2A_G\sigma_G\sigma_\omega} \tag{18}$$

and the chirp is

$$u = \frac{1}{\sigma_t}\sqrt{\frac{2\sigma_{BW}^4}{2\sigma_{BW}^2 + (1-A_G^2)\sigma_G^2} - \sigma_\omega^2} \tag{19}$$

Now we can identify two regimes. When δ_u is large compared to one, Eqs. (14) and (16) show that σ_{BW} reduces to $u\sigma_t$, and σ_G becomes $u^2/2\sigma_\omega^2$. Then, neglecting for the moment the spectrometer resolution, our predictions for both σ_t and u (as in Eqs. (18) and (19)) become independent of the SASE bandwidth. In the opposite limit, the spectral bandwidth reduces to roughly the SASE bandwidth, while the width of G_2 becomes roughly independent of the SASE bandwidth. As such, σ_t remains insensitive to σ_ω while u becomes heavily sensitive to σ_ω. Thus we conclude that regardless of the chirp value, our reconstructions of the bunch length and spectrometer resolution are relatively insensitive to our knowledge of the SASE bandwidth. The chirp, on the other hand, can be quite sensitive to σ_ω if $u\sigma_t/\sigma_\omega \simeq 1$, but becomes less and less sensitive as this parameter grows.

Let us consider this concretely in the case of the previous section. We plot the reconstructed pulse length and chirp as a function of the SASE bandwidth estimate in Fig. 2 for two different values of the chirp, indicated in the legend. Dashed lines represent the true value. In the top figure, it is clear that at both chirp working points the estimate of the pulse length is relatively insensitive to the SASE bandwidth. The chirp,

ISBN: 978-3-95450-220-2 ISSN: 2673-5474 doi: 10.18429/JACoW-FEL2022-MOP07

on the other hand, portrays a relatively weak dependence on bandwidth for the larger chirp case, but a stronger one for the weaker chirp case. We note that this reconstruction method will be most relevant when the chirp is larger anyways, so this does not substantially limit its applicability.

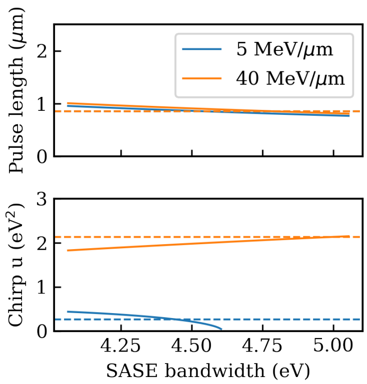

Figure 2: Dependence of pulse length and chirp reconstruction on the estimate of the SASE bandwidth.

CONCLUSIONS

We have performed an analysis of FEL intensity fluctuations when the electron beam is chirped and demonstrated that the combination of the spectral intensity correlation and the average spectrum provides sufficient information to reconstruct the X-ray pulse length, the e-beam chirp, and the resolution of the spectrometer used for the measurement. The reconstructions are technically dependent on a guess of the SASE bandwidth but are found to be insensitive to it in regimes where the reconstruction would be useful. We have validated our method using 1D FEL simulations. Further validation with 3D FEL simulations and experiments will be the subject of future work.

ACKNOWLEDGEMENTS

Authors would like to thank E. Hemsing and W. Fawley (SLAC) for useful discussions on the topic.

REFERENCES

[1] C. Behrens *et al.*, “Few-femtosecond time-resolved measurements of x-ray free-electron lasers,” *Nat. Commun.*, vol. 5, no. 1, pp. 1–7, 2014. `doi:10.1038/ncomms4762`

[2] J. Krzywinski, E. Saldin, E. Schneidmiller, and M. Yurkov, “A new method for ultrashort electron pulse-shape measurement using synchrotron radiation from a bending magnet,” *Nucl. Instrum. Methods Phys. Res., Sect. A*, vol. 401, no. 2-3, pp. 429–441, 1997. `doi:10.1016/S0168-9002(97)00987-X`

[3] M. S. Zolotorev and G. V. Stupakov, “Spectral Fluctuations of Incoherent Radiation and Measurement of Longitudinal Bunch Profile,” in *Proc. PAC'97*, Vancouver, Canada, May 1997.

[4] F. Sannibale, G. Stupakov, M. Zolotorev, D. Filippetto, and L. Jägerhofer, “Absolute bunch length measurements by incoherent radiation fluctuation analysis,” *Phys. Rev. Spec. Top. Accel Beams*, vol. 12, no. 3, p. 032 801, 2009. `doi:10.1103/PhysRevSTAB.12.032801`

[5] I. Lobach *et al.*, “Transverse beam emittance measurement by undulator radiation power noise,” *Phys. Rev. Lett.*, vol. 126, p. 134 802, 13 2021. `doi:10.1103/PhysRevLett.126.134802`

[6] A. Lutman *et al.*, “Femtosecond x-ray free electron laser pulse duration measurement from spectral correlation function,” *Phys. Rev. Spec. Top. Accel Beams*, vol. 15, no. 3, p. 030 705, 2012. `doi:10.1103/PhysRevSTAB.15.030705`

[7] A. Lutman, Z. Huang, J. Krzywinski, J. Wu, D. Zhu, and Y. Feng, “Statistical characterization of an x-ray FEL in the spectral domain,” in *Society of Photo-Optical Instrumentation Engineers (SPIE) Conference Series*, vol. 10237, 2017, paper 102370H, 102370H. `doi:10.1117/12.2268918`

[8] S. Serkez *et al.*, “Wigner distribution of self-amplified spontaneous emission free-electron laser pulses and extracting its autocorrelation,” *J. Synchrotron Radiat.*, vol. 28, no. 1, pp. 3–17, 2021. `doi:10.1107/S160057752001382X`

[9] S. Krinsky and Z. Huang, “Frequency chirped self-amplified spontaneous-emission free-electron lasers,” *Phys. Rev. Spec. Top. Accel Beams*, vol. 6, no. 5, p. 050 702, 2003. `doi:10.1103/PhysRevSTAB.6.050702`

[10] E. L. Saldin, E. A. Schneidmiller, and M. Yurkov, “Statistical properties of radiation from vuv and x-ray free electron laser,” *Opt. Commun.*, vol. 148, no. 4-6, pp. 383–403, 1998. `doi:10.1016/S0030-4018(97)00670-6`

ISBN: 978-3-95450-220-2 ISSN: 2673-5474 doi: 10.18429/JACoW-FEL2022-MOP09

ORIGIN OF ECHO-ENABLED HARMONIC GENERATION*

Vladimir N Litvinenko, Stony Brook, NY, USA

Abstract

In this paper I present an overview of two preprints that were published at Budker Institute of Nuclear Physics in 1980. These original publications describing harmonic generation technique which has the same foundation as Echo-Enabled Harmonic Generation (EEHG). They recently become available online, but they are still unknown to FEL community. This paper is an attempt to current this omission.

INTRODUCTION

When I first read about EEHG [1], it vaguely reminded me of a theory developed at Novosibirsk Institute of Nuclear Physics (BINP) in late 1970s. But I was not 100% sure that my memory of decades-old events was correct.

Recently, the BINP made their preprint available on the web [2] and I was able to confirm that technique proposed by I.G. Idrisov and V.N. Pakin [3, 4] based on the similar principles to those described in [1]. In this presentation I would like to briefly review these original papers and give credit to early inventors of this innovative high-harmonic generation technique.

These papers, see Fig. 1, were written in Russian in form of preprints and were not available outside the Iron Curtain –- a typical totalitarian method of preventing the exchange of information. Hence, in general, only people from BINP had direct exposure to these findings. The goal of this short

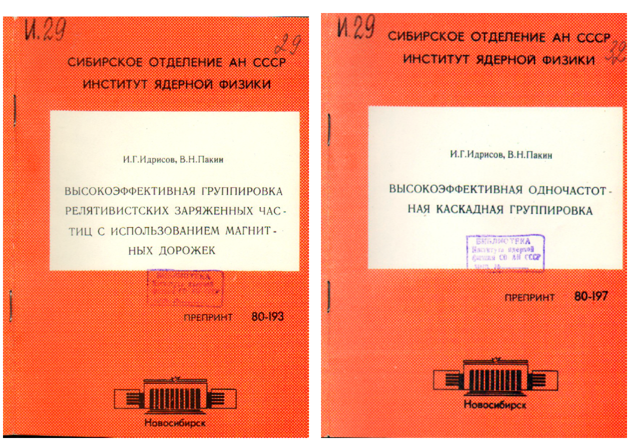

Figure 1: Cover pages of the two preprints.

paper is to give historic perspective on EEHG and to provide FEL community with references to these original papers. I attempted to translate snippets of the original texts and use as many as possible of original illustrations. Unfortunately, quality of some illustrations is poor.

* Work supported by DE-SC0020375 grant from the Office of High Energy Physics, US Department of Energy.

CONTENT OF TWO PREPRINTS

It is impossible to include all text, formulae, figures, and tables from two preprints in this 4-page paper. When it is necessary, I will put in brackets references to these preprints. For example, Fig. [3](3) or Eq. [4](5) will mean Fig. 3 in Ref. [3] and Eq. (5) in Ref. [4], correspondingly. Similarly, Section [3](2.3) means section 2.3 in Ref. [3].

Abstract [3](1) We demonstrate possibility of high efficiency bunching of relativistic beams using magnetic compressors. We show that amplitude of the current in in first harmonic is possible to increase to 1.9·I_0 and the current in 10th harmonic to 1.8·I_0 (where I_0 is the current in un-bunched beam), or even higher….. High efficiency in amplitudes of high harmonics is achieved using strong compression (to be exact – over-compression using large *R56 - VL*) at initial stages and very strong (increasing) energy modulation in the later stages of the bunching.

Abstract [4](1) We show in this paper that using strong compression (e.g. over-compression) in first compressors, followed by increasing amplitude of energy modulation in the following steps of cascade bunching system allows to increase efficiency of the modulation to 1.76·I_0, 1.94·I_0 and 1.98·I_0 (where I_0 is the current in un-bunched beam) using two, three and four cascades, correspondingly.

[4](2) KINEMATIC APPROACH

[4](2.1) *Cascade Bunching*

Figure 2 [4](1) shows a typical schematic of cascade bunching.

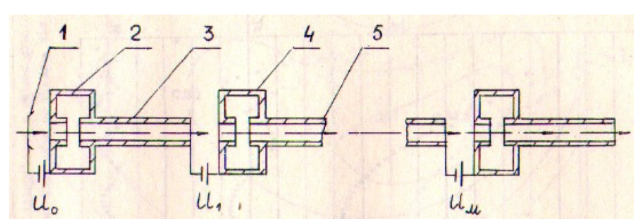

Figure 2: [4](1) Schematic of multi-stage bunching.

A continuous beam with current I_0 from the cathode (1) is accelerated to energy eU_0 and passes through first RF cavity (2), where its energy (velocity) modulated by RF voltage U_{m1}. The drift (3) turns energy modulation into density (current) modulation…. This process is repeated with U_1, U_2, … representing modulation at each stage.

[4](2.2) *Idealized Equations for Phase Motion – Efficiency of Harmonic Generation*

For simplification, let's consider a reference particle which does passing all cavities at zero-crossings:

$$U_1 = U_2 = \dots = 0$$

ISBN: 978-3-95450-220-2 ISSN: 2673-5474 doi: 10.18429/JACoW-FEL2022-MOP09

…We assume that relative energy modulation is small that second order effects can be neglected, and that depth of energy modulation is increasing from stage to stage. …

These assumptions allow us to write following set of equations:

$$\varphi_1 = \varphi - \chi_1 \cdot \sin\varphi \qquad (1)$$

with compression parameter

$$\chi_1 = \frac{\alpha_1 \theta_1}{2} \qquad (2)$$

where θ_1 is the drift parameter[1] and

$$\alpha_1 = \frac{U_1}{U_0}; \;\; \alpha_i = \frac{U_i}{U_0}; \;\; \alpha_1 \ll \alpha_2 \ll \ldots \ll 1\,, \qquad (3)\ \underline{[4](3)}$$

being the depth energy modulation in first section[2]. Then at the exit of 2 stages we have [4](4):

$$\begin{aligned}\varphi_2 = \varphi_1 - \chi_2 \cdot \sin\varphi_1 = (\varphi - \chi_1 \cdot \sin\varphi) \\ - \chi_2 \cdot \sin(\varphi - \chi_1 \cdot \sin\varphi i)\end{aligned} \qquad (4)$$

By induction, at k[th] stage, we can write Eq. [4](5):

$$\begin{aligned}\varphi_k = \varphi_{k-1} - \chi_k \cdot \sin\varphi_{k-1} = (\varphi i_{k-2} - \chi_{k-1} \cdot \sin\varphi_{k-2}) \\ -\chi_k \cdot \sin(\varphi_{k-2} - \chi_{k-1} \cdot \sin\varphi_{k-2}) = \ldots\end{aligned} \qquad (5)$$

We expand the beam current at the exit of k[th] stage [4](6):

$$i_k = I_o \left(1 + 2\sum_{n=1}^{\infty} f_{n,k}(\chi_1, \chi_2, \ldots \varphi_k)\right) \cos n\varphi_k \qquad (6)$$

where Fourier coefficients $f_{n,k}$ represents amplitudes of n[th] harmonic in beam current units of $2I_o$, and therefore, the maximum possible efficiency of generating n[th] harmonics [4](7):

$$\eta(n,k) = f_{n,k} = \frac{1}{\pi} \int_0^{\pi} \cos(\varphi_k(\chi_1, \chi_2, \ldots \varphi))d\varphi \qquad (7)$$

Integral (6) can be analytically evaluated for $k = 1$, but for arbitrary k should be evaluated numerically.

[4](2.3) *Results of Numerical Simulations*

To find maximum possible efficiency Eq. (7) it is necessary to find the extremum of $f_{n,k}(\chi_1, \chi_2, \ldots \chi_k)$. We used the Gauss-Seidel method described in D.J. Wild, *Extremum Methods*, Nauka, Moscow, 1967. Results for systems with two and three stages are shown in Tables 1 and 2. It is possible to notice that parameters χ approaching constant values for high harmonic numbers, which we could call "asymptotic compression parameters".

We calculated efficiencies of first 50 harmonics for compression parameters χ close to asymptotic values and summarized them in Table 3.

K = I	χ_1 = I,08		
K = 2	χ_1 = 2,08	χ_2 = I,08	
K = 3	χ_1 = 3,60	χ_2 = I,92	χ_3 = I,05

[1] Since focus of these papers was on non-relativistic devices, authors used not a modern notation such as $R_{56} = \theta_1/2$

[2] In modern language relevant to EEHG.

Table 1: [4](1) Maximum efficiency for system with two stages.

n	$\eta_e(n,2)_{макс}$	χ_1	χ_2
I	0,879	3,II	I,5I
2	0,842	2,82	I,33
3	0,8I9	2,65	I,25
5	0,790	2,47	I,I8
I0	0,749	2,24	I,II

Table 2: [4](2) Maximum efficiency for system with three stages.

n	$\eta_e(n,3)_{макс}$	χ_1	χ_2	χ_3
I	0,97I	4,08	2,75	I,28
2	0,962	3,97	2,50	I,20
I0	0,937	3,60	I,92	I,05

Table 3: [4](3) Efficiencies of harmonic generation in systems with one, two and three stages.

n	$\eta_e(n,1)$	$\eta_e(n,2)$	$\eta_e(n,3)$
I	0,465	0,823	0,959
3	0,349	0,778	0,947
I0	0,269	0,740	0,937
30	0,2I3	0,672	0,9I4
50	0,I70	0,570	0,878

This table shows that $\eta(n,k)$ remains large for $n > 10$ for two stage, and especially for three stage system. It means that current distribution approaching an ideal, δ-function-like, distribution. Figure 3 [3](2) illustrates phases at the exits of the first, second and third stages. … Figures 4 and 5 show that the area of efficient harmonic generation is reduces for higher harmonics … Further numerical studies, not included in this preprint, showed that area with high efficiency of harmonic generation increases when number of cascades is increased.

$$\alpha_1 = \frac{\delta\gamma_1}{\gamma_0}$$

[4](2.3) *Discussions*

Our studies showed that large compression parameters are needed for high efficiency of harmonic generation in multistage system … Our simulations showed that inclusion of modest velocity spreads does not significantly affect efficiency of harmonic generation with $n \leq 10$ …

Figure 3 shows the dependence of phases at the exits to that at the entrance of the first, second and third stages. Crosses show them for compression parameters optimal for first (fundamental) harmonic. Dots are compression parameters close to asymptotic values. 50 traces were used.

ISBN: 978-3-95450-220-2 ISSN: 2673-5474 doi: 10.18429/JACoW-FEL2022-MOP09

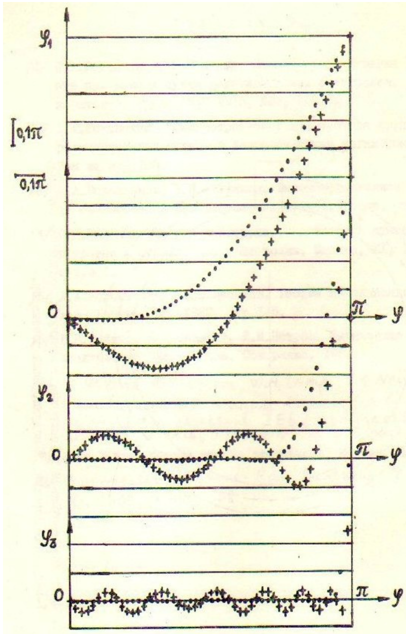

Figure 3: [3](2) Dependence of phases at the exits of the first, second and third stages on that at the entrance of the system.

Figures 4 and 5 show contour plots if the efficiencies for generating first (fundamental) and fifth harmonics in two stage system.

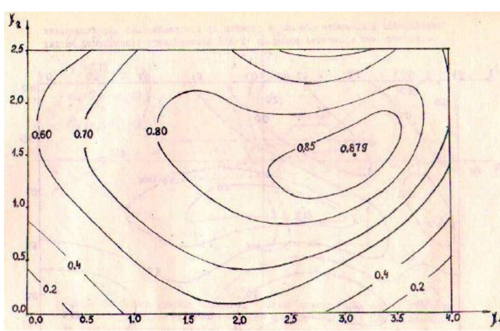

Figure 4: [4](3) Efficiency contour plot for first harmonic in two stage system as function of $\chi_{1,2}$.

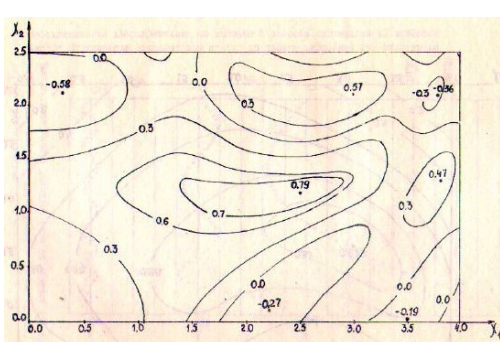

Figure 5: [4](4) Efficiency contour plot for fifth harmonic in two stage system as function of $\chi_{1,2}$.

Figure 6 show an example of the phase space evolution in two-stage system with $\chi_1 = 3.12$ and $\chi_2 = 1.51$ and $\alpha_2/\alpha_1 = 5$ …

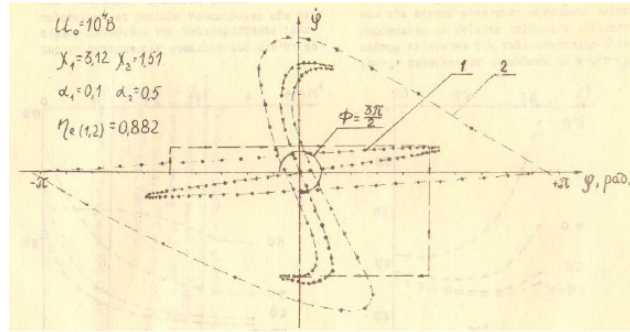

Figure 6: [4](5) Location of test particles in the longitudinal phase space $(\varphi, \dot{\varphi})$. Curve 1 – at the exits of the stage one; Curve 2 – at the exit of stage 2.

To simulate the evolution in this two-stage system 101 test particles were used. Arrows in the figure show phase trajectories of the particles with maximum perturbation in the first stage of the system. One can see that the location of these particles rotated in the phase-space by $\Phi = 3\pi/2$ with respect to initial position The overall particle flow resembles whirling about the origin with strong phase compression towards the center. … Increasing number of stages increases the number of swirls with critical trajectories rotating by $5\pi/2, 7\pi/2$, etc.

[3](2.4) *Discussions of Results*

The necessity of applying strong energy modulation and compression parameters to achieve effective harmonic generation, $f_{n,k}$ is related a sine-wave modulation of the energy… Hence, the goal of effective bunching is to compress as many particles as possible (locate in interval of initial phases of $\pm\pi/2$) close to the origin…

Figure 7 shows step by step evolution of particles in a two-stage system with large ratio of energy modulation in the first and the second sections: $\alpha_2/\alpha_1 = 9$.

[3](2.4) *Conclusions*

Our investigations showed that use of multi-stage systems with high compression parameters provides for high efficiency bunching and harmonic generation.

This concludes the review of these two preprints. Authors also discussed effects of space charge, which I omitted for compactness and relevance to EEHG.

DISCUSSIONS AND CONCLUSION

It is rather obvious that focus of two preprints was on bunching of relatively low energy beams used in klystrons, even though relativistic effects were considered in Ref. [3]. Vinokurov and Skrinsky clearly described both similarity and differences between beam dynamics in optical

ISBN: 978-3-95450-220-2 ISSN: 2673-5474 doi: 10.18429/JACoW-FEL2022-MOP09

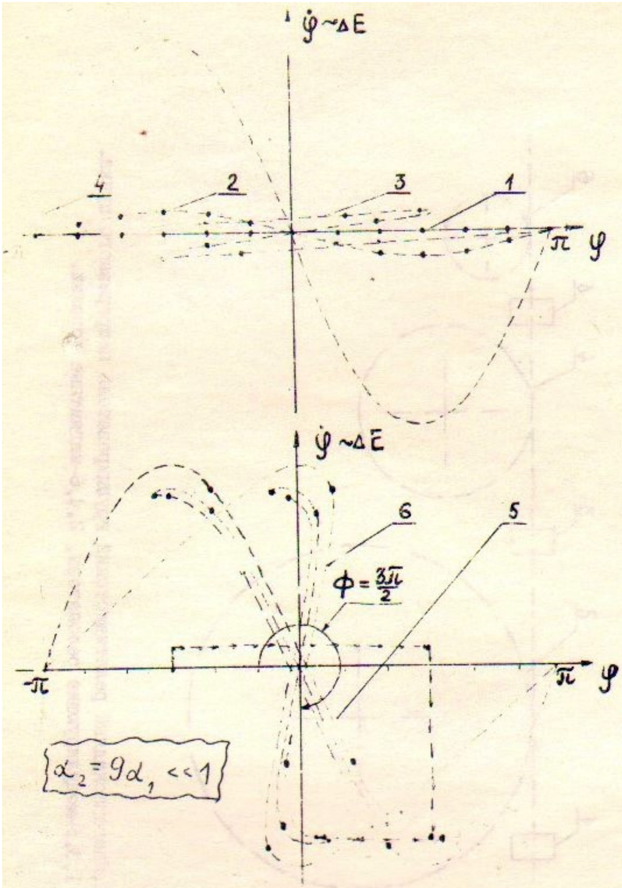

Figure 7: [3](5) particle's evolution in the longitudinal phase space for a two-stage system. Curves in these plots are as follows: 1 – initial particle's positions; 2 – positions after energy modulation in first section; 3 - positions after the first drift; 4 - energy modulation in the second section; 5 - positions after energy modulation in the second section; 6 - positions after second drift.

klystron [5], i.e. in an FEL, and its low energy cousin. Since then, it became apparent that many ideas, including harmonic generation, are applicable – albeit with careful formulation – to FELs. One of very important considerations in for FEL is clearly including well-known bunching suppressions caused by the uncorrelated energy spread [5]:

$$\rho_k \to \rho_k \cdot exp\left(-\frac{1}{2}\left(\frac{kR_{56}\sigma_\gamma}{\gamma}\right)^2\right) ,$$

where is k-vector of the radiation.

Still, kinematics of the efficient high harmonic generation in FELs, known as EEHG [1], has the same origin as that described in the two preprints: (a) after first energy modulation bunch is over compressed to create filamentation in beam energy; (b) applying second energy modulation at the same frequency and optimum R_56, transfers filamentation into the longitudinal density modulation – see Fig. 8.

Finally, one of the interesting hints from these original preprints is that there is potential of furthering efficiency

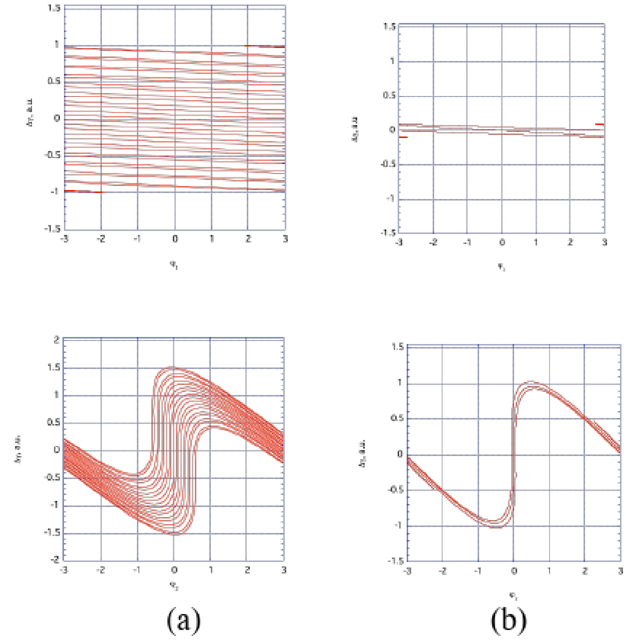

Figure 8: Phase space diagrams: top is after first section, and bottom – after the second section. Two "EEHG" schemes generate the same amplitude of harmonics but use different ratio between amplitude of energy modulation: (a) $\delta\gamma_1 = \delta\gamma_2$; (b) $\delta\gamma_1 = \delta\gamma_2/10$. Vertical scale is in units of $\delta\gamma_1$.

of high harmonic generation by using varying strengths of modulation in two, three, or even more, bunching stages. With modern computers these possibilities can be easily explored [6].

REFERENCES

[1] G. Stupakov, "Using the Beam-Echo Effect for Generation of Short-Wavelength Radiation", *Phys. Rev. Lett.*, vol. 102, p. 074801, 2009. doi:10.1103/PhysRevLett.102.074801

[2] https://www.inp.nsk.su/librarydb

[3] I.G. Idrisov and V.N. Pakin, "High efficiency bunching of ultra-relativistic beams using magnetic compressors", Preprint 80-192 of Institute for Nuclear Physics, October 3, 1980, Novosibirsk, Russia (in Russian).

[4] I.G. Idrisov and V.N. Pakin, "High efficiency cascade bunching using a single frequency modulation" Preprint 80-197 of Institute for Nuclear Physics, October 3, 1980, Novosibirsk, Russia (in Russian)

[5] N. A. Vinokurov and A. N. Skrinsky, Preprint No. INP 77-59, 1977, Novosibirsk, Russia.

[6] X. Yang, G. Penn, L. H. Yu, V. Smaluk, and T. Shaftan, "Optimization of echo-enabled harmonic generation toward coherent EUV and soft X-ray free-electron laser at NSLS-II", *Sci. Rep.*, vol. 12, p. 9437, 2022. doi:10.1038/s41598-022-13702-3

ISBN: 978-3-95450-220-2 ISSN: 2673-5474 doi: 10.18429/JACoW-FEL2022-MOP19

FIRST COMMISSIONING OF THE PROOF-OF-PRINCIPLE EXPERIMENT ON A THz SASE FEL AT THE PITZ FACILITY

P. Boonpornprasert*, Z. Aboulbanine, G. Adhikari, N. Aftab, R. General, G. Georgiev, J. Good, M. Gross, L. Heuchling, A. Hoffmann, M. Homann, L. Jachmann, D. Kalantaryan, W. Köhler, G. Koss, M. Krasilnikov, X.-K. Li, A. Lueangaramwong, S. Maschmann, D. Melkumyan, F. Müller, R. Netzel, R. Niemczyk, A. Oppelt, B. Petrosyan, S. Philipp, M. Pohl, H. Qian, A. Sandmann-Lemm, C. Richard, C. Rüger, M. Schade, E. Schmal, J. Schultze, F. Stephan, G. Vashchenko, T. Weilbach
Deutsches Elektronen-Synchrotron DESY, Zeuthen, Germany
B. Krause, E. Schneidmiller, M. Tischer, P. Vagin, M. Yurkov
Deutsches Elektronen-Synchrotron DESY, Hamburg, Germany
A. Brachmann, N. Holtkamp, H.-D. Nuhn
SLAC, Menlo Park, CA 94025, United States

Abstract

Research and development of an accelerator-based THz source prototype for pump-probe experiments at the European XFEL are ongoing at the Photo Injector Test Facility at DESY in Zeuthen (PITZ). A proof-of-principle experiment to generate THz SASE FEL radiation using an LCLS-I undulator driven by an electron bunch from the PITZ accelerator has been prepared. After four years of designs and construction, the first commissioning with an electron beam was started in July 2022. This paper presents and discusses the experience and results of the first commissioning.

INTRODUCTION

The European XFEL has planned to perform THz pump–X-ray probe experiments at the full bunch repetition rate for users. A promising concept to provide the THz pulses with a pulse repetition rate identical to that of the X-ray pulses is to generate them using an accelerator-based THz source [1, 2]. The Photo Injector Test Facility at DESY in Zeuthen (PITZ) is an ideal machine as a prototype for developments of the THz source [3]. Proof-of-principle experiments to generate the THz SASE FEL by using an LCLS-I undulator driven by a high-charge (2-4 nC) electron bunch from the PITZ accelerator has been planned and studied. Start-to-End simulations for this setup, i.e. beam momentum of about 17 MeV/c, a photocathode laser pulse duration of 10 ps FWHM and a peak current of 200 A, yielded a THz pulse energy of about 0.5 mJ at a central wavelength of 100 µm [4–6].

The PITZ beamline has been extended and improved for the proof-of-principle experiments. A schematic overview of the PITZ beamline and the extension into a tunnel annex currently under installation is shown in Fig. 1. The beamline extension consists of a bunch compressor, an LCLS-I undulator, two beam dumps, magnets, screen stations, and other diagnostic devices. More information on the progress of the beamline extension is reported in [7].

* prach.boonpornprasert@desy.de

In July 2022, screen stations and magnets in the straight section of the extended beamline were installed and operable. We performed the first commissioning of the extended beamline by transport and matching a beam with a bunch charge of 100 pC through the undulator. Then, the transport and matching were repeated with higher bunch charges, 500 pC and 1 nC, respectively. We also measured the output radiation from the undulator using a THz pyroelectric detector.

CORRECTION AND STOP COILS

Beam transport and matching through the undulator are crucial for the first commissioning. For beam momentum of about 17 MeV/c, the transverse gradient of the undulator will lead to a significant off-axis trajectory in the horizontal plane [8]. To compensate the effect of the horizontal gradient on the beam path, a pair of correction coils was designed and installed at the undulator as shown in Fig. 2.

Five identical pairs of short coils are installed uniformly along the longitudinal axis of the undulator. Each pair of short coils is designed to stop a 20 MeV/c beam inside the undulator by horizontally bending the beam up to 10 mrad (applied a current of 3.3 A) to the vacuum pipe for measuring energy gain curve of the SASE FEL. Figure 3 shows the design of the stop coils and the first pair of stop coils installed at the undulator.

BEAM COMMISSIONING

For the first beam commissioning in the undulator, an electron beam with a 100 pC bunch charge was considered, which is much lower than our nominal charge of 4 nC. With a lower bunch charge, the hardware, e.g., screen stations and magnets, could be tested while being protected from high radiation exposure. A smaller beam size is achievable at lower charges, which is beneficial to transport the beam in the narrow vacuum chamber and to test the matching procedure in the undulator. The machine and beam parameters are summarized in Table 1, where the gun and booster phases are the relative phases with respect to the maximum mean momentum gain (MMMG).

ISBN: 978-3-95450-220-2 ISSN: 2673-5474 doi: 10.18429/JACoW-FEL2022-MOP19

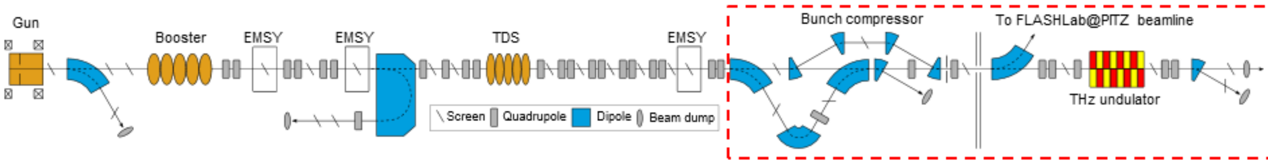

Figure 1: Schematic overview of the complete PITZ beamline. The beamline modification and extension for the proof-of-principle experiments to generate the THz SASE FEL at PITZ is surrounded by the red dashed box.

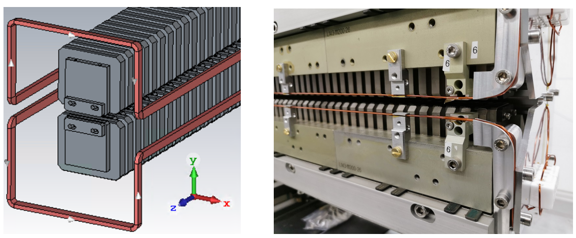

Figure 2: Design of the pair of compensation coils (left) and the pair of the compensation coils installed at the undulator (right).

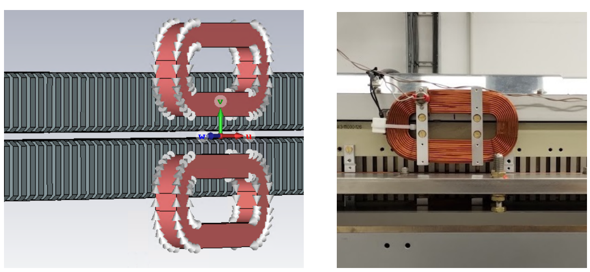

Figure 3: Design of the pair of stop coils (left) and the pair of stop coils installed at the undulator (right), the bottom stop coil is behind the frame.

Table 1: Machine and Beam Parameters for the First Commissioning

Parameters	**Values**
Laser distribution	Gaussian
Laser pulse duration	7 ps FWHM
Gun gradient	57.55 MV/m
Gun phase	0 degree
Booster gradient	12.25~15.93 MV/m
Booster phase	0~45°
Undulator periods	3 cm × 113
Undulator parameter	3.49
Vacuum chamber size	11 mm and 5 mm
Vacuum chamber length	3.4 m
Bunch charge	0.1-1 nC
Beam emittance	>1.5 mm mrad
Beam momentum	17 MeV/c
Resonance wavelength	100 µm

Beam Characterization, Transport and Matching at 100 pC

The photocathode RF gun was driven by a longitudinally Gaussian laser (7 ps FWHM). A beam shaping aperture (BSA) of 1 mm diameter was applied to cut out a flattop transverse distribution. The beam was accelerated by the gun to a momentum of 6.3 MeV/c and then by the booster accelerator to 17 MeV/c, which corresponds to the resonance wavelength of 100 µm. For the 100 pC beam, the emittance was measured using the slit-scan method at several locations downstream of the booster. Figure 4 shows the transverse phase spaces at the measurement site closest to the booster (z = 5.28 m from the cathode).

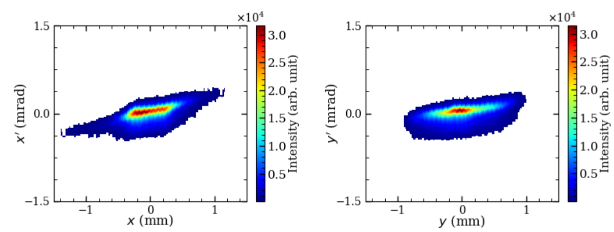

Figure 4: Phase spaces in (left) horizontal and (right) vertical planes of the 100 pC beam, with normalized emittance of 1.5 mm mrad.

Since the undulator is about 25 m downstream of the booster accelerator, the beam needs to be focused by several quadrupole magnets before being matched to the undulator. We have established a focusing procedure that only involves the increase of the amplitude of the quadrupole currents after degaussing. This has allowed us to recover the beam easily after temporary shutdowns, which are common during the commissioning stage. The beam matching procedure discussed in [9] was also applied and proven effective. The measured beam envelop along the beamline is shown in Fig. 5 (Top). The correction coils were used for optimizing the beam trajectory in the undulator and a flat beam profile was observed at the undulator exit as shown in Fig. 5 (Bottom), which agreed with the simulation results.

Beam Transport and Matching at 1 nC

After successful beam transport in the undulator at 100 pC, the bunch charge was increased, first to 500 pC and then to 1 nC, with similar focusing and matching procedures. Figure 6 shows the 1 nC beam transport and its transverse profile at the undulator exit. The beam size for 1 nC was much bigger than that for 100 pC and was also not flat, due to several reasons. First, the photocathode laser used for 100 pC was broken and another laser with a much smaller spot size was

ISBN: 978-3-95450-220-2 ISSN: 2673-5474 doi: 10.18429/JACoW-FEL2022-MOP19

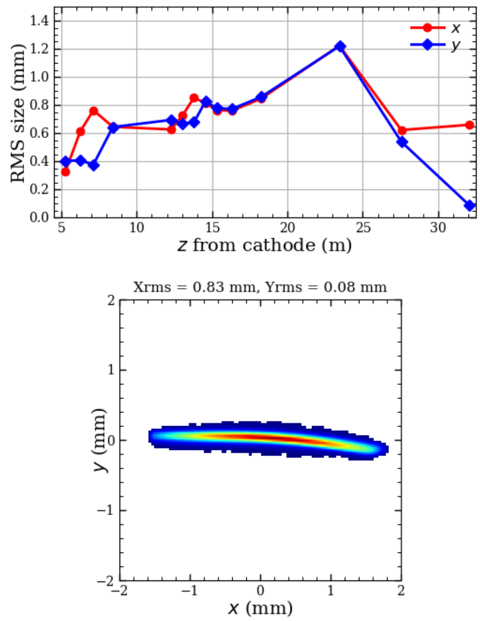

Figure 5: (Top) Transport of the 100 pC beam from the booster exit to the undulator exit and (Bottom) the beam profile at the undulator exit (z ~ 32 m).

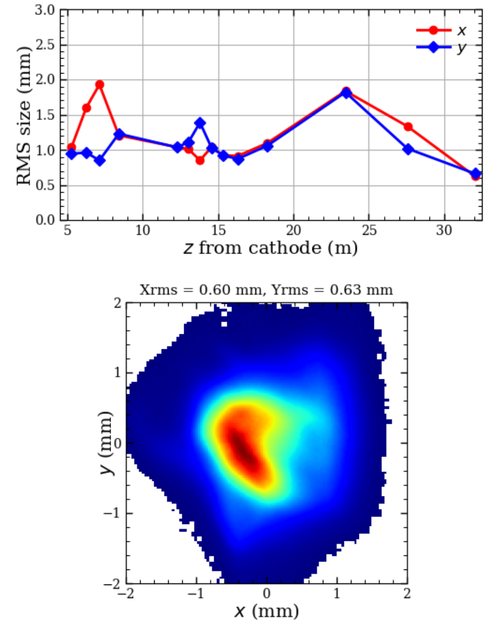

Figure 6: (Top) Transport of the 1 nC beam from the booster exit to the undulator exit and (Bottom) the beam profile at the undulator exit (z ~ 32 m).

put into operation for 1 nC. This means much stronger space charge effects during emission and acceleration in the gun. Second, the matching procedure depended on simulations, which were not done for the latter laser but for the laser used for 100 pC. Even though, the beam was still small enough to fit the vacuum chamber. The replacement laser couldn't produce more than 1 nC. After fixing the broken laser, the bunch charge will be increased up to 4 nC for further commissioning.

RADIATION MEASUREMENT

The first screen station downstream of the undulator is equipped with an in-vacuum gold-coating mirror to deflect the radiation from the undulator to a THz pyroelectric detector through a vacuum diamond window. The mirror has a circular aperture with a diameter of 5 mm to allow the electron beam to go through without hitting the mirror. The radiation transmitted through the diamond window is collected by an aluminum collector cone and transported to the detector. The measured signal from the detector is amplified by a voltage preamplifier and measured by an oscilloscope. The first measured waveform of the radiation from the undulator is shown in Fig. 7. An average pulse energy of 421±6 nJ was measured when the 1-nC beam at 45° off-crest booster phase passed through the undulator.

CONCLUSION AND OUTLOOK

The first commissioning of the extended PITZ beamline with a 100-pC beam was done successfully. We could transport the beam through the undulator, and the matching pro-

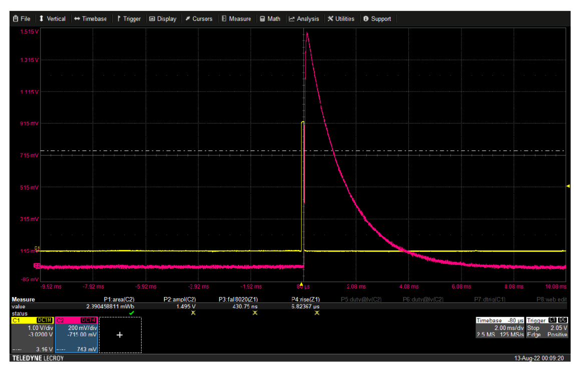

Figure 7: A screenshot of the oscilloscope shows the first measured waveform of the radiation from the undulator.

cedure was proven effective. Then, commissioning with a 1 nC beam was done, and we could measure a radiation pulse energy of 421 nJ from the undulator when operating at 45° off-crest booster phase.

Recently, commissioning with higher bunch charges, 2 – 3 nC, has been performed. Measurements of the THz generation have been taken and the statistics properties analysis reflects the expected SASE performance [10]. For further commissioning, a 3 THz band-pass filter will be used to verify the wavelength of radiation pulses. The design and installation of a THz diagnostic station are ongoing. This station can measure the spectral and transverse profiles of the radiation pulses using a Michelson interferometer and a THz camera, respectively. Installation of the THz diagnostic station, the second beam dump, and other devices are expected to be finished and will be commissioned this fall.

ISBN: 978-3-95450-220-2 ISSN: 2673-5474 doi: 10.18429/JACoW-FEL2022-MOP19

After the commissioning phase, we will continue improving the output FEL properties. A seeding scheme can be used to improve the coherent properties and shot-to-shot stability. Simulation studies of seeding options for THz FEL at PITZ are reported in [11]. We also plan to compress the beam to ultra-short (sub-ps) bunch using the bunch compressor and produce superradiant undulator radiation [12].

ACKNOWLEDGEMENTS

This work was supported by the European XFEL research and development program.

REFERENCES

[1] P. Zalden *et al.*, "Terahertz Science at European XFEL", European XFEL, Schenefeld, Germany, Rep. XFEL.EU TN-2018-001-01.0, 2018.

[2] E. Schneidmiller, M. V. Yurkov, M. Krasilnikov, and F. Stephan, "Tunable IR/THz Source for Pump Probe Experiments at the European XFEL", in *Proc. FEL'12*, Nara, Japan, Aug. 2012, paper WEPD55, pp. 503–506.

[3] P. Boonpornprasert, "Investigations on the Capabilities of THz Production at the PITZ Facility", Department of Physics, Universität Hamburg, Hamburg, Germany, 2020.

[4] M. Krasilnikov, P. Boonpornprasert, H.-D. Nuhn, E. Schneidmiller, F. Stephan, and M. V. Yurkov, "Start-to-End Simulations of THz SASE FEL Proof-of-Principle Experiment at PITZ", in *Proc. ICAP'18*, Key West, Florida, USA, Oct. 2018, pp. 246–252. doi:10.18429/JACoW-ICAP2018-TUPAF23

[5] X. Li *et al.*, "Design Studies of a Proof-of-Principle Experiment on THz SASE FEL at PITZ", in *Proc. IPAC'19*, Melbourne, Australia, May 2019, pp. 1713–1716. doi:10.18429/JACoW-IPAC2019-TUPRB018

[6] X. Li *et al.*, "Progress in Preparing a Proof-of-Principle Experiment for THz SASE FEL at PITZ", in *Proc. FEL'19*, Hamburg, Germany, Aug. 2019, pp. 41–44. doi:10.18429/JACoW-FEL2019-TUP002

[7] T. Weilbach *et al.*, "Status of the THz@PITZ Project - The Proof-of-Principle Experiment on a THz SASE FEL at the PITZ Facility", in *Proc. IPAC'22*, Bangkok, Thailand, Jun. 2022, pp. 1033–1036. doi:10.18429/JACoW-IPAC2022-TUPOPT016

[8] M. Krasilnikov *et al.*, "Modeling the Magnetic Field of the LCLS-I Undulator for THz@PITZ", in *Proc. IPAC'21*, Campinas, Brazil, May 2021, pp. 3855–3858. doi:10.18429/JACoW-IPAC2021-THPAB049

[9] X. Li *et al.*, "Matching of a Space-Charge Dominated Beam into the Undulator of the THz SASE FEL at PITZ", in *Proc. IPAC'21*, Campinas, Brazil, May 2021, pp. 3244–3247. doi:10.18429/JACoW-IPAC2021-WEPAB257

[10] M. Krasilnikov *et al.*, "First Lasing of the THz SASE FEL at PITZ", presented at FEL'2022, Trieste, Italy, Aug. 2022, paper MOA08, this conference.

[11] G. Georgiev *et al.*, "Simulations of Seeding Options for THz FEL at PITZ", presented at FEL'2022, Trieste, Italy, Aug. 2022, paper TUP40, this conference.

[12] N. Chaisueb, P. Boonpornprasert, M. Krasilnikov, X.-K. Li, A. Lueangaramwong, and S. Rimjaem, "Numerical Simulation of a Superradiant THz Source at the PITZ Facility", in *Proc. IPAC'22*, Bangkok, Thailand, Jun. 2022, pp. 1063–1066. doi:10.18429/JACoW-IPAC2022-TUPOPT027

ISBN: 978-3-95450-220-2 ISSN: 2673-5474 doi: 10.18429/JACoW-FEL2022-MOP20

OPTICAL-CAVITY BASED SEEDED FEL SCHEMES TOWARD HIGHER REPETITION RATE AND SHORTER WAVELENGTHS

G. Paraskaki*, S. Ackermann, DESY, Hamburg, Germany
G. Geloni, European XFEL, Hamburg, Germany
B. Faatz, C. Feng, B. Liu, H. Sun, SARI, Shanghai, China

Abstract

More and more high-gain SASE FELs operate at high repetition rates, either in burst or in continuous wave mode of operation, offering an unprecedented number of electron bunches per second. External seeding techniques provide high quality FEL pulses of full coherence and shot-to-shot stability but cannot keep up with MHz repetition rates of such FELs due to their dependence on the seed laser repetition rate. One attractive solution to overcome this limitation is to employ an optical cavity to store radiation that acts as a seed for the electron bunches arriving at high repetition rates. Such a scheme not only allows seeded operation at multi-MHz repetition rates but also introduces the possibility to achieve seeded radiation at shorter wavelengths, overcoming the hurdle of insufficient power availability of seed laser systems in the vacuum ultraviolet (VUV) wavelength range. Here, we present different optical-cavity-based schemes and we give an overview of their unique capabilities together with simulation results.

INTRODUCTION

Most high-gain Free-Electron Laser (FEL) facilities have so far delivered radiation which is transversely coherent, but longitudinally contains spikes that are not correlated in time. The main reason for this is that the radiation is built up from noise in a single pass and the statistics of the initial noise cause a noisy output [1]. Several schemes have been proposed to increase the longitudinal coherence of FEL radiation without the decrease in the pulse energy implied by monochromatization. However, this has turned out to be a challenge, especially at high repetition rates and some wavelength ranges.

One promising direction to improve the longitudinal coherence is a scheme called self-seeding [2, 3], where the amplification process of the radiation starts from noise. The amplified FEL radiation is then monochromatized and serves as a seed for further amplification in a second stage where a clean spectrum can be achieved. This scheme works well for hard x-rays and high repetition rate when heat loading of crystals is not critical [4]. The disadvantage is that it has relatively large intensity fluctuations.

Another interesting direction is to use external seeding techniques [5, 6] to achieve fully coherent FEL pulses. In this paper, we focus on the limits of external seeding and present a scheme that overcomes them. The limitations are twofold, namely the limit of available energy of the seed laser at short wavelength and at high repetition rates. Typically, at wavelengths below 200 nm the intensity of seed lasers reduces significantly. And with the required seed energy, there is no laser available that exceeds approximately a few tens of kHz repetition rate. For these reasons, in this paper we study an alternative solution aiming at external seeding without the need of a high repetition rate and powerful seed laser system.

The simulations shown in this paper make use of the high gain harmonic generation (HGHG) external seeding scheme [5, 7]. We increase the repetition rate of the scheme by using an optical cavity that recirculates a seed at high repetition rates. The FEL process is simulated with Genesis 1.3 [8] while the treatment of the radiation field in the optical cavity is done in ocelot [9]. As examples, we show simulations performed using parameters of FLASH [10] and of the Shenzhen FEL.

SIMULATIONS PERFORMED

For this study, parameters for FLASH and for the Shenzhen FEL have been taken as example, as shown in Table1. Because the main interest is in the shortest achievable wavelength, which should be 4 nm at FLASH and 2.5 nm at the Shenzhen FEL, only the shortest seed wavelength, which is assumed to be 50 nm is studied in this paper.

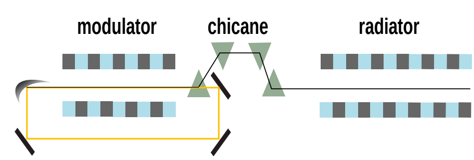

Figure 1: Geometry simulated for FLASH for a cavity-based HGHG setup. Important simulation parameters are given in Table 1.

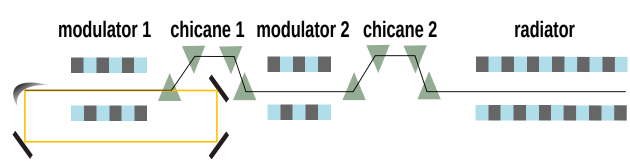

Figure 2: Geometry simulated for the Shenzhen FEL for a cavity-based harmonic optical klystron. Important simulation parameters are given in Table 1.

In both schemes, the process can be initiated by an external seed laser, which seeds the first bunch in a train. After

* georgia.paraskaki@desy.de

ISBN: 978-3-95450-220-2 ISSN: 2673-5474 doi: 10.18429/JACoW-FEL2022-MOP20

Table 1: FLASH and Shenzhen parameters used for the simulations.

	FLASH	Shenzhen
Electron beam		
Beam energy	1.35 GeV	2.53 GeV
Peak current	1 kA	0.8 kA
Emittance, norm. (x,y)	1 mm · mrad	0.5 mm · mrad
Energy spread	0.12 MeV	0.16 MeV
Bunch length	100 µm	120 µm
Modulator Undulator	**planar**	**planar**
Period	60 mm	50 mm
K_{rms}	3.2	9.80 / 4.75
Segment length	2.7 m	3 m
Number of segments	1+1	2+1
Main Undulator	**planar**	**planar**
Period	30 mm	20 mm
K_{rms}	0.97	3.21
Segment length	2.16 m	4 m
Number of segments	12	4

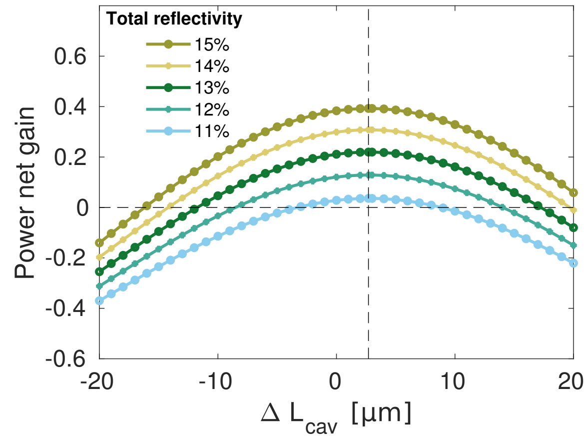

Figure 3: For a different set of total reflectivities of the cavity, a different detuning of the cavity offers zero power net gain and thus steady state. To reach this steady state, a power build-up is required at a detuning that offers positive power net gain.

the seed pulse has modulated the electron beam inside the modulator, it is recirculated to overlap with the next bunch in the train of bunches. In this case, the seed laser is amplified in the modulator to compensate for resonator losses. This has as advantage that the seed power is relatively stable from the start. However, it is difficult to find a seed laser with enough power at short wavelengths. This has been described in Refs. [11–14].

As alternative, one can also start from noise. In this case, initially, several bunches out of the bunch train are needed to build up enough power that could act as seed (power build-up regime). Once this power level is reached, the recirculated seed power needs to be stabilized at this level (steady-state regime). A higher power would mean a larger induced energy spread that would prevent amplification at the harmonic of interest in the amplifier downstream, and is thus undesired. The process starting from noise is studied in this paper for FLASH and the Shenzhen FELs with final wavelengths of 4.17 and 2.5 nm, respectively. In both cases, a 50 nm seed is assumed and the seeding scheme used is high-gain harmonic generation (HGHG) [5, 7].

RESONATOR CONFIGURATION FOR FLASH

The simplest resonator amplifier configuration uses a modulator inside a resonator, where the downstream mirror is placed inside the bunching chicane as shown in Fig. 1. In the case starting from shot noise, it is difficult to control the gain to transition from the power build-up to the steady-state regime. Different methods to control the gain are discussed in [13] and here we take advantage of the gain dependence on the cavity length. By detuning the cavity length, a transition from positive net gain to zero net gain is possible. Here, net gain is defined as $(P_{n+1} - P_n)/P_n$, where P_n and

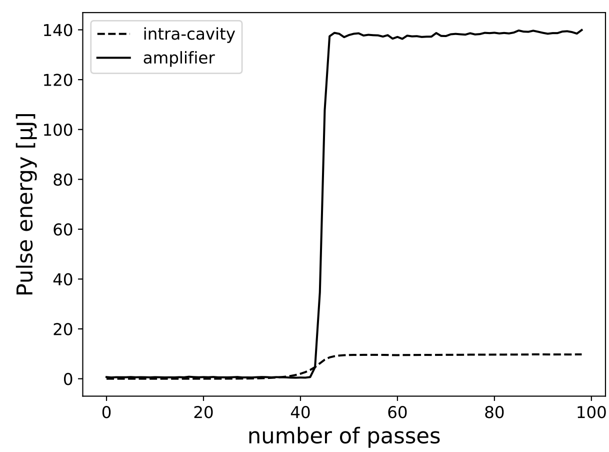

Figure 4: Pulse energy per pass in cavity (50 nm radiation) and at the amplifier (4.167 nm radiation). The steady state is achieved after switching the cavity detuning from 2.7 µm to −14.1 µm. The total reflectivity is set at 14%.

P_{n+1} are the peak input power of the nth and the nth+1 pass, respectively. As can be seen in Fig. 3, for a total reflectivity of 14%, detuning the cavity length by −14.1 µm (applied to passes ≥45 in Fig. 4) results in zero net gain and a steady state. Maximum gain occurs at a detuning of 2.7 µm which can be used in the first passes to build up power (applied to passes <45 in Fig. 4). The transition from building up power to stabilizing the power level can be thus achieved with a relative change in the cavity detuning of 16.8 µm. The output FEL pulses at steady state are shown in Fig. 5.

RESONATOR CONFIGURATION

ISBN: 978-3-95450-220-2 ISSN: 2673-5474 doi: 10.18429/JACoW-FEL2022-MOP20

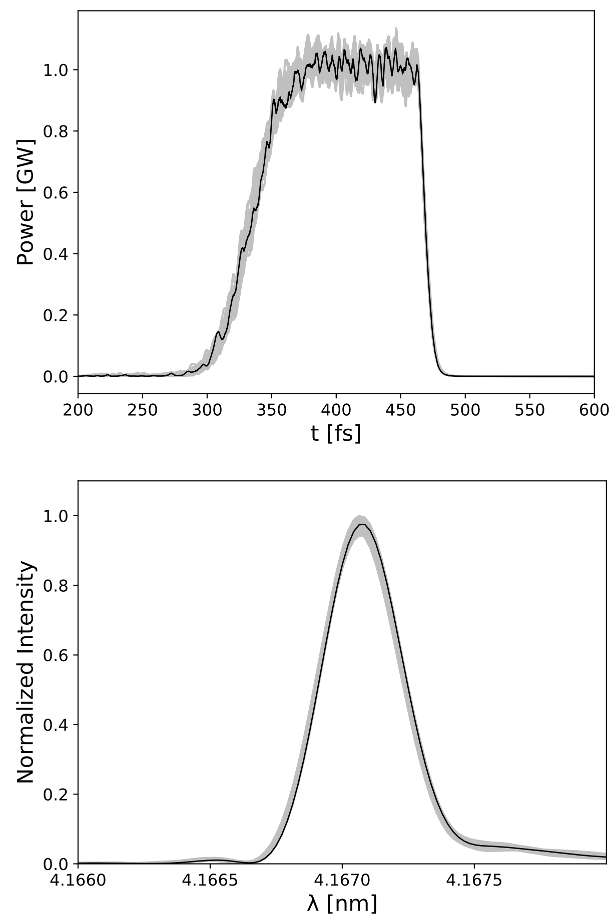

Figure 5: Output FEL radiation of the amplifier of scheme shown in Fig. 1 in steady state, between passes 50 and 100. In (a) we show the power profiles after 25 m and in (b) we show the spectra at the same position.

FOR SHENZHEN

With a resonator HGHG scheme as described above, the 4 nm output wavelength resulting as the 12th harmonic of the 50 nm is close to the shortest possible output wavelength with the given scheme. This limitation is posed by both the shortest fundamental wavelength possible (limited by the broadband mirror reflectivity) and the highest harmonic possible (limited by the energy spread required to get bunching at a given harmonic). However, by using an optical klystron, where modulator 2 shown in Fig. 2 is a harmonic of modulator 1, an increased harmonic number can be achieved. We refer to this scheme as harmonic optical klystron (HOK) and more information can be found in [14, 15]. In this case, for convenience of the simulation, the transition from power build-up to steady-state regime shown in Fig. 6 is done by artificially reducing the reflectivity.

With the HOK, the frequency up-conversion will be higher than the standard HGHG as discussed in [15] even in a single pass. The advantage of the optical cavity is that the fundamental wavelength in the first modulator can be as low as the 50 nm simulated here which can result, after 2 frequency

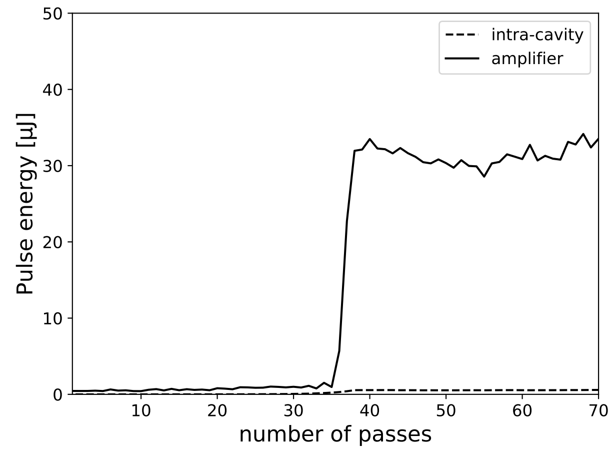

Figure 6: Pulse energy per pass in cavity (50 nm radiation) and at the amplifier (2.512 nm radiation). The steady state is achieved after switching the reflectivity from 7.8% to 5.8%.

up-conversions, at the 20th harmonic of the fundamental wavelength at 2.5 nm. The output FEL at the steady state at this wavelength is shown in Fig. 7.

It is worth noticing, that when an optical klystron scheme is used, a very low recirculating power is required to achieve sufficient energy modulation. More details on the self-amplification process can be found in [16, 17].

SUMMARY AND OUTLOOK

The simulations so far have shown that it is possible to obtain FEL properties of a seeded FEL, using the recirculating field of an optical cavity as seed. Starting with a resonator of 50 nm, which is probably close to the shortest wavelength that can be stored in a broadband resonator, simulations show that wavelengths down to 4.17 nm at the 12th harmonic (foreseen at FLASH) or 2.5 nm at the 20th harmonic (foreseen at the Shenzhen FEL) can be achieved at high repetition rates. Further studies on the resonator geometry and start-to-end simulations are crucial for an experimental verification of these schemes.

ACKNOWLEDGMENT

This work was supported by the National Natural Science Foundation of China (12122514 and 11975300) and Shanghai Science and Technology Committee Rising-Star Program (20QA1410100). G. Paraskaki was supported by the Impuls- und Vernetzungsfond der Helmholtz-Gemeinschaft e.V. within the CAS-Helmholtz International Laboratory on Free-Electron Laser Science and Technology (CHILFEL), Grant No. InterLabs-0002. B. Faatz was Funded by Chinese Academy of Sciences President's International Fellowship Initiative (PIFI), Grant No. 2020FSM0003.

REFERENCES

[1] P. R. Ribic and G. Margaritondo, "Status and prospects of x-ray free-electron lasers (x-FELs): a simple presentation",

ISBN: 978-3-95450-220-2 ISSN: 2673-5474 doi: 10.18429/JACoW-FEL2022-MOP20

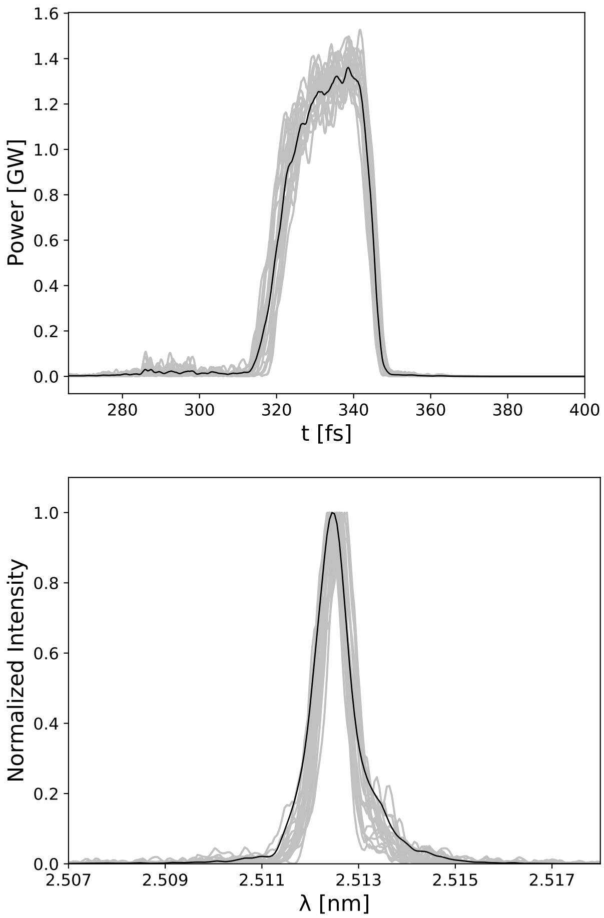

Figure 7: Output FEL radiation of the amplifier of scheme shown in Fig. 2 in steady state, between passes 38 and 70. In (a) we show the power profiles after 15 m and in (b) we show the spectra at the same position. The spectra are normalized to their respective maximum.

J. Phys. D: Appl. Phys, vol. 45, p. 213001, 2012. doi:10.1088/0022-3727/45/21/213001

[2] J. Feldhaus *et al.*, "Possible application of x-ray optical elements for reducing the spectral bandwidth of an X-ray SASE FEL", *Opt. Commun.*, vol. 140(4), pp. 341–352, 1997. doi:10.1016/S0168-9002(97)00451-8

[3] G. Geloni *et al.*, "A novel self-seeding scheme for hard X-ray FELs", *J. Mod. Opt.*, vol. 58, pp. 1391–1403, 2011. doi:10.1080/09500340.2011.586473

[4] S. Liu *et al.*, "Preparing for High-Repetition Rate Hard X-Ray Self-Seeding at the European X-Ray Free Electron Laser: Challenges and opportunities". *Phys. Rev. Accel. Beams*, vol. 22, p. 060704–060704, 2019. doi:10.1103/PhysRevAccelBeams.22.060704

[5] L. H. Yu and J. Wu, "Theory of high gain harmonic generation: an analytical estimate", *Nucl. Instr. and Meth. A*, vol. 483, pp. 493-498, 2002. doi:10.1016/S0168-9002(02)00368-6

[6] G. Stupakov, "Using the Beam-Echo Effect for Generation of Short-Wavelength Radiation", *Phys. Rev. Lett.*, vol. 102, p. 074801, 2009. doi:10.1103/PhysRevLett.102.074801

[7] E. Allaria *et al.*, "Highly coherent and stable pulses from the FERMI seeded free-electron laser in the extreme ultraviolet", *Nat. Photon*, vol. 6, pp. 699–704, 2012. doi.org/10.1038/nphoton.2012.233

[8] S. Reiche, "GENESIS 1.3: a fully 3D Time-Dependent FEL Simulation Code", *Nucl. Instr. and Meth. A*, vol. 429, p. 243, 1999. doi.org/10.1016/S0168-9002(99)00114-X

[9] S. Serkez and S. Tomin, "OCELOT: a versatile computational tool for light sources", https://github.com/ocelot-collab, 2016

[10] J. Rossbach *et al.*, "10 years of pioneering X-ray science at the free- electron laser FLASH at DESY", *Phys. Rep.*, vol. 808, pp. 1–74, 2019. doi:10.1016/j.physrep.2019.02.002

[11] S. Ackermann *et al.*, "Novel method for the generation of stable radiation from free-electron lasers at high repetition rates". *Phys. Rev. Accel. Beams*, vol. 23, p. 071302, 2020. doi:10.1103/PhysRevAccelBeams.23.071302.

[12] G. Paraskaki *et al.*, "Optimization and stability of a high-gain harmonic generation seeded oscillator amplifier". *Phys. Rev. Accel. Beams*, vol. 24, p. 034801, 2021. doi:10.1103/PhysRevAccelBeams.24.034801.

[13] G. Paraskaki *et al.*, "Advanced Scheme to Generate MHz, Fully Coherent FEL Pulses at nm Wavelength", *Appl. Sci.*, vol. 11, p. 6058, 2021. doi.org/10.3390/app11136058.

[14] H. Sun *et al.*, "Seeding with a harmonic optical klystron resonator configuration in a high repetition rate free electron laser". *Phys. Rev. Accel. Beams*, vol. 25, p. 060701, 2022. doi:10.1103/PhysRevAccelBeams.25.060701.

[15] H. Sun *et al.*, "High repetition rate seeded free-electron laser with a harmonic optical klystron in high-gain harmonic generation", presented at the 40th International Free Electron Laser Conference (FEL'22), Trieste, Italy, Aug. 2022, this conference.

[16] J. Yan *et al.*, "Self-amplification of Coherent Energy Modulation in Seeded Free-Electron Lasers", *Phys. Rev. Lett.*, vol. 126, p. 084801, 2021. doi:10.1103/PhysRevLett.126.084801

[17] G. Paraskaki *et al.*, "High repetition rate seeded free electron laser with an optical klystron in high-gain harmonic generation", *Phys. Rev. Accel. Beams*, vol. 24, p. 120701, 2022. doi:10.1103/PhysRevAccelBeams.24.120701

ISBN: 978-3-95450-220-2 ISSN: 2673-5474 doi: 10.18429/JACoW-FEL2022-MOP21

GENERATION OF X-RAY VORTEX BEAMS IN A FREE-ELECTRON LASER OSCILLATOR

N.S. Huang, Shanghai Synchrotron Radiation Facility, Shanghai, China
H.X. Deng*, Shanghai Advanced Research Institute, Chinese Academy of Sciences, Shanghai, China
J.W. Yan, European XFEL, Schenefeld, Germany

Abstract

Light with orbital angular momentum (OAM) provides new insights into a wide range of physical phenomena and has engendered advanced applications in various fields. Currently, research interest in X-ray OAM is rapidly expanding. Here, we report a straightforward method capable of generating intense OAM beams from an X-ray free-electron laser oscillator (XFELO). This method leverages Bragg mirrors and longitudinal-transverse mode coupling to enable mode selection in a conventional XFELO configuration, thereby natively producing fully coherent hard X-ray beams carrying OAM. Simulation results indicate that fully coherent hard X-ray OAM beams can be generated without the need for optical mode converters. This simple approach can significantly advance the creation of X-ray OAM while stimulating the development of novel experimental methods.

INTRODUCTION

Optical vortices are spirally phased beams, which have a phase dependence of $\exp(il\phi)$, where l denotes the topological charge and ϕ denotes the azimuthal coordinate in the plane perpendicular to the beam propagation. As demonstrated, the orbital angular momentum (OAM) of optical vortices is l [1]. The past few decades have seen a succession of breakthroughs in vortex and OAM applications, including ultra-high resolution imaging, microparticle manipulation using optical tweezers, high-capacity communications, quantum optics, and laser thermal noise reduction in gravitational wave detection. Although X-ray OAM is much less common, the interaction of matter and X-ray optical vortices is expected to give rise to new phenomena. This capability allows X-ray OAM to open up new opportunities for characterizing different material properties. In particular, XFEL is able provide unprecedentedly bright X-ray vortices, which will significantly stimulate the development of experiments and methods.

Recent advances have led to the generation of OAM beams in single-pass seeded XFEL with fundamental Gaussian mode lasers and helical undulators [2]. Generally, two schemes have been developed to generate FEL OAM pulses. The first scheme uses spirally microbunched electron beams to produce OAM light, which can be generated by the high harmonic interaction of the lasers and electron beams in a helical undulator. The second one is based on the harmonic emission of the helical undulator, which carries OAM natively. In this scheme, the electron beam is microbunched at harmonic wavelength of a helical undulator via a fundamental Gaussian mode lasers, and then sent to pass through the helical undulator to generate OAM light. This scheme is also compatible with after burner mode.

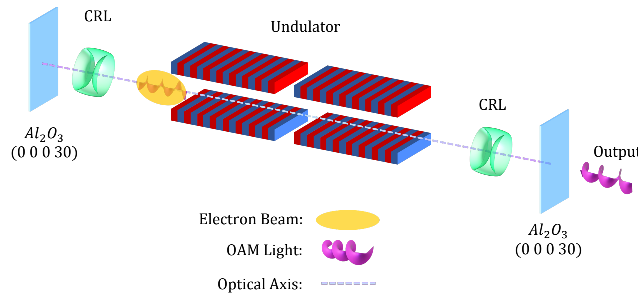

Figure 1: Scheme to generate X-ray OAM beams by using a typical configuration of the XFELO. Compound refractive lenses (CRLs) are used for X-ray focusing.

Unlike single-pass FELs to produce OAM beams, XFELO is well suited to produce coherent radiation with high power and high repetition rates in the hard X-ray regime. XFELO to generate OAM beams (see Fig. 1) can use a newly proposed method [3], which essentially facilitates the preservation of OAM beam amplification at the fundamental wavelength and avoids the need for external optical elements. The method is very simple, as it requires only the adjustment of the resonant condition of XFELO operation. The method is based on the important fact that the resonant condition for each transverse mode is slightly different. As a result, the gain profile of each transverse mode is shifted over the spectrum. The combined effect is that XFELO can operate in a specific spectral regime in which radiation in a high-order transverse mode can be obtained at maximum gain. Because the laser saturation state is only governed by the gain and cavity loss, this effect enables XFELOs to select transverse modes that carry OAM.

OAM MODES IN XFELO

We start with the Laguerre–Gaussian (LG_p^l) modes that can possess arbitrary OAM [1], where l denotes any real integer for the azimuthal mode and p is zero or any positive integer for the radial mode. With the LG_p^l basis modes, the transversely dominated FEL radiation fields can be described

* denghx@sari.ac.cn

ISBN: 978-3-95450-220-2 ISSN: 2673-5474 doi: 10.18429/JACoW-FEL2022-MOP21

as $E(r,\phi,z)=\sum_{p,l}a_{p,l}u_{p,l}$, and $u_{p,l}$ can be expressed as

$$u_{p,l}(r,\phi,z)=\frac{C_{p,l}}{w}\left(\frac{r\sqrt{2}}{w}\right)^{|l|}L_p^{|l|}\left(\frac{2r^2}{w^2}\right)\exp\left(\frac{-r^2}{w^2}\right)$$
$$\times\exp(il\phi)\exp\left[-i(2p+|l|+1)\tan^{-1}\frac{z}{z_R}\right], \quad (1)$$

in which $C_{p,l}$ denotes a normalization constant, L_p^l is the associated Laguerre polynomial, $z_R=\pi w_0^2/\lambda$ denotes the Rayleigh length with wavelength λ and beam waist w_0, and the spot size parameter along the beam propagation is given by $w(z)=w_0(z^2/z_R^2+1)^{1/2}$. Clearly, the helical spatial phase term of $\exp(il\phi)$ is presented. Here, we first consider the higher azimuthal modes with the fundamental radial mode of $p=0$ for simplicity. Thus, $a_{p,l}$, $u_{p,l}$, and LG_p^l can be respectively written as a_l, u_l, and LG^l, where $p=0$ is assumed and its implications will be presented later.

An important factor to be considered in the gain is the extra phase term $(2p+|l|+1)\tan^{-1}z/z_R$ in Eq. (1), which is the Gouy phase. The presence of the Gouy phase increases the phase velocity of the radiation field, therefore requiring a faster electron velocity to maintain resonance [4]. Hence the FEL resonant wavelength is slightly different for each LG_p^l mode.

For an XFELO, the averaged deviation over the undulator can be given by [5]

$$\left\langle\frac{\Delta\lambda}{\lambda_r}\right\rangle\approx\frac{2(2p+|l|+1)\tan^{-1}(L_u/2z_R)}{2\pi N_u} \quad (2)$$

where L_u denotes the undulator length. Making use of the well-known small-signal gain, the gain spectrum for each mode is given by $G_l\left[\nu-2(2p+|l|+1)\tan^{-1}(L_u/2z_R)\right]$. Figure 2 shows the theoretical prediction of the gain spectrums. The shift is determined by Eq. (2), while the gain curve is scaled by the “filling factor” describing the overlap between the radiation and the electron beam

Figure 2 displays gain spectrums for different modes and the reflectivity of the sapphire (0 0 0 30) at 14.3 keV. The maximum gain is normalized to one. Notably, the width of the reflectivity is much narrower than that of the gain spectrum, seen in the small plot in the Fig. 2. Therefore, in the high-reflectivity regime, the radiation only in the $\mathrm{LG}^{\pm1}$ modes could obtain the maximum gain. This effect enables XFELO to amplify $\mathrm{LG}^{\pm1}$ carrying OAM to reach saturation. Important to note is that Bragg reflection does not directly filter out the $\mathrm{LG}^{\pm1}$ radiation from the mixed one but fixes the spectral regime. The radiation in $\mathrm{LG}^{\pm1}$ modes can reach saturation because it sustains the maximum gain over the other modes in each pass. As the gain process repeats, the mode competition effect provides the selection of the $\mathrm{LG}^{\pm1}$ mode.

Also, it should be noted that higher radial mode p affects the optimal detuning of the gain, since the gain spectrum is a function of $2p+|l|$. Besides, the coupling efficiency between each p modes is non-zero during FEL amplification.

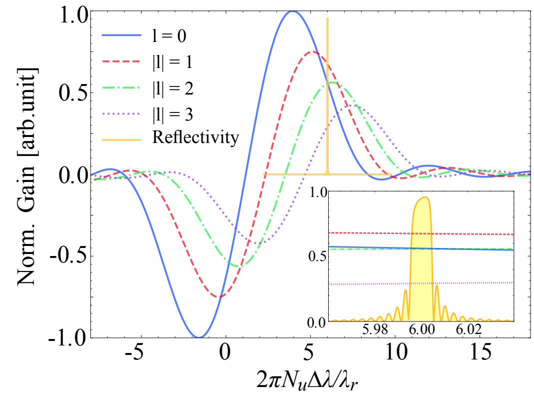

Figure 2: (a) The normalized filling factor $\mathrm{F}_l/\mathrm{F}_0$. (b) The normalized gain for different l modes, while the yellow line indicates the reflectivity of the sapphire (0 0 0 30) at 14.3 keV. Obviously, the reflectivity can select the gain. The parameters based on a realistic scenario: $f_\perp(r,\phi)=\exp(-r^2/2r_e^2)$, $f_E(\eta)=\exp(-\eta^2/2\sigma_\eta^2)/\sqrt{2\pi}\sigma_\eta$, $\sigma_\eta=0.01\%$, $2r_e^2/w_0^2=3$, $z_R=15$ m, $L_u=20$ m, and $p=0$.

Consequently, this effect has an impact on the amplification of modes with $|l|>=2$. For example, if the detuning is set by $2p+|l|=2$, three modes can be found to share the optimal detuning: $p=1, l=0$ and $p=0, l=\pm2$. Therefore, the amplification of $l=\pm2$ may be difficult without the suppression of modes of $p>0$. Fortunately, for $|l|=1$ modes with the detuning of $2p+|l|=1$, p must be zero, and its effect is naturally suppressed. Therefore, XFELOs can generate robust OAM modes with $|l|=1$, as verified by the following simulations.

SIMULATIONS

The baseline case of the SHINE provides electron bunches of 100 pC total charge, which is compressed to 1500 A peak current. The slice emittance is about 0.4 µm, while the slice energy spread blew 0.01%. The basic parameters are listed in Table 1. The operation of the XFELO requires a relatively long electron bunch with a linear energy chirp due to the ultra-narrow spectral acceptance of the crystal Bragg reflection. Therefore, we choose a peak current of 750 A and a 20 m long undulator that is divided into 4 segments.

Table 1: Electron Beam and Undulator Parameters

Parameter	Value	Unit
Electron beam energy	8	GeV
Slice energy spread	0.8	MeV
Normalized emittance	0.4	mm·mrad
Total charge	100	pC
Photon energy	0.75	keV
Undulator period length	26	mm
Undulator segment length	4	m

ISBN: 978-3-95450-220-2 ISSN: 2673-5474 doi: 10.18429/JACoW-FEL2022-MOP21

We perform a simulation with a photon energy of 9.81 keV. The simulation results are shown in Fig. 3 and Fig. 4. Figure 3 shows the pulse energy as a function of the round trips and the evolution of the transverse mode. The saturation power reaches 200 µJ, approaching the level of Gaussian mode operation. In the short period ranging from 20 to 50 round trips, mode competition or mode completion is observed to occur. As a consequence, a short time period is required for completing the symmetric doughnut-like transverse intensity profile and the helical phase. The final outcome is robust because the system steady state is determined by the gain that is tuned for the mode with $l = -1$.

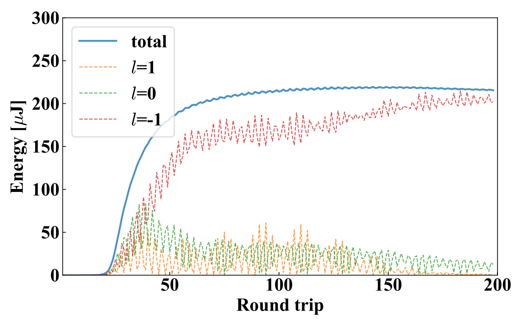

Figure 3: Cavity output energy growth. The total output energy is about 200 µJ.

At saturation, the characteristic hollow profile and helical phase can be observed in Fig. 4. It is obvious from the phase distribution that the dominant mode is the $l = -1$, $p = 0$ LG mode. The intensity of modes $l \neq -1$ is negligible. The longitudinal power profile and the spectrum are shown in Fig. 4. While the total power increases up to 200 µJ, the peak power exceeds 1.5 GW with the FWHM spectrum width of 40 meV.

CONCLUSION

XFELO holds the ability to directly generate optical vortex, without the need for external optical elements. The proposed method is based on the coupling of longitudinal and transverse modes, which enables the Bragg crystal to serve as a “selector” in the transverse modes by maximizing the gain of the mode of interest. Compared to previous schemes, the generation of OAM light in XFELO does not require a helical undulator and a seed laser. Thus, this approach significantly reduces both the electron-beam-control elements and the external optical elements, thereby significantly increasing the optical efficiency. XFELO is expected to stimulate the development of new experiments in areas such as imaging and quantum optics.

ACKNOWLEDGEMENTS

This work was supported by the National Key Research and Development Program of China (2018YFE0103100), the National Natural Science Foundation of China (12125508, 11935020), Program of Shanghai Academic/Technology Research Leader (21XD1404100), and Shanghai Pilot Program for Basic Research – Chinese Academy of Science, Shanghai Branch (JCYJ-SHFY-2021-010).

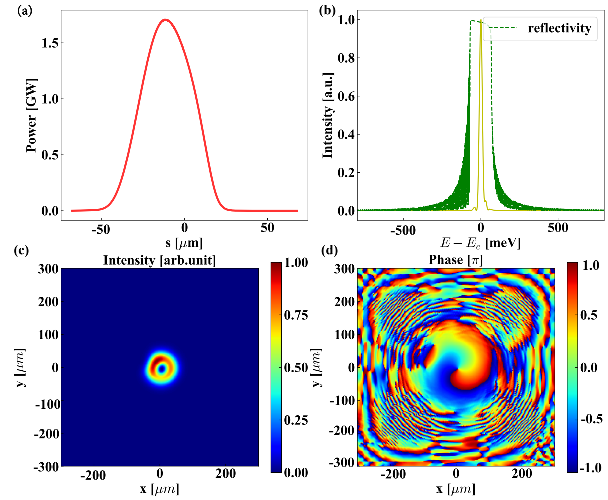

Figure 4: (a) Longitudinal power profile. (b) Spectrum. (c) Transverse profile. (d) Phase distribution. The transverse profile and phase of the lightreveal a OAM mode of $l = -1$ at saturation. A peak power of 1.5 GW with a spectral width (FWHM) of 40 meV can be obtained.

REFERENCES

[1] L. Allen, M. W. Beijersbergen, R. J. Spreeuw, and J. P. Woerdman, “Orbital angular momentum of light and the transformation of Laguerre-Gaussian laser modes,” *Phys. Rev. A*, vol. 45, no. 11, pp. 8185–8189, 1992. doi:10.1103/PhysRevA.45.8185

[2] E. Hemsing, A. Marinelli, and J. B. Rosenzweig, “Generating optical orbital angular momentum in a high-gain free-electron laser at the first harmonic,” *Phys. Rev. Lett.*, vol. 106, no. 16, p. 164 803, 2011. doi:10.1103/PhysRevLett.106.164803

[3] N. Huang and H. Deng, “Generating X-rays with orbital angular momentum in a free-electron laser oscillator,” en, *Optica*, vol. 8, no. 7, p. 1020, 2021. doi:10.1364/OPTICA.428341

[4] C. Pellegrini, A. Marinelli, and S. Reiche, “The physics of x-ray free-electron lasers,” *Rev. Mod. Phys.*, vol. 88, no. 1, 2016. doi:10.1103/RevModPhys.88.015006

[5] B. Faatz, R. W. Best, D. Oepts, and P. W. Van Amersfoort, “Control of the transverse mode distribution in free electron lasers,” *Pure Appl. Opt.*, vol. 2, no. 3, pp. 195–210, 1993. doi:10.1088/0963-9659/2/3/006

ISBN: 978-3-95450-220-2 ISSN: 2673-5474 doi: 10.18429/JACoW-FEL2022-MOP22

SIMULATION STUDIES FOR THE ASPECT PROJECT AT EUROPEAN XFEL

J. W. Yan*, G. Geloni, C. Lechner, S. Serkez, European XFEL, Schenefeld, Germany
Y. Chen, M. Guetg, C. Heyl, E. Schneidmiller
Deutsches Elektronen-Synchrotron DESY, Hamburg, Germany

Abstract

Intense attosecond pulses generated by x-ray free-electron lasers (XFEL) are promising for attosecond science, for example, to study the quantum mechanical motion of electrons in molecules. This paper presents numerical simulations of the generation of attosecond soft and hard x-ray FEL pulses with the chirp-taper and the enhanced self-amplified spontaneous emission methods, based on the parameters of the European XFEL. To overcome the coherence time barrier, a modification of the chirp-taper scheme is used in the case of soft x-rays. The results show that several hundred attosecond pulses can be obtained at both 700 eV and 6 keV photon energies.

INTRODUCTION

As a new generation of light sources, x-ray free-electron lasers (XFELs) are indispensable tools for a wide range of research fields. The demand for attosecond XFEL pulses is increasing rapidly in recent years. Several methods have been proposed to shorten the FEL pulse duration [1]. Many of these schemes employ an external laser to modulate an electron beam and let only a short part of the electron beam lase effectively, such as the chirp-taper [2, 3] and the enhanced self-amplified spontaneous emission (ESASE) schemes [4].

In the chirp-taper scheme, an electron beam is modulated through the interaction with a few-cycle intense laser in a few-period wiggler, and a strong energy chirp is introduced, which inhibits lasing. Reverse taper is used to compensate this effect in a short part of the electron beam, the one with the strongest energy chirp. In addition to the energy modulation, the ESASE scheme relies on the creation of high-current spikes in short parts of the electron beam, with the help of a dispersive section (a chicane) following the energy modulator. Due to the high current levels, in the ESASE scheme, space-charge interactions play a particularly important role. We are currently setting up a project dedicated to the generation AttoSecond Pulses with eSASE and Chirp-Taper schemes (ASPECT) at the European XFEL [5]. ASPECT will initially serve two of the three SASE line at the European XFEL, SASE1 and SASE3, which are respectively specialized in the production of hard and soft x-rays.

The schematic layout of the ASPECT project is shown in Fig. 1. The energy modulation section is placed before SASE1, where external laser and electron beam interact in a two-period wiggler. The energy-modulated beam can be transported to both SASE1 and SASE3. The ESASE scheme is enabled by the two chicanes located, respectively, before SASE1 and SASE3.

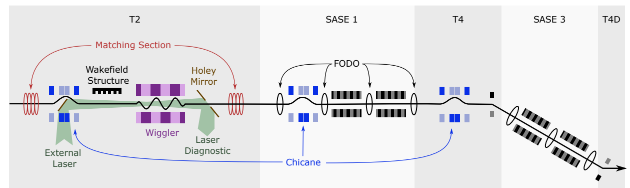

Figure 1: Schematic layout of the ASPECT project.

CHIRP-TAPER SCHEME

We analyze the performance of the chirp-taper scheme for two case studies covering the generation of hard (6 keV) and soft (700 eV) x-ray radiation. A 14 GeV electron beam with a flat-top current of 2500 A is used in both simulations. The electron beam is modulated by a laser with a wavelength of 1030 nm, a pulse energy of several mJ (see below) and an FWHM pulse duration of 4 fs in the two-periods wiggler with a period of 0.7 m. The simulations for the hard and soft x-ray cases are respectively based on the parameters of SASE1 and SASE3 [5], made up of 5 m-long segments, respectively with 40 mm and 68 mm period, followed by 1.1 m-long intersections.

Hard X-Ray Case

In the hard x-ray case, the pulse energy of the laser is selected as 4 mJ. The energy modulation induced by the laser is calculated by theoretical analysis [6] and three-dimensional numerical analysis [7, 8]. As shown in Fig. 2, the two methods yield very similar results. An energy modulation amplitude of around 30 MeV can be obtained.

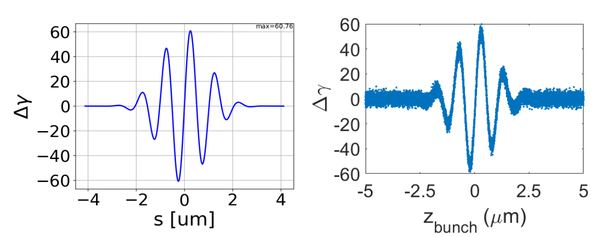

Figure 2: Energy modulation induced by the laser, obtained by theoretical analysis (left) and three-dimensional simulation (right). The bunch head is to the right.

A reverse step-taper is applied in SASE1, and the dimensionless undulator parameter K increases by 0.0013 in each undulator segment. Figure 3 shows the evolution of the

* jiawei.yan@xfel.eu

ISBN: 978-3-95450-220-2 ISSN: 2673-5474 doi: 10.18429/JACoW-FEL2022-MOP22

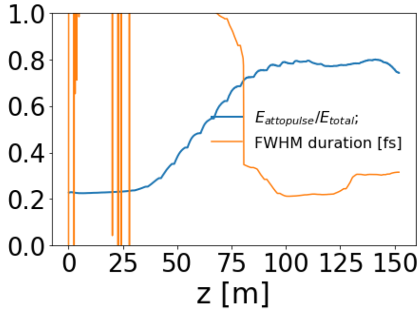

Figure 3: The change of pulse duration and contrast along the undulator.

pulse duration and contrast along the undulator. Figure 4 presents the power profile of the FEL pulse at the position of 130 m down the SASE1 undulator, where the peak power, FWHM duration, and contrast of the pulse are 86 GW, 278 as, and 78%, respectively.

A stability analysis of the FEL performance related to the carrier-envelope phase (CEP) [9] of the optical laser is shown in Fig. 5. Each point in Fig. 5 represents the average value of 10 simulation runs (referring to different shot noise initial conditions) with a certain CEP change. For most applications, we estimate that pulses are satisfactorily stable within ± 0.2 pi phase change.

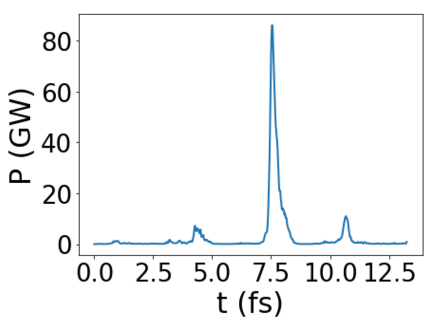

Figure 4: Power profile of the 6 keV FEL pulse at the position of 130 m.

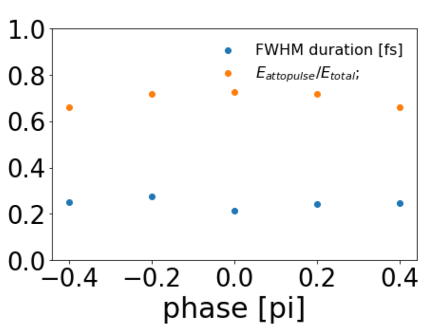

Figure 5: CEP stability analysis of the chirp-taper scheme at 6 keV.

Soft x-ray case

The radiation coherence time increases with the target wavelength. In the soft x-ray range it becomes longer than the lasing window, and poses a limit to the obtainable pulse duration. Here, we employ a modified chirp-taper scheme [3] to ease this performance limitation at 700 eV. As shown in Fig. 6, in the modified chirp-taper scheme, a first stage of the SASE3 undulator with an excessive reverse taper is used to suppress lasing, while obtaining a strong bunching. A second stage composed of one or two undulator segments is works as radiator with decreased slippage. Intense, short FEL pulses can be obtained at the second stage through careful optimization of the undulator strength.

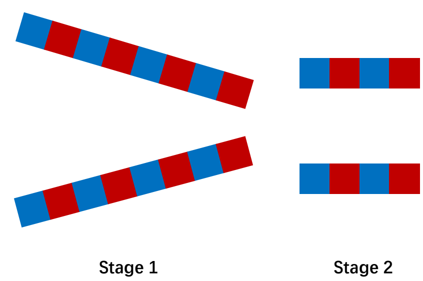

Figure 6: Schematic layout of the modified chirp-taper scheme at SASE3.

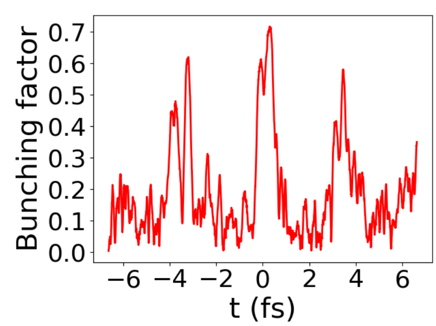

Figure 7: Bunching factor distribution at the exit of the first stage.

Here the pulse energy of the laser is chosen as 5 mJ. An energy modulation amplitude of 34.7 MeV can be obtained in this case. The K in the first stage increases by 0.0122 in each undulator segment to ensure a suitable excessive taper. The bunching factor distribution of the beam at the exit of 10 undulator segments is shown in Fig. 7.

Then the electron beam is sent to the second stage, which consists of one undulator segment. Fig. 8 shows FEL pulse duration, peak power, and contrast at the exit of the second stage as a function of the K parameter of the second stage. The value $K = 9$ is selected as a balanced solution. As presented in Fig. 9, an FEL pulse with a peak power of 22.6 GW, an FWHM duration of 446 as, and a contrast of 81.6% can be obtained. The CEP stability analysis shown in Fig. 10 indicates that the modified chirp-taper scheme holds similar stability compared to the normal chirp-taper scheme.

ISBN: 978-3-95450-220-2 ISSN: 2673-5474 doi: 10.18429/JACoW-FEL2022-MOP22

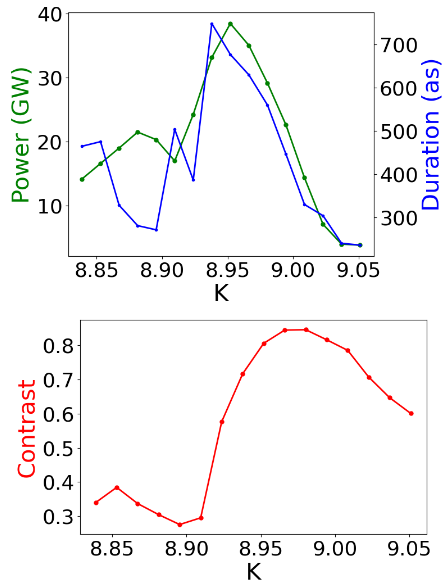

Figure 8: Scanning of the undulator strength of the second stage.

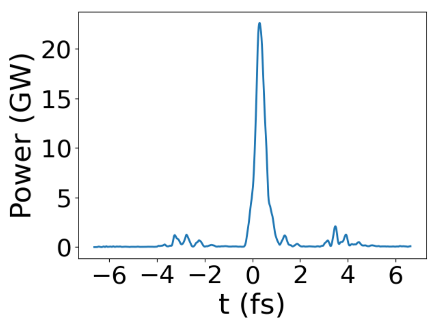

Figure 9: Power profile of the 700 eV FEL pulse at the exit of the second stage.

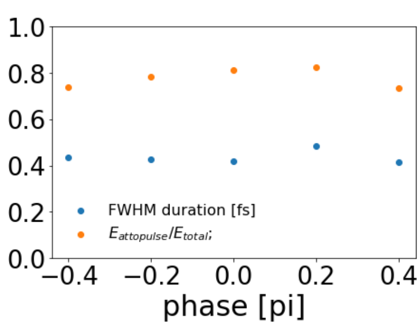

Figure 10: CEP stability analysis of the chirp-taper scheme at 700 eV.

ESASE SCHEME

We further analyzed the performance of the ESASE scheme at 700 eV. A 14 GeV electron beam with a flat-top current of 5000 A is used. Similar to the chirp-taper scheme, the laser is used to modulate the electron beam at the two-period wiggler. In this case, the pulse energy is selected as 4 mJ. The obtained energy modulation is the same as the one shown in Fig. 2.

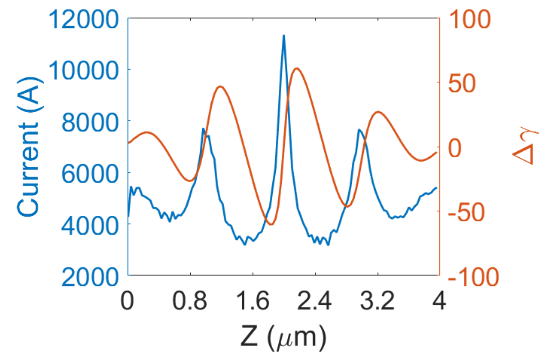

Figure 11: Energy modulation induced by the laser and current profile of the electron beam for the ESASE scheme.

The chicane and arc placed in front of the SASE3 are used to provide a total positive R_{56} of 40 µm. The electron beam is well compressed before passing through SASE3. The current profile of the electron beam after compression is presented in Fig. 11. Due to the high-current spike, the scheme benefits from a strong space charge effect in the SASE3 undulator section [10]. Preliminary analysis shows that intense FEL pulses with an FWHM around 200 as can be obtained at the position of 30 – 40 m. Figure 12 shows the obtained FEL power profile at 43 m, where the peak power is 27.3 GW and FWHM duration is 182 as.

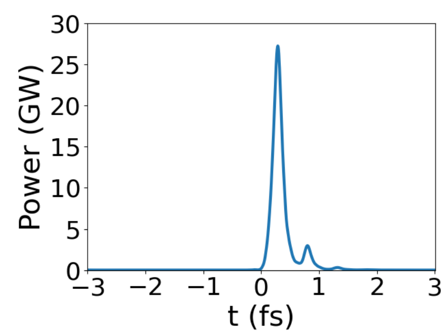

Figure 12: Power profile of the 700 eV FEL pulse obtained with the ESASE scheme.

CONCLUSION

In summary, the generation of attosecond XFEL at European XFEL with the chirp-taper scheme and ESASE scheme is analyzed. Preliminary simulation results show that both schemes are promising to provide several hundred attosecond XFEL pulses at both 700 eV and 6 keV photon energies. More systematically optimization based on start-to-end simulations is required to further improve the performance. Moreover, the possibilities of utilizing the self-modulation [11] in the wiggler to replace the external laser require further exploration.

ISBN: 978-3-95450-220-2 ISSN: 2673-5474 doi: 10.18429/JACoW-FEL2022-MOP22

REFERENCES

[1] S. Serkez *et al.*, "Overview of options for generating high-brightness attosecond x-ray pulses at free-electron lasers and applications at the european xfel," *J. Opt.*, vol. 20, no. 2, p. 024005, 2018.

[2] E. L. Saldin, E. A. Schneidmiller, and M. V. Yurkov, "Self-amplified spontaneous emission fel with energy-chirped electron beam and its application for generation of attosecond x-ray pulses," *Phys. Rev. ST Accel. Beams*, vol. 9, no. 5, p. 050702, 2006.

[3] E. Schneidmiller, "Application of a modified chirp-taper scheme for generation of attosecond pulses in extreme ultraviolet and soft x-ray free electron lasers," *Phys. Rev. Accel. Beams*, vol. 25, no. 1, p. 010701, 2022.

[4] A. A. Zholents, "Method of an enhanced self-amplified spontaneous emission for x-ray free electron lasers," *Phys. Rev. ST Accel. Beams*, vol. 8, no. 4, p. 040701, 2005.

[5] W. Decking *et al.*, "A mhz-repetition-rate hard x-ray free-electron laser driven by a superconducting linear accelerator," *Nat. Photonics*, vol. 14, no. 6, pp. 391–397, 2020.

[6] A. Zholents and M. Zolotorev, "Attosecond x-ray pulses produced by ultra short transverse slicing via laser electron beam interaction," *New J. Phys.*, vol. 10, no. 2, p. 025005, 2008.

[7] H.-X. Deng, T.-Y. Lin, J. Yan, D. Wang, and Z.-M. Dai, "Three-dimensional numerical investigations of the laser-beam interactions in an undulator," *Chinese Phys. C*, vol. 35, no. 3, p. 308, 2011.

[8] J. Yan *et al.*, "First observation of laser–beam interaction in a dipole magnet," *Adv. Photonics*, vol. 3, no. 4, p. 045003, 2021.

[9] D. J. Jones *et al.*, "Carrier-envelope phase control of femtosecond mode-locked lasers and direct optical frequency synthesis," *Science*, vol. 288, no. 5466, pp. 635–639, 2000.

[10] G. Geloni, E. Saldin, E. Schneidmiller, and M. Yurkov, "Longitudinal impedance and wake from xfel undulators. impact on current-enhanced sase schemes," *Nucl. Instr. and Meth. A*, vol. 583, no. 2-3, pp. 228–247, 2007.

[11] J. Duris *et al.*, "Tunable isolated attosecond x-ray pulses with gigawatt peak power from a free-electron laser," *Nat. Photonics*, vol. 14, no. 1, pp. 30–36, 2020.

ISBN: 978-3-95450-220-2 ISSN: 2673-5474 doi: 10.18429/JACoW-FEL2022-MOP27

UNAVERAGED SIMULATION OF SUPERRADIANCE IN FEL OSCILLATORS

R. Hajima†, National Institutes for Quantum Science and Technology, Kizugawa, Japan

Abstract

Generation of few-cycle FEL pulses with a high extraction efficiency was achieved at infrared FEL oscillators. The observed lasing can be understood as superradiance, radiation from bunched electrons in the slippage region. In the superradiant FEL oscillators, the high-extraction efficiency is accompanied by significant energy variation of the electrons during the undulator. Therefore, numerical studies of such FELs should be conducted by unaveraged simulation codes, in which macroparticles are not bound to specific bunch slices. In this paper, evolution of optical pulses in superradiant FEL oscillators is studied by using one-dimensional and three-dimensional unaveraged codes.

INTRODUCTION

Few-cycle optical pulses are generated with a high-extraction efficiency at a free-electron laser oscillator operated with specific parameters: slippage length, bunch length, gain parameter, cavity length detuning, and round-trip loss [1,2]. In this lasing, the peak intensity (I_p) and the pulse duration (τ) show the scaling law with respect to the number of electrons contributing to the lasing, $I_p \propto N^2$, $\tau \propto 1/N$. Since this scaling law is identical to that of superradiance in a two-level system [3], the lasing is also called superradiance in an FEL oscillator.

Thanks to the few-cycle pulse generation with high-extraction efficiency, a superradiant FEL oscillator operated in infrared wavelengths can provide high-intensity laser pulses exceeding the threshold of tunneling ionization of atoms and molecules, ~10^{13} W/cm^2, and could potentially be used for intense light field science including high-harmonic generation for attosecond X-ray pulses [4].

The study of superradiant FELs also leads to a deeper understanding of the resonant light-matter and light-electron interactions through analogies with superradiance in two-level systems.

Numerical simulations are essential for experimental planning and data analysis of superradiant FEL oscillators, as well as for a deeper understanding of the physics of the high-efficiency few-cycle pulse generation. However, it has been found that so-called average codes widely used in FEL simulations do not give correct results in simulations of superradiance FEL oscillators and that unaveraged codes are necessary. In this paper, we report on superradiance FELO simulations using one-dimensional and three-dimensional unaveraged codes.

† hajima.ryoichi@qst.go.jp

SUPERRADIANCE IN TWO-LEVEL SYSTEMS

In order to compare the role of quantum fluctuations in superradiance in two-level systems with the role of shot noise in superradiant FEL oscillators, here we review the Bloch sphere representation of superradiance in two-level systems and calculate pulse waveforms of the superradiance.

The Bloch sphere is a geometrical representation to describe a pair of mutually orthogonal states and their superposition. Here we define the north and south poles of the Bloch sphere as the upper and lower levels in a two-level system and assume all the atoms are initially in the upper level. If there were no quantum fluctuations, all atoms would continue to exist in the upper level, like an inverted pendulum maintaining its posture, and no radiation would occur from the system. In a realistic system, due to quantum fluctuations originating from spontaneous radiation and background thermal radiation, the atoms in the upper level decay to the lower level to emit cooperative radiation, i.e., superradiance [5,6,7].

The radiation waveform from the two-level system was calculated according to the paper [4] and plotted in Fig. 1, in which the initial tipping angle to simulate the quantum fluctuation was assumed to be $\theta_i = 10^{-3}, 10^{-4}, 10^{-5}$. It is shown that the evolution of the pulses depends on the initial tipping angle and the faster the pulses rise with the larger θ_i.

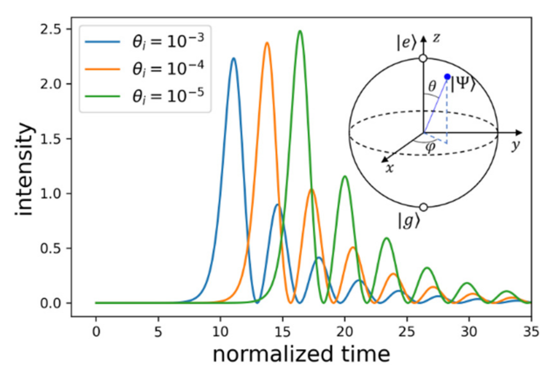

Figure 1: Superradiance of a two-level system calculated by the Burhan-Chiao model with different initial tipping angles, $\theta_i = 10^{-3}, 10^{-4}, 10^{-5}$. The Bloch vector representation of the two-level system is also depicted.

ISBN: 978-3-95450-220-2 ISSN: 2673-5474 doi: 10.18429/JACoW-FEL2022-MOP27

SIMULATIONS WITH A ONE-DIMENSIONAL UNAVERAGED CODE

In widely used FEL simulation codes, a number of macroparticles are prepared in each bunch slice and their motion is tracked taking into account their interaction with the radiation and the undulator fields. The evolution of the radiation field is, then, calculated by averaging the phase of macroparticles over at least one radiation wavelength [8]. The FEL code is called 'averaged code'.

The averaged codes are, however, not appropriate for the simulation of infrared FEL oscillators with large extraction efficiency because the assumption that the macroparticles are bound to a bunch slice is not valid for a high-efficiency FEL oscillator, in which some of the electrons move across bunch slices due to large energy variation. We, therefore, adopted unaveraged codes in the present study. The code was developed by modifying our one-dimensional simulation code [9] according to the paper describing the unaveraged simulation algorithm [10]. In the following simulations, we assumed a perfectly synchronized FEL oscillator, i.e., the cavity-detuning length equal to zero, with the parameters listed in Table 1.

Table 1: Simulation Parameters

Number of the undulator period	52
Normalized slippage distance	1
Cavity round trip loss	0.03
Cavity detuning length	0
Rectangular bunch	
Normalized bunch length	0.5
FEL parameter at peak	4.15×10^{-3}
Parabolic bunch	
Normalized full bunch length	0.5
FEL parameter at peak	4.76×10^{-3}
Gaussian bunch	
Normalized RMS bunch length	0.0625
FEL parameter at peak	6.11×10^{-3}

We investigated, in a previous study, the role of shot noise in a perfectly synchronized FEL oscillator and found that the shot noise plays an important role in sustaining the lasing after the onset of saturation as well as initiating the lasing [2]. The fact can be confirmed again from the results of averaged simulations shown in Fig. 2. In this figure, we plotted two macro pulses, one for a simulation including shot noise, and the other for turning off the shot noise after the 600-th round trip. We can see that lasing cannot sustain without the shot noise after the saturation.

FEL macropulses obtained by the averaged and unaveraged codes are plotted in Fig. 3. The difference in the rise of macropulse can be attributed to the difference in the effective amplitude of the shot noise. In the unaveraged code, coherent spontaneous emission is inherently taken into account, then the shot noise amplitude depends on the bunch shape, i.e., the rectangular bunch shows a fast start-up because of a large coherent spontaneous emission at the FEL

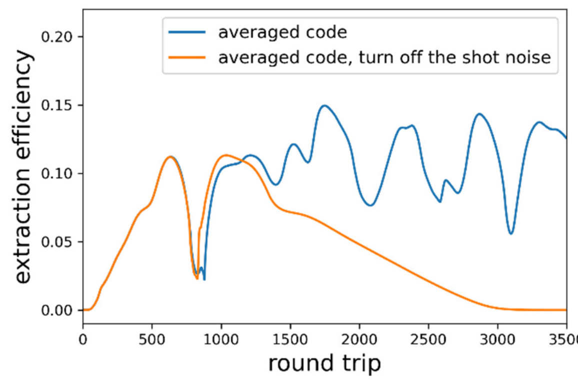

Figure 2: Evolution of macropulses at the perfectly synchronized FEL oscillator calculated by the averaged code. A simulation with turning off the shot noise after the 600th round trip (orange line).

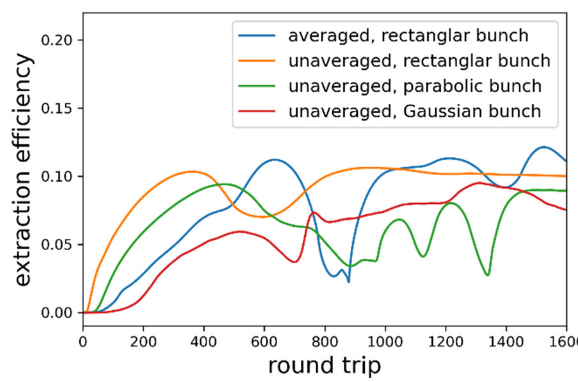

Figure 3: Evolution of macropulses at the perfectly synchronized FEL oscillator calculated by the averaged and unaveraged codes. Three different bunch shapes were assumed in the unaveraged code.

wavelength. Note that incoherent shot noise is introduced both in averaged and unaveraged codes according to the Penman-McNeil algorithm [11].

In Fig. 4, we plot FEL pulse waveforms at the 1600-th round trip for each simulation. The yellow and green patterns in the plots represent electron bunch positions at the entrance and exit of the undulator. The FEL pulses have the main pulse with a steep leading edge and following subpulses. Of the four plots, especially (B) and (C) exhibit ringing similar to the superradiance of two-level systems shown in Fig. 1.

Here we focus on the location of the main peak in the four plots. The leading edge of optical pulses at the perfectly synchronized FEL oscillators is governed by shot noise. The electrons initiate interaction with the radiation field in the shot noise region and induce energy modulation and density modulation to pass their energy to the optical pulse while slipping backward in the optical pulse. The formation of energy and density modulation occurs early in the process when the shot noise has a large amplitude. This is the reason why the main peak shifts forward in the simulation with the rectangular bunch.

ISBN: 978-3-95450-220-2 ISSN: 2673-5474 doi: 10.18429/JACoW-FEL2022-MOP27

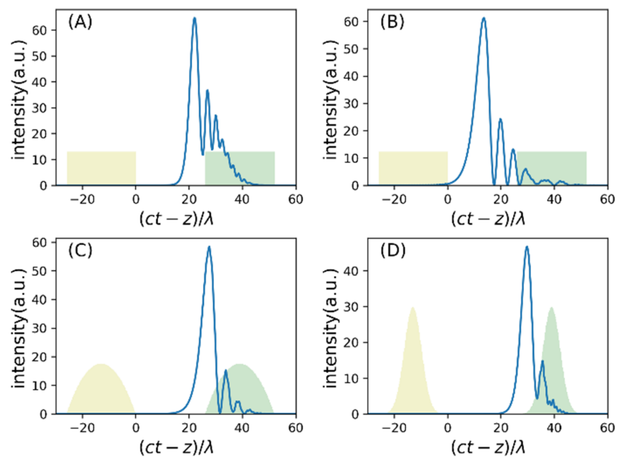

Figure 4: FEL pulses at the 1600-th round trip. (A) averaged code, (B) unaveraged code with a rectangular bunch (C) unaveraged code with a parabolic bunch, and (D) unaveraged code with a Gaussian bunch. The yellow- and green-filled patterns represent electron bunch positions at the entrance and exit of the undulator.

This relationship between the main peak position and the shot noise is completely the same as the superradiance in the two-level systems we discussed in the previous section. The shot noise in the superradiance FEL plays the same role as the initial tipping angle, quantum fluctuation, in the two-level system, which is necessary to initiate the cooperative radiation.

The period of the ringing formed in the slippage region is determined by the operation parameters of the FEL oscillator [1]. In Fig. 4, we found that the number of subpulses also varies with the amplitude of the shot noise.

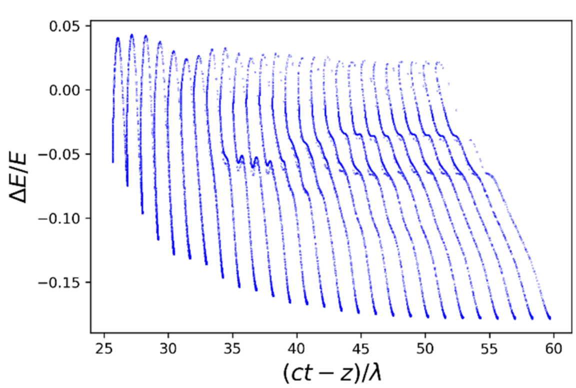

Figure 5: Macroparticles in the phase plane after the undulator at the 1600th round trip (unaveraged code with a parabolic bunch).

In our unaveraged simulations, the extraction efficiency at the 1600-th round trip is 8.9% for a parabolic bunch. In such high-efficiency lasing, macro particles may have deformation due to longitudinal slippage across bunch slices. In Fig.5, we plot macroparticles in the phase plane after the undulator at the 1600-th round trip calculated by the unaveraged code with a parabolic bunch.

The macroparticles have a large energy spread in addition to the density modulation equal to the radiation wavelength. Some of the macroparticles lose a large amount of their energy and slip backward across bunch slices to stretch the bunch. It can be confirmed again that the assumption of the averaged code, that macroparticles are bound to bunch slices, does not hold in superradiant FEL oscillators.

SIMULATIONS WITH A THREE-DIMENSIONAL UNAVERAGED CODE

We adopted a three-dimensional unaveraged code, Puffin [12], for the simulation of superradiance FEL oscillators. Puffin is an unaveraged code in absence of the slowly varying envelope approximation (SVEA), wiggler period averaging approximations, and phase averaging operation for macroparticles. Puffin was originally developed for simulations of single-pass FELs but can be combined with an optical pulse propagation code, OPC [13], to simulate FEL oscillators.

Figure 6 is an example of Puffin simulation result with the parameters listed in Table 2. The pulse is at the center of the undulator after 60 round trips. The extraction efficiency at the 60-th round trip is 5.2%. In the simulation, oscillation of radiation electric field is reproduced because the code does not use the envelope approximation. We confirmed the formation of a superradiant pulse and deformation of the electron bunch due to the large extraction efficiency.

Table 2: Parameters for Puffin Simulation

Number of the undulator period	52
Undulator parameter (peak)	1.34
Undulator pitch (cm)	3.3
Cavity round trip loss	0.03
Cavity detuning length	0
Rayleigh length (m)	0.75
Electron beam energy (MeV)	27.0
Electron bunch charge (pC)	400
Electron bunch length (rectangular with round edges)	
full bunch length (ps)	0.5
Normalized emittance (mm-mrad)	3
Energy spread (rms)	0.1%

Some issues need to be considered for comparing the three-dimensional simulations with experimental results and also with theory. In FEL oscillators, the FEL radiation profile in the transverse plane is determined by the resonator eigenmode and $w_0 = 1.5$ mm in our simulation. The spontaneous radiation, on the other hand, has a dimension determined by the electron beam, 0.13×0.25 mm^2 in our case, and has a large fluctuation of the phase and intensity within the dimension due to the incoherent property. In the simulation, we set the transverse grid size at 15×15 mm^2

ISBN: 978-3-95450-220-2 ISSN: 2673-5474 doi: 10.18429/JACoW-FEL2022-MOP27

with 501×501 grid points, which were limited by the computer resource available.

Figure 7 shows transverse profiles of the optical pulse, beam slices at the main peak and beam slices at the leading edge, after 60 round trips. We can see that the transverse grid points are fine enough to simulate the radiation field at the main peak, but the slices at the leading edge contain numerous sharp peaks whose width is comparable to the grid interval.

Since the spontaneous emission plays an important role in the perfectly synchronized FEL oscillator, the transverse grid points must be fine enough compared to the electron beam size and the entire grids must be large enough to cover both the incoherent spontaneous radiation and the amplified radiation. This constraint increases the cost of the simulation.

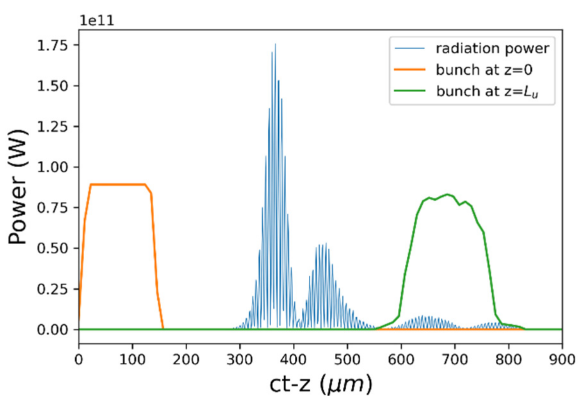

Figure 6: FEL pulse calculated by Puffin with the parameters listed in Table 2. The pulse is at the center of the undulator after 60 round trips.

SUMMARY

We presented one- and three-dimensional simulations of superradiant FEL oscillators with averaged and unaveraged codes. The FEL pulse evolution with high extraction efficiency requires simulations using unaveraged codes that allow macroparticles to move freely within the bunch, rather than averaged codes that assume macroparticles bound to a bunch slice. Unaveraged codes automatically incorporate the effects of coherent radiation according to the electron bunch shape. The coherent radiation becomes effective shot noise and results in a faster rise in the macropulse, and a forward shift of the main peak in the micropulse. The analogy between quantum fluctuations (initial tipping angle) in superradiance of two-level systems and spontaneous emission in superradiant FEL oscillators is also reconfirmed.

ACKNOWLEDGEMENTS

This work was supported by MEXT Q-LEAP (JPMXS0118070271) and JSPS KAKENHI (22H03881). The author thanks Brian McNeil and Pornthep Pongchalee for assistance with the Puffin simulation.

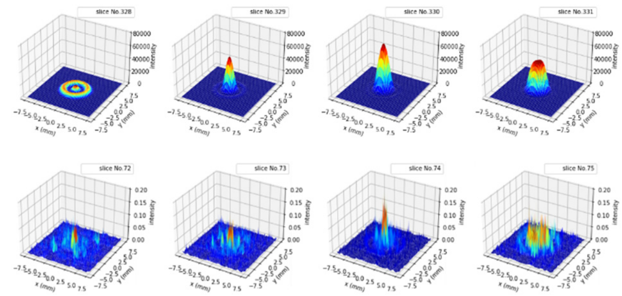
Figure 7: Transverse profiles of the optical pulse after 60 round trips. (Upper column) Beam slices at the main peak, (Lower column) beam slices at the leading edge.

REFERENCES

[1] N. Piovella, "Transient regime and superradiance in a short-pulse free-electron-laser oscillator", *Phys. Rev. E*, vol. 51, p. 5147, 1995. doi:10.1103/PhysRevE.51.5147

[2] R. Hajima, "Few-Cycle Infrared Pulse Evolving in FEL Oscillators and Its Application to High-Harmonic Generation for Attosecond Ultraviolet and X-ray Pulses", *Atoms*, vol. 9, 15, 2021. doi:10.3390/atoms9010015

[3] R.H. Dicke, "Coherence in Spontaneous Radiation Processes", *Phys. Rev.*, vol. 93, p. 99, 1954. doi:10.1103/PhysRev.93.99

[4] R. Hajima and R. Nagai, "Generating Carrier-Envelope-Phase Stabilized Few-Cycle Pulses from a Free-Electron Laser Oscillator", *Phys. Rev. Lett.*, vol. 119, p. 204802, 2017. doi:10.1103/PhysRevLett.119.204802

[5] D.C. Burnham and R.Y. Chiao, "Coherent Resonance Fluorescence Excited by Short Light Pulses", *Phys. Rev.*, vol. 188, p. 667, 1969. doi:10.1103/PhysRev.188.667

[6] D.J. Heinzen, J.E. Thomas, M.S. Feld, "Coherent Ringing in Superfluorescence", *Phys. Rev. Lett.*, vol. 54, p. 677, 1985. doi:10.1103/PhysRevLett.54.677

[7] K. Cong et al., "Dicke superradiance in solids", *J. Opt. Soc. America B*, vol. 33, C80, 2016. doi:10.1364/JOSAB.33.000C80

[8] C.A. Brau, *Free-Electron Lasers*, Academic Press, Inc., 1990.

[9] R. Hajima and R. Nagai, "Generation of a Self-Chirped Few-Cycle Optical Pulse in a FEL Oscillator", *Phys. Rev. Lett.*, vol. 91, p. 024801, 2003. doi:10.1103/PhysRevLett.91.024801

[10] B.W.J. McNeil, G.R.M. Robb, D.A. Jaroszynski, "Self-amplification of coherent spontaneous emission in the free electron laser", *Opt. Comm.*, vol. 165, p. 65, 1999. doi:10.1016/S0030-4018(99)00222-9

[11] C. Penman, B.W.J. McNeil, "Simulation of input electron noise in the free-electron laser", *Opt. Comm.*, vol. 90, p. 82, 1992. doi:10.1016/0030-4018(92)90333-M

[12] L.T. Campbell and B.W.J. McNeil, "Puffin: A three dimensional, unaveraged free electron laser simulation code", *Phys. Plasma*, vol. 19, p. 093119, 2012. doi:10.1063/1.4752743

[13] J. G. Karssenberg, P. J. M. van der Slot, I. V. Volokhine, J. W. J. Verschuur, and K.-J. Boller, "Modeling paraxial wave propagation in free-electron laser oscillators", *J. Appl. Phys.*, vol. 100, p. 093106, 2006. doi:10.1063/1.236325

ISBN: 978-3-95450-220-2 ISSN: 2673-5474 doi: 10.18429/JACoW-FEL2022-MOP28

LASER-INDUCED GAS BREAKDOWN AT KU-FEL

R. Hajima†, National Institutes for Quantum Science and Technology, Kizugawa, Japan
H. Zen, H. Ohgaki, Kyoto University, Uji, Japan

Abstract

We have observed laser-induced breakdown of gases at KU-FEL, the FEL oscillator at Kyoto University, in which few-cycle FEL pulses are generated due to superradiance. In the thermionic cathode mode with a repetition rate of 2856 MHz and a wavelength of 10 µm, the breakdown was observed in air, nitrogen, and argon, while weak luminescence from nitrogen was observed in the photocathode mode operation (29.75 MHz, 8.7 µm). We discuss the mechanism of each phenomenon. The difference in the two operation modes can be explained by the diffusion of electrons between the micropulses.

INTRODUCTION

Free-electron laser oscillators operated in the superradiant regime provide ultrashort infrared pulses with durations of only a few optical cycles. In such lasing, the peak intensity of FEL pulses increases in proportion to the square of the number of electrons. The intensity of the FEL pulses after appropriate focusing, thus, can exceed the threshold of tunnel ionization in atoms and molecules (> 10^{13}W/cm^2), making it possible to develop intense light field science in the long-wavelength infrared region (8-15 µm), where solid-state lasers are difficult to be applied [1].

In this paper, we report recent results from gas-induced breakdown experiments at KU-FEL, the FEL oscillator at Kyoto University, which can be operated in the superradiant regime to produce few-cycle FEL pulses with a high extraction efficiency [2,3].

LASER-INDUCED GAS BREAKDOWN

Laser-induced gas breakdown occurs by the multiphoton ionization process at low pressures and in the case of short pulses (sub-nanosecond). For high-pressure cases, collision cascade ionization dominates [4,5]. Since our experiment is in the high-pressure case, the collision cascade ionization is reviewed here.

The breakdown is initiated by a few free electrons, seed electrons, in the illuminated region. Seed electrons are produced by multiphoton ionization of gas molecules or airborne particles. Cosmic radiation is also a source of seed electrons. Once seed electrons are produced, the electrons gain energy from the laser field by inverse bremsstrahlung, the three-body collision of a photon, an electron, and a heavy particle, and after a number of collisions, the electron energy becomes high enough to induce another ionization. This cascade ionization continues until a sufficient number of free electrons are produced to induce breakdown in the focal spot. The number of free electrons at the breakdown is about 10^{13} [5].

The number of electrons, n, in the cascade process varies according to [4,5]

$$\frac{dn}{dt} = (\nu_i - \nu_a)n - \nabla^2(Dn) - \beta n^2 ,$$

where ν_i is the ionization frequency, ν_a is the attachment frequency, D is the diffusion, and β is the recombination coefficient. The electron energy (ε) gained by the inverse bremsstrahlung is given by

$$\frac{d\varepsilon}{dt} = \frac{e^2 E_{rms}^2 \nu_{eff}}{m\left(\omega^2 + \nu_{eff}^2\right)},$$

where E_{rms} is the rms electric field of the laser, e and m is the electron charge and mass, ω is the laser frequency and ν_{eff} is the effective electron heavy particle collision frequency. The effective collision frequency for air is $\nu_{eff} = 5.3 \times 10^9 p$, with p in torr [6].

Assuming the number of initial and final free electrons in the cascade process, $n_i = 1$ and $n_f = 10^{13}$, we can evaluate the number of cascade generation $k = \ln\left(n_f/n_i\right)/\ln 2 \approx 43$. The laser energy deposition for achieving the breakdown, then, must be larger than kE_I, where E_I is the ionization energy. This requirement of the energy deposition leads to the threshold of the laser energy fluence, F_{th}, for the breakdown, neglecting the particle and energy loss:

$$F_{th} = \frac{kE_I\left(\nu_{eff}^2 + \omega^2\right)}{4\pi r_0 c \nu_{eff}},$$

where r_c is the classical electron radius. For a laser wavelength of 10 µm, and nitrogen gas of 1.0×10^5 Pa, we obtain $F_{th} = 8$ J/cm^2. Once the laser wavelength and the pulse length are given, the intensity threshold for the gas

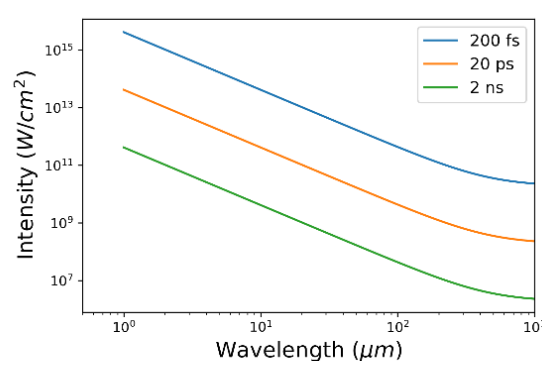

Figure 1: Laser-induced breakdown threshold calculated for nitrogen of 1.0×10^5 Pa and laser pulses with different durations, 200 fs, 20 ps, and 2 ns.

† hajima.ryoichi@qst.go.jp

ISBN: 978-3-95450-220-2 ISSN: 2673-5474 doi: 10.18429/JACoW-FEL2022-MOP28

breakdown can be evaluated. We plot the intensity threshold for nitrogen gas of 1.0×10^5 Pa in Fig. 1.

GAS BREAKDOWN EXPERIMENTS AT KU-FEL

In KU-FEL, the 4.5-cell RF electron gun equipped with a single-crystal LaB_6 cathode can be operated in either thermionic or photocathode mode. In the thermionic cathode mode, electron bunches with charges up to 60 pC are accelerated at 2856 MHz repetitions, while repetitions and bunch charges in the photocathode operation are 29.75 MHz and 200 pC. Since the peak intensity and duration of an FEL pulse in the superradiant regime scale as the number of electrons, the photocathode mode exhibits a higher extraction efficiency and a shorter pulse [2, 3]. Operation parameters for the gas breakdown experiments are listed in Table 1.

Table 1: Parameters for FEL Pulses

	thermionic	photocathode
Wavelength	10 μm	8.7 μm
Macropulse duration	7 μs	7 μs
Macropulse repetition	2 Hz	2 Hz
Micropulse duration (FWHM)	270 fs	150 fs
Micropulse repetition	2856 MHz	29.75 MHz
FEL pulse energy at the experimental station (*)	4 μJ	30 μJ

(*) maximum values in a macropulse

When FEL pulses from the thermionic cathode mode are focused in the air, breakdown emission with a popping sound was observed. In the photocathode mode, however, no breakdown occurred despite the higher pulse energy. To understand these results, a detailed experiment was conducted.

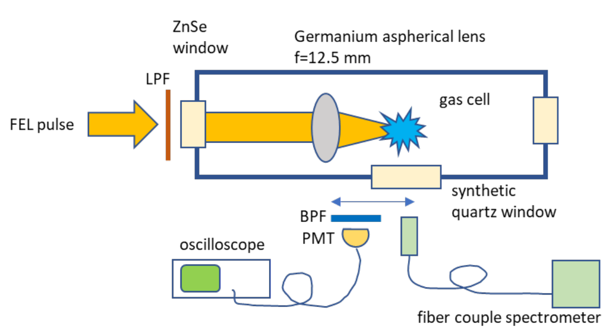

Figure 2: Experimental setup for the laser-induced gas breakdown measurements.

Figure 2 shows the experimental setup. FEL pulses were injected into the gas chamber through a long pass filter to suppress the FEL high-harmonics (7.3 μm-LPF Edmund #68-662) and an AR-coated ZnSe window. The pulses were focused by an AR-coated Germanium aspherical lens (f=12.7 mm Edmund #89-607). The spectrum of optical emission from the laser-induced breakdown was measured by a fiber-coupled spectrometer (ASEQ LR1-B) and a waveform was recorded with a band-pass filter and a photomultiplier tube (Hamamatsu Photonics R1477) connected to an oscilloscope. The experiment was conducted with the thermionic cathode mode. The spot size at the focal point was 13 μm ($1/e^2$ radius), which corresponds to the peak intensity of 7×10^{12} W/cm^2.

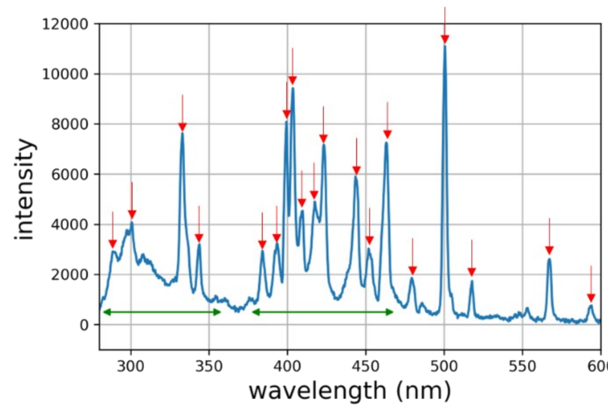

Figure 3: Emission spectrum of the laser-induced breakdown from nitrogen gas at 1.7×10^5 Pa. The red arrows are emission lines for nitrogen atomic ions (N-II). The green arrows correspond to emission bands of nitrogen molecules ($C^3\Pi_u \rightarrow B^3\Pi_g$ and $B^2\Sigma_u^+ \rightarrow X^2\Sigma_g^+$).

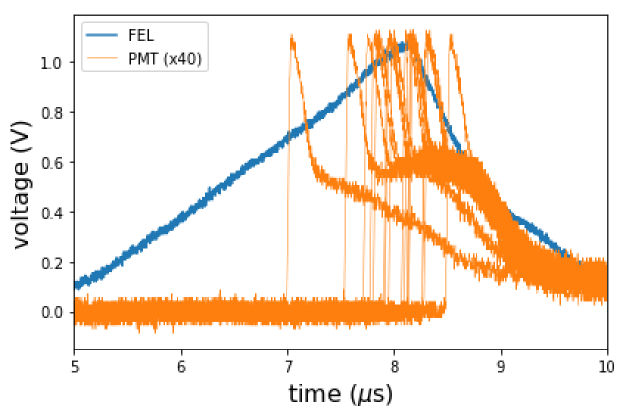

Figure 4: Waveforms of FEL macropulse and emission from the breakdown of nitrogen gas (1.0×10^5 Pa, no filter at PMT).

Figure 3 is an example of the emission spectrum from the laser-induced breakdown in nitrogen gas at 1.7×10^5 Pa (raw spectrum before CCD sensitivity correction). Emission lines were identified by referring to the database [7], and most of them were assigned to the excited levels of the monovalent ions of nitrogen atoms (N-II). The broad spectra indicated by the green arrows in the figure are the wavelength regions corresponding to the transitions between the excited levels of the nitrogen molecule ($C^3\Pi_u \rightarrow$

ISBN: 978-3-95450-220-2 ISSN: 2673-5474 doi: 10.18429/JACoW-FEL2022-MOP28

$B^3\Pi_g$, $B^2\Sigma_u^+ \rightarrow X^2\Sigma_g^+$), but the lines for each rotational level in the transition were not separated due to the limited resolution of the spectrometer.

Waveforms of the emission without a band-pass filter for nitrogen at 1.0×10^5 Pa are plotted in Fig. 4. The figure shows that emission occurs at an arbitrary timing in the macropulse, suggesting that stochastic events dominate the breakdown. The emission has a decay time on the order of microseconds. In the experiment, the gas pressure varied from 0.6×10^5 to 1.7×10^5 Pa, and we found a higher probability of emission for higher gas pressure.

In the photocathode mode operation, we focused FEL pulses in the air with a ZnSe aspherical lens (f=12.7 mm, Thorlabs AL72512-E3). No strong emission of breakdown with a popping sound was observed in this experiment, but weak emission was detected by a photomultiplier tube (PMT, Hamamatsu Photonics R2658). Figure 5 shows an emission waveform measured by the PMT with a bandpass filter of 337 nm (Edmund #89-607).

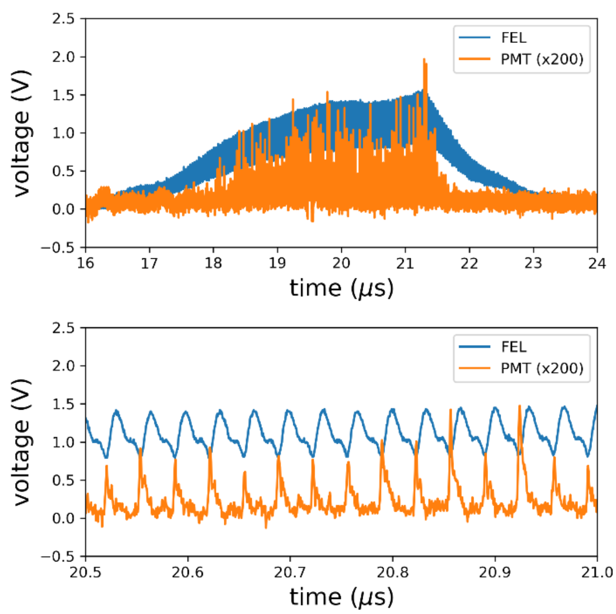

Figure 5: Waveforms of FEL pulse and PMT signals with a bandpass filter of 337 nm.

DISCUSSION

Two points need to be examined to interpret the breakdown observed in the thermionic cathode experiment in terms of conventional theory. One is the source of seed electrons and the other is the process of cascade ionization.

Ionization caused by cosmic rays is estimated to be 2 events/s/cm^3 in the atmosphere [8], which is negligible for the FEL's pulse length and spot size, so the seed electron should be of the FEL pulse origin. The photoionization rate of nitrogen molecules calculated by the molecular ADK model [9] with the experimental peak intensity is, however, insufficient to explain the production of seed electrons. We, therefore, consider the seed electrons were generated by photoionization of airborne particles or oil mist from the rotary pump.

In the introduction, we evaluated the breakdown threshold, $F_{th} = 8$ J/cm^2, for a laser wavelength of 10 μm, and nitrogen gas of 1.0×10^5 Pa. The experimental fluence of a micropulse at the focal spot, 1.6 J/cm^2, was far below the threshold. Hence, it is suggested that the cascade ionization was built up during a pulse train containing many micropulses.

The buildup of cascade ionization in a pulse train is suppressed by electron diffusion between micropulses. Using a plasma database of diffusion coefficient [10], calculations of electron diffusion at micropulse interval show that the electron density at the focal spot is reduced to 14% during the pulse interval, 350 ps, for the thermionic cathode mode, and reduced to 10^{-8} at the photocathode mode, where the pulse interval is 33.6 ns. We consider that the absence of discharge emission in the photocathode operation is due to the electron diffusion between micropulses.

The emission of 337 nm observed at the photocathode mode is the fluorescence of nitrogen molecules, corresponding to the transition between the lowest rotational levels of $C^3\Pi_u$ and $B^3\Pi_g$. In an experiment using a solid-state laser with a wavelength of 1.6 μm, it was confirmed that the intensity of 337-nm emission of nitrogen is consistent with the calculated tunnel ionization yield [11]. The nonlinear variation of the PMT signal with respect to the FEL pulse intensity shown in Fig. 5 suggests that the molecular transition for the 337-nm emission is triggered by strong-field ionization.

SUMMARY AND OUTLOOK

Emission from gases was observed with few-cycle long-wavelength infrared pulses at KU-FEL. The emission shows different aspects for the thermionic and photocathode modes. In the thermionic mode with a repetition rate of 2856 MHz, cascade ionization developed during a pulse train results in laser-induced breakdown. In the photocathode mode, we observed the fluorescence from excited nitrogen molecules generated by strong-field ionization. Further experiments will be continued to investigate these emission phenomena in more detail. We expect that wavelength-tunable, high-repetition-rate FEL oscillators will bring new possibilities to intense light field science in long-wavelength infrared.

ACKNOWLEDGEMENTS

This work was supported by MEXT Q-LEAP (JPMXS0118070271), IAE ZE Research Program (ZE2022B-23) and JSPS KAKENHI (22H03881).

REFERENCES

[1] R. Hajima, "Few-Cycle Infrared Pulse Evolving in FEL Oscillators and Its Application to High-Harmonic Generation for Attosecond Ultraviolet and X-ray Pulses", *Atoms*, vol.9, Iss.1, 15, 2021, doi:10.3390/atoms9010015

ISBN: 978-3-95450-220-2 ISSN: 2673-5474 doi: 10.18429/JACoW-FEL2022-MOP28

[2] H. Zen, H. Ohgaki, and R. Hajima, "High-extraction-efficiency operation of a midinfrared free electron laser enabled by dynamic cavity desynchronization", *Phys. Rev. Accel. Beams*, vol. 23, p. 070701, 2020, doi:10.1103/PhysRevAccelBeams.23.070701

[3] H. Zen, H. Ohgaki, R. Hajima, "Record high extraction efficiency of free electron laser oscillator", *Appl. Phys. Express*, vol. 13, p. 102007, 2020, doi:10.35848/1882-0786/abb690

[4] M. Young and M. Hercher, "Dynamics of Laser‐Induced Breakdown in Gases", *J. Appl. Phys.*, vol. 38, p. 4393, 1967, doi:10.1063/1.1709137

[5] K.V. Kubarev, Ya. V. Getmanov, O.A. Shevchenko, P.V. Koshlyakov, "Threshold Conditions for Terahertz Laser Discharge in Atmospheric Gases", *J. Infrared Milli. Terahz. Waves*, vol. 38, pp. 787-798, 2017, doi:10.1007/s10762-017-0380-3

[6] J. Stricker, J.G. Parker, "Experimental investigation of electrical breakdown in nitrogen and oxygen induced by focused laser radiation at 1.064 μ", *J. Appl. Phys.*, vol. 53, p. 851, 1982, doi:10.1063/1.330592

[7] NIST Basic Atomic Spectroscopic Data, https://physics.nist.gov/PhysRefData/Handbook/Tables/nitrogentable2.htm

[8] W.M. Lowder and H.L. Beck, "Cosmic-ray ionization in the lower atmosphere", *J. Geophysical Research*, vol. 71, p. 4661, 1966, doi:10.1029/JZ071i019p04661

[9] X. M. Tong, Z. X. Zhao, and C. D. Lin, "Theory of molecular tunneling ionization", *Phys. Rev. A*, vol. 66, p. 033402, 2002, doi:10.1103/PhysRevA.66.033402

[10] Plasma Data Exchange Project, https: //nl.lxcat.net/home

[11] N. Saito, N. Ishii, T. Kabai and J. Itatani, "All-optical characterization of the two-dimensional waveform and the Gouy phase of an infrared pulse based on plasma fluorescence of gas", *Opt. Exp.*, vol. 26, p. 24591, 2018, doi:10.1364/OE.26.024591

ISBN: 978-3-95450-220-2 ISSN: 2673-5474 doi: 10.18429/JACoW-FEL2022-MOP31

ANALYSES SUPPORTING THE 2-COLOR UPGRADE TO THE IR FEL AT FHI, BERLIN*

A. M. M. Todd†, AMMTodd Consulting, Princeton Junction, USA
W. B. Colson, WBC Physics, Carmel, USA
D. H. Dowell, SLAC, Menlo Park, USA
S. C. Gottschalk, STIMagnetics, Woodinville, WA, USA
J. W. Rathke, JW Rathke Engineering Services, Centerport, USA
T. J. Schultheiss, TJS Technologies, Commack, USA
L. M. Young, LMY Technology, Lincolnton, GA, USA
W. Schöllkopf, M. De Pas, S. Gewinner, H. Junkes, G. Meijer, G. Helden, FHI, Berlin, Germany

Abstract
This paper provides a summary of the analyses that led to the definition of the 2-color upgrade of the IR FEL at the Fritz-Haber-Institut (FHI), Berlin. We briefly cover several different aspects of the design, beginning with the beam dynamics of the second far-IR (FIR) beamline, engineering considerations of that physics design, and the FEL physics that defined the short-Rayleigh-range undulator, as well as aspects of the undulator design itself. Additionally, we touch on the approach to 2-color operation and considerations for the FIR optical transport to users. The status of commissioning is described in a parallel paper [1].

INTRODUCTION

The FHI mid-IR (MIR) FEL first lased on February 14, 2012 [2]. Since November 2013, it has provided continuous 3 to 60 µm radiation service to users, resulting in more than 80 peer-reviewed publications [3].

In 2018, FHI embarked upon an ambitious upgrade project to add a FIR FEL beamline that could deliver radiation from 5 to 166 µm. By adding a 2-degree deflecting cavity right after the second linac, alternately, 2-color, 500 MHz pump-probe radiation can be delivered to experiments on the MIR and FIR beamlines, which are separated by 4 degrees, when the new FEL is commissioned.

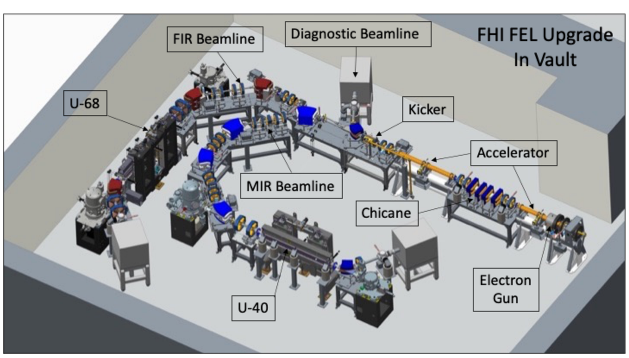

Figure 1: Engineering schematic showing the FHI FEL MIR and FIR electron beamlines in the vault.

* Work supported by the Max-Planck-Gesellschaft, Munich, Germany.
† ammtodd@fhi-berlin.mpg.de

This paper describes the analysis that underpinned the FIR FEL physics and engineering design illustrated in Fig. 1. It touches on the beam dynamics and engineering analyses of the electron beamline, the undulator FEL physics and engineering, the FIR optical transport and scanner magnet calibration measurements used in the beam dynamics calculations.

BEAM DYNAMICS

We concentrate on the most difficult 18 MeV energy operation at the longest wavelengths (166 µm with the minimum 32 mm undulator gap). Figure 2 shows a TRACE3D [4] plot for the FIR electron beamline beginning after the accelerator at the left edge to the beam dump at the right edge. Note that the dispersion trace (gold) goes to zero at the center of the U-68 undulator indicating that the 94-degree pre-undulator FIR bend is achromatic. The horizontal U-68 match has a waist in mid-undulator, while the near constant vertical trace illustrates the proper match in the vertically focusing undulator.

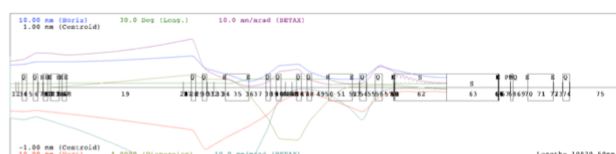
Figure 2: TRACE3D 5ε beam envelope simulation of the FIR electron beamline with achromaticity in the centre of the undulator (gold trace) and an excellent match (horizontal/blue - vertical/red) to the U-68 undulator (62 and 63).

Using identical post-linac parameters, the corresponding Fig. 3 TSTEP [5] simulation for this case shows the revised FIR achromat delivers a 2.5 ps, 100 keV FWHM beam to the FIR undulator for FEL physics analysis.

The most difficult operating scenario will occur for 2-color FEL operation where, for any given beam energy, we are short of beam matching variables on the U-68 beamline. Our plan is to utilize quadrupoles QB05 and QB06 after linac 2, and QC04 and QC05 ahead of U-68, to produce waists in the middle and the near constant matched vertical beam size through U-68, at the longest wavelength. For the MIR beamline, we use the matched FIR values for the two magnets after linac 2, adjusting QC01 and QC02,

ISBN: 978-3-95450-220-2 ISSN: 2673-5474 doi: 10.18429/JACoW-FEL2022-MOP31

ahead of U-40 and two of the MIR mid-achromat triplet magnets, to provide a similar match for U-40 at the minimum gap yielding 50 µm radiation.

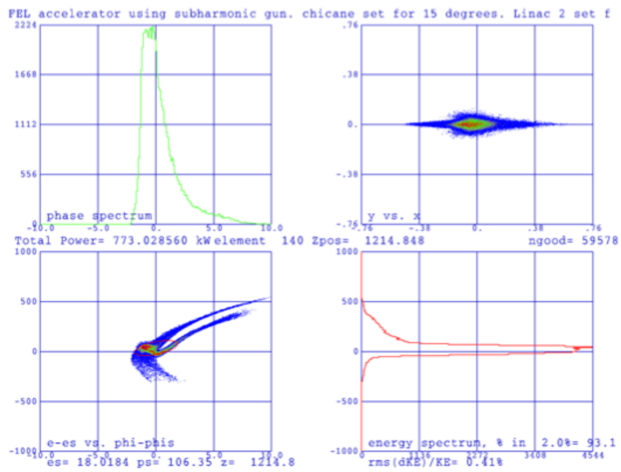

Figure 3: TSTEP simulation of the FIR electron beamline showing the 2.5 ps, 100 keV beam at the entry to U-68.

As shown in Fig. 4, given there is no undulator horizontal focusing, the horizontal beam remains well matched during a gap scan, but the vertical beam starts to exhibit betatron oscillations as the undulator opens. At maximum FIR gap for 31 µm radiation, the vertical match has deteriorated significantly, but the maximum vertical beam size is still less than 2 mm rms, which still fits nicely inside the larger FIR optical mode and should lase adequately. If necessary, we will have the control system vary the key focusing quadrupole magnets with gap size to maintain the focus in the two undulators, though we are reluctant to introduce this added complexity.

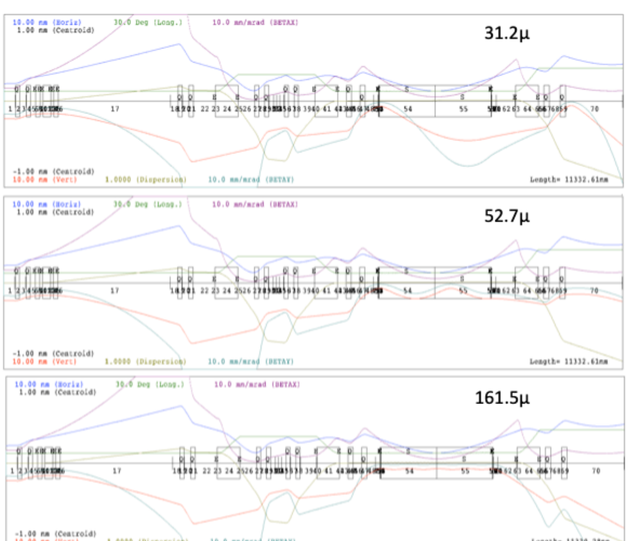

Figure 4: TRACE3D 5ε beam envelope simulation of the FIR electron beamline during a gap scan at 18 MeV showing the loss of vertical focusing (red trace) as the U-68 gap opens from bottom to top.

BEAMLINE ENGINEERING ANALYSIS

The major FIR engineering issues cantered on the performance of the deflector cavity, the design of the very large gap DF dipole magnets because of the large, short Rayleigh range oscillator FIR optical beam envelope on each side of U-68, and the output FIR beam dump window. Figure 5 shows the axial deflecting electric field and thermal analysis for the cavity which was fabricated by Research Instruments GmbH. All potential issues were addressed in the analysis and fabrication, so we are confident that these components will deliver their required performance.

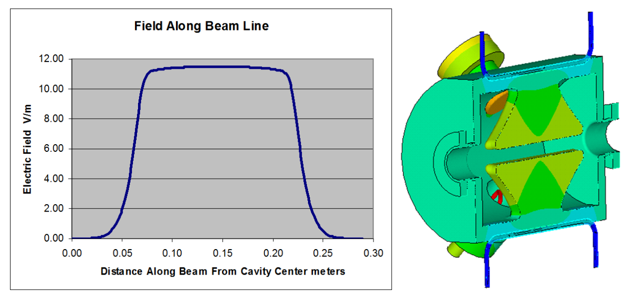

Figure 5: Flat deflecting cavity transverse electric field (left) and thermal analysis of the cavity indicating the predicted small temperature variation of the design (right).

U-68 UNDULATOR ANALYSIS

The undulator design challenge was to provide a nominally non-steering, non-offset, gap-tapered end design to reduce scraping of the 166 µm optical mode at a gap of 32 mm for the 18 MeV electron beam energy. Simultaneously, the entry needed to have a minimal gap dependence to keep the trajectory straight enough that the 40 turn upstream electromagnetic (EM) coils could turn the beam to maintain good optical mode overlap under all operating conditions. A radiation resistant, wedged-pole hybrid with grain boundary diffusion was chosen.

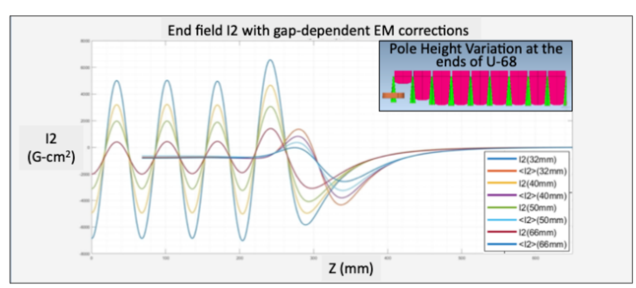

Figure 6: Field integral, I2, from FEA with gap-dependent EM correction for the entry to U-68. The inset shows the pole height variation.

Signature-based finite element analysis (FEA) with metaheuristic, genetic optimization was performed. The heights of the first three poles and the first two magnets were varied and confirmatory, non-signature, multi-gap, full 3D FEA was performed as shown in Fig. 6. Mechanical design of the ends imposed added constraints and requirements. The FEA model illustrates the range of pole and

ISBN: 978-3-95450-220-2 ISSN: 2673-5474 doi: 10.18429/JACoW-FEL2022-MOP31

magnet heights with the first pole 5.65 mm shorter than the center poles. Features like steel strong backs, EM and clamping bolt holes, pole clamp ears and the nominal 0.3mm air gap between poles and magnets were included.

FEL PHYSICS

We have designed a short 68 cm Rayleigh range oscillator undulator to deliver FIR radiation from 5 to 166 µm. The 2.5 ps beam in the 30 period, 68 mm undulator delivers the 166 µm radiation at the minimum gap of 32 mm for 18 MeV operation. The mode is large at the 8 cm diameter optical cavity mirrors but has 96 % of the radiation in the fundamental mode and optimizes to a 6 mm diameter outcoupling hole under these conditions. For the shortest wavelengths, a 1 mm diameter outcoupling hole is preferred.

Figure 7 shows the optical pulse shape and the spectrum for this 166 µm operation point. Saturation occurs in 2.4 µs and the final spectral width is 2.5 %. Thus, we are very encouraged by these FEL physics simulations.

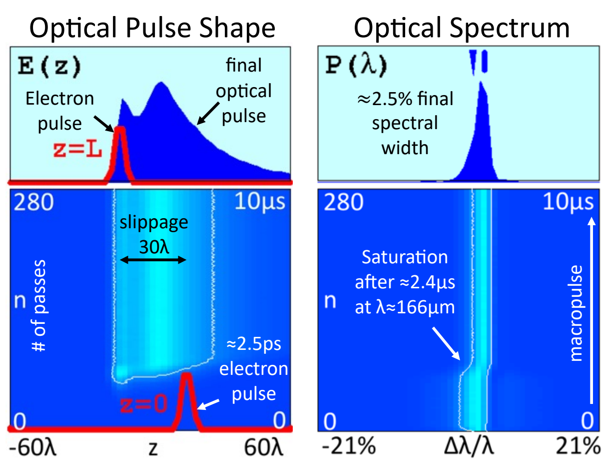

Figure 7: FIR output radiation performance at 166µm.

OPTICAL TRANSPORT

The first experimental FIR target will be the so-called "X4" location upstairs in the FHI user center. The revised MIR optical transport is already successfully in operation.

We have defined an FIR optical transport solution but are waiting for the X4 users to finalize their requirements for optical waist size, pump-probe timing, and target orientation. The baseline geometry from the entrance to the optical diagnostic room and onward upstairs to X4 is shown in Fig. 8 for the MIR (blue) and FIR (orange) optical transport lines. A trombone on the FIR beam line may have to be added to control arrival times between the two lines for pump-probe experiments.

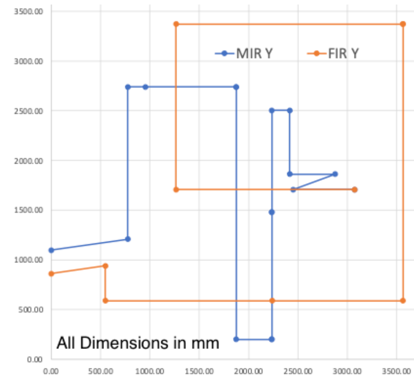

Figure 8: MIR and FIR optical transport in the optical diagnostic room and the upstairs X4 experiment.

The existing MIR and baseline FIR optical transport is shown in Fig. 9, illustrating the waists in the optical diagnostic room and at the X4 target. Both 3.5 w waists at the X4 target are less than 2.5 cm.

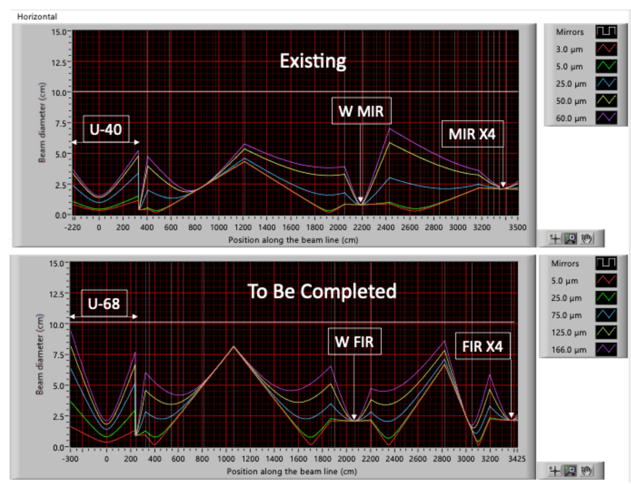

Figure 9: MIR and FIR 3.5w optical transport IR beam envelope transport to the X4 experimental target.

CONCLUSIONS

The design and analysis of the FHI far-IR (FIR) electron and optical beamlines has been completed with all key components delivered and installed.

The redesigned single-achromat FIR beamline has improved emittance delivery at the U-68 undulator for effective FIR lasing. The kicker performance has been verified. Magnetic measurement of key magnets was completed using the magnet scanner system installed at FHI.

Excellent user FIR power performance from 5 – 166 µm is predicted for the FIR beamline in stand-alone and 2-color operation. MIR optical transport to the user X4 target is in operation and the FIR design that will permit 2-color FEL operation is completed awaiting user confirmation and procurement.

The existing mid-IR (MIR) has been recommissioned and regular user operations are ongoing.

ISBN: 978-3-95450-220-2 ISSN: 2673-5474 doi: 10.18429/JACoW-FEL2022-MOP31

REFERENCES

[1] W. Schöllkopf *et al.*, "2-color Upgrade of the IR FEL at FHI Berlin", presented at FEL '22, Trieste, Italy, Aug. 2022, paper MOP23, this conference.

[2] W. Schöllkopf *et al.*, "First Lasing of the IR FEL at the Fritz-Haber-Institut Berlin", in *Proc. FEL'12*, Nara, Japan, Aug. 2012, paper MOOB01, `doi:10.18429/JACoW-FEL2012-MOOB01`

[3] W. Schöllkopf *et al.*, "The New IR FEL Facility at the Fritz-Haber-Institut in Berlin", in *Proc. FEL'14*, Basel, Switzerland, Aug. 2014, paper WEB04, pp. 629-634.

[4] TRACE3D, `https://laacg.lanl.gov/laacg/services/traceman.pdf`

[5] TSTEP, `https://tstep.lmytechnology.com`

40th International Free Electron Laser Conference,Trieste JACoW Publishing
ISBN: 978-3-95450-220-2 ISSN: 2673-5474 doi: 10.18429/JACoW-FEL2022-MOP32

MODELLING OF SUB-WAVELENGTH EFFECTS IN A FEL OSCILLATOR

P. Pongchalee[1,2,3], B.W.J. McNeil[1,2]
[1]SUPA, Department of Physics, University of Strathclyde, Glasgow, UK
[2]Cockcroft Institute, Warrington, WA4 4AD, UK
[3]ASTeC, STFC Daresbury Laboratory, Warrington, WA4 4AD, UK

Abstract

Previous studies of FEL oscillators typically use averaged simulation codes which cannot model sub-wavelength effects, such as Coherent Spontaneous Emission from the electron pulse. In this paper, the unaveraged FEL simulation code Puffin is used with the optics code Optical Propagation Code (OPC) to model a FEL oscillator in three dimensions, enabling sub-wavelength effects to be modelled at the FEL interaction and cavity length scales. Results show that coherence spontaneous emission (CSE) can drive the FEL interaction during the start-up phase in the cavity. Further, cavity detuning effects at the sub-wavelength scale can have an effect upon the FEL output from start-up through to the steady state output. While the effects are demonstrated here at a fundamental level, it can be expected that they may be reduced due to limitations such as electron beam and/or cavity length jitter at the radiation wavelength scale. Such effects will need to be further investigated.

INTRODUCTION

When modelling the short pulse effects here, both the coherent and shot-noise spontaneous emission from the electron beam are taken into consideration. CSE has the potential to dominate the overall amplification of the FEL start-up process in an undulator when it is operating, particularly in the low-gain regime of FEL operation. CSE is primarily caused by a short electron beam that has a fine structure at the wavelength scale, such as a sharp-edge rectangular beam. For a short-pulse FEL oscillator, a better understanding of such sub-wavelength effects is needed and a preliminary study is presented here.

Previously, Puffin [1] and OPC [2] were operated together to simulate a RAFEL oscillator model operating in the steady-state [3], but without considering any detailed effects of coherence spontaneous emission (CSE). The effect of CSE occurs with relatively short electron bunch lengths e.g. when they are shorter or comparable to the slippage length. The use of an unaveraged FEL code, Puffin enables the modelling of CSE effects and, together with OPC, can simulate the optical components for an optical cavity at the sub-wavelength scale. A full 3D unaveraged model of a short pulse FEL oscillator can be achieved.

In this paper an FEL oscillator design operating with the near-concentric resonator in the mid-infrared regime is then described. We first demonstrate the simulation of the FEL oscillator when the optical cavity length is detuned from resonance by integer factors of 0.05 of a radiation wavelength.

THE SIMULATION MODEL

FEL and Optics Codes

The conversion of the radiation field between Puffin and OPC has been described in [3]. The two codes are run sequentially staring from, the Puffin si mulation of electron/light interaction inside the undulator. The output field at the undulator exit from Puffin is then translated into OPC format to propagate further in the optical oscillator including mirrors and optical path length adjusting due to cavity non-resonance. OPC propagates the radiation field to the undulator entrance, where it is translated back into Puffin field format and is used as a seed for the Puffin input file for the subsequent pass.

Simulation Parameters

In the example presented here, we use parameters as given in Table 1. The parameters used are very similar to those of the IR-FEL of [4]. A curved pole undulator is used to keep the beam size constant throughout the undulator length [5]. The undulator module of length 1.8m consists of the 40 periods of $\lambda_u = 4.5$ cm. The symmetric transverse size of the beam is matched into the curved undulator lattice with $\sigma_{x,y} = 311.8$µm. The temporal shape of the beam current is rectangular of duration 400 fs. The electron beam energy and undulator parameters give a radiation wavelength in the mid-infrared wavelength regime of 6 µm. The electron beam length is then equal to 20λ.

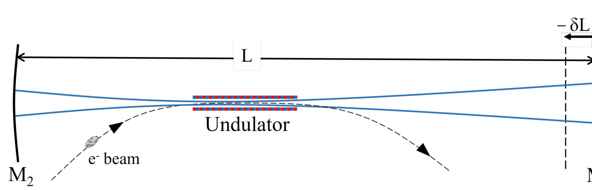

Figure 1: a diagram of the FEL oscillator used in the simulation

The optical cavity is designed as a near-concentric resonator with a Rayleigh length of 52 cm. Two mirrors make up the optical cavity (see Fig. 1). The first mirror is placed after the undulator exit with an output coupling that can be partially transmissive or use a hole out-coupling. The second mirror that forms the simple cavity is then placed before the undulator entrance. When the distance between the two mirrors gives a round-trip propagation time equal to the electron beam repetition rate, the cavity has zero length detuning. The optical beam waist position will be in the cen-

ISBN: 978-3-95450-220-2 ISSN: 2673-5474 doi: 10.18429/JACoW-FEL2022-MOP32

tre of the undulator and the Rayleigh length is approximately one-third of the undulator length.

Table 1: Summary of FEL oscillator parameters

Electron beam parameters	
Electron energy (MeV)	50
Bunch charge (pC)	100
Bunch length (fs)	400
Normalised emittance (x,y) (mm mrad)	12/12
Peak current (mA)	250
Transverse size, $\sigma_{x,y}$ (μm)	311.8
Bunch repetition (MHz)	10
Undulator	
Undulator type	Curved pole
Polarisation	Linear
Undulator parameter (rms)	1.25
Pitch (cm)	4.5
Number of periods	40
Oscillator	
Rayleigh length (m)	0.52
Cavity length (m)	14.9896
Mirror 1 radius (m)	9.00024
Mirror 1 reflectivity	0.960
Mirror 2 radius (m)	6.064
Mirror 2 reflectivity	0.999

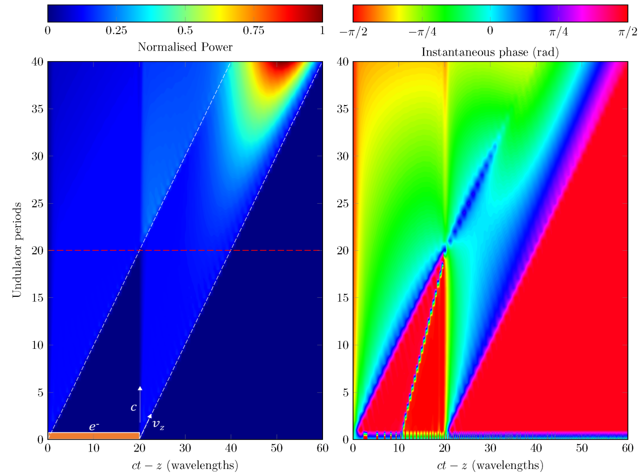

Figure 2: Contour plot of the FEL power evolution (left) and phase (right) inside the undulator as it evolving through the undulator length during the first pass through the oscillator. The power starts from electron beam shot noise and CSE. The electron beam (bottom left) moves left-to-right in the radiation window frame as it propagates through the undulator.

RESULTS

The power evolution of the radiation field within the undulator over the first trip within the cavity is plotted in Fig. 2 together with the position of the electron pulse at the start of the undulator (bottom left). The electron beam then moves from left-to-right in the radiation window as it propagates at a velocity $< c$ through the undulator. A CSE wavefront is generated by the trailing edge of the electron beam, located at $ct - z = 20\lambda$ at the start of the undulator. The temporal position of 20 wavelengths, which is equivalent to the length of an electron bunch, led directly to the appearance of the CSE which propagates vertically (equal to the speed of light) and has a greater power than any spontaneous shot-noise.

The slippage of the electron pulse behind the radiation causes the radiation gain to occur initially towards the rear of the optical pulse, which in turn causes the centroid of the optical pulse to travel at a velocity that is slightly slower than the speed of light. A similar effect takes place during successive passes: the rear part of the pulse is amplified first, and as a result, the pulse's centroid velocity becomes gradually slower than the speed of light with each successive pass. In due time, the optical pulse and the electron beam start to become decoupled from one another. As seen in Fig. 3, the FEL power and phase evolution as the function of cavity roundtrip number, the power is slightly shifted towards the rear of the pulse after every roundtrip so that the peak power propagates at a velocity $< c$. The pulse is amplified from the first pass through the cavity and reaches a maximum energy at pass number ~20, then slightly decays until decoupling from the electrons around pass number 80.

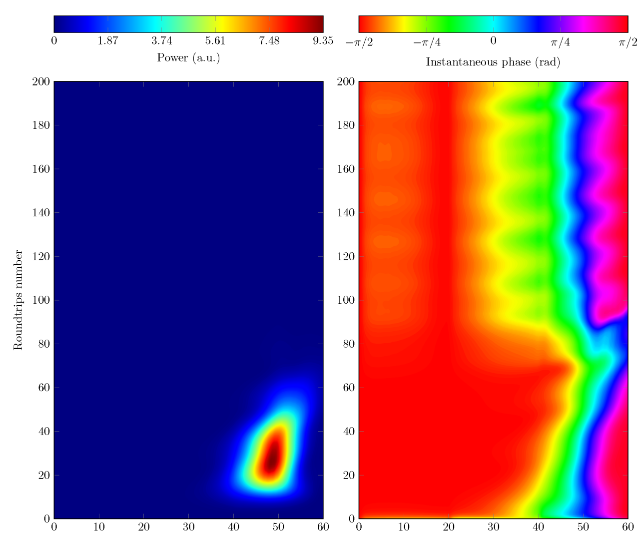

Figure 3: Contour plot of the FEL power evolution as a function of roundtrips number for zero cavity detuning. It is observed that the radiation pulse power propagates at a velocity less than the speed of light.

Cavity shortening, or detuning, can be implemented so that the time dilation that occurs between the optical pulse and the electron bunch can be adjusted. When the cavity is shorter, the optical pulse arrives sooner than it would in

ISBN: 978-3-95450-220-2 ISSN: 2673-5474 doi: 10.18429/JACoW-FEL2022-MOP32

the event of zero detuning and can help mitigate the 'slower pulse' effects observed in Fig. 3 and the interaction region is no longer confined towards the rear of the electron bunch. For the sake of simplicity, here we use the notation of a positive cavity detuning to express a shortening of the cavity. Thus, a cavity detuning length $\delta L > 0$ means the cavity is shortened by this length and the light pulse travels a shorter distance of $2\delta L$ each round-trip. Note that the utilisation of Puffin allows a sub-wavelength adjustment of cavity detuning with a minimum resolution equal to the distance between adjacent nodes of the radiation field sampling. In this particular instance, the simulations make use of 21 nodes for each radiation wavelength within Puffin. This allows the cavity detuning δL to be changed in units of 0.05λ, giving a cavity roundtrip distance change of the radiation of $2\delta L = 0.1\lambda$.

Figure 4 plots the effect of detuning the cavity away from resonance on the radiation pulse energy as a function of roundtrip number, for a range of sub-wavelength cavity detuning $0.0 < 2\delta L < \lambda$. The corresponding effect on the

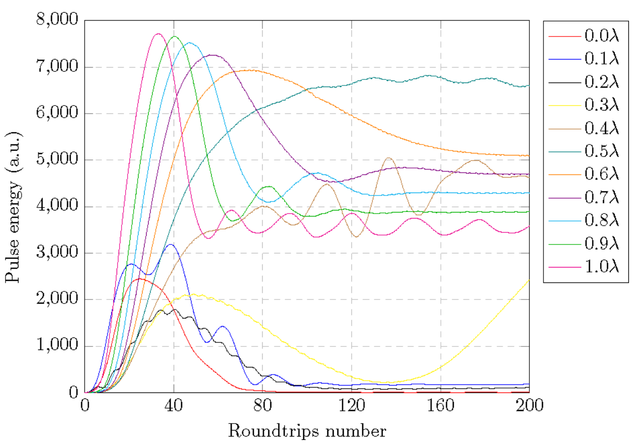

Figure 4: Pulse energy as the function of roundtrips number for a range of sub-wavelength cavity detunings , $0.0 < 2\delta L < \lambda$.

steady-state (post) saturation pulse energy as a function of the sub-wavelength cavity detuning is shown in Fig. 5. The steady-state energy was obtained by averaging between passes 100 to 200. When certain detuning values are used, running additional simulations is necessary. The plot demonstrates that the optimal position with regard to the pulse energy is located at the position of roundtrip distance changes of length $2\delta L = 0.5\lambda$, which is equivalent to shortening the cavity length by 1.5 µm.

The contour plot of the FEL power evolution of this optimised case is shown in Fig. 6. The radiation power, evolving over multiple passes, is seen to propagate from the trailing edge of the electron beam to the front over multiple passes. The optical pulse reaches a quasi steady-state saturation with the constant power output and stabilised phase after ~200 cavity round trips.

Preliminary results, not shown here, for different levels of feedback of the radiation, by changing the output mirror coupling, shows that as the feedback is decreased, the number of round trips to saturation increases and the saturated radiation pulse energy decreases in agreement with previous studies.

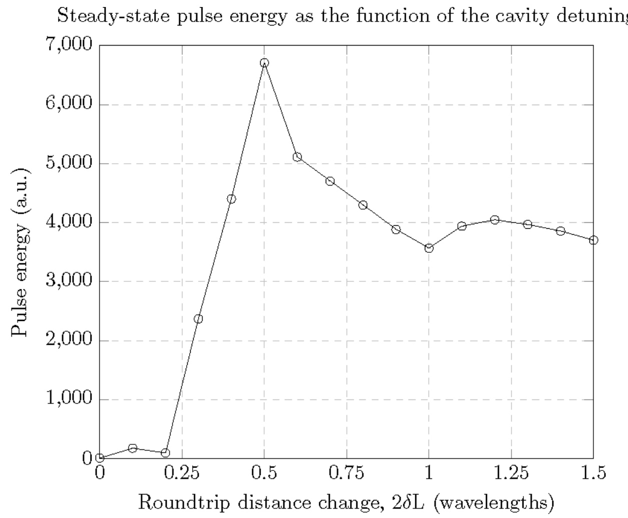

Figure 5: Steady-state (saturated) pulse energy at the undulator exit from Puffin-OPC simulation vs cavity detuning $2\delta L$ in units of radiation wavelengths for a total reflectivity $R = 0.96$.

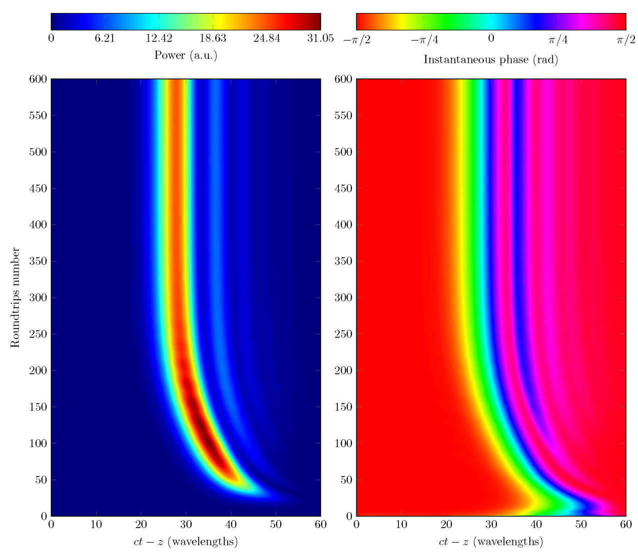

Figure 6: Contour plot of the FEL radiation power and phase evolution as a function of roundtrip number for an optimal cavity detuning of $2\delta L = 0.5\lambda$.

CONCLUSION

The work presented here is the first simulations of sub-wavelength effects in an optical cavity FEL. In addition to the self-seeding effects of the CSE generation, which is greater than the shot-noise for the parameters used, interesting effects in the sub-wavelength cavity detuning have been observed. The results presented are at a preliminary stage, but a tentative conclusion is that the research deserves further investigation from which potential benefits may arise.

ISBN: 978-3-95450-220-2 ISSN: 2673-5474 doi: 10.18429/JACoW-FEL2022-MOP32

For example, when compared to the research of [4], the modelling of CSE self-seeding may be able to produce results that are comparable to those of the externally-seeded model. With the assistance of sub-wavelength cavity adjustment, CSE appears to have the ability to self-seed and stabilise the FEL output. Furthermore, such modelling of sub-wavelength effects in a FEL oscillator, including CSE generation and sub-wavelength cavity detuning, will help provide a more detailed understanding of the fundamental workings of a FEL oscillator. Further modelling of carrier-envelope phase (CEP) stabilisation utilising a passive CSE seeded method, and other CEP design methods should be able to be developed.

ACKNOWLEDGEMENTS

This work is supported by Science and Technology Facilities Council (Agreement Number 4163192 Release#3); Engineering and Physical Sciences Research Council (Grant EP/M011607/1, Grant EP/K000586/1).

REFERENCES

[1] L. Campbell and B. McNeil, "Puffin: A three dimensional, unaveraged free electron laser simulation code," *Phys. Plasma*, vol. 19, no. 9, p. 093 119, 2012. doi:10.1063/1.4752743

[2] J. Karssenberg, P. J. van der Slot, I. Volokhine, J. W. Verschuur, and K.-J. Boller, "Modeling paraxial wave propagation in free-electron laser oscillators," *J. Appl. Phys.*, vol. 100, no. 9, p. 093 106, 2006. doi:10.1063/1.2363253

[3] P. Pongchalee and B. W. J. M, "Unaveraged Simulation of a Regenerative Amplifier Free Electron Laser," in *Proc. FEL'19*, Hamburg, Germany, Aug. 2019, pp. 106–109. doi:10.18429/JACoW-FEL2019-TUP026

[4] R. Hajima and R. Nagai, "Generating carrier-envelope-phase stabilized few-cycle pulses from a free-electron laser oscillator," *Phys. Rev. Lett.*, vol. 119, no. 20, p. 204 802, 2017. doi:10.1103/PhysRevLett.119.204802

[5] J. Henderson, L. T. Campbell, B. W. J. McNeil, and A. R. Maier, "The Implementation of 3D Undulator Fields in the Unaveraged FEL Simulation Code Puffin," in *Proc. FEL'14*, Basel, Switzerland, Aug. 2014, 416–418, paper TUP022.

40th International Free Electron Laser Conference,Trieste JACoW Publishing
ISBN: 978-3-95450-220-2 ISSN: 2673-5474 doi: 10.18429/JACoW-FEL2022-MOP33

REPORT ON THE FELIX WAVELENGTH RANGE EXTENSION

Victor Claessen†, Marije Barel, René van Buuren, Alexander van der Meer, Paul Pijpers, Britta Redlich, Michel Riet, Wouter Stumpel, Guus Tielemans, Arjan van Vliet, Bryan Willemsen,
FELIX Laboratory, Radboud University and NWO, Nijmegen, The Netherlands
Stephen Gottschalk, STI Magnetics, Woodinville, WA, United States

Abstract

The FELIX Laboratory, located at Radboud University in Nijmegen, The Netherlands, is operating a suite of FELs serving an international user community with infrared and THz radiation from 5 to 1500 micron operating three FELs in parallel and providing beam to 16 dedicated user end stations. Recently, FELIX has upgraded its most frequently used FEL-2 beamline. The 38 period, 65 mm Halbach-type SmCo undulator, originally built for the UK-FEL project in the mid 80's, which had been successfully used for the short-wavelength FEL for almost 30 years, was replaced by a new undulator. This 50 period, 40 mm NdFeB hybrid undulator was built in close collaboration with STI magnetics and the FEL group of FHI/MPG in Berlin. Together with a new resonator cavity it allows an extension of the fundamental range from 5 µm to sub-3 µm, while keeping the desirable good spectral overlap with the longer wavelength FEL-1 branch. The upgraded FEL-2 beam line produced first light at the end of April 2022 and commenced serving regular user experiments in early May.

DESIGN

Undulator

Driven by user request for more power in the 2000 – 3000 wavenumber range (i.e. 3 – 5 µm), we decided to upgrade the FEL2 undulator. With the estimated parameters (Table 1) for our accelerator, we did calculations with software constructed on Benson's version [1] of FEL CAD [2] to determine appropriate undulator parameters.

Table 1: FELIX FEL-2 accelerator parameters

Parameter	Value
Beam energy	25 – 50 MeV
Pulse length	0.7 ps
Energy spread	0.3%
Emittance	50 mm mrad
Bunch charge	200 pC

Table 2: U40 undulator parameters

Parameter	Value
Type	Planar hybrid, NdFeB
Period	40 mm
# of periods	50
Length	2 m
K_{RMS}	0.5 – 1.6

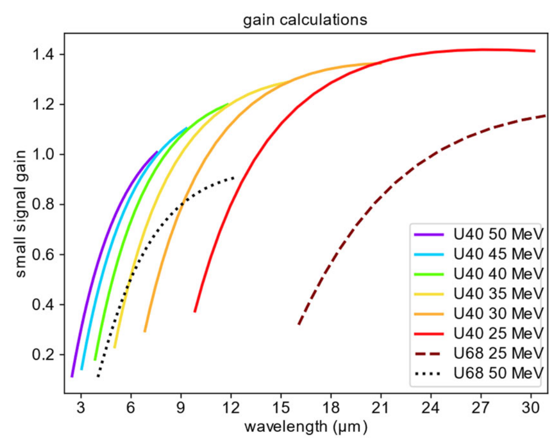

Figure 1: gain calculations for the proposed 40 mm undulator for FEL-2 showing that the 3 – 30 µm region is well covered (solid lines), offer more gain in the 3 – 5 µm region than the 68 mm undulator (dotted line), and maintain good overlap with the highest energy of FEL-1 (dashed line).

As it turns out, the best results (Table 2) were obtained using a 40 mm undulator (Fig. 1) similar to that of the FHI FEL [3], and this design was therefore accepted with slight modifications.

Resonator

A new resonator (Table 3) was built around the new undulator. Since optical cavity stability is more critical at lower wavelengths, particular care was taken to isolate the cavity mirrors from vibrations in the laboratory by mounting them on heavy blocks of granite (Fig. 2).

Table 3: Resonator parameters

Parameter	Value
Type	near-concentric
Frequency	25 MHz
Length	5.9993 m
Rayleigh range	0.85 m
Outcoupling hole	0.9, 1.2, 1.6, 2.1, 2.8, 3.7 mm

† victor.claessen@ru.nl

ISBN: 978-3-95450-220-2 ISSN: 2673-5474 doi: 10.18429/JACoW-FEL2022-MOP33

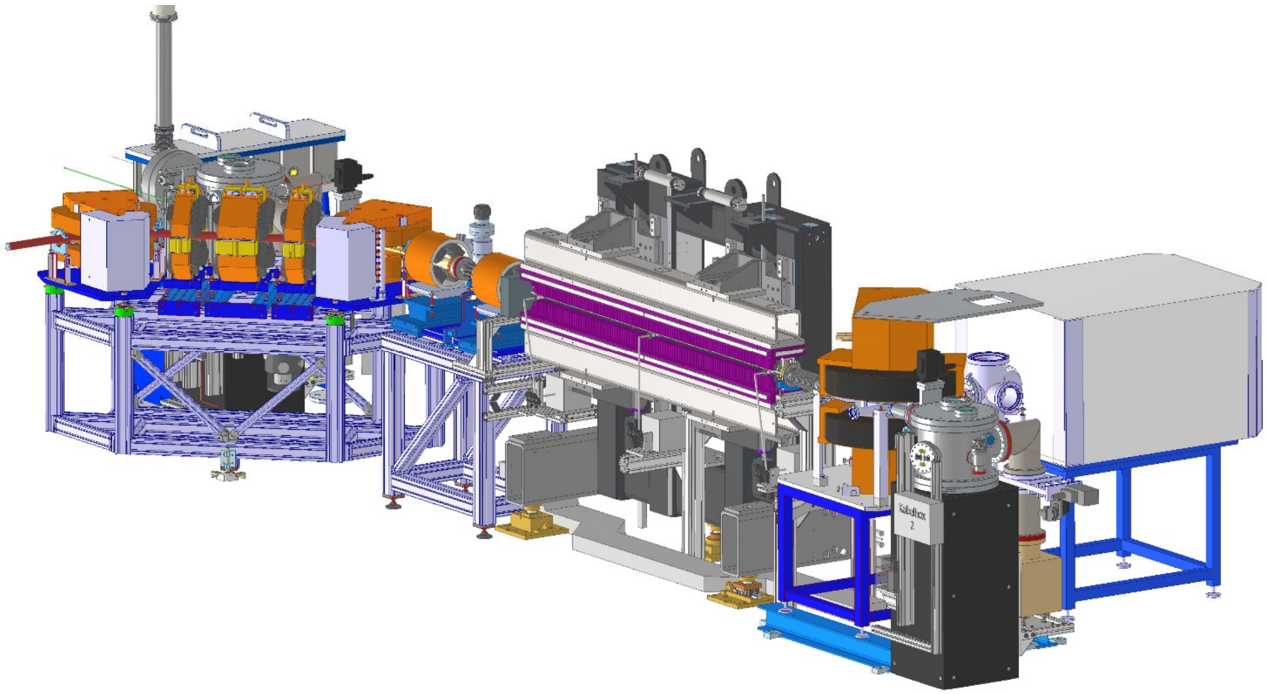

Figure 2: Illustration of the new FEL-2 beam line design showing the new undulator as well as the cavity mirror vacuum chambers mounted on granite blocks.

FEL PERFORMANCE

Gain

During a brief intermezzo in user operation some exploratory gain measurements were performed using a fast MCT detector: a single point at 35 MeV - 200 pC - 9 µm (Fig. 3), and a series at several wavelengths at 32 MeV - 400 pC (Figs. 4 and 5).

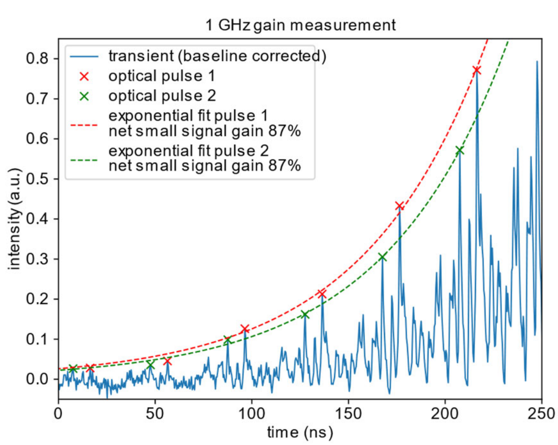

Figure 3: 1 GHz - 200 pC gain measurement at 9 µm. The rise of two out of the forty circulating pulses were fitted with an exponential function yielding a net small signal gain of 87%. After correction for the round-trip loss of 15%, the small signal gain is determined to be 102%.

The growth of the optical pulse was fitted in the small signal regime and corrected for round-trip cavity loss (measured to be around 15% for the 2.8 mm hole outcoupling mirror). The single measurement at 200 pC (small signal gain 102%) corresponds well to the calculated value (100%). The results at 400 pC indicate that the estimated accelerator parameters do not hold at this bunch charge and fit better to a bunch length of 1.5 ps and 0.5% energy spread (Fig. 5), for instance. More detailed measurements are proposed.

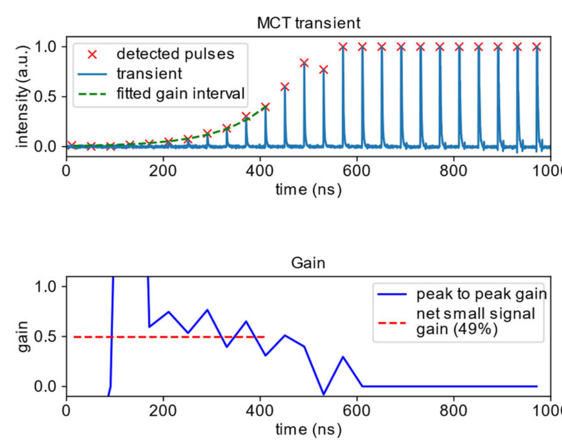

Figure 4: 25 MHz - 400 pC gain measurement at 8 µm. The rise of the optical pulse in the transient MCT signal was fitted to an exponential function between 1% and 50% of the scope saturation level to obtain a net small signal gain of 49% (top). Comparison between peak to peak gain and fitted net small signal gain (bottom).

ISBN: 978-3-95450-220-2 ISSN: 2673-5474 doi: 10.18429/JACoW-FEL2022-MOP33

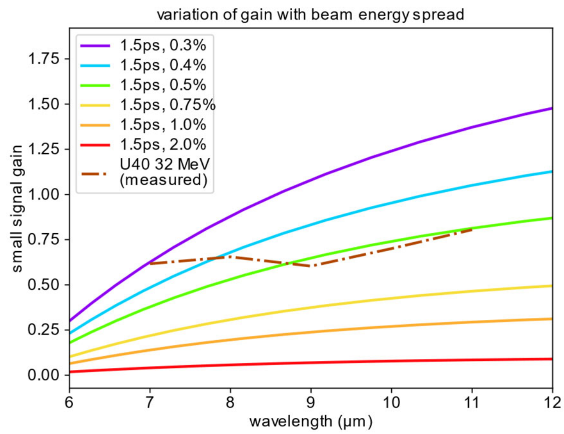

Figure 5: Variation of calculated gain with beam energy spread for a 32 MeV - 400 pC beam (solid lines) and measured gain (brown dash-dotted line).

Power

Initial optical power scans were made at selected electron beam energies covering most of the new range for FEL2 (Fig. 6). Comparison with the wavelength range generated for the highest beam energy in FEL1 shows that a good spectral overlap between the two beam lines was maintained. The power scans were made at 2λ detuning, yielding a typical 0.25 – 0.5% RMS spectral width.

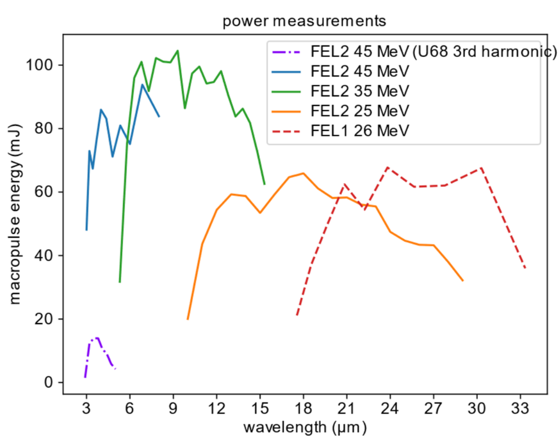

Figure 6: FEL output power vs wavelength scans at various beam energies (solid lines). It is obvious that the power of the U40 on the fundamental exceeds that of the U68 on the third harmonic (purple dash-dotted line). The desired spectral overlap with the highest beam energy of the FEL-1 beam line is also shown (red dashed line).

FIRST APPLICATION

Our in-house users had been unable to observe the CH stretch vibration on the IR spectrum of protonated C60 with the limited power of FEL-2/U68 operating on the third harmonic. Using the improved power of FEL-2/U40 in the 2000 – 3000 wavenumber range, they have found the CH stretch vibration around 2820 wavenumbers (3.55 μm) (Fig. 7).

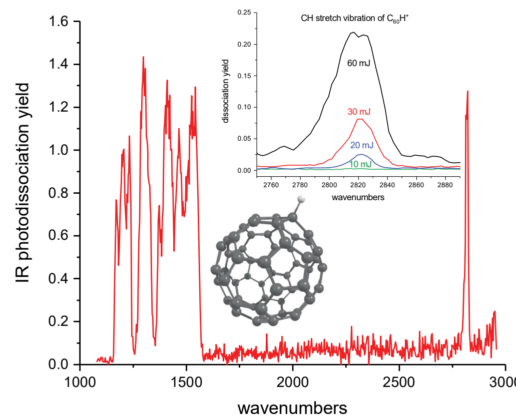

Figure 7: Observation of the CH stretch vibration of protonated C60 (inset, bottom) at 2820 wavenumbers with IR action spectroscopy using the newly available power of the upgraded FEL-2 beam line. This was not possible with the previously available power (inset, top).

CONCLUSION

The range of the FELIX FEL-2 was extended from 5 μm to sub-3 μm with satisfactory output power while maintaining the desired spectral overlap with the FELIX FEL-1 beamline, and FEL-2 has started serving users.

REFERENCES

[1] S. Benson, “FEL CAD v1.1”, Jefferson Lab, Newport News, VA, United States, unpublished.

[2] D. C. Nguyen, S. M. Gierman, P. G. O'Shea, “An FEL design code running on Mathcad™”, *Nuclear Instruments & Methods in Physics Research Section A-accelerators Spectrometers Detectors and Associated Equipment*, vol. 358, pp. ABS67-ABS68, 1995. doi:10.1016/0168-9002(94)01567-8

[3] S. Gottschalk, T. DeHart, R. Kelly, M. Offenbacker, A. Valla, H. Bluem, D. Dowell, J. Rathke, A. M. M. Todd, S. Gewinner, H. Junkes, G. Meijer, W. Schöllkopf, W. Zhang, U. Lehnert, “Design and Performance of the Wedged Pole Hybrid Undulator for the Fritz-Haber-Institut IR FEL”. *Proceedings of FEL’12*, Nara, Japan, 2013 pp. 575-578. doi:10.18429/JACoW-FEL2012-THPD13

ISBN: 978-3-95450-220-2 ISSN: 2673-5474 doi: 10.18429/JACoW-FEL2022-MOP34

LASING PERFORMANCE OF THE EUROPEAN XFEL*

W. Decking †, M. Scholz, Deutsches Elektronen-Synchrotron, Hamburg, Germany

Abstract

The European XFEL operates with 3 different SASE FELs served by variable gap undulators. In addition, the electron energy of the superconducting linear accelerator is varied between 8.0 and 17.5 GeV to cover a photon energy range from 250 eV to 30 keV. We will present SASE performance data collected over the past 5 years of operation and compare them with theoretical predictions.

INTRODUCTION

The European XFEL is in operation since 2017 [1]. With its powerful superconducting accelerator, a flexible beam distribution system and three long, moveable gap, undulators it can provide a wide range of X-ray radiation spanning two orders of magnitude from 250 eV to 30 keV. In this paper we will focus on the peak and average performance of the FELs operated in standard self-amplified spontaneous emission (SASE) mode. Other operation modes like Hard X-ray Self-Seeding are implemented but will not be considered here.

The superconducting accelerator can accelerate up to 27000 bunches/second to an energy of 17.5 GeV. It is operated in burst mode, i.e. with a 10 Hz repetition of a 600 µs long RF pulse that accommodates electron bunches with a repetition rate of up to 4.5 MHz. bunches are produced in a radio-frequency photo-injector at charges between 20 pC to 1 nC. Operating ranges of the accelerator and undulator parameters are summarized in Table 1.

Table 1: Accelerator and undulator parameters

	Range	Typical
Energy - GeV	8 – 17.5	14
# of bunches/s	10 – 27000	13500
Bunch charge pC	20 – 1000	250
	SASE1/2	**SASE3**
K Parameter	3.9 – 1.65	9.0 – 4.08
Number of 5 m cells	35	21

Bunches are distributed with a fast kicker system into two electron beamlines, where one is presently hosting the hard X-ray undulator SASE2, while the other passes the beam through the hard X-ray undulator SASE1 first, before entering the soft X-ray undulator SASE3. The fast kicker system can also discriminate between SASE1/SASE3 bunches by applying a bunch specific betatron oscillation, thus suppressing lasing in either of the two undulators. The kicker system also allows to send individual bunches into a beam dump before the undulators, this gives the opportunity to vary the average X-ray power by up to 3 orders of magnitude (i.e. 1 to 1000 pulses per RF burst) on user demand.

* Work supported by European XFEL GmbH
† winfried.decking@desy.de

LASING PERFORMANCE DATA

In the following we will present an analysis of all FEL intensity data that has been collected over the last 5 years. Electron energies between 8.0 and 17.5 GeV are covered, with pre-dominant operation at 14 GeV (75 % of the time). Only data points at 250 pC bunch charge have been considered. The FEL intensity is measured with an X-ray gas monitor (XGM) [2] providing a data-point every 0.1 s. One should note that the XGM signal observed is an averaged signal with a sliding average of 30 s. The data is processed by binning the respective intensity values into1 keV (Hard X-ray undulators), resp. 0.1 keV intervals, where the average is calculated after removing the lower 10% of the measurements (attributed to tuning or early operation), and the upper 1% (attributed to gain switching in the XGM, leading temporarily to too high values). In addition, the data is compared to the calculated maximum intensity at saturation for optimized electron energies [3].

A gain curve is measured by successively moving the 5 m long undulator segments (cells) out of resonance and monitoring the XGM signal. In addition, a fast and more sensitive, but uncalibrated, signal ("HAMP") is used to obtain reliable data at low intensities. The calibration is obtained in intensity regimes where the XGM continues to measure reliably.

SASE1

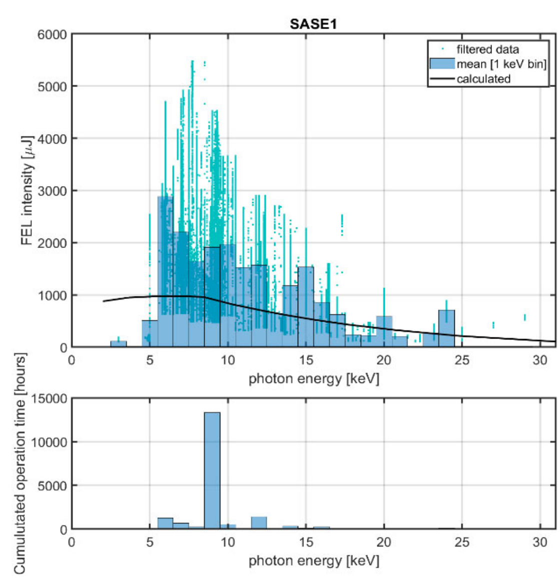

Figure 1: Upper plot: 5-year SASE intensities at SASE1 (cyan dots), and the average value in selected photon ranges (blue bars), compared to calculated intensities for optimized electron energies (black line). Lower plot: Cumulated operation hours within the respective photon energy range.

ISBN: 978-3-95450-220-2 ISSN: 2673-5474 doi: 10.18429/JACoW-FEL2022-MOP34

The SASE1 undulator has been the first FEL in operation at the European XFEL. It uses the "straight" beam and operates predominantly at around 9.3 keV (see Fig. 1 lower). Pulse intensities of 5 mJ have been reached in the 5 – 10 keV range, a factor of 4 to 5 above the calculated value at saturation (see Fig. 1 upper). This can be achieved with power tapering, benefitting from the long undulators, as is shown in the gain curve in Fig. 2.

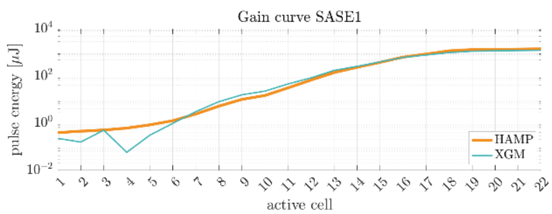

Figure 2: Typical gain curve for SASE1 at 9.3 keV, showing to reach saturation after about 17 active cells. Note that the undulator has a total length of 35 cells.

It is also interesting to look at the usage of bunches summarized in Fig. 3. The dominating time the SASE1 FEL is used in single bunch mode (i.e. 1 bunch per 10 Hz). This mode is used for experiment set-up and alignment. Once data taking starts, the number of bunches is increased to 352 bunches per RF burst (the present limit for the detector read-out) with a 1.1 MHz spacing. Other typical bunch numbers are 200 bunches at 0.55 MHz, this time the sample delivery and the length of the available RF pulse are the defining factors.

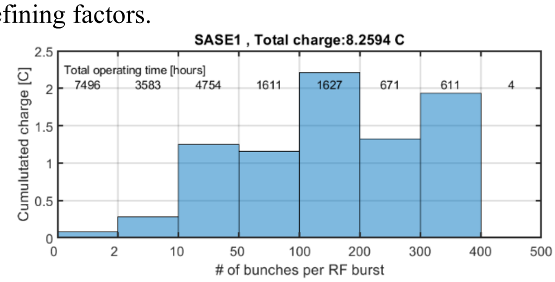

Figure 3: Accumulated charge at different bunch frequencies and total number of operating hours at these frequencies.

SASE2

SASE2 is the second hard X-ray undulator and came into operation about one year after SASE1. It is placed in an electron beamline behind a 2.2 deg arc. The performance of SASE2 shows similar behaviour as SASE1, but with overall about 30% less intensity in average and peak (see Fig. 4). This is also manifested in a longer typical gain length (see Fig. 5) and attributed to several causes:

- The electron phase space quality in the arc suffers under certain circumstances.
- The photon energy is changed more often and thus less tuning time is spent at a fixed setting.

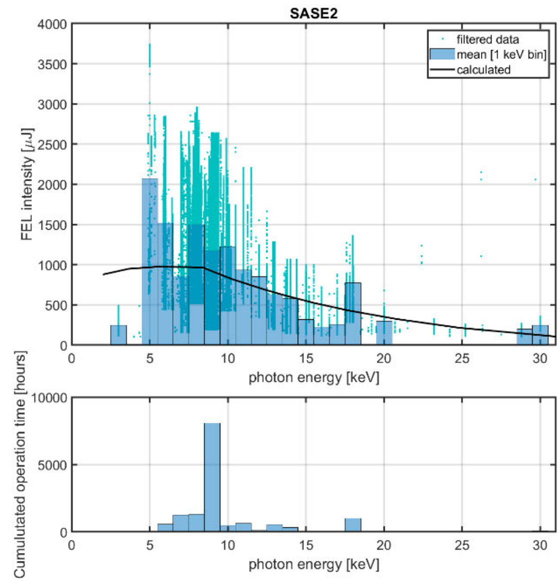

Figure 4: Upper plot: 4-year SASE intensities at SASE2 (cyan dots), and the average value in selected photon ranges (blue bars), compared to calculated intensities for optimized electron energies (black line). Lower plot: Cumulated operation hours within the respective photon energy range.

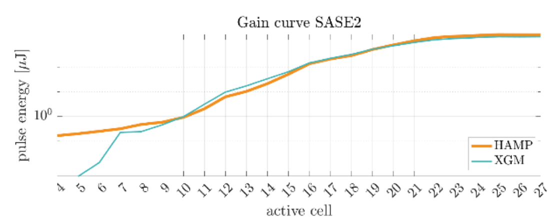

Figure 5: Typical gain curve for SASE2 at 9.0 keV, showing to reach saturation after about 21 active cells. Note that the undulator has a total length of 35 cells.

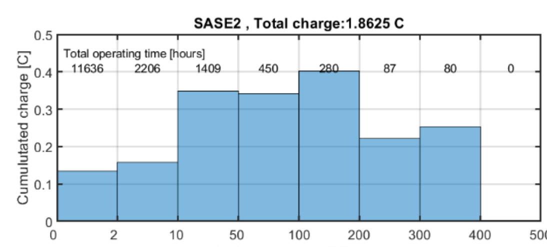

Figure 6: Accumulated charge at different bunch frequencies and total number of operating hours at these frequencies.

SASE2 is operated more often in single-bunch mode as can be seen in Fig. 6.

ISBN: 978-3-95450-220-2 ISSN: 2673-5474 doi: 10.18429/JACoW-FEL2022-MOP34

SASE3

The soft X-Ray undulator SASE3 is placed after the SASE1 undulator. In order to avoid electron beam deterioration from SASE1 bunches, electron bunches that are supposed to lase in SASE3 are put on a betatron oscillation in SASE1 to avoid lasing. Thus, a fresh bunch can be used all the time. Of course, all bunches are passing through each of the two undulators, and the beamlines have to deal with the background produced by incoherent synchrotron radiation or not fully suppressed lasing.

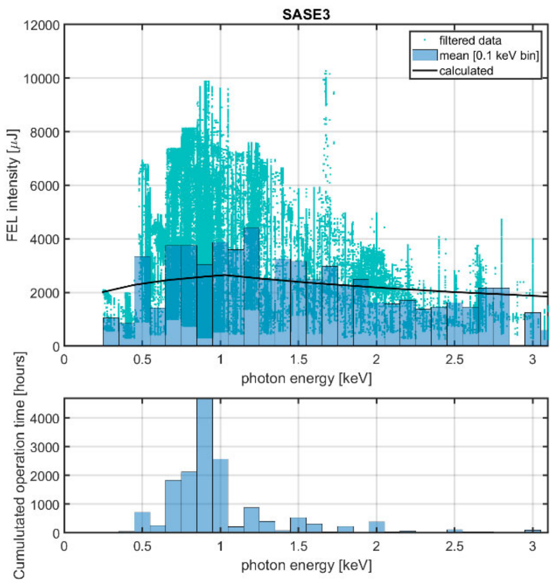

Figure 7: Upper plot: 5-year SASE intensities at SASE3 (cyan dots), and the average value in selected photon ranges (blue bars), compared to calculated intensities for optimized electron energies (black line). Lower plot: Cumulated operation hours within the respective photon energy range.

As can be seen by Fig. 7 the photon energy range of SASE3 is explored in a wider range. Operation at energies below 500 eV is only possible at accelerator energies of 8 GeV or so, at the same time forbidding the operation of the hard X-ray undulators above 6 keV. Due to the large total length of the undulator (21 cells) and the large electron energy, high intensities can be reached. Figure 8 is an example of a gain curve with early saturation ad a long power taper. But often high intensity is not the figure of merit, but rather spectral purity or transverse coherence, thus requiring to operate just at saturation. Another mode that is used frequently is the operation at two colours, using a split undulator and an electron delay chicane.

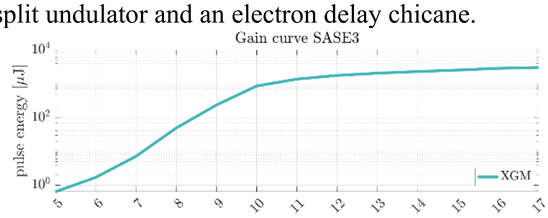

Figure 8: Typical gain curve for SASE3 at 1.0 keV, showing early saturation and a long power taper. The sensitive "HAMP" detector was not available during this measurement.

The bunch usage shows a similar pattern with a dominant use of single-bunches for set-up and alignment purposes and multi-bunch operation for data taking. Compared to SASE1 the used number of bunches per RF burst is in general lower (see Fig. 9). This is driven by the processes that are studied in the experiment, often requiring bunch repetition rates in the 100 kHz regime, and thus limiting the total number of pulses that can be delivered within one RF burst.

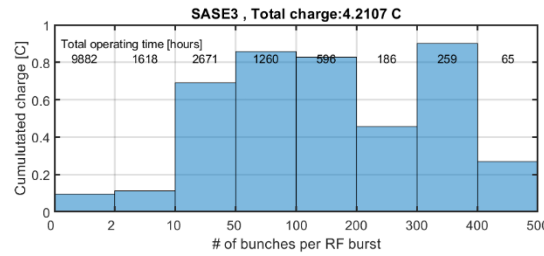

Figure 9: Accumulated charge at different bunch frequencies and total number of operating hours at these frequencies.

CONCLUSION

We have summarized the SASE performance in terms of photon intensity for all three SASE beamlines of the European XFEL. Average intensities meet the calculated values at saturation, while peak intensities exceed these by a factor of four. Intensity is usually not the only key performance parameter, and optimizing those others often compromises the peak intensity that can be reached. The potential of multi-bunch operation is underlined by the usage of long bunch trains in all beamlines for data taking. It should be noted that nevertheless only about 10 % of the available electron bunches are used on average. Optimization of set-up procedures, detector and sample delivery development have thus the potential to yield even more experimental data.

ACKNOWLEDGEMENTS

The data presented here is the result of the work of all staff at DESY and European XFEL that contribute to the successful operation of the European XFEL. The authors wish to thank them all and acknowledge each individual contribution.

REFERENCES

[1] W. Decking *et al.*, "A MHz-repetition-rate hard X-ray free-electron laser driven by a superconducting linear accelerator", *Nat. Photonics*, vol. 14, pp. 391–397, 2020. doi:10.1038/s41566-020-0607-z

[2] T. Maltezopoulos *et al.*, "Operation of X-ray gas monitors at the European XFEL", *J. Synchrotron Rad.*, vol. 26, pp. 1045–1051, 2019. doi:10.1107/S1600577519003795

[3] E.A. Schneidmiller and M. V. Yurkov, "Photon beam properties at the European XFEL - Saturation tables (Dec 2018 rev.)", unpublished.

ISBN: 978-3-95450-220-2 ISSN: 2673-5474 doi: 10.18429/JACoW-FEL2022-MOP36

FLEXIBLE OPERATION MODES FOR EUXFEL

M. W. Guetg*, B. Beutner, J. Branlard, F. Brinker, W. Decking, I. Hartl, R. Kammering, D. Lipka, N. Lockmann, N. Mirian, E. Schneidmiller, H. Tünnermann, T. Wamsat, DESY, Hamburg, Germany
G. Geloni, N. Gerasimova, N. Kujala, S. Serkez, XFEL GmbH, Schenefeld, Germany

Abstract

A major challenge in single-linac-multiple undulator setups like EuXFEL is generating individually shaped photon pulses for each of the undulator lines, especially when working in an operation mode where a single pulse train, or cw stream, feeds all undulator lines. This work presents the experimental verification of a flexible delivery scheme feeding all three undulator lines of EuXFEL with electron bunches individually shaped in charge, compression and optics from a single RF pulse burst.

SETUP

European XFEL (EuXFEL) consists of a single linac which feeds three undulator lines. All undulator lines are fed in parallel, receiving electron pulses that originate from RF pulse trains with a repetition rate of 10 Hz. Each pulse train consists of up to 2700 pulses with a maximal repetition rate of 4.5 MHz. A beam distribution system with a fast and a slow kicker system distributes the pulses between the three undulator lines. The fast kicker system works on a bunch-to-bunch rate and is used to dump superfluous pulses as well as to create soft-kicked pulses for lasing suppression in the fresh-bunch [1, 2] setup. The slow kicker system is used to distribute the beam into one of the two undulator branches.

In most operation modes, the first part of each RF pulse train is used to stabilize the beam through transverse and longitudinal intra-train feedbacks and then dumped after the linac without passing any undulator lines and subsequently not producing any X-rays. The next part of the train is sent in bulk towards the first undulator line (Fig.1, colored in purple). The following part is dumped again in order to provide a transition time (about 30 µs) which is required to relax the slow kicker of the beam distribution system. The last part of the pulse train is used to deliver pulses to two undulator lines that follow one another (Fig. 1, colored in blue and green). Each of the three lines is operated exclusively by allowing the lasing only in one line while suppressing it in the other two. To maximize the available RF time for each experiment, the two serial undulators receive bunches in an interleaved mode. In summary, there are two undulator lines which receive beam in an interleaved mode with a maximum repetition rate of 4.5 MHz and one undulator line which is separated by about 30 µs from the other lines. The repetition rate and number of pulses at each undulator line can be lowered by dumping individual pulses in the linac dump.

* marc.guetg@desy.de

METHODS

We investigated two options to shape the duration of pulses within a single pulse train, which is necessary to provide pulses of different durations for each of the undulator lines. The first option is to exploit the gun laser system, which consists of an acoustic-optical modulator (AOM) in front of the amplifier [3, 4]. This system is designed to keep the charge constant along the entire pulse train, however, this system is also able to create pulses of varying charge along the pulse train. The achievable charge profiles along the pulse train underlie only two limitations. First, the charge cannot be larger than what the laser pulse allows for an unattenuated pulse. Second, there have to be high charge pulses in regular intervals to prevent building up an inversion state in the laser gain medium. Since the AOM is able to react at a 4.5 MHz scale, this system is able to customize the bunch length for all three undulator lines even if the two serial undulator lines are operated in an interleaved mode.

The second option for longitudinal shaping along the pulse train is to use the RF system, which allows to modulate both amplitude and phase of wave in the cavity along the pulse train [5, 6], thereby effectively changing the energy chirp and thus compression of the beam. The maximal frequency of transitions between different states depends on the characteristics of the klystron as well as the quality factor of the super-conducting RF cavity and allows for different compression states for different sections of the pulse train, but not for the individual pulses of the train. Therefore, this option is only suitable when the undulator lines are operated in a non-interleaved mode.

These two options are not exclusive. Combining the two techniques allows to operate with lower charge while still correcting the compression setting individually for optimal performance of all undulator lines. Furthermore, there is the possibility to use multiple RF flat-tops in phase and amplitude in the gun to correct for the different space charge in the low energy regime and thus improve the optical mismatch by exposing the electron to a different electric field.

RESULTS

Reducing the charge is the most flexible way to reduce the pulse duration. It allows for nearly full flexibility of the pulse patterns within a pulse train. Unfortunately, changing the charge leads to different effective compression given similar RF settings, which in turn leads to a miscompressed beam as shown in Fig. 2. It is important to note that the increase in electron pulse duration does not necessarily transfer to the photon pulse, which could still be significantly shorter due

ISBN: 978-3-95450-220-2 ISSN: 2673-5474 doi: 10.18429/JACoW-FEL2022-MOP36

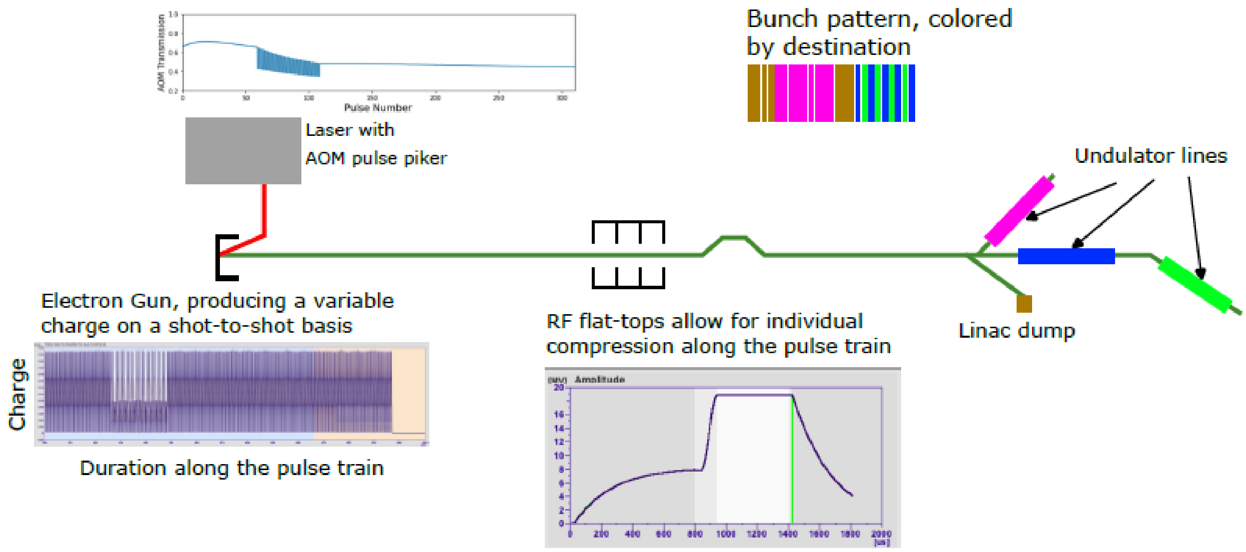

Figure 1: Schematic layout of EuXFEL with its pulse trains feeding three undulator lines. The laser AOM absorber located close to the electron gun allows to arbitrarily shape the charge profile. The modulated RF flat-top allows for different compression along the pulse train. Note the different time scales of the two options making them appropriate for different delivery modes (depending on destination).

to non-linear compression of the beam. However, it does lead to quite non-uniform lasing along the pulse.

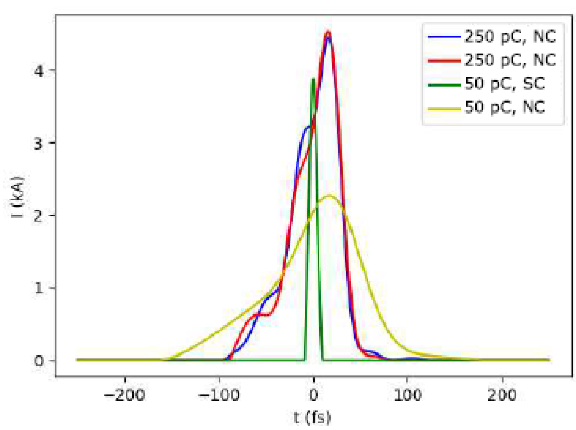

Figure 2: Temporal reconstruction of the electron beam using the CRISP spectrometer [7] for different charges and compressions. Here, NC (nominal compression) is optimized for 250 pC and SC (short-pulse compression) is optimized for 50 pC. Note that a lower charge with non-optimized compression can lead to longer electron pulses.

We did several measurement campaigns for both hard and soft X-rays showing that the variable charge setup without compression didn't have any effect on any of the other beam lines. Furthermore, no cross-talk between beam lines was observed when utilizing non-linear and nominal compression in an non-interleaved operation mode. Figure 3 demonstrates this for both altered compression as well as charge. A soft X-ray measurement campaign during an experimental user delivery run shows that indeed lowering the charge results in shorter photon pulse duration (Table 1). A more targeted effort would likely result in higher intensities.

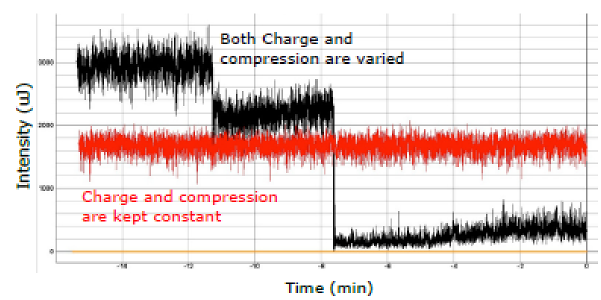

Figure 3: Intensity of two beamlines in parallel operation. The black beamline is tuned in both charge and compression while the red beamline is kept constant and does not experience any cross-talk from the other beamlines effort.

Lowering the charge also benefited extreme non-linear compression cases. Even though non-linear compression had already been implemented in the past for all three undulator lines and was used for a user delivery for hard X-rays, such extreme cases always showed increased intensity fluctuations. Furthermore, the compression feedbacks were hard pressed to keep the condition over the entire 4 days of user delivery. The combination with lower charge allowed to stabilize the intensity jitter and operate in a more stable compression regime in general. Combining reduced charge of individual pulses with altered compression along the pulse train proved to be reliable and stable over a 16h run. During this time we were able to run all feedbacks including the

ISBN: 978-3-95450-220-2 ISSN: 2673-5474 doi: 10.18429/JACoW-FEL2022-MOP36

Charge (pC)	Intensity (μJ)	Estimated photon duration	Stability
250	5000	16 fs	
200	4600	14 fs	95%
150	3200	11 fs	94%
100	2300	8 fs	92%
75	1600	6.5 fs	92%
50	500	5 fs	89%
50*	800	4.8 fs	83%
30*	400	3.6 fs	89%
20*	200	2 fs	81%

Table 1: Results from a single beam time at 1 keV. The top values correspond to non-adjusted compression whereas for the bottom ones (with *) the compression was adjusted. The photon pulse duration was estimated utilizing the photon spectral analysis to measure the photon group duration.

transverse and longitudinal intra-train feedbacks, stabilizing both the pointing as well as the arrival time of the photon beam with this operation mode. Furthermore, the combination of those two techniques allowed for significantly shorter pulses. In the extreme case of 15 pC this resulted in 1% of single spike events at 1 keV. Specific optimisation of this mode remains for future exploration. Some exemplary spectra are shown in Fig. 4.

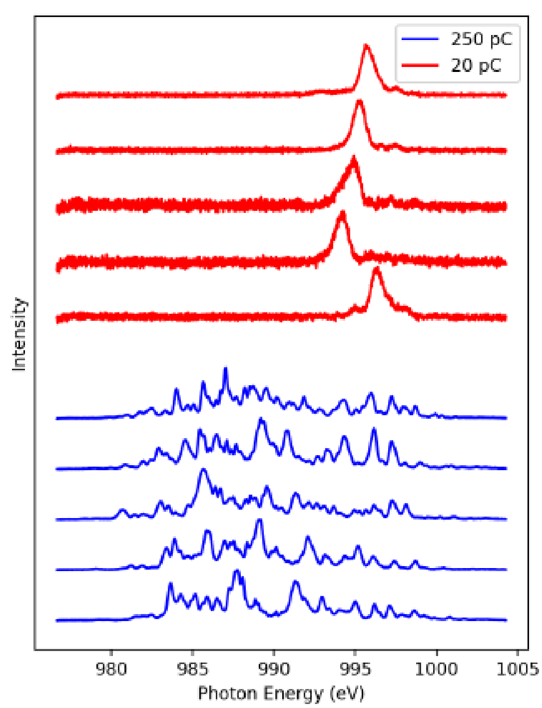

Figure 4: Selected photon spectra for both nominal (250 pC) and low charge (20 pC) with optimized compression.

We also studied the possibility to use different gun RF flat-tops in phase and amplitude to correct for the different space charge and thus matching condition. The optical mismatch due the altered charge was not too severe to hinder beam transport or significantly deteriorate beam quality, with the obvious exception of the optical mismatch itself. However, this mismatch was corrected for in front of each of the undulator lines, thereby allowing for full flexibility. The additional complexity of the operation mode therefore outweighed its benefits.

DISCUSSION

The proposed methods allow for additional operational flexibility at the EuXFEL with its several undulator lines fed by a single linac. It offers pulse length control on a shot-to-shot (4.5 MHz) level as well as a higher flexibility for a different flat-top configuration. In principle, this method can be used complementary to other methods like fresh-slice [8–10], enabling more stable operation. These results might be of interest for the community since they offer an easily implementable way to shape the pulse duration in single linac-multiple undulator line settings, given that several facilities with with this layout will be commissioned in the near future.

ACKNOWLEDGEMENTS

We would like to thank the machine operators at DESY as well as the photon instruments at EuXFEL for their excellent support.

REFERENCES

[1] L. Fröhlich *et al.*, “Multi-Beamline Operation at the European XFEL”, in *Proc. FEL’19*, Hamburg, Germany, Aug. 2019, pp. 335–338. doi:10.18429/JACoW-FEL2019-WEP008

[2] S. Liu *et al.*, “Parallel Operation of SASE1 and SASE3 at the European XFEL”, in *Proc. FEL’19*, Hamburg, Germany, Aug. 2019, pp. 25–28. doi:10.18429/JACoW-FEL2019-TUA01

[3] L. Winkelmann *et al.*,"Compact Photo-Injector and Laser-Heater Drive Laser for the European X-ray Free Electron Laser Facility," in *Proc. Conference on Lasers and Electro-Optics (CLEO)*, San Jose, USA, Aug. 2018, paper 18023557

[4] L. Winkelmann *et al.*, "Flexible Pulse-Train Amplitude Shaping for the European XFEL Photoinjector Laser", in *8th EPS-QEoD Europhoton Conference*, Barcelona, Spain, Sep. 2018, paper ThA1.8

[5] V. Ayvazyan *et al.*, “Low Level RF Control Implementation and Simultaneous Operation of Two FEL Undulator Beamlines at FLASH”, in *Proc. ICALEPCS’15*, Melbourne, Australia, Oct. 2015, pp. 42-45. doi:10.18429/JACoW-ICALEPCS2015-MOC3O07

[6] V. Ayvazyan *et al.*, "Alternating gradient operation of accelarating modules at FLASH", in *Proc. 11th European Particle Accelerator Conference (EPAC’08)*, Genoa, Italy, Jun. 2008, paper TUPP001

[7] N. Lockmann *et al.*, "Noninvasive THz spectroscopy for bunch current profile reconstructions at MHz repetition rates", *Phys.*

ISBN: 978-3-95450-220-2 ISSN: 2673-5474 doi: 10.18429/JACoW-FEL2022-MOP36

Rev. Accel. Beams, vol. 23, p. 112801, 2020. doi:10.1103/PhysRevAccelBeams.23.112801

[8] A.A. Lutman *et al.*, "Fresh-slice multicolour X-ray free-electron lasers", *Nat. Photonics*, vol. 10, pp. 745–750, 2016. doi:10.1038/nphoton.2016.201

[9] S. Serkez, "Short pulses and 2-color capabilities at the SASE3 FEL line of the European XFEL", presented at the 40th International Free Electron Laser Conference (FEL'22), Trieste, Italy, Aug. 2022, this conference.

[10] W. Qin *et al.*, "Corrugated structure system for fresh-slice application at the European XFEL", presented at the 40th International Free Electron Laser Conference (FEL'22), Trieste, Italy, Aug. 2022, this conference.

ISBN: 978-3-95450-220-2 ISSN: 2673-5474 doi: 10.18429/JACoW-FEL2022-MOP37

STATUS OF THE FREE-ELECTRON LASER USER FACILITY FLASH

K. Honkavaara*, C. Gerth, M. Kuhlmann, J. Roensch-Schulenburg,
L. Schaper, S. Schreiber, R. Treusch, M. Vogt, J. Zemella
Deutsches Elektronen-Synchrotron DESY, Hamburg, Germany †

Abstract

FLASH, the free-electron laser user facility at DESY, delivers XUV and soft X-ray radiation for photon experiments since 2005. It is driven by a superconducting linear accelerator, and has two undulator lines (FLASH1 and FLASH2). A third electron beam line hosts the plasma-wakefield experiment FLASHForward. Presently, the FLASH facility is undergoing an extensive refurbishment and a substantial upgrade (FLASH2020+). In this paper we summarize the FLASH operation in 2019-2021, and report on the main upgrades realized in a shutdown from November 2021 to August 2022.

INTRODUCTION

FLASH [1–5] at DESY (Hamburg, Germany) is a XUV and soft x-ray FEL user facility. It originates from the TESLA Test Facility (TTF) Linac [6], which was constructed at DESY in mid 1990's to test the feasibility of high gradient superconducting accelerator technology. The present FLASH facility (originally called "VUV-FEL at TTF2") was constructed in 2003-2004. User operation started in summer 2005, and since summer 2014 two undulator lines (FLASH1 and FLASH2) are operated in parallel. FLASH2 user operation started in April 2016.

In order to keep FLASH a state-of-the-art FEL user facility, refurbishments and upgrades are on-going within the framework of the FLASH2020+ project [7–9]. The main goals are to establish a high repetition rate seeding (up to 1 MHz) at FLASH1, and to extend the wavelength range at FLASH2 down to the oxygen K-edge (2.3 nm). Installation of an APPLE III undulator as a third-harmonic afterburner at FLASH2 will enable FEL radiation with variable, in particular circular polarisation, well suited for magnetic studies, e.g. at the L-edges of Fe, Co and Ni.

The first upgrade shutdown started in November 2021 with the goal to increase the electron beam energy to 1.35 GeV. High repetition rate seeding is planned to be installed in 2024/25.

This paper reports on the status of the FLASH facility and its operation in 2019-2021, and summarizes the main installations during the 2021/22 shutdown. Part of this material has been presented in previous conferences, most recently in [10, 11].

FLASH FACILITY

FLASH consists of a photoinjector, a superconducting linac, two undulator lines (FLASH1 and FLASH2), and two experimental halls. A schematic layout of the facility as it was operated until November 2021 is shown in Fig. 1. In addition, FLASH hosts a seeding experiment Xseed [12], and a plasma-wakefield experiment FLASHForward [13].

The photoinjector, consisting of a normal conducting RF-gun with an exchangeable Cs_2Te photocathode, and three injector lasers, generates a high quality, bunched electron beam. The superconducting linac has seven TESLA type 1.3 GHz accelerator modules with eight 9-cell Niobium cavities each. The maximum electron beam energy, before the energy upgrade in 2022, was 1.25 GeV. A third harmonic (3.9 GHz) module, to linearize the longitudinal phase space, is installed downstream of the first accelerator module. Two magnetic chicane bunch compressors (C-shape and S-shape) are used to compress the electron bunches to the peak currents required for the lasing process. FLASH2 has an additional bunch compressor downstream of the extraction beamline.

Superconducting RF cavities allow operation with long RF-pulses (up to 800 µs), and thus with long electron bunch trains. The number of electron bunches (1 to 500 in user operation), and their spacing within the bunch train, is variable, e.g. 500 bunches with 1 µs (1 MHz) spacing, or 50 bunches with 10 µs (100 kHz) spacing. The bunch train is shared between FLASH1 and FLASH2, which are operated simultaneously [14], both with the full 10 Hz bunch train repetition rate. The switching between FLASH1 and FLASH2 within the bunch train is realized by a kicker-septum system downstream of the last accelerator module. FLASH2 and FLASHForward electron beam lines are separated from each other in the end of the extraction line by a DC-dipole, and thus only one of them can be operated at a given time.

FEL radiation is produced using the SASE (Self Amplified Spontaneous Emission) process. FLASH1 has six 4.5 m long fixed gap (12 mm) undulator modules, FLASH2 twelve 2.5 m long variable gap (minimum 9 mm) undulators. FLASH1 photon wavelength range in the fundamental is from 4.2 nm to slightly above 50 nm. In addition, FLASH1 has a planar electromagnetic undulator downstream of the SASE undulators, and can deliver, on request, also tunable THz radiation (1-300 THz) [15]. FLASH2 provides FEL radiation at wavelengths between 4 nm and 90 nm (fundamental). Thanks to variable gap undulators, fast automated wavelength scans are possible at FLASH2.

Both FLASH1 and FLASH2 have an own transverse deflecting RF structure (TDS) for longitudinal electron bunch diagnostics. FLASH1 has an S-band TDS ("LOLA") [16] located upstream of the SASE undulators, and FLASH2 has, downstream of its undulators, two variable polarization X-band structures ("PolariX") [17].

* katja.honkavaara@desy.de
† for the FLASH team

ISBN: 978-3-95450-220-2 ISSN: 2673-5474 doi: 10.18429/JACoW-FEL2022-MOP37

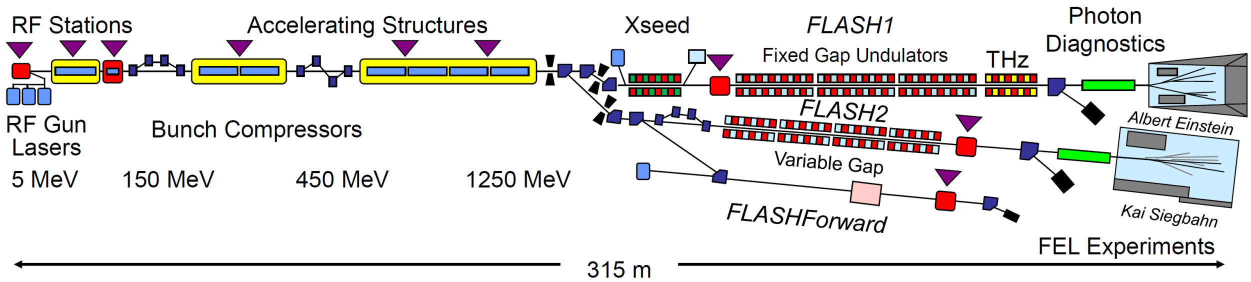

Figure 1: Schematic layout of the FLASH facility in 2019-2021 (not to scale).

OPERATION 2019-2021

In a standard operating year, the FLASH accelerator has 7500 h of scheduled beam operation: 60% of it is dedicated to FEL user operation (4500 h per year), 30% to developments to improve the performance as a user facility, and 10% to general accelerator physics research and developments, such as seeding and plasma-wakefield acceleration. If only one of the undulator lines (FLASH1 or FLASH2) is operated for user experiments, beam time with restricted parameters is provided for developments in the other one. For example, the beam time for FLASHForward is significantly increased, since part of it is scheduled in parallel to the FLASH1 photon user experiments.

The last normal operation year was 2019 with 7476 h of beam operation. Of these, 4601 h (61%) were devoted to user experiments, 1988 h (27%) to FEL and photon beamline developments, and 887 h (12%) to accelerator physics R&D.

In 2020, about 4600 h were originally allocated to user experiments. However, due to the COVID-19 pandemic, FLASH beam operation was stopped for about two months, and two user blocks in spring and early summer 2020 had to be canceled. Part of this time could be used for important cryogenics tests (1272 h). The user operation was resumed in August 2020 with a rearranged schedule. Also in the second half of 2020, due to travel restrictions and other COVID-19 related issues, some experiments had to be canceled or postponed. Finally the FLASH accelerator could deliver beam for 5101 h in 2020. Of these, 3024 h (59%) were devoted to user experiments. In addition, FLASH provided 1732 h for FEL and photon beamline related studies and another 345 h for accelerator developments, mainly for FLASHForward.

In 2021, despite of the continuing COVID-19 pandemic, and the scheduled shutdowns in the beginning and in the end of the year, the FLASH accelerator delivered beam for 6716 h from February to mid November 2021: 3857 h (57%) for user experiments, 2393 h for FEL developments, and 466 h for accelerator R&D.

FEL user operation

At FLASH, differently to many other FEL user facilities, the user beam time hours include also the set-up and tuning times prior to each experiment. Tailoring of the electron and photon beam for the specific demands of the designated experiment takes typically 6-12 h, depending on the required parameters. During the experiment itself, additional tuning is rarely required.

Figure 2 summarizes the FLASH1 and FLASH2 user operation of years 2019, 2020, and 2021.

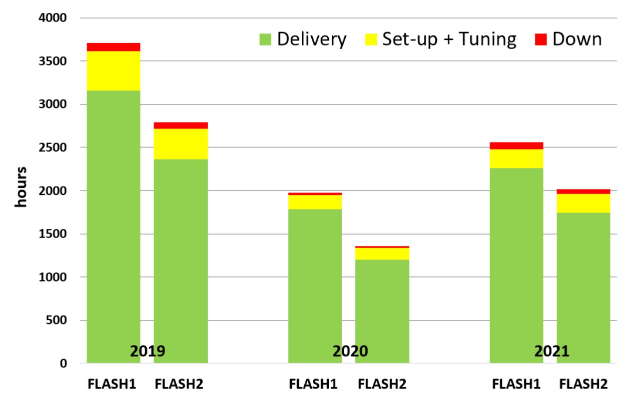

Figure 2: FLASH user operation 2019-2021.

In 2019, the FLASH accelerator was operated 4601 h for user experiments. Thanks to simultaneous experiments at FLASH1 and FLASH2 (about 40% of the user time), a total of 6502 h of beam time could be provided for user experiments: 3710 h at FLASH1 and 2792 h at FLASH2. The set-up and tuning took 12-13% of the user time, and downtime due technical or other failures was 2.6% (FLASH1) and 2.7% (FLASH2).

During the 3024 h of user operation in 2020, 1979 h were provided to FLASH1 users and 1356 h to FLASH2 users. The fraction of parallel operation was reduced to about 10% only, mainly caused by pandemic boundary conditions. Set-up and tuning times were 8-10%, and downtime was at the record low: 1.4% (FLASH1) and 1.3% (FLASH2).

In 2021, the beam time for user experiments was 3857 h. Especially the first half of the year was still hampered with COVID-19 issues, which complicated again the scheduling. As a consequence, FLASH1 and FLASH2 could serve users in parallel only 20% of the time. The user beam time realized at FLASH1 was 2559 h, and 2015 h at FLASH2. Set-up and tuning times in 2021 were similar than in 2020 (8-11%), but downtime was slightly increased to 3.2% (FLASH1) and 2.6% (FLASH2). The main reasons were frequent power glitches in August 2021, failures of aged hardware of control systems, and one single event involving a radio frequency

ISBN: 978-3-95450-220-2 ISSN: 2673-5474 doi: 10.18429/JACoW-FEL2022-MOP37

(RF) station. Measures have been taken to avoid these failures in the future, and in particular to minimize the effects of power glitches on sensitive sub-systems.

In a regular operation year with two calls for proposals, FLASH has typically 65-70 submitted photon experiment proposals; beam time can be allocated to about 45% of them. In addition, part of the user time (10%) is reserved for in-house research. The topics of experiments are manifold, ranging from studies of chemistry in action and (quantum) materials during transformations, to fundamental processes within atoms, molecules and biological building blocks. A few examples of recent experiments carried out at FLASH are ultrafast magnetization dynamics in ferromagnetic alloys [18], chemical shifts in molecules [19], and real time observations of oscillating charge densities upon ionization of a molecule [20].

An experiment analyzing the relaxation time scales in core level photo excited molecules is an example of very demanding beam parameters: simultaneous lasing at 17.7 nm (fundamental) and 5.9 nm (third harmonic) with equal pulse energies (few µJ), together with pulse duration below 50 fs, and long pulse trains (40 pulses per train with 10 µs spacing). The creative solution to realize this was to use a mixture of HLSS (harmonic lasing self-seeded) [21], and two-color lasing [22] approaches. More details can be found in [23].

Accelerator R&D

Xseed seeding experiments at FLASH1 are dedicated to research of novel seeding techniques and testing of concepts related to seeding implementation within the FLASH2020+ project. In summer 2021 Xseed demonstrated, for the first time worldwide, that operation of HGHG (High Gain Harmonic Generation) external seeding is possible, also when the other beam line (FLASH2) is *simultaneously* operated with SASE [12]. The complexity of the simultaneous operation is due the different longitudinal electron beam parameters required for seeding and SASE processes; the electron bunches in the first (seeding at Xseed) and the second (SASE at FLASH2) part of the bunch train need to be tailored very differently. This is possible at FLASH thanks to the adjustable bunch charge and the flexible LLRF system allowing different accelerating amplitudes and phases (i.e. different compression) for the two parts of the bunch train.

The ultimate goal of the beam-driven plasma-wakefield experiment FLASHForward [13] is to demonstrate energy-efficient, beam-quality-preserving, high-average-power plasma acceleration, simultaneously and all at the level required for application to current and future FELs. Recent progress has been diverse and rapid, for example with the first demonstration of energy-spread preservation in a plasma accelerator via efficient beam-loading of the plasma wake [24, 25] as well as the recent fundamental result establishing that the MHz repetition rates required by FEL users can in principle be supported in plasma-wakefield schemes [26].

SHUTDOWN 2021/2022

A nine months upgrade and refurbishment shutdown started in mid of November 2021. It is the first of the two shutdowns in the framework of the FLASH2020+ project.

The main goal of this shutdown is to increase the maximum electron beam energy to 1.35 GeV, which will allow FLASH to lase at about 20% shorter wavelengths than before, thus reaching deeper into the water window. The energy upgrade is realized by exchanging two accelerator modules with new ones having increased performance in terms of cavity gradients and RF-regulation (e.g. piezo-tuners). In addition, the RF distribution system of two other accelerator modules has been upgraded, and now all modules have an optimized RF power performance allowing to maximize the overall accelerating gradient.

Other upgrades are the installation of a laser heater system, and the replacement of the second bunch compressor (S-shape) by mechanically movable C-chicane allowing not only an adjustment of the deflection angle, but also installation of quadruples between the dipoles [27]. The shutdown is also used for refurbishment of the cryogenic and cooling water systems. In addition, a new photocathode laser system is under preparation. At FLASH2 the electron beam line has been modified to enable the installation the afterburner undulator, which is foreseen in summer 2023.

OUTLOOK

FLASH beam operation resumes in autumn 2022, followed by 1.5 years of user operation. The next shutdown, dedicated to upgrade FLASH1 for seeding operation is scheduled to start in summer 2024.

The on-going refurbishments and the further upgrades ensure that FLASH will stay a state-of-the-art FEL user facility for many years to come.

ACKNOWLEDGMENT

We thank all our colleagues for their engagement in the operation and continuous upgrading of the FLASH facility. Special thanks are due to the DESY technical staff for their great effort during the 2021/22 shutdown.

REFERENCES

[1] W. Ackermann *et al.*, “Operation of a free-electron laser from the extreme ultraviolet to the water window”, *Nat. Photonics*, vol. 1, pp. 336–342, 2007. doi:10.1038/nphoton.2007.76

[2] K. Tiedtke *et al.*, “The soft x-ray free-electron laser FLASH at DESY: beamlines, diagnostics and end-stations”, *New J. Phys.*, vol. 11, p. 023029, 2009. doi:10.1088/1367-2630/11/2/023029

[3] S. Schreiber and B. Faatz, “The free-electron laser FLASH”, *High Power Laser Sci. Eng.*, vol. 3, p. e20, 2015. doi:10.1017/hpl.2015.16

[4] B. Faatz *et al.*, “Simultaneous operation of two soft x-ray free-electron lasers driven by one linear accelerator”, *New J.*

ISBN: 978-3-95450-220-2 ISSN: 2673-5474 doi: 10.18429/JACoW-FEL2022-MOP37

Phys., vol. 18, p. 062002, 2016. doi:10.1088/1367-2630/18/6/062002

[5] K. Honkavaara and S. Schreiber, "FLASH: The Pioneering XUV and Soft X-Ray FEL User Facility", in *Proc. 39th Int. Free Electron Laser Conf. (FEL'19)*, Hamburg, Germany, Aug. 2019, paper THP074, pp. 734–737. doi:10.18429/JACoW-FEL2019-THP074

[6] D. A. Edwards, Ed., "TESLA Test Facility Linac, Design Report", DESY, Hamburg, Rep. TESLA-1995-01, March 1995.

[7] M. Beye *et al.* "FLASH2020+, Conceptual Design Report", DESY, Hamburg, 2020. doi:10.3204/PUBDB-2020-00465

[8] L. Schaper, E. Allaria, *et al.*, "Flexible and Coherent Soft X-ray Pulses at High Repetition Rate: Current Research and Perspectives", *Appl. Sci.*, vol. 11, p. 9729, 2021. doi:10.3390/app11209729

[9] L. Schaper *et al.*, "FLASH2020+ Project Progress: Current installations and future plans", presented at the 40th Int. Free Electron Laser Conf. (FEL'22), Trieste, Italy, Aug. 2022, paper TUP51, this conference.

[10] S. Schreiber, J. Roensch-Schulenburg, *et al.*, "Status Report of the Superconducting Free-Electron Laser FLASH at DESY", in *Proc. 12th Int. Particle Accelerator Conf. (IPAC'21)*, Campinas, Brazil, May 2021, paper TUPAB115, pp. 1659–1662. doi:10.18429/JACoW-IPAC2021-TUPAB115

[11] M. Vogt *et al.*, "Status of the Superconducting Soft X-Ray Free-Electron Laser User Facility FLASH", in *Proc. 13th Int. Particle Accelerator Conf. (IPAC'22)*, Bangkok, Thailand, June 2022, paper TUPOPT005, pp. 1006–1009. doi:10.18429/JACoW-IPAC2022-TUPOPT005

[12] S. Ackermann *et al.*, "First Demonstration of Parallel Operation of a Seeded FEL and a SASE FEL", presented at the 40th Int. Free Electron Laser Conf. (FEL'22), Trieste, Italy, Aug. 2022, paper TUP41, this conference.

[13] R. D'Arcy *et al.*, "FLASHForward: plasma wakefield accelerator science for high-average-power applications", *Phil. Trans. R. Soc. A*, vol. 377, p. 20180392, 2019. doi:10.1098/rsta.2018.0392

[14] J. Roensch-Schulenburg *et al.*, "Experience with Multi-Beam and Multi-Beamline FEL-Operation", *J. Phys.: Conf. Series*, vol. 874, p. 012023, 2017. doi:10.1088/1742-6596/874/1/012023

[15] R. Pan *et al.*, "Photon diagnostics at the FLASH THz beamline", *J. Synchrotron Radiat.*, vol. 26, pp. 700–707, 2019. doi:10.1107/S1600577519003412

[16] M. Yan *et al.*, "First Realization and Performance Study of a Single-Shot Longitudinal Bunch Profile Monitor Utilizing a Transverse Deflecting Structure", in *Proc. 2nd Int. Beam Instrumentation Conf. (IBIC'13)*, Oxford, UK, Sep. 2013, paper TUPC36, pp. 456–459.

[17] B. Marchetti *et al.*, "Experimental demonstration of novel beam characterization using a polarizable X-band transverse deflection structure", *Sci. Rep.*, vol. 11, p. 3560, 2021. doi:10.1038/s41598-021-82687-2

[18] X. Liu *et al.*, "Sub-15-fs X-ray pump and X-ray probe experiment for the study of ultrafast magnetization dynamics in ferromagnetic alloys", *Opt. Express*, vol. 29, pp. 32388-32403, 2021. doi:10.1364/OE.430828

[19] D. Mayer *et al.*, "Following excited-state chemical shifts in molecular ultrafast x-ray photoelectron spectroscopy", *Nat. Commun.*, vol. 13, p. 198, 2022. doi:10.1038/s41467-021-27908-y

[20] D. Schwickert *et al.*, "Electronic quantum coherence in glycine molecules probed with ultrashort x-ray pulses in real time", *Sci. Adv.*, vol. 8, p. eabn6848, 2022. doi:10.1126/sciadv.abn6848

[21] E. A. Schneidmiller *et al.*, "First operation of a harmonic lasing self-seeded free electron laser", *Phys. Rev. Accel. Beams*, vol. 20, p. 020705, 2017. doi:10.1103/PhysRevAccelBeams.20.020705

[22] E. A. Schneidmiller *et al.*, "Two-Color Operation of FLASH2 Undulator", in *Proc. 39th Int. Free Electron Laser Conf. (FEL'19)*, Hamburg, Germany, Aug. 2019, paper TUP055, pp. 168–171. doi:10.18429/JACoW-FEL2019-TUP055

[23] J. Roensch-Schulenburg *et al.*, "A combination of harmonic lasing self-seeded FEL with two-color lasing", presented at the 40th Int. Free Electron Laser Conf. (FEL'22), Trieste, Italy, Aug. 2022, paper MOP41, this conference.

[24] C. A. Lindstrøm *et al.*, "Energy-Spread Preservation and High Efficiency in a Plasma-Wakefield Accelerator", *Phys. Rev. Lett.*, vol. 126, p. 014801, 2021. doi:10.1103/PhysRevLett.126.014801

[25] S. Schroeder *et al.*, "High-resolution sampling of beam-driven plasma wakefields", *Nat. Commun.*, vol. 11, p. 5984, 2020. doi:10.1038/s41467-020-19811-9

[26] R. D'Arcy *et al.*, "Recovery time of a plasma-wakefield accelerator", *Nature*, vol. 603, pp. 58–62, 2022. doi:10.1038/s41586-021-04348-8

[27] M. Vogt and J. Zemella, "A New 2nd Bunch Compression Chicane for the FLASH2020+ Project", in *Proc. 12th Int. Particle Accelerator Conf. (IPAC'21)*, Campinas, Brazil, May 2021, paper TUPAB102, pp. 1618 –1621. doi:10.18429/JACoW-IPAC2021-TUPAB102

ISBN: 978-3-95450-220-2 ISSN: 2673-5474 doi: 10.18429/JACoW-FEL2022-MOP38

CORRUGATED STRUCTURE SYSTEM FOR FRESH-SLICE APPLICATIONS AT THE EUROPEAN XFEL

W. Qin*, M. Guetg, W. Decking, N. Golubeva, J. Guo†, S. Liu, T. Wohlenberg, I. Zagorodnov
Deutsches Elektronen-Synchrotron, Hamburg, Germany
E. Gjonaj, Technische Universität Darmstadt, Darmstadt, Germany

Abstract

Fresh-slice lasing using wakefield induced time-dependent orbit oscillation is capable of producing high intensity two-color XFEL pulses and high power short pulses at femtosecond level. At the European XFEL, a corrugated structure system for fresh-slice applications for both the hard x-ray beamline SASE1 and the soft x-ray SASE3 beamline is being developed and implemented. In this contribution, we present the novel design of the corrugated structure system.

INTRODUCTION

X-ray free-electron lasers (XFELs) [1–5] have been significant over the past decade in a broad range of scientific experiments by providing the brightest x-ray pulses. Utilizing various methods, from injector laser shaping to special accelerator and undulator configuration, the XFEL pulses are highly customizable in time and frequency domain. Fresh-slice techniques, which selectively suppress or enable the FEL lasing in localized slices of the electron bunch in different undulator sections, have been very successful in providing tailored x-ray pulses with high efficiency. Many fresh-slice schemes [6–9] employ a parallel-plate corrugated structure [10, 11] to produce transverse to longitudinal correlation from the dipole wakefield of the structure. Meanwhile, non-zero quadrupole wakefield of such structures can cause slice-dependent mismatch [12, 13] and sometimes hinder the advanced applications. The quadrupole effect is usually compensated by orthogonally placed modules or minimized by using small incoming electron bunch sizes.

As the first high-repetition-rate XFEL facility, the European XFEL [4] has seen significant progress in advanced lasing scheme development since operational in 2017. The European XFEL consists of three undulator lines: the hard x-ray lines SASE1 and SASE2 and the soft x-ray line SASE3. The electron bunches are distributed via long pulse KL kicker [14] to the south branch (SASE2) or the north branch (SASE1/3). The SASE3 undulator line is located after the SASE1 undulators, and hence shares the same electron beam path with SASE1. Parallel operation of SASE1 and SASE3 [15–17] is enabled by using bunch-by-bunch KS fast kickers [18] to steer the SASE3 bunches such that they present large orbit oscillation in SASE1 undulators and remain fresh for lasing in SASE3 undulators.

The common beam path shared by SASE1 and SASE3 makes it possible to setup wakefield-based fresh-slice applications for two beamlines with only one corrugated structure. Meanwhile, it also places challenges to the design of the corrugated structure system since it is preferable to operate SASE1 and SASE3 in parallel, i.e., having only one of the two beamlines operate in fresh-slice mode while the other beamline operate in standard mode. Besides, the system has to accommodate the megahertz repetition rate of electron bunches with a distance much below 1 mm between the electron bunches and the corrugated structure.

In this paper, we present the design of the corrugated structure system for fresh-slice applications at the European XFEL. The corrugated structure is located after the SASE2 bunch extraction area and before the SASE1 undulator. Special optics has been designed to allow small distance between the electron bunches and the corrugated structure. Long pulse kickers combined with correctors are designed to separate the SASE1 and SASE3 bunches in the corrugated structure area. Furthermore, a novel L-shape configuration of the corrugated structure has been designed to compensate the quadrupole component of the wakefield. This paper is arranged as the following. We first introduce the special optics and bump orbit design. Then we show the wakefield of the L-shaped corrugated structure. In the last section we present our discussions and conclusion.

OPTICS AND ORBITS

The existing optics before the SASE1 undulator line is a FODO transport line followed by a matching section. The average beta function is about 30 m with peak up to about 50 m. The existing optics is challenging for the corrugated structure operation in two aspects. First, the large beta function makes the time-dependent focusing effect caused by the quadrupole wakefield component significant. Second, a large beta function corresponds to large beam halo extension and can cause significant particle loss in the corrugated structure and further deposit large amount of radiation dose in the undulators, especially when it is operated at a megahertz repetition rate [19].

A special optics with low beta function in both x and y directions around the corrugated structure area has been designed. Two new quadrupoles are inserted in the beamline to help create the low beta region as well as match back to the designed undulator optics. The special optics maintains the possibility to switch back to nominal optics. The created low beta region, as shown in Fig. 1(a), has a beta function of about 9 m to 12 m in both x and y planes over 6-meter-long corrugated structure area (indicated as red rectangle in Fig. 1(b)). The low beta optics reduces the electron beam

* weilun.qin@desy.de
† Currently at Zhangjiang Laboratory, Shanghai, China

ISBN: 978-3-95450-220-2 ISSN: 2673-5474 doi: 10.18429/JACoW-FEL2022-MOP38

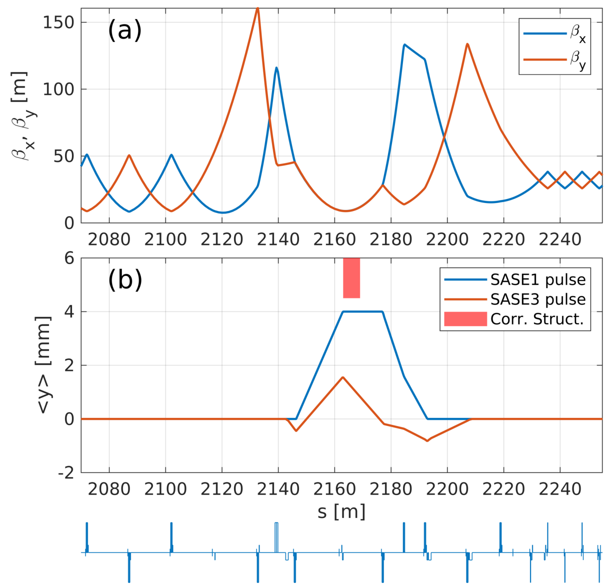

Figure 1: Special low beta optics (a) and orbit separation of SASE1 and SASE3 bunches (b) around the corrugated structure area. The horizontal axis *s* indicates the position of elements in the tunnel. The corrugated structure is indicated as a red rectangle in the middle plot (b).

size such that the quadrupole effect is reduced. Meanwhile, it also reduces the beam halo extension such that the electron bunches can approach the corrugated structure surface as close as possible with a megahertz repetition rate. Detailed beam loss studies for the low beta optics have been presented in [19].

The corrugated structure, indicated as red rectangle in Fig. 1(b), is a motor-free L-shape structure attached at the chamber wall. The distance between the corrugations and the nominal electron beam centroid is 4.5 mm, a distance large enough to make it transparent in nominal operation. The bunches aimed for fresh-slice applications, the SASE1 pulse in blue line in Fig. 1(b), are vertically bumped by four correctors to a 4 mm deviation orbit from the zero orbit. The distance between the bunches and the corrugated structure can be tuned via adjusting the bump strength. With one extra long pulse KL kicker placed before the first bump corrector, SASE3 bunches can be separated with SASE1 bunches with a separation of more than 2.5 mm along the corrugated structure. The orbit difference is then cancelled by another two KL kickers so that both bunches can go through SASE1 undulators. It is very convenient in such configuration to switch to SASE3 bunches operating in fresh-slice mode while SASE1 bunches in nominal mode, simply by imposing a soft kick in the x-plane on the 4-mm bumped bunches with the existing bunch-by-bunch fast kicker upstream.

WAKEFIELDS OF THE L-SHAPED CORRUGATED STRUCTURE

A front view of the L-shaped corrugated structure is shown in Fig. 2, where two single-plate corrugated structures with 0.5 mm corrugation depth (orange area) are stacked together to form an L-shape. The corrugations have a period of 0.5 mm with 0.25 mm opening. Electron bunch orbits along the corrugated structure are indicated by coloured dots, where the purple one (O) represents the orbit for both SASE1 and SASE3 pulses in nominal operation, the blue one (A) represents SASE1 (SASE3) pulses in fresh-slice mode, SASE3 (SASE1) pulses in this case will go through the orbit indicated by the orange dot (C), as already shown in Fig. 1(b). A standard single-plate configuration is also achieved by horizontally bumping the electron beam into the center of the 6 mm-long horizontal wing (red dot B), where the wake contribution from the vertical wing is negligible.

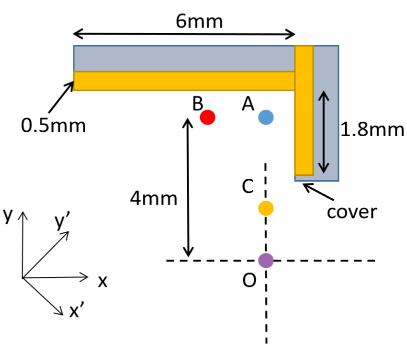

Figure 2: Sketch of the L-shape corrugated structure (rectangle) and operation beam orbits (colored dots). The corrugated areas are marked by orange rectangles.

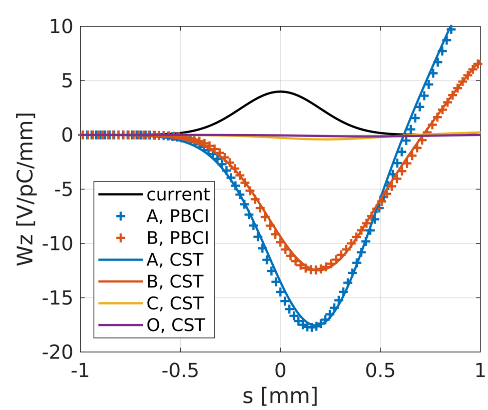

Figure 3: Longitudinal wakes of the L-shape corrugated structure for a gaussian electron bunch with 200 µm RMS bunch length.

The wakefields of the L-shape corrugated structure at interested beam positions have been investigated with CST Particle Studio [20]. The wakefields for position A and B were also benchmarked with the code PBCI [21]. The electron bunch simulated is gaussian in charge profile with 200 µm RMS bunch length. Figure 3 shows the longitudinal wakefields for electron bunches at different orbits. Note here in this paper the wakefields are stationary wakefields normalized to the length of the structure. It can be seen that longitudinal wakefield at the L-shape operation point A (blue crosses and blue line) is about a factor of $\sqrt{2}$ larger than

ISBN: 978-3-95450-220-2 ISSN: 2673-5474 doi: 10.18429/JACoW-FEL2022-MOP38

that of the single plate operation point B (red crosses and red line), which is 3 mm far from the vertical wing. At nominal operation orbit O (purple), the longitudinal kick experienced is vanished. At fresh-slice mode, the non-fresh-slice bunch at orbit C experiences very small residual kick mainly from the vertical wing. The kick becomes even smaller along the 6 m structure, as the orbit separation becomes larger.

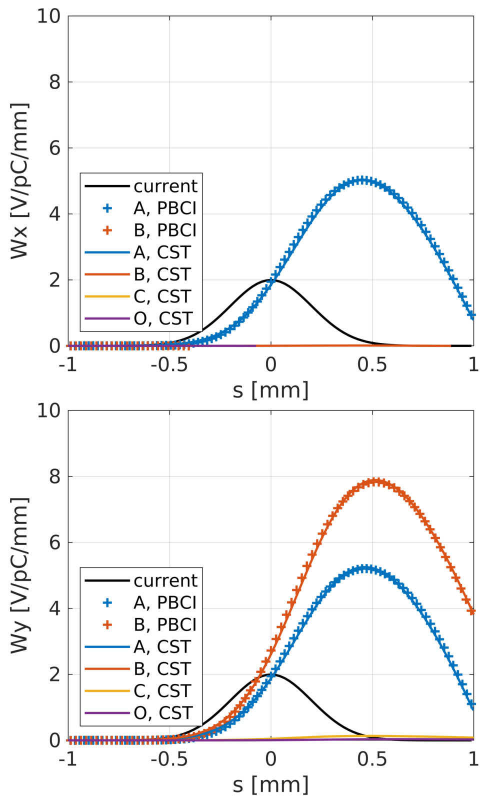

Figure 4: Transverse dipole wakes of the L-shape corrugated structure for a gaussian electron bunch with 200 µm RMS bunch length.

Figure 4 shows the transverse dipole wakefields for electron bunches at different orbits. At L-shape mode position A (blue crosses and blue line), the bunch experiences equal kick in both x and y directions, while at single plate mode position B (red crosses and red line), the dipole kick is only in vertical direction. The amplitude of the combined dipole wakefield for L-shape mode is slightly smaller than that of the single-plate mode, with a rotated kick angle of 45°. Transverse dipole wakefields for position C and position O are small enough for the structure to be transparent.

The compensation of the quadrupole wakefield is illustrated in Fig. 5, where we have calculated the quadrupole wakefield for orbit A along a 45° rotated axis y′ (shown in Fig. 2). It can be seen that the quadrupole wakefield at bunch tail for L-shape operation orbit A (blue crosses and blue line) is very much reduced to about only 20% of the single plate mode orbit B (red crosses and red line).

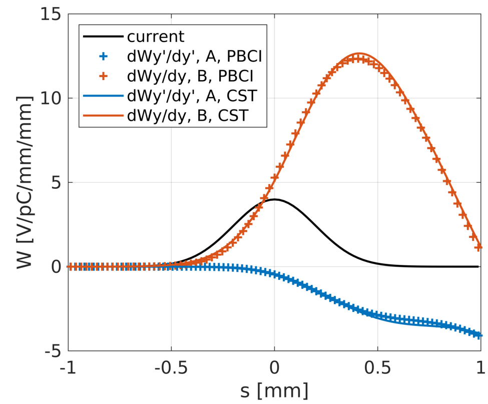

Figure 5: Transverse quadrupole wakes of the L-shape corrugated structure for a gaussian electron bunch with 200 µm RMS bunch length.

DISCUSSION AND CONCLUSION

We have introduced the corrugated structure system for fresh-slice applications at the hard x-ray line SASE1 and soft x-ray line SASE3 at the European XFEL. The corrugated structure system is unique in multiple aspects. It is mounted on the chamber wall without motor and the electron bunches are sent toward the structure by an orbit bump to experience the wakefield kick, making it inexpensive, easy to build and operate. The system is designed with a novel L-shape configuration, enabling the possibility to compensate the quadrupole wakefield component. A corrector-kicker combination is designed to provide the bump as well as separate the SASE1 and SASE3 bunches, allowing bunches for only one of the two beamlines to be kicked by the wakefield. It should be noted that the wakefields simulated here are for a bunch 10 times longer than what is delivered at the European XFEL. Further calculations on the wakefields of the realistic electron bunch are ongoing. Moreover, current beam tracking and FEL performance estimation are based on empirical relation of wakefields between the L-shape corrugated structure and single-plate corrugated structure obtained in this paper. Installation will be carried out in the winter shutdown of 2022 and commissioning will start after the beam restart.

REFERENCES

[1] P. Emma *et al.*, “First Lasing and Operation of an Ångstrom-Wavelength Free-Electron Laser,” *Nat. Photonics*, vol. 4, no. 9, pp. 641–647, 2010. `doi:10.1038/nphoton.2010.176`

[2] T. Ishikawa *et al.*, “A compact x-ray free-electron laser emitting in the sub-ångström region,” *Nat. Photonics*, vol. 6, no. 8, pp. 540–544, 2012. `doi:10.1038/nphoton.2012.141`

[3] H.-S. Kang *et al.*, “Hard X-Ray Free-Electron Laser with Femtosecond-Scale Timing Jitter,” *Nat. Photonics*, vol. 11, no. 11, pp. 708–713, 2017. `doi:10.1038/s41566-017-0029-8`

ISBN: 978-3-95450-220-2 ISSN: 2673-5474 doi: 10.18429/JACoW-FEL2022-MOP38

[4] W. Decking *et al.*, "A MHz-Repetition-Rate Hard X-ray Free-Electron Laser Driven by a Superconducting Linear Accelerator," *Nat. Photonics*, vol. 14, no. 6, pp. 391–397, 2020. doi:10.1038/s41566-020-0607-z

[5] E. Prat *et al.*, "A compact and cost-effective hard x-ray free-electron laser driven by a high-brightness and low-energy electron beam," *Nat. Photonics*, vol. 14, no. 12, pp. 748–754, 2020.

[6] A. A. Lutman *et al.*, "Fresh-slice multicolour X-ray free-electron lasers," *Nat. Photonics*, vol. 10, no. 11, pp. 745–750, 2016. doi:10.1038/nphoton.2016.201

[7] C. Emma *et al.*, "Experimental demonstration of fresh bunch self-seeding in an x-ray free electron laser," *Appl. Phys. Lett.*, vol. 110, no. 15, p. 154 101, 2017. doi:10.1063/1.4980092

[8] A. A. Lutman *et al.*, "High-power femtosecond soft x rays from fresh-slice multistage free-electron lasers," *Phys. Rev. Lett.*, vol. 120, p. 264 801, 26 2018. doi:10.1103/120.264801

[9] J. P. Duris *et al.*, "Controllable x-ray pulse trains from enhanced self-amplified spontaneous emission," *Phys. Rev. Lett.*, vol. 126, no. 10, p. 104 802, 2021. doi:10.1103/PhysRevLett.126.104802

[10] Z. Zhang *et al.*, "Electron beam energy chirp control with a rectangular corrugated structure at the linac coherent light source," *Phys. Rev. ST Accel. Beams*, vol. 18, no. 1, p. 010 702, 2015. doi:10.1103/PhysRevSTAB.18.010702

[11] K. Bane, G. Stupakov, and I. Zagorodnov, "Analytical formulas for short bunch wakes in a flat dechirper," *Phys. Rev. Accel. Beams*, vol. 19, no. 8, p. 084 401, 2016. doi:10.1103/PhysRevAccelBeams.19.084401

[12] W. Qin, Y. Ding, A. A. Lutman, and Y.-C. Chao, "Matching-based fresh-slice method for generating two-color x-ray free-electron lasers," *Phys. Rev. Accel. Beams*, vol. 20, no. 9, p. 090 701, 2017. doi:10.1103/PhysRevAccelBeams.20.090701

[13] Y.-C. Chao *et al.*, "Control of the lasing slice by transverse mismatch in an x-ray free-electron laser," *Phys. Rev. Lett.*, vol. 121, no. 6, p. 064 802, 2018. doi:10.1103/PhysRevLett.121.064802

[14] F. Obier, W. Decking, M. Hüning, and J. Wortmann, "Long Pulse Kicker for European XFEL Beam Distribution," in *Proc. FEL'19*, Hamburg, Germany, 2019, pp. 357–359. doi:10.18429/JACoW-FEL2019-WEP014

[15] L. Fröhlich *et al.*, "Multi-Beamline Operation at the European XFEL," in *Proc. FEL'19*, Hamburg, Germany, 2019, pp. 335–338. doi:10.18429/JACoW-FEL2019-WEP008

[16] S. Liu *et al.*, "Parallel Operation of SASE1 and SASE3 at the European XFEL," in *Proc. FEL'19*, Hamburg, Germany, 2019, pp. 25–28. doi:10.18429/JACoW-FEL2019-TUA01

[17] M. Guetg, J. Branlard, W. Decking, N. Mirian, and B. Beutner, "Flexible operation modes for EuXFEL," in *Proc. FEL'22*, Trieste, Italy, 2022.

[18] F. Obier, W. Decking, M. Hüning, and J. Wortmann, "Fast Kicker System for European XFEL Beam Distribution," in *Proc. FEL'19*, Hamburg, Germany, 2019, pp. 353–356. doi:10.18429/JACoW-FEL2019-WEP013

[19] J. Guo *et al.*, "Beam loss study for the implementation of corrugated structure at the european xfel," *Nucl. Instrum. Methods Phys. Res., Sect. A*, vol. 1034, p. 166 780, 2022. doi:10.1016/j.nima.2022.166780

[20] CST-Computer Simulation Technology, *CST Particle Studio*. http://www.cst.com

[21] E. Gjonaj *et al.*, "Large scale parallel wake field computations for 3d-accelerator structures with the PBCI code," in *Proc. of ICAP'06*, Chamonix, France, 2006, paper MOM2IS02.

ISBN: 978-3-95450-220-2 ISSN: 2673-5474 doi: 10.18429/JACoW-FEL2022-MOP39

AN ATTOSECOND SCHEME OVERCOMING COHERENCE TIME BARRIER IN SASE FELs

E.A. Schneidmiller*, Deutsches Elektronen-Synchrotron DESY, Hamburg, Germany

Abstract

In Self-Amplified Spontaneous Emission Free Electron Laser (SASE FEL) based short-pulse schemes, pulse duration is limited by FEL coherence time. For hard X-ray FELs, coherence time is in a few hundred attosecond range while for XUV and soft X-ray FELs it is in the femtosecond regime. In this paper the modification of so-called chirp-taper scheme is developed that allows to overcome the coherence time barrier. Numerical simulations for XUV and soft X-ray FEL user facility FLASH demonstrate that one can generate a few hundred attosecond long pulses in the wavelength range 2 - 10 nm with peak power reaching hundreds of megawatts.

INTRODUCTION

Attosecond science [1] is rapidly developing nowadays thanks to the laser-based techniques such as chirped-pulse amplification and high-harmonic generation. There are also different schemes proposed for generation of attosecond X-ray pulses in free electron lasers [2–9]. Many of these schemes make use of a few-cycle intense laser pulse to modulate electron energy in a short undulator, and then to make only a short slice (a fraction of wavelength) efficiently lase in a SASE undulator. In particular, in the chirp-taper scheme [7], a slice with the strongest energy chirp is selected for lasing by application of a strong reverse undulator taper that compensates FEL gain degradation within that slice. The lasing in the rest of the bunch is strongly suppressed due to uncompensated reverse taper.

Creation of a short lasing slice can also be done without using a laser. In particular, nonlinear compression of multi-GeV electron beams [10] and self-modulation in a wiggler of a bunch with the special temporal shape [11] allowed to generate a few hundred attosecond long pulses at the Linac Coherent Light Source (LCLS). However, creation of sub-femtosecond features in the electron bunch at lower electron energies ($\simeq$ 1 GeV) is problematic.

Typically, pulse duration in SASE-based short-pulse schemes is limited by FEL coherence time [12]. For hard X-ray FELs, coherence time is usually in a few hundred attosecond range. For such a case an adequate choice of a laser could be a Ti:Sapphire system providing a few mJ within 5 fs (FWHM) with the central wavelength at 800 nm. However, for XUV and soft X-ray regimes the coherence time is in femtosecond range, and a longer wavelength laser is needed [13] to match a lasing slice duration and coherence time. In this contribution a simple method, proposed in [14], is described.

* evgeny.schneidmiller@desy.de

PRINCIPLES OF OPERATION

Conceptual representation of the attosecond scheme is shown in Fig. 1. Few-cycle laser pulse is used to modulate a central part of an electron bunch in energy in a short (typically, two-period) modulator undulator. The wavelength λ_L is chosen such that the lasing slice is much shorter than FEL coherence length. In particular, for generation of attosecond pulses in XUV and soft X-ray regime one can consider Ti:sapphire laser. A typical shape of energy modulation after the modulator undulator is shown in Fig. 2.

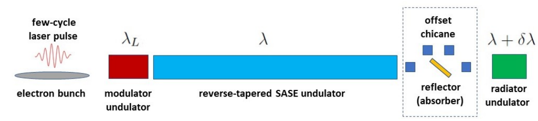

Figure 1: Conceptual scheme for generation of attosecond pulses. Dashed rectangle illustrates a particular realization of suppression (separation) of a radiation background from the SASE undulator.

Then the bunch enters a long SASE undulator tuned to a wavelength λ. The undulator is operated in the same way as in the classical chirp-taper scheme [7]: it is reverse-tapered to compensate for the energy chirp within the central slice (positioned at $t = 0$ in Fig. 2). In this way the FEL gain degradation within this slice is avoided, and the amplification proceeds up to the onset of saturation. The rest of the bunch suffers from the uncompensated reverse taper, and the lasing is strongly suppressed (except maybe for two satellites positioned around $t = \pm 2.7$ fs on Fig. 2 with the negative time derivative). The difference with the standard scheme is that now the central lasing slice is much shorter than FEL coherence time. The distribution of bunching (density modulation amplitude) is rather narrow and is localized at the end of that slice but the radiation slips forward, and a relatively long pulse (on the order of coherence time) is produced. The next task is to get rid of this relatively long radiation pulse (as well as of the background radiation from the rest of the bunch) while preserving the bunching. This can be done in different ways. In Fig. 1 a possible realization is illustrated: an offset chicane with a reflector or absorber inside. Alternative options are discussed below in this Section: excessive reverse taper, an achromatic bend, a kick with a quadrupole, a dogleg, and a harmonic afterburner.

Finally, the microbunched beam radiates in a short radiator undulator. The bunching is strong in the central slice, it is weaker in the two satellites around $t = \pm 2.7$ fs, and much weaker in the rest of the bunch. Note that reverse tapering is

ISBN: 978-3-95450-220-2 ISSN: 2673-5474 doi: 10.18429/JACoW-FEL2022-MOP39

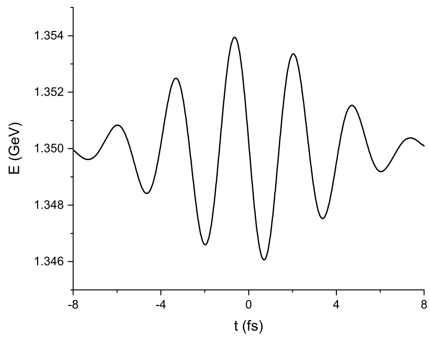

Figure 2: Energy modulation induced by the laser. Bunch head is on the left side.

very efficient in suppression of the radiation but the bunching can reach high values, depending on conditions [15]. We use sufficiently strong chirp and taper to make sure that the the bunching stays at low level in the whole bunch except for the mentioned slices. In addition to that, another feature of the process is used to strongly suppress the ratiation from unwanted parts of the bunch, including satellites. Namely, the central slice is stretched in the main undulator due to a strong energy chirp so that the frequency of the bunching is red-shifted with respect to the resonance frequency at the entrance of SASE undulator. The satellites have a weaker red shift. The rest of the bunch also has a red shift due to undulator taper [16] but it is even weaker. The radiator undulator is set to the resonance with the central slice, and the number of periods is approximately equal to the number of cycles of density modulation within that slice. The other parts of the bunch are non-resonant and radiate very weakly. Below in this Section the operation of the radiator is discussed in more details.

As a result, few hundred attosecond long pulses with low background can be produced in XUV and soft X-ray ranges. The prerequisite for operation of this scheme is a sufficiently long SASE undulator. Note that there is always the range of photon energies at XUV and X-ray FEL facilities for which the saturation occurs well before the undulator end, and there is a reserve for operation with different advanced schemes.

Chirp-Taper Compensation Effect

If there is a linear energy chirp at the undulator entrance, it can have a significant effect on SASE FEL properties, in particular on the gain. The strength of this effect can be characterized by the energy chirp parameter [7]:

$$\hat{\alpha} = -\frac{d\gamma}{dt}\frac{1}{\gamma_0\omega_0\rho^2} , \tag{1}$$

where ρ is the well-known FEL parameter [12, 17], and γ is relativistic factor. Factor γ_0 for a reference particle and reference frequency ω_0 are connected by the FEL resonance condition: $\omega_0 = 2ck_w\gamma_0^2/(1+K^2/2)$. Here K is the undulator parameter and $k_w = 2\pi/\lambda_w$ with λ_w being the undulator period.

It was shown in [7] that a degrading effect of a linear energy chirp on SASE FEL gain can be compensated for by applying a linear undulator taper as soon as the following condition is satisfied:

$$\frac{dK}{dz} = -\frac{(1+K_0^2/2)^2}{K_0}\frac{1}{\gamma_0^3}\frac{d\gamma}{cdt} \tag{2}$$

Here K_0 is the value of undulator parameter at the undulator entrance. Note that the condition in Eq. (2) is applicable when $4\pi\rho\hat{\alpha} \ll 1$, and a perfect compensation is only possible in the limit $\rho \to 0$. However, for practical applications a perfect compensation is usually not required.

Chirp-Taper Compensation for a Short Lasing Slice

Operation of SASE FELs with short bunches was studied in [18, 19]. A relevant parameter to characterize an effect of bunch length on FEL operation is $\rho\omega\sigma_z/c$ with σ_z being rms bunch length. When this parameter is smaller than one (i.e. when bunch is shorter than FEL coherence length $c(\rho\omega)^{-1}$), one can observe an increase of saturation length and a reduction of FEL efficiency.

The condition in Eq. (2) is also valid for short bunches or for short lasing slices (as it was mentioned above, an ideal compensation is only possible when $\rho \to 0$). In this paper we deal with long bunches but short lasing slices having the strongest laser-induced energy chirp. For such a case, instead of σ_z one can consider a reduced laser wavelength, $\lambda_L/(2\pi)$. Thus, a relevant parameter is now $\rho\lambda_L/\lambda$ where $\lambda = 2\pi c/\omega$ is the FEL wavelength. It follows from numerical simulations with laser-modulated beam that an increase of saturation length for a short lasing slice with respect to a normal SASE with long bunches can be approximated as follows:

$$\frac{L_{\mathrm{sat}}}{L_{\mathrm{sat}}^{(\text{long bunch})}} \simeq \left(\rho\frac{\lambda_L}{\lambda}\right)^{-1/2} \quad \text{for} \quad \rho\frac{\lambda_L}{\lambda} < 1 \tag{3}$$

The dependence is similar to that for short bunches [18, 19]. For the purpose of the proposed scheme, one should stop at the onset of saturation (typically 80% to 90% of saturation length) to avoid an increase of the width of bunching distribution within the lasing slice. Thus, a total increase of the required undulator length can be acceptable in many practical cases even for a small parameter $\rho\lambda_L/\lambda$.

Suppression of Background from the Main Undulator

One of the advantages of the proposed scheme is that one can get a clean attosecond pulse from the afterburner. However, we need to get rid of the background produced in the main undulator. Let us consider possible ways of doing this.

Excessive Reverse Taper Reverse taper is efficient in suppression of the radiation, although under some conditions

ISBN: 978-3-95450-220-2 ISSN: 2673-5474 doi: 10.18429/JACoW-FEL2022-MOP39

the bunching can survive [15]. In case of the considered scheme one can apply reverse taper which is stronger than the one needed for compensation of the energy chirp in the main lasing slice. With some delay of the saturation, one can get a strong bunching there but almost no radiation. Excess of reverse taper would then be even stronger in the adjacent slices with the same sign of energy chirp but a weaker amplitude. There one can suppress the radiation even stronger, and the bunching factor saturation is delayed also stronger than in the main slice. In general, the intensity of the radiation from the main undulator can be made sufficiently small. Then, in the radiator a strong power is produced only within the main slice, also due to a frequency offset mentioned above [1]. A disadvantage of this method is that it requires a longer main undulator which is not always possible. Also, bunching within the main slice can be weaker than in a case without over-compensation, depending on parameters.

Achromatic Bend or a Kick with a Quadrupole Another way to produce clean attosecond pulses in the afterburner is to create an angle between the radiation from the main SASE undulator and from the radiator by using an achromatic bend [20] or a kick with a quadrupole [21]. The latter technique (in combination with reverse taper) was successfully used for generation of circularly polarized radiation with high purity at LCLS [22].

Chicane or Dogleg One can also create an offset between the electron beam and the radiation from the SASE undulator with the help of a chicane, as shown in Fig. 1. Then the radiation is either absorbed directly or reflected to an absorber. A possible difficulty is that the longitudinal dispersion, characterized by a transfer matrix coefficient R_{56}, is generated in the chicane. This can be a useful effect: additional bunching can be created, so that one can stop earlier in SASE undulator; moreover the lasing slice is stretched even stronger which helps in suppression of background in the radiator. The upper limit on R_{56} is given by the condition that the beam modulations are not smeared in the dispersive element [23]:

$$R_{56} < \frac{\lambda}{2\pi}\frac{\gamma}{\sigma_\gamma} \tag{4}$$

where σ_γ is uncorrelated energy spread in units of the rest energy.

Note that the two functions of the chicane (a technically reasonable offset and an optimal R_{56}) should be matched which is not always easy to do. A more flexible system could be a chicane with quadrupoles in the dispersion regions [24] so that one can efficiently control R_{56} while the required offset is kept.

Another possible solution is a dogleg that creates a sufficient offset but the R_{56} is typically too small to influence longitudinal dynamics.

[1] Note that in some cases a regular undulator segment (if it is sufficiently short) with optimized K value can play a role of the radiator undulator.

Harmonic Afterburner Radiation at the even harmonics of SASE undulator is weak. Thus, tuning the radiator to the second harmonic, for example, would help to provide low-background attosecond pulses. Radiation at the fundamental of the undulator can be filtered out if it disturbs an experiment.

Suppression of Satellites in the Afterburner

One of the problems of laser-based methods for production of the attosecond pulses is an insufficient contrast of laser modulation that leads to generation of satellite pulses shifted in time by a cycle of the laser light [6]. They are weaker than the main pulse but can still be a problem for user experiments. In the proposed scheme we rely not only on a less efficient generation of bunching for the satellites, but also (and mainly) on the fact the frequency of bunching in the main slice is different (more red-shifted) from that in the satellites. In the case when the chirp is compensated by the undulator taper, the red shift due to a decompression in the main undulator can be estimated as

$$C \simeq \frac{1}{1 - 2\lambda N_{und}\frac{d\gamma}{c\gamma_0 dt}}\,, \tag{5}$$

where N_{und} is a number of periods in the main undulator, and $2\lambda N_{und}$ is the R_{56} of the main undulator. The time derivative of energy is negative in the considered case, so that the compression factor C is smaller than one.

The radiator is tuned to the frequency of the main slice, and the radiation from the adjacent slices is strongly suppressed because of the offset from resonance. Spectral properties of the radiator are characterized by the well-known sinc-function:

$$f_1(\omega) = \left(\frac{\sin(N_w\pi\frac{\omega-\omega_r}{\omega_r})}{N_w\pi\frac{\omega-\omega_r}{\omega_r}}\right)^2 \tag{6}$$

Here ω_r is the resonance frequency of the radiator and N_w is the number of periods. The latter parameter should be chosen such that it is approximately the same as the number of cycles in the bunching distribution within the main lasing slice[2]. At the same time, as it can be seen from Eq. (6), for an efficient suppression one needs to satisfy the condition $N_w \geq \omega_m/(\omega_s - \omega_m)$ with ω_m being the frequency of bunching in the main slice and ω_s in the satellites. One can even adjust parameters such that the satellites are positioned in frequency domain at the zeros of the sinc function, i.e. when $N_w \simeq n\omega_m/(\omega_s - \omega_m)$, where n is a natural number. In this case the suppression will be especially effective.

The density modulations in the bulk of the beam (not modulated by the laser) are much weaker than those on the slopes. In addition, they have a much larger frequency offset from the resonance in the radiator, so that the radiation is strongly suppressed. As a result, one can obtain a clean attosecond pulse from the radiator.

[2] A larger number of periods would lead to unnecessary pulse lengthening, while a smaller number of periods would reduce FEL power.

ISBN: 978-3-95450-220-2 ISSN: 2673-5474 doi: 10.18429/JACoW-FEL2022-MOP39

NUMERICAL SIMULATIONS FOR FLASH

In the first XUV and soft X-ray FEL user facility FLASH [25, 26] the electron bunches with maximum energy of 1.25 GeV are distributed between the two undulator lines. The facility operates in the wavelength range 4 - 60 nm with long pulse trains (several hundred pulses) following with 10 Hz repetition rate. After the planned upgrade, the electron energy will reach 1.35 GeV, this energy is used in numerical simulations. Electron bunches with the charge 100 pC and the following quality [27] are considered in this paper: peak current 1.5 kA, normalized emittance 0.5 mm mrad, uncorrelated energy spread 200 keV. Note that a relatively high longitudinal brightness (100 keV for peak current of 1 kA) was measured at FLASH [28], and low emittances are also routinely measured in the injector. Parameters of the second undulator line FLASH2 are used in the simulations. Segmented variable-gap undulator with the period of 3.14 cm and the maximum K about 2.7 consists of twelve 2.5 m long segments with quadrupoles in the intersections. Average beta-function of the FODO structure is 7 m. Modulator undulator has two periods with the period length of 15 cm and the K value of 12. The Ti:Sapphire laser system generates 5 fs long pulses (FWHM intensity), a pulse energy is 0.25 mJ. The Rayleigh length is chosen to be 1 m. Energy modulation of the electron beam for this parameter set of laser-modulator system is presented in Fig. 2, the maximum energy deviation is 4 MeV. FEL simulations were performed with the code SIMPLEX [29].

Let us consider the case when energy-modulated beam (see Fig. 2) radiates in FLASH2 undulator tuned to 4 nm at the entrance ($K_0 = 1.25$). Since the parameter ρ for the considered beam and undulator parameters is 1.9×10^{-3}, one can use Eq. (1) to find that $\hat{\alpha} \simeq 4$ for the central slice. The reverse step-taper is applied such that K increases by 0.025 in each undulator segment, we use ten segments in simulations. The corresponding parameter of taper strength [15] is $\beta \simeq -2.4$. Note that the chosen reverse taper is 20% stronger than the one needed for the perfect compensation. This helps reduce background from the main undulator without affecting significantly the generation of strong bunching within the central slice. However, a much stronger excessive reverse taper would lead to a significant increase of the undulator length and cannot be considered as the main method of background reduction for given parameters.

Let us discuss an increase of undulator length with respect to that needed for saturation of long bunch with the same slice parameters (which is 18 m). The parameter $\rho\lambda_L/\lambda$ is 0.38 in the considered case, so that an increase of saturation length is about 60 % according to Eq. (3). We do not aim at reaching saturation since there is a broadening of the bunching distribution at that point. Lasing is stopped a bit earlier, at about 90 % of the saturation length, so that the required increase of the undulator length is about 40 % (from 18 m to 25 m).

The distribution of bunching factor in the modulated part of the bunch at the exit of the tenth undulator segment is

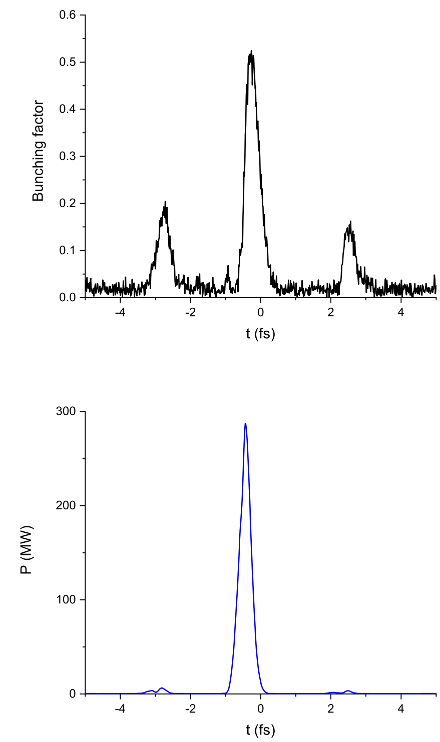

Figure 3: Bunching factor at the entrance to the radiator (upper plot) and power at its exit (lower plot) for a single shot. Bunch head is on the left side.

shown for a single shot in Fig. 3 (upper plot). One can see not only strong bunching within the central lasing slice but also a significant bunching in the satellites. In this simulation we assume that the R_{56} between the main undulator and the radiator is negligible (to avoid an effect on bunching distribution it should be below $\simeq 1$ µm). Thus, the electron beam without modifications is sent to the radiator while the radiation from the main undulator is suppressed with the help of one of the methods discussed in the previous Section.

The radiator is the short undulator with 40 periods, period length of 2.5 cm and the undulator parameter 1.804. In Fig. 3 (lower plot) one can see the temporal profile of radiation pulse at 4.7 nm emitted by the beam with bunching shown in Fig. 3 (upper plot). The wavelength increase is due to stretching of the central slice in the main undulator, as discussed in Section II.D. One can also see that satellites are strongly suppressed despite a significant bunching factor, the mechanism is explained above. Total background (that includes satellites and the radiation produced in the bulk of the beam) does not exceed a few per cent level. More details of the simulations (including 2 nm and 9 nm cases) can be found in [14].

REFERENCES

[1] P. B. Corkum and F. Krausz, “Attosecond science”, *Nat. Phys.*, vol. 3, p. 381, 2007. doi:10.1038/nphys620

ISBN: 978-3-95450-220-2 ISSN: 2673-5474 doi: 10.18429/JACoW-FEL2022-MOP39

[2] E. L. Saldin, E. A. Schneidmiller, and M. V. Yurkov, "Scheme for attophysics experiments at a X-ray SASE FEL", *Opt. Commun.* vol. 212, p. 377, 2002. doi:10.1016/S0030-4018(02)02008-4

[3] E. L. Saldin, E. A. Schneidmiller, and M. V. Yurkov, "Terawatt-scale sub-10-fs laser technology – key to generation of GW-level attosecond pulses in X-ray free electron laser", *Opt. Commun.* vol. 237, pp. 153–164, 2004. doi:10.1016/j.optcom.2004.03.070

[4] A. A. Zholents and W. M. Fawley, "Proposal for Intense Attosecond Radiation from an X-Ray Free-Electron Laser", *Phys. Rev. Lett.*, vol. 92, p. 224801, 2004. doi:10.1103/PhysRevLett.92.224801

[5] P.Emma *et al.*, "Attosecond X-ray Pulses in the LCLS using the Slotted Foil Method", in *Proc. FEL'04*, Trieste, Italy, Aug.-Sep. 2004, paper TUBIS01, pp. 333–338.

[6] A. A. Zholents and G. Penn, "Obtaining attosecond x-ray pulses using a self-amplified spontaneous emission free electron laser", *Phys. Rev. ST Accel Beams*, vol. 8, p. 050704, 2005. doi:10.1103/PhysRevSTAB.8.050704

[7] E. L. Saldin, E. A. Schneidmiller, and M. V. Yurkov, "Self-amplified spontaneous emission FEL with energy-chirped electron beam and its application for generation of attosecond x-ray pulses", *Phys. Rev. Spec. Top. Accel Beams*, vol. 9, p. 050702, 2006. doi:10.1103/PhysRevSTAB.9.050702

[8] Y. Ding *et al.*, "Generation of attosecond x-ray pulses with a multicycle two-color enhanced self-amplified spontaneous emission scheme", *Phys. Rev. ST Accel Beams*, vol. 12, p. 060703, 2009. doi:10.1103/PhysRevSTAB.12.060703

[9] D. Xiang, Z. Huang, and G. Stupakov, "Generation of intense attosecond x-ray pulses using ultraviolet laser induced microbunching in electron beams", *Phys. Rev. ST Accel Beams*, vol. 12, p. 060701, 2009. doi:10.1103/PhysRevSTAB.12.060701

[10] S. Huang *et al.*, "Generating Single-Spike Hard X-Ray Pulses with Nonlinear Bunch Compression in Free-Electron Lasers", *Phys. Rev. Lett.*, vol. 119, p. 154801, 2017. doi:10.1103/PhysRevLett.119.154801

[11] J. Duris *et al.*, "Tunable isolated attosecond X-ray pulses with gigawatt peak power from a free-electron laser", *Nat. Photonics*, vol. 14, p. 30, 2020. doi:10.1038/s41566-019-0549-5

[12] E. L. Saldin, E. A. Schneidmiller, and M. V.Yurkov, *The Physics of Free Electron Lasers*, Springer, Berlin, 1999

[13] W. M. Fawley, "Production of ultrashort FEL XUV pulses via a reverse undulator taper", *Nucl. Instrum. Methods Phys. Res., Sect. A*, vol. 593, p. 111, 2008. doi:10.1016/j.nima.2008.04.051

[14] E. A. Schneidmiller, "Application of a modified chirp-taper scheme for generation of attosecond pulses in extreme ultraviolet and soft x-ray free electron lasers", *Phys. Rev. Accel. Beams*, vol. 25, p. 010701, 2022. doi:10.1103/PhysRevAccelBeams.25.010701

[15] E. A. Schneidmiller and M. V. Yurkov, "Obtaining high degree of circular polarization at x-ray free electron lasers via a reverse undulator taper", *Phys. Rev. ST Accel Beams*, vol. 16, p. 110702, 2013. doi:10.1103/PhysRevSTAB.16.110702

[16] Z. Huang and G. Stupakov, "Free electron lasers with slowly varying beam and undulator parameters", *Phys. Rev. ST Accel Beams*, vol. 8, p. 040702, 2005. doi:10.1103/PhysRevSTAB.8.040702

[17] R. Bonifacio, C. Pellegrini and L. M.Narducci, "Collective instabilities and high-gain regime in a free electron laser", *Opt. Commun.*, vol. 50, p. 373, 1984. doi:10.1016/0030-4018(84)90105-6

[18] R. Bonifacio *et al.*, "Spectrum, temporal structure, and fluctuations in a high-gain free-electron laser starting from noise", *Phys. Rev. Lett.*, vol. 73, p. 70, 1994. doi:10.1103/PhysRevLett.73.70

[19] E. L. Saldin, E. A. Schneidmiller, and M. V. Yurkov, "Statistical properties of radiation from SASE FEL driven by short electron bunches", *Nucl. Instrum. Methods Phys. Res., Sect. A*, vol. 507, p. 101, 2003. doi:10.1016/S0168-9002(03)00847-7

[20] G. N. Kulipanov, A. S. Sokolov and N. A. Vinokurov, "Coherent undulator radiation of an electron beam, microbunched for the FEL power outcoupling", *Nucl. Instrum. Methods Phys. Res., Sect. A*, vol. 375, p. 576, 1996. doi:10.1016/0168-9002(96)00038-1

[21] J. P. MacArthur, A. A. Lutman, J. Krzywinski, and Z. Huang, "Microbunch Rotation and Coherent Undulator Radiation from a Kicked Electron Beam", *Phys. Rev. X*, vol. 8, p. 041036, 2018. doi:10.1103/PhysRevX.8.041036

[22] A.A.Lutman *et al.*, "Polarization control in an X-ray free-electron laser", *Nat. Photonics*, vol. 10, p. 468, 2016. doi:10.1038/nphoton.2016.79

[23] G. Geloni, M. Guetg, S. Serkez, and E. Schneidmiller, "Revision of optical klystron enhancement effects in self-amplified spontaneous emission free electron lasers", *Phys. Rev. Accel. Beams*, vol. 24, p. 090702, 2021. doi:10.1103/PhysRevAccelBeams.24.090702

[24] N. Thompson, "XFEL Isochronous Chicanes: Feasibility Study", in *Proc. FEL'19*, Hamburg, Germany, Aug. 2019, pp. 658–660. doi:10.18429/JACoW-FEL2019-THP033

[25] W. Ackermann *et al.*, "Operation of a free-electron laser from the extreme ultraviolet to the water window", *Nat. Photonics*, vol. 1, p. 336, 2007. doi:10.1038/nphoton.2007.76

[26] K. Tiedtke *et al.*, "The soft x-ray free-electron laser FLASH at DESY: beamlines, diagnostics and end-stations", *New J. Phys.*, vol. 11, p 023029, 2009. doi:10.1088/1367-2630/11/2/023029

[27] J. Zemella and M. Vogt, "Optics & Compression Schemes for a Possible FLASH Upgrade", in *Proc. IPAC'19*, Melbourne, Australia, May 2019, pp. 1744–1747. doi:10.18429/JACoW-IPAC2019-TUPRB026

[28] C. Lechner *et al.*, "Experimental Test of Longitudinal Space-Charge Amplifier in Optical Range", in *Proc. IPAC'19*, Melbourne, Australia, May 2019, pp. 3267–3270. doi:10.18429/JACoW-IPAC2019-WEPTS061

[29] T. Tanaka, "*SIMPLEX*: simulator and postprocessor for free-electron laser experiments", *J. Synchrotron Radiat.*, vol. 22, p. 1319, 2015. doi:10.1107/S1600577515012850

ISBN: 978-3-95450-220-2 ISSN: 2673-5474 doi: 10.18429/JACoW-FEL2022-MOP40

SASE OPTIMIZATION APPROACHES AT FLASH

J. Roensch-Schulenburg*, M. Czwalinna, K. Honkavaara, A. Eislage, V. Kocharyan, M. Kuhlmann, S. Schreiber, R. Treusch, M. Vogt, J. Zemella
Deutsches Elektronen-Synchrotron DESY, Hamburg, Germany

Abstract

The free-electron laser FLASH at DESY can produce SASE-FEL pulses from the extreme ultraviolet to the soft X-ray regime. A superconducting linear accelerator drives two undulator lines (FLASH1 and FLASH2). The FLASH1 undulator beam line contains six fixed gap undulator which implies that the SASE wavelength can only be changed via the electron beam energy, while FLASH2 contains twelve variable gap undulators. Preparing different charges and compression schemes in the two parts of the bunch trains for the two undulator beamlines allows to adjust the phase space in wide range and meet the various requirements of photon pulse trains properties. In order to improve the SASE performance, reference files for standard energies and standard charges are regularly prepared. In the FLASH2 undulator beamline beam-based alignment and phase shifter scans have been applied to improve SASE operations and FEL beam quality. Improving set-up and tuning procedures allow to decrease setup times and optimize performance and stability. Procedures and optimization of FEL parameters towards a reliable SASE-FEL operation as well as the achieved results are discussed.

INTRODUCTION

FLASH [1–5] at DESY (Hamburg, Germany) is a free-electron laser (FEL), operated as a user facility since summer 2005. FLASH contains a normal conducting RF photo-injector with Cs_2Te-cathode and a superconducting linac which allows the acceleration of long bunch trains with several thousand electron bunches per second in 10 Hz bursts of up to 800 µs length. Downstream of the first accelerator module a third harmonic module is installed, to linearize the longitudinal phase space distribution of the bunch, followed by bunch compressor at a beam energy of 150 MeV. Another bunch compressor is installed after the third accelerator module, where the beam has reached an energy of 450 MeV.

The bunch trains are divided into two parts generated by two independent photo-injector lasers with selectable charge. A kicker-septum combination after the seventh accelerator module allows to split the bunch trains and serve two beamlines in parallel. The RF properties of the two beamlines can be chosen independently within a certain range allowing to adjust the phase space properties of the bunches. In standard operation the two beamlines are the undulator beamlines FLASH1 and FLASH2. FLASH2 beam can be diverted towards the plasma wakefield acceleration experiment FLASHForward in the FLASH3 beamline [6] by means of a DC dipole.

The FLASH1 beamline contains a seeding experiment Xseed [7], followed by a transverse deflecting structure (LOLA) [8] for longitudinal diagnostics. The SASE (Self Amplified Spontaneous Emission) undulator consists of six 4.5 m long fixed gap undulators. The fundamental wavelength of the FEL radiation based on the SASE ranges from 4.2 nm to about 50 nm.

The upgrade project "FLASH2020+" [9, 10] includes an energy upgrade from 1250 MeV to 1350 MeV which extends the wavelength range deeper into the water window and a seeding concept at FLASH1 using variable gap undulators.

The FLASH2 beamline contains an additional bunch compressor to further increase the flexibility of the compression. The undulator beamline in FLASH2 contains twelve 2.5 m long variable gap undulator segments. The tunable gap allows to control the undulator parameter K and thus the lasing wavelength in a certain range, depending on the electron beam energy. Behind these undulators a novel Apple-III type undulator will be installed next year as an afterburner which will cover the L-edge of the magnetic 3d metals (at about 1.8 to 1.4 nm) with variable polarization in the third harmonic of the FEL radiation. FLASH2 was equipped recently with a transverse deflecting structure (PolariX) [11, 12].

REFERENCE FILES

Since the FLASH1 undulators are fixed gap undulators employing each wavelength change in FLASH1 goes along with an energy change and thus a new setup of the linac and a new setup in beamline FLASH2. Smaller energy changes can be reached by scaling the magnet currents with the beam energy, but larger changes require a change in the optics. In order to improve the SASE performance and reduce the setup times, reference files for the standard energies 450 MeV, 750 MeV, and 1100 MeV are regularly prepared. The setup is done close to the theoretical energy profile. The goal is to prepare three reproducible, well-documented starting points (reference files) from which a non-expert can reach all standard machine states with a decent SASE pulse energy and long bunch trains with at most moderate beam losses, essentially by scaling the magnet currents. For the 450 MeV-reference file all accelerating modules after the second bunch compressor (ACC4,5,6 and 7) are set to zero volatage. For the 750 MeV-reference file only the last two accelerating modules (ACC6 and 7) are set to zero. In the 1100 MeV-reference file all accelerating modules are used at a high gradient, but not the maximum gradient.

Table 1 indicates the energy/wavelength ranges in which the reference files are applied. Beam energies smaller than

* juliane.roensch@desy.de

ISBN: 978-3-95450-220-2 ISSN: 2673-5474 doi: 10.18429/JACoW-FEL2022-MOP40

450 MeV are reached by decelerating the bunch after the second bunch compressor. The space charge dominated beam

Table 1: Reference File – Range of Usage

Reference file beam energy (MeV)	450	750	1100
energy scaling range (MeV)	350 – 600	600 – 925	925 – 1250
wavelength range (nm)	52 – 17.6	17.6 – 7.4	7.4 – 4.2

from the RF-gun is matched (on-crest, for reference charge of 400 pC and a reference laser beam spot and pulse duration) into the design optics of the 1st compressor chicane before setting up the reference files. This matching is universal for all final beam energies and is thus done once for all reference files. The main idea is to keep the magnetic injector settings up to the second bunch compressor (beam energy: 450 MeV) identical for all reference files. During the reference-file setup the dispersion of all dispersive section is closed and the spurious dispersion is minimized.

All reference files are prepared with a standard charge of 400 pC in FLASH1 and 300 pC in FLASH2. The difference in charge between FLASH1 and FLASH2 is caused by the fact that the bunches are generated by two different injector lasers with different pulse duration (6.5 ps and 4.5 ps, truncated Gaussian). A transverse beam size at the photocathode of 1.2 mm has been chosen. The charge is adjusted such that the initial peak currents of the bunches in FLASH1 and FLASH2 are the same.

Then SASE is maximized, losses are minimized and the capability to run long bunch trains without losses is checked in both beamlines. Finally all FLASH magnets are cycled to compensate for hysteresis effects and reach a high reproducibility of the reference files. This procedure partly requires to cycle the magnets one-by-one to be able to restore the optimized conditions (pulse energy, losses, etc.).

All reference files are setup in FLASH2 for the shortest possible FEL wavelength (largest undulator gap) since this state has the longest gain length and is most sensitive to the undulator orbit. Tapering is not applied to deviations in the undulator setting for the reference files since optimal tapering can be quite different for each setup.

BALLISTIC BEAM-BASED ALIGNMENT

In FLASH2 quadrupole beam-based alignment (BBA) is applied twice a year to the undulator beamline to improve SASE performance and FEL beam quality. The ballistic BBAs have increased the FEL performance by up to about 50% in the past. The frequency (∼ every 6 months) has proven a good compromise between minimizing the effort and maximizing the reproducibility.

As a starting point of the BBA procedure we load and reinstate a recent, machine state with high FEL pulse energy and low losses. This defines our initial reference orbit. Then the ambient field correctors are set to their nominal values in order to compensate the earth magnetic field. All other steerer- and phase shifter-currents are set to zero and the undulators are opened to exclude the influence of undulator focusing. A special optics which matches well into a long flat waist with all intra-undulator quadrupoles off is loaded into the quads upstream of the undulator section. All quads are cycled to zero field. We use the launch steerers upstream of the undulators to optimize transmission close to the initial reference orbit inside the undulators. Then the orbit feedback is adjusted such, that it corrects only the orbit upstream the undulator section. Afterwards we iterate through the quadrupoles one by one using the following procedure:

- switch quadrupole on and drive some reasonable current;
- correct the emerged difference orbit using the corresponding quadrupole movers;
- store the new mover set points;
- cycle quad to zero field and switch off.

Finally an angle correction based on a linear regression through the new mover set points is applied in order to correct the radiation direction towards the user experiment. The results achieved during the ballistic BBA procedure are included into the following generation of reference files.

PHASE SHIFTER SCANS

The twelve FLASH2 SASE undulator sections are separated by intersections with a phase shifter, Beam-position-monitors with a resolution of 2 μm, quadrupoles and steerer. The phase shifters are electromagnetic chicanes which have to be tuned to enable the constructive interference of the radiation of the subsequent undulators for all wavelengths. The required current of all FLASH2 chicanes based on the magnetic measurement results are calculated by an analytical function (2nd order polynomials) for each phase shifter depending only on the K-parameter of the adjacent undulators. This relation is implemented in a server which automatically applies the phase shifter currents whenever the undulator gap is moved. An additional manual offset was introduced to be selected deliberately by machine operators [13].

The FLASH2 phase shifter scans have been performed with the aim to improve SASE operations and FEL beam quality. An increase of pulse energies could be achieved. But, since the total undulator length of 30 m is quite small while the bandwidth is large compared to a hard-X-ray FEL, the influence of phase shifter scans is limited and one has to carefully distinguish between orbit and phase changes.

USER SET-UP

A set-up and tuning procedure has been developed to decrease the setup times and optimize performance and stability of FLASH. Typically, the setup starts from the well-maintained reference files, where important, but time con-

ISBN: 978-3-95450-220-2 ISSN: 2673-5474 doi: 10.18429/JACoW-FEL2022-MOP40

suming steps, like closing the dispersion, and injector matching have already been performed. Setup usually begins with checking the on-crest phases of the gun and all accelerator modules. The sub train durations for FLASH1 and FLASH2 and their bunch repetition frequencies are set according to the conditions requested by the two experiments running in parallel simultaneously in both beamline. After recovering the reference state, i.e. after loading the file and establishing transmission and SASE, the settings are scaled to the required beam energy. The required beam energy is completely fixed by the requested FLASH1 wavelength due to the fixed gap undulators of FLASH1. The set-up is optimized for the requested special user conditions, including SASE optimization, the adjustment of the bunch number with low losses and of the bunch charge. High charge is mainly required for the operation of the THz-undulator to achieve high power. Lower bunch charge is used when tuning SASE for short FEL pulses. Tuning for short FEL pulses is done using the transverse deflecting structures LOLA (FLASH1) and PolariX (FLASH2) [8, 11, 12]. Afterwards compression feedbacks and orbit feedbacks are activated and optimized.

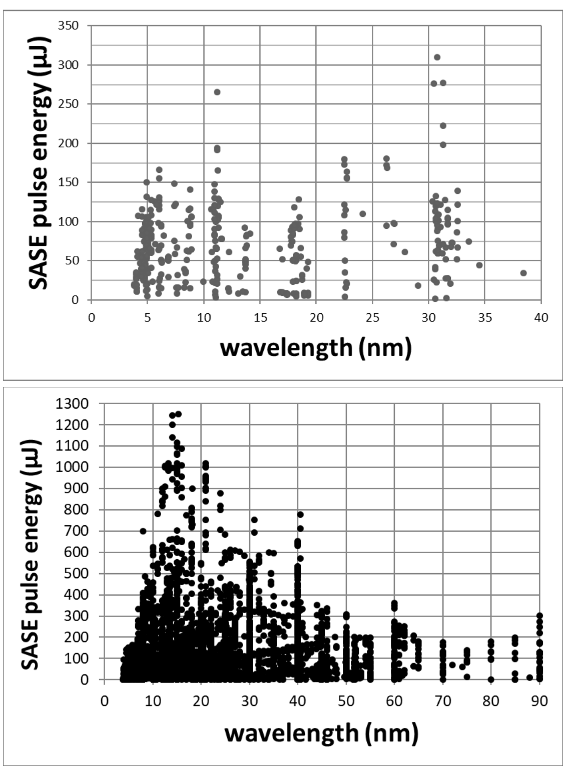

Figure 1: Examples of single pulse SASE energies as a function of the wavelength reached in FLASH1 (top) and FLASH2 (bottom).

Figure 1 shows examples of SASE pulse energies reached in FLASH1 and FLASH2. The range of parameter is quite large since the requirements of the experiments differ strongly. Many user-experiments are more interested in short pulses than in high pulse energies.

OUTLOOK

In the ongoing upgrade and refurbishment shutdown that started in November 2021, two old accelerator modules (modules 2 and 3) have been replaced by modern modules with higher maximum gradient. Thus the beam energy of the injector section is planned to increase from 450 MeV to 550 MeV. In addition the waveguide distribution of two of the linac modules (module 4 and 5) has been optimized. So we are positive that the maximum final beam energy will increase from 1250 MeV to 1350 MeV. The reference file parameter range discussed in Table 1 will be adapted to the parameters shown in Table 2. We note here that after the next upgrade shutdown 2024/25 where FLASH1 will be equipped with variable gap undulators and we plan to run the machine with three fixed reference energies, 750 MeV, 950 MeV, and 1350 MeV only, i.e. without further energy scaling as we do now.

Table 2: Reference File - Range of Usage from 2022 to 2024

Reference file beam energy (MeV)	**550**	**850**	**1200**
energy scaling range (MeV)	350 — 700	600 — 1025	1025 — 1350
wavelength range (nm)	52 — 13	13 — 6	6 — 3.5

We are looking forward to further improve our lasing performance after recommissioning FLASH after the present shutdown [5, 10, 14]. We will study the influence of the laser-heater on the SASE performance in the XUV and soft X-ray range.

REFERENCES

[1] W. Ackermann *et al.*, “Operation of a free-electron laser from the extreme ultraviolet to the water window”, *Nat. Photonics*, vol. 1, pp. 336–342, 2007. doi:10.1038/nphoton.2007.76

[2] B. Faatz *et al.*, “Simultaneous operation of two soft x-ray free-electron lasers driven by one linear accelerator”, *New J. Phys.*, vol. 18, p. 062002, 2016. doi:10.1088/1367-2630/18/6/062002

[3] J. Rossbach, J. R. Schneider, and W. Wurth, “10 years of pioneering X-ray science at the free-electron laser FLASH at DESY”, *Phys. Rep.*, vol. 808, pp. 1–74, 2019. doi:10.1016/j.physrep.2019.02.002

[4] K. Honkavaara and S. Schreiber, “FLASH: The Pioneering XUV and Soft X-Ray FEL User Facility ”, in *Proc. 39th Int. Free Electron Laser Conf. (FEL’19)*, Hamburg, Germany, Aug. 2019, paper THP074, pp. 734–737. doi:10.18429/JACoW-FEL2019-THP074

[5] K. Honkavaara, C. Gerth, M. Kuhlmann, J. Rönsch-Schulenburg, L. Schaper, R. Treusch, M. Vogt, J. Zemella, and S. Schreiber, “Status of the Free-Electron Laser User Facility FLASH”, presented at the 40th Int. Free Electron Laser Conf. (FEL’22), Trieste, Italy, Aug. 2022, paper MOP37, this conference.

ISBN: 978-3-95450-220-2 ISSN: 2673-5474 doi: 10.18429/JACoW-FEL2022-MOP40

[6] R. D'Arcy *et al.*, "FLASHForward: plasma wakefield accelerator science for high-average-power applications", *Phil. Trans. R. Soc. A*, vol. 377, p. 20180392, 2019. `doi:10.1098/rsta.2018.0392`

[7] S. Ackermann *et al.*, "First Demonstration of Parallel Operation of a Seeded FEL and a SASE FEL", presented at the 40th Int. Free Electron Laser Conf. (FEL'22), Trieste, Italy, Aug. 2022, paper TUP41, this conference.

[8] M. Yan *et al.*, "First Realization and Performance Study of a Single-Shot Longitudinal Bunch Profile Monitor Utilizing a Transverse Deflecting Structure", in *Proc. 2nd Int. Beam Instrumentation Conf. (IBIC'13)*, Oxford, UK, Sep. 2013, paper TUPC36, pp. 456-459. `https://jacow.org/ibic2013/papers/tupc36.pdf`

[9] M. Beye *et al.*, "FLASH2020+, Conceptual Design Report", DESY, Hamburg, 2020. `doi:10.3204/PUBDB-2020-00465`

[10] L. Schaper *et al.*, "FLASH2020+ Project Progress: Current Installations and Future Plans", presented at the 40th Int. Free Electron Laser Conf. (FEL'22), Trieste, Italy, Aug. 2022, paper TUP51, this conference.

[11] B. Marchetti *et al.*, "Experimental demonstration of novel beam characterization using a polarizable X-band transverse deflection structure", *Sci. Rep.*, vol. 11, p. 3560, 2021. `doi:10.1038/s41598-021-82687-2`

[12] M. Vogt, J. Rönsch-Schulenburg, S. Schreiber, and F. Christie, "RF Commissioning and First Beam Operation of the PolariX Transverse Deflecting Structures in the FLASH2 Beamline", presented at the 40th Int. Free Electron Laser Conf. (FEL'22), Trieste, Italy, Aug. 2022, paper WEP22, this conference.

[13] M. Tischer, P. Neumann, A. Schöps, and P. Vagin, "Phase shifter for the FLASH2 FEL", in *Proc. 5th Int. Particle Accelerator Conf. (IPAC'14)*, Dresden, Germany, May 2014, pp. 2010–2012. `doi:10.18429/JACoW-IPAC2014-WEPRO032`

[14] M. Vogt, Ch. Gerth, K. Honkavaara, M. Kuhlmann, J. Rönsch-Schulenburg, L. Schaper, S. Schreiber, R. Treusch, and J. Zemella, "Status of the Superconducting Soft X-ray Free-Electron Laser User Facility", in *Proc. 13th Int. Particle Accelerator Conf. (IPAC'22)*, Bangkok, Thailand, June 2022, pp. 1006–1009. `doi:10.18429/JACoW-IPAC2022-TUPOPT005`

ISBN: 978-3-95450-220-2 ISSN: 2673-5474 doi: 10.18429/JACoW-FEL2022-MOP41

A COMBINATION OF HARMONIC LASING SELF-SEEDED FEL WITH TWO-COLOR LASING

J. Rönsch-Schulenburg*, M. Kuhlmann, E. Schneidmiller, S. Schreiber, M. Vogt
Deutsches Elektronen-Synchrotron DESY, Hamburg, Germany

Abstract

The free-electron laser FLASH at DESY can produce SASE-FEL pulses in the extreme ultraviolet to the soft X-ray region. The flexibility of the variable gap undulators in the FLASH2 beamline opens a wide range of scientific opportunities. Different advanced lasing schemes have been tested in the past years, like the "frequency doubler" scheme, "two-color lasing", and "harmonic lasing self-seeded FEL" (HLSS). A recent user experiment required parameters not yet provided: a similar power in the fundamental and the third harmonic. To fulfill these requirements, a new way of lasing had to be developed ad hoc. A combination of HLSS and two-color lasing has been identified as the appropriated scheme to deliver a tailored two-color beam to the user experiment. In this article we describe difficulties of the setup and discuss the results achieved.

INTRODUCTION

FLASH [1–5] at DESY (Hamburg, Germany) is a free-electron laser (FEL) user facility. FLASH has been operated as an FEL user facility since summer 2005. FLASHs superconducting linac allows the acceleration of long bunch trains with several thousand electron bunches per second in 10 Hz bursts of up to 800 µs length. The bunch trains are divided into two parts with, in a certain range, independent RF-properties. A kicker-septum-based beam-switchyard allows to serve two beamlines in parallel. FLASH consists of two undulator beamlines (FLASH1 and FLASH2) and a plasma wakefield acceleration experiment FLASHForward (FLASH3) [6]. In FLASH1 the generation of FEL radiation based on the SASE (Self Amplified Spontaneous Emission) process is defined by the electron beam energy, due to fixed gap undulators. The fundamental FLASH1 wavelength provided for user experiments ranges from 4.2 nm to about 50 nm. In addition, FLASH1 hosts a seeding experiment Xseed [7]. In order to continue the operation of FLASH as a state-of-the-art FEL user facility, a substantial upgrade and refurbishment project, "FLASH2020+" was initiated. It includes seeding at FLASH1 using variable gap undulators [8]. The undulator beamline in FLASH2 contains twelve variable gap undulator segments. The tunable gap allows to control the undulator parameter K and thus the lasing wavelength in a certain range, depending on the electron beam energy. These variable gap undulators allow to implement novel techniques for radiation generation in addition to the standard SASE FEL operation at varying wavelength, ranging from 4 nm to about 90 nm.

* juliane.roensch@desy.de

60% of the available operation time is dedicated to user experiments. Every experiment has its own requirements of photon pulse properties and demands on quality and stability. We optimize each individual setup in order to fulfill all the requested parameters of the experiments.

TWO COLOR LASING AT FLASH

Employing novel lasing schemes potentially allows to significantly optimize the radiation properties, like increasing of the FEL pulse energy, improvement of the longitudinal coherence, control of polarization, extension of the wavelength range and multi-color mode of operation. Different innovative FEL developments have been realized at FLASH2. Using "Post-saturation undulator tapering" an increase of the radiation pulse energies above 1 mJ has been established [9, 10] and also high contrast of the afterburner radiation with reverse undulator tapering scheme has been demonstrated [11, 12].

The frequency doubler scheme [13] allows the operation in a two-color mode (with double frequency) and operation at shorter wavelengths with respect to the standard SASE scheme. At FLASH2 operating in the water window has been demonstrated with a wavelength of 3.1 nm.

Applying Harmonic Lasing Self Seeded FEL (HLSS) [14, 15] a significant increase in spectral brightness has been achieved and the coherence time has been increased noticeable. The HLSS scheme starts with harmonic lasing in the linear regime in the first part of the undulator. In the second part of undulator the K is reduced such that the harmonic becomes the fundamental and the harmonic output serves as "seed" which reduces the gain length and increases the FEL pulse energy. The graph in the middle of Fig.1 describes schematically the undulator setting for the HLSS.

Two-color lasing [16] can be set up in different configurations, but at FLASH2 a scheme based on alternating undulator tunes was found to be beneficial. The graph on top in Fig.1 shows a schematic of the setup for two-colors lasing based on alternating tunes. All odd undulator segments are tuned to the wavelength λ_1 and all even segments to λ_2. The amplification in the FEL process of the electromagnetic wave with the wavelength λ_1 is disrupted as soon as the electron bunch leaves a segment tuned to the wavelength λ_1 and enters a segment tuned to λ_2. However, energy modulations in the electron bunch, continue to get transformed into density modulations. Due to its longitudinal dispersion, the additional bunching in the λ_2 undulator segment quickly radiates a stronger field than the one coming from the previous λ_1 segment, which is diffracted in addition, and the FEL process continues with higher amplitudes. Thus, in

ISBN: 978-3-95450-220-2 ISSN: 2673-5474 doi: 10.18429/JACoW-FEL2022-MOP41

FLASH2 the alternation of the undulator tunes generates a higher pulse energy for both colors than tuning all segments at the beginning of the undulator to λ_1 and the last ones to λ_2. Another important advantage of this scheme is that the longitudinal source positions of both colors are close to each other.

SPECIAL TWO COLOR LASING SETUP FOR USERS

Some photon experiments require two different soft X-ray wavelengths. The choice of the optimum lasing scheme depends on the demands of the individual experiment. For a user-experiment analyzing the relaxation timescales in core level photo excited molecules, required lasing at 17.7 nm and 5.9 nm in parallel, both at a similarly high power. An FEL pulse duration shorter than 50 fs in a bunch train of 40 bunches with 100 kHz repetition rate was required for the optimum experimental conditions.

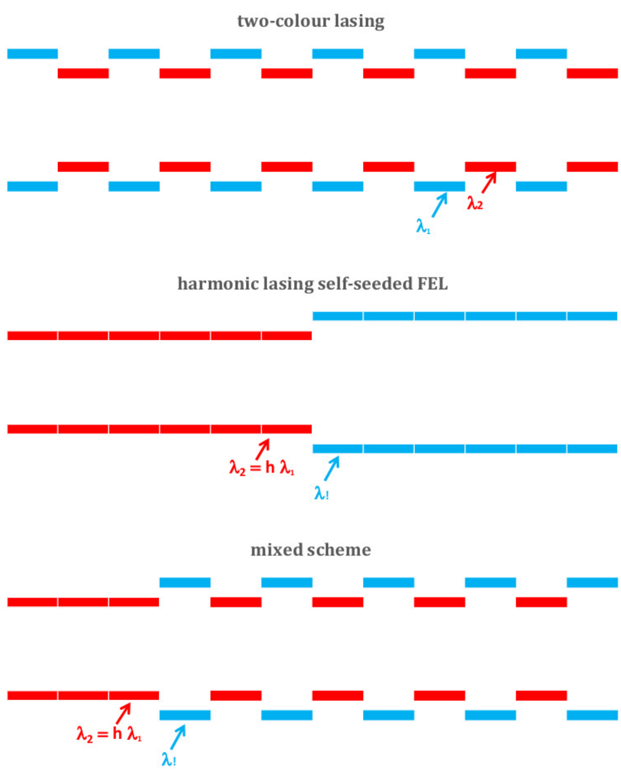

Figure 1: Tuning of the gaps of the undulator segments in the two-color lasing scheme based on alternating tunes (top), the harmonic lasing self-seeded (HLSS) scheme (center) and a mixture of both schemes used to optimize the special requirements of a certain user experiment (bottom).

Since it was shown in [14, 15] that the FEL pulse energy in a harmonic lasing self-seeded configuration exceeds conventional SASE by 50 % this scheme would be a good choice if only the pulse energy in the harmonic is considered. Unfortunately, the fundamental wavelength is eroded in this scheme and cannot be transported to the photon experiment, since the focal points are far away from each other.

Two-color lasing based on alternating tunes offers the possibility to generate the focal point of both wavelength close to each other. The disadvantage is that it does not use the 3rd harmonic relation of the two wavelengths to each other. This leads to a waste of the higher output power in the harmonic.

Therefore, we decide in favour of a mixture of these two configurations, shown in Fig. 1 (bottom). The first three undulators were tuned to 17.7 nm to allow the fundamental wavelength to gain intensity and develop 3rd harmonic bunching content. Downstream two-color lasing based on alternating tunes was applied to increase the intensity of the fundamental as well as the 3rd harmonic and fix their foci at similar longitudinal positions. An electron beam energy of 1.04 GeV was chosen to reach both 5.9 nm and 17.7 nm, and to enable a small wavelength scanning range to allow resonance scans. After an initial resonance scan both wavelengths were fixed and ran very stable.

The photon pulse energy is measured using two different gases in X-ray gas monitor detectors (XGMDs) with known cross sections for λ_1 and λ_2. The transmission value from the XGMD located in the accelerator tunnel to the one in the experimental hall needs to be measured exactly for both colors independently for an exact pulse energy measurement. The determination of the transmission is a touchy process since the bunching effect needs to be preserved while detuning one wavelength. An online measurement tool of the SASE pulse energy of both colors was used for tuning in which XGMDs and the online photo-ionisation spectrometer's (OPIS) were linked. A photon pulse energy of about 4 µJ at 5.9 nm and 35 µJ at 17.7 nm using the mixed undulator configuration has been achieved. For SASE operation at 1.04 GeV and 5.9 nm the saturation length is about 30 m. Thus, the reached pulse energy at 5.9 nm tuning only 5 undulators with a total length of 12.5 m is impressive, because it uses the third harmonic of the 17.7 nm radiation as a seed and profits from the bunch achieved in the undulators tuned to 17.7 nm and shortens the gain length of the 3rd harmonic compared to the fundamental at 5.9 nm.

In order to achieve the required photon pulse duration below 50 fs, the bunch charge was reduced to 250 pC and measurements using a transverse deflecting structure (TDS) has been performed. The PolariX-TDS [17] is located downstream the undulator and thus allow to determine the lasing part of the electron bunch [18]. Figure 2 shows the measurement of the longitudinal phase space distribution (top) and the current density distribution (bottom) of a lasing bunch, done after finalizing the setup. The bunch itself is rather long but it has a high peak current inside a well concentrated short longitudinal region. In this part the local energy spread was enhanced and the centroid energy was reduced as is predicted by FEL theory. Hence this very short part was potentially the lasing part of the bunch and therefore the photon pulse (ignoring slippage) was potentially also within the specifications.

ISBN: 978-3-95450-220-2 ISSN: 2673-5474 doi: 10.18429/JACoW-FEL2022-MOP41

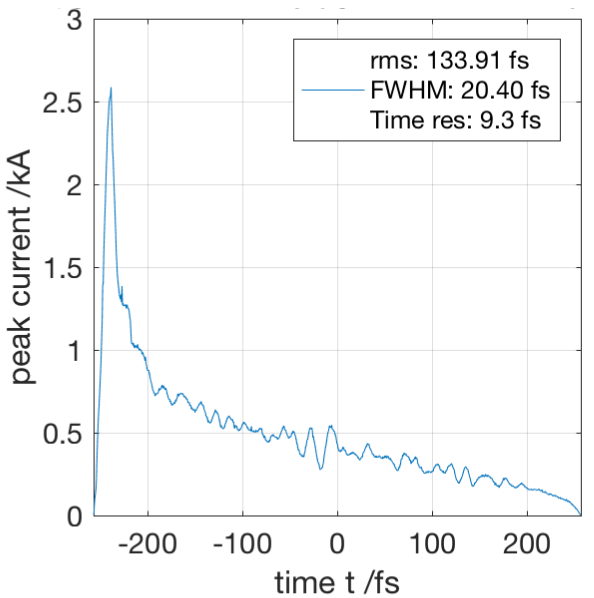

Figure 2: The plot shows the measured longitudinal phase space distribution (top) and the current density distribution (bottom) of the electron bunch using a transverse deflecting cavity downstream the FLASH2 undulator section. The measurement has been performed during lasing at 5.9 nm and at 17.7 nm using the mixed undulator configuration, shown in Fig. 1.

OUTLOOK

We try to further improve the FEL performance of the FLASH by optimizing different lasing schemes. The installation of an APPLE III type variable-polarisation third-harmonic afterburner in the FLASH2 beamline will further increase the flexibility of the FLASH2 lasing schemes [19]. The generation of a few hundred attosecond long pulses at FLASH is of high interest and is discusses in [20] and [21].

REFERENCES

[1] W. Ackermann *et al.*, "Operation of a free-electron laser from the extreme ultraviolet to the water window", *Nat. Photonics*, vol. 1, pp. 336–342, 2007. doi:10.1038/nphoton.2007.76

[2] B. Faatz *et al.*, "Simultaneous operation of two soft x-ray free-electron lasers driven by one linear accelerator", *New J. Phys.*, vol. 18, p. 062002, 2016. doi:10.1088/1367-2630/18/6/062002

[3] J. Rossbach, J. R. Schneider, and W. Wurth, "10 years of pioneering X-ray science at the free-electron laser FLASH at DESY", *Phys. Rep.*, vol. 808, pp. 1–74, 2019. doi:10.1016/j.physrep.2019.02.002

[4] K. Honkavaara and S. Schreiber, "FLASH: The Pioneering XUV and Soft X-Ray FEL User Facility", in *Proc. FEL'19*, Hamburg, Germany, Aug. 2019, pp. 734–737. doi:10.18429/JACoW-FEL2019-THP074

[5] K. Honkavaara, *et al.*, "Status of the Free-Electron Laser User Facility FLASH", presented at the 40th Int. Free Electron Laser Conf. (FEL'22), Trieste, Italy, Aug. 2022, paper MOP37, this conference.

[6] R. D'Arcy *et al.*, "FLASHForward: plasma wakefield accelerator science for high-average-power applications", *Philos. Trans. R. Soc. London, Ser. A*, vol. 377, p. 20180392, 2019. doi:10.1098/rsta.2018.0392

[7] S. Ackermann *et al.*, "First Demonstration of Parallel Operation of a Seeded FEL and a SASE FEL", presented at the 40th Int. Free Electron Laser Conf. (FEL'22), Trieste, Italy, Aug. 2022, paper TUP41, this conference.

[8] L. Schaper *et al.*, "FLASH2020+ Project Progress: Current Installations and Future Plans", presented at the 40th Int. Free Electron Laser Conf. (FEL'22), Trieste, Italy, Aug. 2022, paper TUP51, this conference.

[9] E. A. Schneidmiller and M.V. Yurkov, "The universal method for optimization of undulator tapering in FEL amplifiers", in *Proc. Advances in X-ray Free-Electron Lasers Instrumentation III*, Prague, Czech Republic, vol. 9512, p. 951219, 2015. doi:10.1117/12.2181230

[10] E. A. Schneidmiller and M.V. Yurkov, "Optimization of a high efficiency free electron laser amplifier", *Phys. Rev. ST Accel Beams*, vol. 18, p. 030705, 2015. doi:10.1103/PhysRevSTAB.18.030705

[11] E. A. Schneidmiller and M.V. Yurkov, "Obtaining high degree of circular polarization at x-ray free electron lasers via a reverse undulator taper", *Phys. Rev. ST Accel Beams*, vol. 16, p. 110702, 2013. doi:10.1103/PhysRevSTAB.16.110702

[12] E. Schneidmiller and M. V. Yurkov, "Reverse Undulator Tapering for Polarization Control at XFELs", in *Proc. IPAC'16*, Busan, Korea, May 2016, pp. 722–724. doi:10.18429/JACoW-IPAC2016-MOPOW008

[13] J. Feldhaus *et al.*, "Efficient frequency doubler for the soft X-ray SASE FEL at the TESLA Test Facility", *Nucl. Instrum. Methods Phys. Res., Sect. A*, vol. 528, pp. 471-475, 2004. doi:10.1016/j.nima.2004.04.134

[14] E. A. Schneidmiller, and M.V. Yurkov, "Harmonic lasing in x-ray free electron lasers", *Phys. Rev. ST Accel Beams*, vol. 15, p. 080702, 2012. doi:10.1103/PhysRevSTAB.15.080702

[15] E. Schneidmiller and M. V. Yurkov, "Studies of Harmonic Lasing Self-seeded FEL at FLASH2", in *Proc. IPAC'16*, Busan, Korea, May 2016, pp. 725–728. doi:10.18429/JACoW-IPAC2016-MOPOW009

[16] E. Schneidmiller *et al.*, "Two-Color Operation of FLASH2 Undulator", in *Proc. FEL'19*, Hamburg, Germany, Aug. 2019, pp. 168–171. doi:10.18429/JACoW-FEL2019-TUP055

[17] B. Marchetti *et al.*, "Experimental demonstration of novel beam characterization using a polarizable X-band transverse deflection structure", *Sci. Rep.*, vol. 11, p. 3560, 2021. doi:10.1038/s41598-021-82687-2

[18] M. Vogt, J. Rönsch-Schulenburg, S. Schreiber, and F. Christie, "RF Commissioning and First Beam Operation of the PolariX Transverse Deflecting Structures in the FLASH2 Beamline", presented at the 40th Int. Free Electron Laser Conf. (FEL'22), Trieste, Italy, Aug. 2022, paper WEP22, this conference.

ISBN: 978-3-95450-220-2 ISSN: 2673-5474 doi: 10.18429/JACoW-FEL2022-MOP41

[19] M. Beye, *et al.*, "FLASH2020+, Conceptual Design Report", DESY, Hamburg, 2020. doi:10.3204/PUBDB-2020-00465

[20] E. Schneidmiller, "An attosecond scheme overcoming coherence time barrier in SASE FELs", presented at the 40th Int. Free Electron Laser Conf. (FEL'22), Trieste, Italy, Aug. 2022, paper MOP39, this conference.

[21] E. Schneidmiller, "Application of a modified chirp-taper scheme for generation of attosecond pulses in extreme ultraviolet and soft x-ray free electron lasers", *Phys. Rev. ST Accel Beams*, vol. 25, p. 010701, 2022. doi:10.1103/PhysRevAccelBeams.25.010701

ISBN: 978-3-95450-220-2 ISSN: 2673-5474 doi: 10.18429/JACoW-FEL2022-MOP45

SASE-FEL STOCHASTIC SPECTROSCOPY INVESTIGATION ON XUV ABSORPTION AND EMISSION DYNAMICS IN SILICON

D. De Angelis†, E. Principi, D. Fausti[1], L. Foglia, R. Mincigrucci, E. Pedersoli, J. S. Pelli Cresi, K. J. Prince, F. Capotondi, Elettra-Sincrotrone Trieste, Trieste, Italy
E. Razzoli, C. Svetina, Paul Scherrer Institut, Villigen, Switzerland
Y. Klein, S. Shwartz, Physics Department and Institute of Nanotechnology and advanced Materials, Bar Ilan University, Ramat Gan, Israel
I. A. Vartaniants, Deutsches Elektronen-Synchrotron DESY, Hamburg, Germany
[1]also at Department of Physics, Università degli Studi di Trieste, Trieste, Italy

Abstract

Time-resolved high-resolution emission/absorption spectroscopy appears to be strategic in fundamental matter physics investigation as well as in functional materials characterization. For example, chemical activity can be investigated on the basis of absorption edge spectroscopy, magnetic spin status can be probed via resonant dichroic effects by means of Faraday (in transmission) or Kerr (in reflection) effects, molecular chirality can be resolved with high accuracy using combining photons with variable energy and polarizations. Typically, all such applications of high-resolution time resolved absorption spectroscopy require a pulsed radiation source and narrow bandwidth emission line, along with a large data statistic to resolve level the characteristic signal from the sample above the instrumental noise. In this work we will demonstrate a novel experimental approach, originally demonstrated in hard X-ray regime, aimed to retrieve high resolution absorption and emission spectra with sub-picosecond time resolution, by exploiting the stochastic nature of the wide-band self-amplified spontaneous emission (SASE) FEL radiation provided tuning FERMI in optical klystron mode. We got advantage of the two spectrometers available at the TIMEX beamline to reconstruct a 2D emission/absorption spectrum map of a Si crystalline thin film sample. To do so, we applied the singular value decomposition approach on a large ensemble of incoming and outgoing single-pulse spectra; by applying Tikhonov regularization, we were able to obtain absorption spectra with an energy resolution of few tens of meV (comparable to the maxima resolution of the used spectrometer). Moreover, emission lines due to spontaneous emission of the electron de-excitation are clearly resolved after the inversion of the ensemble of spectra fluctuation before and after the sample. Finally, by using this stochastic approach correlating the spectral fluctuation of the source to sample response, we performed a time resolved characterization of the Si L_{23}-edge and Si emission line at 99.3 eV, by pumping the Si sample with the visible laser (390 nm) below damage threshold (i.e. deposit on the sample surface about 20 mJ/cm^2). Using this approach, we were able to combine time resolved XAS and XES spectra, and we ascribed the observed dynamics to a consequence of the bond softening phenomenon occurring in our sample after the visible light excitation.

INTRODUCTION

In the last decades, the introduction of soft X-ray radiation from synchrotron sources gave an impressive boost to the study of the electronic and structural properties of condensed matter. Their high brilliance, together with their high energy resolution, allow nowadays to spectroscopically characterize samples with high chemical and structural sensitivity. For this reason, synchrotron spectroscopy is extensively used in an increasingly large ensemble of scientific field. Soft X-ray emission/absorption spectroscopy with high-resolution (tens of meV) and picosecond time resolution appears to be strategic in fundamental matter physics investigation as well as in functional materials characterization. FELs have been considered as extremely powerful tools for their capability of delivering high brilliance and high coherent radiation. Such characteristics boosted the research on nonlinear photonics, condensed matter physics in extreme pressure and temperature condition, diffraction and projection imaging. Free-electron laser appeared as a steppingstone to the investigation of the femto- and picosecond timescale dynamics in condensed matter systems. Indeed, nowadays a pump probe scheme is typically implemented in the experimental scheme in order to bring the sample in the excited state to measure its dynamics with the short FEL pulses. Such a measurement approach appears to be of large interest in the context of chemical reaction, structural, electronic and magnetic dynamics and it is widely employed also at FERMI, using the FEL radiation as probe or pump, together with a UV-Vis-IR laser. Recently, also the possibility to have a FEL-FEL pump-probe scheme at FERMI has been introduced with the commissioning of the AC-DC delay line [1]. It is clearly of great interest to introduce spectroscopic techniques in the FEL framework, taking advantage from its peak high brilliance and, in case of seeded FEL, its high energy resolution. Nevertheless, there were some issues, up to now, preventing the efficient implementation of high-performance spectroscopic techniques in combination with FEL strong points.

* Work supported by Elettra-Sincrotrone Trieste
† dario.deangelis@elettra.eu

ISBN: 978-3-95450-220-2 ISSN: 2673-5474 doi: 10.18429/JACoW-FEL2022-MOP45

The main bottleneck in the development of such methodologies is, in general, the low efficiency in photon energy scan, which can be achieved substantially by using two alternative approaches based on the type of source, i.e.: by tuning the radiation wavelength of a seeded FELs, or by monochromatizing the emission of a SASE FELs. The main issue in scanning the photon energy in seeded configuration is related to the FEL tuning, that involves the whole machine and can be so time demanding that a typical hundred point-energy scan would require several hours, reducing considerably the efficiency of time resolved XAS studies during a few-days beamtime. On the other hand, when using wide-band SASE FEL, a reduction in the photon flux and an increase on the pulse duration is introduced due to the presence of the monochromator. At FERMI, by the correlation spectroscopy method, we were able to exploit the high intensity flux of the FEL, operated in SASE mode, and we collected high resolution absorption spectra in few minutes, reaching the efficiency of a typical synchrotron radiation beamline.

In this work we report on the results obtained in the investigation of the structural and electronic dynamical properties of crystalline silicon. In particular, we wanted to explore the bond softening phenomenon that occurs when Si is exposed to a femtosecond laser excitation. The phenomenon has been experimentally observed, although indirectly, on freestanding polycrystalline Si membranes as an exponential decay of X-ray diffraction signal, due to an exponential atomic heating with a well-defined time constant [2]. This heating behaviour has been later described by an ab-initio simulation [3]. In the theoretical framework used by Zijlstra et al., it has been calculated that a Si system can undergo thermal phonon squeezing when excited below the Lindemann stability limit and, moreover, the time constant associated to the process depends on the number of electron-hole pair per unit volume that are generated by the laser pulse. Our aim was to investigate the modification of the electronic structure of Si, due to the laser induced bond softening, by absorption and emission spectroscopy.

For this investigation, X-ray absorption spectroscopy of the $L_{2,3}$-edge of Si provides information about the electronic structure close to the fermi energy and represents an efficient tool to explore the band modification induced by the femtosecond laser. The correlation spectroscopy method showed to be the ideal tool for such kind of investigation.

METHOD

Experimental Setup

The measurements were performed at the EIS-TIMEX beamline at the FERMI FEL facility in Trieste (Italy) [4]. The beamline is optimized for pump-probe measurements in FEL/FEL or UV-vis/FEL configuration. Two spectrometers are available, one before and one after the experimental chamber, both operated in single pulse detection mode at the same frequency as the FEL (50 Hz) (Fig. 1). The first one, called PRESTO [5], allows to characterize the spectral content of each single pulse, by imaging the

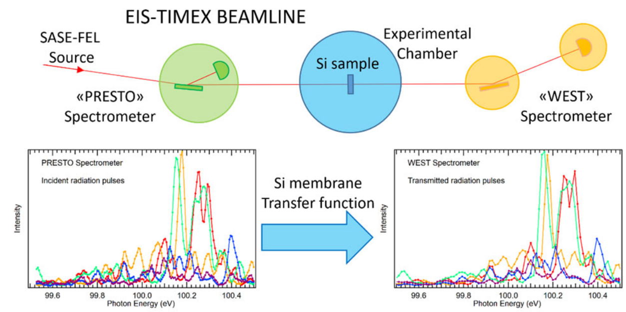

Figure 1: On the upper part of the figure, the scheme of the TIMEX beamline is reported; below, an example of the SASE spectra produced by FERMI during the experiment, measured by the two spectrometers.

energy dispersion of the first diffraction order of its reflecting grating; the latter, called WEST, is designed to collect light after the interaction with the sample. The resolving power of the two spectrometers is ~10^4. The sample was a ultra-polished crystalline Si membrane oriented in a [0,0,1] direction, 200 nm thick, provided by Norcada.

The FEL was operated in optical klystron SASE mode, so to maximize the radiation bandwidth and, at the same time, to achieve a spike spectral distribution, that is of strategic importance for the efficiency of the analysis method.

Data Analysis

We treated the spectra acquired upstream and downstream the sample by applying the correlation spectroscopy method as described by Kayser [6]. In this method, the acquired spectra are considered as vectors defined in the space of photon energies. The method consists in retrieving, from a sufficiently large dataset of incoming and outgoing spectra, the matrix that maps the sample response to the incoming stimulus. In this approach, the off-diagonal terms of retrieved matrix will appear as the Inelastic X-ray Scattering (IXS) of the sample response (Fig. 2a). In this way, the reconstruction of the IXS image is obtained as the solution of an ill-posed linear problem. The large shot to shot variability of the photon energy distribution provided by the SASE FEL is the key feature that makes this data analysis method efficient. Indeed, FEL pulses with different spectral content correspond to linearly independent vectors in the photon energies space; therefore, the spectral variability allows to explore the vector space and to efficiently reconstruct the IXS image. Considering a 1000-pixel detector for the two spectrometers, we have a 1000 vector basis in our energies space, so, in principle, we will need at least 1000 linearly independent SASE pulses to completely solve the linear system of equations. The stochastic nature of the SASE generation, ensures the linear independence also between consecutive pulses. Nonetheless, in our experience, we observed that from 50000 to 100000 pulses are needed to have a statistically significant dataset; this can be attributed to the finite detector dynamic range and signal-to-noise ratio. With a number of vectors larger than the dimension of the basis, the linear problem is over-defined and requires the datasets to be divided in

ISBN: 978-3-95450-220-2 ISSN: 2673-5474 doi: 10.18429/JACoW-FEL2022-MOP45

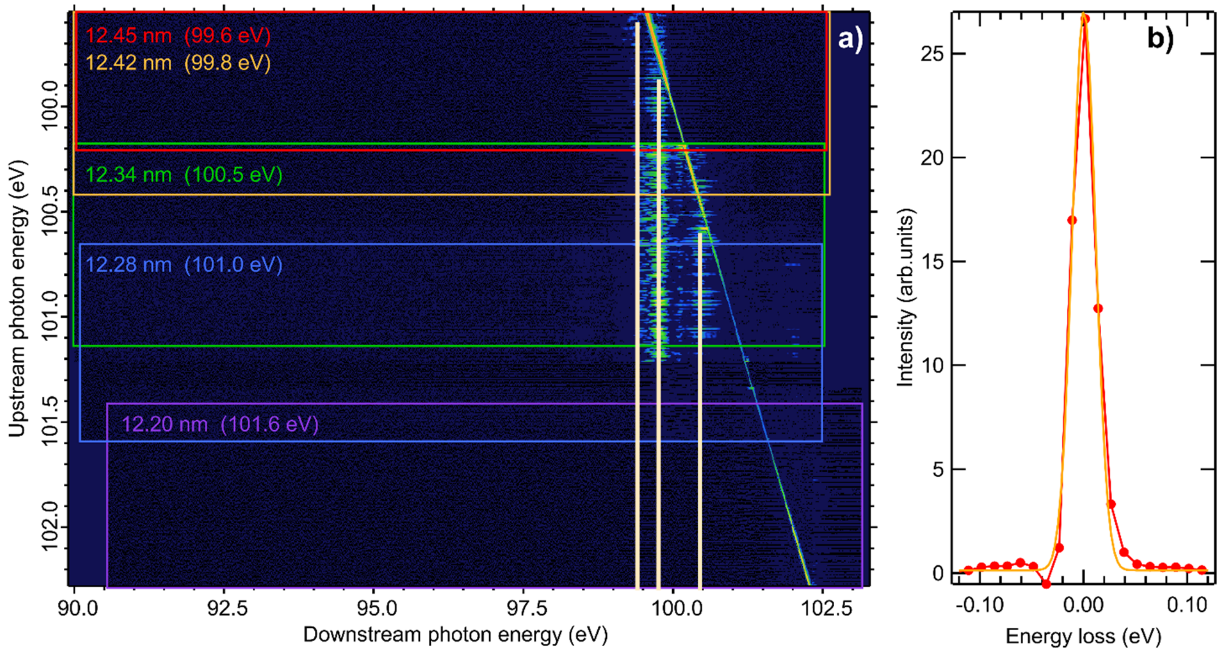

Figure 2: a) Reconstructed IXS map for the Si sample; b) Transverse profile of the elastic line extracted from a no-sample measurement: from FWHM, we estimate an energy resolution of about 30 meV.

smaller parts and the linear problem to be solved separately for each subset of data, averaging the solutions in the following. Moreover, as shown in Fig. 2a, since the signal will be concentrated along the diagonal (the sample XAS spectrum, in the case of transmission) and along lines on the lower-left part of the image (the sample XES spectrum, in the case of emission), a large number of pixels will show very small or null values. To address this relatively common ill-posed problem, we employed the Tikhonov regularization method.

We estimated the energy resolution of this technique by considering the sum of squared errors of PRESTO and WEST. At 100 eV, this value is of the order of 10 meV for both spectrometers. The energy resolution we can therefore expect from our measurement will not be better than 14 meV (the quadrature sum of the two spectrometers resolution). For the sake of an experimental validation of this esteem, we acquired a dataset keeping the sample outside the FEL beam path. The so obtained IXS image, in the ideal case, corresponds to a diagonal transformation matrix; in the real case we expect a Gaussian distribution of the values around the diagonal, generated by the finite energy resolution of the spectrometers. We analysed the transverse profile of the diagonal line by fitting the line-shape with a Gaussian profile (Fig. 2b) and we retrieve a variance value of about 15 meV, which is consistent with the calculated resolution and demonstrates the effectiveness of the correlation method in preserving the energy resolution of the experimental setup.

RESULTS AND DISCUSSION

Static Measurements

As a first investigation on the Si sample, we performed an absorption/emission measurement across the $L_{2,3}$-edge. The SASE-mode FEL was set to five different photon energy configurations in order to collect dataset on an energy range covering the full $L_{2,3}$-edge from about 99.0 eV to 102.5 eV. For each energy configuration we collected 10^5 pulse spectra and we calculated the IXS image. Figure 2a shows in the same plot the result of the five reconstructions. The diagonal (elastic) feature is clearly distinguishable, along with a series of emission lines al lower energies.

In Fig. 3 the integrated profile along the diagonal is showed and compared to the transmission spectra obtained by a seeded FEL scan, a ghost spectroscopy measurement [7] a synchrotron measurement and the spectrum stored in the CXRO X-ray database. In the absorption profile (Fig. 3) we can recognize the fingerprint of the Si L-edge, accordingly with the results reported in literature for silicon nanocrystals [6]. It is worth noting, from the technical point of view, that this result was obtained with five 30-minute acquisition at 50 Hz. In terms of time efficiency, signal-to-noise ratio and energy resolution, this technique appears to

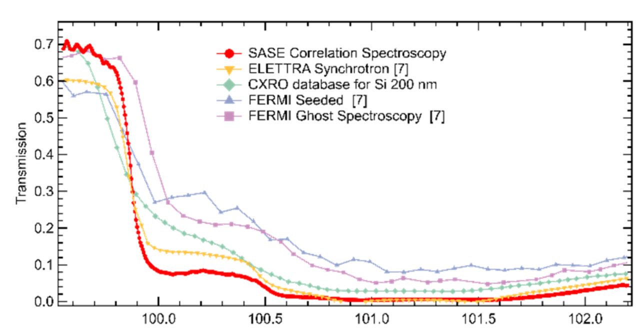

Figure 3: Longitudinal profile of the elastic line, i.e. Si $L_{2,3}$ absorption edge; comparison with other standard measurement techniques.

ISBN: 978-3-95450-220-2 ISSN: 2673-5474 doi: 10.18429/JACoW-FEL2022-MOP45

be competitive with respect to a synchrotron-based measure. A minor drawback of this correlation spectroscopy technique on the time efficiency appears when the energy range of interest becomes larger than the SASE spectral bandwidth (i.e. few eV); in that case, a SASE wavelength change is necessary, which implies, for the FERMI FEL, a few minutes machine optimization in addition to the acquisition time. Emission line profiles are visible in Fig. 2a. The XES features appear to be in good agreement with the c-Si fingerprints [8,9]. It is important to notice that we are able to observe only the on-axis emission from the sample, by construction of the WEST spectrometer, whose vertical acceptance angle is about 2 degrees. Nevertheless, the large dynamic range of the Andor Ikon CCD detector allowed to collect a sufficiently high statistic to describe the emission features.

Dynamic Measurements

A visible-XUV pump-probe experiment was performed after the static measurement to explore the electronic dynamics of the c-Si under femtosecond visible excitation.

As a pump source, we used the FERMI Seed Laser for Users (SLU) tuned at 392 nm (3.16 eV), characterized by 80 fs pulse length. The visible pump fluence was set at about 20 $mJ \cdot cm^{-2}$ in order to avoid sample damage in the time needed for the delay scan, which required about eight hours. We considered in our analysis the L-edge transmission profile, together with the emission lines intensity.

Transmission profiles are reported in Fig. 4. With the aim of obtaining a semi-quantitative result, we used a logistic function to fit the transmission drop around 100 eV. We observe that, while the position of the edge in energy remains constant, the steepness of the edge increases few picoseconds after the visible excitation and tends to recover in about 200 ps in an asymmetric way. The shape of the edge recovers in a shorter time for energies below 100 eV. Thanks to the good signal to noise ratio we reached on the most intense emission line, the one at 99.3 eV, we can observe a dynamic behaviour in its intensity, which seems to follow that of the edge steepness. We observe a 30% increase in the emission intensity within the first ten picoseconds after the pump excitation and then a recovery which lasts for about 200 ps. As predicted in literature [3,10] a femtosecond light pulse with an energy above the Si bandgap can induce a widening of the VB in k-space and a consequent increase in the electronic density of states at the top of the VB. The modification is expected to be transient and to recover to the initial condition in a timescale that directly depends on the delivered excitation energy. This considered, the modification in the electronic structure we were able to observe are reasonably the effect of the afore mentioned bond softening phenomenon.

CONCLUSION

In this work we demonstrated the efficiency of the stochastic spectroscopy as an experimental strategy to perform high energy resolution spectroscopy in a SASE FEL-based experiment. We used this approach to investigate the dynamic behaviour of silicon when excited with visible light. This kind of measurements are of fundamental importance to understand the electronic, structural and chemical properties of materials, especially in the field of novel functional materials. For this reason, we expect this experiment to be the beginning of a new series of investigations in condensed matter structural dynamics performed at FELs.

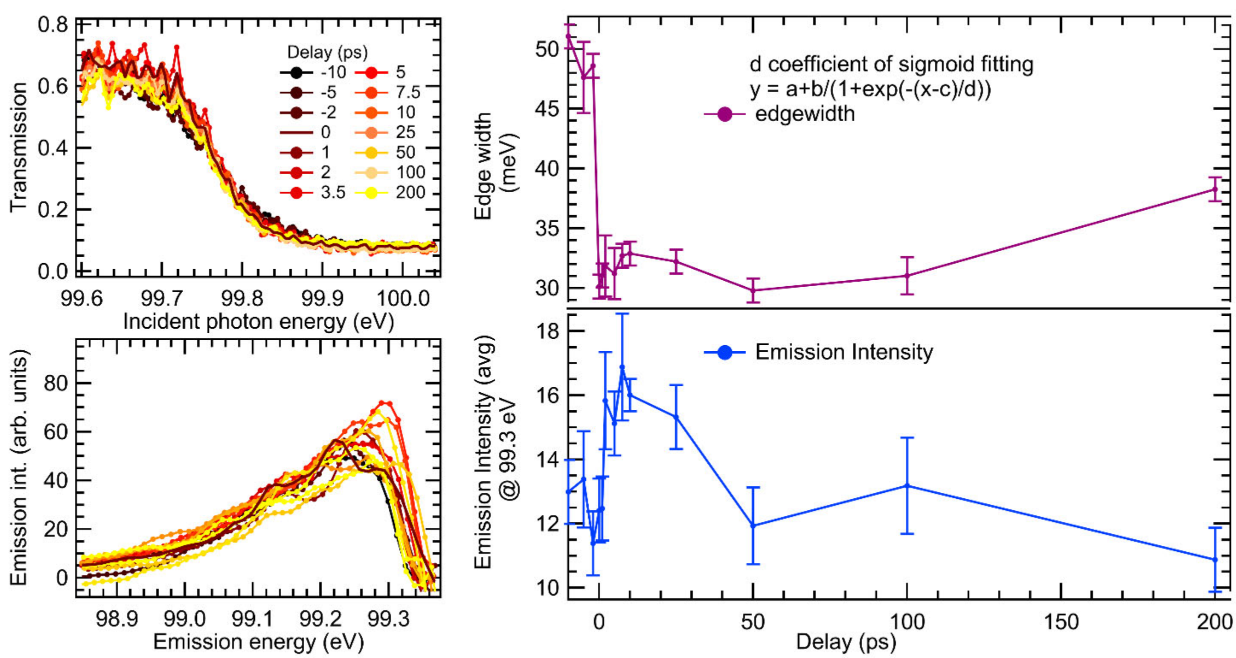

Figure 4: In the upper part of the figure the silicon transmission profile is reported for different delay times (on the left) and the edge width as a function of the delay (on the right); On the lower part, the emission intensity evolution is displayed in the same way, as a function of delay.

ISBN: 978-3-95450-220-2 ISSN: 2673-5474 doi: 10.18429/JACoW-FEL2022-MOP45

REFERENCES

[1] A. Simoncig, M. Manfredda, G. Gaio, N. Mahne, L. Raimondi, M. Zangrando, *et al.*, "AC/DC: The FERMI FEL Split and Delay Optical Device for Ultrafast X-ray Science". *Photonics*, vol. 9, no. 5, p. 314, 2022. `doi:10.3390/photonics9050314`

[2] M. Harb, R. Ernstorfer, T. Dartigalongue, C. T. Hebeisen, R. E. Jordan, and R. D. Miller, "Carrier relaxation and lattice heating dynamics in silicon revealed by femtosecond electron diffraction". *J. Phys. Chem. B*, vol. 110, no. 50, pp. 25308-25313, Nov. 2006. `doi:10.1021/jp064649n`

[3] E. S. Zijlstra, A. Kalitsov, T. Zier, and M. E. Garcia, "Squeezed thermal phonons precurse nonthermal melting of silicon as a function of fluence", *Phys. Rev. X*, vol. 3, iss. 1, p. 011005, Jan. 2013. `doi:10.1103/PhysRevX.3.011005`

[4] C. Masciovecchio, A. Battistoni, E. Giangrisostomi, F. Bencivenga, E. Principi, and M. Zangrando, "EIS: the scattering beamline at FERMI", *J. Synchrotron Radiat.*, vol. 22, no. 3, pp. 553-564, 2015. `doi:10.1107/S1600577515003380`

[5] C. Svetina, D. Cocco, N. Mahne, L. Raimondi, E. Ferrari, and M. Zangrando, "PRESTO, the on-line photon energy spectrometer at FERMI: design, features and commissioning results", *J. Synchrotron Radiat.*, vol. 23, no. 1, pp. 35-42, 2016. `doi:10.1107/S1600577515021116`

[6] Y. Kayser, C. Milne, P. Juranić, L. Sala, J. Czapla-Masztafiak, J. Szlachetko, *et al.*, "Core-level nonlinear spectroscopy triggered by stochastic X-ray pulses", *Nat. Commun.*, vol. 10, no. 1, pp. 1-10, Oct. 2019. `doi:10.1038/s41467-019-12717-1`

[7] Y. Klein, E. Strizhevsky, F. Capotondi, D. De Angelis, L. Giannessi, M. Pancaldi, *et al.*, "High-resolution absorption measurements with free-electron lasers using ghost spectroscopy", in preparation to be submitted to a journal.

[8] L. Šiller *et al.*, "Core and valence exciton formation in x-ray absorption, x-ray emission and x-ray excited optical luminescence from passivated Si nanocrystals at the Si L2, 3 edge", *J. Phys.: Condens. Matter*, vol. 21, no. 9, p. 095005, Jan 2009. `doi:10.1088/0953-8984/21/9/095005`

[9] D. H. Tomboulian, and D. E. Bedo, "Absorption and Emission Spectra of Silicon and Germanium in the Soft X-Ray Region", *Phys. Rev.*, vol. 104, p. 590, Nov. 1956. `doi:10.1103/PhysRev.104.590`

[10] T. Zier, E. S. Zijlstra, and M. E. Garcia, "Silicon before the bonds break", *Appl. Phys. A*, vol. 117, no. 1, pp. 1-5, Oct. 2014. `doi:10.1007/s00339-014-8316-4`

ISBN: 978-3-95450-220-2 ISSN: 2673-5474 doi: 10.18429/JACoW-FEL2022-MOP46

FEL PERFORMANCE OF THE EuPRAXIA@SPARC_LAB AQUA BEAMLINE

F. Nguyen*, A. Petralia, A. Selce, ENEA–Frascati, Frascati, Italy
C. Boffo, Fermilab, Batavia IL, USA
M. Castellano, M. Del Franco, Z. Ebrahimpour, M. Ferrario, A. Ghigo, L. Giannessi,
A. Giribono, A. Marcelli, C. Vaccarezza, F. Villa, INFN–LNF, Frascati, Italy
A. Cianchi, F. Stellato, University of Tor Vergata and INFN–Roma Tor Vergata, Rome, Italy
M. Coreno[1], CNR–ISM and Elettra, Trieste, Italy
P. Iovine, University La Sapienza, Rome and INFN–Napoli, Naples, Italy
N. Mirian, DESY, Hamburg, Germany
M. Opromolla, V. Petrillo, University of Milan and INFN–Milano, Milan, Italy
[1] also at INFN–LNF, Frascati, Italy

Abstract

The AQUA beamline of the EuPRAXIA@SPARC_LAB infrastructure consists of a Free-Electron Laser facility driven by an electron beam with 1 GeV energy, produced by an X-band normal conducting LINAC followed by a plasma wakefield acceleration stage, with the goal to deliver variable polarization photons in the 3-4 nm wavelength range. Two undulator options are considered for the AQUA FEL amplifier, a 16 mm period length superconducting undulator and an APPLE-X variable polarization permanent magnet undulator with 18 mm period length. The amplifier is composed by an array of ten undulator sections 2m each. Performance associated to the electron beam parameters and to the undulator technology is investigated and discussed.

INTRODUCTION

The EuPRAXIA project is expected to realize and demonstrate use of plasma accelerators delivering high brightness beams up to 1-5 GeV for users [1]. During the first phase, the Free-Electron Laser (FEL) facility EuPRAXIA@SPARC_LAB will be constructed at the INFN-LNF laboratory [2]. This will be driven by the beam accelerated to 1 GeV energy within the plasma wakefield accelerator (PWFA) scheme, where a properly tailored electron bunch is injected into the plasma wave [3].

The AQUA [1] FEL beamline of the project will be operated in Self-Amplified Stimulated Emission (SASE) mode with 3-4 nm target wavelength, *i.e.* 310-410 eV photon energy, where water is almost transparent to radiation, while nitrogen and carbon are absorbing and scattering. This range belongs to the so called *water window*, where for instance 3D images of biological samples can be obtained processing several X-ray patterns by means of coherent diffraction imaging experiments: an ideal technique that could allow to reconstruct images of viruses or cells in their native environment [4].

CHOICE OF THE UNDULATORS

Table 1 shows the electron beam values expected and assumed for the undulators assessment and for evaluating the AQUA FEL performance. The Linac driving the AQUA

Table 1: Electron Beam Parameters

Quantity	Value
Charge Q	30 pC
Energy E_{beam}	1 GeV
Peak current I_{peak}	1.8 kA
RMS bunch length σ_z	2 µm
Proj. normalized x, y emittance ε_n	1.7 mm mrad
Slice normalized x, y emittance ε_n	0.8 mm mrad
Proj. fractional energy spread $\sigma_{\delta,p}$	0.95 %
Slice fractional energy spread $\sigma_{\delta,s}$	0.05 %

FEL includes two pairs of eight X-band accelerating cavities, separated by a magnetic bunch compressor and followed by the PWFA module. The final design of the layout is still in progress, with the following main features:

- peak current from the S-band photoinjector;
- slice energy spread goal of 0.05 % or lower;
- energy spread and transverse quantities under control operating at 0.85 GeV/m accelerating gradient.

In addition to the coherent imaging opportunities mentioned before, the chance to have variable and selectable X-rays allows to study [5] chemical properties of materials by means of switchable FEL polarization. Thus, the main requests to the undulator configuration are the following:

- deflection strength $K \simeq 1$ at resonant $\lambda \simeq$ 3-4 nm;
- selectable linear and circular polarization;
- some contingency in the total active length;
- some flexibility in the wavelength tuning range.

Figure 1 shows the FEL saturation length as a function of undulator period and resonant wavelength, evaluated with

* federico.nguyen@enea.it
[1] Water in Latin.

ISBN: 978-3-95450-220-2 ISSN: 2673-5474 doi: 10.18429/JACoW-FEL2022-MOP46

the 1D FEL performance scaling laws [6] assuming the parameters of Table 1 for a planar permanent magnet out-of-

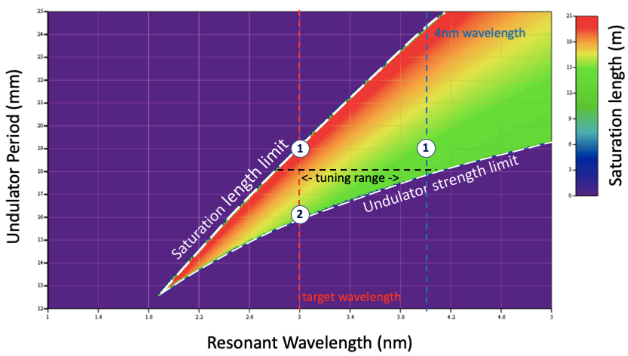

Figure 1: Saturation length contour plot as a function of undulator period and resonant wavelength.

vacuum undulator with remanent field strength $B_r = 1.2$ T and minimum gap of 6 mm. From Fig. 1 it results that:

(1) $\lambda_u = 18$ mm period implies some tuning range, plus a wide saturation length contingency, especially if operating at 4 nm resonant wavelength.

(2) $\lambda_u = 16$ mm period increases the saturation length limit, but with almost no wavelength tuning range, because of the deflection strength limit;

The adopted undulator solution is the Apple-X [7–9] with 18 mm period and remanent field strength $B_r = 1.35$ T. The design envisages a 5 mm external diameter vacuum chamber for electrons propagation. The minimum feasible gap is 1.5 mm, as the compromise between the requested field

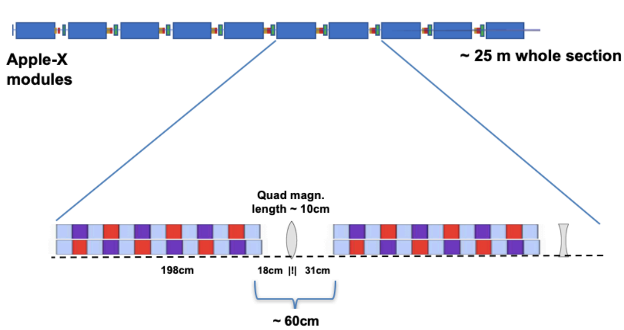

Figure 2: AQUA schematic undulator layout.

strength and mechanical constraints of the magnets. This structure allows to achieve $K_{\max} = 1.2$ ($K_{\max} = 1.7$) in case of circular (linear) polarization.

BASELINE UNDULATOR LAYOUT

The AQUA baseline SASE undulator section consists of 10 modules, each with a length of 110 periods ≃ 2 meters.

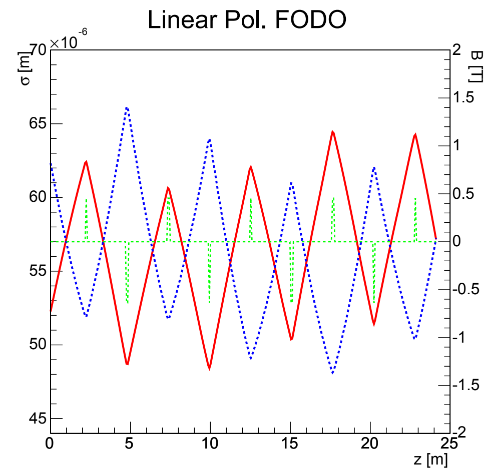

Figure 3: Horizontal (red solid line) and vertical (blue dotted line) profile of the electron beam inside the undulator plus FODO sections in LP mode: the green spots indicate the integral gradient field values specified on the right y-axis.

Figure 2 shows the scheme of the undulator line, featuring the inset zoom of the magnetic unit cell made of the undulator and FODO sections. The magnetic length of the quadrupoles is about 10 cm. For a 1 GeV electron beam energy, the choice to have the intra-undulator distance of about 60 cm, together with Twiss average $\beta_{x,y}$ parameter and K values constrain the quadrupole integral gradient fields requested to operate the Apple-X modules at 4 nm wavelength, in either linear (LP) or circular (CP) polarization.

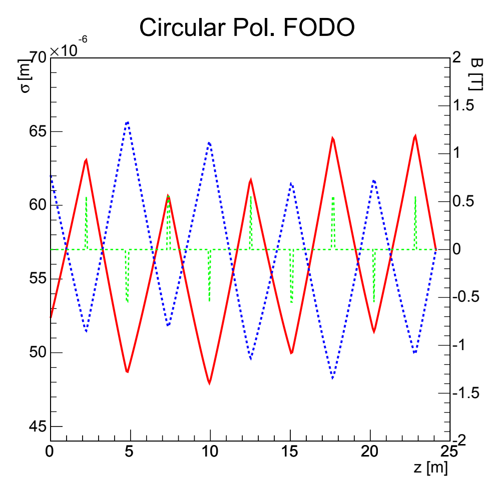

Figure 4: Horizontal (red solid line) and vertical (blue dotted line) profile of the electron beam inside the undulator plus FODO sections in CP mode: the green spots indicate the integral gradient field values specified on the right y-axis.

Figures 3 and 4 show the transverse profile of the electron beam subject to the undulator plus FODO sections in respectively LP and CP operations with $\langle \beta_{x,y} \rangle = 8$ m. The integral gradient field values are indicated by means of green spots indicating values on the y-axis specified on the right.

ISBN: 978-3-95450-220-2 ISSN: 2673-5474 doi: 10.18429/JACoW-FEL2022-MOP46

The behavior of the integral gradient field values is investigated with raising the electron beam energy, while keeping constant all other parameters. In order to accommodate the same focusing factors, integral gradient fields have to be increased. Figure 5 shows that field values stay on the order

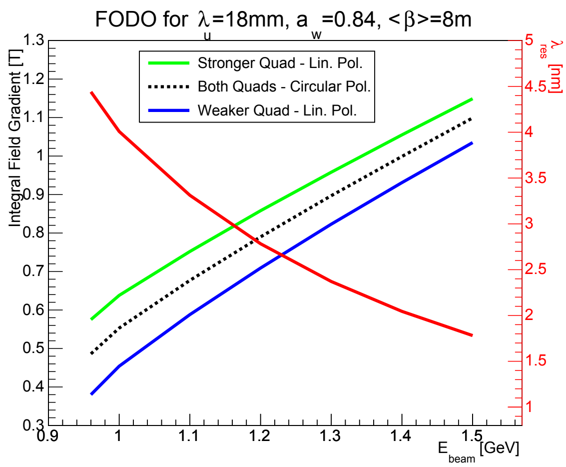

Figure 5: Integral gradient field values and resonant wavelength as a function of electron beam energy.

of about 1 T, or even smaller for both polarization modes, with asymmetric quadrupole field strengths in the LP FODO configuration, as expected. The following considerations are drawn:

- quadrupole field strengths are such to sustain even higher beam energies, and so shorter wavelengths with the same undulators;
- if $E_{\text{beam}} = 1.2\,\text{GeV}$, it is possible to operate at 3 nm wavelength with the same quadrupole and undulator devices, and with larger saturation length and pulse energy contingencies than with $E_{\text{beam}} = 1\,\text{GeV}$.

FEL performance can be enhanced with respect to the baseline design by adding upstream the planar NbTi superconducting undulator prototype under development in collaboration with the Fermi National Accelerator Laboratory [10].

FEL PERFORMANCE

With the electron beam parameters of Table 1 and same FEL scaling laws, the number of photons per pulse N_γ/pulse is evaluated for both polarization modes. Figure 6 shows the number of photons per pulse, evaluated as a function of resonant wavelength and electron beam energy for LP (top) and CP (down). Tunability is achieved in both beam energy and undulator gap:

- undulator gap gives limited lever arm;
- wider tunability in CP than in LP mode;
- by increasing the beam energy, there is the chance to probe water window with $N_\gamma/\text{pulse} \sim 10^{11}$ yields at 4 nm (LP) and 3 nm (CP) wavelengths.

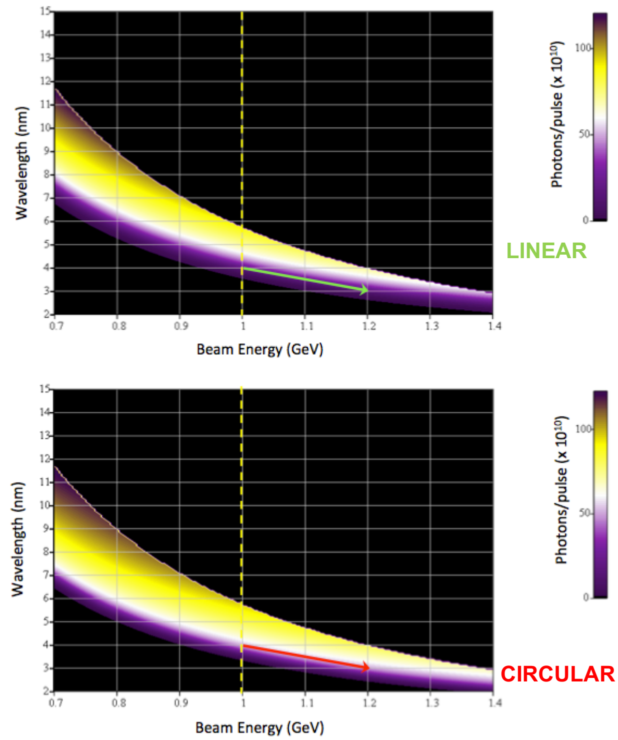

Figure 6: Number of photons per pulse contour plot as a function of resonant wavelength and electron beam energy for linear and circular polarizations.

The average electron beam slice parameters are used to perform 3D time dependent simulations with the `Genesis1.3` code [11] assuming four undulator plus related FODO magnetic lattice configurations: linear and circular polarizations

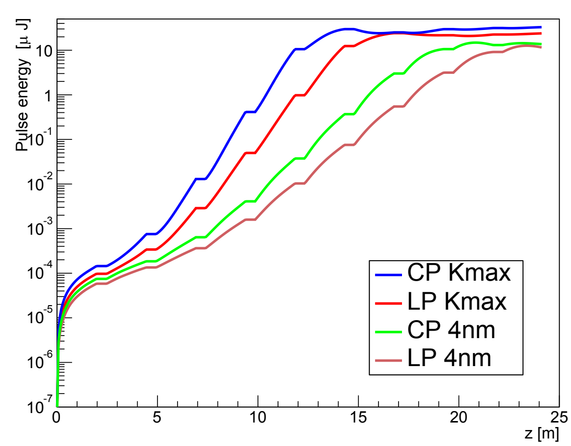

Figure 7: Growth of the FEL pulse energy along the propagation coordinate for the specified working points.

targeting 4 nm and 5.75 nm wavelengths, the latter being associated to the K_{max} deflection strength parameter. The ideal Gaussian current profile is assumed with $I_{\text{peak}} = 1.8\,\text{kA}$ and $Q = 30\,\text{pC}$. Figure 7 shows the growth of the FEL pulse energy along the propagation coordinate, and Table 2 lists the

ISBN: 978-3-95450-220-2 ISSN: 2673-5474 doi: 10.18429/JACoW-FEL2022-MOP46

Table 2: FEL Performance Summary of the 4 nm and 5.75 nm Wavelengths Working Points for both polarizations

Working point	**LP K_{max}**	**LP 4 nm**	**CP K_{max}**	**CP 4 nm**
resonant λ [nm]	5.75	4.01	5.75	4.01
photon energy [eV]	215	309	215	309
matching $\langle\beta\rangle$ [m]	6	8	6	8
Pierce ρ_{1D} $[10^{-3}]$	1.8	1.4	2.0	1.5
gain length$_{1D}$ [m]	0.56	0.79	0.41	0.57
satur. length [m]	16.8	23.4	14.3	20.8
satur. ⟨power⟩ [GW]	0.39	0.24	0.49	0.28
exit E_{pulse} [μJ]	23.9	11.6	33.0	13.7
exit bandwidth [%]	0.15	0.09	0.22	0.12
exit pulse length$_{RMS}$ [fs]	6.10	3.50	6.12	3.76
exit divergence [mrad]	0.032	0.023	0.031	0.022
exit trans. size [μm]	200	130	190	130
exit N_γ/pulse $\left[10^{11}\right]$	6.9	2.3	9.5	2.8

main parameters characterizing the FEL performance of the AQUA beamline for the working points under investigation.

CONCLUSION

The AQUA undulator section and related magnetic lattice targeting 3-4 nm wavelengths are designed, and they are able to sustain $E_{beam} > 1$ GeV energies. This consideration paves the way to operate at the water window range with enhanced contingency in terms of saturation length and pulse energy. Reference beam parameters are used for time dependent simulations for both linear and circular polarizations, at 5.75 nm and 4 nm working points: the goal to produce a photon yield of $N_\gamma/\text{pulse} \simeq \mathcal{O}(10^{11})$ is within reach.

REFERENCES

[1] R. W. Aßmann *et al.*, "EuPRAXIA Conceptual Design Report" *Eur. Phys. J. ST*, vol. 229, no. 24, p. 3675, 2020.doi:10.1140/epjst/e2020-000127-8 [erratum *Eur. Phys. J. ST*, vol. 229, p. 11, 2020. doi:10.1140/epjst/e2021-100018-5]

[2] M. Ferrario *et al.*, "EuPRAXIA@SPARC_LAB Design study towards a compact FEL facility at LNF", *Nucl. Instrum. Methods Phys. Res., Sect. A*, vol. 909, p. 134, 2018. doi:10.1016/j.nima.2018.01.094

[3] P. Chen, J. M. Dawson, R. W. Huff, and T. Katsouleas, "Acceleration of Electrons by the Interaction of a Bunched Electron Beam with a Plasma", *Phys. Rev. Lett.*, vol. 54, p. 693, 1985. 10.1103/PhysRevLett.54.693 [erratum *Phys. Rev. Lett.*, vol. 55, p. 1537, 1985. doi:10.1103/PhysRevLett.55.1537]

[4] A. Balerna *et al.*, "The Potential of EuPRAXIA@SPARC_LAB for Radiation Based Techniques", *Condens. Matter*, vol. 4, p. 30, 2019. doi:10.3390/condmat4010030

[5] E. Roussel *et al.*, "Polarization Characterization of Soft X-Ray Radiation at FERMI FEL-2", *Photonics*, vol. 4, p. 29, 2017. doi:10.3390/photonics4020029

[6] Ming Xie, "Design Optimization for an X-Ray Free Electron Laser Driven by SLAC Linac", in *Proc. PAC'95*, Dallas, TX, USA, May 1995, paper TPG10, pp. 183–185.

[7] P. Li, T. Wei, Y. Li, and J. Pflueger, "Magnetic design of an Apple-X afterburner for the SASE3 undulator of the European XFEL", *Nucl. Instrum. Methods Phys. Res., Sect. A*, vol. 870, p. 103, 2017. doi:10.1016/j.nima.2017.07.023

[8] T. Schmidt and M.Calvi, "APPLE-X Undulator for the SwissFEL Soft X-ray Beamline Athos", *Synchrotron Radiat. News*, vol. 31, p. 35, 2018. doi:10.1080/08940886.2018.1460174

[9] A. Petralia *et al.*, "Short Period Apple-X Undulator Modeling for the AQUA Line of the future EuPRAXIA@SPARC_LAB Facility", presented at the 40th International Free Electron Laser Conference (FEL'22), Trieste, Italy, Aug. 2022, paper WEP38, this conference.

[10] C. Boffo *et al.*, "Design of the Superconducting Undulator for EuPRAXIA@SPARC_LAB"', presented at the 40th International Free Electron Laser Conference (FEL'22), Trieste, Italy, Aug. 2022, paper WEP39, this conference.

[11] S. Reiche, "GENESIS 1.3: a fully 3D time-dependent FEL simulation code", *Nucl. Instrum. Methods Phys. Res., Sect. A*, vol. 429, p. 243, 1999. doi:10.1016/S0168-9002(99)00114-X

ISBN: 978-3-95450-220-2 ISSN: 2673-5474 doi: 10.18429/JACoW-FEL2022-MOP47

SIMULATION STUDIES OF SUPERCONDUCTING AFTERBURNER OPERATION AT SASE2 BEAMLINE OF EUROPEAN XFEL

C. Lechner*, S. Casalbuoni, G. Geloni, B. Marchetti,
S. Serkez, H. Sinn, European XFEL, Schenefeld, Germany
E. Schneidmiller, DESY, Hamburg, Germany

Abstract

European XFEL is a multi-beamline x-ray free-electron laser (FEL) user facility driven by a superconducting accelerator with a nominal photon energy range from 250 eV to 25 keV. An afterburner undulator based on superconducting undulator technology is currently being planned to enable extension of the photon energy range towards harder x-rays. This afterburner undulator would be installed downstream of the already operating SASE2 FEL beamline, emitting at the fundamental or at a harmonic of the upstream SASE2 undulator. In this contribution we present a first simulation study of the impact of undulator mechanical tolerances for operation of the afterburner undulator at the fundamental of SASE2.

INTRODUCTION

European XFEL plans to develop superconducting undulator (SCU) technology as part of its facility development program. Combining the high electron beam energies available at European XFEL [1] with short-period SCUs allows for the generation of harder x-rays. At the exit of the already existing SASE2 hard X-ray permanent magnet undulator (PMU) beamline, the installation of six SCU modules, each housing two 2-meter-long superconducting undulator coils in a cryostat, is planned resulting in a total magnetic length of 24 m. In between the two 2-meter-long SCU coils there are two sets of superconducting Helmholtz coils to correct for the field integrals and a superconducting phase shifter. Between each module there is a room temperature intersection with a permanent magnet phase shifter, quadrupole and diagnostics, as in the PMU line. A detailed description of the European XFEL SCU afterburner project is given in Ref. [2].

In the SASE2 PMU beamline the high-brightness electron bunches arriving from the superconducting linear accelerator of European XFEL drive the self-amplified spontaneous emission (SASE) FEL process [3–6]. During this exponential amplification process, longitudinal density and energy modulations at a period given by the fundamental light wavelength $\lambda_1 = \frac{\lambda_u}{2\gamma_0^2}\left(1 + K^2/2\right)$ are generated. Close to saturation, these microbunches can carry rich harmonic content (at even and odd harmonics), which is the result of non-linear harmonic generation (NHG) [3–5, 7, 8].

After undergoing pre-conditioning by the FEL process in the SASE2 PMU, the bunched electrons enter the SCU beamline. If the SCU is tuned to the same wavelength as the PMU ($\lambda_{1,\mathrm{SCU}} = \lambda_{1,\mathrm{PMU}}$), the power growth continues in the SCU. The SCU can also be tuned to harmonic h of the PMU ($\lambda_{1,\mathrm{SCU}} = \lambda_{1,\mathrm{PMU}}/h$). In the case $h = 2$ that was studied in Ref. [9], the $h = 2$ bunching generated in the PMU drives coherent emission at the fundamental of the SCU. In Ref. [9], simulations of the photon performance of the SCU at photon energies between 30 keV and 60 keV (for operation of the SCU at $h = 1$ or $h = 2$) are described. The estimated number of photons per pulse is larger than $3 \cdot 10^9$ in 30 fs (at 60 keV) and exceeds the number of photons per pulse calculated in Ref. [2] for a 1×1-mm^2 pinhole at 30 m from typical short-period undulators at high energy diffraction limited storage rings by more than two orders of magnitude in pulses more than 5000 times shorter [2].

In this contribution, the impact of undulator tolerances on the photon output (at $h = 1$) is studied.

SIMULATIONS

The numerical simulations are based on the FEL simulation code "GENESIS 1.3", version 2 [10] and on software built around functionality provided by the OCELOT software package [11, 12] to set up, control, and post-process the simulation runs. As the two undulator beamlines in the system under study have different undulator periods (SASE2: 40 mm, SCU: 18 mm), each undulator beamline requires a dedicated run of "GENESIS 1.3". At the beginning of the first run, an ideal flat-top electron bunch distribution is generated with the initial slice parameters as compiled in Table 1. After tracking the electron bunch and light field along the SASE2 PMU, they are stored in files. For operation of the SCU at the identical wavelength as the SASE2 PMU ($h = 1$),

Table 1: Simulation parameters ($h = \lambda_{1,\mathrm{PMU}}/\lambda_{1,\mathrm{SCU}}$).

Parameter	**Value**
electron beam energy	16.5 GeV
initial energy spread	3 MeV
bunch peak current	5 kA
bunch length	1 μm
normalized emittance	0.4 mm mrad
$\langle\beta\rangle$	30 m
SCU operation at harmonic h	$h = 1$ or $h = 2$
undulator period of SCU	18 mm
maximum K parameter of SCU	3.06
total magnetic length of SCU system	24 m

* christoph.lechner@xfel.eu

ISBN: 978-3-95450-220-2 ISSN: 2673-5474 doi: 10.18429/JACoW-FEL2022-MOP47

these files are loaded at the beginning of the second simulation run. For the SCU tuned at the second harmonic ($h = 2$), the procedures described in Ref. [9] are applied instead.

Currently, the simulation model does not take into account several effects: (i) Energy losses due to synchrotron radiation (SR) in the undulators and due to wakefields (SR-induced growth of energy spread is included in the simulations); (ii) the undulators (PMU and SCU) are currently not tapered; and (iii) an ideal flat-top electron bunch with identical slice parameters is currently assumed.

Simulations: Undulator Tolerances

The manufacturing process of the SCU coils introduces deviations from the nominal yoke geometry and in the position of the superconducting winding package [13], resulting in deviations of the magnetic field (and so, in errors of the dimensionless undulator parameter K). To assess the impact of these local variations of the K parameter on the photon performance of the SCU, a software solution based on previous tolerance studies [14,15] was integrated into the existing simulation framework.

Random errors are introduced by changing the K parameter of every half-period of the undulator by a small amount. In the present work, these K errors are normally distributed with rms deviations of $\Delta K/K_0$ of $1.5 \cdot 10^{-3}$ or $3.0 \cdot 10^{-3}$. In any case, the (maximum) absolute relative deviation $|\Delta K/K_0|$ of every pole is limited to $\Delta K_{\max}/K_0 = 6 \cdot 10^{-3}$. A direct consequence of these deviations is that the average position of the electron beam travelling along the undulator is typically no longer on-axis. By adjusting the magnetic fields at the entrance and exit of every coil, its first and second field integrals are set to zero and the beam is leaving the coil again on-axis. Finally, the slippage effect resulting from the electrons travelling under an angle (caused by the field errors) is estimated and corrected for.

Simulations: Phase Shifter Scans

While integrating the functionality required for undulator tolerance studies (as described above) into the software controlling the "GENESIS 1.3" simulation runs, we implemented also the possibility for the user to manipulate all phase shifters in the SCU system and the phase shifter at the interface between the last PMU in SASE2 and the SCU. Carrying out simulations for different settings of a selected phase shifter corresponds to a phase shifter scan. Figure 1 shows such a scan of the phase shifter at the SASE2/SCU interface with 10 scan steps and 5 simulated events per scan step (all simulations were done with a different shot noise seed). Such scans of the phase shifter at the SASE2/SCU interface with the two undulator coils of the following cryostat energized may be interesting for the commissioning of S-PRESSO [2], a pre-series undulator module, as the sinusoidal modulation demonstrates the coupling between the bunched electron beam and the light field in the undulator.

All phase shifters in the simulated undulator beamlines that are not explicitly manipulated by the user are set to the smallest possible value that results in the microbunches and

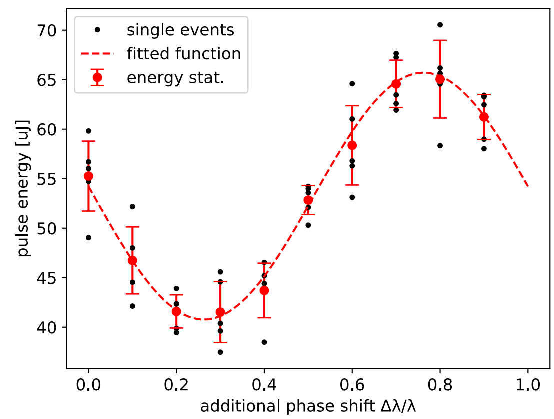

Figure 1: Scan of phase shifter at SASE2/SCU interface. Parameters are: photon energy 30 keV ($h = 1$), 27 active SASE2 undulator modules, $\Delta K/K_0 = 3.0 \cdot 10^{-3}$, 10 scan steps, and 5 shots per step. The indicated photon pulse energies are after one SCU cryomodule with 4 m of superconducting undulator.

the light field to be in phase again when entering the subsequent undulator module (i.e. in the intersection between two undulator modules the light field advances the electron bunch by $n \cdot \lambda_{1,\mathrm{SCU}}$, with n integer). As the phase shifters further delay the electrons with respect to the light field, the smallest possible n is given by the slippage in a drift section (having the length of the intersection). In the lattice file generated while configuring an FEL simulation run, this strategy corresponds to the strength parameter of the `AD` elements (used to fill the intersections between the undulators) being significantly smaller than that of the `AW` elements (the undulators, see Ref. [16]).

The optimum settings are found by scanning the phase shifters one-by-one. The first phase shifter being scanned is the permanent magnet phase shifter at the interface between SASE2 and the SCU (the upstream phase shifters in SASE2 were not scanned). The phase-dependency of the photon pulse energy is recorded at the exit of the first cryostat of the SCU beamline and from fitting a cosine function (illustrated by the dashed line in Fig. 1), the phase shift maximizing the photon pulse energy is found. Also the settings for the other permanent magnet phase shifters in the SCU beamline are determined by observing the photon pulse energy after the subsequent cryostat (containing two 2-meter-long undulator coils). The superconducting phase shifters (installed inside of the cryostats between the two undulator coils) are optimized by observing the photon pulse energy at the exit of their cryostat.

Having determined the phase shifter settings, a set of 20 simulation runs is performed. Every simulation run uses a different shot noise seed. The evolution of the average photon pulse energy and the respective standard deviation are computed and indicated as solid line and colored band, respectively. Figure 2a shows the impact of the phase shifter

ISBN: 978-3-95450-220-2 ISSN: 2673-5474 doi: 10.18429/JACoW-FEL2022-MOP47

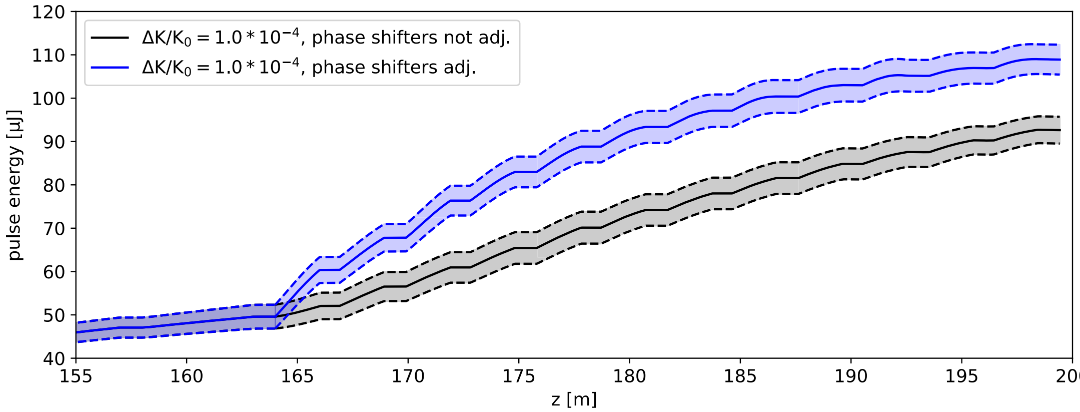

(a) Impact of optimization procedure for $\Delta K/K_0 = 10^{-4}$: Before (black) and after phase shifter scan (blue)

.

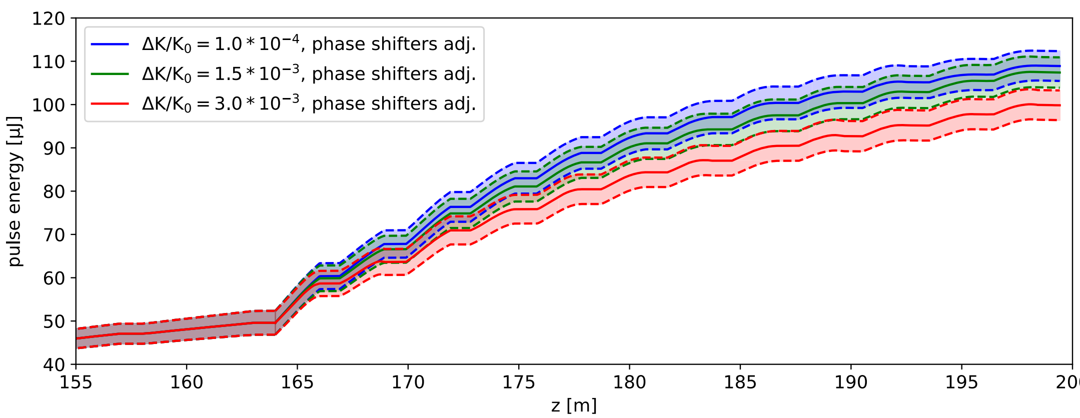

(b) Optimized phase shifter configurations for different values of $\Delta K/K_0$.

Figure 2: Evolution of the photon pulse energy along the SCU beamline for $\Delta K/K_0 = 10^{-4}$ *(a)* and various $\Delta K/K_0$ *(b)*. Energy statistics over 20 simulation runs, solid line indicates mean value, half-width of colored band indicates standard deviation. Simulations for photon energy 30 keV and $N_1 = 27$ active SASE2 undulators. The SCU beamline begins at approx. 164 m.

scan procedure on photon pulse energy for a photon energy of 30 keV, $N_1 = 27$ active SASE2 undulators (as in Ref. [9]), and $\Delta K/K_0 = 10^{-4}$. We note that the case $\Delta K/K_0 = 10^{-4}$ exhibits only very small pulse energy deviations from the simulation result obtained without undulator tolerances. We use $\Delta K/K_0 = 10^{-4}$ as "ideal" case since the current software structure requires a non-zero undulator error for the phase shifter manipulation code to be active.

In Figure 2b the impact of different amplitudes of undulator error on the energy of the 30-keV photon pulse can be seen. All cases were optimized individually using the above procedure. While the pulse energy at the end of the SCU afterburner beamline for $\Delta K/K_0 = 1.5 \cdot 10^{-3}$ is very close to the case $\Delta K/K_0 = 10^{-4}$, for the case $\Delta K/K_0 = 3.0 \cdot 10^{-3}$ it is reduced by about 8 %.

Figure 3 shows the evolution of photon pulse energy for a photon energy of 40 keV and 31 active SASE2 undulators for $\Delta K/K_0$ of $1.0 \cdot 10^{-4}$, $1.5 \cdot 10^{-3}$, and $3.0 \cdot 10^{-3}$, respectively. For 40 keV and $\Delta K/K_0 = 3.0 \cdot 10^{-3}$ the photon pulse energy was reduced by about 10 %. The higher growth rates of the photon pulse energies after entering the SCU illustrate the advantage of short-period superconducting undulators at high photon energies.

Simulations: Planned Steps

The simulations described above were carried out with version 2 of the FEL simulation code "GENESIS 1.3" [10]. It is planned to add the currently not-included effects mentioned above to the simulation model.

The new version 4 of "GENESIS 1.3" [17] is currently under active development and has important new features such as the so-called "one4one" simulation mode. In this mode the actual electrons are tracked (instead of the macroparticles used in version 2), allowing to re-slice the electron bunch distribution in harmonic up-conversion operations, which enables simulation studies of advanced FEL schemes.

Simulations based on this new version are currently under preparation. As part of this process, we contributed code

ISBN: 978-3-95450-220-2 ISSN: 2673-5474 doi: 10.18429/JACoW-FEL2022-MOP47

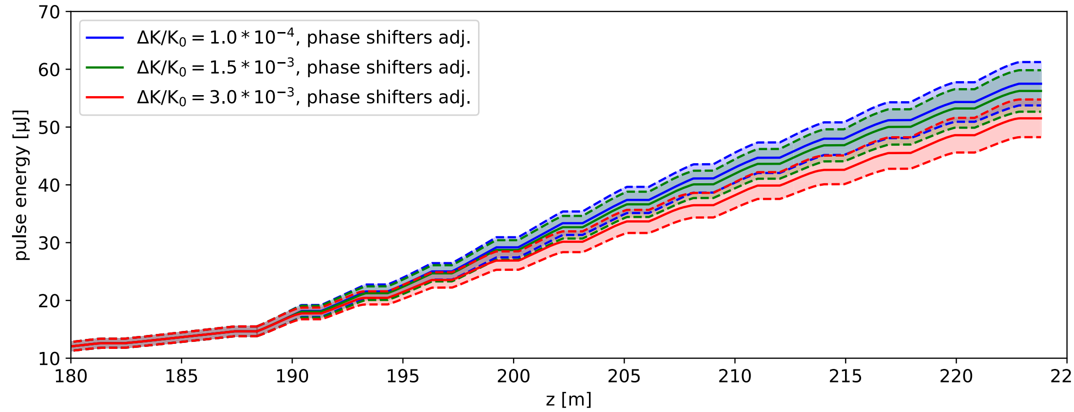

Figure 3: Evolution of the photon pulse energy along the SCU beamline for a photon energy of 40 keV and $N_1 = 31$ active SASE2 undulators. Energy statistics over 20 simulation runs, solid line indicates mean value, half-width of colored band indicates standard deviation. The SCU beamline begins at approx. 189 m.

implementing functionality especially useful for simulations at the very short wavelengths of interest for this project.

CONCLUSION

We extended our simulation framework for the study of SCU afterburner operation at SASE2 beamline of European XFEL with functionality for the study of undulator mechanical tolerances. For the parameters studied in this contribution (compiled in Table 1; photon energies 30 keV and 40 keV; rms $\Delta K/K_0$ up to $3 \cdot 10^{-3}$), we find that the undulator mechanical tolerances do not result in a significant reduction in photon pulse energy. By optimizing the phase shifter settings in the currently untapered undulator, the FEL performance was improved (compare for instance Ref. [18]), in particular the pulse energy growth at the entrance of the SCU.

ACKNOWLEDGEMENTS

The numerical simulations were supported by the Maxwell computational resources operated at Deutsches Elektronen-Synchrotron DESY, Hamburg, Germany.

REFERENCES

[1] W. Decking *et al.*, "A MHz-repetition-rate hard X-ray free-electron laser driven by a superconducting linear accelerator", *Nature Photonics*, vol. 14, pp. 391–397, 2020, `doi:10.1038/s41566-020-0607-z`.

[2] S. Casalbuoni *et al.*, "A pre-series prototype for the superconducting undulator afterburner for the European XFEL", in *Proc. of the 14th Intl. Conf. on Synchrotron Radiation Instrumentation (SRI2021)*, Hamburg, Germany, to appear in *Journal of Physics: Conference Series*, 2022.

[3] Z. Huang and K.-J. Kim, "Review of x-ray free-electron laser theory", *Phys. Rev. ST Accel. Beams*, vol. 10, p. 034801, 2007, `doi:10.1103/PhysRevSTAB.10.034801`.

[4] C. Pellegrini, A. Marinelli and S. Reiche, "The physics of x-ray free-electron lasers", *Rev. Mod. Phys.*, 88, p. 015006, 2016, `doi:10.1103/RevModPhys.88.015006`.

[5] K.-J. Kim, Z. Huang and R. Lindberg, *Synchrotron Radiation and Free-Electron Lasers*, Cambridge, United Kingdom: Cambridge University Press, 2017, `doi:10.1017/9781316677377`.

[6] P. Schmüser, M. Dohlus, J. Rossbach and C. Behrens, *Free-Electron Lasers in the Ultraviolet and X-Ray Regime: Physical Principles, Experimental Results, Technical Realization*. Berlin, Germany: Springer, 2014, `doi:10.1007/978-3-319-04081-3`.

[7] A. Tremaine, *et al.*, "Experimental Characterization of Nonlinear Harmonic Radiation from a Visible Self-Amplified Spontaneous Emission Free-Electron Laser at Saturation", *Phys. Rev. Lett.*, 88, p. 204801, 2002, `doi:10.1103/PhysRevLett.88.204801`.

[8] D. Ratner, *et al.*, "Second and third harmonic measurements at the linac coherent light source", *Phys. Rev. ST Accel. Beams*, vol. 14, p. 060701, 2011, `doi:10.1103/PhysRevSTAB.14.060701`.

[9] C. Lechner, *et al.*, "Simulation studies of superconducting afterburner operation for the European XFEL", in *Proc. 14th Intl. Conf. on Synchrotron Radiation Instrumentation (SRI2021)*, Hamburg, Germany, to appear in: *Journal of Physics: Conference Series*, 2022.

[10] S. Reiche, "GENESIS 1.3: a fully 3D time-dependent FEL simulation code", *Nucl. Instrum. Meth.* A, vol. 429, pp. 243–248, 1999, `doi:/10.1016/S0168-9002(99)00114-X`.

[11] S. I. Tomin, I. V. Agapov, M. Dohlus, and I. Zagorodnov, "OCELOT as a Framework for Beam Dynamics Simulations of X-Ray Sources" in *Proc. 8th Intl. Particle Accelerator Conf. (IPAC'17)*, Copenhagen, Denmark, May 2017, paper WEPAB031, pp. 2642–2645, `doi:/10.18429/JACoW-IPAC2017-WEPAB031`.

[12] OCELOT Source Code `https://github.com/ocelot-collab/ocelot` (last access Apr 9, 2022).

ISBN: 978-3-95450-220-2 ISSN: 2673-5474 doi: 10.18429/JACoW-FEL2022-MOP47

[13] V. Grattoni, S. Casalbuoni, and B. Marchetti, "Tolerance Study on the Geometrical Errors for a Planar Superconducting Undulator", in Proc. 13th Intl. Particle Accelerator Conf. (IPAC'22), Bangkok, Thailand, May 2022, paper THPOPT060, pp. 2734–2736.

[14] S. Serkez, *et al.*, "Super-X: Simulations for Extremely Hard X-Ray Generation With Short Period Superconducting Undulators for the European XFEL", in *Proc. 39th Intl. Free-Electron Laser Conf. (FEL'19)*, Hamburg, Germany, August 2019, paper TUP061, pp. 191–194, `doi:/10.18429/JACoW-FEL2019-TUP061`.

[15] B. Marchetti, S. Casalbuoni, V. Grattoni, and S. Serkez, "Analysis of the error budget for a superconducting undulator SASE line at European XFEL", in *Proc. of the 14th Intl. Conf. on Synchrotron Radiation Instrumentation (SRI2021)*, Hamburg, Germany, to appear in: *Journal of Physics: Conference Series*, 2022.

[16] Manual of "GENESIS 1.3", version 2, online: `http://genesis.web.psi.ch/download/documentation/genesis_manual.pdf`, last access Aug 15, 2022.

[17] Source Code of "GENESIS 1.3", version 4 `https://github.com/svenreiche/Genesis-1.3-Version4` (last access Aug 3, 2022).

[18] D. Ratner, A. Chao, Z. Huang, "Enhancing FEL Power with Phase Shifters", in *Proc. 20th Intl. Free-Electron Laser Conf. (FEL'07)*, Novosibirsk, Russia, paper MOPPH023, pp. 69–72.

ISBN: 978-3-95450-220-2 ISSN: 2673-5474 doi: 10.18429/JACoW-FEL2022-MOP50

PROPOSED FEL SCHEMES AND THEIR PERFORMANCE FOR THE SOFT X-RAY FREE ELECTRON LASER (SXL) AT THE MAX IV LABORATORY

F. Curbis*, W. Qin†, M. Pop, S. Pirani
S. Werin Physics Department, Lund University, Lund, Sweden
J. Andersson, L. Isaksson, B. Kyle‡, F. Lindau, E. Mansten, H. Tarawneh,
P. Fernandes Tavares, S. Thorin, A. Vorozhtsov, MAX IV laboratory, Lund, Sweden
P. Eng-Johnsson, Atomic Physics, Lund University, Lund, Sweden
V. Goryashko, P. Salen, FREIA Laboratory, Uppsala University, Uppsala, Sweden
A. Nilsson, M. Larsson, S. Bonetti, Stockholm University, Stockholm, Sweden
Jonas A. Sellberg, KTH Royal Institute of Technology, Stockholm, Sweden

Abstract

The existing MAX IV 3 GeV linac could drive, with minor improvements, a soft X-ray Free Electron Laser and the aim of the SXL project has been so far to deliver a conceptual design of such a facility in the 1—5 nm wavelength range. The project was initiated by a group of Swedish users of FEL radiation and the design work was supported by the Knut and Alice Wallenberg foundation and by several Swedish universities and organizations (Stockholm, Uppsala, KTH Royal Institute of Technology, Stockholm-Uppsala FEL center, MAX IV laboratory and Lund University). In this paper we will focus on the baseline FEL performance based on two different accelerator operation modes (medium and short pulses) and give some hints of future developments after the first phase of the project, such as two-pulses/two-colours and HB-SASE.

INTRODUCTION

The Science case for a Swedish Soft X-ray FEL was initially defined during and international workshop held in Stockholm in March 2016 with more than 100 participants [1]. The original idea was to take advantage of the existing 3 GeV linac at the MAX IV laboratory, which was from the conceptual phase thought to be a driver for a Free-electron laser, and "quickly" build a beamline in the Short Pulse Facility (SPF) [2] area. With the support of the Wallenberg foundation, some major universities in Sweden contributed, together with the MAX IV laboratory, to a conceptual design report (CDR) that was ready in March 2021 [3]. The CDR focuses on different aspects of the SXL as a FEL user facility (science, experimental stations, beamline, undulators, linac driver, electron gun source, timing and synchronization). These matters were investigated from a conceptual point of view in order to satisfy the needs of the user case and design a competitive and up-to-date machine. While initially limiting the scope we kept in mind possible future upgrades and different modes of operations.

A new workshop has been held in Stockholm in June 2022 to renew the Science Case.

* francesca.curbis@maxiv.lu.se
† now at Deutsches Elektronen-Synchrotron DESY, Hamburg, Germany
‡ now at ISIS Neutron and Muon Source, STFC/RAL, Didcot, UK

OVERVIEW OF THE SXL FEL

SXL (Soft X-ray laser) will cover a wavelength range from 1 to 5 nm with rather short pulse duration (from tens of femtoseconds down to a few femtoseconds, in the first phase) [4]. This source can accommodate the user requirements for a large variety of experiments in four main areas: AMO physics, condensed matter, Chemistry and Life Science [5]. The underlying idea in the conceptual design phase has been to keep the machine flexible for future expansions and enhancing some typical features like the embedded broad spectrum of pump sources. Table 1 summarizes the main parameters of the SXL photon beam.

Table 1: Main SXL Parameters

Wavelength range	1 – 5nm
Photon energy	≈ 0.25 – 1 keV
Pulse duration	1 – 30 fs
Repetition rate	100 Hz
Energy per pulse	0.015 – 1.5 mJ
Peak brightness	10^{-33} Ph./s/mm^2/mrad^2/0.1%BW

The Existing Linac

The SXL will be driven by the 3 GeV S-band linac currently injecting into the MAX IV 1.5 and 3 GeV storage rings and the Short Pulse Facility (SPF). As of today, a photo cathode gun and two bunch compressors can provide 100 fs long pulses for the SPF with a normalised emittance below 1 µm. In the MAX IV linac the bunches are compressed using two double-achromat structures (BC1 and BC2), which provide also passive magnetic linearization. A detailed description of the MAX IV linac and its performance can be found elsewhere [6, 7]. The baseline FEL performance is based on two different accelerator operation modes: a high charge-medium pulse (1A) and a low charge-short pulse (1B). Both pulses display a residual energy chirp which it is not typical in other FELs, but at the same time a very high peak current can be achieved, which help the FEL process. More details about beam dynamics, collective effects and technical solutions that will be adopted can be found in the SXL CDR [3]. The layout of the MAX IV linac with the upgrades envisaged for SXL is shown in Fig. 1.

ISBN: 978-3-95450-220-2 ISSN: 2673-5474 doi: 10.18429/JACoW-FEL2022-MOP50

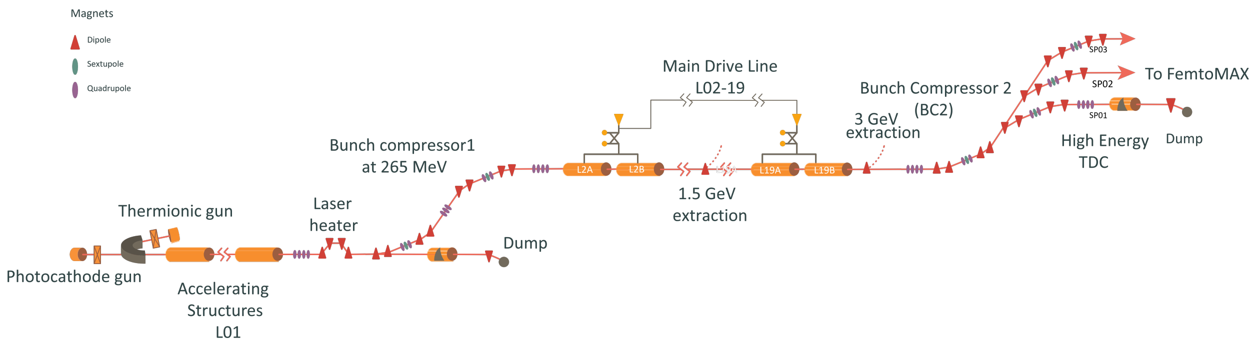

Figure 1: Layout of the MAX IV linac with the foreseen upgrades for SXL.

In particular, in the SP01 line (the lower beamline in the layout) the installation of a high-energy transverse deflecting cavity is currently underway and this device will soon allow a careful characterization of the longitudinal phase space of the electron beam from the linac [8].

Undulators

The proposed undulators for SXL are a compact type of APPLE-X, with a structure composed of four permanent magnet blocks with triangular shape. They are disposed radially at equal distance around the electron beam axis. This symmetric structure allows to achieve, at the same gap, the same energy range at all polarizations. Tuning the polarization can be obtained shifting two magnets sub-girders longitudinally. By moving the magnet arrays radially, i.e., adjusting the magnetic gap, it is possible to change the resonant wavelength. The main parameters of the APPLE-X undulator are shown in Table 2.

Figure 2: View of the compact APPLE-X undulator.

In order to verify the feasibility of the design, a full-size prototype will be built in the framework of LEAPS-INNOV.

Table 2: APPLE X Undulator Parameters

Magnet material	SmCo
Period length	40 mm
Magnetic gap range	8 to 17.3 mm
required effective K range	3.9 to 1.2
Max. gap / min eff. K	28 mm / 0.55
Magnetic length	2 m

BASIC FEL DESIGN AND ITS PERFORMANCE

The layout of the SXL undulator line consists of two sections of 10 undulators each (see Fig. 3). A big 5 m-long chicane is placed in between the two sections and this device will allow to delay the electron beam for two-pulse/two-colour operations or, if required, for "self-seeding". Full polarization control and tunability in the desired wavelength range will be guaranteed by the 2 m-long APPLE-X undulators (see previous section).

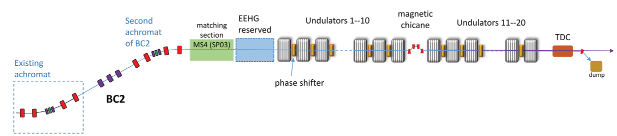

Figure 3: Detail of the FEL undulators line.

A distance of 1 m, is kept in between the undulators (intrasections) in order to to accommodate the required focusing magnets, some diagnostics and other elements needed for the vacuuum system. A FODO lattice is obtained with one quadrupole magnet in each intrasection with alternating focusing and after optimization an average value for the beta functions of 7 m has been chosen for the nominal case. The intra-undulator sections will be also equipped with compact but very strong delay chicanes which will have a threefold usage: as normal phase shifters; as delay lines for HBSASE; as shifting elements to translate the beam to orbits with different offsets.

As it can be seen from Fig. 3, some space is reserved in front of the undulators for accommodating a matching section, a de-chirper and the foreseen EEHG seeding setup.

On the opposite end of the undulator line, a transverse deflecting cavity will be installed to enable a full temporal diagnostics of the electron beam after lasing and to help tuning the performance of the FEL.

Phase 1 - SASE Mode

The phase 1 of SXL will rely on the SASE regime produced by the medium (1A) and the short (1B) electron bunches coming from the linac. In this section we will present the performance at 1 nm of the 1A and 1B pulses respectively in more detail and then refer to a table for the results obtained at 5 nm.

ISBN: 978-3-95450-220-2 ISSN: 2673-5474 doi: 10.18429/JACoW-FEL2022-MOP50

With the 1A bunch, for the shortest wavelength (1 nm), an active length of 26 meters is sufficient to reach saturation, leaving about 14 m (7 modules) of undulator available for post-saturation tapering. In our simulations, a quartic (fourth order) taper profile has been optimized to maximize the output pulse energy, which increases to about 700 µJ at 1 nm and 1500 µJ at 5 nm, while the bandwidth remains about the same. The FEL power and the spectrum at 1 nm can be seen in Fig. 4.

For the short bunch (1B) we do not apply tapering to the undulators. The pulse length of the photon beam is slightly under 1 fs and the spectrum displays a relative small bandwidth (see Fig. 5 FEL power and spectrum at 1 nm).

In Table 3 we report a summary of the performance at 1 and 5 nm for the long pulse (1A) with and without tapering and for the short pulse (1B).

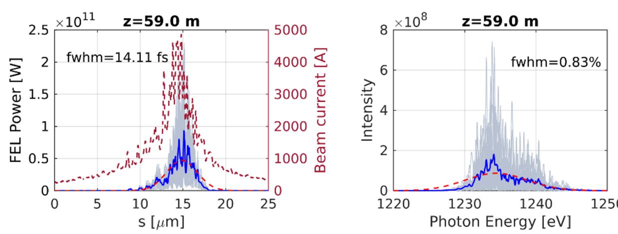

Figure 4: FEL power (left) and spectral intensity (right) obtained with the "long" pulse (1A).

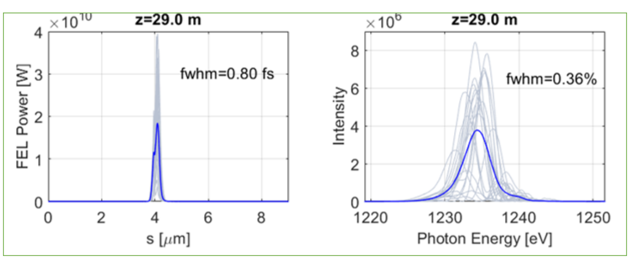

Figure 5: FEL power (left) and spectral intensity (right) obtained with the short pulse (1b).

PHASE 2 - MORE ADVANCED CONCEPTS

As previously mentioned, in the second phase of the project more advanced concepts will be employed in order to improve the features of SXL. In particular, from indications in the science case, three areas have been chosen: ultra-short pulses, coherence enhancement and seeding for improving the stability. We believe that some of the advanced schemes will be facilitated by flattening the long phase space of the electron beam and at the moment we are studying the implementation of conventional de-chirpers combined with overcompression [9]. The de-chirped beam displays a long flat top region in the longitudinal phase space which is compatible with HB-SASE operations [10]. Echo Enabled Harmonic Generation (EEHG) has been studied in a defined wavelength range (3 to 5 nm) and encouraging results have been obtained even with the chirped beam. More details are presented in [11]. FEL jitter studies have been performed with start-to-end simulations [12] with results indicating a very stable performance of the linac in terms of arrival time jitter and compression.

Two-Pulses/Two-Colours

Following the user demands, two colour-two pulses will also be a key feature of the SXL. Different concepts have been studied to target various time and colour separations. The most straightforward is the split-undulator scheme [13] which will allow to produce two pulses with different wavelengths and the strong chicane after the tenth undulator will ensure a variable delay between the two pulses spanning between 100 fs and 1 ps. Various wavelength combinations were studied both with the long (1A) and the short (1B) pulses, and simulations show that almost 1 keV could be reached also in this configuration. In Fig. 6 we report two examples of these results, one obtained with the long pulse (535 eV and 930 eV) and one with the short pulse (310 eV and 248 eV).

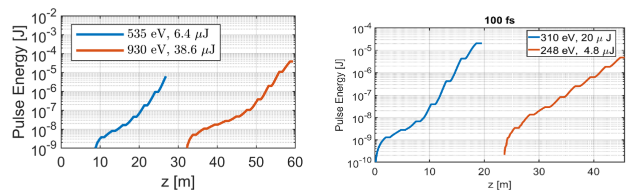

Figure 6: FEL pulse energy for the two colour option with the long bunch (left) and the short bunch (right).

In simulations we observed a variation of the properties of the second colour (pulse energy and bandwidth) depending on the delay applied by the big chicane. This effect has been observed also experimentally at European XFEL [14] (data not shown here).

Longer separation (>1 ps) between the two colours can be obtained accelerating two bunches in different RF buckets [15], with discrete steps of 330 ps. Optical methods (like an optical delay line at the experiment) could be used to make possible the "zero-delay" and the cross-over. Besides, steering the electron beam differently in the two undulator sections will produce photon beams with different pointing and this will help the separation and the manipulation of the two colours at the sample.

HBSASE

In order to get a stable central wavelength and a narrower spectrum, we considered HBSASE as some sort of seeding technique to be applied to the SXL. As it was already mentioned, the residual energy chirp present in the electron pulse at the end of the MAX IV linac cannot be removed by conventional de-chirpers, as it is the opposite. To overcome this problem, we studied the possibily to flip the sign of the chirp by overcompressing the electron pulse and then applying a two-plate wakefield de-chirper. The resulting pulse displays a flat longitudinal phase space with a long enough

ISBN: 978-3-95450-220-2 ISSN: 2673-5474 doi: 10.18429/JACoW-FEL2022-MOP50

Table 3: Overview of the SXL FEL Performance for the Mildly Compressed Bunch (1A) and the Highly Compressed Bunch (1B)

	1A - standard		**1A - tapering**		**1B**	
	1 nm	5 nm	1 nm	5 nm	1 nm	5 nm
Pulse energy (μJ)	130	220	660	1500	15	20
Peak Power (GW)	14	36	50	56	15	12
Photons per pulse	6.6×10^{11}	5.5×10^{12}	3.3×10^{12}	3.8×10^{13}	7.6×10^{10}	5×10^{11}
Pulse duration (fs) [FWHM]	9.3	5.2	14	26	0.8	1.2
Bandwidth (%) [FWHM]	0.5	0.7	0.8	1.2	0.4	0.8
Brightness (Ph./s/mm^2/mrad^2/0.1%BW)	2.5×10^{33}	1×10^{33}	3.5×10^{33}	1×10^{32}	4×10^{33}	1.5×10^{32}

plateau. This electron beam has been used in HBSASE simulations [9] cross-check the overcompressing method and encouraging results show a narrowing of the spectrum and a good central wavelength stability.

CONCLUSIONS

In this paper we presented the main features of the FEL in the SXL project which has been from the beginning a user-driven initiative to capitalizes on the existing infrastructure to open research opportunities that are currently not possible at any other beamline at MAX IV. In particular we focused on the FEL schemes which will be introduced at different stages, starting with SASE and, thanks to the flexibility of the setup, continuing with two-pulses/two-colours and different "seeding" schemes. In general the design of SXL will provides competitive performance that can enable the experiments proposed in the science case. The SXL will produce very short pulses with very good stability. A wide range of pump options will be present from the begining and will used in combination with two-pulses/two-colours schemes with variable delays. The FEL design is flexible and will allow further development for example with seeding schemes (HBSASE, EEHG, self-seeding). If realized in short term SXL be an internationally competitive facility.

ACKNOWLEDGEMENTS

The SXL Design study was partly financed by the Knut and Alice Wallenberg foundation (`https://kaw.wallenberg.org/`). The simulations are supported by the Center for scientific and technical computing at Lund University (LUNARC: `http://www.lunarc.lu.se/`).

REFERENCES

[1] Indico, `https://indico.maxiv.lu.se/event/141/`

[2] H. Enquist *et al.*, “FemtoMAX – an X-ray beamline for structural dynamics at the short-pulse facility of MAX IV,” *J. Synchrotron Radiat.*, vol. 25, pp. 570–579, 2018. `doi:10.1107/S1600577517017660`

[3] SXL Conceptual Design Report, `https://www.maxiv.lu.se/beamlines-accelerators/accelerators/soft-x-ray-laser/`

[4] W. Qin *et al.*, “The FEL in the SXL project at MAX IV,” *J. Synchrotron Radiat.*, vol. 28, pp. 707–717, 2021. `doi:10.1107/S1600577521003465`

[5] The Soft X-Ray Laser@MAX IV, A Science Case for SXL, `https://indico.maxiv.lu.se/event/141/attachments/34/45/SXL_science_case_161102.pdf`

[6] S. Thorin *et al.*, “Bunch Compression by Linearising Achromats for the MAX IV Injector,” in *Proc. FEL'10*, Malmö, Sweden, Aug. 2010, paper WEPB34, pp. 471-474.

[7] S. Thorin *et al.*, “Experience and Initial Measurements of Magnetic Linearisation in the MAX IV Linac Bunch Compressors”, in *Proc. FEL'17*, Santa Fe, NM, USA, Aug. 2017, pp. 273–275.

[8] J. Lundquist, F. Curbis, and S. Werin, “Virtual Diagnostic for Longitudinal Phase Space Imaging for the MAX IV SXL Project,” presented at FEL'22, Trieste, Italy, 2022, paper WEP25, this conference.

[9] S. Pirani, F. Curbi, M. Pop and S. Werin, “Control of the longitudinal phase and benchmarking to HBSASE,” presented at FEL'22, Trieste, Italy, 2022, paper TUP62, this conference.

[10] N.R. Thompson and B.W.J. McNeil, “Mode locking in a free-electron laser amplifier,” *Phys. Rev. Lett.* vol. 100, p. 203901, 2008. `doi:10.1103/PhysRevLett.100.203901`

[11] M.A. Pop *et al.*, “Analysis of the effect of energy chirp in implementing EEHG at SXL,” in *Proc. IPAC'21*, Brazil, 2021. `doi:10.18429/JACoW-IPAC2021-TUPAB082`

[12] S. P. Pirani *et al.*, “Start-to-End study on laser and RF jitter effects for MAX IV SXL”, in *Proc. IPAC'21,* Brazil, 2021. `doi:10.18429/JACoW-IPAC2021-MOPAB266`

[13] A. Lutman *et al.*, “Experimental Demonstration of Femtosecond Two-Color X-Ray Free-Electron Lasers,” *Phys. Rev. Lett.,* vol. 110, p. 134801, 2013. `doi:10.1103/PhysRevLett.110.134801`

[14] G. Geloni and S. Serkez, FELs of Europe workshop in Dresden, April 25-27, 2022.

[15] F.-J. Decker *et al.*, “Two Bunches with ns-separation with LCLS,” in *Proc. FEL'15*, Daejeon, Korea, Aug. 2015. `doi:10.18429/JACoW-FEL2015-WEP023`

ISBN: 978-3-95450-220-2 ISSN: 2673-5474 doi: 10.18429/JACoW-FEL2022-MOP51

SHORT FEL PULSES WITH TUNABLE DURATION FROM TRANSVERSELY TILTED BEAMS AT SwissFEL

P. Dijkstal[1], E. Prat*, S. Reiche, Paul Scherrer Institut, Villigen, Switzerland
[1]also at Department of Physics, ETH Zurich, Switzerland

Abstract

FEL pulses with an easily tunable duration are of great benefit to user experiments with high requirements on the temporal resolution. A transverse beam tilt is well suited to shorten the pulse duration in a controlled manner. We consider three methods of tilt generation: rf deflecting structures, lattice dispersion in combination with an energy chirp, and transverse wakefields from C-band accelerating cavities. We use monochromator scans in combination with an energy-chirped beam to diagnose the reduction in pulse duration.

INTRODUCTION

Exploration of matter and its dynamics on the sub-nanometer space and sub-femtosecond time scales are allowed by the recent progress in X-ray free-electron lasers (XFELs). Some experiments require photon pulses that are shorter than those emitted in the standard operation mode of SASE hard X-ray FEL facilities. For reference, the Aramis undulator beamline at SwissFEL [1] usually delivers pulse durations in the range of 40–60 fs (all pulse durations refer to FWHM: full width at half maximum values). For example, an experiment at LCLS [2] performed double-core-hole spectroscopy on CO molecules, and requested X-ray pulses with durations of about 10 fs [3]. Also at SwissFEL, several times over the past two years users requested pulses with durations between 5 and 20 fs.

Most methods of short pulse generation are based on suppressing the SASE process for selected longitudinal parts (slices) of the bunch. Different slice properties of the electron beam can be spoiled or interrupted: the energy spread [4, 5]; the transverse optics matching [6]; the emittance [7–9]; and the trajectory (beam tilt, this contribution).

A beam tilt is a correlation between the transverse (x, x' or y, y') and temporal (t) coordinates of particles in a bunch. For an efficient FEL process, the electron beam needs to be aligned to the path of the emitted photon beam. Parts of the beam that travel off-axis receive a collective steering effect (i.e., dipole kicks) from the quadrupoles, such that their trajectory oscillates. Therefore, all parts of a linearly tilted beam except one region, usually the core, travel off-axis in an undulator section and do not have a constant transverse overlap with the FEL pulse. The threshold of orbit misplacement, above which the FEL process is suppressed, depends on the photon energy and on electron beam parameters such as the transverse beam size [10–12]. This method of selective FEL pulse suppression is routinely used at LCLS [13–15] and at SwissFEL [16, 17]. In this contribution we perform a systematic comparison of three methods of beam tilt generation.

* eduard.prat@psi.ch

SwissFEL

We report on measurements at the SwissFEL facility [1], schematically shown in Fig. 1. Electron bunches with a nominal charge of 200 pC originate from an rf photocathode with a repetition rate of up to 100 Hz and are accelerated to an energy of up to 6 GeV in several accelerating sections. Two bunch compressors (BC1 and BC2), acting in the horizontal plane, shorten the bunch length. An isochronous energy collimator is located after the last accelerating section (Linac 3). Two rf transverse deflecting structures (TDS) [19], streaking in the vertical plane, can be used in combination with a profile monitor [20] to measure longitudinal electron properties such as bunch length and current profile, as well as horizontal slice properties such as slice emittance, beam tilt and optics mismatch [21]. The Aramis undulator beamline contains 13 planar variable-gap undulator modules with a period of 15 mm, a maximum undulator parameter (K) of 1.8 and a total length of 4 m. The FEL radiation wavelength can be set between 1 and 7 Å. Photon pulse energies and spectra are measured by a gas detector [22] and a single-shot photon spectrometer (PSSS), respectively [23, 24]. In case the acceptance of the PSSS (approx. 0.76%) is insufficient, a monochromator followed by a photodiode is suitable for measuring the average spectral intensity over a larger photon energy range.

Furthermore, the recently developed passive streaker diagnostics allow for an indirect reconstruction of the FEL power profile through measurements of the electron beam longitudinal phase space after the undulator section [18]. At the time the measurements discussed later were performed, this type of diagnostics was not yet available.

BEAM TILT GENERATION

We consider three different ways to impose a mostly linear beam tilt (streaking the beam), as previously suggested [25]:

A) A TDS after Linac 3 directly imposes a linear beam tilt through time-dependent electromagnetic fields.
B) A beam can excite transverse electromagnetic fields (wakefields) that act back on itself. The head does not experience a deflecting force and remains unperturbed on its trajectory. Trailing slices experience progressively growing forces. The C-band accelerating rf cavities in Linac 3 with their periodic surface modulation (see Fig. 3) are suitable for this purpose.

ISBN: 978-3-95450-220-2 ISSN: 2673-5474 doi: 10.18429/JACoW-FEL2022-MOP51

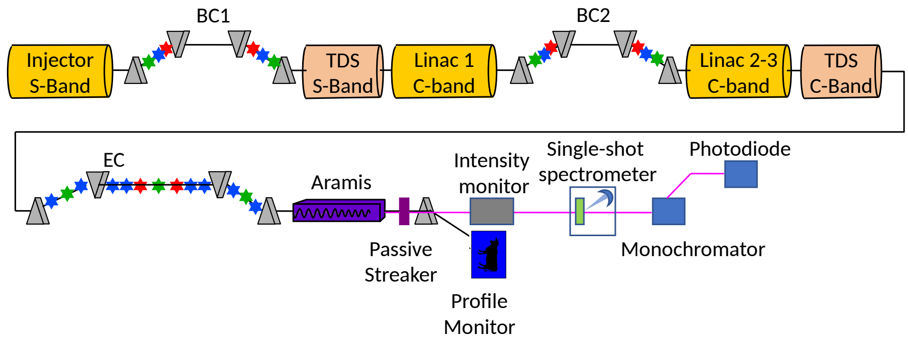

Figure 1: A schematic overview of the SwissFEL accelerator and the Aramis beamline. The red stars indicate sextupoles, blue stars indicate quadrupoles and green stars indicate skew quadrupoles placed in dispersive locations. The passive wakefield streaker diagnostics [18] was not yet available at the time the measurements presented here were performed. However they would be useful for similar studies conducted in the future.

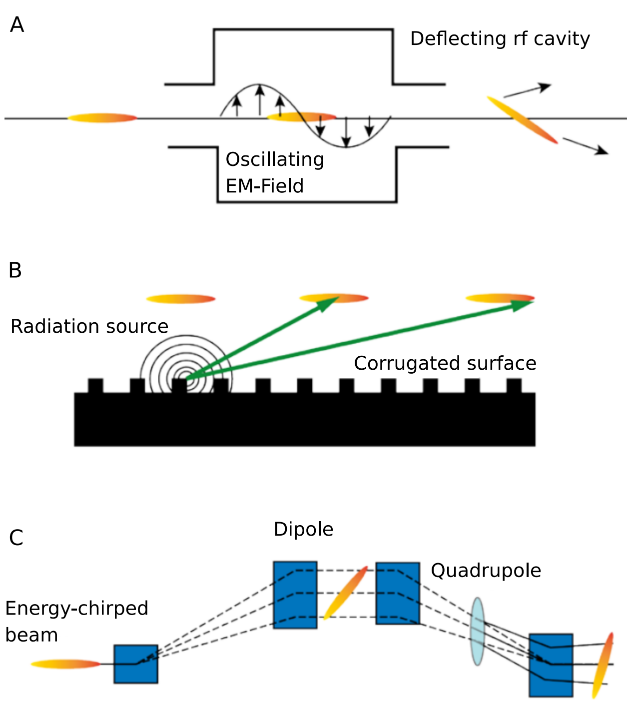

Figure 2: A sketch for three different methods of beam tilt generation: direct streaking with a TDS (A), transverse wakefields (B), and dispersion (C). The orange ellipses depict the same bunch at different positions along the lattice.

C) Transverse dispersion is introduced to an energy chirped electron beam. The dispersion can be generated, for instance, by variation of the quadrupole strength in a dispersive section.

Figure 2 schematically explains the three methods.

EXPERIMENTAL RESULTS

In the following we explain the beam characterization and provide details about the monochromator scans and how to interpret them. Then we show experimental results from the three different beam tilt generation methods.

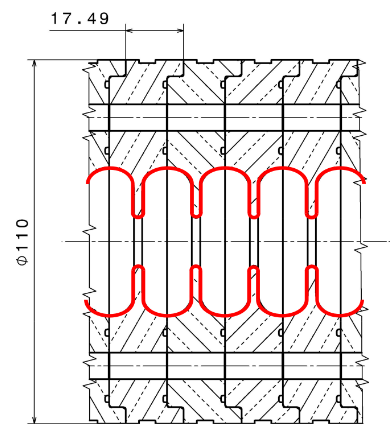

Figure 3: Cross-section of a SwissFEL accelerating C-band cavity. The surface is highlighted in red.

Beam Characterization

We set up the large-bandwidth operation mode [16, 26], meaning that the electron beam exhibited a significant energy chirp. As a consequence of the FEL resonance condition also the FEL pulse was energy-chirped, such that there is a correlation between the longitudinal position of a slice that emits radiation, and the radiation frequency. Therefore, smaller FEL bandwidths translate to shorter pulses. We assume that the chirp is linear, in which case the reduction in pulse duration is proportional to the reduction in bandwidth. It follows for the calibration factor χ between time and photon energy:

$$\chi = \frac{\sigma_t}{2\sigma_\delta E_{\mathrm{ph}}}, \tag{1}$$

with the bunch duration σ_t, the relative enery spread σ_δ and the central photon energy E_{ph}.

We measured the bunch length ($\sigma_t = 31.6$ fs) using the rf deflector after Linac 3, and we measured the relative projected energy spread of the beam ($\sigma_\delta = 0.58\%$) in the EC. The electron beam energy E_0 in the undulator section was 4.88 GeV. The central photon energy E_{ph} was 7.1 keV ($\lambda_R = 1.75$ Å), with an average pulse energy from the un-

ISBN: 978-3-95450-220-2 ISSN: 2673-5474 doi: 10.18429/JACoW-FEL2022-MOP51

tilted beam of approx. 150 μJ. We assume systematic uncertainties in the dispersion function on the order of 10%, and uncertainties of the same order for the bunch duration measurement. This results in an error on the order of 15% in χ, and by extension in all pulse durations mentioned in the following. Using the parameters mentioned earlier in Eq. (1) yields χ = 0.39 fs/eV. A reference monochromator scan for the untilted beam has a FWHM bandwidth of 155 eV. The calibration reveals that an approximately 60 fs long section of the untilted electron beam contributed to the FWHM bandwidth.

Interpretation of Results

In the following we show monochromator measurements of FEL pulses generated by tilted beams. At each monochromator set value the signal from 100 shots was measured. The plots discussed later show the average spectral intensity, with error bars representing the estimated standard errors of the means, i.e., the statistical rms error divided by the square root of the number of measurement points. The resulting spectra are broadened by the central photon energy jitter. Due to the experiments being conducted in large-bandwidth mode, also an orbit trajectory jitter translates to a central photon energy jitter, since different parts of the tilted beam are aligned. Thus, the measured spectral width from a monochromator scan is only an upper limit of the real single-shot spectral width. A further ambiguity appears in the observed reduction of the measured spectral power relative to the reference spectrum from an untilted beam. It can be caused by either a jitter in the central photon energy, or by the detrimental effects of the method of beam tilt generation.

Transverse Deflectors

For the first part of the experiment, we used the TDS before the EC to generate a vertical beam tilt. We performed monochromator scans for rf voltages of 10, 15, and 17 MV. For larger voltages we did not detect a signal at the photo diode. For each voltage we also measured at slightly different rf phases. After setting the aforementioned TDS voltages, the average photon pulse energy was reduced to respectively 20, 10, and 2 μJ (from 150 μJ). The colored lines in the top left plot of Fig. 4 are average photon spectra from monochromator scans. For better visibility, the center right plot shows only the colored lines. The difference between the colors is the TDS phase. Despite the large reduction in average pulse energy, the bandwidth for the 10 MV case is still significantly large. From the reasoning explained earlier, we conclude that the average bandwidth measured after the monochromator is dominated by rf and beam arrival time jitter, and that the pulse durations cannot be determined using multi-shot measurements. Therefore, different methods of photon diagnostics are required for future measurements involving short beams from a beam tilt generated by an rf deflector. Such methods could either be the statistical analysis of single-shot spectrum measurements [27, 28], or the recently developed passive wakefield streaker diagnostics [18].

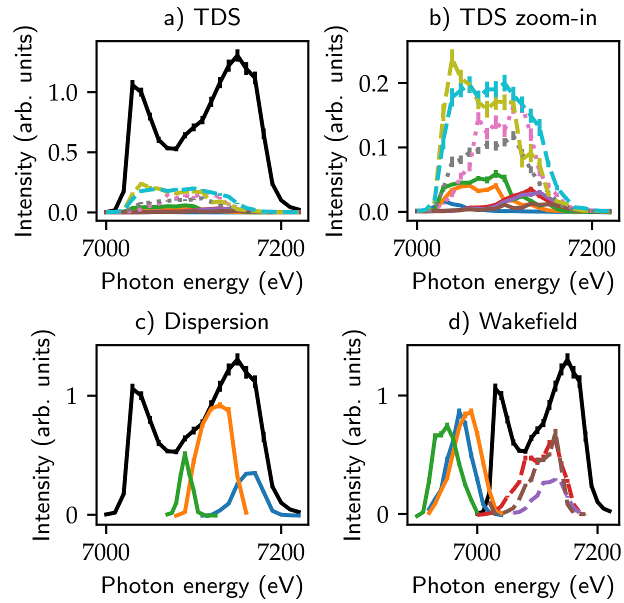

Figure 4: Monochromator scans of FEL pulses emitted by tilted beams. The reference measurement from the untilted beam is shown in black. (a,b): tilt generated with a TDS. The right plot is a repetition of the left plot but without the reference photon spectrum. The dashed curves (cyan and yellow) correspond to a voltage of 10 MV, the dotted curves (pink and gray) to a voltage of 15 MV and the remaining, solid curves to a voltage of 17 MV. The different measurements for the same TDS voltages were taken with different set values of the TDS phase. (c): tilt generated with dispersion. The color code corresponds to the current change in a quadrupole in the EC: −1 A, blue; +1 A, orange; +2 A, green. (d): tilt generated with wakefields of the rf cavities in Linac 3 in horizontal (solid) and vertical (dashed) direction.

Lattice Dispersion

We also tried the dispersion method of beam tilt generation. Due to time limitations, we chose the simplest possible setup: we varied only one quadrupole (the third one between the two central dipoles of the EC) without correcting for the change in transverse optics. We changed the quadrupole current by −1 A, +1 A and +2 A relative to the original set value of 20 A. Beam losses prevented larger current changes. The bottom left plot in Fig. 4 shows the recorded monochromator scans. The bandwidth was reduced to about 40 eV (−1 A and +1 A), and to about 13 eV (+2 A). In two of the three cases, the peak spectral FEL intensity is well preserved compared to the reference case (black), which points to a stable central energy and a small impact of the deteriorating effects of this method of beam tilt generation. According to the earlier performed calibration from spectral bandwidth to pulse duration, bandwidths of 40 eV and 13 eV correspond to FWHM pulse durations of 16 fs and 5.2 fs. This is a reduction by up to a factor of 11 compared to the standard case (60 fs).

ISBN: 978-3-95450-220-2 ISSN: 2673-5474 doi: 10.18429/JACoW-FEL2022-MOP51

Transverse Wakefields

Finally, we used the transverse wakefields of the accelerating C-band rf structures in Linac 3. We used first a horizontal, then a vertical corrector magnet to bring the beam trajectory close to the rf cavity surfaces. The corrector currents were varied until the introduced beam loss became too large. The bottom right plot of Fig. 4 shows the resulting monochromator spectra. The spectral intensity of the shorter FEL pulses is relatively high in most cases, pointing to a small central energy jitter and tolerable detrimental effects. The bandwidths were generally in the range between 35 and 50 eV, indicating FWHM pulse durations between 14 and 20 fs. A peculiarity is that for the horizontal beam tilt (solid lines), the measured photon energies are outside the range of the reference photon spectrum. The energy feedback system was the likely culprit. It uses a dispersive beam position monitor in the EC as its input signal, such that a horizontal trajectory change can be misinterpreted as a beam energy drop. The feedback would then increase the effective voltage of the rf cavities in Linac 3.

CONCLUSION

We investigated the generation of short FEL pulses using tilted electron beams, and were able to shorten the FEL pulse duration with high flexibility in a simple way. From the three methods of beam tilt generation, the lattice dispersion method was most successful, since the range in tunability was the largest. The transverse wakefields from the accelerating C-band cavities also worked reasonably well, although the tunability is reduced compared to the dispersion method. We expect better results from dedicated wakefield sources such as dielectric or corrugated structures. These devices were not yet available at the time of the measurement. The TDS method is strongly affected by rf phase or beam arrival time jitter and would need different methods of photon diagnostics to evaluate. We performed such measurements, and plan to analyze the data in the near future. The generation of FEL pulses with tunable duration down to few fs through beam tilts is now a standard feature available to our users.

The raw data for all results shown in this document will be available from 2023 onward [29].

ACKNOWLEDGMENTS

We thank all technical and operation teams at SwissFEL. The work of P. Dijkstal in the context of this project was supported by the Swiss National Science Foundation under grant 200021_175498.

REFERENCES

[1] E. Prat *et al.*, "A compact and cost-effective hard x-ray free-electron laser driven by a high-brightness and low-energy electron beam," *Nature Photonics*, vol. 14, no. 12, pp. 748–754, 2020. doi:10.1038/s41566-020-00712-8

[2] P. Emma *et al.*, "First lasing and operation of an ångstrom-wavelength free-electron laser," *Nat. Photonics*, vol. 4, no. 9, pp. 641–647, 2010. doi:10.1038/nphoton.2010.176

[3] N. Berrah *et al.*, "Double-core-hole spectroscopy for chemical analysis with an intense x-ray femtosecond laser," *PNAS*, vol. 108, no. 41, pp. 16 912–16 915, 2011. doi:10.1073/pnas.1111380108

[4] A. Marinelli *et al.*, "Optical shaping of x-ray free-electron lasers," *Phys. Rev. Lett.*, vol. 116, no. 25, p. 254 801, 2016. doi:10.1103/physrevlett.116.254801

[5] D. Cesar *et al.*, "Electron beam shaping via laser heater temporal shaping," *Phys. Rev. Accel. Beams*, vol. 24, p. 110 703, 11 2021. doi:10.1103/PhysRevAccelBeams.24.110703

[6] Y.-C. Chao, W. Qin, Y. Ding, A. A. Lutman, and T. J. Maxwell, "Control of the lasing slice by transverse mismatch in an x-ray free-electron laser," *Phys. Rev. Lett.*, vol. 121, p. 064 802, 6 2018. doi:10.1103/PhysRevLett.121.064802

[7] P. Emma *et al.*, "Femtosecond and subfemtosecond x-ray pulses from a self-amplified spontaneous-emission–based free-electron laser," *Phys. Rev. Lett.*, vol. 92, p. 074 801, 7 2004. doi:10.1103/PhysRevLett.92.074801

[8] Y. Ding *et al.*, "Generating femtosecond x-ray pulses using an emittance-spoiling foil in free-electron lasers," *Appl. Phys. Lett.*, vol. 107, no. 19, p. 191 104, 2015. doi:10.1063/1.4935429

[9] A. Marinelli *et al.*, "Experimental demonstration of a single-spike hard-x-ray free-electron laser starting from noise," *Appl. Phys. Lett.*, vol. 111, no. 15, p. 151 101, 2017. doi:10.1063/1.4990716

[10] P. Emma, R. Carr, and H.-D. Nuhn, "Beam-based alignment for the lcls fel undulator," *Nucl. Instrum. Methods Phys. Res., Sect. A*, vol. 429, no. 1, pp. 407–413, 1999. doi:10.1016/S0168-9002(99)00117-5

[11] T. Tanaka, H. Kitamura, and T. Shintake, "Consideration on the BPM alignment tolerance in x-ray FELs," *Nucl. Instrum. Methods Phys. Res., Sect. A*, vol. 528, no. 1-2, pp. 172–178, 2004. doi:10.1016/j.nima.2004.04.040

[12] J. P. MacArthur, A. A. Lutman, J. Krzywinski, and Z. Huang, "Microbunch rotation and coherent undulator radiation from a kicked electron beam," *Phys. Rev. X*, vol. 8, no. 4, p. 041 036, 2018. doi:10.1103/physrevx.8.041036

[13] A. A. Lutman *et al.*, "Fresh-slice multicolour x-ray free-electron lasers," *Nat. Photonics*, vol. 10, no. 11, pp. 745–750, 2016. doi:10.1038/nphoton.2016.201

[14] A. A. Lutman *et al.*, "High-power femtosecond soft x rays from fresh-slice multistage free-electron lasers," *Phys. Rev. Lett.*, vol. 120, no. 26, p. 264 801, 2018. doi:10.1103/physrevlett.120.264801

[15] M. W. Guetg, A. A. Lutman, Y. Ding, T. J. Maxwell, and Z. Huang, "Dispersion-based fresh-slice scheme for free-electron lasers," *Phys. Rev. Lett.*, vol. 120, p. 264 802, 26 2018. doi:10.1103/PhysRevLett.120.264802

[16] E. Prat, P. Dijkstal, E. Ferrari, and S. Reiche, "Demonstration of large bandwidth hard x-ray free-electron laser pulses at SwissFEL," *Phys. Rev. Lett.*, vol. 124, no. 7, p. 074 801, 2020. doi:10.1103/physrevlett.124.074801

[17] E. Prat *et al.*, "Widely tunable two-color x-ray free-electron laser pulses," *Phys. Rev. Res.*, vol. 4, p. L022025, 2 2022. doi:10.1103/PhysRevResearch.4.L022025

ISBN: 978-3-95450-220-2 ISSN: 2673-5474 doi: 10.18429/JACoW-FEL2022-MOP51

[18] P. Dijkstal *et al.*, "Self-synchronized and cost-effective time-resolved measurements at x-ray free-electron lasers with femtosecond resolution," *Phys. Rev. Res.*, vol. 4, p. 013 017, 1 2022. doi:10.1103/PhysRevResearch.4.013017

[19] P. Craievich, R. Ischebeck, F. Loehl, G. L. Orlandi, and E. Prat, "Transverse Deflecting Structures for Bunch Length and Slice Emittance Measurements on SwissFEL," in *Proc. FEL'13*, New York, NY, USA, Aug. 2013, pp. 236–241. https://jacow.org/FEL2013/papers/TUPSO14.pdf

[20] R. Ischebeck, E. Prat, V. Thominet, and C. Ozkan Loch, "Transverse profile imager for ultrabright electron beams," *Phys. Rev. ST Accel Beams*, vol. 18, no. 8, p. 082 802, 2015. doi:10.1103/physrevstab.18.082802

[21] E. Prat *et al.*, "Generation and characterization of intense ultralow-emittance electron beams for compact x-ray free-electron lasers," *Phys. Rev. Lett.*, vol. 123, p. 234 801, 23 2019. doi:10.1103/PhysRevLett.123.234801

[22] K. Tiedtke *et al.*, "Gas detectors for x-ray lasers," *J. Appl. Phys.*, vol. 103, no. 9, p. 094 511, 2008. doi:10.1063/1.2913328

[23] P. Juranić *et al.*, "Swissfel aramis beamline photon diagnostics," *J. Synchrotron Radiat.*, vol. 25, no. 4, pp. 1238–1248, 2018. doi:10.1107/s1600577518005775

[24] C. David *et al.*, "Spectral monitoring at SwissFEL using a high-resolution on-line hard X-ray single-shot spectrometer," *J. Synchrotron Radiat.*, vol. 28, no. 6, 2021. doi:10.1107/S1600577521009619, *Cc by 4.0*. https://creativecommons.org/licenses/by/4.0/

[25] E. Prat, S. Bettoni, and S. Reiche, "Enhanced x-ray free-electron-laser performance from tilted electron beams," *Nucl. Instrum. Methods Phys. Res., Sect. A*, vol. 865, pp. 1–8, 2017. doi:10.1016/j.nima.2016.06.135

[26] Á. Saá Hernández, E. Prat, S. Bettoni, B. Beutner, and S. Reiche, "Generation of large-bandwidth x-ray free-electron-laser pulses," *Phys. Rev. Accel. Beams*, vol. 19, no. 9, p. 090 702, 2016. doi:10.1103/physrevaccelbeams.19.090702

[27] Y. Inubushi *et al.*, "Determination of the pulse duration of an x-ray free electron laser using highly resolved single-shot spectra," *Phys. Rev. Lett.*, vol. 109, no. 14, p. 144 801, 2012. doi:10.1103/physrevlett.109.144801

[28] A. A. Lutman *et al.*, "Femtosecond x-ray free electron laser pulse duration measurement from spectral correlation function," *Phys. Rev. ST Accel Beams*, vol. 15, p. 030 705, 3 2012. doi:10.1103/PhysRevSTAB.15.030705

[29] P. Dijkstal, "Temporal fel pulse shaping and diagnostics at swissfel with tilted electron beams," 2022, Embargoed access until 01.01.2023. doi:10.5281/zenodo.6809306

ISBN: 978-3-95450-220-2 ISSN: 2673-5474 doi: 10.18429/JACoW-FEL2022-MOP53

TWO-COLOR FEL BY LASER EMITTANCE SPOILER

C. Vicario†, C. Arrell, S. Bettoni, A. Dax, P. Dijkstal, M. Huppert, E. Prat, S. Reiche, A. Trisorio
Paul Scherrer Institut, Villigen, Switzerland
A. Lutman, SLAC National Accelerator Laboratory, Menlo Park, CA

Abstract

A novel and noninvasive method for two-color X-ray generation is demonstrated at SwissFEL. In the setup, a short laser pulse is overlapped with the primary photocathode laser to locally spoil the beam emittance and to inhibit the FEL emission. This, together with a chirped electron pulse, results in X-ray emission at two colors delayed in time. High-energy, high-stability, independent control of the duration and of the intensity of the two colors are demonstrated. The laser emittance spoiler enables shot-to-shot selection between one and two-color FEL emission and further, it is compatible with high repetition-rate FELs, as it does not contribute to beam losses.

INTRODUCTION

X-ray free electron lasers (FELs) are largely used for time-resolved studies of photoinduced processes at ultrafast timescale with wide applications in biology, femtochemistry, physics and material science [1-5].

These experiments are usually carried out by combining a conventional laser pump pulse with an X-ray FEL probe. For such studies, the reduction of the temporal jitter between the pump and the probe pulses down to fs- level is a persistent challenge [6]. X-ray pump, X-ray probe experiments employing a two-color FEL are expected to drastically reduce the temporal jitter while the two-wavelengths can be tuned to selectively excite and to probe two different resonances [7, 8].

A two-color FEL output can be achieved by the uneven tuning of the undulator resonance or by the manipulation of the electron bunch properties, see references in [9]. Both approaches are implemented with a dedicated setting of the accelerator or the undulator which is often not optimized for FEL output and required a long preparation time.

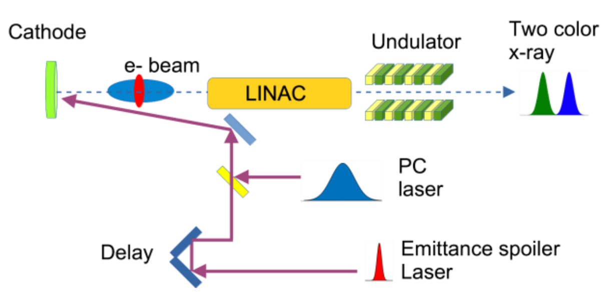

Figure 1: Layout of the two-color FEL scheme based on the laser emittance spoiler.

† email address carlo.vicario@psi.ch

EXPERIMENTAL SETUP

This proceeding reports on a new method for the generation of a two-color FEL by electron beam emittance spoiling realized with a second photocathode laser [9]. Different from other techniques, the present method is able to produce two-color X-rays using the optimal FEL settings as it does not require a dedicated accelerator and undulator retuning. In this way it is possible to reduce the preparation time and save beam-time for the user experiment. The two-color by laser emittance spoiler enables shot-to-shot switching between two and single color. It is directly applicable to high-average power x-ray FELs because it is not introducing beam losses such as in the case of the two-color obtained with double-slot foil. The laser emittance spoiler concept is sketched in Fig. 1. A ps-laser pulse (emittance spoiler) is overlapped on the longer photocathode (PC) laser. The excess of charge spoils locally the slice emittance, preventing the FEL amplification. The part of the bunch not interacting with the laser spoiler still produces FEL emission at two wavelengths due to the linear energy chirp accumulated along the linear accelerator.

We experimentally demonstrated the two-color FEL by laser emittance spoiler at the hard X-ray branch of SwissFEL (Aramis) [1]. At the photoinjector, 300 MeV, 200 pC electron bunches at 100 Hz are generated from a Cs_2Te photocathode in a RF gun. The linear accelerator boosts the beam energy up to 3.15 GeV for the soft x-ray FEL (Athos) and to 5.8 GeV for the Aramis FEL. Two bunch compressors at 0.3 and 2.1 GeV reduce the bunch length to a few tens of fs. The Aramis undulator consists of 13 planar variable-gap modules of 4 m length each and magnetic period of 15 mm. This line produces radiation over the photon energy range 2-12 keV. The FEL pulse energies and spectra are measured by a gas detector and a single-shot spectrometer, respectively.

Table 1: Parameters of the PhotoCathode (PC) and the emittance spoiler laser.

Parameters	**Nominal PC laser**	**Emittance-spoiler laser**
Wavelength (nm)	260	260
Pulse duration (ps)	6.6	0.95
Diameter (mm)	1	2
Generated bunch charge (pC)	200	11-34

ISBN: 978-3-95450-220-2 ISSN: 2673-5474 doi: 10.18429/JACoW-FEL2022-MOP53

In Table I, the main parameters of the PC and emittance spoiler lasers at the photocathode are reported. Both the lasers consist of a low-noise Yb-based oscillator and a diode-pumped Yb:CaF_2 regenerative amplifier running at 100 Hz [10]. The laser is frequency quadrupled in the deep-UV at a photon energy above the Cs_2Te work function. The timing jitter between the two lasers was measured to be below 20 fs rms [11]. The deep-UV laser pulses of the two systems are stretched in time with transmissive diffraction gratings. This system is bypassed for the spoiler laser to keep pulse duration below 1 ps. The emittance spoiler laser pulse can be derived from the same PC laser in front of the stretcher. However, for the present experiment, we used a second laser which gives more flexibility to explore the optimal parameters for the two-color FEL mode. In this configuration, the laser spoiler can be triggered on shot-to-shot basis, and it can be easily delayed and controlled in energy.

At SwissFEL, an emittance of 430 nm is required for the full bunch to radiate at the shortest wavelength (1 Å) [1]. With the ps-laser, the emittance can be spoiled at the center of the bunch well beyond this limit preventing the FEL emission. In this way, only the front and the end of the bunch having low emittance will therefore contribute to the FEL and will produce a two-color spectrum.

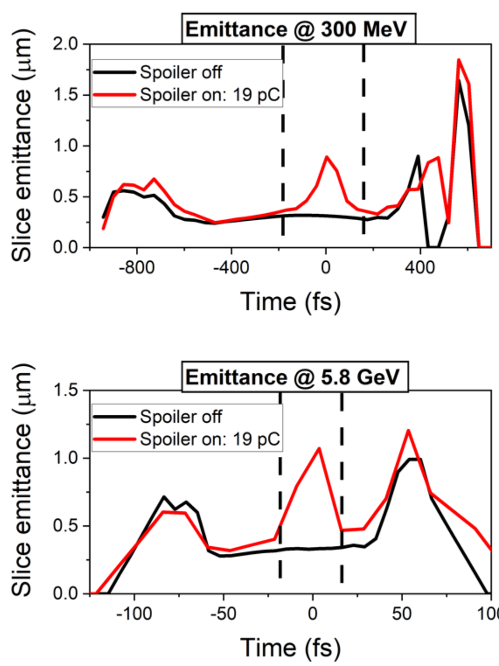

Figure 2: Slice emittance at the injector (top) and at the undulator entrance (down) when the laser emittance spoiler is off (black curves) and on (red curves).

EXPERIMENTAL RESULTS

We measured the electron beam slice emittance at the injector and upstream the undulator for laser emittance spoiler on and off. The results are reported in Fig. 2. The PC laser intensity is adjusted for the generation of the nominal 200 pC bunch. The dashed lines indicate the overlap window between the PC and the emittance spoiler lasers. If the emittance spoiler laser is off (black curve), the slice emittance at low energy (upper plot) stays constant in the central part of the bunch with a value of about 0.32 µm, well below the emittance limit for the FEL emission mentioned before. When the spoiler generates a charge of 19 pC (red curve) the emittance increases sufficiently to prevent completely the lasing. The emittance peak is preserved to the undulator entrance as reported in the lower plot of Fig. 2. The temporal structure of the two-color FEL can be estimated by the slice emittance of Fig. 2 lower plot. The FEL emission occurs at the minima of the emittance in two few tens of femtosecond long pulses separated by about 40 fs.

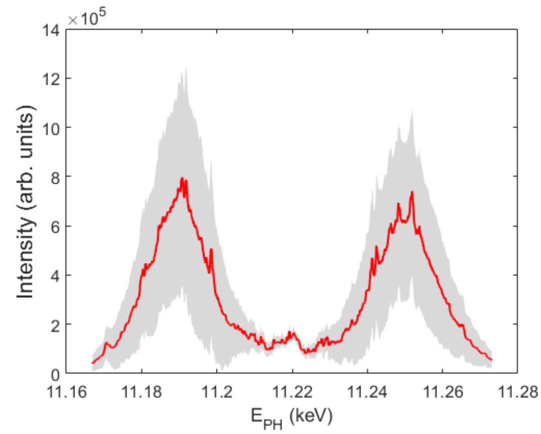

Figure 3: Two-colour FEL spectra at 11.2 keV. The grey area and the red curve show 6000 consecutive FEL spectra and their average.

The two-color FEL by laser emittance spoiler provides well separated two color and excellent spectral shape stability. Figure 3 displays 6000 consecutive SwissFEL spectra recorded at a photon energy of 11.2 keV with relative photon energy separation of 0.5%. The grey area and the red curve display the FEL spectra and their average. The result clearly shows that two-color FEL spectrum with well-separated photon peaks can be reached for all the shots. The photon energy offset between the two colors and the peak wavelength remain stable. The present two-color scheme works well over the entire wavelength range accessible by the FEL. At SwissFEL, by enlarging the energy spread of the beam a maximum relative wavelength separation up to 2% can be expected.

By changing the relative delay T between the emittance spoiler and the PC laser, it is possible to control the relative intensity, the spectral width and the duration of the two individual colors. Figure 4 shows the averaged FEL spectra around 12 keV obtained by changing T. The delay between the two laser is reported on the side of each curve. When the emittance spoiler pulse overlaps with the centroid of the PC laser pulse, at $T = 0$, the two X-ray colors have the same intensity as expected for uniform FEL lasing along the bunch. We calculated the FWHM the durations of the longer and shorter wavelength color as a function of the spoiler delay T. These values are retrieved by fitting the second order spectral correlation function with the model

ISBN: 978-3-95450-220-2 ISSN: 2673-5474 doi: 10.18429/JACoW-FEL2022-MOP53

derived in [12]. The duration of the two colors at $T = 0$ ps, are calculated to be 7 and 11.3 fs for the high and low energy photon. These values are consistent with the emittance temporal profile at high energy obtained in the same experimental conditions reported in Fig. 2. For $T = \pm\, 0.66$ ps the two-color spectrum can be drastically unbalanced towards the high or low energy color and the pulse duration change accordingly [9]. These uneven spectra may be useful to generate the pump and the probe X-ray pulses in time-resolved experiments. With delays of the spoiler pulse larger ±1 ps the single spectral line FEL is recovered. Adjusting the spoiler delay, the duration of the two FEL colors is significantly unbalanced and can be reduced to a minimum value of 6 and 9 fs FWHM for the long and short wavelength pulses [9].

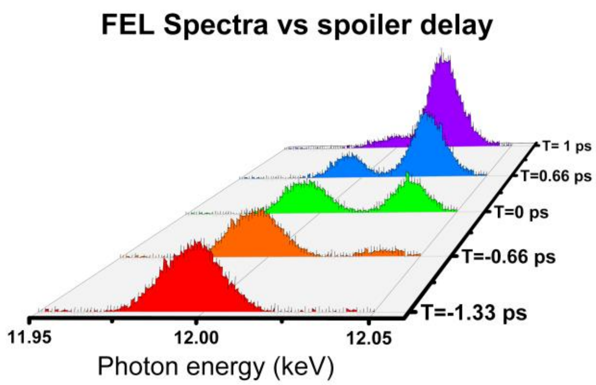

Figure 4: In the figure the two-color X-ray spectra are shown as function of the laser emittance spoiler delay reported on the side. By changing the delay between of the laser emittance spoiler it is possible to unbalance the intensity of the two X-ray colors.

We also characterized the temporal properties of the two-color X-ray pulse. The power profile of the FEL pulse versus time is obtained with the recently developed passive wakefield streaker diagnostics [13]. The indirect measurement of the FEL power evolution is based on the alteration in the final longitudinal phase space (LPS) of the electron beam when the undulators are tuned to their nominal strengths (lasing-enabled), or are randomly detuned (lasing-disabled) [14]. In fact, as a consequence of the FEL, the slice energy spread after the undulators is increased when the FEL is enabled.

In the passive wakefield streaker the LPS is obtained from the transverse electron distribution on a beam monitor located in a dispersive section after the passive streaker. The time coordinates are retrieved by inverting the nonlinear wakefield streaking in horizontal direction through an iterative process. The energy coordinates can be accessed easily due to the linear lattice dispersion in the vertical plane.

Figure 5 reports the LPS and the power profiles of the FEL obtained with the passive wakefield streaker. For these measurements the FEL is operated at 6.6 keV. The top row shows the LPS when the FEL is disabled for laser emittance spoiler off (left) and on (right). The middle row, instead, displays the longitudinal phase space when the FEL is enabled for laser emittance spoiler off (left) and on (right). The corresponding FEL pulse energies are reported in the pictures. At the bottom row the retrieved temporal evolution of the FEL pulse is shown for one (left) and two-color emission (right). Two well-separated FEL wavelength are obtained already with a charge of 6 pC generated by laser emittance spoiler. When the intensity of the laser emittance spoiler is increased, the FEL emission from larger part of the beam is prevented and the temporal separation of the two colors increases. It is worth noting that no special tuning of the machine is required for the two-color mode. This makes the present method very efficient: at 6 pC spoiler, in the two wavelengths a total pulse energy of 604 µJ, corresponding to about 67% of the energy measured for standard SASE single X-ray color (900 µJ). The energy fluctuations for single and two-color FEL are comparable confirming the robustness of the laser emittance spoiler scheme.

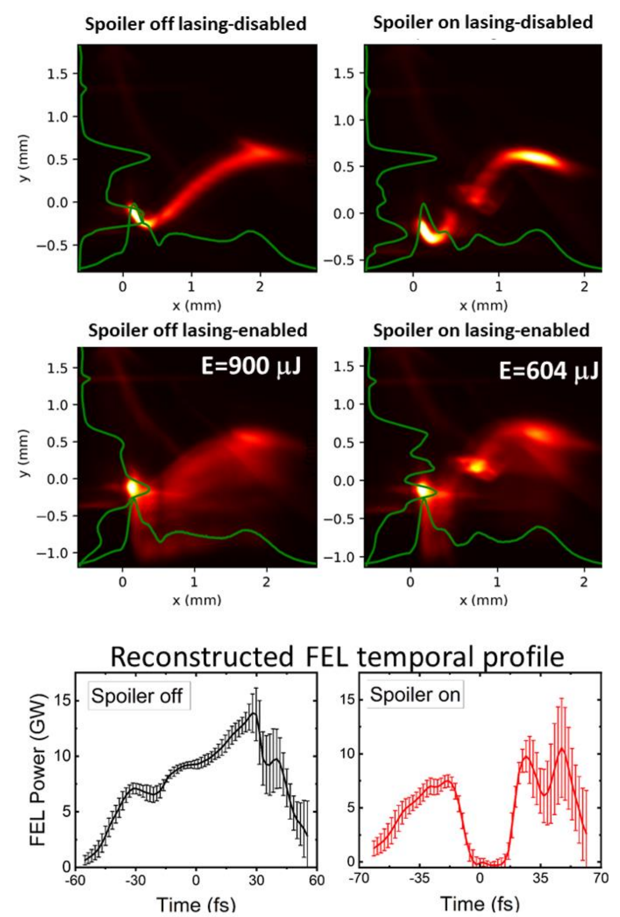

Figure 5: Reconstructed FEL pulse temporal profiles for spoiler off (left) and on (right) using the passive wakefield streaker diagnostics [13] after the hard X-ray Aramis undulator. The top and the middle plot shows the longitudinal phase space when the FEL is disabled and enabled respectively. The one and two color FEL temporal profile is shown at the bottom graphs.

ISBN: 978-3-95450-220-2 ISSN: 2673-5474 doi: 10.18429/JACoW-FEL2022-MOP53

We finally performed a direct measurement of the photon temporal distribution of the two-color FEL with the photon arrival and length monitor (PALM) [15]. This diagnostic relies on THz streaking to measure both the arrival time and the pulse distribution of the incoming X-ray FEL pulses. The THz streaking field is generated from the experimental pump laser. Figure 6 show the streaking trace for single color (top figure) and two-color (low figure) FEL. The measurements are done alternating one and two colors on shot-to-shot base by triggering the laser emittance spoiler at half of the FEL repetition rate (50 Hz).

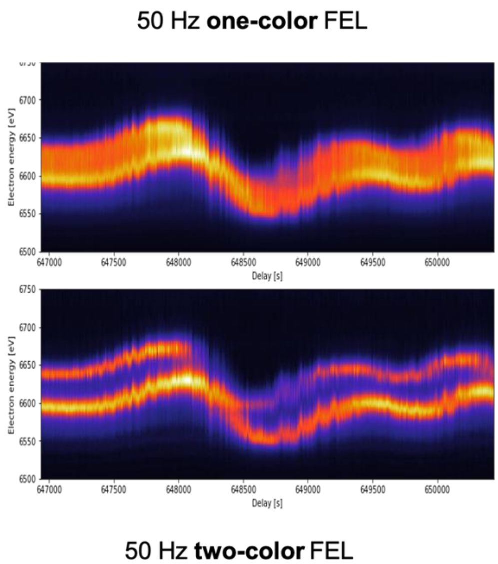

Figure 6: PALM measurement of the one (top graph) and two-colour (lower graph) FEL switched on shot-to-shot base. The vertical and the horizontal axes reports the photon energy and the time scale. Two wavelengths delayed in time are clearly visible in the lower graph.

CONCLUSION

In conclusion, we presented a simple and robust method to generate a two-color hard X-ray FEL. This novel approach relies on a laser emittance spoiler overlapped with the nominal photocathode laser. It enables the generation of two-color FEL pulses with high energy and spectral stability (energy up to 67% of the nominal FEL and comparable stability). The two-color mode requires negligible interference to the machine setup and can be activated on shot-to-shot base for sophisticated lock-in detection schemes for pump-probe experiments. The accessible range of wavelengths, color and temporal separation of the two pulses depends on the electron bunch energy, chirp and duration. The present scheme does not contribute to additional charge losses along the machine and is therefore well suitable for high-repetition rate X-ray lasers. The reliability of the method and the ease of the setup responds to the demand of the FEL scientific community for lower risk two-color configurations to be used in advanced x-ray pump, x-ray probe experiments.

ACKNOWLEDGEMENTS

We thank all the SwissFEL technical groups for their commitment and support.

REFERENCES

[1] C. Milne *et al.,* "SwissFEL: The Swiss X-ray Free Electron Laser", *Appl. Sci.*, vol. 7(7), p. 720, 2017. doi: 10.3390/app7070720

[2] E. Allaria *et al.*, "Highly coherent and stable pulses from the FERMI seeded free-electron laser in the extreme ultraviolet", *Nat. Photonics,* vol. 6, p.699, 2012. doi: 10.1038/nphoton.2012.233

[3] T. Ishikawa *et al.*, "A compact X-ray free-electron laser emitting in the sub-ångström region", *Nat. Photonics,* vol. 6, p.540, 2012. doi: 10.1038/nphoton.2012.141

[4] C. Bostedt *et al.*, "Linac Coherent Light Source: The first five years", *Rev. Mod. Phys.*, vol. 88, p. 015007, 2017. doi: 10.1103/RevModPhys.88.015007

[5] H.-S. Kang *et al.*, "Hard X-ray free-electron laser with femtosecond-scale timing jitter", *Nat. Photonics*, vol. 11, p. 708, 2017. doi: 10.1038/s41566-017-0029-8

[6] S. Schulz *et al.* "Femtosecond all-optical synchronization of an X-ray free-electron laser", *Nat. Commun.*, vol. 6, p. 5938, 2015. doi:10.1038/ncomms6938

[7] S. Serkez, *et al.*, "Opportunities for Two-Color Experiments in the Soft X-ray Regime at the European XFEL", *Appl. Sci.*, vol. 10, p. 2728, 2020. doi: 10.3390/app10082728

[8] F. Tissandier *et al.*, "Two-Color Soft X-Ray Lasing in a High-Density Nickel-like Krypton Plasma", *Phys. Rev. Lett.*, vol. 124, p. 133902, 2020.
doi: 10.1103/PhysRevLett.124.133902

[9] C. Vicario *et al.,* "Two-color x-ray FEL by photocathode laser emittance spoiler", *Phys. Rev. Accel. Beams*, vol. 24, p. 060703, 2021.
doi:10.1103/PhysRevAccelBeams.24.060703

[10] S. Bettoni *et al.,* "Overview of SwissFEL dual-photocathode laser capabilities and perspectives for exotic FEL modes", *High Power Laser Sci. Eng.,* vol. *9*, p. E51, 2021 doi: 10.1017/hpl.2021.36

[11] A. Dax *et al.,* "Arrival time fluctuation of the SwissFEL photocathode laser: characterization by a single color balanced cross correlator", *Opt. Express*, vol. 30(9), pp. 15495-15511, 2022. doi: 10.1364/OE.444679

[12] A. A. Lutman *et al.,* "Femtosecond x-ray free electron laser pulse duration measurement from spectral correlation function", *Phys. Rev. ST Accel. Beams*, vol. 15, p. 030705, 2012. doi: 10.1103/PhysRevSTAB.15.030705

[13] P. Dijkstal *et al.*, "Self-synchronized and cost-effective time-resolved measurements at x-ray free-electron lasers with femtosecond resolution", *Phys. Rev. Res.,* vol. 4, p. 013017, 2022. doi:10.1103/PhysRevResearch.4.013017

[14] Y. Ding *et al.*, "Femtosecond x-ray pulse temporal characterization in free-electron lasers using a transverse deflector", *Phys. Rev. Spec. Top. Accel. Beams*, vol. 14, p. 120701, 2011. doi: 10.1103/physrevstab.14.120701

[15] P. N. Juranić *et al.*, "A scheme for a shot-to-shot, femtosecond-resolved pulse length and arrival time measurement of free electron laser X-ray pulses that overcomes the time jitter problem between the FEL and the laser", *J. Instrum.,* vol. 9, p. P03006, 2014.

ISBN: 978-3-95450-220-2 ISSN: 2673-5474 doi: 10.18429/JACoW-FEL2022-MOP55

SUPERRADIANT AMPLIFICATION TO PRODUCE ATTOSECOND PULSES IN SOFT X-RAY REGIME VIA LINEAR REVERSE TAPER WITHIN UNDULATOR SECTION

Longdi Zhu [1], Sven Reiche, Paul Scherrer Institute, Villigen, Switzerland
Eugenio Ferrari, DESY, Hamburg, Germany
[1] also at Swiss federal institute of technology Lausanne (EPFL), Lausanne, Switzerland

Abstract

Laser pulses of sub-femtosecond duration can be used to track the motion of electrons in the inner shell, which is needed in a variety of advanced experiments. Although this has been accomplished in XUV and hard X-rays in a free-electron-laser facility, it remains a challenge in the soft X-ray region due to the relatively high photon energies and large slippage in the undulator. In this contribution, we present a method to achieve a pulse sequence of ~ 120 attosecond each in average at 293.8 eV photon energy (4 nm wavelength), which covers the K-shell absorption of Carbon. The key is to create a linear undulator taper within each undulator module by rotating a transverse gradient undulator (TGU) at a small angle. The TGU technique is usually referred to minimise the energy spread effect in Laser-driven plasma accelerator, while in this paper we demonstrate that it can also be used to generate short pulses.

INTRODUCTION

Free-electron-laser (FEL) is an X-ray light source [1]. It has many advantages, such as gigawatt power, femtosecond pulse duration and tunable wavelength, opening up experimental opportunities for multiple scientific disciplines including biology, chemistry and physics [2–6]. In this proceeding, we present a method of generating attosecond pulse train (APT) at 4nm radiation wavelength, a scale at which the SASE coherence length is rather large. The consequence of the large coherence length is that the FEL spikes slip out of the electrons and increases the pulse duration, which is the main difficulty in soft x-ray regime.

The compensation of slippage by undulator taper has been discussed in [7, 8], we extend the range of radiation wavelength to 4 nm, where radiations slide significantly into fresh slices and bunch electrons, it is called superradiant regime [9–16]. The compensation of slippage effect is difficult as the process of superradiance is highly non-linear. In this contribution, we propose an original method, combining the energy modulation, phase shifter and taper inside an undulator module. The novelty of the method lies on the strong reverse [17, 18] taper within undulator section by rotated TGU [19] to reduce the effective period number in undulator. If the taper is reverse and its strength is extreme large, only the electrons on which FEL spike stands can effectively lase, while others are suppressed [18]. Based on the parameters in SwissFEL Athos undulator, the simulation result using GENESIS 1.3 code [20] shows that it is possible to generate pulse trains averaging ~120 attosecond, which is much shorter than typical pulse duration in SASE, which is several femtosecond [21].

METHOD

Step 1: Energy Modulation by Seeding Laser

Assuming an electron beam, cold and long, beam current is homogeneous everywhere, travelling through a modulator and a main undulator. The energy modulation is induced by the interaction between electron beam and an external conventional laser, the laser Rayleigh length z_R matchs the modulator length $L_m = N_m \cdot \lambda_m$, where N_m is the modulator period number [22]. For relativistic electrons with velocity $\beta_s \approx 1$, the modulated electron is supposed to have same periodicity as the laser beam [22]. The result of the seeding is a sinusoidal energy modulated beam with large amplitude. For the following discussion we choose a fixed value for the achieved energy modulation of 1% and a laser wavelength of 800 nm.

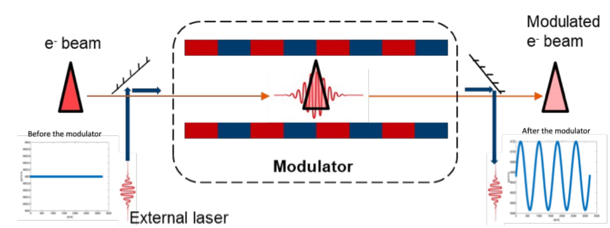

Figure 1: The external Ti-Sapphire 800 nm seeding laser induces a large energy modulation in modulator.

We are interested in the linewidth of resonance $\Delta\omega/\omega \approx \frac{1}{N_u}$, in the undulator. As we assume cold beam, the linewidth is not limited by energy spread, nor emittance. For high-gain case, if electrons do not lose significant energy compared to the total energy, the linewidth is of the order of ρ - FEL parameter [23, 24]. Since the amplitude of energy modulation is 1% and the FEL parameter $\rho \sim 10^{-3}$, for given undulator parameter K, only electrons within the linewidth satisfy the resonance condition and lase significantly photons. The gain in the rest of electron bunch (for both the unmodulated beam fraction and modulated beam with chirp of opposite direction) are strongly reduced or even suppressed, when electrons are out of resonance. Therefore, it is not the whole electron beam that is emitting light, but the resonant electron beam, which is very short.

ISBN: 978-3-95450-220-2 ISSN: 2673-5474 doi: 10.18429/JACoW-FEL2022-MOP55

Step 2: Slippage Mitigation by Taper on Energy-Modulated Beam

In undulator, the central radiation wavelength λ_r is written as :

$$\lambda_r = \frac{\lambda_u}{2\gamma^2}\left(1 + \frac{K^2}{2}\right) \tag{1}$$

where λ_u is undulator period, γ is dimensionless Lorentz factor, K is undulator parameter.

Given the speed of light being always greater than that of electrons and the electrons move in sinusoidal orbits instead of the straight path as of photons, the phase difference between electrons and emitted photons accumulates over longitudinal coordinate z. The FEL radiation precedes electrons by one radiation wavelength λ_r per one undulator period λ_u

As we know the slippage length as well as energy modulation of electron beam, we can taper the magnetic field in undulator so that the resonance condition is fulfilled within the FEL bandwidth. When fully optimized, the only one spike of FEL radiation being tracked gets constantly amplified, though it slides into different part of the beam with different energy [22]. The energy modulation amplitude is of 10^{-2} scale, while the linewidth is of 10^{-3} scale, the resulting pulse duration is much shorter. The method is also discussed in [25], where it reports numerical result of a typical pulse FWHM duration of 340 attosecond for radiation wavelength at 1.22 nm.

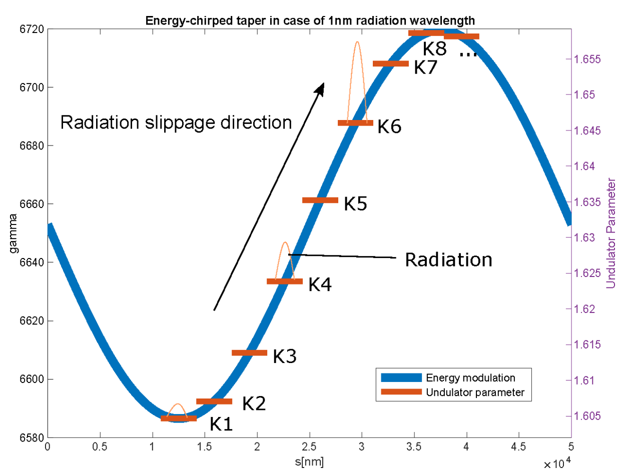

Figure 2: Slicing of energy-modulated beam for 1 nm radiation wavelengths, The "K1" means undulator parameter in the 1st module, starting from the bottom of the modulation, the slippage in one module is around 55 nm (1 nm · 52 + 3 nm), the 3 nm is the slippage calculated for the drift. Radiations, which are initiated from the first undulator section, get amplified when slipping along the energy-modulated beam, it takes around 8 sections to reach the top of the modulation, which is 400 nm distance from the bottom.

Step 3: Enforced Periodicity by Phase Shifters

In the dynamics of slicing, two points are worth noting: the first point is that the energy change of the electrons is not uniform during the slippage; for example, in Fig. 2, the electron energy varies more in the middle part of the modulation and less at the top and bottom. In addition, the gradient of energy deviation becomes progressively larger from U1 (meaning the first undulator section) to U4, while the energy variation decreases from U5 to U8. These have a detrimental effect on the generation of short pulses. The second point is even more important: the undulator parameter remains almost constant from U7 to U9, the slicing effect is greatly weakened, pulse duration is actually increased between U7 and U9.

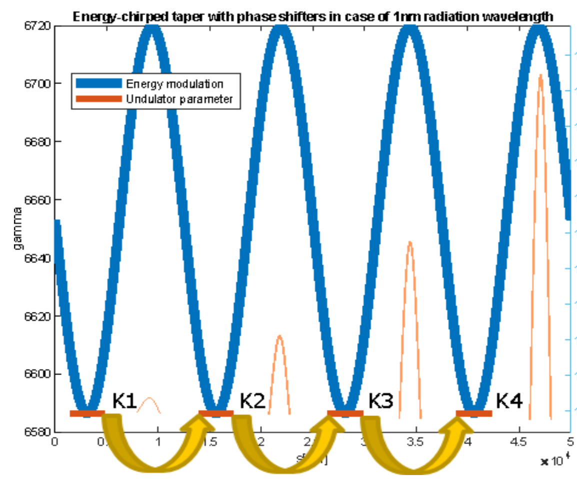

Figure 3: Enforced periodicity by phase shifters after each undulator section. It turns out that resonance occurs only for electrons with the lowest energy in energy modulation. And the amplification process is actually faster.

To avoid the increase in pulse duration, phase shifters are used after each undulator module. The phase shifters, also known as delaying magnetic chicanes, are capable of delaying the electron beam by a small distance, ranging from a few nanometers to hundreds of nanometers. Owing to the periodicity of the energy modulation, the shifter can add delay after each undulator module, keeping the total slippage to 800 nm, same as the period of energy modulation. The FEL radiation, when it begins to slide in the next module, actually experiences the same trajectory along the energy modulation. The method is also called mode-lock [26], as we keep phase locked from module to module. This has the advantage that we only need one undulator parameter value to tune all undulator modules, which significantly reduces the amount of work in the experiment.

Step 4: Reverse Linear Taper via Rotated TGU

The above method works well at a radiation wavelength of 1 nm, where the radiated pulse duration matches the length of the slippage in Athos undulator [27]. However, it is not sufficient to keep the duration short when operating at longer wavelengths, where the slipping effect is much larger. As a direct consequence, the FEL spike slips out of the resonant slice of the beam before the end of one section. As discussed in introduction, we observed strong superradiation

ISBN: 978-3-95450-220-2 ISSN: 2673-5474 doi: 10.18429/JACoW-FEL2022-MOP55

when observing the electron energy extraction at 4 nm radiation wavelength. As described in [9], strong superradiation implies that slippage along long electron beams, in which case the tail of the beam is constantly emitting light and the emitted radiation is used to bunch electrons, the tail of the beam radiate as the scaling of N_e^2, where N_e is the number of electrons.

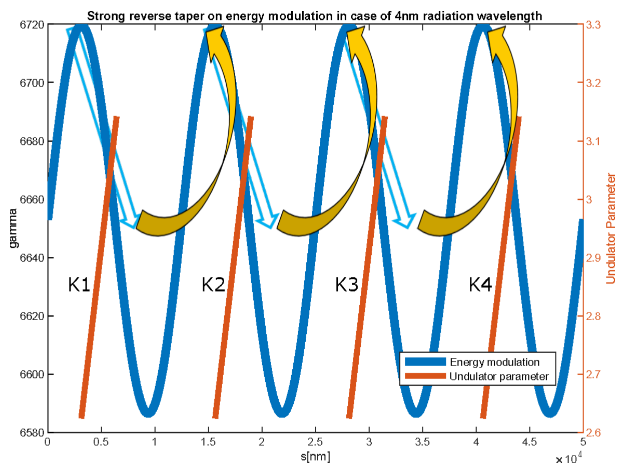

Figure 4: Strong reverse taper via rotated TGU to generate short pulses for longer wavelength radiation. The radiation initiated at the top of the modulation follows the blue arrow. When one section is finished, the delaying magnetic chicane shifts the beam, let the radiation jump to top of the modulation again but in one period behind, as yellow arrow indicates.

Changing the delay between sections, or slightly adjusting undulator parameters, does not affect the slippage effect, as radiations slip out anyway. An effective way to mitigated slippage effect is to apply a strong reverse undulator taper [17, 18] in the undulator section, as described in Fig. 4. The preliminary numerical study suggests a compression of electron beam, to make FEL radiation pulses better contrast compared to background noise.

This is the reason the radiation starts from the top of the beam, instead of the bottom. The Athos undulator has transverse gradient undulator (TGU) profile [28]. By rotating the undulator with a small angle (maximum 0.5 mrad), the transverse configuration is converted to longitudinal direction. The way to obtain longitudinal gradient undulator parameter is illustrated in Fig. 5.

It is difficult to describe the process analytically , as superradiance is highly nonlinear. However, qualitative analysis is possible: Since the taper is excessive reverse, the radiation in main undulator is largely suppressed [18], it requires longer undulator periods to reach saturation. When FEL spikes slip out of the pre-bunched slice, there is almost no radiation, therefore, short pulses are preserved.

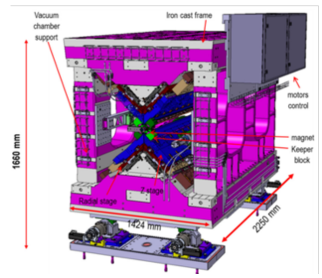

(a) Athos undulator

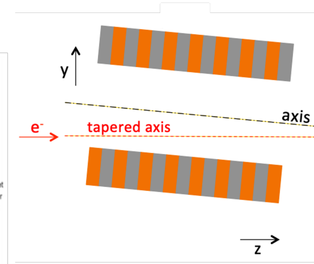

(b) Rotating TGU and convert the transverse configuration to longitudinal direction.

Figure 5: Illustration of how to generate longitudinal gradient undulator parameters on the Athos beamline.

Table 1: Simulation Parameters

Parameters	Value
Beam parameters	
Beam energy	3.4 GeV (γ = 6653)
Bean energy spread	0.511 MeV
Beam peak current	8 kA
Beam emittance	0.3 µm
Bunch length	133 fs
Bunch charge	400 pC
Modulator parameters	
Seeding laser wavelength	800 nm
Modulation amplitude	34 MeV
Modulator period length	0.2 m
Modulator period number	8
Main undulator parameters	
Number of modules	16
Undulator period number	52
Undulator period length	0.038 m
Undulator parameter K	2.6243276 - 3.1414939
Delay in phase shifter	590 nm
Inter-module distance	0.75 m
Central radiation wavelength	4 nm

NUMERICAL RESULTS AT ATHOS UNDULATOR

In SwissFEL Athos beamline [3, 27], there are 16 equal undulator sections, each of them is followed by intersection part , where there is a phase shifter, a quadrupole and a drift. The simulation parameters are listed in table 1, the beam is compressed from 3 kA to 8 kA before entering undulator to let the FEL radiation pulses better contrast compared to background noise. We show the simulation results with four plots: the energy gain (Fig. 6), the spectrum (Fig. 7), the example pulse structure at the optimum location (Fig. 8) and the resulting average pulse duration (Fig. 9). In the Fig. 6: In every module, there is an exponential rate amplification at the early part, but it stops when FEL spikes slide out of the resonant slice. The optimum point observed from the gain

ISBN: 978-3-95450-220-2 ISSN: 2673-5474 doi: 10.18429/JACoW-FEL2022-MOP55

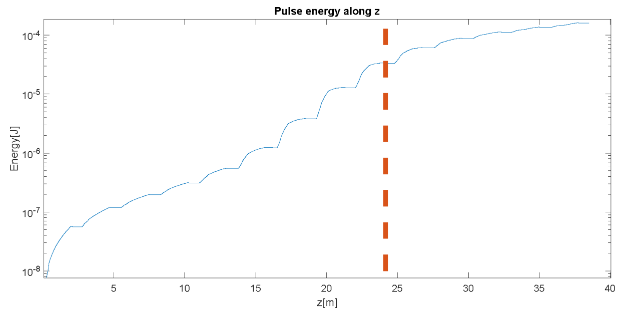

Figure 6: FEL pulse energy

length is at the end of the 9th undulator module, $z = 24.16m$, where we plot a red dotted line.

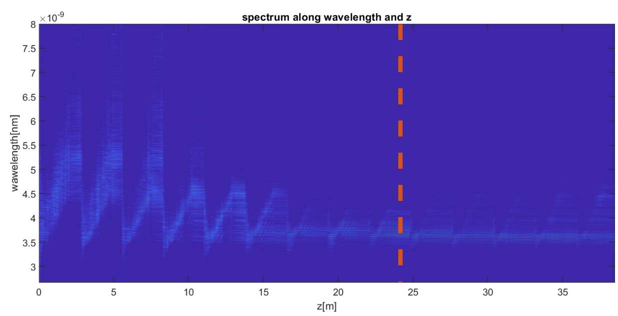

Figure 7: Wavelength spectrum

For the spectrum in Fig. 7, in the first 4 undulator modules, the bandwidth is pretty large, due to the large taper. However, as radiations are amplified, the bandwidth gets narrow between the 5th to 7th section. Later until the 9th section, the bandwidth is much narrower compared to the taper profile. The "blue shift" of the wavelength is reported and discussed in [11].

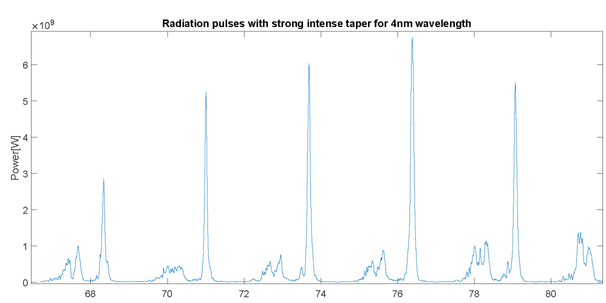

Figure 8: Pulse structure at $z = 24.16m$

We show an example of radiation pulse train, the well-structured short pulses start from the top of the modulation. The side pulses, which are from the modulation bottom can hardly be removed, their intensity is lower owing to the slight beam compression before undulator.

We measure the average pulse duration of short pulses and plot it versus z with errorbar, At the optimum point $z = 21.16$ m, the duration is 118 ± 50.5 attosecond.

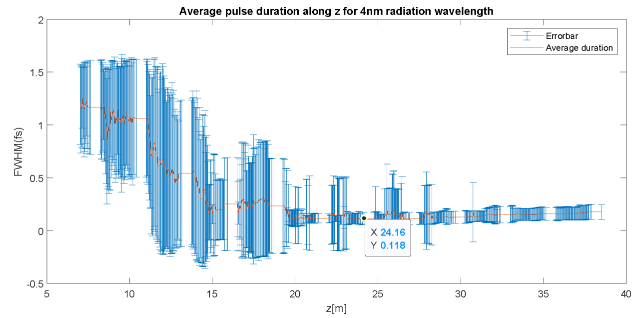

Figure 9: Average pulse duration

CONCLUSION

We have proposed an original method to generate ultra-short pulse train. The results of ~ 120 attosecond average duration at 4 nm radiation wavelength is promising, compared to the state-of-art research [18, 25]. Slippage effect is the main limitation when generating short pulses in soft X-ray regime. The slicing together with phase shifters and strong reverse taper by rotated TGU can largely mitigate the slippage effect. Further optimization will be investigated by different energy modulation profile.

REFERENCES

[1] P. Emma *et al.*, "First lasing and operation of an ångstrom-wavelength free-electron laser", *Nat. Photonics*, vol 4, pp. 641–647, 2010.
`doi:10.1038/nphoton.2010.176`

[2] C. Bostedt *et al.*, "Linac Coherent Light Source: The first five years", *Rev. Mod. Phys.*, vol. 88, p. 015007, 2016.
`doi:10.1103/RevModPhys.88.015007`

[3] E. Prat *et al.*, "A compact and cost-effective hard X-ray free-electron laser driven by a high-brightness and low-energy electron beam", *Nat. Photonics*, vol. 14, pp. 748–754, 2020.
`doi:10.1038/s41566-020-00712-8`

[4] B. W. J. McNeil and N. R. Thompson, "X-ray free-electron lasers", *Nat. Photonics* vol 4, pp. 814–821, 2010.
`doi:10.1038/nphoton.2010.239`

[5] C. Pellegrini *et al.*, "The physics of x-ray free-electron lasers", *Rev. Mod. Phys.*, vol. 88, p. 015006, 2016.
`doi:10.1103/RevModPhys.88.015006`

[6] Z. Huang and Kwang-Je Kim, "Review of x-ray free-electron laser theory", *Phys. Rev. ST Accel. Beams*, vol. 10, p. 034801, 2007.
`doi:10.1103/PhysRevSTAB.10.034801`

[7] E.L. Saldin *et al.*, "Self-amplified spontaneous emission FEL with energy-chirped electron beam and its application for generation of attosecond x-ray pulses", *Phys. Rev. ST Accel. Beams*, vol. 9, p. 050702, 2006.
`doi:10.1103/PhysRevSTAB.9.050702`

[8] E. A. Schneidmiller *et al.*, "Optimization of a high efficiency free electron laser amplifier", *Phys. Rev. ST Accel. Beams*, vol. 18, p. 030705, 2015.
`doi:10.1103/PhysRevSTAB.18.030705`

ISBN: 978-3-95450-220-2 ISSN: 2673-5474 doi: 10.18429/JACoW-FEL2022-MOP55

[9] R. Bonifacio *et al.*, "Physics of the high-gain FEL and superradiance", *La Rivista del Nuovo Cimento*, vol. 13, no. 1, pp. 69, 1990.
doi:10.1007/BF02770850

[10] T. Watanabe *et al.*, "Experimental Characterization of Superradiance in a Single-Pass High-Gain Laser-Seeded Free-Electron Laser Amplifier", *Phys. Rev. Lett.*, vol. 98, p. 034802, 2007
doi:10.1103/PhysRevLett.98.034802

[11] L. Giannessi *et al.*, "Superradiant Cascade in a Seeded Free-Electron Laser", *Phys. Rev. Lett.*, vol. 110, p. 044801, 2013.
doi:10.1103/PhysRevLett.110.044801

[12] L. Giannessi *et al.*, "The free-electron laser harmonic cascade", *New J. Phys.*, vol. 8, p. 294, 2006.
doi:10.1088/1367-2630/8/11/294

[13] R. Bonifacio and F. Casagrande,"The superradiant regime of a free electron laser", *Nucl. Instrum. Methods Phys. Res., Sect. A*, vol. 239, p. 36, 1985.
doi:10.1016/0168-9002(85)90695-3

[14] R. Bonifacio *et al.*, "The superradiant regime of a FEL: Analytical and numerical results", *Nucl. Instrum. Methods Phys. Res., Sect. A*, vol. 296, p. 358, 1990.
doi:10.1016/0168-9002(90)91234-3

[15] R. Bonifacio *et al.*, "Slippage and superradiance in the high-gain FEL: Linear theory", *Opt. Commun.*, vol. 68, p. 369, 1988.
doi:10.1016/0030-4018(88)90234-9

[16] A. Gover *et al.*, "Superradiant and stimulated-superradiant emission of bunched electron beams", *Rev. Mod. Phys.*, vol. 91, p. 035003, 2019.
doi:10.1103/RevModPhys.91.035003

[17] E. A. Schneidmiller and M. V. Yurkov, "Obtaining high degree of circular polarization at x-ray free electron lasers via a reverse undulator taper", *Phys. Rev. ST Accel. Beams*, vol. 16, p. 110702, 2013.
doi:10.1103/PhysRevSTAB.16.110702

[18] E. A. Schneidmiller, "Application of a modified chirp-taper scheme for generation of attosecond pulses in extreme ultraviolet and soft x-ray free electron lasers", *Phys. Rev. Accel. Beams*, vol. 25, p. 010701, 2022.
doi:10.1103/PhysRevAccelBeams.25.010701

[19] Z. Huang *et al.*, "Compact X-ray Free-Electron Laser from a Laser-Plasma Accelerator Using a Transverse-Gradient Undulator", *Phys. Rev. Lett.*, vol. 109, p. 204801, 2012.
doi:10.1103/PhysRevLett.109.204801

[20] S. Reiche, "GENESIS 1.3: a fully 3D time-dependent FEL simulation code", *Nucl. Instrum. Methods Phys. Res., Sect. A*, Vol. 429, p. 243-248, 1999.
doi:10.1016/S0168-9002(99)00114-X

[21] J. Röensch-Schulenburg *et al.*, "Short SASE-FEL Pulses at FLASH", in *Proc. FEL'13*, New York, NY, USA, Aug. 2013, paper TUPSO64, pp. 379–382.

[22] E. Hemsing *et al.*, "Beam by design: Laser manipulation of electrons in modern accelerators", *Rev. Mod. Phys.*, vol. 86, pp. 897–941, 2014.
doi:10.1103/RevModPhys.86.897

[23] J.R. Pierce, "Traveling-Wave Tubes", *Van Nostrand Co.*, vol. 29, no. 4, pp. 608-671, 1950.
doi:10.1002/j.1538-7305.1950.tb03654.x

[24] R. Bonifacio *et al.*, "Collective instabilities and high-gain regime in a free electron laser", *Opt. Commun.*, vol. 50, pp. 373-378, 1984.
doi:10.1016/0030-4018(84)90105-6

[25] J. Duris *et al.*, "Superradiant amplification in a chirped-tapered x-ray free-electron laser", *Phys. Rev. Accel. Beams*, vol. 23, p. 020702, 2020.
doi:10.1103/PhysRevAccelBeams.23.020702

[26] N. R. Thompson and B. W. J. McNeil,"Mode Locking in a Free-Electron Laser Amplifier", *Phys. Rev. Lett.*, vol. 100, p. 203901, 2008.
doi:10.1103/PhysRevLett.100.203901

[27] R. Abela *et al.*, "The SwissFEL soft X-ray free-electron laser beamline: Athos", *J. Synchrotron Radiat.*, vol. 26, pp. 1073-1084, 2019. doi:10.1107/S1600577519003928

[28] M. Calvi *et al.*, "Transverse gradient in Apple-type undulators", *J. Synchrotron Radiat.*, vol. 24, pp. 600-608, 2017. doi:10.1107/S1600577517004726

ISBN: 978-3-95450-220-2 ISSN: 2673-5474 doi: 10.18429/JACoW-FEL2022-MOP57

LOW-EMITTANCE BEAM INJECTION FROM SACLA TO SPring-8

T. Hara†, RIKEN SPring-8 Center, Sayo, Japan
On behalf of RIKEN-JASRI joint project team

Abstract

The SACLA linear accelerator has been successfully used as a full-energy injector of the SPring-8 storage ring since 2020. The beam injection from SACLA is a part of the SPring-8 upgrade project, called SPring-8-II, which requires low-emittance beams for injection due to its small beam aperture. In order to perform the beam injection in parallel with XFEL operation, three accelerators are virtually constructed in a control system of SACLA. Thus, the electron beam parameters, such as beam energies, are independently tuned for the beam injection and two XFEL beamlines. By shutting down a dedicated old injector, electricity consumption has been reduced by roughly 20-30 % and additional maintenance costs are no more necessary.

INTRODUCTION

The beam injection from SACLA has been started as a part of the SPring-8 upgrade project, called SPring-8-II [1, 2]. A small dynamic aperture is a common issue for all recent low-emittance storage rings with multi-bend optics [3]. In SPring-8-II, traditional off-axis beam injection will be employed using an in-vacuum septum magnet and low-emittance beams [4]. Thus, the low-emittance beam of SACLA is indispensable for beam injection.

Figure 1 is a schematic layout of the SACLA facility [5]. There are two XFEL beamlines (BL2, BL3) and a soft x-ray FEL beamline (BL1). BL1 operates independently from the SACLA main linear accelerator by using a dedicated 800 MeV linear accelerator, which was originally constructed as SCSS, a proto-type accelerator of SACLA [6, 7]. BL2 and BL3 share the electron beam of the SACLA main linear accelerator. A switchyard is installed at the end of the linear accelerator and 60 Hz electron bunches are distributed pulse by pulse [8, 9]. For the beam injection, the electron bunches are deflected to a beam transport line named XSBT (XFEL to Storage ring Beam Transport).

The use of SACLA as an injector not only brings small emittance, but also it contributes to electricity saving and facility related cost reduction. In case of a dedicated injector, accelerators should be always maintained in operating condition just for sparsely occurred top-up injection. On the other hand, a linear accelerator of XFEL is already in operation to provide photon beams to its users, so no additional electricity or operation cost is required by just using a small number of electron bunches for top-up injection.

BEAM INJECTION

Figure 2 shows the stored current of SPring-8 during the beam injection from SACLA. It takes about 10 minutes to fill up the ring with 100 mA, which is a nominal stored current of SPring-8. During the 10 Hz injection, XFEL operation is suspended. Once the stored current reaches 100 mA, it is maintained by top-up injection, which is performed in parallel with XFEL operation. When the stored current decays below a certain threshold, SPring-8 sends a request of beam injection to SACLA. A typical frequency of top-up injection is 2-3 times every minute.

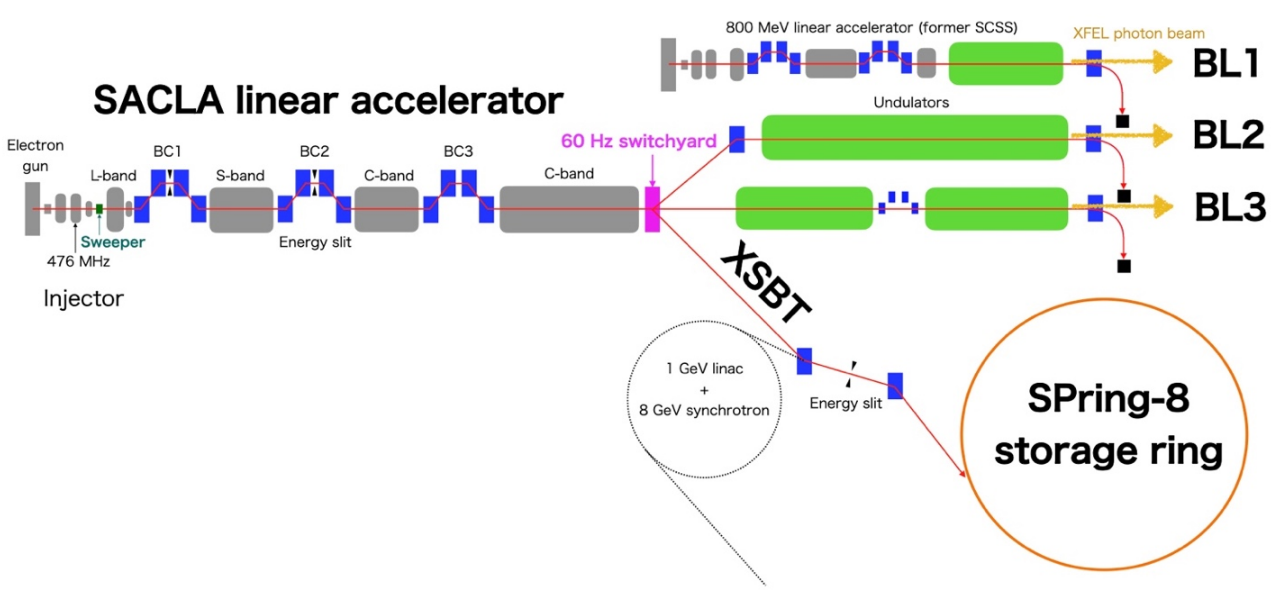

Figure 1: Schematic layout of the SACLA facility.

† toru@spring8.or.jp

ISBN: 978-3-95450-220-2 ISSN: 2673-5474 doi: 10.18429/JACoW-FEL2022-MOP57

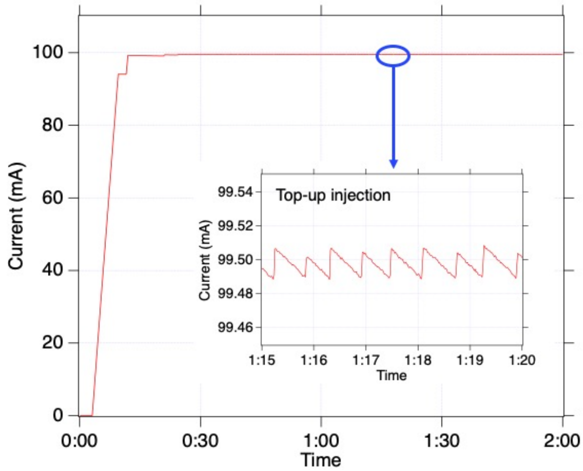

Figure 2: Stored current of SPring-8. The electron beam is injected from SACLA by 10 Hz and the stored current is maintained by top-up injection.

In SACLA, the accelerated electron bunches are distributed pulse by pulse to three destinations, which are the two XFEL beamlines (BL2 and BL3) and the beam transport to the storage ring (XSBT). In order to control the bunch destinations, several distribution patterns for a period of one second are prepared in advance and stored in a master controller. According to the distribution pattern, the master controller sends a 16-bit bunch tag, which contains the information on the bunch destination, to accelerator components through a reflective memory network [10, 11]. Once the components receive the bunch tag, they operate with prestored parameters for each beam destination, such as RF parameters and a direction of beam deflection at the switchyard. For the top-up injection, a destination pattern including XSBT is loaded to the master controller when SACLA receives a beam injection request from SPring-8. Then the electron beam is injected to the ring in the next second.

The energy of the beam injection should be fixed at 8 GeV, while it is often changed for XFEL beamlines [12]. In order to tune the two XFEL beamlines and the beam injection independently, measured data are saved in a database with the bunch tag. Thus, an energy feedback or machine tuning can be individually applied to each destination. Figure 3 shows three beam orbits measured and displayed separably by destination.

Different beam energies result in different quadrupole focusing strengths. Consequently, transverse beam envelop mismatch occurs. At present, the transverse envelops are re-matched downstream the switchyard, but 21 pulsed quadrupoles are now in preparation for individual control of the transverse beam envelops.

The reference clocks of SACLA (238 MHz) and SPring-8 (508 MHz) do not have a multiple relation, so the injection timing naturally goes off with respect to the target RF bucket of SPring-8 by maximum ±2.1 ns (one period of 238 MHz). In order to synchronize the two accelerators, two steps are taken [13]. When the beam injection is requested from SPring-8, the best injection timing is searched first. By delaying the injection by up to 40 ring revolution periods (~197 µs), there should be a point where the timing difference takes its minimum (< 105 ps). As a second step, slight frequency modulation is applied to the reference clock of SACLA to finely synchronize the two accelerators. The developed timing system achieves final synchronization of the two accelerators within 3.8 ps (rms).

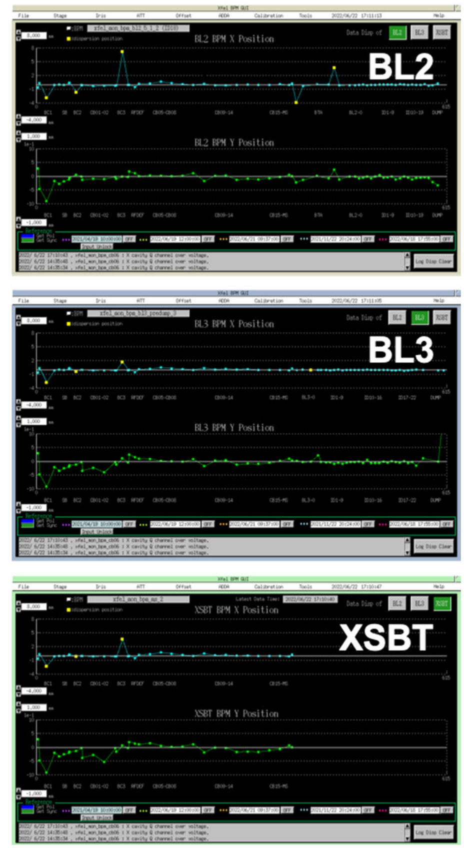

Figure 3: Electron beam orbits measured and displayed by destination. Top blue lines and bottom green lines show horizontal and vertical orbits respectively in each window.

When the injector was switched to the SACLA linear accelerator, we encountered two issues, which are bunch purity and magnetic hysteresis of the switchyard.

The bunch purity, which represents a ratio of bunch charges between beam injected RF buckets and empty buckets, is important for time-resolved experiments of the ring, such as nuclear resonance scattering. The bunch purity of 10^{-8}~10^{-10} is routinely requested at SPring-8 [14]. However, when the beam is injected to the target RF bucket from SACLA, a small number of electrons are also injected 18 ns after the target bucket. After detailed investigations, it is found that some electrons make a roundtrip between a 476 MHz RF cavity and an L-band accelerator in the SACLA injector section (Fig. 1) [2]. Then these electrons are accelerated to the final beam energy having a delay of 18 ns and injected to the ring. In order to remove these undesired electrons, an electron sweeper and an RF knock out system have been introduced in the SACLA injector section and the SPring-8 storage ring respectively, and bunch purity of 10^{-10} is now achieved.

ISBN: 978-3-95450-220-2 ISSN: 2673-5474 doi: 10.18429/JACoW-FEL2022-MOP57

Magnetic hysteresis of a kicker magnet of the switchyard deviates the beam orbit inside XFEL undulators after the beam injection, because the kicker magnet is excited by reversed polarity. In order to erase residual magnetization, the kicker magnet is excited with a blank pulse after the beam injection and the kicker excitation currents of following three pulses are finely adjusted. Figure 4 is histograms of XFEL photon beam horizontal positions observed at BL3. After taking a hysteresis correction procedure, the pointing stability of the photon beam becomes sufficiently small compared to its size of 500 µm (FWHM).

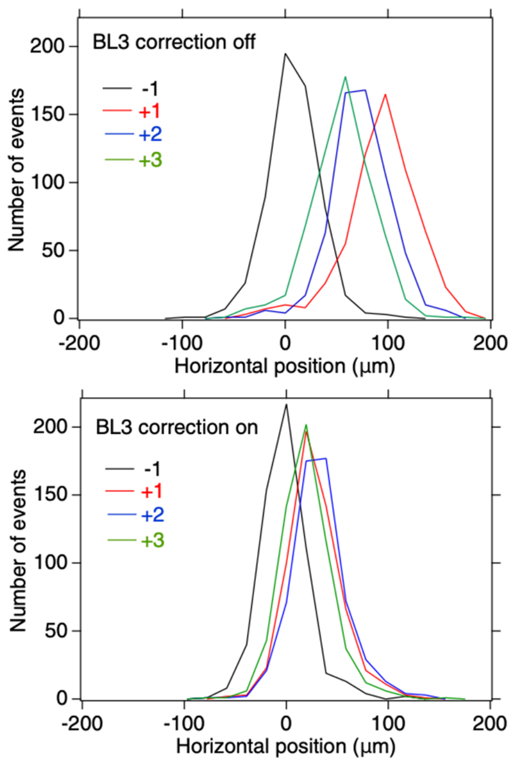

Figure 4: Histograms of XFEL photon beam horizontal positions observed at 40 m downstream of the BL3 undulator end. The cases for hysteresis correction off (up) and on (bottom) are shown. The numbers in different colors correspond to the pulse sequence with respect to the beam injection (0).

EMITTNCE GROWTH

The transverse beam profiles observed on a screen close to the injection point of SPring-8 are shown in Fig. 5 [15]. The emittance of the beam injected from SACLA is estimated to be about 1 nm·rad and that from the old injector (an 8 GeV synchrotron) is 200 nm·rad. Although the projected emittance of the SACLA linear accelerator is 0.15 nm·rad, it increases by an order of magnitude along the beam transport (XSBT). However, it is still small enough compared with the requirement for SPring-8-II, which is around 10 nm·rad.

Figure 6 shows projected emittance growth at XSBT calculated by Elegant [16]. Black lines show the emittance including CSR (Coherent Synchrotron Radiation) and SR (incoherent Synchrotron Radiation) effects, while blue lines consider only SR effects and red lines exclude both effects. Along XSBT, there are 20 horizontal and 6 vertical bending magnets, whose bending radius is around 20 m. The first half of XSBT (z = 0~300 m in Fig. 6) was newly build together with SACLA, whose lattice is DBA (Double Bend Achromat). The last half (z = 300~600 m in Fig. 6) is reuse of an old transport line with a FODO lattice.

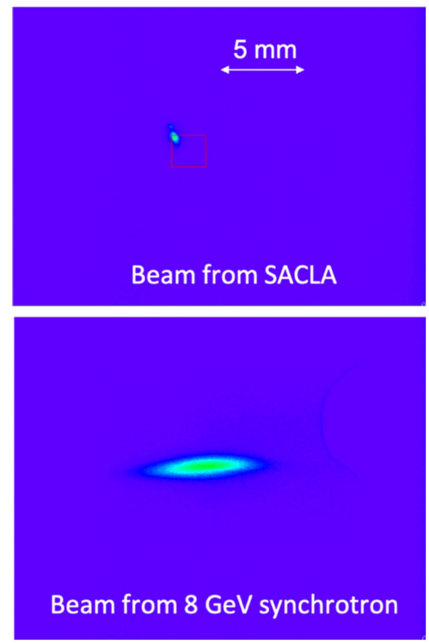

Figure 5: Transverse beam profiles of the electron beam from SACLA and the old injector (8 GeV synchrotron).

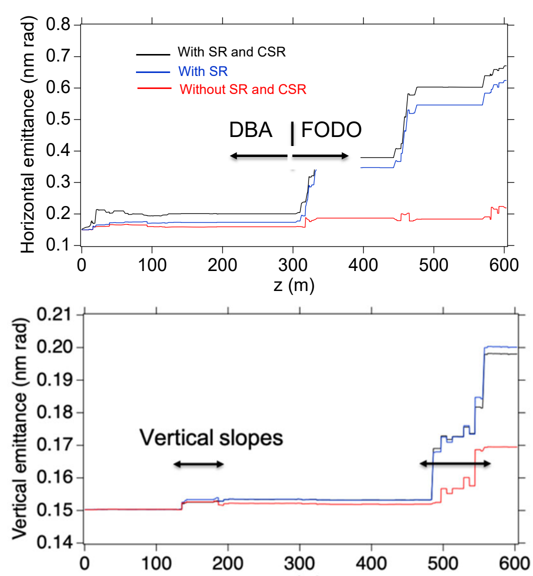

Figure 6: Calculated projected emittance growth along XSBT in horizontal (up) and vertical (bottom) planes.

In Fig. 6, the emittance growth ($\Delta\varepsilon_{x,y}$) is mainly explained by quantum excitation of synchrotron radiation [2]. It is expressed by

ISBN: 978-3-95450-220-2 ISSN: 2673-5474 doi: 10.18429/JACoW-FEL2022-MOP57

$$\Delta\varepsilon_{x,y} = \frac{55 r_e \hbar \gamma^5}{48\sqrt{3} m_e c}\int \frac{\mathcal{H}_{x,y}(z)}{\rho_{x,y}^3(z)} dz, \quad (1)$$

where r_e, $\hbar$, γ, m_e and c are the classical electron radius, Dirac's constant, Lorentz factor, electron rest mass and speed of light in vacuum. $\mathcal{H}_{x,y}$ is defined as $\mathcal{H}_{x,y} = \beta_{x,y}\eta'^2_{x,y} + 2\alpha_{x,y}\eta_{x,y}\eta'_{x,y} + \gamma_{x,y}\eta^2_{x,y}$ with Twiss parameters (α, β, γ), a linear dispersion function and its derivative (η, η'). ρ is a bending radius and the integration is taken along a beam trajectory (z) [17, 18]. In a storage ring, quantum excitation and radiation damping are balanced at ring emittance after many turns around the ring. On the other hand, the electron beam passes a beam transport only once. Then the emittance reduction due to radiation damping, which can be expressed as

$$\Delta\varepsilon_{x,y} \approx -\frac{2 r_e \gamma^3}{3}\int \frac{\varepsilon_{x,y}(z)}{\rho_{x,y}^2(z)} dz, \quad (2)$$

becomes almost ineffective for small emittance beams. In the case of XSBT, the emittance damping of Eq. (2) is three orders of magnitude smaller than the emittance growth caused by quantum excitation (Eq. (1)).

Since the electron bunch is immediately lengthened at the entrance of XSBT, the emittance growth due to CSR effects is limited. The emittance increase observed on the red lines in Fig. 6 attributes to nonlinear dispersion [2].

CONCLUSION

The electron beam injection from SACLA to SPring-8 has been successfully achieved, and the linear accelerator of SACLA is now used as a low-emittance full energy injector of the SPring-8 storage ring. Although emittance growth due to quantum excitation of synchrotron radiation is observed at the beam transport, it still remains small enough for the future SPring-8-II. The old injector composed of a 1 GeV linear accelerator and an 8 GeV synchrotron booster ring were shut down in 2021, which led to significant saving of energy consumption and operation costs.

ACKNOWLEDGEMENTS

The author thanks all the members of the project and the operators of SPirng-8 and SACLA for their contributions.

REFERENCES

[1] H. Tanaka *et al.*, "SPring-8 upgrade project", in *Proc. IPAC'16*, Busan, Korea, May 2016, pp. 2867-2870. doi:10.18429/JACoW-IPAC2016-WEPOW019

[2] T. Hara *et al.*, "Low-emittance beam injection for a synchrotron radiation source using an X-ray free-electron laser linear accelerator", *Phys. Rev. Accel. Beams*, vol. 24, p. 110702, 2021. doi:10.1103/PhysRevAccelBeams.24.110702

[3] K. Soutome, T. Hiraiwa, and H. Tanaka, "Update of Lattice Design of the SPring-8-II Storage Ring Towards 50 pmrad", in *Proc. IPAC'22*, Bangkok, Thailand, Jun. 2022, pp. 477-480. doi:10.18429/JACoW-IPAC2022-MOPOTK017

[4] S. Takano *et al.*, "Renovation of off-axis beam injection scheme for next-generation photon sources", in *Proc. IPAC'19*, Melbourne, Australia, May 2019, pp. 2318-2321. doi:10.18429/JACoW-IPAC2019-WEPMP009

[5] T. Ishikawa *et al.*, "A compact X-ray free-electron laser emitting in the sub-ångström region", *Nat. Photonics*, vol. 6, pp. 540, 2012. doi:10.1038/nphoton.2012.141

[6] T. Shintake *et al.*, "A compact free-electron laser for generating coherent radiation in the extreme ultraviolet region", *Nat. Photonics*, vol. 2, p. 555-559, 2008. doi:10.1038/nphoton.2008.134

[7] S. Owada *et al.*, "A soft X-ray free-electron laser beamline at SACLA: The light source, photon beamline and experimental station", *J. Synchrotron Radiat.*, vol. 25, pp. 282-288, 2018. doi:10.1107/S1600577517015685

[8] T. Hara *et al.*, "Pulse-by-pulse multi-beamline operation for x-ray free-electron laser", *Phys. Rev. Accel. Beams*, vol. 19, p. 020703, 2016. doi:10.1103/PhysRevAccelBeams.19.020703

[9] T. Hara *et al.*, "High peak current operation of x-ray free-electron laser multiple beam lines by suppressing coherent synchrotron radiation effects", *Phys. Rev. Accel. Beams*, vol. 21, p. 040701, 2018. doi:10.1103/PhysRevAccelBeams.21.040701

[10] H. Maesaka *et al.*, "On-demand beam route and RF parameter switching system for time-sharing of a linac for x-ray free-electron laser as an injector to a 4th-generation synchrotron radiation source", in *Proc. IPAC'19*, Melbourne, Australia, May 2019, pp. 3427-3430. doi:10.18429/JACoW-IPAC2019-THYYPLS1

[11] T. Fukui *et al.*, "The design of the control system for the SACLA/SPring-8 accelerator complex to use the linac of SACLA for a full-energy injector of SPring-8", in *Proc. IPAC'19*, Melbourne, Australia, May 2019, pp. 2529-2531. doi:10.18429/JACoW-IPAC2019-WEPGW029

[12] T. Hara *et al.*, "Time-interleaved multienergy acceleration for an x-ray free-electron laser facility", *Phys. Rev. ST Accel. Beams*, vol. 16, p. 080701, 2013. doi:10.1103/PhysRevSTAB.16.080701

[13] T. Ohshima, H. Maesaka, N. Hosoda, and S. Matsubara, "Timing synchronization system for beam injection from the SACLA linac to the SPring-8 storage ring", in *Proc. IPAC'19*, Melbourne, Australia, May 2019, pp. 3882-3885. doi:10.18429/JACoW-IPAC2019-THPRB034

[14] K. Tamura and T. Aoki, "Single bunch purity during SPring-8 storage ring top-up operation", in *Proc. 1st Annual Meeting of Particle Accelerator Society of Japan and the 29th Linear Accelerator Meeting in Japan*, Funabashi, Japan, Aug. 2004, pp. 581-583.

[15] S. Takano, M. Masaki, T. Masuda, and A. Yamashita, "OTR based monitor of injection beam for top-up operation of the SPring-8", in *Proc. DIPAC2005*, Lyon, France, Jun. 2005, pp. 72-74.

[16] M. Borland, "Simple method for particle tracking with coherent synchrotron radiation", *Phys. Rev. ST Accel. Beams*, vol. 4, p. 070701, 2001. doi:10.1103/PhysRevSTAB.4.070701

[17] M. Sands, "The physics of electron storage rings: An introduction", SLAC Report No. 121, 1970.

[18] H. Wiedemann, in *Particle Accelerator Physics*, 4th ed., Springer International publishing, New York, USA, 2015.

ISBN: 978-3-95450-220-2 ISSN: 2673-5474 doi: 10.18429/JACoW-FEL2022-MOP63

DETAIL STUDY FOR THE LASER ACTIVATING REFLECTIVE SWITCH FOR THZ FREE ELECTRON LASER

K. Kawase†, National Institutes for Quantum Science and Technology, Kizugawa, Japan

Abstract

THz free electron laser at SANKEN, Osaka university generates a train of THz pulses with the interval of 27 MHz in the repetition of 5 Hz. The number of pulses in a train is about 100. Single pulse energy exceeds 200 μJ at the carrier frequency of 4.5 THz. To extract a single pulse from the train, the reflective switch of the electron-hole plasma on the surface of Gallium Arsenide wafer driven by the Ti:sapphire laser pulse was constructed and the characteristics of the switch is studied. By evaluating also the characteristics of silicon and germanium wafers, the comparison experiments are performed. In addition, the study for carrier dynamics with the time scale of microseconds by measuring the variations of reflected and transmitted THz pulses with the interval of 27 MHz are being conducted. We report the recent results of the switching for the THz pulse and its time evolution in this conference.

INTRODUCTION

A free electron laser (FEL) oscillator is that the light is amplified and oscillated by going roundtrip inside a cavity similar to conventional lasers. A part of the light inside the cavity is extracted according to the coupling of the resonator mirror. In case of the radiofrequency linac, the electron beam consists of the bunch train with the duration of a few ten picoseconds for each bunch, thus, the FEL has also a form of the bunch train with the similar duration. On the other hand, an isolated pulse is more useful depending on the experimental demands. Therefore, the researches of the semiconductor reflective switching driven by visible or near infrared pulse lasers have been conducted at several FEL facilities [1 - 9].

The semiconductor reflective switching is that the intense laser pulse generates the high dense carrier plasma on the surface of the semiconductor sheet, which is undoped with high transparency on the wavelength range from mid to far infrared, and the plasma reflects the FEL pulses in a short time. When the plasma density on the surface of the semiconductor exceeds a critical density, the reflectivity is high, but the reflection, absorption and transmission of the FEL competes when the density is lower than that. Because the characteristics of the reflection, absorption and transmission of the radiation depends on the carrier density, the evolution of the carrier density is a fundamental property on the response of the semiconductor reflective switches. Thus, the detail studies for the evolution of the laser activating reflective switching for different semiconductors are useful and interesting. We performed the experimental studies of the evolution of reflective switching for gallium arsenide (GaAs), germanium (Ge) and silicon (Si) using the FEL at the range of THz frequency.

EXPERIMENT

The experiments were conducted using THz FEL at the Institute of Scientific and Industrial Research, Osaka University (SANKEN THz-FEL, formerly named ISIR THz-FEL). This FEL covers the wavelength range from 50 to 100 μm (3 to 6 THz) in practical. The pulse interval is 27 MHz and the duration of a pulse train is about 8 μs. The repetition of operation is 5 Hz. The details of the accelerator and FEL apparatuses are shown in the previous reports [10].

The THz FEL beam is transported inside the vacuum duct and extracted to the experimental area through a diamond window. The beam is down-collimated with two off-axis parabola mirrors and injected to the semiconductor wafer as the switching material with Brewster's angle. Samples was undoped semiconductor wafers of GaAs, Ge and Si with the thickness of 0.5 mm. The pulse energy reflected from the switch and the energy of transmitted pulse train were measured by energy meter system (Coherent, Inc.). As the sensor heads, J10MB-LE with higher sensitivity for the reflected pulse and J50MB-LE with lower sensitivity for the transmitted train were used. For time resolved measurements, the pyroelectric detector (P5-00, Molectron, Inc.) was used.

As a driving laser for the semiconductor reflective switching, Ti:sapphire regenerative amplifier laser system with the nominal FWHM pulse duration of 100 fs (Spitfire, SpectraPhysics, Inc.) was used. The laser pulses are synchronized to the timing system of the linac. The irradiation timing on the wafer was tuned with the optical delay line consisting of two mirrors mounted on the motorized linear stage with the stroke of 100 mm and the cable delay line installed in the laser timing system. The irradiation fluence was tuned with the half waveplate before the polarizer. The photograph of the experimental setup is shown in Fig. 1.

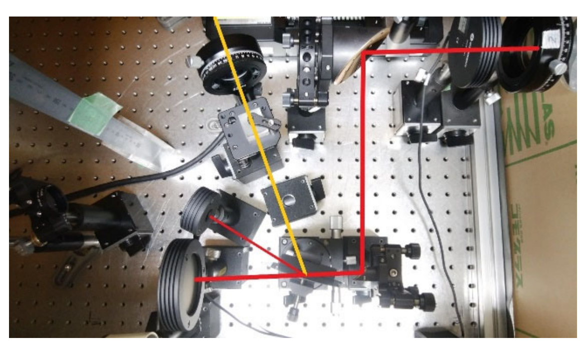

Figure 1: Experimental setup.

† kawase.keigo@qst.go.jp

ISBN: 978-3-95450-220-2 ISSN: 2673-5474 doi: 10.18429/JACoW-FEL2022-MOP63

RESULTS AND DISCUSSION

The variation of the reflected pulse energy of THz FEL from the GaAs wafer by changing the irradiation timing with the optical delay stage is shown in Fig. 2. In this experiment, the reflected pulse energy monotonically decreases according to the irradiation timing after the peak reflection. The higher irradiation fluence results in the longer decay constant. Figure 3 shows the variations of the reflected pulse energy for different irradiation fluences in longer time range increasing the cable delay line in the laser timing system. These curves are well fit to an exponential function and the decay constants depend on the irradiation fluence. In this experiment, the decay constant at the maximum fluence is 3.3 ns. This value is enough smaller than the FEL pulse interval of 37 ns in case of SANKEN FEL.

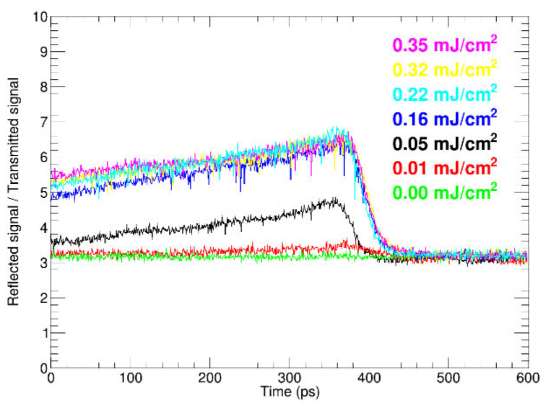

Figure 2: Variation of the reflected signal from the GaAs by changing the laser timing with the optical delay stage.

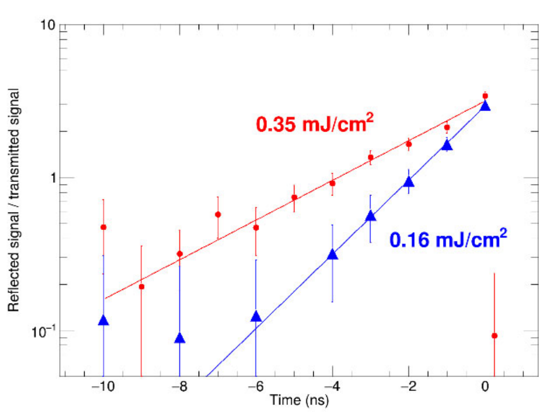

Figure 3: Variation of the reflected signal from the GaAs by changing the laser timing with the cable delay. The decay slope depends on the irradiation fluence of the activating laser pulse. The decay constants are 3.3 ns for 0.35 mJ/cm^2 and 1.8 ns for 0.16 mJ/cm^2 in this experiment, respectively. One data point after 0 ns corresponds to the 600 ps timing in Fig. 2.

In contrast, the waveforms of the fast pyroelectric detector observing reflected pulses from Ge and Si are shown in Fig. 4. The decay constants for Ge and Si are 36 ns and 64 ns, respectively, which are one order larger than that for GaAs in similar irradiation fluence. It may be considered the result from the difference of the transition types between the direct and indirect. One of the possible reasons why the difference between Ge and Si is the difference of the thickness of plasma layer on each surface. The extinction coefficient of Ge is one order higher than that of Si. Thus, in case of Ge, the carrier density on surface is higher but the thickness of plasma layer is thinner than Si. Because the transition process from conduction band to valence band in the indirect-transition semiconductor proceeds through the propagation of lattice vibration and the diffusion of carriers, the decay constants depend on the thickness of generated plasma layer. The detail of this consideration is one of future issues in this study.

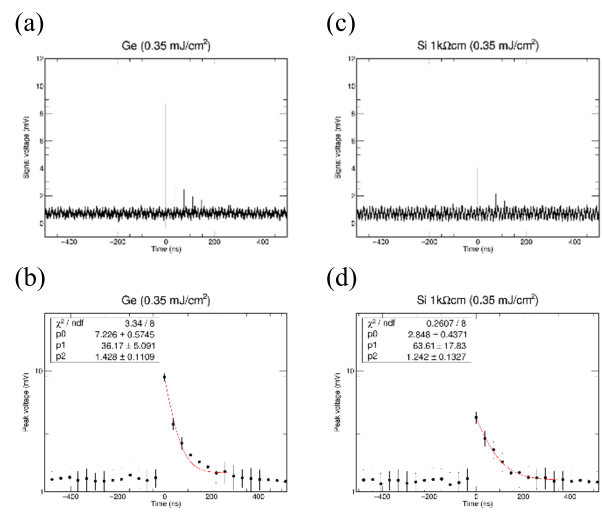

Figure 4: Reflected signals for (a, b) Ge and (c, d) Si. The upper plots are 50 times averaged waveform data, and the lowers are peaks data extracted from uppers. The fitting function is $f(t) = p0 \times \exp(-t/p1) + p2$, where $f(t)$ is the peak voltage and t is time. The parameter $p1$ corresponds to the decay constant.

CONCLUSION

By studying the evolution of the laser activating semiconductor switching of GaAs, we confirmed the decay constant of the reflected pulse energy is a few ns. Thus, we can extract a single pulse from the THz pulse train with the interval of 37 ns at SANKEN FEL using GaAs. In case of Ge and Si differing from GaAs, the decay constants of the reflected energy are a few ten ns. The experimental results suggest that decay constant depends on the generated carrier density. By using the THz FEL with the pulse interval of 37 ns, it is possible to make systematic study for the dynamics of the laser-activated carriers on semiconductor surface.

ISBN: 978-3-95450-220-2 ISSN: 2673-5474 doi: 10.18429/JACoW-FEL2022-MOP63

ACKNOWLEDGEMENTS

A part of this work is supported by MEXT Q-LEAP (contract No. JPMXS0118070271), JSPS KAKENHI (20K12491) and Cooperative Research Program of "Network Joint Research Center for Materials and Devices".

REFERENCES

[1] J. P. Kaminski, J. S. Spector, C. L. Felix, D. P. Enyeart, D. T. White, and G. Ramian, "Far-infrared cavity dumping coupling of the UC Santa Barbara free-electron laser", *App. Phys. Lett.* vol. 57, pp. 2770-2772, Dec. 1990. doi:10.1063/1.103782

[2] F. A. Hegmann and M. S. Sherwin, "Generation of picosecond far-infrared pulses using laser-activated semiconductor reflection switches", in *Proc. SPIE*, vol. 2842, pp. 90-105, Dec. 1996. doi:10.1117/12.262736

[3] E. H. Haselhoff, G. M. H. Knippels, P. W. van Amersfoort, "Slicing single micropulses at FELIX*", Nucl. Instrum. Methods Phys. Res., Sect. A*, vol. 358, pp. ABS28–ABS29, Apr. 1995. doi:10.1016/0168-9002(94)01259-8

[4] M. F. Doty, B. E. Cole, B. T. King, and M. S. Sherwin, "Wavelength-specific laser-activated switches for improved contrast ratio in generation of short THz pulses", *Rev. Sci. Instrum.*, vol. 75, pp. 2921–2925, Sep. 2004. doi:10.1063/1.1783594

[5] S. Takahashi, G. Ramian, and M. S. Sherwin, "Cavity dumping of an injection-locked free-electron laser", *Appl. Phys. Lett.*, vol. 95, Dec. 2009, 234102. doi:10.1063/1.3270041

[6] X. Wang, T. Nakajima, H. Zen, T. Kii, and H. Ohgaki, "Damage threshold and focusability of mid-infrared free-electron laser pulses gated by a plasma mirror with nanosecond switching pulses", *Appl. Phys. Lett.*, vol. 103, Nov. 2013, 191105. doi:10.1063/1.4828995

[7] W. Seidel and S. Winnerl, "A Laser-activated Plasma Switch for the Extraction of Single FELBE Radiation Pulses", in *Proc. FEL'10*, Malmö, Sweden, Aug. 2010, paper TUPA02, pp. 210-211.

[8] J. Schmidt, S. Winnerl, W. Seidel, C. Bauer, M. Gensch, H. Schneider, and M. Helm, "Single-pulse picking at kHz repetition rates using a Ge plasma switch at the free-electron laser FELBE", *Rev. Sci. Instrum.*, vol. 86, 063103, June 2015. doi:10.1063/1.4921864

[9] K. Kawase, R. Kato, A. Irizawa, M. Fujimoto, K. Furukawa, K. Kubo, G. Isoyama, "Single picosecond THz pulse extraction from the FEL macropulse using a laser activating semiconductor reflective switch", in *Proc. FEL'15*, Daejeon, Korea, Aug. 2015, pp. 430-432. doi:10.18429/JACoW-FEL2015-TUP029

[10] K. Kawase, M.Nagai, K. Furukawa, M. Fujimoto, R. Kato, Y. Honda, G. Isoyama, "Extremely high-intensity operation of a THz free-electron laser using an electron beam with a higher bunch charge", *Nucl. Instrum. Methods Phys. Res., Sect. A*, vol. 960, Apr. 2020, 163582. doi:10.1016/j.nima.2020.163582

ISBN: 978-3-95450-220-2 ISSN: 2673-5474 doi: 10.18429/JACoW-FEL2022-TUAI1

CASCADED AMPLIFICATION OF ATTOSECOND X-RAY PULSES: TOWARDS TW-SCALE ULTRAFAST X-RAY FREE-ELECTRON LASERS*

P. L. Franz†, Z. Guo, R. Robles, Stanford University, Stanford, CA, USA
D. K. Bohler, D. Cesar, X. Cheng, T. Driver, J. P. Duris, A. Kamalov, S. Li,
R. Obaid, N. S. Sudar, A. L. Wang, Z. Zhang, J. P. Cryan, A. Marinelli
SLAC National Accelerator Laboratory, Menlo Park, CA, USA

Abstract

The natural time scale of valence electronic motion in molecular systems is on the order of hundreds of attoseconds. Consequently, the time-resolved study of electronic dynamics requires a source of sub-femtosecond pulses. Pulses in the soft x-ray domain can access core-level electrons, enabling the study of site-specific electron dynamics through attosecond pump/probe experiments. As time-resolved pump/probe experiments are nonlinear processes, these experiments require high brightness attosecond x-ray pulses. The X-ray Laser-Enhanced Attosecond Pulses (XLEAP) collaboration is an ongoing project for the development of attosecond x-ray modes at the Linac Coherent Light Source (LCLS). Here we report development of a high power attosecond mode via cascaded amplification of the x-ray pulse. We experimentally demonstrate generation of sub-femtosecond duration soft x-ray free electron laser pulses with hundreds of microjoules of energy. In conjunction with the upcoming high repetition rate at LCLS-II, these tunable, high intensity attosecond capabilities enable new nonlinear spectroscopic techniques and advanced imaging methods.

INTRODUCTION

Valence electronic motion in molecular systems is on the order of hundreds of attoseconds. Consequently, the time-resolved study of electron dynamics requires a source of sub-femtosecond pulses.

The X-Ray Laser-Enhanced Attosecond Pulses (XLEAP) collaboration is an ongoing project for the development of attosecond capabilities at the Linac Coherent Light Source (LCLS). The XLEAP project has previously demonstrated the generation of isolated soft x-ray attosecond pulses with pulse energy millions of times larger than any other source of isolated attosecond soft x-ray pulses, with a median pulse energy of 10 µJ and median pulse duration of 280 as at 905 eV photon energy [1]. Here we report the recent development of a high power attosecond mode via cascaded amplification of the x-ray pulse. We experimentally demonstrate generation of soft x-ray free electron laser pulses with hundreds of microjoules of energy.

* This work was supported by US Department of Energy Contracts No. DE-AC02-76SF00515.
† FRANZPL@STANFORD.EDU

CASCADED AMPLIFICATION

A density perturbation is introduced in the electron beam by laser pulse stacking at the photocathode [2]. The perturbation is amplified to a high current spike by acceleration and then beam compression in downstream wigglers and a magnetic chicane.

In the first cascade stage, the undulator taper is matched to the energy chirp of the electron beam at the current spike to produce the initial enhanced self-amplified spontaneous emission (ESASE) [3] x-ray pulse. The bunch is then delayed relative to the pulse by a second magnetic chicane, allowing the radiation to slip onto a fresh slice of the bunch. This seeds the FEL process and amplifies the pulse in the second cascade stage (Fig. 1).

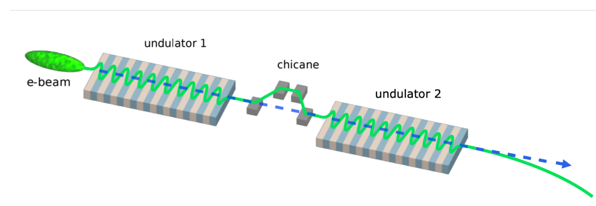

Figure 1: Schematic of the two-stage cascade. Cathode shaping has been used to create an ESASE current spike in the electron beam prior to the first undulator stage.

PRELIMINARY RESULTS

We have experimentally demonstrated the generation of soft x-ray pulses with hundreds of microjoules of energy using cascaded amplification in two FEL stages at LCLS. Figure 2 shows the pulse energy as a function of the number of undulator sections in the second stage. Using ten undulators the highest energy shots have over 300 µJ of pulse energy.

The highest energy pulses also have sufficient bandwidth to have sub-femtosecond duration near the fourier transform limit (Fig. 3). Previous XLEAP configurations have been within a factor of 2 of the fourier transform limit [1].

In the electron beam phase space, energy loss from reamplification in the second stage is seen as the lasing spike in the head of the beam (Fig. 4). The ESASE pulse initially lases at the current spike near the center of the beam, and is then slipped ahead to the fresh, non-chirped head of the beam. Energy loss from lasing in the head is visible when the second undulator stage is inserted, indicating that amplification of the ESASE pulse is taking place. Figure 5

ISBN: 978-3-95450-220-2 ISSN: 2673-5474 doi: 10.18429/JACoW-FEL2022-TUAI1

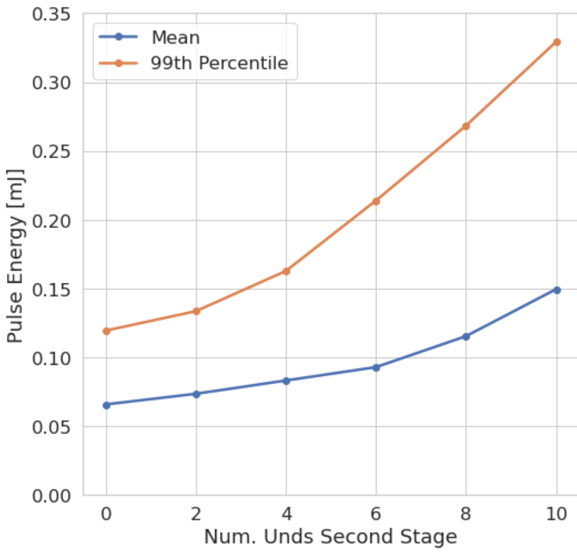

Figure 2: Distribution of pulse energies for different numbers of undulator segments in the second undulator stage.

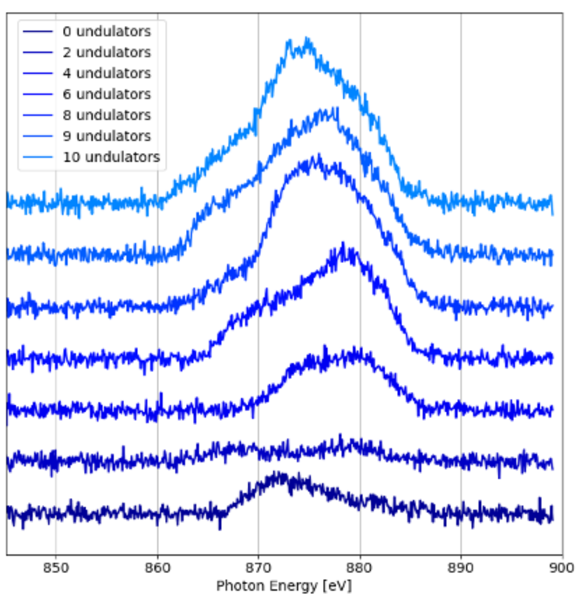

Figure 3: Example spectra are shown for different numbers of undulators in the second stage. The highest energy shots occur in the 10 undulator configuration, and have sufficient bandwidth for generation of sub-femtosecond pulses.

shows the joint distribution of pulse energy and bandwidth. The two quantities are correlated, with the most intense shots exhibiting the largest bandwdith. This is consistent with soliton-like superradiant amplification [4, 5], where the pulse duration decreases as the peak power increases.

CONCLUSION

The preliminary results suggest we can deliver a high power, sub-femtosecond duration soft x-ray mode at LCLS. This setup is scalable to the upcoming high repetition rate at LCLS-II. Analysis using angular streaking [6] of the experimental soft x-ray pulses to reconstruct the temporal profile of the x-ray pulses and fully characterize peak power is currently ongoing.

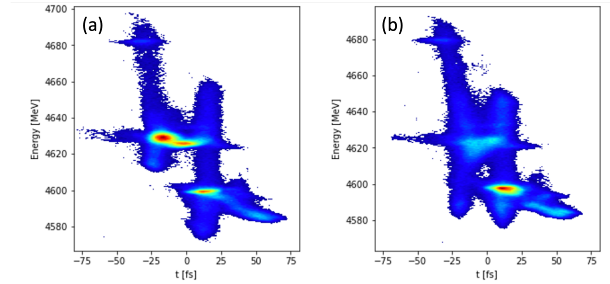

Figure 4: Representative electron bunch time-energy phase space distribution after the undulators. (a) Zero undulators in the second stage and 0.127 mJ pulse energy, (b) 10 undulators in the second stage and 0.328 mJ pulse energy. The ESASE pulse is initially lased at the current spike at the center of the beam (t = 12 fs). Energy loss from reamplification in the second stage is seen as the lasing spike in the head of the beam (t = -25 fs).

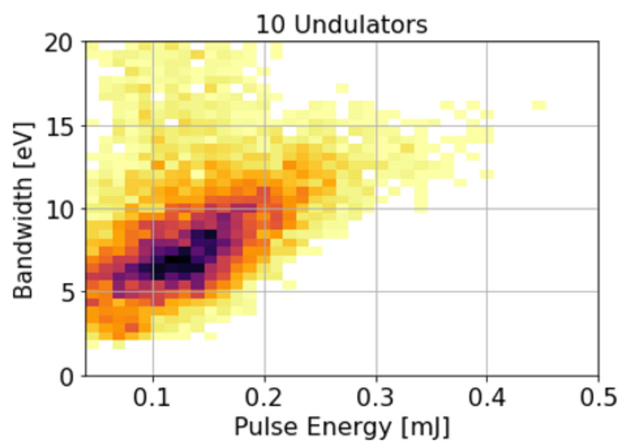

Figure 5: Distribution of bandwidth and pulse energies.The broadening of bandwidth with pulse energy is characteristic of superradiant lasing.

We are able to achieve highest pulse energy by inserting more undulator segments into the second stage; however, this may increase the SASE background. Future work will investigate scrambling the second undulator stage in order to suppress SASE background in this mode. Additionally, the broadening of bandwidth with pulse energy is characteristic of superradiant lasing. It is of interest to further study the lasing process in the second stage through start-to-end simulations.

ACKNOWLEDGMENTS

Travel to FEL2022 supported by the Robert H. Siemann Fellowship.

ISBN: 978-3-95450-220-2 ISSN: 2673-5474 doi: 10.18429/JACoW-FEL2022-TUAI1

REFERENCES

[1] J. Duris *et al.*, "Tunable isolated attosecond X-ray pulses with gigawatt peak power from a free-electron laser,", *Nature Photonics*, vol. 14, p. 30–36, 2020. doi:10.1038/s41566-019-0549-5

[2] Z. Zhang *et al.*, "Experimental demonstration of enhanced self-amplified spontaneous emission by photocathode temporal shaping and self-compression in a magnetic wiggler," *New J. Phys*, vol. 22, p. 083030, 2020. doi:10.1088/1367-2630/aba14c

[3] A. Zholents, "Method of an enhanced self-amplified spontaneous emission for x-ray free-electron lasers," *Phys. Rev. ST Accel. Beams*, vol. 8, p. 040701, 2005. doi:10.1103/PhysRevSTAB.8.040701

[4] R. Bonifacio *et al.*, "Superradiance in the high-gain free-electron laser," *Phys. Rev. A*, vol. 40, p. 4467, 1989. doi:10.1103/PhysRevA.40.4467

[5] K. Kim, Z. Huang and R. Lindberg. *Synchrotron Radiation and Free-Electron Lasers*, Cambridge, UK: Cambridge Univ. Press, 2017.

[6] S. Li *et al.*, "Characterizing isolated attosecond pulses with angular streaking," *Opt. Express*, vol. 26, pp. 4531–4547, 2018. doi:10.1364/OE.26.004531

ISBN: 978-3-95450-220-2 ISSN: 2673-5474 doi: 10.18429/JACoW-FEL2022-TUBO3

COMPARISON OF TRANSVERSE COHERENCE PROPERTIES IN SEEDED AND UNSEEDED FEL

M. Pop*, F. Curbis, S. Werin, Physics department, Lund University, Lund, Sweden
A. Simoncig, C. Spezzani, D. Garzella, E. Allaria , G. De Ninno, G. Perosa,
G. Penco, L. Foglia , L. Giannessi, M. Zangrando, M. Trovo,
M. Manfredda , N. Mahne, N. Mirian, P. R. Ribic,
S. Di Mitri , S. Spampinati, Elettra-Sincrotrone, Trieste, Italy
G. Geloni, European XFEL, Hamburg, Germany
N. Mirian, Deutsches Elektronen-Synchrotron (DESY), Hamburg, Germany

Abstract

The transverse coherence of the source is an important property for FEL experiments. Theory and simulations indicated different features for seeded and unseeded FELs but so far no direct comparison has been pursued experimentally on the same facility. At FERMI FEL one has the unique possibility to test both SASE and seeded configurations under the same operating conditions. In this contribution we present the experimental results of the characterization of transverse coherence with special attention to the evolution of this fundamental property.

INTRODUCTION

Novel investigation techniques such as diffractive imaging [1] and X-ray holography [2] require high levels of transverse coherence from the free electron laser (FEL) source. An X-ray FEL is usually driven by a high current, low emittence and low energy spread electron beam. To achieve ultra relativistic velocities and high currents, the electron beam is accelerated by a linear accelerator and compressed by dispersive sections called bunch compressors. After acceleration the beam is then fed through and undulator line called radiator where the interaction between the electrons and the electromagnetic field, which they themselves produce, exponentially amplifies the latter. The resulting FEL radiation is highly brilliant and highly coherent.

Taking advantage of the capabilities of FERMI FEL-2, we were able to study two distinct modes of operating an FEL: self amplified spontaneous emission (SASE) and seeded. The first option is able to produce gigawatts of power by directly sending the electrons through the radiator, without any prior phase space shaping [3–6]. The longitudinal coherence of SASE radiation can be improved if the FEL is seeded [7–9]. The most common seeding scheme, in the XUV range, is the high gain harmonic generation or HGHG. First, an external laser co-propagating with the electron beam inside an undulator, called modulator, imprints an energy modulation onto the electron beam. Then the energy modulation is transformed into density modulation in a dispersive section. Such density modulation exhibits bunching not only at the fundamental harmonic but, with diminishing intensities, also at higher harmonics. By this mechanism HGHG FELs can produce longitudinally coherent radiation at harmonics of the wavelength an external, optical laser.

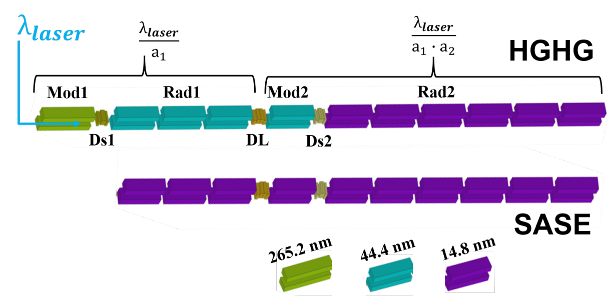

Figure 1: Schematic layout of FERMI FEL-2 operated in cascaded HGHG (top) and SASE (bottom) modes. The undulators are color-coded to the resonant wavelength they were set during the experiment.

Previous work showed that both SASE [10, 11] and seeded [12] FELs reach high degrees of transverse coherence. Furthermore, semi-analytical and simulation studies indicated that in a SASE FEL the transverse coherence is built up during the amplification process, reaching a maximum before intensity saturation. Aiming at qualitatively comparing the evolution of transverse coherence, this contribution presents the first experimental confirmation of the early saturation of this property in SASE FELs. A more in-depth description and analysis is presented in the original paper describing this experiment [13].

EXPERIMENTAL SETUP

The aim of our experiment was to estimate the transverse coherence properties of the FERMI FEL-2, operated in cascaded HGHG (seeded) and SASE modes. By progressively tuning out radiators, it is possible to obtain a transverse coherence gain curve which can be used to investigate how coherence is built up in the two types of FEL.

FERMI FEL-2 is usually run in fresh-bunch cascaded HGHG mode [14], which can produce longitudinally coherent pulses down to a few nanometers. However, for this

* corresponding author: mihai.pop@maxiv.lu.se

ISBN: 978-3-95450-220-2 ISSN: 2673-5474 doi: 10.18429/JACoW-FEL2022-TUBO3

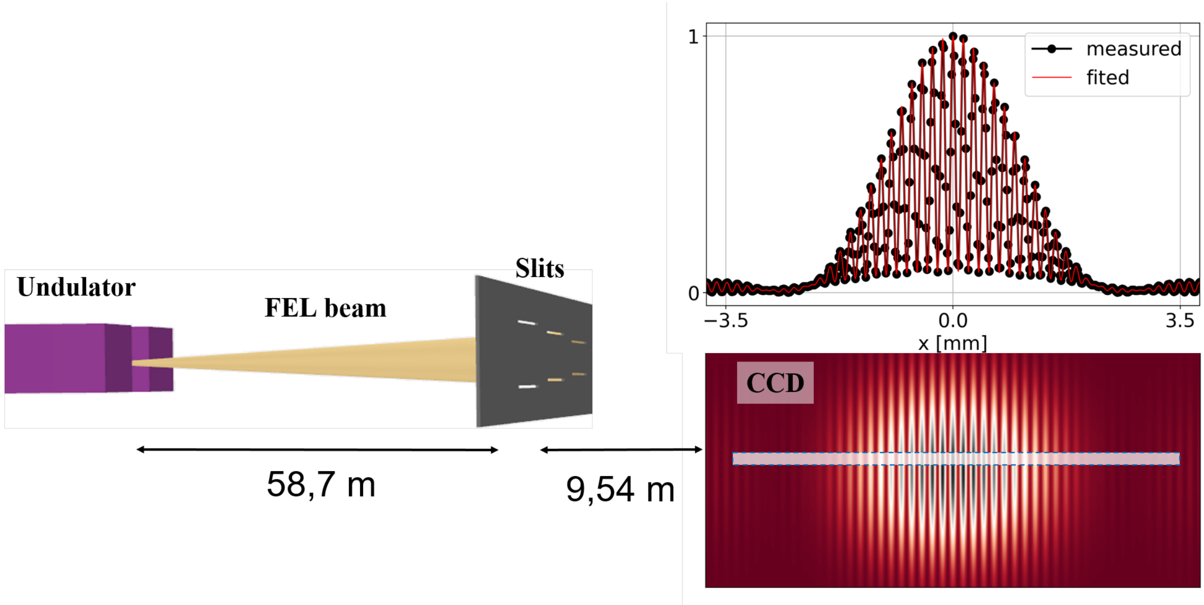

Figure 2: Layout of the measurement setup. The FEL radiation propagates 58.7 m from the end of the last undulator to the slits. The diffracted light travels 9.54 m from the slits to a CCD. The 1D interference pattern(top right) is obtained by averaging along the vertical direction of the area highlighted in white on the CCD.

experiment we chose as final radiation wavelength 14.8 nm to be able to obtain significant radiation amplification for the SASE mode of operation. As show in Fig. 1, the external laser wavelength was 266.4 nm and in the first stage the radiator was set to the 6^{th} harmonic, 44.4 nm. The second stage was made resonant to the third harmonic of the second stage, i.e., 14.8 nm. In SASE operation all undulators, with the exception of the first modulator which was fully opened, were set resonant to the final 14.8 nm wavelength.

The figure of merit we used to characterize the transverse coherence was the total degree of transverse coherence ζ [15]. In the Gauss-Schell model [11] the procedure for obtaining ζ involves determining the transverse coherence length l_c and the radiation transverse size σ. The transverse coherence length is deduced by fitting the decay of the degree of coherence $\boldsymbol{g}$ as a Gaussian. The degree of coherence is obtained by fitting the intensity of the interference pattern form a *Young double-slit* experiment to a theoretical function $I_{fit}(w, d, z, \boldsymbol{g}, ..)$ that takes into account the width w and separation d of the slits, the propagation distance from the slits to the screen z and the degree of coherence $\boldsymbol{g}$ among other things. The special fitting function used in our experiment is detailed in the appendix of the original paper [13].

The layout of the experimental setup for measuring transverse coherence is presented in Fig. 2. The diffraction pattern is recorded on a CCD camera capable of detecting single shot images. For this experiment we only investigated the horizontal direction (OX) but we expect the vertical direction to yield similar results.

RESULTS

As mentioned in the previous section, by performing the Young double-slit experiment at various slit separations one can obtain the transverse coherence length. In Fig. 3 we plot the decay of the degree of coherence $\boldsymbol{g}$ as the slit separation increases. The fitted coherence lengths are $l_{c_x}^{SASE} = 1.88 \pm 0.2$ mm and $l_{c_x}^{HGHG} = 2.2 \pm 0.1$ mm for SASE and HGHG modes of operation respectively.

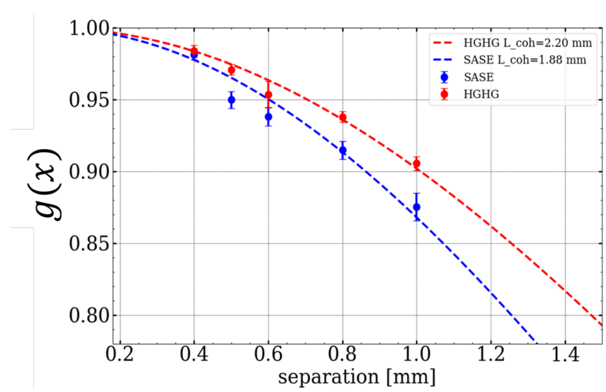

Figure 3: Measured (dots with error bars) an fitted (dashed lines) for HGHG (red) and SASE (blue) modes of operation.

The transverse coherence sizes, of the two modes were measured to be $\sigma_x^{SASE} = 1.25 \pm 0.05$ mm and $\sigma_x^{HGHG} = 1.38 \pm 0.1$ mm. These measurements, in conjunction with the transverse coherence length give the following values for the total degree of transverse coherence $\zeta_x^{SASE} = 0.6 \pm 0.03$ and $\zeta_x^{HGHG} = 0.62 \pm 0.02$.

By opening the gap of more and more undulators, we were able to obtain snapshots of the FEL radiation at different

ISBN: 978-3-95450-220-2 ISSN: 2673-5474 doi: 10.18429/JACoW-FEL2022-TUBO3

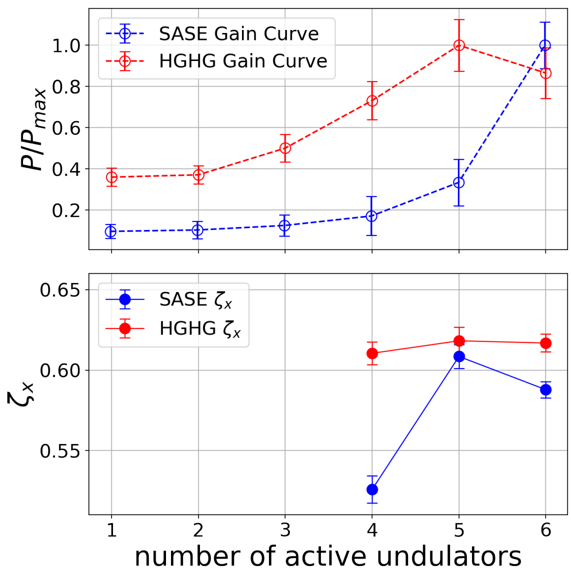

Figure 4: Intensity gain curve (top) and total degree of coherence evolution (bottom) for HGHG (red) and SASE (blue) modes of operation.

stages in the the gain process, both in terms of radiation intensity but also in terms of transverse coherence. In Fig. 4 we plot the evolution of radiation intensity (top) and transverse coherence (bottom) as a function of number of active undulators for SASE and seeded modes of operation using the transverse coherence measurement procedure described in the previous section. As stated in [13] even though the radiation intensity did not reach saturation in the available undulator length, we did manage to achieve saturation of transverse coherence.

The evolution of transverse coherence, Fig. 4 (bottom), suggests qualitatively different mechanisms for building up this property in the two modes of operation (SASE and HGHG). In the seeded case, we observe an almost constant value for transverse coherence along the gain curve, while for SASE there is a visible evolution, indicating that transverse coherence is built up similarly to longitudinal coherence. The HGHG trend suggests that seeded modes of operation "inherit" the transverse coherence from the seed laser.

The different buildup processes of seeded and SASE FEL's transverse coherence observed in the gain based data is confirmed by a complementary measurement in which the energy spread of the electron beam is varied. By using a laser heater system [16], one can induce extra, uncorrelated, energy spread into the electron beam. This has the effect of changing the gain length of the FEL. We can thus change the position in the gain curve at which we measure the transverse coherence by modifying the energy spread. In Fig. 5 we can see that the change in energy spread has a similar effect on the intensity (magenta trace) on the SASE (top) and HGHG (bottom) modes of operation. However, looking at the scaled transverse coherence we find considerably different trends between SASE and HGHG. While for HGHG it maintains at an almost constant level, for SASE the transverse coherence seems to be highly dependent on the position in the gain curve. These measurements agree qualitatively with the measurements based on tuning out undulators and strengthen the interpretation that transverse coherence develops by fundamentally different mechanisms in SASE and seeded FEL.

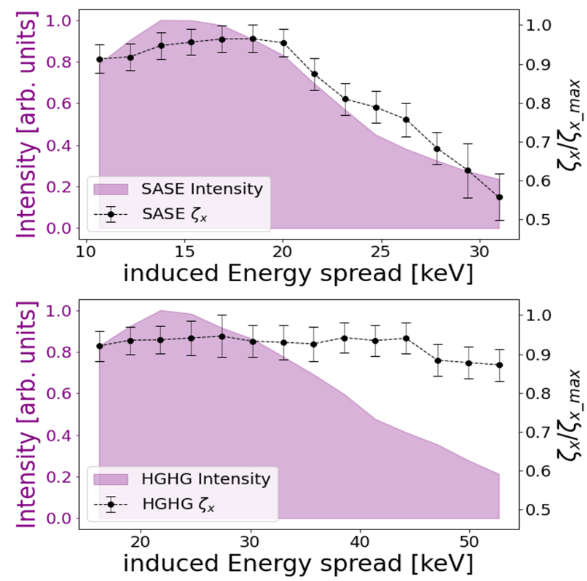

Figure 5: Intensity variation (magenta) and scaled total degree of coherence (black) with induced electron energy spread, for SASE (top) and HGHG (bottom) modes of operation.

CONCLUSIONS

At FERMI FEL-2 we were able to compare, for the first time, the HGHG and SASE modes of operation in terms of transverse coherence. In our experimental setup SASE and HGHG FEL reached similar maximum values of transverse coherence. Furthermore our data shows that the way in which the two modes of operation develop transverse coherence is fundamentally different. While in the SASE process transverse coherence is built up and reaches a maximum earlier than power saturation, in HGHG the FEL starts of with a high degree of transverse coherence and maintains it all through the amplification process.

ACKNOWLEDGEMENTS

We would like to thank the entire team of FERMI FEL for their support during and after the experiment.

REFERENCES

[1] H. N. Chapman *et al.*, "Femtosecond diffractive imaging with a soft-X-ray free-electron laser," *Nat. Phys.*, vol. 2, no. 12, pp. 839–843, 2006. doi:10.1038/nphys461

ISBN: 978-3-95450-220-2 ISSN: 2673-5474 doi: 10.18429/JACoW-FEL2022-TUBO3

[2] C. J. Jacobsen, "X-ray microscopy using FELs: possibilities and challenges," in *Proc. SPIE 3925*, International Society for Optics and Photonics, vol. 3925, 2000, pp. 16–25. doi:10.1117/12.384260

[3] R. Bonifacio, C. Pellegrini, and L. Narducci, "Collective instabilities and high-gain regime in a free electron laser," 6, vol. 50, 1984, pp. 373–378. doi:10.1016/0030-4018(84)90105-6

[4] E. Saldin, E. V. Schneidmiller, and M. V. Yurkov, *The physics of free electron lasers*. Springer Science & Business Media, 1999.

[5] L. H. Yu, "Generation of intense uv radiation by subharmonically seeded single-pass free-electron lasers," *Phys. Rev. A*, vol. 44, pp. 5178–5193, 1991. doi:10.1103/PhysRevA.44.5178

[6] P. Emma *et al.*, "First lasing and operation of an ångstrom-wavelength free-electron laser," English (US), *Nat. Photonics*, vol. 4, no. 9, pp. 641–647, 2010. doi:10.1038/nphoton.2010.176

[7] L.-H. Yu *et al.*, "High-Gain Harmonic-Generation Free-Electron Laser," *Science*, vol. 289, no. 5481, pp. 932–934, 2000. doi:10.1126/science.289.5481.932

[8] E. Allaria *et al.*, "Highly coherent and stable pulses from the FERMI seeded free-electron laser in the extreme ultraviolet," *Nature Photonics*, vol. 6, no. 10, pp. 699–704, 2012. doi:10.1038/nphoton.2012.233

[9] P. R. Ribič *et al.*, "Coherent soft X-ray pulses from an echo-enabled harmonic generation free-electron laser," *Nat. Photonics*, vol. 13, no. 8, pp. 555–561, 2019. doi:10.1038/s41566-019-0427-1

[10] R. Ischebeck *et al.*, "Study of the transverse coherence at the ttf free electron laser," *Nucl. Instrum. Methods Phys. Res., Sect. A*, vol. 507, no. 1, pp. 175–180, 2003, Proceedings of the 24th International Free Electron Laser Conference and the 9th Users Workshop. doi:10.1016/S0168-9002(03)00866-0

[11] I. A. Vartanyants and A. Singer, "Coherence properties of hard x-ray synchrotron sources and x-ray free-electron lasers," *New J. Phys.*, vol. 12, no. 3, p. 035 004, 2010. doi:10.1088/1367-2630/12/3/035004

[12] O. Y. Gorobtsov *et al.*, "Seeded X-ray free-electron laser generating radiation with laser statistical properties," *Nat. Commun.*, vol. 9, no. 1, p. 4498, 2018. doi:10.1038/s41467-018-06743-8

[13] M. Pop *et al.*, "Single-shot transverse coherence in seeded and unseeded free-electron lasers: A comparison," *Phys. Rev. Accel. Beams*, vol. 25, p. 040 701, 4 2022. doi:10.1103/PhysRevAccelBeams.25.040701

[14] E. Allaria *et al.*, "Two-stage seeded soft-X-ray free-electron laser," *Nat. Photonics*, vol. 7, no. 11, pp. 913–918, 2013. doi:10.1038/nphoton.2013.277

[15] J. W. Goodman, *Statistical optics*. John Wiley & Sons, 2015.

[16] S. Spampinati *et al.*, "Laser heater commissioning at an externally seeded free-electron laser," *Phys. Rev. ST Accel. Beams*, vol. 17, p. 120 705, 2014. doi:10.1103/PhysRevSTAB.17.120705

ISBN: 978-3-95450-220-2 ISSN: 2673-5474 doi: 10.18429/JACoW-FEL2022-TUCO3

FEL RESONANCE OF CIRCULAR WAVEGUIDE MODES

A. Fisher*, P. Musumeci
Department of Physics and Astronomy, University of California Los Angeles, USA

Abstract

The THz gap is a region of the electromagnetic spectrum where high average and peak power radiation sources are scarce while scientific and industrial applications grow in demand. Free-electron laser coupling in a magnetic undulator can provide radiation generation in this frequency range, but slippage effects require the use of relatively long and low current electron bunches in the THz FEL, limiting the amplification gain and output peak power. The introduction of a waveguide can contain the radiation and match the radiation group velocity to the electron beam longitudinal velocity, allowing strong compression of the beam to provide seeding for a high efficiency THz FEL. We discuss the resonance and implementation of the waveguide modes in GPTFEL and consider simulations of the THz FEL, targeting resonance with the TE11 and TE12 modes.

INTRODUCTION

Recent experimental results have shown that large energy conversion efficiencies in a THz free electron laser can be achieved with strong undulator tapering and by introducing a waveguide to match the radiation group velocity to the electron beam longitudinal velocity [1]. The experiment relied on the coupling between the helical trajectory of the electrons and the fundamental lowest frequency TE11 mode of the waveguide. In this paper, we consider the resonance of higher order waveguide modes beyond the TE11 mode.

The paper is organized as follows. First we define the circular waveguide modes in general form. Next we describe the implementation in GPTFEL [2] and compare the simulated gain lengths in a untapered undulator amplifier to analytical expressions from the 1D theory. Finally, we compare single-mode and multi-mode simulations of a THz FEL at zero-slippage resonance for the TE11 mode and then the TE12 mode using planned experiment parameters.

CIRCULAR WAVEGUIDE MODES

TE and TM modes for a circular waveguide are written in terms of the the longitudinal fields H_z and E_z, respectively. For brevity, we present equations only for TE radiation modes as they couple more effectively to the electron beam in the undulator. A general description of circular waveguide modes can be found in most electrodynamics textbooks [3].

The discrete TE waveguide modes are solutions of a 2D Helmholtz equation

$$\left[\frac{\partial^2}{\partial\rho^2}+\frac{1}{\rho}\frac{\partial}{\partial\rho}+\frac{1}{\rho^2}\frac{\partial^2}{\partial\phi^2}+k_\perp^2\right]H_z=0, \qquad \left.\frac{\partial H_z}{\partial n}\right|_{\rho=R}=0$$
$$H_z^{mn}=H_0 J_m\left(k_{mn}\rho\right)e^{\pm im\phi} \tag{1}$$

* afisher000@g.ucla.edu

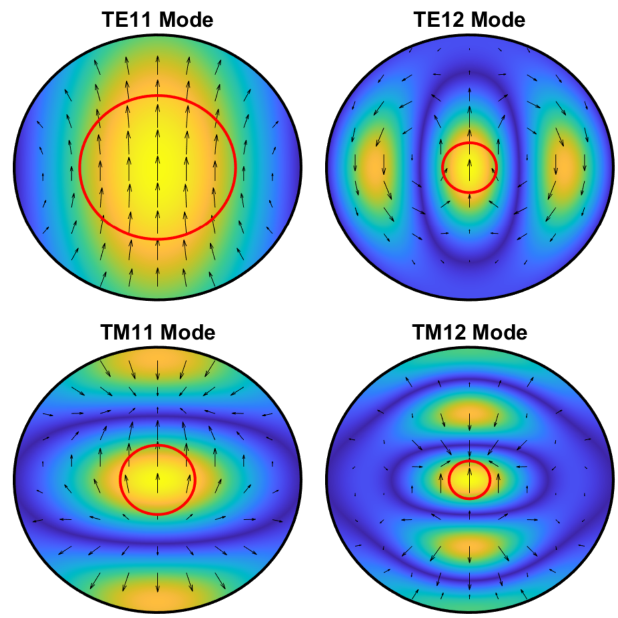

Figure 1: Waveguide Modes. Red circles show electron trajectory and amplitude of $\vec{v}_z \cdot \vec{E}_\perp^{mn}$ is shown by colormap.

for $m = 0, 1, \ldots$ and $n = 1, 2, \ldots$ where $k_{mn} = w_{mn}/R$, w_{mn} is the n^{th} zero of the derivative of the m^{th} Bessel function ($J_m'(w_{mn}) = 0$), R is the waveguide radius, and H_0 is a normalization constant. The transverse fields are given by

$$\vec{E}_\perp^{mn}=\frac{-i\omega\mu}{k_{mn}^2}\left[\hat{z}\times\nabla_\perp H_z^{mn}\right] \tag{2}$$
$$\vec{H}_\perp^{mn}=\frac{\omega\epsilon}{k_z}\left[\hat{z}\times\vec{E}_\perp^{mn}\right]. \tag{3}$$

We choose $H_0 = \frac{\sqrt{2}k_{mn}}{\mu\omega}$ to normalize $|\vec{E}_\perp^{mn}|^2$ to 1.

Due to the symmetry of the spiraling electron trajectory, only TE and TM modes with $m = 1$ allow for net energy exchange with an electron over an undulator period. The first four of these modes are shown in Fig. 1. The red circles show the trajectory radius of the electron beam at the zero-slippage resonance and the colormap shows the amplitude of $\vec{v}_e \cdot \vec{E}_\perp^{mn}$.

The ratio of electron beam trajectory radius to waveguide radius is essentially independent of resonant frequency or beam energy and is given by $\frac{r_{\text{traj}}}{R} = \frac{K}{\sqrt{1+K^2}}\frac{\beta_z}{w_{mn}}$ where K is the undulator strength parameter, and β_z is the dimensionless relativistic longitudinal velocity. For TM modes, w_{mn} is the n^{th} zero of the m^{th} Bessel function ($J_m(w_{mn} = 0)$). While there are tight trajectory tolerances to ensure an effective energy exchange, the decreasing ratio suggests that higher modes could be used to target high frequencies in

ISBN: 978-3-95450-220-2 ISSN: 2673-5474 doi: 10.18429/JACoW-FEL2022-TUCO3

cases where the gain of the TE11 mode is limited by charge transmission and wakefield effects.

We simulate the FEL interaction using GPTFEL [2] which expands the radiation field into frequency and spatial modes as

$$\vec{\mathbf{E}}(\vec{x}, z, t) = \sum_{m,n} a_{mn}(t)\vec{\Theta}_{mn}(\vec{x}, k_{mn}, t)e^{ik_{mn}z-i\omega_{mn}t} \quad (4)$$

where a_{mn} is a complex amplitude, $\vec{\Theta}_{mn} = \vec{E}^{mn}_{\perp} + \vec{E}^{mn}_{z}$ is the mode electric field, and m, n index the frequency and spatial modes, respectively.

The change in amplitude is driven by the dot product of the mode with the electron beam current density [4].

$$\dot{a}_{mn} = -\sum_{j} \frac{q_j}{2\epsilon_0 A_{mn}}(\vec{\mathbf{v}}_j \cdot \vec{\Theta}^*_{mn,j})e^{-ik_{mn}z_j+i\omega_{mn}t} \quad (5)$$

where j indexes the macroparticles, q_j is macroparticle charge, and A_{mn} is the effective mode area.

The effective mode areas are the same for TE and TM modes and are given by

$$\begin{aligned} A_{mn} &= \int |\Theta_{mn}|^2 dr_{\perp} \\ &= \frac{4\pi}{k^2_{mn}} \int_0^{k_{mn}R} \left[\frac{m^2}{x} J_m(x)^2 + xJ'_m(x)^2\right] dx. \end{aligned} \quad (6)$$

AMPLIFIER GAIN LENGTHS

We benchmark simulations of higher order modes by comparing the gain length for a amplifier using a simplified case with no space charge, beam energy spread, or emittance. Electron beams are initialized with a gaussian longitudinal charge distribution ($\sigma_z = 4\lambda$) and a peak current of 20 A. The untapered undulator has a field strength of $B_0 = 730$ mT and period $\lambda_u = 3.2$ cm. The nominal beam energy and waveguide radius are chosen to satisfy the zero-slippage waveguide condition for a frequency of 165 GHz. The amplifier is seeded with a 1% bunching factor using GPT's AddZoscillation function, taking into account the beam compression experienced upon entering the undulator due to a reduced longitudinal velocity.

The theoretical expression for energy modulation includes the electric field mode to account for a reduction in the experienced field by the particle off axis.

$$\frac{d\gamma_j}{dz} = \frac{-ecK|\Theta_j|}{\sqrt{2}mc^3\gamma_0}\Re\left(ae^{i\theta_j}\right) \quad (7)$$

where K is the rms normalized vector potential, $\Theta_j = \Theta_{mn,j}$, $a = a_{mn}$, and θ is the ponderomotive phase. The factor for resonant electrons is $|\Theta_0| \approx 0.65$ for TE modes and $|\Theta_0| \approx 0.88$ for TM modes.

The one dimensional gain length is $L_{g,1D} = \lambda_u/4\pi\sqrt{3}\rho$ where the dimensionless Pierce parameter is given by

$$\rho = \left(\frac{K^2\lambda_u^2 I|\Theta_0|^2}{16\pi\gamma_0^3 A_{mn} I_A}\right)^{1/3} \quad (8)$$

Table 1: Gain Length Simulations

Mode	L_g (cm)	$L_{g,1D}$ (cm)
TE11	9.9	8.7
TM11 (no Ez)	29.7 (12.2)	10.1
TE12	16.4	13.6

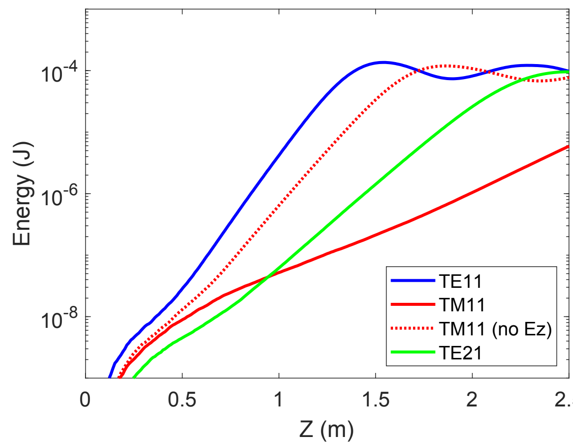

Figure 2: Untapered amplifier simulations for individual modes.

and $I_A = \frac{4\pi\epsilon_0 mc^3}{e}$=17045 A is the Alfven current.

1 shows the measured and theoretical gain lengths for the TE11, TM11, and TE12 modes for the energy data shown in Fig. 2. The measured gain lengths are within 20% of theory and at least part of the discrepancy can be explained by dispersive effects. Only one spatial waveguide mode was used in each simulation and the electron beam energy was tuned to minimize the gain length. It has already been seen that a positive energy detuning produces stronger results in the THz waveguide FEL due to broadening of the dispersion curves from the finite FEL bandwidth, and also finite beam energy spread and emittance. The longitudinal electric field of the TM11 mode accelerates resonant particles, countering the energy modulation of the FEL and greatly increasing the radiation gain length. For comparison, we include a simulation for TM11 where we have unphysically set $E_z = 0$.

The FEL coupling is reduced for higher order modes due to an increasing mode area. This would require weaker undulator tapering limiting the single pass gain of a THz FEL. However this could be countered by the ability to transmit more charge through the larger waveguide.

WAVEGUIDE FEL SIMULATION

An experiment is being planned on the Pegasus beamline at UCLA to produce 0.33 THz radiation from a 7.4 MeV electron beam with high efficiency in a single pass. The experiment parameters and beam transport are discussed in [5]. The electron beam is compressed to provide a significant bunching factor ($b \approx 0.8$) that seeds the THz waveguide FEL. The waveguide radius is chosen for resonance with

ISBN: 978-3-95450-220-2 ISSN: 2673-5474 doi: 10.18429/JACoW-FEL2022-TUCO3

the TE11 mode, and it is expected that higher order modes will have negligible effect due to the higher cutoff frequencies. To confirm, we compare the FEL interaction of the compressed beam in single-mode (TE11 only) and multi-mode (TE11-TM12) simulations. Figure 3 confirms that the higher order modes are almost entirely suppressed. There is a slight decrease in the TE11 spectra corresponding to a 5% decrease in total pulse energy, but in practice this is negligible when compared to the effects of undulator field tuning errors and charge transmission on the total energy. The simulated efficiency is 24%.

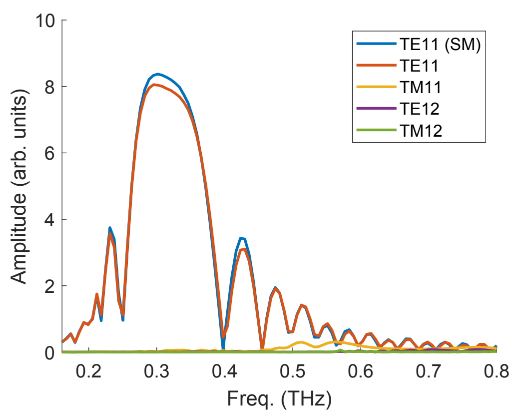

Figure 3: Single-mode (SM) and multi-mode spectra of THz FEL with zero-slippage resonance for TE11.

Another interesting question is how the single-mode and multi-mode simulations compare for resonance at the TE12 mode with a larger waveguide radius. The tapering was reduced and the charge was doubled to ensure resonance through the entire undulator. The final simulated efficiency was 15%. We see in Fig. 4 that the TE11 and TM11 do present themselves in the multi-mode simulation, while the TM12 mode is still suppressed. This makes sense as the TE11 and TM11 modes will not satisfy zero slippage, but will satisfy the FEL phase resonance condition, $k_z + k_u = \omega/c\beta_z$, at two frequencies due to the quadratic waveguide dispersion. The expected frequencies are 0.02 THz and 0.60 THz for TE11 and 0.10 THz and 0.53 THz for TM11, which agrees well with Fig. 4. The lower frequencies (outside the range of the simulation) experience a larger slippage than the higher frequencies as can be seen by comparing the group velocities relative to the electron beam. While lower frequencies do see larger bunching factors, the bunching is still large (0.59) at higher frequencies (0.60 THz). Finally, $|\Theta_0| \approx 1$ for the TE11 and TM11 modes.

CONCLUSION

Waveguides can be used to overcome FEL slippage at long radiation wavelengths by matching the subluminal group velocity to the longitudinal electron beam velocity. We show how circular waveguide modes can be simulated in GPT-FEL and display the couplings in theoretical expression and 1D amplifier simulations. We confirm that modes at higher

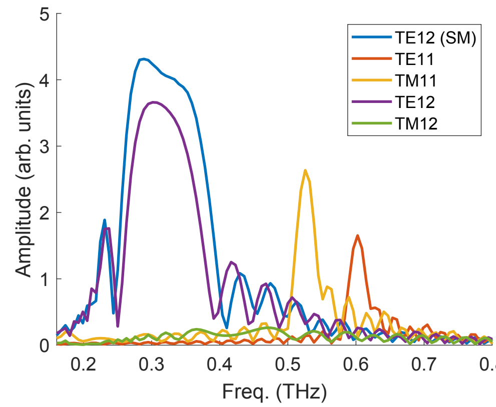

Figure 4: Single-mode (SM) and multi-mode spectra of THz FEL with zero-slippage resonance for TE12.

resonances are suppressed due to their high cutoff frequencies with simulations of a THz waveguide FEL. Finally, we considered the possibility of resonating with a higher order mode, and find that other modes are excited by satisfying the FEL phase resonance condition with slippage.

ACKNOWLEDGMENTS

This work was supported by DOE grant No. DE-SC0009914 and a fellowship from the Julian Schwinger Foundation for physics research.

REFERENCES

[1] A. Fisher *et al.*, “Single-pass high-efficiency terahertz free-electron laser,” *Nature Photonics*, pp. 1–7, 2022. doi:10.1038/s41566-022-00995-z

[2] A. Fisher, P. Musumeci, and S. Van der Geer, “Self-consistent numerical approach to track particles in free electron laser interaction with electromagnetic field modes,” *Physical Review Accelerators and Beams*, vol. 23, no. 11, p. 110 702, 2020.

[3] A. Zangwill, *Modern electrodynamics*. Cambridge University Press, 2013.

[4] A. Gover *et al.*, “Superradiant and stimulated-superradiant emission of bunched electron beams,” *Reviews of Modern Physics*, vol. 91, no. 3, p. 035 003, 2019.

[5] A. Fisher *et al.*, “Simulating Beam Transport with Permanent Magnet Chicane for THz Fel,” in *Proc. IPAC’22*, Bangkok, Thailand, 2022, paper TUPOPT032, pp. 1077–1080. doi:10.18429/JACoW-IPAC2022-TUPOPT032

ISBN: 978-3-95450-220-2 ISSN: 2673-5474 doi: 10.18429/JACoW-FEL2022-TUCO4

SYNCHRONIZED TERAHERTZ RADIATION AND SOFT X-RAYS PRODUCED IN A FEL OSCILLATOR

M. Ruijter*, A. Bacci, I. Drebot, M. Rossetti Conti, A. R. Rossi, S. Samsam[1], L. Serafini
INFN-Section of Milan, Milan, Italy
[1]also at Università La Sapienza, Rome, Italy
M. Opromolla[2], V. Petrillo[2], Università degli Studi di Milano, Milan, Italy
[2]also at INFN-Section of Milan, Milan, Italy

Abstract

We present a scheme to generate synchronized THz and Soft X-ray radiation pulses by using a Free-Electron Laser Oscillator driven by a high repetition rate (of order 10-100 MHz) energy recovery linac. The backward THz radiation in the oscillator cavity interacts with a successive electron bunch, thus producing few 10^5 Soft/Hard X-ray photons per shot (namely 10^{12}-10^{13} photons/s) via Thomson back-scattering, synchronized with the mJ-class THz pulse within the temporal jitter of electron beams in the superconducting linac (< 100 fs). Detailed simulations have been performed in order to assess the capability of the scheme for wavelengths of interest, between 10 and 50 µm for the TeraHertz radiation and $0.5 - 3$ nm for the X-rays.

INTRODUCTION

Researches at the science frontiers need tunable, brilliant and coherent radiation pulses. Two synchronized different wavelengths are required for testing phenomena on different time scales or for pump and probe experiments [1–3]. The combination of THz radiation sources with the most advanced X-ray facilities is so promising that the laboratories allocating the most brilliant X-ray sources, namely Synchrotrons and Free-Electron Lasers (FELs), are also endowed with THz sources to be coupled with the X-rays [4,5]. However, in this way, these experiments can be exclusively carried out in huge laboratories, limiting the diffusion of this research technique. Regarding the THz generation, much interest converges on FELs, widely tunable and delivering high quality pulses presenting energy stability, polarization, spectral and spatial optimal distribution. THz FELs operate mainly as oscillators, i.e. they are equipped with resonators confined by mirrors [6–10]. This operational mode guarantees compactness, relaxed requirements of the electron bunch quality and the fact that oscillators are suitable for Super Conducting (SC) Linacs, allowing the generation of powerful quasi-cw light. The dual source (THz plus X-rays) we expose here (see also [11]) exploits the fact that the THz radiation generated by the passage of successive electron bunches in the FEL undulator, driven by a SC ERL, propagates at each round trip inside the cavity, first forward towards the front mirror and then backward to the rear mirror. After the reflection, the radiation hits a successive electron bunch in a condition suitable for Thomson back-scattering. THz FEL intracavity pulses with mJ-class energy at 15-50 µm of wavelength, driven by 20-100 MeV energy electron bunches, can deliver up to few 10^5 soft X-ray photons per shot by Thomson back-scattering at a rate of 10-100 MHz and synchronized with the THz radiation. The total of 10^{12}-10^{13} X photons generated per second can be useful in many imaging fields (see Ref. [3]). This source is more compact and less expensive than Synchrotrons and Soft X-ray FELs, can be developed in small/medium size laboratories, hospitals or university campuses and represents an elementary upgrade of a basic THz FEL Oscillator. Section II describes the generalities of the double source constituted by a THz Free-Electron Laser Oscillator and by a X-ray Thomson source driven by the same electron beam. Section III presents the numerical results of the FEL and Thomson sources. We conclude by presenting considerations about the optimal layout and discussing the possibility of developing such a device.

* Marcel.Ruijter@mi.infn.it

DUAL SOURCE GENERALITIES

A SC Energy Recovery Linac (ERL) is required because the FEL Oscillator is based on the passage of successive electron beams at large repetition rate inside the undulator and the energy recovery option allows for sustainable radiation generation. The ERL is similar to those described in [9, 10]. Table 1 presents values of the electron beam parameters given by start to end simulations. The electron beam provides THz radiation with interesting properties and, at the same time, suitable for driving Thomson back-Scattering.

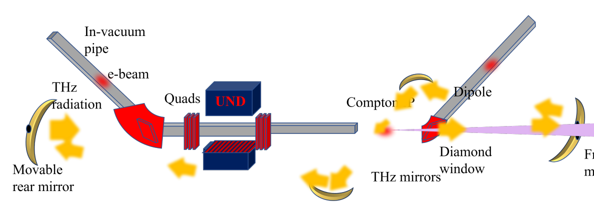

Figure 1: Dual source of THz and X-ray radiation. The cavity is constituted by four mirrors. The Thomson interaction point is on the right. E-beam and THz radiation interact at angle.

Figure 1 shows an option based on a four mirror cavity of the radiation source layout. After the first reflection off-axis, the radiation is obliquely sent to the Thomson interaction point (IP) by a second mirror, the scattering taking therefore place at a small angle. The THz radiation circumvents the

ISBN: 978-3-95450-220-2 ISSN: 2673-5474 doi: 10.18429/JACoW-FEL2022-TUCO4

undulator. The focusing needed for increasing the luminosity of the process is provided by the mirrors surrounding the IP. This configuration is quite usual in Thomson sources based on lasers in Fabry-Peròt cavities [12–14]. The radiation should arrive exactly synchronized to a successive electron beam at the beginning of the undulator, so that $L_{rt} = n\Delta l$ (n integer), Δl being the electron bunch-to bunch inter-distance and L_{rt} the round trip. The Thomson IP is set in a position where the length L_c of the path the radiation covers for coming back to this same point after the reflection equals a multiple of the distance between two electron bunches, i.e., $L_c = n'\Delta l$ (n' integer). The THz radiation, propagating backward, crosses a successive electron bunch and scatters X-ray radiation in the direction of the electrons at the same repetition rate. Since the X-ray and the THz radiation flowing through the front mirror are generated in sequence by two successive bunches of the electron beam train, they are naturally synchronized within the characteristic temporal jitters of the SC accelerator. The possible combinations of THz and X-ray wavelengths produced by the device are analysed in Fig. 2. The resonance condition of the FEL oscillator is $\lambda_{THz} = \lambda_w(1 + a_w^2)/(2\gamma^2)$, where $\gamma = E/mc^2$ is the Lorentz factor of the electron beam, λ_w and a_w the period and the undulator parameter. Figure 2

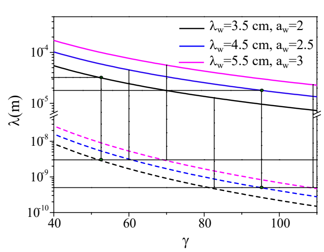

Figure 2: Wavelength of the THz and X-ray radiation vs. electron Lorentz factor γ. Solid lines: THz radiation produced with the FEL oscillator. Dashed lines: X-ray radiation generated by means of Thomson back-scattering.

shows the resonant values λ_{THz} as a function of γ ranging from 40 (20 MeV) to 110 (55 MeV), for various values of the undulator period λ_w between 3.5 cm and 5.5 cm at values of a_w between 2 and 3 respectively. The undulator can be tuned to cover a wide THz wavelength range with relatively low electron energy values. By changing a_w, a wider range of wavelengths can be produced.

In the same graph, the Compton radiation wavelength $\lambda_X \simeq \lambda_{THz}/(4\gamma^2)$ generated by the scattering between the electron beam and the THz pulses is also presented (dotted lines), thus showing the couples of THz/X-ray wavelengths simultaneously generated. Interesting wavelengths in the soft-tender X-ray regime are, for instance, the water window at λ =3 nm [15] or the spectroscopy range around 0.5 nm [16]. THz radiation at 30-55 μm can be paired with X-rays in the water window at 3 nm. With the same undulator, THz radiation in the range 13-25 μm generates X rays at

Table 1: Electron beam characteristics at the undulator entrance

Quantity	Unit	Value
Energy	MeV	20-100
Charge	pC	100-200
Energy spread	%	0.1-1
Slice emittance	mm mrad	0.6-2
Transverse size	mm	0.1-0.25
Length	mm	0.5-5
Average current	mA	<7-8

λ =0.5 nm. Sustainable undulator lengths (few meters) and reasonable peak currents (7 A $< I <$ 25 A), in the range attainable by a SC high repetition rate accelerator, are considered. Electron beams with 150 pC of charge, 15-20 A of peak current, reasonable values of emittance (< 2 mm mrad) and energy spread ($< 5 \times 10^{-3}$) could produce more than 1 mJ of intra-cavity (IC) radiation energy at 10-50 μm of wavelength in less than 2 m of undulator, with extra-cavity (EC) pulses of tens of μmJ. The intra-cavity THz pulse constitutes the scattering radiation in the Inverse Compton process, generating N_X photons at λ_X. The number of X-ray photons per shot N_X can be indeed estimated as [17]:

$$N_X = \sigma_{Th} \frac{N_e N_{THz}}{2\pi({\sigma_e}^2 + {\sigma_{THz}}^2)}. \tag{1}$$

Being σ_{Th}= $6.65 \times 10^{-29} m^2$ the Thomson cross section, $N_e = Q/e = 1.25 \times 10^9$, σ_e = 100 μm, $N_{THz} = E_{IC}/(h\nu_{THz})= E_{IC}\lambda_{THz}/(hc) \simeq$ 2-5 $\times 10^{17}$, the system produces an amount of about 10^5 X-ray photons per shot in the whole spectrum, provided that $\sigma_{THz} \leq 0.3$ mm. At a repetition rate of about 50 MHz, the source could deliver to users 5×10^{12} X-ray photons/s together with $2 - 5 \times 10^{23}$ THz photons/s.

NUMERICAL RESULTS

The FEL emission is first computed starting from noise. The radiation electric field is extracted over a three-dimensional grid at the end of the undulator and transported through the cavity. After reflection by the rear mirror, the radiation pulse seeds a next electron beam in the subsequent passage inside the undulator. The process is then reiterated up to saturation. The FEL simulation has been carried out by using the FEL code Genesis 1.3 [18]. The total losses *Loss* are given by the sum of several terms, namely the fraction of energy extracted from the system, the absorption of the mirrors, the losses on the lenses, the effect of the holes and the mismatch between the radiation and electron area at the beginning of the undulator. The last term, connected to the filling factor, is widely dominating. For taking into account the jitters in energy of the linac, a sequence of electron bunches different one from each other both microscopically and macroscopically, have been prepared and injected into the undulator. The macroscopic shot to shot beam varia-

ISBN: 978-3-95450-220-2 ISSN: 2673-5474 doi: 10.18429/JACoW-FEL2022-TUCO4

tions include the random change of the electron energy by 1 per mill, the tuning between electron beam and radiation within 100 fs of time delay and the transverse overlapping with 50 µm of pointing jitter. Due to their different velocities, the radiation field travelling inside the cavity overtakes the electron beam. The pulse, therefore, needs to be delayed by the total slippage length at the successive round trip. Implementing a slight shortening of the cavity length, the radiation turns out to be synchronized with the next bunch at the undulator entrance, within the temporal jitter.

Table 2: Characteristics of undulator, FEL and Thomson sources.(repetition rate at 5×10^7 Hz). E_{IC} and E_{EC} indicate the intra-cavity and extra-cavity radiation energy respectively; size, div and P_{EC} are the output radiation size, divergence and the extra-cavity radiation power level. Mirror losses at 2%. $/n$ means per shot.

Quantity	**Unit**					
λ_w	cm	3.5	3.5	4.5	4.5	4.5
a_w		2.33	2	2.95	2	2
L_{und}	m	2	2	1.7	1.7	1.7
γ		55.5	81.5	65	55.5	86
λ_{THz}	µm	36	13.2	51.6	36	15
E_{IC}	mJ	3	3.38	1	2.1	2.8
E_{EC}	μJ	60	67	20	42	56
N_{IC}/n	$\times 10^{17}$	5.5	2.6	2.5	3.8	2.1
N_{IC}/s	$\times 10^{25}$	2.75	1.3	1.25	1.9	1.05
N_{EC}/n	$\times 10^{15}$	11	5.2	5	7.6	4.2
N_{EC}/s	$\times 10^{23}$	5.5	2.6	2.5	3.8	2.1
bw	%	4	2.6	1	2.5	2.15
size	mm	2.7	1.6	3	3	2.2
div	mrad	3.5	1.8	6	4	3.7
P_{EC}	kW	3	3.4	1	2.1	2.8
λ_X	nm	3	0.5	3	3	0.5
size in IP	µm	180	65	250	180	75
N_X/n	$\times 10^5$	1.7	1.05	1.27	1.19	0.96
N_X/s	$\times 10^{12}$	8.5	5.3	6.3	6	4.8
${N_X}^{coll}$/n	$\times 10^5$	0.41	0.42	0.23	0.29	0.37
${N_X}^{coll}$/s	$\times 10^{12}$	2.2	2.25	1.15	1.45	1.85

With the electron beam parameters in the range of Table 1, Q= 250 pC, I_{peak}=20 A , $\epsilon_n = 1.4 mmmrad$, energy spread $\Delta E = 100 keV$ and varying energies with jitter of $2x10^{-4}$, five reference cases have been studied: two based on an undulator with period $\lambda_w = 3.5$ cm and three with $\lambda_w = 4.5$ cm. The data and the results are summarized in Table 2. THz radiation energies larger than 1 mJ are always obtained for wavelengths between 13 and 50µm, with undulator lengths larger than 1.5 m. Figure 3 shows the energy growth as a function of the round trip number inside the cavity, in the case of cavity losses at 2%. The radiation power profiles at saturation are instead shown in Fig. 4. In some cases, the power shape is multi-spiky, resulting in a broad and polichromatic spectrum.

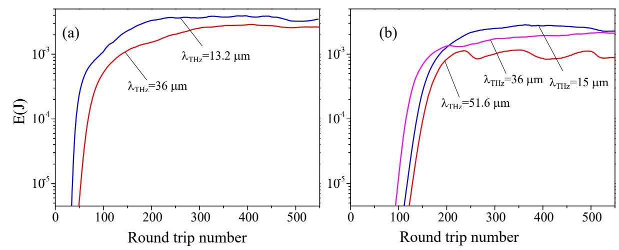

Figure 3: Intra-cavity radiation energy growth E(J) vs. number of shots N. Window (a): undulator period $\lambda_w = 3.5$ cm; red: $\gamma = 55.5$, $\lambda = 36$ µm; blue: $\gamma = 81.5$ $\lambda = 13.2$ µm. Window (b): undulator period $\lambda_w = 4.5$ cm; red: $\gamma = 65$, $\lambda = 51.6$ µm; magenta: $\gamma = 55.5$, $\lambda = 36$ µm; blue: $\gamma = 86$, $\lambda = 15$ µm.

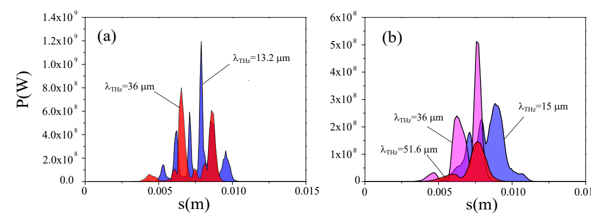

Figure 4: Intra-cavity radiation power profile P(W) vs coordinate s(m)=t(s)c. Window (a): undulator period $\lambda_w = 3.5$ cm; red: $\gamma = 55.5$, $\lambda = 36$ µm; blue: $\gamma = 81.5$, $\lambda = 13.2$ µm. Window (b): undulator period $\lambda_w = 4.5$ cm; red: $\gamma = 65$, $\lambda = 51.6$ µm; magenta: $\gamma = 55.5$, $\lambda = 36$ µm; blue: $\gamma = 86$, $\lambda = 15$ µm.

The example of cavity sketched in Fig. 5 is a four mirror unstable cavity in a bow-tie configuration. The mirrors are spherical and constitute a telescopic system, surrounding the Compton IP, which provides the focusing needed for increasing the luminosity of the system. Cavities of this kind has been used in Thomson Scattering Sources, for instance in BriXSinO [13] or ThomX [14]. The radiation exits the undulator (point 1) with assigned waist size w_1 and curvature radius R_1, provided by the GENESIS 1.3 calculations. The

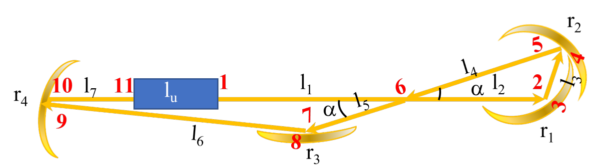

Figure 5: Dual source of THz and X-ray radiation. The cavity is constituted by four mirrors, one of them (r_1) holed for THz and X-ray extraction. The Compton interaction is in point 6, the focusing being realized by the mirrors themselves. Electron beam and THz radiation interact at an angle α of few degrees.

THz radiation must hit the holed front mirror with a size

ISBN: 978-3-95450-220-2 ISSN: 2673-5474 doi: 10.18429/JACoW-FEL2022-TUCO4

$w_2(>> w_1)$ large enough to guarantee a fraction of few percent of extra-cavity radiation with a hole of few mm radius, namely $w_2 \simeq 10$ cm. For the THz pulse propagation, we follow the ABCD model of the Gaussian beams. The length between the end of the undulator and the mirror (point 2) is then chosen in such a way that $w_2 =\simeq 0.1m$. A waist at the IP (point 6) of the order of 1.5×10^{-4} m entails a focusing distance $l_4 \simeq 3.14$ m. The radiation reflected on mirror 1 should encounter a successive electron bunch in the IP, leading to $l_2 + l_3 + l_4 = m\Delta l$ (m integer and Δl the bunch-to-bunch separation). With an angle of collision of 2°, $l_2 \simeq 2.6$ m and $l_3 \simeq 0.24$ m. The total round trip length should also be an integer multiple n of Δl, namely $l_5 + l_6 + l_7 + l_u + l_1 \simeq n\Delta l$. The radiation should arrive consistently matched with the undulator (point 11). This condition is guaranteed by values of $w_{11} \simeq 7.510^{-3}$ m and $R_{11} = -1$ m, leading to $l_5 = 0.27$ m, $l_6 = 14.72$ m and $l_7 = 0.24$ m. The resulting round trip length is 36 m and the linear dimension of the cavity is about 18 m. The mirrors turn out to have the following curvature radii: $r_1 \simeq 27.3$ m, $r_2 \simeq 3.14$ m, $r_3 \simeq 0.27$ m and $r_4 = 0.39$ m. Radiation with wavelengths up to 50 µm can be transported and focused with these same curvature lengths, by operating slight adjustments of the position of the mirrors. The interaction between the electron beam and the THz radiation propagating backward has been investigated with the classical model The radiation in the IP can be focused down to $\sigma_{THz} \simeq 65 - 75$ µm in the case of $\lambda_{THz} \simeq 13 - 15$ µm and to about 150-250 µm for λ =36-51µm. Figure 6 presents the dependence of the total X-ray flux on the THz radiation size σ_{THz} for 3 nm of X-ray wavelength (window(a)) and 0.5 nm (window (b)). A suitable focusing allows to exceed 10^5 X-ray photon per shot. Figure 7 shows the number of photons N_X (solid lines, left axis) and the bandwidth b_w (dotted lines, right axis) obtained with different collimation angles θ_{coll}, for a THz focusing reference value $\sigma_{THz} \simeq 5\lambda_{THz}$. The number of photons strongly depends on the THz intensities. The cases obtained with the shorter undulator period generate more intense X rays.

The results, collected in Table 2, have been obtained by collimating the output yield in a proper angle $\theta_{coll} \simeq 10$ mrad for a bandwidth of about 10 %. Narrower or broader spectra can be achieved by varying the collimation angle, as presented in Fig 7. Figure 8 shows the spectra of the X-ray radiation at 3 nm (window (a)) and 0.5 nm (window (b)) collimated at a bandwidth of 10%, for the five reference cases. Figure 9 presents the effect of the presence of a collision angle. The case with $\lambda_{THz} = 15$ µm and cavity losses at 2%, 4% and 6% has been analysed as function of the interaction angle α ($\alpha = 0$ for head to head collisions). The data show a contained decrease of the photon number that remains quite negligible for angles below 5°. The Rayleigh length of the X radiation is of order of tens meters and its size on the front mirror much smaller than the dimension of the hole, allowing the extraction of the X-rays from the cavity without problems.

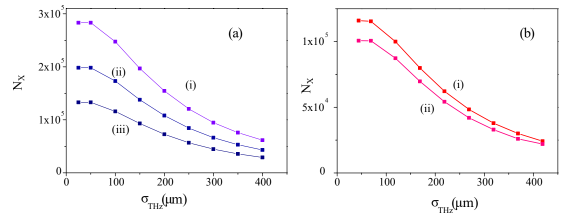

Figure 6: Total number of X-ray photons N_X as function of rms dimension of the THz pulse in the IP, σ_{THz}(µm). Window (a): $\lambda_X = 3$ nm, (i) $\lambda_w = 3.5$ cm, $\lambda_{THz} = 36$ µm; (ii) $\lambda_w = 4.5$ cm, $\lambda_{THz} = 36$ µm; (iii) $\lambda_w = 4.5$ cm, $\lambda_{THz} = 51.6$ µm. Window (b): $\lambda_X = 0.5$ nm, (i) $\lambda_w = 3.5$ cm, $\lambda_{THz} = 13.2$ µm; (ii) $\lambda_w = 4.5$ cm, $\lambda_{THz} = 15$ µm.

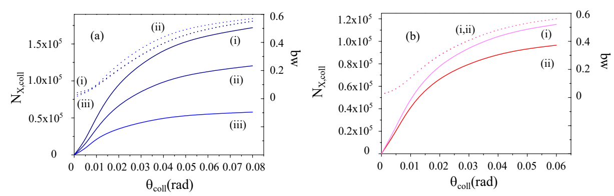

Figure 7: Number of photons $N_{X,coll}$ (solid lines) and bandwidth (dotted lines) as function of collimation angle θ_{coll}(rad). Window (a): $\lambda_X = 3$ nm, (i) $\lambda_w = 3.5$ cm, $\lambda_{THz} = 36$ µm; (ii) $\lambda_w = 4.5$ cm, $\lambda_{THz} = 36$ µm; (iii) $\lambda_w = 4.5$ cm, $\lambda_{THz} = 51.6$ µm. Window (b): $\lambda_X = 0.5$ nm, (i) $\lambda_w = 3.5$ cm, $\lambda_{THz} = 13.2$ µm; (ii) $\lambda_w = 4.5$ cm, $\lambda_{THz} = 15$ µm. In window (b), the bandwidths relevant to cases (i) and (ii) are not distinguishable.

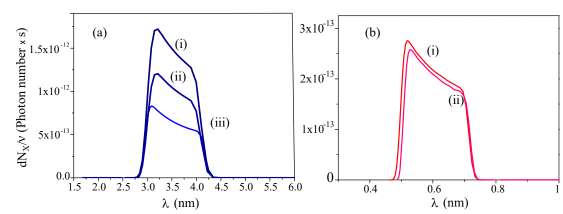

Figure 8: Spectrum of the collimated X-ray radiation for bandwidth of 10%. Window (a): $\lambda_X = 3$ nm, (i) $\lambda_w = 3.5$ cm, $\lambda_{THz} = 36$ µm; (ii) $\lambda_w = 4.5$ cm, $\lambda_{THz} = 36$ µm; (iii) $\lambda_w = 4.5$ cm, $\lambda_{THz} = 51.6$ µm. Window (b): $\lambda_X = 0.5$ nm, (i) $\lambda_w = 3.5$ cm, $\lambda_{THz} = 13.2$ µm; (ii) $\lambda_w = 4.5$ cm, $\lambda_{THz} = 15$ µm.

CONCLUSIONS

The dual source we have presented here, delivering simultaneously THz and X-ray radiation, has a compact footprint and can therefore be installed in medium size laboratories, hospitals or university campuses. It is based on a relatively simple upgrade of a THz FEL Oscillator, consisting in the addition of a telescopic system surrounding the Compton Interaction Point, placed in the center of the cavity. A possi-

ISBN: 978-3-95450-220-2 ISSN: 2673-5474 doi: 10.18429/JACoW-FEL2022-TUCO4

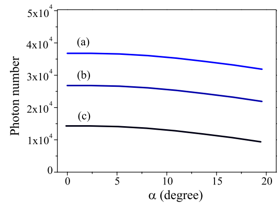

Figure 9: Number of photons of the collimated X-ray radiation for bandwidth at 10% as function of the complementary angle α between electron beam and THz radiation (head to head interaction $\alpha = 0$.) λ_w=4.5 cm, $\lambda_{THz} = 15$ µm. $\lambda_X = 0.5$ nm, (a): $L_c = 2\%$, (b): $L_c = 4\%$, (c): $L_c = 6\%$.

ble geometry of the cavity, a bow-tie configuration with four mirrors, have been discussed. The undulator should occupy part of the region between the telescopic system and the front mirror. The dimension and the cost of the device are almost the same of those of a THz oscillator. The THz radiation generated in an FEL Oscillator propagating backward in the cavity hits a successive electron bunch producing soft X-rays via Thomson back-scattering. In this condition, THz FEL intracavity pulses with mJ-class energy at 15-50 µm of wavelength, driven by 20-100 MeV energy electron bunches, can deliver up to few 10^5 soft X-ray photons per shot by Compton back-scattering at a rate of 10-100 MHz, synchronized with the THz radiation. Two possible undulator choices at λ_w=3.5 and 4.5 cm have been described. More than 10^{17} THz photons per shot are emitted intra-cavity by the FEL Oscillator, meaning more than 10^{15} per shot to the extra-cavity users, and drive more than 10^5 X-ray photons per shot. These numbers, multiplied by the repetition rate of the source, namely 10-100×10^6 Hz, give 10^{22} – 10^{23} THz photons/s, coupled with more than 10^{12} X-ray photons/s. Open technological challenges are the implementation of the cavity elements, such as mirrors, lenses and windows, issues that should be studied within a work of conceptual and technical design.

REFERENCES

[1] J. J, Turner, "Combining THz laser excitation with resonant soft X-ray scattering at the Linac Coherent Light Source", *J. Synchrotron Rad.*, vol. 22, pp. 621–625, 2015. doi:10.1107/S1600577515005998

[2] Hoffmann M. C. and Turner J. J. "Ultrafast X-ray Experiments Using Terahertz Excitation, *Synchrotron Radiat. News* vol. 25, pp. 17–24, 2012. doi:10.1080/08940886.2012.663318

[3] C. Koral *et al.*, "Multi-Pass Free Electron Laser Assisted Spectral and Imaging Applications in the Terahertz/Far-IR Range Using the Future Superconducting Electron Source BriXSinO", *Front. Phys.*, vol. 10, p. 725901, 2022. doi:10.3389/fphy.2022.725901

[4] Z. Zhang *et al.*, "A high-power, high-repetition-rate THz source for pump–probe experiments at Linac Coherent Light Source II", *J. Synchrotron Radiat.*, vol. 27, pp. 890-901, 2020. doi:10.1107/S1600577520005147

[5] E. Zapolnova *et al.*, "THz pulse doubler at FLASH: double pulses for pump–probe experiments at X-ray FELs", *J. Synchrotron Rad.*, vol. 25, pp. 39-43, 2018. doi:10.1107/S1600577517015442

[6] *Free-electron laser at Jefferson Laboratory*, from 'Jefferson Lab.' website: https://www.jlab.org/FEL/

[7] S. Winnerl *et al.*, ""2006 Joint 31st International Conference on Infrared Millimeter Waves and 14th International Conference on Teraherz Electronics, 2006, pp. 159-159. https://doi:10.1109/ICIMW.2006.368367.

[8] N. Vinokurov *et al.*, "Status of the Novosibirsk High Power Terahertz FEL", in *Proc. FEL'06*, Berlin, Germany, Aug.-Sep. 2006, paper TUCAU03, pp. 492–495.

[9] Serafini L. *et al.*, *BriXSinO Conceptual Design Report*, https://marix.mi.infn.it/brixsino-docs/(2021)

[10] V. Petrillo *et al.*, "High brilliance Free-Electron Laser Oscillator operating at multi-MegaHertz repetition rate in the short-TeraHertz emission range", *Nucl. Instrum. Methods Phys. Res., Sect. A*, vol. 1040, p. 167289, 2022. doi:10.1016/j.nima.2022.167289

[11] V. Petrillo *et al.*, "Synchronised TeraHertz Radiation and Soft X-rays Produced in a FEL Oscillator", *Appl. Sci.*, vol. 12, p. 8341, 2022. doi:10.3390/app12168341

[12] P. Cardarelli *et al.*, "BriXS, a new X-ray inverse Compton source for medical applications", *Physica Med.*, vol. 77, pp. 127–137, 2020. doi:10.1016/j.ejmp.2020.08.013

[13] E. Suerra *et al.*, "A new method for spatial mode shifting of stabilized optical cavities for the generation of dual-color X-rays", *Nucl. Instrum. Methods Phys. Res., Sect. A*, vol. 1019, p. 165852, 2021. doi:10.1016/j.nima.2021.165852

[14] K.Dupraz *et al.*, "The ThomX ICS source", *Phys. Open*, vol. 5, p. 100051, 2020. doi:10.1016/j.physo.2020.100051

[15] M. Weikum *et al.*, "Status of the Horizon 2020 EuPRAXIA conceptual design study", *J. Phys.: Conf. Ser.*, vol. 1350, p. 012059, 2020. doi:10.1088/1742-6596/1350/1/012059

[16] L. Serafini *et al.*, "MariX, an advanced MHz-class repetition rate X-ray source for linear regime time-resolved spectroscopy and photon scattering", *Nucl. Instrum. Methods Phys. Res., Sect. A*, vol. 930, pp. 167–172, 2019. doi:10.1016/j.nima.2019.03.096

[17] N. Ranjan *et al.* "Simulation of inverse Compton scattering and its implications on the scattered linewidth", *Phys. Rev. Accel. Beams*, vol. 21, p. 030701, 2018. doi:10.1103/PhysRevAccelBeams.21.030701

[18] S. Reiche, "GENESIS 1.3: a fully 3D time-dependent FEL simulation code", *Nucl. Instrum. Methods Phys. Res., Sect. A*, vol. 429, pp. 243–248, 1999. doi:10.1016/S0168-9002(99)00114-X

ISBN: 978-3-95450-220-2 ISSN: 2673-5474 doi: 10.18429/JACoW-FEL2022-TUP01

A PULSE SHAPER FOR DIRECT GENERATION OF 515 nm 3D ELLIPSOIDAL PULSES AT PITZ

A. Hoffmann†, J. Good, M. Gross, C. Koschitzki, M. Krasilnikov, H. Qian, F. Stephan
DESY, Zeuthen, Germany

Abstract

In this paper, a cathode laser pulse shaper at 515 nm is presented that will be used for emittance optimizations. In case alkali antimonide photocathodes are used, the shaped green pulses can be applied directly for photoemission while Cs_2Te photocathodes requires second harmonic generation to provide UV laser pulses. Recent tests of CsK_2Sb photocathodes in the high gradient RF gun at PITZ are first steps for the future usage of green laser pulses, which would simplify the requirements for the photocathode laser system, especially for CW operation cases envisioned in future. As long the alkali antimonide photocathodes are not in regular use yet, the laser pulses need to be converted into the UV. The green pulse shaper still simplifies the laser system since two conversion stages from IR to green to UV were needed in the past, which dilutes the quality of the shaped laser pulses. In this paper, a pulse shaper for 515 nm wavelength is presented that is expected to further improve the beam emittance generated by 3D ellipsoidal laser shaping.

INTRODUCTION

X-ray free electron lasers require short, high-brightness electron bunches with up to 1 nC charge. However, high charge and low emittance are conflicting goals due to space charge. To overcome this limitation an electron bunch with linear space charge force should be used which simplifies the electron transport [1]. The electron distribution with a linear space charge field is a uniform ellipsoidal electron bunch. To generate such electron distributions with high bunch charge in photoinjectors, the driving photocathode laser pulse should have a 3D ellipsoidal shape [2]. At the Photo Injector Test Facility at DESY in Zeuthen (PITZ), we investigate the generation of 3D ellipsoidal laser pulse shapes experimentally, among other techniques, mainly by spatial light modulator (SLM) pulse shapers [3-7].

For Cs_2Te photocathodes UV laser pulses have to be used and pulse shaping devices in that wavelength range have either low efficiency or are not suited for high average power. Pulse shaping schemes in the NIR are well established for 800 nm or 1030 nm, but frequency conversion of the shaped pulses to UV is limited by a compromise between conversion efficiency and pulse shape preservation.

In this paper, we present a pulse shaper that operates at 515 nm being a good compromise of having powerful lasers and the availability of efficient pulse shaping devices for operation with 1 MHz repetition rate at several watts of average power. The wavelength of 515 nm has the advantage of direct pulse shaping for CsK_2Sb photocathodes without any frequency conversion step involved and for Cs_2Te only one conversion section for second harmonic generation (SHG) is required to achieve 257 nm wavelength.

The pulse shaper is based on a liquid crystal on silicon spatial light modulator (LCOS SLM) in a 4f zero dispersion stretcher geometry for applying amplitude shaping of chirped pulses. First experiments showing the preservation of a parabolic pulse shape in the UV are presented.

† andreas.hoffmann@desy.de

PULSE SHAPER AND DIAGNOSTICS

Green laser pulses (515 nm, 10 µJ, 265 fs, 1 MHz) are sent through a transmission grating stretcher to generate 10 ps chirped pulses, which afterwards enter the pulse shaper.

Amplitude Shaping

With the advance of LCOS SLMs shaping of femtosecond pulses became a standard technique for generation of user-specified waveforms [8]. Here, we use amplitude shaping of chirped picosecond pulses to mask the desired pulse shape from a Gaussian distribution that is coupled temporally and spectrally. A folded 4f zero dispersion stretcher of a cylindrical lens with the LCOS SLM in the image plane allows for shaping one spatial component and the spectrum. The amplitude shaping is realized by insertion of a quarter-wave plate in the beam path of the shaper. The second pass over the transmission grating at the exit of the shaper serves as a polarization filter. After image rotation by 90 degrees a second shaper is entered allowing to shape the other spatial component. With this, full 3D control over the pulse shape becomes possible. As feedback for the pulse shape optimization a high-resolution Czerny-Turner imaging spectrometer is used.

SHG FROG

Frequency-resolved optical gating (FROG) is a general method for measuring the spectral phase of ultrashort laser pulses and the standard technique for characterizing ultrashort laser pulses. In a FROG measurement a pulse gates itself in a nonlinear-optical medium and the resulting gated piece of the pulse is then spectrally resolved as a function of the delay between the two pulses. Retrieval of the pulse from its FROG trace is accomplished by using a two-dimensional phase-retrieval algorithm [9].

ISBN: 978-3-95450-220-2 ISSN: 2673-5474 doi: 10.18429/JACoW-FEL2022-TUP01

Here, SHG FROG is used, where the 515 nm laser pulses are gated in a BBO crystal and generate 257 nm signal. This FROG geometry is similar to a noncollinear intensity autocorrelator, but instead of a diode a spectrometer serves as the detector.

PULSE SHAPING EXPERIMENTS

Analyzing the resulting pulse shapes after optimization with SHG FROG gives a reconstruction of the green shaped laser pulse. By choosing the focusing geometry and the nonlinear crystal thickness similar to the values that will be later used for frequency conversion to the UV for photoelectron generation with Cs_2Te cathodes, the FROG measurement is limited by similar effects as group velocity mismatch and spatial walk-off.

Hence the FROG reconstruction can be used as a figure of merit for pulse shape preservation during frequency conversion in a nonlinear crystal. Here the generation of a temporally parabolic shaped pulse is studied, which is a good approximation to the later envisioned ellipsoidal pulses. Figure 1 summarizes the pulse shaping experiment. The SLM is optimized with a spectrometer in a feedback loop for generation of parabolic pulses and the corresponding shaper mask is shown in grayscale (black corresponds to zero transmission and white to maximum transmission of the amplitude). Then the shaped pulses are characterized by measuring a SHG FROG trace.

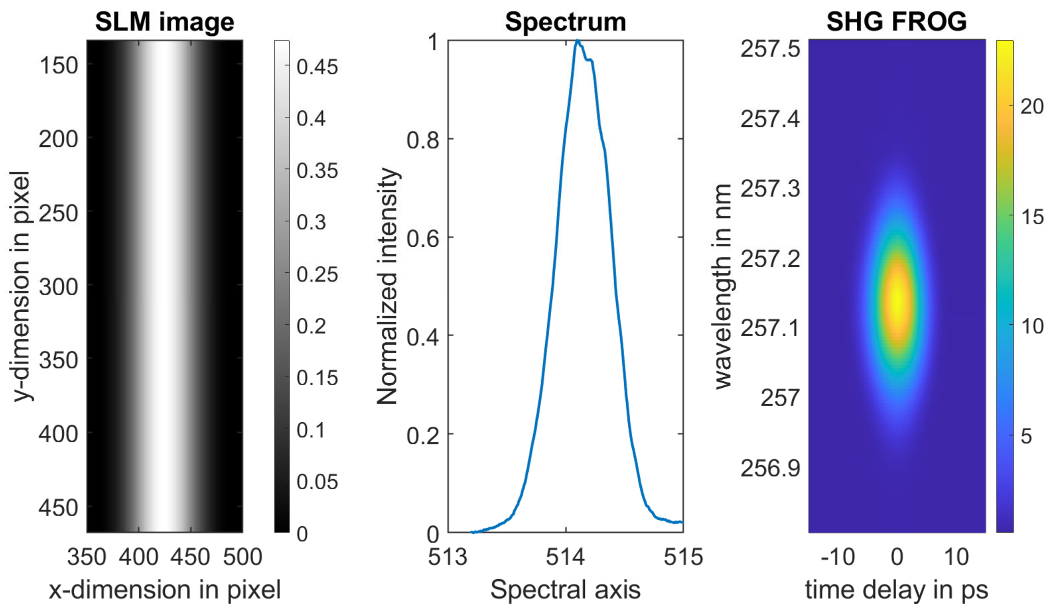

Figure 1: Pulse shaping experiment for a parabolic pulse. Left: Applied mask on the Spatial Light Modulator. Middle: Measured green spectrum after the pulse shaper. Right: Measured SHG FROG trace.

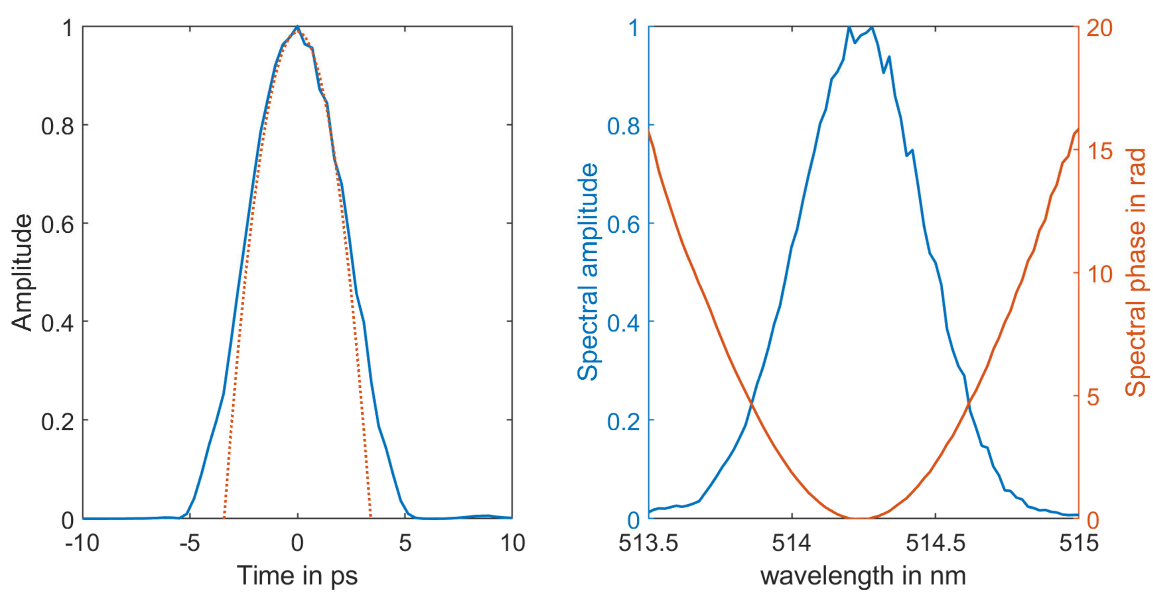

Figure 2: Pulse reconstruction of the parabolic pulse by FROG algorithm. Left: Reconstructed temporal pulse shape (blue) and parabolic fit (orange dotted). Right: Reconstructed spectral amplitude (blue) and phase (orange).

ISBN: 978-3-95450-220-2 ISSN: 2673-5474 doi: 10.18429/JACoW-FEL2022-TUP01

The reconstruction of the shaped green laser pulse is shown in Fig. 2. The temporal pulse shape is in close agreement with a parabolic shape. Compared to the stretched Gaussian input pulses coming into the shaper with a 10 ps FWHM duration, the pulse duration is reduced due to the applied amplitude masking. Deviations from the parabolic shape can be explained by discretisation artefacts of the SLM mask and the frequency conversion in a 0.5 mm thick BBO crystal, similar to the one used for later UV conversion of the pulse for photoelectron generation. This could be improved by adjusting the feedback algorithm for pulse shaping. The width of the spectral amplitude is reduced compared to the input Gaussian pulses due to the amplitude masking. The parabolic shape of the spectral phase is introduced by stretching the 260 fs pulses from the laser to 10 ps.

CONCLUSION

A SLM pulse shaper for 515 nm wavelength has been installed at one of the photocathode lasers at PITZ. Amplitude shaping of the laser pulse will allow for generation of 3D ellipsoidal distributions which can be directly applied to CsK_2Sb photocathodes or require only one conversion step, if Cs_2Te photocathodes are used. As a first experiment the preservation of a parabolic temporal pulse shape undergoing UV conversion was shown, supporting the capabilities of the proposed scheme.

ACKNOWLEDGEMENTS

This work was supported by the European XFEL research and development program.

REFERENCES

[1] G. Ha *et al.*, “Bunch shaping in electron linear accelerators”, *Rev. Mod. Phys*., vol. 94, p. 025006, May 2022. doi:10.1103/RevModPhys.94.025006

[2] Y. Li and J. W. Lewellen, “Generating a Quasiellipsoidal Electron Beam by 3D Laser-Pulse Shaping”, *Phys. Rev. Lett.*, vol. 100, p. 074801, Feb. 2008. doi:10.1103/PhysRevLett.100.074801

[3] T. Rublack et al., “Production of quasi ellipsoidal laser pulses for next generation high brightness photoinjectors”, *Nucl. Instrum. Methods Phys. Res., Sect. A*, vol. 829, pp. 438-441, Sept. 2016. doi:10.1016/j.nima.2015.12.004

[4] S. Yu Mironov *et al.*, “Spatio-temporal shaping of photocathode laser pulses for linear electron accelerators”, *Phys. Usp.* vol. 60, pp. 1039-1050, May 2017. doi:10.3367/UFNe.2017.03.038143

[5] J. Good *et al.*, “Preliminary On-Table and Photoelectron Results from the PITZ Quasi-Ellipsoidal Photocathode Laser System”, in *Proc. 38th International Free-Electron Laser Conference (FEL’17)*, Santa Fe, USA, Aug. 2017, pp. 418-420. doi:10.18429/JACoW-FEL2017-WEP006

[6] H. Qian *et al.*, “Beyond Uniform Ellipsoidal Laser Shaping for Beam Brightness Improvements at PITZ”, in *Proc. 60th ICFA Advanced Beam Dynamics Workshop on Future Light Sources (FLS’18)*, Shanghai, China, Mar. 2018, pp. 146-149. doi:10.18429/JACoW-FLS2018-WEP2PT034

[7] M. Gross *et al.*, “Characterization of Low Emittance Electron Beams Generated by Transverse Laser Beam Shaping”, in *Proc. 12th International Particle Accelerator Conference, (IPAC’21)*, Campinas, Brazil, May 2021, pp. 2690-2692. doi:10.18429/JACoW-IPAC2021-WEPAB040

[8] M. M. Wefers and K. A. Nelson, “Generation of high-fidelity programmable ultrafast optical waveforms”, *Opt. Lett.*, vol. 20, pp. 1047-1049, May 1995. doi:10.1364/OL.20.001047

[9] R. Trebino *et al.*, “Measuring ultrashort laser pulses in the time-frequency domain using frequency-resolved optical gating”, *Rev. Sci. Instrum.*, vol. 68, pp. 3277-3295, Jun. 1997. doi:10.1063/1.1148286

ISBN: 978-3-95450-220-2 ISSN: 2673-5474 doi: 10.18429/JACoW-FEL2022-TUP03

RF PERFORMANCE OF A NEXT-GENERATION L-BAND RF GUN AT PITZ

M. Krasilnikov*, Z. Aboulbanine, G. Adhikari, N. Aftab, P. Boonpornprasert, M.-E. Castro-Carballo, G. Georgiev, J. Good, M. Gross, A. Hoffmann, L. Jachmann, W. Koehler, C. Koschitzki, X.-K. Li, A. Lueangaramwong, D. Melkumyan, R. Niemczyk, A. Oppelt, S. Philipp, M. Pohl, B. Petrosyan, H. Qian, C. Richard, J. Schultze, G. Shu, F. Stephan, G. Vashchenko, T. Weilbach, DESY, Zeuthen, Germany

M. Bousonville, F. Brinker, L. Knebel, D. Kostin, S. Lederer, L. Lilje, S. Pfeiffer, M. Hoffmann, R. Ritter, H. Schlarb, S. Schreiber, H. Weise, M. Wenskat, J. Ziegler, DESY, Hamburg, Germany

Abstract

A new generation of high-gradient normal conducting 1.3 GHz RF gun with 1% duty factor was developed to provide a high-quality electron source for superconducting linac driven free-electron lasers like FLASH and European XFEL. Compared to the Gun4 series, Gun5 aims for a ~50% longer RF pulse length (RF pulse duration of up to 1 ms at 10 Hz repetition rate) combined with high gradients (up to ~60 MV/m at the cathode). In addition to the improved cell geometry and cooling concept, the new cavity is equipped with an RF probe to measure and control the amplitude and phase of the RF field inside the gun. The first characterization of Gun5.1 included measurements of RF amplitude and phase stability (pulse-to-pulse and along 1 ms RF pulse). The dark current was measured at various peak power levels. The results of this characterization will be reported.

INTRODUCTION

The Photo Injector Test Facility at DESY in Zeuthen (PITZ) develops, tests and characterizes high brightness electron sources for FLASH and European XFEL for more than 20 years. Since these user facilities operate superconducting accelerators in pulsed mode, the corresponding normal-conducting L-band RF gun also has to operate with long RF pulses at 10 Hz repetition rate. To obtain high electron beam quality from a photocathode RF gun, a high acceleration gradient at the cathode is required. The peak RF electric field of 60 MV/m at the cathode is considered as a goal parameter for a high brightness L-band photogun. Therefore, the RF gun has to provide stable and reliable operation at high average RF power. The previous gun cavity generation (Gun4) had a maximum RF pulse length of 650 µs, which implies a maximum of 27000 electron bunches per second. Growing interest from the FEL user community for even longer pulse trains motivated developments of the next generation of normal conducting L-band gun cavity (Gun5), which aims for 1 ms RF pulses. Combined with 6.5 MW of peak RF power, this results in a very high average power of ~65 kW. In addition to the improved resonator shape and cooling, Gun5 has a built-in RF probe to directly control the phase and amplitude of the RF field in the cavity. RF conditioning faces issues of stability and reliability. Aspects of pulsed heating and dark current should also be considered.

GUN5.1 SETUP AT PITZ

The RF gun cavity is a 1½-cell normal conducting copper cavity operating in a π-mode standing wave at 1.3 GHz. The Gun5 design includes several major improvements over the Gun4-generation, which are aimed at improving the performance of the gun. An elliptical shape of the internal geometry was applied in order to optimize the distribution of the peak electric field over the cavity surface [1]. Detailed studies to reduce the dark current resulted in an elliptical shape of the cathode hole at the back wall of the cavity [2]. In order to control the RF field in the cavity directly, an RF probe has been integrated in the front wall of the full cell. An optimized cavity cooling system and improved rigidity [1] should mitigate the challenges associated with the 1% duty cycle.

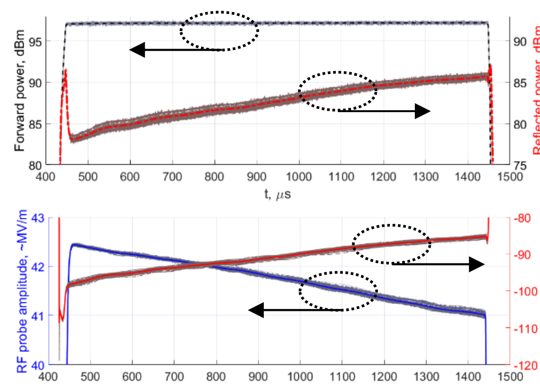

Figure 1: RF signals from 1 ms pulses. Top plot – directional coupler signals. Bottom plot: corresponding RF probe (pickup) signals.

The Gun5.1 RF feed setup was taken over from the waveguide distribution system of the previous generation of guns (Gun4.x) [3], including two waveguides (WG1,2) with two 5MW directional couplers (WG1,2 5 MW), followed by RF windows and a T-combiner in vacuum. The combined RF feed can be controlled by the 10 MW directional coupler (as was the case in recent Gun4.x generation setups) or by the newly installed RF pickup in the cavity. Typical RF signals for 1 ms RF pulses are shown in Fig. 1,

ISBN: 978-3-95450-220-2 ISSN: 2673-5474 doi: 10.18429/JACoW-FEL2022-TUP03

where average pulse profiles are shown over the statistics of 50 subsequent shots (grey traces).

RF GUN CHARACTERIZATION

The standard PITZ procedure for the RF gun conditioning [3] was applied to Gun5.1. Conditioning started on 18th of October 2021 with a repetition rate of 1 Hz, after 10 days the repetition rate was increased to 5 Hz, and then after additional 21 days it was set to 10 Hz. The RF pulse length was increased from 10 µs to 100 µs / 1 ms for 5 Hz / 10 Hz with the peak power slowly ramped for each pulse duration.

Beam Momentum and Dark Current

For beam-based RF calibration, the photoelectron beam momentum was measured as a function of the RF gun launch phase for various levels of peak RF power. The cathode gradient was estimated from the field profile of the π-mode obtained from bead-pull measurements. The measured peak RF power scales as $P_{RF}[MW] \cong 0.00192 \cdot (1 \pm 0.037) \cdot (E_{cath}[MV/m])^2$. The results of the beam measurements are shown in Fig. 2 (left graph), where the calculated cathode gradient and corresponding phases of the maximum mean momentum gain (MMMG) are plotted versus measured maximum beam momentum together with simulated curves.

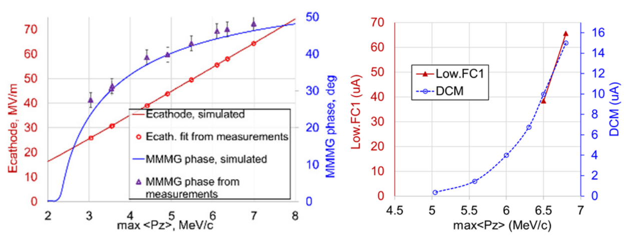

Figure 2: Gun gradient and the mean momentum gain (MMMG) phase (left plot) and the measured dark current (right plot) vs. maximum beam mean momentum.

The dark current measured by the first Faraday cup (LOW.FC1 at z=0.8 m from the cathode) and by the dark current monitor (DCM at z=2.1 m) is shown at the right plot of Fig. 2 as a function of the measured maximum beam momentum as the RF peak power varies. Comparison with the corresponding dark current measurements for Gun4.2 demonstrates a reduction of a factor 3 to 5.

Gun Resonance Temperature and Pulsed Heating

The gun cavity resonance is maintained by thorough water temperature control of the resonator body. The controlling temperature sensor is placed in the copper cavity body at the iris between the half and the full cell and is in between the cooling water and the inner cavity surface. Since the beginning of conditioning, an overall resonance temperature increase of ~5°C was observed. Most of the change occurred within the first 6 weeks, the resonance temperature stabilized 12 weeks after the start of conditioning. The dependences of the resonance temperature on the peak RF power and pulse duration are shown in Fig. 3. The slope of the resonance temperature was measured as ~0.5ºC/5 MW (left plot) at 200 µs RF pulse length, which corresponds to a change in heating by ~10 kW (average power). A resonance temperature growth of ~1.8ºC for ~7 MW peak RF power was observed by increasing the RF pulse length from 10 to 400 µs (right plot).

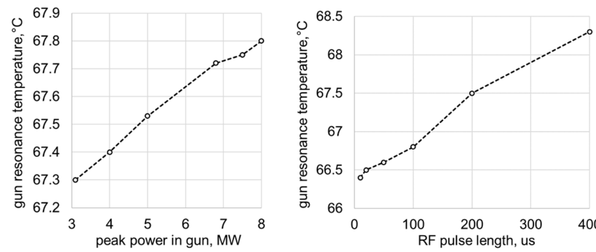

Figure 3: Gun resonance temperature versus peak power for 200 µs RF pulse length (left) and versus pulse length for 7 MW peak power in the gun (right).

Stability

To control the RF gun amplitude and phase, PITZ employs a µTCA-based low level RF (LLRF) system [4], which has large commonalities to those used at the European XFEL and FLASH. The control system allows lossless RF signals acquisition. The LLRF feedback has been tuned at PITZ for 1 ms pulse duration and 6.4 MW peak power in the gun. The results of stability monitoring of 500 subsequent shots are shown in Fig. 4, where the relative amplitude and absolute phase rms jitters along the pulse are plotted. Generally, the shot-to-shot rms jitter is ~0.02% for the amplitude and ~0.02 deg (~40 fs) for the phase.

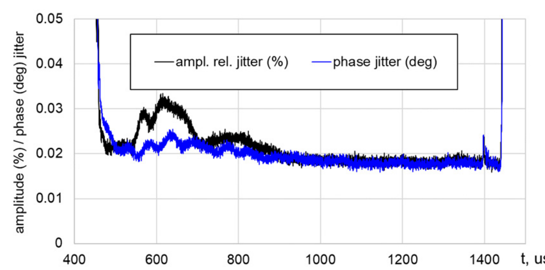

Figure 4: Relative amplitude and absolute phase rms jitters along the RF pulse.

The Gun5.1 cavity detuning due to pulsed heating was measured as 15.6 kHz for 1 ms RF pulse length at E_{cath}~60 MV/m and 11 kHz for 1 ms RF pulse length at E_{cath}~50 MV/m. The latter detuning per pulse length is 24% lower than the detuning measured for Gun4 at 450 µs pulse length.

To check the beam stability along the RF pulse, beam momentum has been measured for 1 ms pulses while scanning the photocathode laser timing position w.r.t. to RF gun pulse while maintaining the same launch phase (MMMG). The LLRF system at PITZ can use either the virtual probe (based on 10 MW directional coupler forward and reflected power signals) or the direct field measurements from the newly implemented RF pickup (real probe). The momentum distribution of electron bunches was

ISBN: 978-3-95450-220-2 ISSN: 2673-5474 doi: 10.18429/JACoW-FEL2022-TUP03

measured in the first dispersive section, yielding mean momentum $\langle P_z \rangle$ and rms momentum spread. The results are plotted in Fig. 5 for both available options of the controlling sensor (virtual and real probe). The linear slope of the mean momentum profile $\frac{1}{\langle P_z \rangle_0}\left|\frac{d\langle P_z \rangle}{dt}\right|$ is a factor of 7 smaller for the real probe case compared to the virtual one (0.0016 (ms)$^{-1}$ versus 0.011 (ms)$^{-1}$, respectively). This is significantly better than the result obtained in 2021 for Gun4.1 with a virtual probe: 0.021 (ms)$^{-1}$ within a 200 µs pulse.

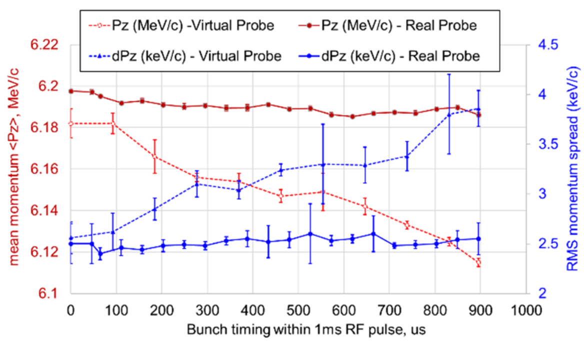

Figure 5: Beam mean momentum and rms momentum spread along the 1 ms RF pulse.

Mini-breakdown Events

Currently, the RF performance of Gun5.1 is limited by what are called as mini-breakdowns within RF pulses detected by the gun cavity pickup and by all directional couplers for reflected power signals. A typical mini-breakdown (mBD) is a short (~10…15 µs) interruption within the first part of an RF pulse (usually the first 30 µs of the flattop), then the amplitude is restored within the characteristic cavity filling time to the nominal amplitude (Fig. 6). The mini-breakdown rate (the ratio of number of "broken" pulses to the total pulse number) was measured to be ~0.05…0.2% at various RF pulse length and peak power levels. It starts to be detectable at an RF pulse length of ~350…400 µs and increases as the peak power increases. All mBD events are always accompanied by a small vacuum pressure spike (from ~$2\cdot10^{-9}$ mbar to 5…$8\cdot10^{-9}$ mbar), which is well below the vacuum interlock threshold. No correlation was found between mBD events and the static magnetic field configuration around the gun and the RF feed system. It is remarkable that the aforementioned location of a mBD within the RF pulse remains approximately the same for various pulse durations and peak power levels. The reason and nature of this distortion in the gun operation is still under investigation. Despite the rather low rate, mBD events could impact the efficiency of the LLRF feedback. This is a probable reason for irregular behaviour of the rms jitter in the first part of the RF pulse measured during 1 ms LLRF tests (Fig. 4).

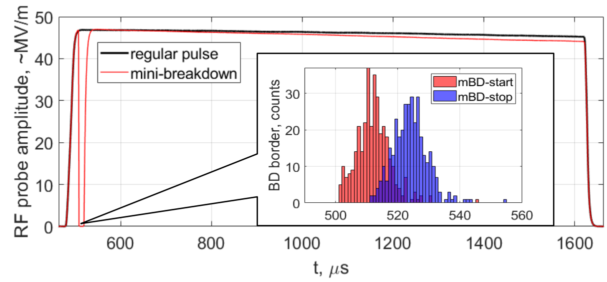

Figure 6: Typical mini-breakdown (mBD) event over regular RF probe 1 ms signal. Inset: 4.5-hour statistics of the mBD event start and end time locations within the RF pulse; the mBD rate over this period was 0.21%.

CONCLUSION

The first prototype of a new generation high-gradient normal conducting 1.3 GHz RF gun (Gun5.1), developed for 1 ms RF pulse operation at the European XFEL and FLASH, has been installed at PITZ for RF conditioning and characterization. The goal of high average RF power of up to 65 kW was achieved. The new cavity is equipped with an RF probe to measure and control the amplitude and phase of the RF field inside the gun cavity. The probe has been put into operation and employed for the LLRF regulation, yielding very good performance (pulse-to-pulse and along 1 ms RF pulse), exceeding that provided by the previously used virtual probe based on directional coupler signals. The measured detuning due to the pulse heating within the RF pulse was measured to be by ~24% lower than for the case of Gun4. The Gun5.1 peak power has been calibrated with electron beam longitudinal momentum measurements. The dark current from Gun5.1 was measured to be 3-5 times lower than the typical values of Gun4.2. A detailed investigation of the mini-breakdown events preventing Gun5.1 from its full performance is currently ongoing.

REFERENCES

[1] V. Paramonov, *et al.*, "Design of an L-band normally conducting RF gun cavity for high peak and average RF power", *Nucl. Instrum. Methods Phys. Res. A*, vol. 854 pp. 113–126, 2017.

[2] G. Shu, *et al.*, "Dark current studies of an L-band normal conducting RF gun", *Nucl. Instrum. Methods Phys. Res.* A, vol. 1010, p. 165546, 2021.

[3] I. Isaev *et al.*, "Conditioning Status of the First XFEL gun at PITZ", in *Proc. FEL'13*, New York, NY, USA, Aug. 2013, paper TUPSO30, pp. 282-286.

[4] J. Branlard, *et al.*, "LLRF commissioning of the European XFEL RF gun and its first linac RF station", in *Proc. IPAC'15*, Richmond, VA, USA, May 2015, pp. 1377-1379. doi:10.18429/JACoW-IPAC2015-TUAD3

.

ISBN: 978-3-95450-220-2 ISSN: 2673-5474 doi: 10.18429/JACoW-FEL2022-TUP04

DEVELOPMENT AND TEST RESULTS OF MULTI-ALKALI ANTIMONIDE PHOTOCATHODES IN THE HIGH GRADIENT RF GUN AT PITZ

S.K. Mohanty[1], H. Qian, Z. Aboulbanine, G. Adhikari, N. Aftab, P. Boonpornprasert, J. Good, M. Gross, A. Hoffmann, M. Krasilnikov, A. Lueangaramwong, R. Niemczyk, A. Oppelt, F. Stephan, T. Weilbach, DESY, Zeuthen, Germany
D. Sertore, L. Monaco, Istituto Nazionale di Fisica Nucleare - LASA, Segrate, Italy
G. Guerini Rocco, C. Pagani, ,Università degli Studi di Milano & INFN, Segrate, Italy
W.Hillert, University of Hamburg, Germany
G. Loisch, DESY, Hamburg, Germany
[1]also at INFN-LASA, Segrate, Italy

Abstract

Multi-alkali antimonide photocathodes can have high quantum efficiency, similar to UV sensitive (Cs_2Te) photocathodes, but with the advantages of photoemission sensitivity in the visible region of the light spectrum and a significant reduction in the mean transverse energy of photoelectrons. A batch of three KCsSb photocathodes was grown on molybdenum substrates via a sequential deposition method in a new preparation system at INFN LASA. Afterward, the cathodes were successfully tested in PITZ's high gradient RF gun. This contribution summarizes the experimental results obtained in both the preparation chamber and the RF gun. Based on those findings, we are now optimizing the recipe of KCsSb and NaKSb(Cs) photocathodes for lower field emission and longer lifetime, and the measurements for the latest photocathode with the improved recipe are also presented.

INTRODUCTION

High brilliance and high current electron beam with MHz repetition rate are the critical components for next-generation X-FEL [1,2]. To obtain these features, it requires an electron source of high quantum efficiency (≥ 1 %), low thermal emittance (< 1 mm. mrad/mm), and long lifetime (>1 week) [3]. In recent years, different studies show that owing to its high QE (quantum efficiency), low emittance, and fast response time in the visible range, KCsSb-based photocathode material has emerged as a prominent candidate for these applications. However, these cathodes have some limiting factors like their high sensitiveness towards the vacuum condition, which reduces their lifetime inside the RF guns.

This kind of photocathode material has successfully been demonstrated in various DC and continuous wave (CW) guns at low gradients (<20 MV/m) [4,5], and the parameters like QE and thermal emittance are found to be very promising. Recently, it has been demonstrated that these kinds of cathodes can sustain a month of long continuous operation inside a QWR SRF gun [6]. However, to improve the brightness of the electron beam in next-generation CW guns, it requires even higher cathode gradients (30-40 MV/m) for various applications. So, our current research domain is mainly focused on developing these materials and exploring their feasibility for high gradient operation at the PITZ RF gun for a future upgrade of the European XFEL facility. For the development part of the KCsSb-based photocathodes, DESY collaborated with INFN LASA, which has long-standing experience in studying and growing of semiconductor-based photocathode material. The first batch of three KCsSb cathodes with different thicknesses has been prepared and successfully tested at the PITZ RF gun. In this paper, the preparation and test results of these photocathodes are presented.

PHOTOCATHODE PREPARATION

As it is reported in previous papers [7-10], a reproducible recipe has been established for KCsSb photocathode in our R&D development system at INFN LASA. As it is described, the molybdenum substrates used in the R&D setup were not suitable to be loaded into an RF gun. So, another UHV preparation chamber has been prepared similar to Cs_2Te photocathode preparation system, which is suitable for producing the cathode film on the standard INFN Mo plugs. The new UHV preparation system has been equipped with the standard UHV devices (pressure gauges, a residual gas analyzer, and manipulators), two vacuum pumps (a combination of sputter-ion pump and NexTorr from SAES Getters), and a newly designed Mo plug heater. A custom-made source for Sb and commercially available Cs, Na, and K dispensers are used for the deposition. Each source is carefully pre-heated before starting of the deposition and calibrated to have the proper evaporation rate during the cathode growth. The usual deposition rate of 1 nm/min is used for the deposition in this case. A total number of four Mo plugs were polished to a mirror-like finishing (reflectivity > 54% at 543 nm w.r.t. 57% theoretical [11]) to allow reflectivity measurements during and after the photocathode growth. All samples are ultrasonically cleaned before loading them into the UHV system. Before the deposition, each cathode plug was heated up to 450 °C for at least one hour to remove the eventual residuals on the surface. By following the R&D experiences, three KCsSb cathodes have been prepared through a sequential deposition method. Out of which, two are thin (Sb=5 nm) and one thick (Sb=10 nm) cathodes. The detailed recipe parameters of produced photo cathodes are discussed in the

† sandeep.mohanty@desy.de

ISBN: 978-3-95450-220-2 ISSN: 2673-5474 doi: 10.18429/JACoW-FEL2022-TUP04

ref. [12]. The spectral response and reflectivity have been measured after the production and are reported in Fig. 1.

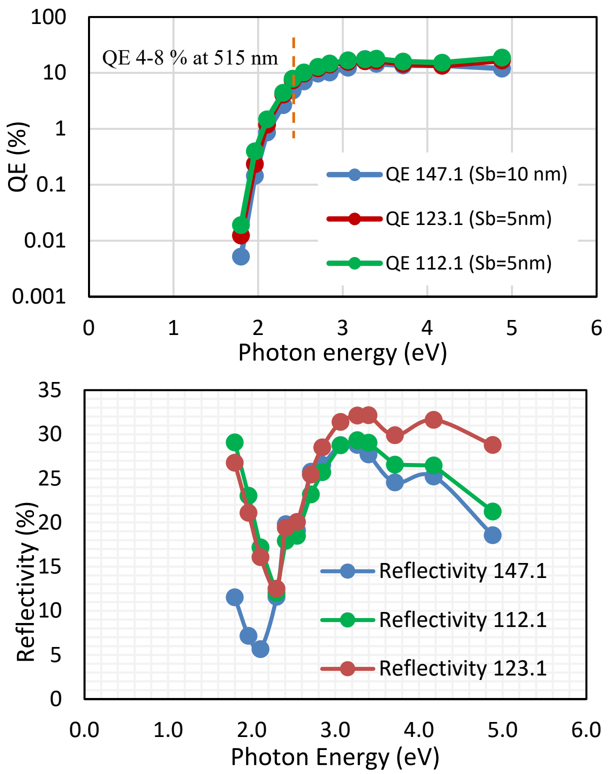

Figure 1: KCsSb photocathode spectral responses and reflectivity: 147.1 (thick, 10 nm of Sb), 123.1, and 112.1 (thin, 5 nm of Sb).

The QE at 515 nm has been recorded at 4-8 % for thick and thin cathodes, respectively, just after the production. Afterward, these cathodes were transferred to the portable UHV suitcases and transported to PITZ for testing.

PITZ PHOTOINJECTOR

The Photo Injector Test facility at DESY, Zeuthen site (PITZ) is mainly dedicated to the development and optimization of high brightness electron sources for free-electron lasers (FELs) like FLASH and European XFEL [13]. The normal conducting L-band radio frequency (RF) gun cavity generates about 6 MeV electron beams with bunch charges up to several nC, with a peak acceleration field of ~60 MV/m.

PHOTOCATHODE STUDIES

The cathodes survived during the transport. The QEs (at 515 nm) of photocathodes were measured after the arrival at the PITZ facility, and the values are similar to those measured at LASA. Afterward, these cathodes were inserted into the gun. The QE maps of these cathodes were uniform throughout the surface, and the map of one of the cathodes is reported in Fig 2.

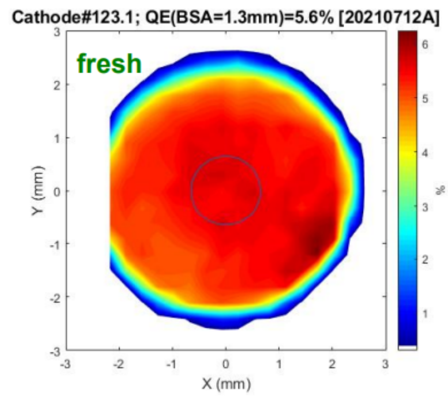

Figure 2: QE map of cathode #123.1 (Sb= 5nm) at 515nm.

During cathode conditioning in the RF gun, it has been observed that when the cathode gradient was increased above 30-40 MV/m, many vacuum trips happened compared to the past Cs_2Te cathode conditioning. During these trips, sometimes, the vacuum pressure increases to $1 \cdot 10^{-7}$ mbar. These vacuum events play a significant role in the quick QE degradation of the photocathodes. The vacuum level history during the conditioning of one of the cathodes (cathode #123.1) is presented in Fig. 3.

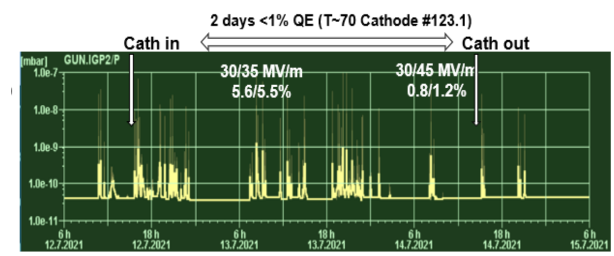

Figure 3: Vacuum level history during the conditioning of cathode #123.1.

These vacuum events happened with all three cathodes during conditioning; as a consequence, the QE was degraded to below 1% within an average of 48 hours. The QE of the photocathode was also observed to be slowly degraded without these vacuum events. In the case of KCsSb photocathodes, it has been previously demonstrated that its reactiveness towards the residual gases like carbon monoxide, carbon dioxide, oxygen, and hydrocarbons, which has a significant role in its short operational lifetime [14]. Figure 4 reports the mass spectrum of the residual gas traces in the cavity with and without RF power.

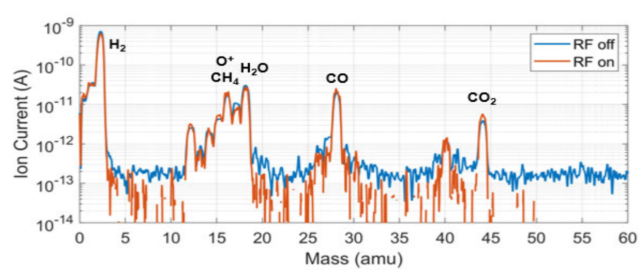

Figure 4: Mass spectrum of the residual gas in the cavity with and without RF power.

ISBN: 978-3-95450-220-2 ISSN: 2673-5474 doi: 10.18429/JACoW-FEL2022-TUP04

It is clearly shown that there is a relatively high amount of traces of these residual gases present inside the gun, and it could potentially be one of the primary reasons for the degradation of the QE of these cathodes. Thermal emittance measurements have been carried out of all three cathodes using thermal emittance imaging techniques at different cathode emission gradients & wavelengths of light (i.e., 515 nm & 257 nm). The measured values are reported in Table 1.

Table 1: Thermal Emittance at Different Cathode Gradients & Wavelengths of Light

Wave-lengths	**Cathode gradient (MV/m)**	**Thermal emittance (mm. mrad/mm)**
515 nm	19	0.6
	29	0.7
257 nm	19	1

As we know, the intrinsic emittance of a photocathode is mainly related to the MTE (mean transverse energy) of the emitted electrons, and the MTE at a specific wavelength can be defined by Eq. (1) [15].

$$MTE = 1/3\ (E_{ph} - E_{th}) \quad (1)$$

Where E_{ph} is the photon energy, and E_{th} is the photoemission threshold (Eg+Ea, where Eg is the energy gap and Ea the electron affinity). As we can see in Table 1, the thermal emittance measured at a higher cathode gradient (29 MV/m) was slightly higher than the value measured at 19MV/m. The potential reason could be the reduction in the cathode's work function due to the Schottky effect, which could increase the MTE.

The dark current has been measured as a function of the main solenoid current at different cathode gradients at the first Faraday Cup, located ~0.8m downstream of the cathode [16]. The results are shown in Fig. 5.

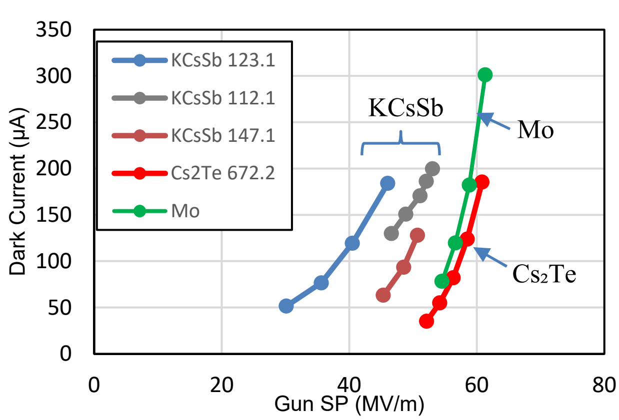

Figure 5: Dark current measurement at different cathode gradients.

The dark current from KCsSb cathodes was relatively higher by a factor of 2 to 5 than the one from Cs_2Te cathodes, which is potentially due to the lower photoemission threshold of KCsSb = 1.9 eV compared to Cs_2Te = 3.5 eV [17]. The lower dark current from the Mo cathode confirmed that the major contribution of the dark current comes from the cathode film itself.

A comparison of 100 pC projected emittance, measured at a cathode gradient of 40 MV/m between KCsSb & Cs_2Te photocathode, is presented in Table 2.

Table 2: Comparison of 100 pC Projected Emittance between KCsSb & Cs_2Te Photocathode

Measurements	**Cs_2Te 1µm.rad/mm**	**KCsSb 0.7µm.rad/mm**	**Unit**
95% rms emit.	0.36	0.28	µm.rad
Gauss emit.	0.33	0.25	µm.rad
4d brightness	760	1209	pC(µm.rad)²

It has been observed that the overall emittance was reduced to about ~23%, and the 4D brightness was increased up to 60% for KCsSb cathode compared to Cs_2Te.

Due to the high dark current, the response time measurements for cathode 147.1(Sb=10 nm) could only be possible to perform. The photoemission mechanism for semiconductor-based photocathodes could be understood by the three-step model. During the transport of a photoexcited electron (towards the surface) in a semiconductor photocathode, the electron motion can be affected by numerous scattering processes (i.e., electron-phonon). As a consequence, there is a delay between the photon's arrival at the cathode and the emission of an electron (excited by this photon) from the cathode. This delay causes lengthening of the extracted electron bunch with respect to the original light pulse. The shape of the emission curve is called the cathode response function, and its characteristic time constant is denoted as the cathode response time. Two laser pulses with known optical delay have been shone on the cathode for the response time measurement to calibrate the beam temporal response at the photoemission. The detailed procedure is already discussed in the ref. [18]. The cathode response time was measured for cathode #147.1 when its QE was already degraded to 0.4%. At this stage, the surface chemistry of the cathode could potentially be changed. However, the preliminary results show that the response time is below the resolution of 100 fs for the KCsSb cathode, compared to a response time of ~200 fs for the Cs_2Te photocathode.

After the test of these photocathodes at PITZ, they were again transported to LASA. The spectral response and reflectivity have been measured for these "used" cathodes and are compared in Fig. 6 with the values measured just after the production. From Fig. 6, it shows that the photoemission threshold of cathode 147.1 and 112.1 is increased from 1.79 eV to 2.08 eV, and a shoulder has appeared at the low photon energy for cathode 123.1. This new spectral behavior of these used cathodes elucidates the potential oxidation of cathode films. This kind of spectral behavior has previously been observed and interpreted through XPS investigation [19]. The difference in the spectral behavior

ISBN: 978-3-95450-220-2 ISSN: 2673-5474 doi: 10.18429/JACoW-FEL2022-TUP04

between the cathodes 123.1 and 147.1,112.1 could be construed as these cathodes being buried under a thin and thick alkali suboxide layer, respectively [19].

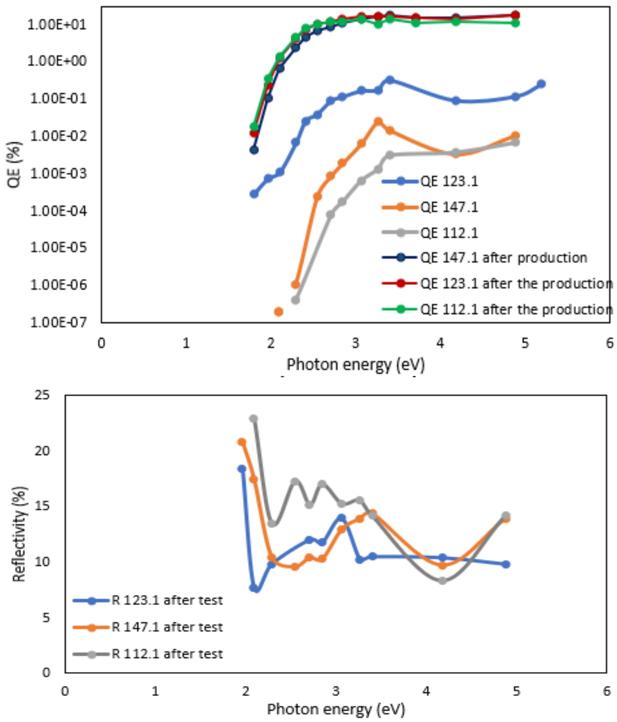

Figure 6: Spectral response and reflectivity measurements of the three cathodes after usage in the RF gun. The spectral response of the three fresh cathodes is shown for comparison.

NEW R&D DEVELOPMENT

To further improve the KCsSb photocathode recipe, we explored the effect of different deposition rates on the cathode properties. A new cathode KCsSb-8 has been grown in the R&D preparation system. We have deposited 5 nm of Sb at 90 °C, followed by K at 130 °C and Cs at 120 °C. During the K deposition, we kept the deposition rate at 0.2 to 0.4 nm/min (compared to 1 nm/min before), whereas in the Cs case, the deposition rate was maintained at 0.3 to 0.6 nm/min (compared to 1 nm/min earlier). Due to different deposition rates and slightly improved substrate temperature (i.e., 130 °C) during K deposition, we observed a significantly higher QE, of about 1.2 % at 543 nm for KSb compound, compared to previous QEs of about 0.2 % at 543 nm. A comparison of the QE curve during K deposition of all produced R&D cathodes is presented in Fig. 7.

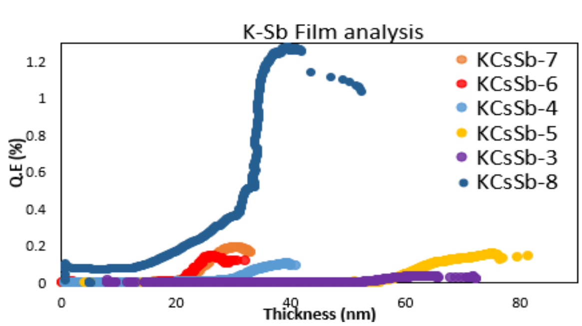

Figure 7: Comparison of the QE during K deposition of all produced R&D cathodes.

The final QE of the KCsSb-8 cathode was measured as 5.1 % at 543 nm (2-5% previously) and 8.84 % at 515 nm (4-8% previously). The optical characterization of this cathode is currently underway, and we will report the outcome shortly.

Conclusion

The first batch of three green cathodes was tested in a high gradient RF gun at PITZ. The results in terms of QE, thermal emittance, and response time are very promising. However, the limiting factors are high dark current and short operational lifetime. To overcome these drawbacks, we are currently improving our cathode recipe. The new co-evaporation technique will be introduced in our production system to explore its effect on the operation of our photocathodes in RF guns in the future.

ACKNOWLEDGEMENT

This work was supported by the European XFEL research and development program.

REFERENCES

[1] Y. Ding *et al.*, "Measurements and simulations of ultralow emittance and ultrashort electron beams in the linac coherent light source", *Phys. Rev. Lett.* vol. 102, p. 254801, 2009. doi: 10.1103/PhysRevLett.102.254801

[2] R. Akre *et al.*, "Commissioning the linac coherent light source injector", *Phys. Rev. Spec. Top. Accel. Beams*, vol. 11, p. 030703, 2008.
doi:10.1103/PhysRevSTAB.11.030703

[3] F. Sannibale *et al.*, "Schemes and challenges for electron injectors operating in high repetition rate X-ray FELS", *Journal of Modern Optics*, vol. 58, p. 1419, 2011. doi: 10.1080/09500340.2011.601328

[4] L. Cultrera *et al.*, "Photocathode behavior during high current running in the Cornell energy recovery linac photoinjector", *Phys. Rev. Spec. Top. Accel. Beams*, vol. 14, p. 120101, 2011
doi:10.1103/PhysRevSTAB.14.120101

[5] H.J. Qian *et al.*, "Alkali Cathode Testing for LCLS-II at APEX", in *Proc. FEL'15*, Daejeon, Korea, Aug. 2015, pp. 280-284. doi:10.18429/JACoW-FEL2015-MOD03

[6] E. Wang, V. N. Litvinenko, I. Pinayev, *et al.* "Long lifetime of bialkali photocathodes operating in high gradientsuperconducting radio frequency gun", *Sci. Rep.*, vol. 11, p. 4477, 2021. doi: 10.1038/s41598-021-83997-1

[7] D. Sertore, P. Michelato, L. Monaco, and C. Pagani, "R&D Activity on Alkali-Antimonied Photocathodes at INFNLasa," in *Proc. IPAC'18,* Vancouver, Canada, Apr.-May 2018, pp. 4284–4286. doi:10.18429/JACoW-IPAC2018-THPMF088

[8] D. Sertore, G. G. Rocco, P. Michelato, S. K. Mohanty, L. Monaco, and C. Pagani, "Photocathode Activities at INFN LASA", in *Proc. IPAC'19,* Melbourne, Australia, May 2019, pp. 2203–2206. doi:10.18429/JACoWI-PAC2019-TUPTS117

ISBN: 978-3-95450-220-2 ISSN: 2673-5474 doi: 10.18429/JACoW-FEL2022-TUP04

[9] S. K. Mohanty, G. G. Rocco, P. Michelato, L. Monaco, C. Pagani, and D. Sertore, "Development of a Multialkali Antimonide Photocathode at INFN LASA", in *Proc. FEL'19,* Hamburg, Germany, Aug. 2019, pp. 448–451. doi:10.18429/JACoW-FEL2019-WEP053

[10] S. K. Mohanty *et al.,* "Development of Multi-Alkali Antimonides Photocathodes for High-Brightness RF Photoinjectors", in *Proc. IPAC'21*, Campinas, Brazil, May 2021, pp. 1416–1419. doi:10.18429/JACoW-IPAC2021-TUPAB034

[11] E. D. Palik, "Introductory Remarks", in Handbook of Optical Constants of Solids, E. D. Palik, Ed. San Diego, CA, USA: Academic Press, pp. 3-9, 1985. doi:10.1016/B978-0-08-054721-3.50006-X

[12] D. Sertore *et al.,* "R&D on High QE Photocathodes at INFN LASA", in *Proc. IPAC'22*, Bangkok, Thailand, Jun. 2022, pp. 2633-2636. doi:10.18429/JACoW-IPAC2022 THPOPT027

[13] F. Stephan, C. H. Boulware, M. Krasilnikov, J. Bähr, *et al.,* "Detailed characterization of electron sources yielding first demonstration of European X-ray Free-Electron Laserbeam quality", *Phys. Rev. ST Accel. Beams*, vol. 13, p. 020704, 2010. doi:10.1103/PhysRevSTAB.13.020704

[14] A di Bona *et al.,* "Development, operation and analysis of bialkali antimonide photocathodes for high-brightness photo-injectors", *Nucl. Instr. Methods Phys. Res., Sect. A*, vol. 385, issue 3, pp. 385-390, 1997. doi:10.1016/S0168-9002(96)00809-1

[15] D. H. Dowell and J. F. Schmerge, "Quantum efficiency And thermal emittance of metal photocathodes*", Phys. Rev. ST Accel. Beams*, vol. 12, p. 074201, 2009. doi:10.1103/PhysRevSTAB.12.119901

[16] G. Shu *et al*., "Dark current studies of an L-band normal conducting RF gun*", Nucl. Instr. Methods Phys. Res., Sect. A*, vol. 1010, 2021. doi:10.1016/j.nima.2021.165546

[17] D. H. Dowell *et al*., "Cathode R&D for future light sources," *Nucl. Instrum. Methods Phys. Res., Sect. A,* p. 622, 2010. doi:10.1016/j.nima.2010.03.104

[18] G. Loisch *et al*.," Direct measurement of Photocathode time response in a high-brightness photoinjector", *Appl. Phys. Lett.* vol. 120, p. 104102, 2022. doi:10.1063/5.0078927

[19] Leonardo Soriano and Luis Galán, "Interaction of Cesium-Potassium Antimonide Photocathode Materials with Oxygen: an X-Ray Photoelectron Spectroscopy Study*", Jpn. J. Appl. Phys.*, vol. 32, p. 4737, 1993. doi:10.1143/JJAP.32.473

ISBN: 978-3-95450-220-2 ISSN: 2673-5474 doi: 10.18429/JACoW-FEL2022-TUP05

RADIO-FREQUENCY-DETUNING BASED MODELING AND SIMULATION OF ELECTRON BUNCH TRAIN QUALITY

Y. Chen*
Deutsches Elektronen-Synchrotron DESY, Hamburg, Germany

Abstract

A numerical study is carried out on the quality of the electron bunch train produced from a photoinjector based on a frequency-detuning dependent gun coupler kick. The impact of the kick on the emittance of the bunch train is modelled via three-dimensional electromagnetic field maps calculated at detuned frequencies of the gun cavity within long radio-frequency pulses. Beam dynamics simulations are performed in the so-called frequency-detuning regime. Preliminary results are presented and discussed.

INTRODUCTION

Radio-Frequency (RF) photoinjectors provide high brightness electron bunches for modern linear accelerator based free-electron lasers (FEL) [1–7]. At the European XFEL [2] (EuXFEL), the photoinjector [8] consists of an L-Band RF gun, a TESLA type 1.3 GHz module (A1), a 3rd harmonic RF section (AH1), a laser heater and beam diagnostics, as shown in Fig. 1. The 1.6-cell 1.3 GHz RF gun [9] can be operated with an electric field gradient of 60 MV/m on the cathode surface with long RF pulses of up to 650 µs at 10 Hz, allowing the production of 27000 bunches per second at the EuXFEL. The RF power is provided by a 10 MW multi-beam klystron and fed to the gun from the input waveguide via a door-knob transition into the rotationally symmetric coaxial coupler and the gun cavity. A frequency-detuning dependent transient coaxial RF coupler kick is observed and characterized within the RF pulse in [10]. The impacts of the effect on the electron bunch quality along the train are more pronounced towards longer RF pulse operation of the FEL.

Since the first lasing of the EuXFEL in May 2017 [11], a growing trend in the RF pulse length of the gun has been shown for routine user experiments, i.e. from averagely 100 µs in 2017 to first-time operating with 600 µs by the end of 2019, subsequently, stably running with 500 µs and above until the present. With more pronounced frequency-detuning over longer RF macropulses, potential impacts of the above-mentioned RF coupler kick on the bunch quality along the train should be further studied.

METHODOLOGY

Experiments have shown the existence of frequency detuning of the gun cavity within the RF macropulse due to pulse heating [10]. Within the RF pulse, individual electron bunches along the train see the transverse coaxial coupler kick of the gun. The kick is varied as a function of the frequency detuning of the gun cavity. Thus, the variable kick added to different bunches along the train and the resulting impact onto the bunch quality can be modelled as these bunches passing through the gun while experiencing disturbed and detuned RF field distributions of the gun cavity. This method requires RF field calculations at detuned frequencies as well as corresponding beam dynamics simulations using these field maps, as presented in the following two sections.

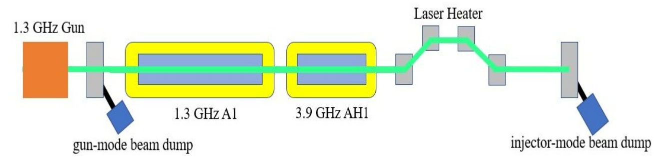

Figure 1: Schematic view of the European XFEL photoinjector (not to scale).

ELECTROMAGNETIC FIELDS

The three-dimensional calculation of the disturbed RF cavity field due to the gun coupler kick is based on the frequency domain solver of Computer Simulation Technology [12]. A computational model with its coordinate system is described in [10]. The frequency detuning (Δf) is defined as the difference between the RF drive frequency (f) and the cavity resonance frequency (f_0), i.e. $\Delta f = f - f_0$. In the following example, the S11 parameter, defined as the ratio of the reflected power over the forward power for a resonant cavity, is tuned to about -25 dB at the resonance. Figure 2 shows the disturbed transverse electric (Ey) and magnetic (Hx) field profiles at different detuned frequencies of the gun cavity, covering a detuning range up to +15 kHz towards a deeper over-heating state of the gun.

SIMULATIONS

Beam dynamics simulations are performed using ASTRA [13]. A simulation setup is sketched in Fig. 1. Electron bunches are tracked with on-crest RF phasing until the exit of the A1 module. The final beam energy is 150 MeV. Note, in addition, that a three-dimensional TESLA cavity field map of the A1 module is also applied [14, 15].

Figure 3 shows a comparison of the projected transverse emittance evolution along the beamline between two simulation cases. One of the cases (blue curve) serves as a reference, in which, under ideal conditions, no coupler kick effects are considered. In the other case (orange curve), a specific situation is emulated: a bunch travels through the gun and the A1 module both of which are described by the

* ye.lining.chen@desy.de

ISBN: 978-3-95450-220-2 ISSN: 2673-5474 doi: 10.18429/JACoW-FEL2022-TUP05

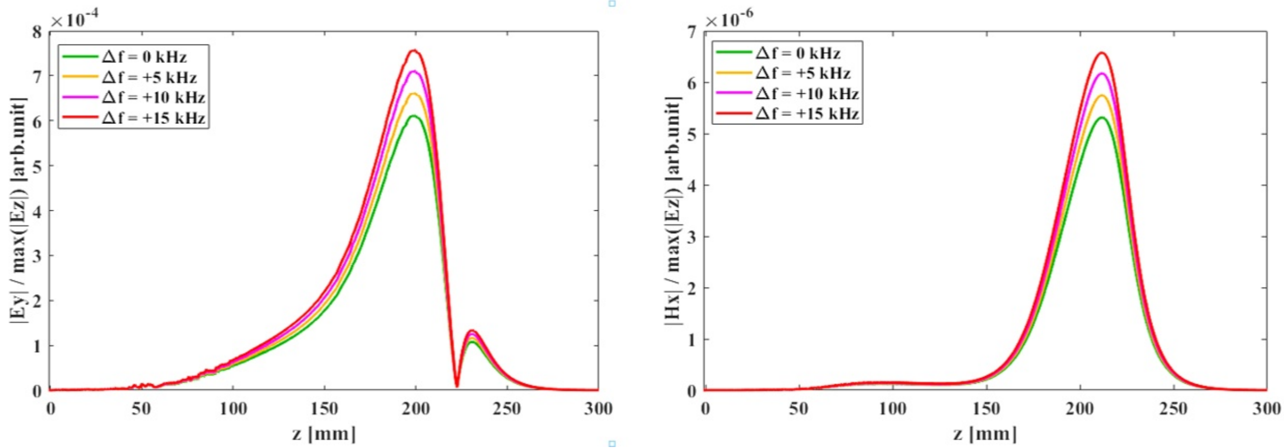

Figure 2: Disturbed RF field distributions with the normalized amplitudes to the accelerating fields at detuned resonance frequencies of the gun cavity. Left: electric fields; right: magnetic fields.

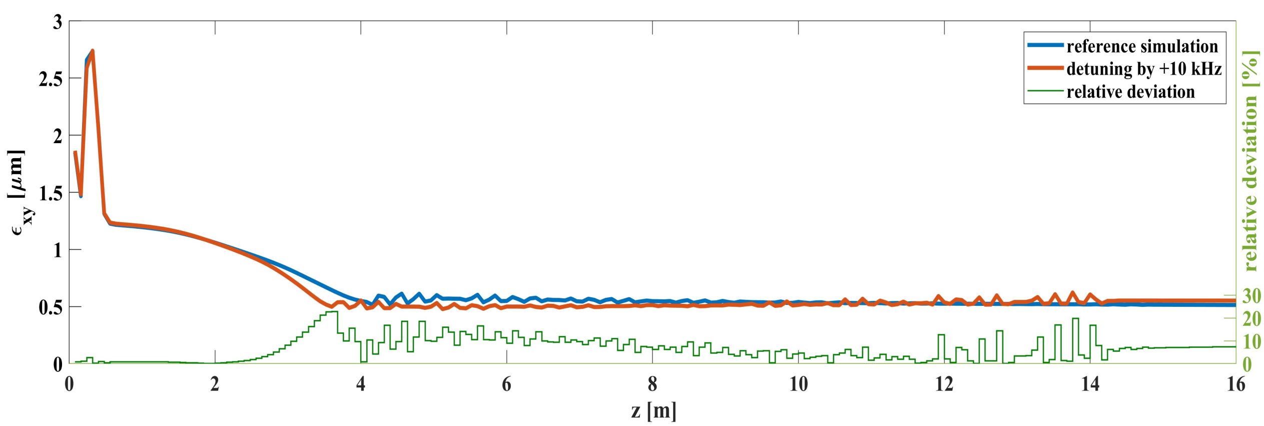

Figure 3: A comparison of the projected transverse emittance along the beamline between a reference simulation (no coupler kicks) and a simulation performed at 10 kHz off-resonance of the gun cavity. The final emittance is calculated at the exit of the A1 module, i.e. about 16 m downstream the cathode, as shown in Fig. 1.

corresponding three-dimensional field maps. Particularly for the gun field map, a 10 kHz frequency detuning is assumed. As an empirical estimation, a simulated 10-kHz detuning of the gun cavity may correspond to about 30 kW power reflection when the gun is practically operated at about 5.4 MW. Other simulation settings are kept the same in both cases. The relative difference in emittance (green curve) is illustrated on the right axis. As a result, for an electron bunch sitting on an intra-RF-pulse location of 10 kHz off the gun resonance, its projected transverse emittance grows by about 7% with respect to an ideal coupler-kick-free case.

Figure 4 shows a relative emittance change as a function of frequency detuning of the gun cavity. The gun solenoid strength is fixed and not explicitly optimized for a smaller transverse emittance at any reference point. In this figure, different detuned frequencies correspond to different locations within the RF macropulse (towards an over-heated state w.r.t. the gun resonance), thereby representing the cases of different electron bunches along the train. This numerical example shows an overall emittance deviation along the bunch train (reflected by the frequency detuning) downstream the A1 module. More specifically, within a 10-kHz detuning of the gun cavity over the RF macropulse, seen by the electron bunch train, the projected emittance change is up to about 22%. It can also be noted that higher frequency detuning towards a deeper over-heated state of the gun is generally more beneficial for the emittance reduction.

A parametric dependency of the effect on the gun solenoid strength is shown in Fig. 5. At a fixed detuned frequency of the gun cavity, it is obvious that the overall emittance at the exit of the A1 module depends on the strength of the gun solenoid. However, at each detuned frequencies of the gun cavity, an optimal gun solenoid strength for achieving an overall optimized transverse emittance after the A1 module may not be the same. This also indicates that the peak to peak variation of the projected transverse emittance along the bunch train may have a parametric dependency on the chosen solenoid strength. These interrelated parametric dependencies (e.g. on RF phases, solenoid strength, orbit at the entrance of the A1 module, etc.) needs to be further clarified.

ISBN: 978-3-95450-220-2 ISSN: 2673-5474 doi: 10.18429/JACoW-FEL2022-TUP05

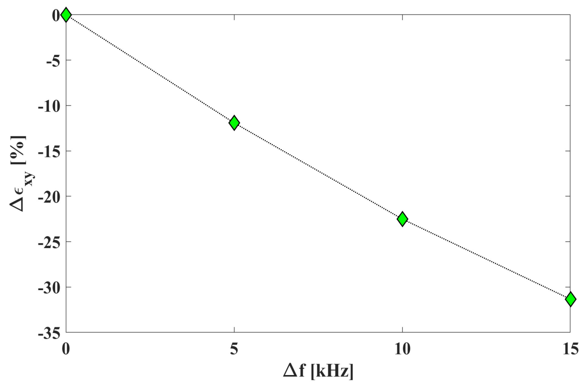

Figure 4: Relative emittance change versus frequency detuning within the RF pulse of the gun cavity. The emittance is calculated at the exit of the A1 module. The gun solenoid strength is fixed.

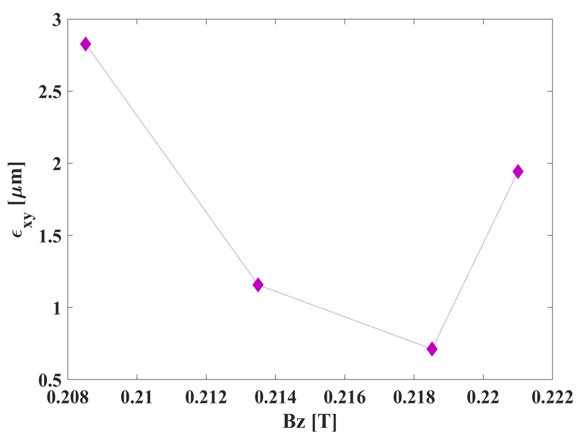

Figure 5: Gun solenoid strength dependency of an optimized projected emittance at a fixed detuned frequency of the gun cavity using on-crest phasing of both the gun and the A1 module.

OUTLOOK

Numerical studies presented in this paper suggest a relative projected transverse emittance change up to 22% along an electron bunch train contained within an RF macropulse of the gun cavity over a frequency detuning of 10 kHz with respect to the resonance. More detailed investigations will be focused on a comparison of the bunch quality with the measurement data, as well as potential impacts onto the FEL performance.

ACKNOWLEDGEMENTS

The author acknowledges support from Deutsches Elektronen-Synchrotron DESY (Hamburg, Germany), a member of the Helmholtz Association HGF and European XFEL GmbH (Schenefeld, Germany). The author thanks Martin Dohlus from DESY for useful discussions on coupler kicks of TESLA cavities and for providing helpful references.

REFERENCES

[1] M. Dohlus *et al.*, “Synchrotron Radiation and Free-Electron Lasers”. In *Landolt-Boernstein New Series*; Myers, S., Schopper, H., Eds.; Springer: Berlin/Heidelberg, Germany, 2013; Volume 21C. doi:10.1007/978-3-642-23053-0$_$41

[2] W. Decking *et al.*, “A MHz-repetition-rate hard X-ray free-electron laser driven by a superconducting linear accelerator”, *Nat. Photonics*, vol. 14, pp.391–397, 2020. doi:10.1038/s41566-020-0607-z

[3] E. Prat *et al.*, “A compact and cost-effective hard X-ray free-electron laser driven by a high-brightness and low-energy electron beam”, *Nat. Photonics*, vol. 14, pp. 748–754, 2020. doi:10.1038/s41566-020-00712-8

[4] P. Emma *et al.*, “First lasing and operation of an ångstrom-wavelength free-electron laser”, *Nat. Photonics*, vol. 2010, vol. 4, p. 641–647. doi:10.1038/nphoton.2010.176

[5] T. Ishikawa *et al.*, “A compact X-ray free-electron laser emitting in the sub-ångström region”, *Nat. Photonics*, vol. 6, pp. 540–544, 2012. doi:10.1038/nphoton.2012.141

[6] H. Kang *et al.*, “Hard X-ray free-electron laser with femtosecond-scale timing jitter”, *Nat. Photonics*, vol. 11, pp. 708–713, 2017. doi:10.1038/s41566-017-0029-8

[7] A. Novokhatski, F.-J. Decker, Y. Nosochkov, and M. K. Sullivan, “The Effect of Wakefields on the FEL Performance”, in *Proc. FEL'15*, Daejeon, Korea, Aug. 2015, pp. 161–165. doi:10.18429/JACoW-FEL2015-MOP055

[8] F. Brinker, “Commissioning of the European XFEL Injector”, in *Proc. IPAC'16*, Busan, Korea, May 2016, pp. 1044–1047. doi:10.18429/JACoW-IPAC2016-TUOCA03

[9] M. Krasilnikov *et al.*, “Experimentally minimized beam emittance from an L-band photoinjector”, *Phys. Rev. Accel. Beams*, vol. 15, p. 100701, 2012. doi:10.1103/PhysRevSTAB.15.100701

[10] Y. Chen *et al.*, “Frequency-detuning dependent transient coaxial rf coupler kick in an *L*-band long-pulse high-gradient rf photogun”, *Phys. Rev. Accel. Beams*, vol. 23, p. 010101, 2020. doi:10.1103/PhysRevAccelBeams.23.010101

[11] H. Weise and W. Decking, “Commissioning and First Lasing of the European XFEL”, in *Proc. FEL'17*, Santa Fe, NM, USA, Aug. 2017, pp. 9–13. doi:10.18429/JACoW-FEL2017-MOC03

[12] Computer Simulation Technology. https://www.3ds.com/.

[13] A Space Charge Tracking Algorithm. https://www.desy.de/~mpyflo/.

[14] P. Piot, M. Dohlus, K. Floettmann, M. Marx, and S. G. Wipf, “Steering and Focusing Effects in TESLA Cavity Due to High Order Mode and Input Couplers”, in *Proc. PAC'05*, Knoxville, TN, USA, May 2005, paper WPAT083, pp. 4135–4137.

[15] 3D TESLA cavity field maps. https://www.desy.de/fel-beam/s2e/codes.html.

ISBN: 978-3-95450-220-2 ISSN: 2673-5474 doi: 10.18429/JACoW-FEL2022-TUP07

PHOTOCATHODES FOR THE ELECTRON SOURCES AT FLASH AND EUROPEAN XFEL

D. P. Juarez-Lopez*, F. Brinker, S. Lederer, S. Schreiber
Deutsches Elektronen-Synchrotron DESY, Hamburg, Germany
L. Monaco, D. Sertore, INFN Milano - LASA, Segrate, Italy

Abstract

The photoinjectors of FLASH at DESY (Hamburg, Germany) and the European XFEL are operated by laser driven RF-guns. In both facilities cesium telluride (Cs_2Te) photocathodes are successfully used since several years. We present recent data on the lifetime and quantum efficiency (QE) of the photocathodes currently in operation. In addition we present the latest data of the cathode #680.1 which holds the operation record time of 1452 days with a total charge extracted of 32.2 C.

INTRODUCTION

The FLASH accelerator is a free-electron laser (FEL) user facility since 2005 [1–4], located in DESY (Hamburg, Germany) and provides ultra-short femtosecond laser pulses in the extreme ultra-violet and soft X-ray wavelengths range with unprecedented brilliance to two photon experimental halls. The macro-pulse repetition rate is 10 Hz with a usable length of the RF pulses of 800 µs. With a micro-bunch frequency of 1 MHz up to 8000 bunches per second are accelerated at FLASH. The bunch charge depends on the requirements on the FEL-light and is usually within a span of 20 pC to 1 nC. After the electron beam is accelerated to 1.25 GeV, the electron bunches are distributed into two different undulator beamlines.

The European XFEL [5] is the longest superconducting linear accelerator in the world driving a hard X-ray free-electron laser. The accelerator is operated by DESY. After a successful commissioning in 2016 [6] and first lasing in May 2017 [7], first user periods have been successfully accomplished [8]. The European XFEL runs now in full swing delivering high brilliance femtosecond short X-ray pulses in the energy range of 0.25 to 25 keV. The European XFEL uses upgraded TESLA type superconducting linac technology similar to FLASH with 10 Hz macro-pulse repetition rate. With a micro-bunch frequency of up to 4.5 MHz and an RF-pulse length of 600 µs, the European XFEL can deliver 27000 bunches per second.

ELECTRON SOURCES

The electron sources of FLASH and the European XFEL are very similar. Both photoinjectors are driven by a normal conducting 1.3 GHz L-band RF-gun, based on the design by [9]. Cs_2Te cathodes have been chosen to generate the photoelectrons bunches in both facilities. The electron bunches at FLASH are generated by three drive laser systems operating at a wavelength of 262 nm and 257 nm [10], while both laser at the European XFEL operates at 257 nm. All Cs_2Te photocathodes have a high quantum efficiency (QE) that keeps the required average laser power for multi-bunch operation in a reasonable regime. The vacuum pressure in the RF-guns during operation is in the low 10^{-9} mbar range. These excellent vacuum conditions are crucial for the lifetime of Cs_2Te cathodes.

Currently the accelerating field at the photocathode during standard operation at FLASH is 50 MV/m and 54 MV/m for the European XFEL. In both facilities the whole gun setups are interchangeable between each other. Gun 3.1 is was in operation at FLASH since 2013 [11] and has been exchanged in December 2019 for Gun 4.4 due to a leak in the cooling water circuit. Installed in 2013, Gun 4.3 was the first RF-gun operated at the European XFEL, during commissioning phase and first user runs. In December 2017 it was exchanged for Gun 4.6 and serves now as hot spare.

The photocathodes are either prepared at INFN-LASA in Milano, Italy, [12] or at DESY Hamburg. The transfer to the accelerators is done with ultra-high-vacuum (UHV) transport boxes, maintaining a pressure in the low 10^{-10} mbar range. The transport boxes can be equipped with up to four cathodes, one place is void. In both facilities a very similar load-lock transfer system is used to insert the Cs_2Te photocathodes under the required UHV conditions into the RF guns [12].

QUANTUM EFFICIENCY AND LIFETIME

QE Measurement Procedure

The QE is monitored after cathode production in the lab where the spectral response is measured with a Hg-lamp for 6 different wavelengths. A QE map is generated after production to understand its uniformity and to be able to compare the map afterwards with in situ measurements.

In situ, the cathode performance is monitored on regular bases. The QE measurements in the gun are always taken under comparable conditions, such as:

- The on-crest accelerating field during the measurements is in the order of 52 MV/m.
- The charge is measured with a toroid right after the RF-gun (uncertainty 1%).
- The launch phase is set to 38° w.r.t. zero crossing. This phase was chosen years ago and kept as reference for all QE measurements.

Regarding the phase, the measurement is neither at the on-crest phase nor at the launch phase during standard operation

* pavel.juarez@desy.de

ISBN: 978-3-95450-220-2 ISSN: 2673-5474 doi: 10.18429/JACoW-FEL2022-TUP07

of the accelerators, which is at 45°. On-crest, about 30% more charge is extracted than at 38°, at 45° about 10% more.

To determine the QE, we measure the charge as function of the laser energy. At FLASH the laser energy is measured by a calibrated pyroelectric joulemeter in front of the vacuum window (uncertainty 2%). At the European XFEL the measurement is done by a photo diode which is cross-calibrated with a pyroelectric detector. To obtain the laser energy at the cathode the transmission of the vacuum window and the reflectivity of the in-vacuum mirror are taken into account in the data analysis. Laser spot at the photocathodes during the measurements is 1.0 mm and 1.2 mm – typical truncated Gaussian spot sizes during operation. The QE is determined by a linear fit of the slope of the measured charge versus laser energy in the region, where space charge effects are negligible. [13]

Lifetime at European XFEL

Cathode #680.1 holds the operation record time of 1452 days with a total charge of 32.2 C extracted (Fig. 1). The cathode was exchanged for #681.1 after its QE dropped significantly to a 2 % level.

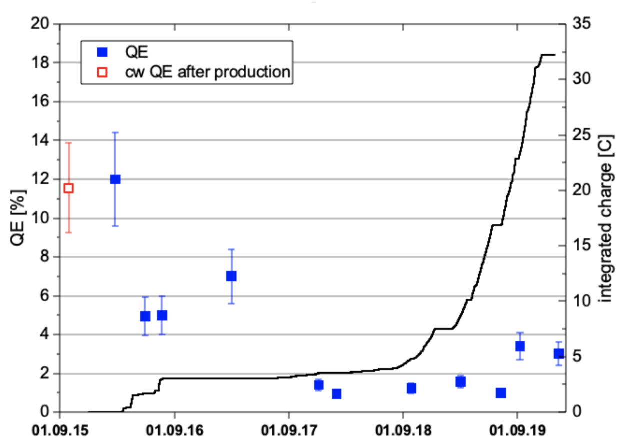

Figure 1: Quantum efficiency (blue solid squares) and integrated charge vs. time (black line) for cathode #680.1, which was in operation at the European XFEL. The red square data point shows the QE right after production measured with a Hg-lamp at 254 nm.

Figure 2 shows the quantum efficiency of cathode #681.1. The cathode is being in operation at the European XFEL since the 14th of January 2020.

Cathode #681.1 has been prepared in September 2015 at DESY and is being in operation since January 2020 at the European XFEL. The QE is being stable after the first year of operation. During operation a total integrated charge of 49.8 C has been extracted from cathode #681.1.

Lifetime at FLASH

Cathode #73.3 was in operation from February 2015 to December 2018. This cathode held the previous record of

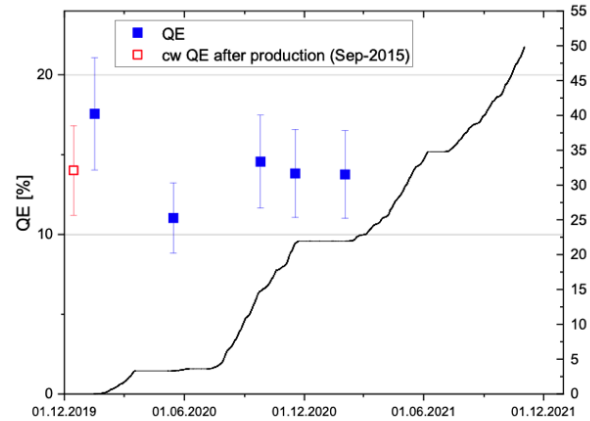

Figure 2: Quantum efficiency (blue solid squares) and integrated charge vs. time (black line) for cathode #681.1, operated at European XFEL. The red square data point shows the QE right after production measured with a Hg-lamp at 254 nm.

1413 days in operation with an integrated charge of 25 C extracted. [14] Since December 2018, the FLASH accelerator operates with cathode #105.2.

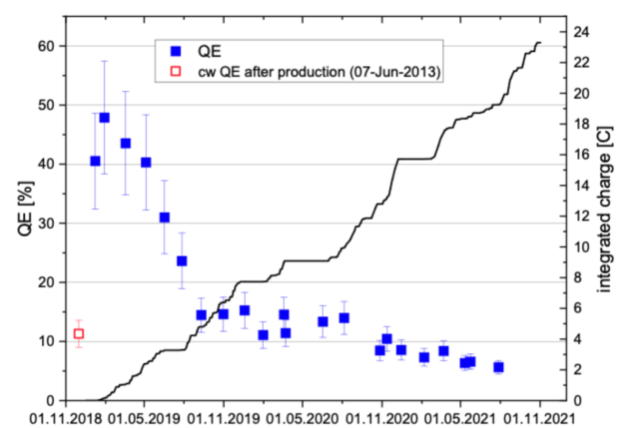

Figure 3: Quantum efficiency (blue solid squares) and integrated charge vs. time (black line) for cathode #105.2, operated at FLASH since December 2018. The red square shows the QE right after production measured with a Hg-lamp at 254 nm.

Figure 3 shows the QE of cathode #105.2 as well as the integrated extracted charge over the whole operation time. The QE has settled at a 7% level with an integrated charge of 23 C up to now.

In addition to the regular QE measurements at FLASH, the homogeneity of electron emission from the photocathodes is studied by QE-maps. For this investigations a small spot laser beam of σ = 25 µm is scanned horizontally and vertically over the cathode in steps of 85 µm. The emitted charge is measured with a high resolution toroid (detection

ISBN: 978-3-95450-220-2 ISSN: 2673-5474 doi: 10.18429/JACoW-FEL2022-TUP07

threshold <1 pC). The laser energy is adjusted such to generate a maximum charge of 10 pC to 20 pC.

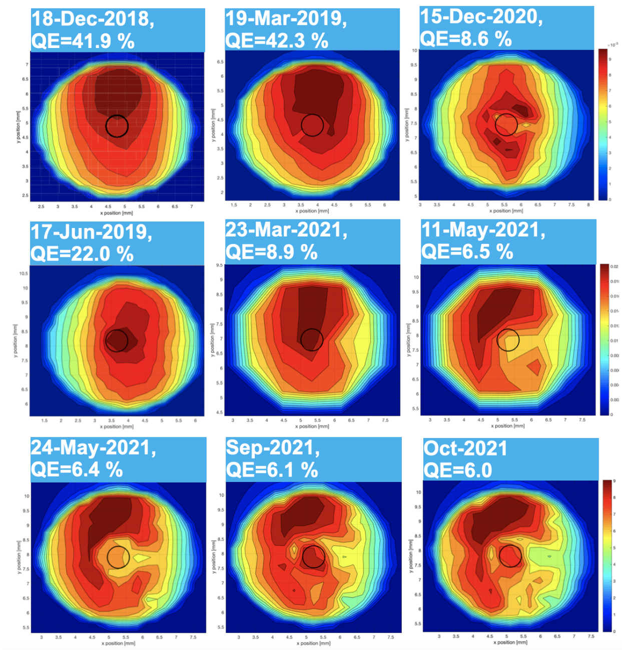

Figure 4: Quantum efficiency map evolution of cathode #105.2 from December 2018 to October 2021. The black ring in the middle indicates the typical size of the laser beam of 1.2 mm during operation.

Figure 4 shows the evolution of QE-maps for cathode #105.2. An non-homogeneous emission over the cathode is observed, the top has a higher QE than the bottom. A decrease of the overall QE is partially compensated by the cleaning effect of the UV laser beam hitting the cathode in the middle. [11, 15, 16].

In order to understand better the QE map measured in the gun, an experiment was performed to understand if the QE at the cathode left/right was actually lower than top/down or is an effect of the narrow acceptance of the last mirror mounted in the gun vacuum, about 70 cm away from the cathode. Due to the 45° angle the mirror has an acceptance of only 5 mm in the horizontal plane, the size of the cathode. In the vertical the acceptance is 10 mm. During the scan, the laser spot is moved with linear stages only and thus moves over the vacuum mirror.

In the experiment, the laser spot angle was changed such, that the laser hits the outer edges of the cathode, keeping the spot in the center of the vacuum mirror. Figure 5 shows the QE maps taken while the laser was moved in order to reach the edges of the cathode. The top maps show the QE map with the laser centered on the cathode and on the vacuum mirror, but moved during the scan on the vacuum mirror. The bottom maps show the QE map with the laser centred on the mirror while hitting the right edge of the cathode (left map) and the top edge of the cathode (right map). Also in this case, the laser was moved over the vacuum mirror during the scan.

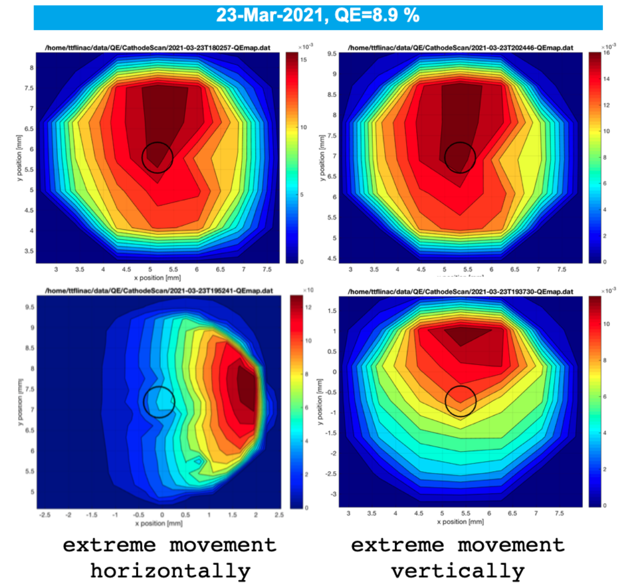

Figure 5: Quantum efficiency map of cathode #105.2 measured on March 2021 with a QE of 8.9%. The top maps: laser centered on the cathode. The bottom maps: laser is hitting the right edge of the cathode (left) and the top edge of the cathode (right).

The high QE at the right/top edges with the laser initially moved to these edge shows, that the limited horizontal acceptance of the vacuum mirror in the usual QE map (top) artificially reduces the QE left/right and is not a real reduction of the QE. The very low QE on the left and bottom of the bottom maps is explained by the same argument with a stronger reduction in the horizontal plane.

In order to solve this systematic issue of the QE map, one should scan the laser spot over the cathode keeping the laser in the middle of the vacuum mirror. This is a complicated procedure which takes a lot of beam time (8 hours) and thus does not allow quick regular scans. The simplified scan is done in 20 minutes and is short enough for regular measurements during FLASH operation.

CONCLUSION

The Cs_2Te photocathodes operated at FLASH and the European XFEL during the last years show a remarkable lifetime. Cathode #680.1 was exchange at the European XFEL holding an operation record of 1452 days with a total extracted charge of 32.2 C. Cathode #681.1 is being used for 910 days with a total extracted charge of 20.7 C.

Cathode #105.2 is in use at FLASH for 1058 days with a total extracted charge of 23.3 C. This cathode has shown a remarkable high quantum efficiency. This cathode proceeds the #73.3 which was in use for 1413 days with an extracted charge of 24.4 C.

ISBN: 978-3-95450-220-2 ISSN: 2673-5474 doi: 10.18429/JACoW-FEL2022-TUP07

ACKNOWLEDGEMENTS

We would like to acknowledge our colleagues from LASA, Milano, Italy and from DESY Hamburg and Zeuthen for their support in cathode preparation and vacuum equipment.

REFERENCES

[1] W. Ackermann *et al.*, "Operation of a free-electron laser from the extreme ultraviolet to the water window", *Nat. Photonics*, vol. 1, pp. 336–342, 2007. doi:10.1038/nphoton.2007.76

[2] S. Schreiber and B. Faatz, "The free-electron laser FLASH", *High Power Laser Science and Engineering*, vol. 3, p. e20, 2015. doi:10.1017/hpl.2015.16

[3] B. Faatz *et al.*, "Simultaneous operation of two soft x-ray free-electron lasers driven by one linear accelerator", *New J. Phys.*, vol. 18, p. 062002, 2016. doi:10.1088/1367-2630/18/6/062002

[4] K. Honkavaara, "Status of the FLASH FEL User Facility at DESY", in *Proc. 38th Int. Free Electron Laser Conf. (FEL'17)*, Santa Fe, NM, USA, Aug. 2017, pp. 14–18. doi:10.18429/JACoW-FEL2017-MOD02

[5] M. Altarelli *et al.* ED., "The European X-Ray Free-Electron Laser - Technical design report", DESY, Hamburg, Germany, Rep. DESY 2006-097, July 2007.

[6] W. Decking and H. Weise, "Commissioning of the European XFEL Accelerator", in *Proc. IPAC'17*, Copenhagen, Denmark, May 2017, pp. 1–6. doi:10.18429/JACoW-IPAC2017-MOXAA1

[7] H. Weise and W. Decking, "Commissioning and First Lasing of the European XFEL", in *Proc. FEL'17*, Santa Fe, NM, USA, Aug. 2017, pp. 9–13. doi:10.18429/JACoW-FEL2017-MOC03

[8] W. Decking *et al.*, "Status of the European XFEL", in *Proc. IPAC'19*, Melbourne, Australia, May 2019, pp. 1721–1723. doi:10.18429/JACoW-IPAC2019-TUPRB020

[9] B. Dwersteg, K. Flöttmann, J. Sekutowicz, and Ch. Stolzenburg, "RF gun design for the TESLA VUV Free Electron Laser", NIM A393, pp. 93–95, 1997. doi:10.1016/S0168-9002(97)00434-8

[10] S. Schreiber, C. Gruen, K. Klose, J. Roensch, and B. Steffen, "Simultaneous Operation of Three Laser Systems at the FLASH Photoinjector", in *Proc. FEL'15*, Daejeon, Korea, Aug. 2015, pp. 459–463. doi:10.18429/JACoW-FEL2015-TUP041

[11] S. Lederer and S. Schreiber, "Cs2Te Photocathode Lifetime at Flash and European XFEL", in *Proc. IPAC'18*, Vancouver, Canada, Apr.-May 2018, pp. 2496–2498. doi:10.18429/JACoW-IPAC2018-WEPMF056

[12] S. Schreiber, P. Michelato, L. Monaco, and D. Sertore, "On the Photocathodes Used at the TTF Photoinjector", in *Proc. PAC'03*, Portland, OR, USA, May 2003, paper WPAB016, pp. 2071–2073.

[13] S. Lederer *et al.*, "Photocathode Studies at FLASH", in *Proc. EPAC'08*, Genoa, Italy, Jun. 2008, paper MOPC072, pp. 232–234.

[14] S. Lederer, F. Brinker, L. Monaco, S. Schreiber, and D. Sertore, "Update on the Photocathode Lifetime at FLASH and European XFEL", in *Proc. FEL'19*, Hamburg, Germany, Aug. 2019, pp. 427–429. doi:10.18429/JACoW-FEL2019-WEP047

[15] S. Schreiber and S. Lederer, "Lifetime of Cs2Te Cathodes Operated at the FLASH Facility", in *Proc. FEL'15*, Daejeon, Korea, Aug. 2015, pp. 464–467. doi:10.18429/JACoW-FEL2015-TUP042

[16] D. Sertore *et al.*, "Cs2Te Photocathode Robustness Studies", in *Proc. EPAC'08*, Genoa, Italy, Jun. 2008, paper MOPC075, pp. 241–243.

ISBN: 978-3-95450-220-2 ISSN: 2673-5474 doi: 10.18429/JACoW-FEL2022-TUP09

GENERATION OF A SUB-PICOSECOND SHEET ELECTRON BEAM USING A 100 fs LASER

M. Asakawa†, S. Yamaguchi, Y. Karaki, H. Matsubara, Y. Miyajima, R. Michishita, T. Shirai, R. Horrii and S. Yoshimatsu, Kansai University, Suita, Japan
M. Nakajima, Institute of Laser Engineering Osaka University, Suita, Japan

Abstract

In this paper, we present the experimental results of a pulsed sheet-like photoelectron bunch generated by irradiating an elliptically focused 100 fs laser. The sheet-like bunch has the same space-charge limitation as the circular bunch. In the contrast, the anisotropic diverging property of the sheet-like bunch was observed: the diverging angle along the minor axis of the photoemission area was greater than that along the major axis. In addition, the net diverging angle of the sheet bunch seemed to be smaller. Based on our results, we propose a new kind of Peirce gun to compensate for the diverging angle along the minor axis.

INTRODUCTION

One of the most promising electron sources is the sub-picosecond laser driven DC photoelectron gun, capable of producing an ultrashort electron bunch with a duration of less than 1 ps and a charge of 10 pC and has been developed specifically for use as an ultrafast electron microscope instrument [1-3]. However, for the radiation source application, which requires a charge of 100 pC, electrons suffer from a strong self-field at the emission surface due to the ultrashort pulse duration, which causes them to increase their phase space volume, as previously reported [4].

In contrast, the sheet electron beam formation is being investigated for high-power microwave sources because the sheet electron beam interacts efficiently with the planar radiative structures [5-8]. Several methods have been studied to form the sheet electron beam: a round beam produced by the thermionic cathode Pierce gun was transformed into a sheet beam using a quadrupole magnet or an asymmetric solenoid lens, a specially designed sheet beam Pierce gun, and direct emission from a blade-like metallic cathode. Those studies aimed to produce a DC or long pulse current.

In this paper, we will present a preliminary attempt to generate a sheet-like electron bunch via photoemission using an elliptically focused 100 fs laser. The focal spot was an ellipse with an ellipticity of 43. With this ellipticity, the circumference of the sheet-like bunch is 4.2 times longer than that of a round beam with the same cross-section. Thus, the sheet-like bunch has a larger surface area. According to Gauss's law, the electric field on the surface of the sheet-like bunch should be significantly reduced. Based on this idea, we investigated the diverging angle of the sheet-like bunch.

EXPERIMENT

Figure 1 shows the experimental apparatus. The driving laser was a Ti:sapphire laser operated at a repetition rate of 1 kHz. At the fundamental wavelength of 800 nm, the average power was 2.5 W and the pulse-duration was 92 fs. At a third harmonic generator, the laser pulse was converted to the ultraviolet pulse with a wavelength of 266 nm (4.65 eV) and an average power of 200 mW. Then, the UV pulse passed through a pair of beam-splitters, changing the injection angle of the laser to the splitters by rotating them, with the transmitted power regulated from 0 to 150 mW. The UV pulse was focused by a convex lens or a cylindrical lens to generate a round electron bunch or a sheet-like bunch, respectively. Finally, the UV pulse was irradiated in a tungsten cathode (φ = 4.52 eV), which was held at the negative voltage, by passing through a single crystalline quartz window placed in the vacuum vessel. With the convex lens, the spot area on the cathode formed an ellipse of $\pi \times 1.5$ (horizontal direction) $\times$ 0.75 (vertical direction) mm^2 due to the injection angle of 60º. The injection angle also resulted in an optical path difference of 2 × 1.5 mm × sin 60º in the incident plane, resulting in a time lag of 8.7 ps at most. The cylindrical lens was placed so that the laser spot had the same area: the expected size was $\pi \times 0.185 \times 6$ mm^2 and the ellipticity was 32. The electron bunch in the region of the emission area should form a line-like shape rather than a sheet because of the short duration of the dive laser. In this case, the time lag was reduced to 2 × 0.185 mm × sin 60º / 3 × 10^{11} mm/s = 1.1 ps.

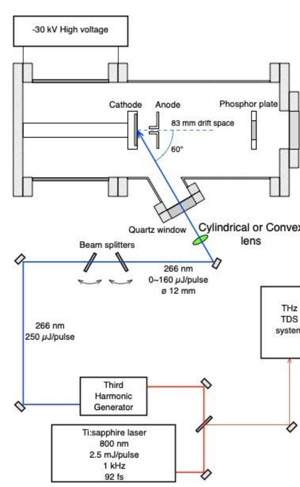

Figure 1: Experimental apparatus.

† asakawa@kansai-u.ac.jp

ISBN: 978-3-95450-220-2 ISSN: 2673-5474 doi: 10.18429/JACoW-FEL2022-TUP09

Then, the photoelectrons accelerated toward a grounded anode. The cathode-anode spacing was set to 10 mm. Electrons in the center of the bunch passed through an aperture with a radius of 1 mm and a thickness of 5 mm drilled at the center of the anode and then ran into a phosphor screen 83 mm from the aperture end. The electron bunch diameter was estimated from the fluorescence image, and the bunch charge was measured on the screen. All experiments were conducted at a pressure of less than 5×10^{-7} Pa.

Figure 2 shows the dependencies of the electron bunch charge at the anode electrode Q_A (a) and that at the phosphor plate Q_P (b) on the laser pulse energy. In Fig. 2 (a), a maximum Q_A of 88 pC and 42 pC was generated by irradiating the laser pulse focused by the convex lens (blue circles) for $V_{KA} = 30$ kV and 10 kV, respectively. These values are close to the space charge limitation charge for the ultrashort electron bunch [2, 9]:

$$Q_{sat} = \varepsilon_0 \frac{V_{KA}}{d} S, \tag{1}$$

which are to be 93.7 pC and 31.3 pC for 30 kV and 10 kV, respectively. The Q_A with the cylindrical lens (red circles) is about 0.8 times lower than that with the convex lens and starts to saturate at a laser energy of 60 μJ. These facts indicate that the laser spot area with the cylindrical lens is smaller than that with the convex lens. The estimated spot area is $\pi \times 6 \times 0.14$ mm^2, which is 80% of the spot area with the convex lens, and the ellipticity is 43.

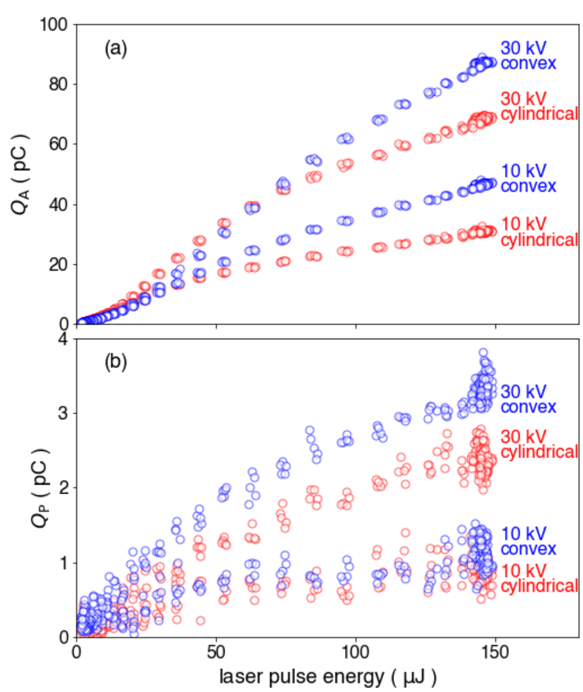

Figure 2: Dependencies of the electron bunch charge (a) at the anode Q_A and (b) at the phosphor plate Q_P on the laser pulse energy for the gun voltages of 10 kV and 30 kV.

In Fig. 2 (b), Q_P with the cylindrical lens was 0.76 times lower than that with the convex lens for $V_{KA} = 30$ kV: the same ratio of Q_A with the cylindrical lens to that with the convex lens. The transmitting rate, Q_P/Q_A, decreased with the laser pulse energy and remained constant at 0.05 for laser energies greater than 70 μJ for the round bunch and the sheet-like bunch. This indicates that the electron bunch increased its cross-section significantly while traveling through the cathode-anode spacing. For $V_{KA} = 30$ kV, Q_P/Q_A decreased to 0.03: the bunch increased its cross section more rapidly, as expected.

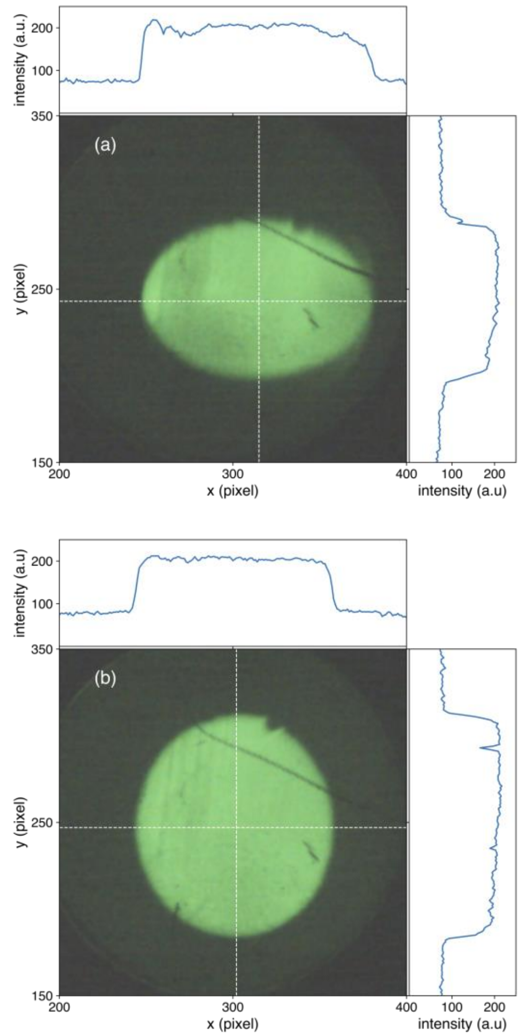

Figure 3: Fluorescence images with the cylindrical lens (a) and with the covex lens (b). The intensity profiles along the dashes lines in the images are also shown.

Figure 3 shows the fluorescence images of electron bunches passing through the anode aperture for $V_{KA} =$ 30 kV. For the examples with the cylindrical lens (upper, (a)) and the convex lens (lower, (b)), Q_A was measured to be 83 pC and 65 pC and Q_P was 3.1 pC and 2.2 pC, respectively. The dark lines in the images were caused by the scars on the phosphor surface from the installation process. In (a), an elliptic image with the major radius along the x-

ISBN: 978-3-95450-220-2 ISSN: 2673-5474 doi: 10.18429/JACoW-FEL2022-TUP09

axis (horizontal direction) was observed with the cylindrical lens. The major and minor radii were 10.0 and 6.7 mm, respectively. This result indicates that electrons had a larger diverging angle along the minor axis of the photoemission area. The same tendency was observed for the case with the convex lens: the image had a minor radius of 8.7 mm along the x-axis, along which the photoemission area had its major radius. In this case, the major radius was 9.8 mm, almost the same as that with cylindrical lens. Comparing these two images, the bunch cross-section (the number of the bright pixels) with the cylindrical lens was 0.75 times smaller than that with the convex lens. These results indicated that the net diverging angle of the central part of the bunch was reduced by increasing the ellipticity of the emission area, as expected.

Figure 4 shows the dependence of the diameter of the phosphor image on Q_A for $V_{KA} = 30$ kV. For all Q_A values, the diameters along the minor axis of the emission area were larger than that along the major axis, and the size relation was

$$D_{m,cy} \gtrsim D_{m,co} > D_{M,co} > D_{M,cy}$$

where subscripts "m" and "M" indicate that the diameter along the minor axis and major axis of the emission area, respectively. Subscripts "cy" and "co" indicate cylindrical lens and convex lens, respectively. The diameter of the bunch increased as the radius of the emission area decreased. For all Q_A, $D_{m,cy}$ and $D_{m,co}$ were almost the same, even though the minor radius of the emission area differed by a factor of 0.14 mm/0.75 mm = 0.187, whereas $D_{M,cy}$ was much smaller than other diameters. The decrease in the net diverging angle is caused by a small diverging angle along the major axis of the highly elliptic emission area. The diameter likewise remained constant for $Q_A > 40$ pC, where the electron gun began to saturate. Even under this condition, the diverging angles were still 60 % of the acceptable angle of the anode aperture $\tan^{-1}(1/5) = 0.197$ rad.

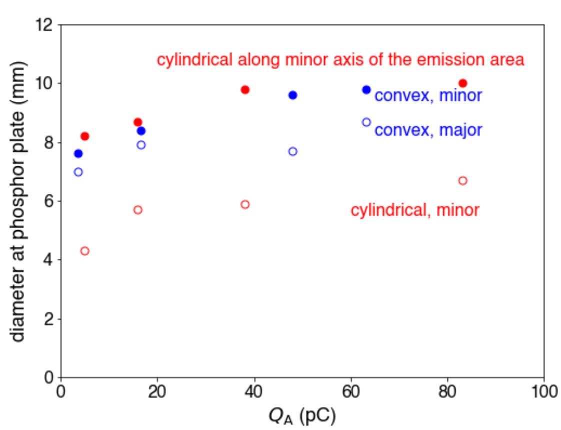

Figure 4: Dependencies of the diameter of the phosphor image on Q_A for $V_{KA} = 30$ kV. Red and blue circles indicate the diameters with the cylindrical lens and the convex lens, respectively.

DISCUSSION

According to Gauss's law, the net radial electric field at the bunch periphery may decrease with the circumference of the bunch cross-section. The circumference of an ellipse with a given area S and ellipticity e is approximately expressed by:

$$C \simeq \sqrt{\pi S}\left[3\left(\frac{1}{\sqrt{e}}+\sqrt{e}\right)-\sqrt{10+3\left(\frac{1}{e}+e\right)}\right]. \qquad (2)$$

An ellipse with an ellipticity of 43 has a circumference that is 4.2 times larger than that of a circle, $C_0 = 2\sqrt{\pi S}$. Thus, a significant reduction in the radial field can be expected near the emission surface, where the emittance growth from the nonlinear radial force is most visible. This could be the reason for the decrease in the net diverging angle of the sheet-like electron bunch. The ratio of the total surface area of the elliptic bunch with thickness t to that of the round bunch is less sensitive to the ellipticity e as

$$\frac{2\sqrt{\frac{S}{\pi}}+g(e)t}{2\left[\sqrt{\frac{S}{\pi}}+t\right]}, \qquad (3)$$

where $g(e)$ denotes the terms depending on e in Eq. (2). A numerical evaluation of the electric field produced by the charged elliptic thin disk predicted that the surface radial field is 1/2.9 less than that of the charged round disk. The longitudinal electric field was also affected by e. To better understand the effects of the ellipticity on the bunch divergence, we are now preparing a pepper-pot emittance measurement system and optics to compensate for the time lag of the photoemission by tilting the laser pulse front to maximize the current density at the photoemission area.

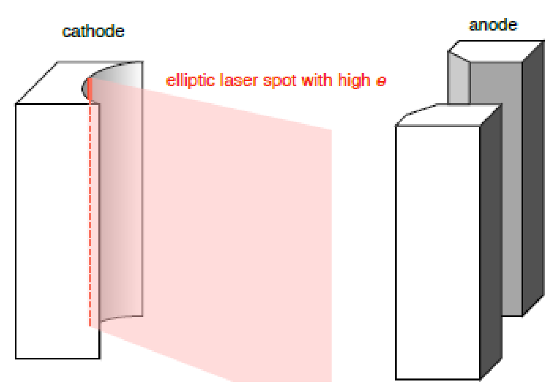

Figure 5: Pierce gun for sheet-like electron bunch.

We are also working on a modified Pierce gun that focuses on the collimation along the minor axis of the sheet-like bunch. Figure 5 shows its schematic view. The cathode surface is rounded inward to compensate for the strong electric field along the minor axis. The rectangle anode provides enough spacing for laser irradiation with a small injection angle. Therefore, the cathode surface can be hollowed out deeply. The optimization of the curvature of the

ISBN: 978-3-95450-220-2 ISSN: 2673-5474 doi: 10.18429/JACoW-FEL2022-TUP09

cathode surface is an important point to study. The sheet-like bunch transport line, including quadrupole magnets, is also being developed for Smith-Purcell and Meta-material radiation [10] experiments. Furthermore, we are also investigating the possibility of transforming the sheet-like bunch into a high-brightness round electron bunch that is suitable for ultrafast electron microscopy and RF accelerators.

CONCLUSION

The generation of a sheet-like electron bunch with a high ellipticity appears to be a promising technique for producing a high-brightness electron beam with an ultra-short duration because the elongation of the circumference of the cross-section reduces the self-field, causing the emittance degradation near the photoemission area. In the experiment, the bunch had a large diverging angle along the minor axis of the emission ellipse at the anode, but it was much smaller along the major axis of the emission ellipse. Furthermore, the diverging angle along the minor axis was almost the same as that of the round beam. Thus, it can be concluded that the net diverging angle of the sheet-like bunch was smaller than that of the round beam. Based on our discussions, we proposed an electron gun with the cathode rounded inward along the minor axis to compensate for the diverging field. This novel type of Pierce gun is currently being developed in our laboratory.

REFERENCES

[1] A. M. Michalik and J. E. Sipe, "Analytic model of electron pulse propagation in ultrafast electron diffraction experiments", *J. Appl. Phys*., vol. 99, p. 054908, 2006. doi:10.1063/1.2178855

[2] J. A. Berger *et al.*, "DC photoelectron gun parameters for ultrafast electron microscopy", *Microsc. Microanal.,* vol. 15, pp. 298-313, 2009. doi:10.1017/S1431927609090266

[3] X. Yang *et al.*, "Toward monochromated sub-nanometer UeM and femtosecond UeD", *Sci. Rep.,* vol. 10, p. 16171, 2020. doi:10.1038/s41598-020-73168-z

[4] M. Asakawa and S. Yamaguchi, "Smith-Purcell radiation emitted by pico-second electron bunches from a 30 keV photo-electron gun", in *Proc. 39th Free Electron Laser Conf. (FEL2019),* Hamburg, Germany, Aug. 2019, pp. 66-68. doi:10.18429/JACoW-FEL2019-TUP012

[5] Z. Wang *et al.*, "High-power millimeter-wave BWO driven by sheet electron beam", *IEEE Trans. Electron Devices,* vol. 60, pp. 471-477, 2013. doi:10.1109/TED.2012.2226587

[6] M. A. Basten *et al.*, "Magnetic quadrupole formation of elliptical sheet electron beams for high-power microwave devices", *IEEE Trans. Plasma Sci.,* vol. 22, pp. 960-966, 1994. doi:10.1109/27.338313

[7] K. T. Nguyen, J. Pasour, E. L. Wright, J. Petillo and B. Levush, "High-perveance W-band sheet-beam electron gun design", in *Proc. 2008 IEEE Int. Vacuum Electron. Conf.,* Monterey, Calif., Apr. 2008, pp. 179-180. doi:10.1109/IVELEC.2008.4556326

[8] S. J. Russell *et al.*, "First observation of elliptical sheet beam formation with an asymmetric solenoid lens", *Phys. Rev. ST Accel. Beams,* vol. 8, p. 080401, 2005. doi: 10.1103/PhysRevSTAB.8.080401

[9] H. Yamamoto *et al.*,"Space-charge limitation of a femtosecond photoinjector", *Int. J. Opt.*, vol. 11, p. 714265, 2011. doi:10.1155/2011/714265

[10] D. Li *et al.*, "Terahertz radiation from combined metallic slit arrays", *Sci. Rep.,* vol. 9, p. 6804, 2019. doi:10.1038/s41598-019-43072

ISBN: 978-3-95450-220-2 ISSN: 2673-5474 doi: 10.18429/JACoW-FEL2022-TUP10

EXPERIMENTAL DEMONSTRATION OF TEMPORALLY SHAPED PICOSECOND OPTICAL PULSES FOR DRIVING ELECTRON PHOTOINJECTORS

R. Lemons *, N. Neveu, J. Duris, A. Marinelli, C. Durfee, S. Carbajo

SLAC National Accelerator Laboratory, 2575 Sand Hill Rd, Menlo Park CA, 94061, USA
Colorado School of Mines, 1500 Illinois St, Golden CO, 80401, USA
University of California, Los Angeles, 420 Westwood Plaza, Los Angeles, CA 90095

Abstract

Next-generation electron photoinjector accelerators, such as the LCLS-II photoinjector, have increasingly tight requirements on the excitation lasers, often calling for tens of picosecond, temporally flat-top, ultraviolet (UV) pulse trains to be delivered at up to 1 MHz. We present an experimental demonstration of temporal pulse shaping for the LCLS-II photoinjector laser resulting in temporally flat-top pulses with 24 ps durations. Our technique is a non-colinear sum frequency generation scheme wherein two identical infrared optical pulses are imparted with equal and opposite amounts of spectral dispersion. The mixing of these dispersed pulses within a thick nonlinear crystal generates a second harmonic optical pulse that is spectrally narrowband with a designed temporal profile [1]. In the experiment, we achieve upwards of 40% conversion efficiency with this process allowing this to be used for high average and peak power applications. These narrowband pulses can then be directly upconverted to the UV for use in driving free electron laser photocathodes. Additionally, we present a theoretical framework for adapting this method to shape optical pulses driving other photoinjector-based applications.

INTRODUCTION

In photoinjectors, electrons are generated via the photoelectric effect with laser pulses comprised of light above the work function of the material. During emission, the temporal intensity profile of the laser pulse can significantly affect electron bunch quality. A key measure of quality is the transverse emittance, ϵ_x, defined as [2]

$$\epsilon_x = \sqrt{\langle x_i^2\rangle\langle x_i'^2\rangle - \langle x_i^2 x_i'^2\rangle} \qquad (1)$$

where x is the transverse position and x' is the corresponding angle with respect to the ideal trajectory. For generation of x-rays from x-ray free electron lasers (XFELs), it is critical to have electron bunches that are generated with low emittance ($< 1.5\ \mu$m), narrow energy spread (ΔE/E $< 10^{-3}$), and good spatial uniformity [3]. The latter two quantities can be improved to some extent after generation through the use of spatio-temporally shaped IR lasers in laser heaters [4–6], however initial transverse emittance is dominantly controlled through the temporal intensity profile of the excitation laser pulse. Conventionally implemented photoexcitation laser profiles are Gaussian in time though other commonly sought-after laser distributions are shown to reduce transverse emittance such as flat-top spatiotemporal profiles resembling cylinders [7] or 3D ellipsoids such that the beam size and intensity vary as a function of time [8].

Producing excitation laser pulses with non-Gaussian temporal intensity profiles and duration on the order of 10s of picoseconds is non-trivial. Pulses of the temporal duration lack the spectral content for shaping methods such as spatial-light modulators [9] or acousto-optic modulators [10] to be effective and are shorter than the response time for direct temporal electro-optic modulators [11]. Additionally, the high-repetition rate and pulse energy requirements of next-generation XFELs such as LCLS-II [12] approaches or exceeds the material damage threshold for these devices [13] further complicating their use for shaping the excitation laser pulses. One method that has seen promise for pulse shaping for XFEL facilities is pulse stacking [14] where multiple copies of a short pulse are coherently added in time to generate the desired composite intensity profile. However, pulses generated with the method have been shown to induce unwanted microbunching [15, 16] on the electron bunch resulting in increased emittance relative to Gaussian distributions. Furthermore, the series of nonlinear conversion stages to upconvert infrared (IR) light to UV light below 270 nm [17, 18] present in all XFEL photo-excitation laser systems is detrimentally affected by non-zero phase structure on the pulses, distorting temporal profiles, complicating shaping efforts, and limiting the applicability to high average power, 24/7 facilities.

We present a non-colinear sum frequency generation (NC-SFG) technique that inherently incorporates temporal intensity shaping [1]. Our method is characterized by the mixing of two highly dispersed pulses (Fig. 1) which combine during sum-frequency generation to generate a pulse with a tailored temporal intensity profile. We expand on Raoult et al [19] of efficient narrowband second harmonic generation in thick crystals by adding third-order dispersion to simultaneously shape the output pulse. This method, which we call dispersion controlled nonlinear shaping (DCNS), can be broadly used to tailor pulses for the reduction of transverse emittance in photoinjector-based instrumentation.

* rlemons@slac.stanford.edu

ISBN: 978-3-95450-220-2 ISSN: 2673-5474 doi: 10.18429/JACoW-FEL2022-TUP10

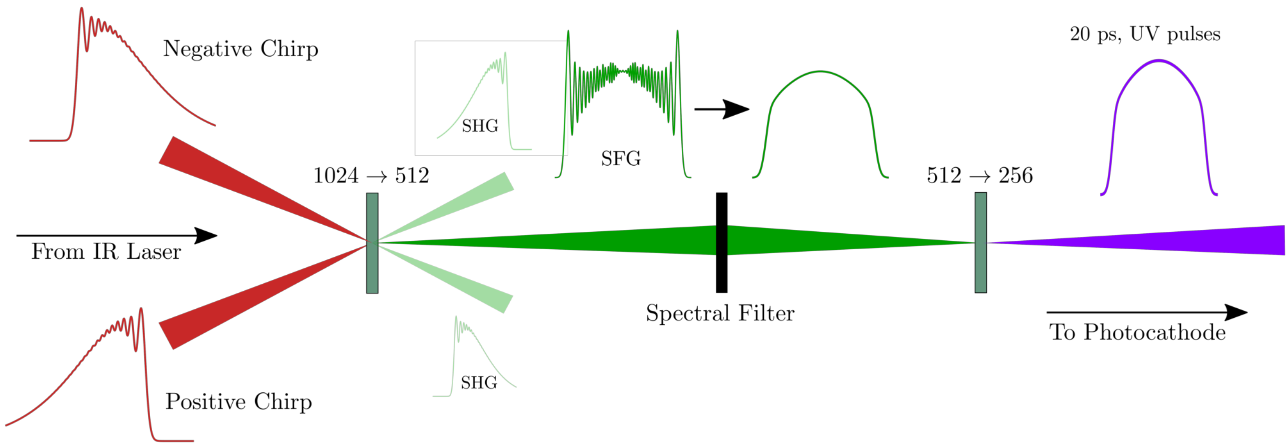

Figure 1: Schematic diagram of the DCNS method being used to generate a temporally flattened UV pulse from equal and oppositely dispersed infrared pulses. The spectral filter included between the two upconversion stages serves to eliminate unwanted oscillations on the edges of the optical pulse

EXPERIMENTAL IMPLEMENTATION

The electric field of a laser pulse in frequency space is given by $E(\omega) = A(\omega)e^{i\varphi(\omega)}$ where $A(\omega)$ is the spectral amplitude, typically modeled as a Gaussian distribution around the central frequency, and $\varphi(\omega)$ is the spectral phase. We define $\varphi(\omega)$ via a Taylor expansion about the central frequency,

$$\varphi(\omega) = \varphi_0 + \varphi_1(\omega-\omega_0) + \frac{\varphi_2}{2!}(\omega-\omega_0)^2 + \frac{\varphi_3}{3!}(\omega-\omega_0)^3 + \frac{\varphi_4}{4!}(\omega-\omega_0)^4 + \ldots \quad (2)$$

where φ_j is the j^{th} derivative of $\varphi(\omega)$ evaluated at ω_0. Dropping the first two terms, which are arbitrary for our purposes, we focus on the next two terms, second order dispersion (SOD), φ_2, and third order dispersion (TOD), φ_3. SOD is a linear instantaneous temporal chirp on the pulse primarily affecting duration while TOD is a quadratic instantaneous chirp creating temporal oscillations on either the leading or falling edge of the pulse. Additionally, we define the ratio $\alpha = \varphi_3/\varphi_2$ (s) allowing us to set pulse duration with SOD and change shape with α.

Our laser system is driven by a Light Conversion Carbide 1024 nm, 40 μJ, 1 MHz, 246 fs commercial laser with an approximately 7 nm full width at half maximum (FWHM) spectral bandwidth. Based on these laser parameters we constructed a matched free-space grating-based optical compressor and stretcher set in an off-littrow configuration designed to impart ± 27.311 ps^2 SOD and ∓ 0.28 ps^3 TOD onto the IR pulses. SOD of this magnitude results in pulses with duration ≈ 300 ps however, it is necessary in order to achieve the proper TOD while maintaining efficiency and physically constructible designs. To correct this excessive SOD without changing TOD, we pass both beams through a chirped volume Bragg grating [20] designed to apply ∓ 24.75 ps^2 of SOD. This leaves the IR pulses with values of SOD and TOD of ± 2.5611 ps^2 and ∓ 0.28 ps^3 respectively which were chosen so that the FWHM of the laser pulse would be 25 ps in time [18] with an approximately flat temporal profile.

Once the spectral phase of the IR pulses was modified, they were used as the two input pulses to the NC-SFG setup. After passing through a 2 mm thick β-barium borate (BBO) crystal, the SFG pulses were passed through two spectral filters centered at 514 nm with a FWHM of 2 nm. The central wavelength of the spectral filters was angle tuned towards 512 nm with one being tuned farther such that the combined effective filter was centered at 512 nm but with a FWHM of $\approx 1nm$. The filtered SFG pulses finally were used to generate the necessary UV pulses in a 1.5 mm BBO crystal and then sent to a difference frequency cross-correlator to measure temporal intensity.

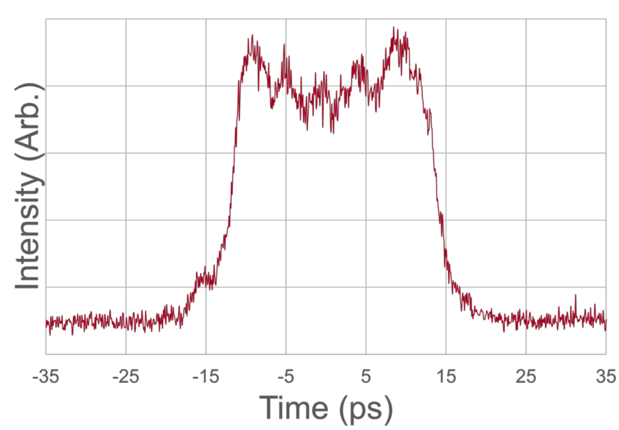

Figure 2: Experimental temporal intensity trace

The UV temporal intensity profile (Fig. 2) has a FWHM duration of 26 ps with 90:10 rise/fall times of 4 ps. The temporal intensity profile is characterized by a significantly longer and flatter peak intensity region than that of a Gaussian with a similar duration. However, there is also a significant oscillation across the plateau of the pulse. This oscillation is likely caused by excessive spectral filtering

ISBN: 978-3-95450-220-2 ISSN: 2673-5474 doi: 10.18429/JACoW-FEL2022-TUP10

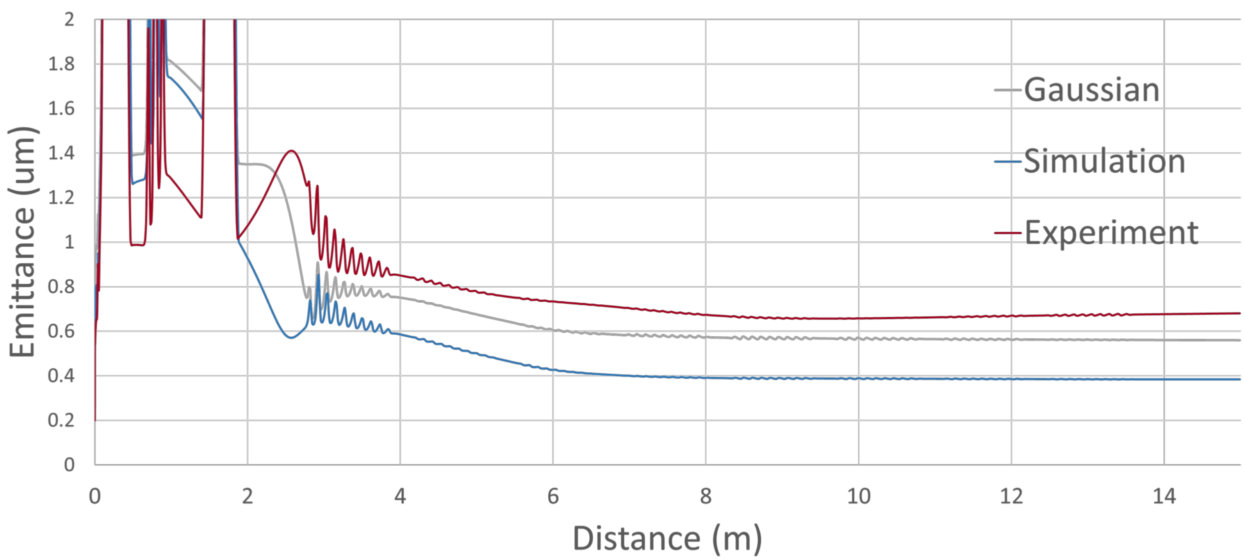

Figure 3: Transverse emittance of electron bunches generated from photo-excitation laser pulses with different temporal intensity profiles from the LCLS-II photocathode over the first 15 meters. The currently implemented Gaussian profile (gray) has a final emittance of 0.55 um while the experimental and simulation DCNS pulses achieve 0.38 um and 0.68 um respectively

in the UV generation crystal due to its thickness limiting the possible spectral acceptance bandwidth. Filtering due to this effect would overshadow the filtering achieved with the two spectral filters on the SFG beam but could be easily corrected by using a thinner BBO crystal.

To evaluate the possible electron generation performance, we simulate the photoinjector system and the first 15 meters of acceleration at LCLS-II. This serves to limit the simulation to a region where space-charge forces are not yet damped by highly relativistic speeds and the effect of the laser is prominent. The simulation code used for e-beam dynamics is OPAL [21], and for particle distribution generation [22]. While supplying the DCNS pulses is straightforward, determining the optimal FWHM and spot size on the cathode is not. The strength of the space charge forces is directly impacted by both the FWHM and spot size, which then impacts how strong the external forces need to be to limit emittance growth. To determine optimal laser and machine settings for an individual temporal profile, the simulation would need to be run in combination with an optimization algorithm such as NSGA-II [23]. In our case, the simulation was run with parameters optimal for the Gaussian distribution and is likely to overestimate the emittance of the other profiles.

Figure 3 displays the emittance of the electron bunches generated by the currently implemented Gaussian beam, the experimental DCNS pulse trace, and a simulated DCNS pulse with the same generation parameters. The simulation DCNS pulse also does not take into account the excessive filtering from the thick UV crystal. All temporal profiles initially have similar emittance values around 0.55 um immediately after the cathode. After the dispersive sections, noted by the sections with significant emittance increase, the emittance from the three profiles settles out to 0.55 um, 0.68 um, and 0. 38 um for the Gaussian, experimental, and simulation profiles respectively. As noted previously, the non-optimal parameters are likely to increase emittance for both the DCNS profiles compared to the Gaussian case, however, the temporal oscillations across the plateau of the experimental profile are the largest contributor to a larger emittance value, and the discrepancy compared to simulation. A temporal profile with reduced or eliminated oscillations is thus likely to exceed the emittance performance of the currently implemented Gaussian profile. This is supported by the simulated DCNS pulse maintaining a 30% decrease in emittance compared to the Gaussian profile and consistent with the results presented in Lemons et al. [1]. As such, the experimentally captured DCNS pulse still represents a significant step toward the implementation of a temporal pulse shaping technique that is compatible with the energies and repetition rates required by next-generation XFELs.

CONCLUSION

Electron emittance, and by extension the electron beam and x-ray beam brightness, can be improved through temporal tailoring of the photoinjector drive laser backing modern and next-generation XFELs. Available shaping methods for tailoring the excitation laser pulse are limited due to the required temporal duration, laser pulse energy, and repetition rate. We present the first experimental application of the DCNS method to generate tailored UV laser pulses capable of driving the LCLS-II photoinjector. We demonstrate the applicability of this method to the high pulse energy and high repetition rate regimes demanded by next-generation XFELs. The generated UV pulses with tailored temporal intensity

ISBN: 978-3-95450-220-2 ISSN: 2673-5474 doi: 10.18429/JACoW-FEL2022-TUP10

profiles are characterized by FWHM of 26 ps, sharp rise/fall time, and a region of extended and flattened peak intensity compared to the currently implemented Gaussian profile. Though the experimental DCNS pulses have temporal intensity oscillations across the plateau, and thus an increased emittance in simulation compared to Gaussian pulses, this is likely caused by a correctable experimental design choice. Electron bunches generated by simulated DCNS pulses using the same experimental parameters, without the conditions leading to the intensity oscillations, have upwards of 30% emittance decrease compared to the Gaussian profile. Our implementation of the DCNS method is a significant step toward realizing a system that can substantially extend the brightness of photoinjector systems worldwide without major configuration changes and thus enhance current scientific capabilities on existing accelerators and reduce the cost of future accelerator facilities.

ACKNOWLEDGEMENTS

We thank Yuantao Ding and Christopher Mayes at SLAC National Accelerator Laboratory for their helpful discussions.

This work is supported by the U.S. Department of Energy, Office of Science, Office of Basic Energy Sciences under Contract No. DE-AC02-76SF00515 and DE-SC0022559.

REFERENCES

[1] R. Lemons, N. Neveu, J. Duris, A. Marinelli, C. Durfee, and S. Carbajo, "Temporal shaping of narrow-band picosecond pulses via noncolinear sum-frequency mixing of dispersion-controlled pulses," *Physical Review Accelerators and Beams*, vol. 25, no. 1, p. 013 401, 2022.

[2] H. Wiedemann, "Particle beams and phase space," in *Particle Accelerator Physics*. 2015, pp. 213–251, doi:10.1007/978-3-319-18317-6_8

[3] Z. Huang and K.-J. Kim, "Review of x-ray free-electron laser theory," *Phys. Rev. ST Accel. Beams*, vol. 10, p. 034 801, 3 2007, doi:10.1103/PhysRevSTAB.10.034801

[4] Z. Huang *et al.*, "Suppression of microbunching instability in the linac coherent light source," *Physical Review Special Topics-Accelerators and Beams*, vol. 7, no. 7, p. 074 401, 2004.

[5] N. Liebster *et al.*, "Laguerre-gaussian and beamlet array as second generation laser heater profiles," *Physical Review Accelerators and Beams*, vol. 21, no. 9, p. 090 701, 2018.

[6] J. Tang *et al.*, "Laguerre-gaussian mode laser heater for microbunching instability suppression in free-electron lasers," *Physical Review Letters*, vol. 124, no. 13, p. 134 801, 2020.

[7] M. Krasilnikov *et al.*, "Experimentally minimized beam emittance from an l-band photoinjector," *Physical Review Special Topics-Accelerators and Beams*, vol. 15, no. 10, p. 100 701, 2012.

[8] O. Luiten, S. Van der Geer, M. De Loos, F. Kiewiet, and M. Van Der Wiel, "How to realize uniform three-dimensional ellipsoidal electron bunches," *Physical review letters*, vol. 93, no. 9, p. 094 802, 2004.

[9] S. Y. Mironov *et al.*, "Shaping of cylindrical and 3d ellipsoidal beams for electron photoinjector laser drivers," *Applied optics*, vol. 55, no. 7, pp. 1630–1635, 2016.

[10] Y. Li, S. Chemerisov, J. Lewellen, *et al.*, "Laser pulse shaping for generating uniform three-dimensional ellipsoidal electron beams," *Physical Review Special Topics-Accelerators and Beams*, vol. 12, no. 2, p. 020 702, 2009.

[11] M. D. Skeldon, "Optical pulse-shaping system based on an electro-optic modulator driven by an aperture-coupled-stripline electrical-waveform generator," *J. Opt. Soc. Am. B*, vol. 19, no. 10, pp. 2423–2426, 2002, doi:10.1364/JOSAB.19.002423

[12] J. Stohr, "Linac coherent light source ii (lcls-ii) conceptual design report," 2011, doi:10.2172/1029479

[13] S. Carbajo and K. Bauchert, "Power handling for lcos spatial light modulators," in *Laser Resonators, Microresonators, and Beam Control XX*, International Society for Optics and Photonics, vol. 10518, 2018, 105181R.

[14] M. Krasilnikov, Y. Chen, and F. Stephan, "Studies of space charge dominated electron photoemission at pitz," in *Journal of Physics: Conference Series*, IOP Publishing, vol. 1238, 2019, p. 012 064.

[15] S. Bettoni *et al.*, "Impact of laser stacking and photocathode materials on microbunching instability in photoinjectors," *Phys. Rev. Accel. Beams*, vol. 23, p. 024 401, 2 2020, doi:10.1103/PhysRevAccelBeams.23.024401

[16] C. Mitchell, P. Emma, J. Qiang, and M. Venturini, "Sensitivity of the microbunching instability to irregularities in cathode current in the lcls-ii beam delivery system," *proceedings NAPAC2016, Oct*, pp. 9–14, 2016.

[17] I. Will, H. I. Templin, S. Schreiber, and W. Sandner, "Photoinjector drive laser of the flash fel," *Optics Express*, vol. 19, no. 24, pp. 23 770–23 781, 2011.

[18] S. Gilevich *et al.*, "The lcls-ii photo-injector drive laser system," in *2020 Conference on Lasers and Electro-Optics (CLEO)*, IEEE, 2020, pp. 1–2.

[19] F. Raoult *et al.*, "Efficient generation of narrow-bandwidth picosecond pulses by frequency doubling of femtosecond chirped pulses," *Optics letters*, vol. 23, no. 14, pp. 1117–1119, 1998.

[20] S. Kaim, S. Mokhov, B. Y. Zeldovich, and L. B. Glebov, "Stretching and compressing of short laser pulses by chirped volume bragg gratings: Analytic and numerical modeling," *Optical Engineering*, vol. 53, no. 5, p. 051 509, 2013.

[21] A. Adelmann *et al.*, *Opal a versatile tool for charged particle accelerator simulations*, 2019.

[22] C. Gulliford, *DistGen: Particle distribution generator*, 2019, https://github.com/ColwynGulliford/distgen

[23] K. Deb, A. Pratap, S. Agarwal, and T. Meyarivan, "A fast and elitist multiobjective genetic algorithm: NSGA-II," *IEEE Trans. Evol. Comp.*, vol. 6, no. 2, pp. 182–197, 2002, doi:10.1109/4235.996017

ISBN: 978-3-95450-220-2 ISSN: 2673-5474 doi: 10.18429/JACoW-FEL2022-TUP11

REAL-TIME PROGRAMMABLE SHAPING FOR ELECTRON AND X-RAY SOURCES

Jack Hirschman*[1,2], Randy Lemons[2,3], Ravi Saripalli[2], Federico Belli[4], and Sergio Carbajo[2,5,6]

[1]Department of Applied Physics, Stanford University, 348 Via Pueblo, Stanford, CA 94305, USA
[2]SLAC National Accelerator Laboratory, 2575 Sand Hill Rd, Menlo Park, CA 94025, USA
[3]Colorado School of Mines, 1500 Illinois St, Golden, CO 80401, USA
[4]School of Engineering and Physical Sciences, Heriot-Watt University, Edinburgh, EH14 4AS, UK
[5]Electrical and Computer Engineering Department, UCLA, 420 Westwood Plaza, Los Angeles, CA 90095, USA
[6]Physics and Astronomy Department, UCLA, 475 Portola Plaza, Los Angeles, CA 90095, USA

Abstract

The next generation of augmented brightness X-ray free electron lasers (XFELs), such as the Linac Coherent Light Source-II (LCLS-II), promises to address current challenges associated with systems with low X-ray cross-sections. Typical photoinjector lasers produce coherent ultraviolet (UV) pulses via nonlinear conversion of an infrared (IR) laser. Fast and active beam manipulation is required to capitalize on this new generation of XFELs, and controlling the phase space of the electron beam is achieved by shaping the UV source and/or via IR shapers [1, 2]. However current techniques for such shaping in the UV rely on stacking pulses in time, which leads to unavoidable intensity modulations and hence space-charge driven microbunching instabilities [3]. Traditional methods for upconversion do not preserve phase shape and thus require more complicated means of arriving at the desired pulse shapes after nonlinear upconversion [4]. Upconversion through four-waving mixing (FWM) allows direct phase transfer, convenient wavelength tunability by easily changeable phase matching parameters, and also has the added advantage of greater average power handling than traditional $\chi(2)$ nonlinear processes [5, 6]. Therefore, we examine a possible solution for e-beam shaping using a machine learning (ML) implementation of real-time photoinjector laser manipulation which shapes the IR laser source and then uses FWM for the nonlinear upconversion and shaping simultaneously. Our presentation will focus on the software model of the photoinjector laser, the associated ML models, and the optical setup. We anticipate this approach to not only enable active experimental control of X-ray pulse characteristics but could also increase the operational capacity of future e-beam sources, accelerator facilities, and XFELs [7].

* jhirschm@stanford.edu

INTRODUCTION AND MOTIVATION

Ground-up design of high power chirped pulse amplification (CPA) systems is not trivial. Choosing the correct hardware and determining limitations for a particular laser system– such as damage thresholds for optics [8] and amplifiers as well as bandwidth limitations for shaping– can be a challenging task, especially for systems involving custom design amplifiers, pre-CPA programmable pulse shapers, or a series of up-/down-conversion stages. Start-to-end (S2E) software models can greatly inform laser system design decisions and aid in understanding limitations or trade-offs in performance parameters. To an even greater extent, as we enter new stages of ML-driven photonics and optical system design [9], the need for S2E-based data generation to inform these ML models and reduce parameter searches in the lab will become increasingly desired. Furthermore, the potential symbiosis between experiment and software model means experiment can improve the S2E models, which in turn can drive improvements in the system design. This relationship with experiment-corrected software model design could even open the possibility for using these models for material design via inverse engineering.

At LCLS-II, we are developing real-time adaptable photoinjector shaping techniques to increase the electron beam brightness and enhance future modes of X-ray lasing operation, some of which may require advanced models, such as machine learning, to determine optimal spatio-temporal distribution of the photoinjector laser pulses. Thus, we have developed and used this S2E model to both determine the limitations of our pulse shaping techniques and to generate data for training the ML models.

MODEL AND RESULTS

The LCLS-II photoinjector laser system starts with an IR mode-locked oscillator shaped in spectral phase and amplitude by an acousto-optic programmable dispersive filter,

ISBN: 978-3-95450-220-2 ISSN: 2673-5474 doi: 10.18429/JACoW-FEL2022-TUP11

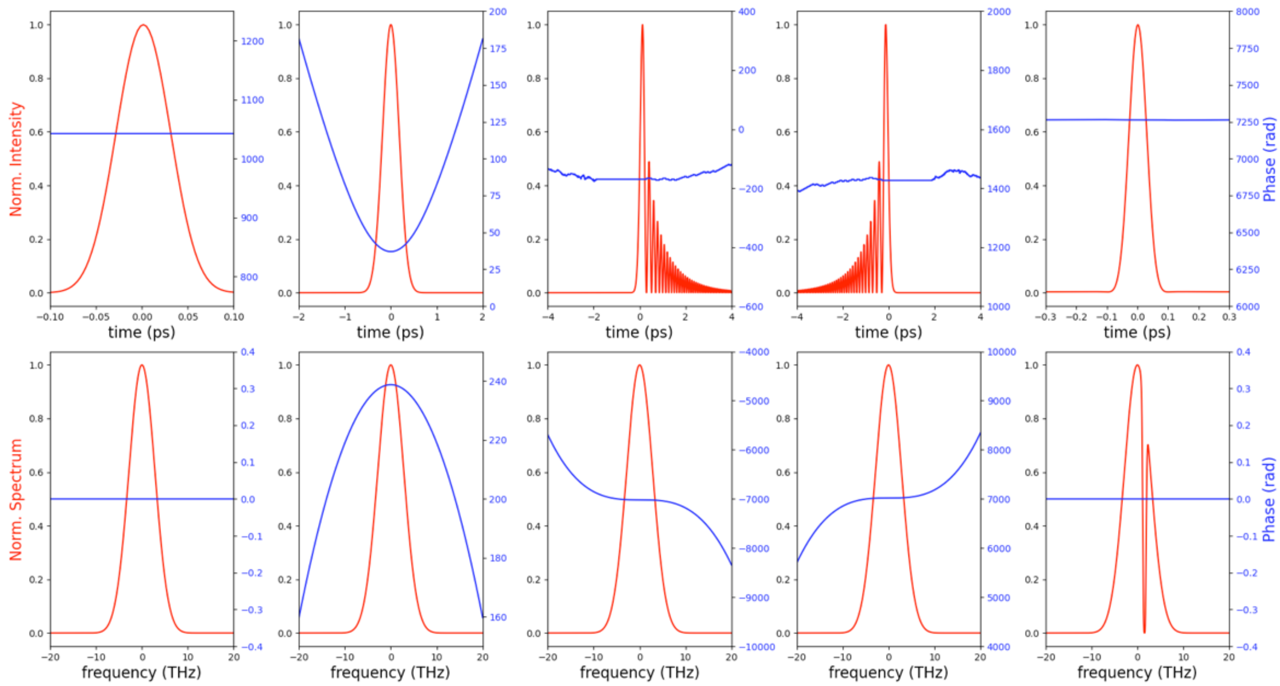

Figure 1: Shows the time domain (top row) intensity (red) and phase (blue) profiles and frequency domain (bottom row) spectrum (red) and spectral phase (blue) for various types of pulse shaping: no shaping (first column), added second-order dispersion (second column), positive third-order dispersion (third column), negative third-order dispersion (fourth column), and spectrum shaping (fifth column).

then amplified by an Yb:KGW regenerative amplifier. The amplified IR beam is finally subject to an ensemble of non-linear upconversion stages including sum frequency generation (SFG) [4], cascaded second harmonic (SH) stages, or FWM to generate UV.

The initial IR pulse in our S2E model is a spectrum collected from our oscillator. We then directly shape the output of our oscillator using a Dazzler [10]. The Dazzler is a programmable acousto-optic device that uses an RF signal to impart a diffraction pattern within a crystal in order to modify the input signal. The S2E model uses seven parameters to perform amplitude and phase modulation where amplitude shaping uses a frequency domain super Gaussian transfer function and phase shaping uses a frequency domain Taylor expansion.

The regenerative amplifier (RA) follows the pulse shaper and amplifies the signal before upconversion. The main tuning parameters for this portion of the model include crystal length, ion density, material emission and absorption cross section spectra, pump power as well as other RA parameters. This simulation uses modified Frantz-Nodvik equations [11] in the wavelength domain to capture the change in spectral shape, the shift in central wavelength, and the build-up in energy. The simulation centers around the emission and absorption peaks for Yb:KGW for the pump and seed processes and does not require phase information.

Lastly, the output of the RA feeds into the upconversion stage. We are currently exploring upconversion through FWM in gas-filled hollow-core fibers. Our aim is to use a pulse shaper in the near infrared to directly control the emission bandwidth, wavelength and phase of the emitted deep-ultraviolet light pulse. Such new generation of light sources would provide light guidance in a hollow-channel over an unmatched spectral band, dynamic control of the linear and nonlinear optical properties by filling the hollow-core with different gases at different pressure or temperatures, and high-average power handling and peak-power delivery, up to kW and GW respectively [5, 6].

The current simulations of the FWM process are based on solving the coupled-mode equations of the complex amplitudes of the three interacting waves with respect to their propagation inside the fiber [12]. The calculations are made in the frequency domain considering a frequency dependent dispersion and nonlinearity of the gas used inside the fiber without resorting to the undepleted pump approximation. This allows for the study of output redistributions of the power among the interacting waves. An optimization is run across various parameters such as gas-type, pressure, inner-core radius, and length of the fiber for different interacting wavelengths to minimize the group-velocity dispersion (GVD) and maximize the conversion efficiency. The simulations show a high conversion efficiency for fiber of 1 m length and 100 μm inner radius filled with Krypton gas at 0.8 bar pressure. The total phase of the nonlinear interaction as a function of the propagation along the fiber length is again realized by solving the coupled-mode equations of the complex amplitudes of the three interacting waves

ISBN: 978-3-95450-220-2 ISSN: 2673-5474 doi: 10.18429/JACoW-FEL2022-TUP11

[12]. To study the spectral phase transfer from the input signal beam (at 1025 nm) to the generated idler beam (at 341 nm) through the FWM process, we assume that the spectral phase of the pump beam remains constant through the FWM process [6]. Then the spectral phase of the FWM signal is realized by plotting a few initial order terms of the Taylor expansion of the spectral phase of the amplifier beam.

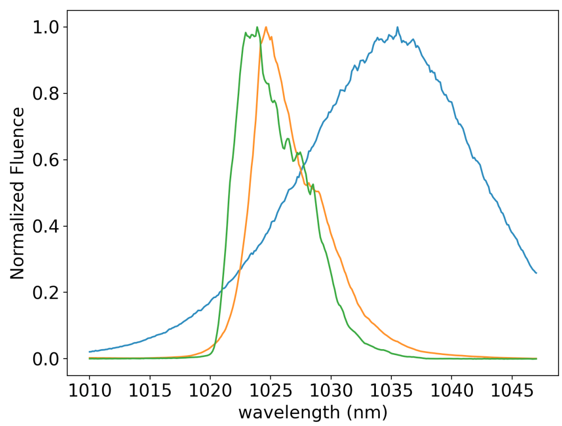

Figure 2: Functioning amplifier model with direct oscillator input (blue) to amplifier with true (green) and simulated (orange) outputs from amplifier.

In our presentation, we will demonstrate the S2E model by showing several portions of the model – IR pulse shaping, amplifier, and FWM. Figure 1 shows the first portion of the S2E model, the pulse shaper. Here, we demonstrate some of the fundamental pulse shaping capabilities. We start by showing the oscillator output, not shaped. Then show added second-order dispersion, positive third-order dispersion, negative third-order dispersion, and spectrum hole carving. These examples are important for several reasons. First, they have specific potential application for the desired pulses for our photoinjector. For example, the second-order dispersion widens the time-domain pulse, so we can bring our pulse shapes closer to the required 25 ps pulse widths. Then for the third-order dispersion, we are able to chirp the pulse. This could be useful for driving instabilities that generate mircobunching in the electron bunch in the XFEL, which is used for generating attosecond X-ray pulses. Apart from specific application to photoinjector shaping, these examples of shaping are what is used for training the ML models where we scan parameter combinations using these types of shaping. Our ML studies will show what the shaping parameters should be based on the method of upconversion used.

In figure 2, the RA operation is shown next. For this, the direct output of the oscillator (blue) is fed into the amplifier model. The simulated output (orange) and the true output (green) are shown. We can see the simulated and true closely match each other, exhibiting similar gain narrowing and output peaks. To yield this result, we used an error

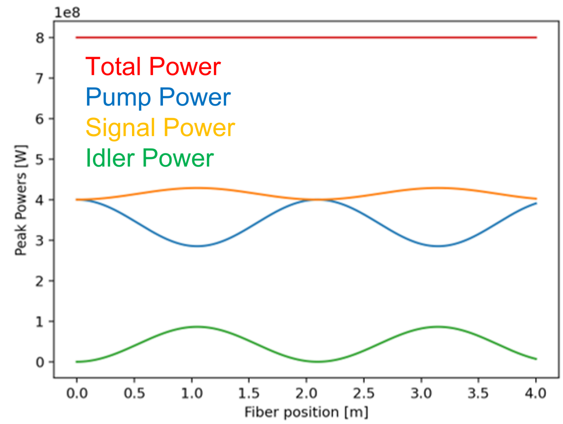

(a)

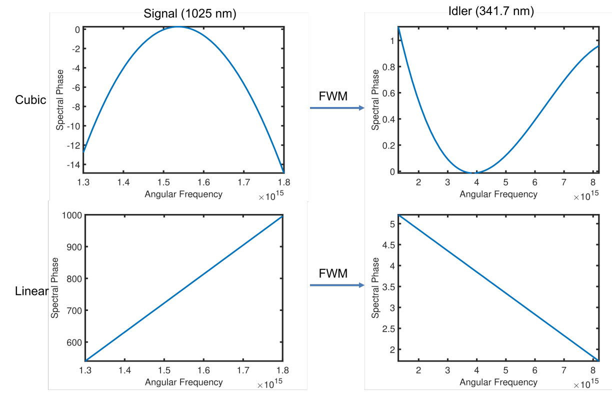

(b)

Figure 3: (a) Energy transfer between the three waves as they propagate within the fiber; (b) Spectral phase transfer signal to idler through FWM process

reduction analysis by tuning amplifier crystal orientation, ion density, and crystal length among other parameters and comparing the simulated output with the true output of the spectrum collected in lab.

Figure 3a shows the power distribution among the three interacting waves along the length of the fiber for the FWM process. The input signal IR beam is at 1025 nm and the pump, generated from the SHG of the signal, is at 512 nm. The idler output beam is thus at 341 nm. In this figure, we can see the total power is conserved over the whole mixing process. Figure 3b shows how the spectral phase of the idler is affected for a linearly- and cubic varying input signal beam phase.

OUTLOOK

Our work on the S2E model for simulating pulse shaping, amplification, and upconversion in our photoinjector laser system demonstrates operational code that can be used for a number of applications including (inverse) designing a laser system, reverse engineering portions of an existing system, and tuning the system's performance parameters. We are currently using this model as part of a

ISBN: 978-3-95450-220-2 ISSN: 2673-5474 doi: 10.18429/JACoW-FEL2022-TUP11

ML-based approach to produce photoinjector laser pulse shapes employing programmable shapers in combination with advanced upconversion techniques. This S2E model will both help us determine optics and diagnostics as well as help determine limits on pulse shaping to avoid damaging our amplifier. Additionally, we will use the model to generate data sets to train ML networks to examine the relationship between generalized pulse shaping and electron beam and X-ray performance.

ACKNOWLEDGMENT

Use of the Linac Coherent Light Source, SLAC National Accelerator Laboratory, is supported by the U.S. Department of Energy, Office of Science, Office of Basic Energy Sciences under Contract No. DE-AC02-76SF00515 and DE-SC0022559. Additionally, this research is supported by a U.S. Department of Defense National Defense Science and Engineering Fellowship.

References

[1] David Cesar *et al.* "Electron beam shaping via laser heater temporal shaping". In: *Physical Review Accelerators and Beams* 24.11 (2021), p. 110703. DOI: 10.1103/PhysRevAccelBeams.24.110703.

[2] Jingyi Tang *et al.* "Laguerre-gaussian mode laser heater for microbunching instability suppression in free-electron lasers". In: *Physical Review Letters* 124.13 (2020), p. 134801. DOI: 10.1103/PhysRevLett.124.134801.

[3] Simona Bettoni *et al.* "Impact of laser stacking and photocathode materials on microbunching instability in photoinjectors". In: *Physical Review Accelerators and Beams* 23.2 (2020), p. 024401. DOI: 10.1103/PhysRevAccelBeams.23.024401.

[4] Randy Lemons *et al.* "Temporal shaping of narrow-band picosecond pulses via noncolinear sum-frequency mixing of dispersion-controlled pulses". In: *Phys. Rev. Accel. Beams* 25 (1 2022), p. 013401. DOI: 10.1103/PhysRevAccelBeams.25.013401. URL: https://link.aps.org/doi/10.1103/PhysRevAccelBeams.25.013401.

[5] Peng Zuo *et al.* "Spectral phase transfer to ultrashort UV pulses through four-wave mixing". In: *Optics Express* 18.15 (2010), pp. 16183–16192. DOI: 10.1364/OE.18.016183.

[6] John E Beetar *et al.* "Thermal effects in molecular gas-filled hollow-core fibers". In: *Optics Letters* 46.10 (2021), pp. 2437–2440. DOI: 10.1364/OL.422983.

[7] Sergio Carbajo. "Light by design: emerging frontiers in ultrafast photon sciences and light–matter interactions". In: *Journal of Physics: Photonics* 3.3 (2021), p. 031001. DOI: 10.1088/2515-7647/ac015e.

[8] Sergio Carbajo and Kipp Bauchert. "Power handling for LCoS spatial light modulators". In: *Laser Resonators, Microresonators, and Beam Control XX*. Vol. 10518. SPIE. 2018, pp. 282–290. DOI: 10.1117/12.2288516.

[9] Goëry Genty *et al.* "Machine learning and applications in ultrafast photonics". In: *Nature Photonics* 15.2 (2021), pp. 91–101. DOI: 10.1038/s41566-020-00716-4.

[10] Pierre Tournois. "Acousto-optic programmable dispersive filter for adaptive compensation of group delay time dispersion in laser systems". In: *Optics communications* 140.4-6 (1997), pp. 245–249. DOI: https://doi.org/10.1016/S0030-4018(97)00153-3.

[11] Peter Kroetz *et al.* "Numerical study of spectral shaping in high energy Ho:YLF amplifiers". In: *Opt. Express* 24.9 (2016), pp. 9905–9921. DOI: 10.1364/OE.24.009905.

[12] Giancarlo Cappellini and Stefano Trillo. "Third-order three-wave mixing in single-mode fibers: exact solutions and spatial instability effects". In: *JOSA B* 8.4 (1991), pp. 824–838. DOI: 10.1364/JOSAB.8.000824.

ISBN: 978-3-95450-220-2 ISSN: 2673-5474 doi: 10.18429/JACoW-FEL2022-TUP16

UNIVERSAL TOOL FOR THZ RADIATION ANALYSIS

M. Gerasimov, E. Dyunin, J. Gerasimov, A. Friedman
Department of Electrical and Electronic Engineering, Ariel University, Ariel, Israel

Abstract

We present here a tool for the 3D THz Radiation Analysis. The tool is a homemade simulation built from scratch in a Python code. A final goal of the simulation is a of designs of a Transmission Line (TL) for a wide tunable broad-spectrum THz radiation source. The TL is designed to be a component of the construction of an innovative accelerator at the Schlesinger Family Center for Compact Accelerators, Radiation Sources & Applications (FEL). A 3D space-frequency tool for a diagnostic of radiation pulse perform by the Wigner Distribution Function (WDF). This EM field is converted to geometric-optical ray representation at any desired resolution. WDF's representation allows to describe the dynamics of field evolution in future propagation, which allows us to determine an initial design of the TL. The EM field representation in terms of rays gives access to the Ray Tracing method and future processing, operating in the linear and non-linear regimes. A parallel processing, with graphics cards can be used which provides great flexibility and as a future preparation that able to apply advanced libraries such as machine learning. The tool can be used to study the phase-amplitude and spectral characteristics of multimode radiation generation in a free-electron laser (FEL), operating in various operational parameters.

INTRODUCTION

Terahertz (THz) radiation refers to electromagnetic waves which lengths are 80 – 1000 µm (corresponding to the 3.75 – 0.3 THz). A main THz radiation feature is transmission through various types of media as plastics, ceramics, paper, textiles wood, etc. They enable to perform non-destructive analysis, also, can detection hidden internal substances. Thus, THz research and applications have become widely popular and accessible [1,2]. In other side, the THz propagation is not straightforward. It has light waves properties on one hand and an electromagnetic on the one other. Hence, the THz propagation calculation is not trivial task. A goal of this work is a characterization of ultra-short of THz source. The source is a FEL under construction at the Schlesinger Family Center for Compact Accelerators, Radiation Sources & Applications, Ariel University Ariel University [3]. This result will impact to planning of an early design of Transmission line (TL) under development. Figure 1 is showing THz FEL Setup (with the TL). A heart is a 6 MeV hybrid photo-injector has been designed and constructed, based on a smaller-scale prototype previously built in UCLA's Particle Beam Physics Laboratory.

Using classical calculation methods as well as commercial software like CST, FDTD, HFSS not achieved a desired result. These contents supposed to supply a limited solution to general problems, because that's how they are designed. It is mostly an environment with a well-defined geometry and likewise the function of the signal itself must have a defined function. Otherwise no calculation will be performed. It is true that the numerical calculation of the problem can also be used. In these cases, reference files built in programs such as MATLAB, PYTHON, etc. are often used. In this case even definition of the initial signal is a problem. The FEL supposed to produce a defined pulse as in a single shot regime. But in reality, it is completely different. As it is already known in advance, each pulse will be different from the previous one due to many influencing parameters, such as: exact laser frequency, exact optical path, laser impact at exactly the same point on the cathode, if all this is met then in addition, the electron beam must pass evenly and radiate in exactly the same direction. Besides, the electron beam must enter the wiggler in exactly the same place. And finally, there are also mechanical vibrations of each component, temperature dependence and many other parameters. Apart from everything that has been detailed so far, the FEL is in the construction stages therefore at this stage an approximate model of the EM field obtained in the previous studies is used [4]. The model represents a total electromagnetic (EM) field on the edge of the source in the frequency domain in terms of cavity eigenmodes, realized in WB3D numerical code.

As mentioned above, the classical methods and the use of commercial software are not suitable in our case, due to excessive demand of memory and calculation resources an extended explanation is shown in the work [5]. This work approach is based on a transform to a light field [6]. In other words, the EM field is represented in terms of optical geometric rays. This representation allows the use of simple geometrical optics techniques, the characterization of the field beam on the aperture. The rays' directions of the allow diagnose the propagation of the EM field in a free space.

In most cases, the WDF [7] is calculated analytically, or calculated in more complicated cases. In this work we calculate the WDF for the general case. The simulation is built in such a way that it will allow future integration of artificial intelligence (AI) techniques. AI will be integrated in the future and should design the smart mirrors for transferring radiation in the most efficient way.

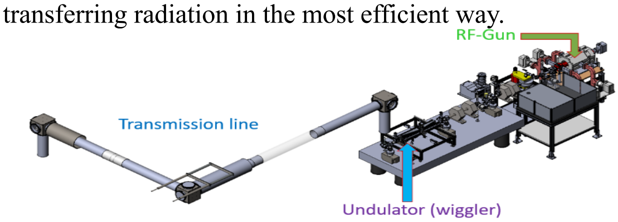

Figure 1: THz FEL Setup at the Schlesinger Center.

ISBN: 978-3-95450-220-2 ISSN: 2673-5474 doi: 10.18429/JACoW-FEL2022-TUP16

Wigner Methodology

The WDF was introduced by E. Wigner [8] as the simplest quantum analogue of the classical phase space distribution function. Originally, it used for find mathematical expectations and probabilities of quantum operators in a classical way as possible. In another form it is a phase-space representation used in optics over 30 years ago [9].

This work present a general approach to Electromagnetic fields (EM), especially inexact description of free electromagnetic wave fields in terms of rays [10] and with emphasis THz radiation systems (see Ref. [11] and references therein).

The evaluation of most important beam parameters (such intensity, phase coherence, beam-width, etc.) during the propagation, following T. Alieva etc. [12], can be described by the pure space or the pure spatial-frequency representation of a stochastic process via its mutual intensity (MI).

By the MI, such beams easy describing with $\Gamma(\boldsymbol{r}_1, \boldsymbol{r}_2) = \langle f(\boldsymbol{r}_1) f^*(\boldsymbol{r}_2)\rangle$ which is a function of four variables: the vectors $\mathbf{r}_1$ and $\mathbf{r}_2$. The brackets for time or spatial averaging and the asterisk * means complex conjugate. In our case, the MI describes the modified correlation between the EM field oscillations at two points $\mathbf{r}_1$ and $\mathbf{r}_2$. Note that $\Gamma(r,r) = \langle |f(r)|^2\rangle$ corresponds to the intensity distribution $\boldsymbol{I}(\mathbf{r})$, so can be measured.

The WDF of an EM Field $W(r,p)$, can be define by its MI, and also, in terms of its directional spectrum [12]:

$$W(r,p) = \int \Gamma(r+\tfrac{\tilde{r}}{2}, r-\tfrac{\tilde{r}}{2}) e^{(-i2\pi p\tilde{r})} d\tilde{r} \tag{1}$$

$$W(r,p) = \int \overline{\Gamma}(p+\tfrac{\tilde{p}}{2}, p-\tfrac{\tilde{p}}{2}) e^{(+i2\pi r\tilde{p})} d\tilde{p} \tag{2}$$

Such a space-frequency description is a typical light field definition [6, 13], or the "Ray Concept" in the Geometrical Optics (GO), or ray optics that is defined by the position and direction of the ray. W(r, p) is the amplitude of a ray passing via the point r with a frequency p (i.e., direction q).

A waveguide output constitute a flat aperture, which is oriented in space perpendicular to the z-axis. For a known monochromatic field distribution on the aperture, the Wigner distribution is defined by:

$$\begin{aligned} W_{\{x,y\}}(x,y,k_x,k_y)\Big|_{z_{aperture}} &= \iint E^*_{\{x,y\}}\left(x-\frac{\tilde{x}}{2}, y-\frac{\tilde{y}}{2}\right)\Big|_{z_{aperture}} \\ &\cdot E_{\{x,y\}}\left(x+\frac{\tilde{x}}{2}, y+\frac{\tilde{y}}{2}\right)\Big|_{z_{aperture}} e^{(+ik_x\tilde{x})} \\ &\cdot e^{(-ik_y\tilde{y})} d\tilde{x}d\tilde{y} \end{aligned} \tag{3}$$

$W_{\{x,y\}}$ are the WDF of $E_{\{x,y\}}$ EM field, x, y are the coordinates on the aperture surface, k_x, k_y are Fourier conjugated variables to the space coordinates. Considering the time-dependence of the EM-field transfers the WDF equations from 4D to 6D-function. In this paper, we concentrate on single-frequency problem.

As the result, the rays from each point *xy* on the aperture are obtained. The direction of each ray is defined by the wave number $\boldsymbol{k} = (k_x, k_y, k_z)$ where

$$k_z = \sqrt{\left(\frac{\omega}{c}\right)^2 - k_x^2 - k_y^2}. \tag{4}$$

The ray amplitude (**I**) is defined by the Wigner distribution:

$$I_x(x,y,k_x,k_y) = W_x(x,y,k_x,k_y) \tag{5}$$

$$I_y(x,y,k_x,k_y) = W_y(x,y,k_x,k_y) \tag{6}$$

In any uniform media, due to the orthogonality of the ray's intensity to the ray wavenumber ($\mathbf{I} \perp \mathbf{k}$):

$$I_z = \begin{cases} -\frac{I_x \cdot k_x + I_y \cdot k_y}{k_z} & k_z \neq 0 \\ 0 & k_z = 0 \end{cases} \tag{7}$$

Thus, in each point (*x,y*) on the aperture with the given field distribution (**E**) we obtain the set of GO rays $\boldsymbol{I}(x,y,k_x,k_y)$. The signal propagation in the space after the aperture is represented by the propagation of the GO rays [14].

RESULTS

Previous Researches of the EM-Field Distribution

The THz radiation generated by an electron beam drifting via planar wiggler in a superradiant regime [15]. A coupled-mode approach expressed in the frequency domain constitute this model [16]. The total electromagnetic field excited by an electron beam drifting through the waveguide in the presence of a wiggler calculated by the WB3D particle simulation code.

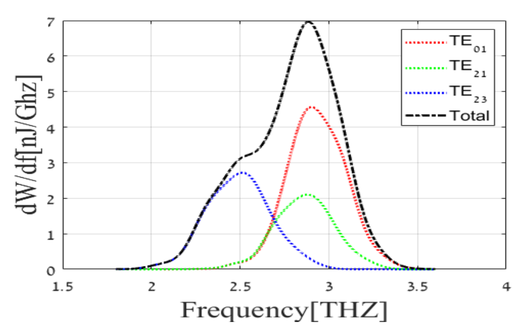

Figure 2: Output amplitude radiation spectrum of Israeli free-electron THz source.

A radiation result reveals that TE_{01}, TE_{21}, and TE_{23} are mainly excited modes. An excitation other waveguide mode is negligible. This output spectrum shown on Fig. 2. A main characteristic frequency points are about 2.89 THz (the peaks of TE_{01} and TE_{21} components), 2.5 THz (the peak of TE_{23} component), and 2.65 THz (the intermediate

ISBN: 978-3-95450-220-2 ISSN: 2673-5474 doi: 10.18429/JACoW-FEL2022-TUP16

point where all the components considered have approximately equal spectral energy flux). The output radiation field at these 3 points are shown in Fig. 3 as spatial profiles. The EM field profile corresponds to the symmetry of the dominant waveguide component at the chosen characteristic frequency. Note, that radiation keeps the boundary conditions at the walls of the rectangular waveguide in which it was excited.

A nice and symmetrical profile to the quarter field obtained at the working frequency. In this resonant frequency a n energy concentrated and transmitted in the middle of the aperture and fades at the edges.

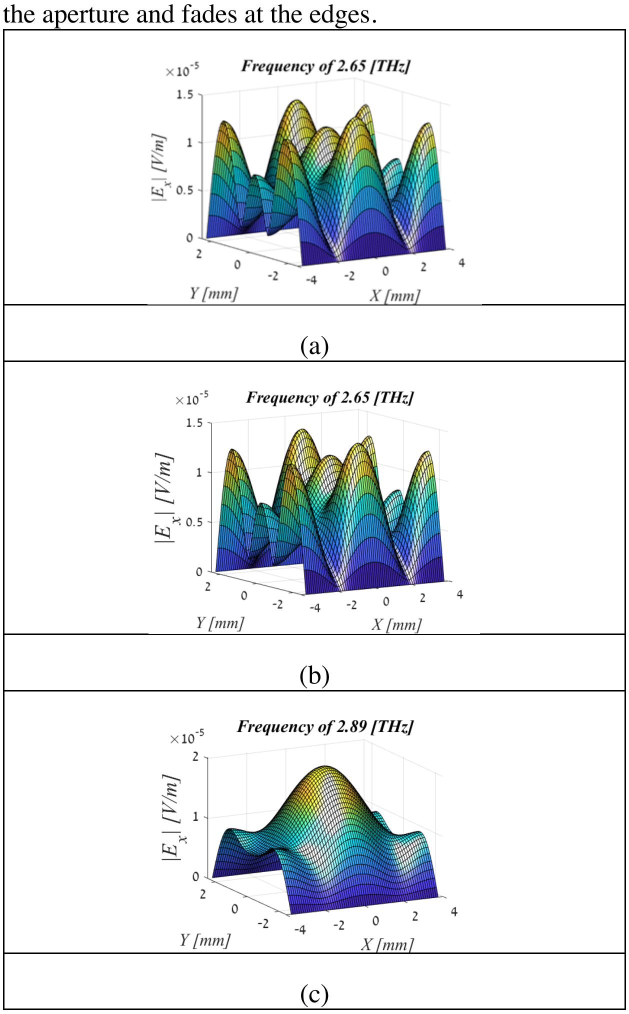

Figure 3: Spatial radiation profiles: (a) f=2.5 THz, (b) f=2.65 THz, (c) f=2.89 THz.

WDF Simulations

The EM field may have *N* dimensions at the desired resolution. The MI is achieved from that respective resolution. A double-resolution is obtained, as result. A number of rays for each position of the field controllable by user (by changing resolution). The WDF has complex amplitude. A K space profiles provide an indication of the future propagation of the rays, which can then be tracked by RT.

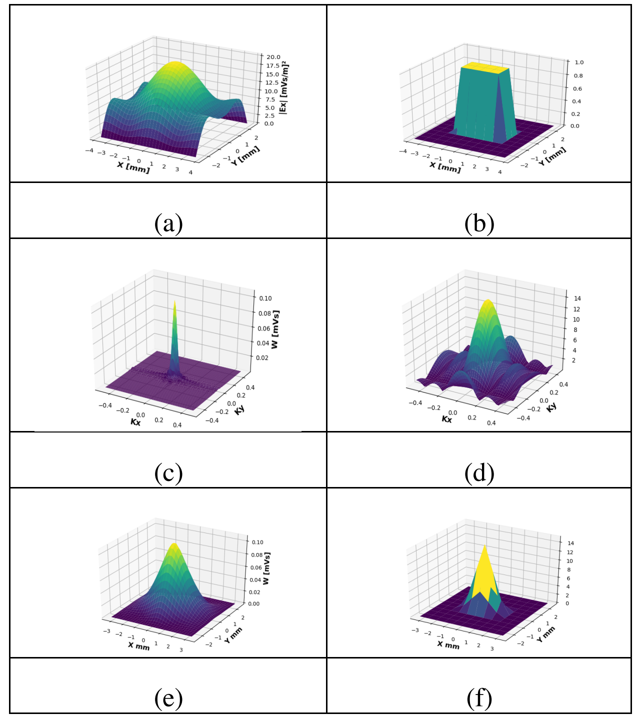

Figure 4: (a) Spatial profile of the output radiation field at the working frequency of 2.89 THz and the test signal and (b) the window function (rectangular pulse). The WDF from the center of the aperture - W_x (X=0, Y=0). (c) Of the radiation field at 2.89 THz. (d) Of the window function. The WDF from the **entire** aperture, only parallel to the Z-axis rays, W_x (K_x =0, K_y =0). (e) Of the radiation field at 2.89 THz. (f) Of the window function.

DISCUSSION AND CONCLUSION

Figure 4a demonstrate The $\mathbf{E_x}$ Field distribution at the output of a waveguide with the test signal (window function) in Figure 4b. Figure 4c demonstrated the WDF at coordinates X=0 and Y=0. An energy is mostly concentrated in the center and therefore, propagates straight in the Z direction. The energy dispersion is neigliable due to small K_x, K_y spread. That means the radiation propagates forward along the Z-axis at working frequency. This indicate most of the radiation is concentrated around the electron beam that is in the center. Obviously, a frequency of synchronization of the electron with an undulator is expressed. The "Pattern" of the original field, repeats by the WDF, as can well be seen in Fig 4c. Figure 4e demonstrates only parallel rays to the Z axis ($k_{\{x,y\}} = 0$) across the entire aperture. Gaussian behavior can be concluded. The code was activated on the test signal for conveniences. A “perfect sync” signal (Figure 4d) for the key coordinates (x=0, y=0) when parallel rays (K_x=0, K_y=0) of entire aperture a “perfect triangle” signal (Figure 4f) is obtained. A theory and analytical calculation is perfectly matches. This emphasizes the correctness of our homemade code. **Funding:** This research was funded by the Ministry of Science and Technology State of Israel, grant number 3-16652, and number 3-16461.

ISBN: 978-3-95450-220-2 ISSN: 2673-5474 doi: 10.18429/JACoW-FEL2022-TUP16

REFERENCES

[1] M. Chamberlain *et al.*, “Opportunities in THz Science”, *Science*, p. 123, 2004. doi:10.2172/899222

[2] S. R. Tripathi, E. Miyata, P. Ben Ishai, and K. Kawase, “Morphology of human sweat ducts observed by optical coherence tomography and their frequency of resonance in the terahertz frequency region,” Sci. Rep., vol. 5, no. March, 2015. doi:10.1038/srep09071

[3] A. Friedman *et al.*, “Configuration and Status of the Israeli THz Free Electron Laser,” in *Proc. FEL 2014,* Basel, Switzerland, Aug. 2014, paper TUP081, pp. 553-555.

[4] Y. Lurie, A. Friedman and Y. Pinhasi, “Single pass, THz spectral range free-electron laser driven by a photocathode hybrid rf linear accelerator,” Phys. Rev. Spec. Top. Accel. Beams, vol. 18, no. 7, pp. 1–9, 2015. doi:10.1103/PhysRevSTAB.18.070701

[5] M. Gerasimov, E. Dyunin, J. Gerasimov, J. Ciplis, and A Friedman, “Application of wigner distribution function for THz propagation analysis,” Sensors, vol. 22, no. 1, 2022 doi:10.3390/s22010240

[6] A. Gershun, “The Light Field,” J. Math. Phys., vol. 18, no. 1–4, pp. 51–151, 1939. doi:10.1002/sapm193918151

[7] M. A. Alonso, “Wigner functions in optics: describing beams as ray bundles and pulses as particle ensembles,” Adv. Opt. Photonics, vol. 3, no. 4, p. 272, 2011. doi:10.1364/aop.3.000272

[8] E. Wigner, “On the quantum correction for thermodynamic equilibrium,” Phys. Rev., vol. 40, no. 5, pp. 749–759, 1932. doi:10.1103/PhysRev.40.749

[9] M. J. Bastiaans, “The Wigner distribution function applied to optical signals and systems,” Opt. Commun., vol. 25, no. 1, pp. 26–30, 1978. doi:10.1016/0030-4018(78)90080-9

[10] M. Alonso, “Exact description of free electromagnetic wave fields in terms of rays,” Opt. Express, vol. 11, no. 23, p. 3128, 2003. doi:10.1364/oe.11.003128

[11] T. Dieing, O. Hollricher, and J. Toporski, Springer Series in Optical Sciences: Preface, vol. 158. 2010.

[12] V. Lakshminarayan, M.L. Calvo, and T. Alieva, "Mathematical Optics: Classical, Quantum, and Computational Methods", pp. 13-51, 2012.

[13] M. Levoy, “Light fields and computational imaging,” Computer (Long. Beach. Calif)., vol. 39, no. 8, pp. 46–55, 2006. doi:10.1109/MC.2006.270

[14] A. Torre, “Linear Ray and Wave Optics in Phase Space,” Linear Ray Wave Opt. Phase Sp., 2005. doi:10.1016/B978-0-444-51799-9.X5000-6

[15] Y. Pinhasi, Y. Lurie and A. Yahalom, “Model and simulation of wide-band interaction in free-electron lasers,” Nucl. Instruments Methods Phys. Res. Sect. A Accel. Spectrometers, Detect. Assoc. Equip., vol. 475, no. 1–3, pp. 147–152, 2001. doi:10.1016/S0168-9002(01)01693-X

[16] L. Schmidt, “Cross sections” Scope (Kalamazoo), vol. 2015, no. 11, p. 6, 2015. doi:10.1201/9781315273839-44a

ISBN: 978-3-95450-220-2 ISSN: 2673-5474 doi: 10.18429/JACoW-FEL2022-TUP17

BRILLIANT X-RAY FREE ELECTRON LASER DRIVEN BY RESONANT MULTI-PULSE IONIZATION INJECTION ACCELERATOR

P. Tomassini[1]*, ELI-NP, Magurele, Romania
[1]also at CNR-INO, Pisa, Italy
L. Giannessi[2], A. Giribono, INFN-LNF, Frascati, Italy
[2]also at ELETTRA, Trieste, Italy
F. Nguyen, ENEA, Frascati, Italy
L. A. Gizzi[3], CNR-INO, Pisa, Italy
[3]also at INFN, Pisa, Italy

Abstract

Laser Wakefield Accelerators are now sufficiently mature to provide GeV scale/high-brightness electron beams capable of driving Free Electron Laser (FEL) sources. Here, we show start-to-end simulations carried out in the framework of the EuPRAXIA project of a Free Electron Laser driven by an LWFA accelerator with the Resonant Multi-Pulse Ionisation Injection (ReMPI) setup. Simulations with this model using a 1 PW Ti:Sa laser system and a 20 cm long capillary, show the injection and acceleration of an electron beam up to 4.5 GeV, with a slice energy spread and a normalized emittance below 4×10^{-4} and 80 nm, respectively. The transport of the beams from the capillary exit to the undulator is provided by a matched beam focusing with a marginal beam-quality degradation. Finally, 3D simulations of the FEL radiation generated inside an undulator show that $\approx 10^{10}$ photons with central wavelength of 0.15 nm and peak power of $\simeq$ 0.3 GW can be produced for each bunch. Our start-to-end simulations indicate that a single-stage ReMPI accelerator can drive a high-brightness electron beam having quality large enough to be efficiently transported to a FEL undulator, thus generating X-ray photons of brilliance exceeding 10^{31} $ph/s/mm^2/mrad^2/0.1\%$ bw.

INTRODUCTION

The use of Laser Wake Field Accelerators (LWFA) to produce beams capable of driving an FEL had been envisaged decades ago [1] due to their potentialities in terms of flexibility and compactness of the source. As the beam-quality required to drive an FEL is extremely demanding, high-quality both particle injection and acceleration schemes are required. In the last decade, therefore, a focus on high-quality injection and acceleration schemes has been provided. Remarkably, this long-term activity led to the first demonstration of FEL lasing in the X-ray range by beams produced a LWF accelerator with a density downramp injector, leading to a $\approx$ 500 MeV high-brightness beam with an estimated normalised emittance of about 200 nm [2]. Recently, an all-optical, high-quality injector using a Two-Color scheme [3] in a resonant wakefield excitation framework, has been proposed and numerically tested in different scenarios [4]. In the Resonant Multi-Pulse Ionisation injection (ReMPI), a tightly

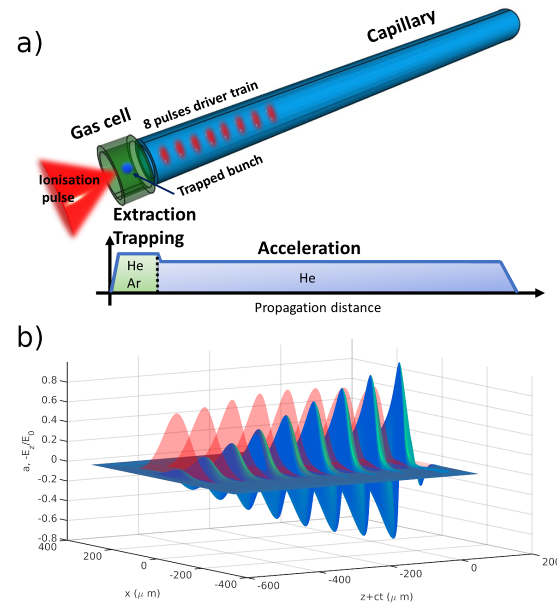

Figure 1: a) The LWFA layout with the ReMPI framework. The target consists of a 2mm long gas-cell filled with a mixture of He and Ar (50% + 50%). A 20 cm long He-filled capillary is placed just after the gas-cell. The large amplitude plasma wave excited by the train is able to catch and accelerate newborn electrons extracted by the fourth-harmonic ionizing pulse. The energy boosting up to 4.5 GeV is obtained by matching the transverse capillary size so as to guide a pulse with waist $w_{matched} = 65\ \mu$m. Inside the capillary, the sub-pulses in the train remain well focused for the whole section, thus providing an efficient driver for the about 4.3 GeV of energy boost. b) Wakefield longitudinal electric field map (blue color) resonantly excited by the train of pulses (red color). Snapshot after 3cm of propagation.

focused, short-wavelength pulse acts as an *ionization* pulse as in the Two-Color scheme. Such a pulse extracts electrons from a dopant (*e.g.* Nitrogen, Argon or Krypton) and can be obtained by frequency doubling (or more) a portion of the Ti:Sa pulse. The remaining largest portion of the Ti:Sa pulse is time shaped as a sequence of (sub) pulses and focused on the target with a long parabola. Such a train of pulses is devoted to the resonant excitation of a large-amplitude

* paolo.tomassini@eli-np.ro

ISBN: 978-3-95450-220-2 ISSN: 2673-5474 doi: 10.18429/JACoW-FEL2022-TUP17

plasma wave that traps the electrons extracted by the subsequent ionization pulse. Therefore, in ReMPI it is possible to avoid the ionization of the dopant atoms by means of the plasma wave driver, by using the resonant reinforcement of the plasma wave drive by low-intensity pulses instead that using high-amplitude long-wavelength single pulses delivered by a dedicated laser system as in [3]. The advantage of using a single Ti:Sa pulse is twofold. Firstly, Ti:Sa laser systems are nowadays a mature, worldwide available technology. Secondly, the usage of a single laser system drops out synchronization jitter issues between the driver and the ionization pulses. The main drawback of ReMPI consists in the additional complexity of the pulse train generation. Such a complexity, however, offers the possibility of exciting the plasma wave with an higher degree of flexibility, by simply modifying the spacing (or time delay) between the pulses of the train. The ReMPI scheme, in turn, offers the possibility of generating *tens of* nm of normalized emittance beams, tunable charge and length, quasi monochromatic beams with additional flexibility in the long-range excitation of the plasma wave so as to obtain either low-energy [5] or multi-GeV high-brigthness beams [6].

Here we investigate the usage of the ReMPI scheme as a single-stage injector/accelerator able to generate FEL oriented, high-brightness 4.5 GeV beams. We show, by means of start-to-end simulations, that ReMPI based accelerators can generate bunches able to drive an FEL in an efficient way, being therefore a valid candidate for compact all-optical high-brilliance FEL systems.

ALL-OPTICAL ACCELERATION OF FEL-QUALITY ELECTRON BEAMS

In our simulated setup (see Fig. 1) a 1PW Ti:Sa laser system was employed. A small fraction of the pulse, converted in fourth harmonics, was tightly focused so as to extract electrons from the K-shell of an high-Z dopant (Argon), thus constituting an ”ionizing pulse”. Those newborn electrons were trapped and accelerated by the plasma wave created by a train of eight sub-pulses (the ”driver train”), obtained by a time shaping of the main portion of the PW pulse. As the driving train enters the density plateau of the injector section (the 2mm long gas-cell filled with a mixture of He and Ar (50% + 50%)), a nonlinear wakefield is resonantly excited by the reinforced action of the longitudinal ponderomotive forces of the train sub-pulses. At the end of the train, where electrons are extracted by the ionizing pulse, a longitudinal electric field with peak value of $E_{z,max} \simeq 0.8E_0$ is found. Here $E_0 \equiv mc^2k_0/e \simeq 98\sqrt{n_e[cm^{-3}]}$ is the nonrelativistic wavebreaking limit. Since the longitudinal electric field exceeds the trapping threshold, newborn electrons from the ionized dopants are suddenly trapped in the same wave bucket and start to be accelerated. The trapped beam possesses a very high transverse quality, being the normalized emittances in the ionizing pulse and in the driver train polarization planes of $\epsilon_{n,x} = 0.080$ μrad and $\epsilon_{n,y} = 0.075$ μrad, respectively. In ReMPI (and also as in the Two Color scheme) extracted electrons have a very small transverse momentum and size after the ionizing pulse passage, due to the pulse low amplitude ($a_{0,ion} = 0.6$) and size ($w_{0,ion} = 4$ μm). As a result of the QFluid simulations [7], a 32 pC charge bunch with a remarkably low normalized emittance of $\epsilon_{n,x} = 0.083$ μrad along the ionizing pulse polarization was obtained at the capillary target end. Moreover, due to a partial overlapping between the ionizing pulse and the last pulse of the train (polarized perpendicularly to the ionization pulse), a quasi-round beam [5] with normalised emittance $\epsilon_{n,y} = 0.078$ μm was also found.

As the ionizing pulse is diffracted away at the capillary entrance (its Rayleigh length is $Z_{R,ion} = \pi w_{0,ion}^2/\lambda_{ion} \simeq 250$ μm), the driving train and the obtained trapped bunch enter into the boosting section, whose inner diameter is matched so as to guide a pulse with waist of $w_{matched} = 65$ μm. Inside the energy boosting section each sub-pulse (but the first one) propagates into a plasma wave excited by the previous pulses of the train, therefore the time evolution of each pulse is unique in the train and different from a standard evolution of a non relativistic pulse inside a capillary. At the end of the capillary density downramp, a 4.5 GeV high-brightness electron beam with peak current of 3.5 kA, projected energy spread of about 2% and slice energy spread at the peak current of 3×10^{-4} has been obtained.

EFFICIENT BEAM TRANSPORT TO THE UNDULATOR

Such beams result to be very appealing for FEL sources thanks to their high brilliance and high quality slice parameters. Beside that, the intrinsic transverse divergence (x') and projected energy spread ($\delta E/E$) are still critical items for beams thus produced. Indeed, typical values for these parameters are at least one order of magnitude higher than ones obtained with conventional accelerators, thus leading to unavoidable emittance spoiling and chromaticity rise once the beam exits the plasma. For this reason, the design of the transfer line needed for matching the electron beam with the FEL remains a challenging step in the machine definition.

In this work the beam matching to the undulator modules is enforced by a 10 m long transfer line consisting in the combination of state-of-the-art permanent and electromagnet quadrupoles. More in details, the beamline is composed of three triplets of permanent quadrupoles (PMQ) - the single triplet relying on 5-10-5 cm long quadrupoles with a nominal gradient of 450 T/m each spaced by 10 cm center-center - and four electromagnet quadrupoles (EMQ). The position and focusing gradients for PMQ quads have been settled aiming to capture the very divergent beam taking advantage of the high magnetic field in a very short distance and trying to avoid spoiling the beam quality because of second order effects. The following EMQ quads, whose positions are settled to match the beam to the FEL requests, gently carry the beam at the FEL entrance and allow for

ISBN: 978-3-95450-220-2 ISSN: 2673-5474 doi: 10.18429/JACoW-FEL2022-TUP17

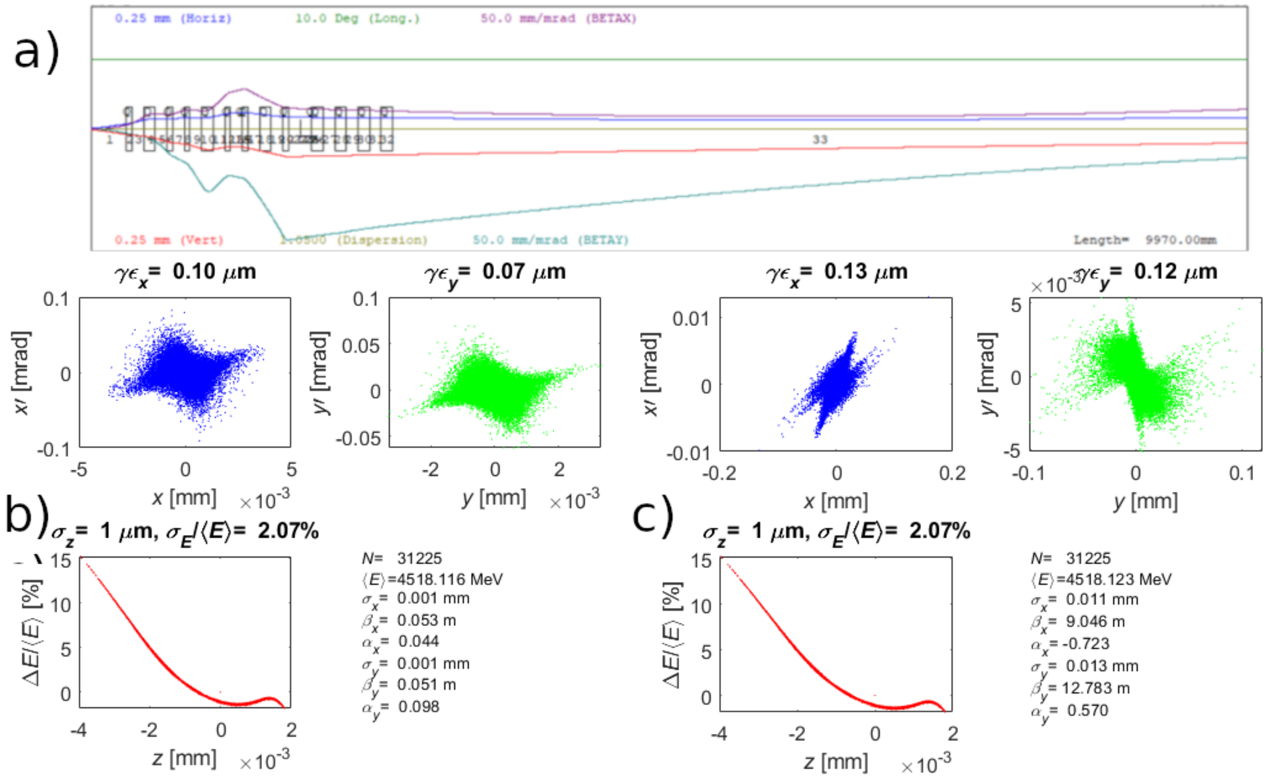

Figure 2: a) Evolution of beam spot size and Twiss parameters of the electron beam lines from the ReMPI stage exit down to the undulator entrance. b), c) Phase space of the electron beam at the beginning (end) of the transport line.

tuning of the Twiss parameters in a wide range acting only on their magnetic field.

The transport beamline matching aims to provide the electron beam, coming from the ReMPI stage, at the undulator entrance with the values of the Twiss functions as close as possible to the ones summarised in Table 1. In details, the electron beam dynamics in the transport line has been explored by means of simulations with Trace3D and Tstep codes (with space-charge effects included) aiming to β_{rms} tunable in the range 8-12 m and absolute alpha functions around 1 with the beam converging in the vertical plane and diverging in the horizontal one. The optimised beam matching as obtained by means of Trace3D simulations and the simulation results are shown in Fig. 2. At first, the matching of the beamline has been obtained with TRACE 3D, then the beam dynamics has been studied with the multi-particle code Tstep, an upgraded version of PARMELA [8].

FREE ELECTRON LASER OUTPUT

The undulator parameters chosen for the present study follow that of the Delta module from the SPARC experimental facility [9]. In more detail, it is a planar undulator with period $\lambda_u = 14$ mm and K=1.145, capable to operate at a gap of about 5 mm and to provide a permanent magnetic field of 1.22 T. With the electron bunches under consideration having an average energy of $E_{beam} = 4.518$ GeV, the expected resonant wavelength is $\lambda_R \simeq 0.148$ nm, equivalent to an X-ray photon energy of about 8.4 keV.

The undulator line consists of 15 modules, each one with length $N_u = 140$ periods, namely $L_u = N_u\,\lambda_u \simeq 2$ m, so that the total active length is about 30 meters. As the undulator has almost negligible focusing power, in order to keep a small transverse size of the electron beam, the periodic magnetic cell has to include alternate gradient quadrupoles in between undulator modules.

Matching the electron beam with the undulator parameters discussed above constrain the requests on the way the transport line is designed [10]. The matching criteria consist of equal average Twiss β values on both horizontal x and vertical y planes, as follows:

Table 1: Twiss coefficients requested at undulator entrance.

	β [m]	α	γ [m^{-1}]
x-plane	8.19	−0.795	0.199
y-plane	12.05	1.162	0.195

$$\langle\beta_{x,y}\rangle \equiv \frac{1}{L_u}\int_0^{L_u}\beta_{x,y}(z)\mathrm{d}z = 10\,m\,. \tag{1}$$

The condition in Eq.(1) is a safe one in order to guarantee an electron beam with about 4.5 GeV energy to be matched over the whole undulator line. Table 1 shows the values of

ISBN: 978-3-95450-220-2 ISSN: 2673-5474 doi: 10.18429/JACoW-FEL2022-TUP17

the Twiss coefficients requested at undulator entrance for the electron beam under discussion to be matched to the chosen undulator line, as a result of the constraints given in Eq.(1).

Since the proposed FEL is operated in SASE configuration, a relevant systematic effect is played by the initial noise power, that fluctuates randomly. In order to evaluate the impact of the numerical noise seed we generated nine additional replicas of the FEL time-dependent simulation by only varying the starting seed. The FEL performance

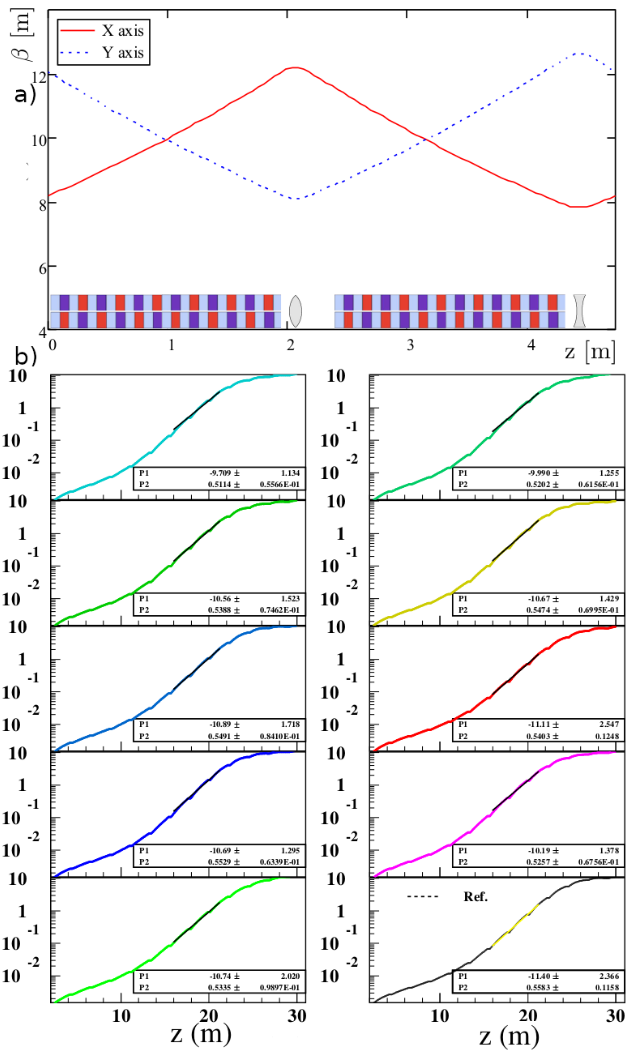

Figure 3: a) Behavior of the Twiss β functions through the magnetic lattice cell of the undulator line. The undulator modules and the focusing, defocusing quadrupoles are sketched indicating their positions. b) Growth of the FEL photon energy per pulse for the nine simulation replicas as specified in the text, compared to the reference one, shown with the dashed line on the right-bottom.

is studied with the `Genesis1.3` simulation code [11], by providing the related full 6D phase space. Figure 3 shows the growth of the pulse energy as a function of the propagation coordinate, in the region where the growth follows the exponential distribution, for the nine simulations calculated with a different noise seed value. The uncertainty associated to this systematics is estimated as the *rms* of the gain length L_G obtained from these simulations:

$$L_G = (1.79 \pm 0.09)\ m \tag{2}$$

The same procedure is applied to the photon pulse energy at the undulator exit and the value reads as

$$E_p(z_{exit}) = (10.8 \pm 0.8)\ \mu J\,. \tag{3}$$

The mean wavelength at the undulator exit is evaluated for each of the nine time-dependent simulations obtained varying the noise seed value. As a result, the wavelength uncertainty associated to this tolerance study is given below:

$$\lambda_{exit} = (0.152568 \pm 0.000031)\ nm \tag{4}$$

The final, averaged on the noise seed, radiation quality showing a brilliance exceeding $10^{31}\frac{ph}{s(\mu mrad)^2(0.1\%bw)}$ is summarised in Table 2.

Table 2: FEL radiation output

$\mathbf{E_p}$ [J]	σ_λ [nm]	**N/s** $[s^{-1}]$	**Brilliance** $[\frac{ph}{s\,(\mu mrad)^2(0.1\%bw)}]$
10	5.5×10^{-5}	8.2×10^{22}	3.0×10^{31}

CONCLUSIONS

By means of start-to-end numerical simulations, we showed that a single-stage 4.5 GeV LWFA accelerator in the ReMPI framework, along with dedicated beam transport line accommodating for the relatively large projected energy spread and large beam divergence, can be employed to drive a SASE-FEL with central wavelength of 0.152 nm. The FEL beamline about 30 m long will generate, at saturation, radiation with $\approx 10^{10}$ photons/shot and brilliance exceeding $10^{31}\frac{ph}{s(\mu mrad)^2(0.1\%bw)}$.

ACKNOWLEDGEMENTS

We acknowledge funding from the European Union's EU Horizon 2020 Research and Innovation Programs "EuPRAXIA"under Grant Agreement No. 653782 and IFAST under Grant Agreement No 101004730.

REFERENCES

[1] `https://alpha-x.phys.strath.ac.uk/`.

[2] W. Wang *et al.*, "Free-electron lasing at 27nm based on laser wakefield accelerator", *Nature*, vol. 595, pp. 516–520, 2021. `doi:10.1038/s41586-021-03678-x`

[3] L.-L. Yu *et al.*, "Two-Color Laser-Ionization Injection", *Phys. Rev. Lett.*, vol. 112, p. 125001, 2014. `doi:10.1103/PhysRevLett.112.125001`

[4] P. Tomassini *et al.*, "The Resonant Multi-Pulse Ionization injection", *Phys. Plasmas*, vol. 24, p. 103120, 2017. `doi:10.1063/1.5000696`

ISBN: 978-3-95450-220-2 ISSN: 2673-5474 doi: 10.18429/JACoW-FEL2022-TUP17

[5] P. Tomassini *et al.*, "High quality electron bunches for a multistage GeV accelerator with resonant multipulse ionization injection", *Phys. Rev. Accel. Beams*, vol. 22, p. 111302, 2019. `doi:10.1103/PhysRevAccelBeams.22.111302`

[6] P. Tomassini *et al.*, "High-quality 5 GeV electron bunches with resonant multi-pulse ionization injection", *Plasma Phys. Control. Fusion*, vol. 62, no. 1, pp. 014010, 2019. `doi:10.1088/1361-6587/ab45c5`

[7] P. Tomassini and A. R. Rossi, "Matching strategies for a plasma booster", *Plasma Phys. Control. Fusion*, vol. 58, pp. 034001, 2016. `doi:10.1088/0741-3335/58/3/034001`

[8] L. M. Young, "PARMELA", Los Alamos National Laboratory report LA-UR-96-1835 (2003) `https://accelconf.web.cern.ch/p03/PAPERS/FPAG029.pdf`.

[9] F. Ciocci *et al.*, Segmented undulator operation at the SPARC-FEL test facility, Proc. SPIE 9512, Advances in X-ray Free-Electron Lasers Instrumentation III, p. 951203, 2015. `doi:10.1117/12.2185099`

[10] M. Quattromini, M. Artioli, E. Di Palma, A. Petralia, and L. Giannessi, " Focusing properties of linear undulators",*Phys. Rev. Accel. Beams*, vol. 15, p. 080704, 2012. `doi:10.1103/PhysRevSTAB.15.080704`

[11] S. Reiche, "GENESIS 1.3: a fully 3D time-dependent FEL simulation code", *Nucl. Instr. Meth.*, vol. 429, pp. 243-248, 1999. `doi:10.1016/S0168-9002(99)00114-X`

ISBN: 978-3-95450-220-2 ISSN: 2673-5474 doi: 10.18429/JACoW-FEL2022-TUP19

STABLE MULTI-DAY PERFORMANCE OF A LASER WAKEFIELD ACCELERATOR FOR FEL APPLICATIONS

J. P. Couperus Cabadağ*, S. Bock, Y-.Y Chang, A. Debus, R. Gebhardt, A. Ghaith, U. Helbig, A. Irman, A. Koehler, M. LaBerge, R. Pausch, T. Püschel, U. Schramm, S. Schöbel, K. Steiniger, P. Ufer, O. Zarini, Helmholtz-Zentrum Dresden - Rossendorf, Dresden, Germany
E. Roussel, Univ. Lille, PhLAM, Lille, France
M.E. Couprie, M. Labat, Synchrotron SOLEIL, Saint-Aubin, France
M. C. Downer, University of Texas at Austin, Austin, Texas

Abstract

We report on the operation of the DRACO Laser Driven electron source for stable multi-day operation for Free Electron Laser (FEL) applications. The nC-class accelerator can deliver charge densities around 10 pC/MeV , <1 mrad rms divergence at energies up to 0.5 GeV and peak currents of over 10 kA [1]. Precise characterisation is paramount for controlled operation, including: spectrally resolved charge diagnostic, coherent optical transition radiation (TR) to resolve microbunch beam structures [2] and TR-based multioctave high-dynamic range spectrometry for sub-fs resolved characterisation of the 10 fs rms electron bunches [3]. Achieved stability allows for systematic exploration of demanding applications, resulting in the recent demonstration of the first LWFA based Beam-driven Plasma Wakefield Accelerator (LPWFA) [4]. Fulfilling the high demands required for FEL operation, the COXINEL manipulation line [5, 6] developed at Synchotron SOLEIL has recently been installed at our facility. Based on successful beam transport of over 13000 shots within 9 experimental days during commissioning, we were able to demonstrate the very first operation of a seeded FEL driven by a laser plasma accelerator [7].

INTRODUCTION

Plasma based wakefield acceleration is an acceleration technique able to achieve extremely high accelerating gradients, not limited by the vacuum breakdown limit, which has the potential to complement conventional accelerators where downsizing is desired. In Laser-plasma Wakefield Acceleration (LWFA), an ultrashort intense laser-pulse propagates through an optically transparent plasma and excites a plasma wake by displacing plasma electrons from its path by ponderomotive force [8]. Alternatively, in beam driven plasma wakefield acceleration (PWFA), a charged particle beam's space charge field similarly excites a plasma wake [9, 10]. For sufficiently high laser driver intensity or peak-current driver beam, all plasma electrons are completely expelled from the driver vicinity, thereby creating a co-propagating near-spherical shaped ion cavity [11, 12], which is able to sustain accelerating gradients above 100 GV/m [13]. Nowadays, compact LWFAs are hosted in many high-power laser facilities worldwide, and are able to provide electrons beams up to several GeVs [14], sub-percent energy spread [15], emittances down to 0.1 mm mrad [16], nanocoulomb charges [1, 17] and inherently short bunch durations in the few femtoseconds range [2, 18] leading to peak currents exceeding 10 kA [1, 2, 19]. LWFA research is currently in a transition phase where a significant ongoing effort to understand and control the underlying physical phenomena takes place aiming at further quality improvement continues [20], while simultaneously a strong effort is being made to improve LWFAs' stability, aiming at applications [21]. Here we present the current status of the DRACO Laser Plasma Accelerator (LPA), and the ongoing effort to achieve stable performance for secondary applications, such as FEL or LPWFA operation.

DRACO LASER PLASMA ACCELERATOR

The DRACO LPA, located at the Helmholtz-Zentrum Dresden-Rossendorf, is driven by the 100 TW line of the 30 fs dual-arm 100 TW & 1 PW DRACO laser system [22]. The DRACO laser is located in a separate room and after compression is transported in-vacuum to a radiation shielded accelerator hutch, which is schematically depicted in Fig. 1. Before experiment and while operating at full laser amplification mode, a wavefront sensor (Phasics SID4) located at the accelerator (see Fig. 1) in closed loop with a deformable mirror at the laser compressor chamber provides focal spot optimization. The spectral phase is measured with spectral-phase interferometry for a direct electric field reconstruction (SPIDER-A.P.E.) in parallel with self-referenced spectral interferometry (WIZZLER-fastlite) in closed loop with an acousto-optic programmable dispersive filter (DAZZLER-fastlite) for correction of dispersion mismatch along the laser amplifier and laser beam transport chain. The LPA performance is further optimized by phase correction on the second order (group velocity) dispersion at the DAZZLER. Active beam stabilization within the amplification system in conjunction with online diagnostics for laser near field and far field monitored at the accelerator hutch (see Fig. 1) ensure shot-to-shot pointing stability. A few-cycle probe beam [23], derived from the main laser pulse, allows to monitor driver laser self-focussing and formation of the wakefield accelerating structure. A sample wakefield is shown in Fig. 2.

Accelerated electron beams can be diagnosed for charge, energy-distribution, (single plane) divergence & pointing using a 0.4 m long 0.9 T permanent magnet dipole. Phosphor-

* j.couperus@hzdr.de

ISBN: 978-3-95450-220-2 ISSN: 2673-5474 doi: 10.18429/JACoW-FEL2022-TUP19

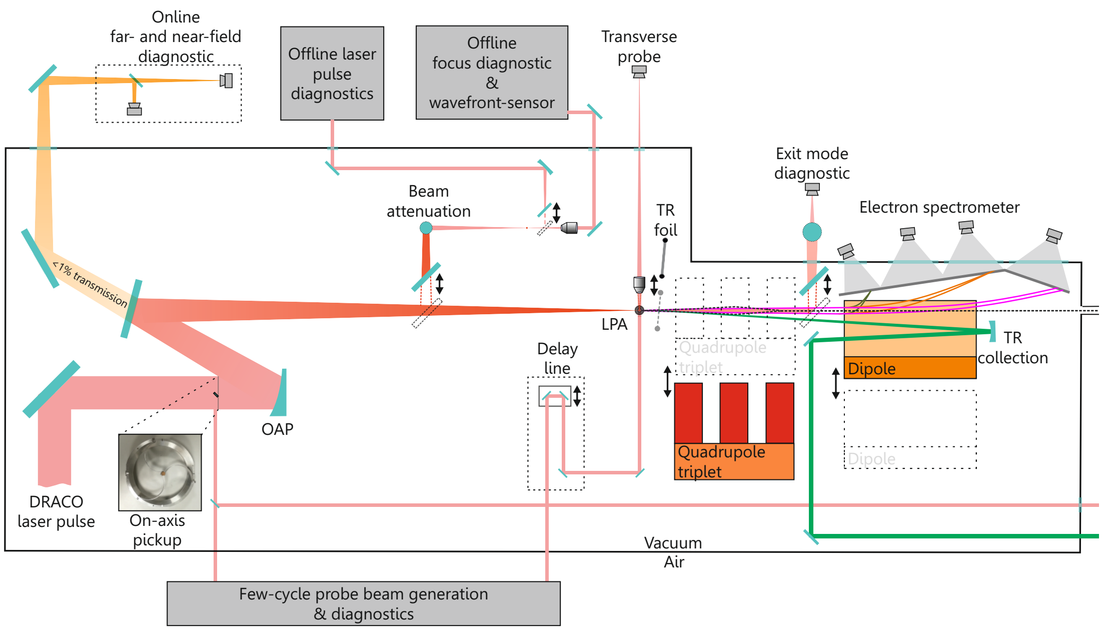

Figure 1: Schematic representation of the DRACO Laser Plasma Accelerator. The 100 TW DRACO laser is focused in a changeable gas target, in which the electron acceleration takes place. The electron beam can be characterized for charge while being spectrally-resolved using a dipole spectrometer. An insertable foil allows for electron beam characterization using Transition Radiation (TR). For FEL operation, a quadrupole triplet (QUAPEVA) can be inserted (while the dipole spectrometer is removed) to transport the beam into the COXINEL beamline.

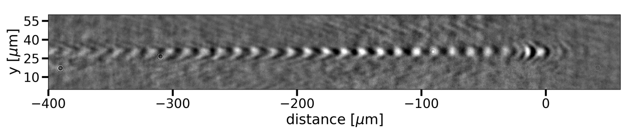

Figure 2: Snapshot image of a laser-driven wakefield capture using the few-cycle probe [23]. The laser is propagating from left to right and 0 µm marks the position of the driver laser.

based scintillating screens (CAWO-OG-16 front), imaged onto 12-bit CMOS cameras, are positioned such that the energy resolution is optimized using point-to-point imaging for energies up to 375 MeV. Higher energies up to 1.3 GeV can be detected in a non-imaging configuration (see Fig. 1). The absolute charge response of the scintillating screens was calibrated using the ELBE (Electron Linac for beams with high Brilliance and low Emittance) accelerator [24]. This calibration is implemented into the electron beam spectrometer, taking into account imaging system and camera efficiency as described in section IV from [24]. The electron beam can be further characterized using (coherent) Transition Radiation (TR). A multi-octave high-dynamic range optical spectrometer allows for single-shot longitudinal characterization of the ultrashort electron bunches. Figure 3 features an example temporal reconstruction of a LWFA electron bunch. The spectrometer and the reconstruction technique is detailed in [2]. Applying spectrally resolved transversally imaging of transition radiation (not included in Fig. 1), further information can be obtained on the transversal electron distribution as is detailed in [3, 25].

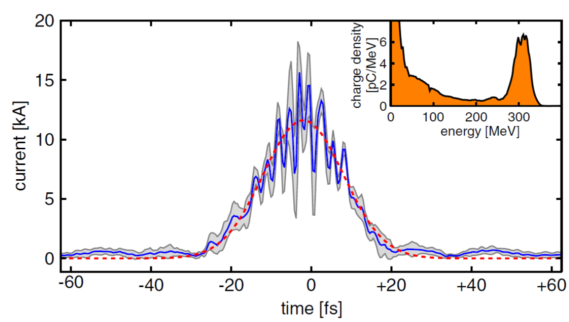

Figure 3: A reconstructed ultrashort STII Laser-wakefield accelerated electron bunch based on the emitted CTR spectrum, the electron spectrum, bunch charge and bunch divergence acquired at single-shot. The electron bunch featured (9.78 ± 0.77) fs rms-bunch duration, (9.40 ± 0.66) kA peak current and sub-structures with ∼ 3.0 fs characteristic periodicity figure from [2].

The dipole spectrometer can be removed from the beam-path to allow beam transport to secondary applications. Recently, the COXINEL beam manipulation line (detailed in [26]) developed by synchrotron SOLEIL, was installed at the DRACO LPA aiming at the demonstration of seeded LPA-driven FEL. A quadrupole triplet (QUAPEVA) [27], designed to capture divergent LPA-generated electron beams and integral part of the COXINEL beamline, was installed directly after the accelerator (see Fig. 1). To allow for seeded FEL, a small fraction of the LPA driver laser is picked up using a 1/2 inch pick-off mirror, see Fig. 1. Third-order

ISBN: 978-3-95450-220-2 ISSN: 2673-5474 doi: 10.18429/JACoW-FEL2022-TUP19

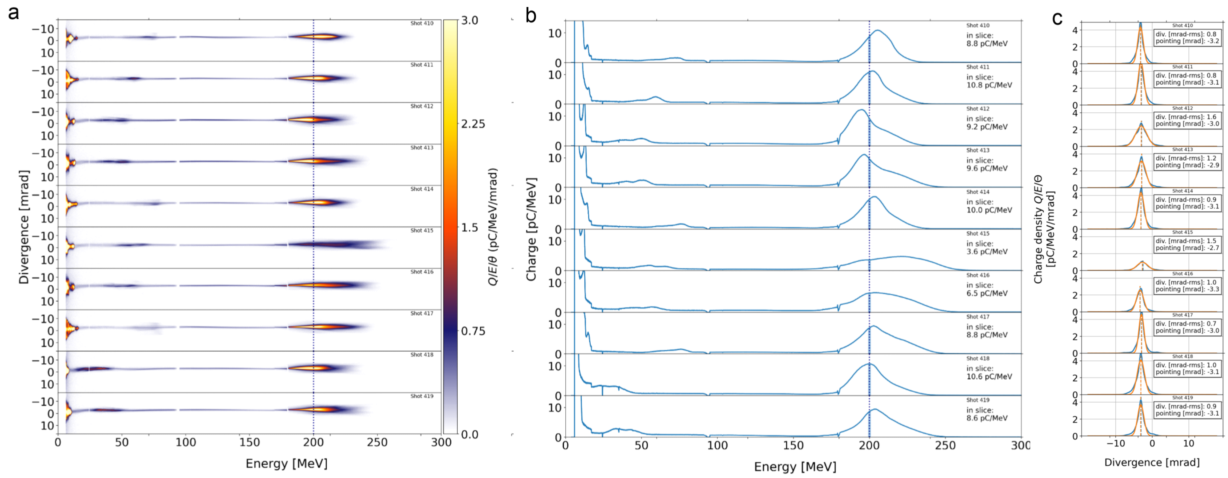

Figure 4: Consecutive shots of the DRACO laser driven electron source optimized for COXINEL parameters. **a** show the spectral distribution and divergence in the spectrometer non-bending plane. **b** shows associated lineouts and the spectral charge density in the 199.5-200.5 MeV energy slice. **c** shows the corresponding pointing and divergence in before mentioned energy slice.

frequency conversion to λ_{seed} = 269 nm is achieved using a set of two BBO-crystals (type 1 SHG & type 1 THG) in combination with a group velocity delay compensation plate and a dual waveplate. A half-λ plate combined with reflective thin polarizing plates allow for step-less adjustment of the seed generation input energy. The short pathway between pick-up, LPA and seed generation assures stable temporal overlap between the seed and electrons at the undulator. Online near- and far-field diagnostics of the seed (see Fig. 1) is used to monitor pointing stability and spatial overlap.

LWFA PERFORMANCE FOR FEL OPERATION

From accelerator point of view there are two main challenges in operating a LWFA-driven FEL. Firstly, the stringent beam quality requirements have to be met. The COXINEL beamline has been specifically designed for LWFA-generated beams, aiming to partially mitigate the, compared to conventional accelerators, typically large energy spread and large divergence [26–29]. Nevertheless, to achieve lasing, beams with divergence around or below 1 mrad-rms and spectral charge densities above ~ 3 pC/MeV are required at the design energy of the COXINEL line [30, 31]. Secondly, both shot-to-shot and long-term stability of the accelerator has to be guaranteed. Shot-to-shot stability is specifically crucial due to the low repetition rate of on LWFA accelerator (typical 0.1 - 0.5 Hz). Low fluctuations allow for quicker beam transport alignment as well as quicker collection of statistical data at low repetition rates nonetheless. Long-term stability has to be ensured as during beamline transport and FEL operation no complete electron beam diagnostics are available. It is desired to reduce the need to retune the accelerator to the absolute minimum, as this involves interrupting beam transport and experiment, i.e. removing the QUAPEVA quadropole triple and inserting the dipole spectrometer.

To generate electron beams, several injection methods are available. In choosing a suitable method, both above-mentioned requirements have to be taken into consideration. At the DRACO LPA, beams have been generated using shock-front injection, reaching an average charge density of (7.5 ± 2.4) pC/MeV, a divergence of (1.0 ± 0.3) mrad-rms and a (3.3 ± 1.6)% relative energy spread. Although these parameters fit the FEL requirements, a large shot-to-shot energy fluctuation of > 5% around the mean energy makes this injection method not suitable until further improvements to its stability have been made. In contrast, the Self-Truncated Ionization Injection (STII) scheme [32] characteristically has a significant larger energy spread due to its larger injection volume, but at the same time is capable to inject large quantities of charge into the accelerator. This allows for a certain degree of shot-to-shot mean energy fluctuation, while still fulfilling the required beam parameters at the design energy of the COXINEL line at every shot.
Employing beam loading [1] to nevertheless limit energy spread, thus safeguarding a sufficiently high spectral charge density, and tailoring [33] the injection scheme leads to robust and stable performance specifically suitable for FEL operation using the COXINEL beamline. Figure 4 shows the performance of the accelerator in the STII scheme, tuned for optimal performance around 200 MeV, the initial design energy of the COXINEL beamline. The broad energy spread compensated for shot-to-shot fluctuations in the mean energy, resulting in an average spectral charge density of (8.7 ± 2.2) pC/MeV at 200 MeV. Meanwhile a divergence of (1.0 ± 0.3) mrad-rms is found in this slice.
The long-term stability of the accelerator can be found in Labat *et al.* [7] (Fig. 5), which presents data gathered during a successful seeded FEL campaign. For this campaign the beamline and accelerator operated at a mean energy of

ISBN: 978-3-95450-220-2 ISSN: 2673-5474 doi: 10.18429/JACoW-FEL2022-TUP19

189 MeV. Presented are sets of sequential shots at different times over two experimental days. The time in between sets are slots where the COXINEL line is operated and thus no spectrometer is available. Accelerator tweaking only occurred and reference shots were only taken when indications of accelerator performance deterioration (e.g. reduction of transported charge in COXINEL line, pointing drift on COXINEL imager screens) occurred. Effectively, time slots of up to over six hours of stable accelerator performance were available. Routine operation, with up to 5000 high-quality shots per day, has been established.

CONCLUSION & OUTLOOK

We presented an overview of the DRACO Laser Plasma Accelerator and its current status for driving secondary applications requiring both high beam quality as well as high shot-to-shot and long-term stability. Its current performance enabled the worldwide first LWFA-driven seeded FEL demonstration [7], on which the LWFA performance was presented in more detail in this proceeding. Another example application enabled by the stable high-quality operation of the DRACO LPA is laser-to-beam-driven wakefield acceleration (LPWFA) presented in more detail in [4, 34].

For future experiments it is envisioned to further improve stability of the accelerator, potentially allowing operation in shock-front injection mode to benefit from a lower beam energy spread.

REFERENCES

[1] J.P. Couperus *et al.*, "Demonstration of a beam loaded nanocoulomb-class laser wakefield accelerator", *Nat. Commun.*, vol. 8, no. 487, 2017. doi:10.1038/s41467-017-00592-7

[2] O. Zarini *et al.*, "Multioctave high-dynamic range optical spectrometer for single-pulse, longitudinal characterization of ultrashort electron bunches", *Phys. Rev. Accel. Beams*, vol. 25, p. 012801, 2022. doi:10.1103/PhysRevAccelBeams.25.012801

[3] A. Lumpkin, M. LaBerge, *et al.*, "Coherent Optical Signatures of Electron Microbunching in Laser-Driven Plasma Accelerators", *Phys. Rev. Lett.*, vol. 125, p. 014801, 2020. doi:10.1103/PhysRevLett.125.014801

[4] T. Kurz, T. Heinemann, *et al.*, "Demonstration of a compact plasma accelerator powered by laser-accelerated electron beams", *Nat. Commun.*, vol. 12, p. 2895, 2021. doi:10.1038/s41467-021-23000-7

[5] M.-E. Couprie *et al.*, "Towards a free electron laser based on laser plasma accelerators", *J. Phys. B*, vol. 47, p. 234001, 2014. doi:10.1088/0953-4075/47/23/234001

[6] M.-E. Couprie *et al.*, "An application of laser-plasma acceleration: towards a free-electron laser amplification", *Plasma Phys. Control. Fusion*, vol. 58, p. 034020, 2016. doi:10.1088/0741-3335/58/3/034020

[7] M. Labat, J.P. Couperus Cabadağ, A. Ghaith, A. Irman, *et al.*, "Seeded free-electron laser driven by a compact laser plasma accelerator", submitted for publication. doi:10.21203/rs.3.rs-1692828/v1

[8] T. Tajima and V. Malka, "Laser plasma accelerators", *Plasma Phys. Control. Fusion*, vol. 62, p. 034004, 2020. doi:10.1088/1361-6587/ab6da4

[9] P. Chen *et al.*, "Acceleration of Electrons by the Interaction of a Bunched Electron Beam with a Plasma", *Phys. Rev. Lett.*, vol. 54, pp. 693-696, 1985. doi:10.1103/PhysRevLett.54.693

[10] J. Rosenzweig *et al.*, "Acceleration and focusing of electrons in two-dimensional nonlinear plasma wake fields", *Phys. Rev. A*, vol. 44, pp. R6189-R6192, 1991. doi:10.1103/PhysRevA.44.R6189

[11] K. Lotov, "Blowout regimes of plasma wakefield acceleration", *Phys. Rev. E*, vol. 69, p. 046405, 2004. doi:10.1103/PhysRevE.69.046405

[12] W. Lu *et al.*, "Nonlinear Theory for Relativistic Plasma Wakefields in the Blowout Regime", *Phys. Rev. Lett.*, vol. 96, p. 165002, 2006. doi:10.1103/PhysRevLett.96.165002

[13] S. Corde *et al.*, "High-field plasma acceleration in a high-ionization-potential gas", *Nat. Commun.*, vol. 7, p. 11898, 2016. doi:10.1038/ncomms11898

[14] A. Gonsalves *et al.*, "Petawatt Laser Guiding and Electron Beam Acceleration to 8 GeV in a Laser-Heated Capillary Discharge Waveguide", *Phys. Rev. Lett.*, vol. 122, p. 084801, 2019. doi:10.1103/PhysRevLett.122.084801

[15] W. Wang *et al.*, "High-Brightness High-Energy Electron Beams from a Laser Wakefield Accelerator via Energy Chirp Control", *Phys. Rev. Lett.*, vol. 117, p. 124801, 2016. doi:10.1103/PhysRevLett.117.124801

[16] G. Plateau *et al.*, "Low-Emittance Electron Bunches from a Laser-Plasma Accelerator Measured using Single-Shot X-Ray Spectroscopy", *Phys. Rev. Lett.*, vol. 109, p. 064802, 2012. doi:10.1103/PhysRevLett.109.064802

[17] J. Götzfried *et al.*, "Physics of High-Charge Electron Beams in Laser-Plasma Wakefields", *Phys. Rev. X*, vol. 10, p. 041015, 2020. doi:10.1103/PhysRevX.10.041015

[18] O. Lundh *et al.*, "Few femtosecond, few kiloampere electron bunch produced by a laser–plasma accelerator", *Nat. Phys.*, vol. 7, pp. 219-222, 2011. doi:10.1038/nphys1872

[19] Y. F. Li *et al.*, "Generation of 20 kA electron beam from a laser wakefield accelerator", *Phys. Plasmas*, vol. 24, p. 023108, 2017. doi:10.1063/1.4975613

[20] M. C. Downer *et al.*, "Diagnostics for plasma-based electron accelerators", *Rev. Modern Phys.*, vol. 90, p. 035002, 2018. doi:10.1103/RevModPhys.90.035002

[21] A. Maier *et al.*, "Decoding Sources of Energy Variability in a Laser-Plasma Accelerator", *Phys. Rev. X*, vol. 10, p. 031039, 2020. doi:10.1103/PhysRevX.10.031039

[22] U. Schramm *et al.*, "First results with the novel petawatt laser acceleration facility in Dresden", *J. Phys. Conf. Ser.*, vol. 874, p. 012028, 2017. doi:10.1088/1742-6596/874/1/012028

[23] S. Schöbel *et al.*, "Effect of driver charge on wakefield characteristics in a plasma accelerator probed by femtosecond shadowgraphy", *New J. Phys.*, in press, 2022. doi:10.1088/1367-2630/ac87c9

ISBN: 978-3-95450-220-2 ISSN: 2673-5474 doi: 10.18429/JACoW-FEL2022-TUP19

[24] T. Kurz *et al.*, "Calibration and cross-laboratory implementation of scintillating screens for electron bunch charge determination", *Rev. Sci. Instrum.*, vol. 89, p. 093303, 2018. doi:10.1063/1.5041755

[25] M. LaBerge *et al.*, "Coherent 3D microstructure of laser-wakefield-accelerated electron bunches", presented at the 40th International Free Electron Laser Conference (FEL'22), Trieste, Italy, Aug. 2022, paper THAI2, this conference.

[26] T. André *et al.*, "Control of laser plasma accelerated electrons for light sources", *Nat. Commun.*, vol. 9, p. 1334, 2018. doi:10.1038/s41467-018-03776-x

[27] F. Marteau *et al.*, "Variable high gradient permanent magnet quadrupole (QUAPEVA)", *Appl. Phys. Lett.*, vol. 111, p. 253503, 2017. doi:10.1063/1.4986856

[28] A. Ghaith *et al.*, "Tunable high gradient quadrupoles for a laser plasma acceleration based FEL", *Nucl. Instrum. Methods Phys. Res. A*, vol. 909, pp. 290-293, 2018. doi:10.1016/j.nima.2018.02.098

[29] E. Roussel *et al.*, "Energy spread tuning of a laser-plasma accelerated electron beam in a magnetic chicane", *Plasma Phys. Control. Fusion*, vol. 62, p. 074003, 2020. doi:10.1088/1361-6587/ab8ca0

[30] A. Loulergue *et al.*, "Beam manipulation for compact laser wakefield accelerator based free-electron lasers", *New J. Phys.*, vol. 17, p. 023028, 2015. doi:10.1088/1367-2630/17/2/023028

[31] M. Labat *et al.*, "Robustness of a plasma acceleration based free electron laser", *Phys. Rev. Accel. Beams*, vol. 21, p. 114802, 2018. doi:10.1103/PhysRevAccelBeams.21.114802

[32] M. Zeng *et al.*, "Self-truncated ionization injection and consequent monoenergetic electron bunches in laser wakefield acceleration", *Phys. Plasmas*, vol. 21, p. 030701, 2014. doi:10.1063/1.4868404

[33] A. Irman *et al.*, "Improved performance of laser wakefield acceleration by tailored self-truncated ionization injection", *Plasma Phys. Control. Fusion*, vol. 60, p. 044015, 2018. doi:10.1088/1361-6587/aaaef1

[34] J. P. Couperus Cabadağ *et al.*, "Gas-dynamic density down-ramp injection in a beam-driven plasma wakefield accelerator", *Phys. Rev. Research*, vol. 3, p. L042005, 2021. doi:10.1103/PhysRevResearch.3.L042005

ISBN: 978-3-95450-220-2 ISSN: 2673-5474 doi: 10.18429/JACoW-FEL2022-TUP22

A NOVEL METHOD FOR GENERATING HIGH-REPETITION-RATE AND FULLY COHERENT EUV FREE-ELECTRON LASER

H. X. Yang[1,2], J. W. Yan[3], H. X. Deng[4,*]
[1]Shanghai Institute of Applied Physics, Chinese Academy of Sciences, Shanghai, China
[2]University of Chinese Academy of Sciences, Beijing, China
[3]European XFEL GmbH, Schenefeld, Germany
[4]Shanghai Advanced Research Institute, Chinese Academy of Sciences, Shanghai, China

Abstract

High-brightness extreme ultraviolet (EUV) light source is strongly required for high-resolution photoelectron spectroscopy, imaging experiments, and EUV lithography. In this work, the self-modulation technique is introduced into seeded FELs, such as high-gain harmonic generation (HGHG), to significantly reduce the requirement of the seed laser power by enhancing coherent energy modulation. Numerical simulations demonstrated that the modified HGHG configuration with the self-modulation technique could generate high-repetition-rate, fully coherent, stable, and kilowatt-scale EUV pulses at a more compact linac-based light source.

INTRODUCTION

High-brightness extreme ultraviolet (EUV) light source is a prerequisite for fundamental science. In terms of EUV high-resolution photoelectron spectroscopy and imaging experiments, high brightness and full coherence characteristics are essential. In terms of EUV lithography (EUVL), high average power (higher than 1 kW) and high stability characteristics are more critical. A high-power, fully coherent, and stable EUV light source is urgently required. Over the past decades, synchrotron radiation (SR) has been supplied as a standard tool for advanced research [1]. The SR light source's limitations are the longitudinally incoherent and the order of tens of picoseconds of pulse duration. With accelerator and undulator technology advancements, free-electron lasers (FELs) with high-intense and ultra-fast characteristics have made enormous progress in cutting-edge applications [2], which is the most promising high-power EUV light source.

Generation of high-brightness EUV radiation pulses requires the combination of a high-repetition-rate electron beam and various operating mechanisms. The steady-state microbunching mechanism-based photon source and storage-ring-based FEL are promising EUV light sources because the electron beam repetition rate in the storage ring can easily reach 100 MHz [3, 4]. However, the drawbacks of the electron beam in the storage ring are the low peak current, the induced energy spread that can limit the FEL extracted power, and the multiple turns stability remains experimentally demonstrated. Besides, the energy recovery linac (ERL) based light source with the self-amplified spontaneous emission (SASE) scheme [5, 6] is another method to produce kW-scale EUV pulses [7]. However, generating high-quality electron beams with high beam energy and high peak current is challenging. The total length of the ERL-FEL typically reaches over 100 m to improve the efficiency of extracted radiation power. Moreover, SASE FEL suffers from longitudinally incoherent and significant shot-to-shot jitter due to the initial shot noise of the electron beam.

Currently, most FEL facilities are based on linac that can produce electron beams with small energy spread, high peak current, and low emittance, thus achieving high single-pass FEL gain. The challenge of producing high average power kW scale EUV from single-pass FEL sources is the demand for high-repetition-rate electron beam or high beam energy. With the advanced superconducting radiofrequency technology, continuous-wave electron beam generation and FEL light source becomes feasible. Seeded FELs inherit the characteristics of the external seed laser, which can generate fully coherent and stable FEL pulses [8–10]. To generate high-repetition-rate EUV pulses in seeded FELs, such as high-gain harmonic generation (HGHG) [8], a UV seed laser of several MHz is required, challenging for state-of-the-art laser technology. Recently, the self-modulation technique has been demonstrated theoretically and experimentally in seeded FELs to reduce the power requirement of the seed laser at least two orders of magnitude by amplifying coherent energy modulation [11]. Thus, externally seeded FELs introducing the self-modulation technique have excellent potential to produce high-repetition-rate, fully coherent, and stable EUV pulses.

In this work, we demonstrate the feasibility of the single-pass FEL facilities to produce high-repetition-rate, fully coherent, and stable kW-scale EUV generation, with its potential application to EUVL. After upgrading the linac and laser systems, this modified HGHG configuration with the self-modulation technique is compatible with existing seeding beamlines.

PHYSICAL DESIGN

In a standard HGHG, an external seed laser interacts with the electron beam in a modulator undulator and imprints a sinusoidal energy modulation. After a dispersion section, the energy modulation is transferred into a density modulation and radiators resonate at the target harmonic of the seed laser. Typically, the energy modulation amplitude is proportional to the harmonic number n. For amplifying the FEL

* denghx@sari.ac.cn

ISBN: 978-3-95450-220-2 ISSN: 2673-5474 doi: 10.18429/JACoW-FEL2022-TUP22

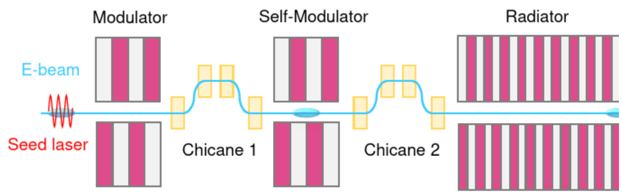

Figure 1: The schematic layout of the self-modulation HGHG configuration. A UV seed laser with lower intensity modulates the energy beam in the modulator. Then, the electron beam is compressed longitudinally by a four-dipole magnetic chicane 1 to enhance the coherent radiation in the self-modulator resonating at the fundamental wavelength of the seed laser. Through the precisely optimized magnetic chicane 2, the electron beam can generate high harmonic radiation toward the EUV region in the following radiator.

radiation in the EUV range, the energy modulation should be increased. The self-modulation technique is employed to the standard HGHG to enhance a larger energy modulation extending to the spectrum wavelength of the EUV. Meanwhile, the seed laser power is significantly lower than that of the standard HGHG, which means the conventional externally seeding scheme HGHG can generate the high-repetition-rate EUV radiation.

The schematic illustration of the self-modulation HGHG is shown in Fig. 1. Compared to the standard HGHG, this configuration introduces one additional self-modulator to generate coherent energy modulation. Generally, the power of the coherent radiation is given by

$$P_{\text{coh}} = \frac{Z_0 \left(K[JJ]_1 L I b_n\right)^2}{32\pi\sigma_x^2\gamma^2} \tag{1}$$

where $Z_0 = 377\ \Omega$ is the vacuum impedance, K is the undulator parameter, $[JJ]_1$ is the planar undulator Bessel factor, L is the self-modulator length, b_n is the n-th bunching factor, I is the peak current, and σ_x is the transverse beam size. Here, the coherent radiation intensity can be further enhanced by precisely optimizing the beam size, the peak current, and the self-modulator length, thus relaxing the requirement of the seed laser system.

To verify the feasibility of the self-modulation HGHG to generate EUV pulses with high average power, the nominal parameters of the SXFEL user facility are adopted, as shown in Table 1, to present some physical design and optimization. The SXFEL user facility was initially designed to generate coherent soft x-ray pulses using externally seeding schemes, such as cascaded HGHG or EEHG. The baseline design is fully compatible with the self-modulation HGHG configuration. The electron beam, seed laser, and undulator parameters are listed in Table 1, the FEL pierce parameter is calculated to 7×10^{-3}, corresponding to the gain length is 0.5 m. The 1.6 m long self-modulator corresponds to a gain length of 3.2 times. Due to the 3-fold gain length being critical for quadratic growth and FEL exponential growth, the coherent energy modulation in the self-modulator is significantly enhanced, producing significant harmonic bunching

Table 1: Main Simulation Parameters of SXFEL User Facility

Specifications	Electron beam
Energy	1.4 GeV
Slice energy spread	50 keV
Normalized emittance	1 mm·mrad
Peak current	700 A (Flat-top)
Bunch charge	600 pC
Specifications	**Seed laser**
Peak power	400 kW (Gaussian)
Duration	1 ps (FWHM)
Wavelength	266 nm
Rayleigh length	5 m
Specifications	**Undulator**
Period of Modulators	0.08 m
Length of Modulators	1.6 m
Period of Radiator	0.05 m
Length of Radiator	16 m

in the wavelength of EUV and broadening the HGHG operating range. By obtaining the same harmonic bunching factor, the self-modulation HGHG introduces an additional energy spread compared to standard HGHG. However, the seed laser power can be reduced by nearly two orders of magnitude, with great potential for high repetition rate operation.

SIMULATION RESULTS

To analyze the feasibility of the self-modulation HGHG, the simulations were carried out with GENESIS [12]. We first introduced a UV seed laser with a peak power of 400 kW, as shown in Table 1, producing an initial weak energy modulation of about 65 keV, corresponding to 1.3 times the slice energy spread. The steady-state simulation is performed to fast optimize the working points of R_{56}s of chicane 1 and chicane 2, as shown in Fig. 2. The maximum bunching factor at the 20th harmonic of the seed laser is about 0.07, with one of the optimal R^1_{56} and R^2_{56} of 0.86 mm and 0.043 mm, respectively.

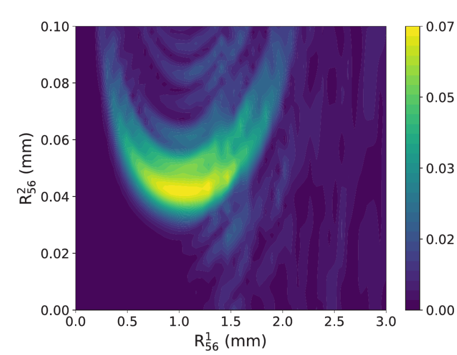

Figure 2: Optimization results of the optimal area of R_{56}s at the 20th harmonic bunching factor, corresponding to EUV wavelength.

ISBN: 978-3-95450-220-2 ISSN: 2673-5474 doi: 10.18429/JACoW-FEL2022-TUP22

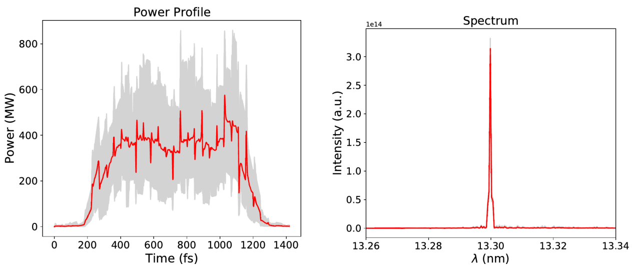

Figure 3: The 100-shot EUV FEL performance using the self-modulation technique after a 4 modules radiator of 16 m. Each grey plot corresponds to a single-shot simulation. The red plot corresponds to the average of all 100 shots.

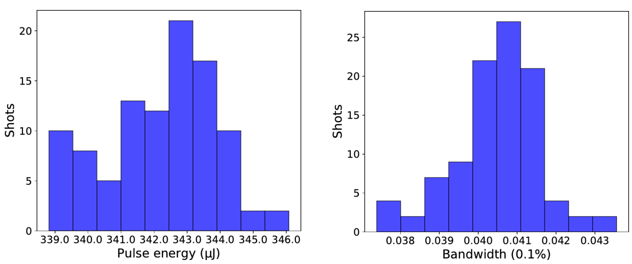

Figure 4: The statistical properties of 100 shots output EUV FEL performance.

FEL Performance

The time-dependent simulations were performed by further precisely optimizing the beam orbit, beam size, and undulator parameters, as shown in Fig. 3. The average EUV pulse energy reaches 342.2 µJ, and the rms pulse energy jitter is 1.7 µJ. The number of photons per pulse is about 2.3×10^{13} Due to the slippage of the self-modulator and shot noise effects, there are several spikes on the power profile. The average FWHM pulse length is about 646.0 fs. The average FWHM bandwidth is about 4.0×10^{-5}, corresponding to a time-bandwidth product of 0.58, approaching the Fourier transform limit. Besides, as shown in Fig. 4, the shot-to-shot pulse energy and relative bandwidth fluctuation is 0.49‰ and 2.8‰, respectively. The enhanced energy modulation amplitude is about 24.5 leading to a lower saturation pulse energy. Based on the self-modulation technique, the seed laser power is only 400 kW, corresponding to the average power of 1.2 W, promising to reach a 3 MHz repetition rate with the existing seed laser system. Assuming that the electron beam generated by the linac can achieve a 3 MHz repetition rate corresponding to an average current of 1.8 mA, the average power of the fully coherent EUV FEL can reach 1 kW. It is worthy that a tapering undulator can be used to extract additional power from the electron beam, which can further increase the average power by a factor of 3 to 5.

Stability Analysis

More numerical simulations were performed to investigate further whether the stability of the output FEL properties is sensitive to the seed laser power. Here, we assumed that the maximum power jitter of the seed laser is ± 6%, corresponding to between 376 kW to 424 kW when the dispersion strength of chicanes is constant. As shown in Fig. 5, a slight increase in the seed laser power can improve the harmonic bunching factor because of a range of working points, such as R_{56} of chicane 2. Besides, according to Fig. 6, both the pulse energy deviation and time-bandwidth product of output spectra as a function of the seed laser power. When the seed laser power is as low as 370 kW, the pulse energy is instead increased while the longitudinal coherence is significantly decreased. Because the introduced seed laser is weak, resulting in a pedestal on the power profile, the SASE background from the shot noise eventually leads to a lower signal-to-noise ratio. Therefore, the shot noise effects need further analysis to verify the self-modulation technique toward shorter wavelength FEL.

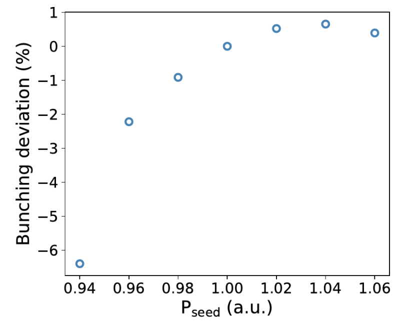

Figure 5: The 20th harmonic bunching deviation versus the seed laser power. The power is normalized by the nominal case of that of 400 kW.

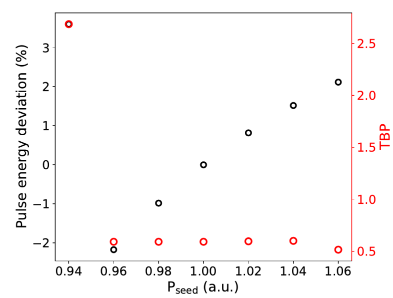

Figure 6: The EUV pulse energy deviation and the time-bandwidth product of output spectra versus the seed laser power. The power is normalized by the nominal case of that of 400 kW.

DISCUSSION

In this work, a novel method for generating high-repetition-rate, fully coherent, stable, and compact EUV FEL is demonstrated by numerical simulations. By reasonably optimizing the working points, one can obtain fully coherent EUV pulses with an average power of 1 kW utilizing a 3 MHz electron beam and a seed laser with an average power of only 1.2 W, significantly improving the efficiency of the EUV spectroscopic experiments. It should be noted that the output EUV pulse intensity can be further enhanced by increasing the electron beam repetition rate and combining it with the fresh bunch technique [13, 14], with the

ISBN: 978-3-95450-220-2 ISSN: 2673-5474 doi: 10.18429/JACoW-FEL2022-TUP22

potential to achieve kW-scale EUV-FEL. In addition, the sensitivity analysis of the novel method to the seed laser power shows that shot noise effects are essential at high harmonic up-conversion numbers. The degradation of FEL coherence should be considered during the optimization of the seed laser, which can be further investigated in future work.

ACKNOWLEDGMENTS

The authors would like to thank N. S. Huang and B. J. Deng for their helpful discussions. This work was supported by the National Key Research and Development Program of China (2018YFE0103100), the National Natural Science Foundation of China (12125508, 11935020), Program of Shanghai Academic/Technology Research Leader (21XD1404100), and Shanghai Pilot Program for Basic Research - Chinese Academy of Science, Shanghai Branch (JCYJ-SHFY-2021-010).

REFERENCES

[1] Z.T. Zhao, "Storage Ring Light Sources", *Reviews of Accelerator Science and Technology*, vol. 03, no. 01, p. 57-76, 2010. doi:10.1142/S1793626810000361

[2] N. Huang, H. Deng, B. Liu, D.Wang, and Z. Zhao, "Features and futures of X-ray free-electron lasers Features and futures of X-ray free-electron lasers", *The Innovation*, vol. 2, no. 2, p. 100097, 2021. doi:10.1016/j.xinn.2021.100097

[3] X. Deng *et al.*, "Experimental demonstration of the mechanism of steady-state microbunching", *Nature*, vol. 590, no. 7847, pp. 576-579, 2021. doi:10.1038/s41586-021-03203-0

[4] J. Lee *et al.*, "Demonstration of a ring-FEL as an EUV lithography tool", *Journal of Synchrotron Radiation*, vol. 27, no. 4, pp. 864-869, 2020. doi:10.1107/S1600577520005676

[5] A. Kondratenko and E. Saldin, "Generating of coherent radiation by a relativistic electron beam in an ondulator", *Part. Accel.*, vol. 10, pp. 207–216, 1980. http://cds.cern.ch/record/1107977/files/p207.pdf

[6] R. Bonifacio, C. Pellegrini, and L. Narducci, "Collective instabilities and high-gain regime in a free electron laser", *Optics Communications*, vol. 50, no. 6, pp. 373–378, 1984. doi:10.1016/0030-4018(84)90105-6

[7] N. Nakamura *et al.*, "Demonstration of proof of concept of the EUV-FEL for future lithography", *Proc. of SPIE*, vol. 11854, 2021. doi:10.1117/12.2600782

[8] L. H. Yu, "Generation of intense uv radiation by subharmonically seeded single-pass free-electron lasers", *Physical Review A*, vol. 44, no. 8, pp. 5178–5193, 1991. doi:10.1103/PhysRevA.44.5178

[9] G. Stupakov, "Using the beam-echo effect for generation of short-wavelength radiation", *Physical Review Letters*, vol. 102, no. 7, pp. 1–4, 2009. doi:10.1103/PhysRevLett.102.074801

[10] H. Deng and C. Feng, "Using off-resonance laser modulation for beam-energy-spread cooling in generation of shortwavelength radiation", *Physical Review Letters*, vol. 111, no. 8, pp. 1–5, 2013. doi:10.1103/PhysRevLett.111.084801

[11] J. Yan *et al.*, "Self-amplification of coherent energy modulation in seeded free-Electron Lasers", *Physical Review Letters*, vol. 126, no. 8, pp. 84801, 2021. doi:10.1103/PhysRevLett.126.084801

[12] S. Reiche, "GENESIS 1.3: a fully 3D time-dependent FEL simulation code", *Physical Review Accelerators and Beams*, vol. 429, no. 1, pp. 243-248, 1999. doi:10.1016/S0168-9002(99)00114-X

[13] L. Hua Yu and I. Ben-Zvi, "High-gain harmonic generation of soft X-rays with the "fresh bunch" technique", *Nuclear Instruments and Methods in Physics Research, Section A: Accelerators, Spectrometers, Detectors and Associated Equipment*, vol. 393, no. 1-3, pp. 96-99, 1997. doi:10.1016/S0168-9002(97)00435-X

[14] K. Zhou *et al.*, "Generating high-brightness and coherent soft x-ray pulses in the water window with a seeded free-electron laser", *Physical Review Accelerators and Beams*, vol. 20, no. 1, pp. 010702, 2017. doi:10.1103/PhysRevAccelBeams.20.010702

ISBN: 978-3-95450-220-2 ISSN: 2673-5474 doi: 10.18429/JACoW-FEL2022-TUP24

HIGH HARMONIC LASING USING ATTOSECOND ELECTRON PULSE COMBS IN PHOTON-INDUCED NEAR-FIELD ELECTRON MICROSCOPY

Y. Pan†, M. Krueger, Physics Department and Solid State Institute, Technion, Haifa, Israel
I. Kaminer, Department of Electrical and Computer Engineering, Technion, Haifa, Israel

Abstract

We propose a new high harmonic lasing mechanism using attosecond electron pulses, which can serve as promising ultra-bright extreme ultraviolet/soft X-ray attosecond laser sources.

INTRODUCTION

Attosecond laser pulses in the extreme ultraviolet/soft X-ray (XUV/SXR) spectral regions are presently available for attosecond pump-probe spectroscopy and extreme ultraviolet lithography for chip manufacturing, ultrafast atomic-scale microscopy, and nonlinear X-ray optics. There are two main approaches to produce attosecond light pulses: high-harmonic generation (HHG) in gas-phase or solid-state matter based on the three-step model [1-3], and X-ray free-electron lasers (XFELs) based on self-amplified spontaneous emission (SASE) and laser seeding processes of relativistic free electrons traveling through an undulator [4, 5].

Here, we propose a novel route of producing attosecond laser pulses, based on the generation of attosecond electron pulse trains in photon-induced near-field electron microscopy (PINEM) [6-8], combined with the SASE principle for light amplification. Our scheme relies on high-density nanotip arrays emitting dense electron bunches [9] that are subsequently modulated with a PINEM-type interaction, enabling high-gain for amplification of XUV/SXR high harmonic radiation.

SETUP

In analogy with the three-step model of HHG (ionization, acceleration, and recombination of an initially bound electron), we call our PINEM-HHG laser scheme the “three-tip” model (see Fig. 1a)), which can create both attosecond electron pulses and attosecond light pulses in a phase-coherent manner: the first tip emits electron pulses triggered by femtosecond laser pulses, with up to 102 electrons per laser pulse per tip [10]; the second tip modulates the electrons through a PINEM interaction with IR light (~800 nm) [7] and creates periodically bunched attosecond electron pulses [11]; the last tip serves as a radiation antenna for generating attosecond XUV/SXR pulses when interacting with the electron pulse train. Our scheme thus combines a tip emitter, a tip modulator, and a tip radiator.

In order to enhance the attosecond radiation power further, we replace the three tips with high-density nanotip arrays. The first tip is replaced by a 2D array (pitch of 100 nm) for generating a high electron charge density, thereby increasing it from 102 to 107 per laser pulse [9]. We also increase the PINEM interaction time (increasing the interaction length to 100 nm, with acceleration gradient field 1 GV/m) by introducing an array modulator with ten nanotips (pitch of 100 nm). As a result, we can achieve the widely spread PINEM spectrum of the order of a few hundred electronvolts, which as a crucial parameter limits the cut-off frequency of the radiation. Indeed, we find a linear scaling law of the cut-off frequency because it linearly depends on the laser-induced energy spread. At last, we realize SASE of XUV/SXR lasing radiation with an array radiator with 100 nanotips with a pitch of 800 nm (to match the period of electron pulse trains), respectively.

RESULTS

In order to assess the efficiency of PINEM-HHG, we devise a fully quantum theory approach based on quantum electrodynamics in the strong-field regime. Typical features of PINEM-HHG are shown in Fig. 1b)-1d). Fig. 1b) shows the HHG spectrum from an attosecond bunched free electron with PINEM spectrum with a spread of 160 eV. The HHG spectrum has a plateau shape and a cut-off at harmonic order $n_{cut\text{-}off}$=150, corresponding to the PINEM spread. Fig. 1c) shows the linear dependence of the cut-off frequency on the laser coupling strength 2|g| and hence on the laser field strength, which is similar to the linear power law in intra-band solid-state HHG [3]. A Fourier transform to the time domain reveals a radiative attosecond pulse train (see Fig. 1d)). We find that the pulse duration in the trains is 20 as, which is on the order of the atomic unit of time (inset of Fig. 1d)) and can hardly be achieved from FEL of relativistic beams [12]. In total, the best-case theoretical estimation of the superradiant XUV/SXR photon emission is $N_{ph}=(N_e\ N_{(tip3)})^2\ \Delta\nu_{sp}\sim 10^{11}$ photon/pulse, with $N_e=10^7$, $N_{(tip3)}=100$ [9] and the emitted photon number per single electron $\Delta\nu_{(q,\ sp)}\sim 10^{-7}$. The N_e^2-dependence stems from the superradiance where many electrons emit coherently, and the $N_{(tip3)2}$-dependence from the SASE process when the photons are emitted spontaneously from the attosecond electron pulses and radiation emission builds up exponentially, until saturation. It is worthy to compare with the practical assessment of the first lasing in LCLS (~1013 photon/pulse), in which the beam has bunched electrons of the order of 109 [5]. However, we stress that practical challenges, such as the large source size of the emitter array and the Coulomb repulsion inside the high-charge electron bunches, will likely render our approach less efficient due to the increase of both the transverse and longitudinal beam emittance. The Coulomb repulsion effect may be mitigated by working at higher electron energies or at longer light pulses and accordingly longer wavelengths (mid/far IR).

From the perspective of free electrons, our PINEM-HHG scheme has many differences compared to atomic HHG and high-harmonic FEL [19]. First, the spectral spread of the electron beam in PINEM is about 1eV, less

ISBN: 978-3-95450-220-2 ISSN: 2673-5474 doi: 10.18429/JACoW-FEL2022-TUP24

than the typical photon energy ($\hbar\omega$=1.6 eV). Hence, there is no classical picture of the electron to explain PINEM-HHG, and a fully quantum-mechanical description must be applied. Second, the averaged kinetic energy of the ultrafast electron pulses is 200 keV, which is easily achievable, different from the typical central energy of the ultra-relativistic free electron beams in X-ray FELs (~1 GeV) that requires beam accelerators. Compared to atomic HHG, the mildly relativistic (γ=1.4) PINEM electrons propagate freely, which is easily coherently manipulated and phase-matched via the currently developed beam techniques.

To achieve coherent lasing, the phase-matching condition for many electrons is very crucial. Another critical issue is the high peak current in the PINEM-HHG scheme. We can generate the femtosecond electron pulses with a large peak current on the scale of 1 kA (107 electron/pulse) via nanotip array emitters [9], which is impossible for strong-field ionization in atoms. Furthermore, since the photons are generated from the scattering between PINEM sidebands, the final HHG photon generation is fundamentally entangled with the final electrons. Consequently, the resulting PINEM-HHG closely depends on electron post-selection. In our estimation, the photon emission rate from a single electron is extremely low ($\Delta\nu$_(q,sp)~10^{-7}), which can be further enhanced by the post-selection. Post-selection of the final electrons to be aligned with the initial PINEM state (after tip 2) can depict which radiation spectra will be created, with one of the options being to retrieve a classical radiation picture from our PINEM-HHG lasing scheme [13].

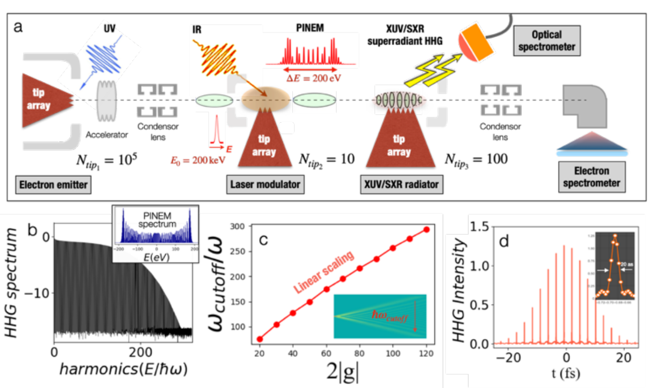

Figure 1: The setup and concept of PINEM-HHG lasing. (a) The "three-tip" model of PINEM-HHG scheme. (b) The HHG spectrum from PINEM-induced attosecond bunched free electrons. The inset is the corresponding PINEM spectrum. (c) The linear scaling law of the HHG cut-off frequency. (d) The generation of attosecond PINEM-HHG laser pulse trains in the XUV/SXR region.

CONCLUSION

We would realize our ambitious PINEM-HHG lasing scheme in two steps. The first goal is to generate both a phase-coherent attosecond electron pulse train and an attosecond XUV/SXR light pulse and correlate them with each other. Since both the electron and light pulses stem from a simultaneous interaction process at the nanotip array radiator, the electrons and photons are coherently phase-correlated and spectrally entangled at the quantum-mechanical level. As a result, the free electron and laser pulses can be used as a promising tool of attosecond pump-probe experiments further to explore ultrafast and subatomic electron dynamics in condensed matters. The second goal is to produce the attosecond laser as the next generation of state-of-the-art sources, which can trigger further applications of nonlinear X-ray optics and strong-field plasma physics.

REFERENCES

[1] P. B. Corkum, "Plasma perspective on strong field multiphoton ionization," *Phys. Rev. Lett.*, vol. 71, pp.1994-1997, 1994. doi:10.1103/PhysRevLett.71.1994

[2] P. M. Paul *et al.*, "Observation of a train of attosecond pulses from high harmonic generation," *Science*, vol. 292, pp. 1689-1692, 2001. doi:10.1126/science.105941

[3] S. Ghimire, A. D. DiChiara, E. Sistrunk, P. Agostini, L. F. DiMauro, and D. A. Reis, "Observation of high-order harmonic generation in a bulk crystal," *Nat. Phys.*, vol. 7, pp. 138-141, 2011. doi:10.1038/nphys1847

[4] J. Madey, "Stimulated emission of bremsstrahlung in a periodic magnetic field," *J. Appl. Phys.*, vol. 42, pp. 1906–1913, 1971. doi:10.1063/1.1660466

[5] P. Emma *et al.*, "First lasing and operation of an ångstrom-wavelength free-electron laser," *Nat. Photonics*, vol. 4, pp. 641-647, 2010. doi:10.1038/nphoton.2010.176

[6] B. Barwick, D. J. Flannigan, and A. H. Zewail, " Photon-induced near-field electron microscopy," *Nature*, vol. 462, pp. 902-906, 2009. doi:10.1038/nature08662

[7] A., Feist, K. E. Echternkamp, J. Schauss, S. V. Yalunin, S. Schäfer, and C. Ropers, "Quantum coherent optical phase modulation in an ultrafast transmission electron microscope," *Nature*, vol. 521, pp. 200-203, 2015. doi:10.1038/nature14463

[8] R. Dahan *et al.*, "Resonant phase-matching between a light wave and a free-electron wavefunction," *Nat. Phys.*, vol. 16, pp. 1123-1131, 2020. doi:10.1038/s41567-020-01042-w

[9] A. Mustonen, P. Beaud, E. Kirk, T. Feurer, and S. Tsujino, " Five picocoulomb electron bunch generation by ultrafast laser-induced field emission from metallic nanotip arrays," *Appl. Phys. Lett.*, vol: 99, p. 103504, 2011. doi:10.1063/1.3631634

[10] R. Bormann, M. Gulde, A. Weismann, S. V. Yalunin, and C. Ropers, "Tip-enhanced strong-field photoemission," *Phys. Rev. Lett.*, vol. 105, p. 147601, 2010. doi: 10.1103/PhysRevLett.105.147601

[11] K. E. Priebe *et al.*, "Attosecond electron pulse trains and quantum state reconstruction in ultrafast transmission electron microscopy," *Nat. Photonics*, vol. 11, pp. 793-797, 2017. doi:10.1038/s41566-017-0045-8

[12] S. Huang *et al.*, "Generating single-spike hard x-ray pulses with nonlinear bunch compression in free-electron lasers," *Phys. Rev. Lett.*, vol. 119, p. 154801, 2017. doi:10.1103/PhysRevLett.119.154801

[13] Y. Pan, and A. Gover, "Spontaneous and stimulated radiative emission of modulated free-electron quantum wavepackets—semiclassical analysis," *J. Phys. Commun.*, vol. 2, p. 115026, 2018. doi:10.1088/2399-6528/aae2ec

ISBN: 978-3-95450-220-2 ISSN: 2673-5474 doi: 10.18429/JACoW-FEL2022-TUP25

FREE ELECTRON LASER SEEDED BY BETATRON RADIATION

A. Ghigo, M. Galletti, V. Shpakov, INFN-LNF, Frascati, Italy
A. Curcio, CLPU, Villamayor, Salamanca, Spain
V. Petrillo[1], Milan University, Milano, Italy
[1]also at INFN-Mi, Milano, Italy

Abstract

In this paper the use of betatron radiation as a seed for the Free Electron Laser (FEL) is presented. The scheme shown can be adopted from all FEL driven by plasma accelerated electron beams via Particle or Laser Wake Field Acceleration. Intense radiation in the region of X ray characterized by a broad spectrum, the betatron radiation, is indeed produced in the plasma acceleration process from the electron passing through the ionized gas. It is proposed to use this radiation, suitably selected in wavelength and properly synchronized, to stimulate the emission of the Free Electron Laser.

INTRODUCTION

The possibility of using a plasma accelerated electron beam to generate Free Electron Laser (FEL) radiation has recently been proven [1]. The European EuPRAXIA project aims to develop FEL facilities using laser wake field acceleration and particle wake field acceleration (PWFA) techniques. In particular, in the INFN Frascati Laboratories, the headquarters of the EuPRAXIA project, an infrastructure will be built that will use the PWFA to generate FEL radiation in X-rays region [2]. The electron beam produced by a low emittance injector is accelerated by an X-band linac and a plasma acceleration section. Due to the intense transverse forces generated in the plasma wave, the electrons of the bunch oscillate emitting the so called betatron radiation. The radiation is emitted in a wide bandwidth in the X ray region and the basic idea is to select a narrow portion of the betatron radiation spectrum with a monochromator and to send this radiation superimposed on the same electrons beam that generated it, towards the magnetic undulator, as shown in Fig.1 [3]. The betatron radiation acts as seed of the Free Electron Laser emission: in EuPRAXIA, if the selected photon energy is matched with undulator fundamental wavelength (4nm), the seeding scheme enhances the number of photons per pulse and improves the pulse-to-pulse temporal stability as happens in the self-seeding scheme [4]. To extend the FEL emission spectrum towards high frequencies, the gap of the undulator can be opened. However, in these conditions, the SASE gain is no longer sufficient to saturate with the parameters of the beam expected at the accelerator output and with the nominal undulator length. It can be shown that by injecting the selected betatron radiation at the highest frequency that the most open undulator would have, it is possible to considerably extend the range of frequencies in which the FEL can saturate.

EXPERIMENTAL SET-UP

In the particle wake field plasma acceleration, a high charge electron bunch, the *driver* bunch, generates the plasma shape, losing energy, while a following low charge bunch, the *witness* bunch, is accelerated. Before entering in the FEL undulator, at the plasma chamber exit, the *driver* and *witness* bunches are dispersed, due to the different energy, in a dispersive section composed by four dipole magnets in a chicane configuration. The deviation angle in the first chicane dipole is large enough to separate the witness from the driver bunch. A collimator, or beam scraper, can be placed to stop the driver bunch. The betatron radiation propagates straight into the vacuum chamber and, as soon as the electron beam is deflected from the straight path, the first optical element of the monochromator is installed.

The betatron radiation is selected in bandwidth and reflected back in the direction of the undulator overlapping the electrons that are leaving the chicane, in the first part of the undulator. Because of the very short electron bunch a perfect synchronization at the entrance of the undulator, at level of tens of femtosecond, is needed. The electron and photon beams started automatically synchronized because generated from the same electron beam. The trajectory length of the photons in the monochromator must compensate the path of the electrons that pass through the magnetic chicane and the delay of the electron, that travel with relativistic factor γ=2000, respect to the photon arrival time.

BETATRON RADIATION

Betatron radiation is the radiation emitted by electrons accelerated in plasma channels. Betatron radiation is emitted forward, and it is due to the betatron oscillations driven by the focusing fields inside the plasma bucket. Due to the very short scale of the betatron oscillations period (typically from mm down to microns, depending on the background electron plasma density), the typical energy of the photons emitted via betatron radiation falls in the X-rays.

Theoretical Introduction

If the scale of the electron energy gain is much longer than the betatron period, it can be assumed that the acceleration occurs adiabatically compared to the betatron dynamics. This allows using the following formula for the energy irradiated I by a single electron per unit photon energy E and

ISBN: 978-3-95450-220-2 ISSN: 2673-5474 doi: 10.18429/JACoW-FEL2022-TUP25

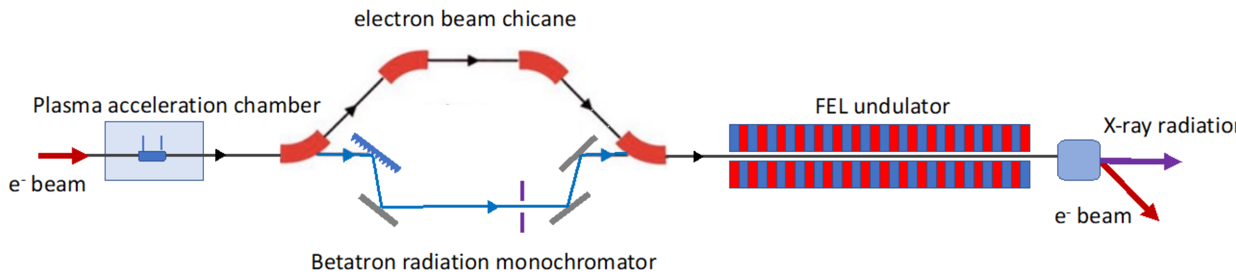

Figure 1: Betatron radiation seeding FEL scheme.

solid angle of observation Ω:

$$\left.\frac{d^2I}{dEd\Omega}\right|_{single} = \int \frac{dz}{L_{acc}} \sum_n \frac{\alpha N_\beta \gamma^2(z) E R_n}{2\hbar\omega_\beta} [C_r^2 + C_z^2\theta^2 - 2C_rC_z\theta\cos\varphi] \quad (1)$$

where α is the fine structure constant, $N_\beta = \omega_\beta L_{acc}/c$ is the number of betatron oscillations over the acceleration length L_{acc} (z is the acceleration axis here), c is the speed of light in vacuum, $\gamma(z)$ is the Lorentz factor of the emitting electron, $\omega_\beta = \omega_p/\sqrt{2\gamma(z)}$ is the betatron frequency related to the plasma frequency $\omega_p = \sqrt{n_e e^2/\varepsilon_0 m_e}$, where n_e is the background electron plasma density, m_e is the electron mass, e is the elementary charge and ε_0 is the vacuum dielectric constant. The summation in Eq. (1) runs over n, the harmonic numbers of the resonance function R_n. Indeed, the plasma channel acts similarly as a wiggler device, therefore lines emission should be in principle expected. In reality, we shall see that being the harmonic frequency related to the betatron amplitude, the finite size of the beam is responsible for spectral broadening. Moreover, in Eq. (1) we have defined:

$$C_r = r_\beta k_\beta \sum_m J_m(\rho_z)[J_{n+2m-1}(\rho_r) + J_{n+2m+1}(\rho_r)] \quad (2)$$

$$C_z = \sum_m 2J_m(\rho_z) J_{n+2m}(\rho_r) \quad (3)$$

$$\rho_z = \frac{E r_\beta^2 k_\beta^2}{8\hbar\omega_\beta} \quad (4)$$

$$\rho_r = \frac{E r_\beta k_\beta \theta \cos\varphi}{\hbar\omega_\beta} \quad (5)$$

$$R_n = sinc^2\left[\frac{\pi N_\beta}{2\gamma^2(z)\hbar\omega_\beta}\left(E - \frac{2n\gamma^2(z)\hbar\omega_\beta}{1+\frac{K_\beta^2}{2}+\gamma^2(z)\theta^2}\right)\right] \quad (6)$$

where r_β is the betatron amplitude, $K_\beta = \gamma(z) r_\beta k_\beta$ is the undulator parameter of the plasma wiggler and $k_\beta = \omega_\beta/c$. Concluding the present section, we introduce the final formula for the calculation of the spectral-angular distribution of the betatron radiation that includes the distribution of the betatron oscillation amplitudes.

Indeed, each electron oscillates with a different amplitude r_β, according to the position within the beam that it had at the entrance of the plasma channel. Given a radial profile of the beam $P(r_\beta)$ (we assume radial symmetry here), the betatron radiation formula becomes:

$$\left.\frac{d^2I}{dEd\Omega}\right|_{beam} = \frac{Q}{e}\int_0^\infty dr_\beta\, r_\beta\, P(r_\beta) \left.\frac{d^2I}{dEd\Omega}\right|_{single} \quad (7)$$

Betatron Radiation from the Witness Bunch

The target parameters of the witness bunch in Eupraxia are resumed in the table below.

Table 1: Witness Bunch Electron Beam Parameters

	In	**Out**
Charge	30 pC	30 pC
Beam size (transverse, rms)	2 μm	2 μm
Beam size (longitudinal, rms)	7 μm	7 μm
Normalized rms emittance	0.6 mm mrad	0.6 mm mrad
Relative energy spread, rms)	0.05 %	0.05 %
Peak current	1.8 kA	1.8 kA
Beam energy (mean)	500 MeV	1 GeV

For the simulation of the radiated betatron spectrum we have assumed a linear energy gain, i.e. γ(z) is a linear function of z, with initial value ~ 1000 at z = 0 and final value ~ 2000 at z = 0.4 m = L_{acc}. Furthermore, we consider a gaussian beam and the background electron plasma density is $n_e = 3 \times 10^{16}$ cm^{-3}. The result of the simulation based on Eq. (7) and on the data reported in table above is shown in Fig. 1.

From Fig. 2 it is possible to infer the number of emitted photons, after integration over E. In particular, the number of photons emitted at 620 eV (2 nm), within a bandwidth of 10 %, is 8.9×10^6, while the number of photons emitted at 310 eV (4 nm) within a bandwidth of 10 %, is 1.4×10^7. Reducing the bandwidth to 1%, we get 1.4×10^6 at 4 nm and 8.9×10^5at 2 nm.

SEEDED FEL SIMULATIONS

The betatron radiation has been used as seed for the FEL emission generated by the witness electron beam. The undulator is the EuPRAXIA high-energy line AQUA [5], with

ISBN: 978-3-95450-220-2 ISSN: 2673-5474 doi: 10.18429/JACoW-FEL2022-TUP25

10 modules with period $\lambda_w = 1.8$ cm for a total length of about 25 m. The initial longitudinal power distribution of the seed has been prepared with random spikes and random phase structure so as to mimic the incoherent structure of the betatron pulse. The witness beam has been matched to the undulator with transverse dimensions $\sigma_x = 69$ µm and $\sigma_y = 44$ µm. The SASE simulation, made with GENESIS 1.3 [6] at 4 nm (Fig. 3, blue curve) shows that the radiation in 25 m is still in the exponential stage, achieving at the undulator end 5.3 µJ of energy, corresponding to 10^{11} photons /shot. Starting with the seed, instead, allows the radiation to reach saturation within 20-22 m, arriving to an energy of 20 µJ, corresponding to $4{\cdot}10^{11}$ photons/shot (red curves). The stability of the pulse is moreover increased.

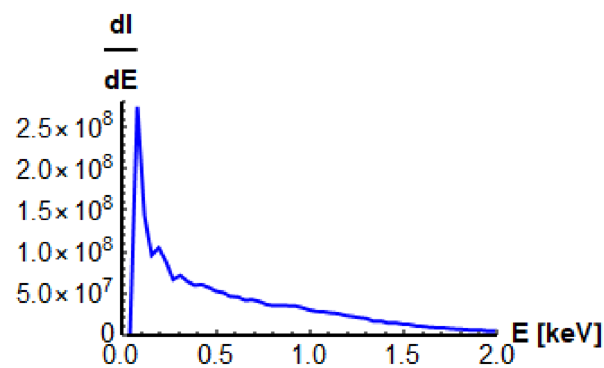

Figure 2: Simulated betatron radiation spectrum emitted by the Eupraxia witness bunch.

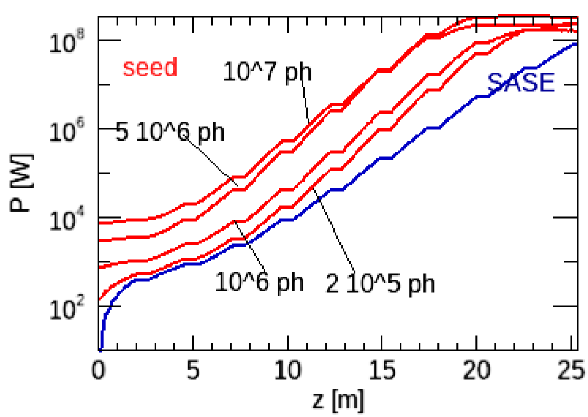

Figure 3: Growth of the FEL radiation at 4 nm along z(m) for the SASE case (blue curve) and various seed values (red curves).

At 3.2 nm (see Fig. 4), the use of the betatron radiation as a seed appears even more advantageous, provided to seed the FEL with at least 2/3 10^6 photons. In this case, in fact, the SASE provides 3 10^9 photons, vs 10^{11} of the seeded operation. Table 2 summarizes the data.

CONCLUSION

The betatron radiation, produced during plasma acceleration by transversely oscillating electrons, can be efficiently used as seeding for FEL.

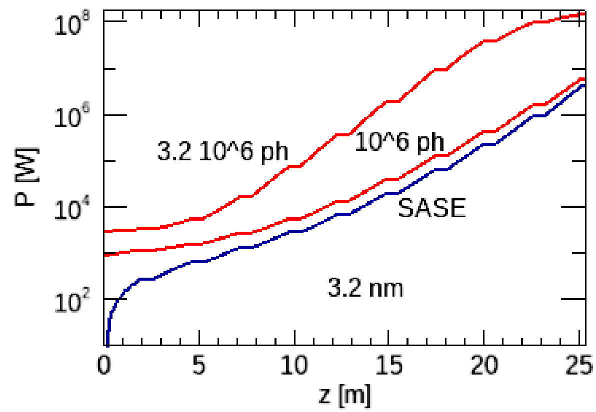

Figure 4: Growth of the FEL radiation at 3.2 nm along z(m) for the SASE case (blue curve) and various seed values (red curves).

Table 2: Summary of FEL Radiation Photon Number and Bandwidth at 4 and 3.2 nm for Different Seed Energies.

λ_{rad}	N_{seed} ph.	N_{rad} ph.	BW
4 nm	0	10^{11}	0.08%
4 nm	10^6	$3{\cdot}10^{11}$	0.12 %
4 nm	5·106	$4{\cdot}10^{11}$	0.12%
3.2 nm	0	$3{\cdot}10^9$	0.1%
3.2 nm	10^6	$5{\cdot}10^9$	0.09%
3.2 nm	$2{\cdot}10^6$	10^{11}	0.09%

The scheme has been proved to be adoptable, from all FEL driven by plasma accelerated electron beams via Particle or Laser Wake Field Acceleration, suitably selecting the suitable wavelength with a proper synchronization, to stimulate the emission of the Free Electron Laser. Among next steps, we will consider the betatron radiation produced by the driver bunch which carries much higher charge and a different spectrum due to the energy. Moreover, the betatron field propagation with the self-consistent phase input for the FEL simulations will be optimized. A more accurate simulation campaign accounting for 3D effects in betatron radiation emission, especially the impact on the final photon number, is envisioned. Finally, having the betatron source optimized, simulations on the betatron radiation stimulating the emission on the higher harmonics will be carried out.

REFERENCES

[1] R. Pompili *et al.*, "Free-electron lasing with compact beam-driven plasma wakefield accelerator", *Nature*, vol. 605, pp. 659–662, 2022. doi: 10.1038/s41586-022-04589-1

[2] M. Ferrario *et al.*, "EUPRAXIA@SPARC_LAB design study towards a compact FEL facility at LNF", *Nucl. Instrum. Methods Phys. Res., Sect. A*, vol. 909, pp. 134–138, 2018. doi:10.1016/j.nima.2018.01.094

ISBN: 978-3-95450-220-2 ISSN: 2673-5474 doi: 10.18429/JACoW-FEL2022-TUP25

[3] A. Ghigo, "Free Electron Laser Seeded by Betatron Radiation", *ACC DIV-01-2022,* 2022.

[4] D. Ratner *et al.,* "Experimental Demonstration of a Soft X-Ray Self-seeded Free-electron Laser", *Phys. Rev. Lett.,* vol. 114, p. 054801, 2015. doi: 10.1103/PhysRevLett.114.054801

[5] F. Nguyen *et al.,* "Design of the Superconducting undulator for EuPRAXIA@SPARC_LAB", presented at the FEL2022, Trieste, Italy, Aug. 2022, paper WEP39, this conference.

[6] S. Reiche, "GENESIS 1.3: a fully 3D time-dependent FEL simulation code", *Nucl. Instrum. Methods Phys. Res., Sect. A,* vol. 429, pp.243-248, 1999. doi:10.1016/S0168-9002(99)00114-X

ISBN: 978-3-95450-220-2 ISSN: 2673-5474 doi: 10.18429/JACoW-FEL2022-TUP26

SPECTRAL CONTROL OF THz SUPER-RADIANT SPONTANEOUS UNDULATOR RADIATION DRIVEN BY ULTRASHORT ELECTRON BEAM WITH ENERGY SPREAD

S.Y. Teng, S.H. Chen, Department of Physics, NCU, Taoyuan, Taiwan
W.Y. Chiang, M.C. Chou, H.P. Hsueh, W.K. Lau, A.P. Lee, NSRRC, Hsinchu, Taiwan
P.T. Lin, Department of Engineering and System Science, NTHU, Hsinchu, Taiwan

Abstract

Intense coherent THz radiation has been generated from an 18-period, hybrid-type U100 planar undulator as it is driven by short relativistic electron pulses produced from the NSRRC photoinjector. However, it is observed that the number of output optical pulse cycles is much less than the number of undulator periods and therefore the radiation spectral bandwidth has been broadened. It is found that the dispersion of undulator with excessive energy spread is responsible for this undesired broadening of THz radiation spectrum. In this study, instead of using rectilinear rf bunch compression (i.e. velocity bunching) in photoinjector linac, we investigate the feasibility of using nonlinear magnetic bunch compression for spectral bandwidth control of coherent THz undulator radiation.

INTRODUCTION

THz radiation is a promising tool for scientific research in a variety fields such as semiconductor, quantum material and biology imaging etc. A linac-based tunable narrow-band THz radiation source has been constructed for novel light source development as well as user applications in NSRRC. It is a superradiant THz FEL facility with a photoinjector linac system providing sub-picosecond few tens MeV electron beam using the so-called velocity bunching technique. Superradiant THz spontaneous undulator radiation (THz SSUR) is then generated from a gap tunable planar undulator as the sub-picosecond beam passing through the device. Velocity bunching is a convenient way and cost effective way to produce ultrashort bunches from photoinjector. However, beam energy spread and the orientation of electron distribution in longitudinal phase space cannot be controlled easily especially when beam energy is not a free parameter and is determined by the resonant condition of undulator radiation. As a result, bunch lengthening of electron beam with excessive energy spread due to undulator dispersion leads to a decrease of output radiation amplitude with time. In this study, we investigate the possibility of using nonlinear dog-leg compressor for manipulation of electron distribution in longitudinal phase space in order to control emission spectrum of the superradiant undulator radiation.

The experimental setup and results of NSRRC THz SSUR source are described and summarized in the next section. Simulation results of photoinjector using ASTRA [1] and the electron beam manipulation through the dog-leg bunch compressor via ELEGANT [2] under different compression ratios are discussed in the third section. In section 4, we describe the results of a self-developed algorithm in which particle motions in the undulator are tracked and the emission profile and spectra are calculated. Conclusions and the direction for future study are discussed in the last section.

EXISTING NSRRC THZ FEL

Schematic layout of the NSRRC THz FEL facility is shown in Fig.1. Currently, an electron beam of maximum kinetic energy up to 62 MeV and a bunch charge of 460 pC are available from the photoinjector system. The electron bunches can be tightly compressed via velocity bunching during rf acceleration when the linac is operated near zero crossing phase. A wrap-around solenoid magnet is installed at the first 2 meters of the 5.2-m booster rf linac to assist beam focusing. In previous experimental study [1], an ultrashort beam of 490 fs bunch duration has been obtained and ~20 μJ super-radiant THz undulator radiation at 0.6 THz is produced from an 18-periods, U100 planar undulator.

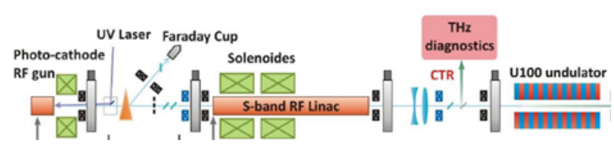

Figure 1: Schematics of the NSRRC THz FEL.

Interferogram of the THz output signal as detected by the Golay cell in auto-correlation measurement shows that the undulator radiation power reduce dramatically with time (Fig. 2). The main reason of this time-dependent power reduction is due to a significant reduction of beam bunching factor when the ultrashort beam with much energy spread traveling along an undulator which has inherent dispersion. In other words, while we are expecting a radiation bandwidth of $1/N_u$ in ideal situation, the coherent radiation power is broadened significantly to ~15%.

ISBN: 978-3-95450-220-2 ISSN: 2673-5474 doi: 10.18429/JACoW-FEL2022-TUP26

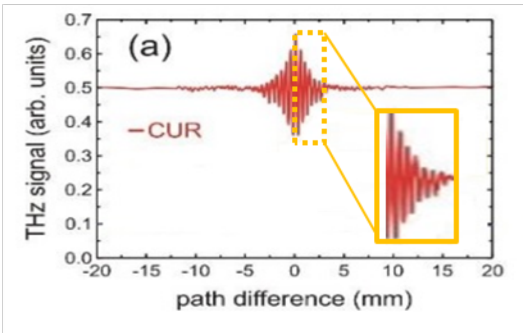

Figure 2: Interferogram of THz signal as detected by the interferometer [3].

MAGNETIC BUNCH COMPRESSION

In order to reduce such spectral broadening due to beam energy spread and undulator dispersion, instead of velocity bunching, we considered to use magnetic bunch compression scheme in which correlated beam energy spread is independently controllable by the accelerating voltage of the chirper linac. We also considered to use dogleg bunch compressor with nonlinear optical element to remove 2[nd]-order beam energy chirp which cannot be done by simple 4-dipole chicane without harmonic rf linac.

Dog-Leg Bunch Compressor

In a future machine upgrade plan (Fig.3), a double dogleg bunch compressor has been designed to perform bunch compression other than velocity bunching. We choose to operate 3-m long chirper linac at zero crossing phase such that there is no beam energy gain from the linac. Resonant beam energy is therefore determined solely by the operational energy of the photoinjector and independent of the maximum energy gain of the chirper linac. Further, the photoinjector can be optimized for high beam brightness. In this case study, the photoinjector beam energy is set at 30 MeV and maximum energy gain of chirper linac is set at about 10 MeV to produce about 3% correlated beam energy spread.

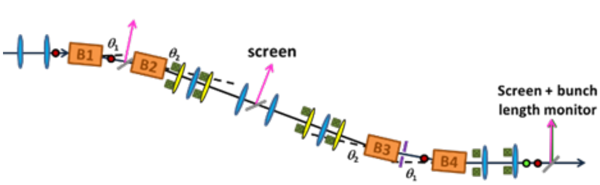

Figure 3: Layout of the double dogleg bunch compressor for the simulation of NSRRC THz FEL linac system.

First order longitudinal dispersion function (i.e. R_{56}) are adjustable by tuning the longitudinal position of dipoles with proper orbit steering [4]. This allow us the to adjust orientation of electron distribution in longitudinal phase space for either over or under compression to fulfil our needs.

Compressed Beam

In this study, the electron beam starting from the photocathode gun is tracked by ASTRA until the injector exit. Output beam data obtained from ASTRA is then transferred to ELEGANT for different bunch compression conditions. Injection beam energy to the dogleg compressor is set at 30 MeV. Photoinjector parameters are optimized to provide a beam with transverse beam emittance less than 2 π·mm-mrad and energy spread less than 160 keV. Chirper linac phase is set at -90° for 10 MeV maximum energy gain to provide ~3% correlated energy spread. Three compression conditions are chosen for comparative study. Namely, the optimal compression case where compression ratio is very large, under compression case with compression ratio of about 20 and over compression case with compression ratio of about 30. Compressed bunch length is about 140 fs in the optimal compression case (i.e. an up-stood beam in longitudinal phase space). Figure 4 shows the orientation of electron distributions in longitudinal phase space for these three different cases.

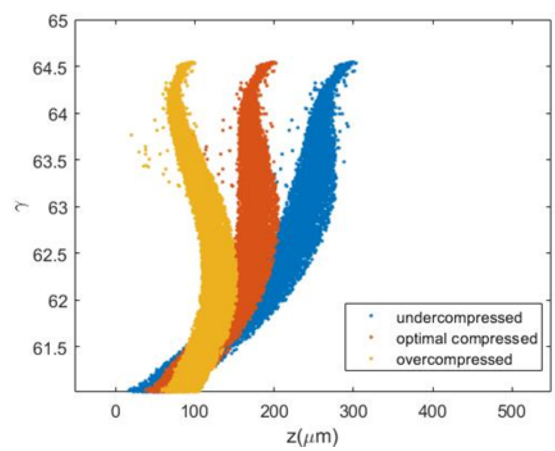

Figure 4: Electron distributions under three different bunch compression conditions: (1) the optimal compression case where compression ratio is very large (red dots), (2) under compression case with compression ratio of about 20 (blue dots) and (3) over compression case with compression ratio of about 30 (yellow dots). Compressed bunch length is about 140 fs in the optimal compression case (i.e. an up-stood beam in longitudinal phase space).

CALCULATION OF SSUR SPECTRA

Multi-particle dynamics in the superradiant THz FEL is simulated by a 3D particle tracking algorithm [5]. Radiation power at any instance are calculated by summing up all Liénard-Wiechart fields from all individual particles at a retarded time. Electron motions in the undulator are tracked by integrating the Lorentz force equation based on the 4[th]-order Runge-Kutta method. Space charge effect is neglected in the simulation by assumption. Radiation power is calculated from Liénard-Weichert potential in a

ISBN: 978-3-95450-220-2 ISSN: 2673-5474 doi: 10.18429/JACoW-FEL2022-TUP26

straightforward manner. This allows us to study evolution of radiation emission in time domain.

Time-Domain Simulation Results

We perform the simulation by importing the electron distributions shown in Fig. 4 into the 3D tracking algorithm for the three cases of bunch compression. Calculation results radiation from U100 undulator are shown in Fig.5. In Fig. 5, the orange line shows the evolution of radiation in case of an optimal compressed beam. This temporal dependence of radiation field is in good agreement with observed signal from interferogram in previous experiment. The radiation power is largest when the beam just entered the undulator. However, due to dispersion of U100, there is a significant decrease in radiation power as the bunch length gets longer when the beam travels along the undulator. For an over-compressed beam, yellow line in Fig.5, the radiation power starts at a lower value and gradually increased to a certain peak and decreases at about the same rate as the optimal compression case. This can be explained by a less severe bunch lengthening in the over-compressed case (see Fig.6).

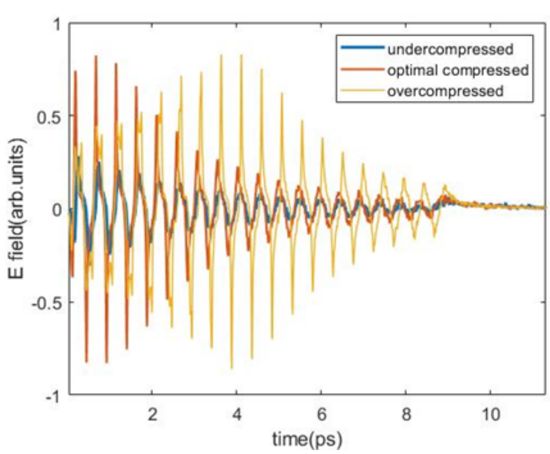

Figure 5: Time domain electric field profile under different condition.

Figure 6 depicts the bunch length evolution along the undulator for the three cases. The bunch lengthening in simulation have similar trends under different conditions except that the beams start at different values. Nevertheless, it is worth noting that the orientation of electron phase space can reduce the effects of dispersion, which gives us a grow profile in yellow line. Thus, the results give a hint that the bunch length have a great impact on super-radiant undulator emission process.

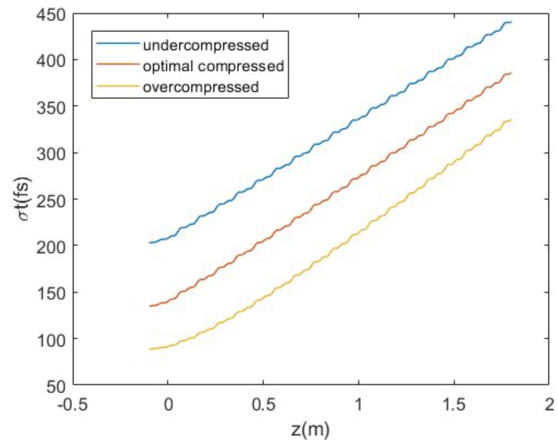

Figure 6: Bunch length evolution in the undulator for the three bunch compression conditions as shown in Fig. 4.

Radiation Spectrum

Fourier transform of the calculated time-dependent fields gives us the spectrum of each condition in Fig. 7. FWHM spectral bandwidth can be deduced from the spectra. They are 7.38%, 8.14% and 8.47% for the over-compressed, optimal and under-compressed cases respectively. The radiation spectrum of the over-compressed beam reveals that slight reduction of radiation bandwidth is possible.

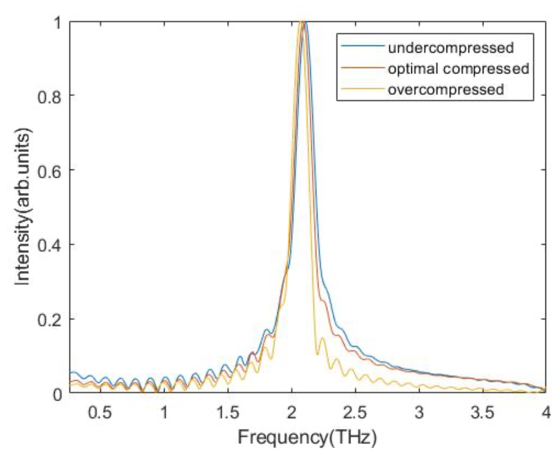

Figure 7: Radiation spectra under different bunch compression conditions.

CONCLUSION

In this simulation study, we obtained a distribution of ~1000 A, 100 fs compressed electron beam from ASTRA/ELEGANT simulation and transfer the output data to simulate electron motion in undulator and get the emitted radiation. Simulation results shows that adequate over compressed beam can help to improve the undulator dispersion effects. The radiation spectrum also pointed out that over compressed beam can reduce radiation bandwidth. Output radiation from three types of beam condition can be obtained at central frequency around 2.05 THz

ISBN: 978-3-95450-220-2 ISSN: 2673-5474 doi: 10.18429/JACoW-FEL2022-TUP26

which meets resonant condition. The properties of the drive beam from the high brightness linac system are by no means optimized. It has to be pointed out that the effect of space charge effect in the undulator is neglected. We believe that it is insignificant for such a relativistic electron beam.

The simulation results give us a direction to enhance the THz undulator source. Further, the effects of undulator and field errors have to be investigated for engineering design.

ACKNOWLEDGEMENTS

This work was supported by the Ministry of Science and Technology (MOST), Taiwan, under Grant numbers of MOST-109-2112-M-213-013, MOST-110-2112-M-213-018, MOST -110-2112-M-008-022.

REFERENCES

[1] K. Flöttmann, ASTRA user manual, 2017 `https://www.desy.de/~mpyflo/Astra_manual/Astra-Manual_V3.2.pdf`

[2] M. Borland, "ELEGANT: A flexible SDDS-compliant code for accelerator simulation", *United States: N. p.,* 2000. `doi:10.2172/761286`

[3] M. C. Chou *et al.*, "Experimental Study of Coherent THz Sources Driven by the NSRRC High Brightness Photo-injector", in *Proc. IPAC'18,* Vancouver, Canada, Apr.-May 2018, pp. 4332-4335. `doi:10.18429/JACoW-IPAC2018-THPMK017`

[4] W. K. Lau, M. C. Chou, N. Y. Huang, A. P. Lee, and J. Wu, "Design of a Dogleg Bunch Compressor with Tunable First-Order Longitudinal Dispersion", in *Proc. FEL'17*, Santa Fe, NM, USA, Aug. 2017, pp. 309-312. `doi:10.18429/JACoW-FEL2017-TUP031`

[5] V. Joshi and S. Ghosh, "Multiparticle time-domain analysis of coherent undulator radiation", *Phys. Rev. Accel. Beams*, vol. 22, p. 020702, 2019. `doi:10.1103/PhysRevAccelBeams.22.020702/`

ISBN: 978-3-95450-220-2 ISSN: 2673-5474 doi: 10.18429/JACoW-FEL2022-TUP32

FACILITY CONCEPT OUTLINES FOR A UK XFEL

D. J. Dunning†, J. A. Clarke, L. S. Cowie, N. R. Thompson, P. H. Williams, ASTeC, STFC Daresbury Laboratory and the Cockcroft Institute, Warrington, UK,
J. L. Collier, J. S. Green, Central Laser Facility, STFC Rutherford Appleton Laboratory, Didcot, UK
J. P. Marangos, Department of Physics, Imperial College London, Blackett Lab, London, UK

Abstract

In early 2019, the UK initiated a project to develop the science case for a UK XFEL, featuring a diverse team of UK scientists and international advisors. Accelerator scientists were engaged to highlight potential future accelerator developments and to develop concept outlines for a facility design meeting the requirements for world-leading capabilities. The UK XFEL Science Case, featuring the concept outlines, was published in late 2020. Subsequent exercises further demonstrated the support of the UK community and the project is soon to enter a more detailed design phase. The concept outlines are reviewed and next steps outlined.

INTRODUCTION

This paper describes the development of facility concept outlines as part of the Science Case for a UK XFEL, which was published in 2020 [1]. The first section outlines the requirements from each of the different science areas, while the second collates them and describes how they impact key technology choices. The third section sets out concept outlines to meet the requirements. The final section outlines next steps for the project, which is funded for a 3-year conceptual design and options analysis phase starting soon.

REQUIREMENTS BY SCIENCE AREA

Each of the Science Case areas set out visions for world leading science, with requirements summarised below, including for photon energy and repetition rate in Fig. 1.

Physics and X-ray Photonics

The key requirements are attosecond pulses (~100 as) across a broad range of photon energies, from 200 eV to hard X-ray, with sub-femtosecond synchronisation to optical lasers. Combination with electrons and other FEL pulses is also of interest. Control of pulse properties, such as polarisation, and through seeding are also highlighted. High repetition rates (> 10 kHz) are strongly preferred as in many examples the anticipated signals are weak and much data must be taken for high fidelity measurements.

Matter in Extreme Conditions

The main requirements are X-ray pulses with high pulse energy (mJ to orders of magnitude higher) and high photon energy (up to 30 – 50 keV), in combination with very high-energy optical lasers. Rep. rate is generally less demanding, due to being relatively low in the high energy lasers that compress the material. However higher rates could be beneficial where the X-ray beam is used to isochroically heat samples. Narrow bandwidth (~10 meV), two-colour capability and sub-μm spot sizes are also called for.

Quantum and Nanomaterials

The key requirements of this science area are soft to very hard X-rays (up to ~50 keV would open up new opportunities), in combination with pump sources across a broad range of wavelengths (THz to visible), as well as two-colour FEL capability. Sub-femtosecond synchronisation is important in all cases. Repetition rate can be as low as 10 Hz in some experiments, due to sample recovery times, but high average flux is needed in others.

Chemical Sciences and Energy

An important requirement is to combine XFEL pulses with a multitude of different sources: accelerator-based THz, electron beam pump sources, along with numerous synchronized laser-based sources. The X-rays should be soft to very hard (> 25 keV for some experiments) and high repetition rate (1 kHz to 1 MHz). For some experiments, a relative bandwidth below 1×10^{-4} is needed. Two-colour FEL operation is also important, with the possibility of delivering various combinations of soft and hard X-rays.

Life Sciences

This area calls for hard X-rays (5 – 25 keV) at rep. rates from 1 kHz to potentially 1 MHz, depending on detector capabilities. Some applications require precise control of the X-ray pulse properties: stability of pulse energy, carrier frequency, instantaneous bandwidth and spectrum. Hard X-ray pulses with up to 4% bandwidth, demonstrated at SwissFEL [2], are of interest. Two-colour FEL operation with large variation in temporal (fs – μs) and energy separation is important, as well as combination with electrons.

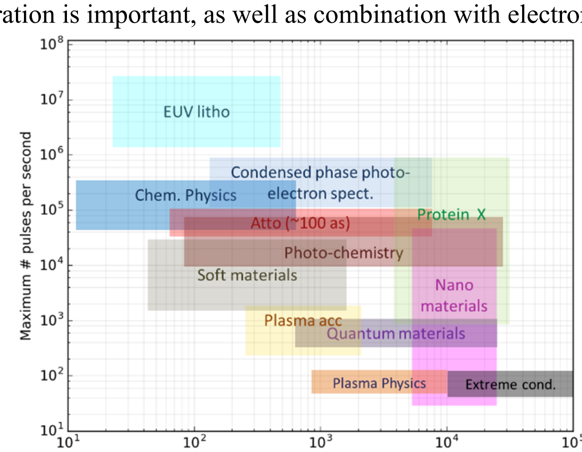

Figure 1: Requirements of different areas of the science case in terms of photon energy and repetition rate.

† david.dunning@stfc.ac.uk

ISBN: 978-3-95450-220-2 ISSN: 2673-5474 doi: 10.18429/JACoW-FEL2022-TUP32

KEY X-RAY REQUIREMENTS AND UNIQUE FACILITY CAPABILITY

This section describes the outcome of collating the requirements across the different science areas to produce a set of key facility capabilities. These are discussed together with the potential accelerator technology and techniques required to deliver unique and world-leading capability.

Soft and Hard X-rays at up to MHz Repetition Rate

The photon energy requirements of the Science Case are predominantly focused on hard and soft X-rays – from approximately 200 eV to 25 keV – as shown in Fig. 1. There is a clear call from the soft x-ray science in particular for high repetition rates (10 kHz to 1 MHz), requiring superconducting accelerator technology to be deployed up to an electron beam energy of at least 2 GeV, as described below (Concept outlines 1 and 2).

To provide hard X-rays up to 25 keV requires electron beam energy up to approximately 7 GeV, assuming reasonably ambitious short period undulators (e.g. superconducting) to allow access to higher photon energies for a given electron beam energy. The repetition rate requirements for hard X-rays cover a wider range from around 100 Hz to 1 MHz. Therefore a fully superconducting accelerator is required to meet all the requirements (Concept outline 1) but a normal conducting accelerator providing up to 1 – 5 kHz repetition rate could meet a large subset of the science (Concept outline 2). Further R&D is required to deliver normal conducting technology with this performance, but it can be anticipated to be possible as part of the baseline design. Superconducting accelerator technology for MHz operation is suitably mature, with two such XFEL facilities already under construction (LCLS-II [3] and SHINE).

Very Hard X-rays with High Pulse Energy (at Lower Repetition Rate)

There is significant interest in photon energies above the current state of the art (25 keV), up to approximately 50 keV, with an associated desire in some cases for very high pulse energy (mJ to orders of magnitude higher). While delivering the requisite photon energies is technically challenging, it is entirely feasible for day one of UK XFEL – the focus would be to determine the most cost-effective route.

The key factors for increasing FEL photon energy are increasing the energy of the electron beam, utilising novel undulator technologies (e.g. superconducting) with reduced undulator period, and improving electron beam quality through ultra-low emittance photo-injectors. A combination of these factors could deliver suitable performance with electron beam energy around 10 GeV, i.e. higher than a machine to deliver sub-25 keV photon energy and moderate pulse energy but substantially lower than European XFEL (17.5 GeV) [4], while being competitive. Advanced techniques to increase pulse energy via improved efficiency should also be pursued.

In general, the specification for very hard x-rays is in science areas requiring lower repetition rate (10 – 100 Hz), as shown in Fig. 1, due to sample recovery time, and auxiliary source limitations. The hybrid accelerator option, Concept outline 2, could potentially trade off repetition rate to increase electron beam energy, and so excel for these science areas. Very advanced concepts such as plasma acceleration are not yet considered to be mature enough to be on the critical path but could potentially be part of an upgrade route.

Reproducibility, High Spectral Purity and Control of Other Pulse Properties

A clear requirement from multiple areas of the Science Case is for greater control of the X-ray pulse properties over the full range of photon energies and repetition rates. This would add a plethora of advantages for the science – from the conceptually simple but critical advantage of shot-to-shot reproducibility, to a host of advanced features in the pulse properties. Seeding can greatly improve the coherence properties and stability of the output. The present state-of-the-art facility for seeding is the FERMI facility [5] in Italy, which has demonstrated the technique up to approximately 400 eV at 50 Hz. A UK XFEL could be confidently expected to provide seeded output with repetition rate orders of magnitude higher at the outset. Furthermore, seeding may be extended to higher photon energies (> 1 keV), for example using the latest non-linear optical laser technology, thereby spanning an important range of critical absorption edges in carbon, nitrogen, oxygen and metals.

Laser seeding to substantially higher than 1 keV is anticipated to require long-term development, however in the shorter term, greater control of the pulse properties at hard X-ray is likely to come from methods such as High-Brightness SASE [6] for higher spectral purity; ongoing R&D into X-ray FEL Oscillators [7] and X-ray seed sources [8] will determine timescales for potential deployment in a UK XFEL. Several areas would also benefit from advanced control of other properties including polarisation, orbital angular momentum, energy chirp, and carrier-envelope phase.

Attosecond Pulses at All Photon Energies, Synchronised to External Sources

The ability to probe structural dynamics at timescales down to attoseconds is one of the defining features of the Science Case. Pulse durations down to approximately 100 as are required across a broad range of photon energies from 200 eV to hard X-ray, with sub-femtosecond synchronisation to optical lasers and other sources. The required pulse durations have recently been demonstrated at existing facilities (e.g. [9]) but there is opportunity to significantly enhance capabilities in terms of synchronisation and applicability across all photon energies. The use of external lasers to control the lasing portion of the electron beam would greatly improve synchronisation to external sources. Given UK strengths in the required technologies, it is fea-

ISBN: 978-3-95450-220-2 ISSN: 2673-5474 doi: 10.18429/JACoW-FEL2022-TUP32

sible for a UK XFEL to implement world-leading capabilities from day one and to further enhance these capabilities throughout the lifetime of the facility.

Multi-colour Modes and Combination Between Sources

Some of the most pressing requirements from the Science Case are for multi-colour FEL operation and combination of X-rays with external sources. The most frequently highlighted requirement of all was to combine X-rays with optical lasers: high repetition rate femtosecond optical pump sources from the deep UV through to far IR, as well as high energy (~100 PW) laser pump sources. THz sources, relativistic electron beams and high magnetic fields at interaction points were also frequently highlighted.

Two-colour or multi-colour FEL capabilities are required by many science areas. Several innovative methods have been developed to retrofit multi-colour FEL capability to existing XFELs [10, 11] – a new facility offers the opportunity to include these in an optimised way, with potentially unique capabilities including extending the range of energy/temporal separation.

High Power EUV / Gamma Source (Multi-MHz Repetition Rate)

Opportunities to develop symbiotically a high power EUV source for lithography and a high brightness γ source for use in nuclear applications were identified. These would benefit from higher repetition rates (up to approximately 100 MHz) but require relatively low electron beam energy (1 GeV). There is potential to incorporate these capabilities as described in the following section.

Other Facility Requirements

While the focus of this paper is on the accelerator capabilities, the Science Case describes the various other features required in a next-generation XFEL facility. More general facility requirements include advanced sample delivery and detectors, data infrastructure and management, user support infrastructure and emphasis on sustainability.

CONCEPT OUTLINES

The process of developing a conceptual facility design to meet the requirements set out above was beyond the scope of the Science Case phase. Nevertheless, three concept outlines were developed for the Science Case – two of which are described here. The third, a fully normal conducting accelerator, would be less well suited to meeting the repetition rate requirements.

Concept Outline 1: Superconducting Accelerator

Concept outline 1 is a high energy (~10 GeV) superconducting accelerator operating with MHz repetition rate, as shown in Fig. 2. By combining high energy and high repetition rate, it covers the full repetition rate-photon energy parameter space required by the science case. High electron energy and advanced (e.g. superconducting) undulators provide access to very high energy per pulse up to very hard x-ray. Fast kickers can be used to distribute bunches between different FEL lines, with the ability to deliver lower repetition rates where required. The linear (i.e. single-pass) layout shown in Fig. 2 would be broadly similar to LCLS-II HE and SHINE. A recirculating option could also be considered to reduce cost, though it would seem less suited to meet very hard X-ray FEL operation.

High repetition rate seeding would be incorporated to as high a photon energy as possible. Beyond this, other high spectral purity techniques would be used such as HB-SASE, and oscillator FELs including XFELO are an option due to MHz repetition rates. Techniques for attosecond pulses could be incorporated at all photon energies. End-stations would be equipped with the most advanced lasers, THz radiation sources and electron beams, for use in combination with the x-rays.

A feature under consideration for both Concept outlines 1 and 2 is to have a second photo-injector towards the end of the main linac. While it is not essential in this case, it offers the opportunity to provide lower energy electron beams to serve the soft and hard x-ray undulator lines independently – or in combination for multi-colour experiments with widely separated photon energies. Soft x-rays with high pulse energy could be generated from the 10 GeV beam if required. A second injector also provides the option of upgrading this region to even higher repetition rate by introducing an energy recovery linac, which could support a high average power EUV FEL and a high brightness gamma ray source.

Concept Outline 2: Hybrid Accelerator

Concept outline 2 is a high energy (~10 GeV) hybrid of two accelerator types as shown in Fig. 2. It features a ~2 GeV superconducting linac, operating to provide MHz repetition rate up to a few keV photon energy. This is coupled to an ~8 GeV advanced normal conducting linac, to provide kHz repetition rate for up to very hard x-ray photon energies.

Operating in this way provides a more targeted approach to covering the repetition rate-photon energy requirements of the science case, as shown in Fig. 2. While it cannot deliver MHz repetition rates at high energy as per Concept outline 1, the hybrid option would likely be more flexible for trading off gradient against repetition rate, meaning it could more efficiently target the very high photon energies required by some areas of the science, albeit at low repetition rate. Preliminary work is ongoing around a baseline of 8 GeV at 1 kHz for the normal conducting section, potentially scaling up to 5 kHz at lower gradient, or to higher energy at lower repetition rate. Again, advanced undulators would be used for maximum reach in terms of photon energy/pulse energy, and fast kickers would distribute bunches between different FEL lines.

ISBN: 978-3-95450-220-2 ISSN: 2673-5474 doi: 10.18429/JACoW-FEL2022-TUP32

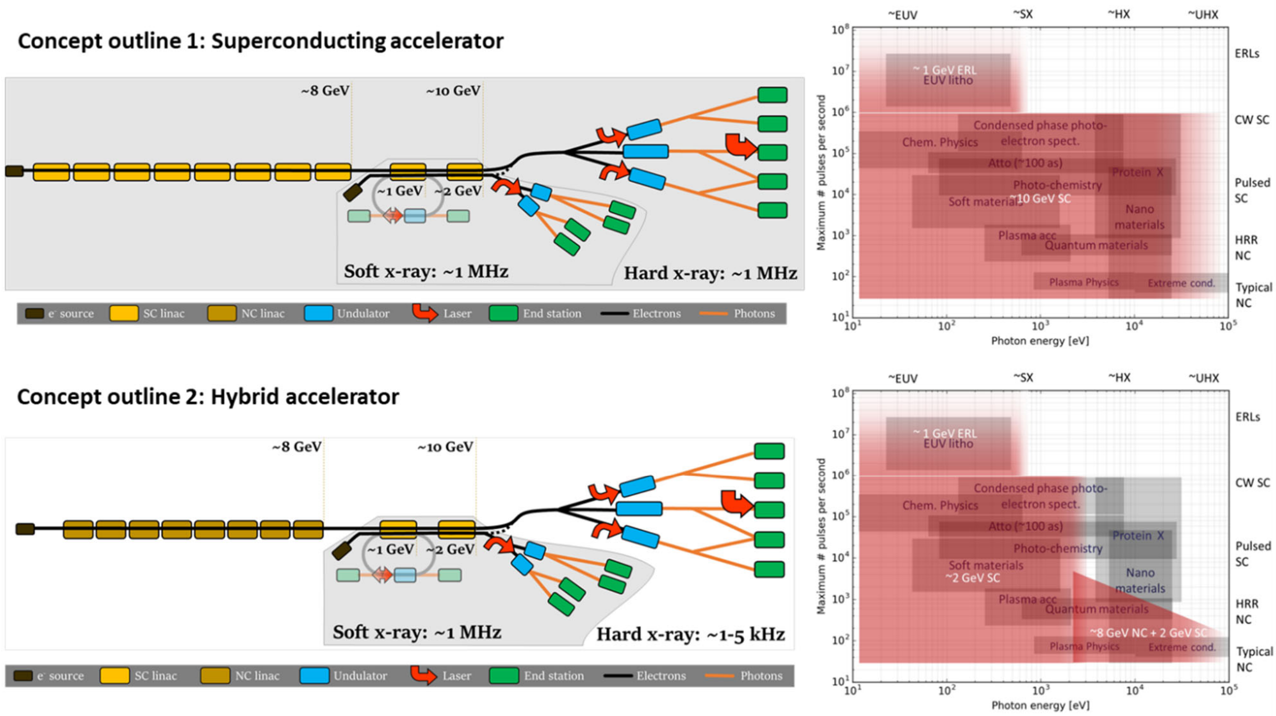

Figure 2: Top: UK XFEL Concept outline 1: superconducting (SC) accelerator. The schematic to the left shows the layout for a ~10 GeV superconducting accelerator facility proposed to meet the science requirements. The plot to the right shows how such a technical solution would cover the repetition rate-photon energy requirements of the science case. Bottom: Concept outline 2: hybrid accelerator. Equivalent schematic for a ~10 GeV hybrid accelerator facility (left) and its coverage of the repetition rate-photon energy requirements of the science case (right) – the sloping region represents a potential trade-off between repetition rate and gradient in the normal-conducting (NC) linac.

Two electron injectors would be essential in this case: an ultra-low emittance, low repetition rate injector for hard x-rays, together with a high-repetition rate injector for soft x-rays. This would also provide opportunity for multi-colour experiments with widely separated photon energies. Soft x-rays with high pulse energy could be generated from the 10 GeV beam if required, albeit at lower repetition rate. A second injector again provides the option of upgrading this region to an energy recovery linac to support a high average power EUV FEL and a high brightness gamma ray source. Alternatively, recirculation around the superconducting section would be a promising future upgrade to extend MHz repetition rates towards hard x-ray.

As for Concept outline 2, high repetition rate seeding, attosecond pulse generation, and high spectral purity techniques could be incorporated, although the use of oscillator FELs would be limited to photon energies where MHz is available (i.e. up to a few keV). An oscillator FEL could potentially be used to seed to higher photon energy. Again, end-stations would be equipped with the most advanced lasers, THz radiation sources and electron beams, for use in combination with the x-rays.

NEXT STEPS

In June 2022, UK Research and Innovation announced funding for the next phase of the project: a 3-year conceptual design and options analysis. The conceptual design and options to build a UK XFEL will be investigated, along with other options, including making significant investments into overseas XFELs to enhance their current capabilities as part of a strategic development to create a next generation XFEL. This next phase of the project is set to start in October 2022.

ACKNOWELDGEMENTS

The authorship of this paper is limited to those on the facility side of the UK XFEL Science Case team, as well as Jon Marangos as project lead. However the innovative contributions from the Science Team members of the project should be recognised, as well as those from a host of additional contributing authors as listed in the Science Case. We are also grateful for input from new members of the emerging design team for the next phase.

REFERENCES

[1] J. P. Marangos *et al.*, "UK XFEL Science Case", UK Research and Innovation, Science and Technology Facilities Council, 2020. `https://www.clf.stfc.ac.uk/Pages/UK-XFEL-science-case.aspx`

[2] E. Prat, and P. Dijkstal, E. Ferrari and S. Reiche, "Demonstration of Large Bandwidth Hard X-Ray Free-Electron Laser Pulses at SwissFEL", *Phy. Rev. Lett.*, vol. 124, no. 7, p. 074801, Feb. 2020. `doi:10.1103/PhysRevLett.124.074801`

ISBN: 978-3-95450-220-2 ISSN: 2673-5474 doi: 10.18429/JACoW-FEL2022-TUP32

[3] R. Schoenlein *et al.*, "New Science Opportunities Enabled by LCLS-II X-Ray Lasers", SLAC National Accelerator Lab., Menlo Park, CA, USA, June 2015. doi:10.2172/1630267

[4] M. Altarelli *et al.*, "XFEL: The European x-ray free electron laser technical design report", DESY, Hamburg, Germany, Jul. 2007. doi:10.3204/DESY_06-097

[5] E. Allaria *et al.* "Highly coherent and stable pulses from the FERMI seeded free electron laser in the extreme ultraviolet", *Nat. Photonics*, vol. 6, p. 699, Sep. 2012. doi:10.1038/nphoton.2012.233

[6] B. W. J. McNeil, N. R. Thompson, and D. J. Dunning, "Transform-Limited X-Ray Pulse Generation from a High-Brightness Self-Amplified Spontaneous-Emission Free-Electron Laser", *Phys. Rev. Lett.*, vol. 110, no. 13, p. 134802, Mar. 2013. doi:10.1103/PhysRevLett.110.134802

[7] K.-J. Kim, Y. Shvyd'ko, S. Reiche, "A proposal for an Xray free-electron laser oscillator with an energy recovery linac", *Phys. Rev. Lett.*, vol. 100, no. 24, p. 244802, Jun. 2008. doi:10.1103/PhysRevLett.100.244802

[8] W. S. Graves *et al.*, "ASU Compact XFEL", in *Proc. FEL'17,* Santa Fe, NM, USA, Aug. 2017, pp. 225-228. doi:10.18429/JACoW-FEL2017-TUB03

[9] J. Duris, *et al.*, "Tunable isolated attosecond X-ray pulses with gigawatt peak power from a free-electron laser", *Nat. Photonics*, vol. 14, pp. 30-36, Jan. 2020. doi:10.1038/s41566-019-0549-5

[10] A. Marinelli *et al.*, "High intensity double-pulse X-ray free-electron laser", *Nat Commun*, vol. 6, p. 6369, Mar. 2015. doi:10.1038/ncomms7369

[11] A. Lutman, T. Maxwell. J. MacArthur, *et al.* "Fresh-slice multicolour X-ray free-electron lasers", *Nature Photon.*, vol. 10, pp. 745-750, Oct. 2016. doi:10.1038/nphoton.2016.201

ISBN: 978-3-95450-220-2 ISSN: 2673-5474 doi: 10.18429/JACoW-FEL2022-TUP33

FAST-GREENS: A HIGH EFFICIENCY FREE ELECTRON LASER DRIVEN BY SUPERCONDUCTING RF ACCELERATOR

P. Musumeci, A. Fisher, P. Denham, J. Jin, Y. Park
Department of Physics and Astronomy, University of California Los Angeles, Los Angeles, CA, USA
R. Agustsson, L. Amoudry, T. Hodgetts, M. Ruelas, A. Murokh
RadiaBeam Technologies, Santa Monica, CA, USA
A. Lumpkin, A. Zholents Argonne National Laboratory, Lemont, IL, USA
D. Broemmelsiek, S. Nagaitsev, J. Ruhan, J. Santucci, G. Stancari, A. Valishev
Fermilab National Laboratory, Batavia, IL, USA
J. Edelen, C. Hall and D. Bruhwiler
RadiaSoft, Boulder, CO, USA

Abstract

In this paper we'll describe the status of the FAST-GREENS experimental program aiming at the demonstration of the high gain TESSA regime using a strongly tapered helical undulator at the FAST facility in Fermilab. The first phase of the experiment is based on the use of the compressed 220 MeV electron beam from the FAST linac and two strongly tapered helical undulators aiming at the generation of high power radiation at 515 nm. We present time-dependent simulation results based on GENESIS and GPTFEL showing that up to 5 % conversion efficiency can be achieved in less than 2 m active interaction length.

INTRODUCTION

Improving the conversion efficiency of relativistic electron beam power into coherent short wavelength radiation is at the center of both scientific and industrial interests as it would enable light sources to reap the benefits of 100 years development in the wall-plug efficiency of charged particle accelerator technology. In the X-ray, it would facilitate ultrahigh intensity X-ray laser pulses for single shot coherent imaging and Schwinger-field physics exploration, in the EUV it would meet the demands of fast throughput material processing (EUV-lithography) and at visible wavelengths it would enable high efficiency, high average and peak power lasers. It is helpful to note that state-of-the-art X-ray sources based on the Free Electron Laser principle take advantage of only a minimal fraction (< 0.1 %) of the available power stored in the beam with most of it simply wasted on the beam dump.

The TESSA program aims at fundamentally addressing this limitation in electron-based coherent radiation generation by exploiting a deeper understanding of the interaction of relativistic electrons with the electromagnetic field in tapered undulator systems, and leveraging the progress in high brightness beam generation and control [1, 2].

The physical concept behind our approach is the so-called Tapering-Enhanced-Superradiant-Stimulated-Amplification regime of FELs where high intensity seed and pre-bunched electron beams are used in combination with strongly tapered undulators to sustain high gradient deceleration over extended distances and convert a large fraction of the beam energy into coherent radiation [3]. The main advantages of this coupling scheme are the absence of nearby boundary or media (i.e. this is a vacuum plane-wave interaction), so that there are basically no mechanisms for the energy to flow out of the particle-field system [4]. In TESSA, the initial conditions for the system allow for particle deceleration at a very high average energy exchange rates (typically in excess of 10 MV/m) larger than in any known FEL, in order to beat the onset of sideband instabilities which have been known for decades to set the limit on tapered FEL energy exchange [5]. Previous experiments based on the TESSA concept [6] demonstrated efficiencies as high as 30 % in the far-infrared. Nevertheless, they were carried out in a very low gain amplification regime resulting in a strong background signal from the seed laser which precluded obtaining direct measurements of the transverse and spectral profiles of the amplified radiation. A recent application of the TESSA concept in the THz regime demonstrated 10 % conversion efficiency in 1 m long tapered helical undulator at 160 GHz [7].

The TESSA initiative at FAST is aimed at demonstrating record high extraction efficiency lasing in a strongly tapered undulator [8]. We seek to obtain the first experimental measurements of spectral and spatial properties of the 515 nm radiation amplified in the high gain TESSA regime (Fig.1). The experiment will start in single-pass mode, but eventually we plan to take advantage of the unique high repetition rate of the FAST linac to demonstrate a very high average power source based on this principle. This source would be intrinsically synchronized with the electron beam and could be used for high flux gamma ray and polarized positron production [9, 10].

Nominal parameters for the FAST beam are reported in Table 1. The experiment is designed assuming an electron beam with 1000 pC charge, compressed to 600 Amp by the magnetic chicane compressor with a normalized emittance of < 3 mm-mrad and a relative energy spread of 0.1 %. The intense green seed pulse of nominal peak power 1 GW (2 mJ in 2 ps in order to homogeneously seed the entire bunch temporal current profile) is obtained from an Yb-based laser

ISBN: 978-3-95450-220-2 ISSN: 2673-5474 doi: 10.18429/JACoW-FEL2022-TUP33

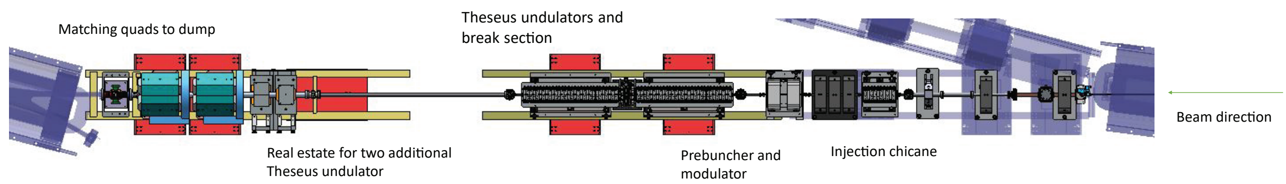

Figure 1: A schematic diagram of the proposed FAST-GREENS beamline. The beam moves from right to left. The injection chicane creates an offset sin the electron beam trajectory to allow the injection of the input seed laser on axis. A modulator-chicane module is used to prebunch the beam at the seed wavelength. The energy is then extracted from the beam using multiple 1 m long undulator sections, separated by a quadrupole doublet to control the transverse beam size. Post-undulator diagnostics section includes matching quadrupoles, and a spectrometer dipole for beam energy measurements.

system that will be installed in a newly refurbished laser room located above the FAST linac.

Table 1: Design Electron Beam, Laser and Undulator Parameters for FAST-GREENS Experiment

Parameter	Unit	Value
Beam Energy	MeV	220
Bunch Charge	nC	1
Peak Current	Amp	600
Bunch Length, FWHM	ps	1.6 ps
Normalized Emittance	mm-mrad	3
Uncorr. energy spread, FWHM	keV	220
Resonant wavelength	nm	515
Input seed power	GW	1
Undulator period	mm	32
Undulator K		2.25-2

GENESIS AND GPT-FEL NUMERICAL MODELS

The layout for the experiment is the result of a large number of technical choices and available hardware. A 8 period helical prebuncher is used to generate the energy modulation that the prebunching chicane converts into density modulation at the entrance of the THESEUS tapered undulator [8].

The input beam transverse parameters can be chosen with some flexibility as the quadrupoles between the prebuncher and the 1st tapered undulator can be varied to match the beam into the FODO channel. In addition, we assume that the optics installed upstream of the prebuncher can be used to ease the beam into the FAST-GREENS transport. In the numerical example studied in this paper the integrated gradient of the combined function quadrupoles located between the prebuncher and undulator is 0.751 T (4.91 T/m for an effective length of 0.153 m) and the initial Twiss parameters are $\alpha_{x,y} = (1.84, 3.18)$ and $\beta_{x,y} = (9.29, 11.55)$ m respectively.

In order to maximize the extraction efficiency [3], the transport lattice in the undulator system is set up by balancing the wiggler natural focusing with a quadrupole doublet in the break sections. For the design quadrupole gradient of 115 T/m (effective magnetic length 30.7 mm), the average matched beta-function in the undulator is 0.7 m. To minimize the foot-print of the break section, the quadrupoles also serve as kickers in conjuction with a small electromagnetic dipole to realize a three-element phase shifter and re-align the bunching and the radiation at the entrance of the tapered undulator sections. The reference electron beam trajectory along the system is shown in Fig. 2 along with the horizontal and vertical spot sizes.

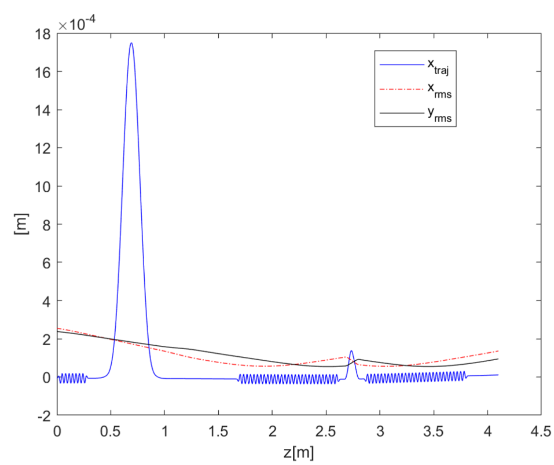

Figure 2: Beam trajectory in the system. The prebunching and phase shifter chicane bumps are clearly visible. The horizontal and vertical spot sizes for a 3 mm-mrad emittance are also shown.

Time-independent Genesis simulations are performed to optimize the tapering of the undulator. In particular we first optimize the seed laser focusing (Rayleigh range and waist position) and the R56 of the bunching chicane. At the same time we vary the undulator tapering gradients and the phase shifter to maximize the output radiation. The outcome of this optimization is shown in Fig.3 and indicate that 5.5 % efficiency could be reached in a system with just two undulators and one break section. For this simulation we used a Rayleigh range of 1.84 m, a waist position 2.2 m and a R_{56} of 20.5 μm for the bunching chicane. The results of time-dependent GENESIS simulations sending the electron bunch in this optimized undulator profile are shown in the Fig. 4 where we also plot the efficiency as a function of

ISBN: 978-3-95450-220-2 ISSN: 2673-5474 doi: 10.18429/JACoW-FEL2022-TUP33

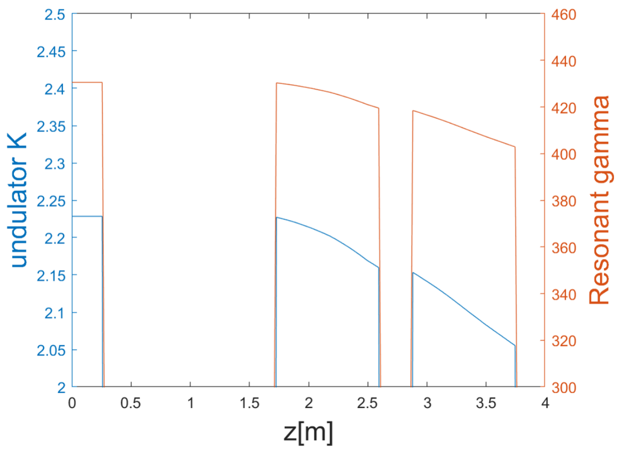

Figure 3: Optimized tapering of the normalized vector potential and resonant energy along the undulator. The undulator period is fixed and the prescribed variation of the undulator K parameter can be obtained by adjusting the gap.

electron bunch length assuming a gaussian current profile. These results have been verified and benchmarked with GPT-FEL [11] which is a new code developed to take advantage of the built-in features of the particle tracer GPT when simulating FEL interaction. GPTFEL allows use to input the actual undulator maps and not the period-average version of them, enabling a better representation of the interaction in the entrance and exit sections of the undulators. Wakefields, transverse and longitudinal space charge effects are all included.

One of the major issue with operating the FEL in the TESSA regime is the strong slippage experienced by the radiation due to the fact that the gain is not exponential. If the electron bunch length is shorter than the total slippage length (2 29 periods undulators + 9 periods prebuncher + 7 period break section, for a total slippage length of 127 fs) then the total efficiency is strongly suffering. Therefore, it will be of great importance to achieve the high peak current in a relatively long (rms bunch length > 0.3 ps) region of the electron beam while at the same time maintaining good emittance and low energy spread. Significant efforts are currently ongoing to explore different approaches to shape the temporal profile of the electron beam from the FAST linac in order to match it to the TESSA application. In order to give a better idea of the tolerances in setting up the beam from the FAST linac, we also show the dependencies of the final efficiency from input uncorrelated energy spread and emittance affect the final output in Fig. 5.

CONCLUSIONS

In summary, in this paper we presented the numerical model for the FAST-GREENS experiment. Two different FEL codes GENESIS and GPTFEL have been used to optimize the tapering design and understand the parameter tolerances. The results of the two numerical simulations

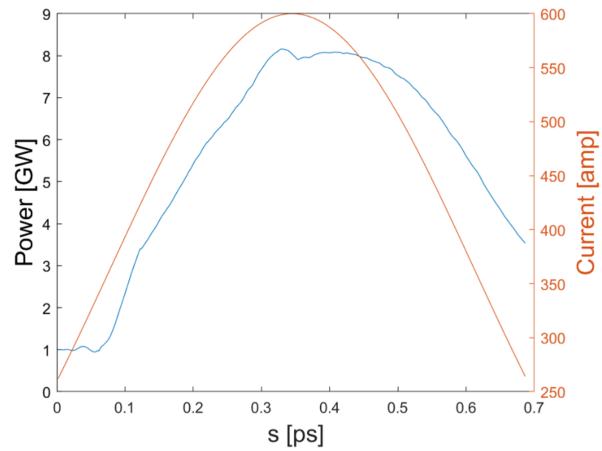

Figure 4: Radiation and beam current profile at the exit of the undulator for a case where the rms bunch length of the beam is 200 fs.

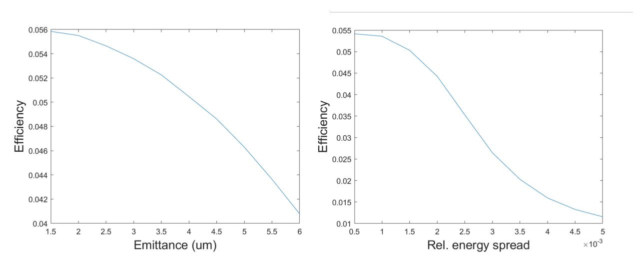

Figure 5: Efficiency of system as a function of input emittance (left) and uncorrelated energy spread (right).

are in excellent agreement with each other and provide a solid foundation for the upcoming experimental investigations. It is foreseen that the model developed here will be coupled with beam dynamics simulation for the evolution of the beam from the photoinjector up to the FAST-GREENS beamline to understand the effect of detailed electron beam distribution on the system performances.

ACKNOWLEDGEMENTS

Work partially supported by DOE grant DE-SC0009914, DE-SC0018559 and DE-SC0017102.

REFERENCES

[1] J. Duris, A. Murokh, and P. Musumeci, “Tapering enhanced stimulated superradiant amplification,” *New J. Phys.*, vol. 17, no. 6, p. 063 036, 2015. doi:10.1088/1367-2630/17/6/063036

[2] J. Duris, P. Musumeci, N. Sudar, A. Murokh, and A. Gover, “Tapering enhanced stimulated superradiant oscillator,” *Phys. Rev. Accel. Beams*, vol. 21, no. 8, p. 080 705, 2018. doi:10.1103/PhysRevAccelBeams.21.080705

[3] C. Emma, N. Sudar, P. Musumeci, A. Urbanowicz, and C. Pellegrini, “High efficiency tapered free-electron lasers with a prebunched electron beam,” *Phys. Rev. Accel. Beams*, vol. 20, no. 11, p. 110 701, 2017. doi:10.1103/PhysRevAccelBeams.20.110701

ISBN: 978-3-95450-220-2 ISSN: 2673-5474 doi: 10.18429/JACoW-FEL2022-TUP33

[4] J. Duris, P. Musumeci, and R. Li, "Inverse free electron laser accelerator for advanced light sources," *Physical Review Special Topics-Accelerators and Beams*, vol. 15, no. 6, p. 061 301, 2012. doi:10.1103/PhysRevSTAB.15.061301

[5] A. Gover *et al.*, "Superradiant and stimulated-superradiant emission of bunched electron beams," *Rev. Mod. Phys.*, vol. 91, p. 035 003, 3 2019. doi:10.1103/RevModPhys.91.035003

[6] N. Sudar *et al.*, "High efficiency energy extraction from a relativistic electron beam in a strongly tapered undulator," *Phys. Rev. Lett.*, vol. 117, p. 174 801, 2016. doi:10.1103/PhysRevLett.117.174801

[7] A. Fisher *et al.*, "Single-pass high-efficiency terahertz free-electron laser," *Nature Photonics*, vol. 16, no. 6, pp. 441–447, 2022.

[8] Y. Park *et al.*, "Tapered helical undulator system for high efficiency energy extraction from a high brightness electron beam," *Nucl. Instrum. Methods Phys. Res., Sect. A*, vol. 1028, p. 166 370, 2022. doi:10.1016/j.nima.2022.166370

[9] Y. K. Wu *et al.*, "Performance and capabilities of upgraded high intensity gamma-ray source at duke university," in *Proc. PAC'09*, Vancouver, Canada, May 2009, pp. 3181–3183.

[10] I. Chaikovska *et al.*, "Positron sources: From conventional to advanced accelerator concepts-based colliders," *J. Instrum.*, vol. 17, no. 05, P05015, 2022. doi:10.1088/1748-0221/17/05/P05015

[11] A. Fisher, P. Musumeci, and S. Van der Geer, "Self-consistent numerical approach to track particles in free electron laser interaction with electromagnetic field modes," *Phys. Rev. Accel. Beams*, vol. 23, no. 11, p. 110 702, 2020. doi:10.1103/PhysRevAccelBeams.23.110702

ISBN: 978-3-95450-220-2 ISSN: 2673-5474 doi: 10.18429/JACoW-FEL2022-TUP35

SIMULATIONS OF ULTRAHIGH BRIGHTNESS BEAMS FROM A PLASMA PHOTOCATHODE INJECTOR

L. H. A. Berman*, A. F. Habib, T. Heinemann, G. G. Manahan, A. Sutherland,
D. Campbell, A. Hewitt, A. Dickson and B. Hidding,
Scottish Universities Physics Alliance, Department of Physics,
University of Strathclyde, Glasgow G4 0NG, UK
The Cockcroft Institute, Warrington, UK

Abstract

Plasma photocathode injectors may enable electron beams with normalised emittance at the nm-rad level from a Plasma Wakefield Acceleration (PWFA) stage [1]. At these emittance levels, and currents at the kA-level, they are ultrahigh 5D brightness beams with the potential to drive advanced light sources. The feasibility of plasma photocathodes was demonstrated at the first Facility for Advanced Accelerator Experimental Tests (FACET-I) at the Stanford Linear Accelerator (SLAC) [2]. Further experiments will aim at realisation of the full 5D and 6D brightness potential at FACET-II [3]. However, a series of milestones must be reached before these beams can be utilised for FELs. For example, electron beams accelerated in plasma-based accelerators inherently have a significant energy chirp due to the multi-GV/m accelerating gradients involved. Since energy chirp and energy spread can be detrimental to the high-gain FEL interaction, an approach has been developed for energy spread minimisation of ultrahigh 5D brightness beams towards ultrahigh 6D brightness via the escort beam approach [4]. Here we discuss ongoing efforts within the framework of the PWFA-FEL project [5], aiming at direct single-bunch production of ultrabright beams with reduced energy spread using beam-loading. We present considerations and results aiming at a balanced optimisation of energy spread, peak current, and emittance from direct plasma photocathode production, and their application to FELs.

INTRODUCTION

Plasma-based particle acceleration uses a plasma as the accelerating medium instead of conventional RF cavities [6]. Either an electron bunch or an intense laser pulse acts as a 'driver' that is sent through the plasma, transversely expelling the plasma electrons but having negligible impact on the heavier ions. This creates a cavity (or 'blowout') devoid of electrons that trails the driver, resulting in an internal longitudinal E-field of gradient on the order of tens of GV/m. This 'wakefield' can trap and accelerate an electron 'witness' bunch. Both the laser and beam-driven varieties, respectively known as laser and plasma wakefield acceleration (LWFA and PWFA), have already been used to demonstrate multi-GeV energy gain [7, 8], with a current record of energy doubling of electrons to 84 GeV [9] . This took less than a metre compared to the km-scale linac that would be needed to achieve a comparable energy gain. If a plasma-based accelerator could be used to drive an FEL this would open up huge additional capacities, and potentially capabilities.

This prospect has gained a lot of interest, and FEL gain has recently been demonstrated for the first time using beams from plasma-based accelerators in the EUV at 27 nm [10] and the IR at 820 nm [11]. However, FEL gain in the x-ray region has not yet been achieved due to the increasingly stringent requirements on the electron witness beam. A key parameter is the normalised transverse beam emittance ε_n since this determines the minimum FEL wavelength that can be accessed via the Pellegrini criterion, $\varepsilon_\mathrm{n} \leq \gamma\lambda_r/4\pi$, where λ_r is the resonant FEL wavelength and γ is the beam Lorentz factor. The other key parameter is the slice energy spread σ_γ/γ of the electron beam, which should be smaller than ρ according to $\sigma_\gamma/\gamma \leq \rho$. Both thresholds are difficult to reach for beams from plasma accelerators today, and increasingly so for lower electron energies and harder resonant wavelengths. Because the electron beam quality obtainable from plasma accelerators is both determined and limited by currently used electron beam generation methods, the x-ray range may remain out of reach. Electron beams of higher quality are necessary for overcoming these limitations in future plasma-based accelerators.

Beam brightness is an important figure of merit for determining suitability for FEL operation [12]. Here we define 5D brightness as $B_\mathrm{5D} = 2I_\mathrm{peak}/\varepsilon_\mathrm{n}^2$, where I_peak is peak current, and 6D brightness as $B_\mathrm{6D} = B_\mathrm{5D}/\sigma_E 0.1\%\mathrm{BW}$ which also takes into account the correlated (projected) energy spread σ_E. Indeed, the obtainable witness beam quality depends heavily on the injection method. Self-injection methods tend to produce lower quality beams due to their dependence on highly nonlinear processes, whereas controlled injection methods may achieve higher beam quality due to the increased stability [13–15].

A novel electron injection method that goes one step further and promises decoupled control over witness properties, and electron beam quality orders of magnitude beyond state-of-the-art is the plasma photocathode injection, also known as 'Trojan Horse' (TH) [1]. In this method the plasma wave blowout is set up in a mixture of two gases, one with a low ionisation threshold (LIT) and one with a high threshold (HIT). Initially only the LIT gas is preionised into a plasma with the HIT gas remaining in a neutral state. An electron bunch driver sets up a wake in the LIT plasma. A low-intensity laser pulse incident in arbitrary orientation then

* lily.berman@strath.ac.uk

ISBN: 978-3-95450-220-2 ISSN: 2673-5474 doi: 10.18429/JACoW-FEL2022-TUP35

ionises the HIT gas in a targeted region around the centre of the blowout, releasing electrons with minimal transverse momentum that are trapped and accelerated to form the witness beam. This witness beam may have 10's of nm-rad scale normalised emittance capable of surpassing the Pellegrini criterion at sub-nm wavelengths and moderate energies. Furthermore, properties such as the witness charge and dimensions can be adjusted by changing the relative gas densities and photocathode laser parameters [3, 16]. The first demonstration of a plasma photocathode-based injection has already taken place at the FACET-I at SLAC in the E-210: Trojan Horse proof-of-concept experiment [2]. The next generation of experiments planned at FACET-II, which have recently commenced operation, will aim to demonstrate the full emittance and brightness potential through a number of avenues e.g. collinear injection geometry and larger blowouts [3].

An issue typically encountered in plasma-accelerated beams is the large negative witness energy chirp, which is detrimental to the FEL process [12]. Energy chirp is of course also an issue in state-of-the-art FELs. Various methods for chirp compensation have been developed, such as the passive dechirper by self-induced wakefields used successfully at LCLS [17]. Similar chirp compensation techniques have also been developed for plasma wakefields [18, 19]. However these involve multiple stages, leading to emittance growth during extraction [20]. While these methods are sufficient to be used with beams that have ~ mm mrad emittance, growth of this magnitude would not be acceptable for the ~ nm rad beams expected from a plasma photocathode. Therefore it is essential to remove the chirp prior to extraction in a single stage for beam quality preservation along the beam transport line. A method that has been devised to achieve this is the multibunch dechirper method [4]. In this method, a second, high-charge 'escort' electron bunch is produced inside the blowout only after the low-charge witness bunch has become sufficiently relativistic and is therefore largely immune to space-charge forces. The escort sits at the same position as the witness where it loads the wakefield, as shown in Fig. 1 via a 1D model. This locally reverses the field gradient so that the energy chirp accumulated so far is counter-rotated at a rate given by the degree of beam-loading such that the chirp is fully compensated by the time the beam exits the plasma. The single stage setup allows the production of beams with ultrahigh 6D brightness, and future experimental demonstration will be aimed at during the E-313 experiment at FACET-II.

DIRECT BEAM-LOADING BY WITNESS BUNCHES FROM TROJAN HORSE

While the multibunch dechirper method is currently seen as the path to highest beam quality in terms of 6D brightness, the plasma photocathode does also offer direct beam-loading by the witness bunch, without the escort beam. Injecting a high charge witness is beneficial for beam current and projected energy spread, which can be directly reduced by

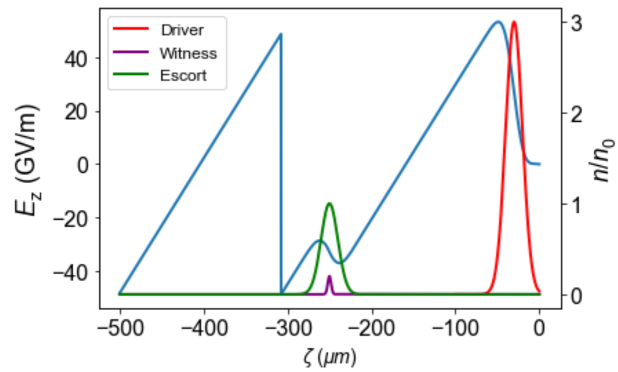

Figure 1: Demonstration of the multibunch dechirper concept in 1D. Blue: Longitudinal on-axis accelerating electric field E_z. Normalised density of drive beam (red), witness beam (purple) and escort beam (green). n_0 is background plasma density.

beam-loading. This comes at the cost of increased emittance due to space-charge forces. Therefore a trade-off can be made with regard to brightness.

Beam-Loading for Energy Spread Reduction

A high-charge electron bunch can locally reduce the accelerating gradient due to beam loading, preventing the accumulation of energy chirp during the acceleration. Beam-loading effects are well-known in the field of plasma-based accelerators [21–23] and can be used for shaping the accelerating gradient of the plasma-based accelerator [4].

Analytical 3D models of the blowout can be used to find approximate values for the witness charge/current that would be required to flatten the wakefield for given plasma density and wakefield electron drive-beam parameters as a precursor to implementing fully-explicit 3D Particle-in-cell (PIC) simulations. Here, we use the generalised model developed by Golovanov *et. al.* [24, 25] in the thin sheath approximation (sheath thickness $\ll$ bubble radius) for an exponential sheath profile [26]. This model qualitatively describes beam-loading effects and allows estimation of the required witness beam charge values for ideal beam-loading in PWFA.

The equations of the generalised model were solved for parameters similar to those expected at the upcoming E-310: Trojan Horse-II experiment at FACET-II. The plasma density is chosen to be $n_e = 1.78 \times 10^{16}$ cm^{-3} to give a plasma wavelength $\lambda_p = 250$ μm, the driver charge is assumed $Q_d = 1.5$ nC, and its length $\sigma_{\mathrm{z,\,d}} = 32$ μm and radius $\sigma_{\mathrm{r,\,d}} = 4.5$ μm [16]. The dimensions of the witness beam generated from the plasma photocathode were fixed at $\sigma_{\mathrm{z,\,w}} = \sigma_{\mathrm{r,\,w}} = 2$ μm, although in reality these are expected to change with Q_w and photocathode laser parameters. Figure 2 shows the effect of beam-loading on the longitudinal wakefield. As witness charge is increased, the local field gradient increases until it is flattened and then overloaded. E_z is shown at the witness location to demonstrate this clearly in (a), (b) and (c) for $Q_w = 100$, 200 and 300 pC. Case (a) shows weak beam-loading, (b) shows near-optimum loading since

ISBN: 978-3-95450-220-2 ISSN: 2673-5474 doi: 10.18429/JACoW-FEL2022-TUP35

the field appears locally flat, while (c) shows a reversal of field gradient which will lead to a positive energy chirp. This analytical estimate can guide refined simulations and experimental realisation of matched beam-loading.

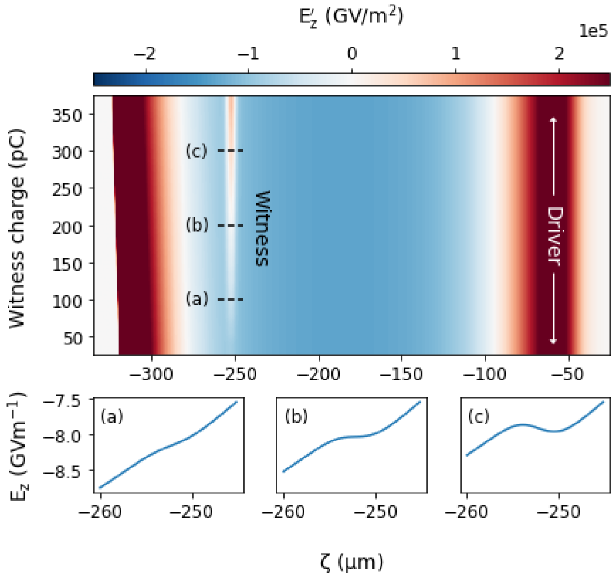

Figure 2: Beam-loading of longitudinal accelerating field E_z by a high-charge witness using analytical 3D models [24–26]. Main figure: first derivative of accelerating field E_z' within the blowout for witness charge vs longitudinal co-moving coordinate ζ. The driver is positioned on the right-hand side and the witness is centred near -250 μm. Loading is observed at the witness position. Lower figures show E_z sections at locations of dotted lines for witness charges of (a) 100 pC, (b) 200 pC and (c) 300 pC. Increasing local flattening of field is observed as witness charge increases.

Tuning Witness Charge

The plasma photocathode has the unique capability to tune witness beam charge via tunneling ionisation, fully decoupled from the underlying wakefield setup, for example by tuning laser intensity via a_0, laser pulse duration τ_0, spot size w_0 or HIT component density. The electron charge yield, shown in Fig. 3 as a function of a_0 and HIT density n_{He}, spans several orders of magnitude. Spot size and pulse duration have been kept constant at 7 μm and 50 fs respectively to match expected injector laser parameters at FACET-II [3]. The laser wavelength is 800 nm and we use a Hydrogen/Helium LIT/HIT mixture. Figure 3 was produced by numerically calculating the Ammosov-Delone-Krainov (ADK)[27] tunnelling ionisation rates and shows plasma photocathode working points suitable to generate required charges for sufficient beam-loading as shown in Fig. 2.

Optimisation of Witness Properties for FEL

The key witness properties for application to an FEL are projected and slice energy spread, current and emittance. Major contributions to the beam emittance are thermal emittance, from phase-mixing and space charge. Estimations [1]

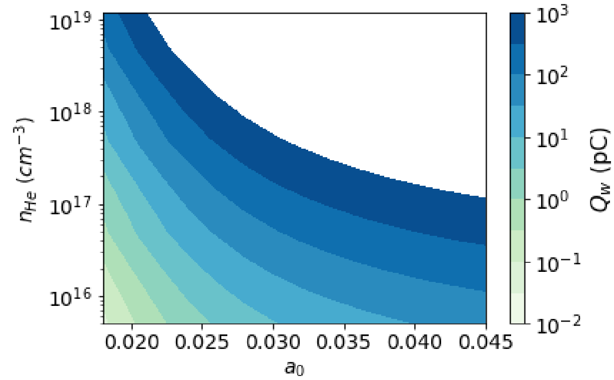

Figure 3: Released witness charge as a function of normalised laser vector potential a_0 and HIT gas density n_{He}. Laser pulse duration $\tau_0 = 50$ fs and waist size $w_0 = 7$ μm

and calculations [28] of thermal emittance and its dependence on a_0 and w_0 have been made, and phase mixing can also be modelled [29, 30]. However, if direct beam-loading is exploited then the emittance is dominated by space charge. Conversely, in low charge scenarios space charge may be ignored and increased residual transverse momentum and/or phase mixing by tuning a_0 or w_0 may take precedence. Increasing n_{He} does not change the ionisation volume and geometry and so does not intrinsically increase thermal emittance or bunch length. It is therefore the first variable of choice for exploration of brightness optimisation strategies.

An initial scan of n_{He} for collinear TH injection was carried out using the VSim 3D PIC code [31] for 1 cm propagation. Grid cell size was 1 μm in the acceleration direction and 1.2 μm transversely. This gives a first estimate of

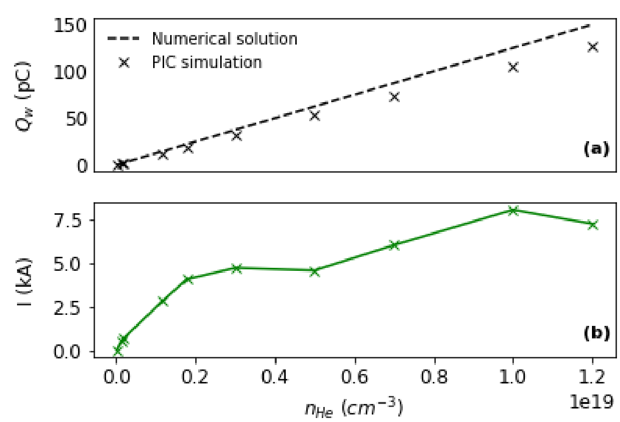

Figure 4: Results from PIC simulations of collinear TH injection. (a) HIT gas density vs witness charge Q_w compared with numerical estimates. (b) peak current I

some possible witness beam parameters. However, resolving beam-loading effects will be addressed using more advanced simulations, requiring significantly more computational resources for this next refinement step. Figure 4a shows the resulting witness charge, which increases linearly with n_{He}.

ISBN: 978-3-95450-220-2 ISSN: 2673-5474 doi: 10.18429/JACoW-FEL2022-TUP35

This matches the numerical estimates sufficiently to confirm their usefulness for fast estimates of charge release.

The obtained beam current in Fig. 4b initially also shows a linear increase, but then develops sublinearly. This is in part due to increasing bunch length from internal space-charge forces. Despite this, multi-kA currents are reached even at witness charges far below those anticipated for optimum loading thanks to few-fs bunch duration. Additionally, the unipolar electric field of the witness itself begins self-ionising the HIT gas once its charge approaches 100 pC. This charge is not trapped and therefore does not act as a source of dark current, but is enough to locally load the wakefield. While this could possibly be advantageous for field flattening, the charge release in these simulations was seen to fluctuate which was reflected in wakefield loading. This increasingly distorts the witness phase-space at high HIT densities and degrades its emittance. Also, the HIT density is already three orders of magnitude greater than the LIT density in this scenario, so further increasing charge release via the HIT density is not a promising path for optimisation.

Instead, this modelling shows that the plasma photocathode laser parameters should be tuned by increasing a_0, w_0 to τ_0 in order to achieve larger witness charges at lower HIT densities. This may then also avoid HIT gas self-ionisation by the witness beam and enable emittance optimisation. Iterative scans and in-depth emittance evolution studies can be used to optimise the beam for application scenarios e.g. guided by the resonance wavelength goal.

APPLICATION TO SOFT XFEL

Figure 4b shows that a 5 kA current is easily reached. Initial scans show that the obtained emittance level for such scenarios will be somewhere between few tens of nm rad (as in the low charge case), and few hundreds of nm rad for heavy beam-loading scenarios. While this may be unacceptable for operation at hard x-ray wavelengths, in which case the multibunch dechirper method can be used, requirements at soft x-ray wavelengths are less stringent. Even if the tens of nm rad emittance of a low-charge witness [3] may be exceeded by an order of magnitude, the Pellegrini criterion may be satisfied over almost the entire soft x-ray range of 1-10 nm even at modest energies. For example, a 1 GeV, 5 kA beam with 300 nm rad normalised emittance satisfies the Pellegrini criterion down to 1.9 nm. At the same time, the obtainable brightness can greatly exceed those at existing linac-driven XFEL facilities [12].

This may also extend to 6D brightness. The slice spread has been estimated for the low charge case in good agreement with simulations as $\sigma_\gamma/\gamma \approx 2\pi/5E_{z,\mathrm{trap}}\, w_0^2/\lambda_\mathrm{L}$ where $E_{z,\mathrm{trap}}$ is the accelerating field at the trapping position [4]. The value of $E_{z,\mathrm{trap}}$ will depend on the plasma density (and driver charge), but also dynamically on the witness charge when beam-loading sets in. For a spot size e.g. of w_0 = 7 μm, $E_{z,\mathrm{trap}}$ ≈ 10-20 GV/m and a final beam energy of 1 GeV the above scaling would lead to $\sigma_\gamma/\gamma \approx$ 0.07-0.15 %.

In Fig. 5, we have used the Xie formalism [32] to calculate the gain length that could be achieved at different wavelengths and emittances for a 1 GeV beam with I = 5 kA and σ_γ/γ = 0.1 %. The undulator peak field B_0 was fixed at 1.3 T while the undulator period λ_u was allowed to vary, and the natural beta function assuming a planar undulator was used. The green region shows where both the Pellegrini and energy spread criteria are fulfilled. Even at this relatively low beam energy, a large portion of the soft x-ray spectrum could be accessed even at non-optimised emittance values. Thanks to the brightness, the gain length is also an order of magnitude lower than conventional XFELs, and there remains much scope for this to be optimised further at any particular wavelength by changing B_0, λ_u and the beta function in addition to (further) beam parameter optimisation.

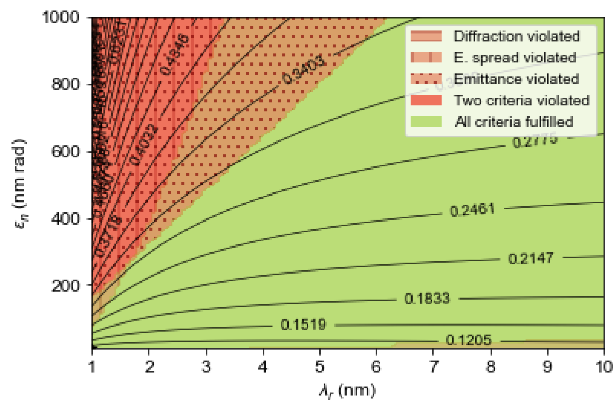

Figure 5: Gain length in wavelength-emittance space for 1 GeV electron beam with I = 5 kA, σ_γ/γ = 0.1 %. Green: Lasing criteria satisfied. Light red: Pellegrini criterion not satisfied. Dark red: energy spread criterion also not satisfied.

CONCLUSION

We are exploring the direct use of plasma photocathodes for beam-loading-based energy spread reduction. This is a simplified, complementary approach for ultrabright beam production when compared to the escort bunch technique [4]. Trade-offs between energy spread and emittance are to be made, but initial explorations indicate that emittance and brightness can be improved by approximately an order of magnitude compared to state-of-the-art, thus potentially enabling soft x-ray FELs with ultrahigh gain already at modest energies.

ACKNOWLEDGEMENTS

This work used computational resources of the National Energy Research Scientific Computing Center, which is supported by DOE DE-AC02-05CH11231, and of Shaheen (Project k1191). This work is supported by the European Research Council (ERC) under the EU Horizon 2020 research and innovation programme (NeXource: Next-generation Plasma-based Electron Beam Sources for High-brightness Photon Science, ERC Grant agreement No. 865877) and by the STFC PWFA-FEL programme ST/S006214/1.

ISBN: 978-3-95450-220-2 ISSN: 2673-5474 doi: 10.18429/JACoW-FEL2022-TUP35

REFERENCES

[1] B. Hidding *et al.*, "Ultracold electron bunch generation via plasma photocathode emission and acceleration in a beam-driven plasma blowout," *Phys. Rev. Lett.*, vol. 108, p. 035 001, 2012. doi:10.1103/PhysRevLett.108.035001.

[2] A. Deng *et al.*, "Generation and acceleration of electron bunches from a plasma photocathode," *Nat. Phys.*, vol. 15, pp. 1–5, 2019. doi:10.1038/s41567-019-0610-9.

[3] A. F. Habib, T. Heinemann *et al.*, "Ultrahigh brightness beams from plasma photoguns," *arXiv:2111.01502 [physics]*, Nov. 2021. doi:arXiv:2111.01502.

[4] G.G. Manahan, A.F. Habib *et al.*, "Single-stage plasma-based correlated energy spread compensation for ultrahigh 6D brightness electron beams," *Nat. Commun.*, vol. 8, no. 15705, 2017. doi:10.1038/ncomms15705.

[5] B. Hidding *et al.*, *STFC PWFA-FEL: Exploratory study of PWFA-driven FEL at CLARA*, https://pwfa-fel.phys.strath.ac.uk/, 2019.

[6] P. Chen *et al.*, "Acceleration of electrons by the interaction of a bunched electron beam with a plasma," *Phys. Rev. Lett.*, vol. 54, no. 7, pp. 693–696, Feb. 1985. doi:10.1103/PhysRevLett.54.693.

[7] M. J. Hogan *et al.*, "Multi-GeV energy gain in a plasma-wakefield accelerator," *Phys. Rev. Lett.*, vol. 95, p. 054 802, 2005. doi:10.1103/PhysRevLett.95.054802.

[8] A. Gonsalves *et al.*, "Petawatt laser guiding and electron beam acceleration to 8 GeV in a laser-heated capillary discharge waveguide," *Phys. Rev. Lett.*, vol. 122, no. 8, p. 084 801, Feb. 2019. doi:10.1103/PhysRevLett.122.084801.

[9] I. Blumenfeld *et al.*, "Energy doubling of 42 GeV electrons in a metre-scale plasma wakefield accelerator," *Nature*, vol. 445, no. 7129, pp. 741–744, Feb. 2007. doi:10.1038/nature05538.

[10] W. Wang *et al.*, "Free-electron lasing at 27 nanometres based on a laser wakefield accelerator," *Nature*, vol. 595, no. 7868, pp. 516–520, Jul. 2021. doi:10.1038/s41586-021-03678-x.

[11] R. Pompili *et al.*, "Free-electron lasing with compact beam-driven plasma wakefield accelerator," *Nature*, vol. 605, no. 7911, pp. 659–662, May 2022. doi:10.1038/s41586-022-04589-1.

[12] S. Di Mitri and M. Cornacchia, "Electron beam brightness in linac drivers for free-electron-lasers," *Phys. Rept.*, vol. 539, pp. 1–48, 2014. doi:10.1016/j.physrep.2014.01.005.

[13] J. Faure *et al.*, "Controlled injection and acceleration of electrons in plasma wakefields by colliding laser pulses," *Nature*, vol. 444, no. 7120, pp. 737–739, Dec. 2006. doi:10.1038/nature05393.

[14] D. Ullmann *et al.*, "All-optical density downramp injection in electron-driven plasma wakefield accelerators," *Phys. Rev. Res.*, vol. 3, no. 4, p. 043 163, Dec. 2021. doi:10.1103/PhysRevResearch.3.043163.

[15] C. G. R. Geddes *et al.*, "Plasma-density-gradient injection of low absolute-momentum-spread electron bunches," *Phys. Rev. Lett.*, vol. 100, no. 21, p. 215 004, May 2008. doi:10.1103/PhysRevLett.100.215004.

[16] A. F. Habib *et al.*, "Plasma accelerator-based ultrabright x-ray beams from ultrabright electron beams," in *Advances in Laboratory-based X-Ray Sources, Optics, and Applications VII*, International Society for Optics and Photonics, vol. 11110, 2019. doi:10.1117/12.2530976.

[17] P. Emma *et al.*, "Experimental demonstration of energy-chirp control in relativistic electron bunches using a corrugated pipe," *Phys. Rev. Lett.*, vol. 112, no. 3, p. 034 801, Jan. 2014. doi:10.1103/PhysRevLett.112.034801.

[18] R. D'Arcy *et al.*, "Tunable plasma-based energy dechirper," *Phys. Rev. Lett.*, vol. 122, p. 034 801, 2019. doi:10.1103/PhysRevLett.122.034801.

[19] R. Pompili *et al.*, "Energy spread minimization in a beam-driven plasma wakefield accelerator," *Nature Physics*, vol. 17, no. 4, pp. 499–503, Apr. 2021. doi:10.1038/s41567-020-01116-9.

[20] M. Scisciò *et al.*, "Parametric study of transport beam lines for electron beams accelerated by laser-plasma interaction," *J. Appl. Phys.*, vol. 119, no. 9, p. 094 905, Mar. 2016. doi:10.1063/1.4942626.

[21] T. C. Katsouleas *et al.*, "Beam loading in plasma accelerators," *Part. Accel.*, vol. 22, pp. 81–99, 1987.

[22] M. Tzoufras *et al.*, "Beam loading by electrons in nonlinear plasma wakes," *Phys. Plasmas*, vol. 16, no. 5, p. 056 705, May 2009. doi:10.1063/1.3118628.

[23] G. Li *et al.*, "Control of electron beam energy-spread by beam loading effects in a laser-plasma accelerator," *Plasma Phys. Control. Fusion*, vol. 62, no. 5, p. 055 004, May 2020. doi:10.1088/1361-6587/ab7c50.

[24] A. A. Golovanov *et al.*, "Generalised model of a sheath of a plasma bubble excited by a short laser pulse or by a relativistic electron bunch in transversely inhomogeneous plasma," *Quantum Electronics*, vol. 46, no. 4, pp. 295–298, Apr. 2016. doi:10.1070/QEL16040.

[25] J. Thomas *et al.*, "Non-linear theory of a cavitated plasma wake in a plasma channel for special applications and control," *Phys. Plasmas*, vol. 23, no. 5, p. 053 108, May 2016. doi:10.1063/1.4948712.

[26] A. A. Golovanov *et al.*, "Analytic model for electromagnetic fields in the bubble regime of plasma wakefield in non-uniform plasmas," *Phys. Plasmas*, vol. 24, no. 10, p. 103 104, Oct. 2017. doi:10.1063/1.4996856.

[27] M. V. Ammosov, N. B. Delone, and V. P. Krainov, "Tunnel ionization of complex atoms and atomic ions in electromagnetic field," *Proc. SPIE.*, vol. 0664, 1986.

[28] C. B. Schroeder *et al.*, "Thermal emittance from ionization-induced trapping in plasma accelerators," *Phys. Rev. ST Accel. Beams*, vol. 17, p. 101 301, 2014. doi:10.1103/PhysRevSTAB.17.101301.

[29] Y. Xi *et al.*, "Hybrid modeling of relativistic underdense plasma photocathode injectors," *Phys. Rev. ST Accel. Beams*, vol. 16, p. 031 303, 2013. doi:10.1103/PhysRevSTAB.16.031303.

[30] X. L. Xu *et al.*, "Phase-space dynamics of ionization injection in plasma-based accelerators," *Phys. Rev. Lett.*, vol. 112, p. 035 003, 2014. doi:10.1103/PhysRevLett.112.035003.

[31] C. Nieter and J. R. Cary, "VORPAL: a versatile plasma simulation code," *J. Comput. Phys.*, vol. 196, pp. 448–473, 2004. doi:10.1016/j.jcp.2003.11.004.

[32] M. Xie, "Design optimization for an X-ray free electron laser driven by SLAC linac," in *Proceedings Particle Accelerator Conference*, vol. 1, Dallas, TX, USA: IEEE, 1995, pp. 183–185. doi:10.1109/PAC.1995.504603.

ISBN: 978-3-95450-220-2 ISSN: 2673-5474 doi: 10.18429/JACoW-FEL2022-TUP39

IMPROVING THE REALISTIC MODELING OF THE EEHG SEED SECTION IN START TO END SIMULATIONS

P. Niknejadi*, S. Ackermann, P. Amstutz, M. Dohlus, E. Ferrari, T. Lang, G. Paraskaki, L. Schaper, E. Schneidmiller, S. Schreiber, M. Vogt, M. Yurkov, DESY 22607 Hamburg, Germany
W. Hillert, F. Pannek, D. Samoilenko, Institute for Experimental Physics
University of Hamburg 20148 Hamburg, Germany
S. Reiche, Paul Scherrer Institut 5232 Villigen PSI, Switzerland
F. Curbis, M. Pop, Lund University and MAX IV Laboratory 22484 Lund, Sweden

Abstract

A tunable and multicolor light source with near Fourier-limited pulses, controlled delay, and fully coherent beam with precisely adjustable phase profiles enables state-of-the-art measurements and studies of femtosecond dynamic processes with high elemental sensitivity and contrast. The start-to-end (S2E) simulations efforts aim to take advantage of the available global pool of software and past and present extensive efforts to provide realistic simulations, particularly for cases where precise manipulation of the beam phase space is concerned. Since tracking of beams with billions of particles through magnetic structures and handover between multiple codes are required, extensive realistic studies for such cases are limited. Here we will describe a workflow that reduces the needed computational resources for the echo-enabled harmonic generation (EEHG) seed section of the FLASH2020+ project.

INTRODUCTION

The rapid progress in the field of x-ray free-electron lasers (XFELs) has opened a new era for photon science [1–4]. The progressively improved properties of x-rays have led to sources with higher brightness by ten orders of magnitude over previously available sources. Consequently, modeling and diagnostics of current and future XFELs have become more and more challenging. For instance, modeling externally seeded free-electron laser (FEL) requires noise suppression and smooth handshaking between multiple codes [5–13]. At FLASH, the first high-gain FEL, an upgrade with a strong emphasis on the research and development towards a fully coherent light source is ongoing. This upgrade program, FLASH2020+ [14,15], peruses high-harmonic generation at high repetition rates in a superconducting seeded FEL. One of this program's goals is to study advanced concepts in beam dynamics, accelerator, and FEL physics through realistic and reliable S2E simulations.

A BRIEF OVERVIEW OF METHODS

In the past year, our focus has been mainly on improving EEHG [16] modeling, which needs multiple handovers between particle tracking and FEL codes. Due to the fine structure of the electron beam in the EEHG scheme, the task involves simulating a large number of particles, which requires a large amount of memory and and limits the possible studies to be conducted on electron beam properties, FEL performance, and properties of the output radiation. The relevant parameters are listed and discussed in reference [14]. In Fig. 1, the adopted workflow for the FLASH2020+ upgrade [15] simulation is shown above the dashed line. In addition, a few of the simulation codes [17–19] reviewed for short segments of the beamline are also listed below the line.

Electron Beam

Seeded FEL output's sensitivity to electron parameter deviations or jitters plays an essential role in the machine's stability. In ideal simulations, we often ignore or isolate the effects of chirp [20], inter-beam scattering, and coherent or incoherent synchrotron radiation [21]. Realistic modeling of the electron beam in the seed section would require (1) starting the simulations in the seed section with a high number of particles and (2) altering simulation codes for chicanes and modulators. To achieve the former, earlier steps of simulations, i.e., gun, and acceleration, need to be modeled with a high number of particles. Therefore, for the full S2E, the electron beam is simulated in sub-bunches using ASTRA [5]. The realistic acceleration and compression are modeled in Impact-Z [6]. However, since these two steps are computationally expensive and time-consuming, elegant and SelaV were benchmarked against Impact-Z for "quiet start" simulations to speed up the scans needed for determining the optimal working points [7,8,11]. While Impact-Z simulations are still in progress, the preliminary optimized beam in elegant is matched and transported to the start of the seed section and then upsampled to be a suitable input for the FEL codes. A detailed analysis is performed to understand contributing factors to microbunching and complement the S2E simulations [22,23]. More importantly, these studies help identify the simulation artifacts, mainly in the noise distribution, in simulations and improve the model.

For the latter, the challenge is up and downsampling the beam for transition between elegant and FEL codes in the seed section. For instance, the genesis output at each modulator's end needs to be downsampled to be a suitable input file for elegant simulations in each chicane. While large particle files are often downsampled for plotting and output of PIC simulations for plasma-accelerators are upsampled

* pardis.niknejadi@desy.de

ISBN: 978-3-95450-220-2 ISSN: 2673-5474 doi: 10.18429/JACoW-FEL2022-TUP39

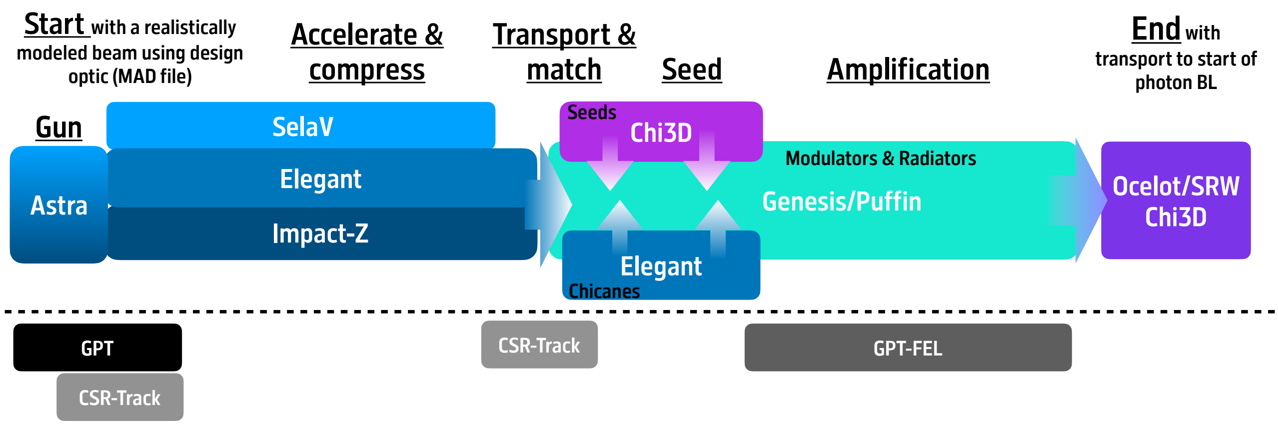

Figure 1: Workflow for the S2E simulations for the FLASH2020+ upgrade

for compact plasma-based FEL S2E simulations, the fine structures of the beam in the EEHG scheme poses additional challenges [24]. For this case, several methods of beam manipulation were studied and compared.

Laser Beam

Studying the impact of laser jitter and imperfections is equally crucial for the Seeded XFEL. For this purpose, S2E simulations of seed lasers are performed in Chi3D [10], which can model the propagation and nonlinear interaction of ultra-short laser pulses in isotropic and birefringent media. The typical output of Chi3D is intensity distribution in space and time as well as peak power and phase. Proper handshaking between Chi3D and FEL codes ensures that all essential frequency content is included. Scans with an ideal laser beam [25] and analytical studies also complement the S2E simulation with realistic seed inputs.

FEL Radiation Fields

The spectral and temporal structure of the radiation pulses in the Seeded FEL can be tailored to the specific needs of many experiments or novel FEL developments such as THz or cavity FEL experiments. In many cases, the fields describing the output of the XFEL are used as input for further simulations. Therefore, dedicated studies to benchmarking a few widely used codes [10, 26, 27] in the post-radiation stage are also part of the S2E simulation workflow.

SUMMARY

The relative plenitude of the computing resources and ease of international collaboration in recent years has significantly contributed to evaluating past efforts, benchmarking different simulation codes, and more accurate studies. These efforts have culminated in a paper, "Review of the state-of-the-art simulation codes for linear particle accelerator based XFELs" [28]. This paper focuses on a subset of available simulation codes which have been continuously upgraded along with the needs of the accelerator and FEL physics community or codes that have been developed recently to answer some of the mentioned needs. Additionally, the comparison and analysis of the methods and workflow presented here will be summarized in another forthcoming paper.

ACKNOWLEDGEMENTS

The authors gratefully acknowledge the Gauss Centre for Supercomputing e.V. (www.gauss-centre.eu) for funding this project by providing computing time through the John von Neumann Institute for Computing (NIC) on the GCS Supercomputer JUWELS [29] at Jülich Supercomputing Centre (JSC). This work is also supported by BMBF within "05K2019-STAR" project.

REFERENCES

[1] P. Emma *et al.*, *Nat. Photonics*, vol. 4, pp. 641–647, 2010. doi:10.1038/nphoton.2010.176

[2] E. Allaria *et al.*, *Nat. Photonics*, vol. 6, pp. 699–704, 2012. doi:10.1038/nphoton.2013.277

[3] E. Hemsing *et al.*, *Nat. Photonics*, vol. 10, pp. 512–515, 2016. doi:10.1038/nphoton.2016.101

[4] P. R. Ribič *et al.*, *Nat. Photonics*, vol. 13, pp. 555–561, 2019. doi:10.1038/s41566-019-0427-1

[5] K. Floettmann "ASTRA", Aug 2022, https://www.desy.de/~mpyflo

[6] J. Qiang *et al.*, *Journal of Computational Physics* vol. 163, pp. 434–451, 2000. doi:10.1006/jcph.2000.6570

[7] P. Amstutz, "SelaV1D", Jun 2022, https://selav.desy.de

[8] P. Amstutz, presented at the FEL2022, Trieste, Italy, Aug. 2022, paper WEBI1, this conference.

[9] T. Lang, "Chi2D and Chi3D ", Aug 2022, http://www.chi23d.com

[10] T. Lang *et al.*, presented at the FEL2022, Trieste, Italy, Aug. 2022, paper TUP43, this conference.

[11] M. Borland, in *Proc. 6th International Computational Accelerator Physics Conference (ICAP 2000)*, September 11-14, 2000, Darmstadt, Germany LS-287, doi:10.2172/761286

ISBN: 978-3-95450-220-2 ISSN: 2673-5474 doi: 10.18429/JACoW-FEL2022-TUP39

[12] S. Reiche, *Nucl. Instr.*, vol. 429, pp. 243-248, 1999. doi:10.1016/S0168-9002(99)00114-X

[13] L. T. Campbell and B. W. J. McNeil, *Phys. Plasm.*, vol. 19, 093119, 2012. doi:10.1063/1.4752743

[14] L. Schaper *et al.*, *Appl. Sci.*, vol. 11, p. 9729, 2021. doi:10.3390/app11209729

[15] E. Ferrari *et al.*, presented at the FEL2022, Trieste, Italy, Aug. 2022, paper TUP42, this conference.

[16] G. Stupakov, *Phys. Rev. Lett.*, vol. 102, p. 074801, 2009. doi:10.1103/PhysRevLett.102.074801

[17] M. J. de Loos and S. B. van der Geer, "General Particle Tracer: A New 3D Code for Accelerator and Beamline Design", in *Proc. EPAC'96*, Sitges, Spain, Jun. 1996, paper THP001G, pp. 1245 – 1247.

[18] A. Fisher *et al.*, *Phys. Rev. Accel. Beams*, vol. 23, pp. 110702, 2020. doi:10.1103/PhysRevAccelBeams.23.110702

[19] M. Dohlus and T. Limberg, "CSRtrack", Aug 2022, https://www.desy.de/fel-beam/csrtrack/

[20] E. Hemsing, *et al. Phys. Rev. Accel. Beams*, vol. 20, p. 060702, 2017. doi:1103/PhysRevAccelBeams.20.060702

[21] S. Di Mitri and S. Spampinati, *Phys. Rev. Accel. Beams*, vol.20, p. 120701, 2017. doi:10.1103/PhysRevAccelBeams.20.120701

[22] D. Samoilenko *et al.*, presented at the FEL2022, Trieste, Italy, Aug. 2022, paper TUP74, this conference.

[23] D. Samoilenko *et al.*, "Discussion on CSR instability in EEHG Simulation", in *Proc. IPAC'21*, Campinas, Brazil, May 2021, pp. 1622–1625. doi:10.18429/JACoW-IPAC2021-TUPAB103

[24] D. Samoilenko *et al.*, "Sensitivity of EEHG Simulations to Dynamic Beam Parameters", in *Proc. IPAC'22*, Bangkok, Thailand, Jun. 2022, pp. 1463–1466. doi:10.18429/JACoW-IPAC2022-TUPOMS024

[25] F. Pannek *et al.*, presented at the FEL2022, Trieste, Italy, Aug. 2022, paper TUP73, this conference.

[26] O. Chubar *et al.*, *Proc. SPIE 4769*, vol. 4769, Optical Design and Analysis Software II, 2002. doi:10.1117/12.481182

[27] I. Agapov *et al.*, *Nuclear Inst. and Methods in Phys. Research Section A* Vol. 768, pp. 151-156, 2014. doi:10.1016/j.nima.2014.09.057

[28] P. Niknejadi *et al.*, in preparation.

[29] D. Alvarez, *Journal of large-scale research facilities*, vol. 7, p. A183, 2021. doi:10.17815/jlsrf-7-183

ISBN: 978-3-95450-220-2 ISSN: 2673-5474 doi: 10.18429/JACoW-FEL2022-TUP40

SIMULATIONS OF SEEDING OPTIONS FOR THz FEL AT PITZ

G. Georgiev*, P. Boonpornprasert, M. Krasilnikov, X.-K. Li
Deutsches Elektronen-Synchrotron DESY, Zeuthen, Germany
W. Hillert, University of Hamburg, Hamburg, Germany

Abstract

A THz FEL is under commissioning at PITZ as a proof-of-principle experiment for a high power and high repetition rate THz source and as an option for THz-driven experiments at the European XFEL. Some of these experiments require excellent coherence and CEP stable THz pulses. In SASE regime, the coherent properties of the FEL radiation are limited. A seeding scheme can be used instead of SASE to improve the coherent properties and shot-to-shot stability. Several options for seeding are considered in simulation for the THz FEL at PITZ: external laser pulse, pre-bunched electron beam, energy modulated electron beam and additional short spike on top of a smooth beam profile. The improvements over SASE in energy, spectral and temporal stability of the THz pulse are presented.

INTRODUCTION

The scientific opportunities of using terahertz (THz) radiation in modern x-ray free electron lasers (FELs) are recognized by the user community of the European XFEL [1]. Intense THz pulses are required for research of non-linear physics in THz-driven pump-probe experiments. The desired THz source is high-power, tunable and operates at a high repetition rate. An accelerator-driven source is a promising option. One concept of accelerator-driven source that matches the requirements is a THz FEL. At present, a proof-of-principle experiment of THz FEL source has achieved first lasing at the Photo Injector Test Facility at DESY in Zeuthen (PITZ) [2]. For this experiment, a LCLS-I undulator was installed in a second tunnel as an extension to the already existing PITZ accelerator.

In addition to high intensity, the ideal THz source should deliver identical and carrier-envelope phase stable pulses with good synchronization (low arrival time jitter). Typically in SASE regime FELs demonstrate significant shot-to-shot fluctuation due to the stochastic nature of the SASE process. This fluctuation manifests itself as final intensity, arrival time and spectral profile differences between shots of the FEL. To achieve more stable shot-to-shot performance, a seeding method is applied to the FEL. Several seeding options are studied in simulation for the THz FEL at PITZ and a summary of the results is given in this text.

SEEDING OPTIONS

The simulations are performed for four seeding options:

- External laser pulse,
- Pre-bunched electron beam [3],
- Energy modulated electron beam, and
- Short electron beam spike on top of main beam current profile.

A common FEL seeding method is the inclusion of a laser pulse along the electron beam in the undulator. In this setup, the FEL acts as an amplifier and inherits the coherent properties of the initial seeding radiation. The main simulation parameter of this seeding option is the seeding pulse power - it has to dominate over the beam noise.

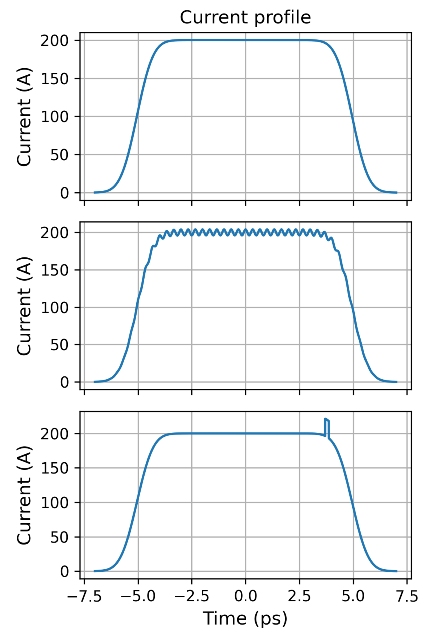

Figure 1: Electron beam current profile for SASE (top), pre-bunched beam with $b = 10^{-2}$ (center) and short 25 A spike (bottom).

Another technique is to deliver longitudinally density-modulated electron beam with the same periodicity as the FEL radiation, also called pre-bunched electron beam, to the undulator. An example is shown in the middle plot of Fig. 1, note the relatively small modulation amplitude. The main parameter of the simulation is the initial bunching factor b [4] given by:

$$b = \frac{1}{N_e}\left|\sum_{k=1}^{N_e} \mathrm{e}^{-i\omega t_k}\right|, \quad (1)$$

where ω is the FEL resonant frequency, N_e is the number of electrons/macroparticles in the beam and t_k is the time coordinate of the kth particle. Sufficient pre-bunching will drive the FEL process and define the properties of the radiation pulse. The density-modulations generated in the simulation code Genesis 1.3 [5] for different bunching values are shown in Fig. 2.

* georgi.georgiev@desy.de

ISBN: 978-3-95450-220-2 ISSN: 2673-5474 doi: 10.18429/JACoW-FEL2022-TUP40

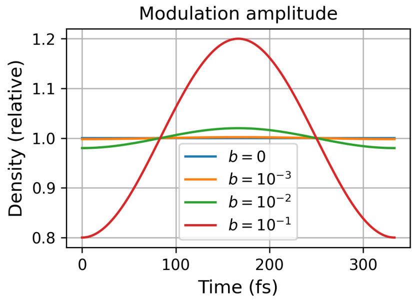

Figure 2: Electron beam current modulation along the duration of one period for different bunching values.

An alternative to pre-bunched beams is sending into the undulator a beam with periodic energy modulation along the beam at the resonant FEL frequency. As the beam travels through the undulator, the energy modulation drives the microbunching process. The main simulation parameter is the amplitude of the energy modulation.

Finally, a seeding option is to introduce a short spike on top of smooth beam current profile that is shorter than the radiation wavelength. Such a spike will radiate coherently from the start of the undulator. The spike radiation acts as a seeding signal that is amplified by the main electron beam in the FEL. A proper position of the spike for this model beam is at the tail of the main electron beam as shown in Fig. 1 bottom plot. Because of the slippage between the radiation and the electron beam inside the undulator, the radiation pulse will move forward relative to the electron beam. Therefore the emission from a seeding spike at the tail of the beam will move towards the head of the beam and the seeding signal will eventually cover the entire beam.

SIMULATION SETUP

The simulations are performed for model electron beams using Genesis 1.3 [6] version 2. While this version is not the most recent, it applies space-charge effects during simulation, which are relevant for the PITZ FEL parameter space. The parameters of the simulated lattice with LCLS-I undulator are given at the top of Table 1. Key beam parameters are given at the bottom of Table 1. The beam emittance and energy spread are assumed to be similar to experiments for few nC-charge beams [7]. The beam current profile is a flat-top with 10 ps FWHM and 2 ps rise time, shown in Fig. 1 top plot, however it may differ depending on the seeding method applied. The current profile is a model for the simulations and not a beam profile measured in experiments. The particle coordinates are generated in a quasi-random fashion to ensure that the macro-particle shot-noise is suppressed at the resonance frequency [5].

SIMULATION RESULTS

The simulation results are presented in Figs. 3 to 6 and for SASE in Table 2. The results for each method are based on 100 shots statistics with different seed number given to the particle generator in the simulation code. The final pulse energy is the average over all shots and the energy fluctuation is calculated as one standard deviation of the energy at the undulator exit. The arrival time for each shot is the time of the centroid of the radiation pulse. Then the arrival time jitter is one standard deviation of the arrival times of all shots. The spectrum fluctuation Δ_s is estimated with the formula:

$$\Delta_s = \frac{\sum \sigma_i}{\sum a_j}, \tag{2}$$

where a_j is the average spectral power of all shots at jth wavelength of the discrete simulation spectum and σ_i is the standard deviation of the spectral power at ith wavelength. The above formula can be derived from

$$\Delta_s = \frac{\sum (\sigma_i/a_i)w_i}{\sum w_j}, \tag{3}$$

where σ_i/a_i is the relative deviation of the spectral power at ith wavelength and $w_i = a_i$ are weights for each wavelength point.

Table 1: Simulation parameters

Parameter	Value
Undulator parameter	3.49
Period length	30 mm
Number of periods	113
Start/end drift	105 mm
Resonant frequency	3 THz
Peak current	200 A
Duration, FWHM	10 ps
Emittance (x, y)	4 mm mrad
Mean energy	17.06 MeV
Energy spread	85.3 keV

Table 2: SASE FEL performance

Parameter	Value
Final energy	35 μJ
Energy fluctuation	27 μJ
Arrival time jitter	667 fs
Spectrum fluctuation	0.826

The results of the simulation with external seeding laser pulse are shown in Fig. 3. At the lowest laser power, there is a relatively small improvement to SASE. When the external pulse power is increased, all studied FEL-pulse parameters continuously improve. At 1 kW laser power the FEL performance is significantly improved compared to SASE.

The bunching factor of pre-bunched beam simulations is scanned from 10^{-6} to 10^{-2} and shown in Fig. 4. Up to bunching factor of 10^{-5}, there is no significant seeding effect and between bunching of 10^{-5} and 10^{-4} there is an improvement of the FEL efficiency. Passing that point, all four parameters are improved with increased bunching factor.

ISBN: 978-3-95450-220-2 ISSN: 2673-5474 doi: 10.18429/JACoW-FEL2022-TUP40

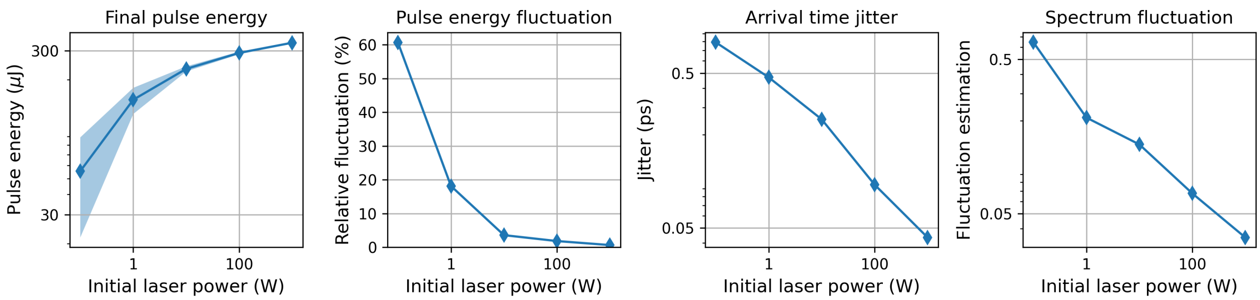

Figure 3: Summary of simulation results with external laser seeding. The laser power varies from 100 mW to 1 kW.

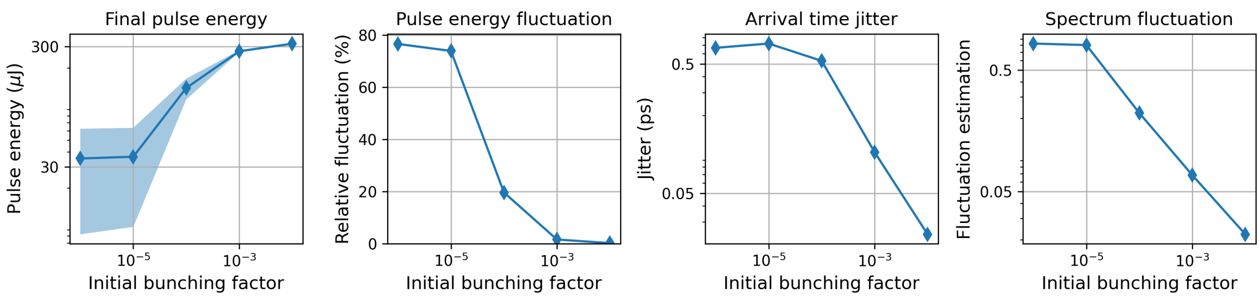

Figure 4: Summary of simulation results with pre-bunched electron beam. The bunching factor varies from 10^{-6} to 10^{-2}.

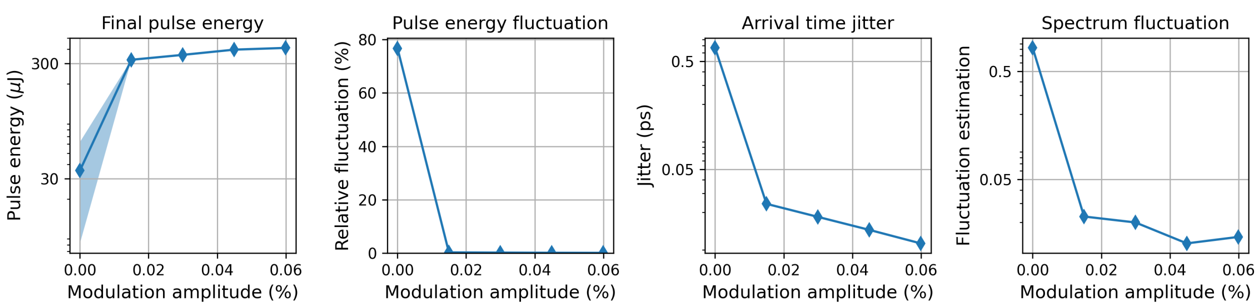

Figure 5: Summary of simulation results with energy modulated electron beam. The modulation amplitude spans from 0 to 10.2 keV.

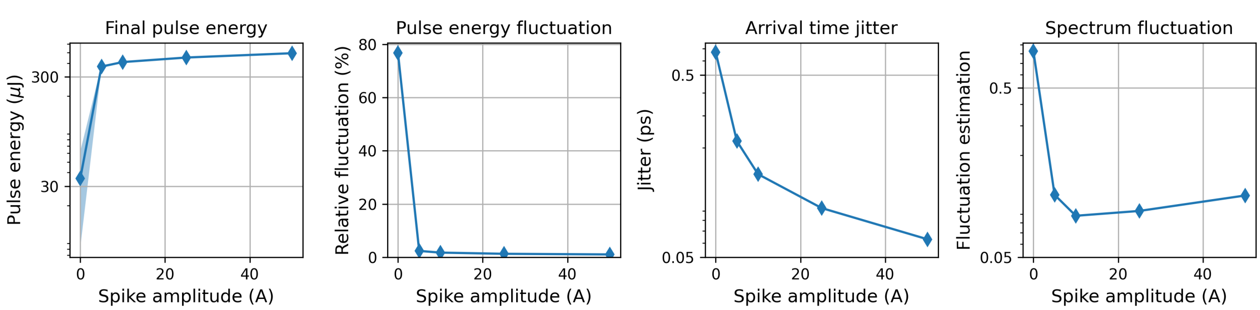

Figure 6: Summary of simulation results with additional short spike for spike currents 0, 5, 10, 25, 50 A.

With an energy modulation amplitude of 2.56 keV (0.015 % of the average electron energy) there is strong seeding effect. Such amplitude of the modulation is difficult to observe, since it is much smaller than the uncorrelated energy spread of 0.5 %. Nevertheless at that point, the FEL is clearly not in SASE regime as indicated by the plots in Fig. 5. One possible explanation is the quick evolution of the energy modulation into bunching with a factor above 10^{-4} in the drift before the undulator. Further increase of

ISBN: 978-3-95450-220-2 ISSN: 2673-5474 doi: 10.18429/JACoW-FEL2022-TUP40

the energy modulation amplitude in the shown range does not change the FEL performance significantly.

Finally, results with a short spike added near the tail of the electron beam are shown in Fig. 6. The spike is created by rearranging macroparticles and increasing the current accordingly. The spike is a flattop with a duration half of that of the radiation period. Adding a 5 A spike to the main electron beam is enough to apply seeding in this simulation. Further increase in the spike current decreases the arrival time jitter and there is minimum of spectral fluctuation at 10 A point.

Overall, significant gains in the FEL performance and stability are achieved in all of the simulated seeding options. For any of them with strong seeding applied, the final FEL pulse energy exceeds 300 µJ while the energy fluctuation is 1 % or lower. Also, the arrival time jitter is below 67 fs (1/5th of the radiation period). Finally, the spectral fluctuation estimation falls under 0.1 (for a short spike, it is 0.088 at 10 A). In comparison to the SASE performance in Table 2, there is a clear improvement.

OUTLOOK

The simulation results thus far are a showcase for the four seeding methods with flattop model beam with 200 A current, but they may not be a complete and fair comparison. The actual choice of seeding method for PITZ also depends on the availability of the method and the electron beam preparation in an experiment. It is challenging to find a suitable and affordable THz source for a seeding pulse in the present. Delivering a pre-bunched beam in the undulator is a promising method for seeding and sub-THz current modulations were observed experimentally at PITZ [8]. The main difficulties of the method are beam transport with space-charge forces and higher modulation frequencies. A solution to the latter is a development of modulation harmonics by non-linear space-charge oscillations during beam transport [9]. Energy modulation can be achieved with a dielectric lined waveguide in the beam path [10], but it is not easy to achieve modulation frequency as high as 3 THz. Finally, a short spike may be generated by hitting the photocathode with two laser pulses simultaneously. One laser pulse is high intensity and smooth over time while the other laser pulse has short duration. The optical beamline and electron transport are left as concerns for this two laser setup.

CONCLUSION

In simulation with model flattop 200 A electron beam, all studied seeding options bring significant improvements to the FEL efficiency and shot-to-shot stability. The necessary seeding strength for each method is also indicated in the presented simulation results. Since overall the seeding effect is comparable in all options, there is a free choice of the most appropriate seeding method to be implemented in PITZ, with most to date research performed for pre-bunched beams.

ACKNOWLEDGEMENTS

This work was supported by the European XFEL research and development program. The author wants to additionally thank Georgia Paraskaki, Fabian Pannek and Anusorn Lueangaramwong from DESY for the helpful discussions.

REFERENCES

[1] P. Zalden *et al.*, "Terahertz science at European XFEL," 2018.

[2] M. Krasilnikov *et al.*, "First lasing of the THz SASE FEL at PITZ," Trieste, Italy, Aug. 2022, this conference, paper MOA08.

[3] R. Huang *et al.*, "Design of a pre-bunched THz free electron laser," *Particles*, vol. 1, no. 1, pp. 267–278, 2018. doi:10.3390/particles1010021

[4] E. Saldin, E. Schneidmiller, and M. V. Yurkov, *The physics of free electron lasers*. Springer Science & Business Media, 1999.

[5] S. Reiche, "Numerical studies for a single pass high gain free-electron laser," DESY, Tech. Rep., 2000.

[6] S. Reiche, "Update on the FEL Code Genesis 1.3," in *Proc. FEL'14*, Basel, Switzerland, Aug. 2014, pp. 403–407. https://jacow.org/FEL2014/papers/TUP019.pdf

[7] X. Li *et al.*, "Matching of a space-charge dominated beam into the undulator of the THz SASE FEL at PITZ," in *Proc. IPAC'21*, Campinas, Brazil, May 2021, pp. 3244–3247. doi:10.18429/JACoW-IPAC2021-WEPAB257

[8] G. Georgiev *et al.*, "Beam preparation with temporally modulated photocathode laser pulses for a seeded THz FEL," in *Proc. IPAC'21*, Campinas, Brazil, May 2021, pp. 2866–2869. doi:10.18429/JACoW-IPAC2021-WEPAB115

[9] P. Musumeci, R. K. Li, and A. Marinelli, "Nonlinear longitudinal space charge oscillations in relativistic electron beams," *Phys. Rev. Lett.*, vol. 106, p. 184 801, 18 2011. doi:10.1103/PhysRevLett.106.184801

[10] F. Lemery *et al.*, "Passive ballistic microbunching of nonultrarelativistic electron bunches using electromagnetic wakefields in dielectric-lined waveguides," *Phys. Rev. Lett.*, vol. 122, no. 4, p. 044 801, 2019. doi:10.1103/PhysRevLett.122.044801

ISBN: 978-3-95450-220-2 ISSN: 2673-5474 doi: 10.18429/JACoW-FEL2022-TUP41

FIRST DEMONSTRATION OF PARALLEL OPERATION OF A SEEDED FEL AND A SASE FEL

S. Ackermann, Ph. Amstutz, F. Christie, E. Ferrari, S. Hartwell, M.M. Kazemi, P. Niknejadi, G. Paraskaki, J. Rönsch-Schulenburg, S. Schreiber, M. Vogt, L. Schaper, J. Zemella,
Deutsches Elektronen-Synchrotron DESY, Hamburg, Germany
E. Allaria, Elettra-Sincrotrone Trieste S.C.p.A., Triest, Italy
W. Hillert, S. Mahmoodi, F. Pannek, D. Samoilenko, A. Thiel,
Hamburg University, Hamburg, Germany

Abstract

The FLASH facility houses a superconducting linac powering two FEL beamlines with MHz repetition rate in 10 Hz bursts. Within the FLASH2020+ project, which is taking care of facility development, one major aspect is the transformation of one of the two FEL beam lines to deliver externally seeded fully coherent FEL pulses to photon user experiments. At the same time the second beam line will use the SASE principle to provide photon pulses of different properties to users. Since the electron beam phase space conducive for SASE or seeded operation is drastically different, here a proof-of-principle experiment using the existing experimental seeding hardware has been performed demonstrating the possibility of simultaneous operation. In this contribution we will describe the setup of the experiment and accelerator. Finally, we will discuss the results and their implications also for the FLASH2020+ project.

INTRODUCTION

FLASH, the Free-Electron Laser user facility in Hamburg, has been delivering high brilliance soft X-ray FEL pulses for user experiments since 2005 [1, 2]. Also, FLASH had been equipped with hardware to study seeded FELs [3]. To address the growing demand of beam time requests, the facility has been upgraded with a second FEL beam line in 2014 [4]. The next upgrade project, FLASH2020+ [5, 6], aims for several augmentations of the facility. Two key components are the higher electron beam energy of now 1.35 GeV and the implementation of external seeding, namely HGHG [7, 8] and EEHG [9] at the high repetition rates FLASH can offer.

Experimental Setup Within the User Facility

The FLASH FEL, as seen in Fig. 1, is driven by a superconducting linear accelerator and can provide up to 800 electron bunches, separated by 1 μs per so-called macro pulse. The bunches can be divided between FLASH1 and FLASH2 during each macro pulse, expending about 50 μs of the burst. This also allows for different RF-parameters for the two bunch trains. The macro pulses are generated at a repetition rate of 10 Hz. In the FLASH1 electron beam line, just upstream the SASE undulators, the experimental seeding hardware called Xseed is located. The setup consists of a seed laser injection where two seeds of a wavelength of 267 nm are coupled in the last dipole of the energy collimation area. For the laser-electron interaction, two planar electromagnetic modulators of orthogonally oriented deflection planes are used, separated by a dispersive chicane of sufficient strength for EEHG seeding. A second, less strong dispersive section completes the modulation section. The electron beam then passes to 10 m of radiator undulators, before the generated radiation is reflected into a diagnostic section inside another chicane. The electron beam is transported through a transverse deflecting structure and dipole magnet before it hits a screen and finally a diagnostic beam dump. During user operation none of the aforementioned components are influencing the beam. Due to the limited repetition rate of the used laser system only one bunch per macro pulse can be used for experimental seeding, while the remaining burst can be used for FLASH2.

EXPERIMENTAL SETUP

The experimental program to achieve parallel operation as a side goal was conducted in June 2021. The parameters used for the demonstration of true parallel operation can be found in Table 1.

Table 1: Parameters Used During the Demostration of Parallel Operation

Electron bunch		
Energy	E	685 MeV
Charge	C	400 pC
Duration	$\tau_{\mathrm{e,rms}}$	391 fs
Peak current	A_{peak}	770 A
Norm. emittance	ε_{x}	0.68 mm mrad
	ε_{y}	0.48 mm mrad
Mismatch para.	μ_{x}	1.10
	μ_{y}	1.07
Mismatch ampl.	M_{x}	1.56
	M_{y}	1.44
Dispersion	D_{x}	≤ 5 mm
	D_{y}	≤ 10 mm
Seed laser		
Wavelength	λ_{seed}	267 nm
Duration	$\tau_{\mathrm{seed,fwhm}}$	200 fs

Six-Dimensional Overlap

The six-dimensional overlap between electron bunch and seed laser pulses at each modulator is achieved by first using

ISBN: 978-3-95450-220-2 ISSN: 2673-5474 doi: 10.18429/JACoW-FEL2022-TUP41

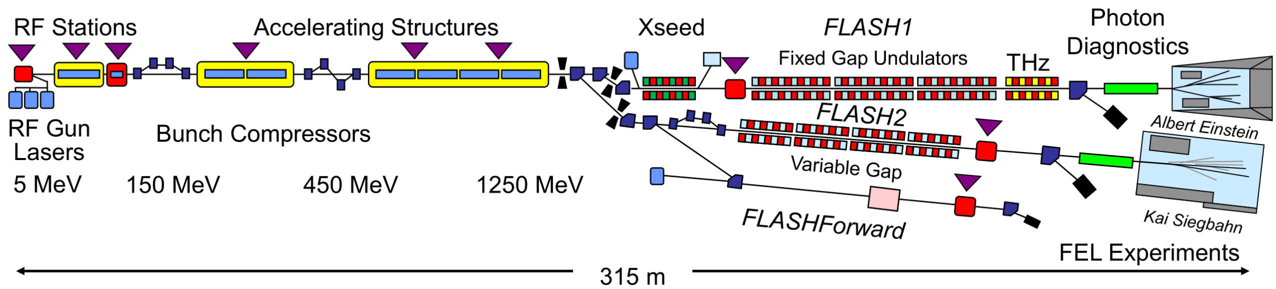

Figure 1: Layout of the FLASH user facility at the time of the experiment in 2021.

screens upstream and downstream of the respective modulator to find spatial overlap. The spectral overlap is ensured by exciting the electromagnetic modulators to the correct currents and tuning the radiator gaps for the correct wavelength of the 7th harmonic of the seed laser. Then the timing between electron beam and seed laser is scanned until the interaction is observable on the image of the transverse deflecting structure as in Fig. 2.

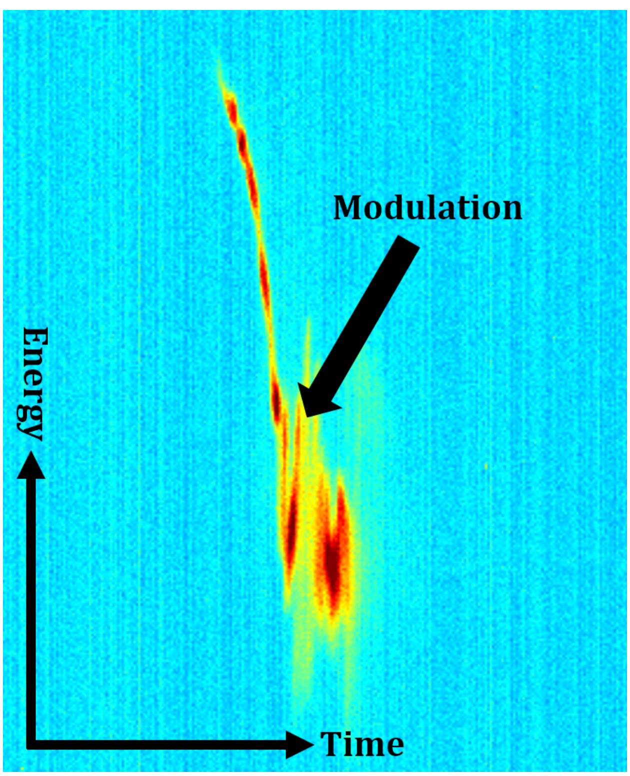

Figure 2: Image of the longitudinal phase-space distribution of the electrons within the bunch after passing the transverse deflecting structure and spectrometer dipole.

In parallel, the FLASH2 beam line was tuned for generation of SASE radiation.

RESULTS

Since the energy detector, a micro channel plate, is also sensitive to the seed laser and electromagnetic showers due to beam losses it is crucial to check that the signal observed is

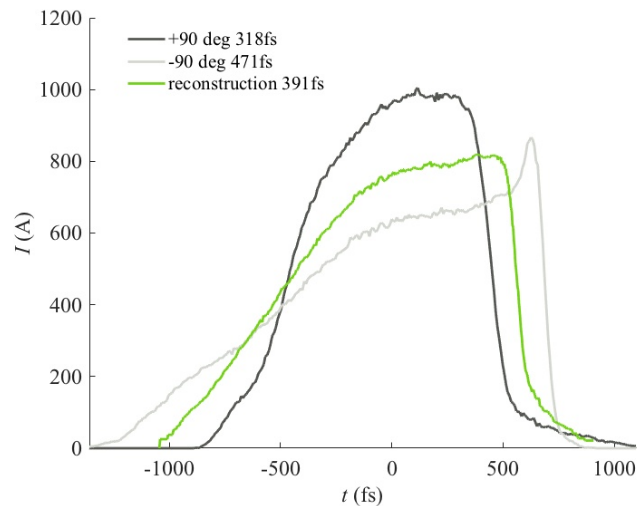

Figure 3: Measurement result of the transverse deflecting structure LOLA with a bunch length of about 391 fs and a peak current of about 770 A.

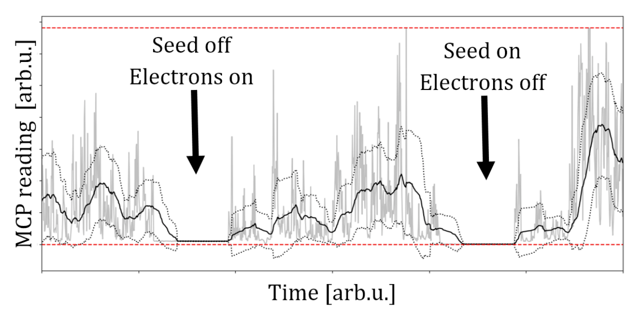

Figure 4: MCP signal. The larger signals come from the seeded radiation and show larger fluctuations. The first dip with visible radiation remaining shows the SASE radiation only, while the second dip shows that without the electron beam, the seed laser is not able to produce a signal exceeding the noise background of the MCP/ADC combo.

really generated by the seeding process. First, the seed laser is off, thus one would expect a lower, yet non-zero, photon pulse energy as the partially compressed electron bunch still generates SASE radiation. This is visible within Fig. 4 where the first dip is where the seed laser was switched off. Here, the SASE signal is clearly lower than the seeded one while still clearly exceeding zero. The second dip in the same

ISBN: 978-3-95450-220-2 ISSN: 2673-5474 doi: 10.18429/JACoW-FEL2022-TUP41

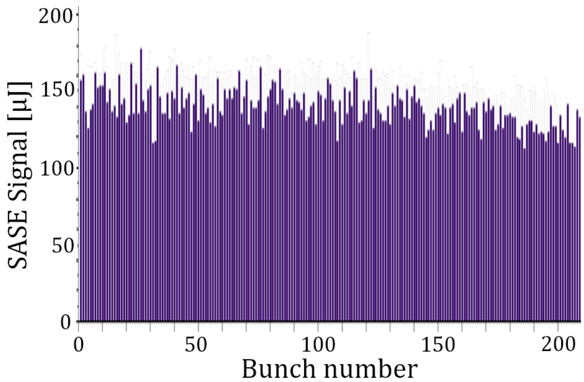

Figure 5: Screenshot of the control system panel showing the SASE pulse energy measured by a gas detector monitor in FLASH2 for a bunch train consisting of 210 bunches. The image shows the electron signal of the GMD, thus the per-pulse produced FEL photon pulse energy.

figure shows the MCP reading when the seed laser is on, but no electron beam present. Here, the signal completely vanishes into the noise floor of the used MCP/ADC combo. With those two measurements one can conclude that the radiation measured on the MCP is requiring the electron beam and laser seed pulse alike, thus it is indeed a seeded signal.

At the same time these experiments were performed the SASE signal at the FLASH2 beamline was exceeding 150 μJ for each of the 210 electron bunches sent to the beam line (see Fig. 5). Again, it is very important to note that the seeded signal was observed at the exact same time when FLASH2 was lasing with this performance.

SUMMARY AND OUTLOOK

We have shown that the setup of a seeded FEL at FLASH1 and a SASE FEL at FLASH2 are not mutually excluding each other. Decent SASE performance can be achieved at the same time as a seeded FEL is operated. This is an important result for FLASH, as it aims to be the first user facility at MHz repetition rate to use a SASE and a seeded FEL beam line simultaneously.

REFERENCES

[1] W. Ackermann *et al.*, "Operation of a free-electron laser from the extreme ultraviolet to the water window", *Nat. Photon.*, vol. 1, no. 6, p. 336, Jun. 2007. doi: 10.1038/nphoton.2007.76

[2] S. Schreiber, "First Lasing in the Water Window with 4.1nm at FLASH", in *Proc. FEL'11*, Shanghai, China, Aug. 2011, pp. 164–165, paper TUOBI2.

[3] S. Ackermann *et al.*, "Generation of Coherent 19-and 38-nm Radiation at a Free-Electron Laser Directly Seeded at 38 nm", *Phys. Rev. Lett.*, vol. 111, no. 11, p. 114801, Sep. 2013. doi: 10.1103/PhysRevLett.111.114801

[4] B. Faatz *et al.*, "Flash II: Perspectives and challenges", *Nucl. Instrum. Methods Phys. Res., Sect. A*, vol. 635, no. 1 supplement , pp. S2 – S5, Apr. 2011. doi: 10.1016/j.nima.2010.10.065

[5] M. Beye (*ed.*), "FLASH2020+: Making FLASH brighter, faster and more flexible:Conceptual Design Report", Deutsches Elektronen-Synchrotron, DESY, Hamburg, 2020. doi: 10.3204/PUBDB-2020-00465

[6] E. Allaria *et al.*, "FLASH2020+ Plans for a New Coherent Source at DESY", in: *Proc. IPAC'21*, Campinas, SP, Brazil, May 2021, pp. 1581-1584. doi: 10.18429/JACOW-IPAC2021-TUPAB086

[7] L. Yu, "Generation of intense uv radiation by subharmonically seeded single-pass free-electron lasers", *Phys. Rev. A*, vol. 44, pp. 5178–5193, Oct. 1991. doi: 10.1103/PhysRevA.44.5178

[8] L. Yu and J. Wu, "Theory of High Gain Harmonic Generation: an Analytical Estimate", *Nucl. Instrum. Methods Phys. Res., Sect. A*, vol. 483, pp. 493–498, May 2002. doi: 10.1016/S0168-9002(02)00368-6

[9] D. Xiang and G. Stupakov, "Echo-enabled harmonic generation free electron laser", *Phys. Rev. ST Accel. Beams*, vol. 12, p. 030702, Mar 2009. doi: 10.1103/PhysRevSTAB.12.030702

ISBN: 978-3-95450-220-2 ISSN: 2673-5474 doi: 10.18429/JACoW-FEL2022-TUP42

STATUS OF THE SEEDING UPGRADE FOR FLASH2020+ PROJECT

E. Ferrari*, S. Ackermann, M. Beye, I. Hartl, S. Hartwell,
T. Lang, S. Mahmoodi, M. Mohammad Kazemi, P. Niknejadi, G. Paraskaki,
L. Schaper, S. Schreiber, M. Tischer, P. Vagin, J. Zemella, J. Zheng
Deutsches Elektronen-Synchrotron (DESY), Hamburg, Germany
Enrico Allaria Elettra-Sincrotrone Trieste S.C.p.A., Basovizza, Italy.
Margarit Asatrian, Wolfgang Hillert, Fabian Pannek, Dmitrii Samoilenko, Andreas Thiel
University of Hamburg, Hamburg, Germany.

Abstract

In the framework of the FLASH2020+ project, the FLASH1 beamline will be upgraded to deliver seeded FEL pulses for users. This upgrade will be achieved by combining high gain harmonic generation and echo-enabled harmonic generation with a wide-range wavelength–tunable seed laser, to efficiently cover the 60-4 nm wavelength range. The undulator chain will also be refurbished entirely using new radiators based on the APPLE- III design, allowing for polarization control of the generated light beams. With the superconducting linac of FLASH delivering electron beams at MHz repetition rate in burst mode, laser systems are being developed to seed at full repetition rates. In the contribution, we will report about the progress of the project.

INTRODUCTION

In the context of the FLASH2020+ project, the whole FLASH machine is undergoing a notable series of upgrades and refurbishments that include the installation of a laser heater, exchange of bunch compressor chicanes as well as an electron beam energy upgrade. They will be realized during two long shutdown periods, the first ending in August 2022 and the next one scheduled for July 2025.

Full seeding capabilities will be implemented at the FLASH1 beamline to provide users with fully coherent and stable FEL radiation at the Fourier limit, with continuous wavelength tunability below 40 nm and full wavelength range spanning from 60 to 4 nm. Polarization control will also be available. All of the above, combined with the high burst repetition rate of FLASH, will provide the user community with a unique lightsource in the VUV soft-X-ray wavelength range.

In Fig. 1, the envisioned FLASH footprint at the end of the upgrade project FLASH2020+ [1] is shown. The machine operation concept will rely on the a single superconducting linac feeding both FEL beamlines in parallel. The bunch properties will need to be compatible both with seeded and SASE operation on FLASH2. To achieve this, a large linear energy chirp will be present for FLASH1 in order to allow for further compression in FLASH2, as well as downstream FLASH1 for THz production. Such operational mode was already successfully demonstrated last year [2].

To implement seeding in FLASH1, we anticipate to utilize two harmonic generation seeding approaches for efficiently cover the tuning range for users, namely HGHG [3] and EEHG [4]. For the longer wavelengths (>20 nm), we foresee to employ HGHG. In fact, by looking at the bunching curve as a function of the harmonic number as reported in Fig. 2, one can observe the higher efficiency in generating coherent bunching of HGHG than for EEHG in this wavelength range.. For harmonic numbers $\gtrsim 15$, i.e., for shorter wavelengths, we plan to rely on EEHG.

Such an ambitious upgrade requires new dedicated state-of-the-art seed lasers and laser transport beamlines, new modulators and radiators undulators, magnetic chicanes, as well as numerical simulations to investigate and optimize the setup.

SIMULATIONS

An extensive series of numerical simulations have been performed for optimizing the setup, using different numerical codes. For the electron part we used a combination of elegant [5] and selav [6], that provide fast exploration of the electron beam properties considering collective effects along the linac. Up to now the input beam distribution has been self-generated, but we plan in the next few months to start using realistic beam distributions generated via ASTRA [7]. For the FEL process we use GENESIS1.3v4 code [8]. The seed laser is also fully simulated using [9].

Three different working points, with electron beam energies of 750, 950 and 1350 MeV, represent our baseline. We plan to have full start-to-end simulations for the linac and FLASH1 beamline soon. For this, we developed a comprehensive toolkit with handshaking between the different codes [10]. Such an approach allows for investigating the impact on the FEL output of different machine parameters. As an example, we evaluated the impact of the large residual linear energy chirp needed for parallel operation on the performance of both HGHG and EEHG. By proper tuning of the resonances, we were able to recover similar FEL pulses as in the case when the beam is flat. We also investigated the power jitter variations of the two seed lasers on the EEHG scheme [11]. We also benchmarked EEHG performance using elegant, in particular to investigate the impact of collective effects, e.g. CSR, on the output radiation properties [12]. Concerning the choice of seeding technique to utilize around the transition in efficiency, see Fig. 2, we performed simula-

* eugenio.ferrari@desy.de

ISBN: 978-3-95450-220-2 ISSN: 2673-5474 doi: 10.18429/JACoW-FEL2022-TUP42

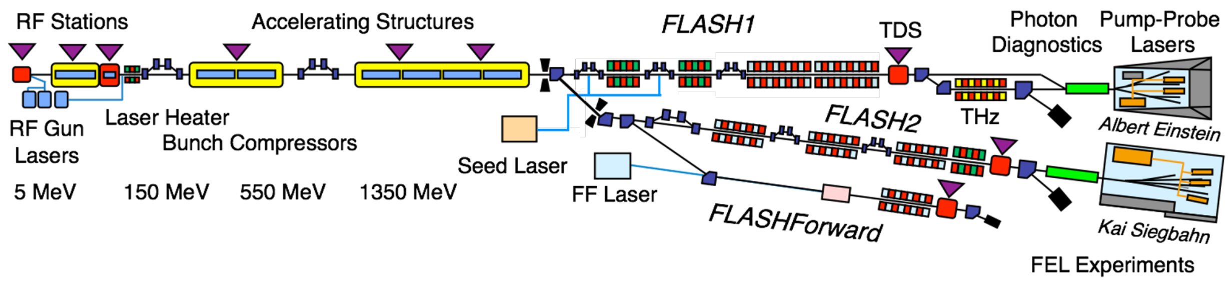

Figure 1: Envisioned FLASH footprint at the end of FLASH2020+ project. The whole machine will undergo a notable series of upgrades and refurbishments, including the installation of a laser heater, exchange of bunch compressor chicanes as well as an electron beam energy upgrade. Full seeding capabilities will be implemented in the FLASH1 beamline.

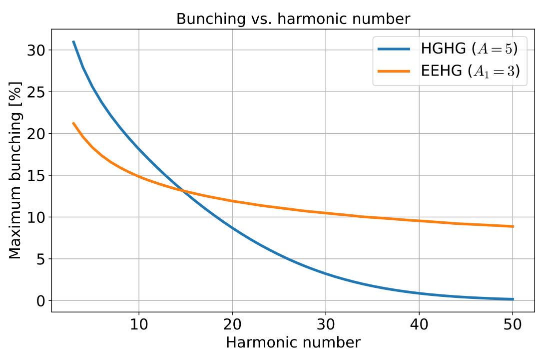

Figure 2: Comparison of the maximum obtainable bunching factor for HGHG and EEHG, according to the equations in [3, 4]. One can notice that for harmonic numbers $\gtrsim 15$, i.e., for shorter wavelengths, EEHG has significantly higher bunching, with reduced energy spread for better amplification. Parameters for HGHG: modulation amplitude $A = 5$, chicane strength B optimized for maximum bunching. Parameters for EEHG: $A_1 = 3$, $B_1 = 32.1$, A_2 and B_2 optimized for maximum bunching.

tions and numerical calculations looking at the performance of EEHG and HGHG [13].

SEED LASERS

A tunable seed laser system is needed in order to have tunable seeded FEL radiation. We will use an OPCPA based system with wavelengths between 297 and 317 nm, allowing for FEL emission in a gap-free spectrum below 40 nm, see Fig. 3.

In the case of EEHG, the first seed will be operated at fixed wavelength of 343 nm. It will be a part of the laser at the end of amplification, branched before seeding the OPCPA. We envision to have the tunable laser almost always on the second modulator, closer to the radiators in order to reduce possible space charge effects when transporting microbunched beams [14].

The parameters for both seed lasers are specified keeping in mind that the beamline will need to provide stable FEL radiation for users in a reliable manner. Hence, it requires

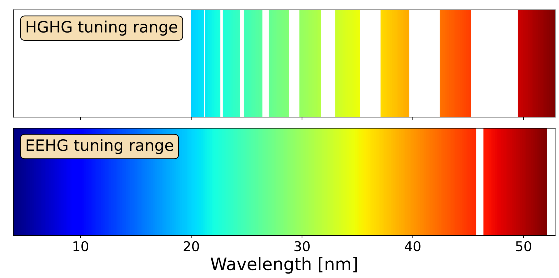

Figure 3: Comparison of the tuning range for the seeded FLASH1 beamline in the case of HGHG and EEHG. Using a seed laser with tuning range of 297–317 nm allows full continuous tunability in EEHG for wavelengths shorter than 40 nm. In the case of EEHG, $n = [-1, -2, -3]$ are considered.

a robust laser system with limited time available for maintenance, as this will generate operational downtimes. The laser system needs to match the repetition rate of FLASH, 10 Hz, as well as the train at 1 MHz internal repetition rate, to realize a fully seeded, high repetition rate source. The pulse duration of Seed1 will be fixed at 500 fs, while Seed2 will be much shorter, on the order of 50 fs as it determines the FEL pulse duration. The chirp for Seed2, which directly influences the output properties of the FEL radiation, will need to be minimized and to stay as constant as possible when changing the laser wavelength. The beam size at the interaction point, located in the middle of each modulator, will be on the order of 600 µm, larger than the electron beam in order to accommodate possible transverse jitters. The transverse position will need to be maintained stable, with maximum variation of 50 µm (rms). The timing stability will need to be better than 50 fs between both lasers, and between the lasers and the electron beam. To satisfy these requirements, both the transverse and the longitudinal alignments will be maintained using feedback loops.

The required wavelength stability for Seed2 will be on the order of 2×10^{-4}, while the time required for wavelength changes less than 10 s for 5% of the tunability range, and 2 minutes for the full wavelength range. This will enable users to perform quick wavelength scans using the FEL radiation. Both lasers will need to deliver hundreds of MW power

ISBN: 978-3-95450-220-2 ISSN: 2673-5474 doi: 10.18429/JACoW-FEL2022-TUP42

for satisfying the seeding requirements. As the laser power fluctuations directly induce FEL output power fluctuations, the seed lasers need to be stable within 2% shot-to-shot and within 4% train-to-train.

The laser system is partially already running for testing and development, in the newly constructed seed laser laboratory located at the FLASH2 extraction. For further details about the laser systems, see [15].

SEED LASER TRANSPORT

We plan to define a handshake position for each of the two seed lasers, located on the laser table in the laser laboratory. The transport will deliver the laser pulses using full Rayleigh imaging from this location till the center of the corresponding modulator. The full laser transport will be enclosed in UHV environment, in order to minimize both the contamination on the optics, as well as to preserve the laser beam properties from degradation due to nonlinear effects.

We will try to maintain the system as simple as possible, reducing the amount of optics and motors inside the tunnel. The optics will be optimized for maximum reflectivity in the wavelength range and specific for each of the seed lasers. The last mirror for each of the two injections will be in machine vacuum, mounted on a remotely controlled manipulator to allow for establish and maintain the transverse alignment between the electrons and the laser. We investigated in a dedicated experiment the minimum distances from the electron beam that will be required to not induce surface charge accumulation, which in turn would negatively impact the trajectory stability.

In the case of Seed2, due to damage threshold concerns, we will utilize different concepts to reduce the risk of damaging the optics and increasing the downtime for users. We will employ both multi-reflection setups, as well as very shallow incidence angles to increase the effective beam size on the optics themselves, thus reducing the effective peak intensity.

For further details concerning the laser transport, see [16].

UNDULATORS AND CHICANES

The whole FLASH1 beamline will be refurbished and most of the undulators will be exchanged. The two modulators will be two identical undulators, longer than the ones presently used for the Xseed project [17] and with adequate periodicity for ensure optimal resonance along the whole seed laser tuning range. We foresee the installation of at least three magnetic chicanes, bending the beam in the vertical direction. They will be used to create the required offset with the electron beam, allowing for the injection of the two seed lasers for EEHG in the corresponding modulators, as well as to provide the tunable longitudinal dispersion required. When using HGHG we plan to simply close the shutter of Seed1 and open modulator1, as well as set the sheering chicane straight. This allows for maintaining the tunable laser on modulator2, hence obtaining tunable seeded FEL radiation in the longer wavelength range. We will keep the option of delivering Seed2 in the first modulator to explore advanced modes, based, e.g., on the optical klystron scheme [18, 19].

For the radiators, we plan to utilize 2.5 m APPLE-III type devices to provide users with variable polarization FEL radiation [20] along the full wavelength range of the beamline. The beamline has sufficient length for 11 cells for possible radiators and will initially be filled depending on budget constraints. Also in the initial phase, we plan to re-use the existing planar devices presently installed for the Xseed experiments for beam transport purposes.

To simplify operations at longer wavelengths, e.g., by shifting the source position towards the users and reduce possible clipping due to the beam pipe, we plan to install further magnetic chicanes in possible empty slots along the beamline. This will also allow us to further explore advanced FEL modes. For further information concerning the undulator beamline design, see [21].

CONCLUSION

We presented the status of the upgrade towards full seeded FLASH1 in the context of the FLASH2020+ project. The progress in the design and realization of the components is on schedule. The installation of the required components will start in 2024 and we foresee the commissioning to start taking place with the 2025 FLASH restart.

FLASH1 will be a unique lightsource, capable of providing users with high repetition, fully coherent and stable FEL radiation with polarization control, at the Fourier limit in the VUV soft-X-rays from 60 to 4 nm.

REFERENCES

[1] L. Schaper *et al.*, "FLASH2020+ project progress: current installations and future plans", presented at the FEL2022, Trieste, Italy, Aug. 2022, paper TUP51, this conference.

[2] S. Ackermann *et al.*, "First demonstration of parallel operation of a seeded FEL and a SASE FEL", presented at the FEL2022, Trieste, Italy, Aug. 2022, paper TUP41, this conference.

[3] L.H. Yu, "Generation of intense uv radiation by subharmonically seeded single-pass free-electron lasers", *Phys. Rev. A*, vol. 44, pp. 5178–5193, 1991. doi:10.1103/PhysRevA.44.5178

[4] G. Stupakov, "Using the beam-echo effect for generation of short-wavelength radiation", *Phys. Rev. Lett.*, vol. 102, p. 074801, 2009. doi:10.1103/PhysRevLett.102.074801

[5] M. Borland, "elegant: a flexible SDDS-compliant code for accelerator simulation", 2000. doi:10.2172/761286

[6] https://selav.desy.de

[7] http://www.desy.de/~mpyflo/

[8] https://github.com/svenreiche/Genesis-1.3-Version4

[9] http://www.chi23d.com

ISBN: 978-3-95450-220-2 ISSN: 2673-5474 doi: 10.18429/JACoW-FEL2022-TUP42

[10] P. Niknejadi *et al.*, “Improving the realistic modelling of the EEHG seed section in start to end simulations”, presented at the FEL’2022, Trieste, Italy, Aug. 2022, paper TUP39, this conference.

[11] F. Pannek *et al.*, “Sensitivity of echo-enabled harmonic generation to seed power variations”, presented at the FEL’2022, Trieste, Italy, Aug. 2022, paper TUP73, this conference.

[12] D. Zhou *et al.*, “Calculation of the CSR effect in EEHG simulations”, presented at the FEL’2022, Trieste, Italy, Aug. 2022, paper TUP74, this conference.

[13] F. Pannek *et al.*, “Comparison of the Spectro-Temporal Properties of Echo-Enabled and High-Gain Harmonic Generation Free-Electron Laser Pulses at the 15th Harmonic”, presented at the FEL’2022, Trieste, Italy, Aug. 2022, paper TUP72, this conference.

[14] S. Khan *et al.*, “Bunching evolution in drifts”, presented at the FEL’2022, Trieste, Italy, Aug. 2022, paper MOP01, these proceedings.

[15] E. Allaria *et al.*, “High repetition rate, ultra-low noise and wavelength stable UV seed laser system for tunable two-color EEHG FEL seeding”, presented at the FEL’2022, Trieste, Italy, Aug. 2022, paper TUP43, this conference.

[16] M.M. Kazemi *et al.*, “Towards seeded high repetition rate FEL: Concept of seed laser beam transport and incoupling”, presented at the FEL’2022, Trieste, Italy, Aug. 2022, paper TUP45, this conference.

[17] L. Schaper *et al.*, “Flexible and coherent soft X-ray pulses at high repetition rate: current research and perspectives”, *Appl. Sci.*, vol. 11, no. 20, 9729, 2021. doi:10.3390/app11209729

[18] H. Sun *et al.*, “High repetition rate seeded free-electron laser with a harmonic optical klystron in high-gain harmonic generation”, presented at the FEL’2022, Trieste, Italy, Aug. 2022, paper TUP69, this conference.

[19] G. Paraskaki *et al.*, “Impact of electron beam energy chirp on optical-klystron-based high gain harmonic generation”, presented at the FEL’2022, Trieste, Italy, Aug. 2022, paper TUP49, this conference.

[20] M. Tischer *et al.*, “Development of APPLE-III undulators for FLASH”, presented at the FEL’2022, Trieste, Italy, Aug. 2022, paper THBI1, this conference.

[21] J. Zemella and M. Vogt, “The new FLASH1 undulator beamline for the FLASH2020+ project”, presented at the FEL’2022, Trieste, Italy, Aug. 2022, paper TUP52, this conference.

ISBN: 978-3-95450-220-2 ISSN: 2673-5474 doi: 10.18429/JACoW-FEL2022-TUP43

HIGH REPETITION RATE, LOW NOISE AND WAVELENGTH STABLE OPCPA LASER SYSTEM WITH HIGHLY EFFICIENT BROADLY TUNABLE UV CONVERSION FOR FEL SEEDING

T. Lang †, M. M. Kazemi, J. Zheng, S. Hartwell, N. Hoang, E. Ferrari,
L. Schaper, I. Hartl
Deutsches Elektronen Synchrotron DESY, Hamburg, Germany
E. Allaria, Elettra-Sincrotrone Trieste S.C.p.A., Basovizza, Italy

Abstract

We present the concept and first results of new seed laser system for the FLASH2020+ project at the FLASH VUV/XUV FEL facility at DESY (Hamburg, Germany). One goal of the project is to build the first high repetition rate, fully coherent FEL light source worldwide ready for user operation in 2025 [1]. The novel optical parametric chirped pulse amplification seed laser system with highly-efficient, broadly-tunable UV conversion is designed to deliver UV pulse energies up to 100 µJ in two seed beams in order to allow for the Echo-Enhanced Harmonic Generation (EEHG) seeding scheme [2]. The temporal structure will match the burst pulse structure of FLASH which can operate with up to 6000 pulses in one second (1 MHz pulse train in 600 µs - 10 Hz bursts). We compare the first experimental results to a start-to-end simulation allowing to predict the system performance regarding tunability, beam quality, stability and pointing, depending on the measured input parameters and fluctuations of the high-power chirped pulse amplification is a pump laser.

INTRODUCTION

FLASH is up-to-date the only free electron laser facility worldwide delivering highly brilliant and spatially coherent VUV laser pulses with high repetition rates for user experiments in two parallel operating FEL beamlines FLASH1 and FLASH2. The facility is currently undergoing a major upgrade in which FLASH1 will be rebuild in order to support a fully spatially and temporally coherent FEL operation utilizing EEHG for gap-free wavelength tuning down to 4 nm and high gain harmonic generation (HGHG) for longer wavelengths between 20 nm to 60 nm.

For both HGHG and EEHG operation the seed laser system needs to provide high power, broadly wavelength tunable UV seeding pulses with excellent stability and beam quality. As illustrated in Fig. 1, the new concept uses two seed laser beams with fixed wavelength at 343 nm (Seed1) and wavelength tunable between 297 nm to 317 nm (Seed2) respectively for EEHG seeding. The HGHG seeding is planned to be operated with the wavelength tunable Seed2 only. The two laser beams will be spatially and temporally overlapped in two modulation undulators. In our design we use three different operational electron energies: 750, 950 and 1350 MeV. In order to imprint sufficient electron energy modulation, the seed laser system is designed to deliver UV pulse energies > 100 µJ and > 50 µJ for Seed1 and Seed2, respectively, while maintaining the high repletion rates of up-to 1 MHz (in-burst) of FLASH. In order to exploit the full capabilities of the narrow-band fully coherent FEL pulses for 24/7 scientific user experiments, the seed laser needs to provide widely tunable, high power UV laser pulses with pulse durations of 50 fs, excellent beam quality and exceptional high short and long-term stability in respect to the seeding wavelength ($< 2\cdot10^{-4}$), pulse-to-pulse energy (< 2%) and pointing jitter (< 20 µrad). Altogether, the requirements on the laser system are beyond state-of-the-art.

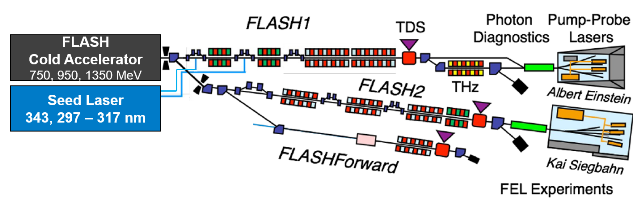

Figure 1: Layout of FLASH VUV/XUV FEL Facility.

Laser Concept

For a successful seeded FEL operation, the laser concept needs to provide stable high energetic, ultra-short UV pulses in combination with high repetition rates and ultra-broad wavelength tunability. Figure 2 shows a schematic of the concept and the power budget of the Seed2 optical chirped pulsed parametric amplification system (OPCPA). The OPCPA is pumped by a commercial Yb:YAG high-power chirped pulse amplifier (CPA, Trumpf/Amphos) and is followed by highly efficient broadband nonlinear UV conversion stages. The amplifier operates under non-thermal equilibrium condition. The 10 Hz pulsed operation with 600 µs long bursts at an in-burst repetition rate of 1 MHz allows for exceptional high in-burst average powers of up-to 5kW. The seed laser oscillator and the Ytterbium fiber laser front-end (FE, NKT-Photonics) provides two outputs. A first output providing 2 W average power is used for seeding the high-power CPA system. Its spectral bandwidth of 2 nm centred at 1030 nm is matched to the amplification bandwidth of the CPA system.

† tino.lang@desy.de

ISBN: 978-3-95450-220-2 ISSN: 2673-5474 doi: 10.18429/JACoW-FEL2022-TUP43

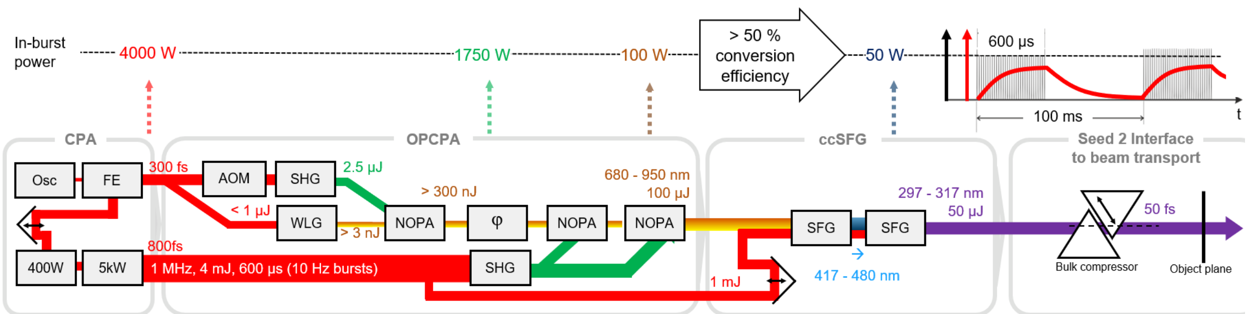

Figure 2: Schematic of all major sub-components of the wavelength tunable part of the seed laser system (SEED 2).

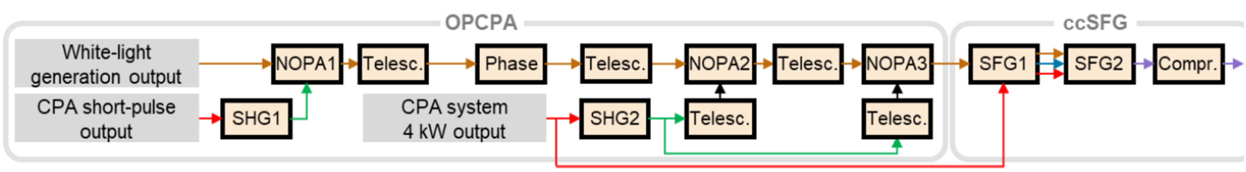

Figure 3: Building blocks of the start-to-end simulation including all second order nonlinear conversion stages as well as propagation and imaging effects.

The CPA system supports compressed pulses of 800 fs duration, which are frequency doubled for pumping the OPCPA. A second output provides laser pulses with 250 fs pulse duration and 5 µJ of pulse energy. This output drives both a filamentation process in a 5 mm YAG crystal to generate a stable white-light super-continuum, as well as first green pumped non-collinear optical parametric amplification (NOPA) to pre-amplify a broad range of the white-light spanning from 680 – 950. An accusto-optical modulator (AOM) in the pump arm of the OPCPA seed generation serves a pulse picker to cut a 1 MHz - 600 µs long pulse burst out of the 3 MHz second FE output port and as a fast actuator to compensate for any in-burst pulse-to-pulse or burst-to-burst energy dynamics in the final output of the seed laser system.

In order to be able to utilize a simple time delay between OPCPA pump and seed pulses for fast and precise wavelength tuning it is necessary to stretch the seed pulses. By applying approximately -8000 fs² of negative chirp (φ) using double chirped mirror pairs (DCMs) the temporal overlap with the < 800 fs green OPCPA pump pulse in the two sub-sequent non-collinear OPA stages (NOPA) results in an amplified spectral bandwidth which just supports the required 50 fs pulses duration. Please note, to the best of our knowledge, the OPCPA technology exclusively offers the advantage of very low heat dissipation in the nonlinear crystal allowing for stable high-power operation under the non-thermal equilibrium conditions as indicated by the red line in the schematic power vs. time plot in Fig. 2.

The negatively chirped tunable OPCPA signal pulses are further converted to the ultra violet spectral range within two sub-sequent sum frequency conversion stages. The cascaded nonlinear up-conversion mixing process using 1 mJ of the narrowband CPA pulses allows for an exceptional high conversion efficiency of more than 50 % (with respect to the OPCPA output) whereas the broad bandwidth, wavelength tunablity and the linear negative chirp, as well as the spatial phase of the of the OPCPA signal pulses are maintained. Due to the linear phase transfer in the conversion stages the negatively stretched UV seed pulses can be compressed utilizing simple UV grade fused silica bulk material. Another advantage of the described phase conservation is the possibility to generate a diverging UV beam which helps to reduce the peak intensity of the UV beam below the laser damage threshold for the first UV optics in the system within a practical propagation length.

The Seed1 beam is produced by comparatively simple third harmonic generation of the CPA output and will not be further discussed in this study.

Start-to-end Simulation and First Results

An extensive numerical study based on a 3+1 dimensional start-to-end simulation code (chi3D) allows for predictions of the entire system performance in terms of output power, tunability, beam quality and stability with respect of the measured input parameters and respective statistical fluctuations and systematic in-burst sweeps. Figure 3 shows the numerical simulation blocks as they map the actual concept of the laser system. The simulation allows for modeling of all nonlinear second order direct and cascaded conversion processes as well as self-phase modulation and self-focusing. The performance of the pump laser system and the super-continuum generation via filamentation in a YAG-crystal are the input parameters for the simulation. Table 1 summarizes the simulation results for the different sub-systems. The standard deviation of all simulation results can be calculated by repeating the simulation with normal distributed input parameters, namely the measured beam properties for the CPA system and the super-continuum generation including pulse energies, pulse durations, spectrum and phase, beam diameter and pointing. Exemplary for all results listed, Fig. 4 shows the UV

ISBN: 978-3-95450-220-2 ISSN: 2673-5474 doi: 10.18429/JACoW-FEL2022-TUP43

pulse energies and the respective histogram for all 467 individual start-to-end simulation runs. Each run was started with a set of random input parameters similar to the measured single shot instabilities and in-burst sweeps of pump laser and white-light seed in terms of: pulse energy, pulse duration, beam pointing and position as well as the relative pump-seed time delays in the NOPA stages.

Table 1: Simulation results listing the values and rms instabilities of each sub system

System	Sub-system	Property	Result
OPCPA	SHG 1	Pulse energy	2.85 µJ 0.3%
	NOPA 1 (PVWC)	Pulse energy	379 nJ 0.9%
	SHG 2	Pulse energy	1.75 mJ 0.5%
	NOPA 2 (TPG)	Pulse energy	29 µJ 5%
		Wavelength	763 nm 0.37 nm
	NOPA 3 (TPG)	Pulse energy	139 µJ 4.9%
		Wavelength	764 nm 0.38 nm
ccSFG	SFG 1	Pulse energy	150 µJ 4.3%
		Wavelength	438 nm 0.12 nm
	SFG 2	Pulse energy	71.6 µJ 2.1%
		Wavelength	307 nm 0.06 nm
		Fourier limit	52.6 fs 0.6%
	Compressor	Pulse duration (FWHM)	56 fs 0.6%
		Peak power	1.3 GW 2.7%

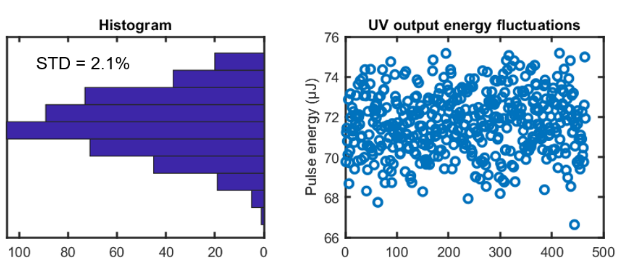

Figure 4: Simulation UV output pulse energy fluctuation and the corresponding histogram.

The theoretical results are confirmed by first experimental studies, showing an outstanding high broadband (50 fs transform limit) OPCPA-Signal to UV conversion efficiency of up to 68 % and excellent beam quality. Furthermore, the numerical predicated improvement of the UV pulse-to-pulse stability compared to the OPCPA output stability could be experimentally reproduced.

The experimental results of the first OPCPA stage (NOPA 1) are also in very good agreement with the simulation results.

CONCLUSION

In conclusion, we presented the concept and a sophisticated start-to-end simulation of the novel seed laser system which is currently under construction within the FLASH2020+ upgrade plan of the soft X-ray FEL facility FLASH at DESY in Hamburg, Germany. The simulation results validate the conceptual design. The simulated pulse energies, pulse durations and wavelength tunability meet the requirements for EEHG seeding of FLASH with a fair safety margin. The simulation results in terms of wavelength and pulse energy stability are very close to the required values. To meet all requirements with good safety margin, further measures for active stabilization of the output parameters are under investigation. Here we plan to utilize fast actuators and feed-forwards or feedback controls. We focus on a fast OPCPA seed-pump pulse timing stabilization as well as in-burst and burst-to-burst pulse energy stabilization using feedback control with the AOM in the pump beam of the first NOPA stage as fast actuator.

REFERENCES

[1] M. Beye, Ed., “FLASH2020+: Making FLASH brighter, faster and more flexible”: *Conceptual Design Report*. Deutsches Elektronen-Synchrotron, DESY, Hamburg, 2020. doi:10.3204/PUBDB-2020-00465

[2] L. Schaper *et al.*, “Flexible and Coherent Soft X-ray Pulses at High Repetition Rate: Current Research and Perspectival” *Appl. Sci.*, vol. 11, p. 9729, 2021. doi:10.3390/app11209729

ISBN: 978-3-95450-220-2 ISSN: 2673-5474 doi: 10.18429/JACoW-FEL2022-TUP44

PHASE-LOCKED HARD X-RAY SELF-SEEDING FEL STUDY FOR THE EUROPEAN XFEL

T. Long[1], S. Huang, K. Liu
State Key Laboratory of Nuclear Physics and Technology, Peking University, Beijing, China
Y. Chen, W. Decking, S. Liu*, N. Mirian, W. Qin
Deutsches Elektronen-Synchrotron (DESY), Hamburg, Germany
G. Geloni†, J. Yan, European XFEL, Schenefeld, Germany
[1]also at DESY, Hamburg, Germany

Abstract

Phase-locked pulses are important for coherent control experiments. Here we present theoretical analyses and start-to-end simulation results for the generation of phase-locked pulses using the Hard X-ray Self-Seeding (HXRSS) system at the European XFEL. As proposed by Sven Reiche *et al.* in "A perfect X-ray beam splitter and its applications to time-domain interferometry and quantum optics exploiting free-electron lasers", 2022, the method is based on a combination of self-seeding and fresh-slice lasing techniques. However, at variance with this reference, here we exploit different transverse centroid offsets along the electron beam. In this way we may first utilize part of the electron beam to produce SASE radiation, to be filtered as seed and then generate HXRSS pulses from other parts of the beam applying appropriate transverse kicks. The final result consists in coherent radiation pulses with fixed phase difference and tunable time delay within the bunch length. This scheme can be useful for coherent control applications such as coherent x-ray pump-probe experiments.

INTRODUCTION

Phase-locking means a fixed phase relation between successive pulses [1] and phase-locked pulses are important for coherent control experiments [2–4]. Usually a split-and-delay scheme is employed to generate phase-locked pulses in the optical to the extreme ultraviolet wavelengths, while it is challenging to produce phase-locked pulses down to the X-ray regime. X-ray free-electron lasers (FELs) deliver photon pulses with extremely high intensity and show remarkable capabilities for researches in physics, chemistry and biology [5,6]. Self-seeding schemes [7–10] can provide nearly fully coherent x-ray FELs and expand their application to a broader range [11]. Several methods have been proposed to generate coherent phase-locked X-ray pulses from externally seeded FELs [12–15] or using self-seeding techniques [16]. In the first case, the achievable wavelength is limited within the soft x-ray spectral region typical of the high gain harmonic generation configuration, while the second scheme can operate in both soft and hard X-ray regimes by properly choosing the self-seeding monochromators. In Ref. [16], the employed method is based on a combination of self-seeding and fresh-slice lasing techniques and can offer much higher phase stability than conventional X-ray split-and-delay approaches.

Here we present theoretical analyses and start-to-end simulation results for the generation of phase-locked pulses using the Hard X-ray Self-Seeding (HXRSS) system at the European XFEL. European XFEL is an X-ray FEL facility based on a superconducting linear accelerator [17]. After the collimation section that follows the main linac, there is an arc [18, 19] that bends selected electron beams from a bunch train to the hard x-ray FEL beamline SASE2, where the HXRSS system is built [20]. There are 35 undulator segments of 5 m length interspaced by 1.1 m sections with magnets elements. For the HXRSS system, two single crystal monochromators and chicanes are installed in two positions: one between 8th and 9th segments, the other one between 16th and 17th segments. This configuration provides the flexibility to increase spectrum signal-to-noise ratio by choosing one- or two-chicane scheme according to difference photon energies, and to mitigate crystal heat load effect by using two-chicane scheme for lower photon energies [20].

At variance with Ref. [16], where different lasing parts of the electron beam are defined by the slotted foil in a dispersion section, here we exploit different transverse centroid offsets along the electron beam. This offsets may be induced by collective coherent synchrotron radiation (CSR) effects [21,22] during the beam transport in the arc upstream of the SASE2 undulators. The method proposed here does not suffer from possible limitation on the beam repetition rate, while the spoiler technique employing slotted foil may do due to radiation losses [23]. In this way we may first utilize part of the electron beam to produce SASE radiation, which is monochromatized as coherent seed to trigger seeded lasing with other parts of the beam that are appropriately kicked on the undulator axis. The final result consists in phase-locked coherent radiation pulses with tunable time delay within the bunch length.

In the following, we will first introduce the slice centroid deviation based scheme to generate phase-locked HXRSS FEL, then CSR effect in the arc before SASE2 at the European XFEL is analysed. Finally the start-to-end simulation is presented.

* shan.liu@desy.de
† gianluca.aldo.geloni@xfel.eu

ISBN: 978-3-95450-220-2 ISSN: 2673-5474 doi: 10.18429/JACoW-FEL2022-TUP44

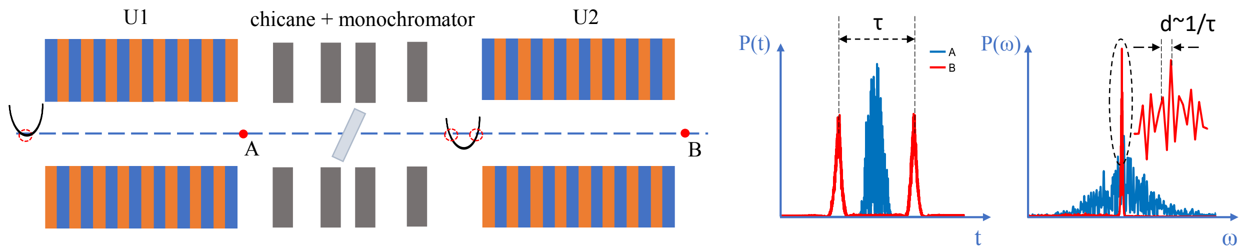

Figure 1: Schematic plot of phase-locked HXRSS FEL generation from electron beam with different slice centroid deviation. In the first undulator U1, the central part of electron beam is kicked on axis (dashed line) and radiate SASE. The SASE pulse is then monochromatized with a Bragg crystal and the electron beam bypasses the monochromator and is realigned with different parts on axis. The delayed electron beam overlaps with the monochromatized seeding wake to generate seeded pulses in the final undulator U2. Different lasing parts of the electron beam are indicated by red dashed circles. Plots on the right are power and spectrum distribution for both SASE and seeded pulses. A and B correspond to positions at the exit of U1 and U2, respectively. An enlarged plot is shown for the central part of the seeded spectrum, as denoted by the black dashed ellipse.

RESULTS

The proposed method for phase-locked HXRSS FEL generation is shown in Fig. 1, where an electron beam with parabolic or V-like shape with different slice centroid deviation is required. Different parts of electron beam lase separately in different stages, as the red dashed circles indicate. In the first stage, central part of electron beam is kicked with magnetic correctors on axis in undulator 1 (U1) for SASE radiation. For efficient interaction between electron beam and FEL pulse, the on-axis lasing part should have a radius approximated as [5] $\sigma_x \sim \sigma_r \sim \sqrt{\lambda_r L_g/(4\pi)}$, where λ_r is the FEL resonant wavelength and L_g the gain length. Other parts of the beam undergo betatron oscillation without lasing due to inefficient overlap with the radiation field, hence beam quality is preserved for these parts.

In the second stage, the SASE pulse is filtered by a single crystal monochromator to generate coherent seeding wake [7] while the electron beam is deflected and delayed by chicane and bypasses the monochromator. In the final stage, electron beam is kicked again with unspoiled parts on axis to overlap with the monochramatized wake to generate seeded lasing in undulator 2 (U2). Delay between the two lasing parts is determined by the kick amount and limited by electron bunch length and quality. The two lasing parts are seeded with the same coherent seed and generated seeded pulses are naturally phase-locked. Radiation power and spectrum are shown for both SASE and seeded lasing at the exit of U1 (A) and U2 (B), respectively. One can see in U1 a single SASE pulse is generated with a broad spectrum, while in U2 coherent twin pulses are generated with a much narrower spectrum. For phase-locked pulses, pulse delay τ in time domain corresponds to the spike distance d in frequency domain, where d $\sim 1/\tau$ and the spike width is inversely proportional to the pulse number (here it's two), as shown in the right plots, where the central part of the seeded spectrum is enlarged in the plugin.

The parabolic or V-like different slice centroid deviation is important for this method to work. Such beam shape can be generated with dispersion-based method [24], where sextupole magnets are placed in the dispersive sections for two-color pulse pairs generation utilizing beams with energy chirp. Here we present initial simulation results to show that it is possible to utilize CSR effect, which is always treated as detrimental in FEL facilities and many methods are proposed to suppress this effect [25, 26].

The desired centroid deviation is introduced through CSR effect, as shown in Fig. 2. Beam head is to the right in all the following figures. The beam transport simulation is carried out with the multi-physics software package OCELOT [27]. An ideal electron beam distribution with electron energy of 14 GeV, beam charge of 250 pC, guassian distribution both in longitudinal and transverse phase space is used as input before the arc, and the arc lattice remains the same with designed dispersion-free optics. It is shown that CSR dominates over other collective effects such as space charge and wakefield influence in the arc [28]. Here among these collective effects only CSR is considered.

The electron beam has a Gaussian current profile with peak value of around 5 kA and FWHM 15 µm. The whole beam slices have nearly zero initial centroid deviation in both transverse direction (Fig. 2(a)). Significant slice centroid deviation is observed after transport through the arc, especially in the horizontal direction x, as shown in Fig. 2(b). Also, energy modulation is induced through the arc, as shown in Fig. 2(c). The modulation process can be understood as that during the transport in the arc, CSR induces energy modulation in the first part of arc, then this energy chirp undergoes dispersion in the last part of arc and results beam centroid deviation at the arc exit. Though the net dispersion of the whole arc is zero, the final part is not. The induced energy chirp and beam centroid deviation is closely related to the beam current profile with a small shift of the maximum modulation position compared to the peak current position.

ISBN: 978-3-95450-220-2 ISSN: 2673-5474 doi: 10.18429/JACoW-FEL2022-TUP44

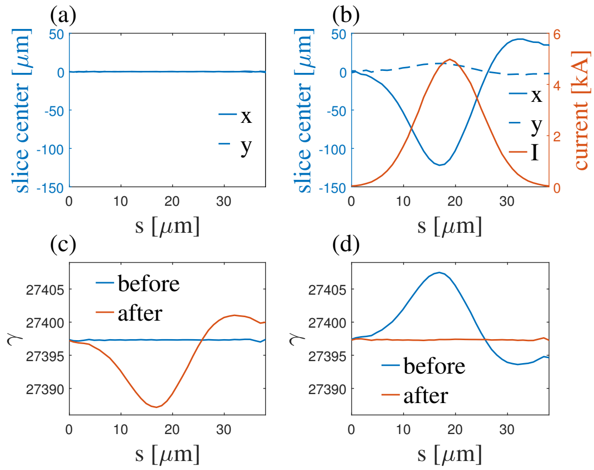

Figure 2: Beam slice properties before and after transport in arc with ideal initial beam distribution at arc entrance. (a) slice center before arc. (b) slice center after arc and beam current profile. (c) slice electron energy (γ) before and after arc. (d) same as (c) with different initial energy distribution.

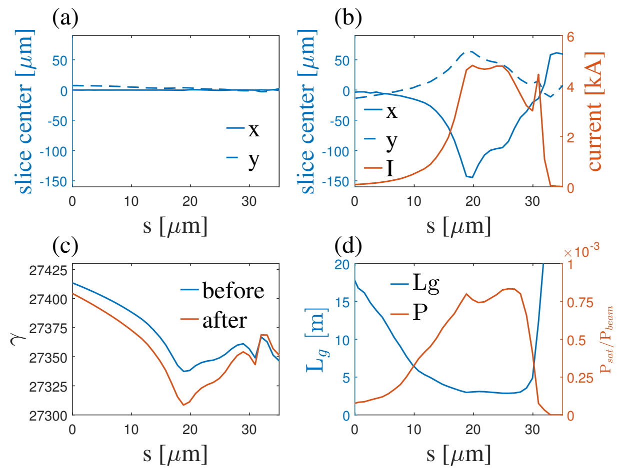

Figure 3: Beam slice properties before and after transport in arc with beam distribution from start-to-end simulation. (a) slice center before arc. (b) slice center after arc and current profile. (c) slice electron energy (γ) before and after arc. (d) theoretical slice gain length and normalized saturation power along the beam at the entrance of the SASE2 undulator beamline.

This shift results in an asymmetric current distribution in the two lasing beam parts in the final seeded lasing stage, which usually results in twin pulses with different power. It is interesting to note that if we use another ideal initial beam distribution with inverse energy modulation of red curve in Fig. 2(c), while other parameters remain the same, then we can get centroid deviated beam as shown in Fig. 2(b) and remove energy chirp as shown in Fig. 2(d) after transport in the arc. This may be beneficial for applications requiring beam centroid deviation while with constant beam energy. Simulations also show that if we turn off CSR effect there will be no energy modulation nor beam centroid deviation after transport in the arc.

Beam properties before and after transport in the arc from start-to-end simulation are shown in Fig. 3. We observe similar centroid deviation and energy modulations as in Fig. 2. Here, the current profile is much more complicated than the ideal Gaussian profile, however, the modulation shape also inherits the current profile with peak modulation position slightly shifted. In Fig. 3(b), horizontal slice centroid deviation at bunch position s=20 μm is x=-145 μm, while at s=17 μm and s=27 μm the two slices have same horizontal deviation of x=-82 μm. The deviation difference is around 63 μm and is larger than the typical transverse lasing width. In the following simulation we first kick slice at position s=20 μm on axis in U1 to radiate SASE then kick slices at s=17 μm and s=27 μm on axis in U2 for seeded lasing.

Beam quality for lasing is shown in Fig. 3(d), where the slice gain length L_g is calculated with Ming Xie's formula [29] and the normalized saturation power $P = P_{sat}/P_{beam}$ is calculated from [30] $P = 1.6\rho(L_{g0}/L_g)^2$ with resonant photon energy of 10 keV, where P_{sat} and P_{beam} are saturated radiation power and beam power, ρ is Pierce parameter, L_{g0} 1D gain length.

FEL lasing process is simulated with GENESIS [31]. We use the start-to-end simulated beam distribution as input at the undulator entrance and single shot simulation results are shown in Fig. 4, with resonant photon energy E_c=10 keV. For the first SASE stage, the gain length is around 3 m and we utilize the first 16 undulator segments, where radiation pulse energy reaches around 340 μJ at the exit of U1, as denoted by point A in Fig. 4(a). SASE power and spectrum are shown in Fig. 4(b) and (c), indicating a single pulse and broad spectrum. A diamond crystal with C(004) reflection and thickness of 100 μm is used to monochromatize the SASE pulse and chicane strength is tuned to delay electron beam by 15 μm to overlap with the seeding wake. The seeded lasing pulse energy increases from several μJ to 70 μJ at point B in the linear gain regime, 320 μJ at point C in saturation regime, and to post saturation with more than 690 μJ. Seeded FEL spectrum at point B is shown in Fig. 4(d). The coherent twin pulses are separated with 10 μm, this delay corresponds to spectrum spike distance of 0.124 eV. The plugin in Fig. 4(d) shows spectrum at [0, 1.24] eV, where one can find exactly 10 spikes in this range, which confirms phase-locking of the coherent twin pulses. However, due to the electron energy and current difference between the two lasing parts, the twin pulses have different power with slightly different central photon energy. The left pulse has lower power and higher photon energy, hence spectrum spikes are only found on the right side. Two spectrum envelopes emerge in saturation regime, as denoted by point C and Fig. 4(e) and (f). The seeded FEL has much narrower spectrum than SASE with FWHM less than 3 eV.

ISBN: 978-3-95450-220-2 ISSN: 2673-5474 doi: 10.18429/JACoW-FEL2022-TUP44

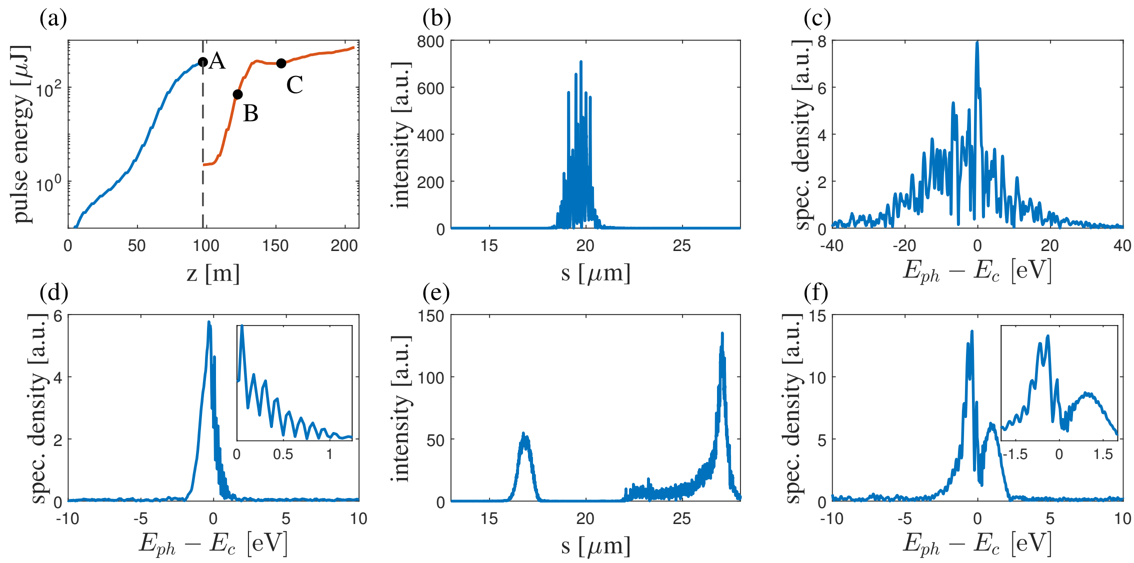

Figure 4: Radiation properties with beam distribution from start-to-end simulation. (a) pulse energy evolution along undulator for first SASE then seeded lasing stages in U1 and U2. (b) and (c) on-axis intensity and spectrum of SASE pulse at position A in (a). (d) on-axis seeded pulse spectrum at position B in (a). (e) and (f) on-axis intensity and spectrum of seeded pulse at position C in (a). The plugins in (d) and (f) show enlarged spectrum center.

CONCLUSION

In summary, a method utilizing different electron beam centroid deviation is proposed to generate phase-locked HXRSS FEL pulses. The centroid deviation can be induced by CSR effects when the beam is transported thorough an arc before the undulator beamline. Different beam parts are steered to lase seperately at different stages. This method is a combination of fresh slice and self-seeding techniques and is naturally suitable for high repetition rate operations. The proposed scheme may well facilitate the coherent x-ray pump-probe experiments.

ACKNOWLEDGEMENTS

We would like to acknowledge helpful discussions with N. Golubeva, S. Tomin and S. Walker. We would also like to thank R. Feidenhans'l for useful discussions and his interest in this work.

REFERENCES

[1] D. Oepts and W. Colson, "Phase locking in an infrared short-pulse free-electron laser", *IEEE J. Quantum Electron.*, vol. 26, no. 4, pp. 723–730, 1990. doi:10.1109/3.53390

[2] B. W. Adams *et al.*, "X-ray quantum optics", *J. Mod. Opt.*, vol. 60, no. 1, pp. 2–21, 2013. doi:10.1080/09500340.2012.752113

[3] S. T. Cundiff and S. Mukamel, "Optical multidimensional coherent spectroscopy", *Phys. Today*, vol. 66, no. 7, pp. 44–49, 2013. doi:10.1063/PT.3.2047

[4] K. Prince *et al.*, "Coherent control with a short-wavelength free-electron laser", *Nat. Photonics*, vol. 10, no. 3, pp. 176–179, 2016. doi:10.1038/nphoton.2016.13

[5] Z. Huang and K.-J. Kim, "Review of x-ray freeelectron laser theory", *Phys. Rev. Spec. Top. Accel Beams*, vol. 10, no. 3, p. 034801, 2007. doi:10.1103/PhysRevSTAB.10.034801

[6] J. C. Spence, U. Weierstall, and H. Chapman, "X-ray lasers for structural and dynamic biology", *Rep. Prog. Phys.*, vol. 75, no. 10, p. 102601, 2012. doi:10.1088/0034-4885/75/10/102601

[7] G. Geloni, V. Kocharyan, and E. Saldin, "A novel self-seeding scheme for hard x-ray FELs", *J. Mod. Opt.*, vol. 58, no. 16, pp. 1391–1403, 2011. doi:10.1080/09500340.2011.586473

[8] J. Amann *et al.*, "Demonstration of self-seeding in a hard-x-ray freeelectron laser", *Nat. Photonics*, vol. 6, no. 10, pp. 693–698, 2012. doi:10.1038/nphoton.2012.180

[9] I. Inoue *et al.*, "Generation of narrow-band x-ray free-electron laser via reflection self-seeding", *Nat. Photonics*, vol. 13, no. 5, pp. 319–322, 2019. doi:10.1038/s41566-019-0365-y

[10] I. Nam *et al.*, "High-brightness self-seeded x-ray free-electron laser covering the 3.5 kev to 14.6 kev range", *Nat. Photonics*, vol. 15, no. 6, pp. 435–441, 2021. doi:10.1038/s41566-021-00777-z

ISBN: 978-3-95450-220-2 ISSN: 2673-5474 doi: 10.18429/JACoW-FEL2022-TUP44

[11] C. Bostedt *et al.*, "Linac coherent light source: The first five years", *Rev. Mod. Phys.*, vol. 88, no. 1, p. 015007, 2016. doi:10.1103/RevModPhys.88.015007

[12] N. Thompson and B. McNeil, "Mode locking in a free-electron laser amplifier", *Phys. Rev. Lett.*, vol. 100, no. 20, p. 203901, 2008. doi:10.1103/PhysRevLett.100.203901

[13] D. Xiang, Y. Ding, T. Raubenheimer, and J. Wu, "Mode-locked multichromatic x rays in a seeded free-electron laser for single-shot x-ray spectroscopy", *Phys. Rev. Spec. Top. Accel Beams*, vol. 15, no. 5, p. 050707, 2012. doi:10.1103/PhysRevSTAB.15.050707

[14] D. Gauthier *et al.*, "Generation of phaselocked pulses from a seeded free-electron laser", *Phys. Rev. Lett.*, vol. 116, no. 2, p. 024801, 2016. doi:10.1103/PhysRevLett.116.024801

[15] A. Wituschek *et al.*, "Tracking attosecond electronic coherences using phase-manipulated extreme ultraviolet pulses", *Nat. Commun.*, vol. 11, no. 1, pp. 1–7, 2020. doi:10.1038/s41467-020-14721-2

[16] S. Reiche, G. Knopp, B. Pedrini, E. Prat, G. Aeppli, and S. Gerber, "A perfect x-ray beam splitter and its applications to time-domain interferometry and quantum optics exploiting free-electron lasers", *PNAS*, vol. 119, no. 7, p. e2117906119, 2022. doi:10.1073/pnas.2117906119

[17] W. Decking *et al.*, "A MHz-repetition-rate hard X-ray free-electron laser driven by a superconducting linear accelerator", *Nat. Photonics*, vol. 14, no. 6, pp. 391–397, 2020. doi:10.1038/s41566-020-0607-z

[18] W. Decking and F. Obier, "Layout of the beam switchyard at the European XFEL", *EPAC08-WEPC073*, Genoa, Italy, 2008.

[19] N. Golubeva, V. Balandin, and W. Decking, "Optics for the Beam Switchyard at the European XFEL", in *Proc. IPAC'11*, San Sebastian, Spain, Sep. 2011, paper WEPC008, pp. 2016–2018.

[20] S. Liu *et al.*, "Preparing for high-repetition rate hard x-ray self-seeding at the European x-ray free electron laser: Challenges and opportunities", *Phys. Rev. Accel. Beams*, vol. 22, no. 6, p. 060704, 2019. doi:10.1103/PhysRevAccelBeams.22.060704

[21] E. L. Saldin, E. A. Schneidmiller, and M. Yurkov, "Radiative interaction of electrons in a bunch moving in an undulator", *Nucl. Instrum. Methods Phys. Res., Sect. A*, vol. 417, no. 1, pp. 158–168, 1998. doi:10.1016/S0168-9002(98)00623-8

[22] M. Dohlus, "Two methods for the calculation of CSR fields", *CM-P00048519, Tech. Rep.*, 2003.

[23] A. Potter *et al.*, "Investigation of the beam losses and radiation loads for the implementation of a slotted foil in the European XFEL", *40th Free Electron Laser Conf.*, vol. WEP16, 2022.

[24] P. Dijkstal, A. Malyzhenkov, S. Reiche, and E. Prat, "Demonstration of two-color x-ray free-electron laser pulses with a sextupole magnet", *Phys. Rev. Accel. Beams*, vol. 23, no. 3, p. 030703, 2020. doi:10.1103/PhysRevAccelBeams.23.030703

[25] V. Yakimenko, M. Fedurin, V. Litvinenko, A. Fedotov, D. Kayran, and P. Muggli, "Experimental observation of suppression of coherent-synchrotron-radiation–induced beam-energy spread with shielding plates", *Phys. Rev. Lett.*, vol. 109, no. 16, p. 164802, 2012. doi:10.1103/PhysRevLett.109.164802

[26] S. Di Mitri, M. Cornacchia, and S. Spampinati, "Cancellation of coherent synchrotron radiation kicks with optics balance", *Phys. Rev. Lett.*, vol. 110, no. 1, p. 014801, 2013. doi:10.1103/PhysRevLett.110.014801

[27] I. Agapov, G. Geloni, S. Tomin, and I. Zagorodnov, "Ocelot: A software framework for synchrotron light source and fel studies", *Nuclear Instruments and Methods in Physics Research Section A: Accelerators, Spectrometers, Detectors and Associated Equipment*, vol. 768, pp. 151–156, 2014. doi:10.1016/j.nima.2014.09.057

[28] I. Zagorodnov, "Beam dynamics in sase2 arc", 2019.

[29] M. Xie, "Exact and variational solutions of 3D eigenmodes in high gain FELs", *Nucl. Instrum. Methods Phys. Res., Sect. A*, vol. 445, no. 1-3, pp. 59–66, 2000. doi:10.1016/S0168-9002(00)00114-5

[30] K.-J. Kim and M. Xie, "Self-amplified spontaneous emission for short wavelength coherent radiation", *Nucl. Instrum. Methods Phys. Res., Sect. A*, vol. 331, no. 1-3, pp. 359–364, 1993. doi:10.1016/0168-9002(93)90072-P

[31] S. Reiche, "Genesis 1.3: a fully 3d time-dependent FEL simulation code", *Nucl. Instrum. Methods Phys. Res., Sect. A*, vol. 429, no. 1-3, pp. 243–248, 1999. doi:10.1016/S0168-9002(99)00114-X

ISBN: 978-3-95450-220-2 ISSN: 2673-5474 doi: 10.18429/JACoW-FEL2022-TUP45

TOWARDS A SEEDED HIGH REPETITION RATE FEL: CONCEPT OF SEED LASER BEAM TRANSPORT AND INCOUPLING

M. M. Kazemi, T. Lang, L. Winkelmann, S. Hartwell, D. Meissner, E. Ferrari, S. Schreiber, L. Schaper and I. Hartl, Deutsches Elektronen-Synchrotron DESY, Hamburg, Germany
E. Allaria, Elettra-Sincrotrone Trieste S.C.p.A., Basovizza, Italy

Abstract

In this contribution we report the concept of seed laser beam transport and incoupling into the electron beamline to achieve the required seeding parameters for FLASH2020+ project. In our concept a defined source point inside the laser lab is imaged to the center of the modulator. This provides the possibility of controlling the delivered seed parameters at the modulators by actuators within the laser system. We illustrate how the total energy transmission is maximized while the risk of laser induced damage of optics is mitigated. The nonlinear effects of high peak power pulse propagation are studied. Considerations for the incoupling of the seed laser into the electron beamline and the concept for laser-electron timing stabilization are presented.

INTRODUCTION

FLASH2020+ is an upgrade project of the FLASH facility at Hamburg. A main goal of the project is to generate fully coherent soft X-ray FEL radiation at a high repetition rate (MHz) [1]. This will be accomplished by utilizing the well-known seeding techniques High Gain Harmonic Generation (HGHG) and Echo-Enhanced Harmonic Generation (EEHG), hence it requires two external seed lasers. The combination will provide seeded FEL radiation with tunable wavelength from 4 to 60 nm.

For HGHG, a tunable UV laser system (Seed2: 297 – 317 nm, 50 fs, < 16 µJ) will modulate the electrons inside the second modulator (Mod2). For EEHG, fixed wavelength (Seed1: 343 nm, 500 fs, < 50 µJ) laser pulses interact with the electrons inside the first modulator (Mod1) which is followed by the interaction of Seed2 and electrons inside the second modulator [2].

Details of the high energy and high repetition rate laser system for seeding are described in [3]. The laser system operates at 10 Hz burst mode with a pulse train of 6000 pulses per second with 1 MHz in a 600 µs long pulse trains. This matches the electron bunch repetition rate structure.

The femtosecond laser pulses will be transported about 28 and 35 m to the first and second modulators, respectively using dedicated transport laser beamlines and incoupling. The laser beamlines pass mainly through radiation protected area. Figure 1 illustrates the overview of the FLASH accelerator, seeding laser lab and the laser beam transport.

FLASH operates 24/7, with limited access (4 – 8 hours per month) for the maintenance and repair of components inside accelerator tunnel. Therefore, our design has to provide proper means to monitor and control the beam parameters and at the same time. minimize the required time and expenses for repair and maintenance.

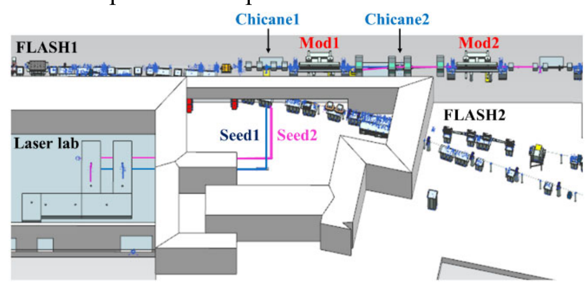

Figure 1: Overview of laser beam transport. Seed1 and Seed2 are coupled into first and second modulators via mirrors installed at the chicanes, where a transversal offset between the laser path and the electrons is presented.

Table 1: Required Seed Laser Beam Parameters Inside Modulators, Mod1 and Mod2

Parameter	Seed1	Seed2
Wavelength (nm)	343	297 – 317
Pulse duration (fs)	500	50
Pulse energy (µJ)	50	16
Peak power (MW)	1 – 100	5 – 300
Polarization	s (perpendicular)	
Beam radius (µm, $1/e^2$)	600	
Beam quality	$M^2 < 1.5$	
Position control (µm)	±500, 20 µm resolution	
Pointing (angle) control (µrad)	±80, 3 µrad resolution	
Position / pointing stability (µm, rms) / (µrad)	50 / 40	
Temporal jitter (fs, rms)	Seed1 to e-beam < 50 Seed2 to Seed1 < 50	

SEED LASER BEAM TRANSPORT

Required Parameters for Seeding

Stable overlap in time and space between seed laser and electron beam inside Mod1 and Mod2 is required to imprint an energy modulation onto the electron bunches. Each of the modulator undulators are about 2.5 m long, the electron beam size is between 100 µm and 200 µm ($1/e^2$, radius) along the modulator and the laser beam size is ~600 µm ($1/e^2$, radius). This beam size ratio ensures that the electron beam is modulated by the uniform pulse energy distribution of the laser beam and providing most stable modulation.

Table 1 summarizes some of the most relevant parameters of the Seed1 and Seed2 laser pulses inside

ISBN: 978-3-95450-220-2 ISSN: 2673-5474 doi: 10.18429/JACoW-FEL2022-TUP45

modulators which need to be concerned by laser beam transport and incoupling.

Interface Between Seed Laser and Beam Transport

The main strategy of beam transport is to reduce the complexity. In this respect, we define an interface between seed laser and beam transport as the source point and the required parameters for seeding are controlled by the seed laser system at the interface.

Figure 2(a) illustrates the scheme of interface between seed laser and beam transport for Seed2. The beam mode matching is done in the astigmatism compensated distance constant (AC-DC) telescopes. First the beam is expanded to reduce the B-integral of propagating inside the bulk compressor (BC). The delay of BC can be used to manage the dispersion through the beam transport. In addition, adaptive optics (e.g. deformable mirror) will be used to optimize the laser wavefront distortion for best seeding performance.

Figure 2(b) shows the evolution of beam waist, pulse duration and the B-integral as the beam propagates from the laser system to the interface plane. The Kerr lensing effect varies at different pulse energies. This can be compensated by the AC-DC telescope to preserve the beam size and divergence at the interface.

Imaging System, Optical Components, Energy Efficiency and LIDT

The seed lasers have to exhibit high pointing and position stability inside modulators. To achieve this, the source point in the laser lab (“interface” in Fig. 2(b), right) is relay imaged into the modulators. A schematic view of the relay imaging for Seed1 and Seed2 with magnification factors 9x and 11x, respectively is shown in Fig. 3. The concept uses two focusing modules that consist of spherical mirrors MS1.10/11&MS1.3 for Seed1 and MS1.11/12&MS2.4 for Seed2.

The Seed2 laser output parameters show 2 µrad position and 1% pointing fluctuations in a start-to-end simulation [3]. We then simulated the transfer of laser position and angle pointing fluctuations through the relay imaging beamline considering 1 µm instability for each of the mirrors. The results show the pointing and position fluctuations of laser beam ~25 µm and 2.2 µrad (rms) inside modulator.

To prevent air turbulences affecting the laser spatial pointing and arrival time, contamination of the optical components and to minimize the nonlinear effects such as B-Integral, the laser beam will be transported under ultrahigh vacuum (UHV) condition < 10^{-6} mbar.

The beam transport and incoupling consist of 12 (13) high reflective (HR) dielectric coated mirrors, 2 samplers (CaF2, uncoated) and 1 vacuum window (uncoated Z-cut UV Fused Silica). We will use HR mirrors with IBS dielectric coating. The reflectivity of these mirrors is higher than 99%, which provides a total energy transmission of about 80% for both Seed1 and Seed2. The main loss factor in here is the uncoated vacuum window which separates laser and electron UHV beamlines.

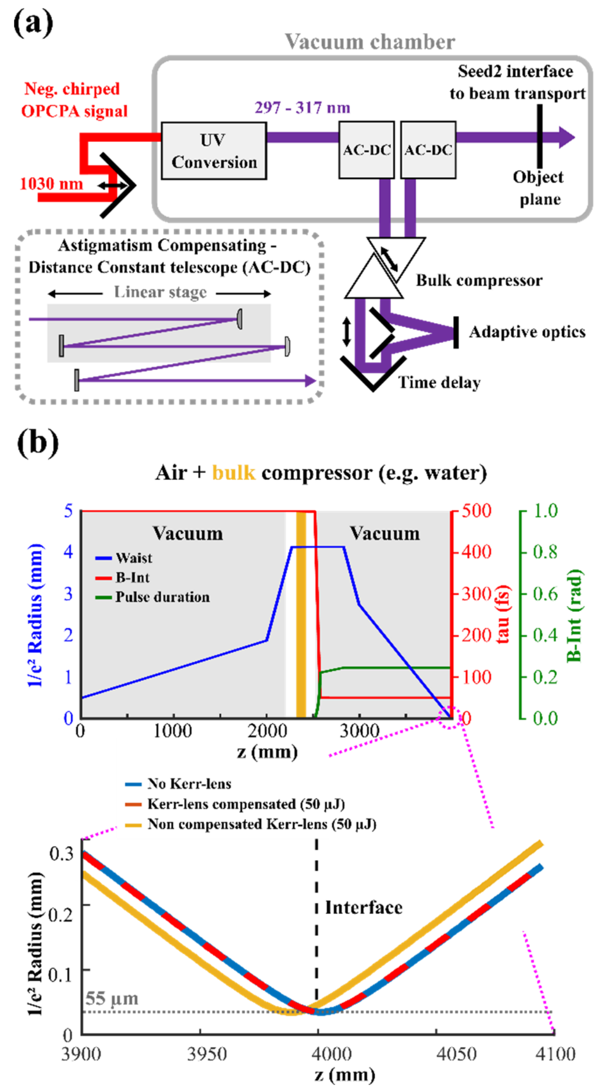

Figure 2: (a) Scheme of the interface between seed laser and beam transport. (b) Beam waist, B-Integral and pulse duration propagation from seed laser to the interface.

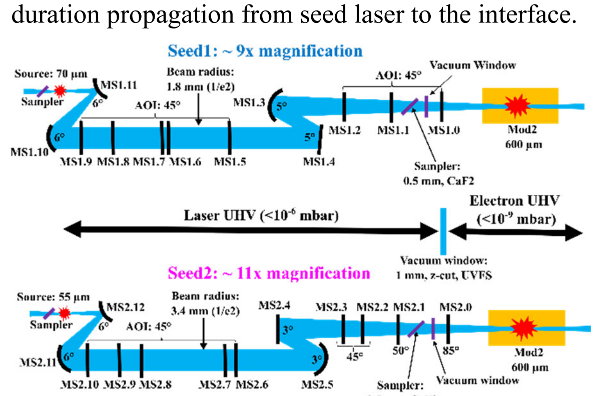

Figure 3: Relay imaging system for Seed1/2.

An important parameter which defines the total transmission and accessibility of the beam transport for seeding is the laser induced damage threshold (LIDT). The

ISBN: 978-3-95450-220-2 ISSN: 2673-5474 doi: 10.18429/JACoW-FEL2022-TUP45

LIDT depends on the pulse duration, wavelength and the repetition rate. As our laser system delivers pulses in special burst mode structure which affect the equilibrium conditions of the coating layers, we try to account of a safety margin in our design. The maximum fluences on the IBS coating HR mirrors for Seed1 is 4 mJ/cm^2. This is much less than the reported LIDT values of such coating at 343 nm with, s-pol: 120 mJ/cm^2, p-pol: 170 mJ/cm^2.

Figure 4 shows the fluence at each mirror through the laser beam transport for Seed2. The fluence on the most of mirrors is kept bellow 0.25 mJ/cm^2 by increasing the beam size or the angle of incidence (AOI). At FERMI at Elettra the incoupling mirror (IBS coating, HR@ 232–267 nm, 50 Hz, 60 – 100 fs, out of vacuum) experiences maximum 1.4 mJ/cm^2 and no damage has been observed. The maximum fluence for Seed2 beam transport is 0.6 mJ/cm^2, but the entire beamline is inside UHV where the coatings in general might have a lower LIDT, therefore a LIDT test for the optics of Seed2 is being planned.

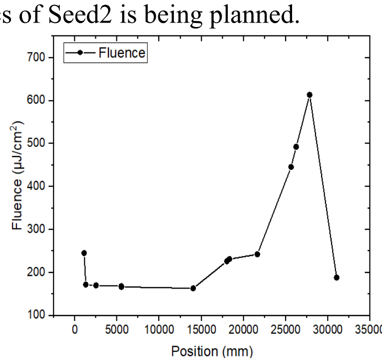

Figure 4: fluence at each mirror (filled circles) through the laser beam transport for Seed2. The fluence on the incoupling mirror (MS2.0), inside electron UHV beamline, is reduced using a grazing incidence angle, AOI = 85°.

B-Integral

The peak intensity of the seed lasers is in the order of tens of GW/cm^2. Thus, it is important to consider possible nonlinear effects such as Kerr lensing that can change the beam waist and position inside modulators. In Fig. 5 the B-Integral and the beam waist for different pulse energies of Seed1 and Seed2 are illustrated. The main contribution to the B-Integral is caused by the propagation through vacuum windows. For Seed2 the total B-Integral and change of beam waist and position inside the modulator is negligible. Seed1 also has a total low B-integral over the beamline. The variation of the beam waist and position for Seed1 can be adjusted and compensated by the AC-DC telescope in the laser system (see Fig. 2).

Incoupling Design

The chicane magnets deflect the electron beam and allow the incoupling and outcoupling of the seed lasers.

An important consideration for the design of the in/outcoupling chambers is the space charge effect. This effect occurs when the high energy electron bunch travels in the vicinity of dielectric substrates and accumulates charges on the surface of the substrate [4]. This effect can cause damage of dielectric coated optics, as well as the deflection of e-beam trajectory.

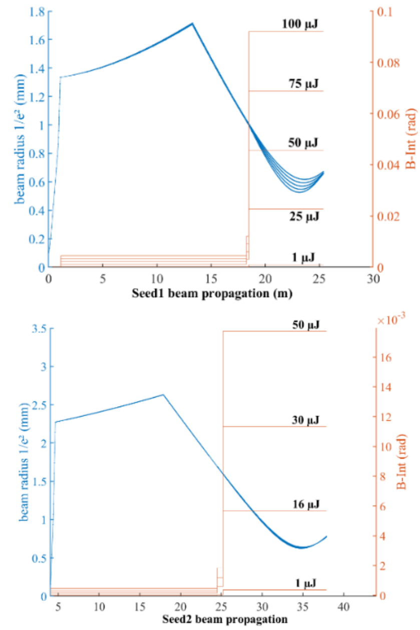

Figure 5: B-Integral and waist propagation of seed lasers for different pulse energies.

Since there is little data available, in a dedicated campaign at FLASH, this effect was studied. Dielectric coatings on glass substrates were located in the vicinity of the electron beam with an energy of 650 MeV and 970 MeV operating with one electron bunch per pulse train. We observed that in the case of 650 MeV, at distances smaller than 0.5 mm, the electron beam position monitors 7.2 m downstream of the testing station shows periodic deflection of the electron beam trajectory (see Fig. 6).

FLASH can operate at much higher electron bunch number, thus a minimum distance of 3 mm between the dielectric mirrors and the electron beam in our design will be considered to prevent the deflection of electron beam and damage of the laser incoupling mirrors.

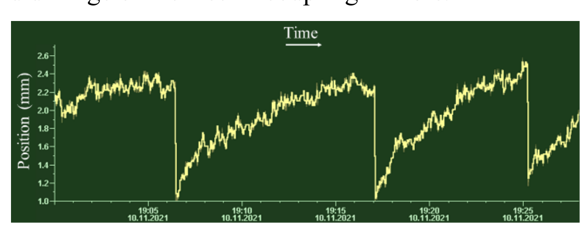

Figure 6: electron beam position after the dielectric mirror shows periodic changes of the electron trajectory.

Diagnostics and control

The design of laser beam transport is aiming to provide on-line and off-line diagnostics through the entire beamline in order to monitor the beam parameters such as position and pulse energy. In addition, at each of the incoupling sections, dedicated laser tables are considered to accommodate the diagnostics for Seed1 and Seed2. Figure 7 illustrates the diagnostic table for the Seed2 incoupling.

ISBN: 978-3-95450-220-2 ISSN: 2673-5474 doi: 10.18429/JACoW-FEL2022-TUP45

There, the laser pulse energy (PE), beam size and profile (CCD) can be monitored. The wavefront sensor (WFS) feedbacks to the adaptive optics (see Fig. 2) to optimize the beam quality.

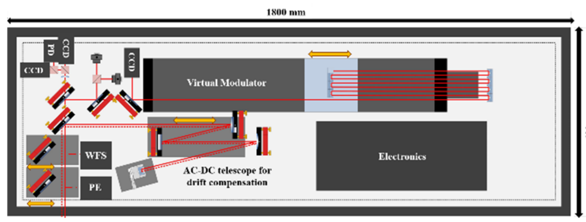

Figure 7: Seed2 diagnostic at incoupling to electron beam.

CCDs will be used to actuate the beamline motorized mirrors in order to establish the transverse overlap between laser and electron beam. A beam stabilization system that uses the beamline cameras and actuators to monitor and preserve the transverse overlap. The virtual modulator will give the possibility to scan the laser beam profile along the real modulators.

For the laser beamline, UHV compatible opto-mechanics that are free of hydrocarbons will be used. The number of movers and actuators will be minimized to reduce the system complexity. Almost all of the beam transport mirrors are selected to be standard 2-inch substrates. We are currently evaluating several choices of mirror mount designs which can be actuated with high resolution and provide low wavefront distortion and sm minimum beam pathlength variation.

Incoupling mirrors have to be compatible with electron beamline UHV requirements which forbid any actuators. Here, we will use out of vacuum actuators that manipulate the components inside vacuum using mechanical feedthroughs. This type of actuators provides only few µm resolution which is not as fine as the nm resolution of laser transport beam opto-mechanics.

To control the transverse overlap, the position of laser beam in respect to the electron beam axis needs to have the adjustment possibility of ±500 µm, with 20 µm resolution along the modulators. The linear manipulators of the incoupling mirrors with few mm of travel range and bellow 5 µm precision can provide the required position modification. The requirements for the laser beam angle is ~80 µrad with 3 µrad resolution. To realize this, the opto-mechanics of incoupling mirrors, MS1.0 and MS2.0, will be used for coarse movements. The fine tuning of the beam position and pointing is provided by the high resolution opto-mechanics of MS1.1 and MS2.1/2.

Seed Laser and Electron Timing

The longitudinal overlap between seed lasers and electron pulses is established by the detection of the electron energy modulation and / or the seeded FEL radiation.

Stable seeding requires low (bellow 50 fs, rms) timing jitter between the two seed lasers and the seed laser and electron bunch. The seed laser system utilizes fast synchronization between the seed laser oscillator (Origami 1030 nm) and an optical fibre link (1550 nm) with timing jitter < 30 fs based on an optical balanced cross-correlator (NIR-OSC BXC) [5].

The 28 to 35 meters of laser beam transport from laser lab to the FLASH tunnel experiences different environmental conditions, e.g., temperatures and humidity, in addition to the ground movements. These will cause changes in the laser beamline path length and consequently the arrival time of laser pulses. We expect timing drifts in the order of several picosecond which have to be compensated.

The concept for the drift compensation for Seed1 and Seed2 is illustrated in Fig. 8. A small portion of the seed laser is mode matched using an AC-DC telescope in the seed laser incoupling section and redirected towards the laser lab through the beam transport. In this way, the relay imaging for the re-directed beam is in principle preserved, which will provide pointing and position stability after the long propagation. The redirected seed laser and oscillator pulses are mixed in a DFG process in the balance cross correlator (UV-OSC BXC). For Seed1 the timing stabilization actuates the translation stage after the THG setup to compensate for the slow drifts. For Seed2 the the slow fibre delay line between oscillator and the NKT front end is actuated to stabilize the timing between laser and the electron beam.

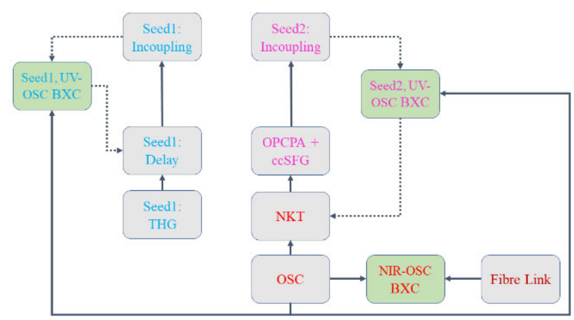

Figure 8: Scheme of the beam transport drift compensation concept.

CONCLUSION

The concept of laser beam transport and incoupling is based on imaging a defined source point from laser room to the modulators. Keeping the complexity low, this design is capable of transporting fs tunable UV pulses with ~80% energy transmission efficiency. The fluence on the optical components of Seed1 is significantly lower than the expected LIDT. For Seed2 further LIDT tests are required to study the risk of damaging optics. The study of nonlinear effect shows that the variation of B-Integral is low and the residual changes can be compensated by a tunable telescope in the laser system. The space charge effect was tested and measures for the incoupling design are taken. The diagnostics of the beam transport and incoupling will provide the possibility to monitor and modify seed laser parameters for optimized FEL performance. A timing stabilization concept is under development to provide low laser arrival time jitter and drift.

ISBN: 978-3-95450-220-2 ISSN: 2673-5474 doi: 10.18429/JACoW-FEL2022-TUP45

REFERENCES

[1] L. Schaper *et al.*, "Flexible and Coherent Soft X-ray Pulses at High Repetition Rate: Current Research and Perspective", *Appl. Sci.*, vol. 11, p. 9729, 2021. doi:10.3390/app11209729.

[2] E. Ferrari *et al.*, "Status of the Seeding Upgrade for FLASH2020+ Project", presented at FEL'22, Trieste, Italy, Aug. 2022, paper TUP42, this conference.

[3] T. Lang *et al.*, "High Repetition Rate, Ultra-Low Noise and -Wavelength Stable UV Seed Laser System for Tunable Two-Color EEHG FEL Seeding", presented at the FEL'22, Trieste, Italy, Aug. 2022, paper TUP43, this conference.

[4] A. I. Novokshonov *et al.*, "Observation of Scintillators Charging Effects at the European XFEL", in *Proc. IBIC'19*, Malmö, Sweden, Sep. 2019, pp. 308-312. doi:10.18429/JACoW-IBIC2019-TUPP011.

[5] S. Schulz *et al.*, "An Optical Cross-correlation Scheme to Synchronize Distributed Laser Systems at FLASH", in *Proc. EPAC'08*, Genoa, Italy, Jun. 2008, paper THPC160, pp. 3366-3368.

ISBN: 978-3-95450-220-2 ISSN: 2673-5474 doi: 10.18429/JACoW-FEL2022-TUP49

IMPACT OF ELECTRON BEAM ENERGY CHIRP ON OPTICAL-KLYSTRON-BASED HIGH GAIN HARMONIC GENERATION

G. Paraskaki*, E. Ferrari, L. Schaper, E. Schneidmiller
Deutsches Elektronen-Synchrotron DESY,
Hamburg, Germany
E. Allaria, Elettra-Sincrotrone Trieste S.C.p.A., Trieste, Italy

Abstract

External seeding schemes allow the generation of stable and fully coherent free electron laser (FEL) radiation but are limited in repetition rates in the order of tens of Hz. This limitation is mainly posed by the limited average power of the seed lasers required to provide hundreds of MW peak power to modulate the electron bunches. An optical-klystron-based high gain harmonic generation (HGHG) scheme, which can be implemented in several existing and upcoming seeded FEL beamlines with minimal to no additional installations, overcomes this limitation by greatly reducing the required seed laser power. In this work, we carefully study the scheme with detailed simulations that include imperfections of electron beam properties such as a quadratic electron beam energy chirp that characterizes existing FEL facilities. We discuss the optimization steps that in these conditions ensure successful operation, opening the path towards exciting science at FELs with fully coherent and high repetition rate FEL radiation.

INTRODUCTION

High-gain Free electron lasers (FELs) generate pulses of high peak power, short duration, high brightness and transverse coherence down to wavelengths in the hard x-ray regime. These unique properties have allowed several state of the art experiments [1, 2]. However, the temporal coherence of FEL pulses is not guaranteed: the original and well-established mode of operation of high-gain FELs self-amplified spontaneous emission (SASE) [3, 4] is initiated by the spontaneous undulator emission that is naturally chaotic and leads to several individual longitudinal modes being amplified.

To improve the temporal coherence, several proposals have come forward with self-seeding [5,6] being a promising method to obtain a single-spike spectrum, however, still suffering from SASE intensity fluctuations. A well-established method to achieve not only near transform-limited pulses but also of unprecedented stability is the external seeding [7, 8]. This family of techniques depends on an external seed laser source that imposes both its coherence and its stability onto the output FEL radiation that is a harmonic of the seed laser wavelength.

While seeded FEL radiation has proven very important for several experiments due to its unique pulse properties, it is limited in terms of repetition rate and shortest output wavelength. Despite the fast progress of lasers, it is still not possible to access lasers that provide sufficient peak power for successful seeded operation at repetition rates exceeding hundreds of Hz. At the same time, there is currently an increasing trend on FELs providing electron bunches at much higher repetition rates of MHz, with FLASH [9] doing this since 2005, European XFEL [10] since 2017 and SHINE [11] together with LCLS-II [12] coming into operation in the near future as continuous-wave-based machines. External seeding cannot keep up with these repetition rates with the currently used seed lasers.

To relax the requirements put on the seed laser systems and therefore increase their repetition rate at a much lower peak power, an alternative seeding scheme has been proposed, the optical-klystron based high gain harmonic generation (OK HGHG) [13, 14]. This scheme combines the already known optical klystron (OK) [15] and high gain harmonic generation (HGHG) [7,16] schemes with the goal to replicate the properties of seeded radiation but with a much lower seed laser power, which in some cases is up to three orders of magnitude smaller [14]. With such a lower power, the repetition rate of the seed laser system can be increased or shorter-wavelength seed laser sources can be used to achieve shorter output wavelengths.

In the following, we take a closer look into this scheme and we study its response to an electron beam energy chirp. While a linear electron beam energy chirp is necessary for compressing the electron bunch and achieving sufficient peak current to drive the FEL amplification in high-gain, higher order terms in longitudinal phase space are typically undesired, but unavoidable. Several factors along the linear accelerator contribute to those high order terms effects with wakefields, space charge and non-linearities in compression being a few of them. In this paper, we isolate a purely quadratic energy chirp and we study its effect on the output FEL pulses of a standard HGHG and an OK-HGHG scheme. We study the 15th harmonic of a 300 nm seed laser wavelength, resulting in 20 nm as output wavelength.

THE LAYOUT

In this section, we briefly review the standard HGHG scheme and the modifications needed for an OK-HGHG scheme. In standard HGHG, we take advantage of a powerful seed laser that modulates the energy of the electrons via

* georgia.paraskaki@desy.de

ISBN: 978-3-95450-220-2 ISSN: 2673-5474 doi: 10.18429/JACoW-FEL2022-TUP49

their interaction along a modulator. When sufficient energy modulation is obtained, it can be exploited in a dispersive section such as a chicane to obtain bunching at harmonics of the seed laser wavelength. As a result, the pre-bunched electron bunch is sent to the radiator and a harmonic of the seed laser wavelength is amplified. The scheme is shown in Fig. 1.

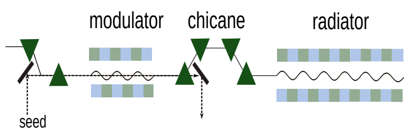

Figure 1: In the standard HGHG scheme, a powerful seed laser, a modulator and a chicane are required to obtain sufficient bunching at a harmonic of the seed laser wavelength at the entrance of the radiator.

While a similar concept remains for the OK-HGHG, the main difference is that the desired energy modulation is achieved in two stages, each of them consisting of a modulator and a chicane. This modified setup is shown in Fig. 2. A much weaker seed laser is used this time to induce a much smaller energy modulation in modulator 1 which is sufficient to obtain bunching at the seed laser wavelength after chicane 1. The pre-bunched electron bunch radiates coherent radiation in modulator 2 and the initially small energy modulation is amplified. This amplified energy modulation can be used in chicane 2 to obtain bunching at a harmonic of the seed laser wavelength.

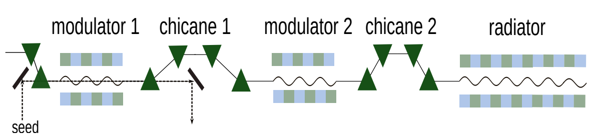

Figure 2: In the OK-HGHG scheme, a seed laser of a much lower power compared to the standard HGHG, two modulators and two chicanes are required to obtain sufficient bunching at a harmonic of the seed laser wavelength at the entrance of the radiator.

SIMULATION RESULTS

In this paper we study the isolated effect of a quadratic chirp. In a previous paper [17] we studied the isolated effect of a linear chirp taking as an example the linear terms in longitudinal phase for typical electron bunches at FLASH2020+ [18, 19]. It was concluded that a linear chirp does not deteriorate the pulse properties neither for the standard HGHG nor for the OK HGHG. After the appropriate optimization, the pulse properties are comparable with those of a flat energy profile with the additional effect of a predictable wavelength shift of the output radiation. The wavelength shift is more significant for the OK HGHG.

Here, we continue our studies by isolating the quadratic terms of two different electron bunch longitudinal phase spaces, one coming from FLASH2020+ [19] where the linear terms are dominant in comparison to the quadratic terms and the other one coming from FERMI [20] where quadratic terms are dominant in some parts of the electron bunch. In this work, we consider electron beams that mimic typical measured (for FERMI) and simulated (for FLASH). The electron beam energy profiles are described with a third degree polynomial $\gamma = \gamma_0 + \gamma_1 s + \gamma_2 s^2 + \gamma_3 s^3$ with the following coefficients for the two facilities:

1. For FERMI: $\gamma_1 = -3.2 \cdot 10^4 m^{-1}$, $\gamma_2 = 27 \cdot 10^7 m^{-2}$, $\gamma_3 = 22.9 \cdot 10^{11} m^{-3}$.
2. For FLASH: $\gamma_1 = -9.7 \cdot 10^4 m^{-1}$, $\gamma_2 = 8.7 \cdot 10^7 m^{-2}$, $\gamma_3 = 5.9 \cdot 10^{11} m^{-3}$.

Real measurements at the two facilities may differ slightly from the used values but the main features that are relevant to our studies are described by the used equations. For easier comparison, we keep the nominal energy γ_0=1467.7 the same for both cases following the parameters used for our previous simulation studies [14, 17]. In order to isolate the contribution of the quadratic chirp to the process, we set the coefficients γ_1 and γ_3 to zero. For the energy profile simulated in Genesis [21], we isolate the quadratic term γ_2 for the two individual cases and we overlap the nominal energy with the peak of the Gaussian seed laser power profile and the center of the flat-top current profile as shown in Fig. 3. An overview of the simulation parameters are shown in Table 1.

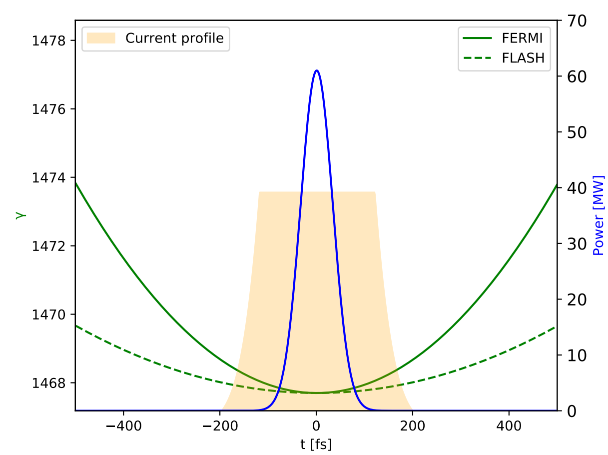

Figure 3: Initial energy profile for the case of FERMI and FLASH together with the input seed laser power profile and the initial current profile. The initial relative timing between the three profiles is kept the same for all simulations shown here.

In Fig. 4 and Fig. 5 we show the simulation results after optimization for the standard HGHG and the OK HGHG, respectively, and for three different cases of an electron bunch with: a flat energy profile, a quadratic energy chirp based on FERMI parameters, and a quadratic energy chirp based on FLASH parameters. For each of these six in total cases, we show the resulting pulse energy along the radiator and the

ISBN: 978-3-95450-220-2 ISSN: 2673-5474 doi: 10.18429/JACoW-FEL2022-TUP49

output pulses' spectra and power profiles. The simulation parameters after optimization are shown in Table 2 and the resulting pulse properties are shown in Table 3.

Comparing the six cases, we notice at the OK-HGHG scheme the effect of the quadratic chirp on the bandwidth of output FEL spectra that has been studied before [20, 22, 23]. The exact broadening depends on chicane strengths, the interplay between the quadratic term of the energy chirp and the duration of the seed which determines the energies sampled along it and the desired harmonic amplified. The smaller quadratic terms at FLASH ($8.7 \cdot 10^7$ vs $27 \cdot 10^7 m^{-2}$) lead to a smaller -but still significant- bandwidth broadening compared to the case of FERMI. It is worth noticing that the effect of bandwidth broadening is negligible for the standard HGHG case and the seed laser power duration (33 fs rms) chosen in our simulations. A longer seed laser and a larger R_{56} would have led to bandwidth broadening too. Overall, we notice that the OK-HGHG scheme is more prone to being affected by an isolated quadratic energy chirp due to its two stages with a rather strong first chicane ($R_{56,1}$=482 µm) that broaden the bandwidth of the bunching profile at this relatively high harmonic 15. It is worth noticing that the seed laser power ratio required for the standard HGHG and OK HGHG in all cases remains the same: the seed laser power used for the OK-HGHG scheme is lower by a factor of 360.

Table 1: Input Simulation Parameters

Electron beam	
Energy	750 MeV
Uncorrelated energy spread	75 keV
Peak current	500 A (flat-top)
Seed laser	
Wavelength	300 nm
rms duration	33 fs (rms)

Table 2: Optimized simulation parameters for standard and the optical klystron (OK) HGHG. Both FERMI and FLASH energy profiles resulted in the same optimized parameters.

Standard HGHG:	**w/o chirp**	**with chirp**
K_{mod}	5.42	5.42
P_{seed}	61 MW	61 MW
R_{56}	38.7 µm	38.7 µm
K_{rad}	1.791	1.793
OK HGHG:	**w/o chirp**	**with chirp**
$K_{\mathrm{mod},1/2}$	5.42/5.42	5.42/5.41
P_{seed}	170 kW	170 kW
$R_{56,1/2}$	482 µm/23.8 µm	482 µm/23.8 µm
K_{rad}	1.789	1.791

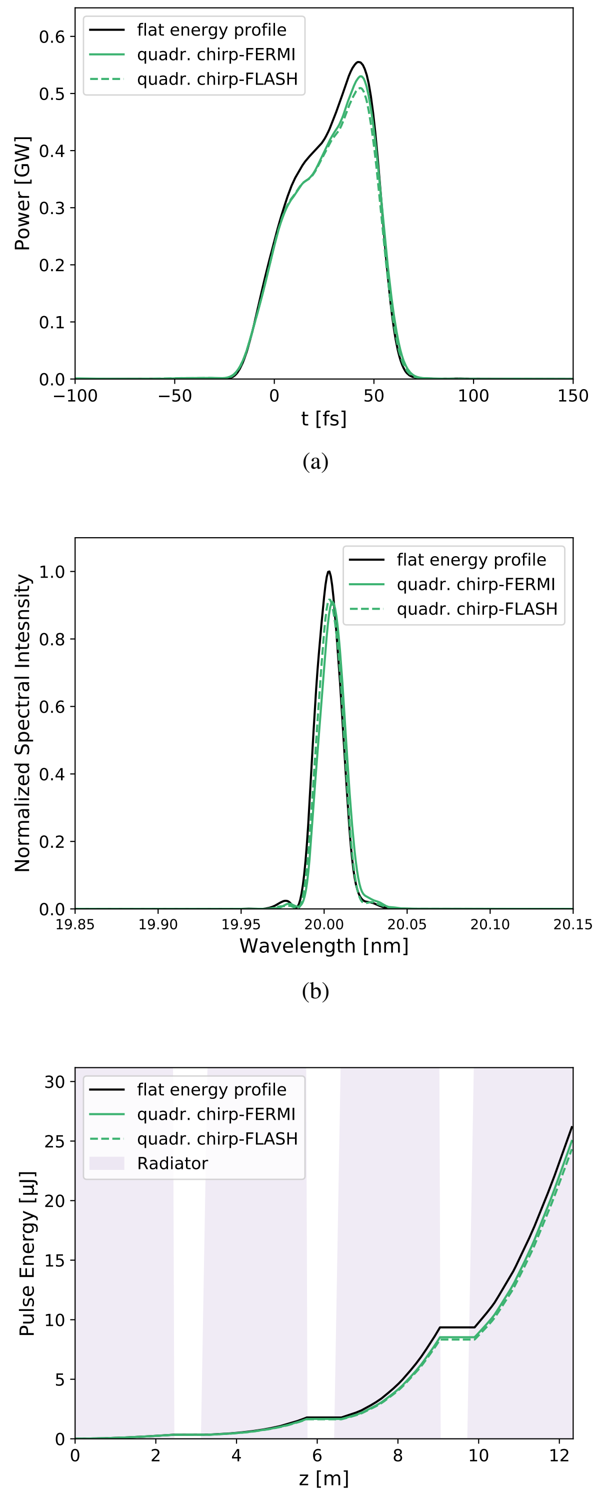

(a)

(b)

(c)

Figure 4: (a) Power profile and (b) spectra of output FEL in a standard HGHG scheme (Fig. 1) with three different electron beam energy profiles. In (c) we show the growth of the pulse energy along radiator.

ISBN: 978-3-95450-220-2 ISSN: 2673-5474 doi: 10.18429/JACoW-FEL2022-TUP49

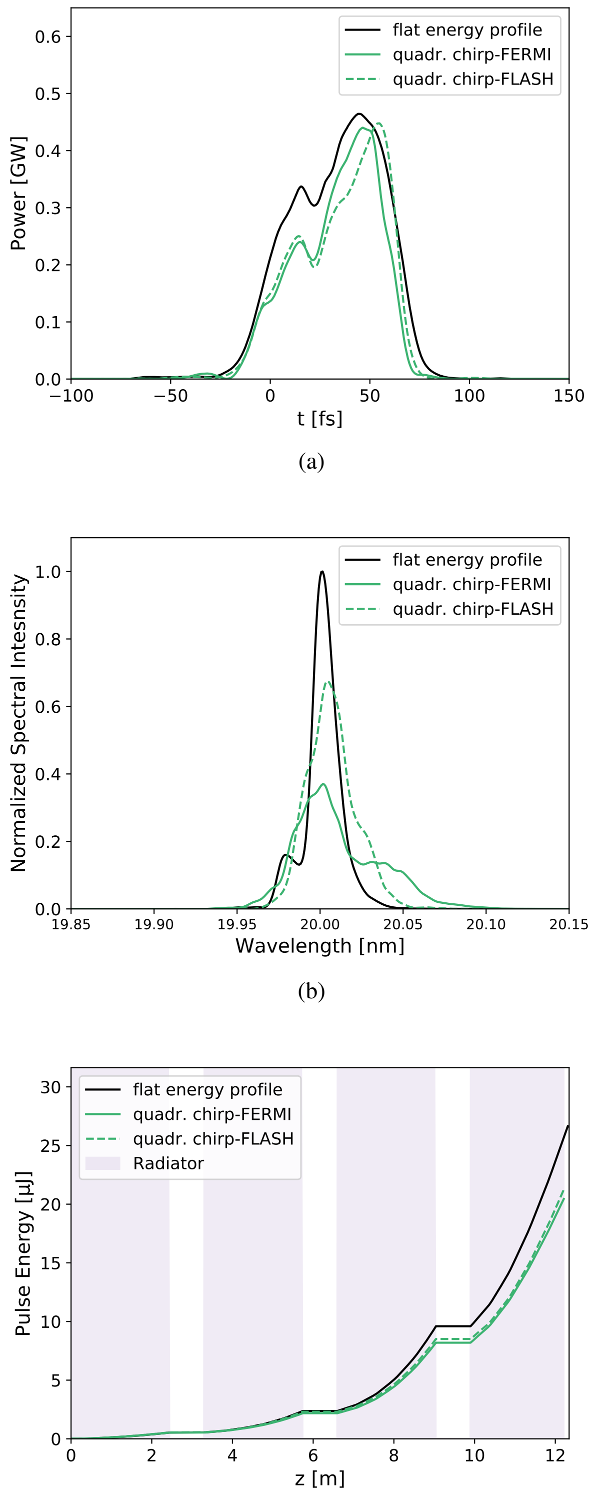

Figure 5: (a) Power profile and (b) spectra of output FEL in an OK-HGHG scheme (Fig. 2) with three different electron beam energy profiles. In (c) we show the growth of the pulse energy along radiator.

Table 3: Pulse properties of the output FEL radiation shown in Figs. 4 and 5.

Standard HGHG:	**w/o chirp**	**with chirp FERMI/FLASH**
Pulse energy	26.4 µJ	25.3 µJ/24.3 µJ
FWHM BW	$8.8 \cdot 10^{-4}$	$8.4 \cdot 10^{-4}/8.7 \cdot 10^{-4}$
rms duration	19.5 fs	20.1 fs/19.9 fs
OK HGHG:	**w/o chirp**	**with chirp FERMI/FLASH**
Pulse energy	27 µJ	20.6 µJ/21.4 µJ
FWHM BW	$7.4 \cdot 10^{-4}$	$1.6 \cdot 10^{-3}/1.4 \cdot 10^{-3}$
rms duration	23.5 fs	21.6 fs/22.8 fs

DISCUSSION AND SUMMARY

In this paper, we studied the isolated effect of the quadratic chirp of typical electron bunches of FLASH2020+ and FERMI. It resulted that the quadratic terms are responsible for a bandwidth broadening of the output FEL which becomes more significant for an increasing harmonic number. In addition, the effect becomes more dominant for the OK-HGHG scheme because of the two stages with the two chicanes before the final amplification.

It should be noted that in reality, there is a number of factors that can contribute to mitigating the effect of bandwidth broadening observed here. First of all, the interplay between the different order terms of the energy profile can smooth out the effect of the quadratic term. When combining more terms we expect to see improved results, especially when linear components are dominant. In addition, different regions of an electron bunch contain different ranges of energies. Since the important factor is the energies sampled by the seed laser profile itself, we can strategically select the temporal position of the seed laser along the electron bunch. In this process, the seed laser pulse duration becomes important, with shorter seed laser pulses minimizing the effect of bandwidth broadening. Since OK HGHG allows for much lower laser pulse energies, there is margin for seed laser manipulation for shorter laser pulses.

Another solution that could be considered is to counteract the quadratic term correlating electron energy in time with a seed laser frequency chirp [20], restoring locally the resonance condition at all longitudinal positions. Finally, another option for experiments that require mitigation of the bandwidth broadening would be to reduce $R_{56,1}$ of the first chicane of OK HGHG, reducing this way the bandwidth broadening observed in the simulations presented here with the compromise of a smaller gain in seed laser power compared to the factor 360 achieved in our simulations. In our following studies, we will focus on the effect of a realistic electron bunch energy profile containing both linear and quadratic terms, as well as other higher order terms when significant.

ISBN: 978-3-95450-220-2 ISSN: 2673-5474 doi: 10.18429/JACoW-FEL2022-TUP49

REFERENCES

[1] P. R. Ribic and G. Margaritondo, "Status and prospects of x-ray free-electron lasers (x-FELs): a simple presentation,"*J. Phys. D: Appl. Phys.*, vol. 45, p. 213001, 2012. doi:10.1088/0022-3727/45/21/213001.

[2] N. Huang, H. Deng, B. Liu, D. Wang, Z. Zhao, "Features and futures of X-ray free-electron lasers", *The Innovation*, vol. 2, no. 2, p. 100097, 2021. doi:10.1016/j.xinn.2021.100097

[3] A. M. Kondratenko and E.L. Saldin, "Generation of coherent radiation by a relativistic electron beam in an ondulator", *Part. Accel.*, vol. 10, pp. 207–216, 1980.

[4] R. Bonifacio, F. Casagrande, and G. Casati, "Cooperative and chaotic transition of a free electron laser Hamiltonian model", *Opt. Comm.*, vol. 40, pp. 219-223, 1982. doi:10.1016/0030-4018(82)90265-6

[5] J. Feldhaus, E. Saldin, J. Schneider, E. Schneidmiller and M. Yurkov, "Possible application of x-ray optical elements for reducing the spectral bandwidth of an x-ray SASE FEL", *Opt. Comm.*, vo. 140, pp.341–352, 1997. doi:10.1016/S0168-9002(97)00451-8

[6] G. Geloni, V. Kocharyan and E. Saldin, "A novel self-seeding scheme for hard X-ray FELs", *J. Mod. Opt.* vol. 58, pp. 1391–1403, 2011. doi:10.1080/09500340.2011.586473

[7] L. H. Yu and J. Wu, "Theory of high gain harmonic generation: an analytical estimate", *Nucl. Instr. Meth.*, vol. 483, pp. 493-498, 2002. doi:10.1016/S0168-9002(02)00368-6.

[8] G. Stupakov, "Using the Beam-Echo Effect for Generation of Short-Wavelength Radiation", *Phys. Rev. Lett.*, vol. 102, p. 074801, 2007. doi:10.1103/PhysRevLett.102.074801.

[9] J. Rossbach, J. R. Schneider, and W. Wurth, "10 years of pioneering x-ray science at the free-electron laser flash at DESY", *Phys. Rep.*, vol. 808, pp.1-74, 2019. doi:10.1016/j.physrep.2019.02.002

[10] D. Nölle, "FEL Operation at the European XFEL Facility", in *Proc. FEL'19*, Hamburg, Germany, Aug. 2019, pp. 766–771. doi:10.18429/JACoW-FEL2019-FRA01.

[11] T. Liu, X. Dong, and C. Feng, "Start-to-end Simulations of the Reflection Hard X-Ray Self-Seeding at the SHINE Project", in *Proc. FEL'19*, Hamburg, Germany, Aug. 2019, pp. 254–257. doi:10.18429/JACoW-FEL2019-TUP087.

[12] E. Hemsing *et al.*, "Soft x-ray seeding studies for the SLAC Linac Coherent Light Source II", *Phys. Rev. Accel. Beams*, vol. 22, p. 110701, 2019. doi:10.1103PhysRevAccelBeams.22.110701.

[13] J. Yan *et al.*, "Self-amplification of Coherent Energy Modulation in Seeded Free-Electron Lasers", *Phys. Rev. Lett.*, vol. 126, p. 084801, 2021. doi:10.1103/PhysRevLett.126.084801.

[14] G. Paraskaki, E. Allaria, E. Schneidmiller, and W. Hillert, "High repetition rate seeded free electron laser with an optical klystron in high-gain harmonic generation", *Phys. Rev. Accel. Beams*, vol. 24, p. 120701, 2021. doi:10.1103/PhysRevAccelBeams.24.120701.

[15] N. A. Vinokurov and A. N. Krinsky, "About the maximum power of an optical klystron on a storage ring", Preprint of INP 77-59, Novosibirsk, 1977.

[16] E. Allaria *et al.*, "Highly coherent and stable pulses from the FERMI seeded free-electron laser in the extreme ultraviolet", *Nat. Photon.* vol. 6, pp. 699–704, 2012. doi:10.1038/nphoton.2012.233.

[17] G. Paraskaki, E. Allaria, E. Ferrari, W. Hillert, L. Schaper, and E. Schneidmiller, "Path to High Repetition Rate Seeding: Combining High Gain Harmonic Generation with an Optical Klystron", in *Proc. IPAC'22*, Bangkok, Thailand, Jun. 2022, pp. 2411–2414. doi:10.18429/JACoW-IPAC2022-THOXSP3.

[18] L. Schaper *et al.*, "Flexible and Coherent Soft X-ray Pulses at High Repetition Rate: Current Research and Perspectives", *Appl. Sci.*, vol. 11, p. 9729, 2021. doi:10.3390/app11209729.

[19] J. Zemella and M. Vogt, "Optics & Compression Schemes for a Possible FLASH Upgrade", in *Proc. IPAC'19*, Melbourne, Australia, May 2019, pp. 1744-1747. doi:10.18429/JACoW-IPAC2019-TUPRB026.

[20] B. Mahieu *et al.*, "Two-colour generation in a chirped seeded free-electron laser: a close look", *Opt. Express*, vol. 21, pp. 22728-22741, 2013. doi:10.1364/OE.21.022728.

[21] S. Reiche, "Genesis 1.3: a fully 3d time-dependent fel simulation code", *Nucl. Instr. Meth.*, vol. 429, pp. 243-248, 1999. doi:10.1016/S0168-9002(99)00114-X.

[22] A. Marinelli, L. Giannessi, C. R. Frascati, C. Pellegrini, and S. Reiche, "Comparison of HGHG and Self Seeded Scheme for the Production of Narrow Bandwidth FEL Radiation", in *Proc. FEL'08*, Gyeongju, Korea, Aug. 2008, paper MOPPH009, pp. 25–28.

[23] C. Feng, D. Wang, and Z. T. Zhao, "Study of the Energy Chirp Effects on Seeded FEL Schemes at SDUV-FEL", in *Proc. IPAC'12*, New Orleans, LA, USA, May 2012, paper TUPPP056, pp. 1724–1726.

ISBN: 978-3-95450-220-2 ISSN: 2673-5474 doi: 10.18429/JACoW-FEL2022-TUP50

AN XFELO DEMONSTRATOR SETUP AT THE EUROPEAN XFEL*

P. Rauer†, W. Decking, Deutsches Elektronen-Synchrotron DESY, Hamburg, Germany
I. Bahns, D. La Civita, J. Gruenert, M. Di Felice, A. Koch,
L. Samoylova, H. Sinn, M. Vannoni, European XFEL GmbH, Schenefeld, Germany
J. Rossbach, Universitaet Hamburg, Hamburg, Germany

Abstract

An X-ray free-electron laser oscillator (XFELO) is a next generation X-ray source promising radiation with full three-dimensional coherence, nearly constant pulse to pulse stability and more than an order of magnitude higher spectral flux compared to SASE FELs. In this contribution the concept of an R&D project for installation of an *XFELO* demonstrator experiment at the European XFEL facility is conceptually presented. It is composed of an X-ray cavity design in backscattering geometry of 133 m round trip length with four undulator sections of 20 m total length producing the FEL radiation. It uses cryocooled diamond crystals and employs the concept of retroreflection to reduce the sensitivity to vibrations. Start to end simulations were carried out which account for realistic electron bunch distributions, inter RF-pulse bunch fluctuations, various possible errors of the X-ray optics as well as the impact of heat load on the diamond crystals. The estimated performance and stability derived from these simulations shall be reported and foreseen issues shall be discussed.

INTRODUCTION

In order to overcome one of the major flaws of SASE based FEL radiation in the hard X-ray regime, which is the low degree of monochromaticity and the lack of of longitudinal coherence, multiple schemes have been proposed and partly realized over the recent years. Promising schemes are the *X-ray Regenerative Amplifier FEL* (XRAFEL) proposed by *Z. Huang* in 2006 [1] and the *X-ray Free Electron Laser Oscillator* (XFELO) proposed by *K.J. Kim* in 2008 [2]. Both schemes are based on trapping FEL radiation inside a X-ray optical cavity, using monochromatizing crystals based on Bragg reflection instead of total reflecting optical mirrors [1, 3]. While the XFELO is closely related to the low gain FELO scheme, the XRAFEL is based on the strong gain FEL amplifier scheme. In the following, both schemes will be summarized under the term *XFELO*. Due the promise of delivering outstanding radiation properties, *XFELO*s have received growing interest in the recent years [3–14].

European XFEL is developing an *XFELO* demonstrator to be installed at the end of one of the hard X-ray undulator lines (SASE1) in the first quarter of 2024. The principal goal of the demonstrator is to prove the working concept - meaning seeding and increasing longitudinal coherence by several orders of magnitude over subsequent round trips, from synchrotron radiation to almost monochromatic FEL amplifier radiation. It is not primarily meant for user-operation, and therefore not optimized to this end.

In this proceeding, the fundamentals of the experimental setup as well as the expected output characteristics shall be sketched. More detailed information will be given in a separate publication [15] or can be looked up in ref. [16].

A PROOF-OF-CONCEPT *XFELO* EXPERIMENT

The X-ray cavity is designed in a simple two crystal backscattering geometry, following the principle of maximum simplicity to avoid mechanical complications. Hence, features like wavelength tunability [3, 7] are omitted. The crystals are two optically thick ($t_C \approx 250\,\mu$m) diamond crystals. This increases the robustness of the setup against thermal load, which is further improved by cooling the diamonds to a temperature of $T = 77$ K [10, 11, 17–19]. In between the crystals, four 5 m long variable gap undulator sections are positioned and two chicanes are used to in- and out-couple the electrons. The crystal to crystal distance is fixed to $L_{C-C} \approx 66.42$ m, which matches an electron bunch repetition rate of $f_{\mathrm{rep}}^{\mathrm{el.}} = 2.25$ MHz, being a common repetition rate at the European XFEL accelerator. Each reflecting crystals is combined with two grazing incidence mirrors aligned orthogonally with respect to each other and the crystal. This forms a so called retroreflector, which may decouple the setup from outer vibrations (see [15] or [16] for reference). Additionally, by applying a slight meridional curvature $R_m \approx 20$ km on the total reflecting mirrors, focusing of the X-ray pulses can be achieved.

In Fig. 1 the evolution of the pulse energy of the *XFELO* demonstrator for a photon energy of $E_c = 9.05$ keV is displayed. The different curves correspond to the X-ray pulse directly after the undulator (blue), reentering the undulator as seed for the subsequent round trip (red) and the transmitted pulse (yellow). The simulations include various different error sources, such as statistical electron beam shot to shot fluctuations common for the European XFEL accelerator [20], crystal misalignment and mirror surface profile error of $h_{\mathrm{rms}} = 1.5$ nm. Figure 1(a), which neglects the impact of heat load on the crystals, shows that the pulse energy trapped inside the X-ray cavity reaches up to very high value, which corresponds in combination with a very small bandwidth of only $\sigma_{E_{\mathrm{ph}}} = 20.4(5)$ meV to unparalleled peak spectral densities. Owing to the simplistic transmission through a thick crystal, only the spectral side lobes regenerated at every round trip are transmitted. This leads to much lower trans-

* Work supported by (FKZ 05K16GU4)
† patrick.rauer@desy.de

ISBN: 978-3-95450-220-2 ISSN: 2673-5474 doi: 10.18429/JACoW-FEL2022-TUP50

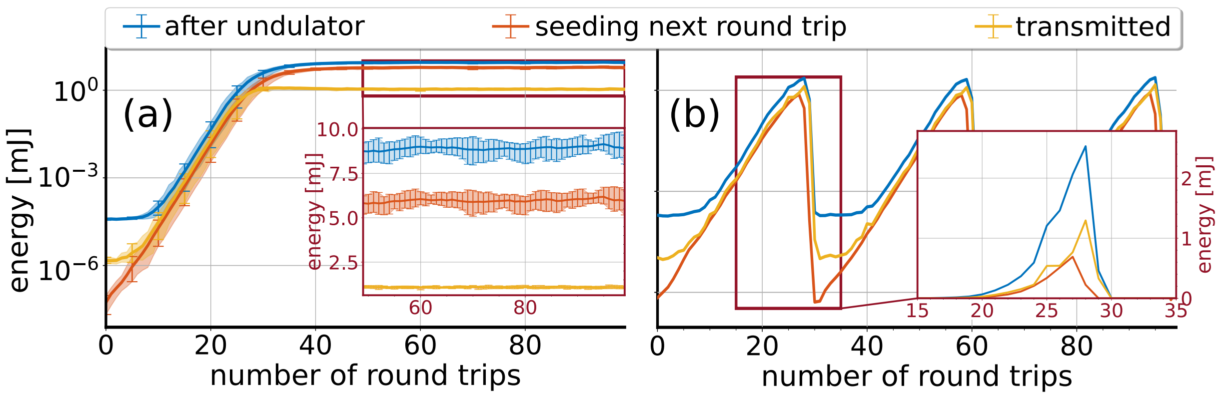

Figure 1: Pulse energy evolution in logarithmic scale for a photon energy of $E_c = 9.05\,\mathrm{keV}$, corresponding to a diamond C 111 orientation, neglecting heat load (a) and including heat load in the calculation (b). The inset show the pulse energies around the maxima in linear scale. The heat load evidently strongly destabilizes the output.

mitted pulse energies at around $Q_{tr} \approx 0.95(5)$ mJ. Yet, still showing a very small bandwidth of only $\sigma_{E_{\mathrm{ph}}} = 69(2)$ meV, the expected peak spectral flux is still much higher compared to SASE.

However, as evident from Fig. 1(b), when including the impact of thermal load into the fully coupled simulations, the output gets strongly destabilized, even at an optimized crystal base temperature of $T_c = 77\,\mathrm{K}$. This is fully understandable, regarding the intense and focussed, X-ray pulses interacting with the crystal at a megahertz repetition rate.

In a more detailed publication [15], the details of the X-ray output characteristics, with and without heat load, as well as its implications on the demonstrator experiment, will be explained in much more detail.

REFERENCES

[1] Z. Huang and R. D. Ruth, "Fully coherent x-ray pulses from a regenerative-amplifier free-electron laser," *Phys. Rev. Lett.*, vol. 96, no. 14, p. 144 801, 2006. doi:10.1103/physrevlett.96.144801

[2] K.-J. Kim, Y. Shvyd'ko, and S. Reiche, "A proposal for an x-ray free-electron laser oscillator with an energy-recovery linac," *Phys. Rev. Lett.*, vol. 100, no. 24, 2008. doi:10.1103/physrevlett.100.244802

[3] K.-J. Kim and Y. V. Shvyd'ko, "Tunable optical cavity for an x-ray free-electron-laser oscillator," *Phys. Rev. Spec. Top. Accel Beams*, vol. 12, no. 3, 2009. doi:10.1103/physrevstab.12.030703

[4] H. P. Freund, P. J. M. van der Slot, and Y. Shvyd'ko, "An x-ray regenerative amplifier free-electron laser using diamond pinhole mirrors," *New J. Phys.*, vol. 21, no. 9, p. 093 028, 2019. doi:10.1088/1367-2630/ab3f72

[5] G. Marcus *et al.*, "Refractive guide switching a regenerative amplifier free-electron laser for high peak and average power hard x rays," *Phys. Rev. Lett.*, vol. 125, no. 25, p. 254 801, 2020. doi:10.1103/physrevlett.125.254801

[6] R. A. Margraf, J. P. MacArthur, G. Marcus, and Z. Huang, "Microbunch Rotation as an Outcoupling Mechanism for Cavity-based X-Ray Free Electron Lasers," no. 11, p. 35, 2021. doi:10.18429/JACoW-IPAC2020-WEVIR03

[7] R. R. Lindberg, K.-J. Kim, Y. Shvyd'ko, and W. M. Fawley, "Performance of the x-ray free-electron laser oscillator with crystal cavity," *Phys. Rev. Spec. Top. Accel Beams*, vol. 14, no. 1, 2011. doi:10.1103/physrevstab.14.010701

[8] R. R. Lindberg, K.-J. Kim, Y. Cai, Y. Ding, and Z. Huang, "Transverse Gradient Undulators for a Storage Ring X-ray FEL Oscillator," in *Proc. FEL'13*, New York, NY, USA, Aug. 2013, pp. 740–748. https://jacow.org/FEL2013/papers/THOBNO02.pdf

[9] T. J. Maxwell *et al.*, "Feasibility Study for an X-ray FEL Oscillator at the LCLS-II," in *Proc. IPAC'15*, Richmond, VA, USA, May 2015, pp. 1897–1900. doi:10.18429/JACoW-IPAC2015-TUPMA028

[10] J. Zemella, C. P. Maag, J. Rossbach, H. Sinn, and M. Tolkiehn, "Numerical Simulations of an XFELO for the European XFEL driven by a Spent Beam," in *Proc. FEL'12*, Nara, Japan, Aug. 2012, pp. 429–432. https://jacow.org/FEL2012/papers/WEPD29.pdf

[11] P. Rauer, I. Bahns, W. Decking, W. Hillert, J. Roßbach, and H. Sinn, "Integration of an XFELO at the European XFEL Facility," pp. 62–65, doi:10.18429/JACoW-FEL2019-TUP009

[12] K. Li and H. Deng, "Systematic design and three-dimensional simulation of x-ray FEL oscillator for shanghai coherent light facility," *Nucl. Instrum. Methods Phys. Res., Sect. A*, vol. 895, pp. 40–47, 2018. doi:10.1016/j.nima.2018.03.072

[13] B. W. Adams and K.-J. Kim, "X-ray comb generation from nuclear-resonance-stabilized x-ray free-electron laser oscillator for fundamental physics and precision metrology," *Phys. Rev. Spec. Top. Accel Beams*, vol. 18, no. 3, 2015. doi:10.1103/physrevstab.18.030711

[14] W. Qin, K.-J. Kim, R. R. Lindberg, and J. Wu, "X-ray FEL Oscillator Seeded Harmonic Amplifier for High Energy Photons," in *Proc. FEL'17*, Santa Fe, NM, USA, 2018, pp. 196–199. doi:10.18429/JACoW-FEL2017-MOP062

[15] P. Rauer *et al.*, "An cavity based x-ray fel demonstrator at the European XFEL facility," to be published, 2022.

[16] P. Rauer, "A Proof-Of-Principle Cavity-Based X-RayFree-Electron-Laser Demonstrator at the European XFEL," Dissertation, Universität of Hamburg, 2022. doi:10.3204/PUBDB-2022-02800

ISBN: 978-3-95450-220-2 ISSN: 2673-5474 doi: 10.18429/JACoW-FEL2022-TUP50

[17] C. P. Maag, I. Bahns, J. Roßbach, H. Sinn, P. Thiessen, and J. Zemella, "An Experimental Setup for Probing the Thermal Properties of Diamond Regarding Its Use in an XFELO," in *Proc. FEL'17*, Santa Fe, NM, USA, Aug. 2017, pp. 200–203. doi:10.18429/JACoW-FEL2017-MOP064

[18] I. Bahns, W. Hillert, P. Rauer, J. Roßbach, and H. Sinn, "Interaction of Powerful Electro-Magnetic Fields With Bragg Reflectors," pp. 673–676, doi:10.18429/JACoW-FEL2019-THP041

[19] B. Yang, S. Wang, and J. Wu, "Transient thermal stress wave and vibrational analyses of a thin diamond crystal for x-ray free-electron lasers under high-repetition-rate operation," *J. Synchrotron Radiat.*, vol. 25, no. 1, pp. 166–176, 2018. doi:10.1107/s1600577517015466

[20] W. Decking *et al.*, "A MHz-repetition-rate hard x-ray free-electron laser driven by a superconducting linear accelerator," *Nature Photonics*, vol. 14, no. 6, pp. 391–397, 2020. doi: 10.1038/s41566-020-0607-z

ISBN: 978-3-95450-220-2 ISSN: 2673-5474 doi: 10.18429/JACoW-FEL2022-TUP51

FLASH2020+ PROJECT PROGRESS: CURRENT INSTALLATIONS AND FUTURE PLANS

L. Schaper†, Ph. Amstutz, N. Baboi, K. Baev, M. Beye, Ch. Gerth, I. Hartl, K. Honkavaara, J. Müller-Dieckmann, R. Pan, E. Plönjes-Palm, O. Rasmussen, J. Rönsch-Schulenburg, E. Schneidmiller, S. Schreiber, K. Tiedtke, M. Tischer, S. Toleikis, R. Treusch, M. Vogt, L. Winkelmann, M. Yurkov, J. Zemella
Deutsches Elektronen Synchrotron DESY, Hamburg, Germany

Abstract

The FLASH2020+ project has started to transform the FLASH facility to broaden the facility profile and meet demands of future user experiments. In a nine-month lasting shutdown until August 2022 the linear accelerator of the FLASH facility has, among others, been upgraded with a laser heater, new bunch compressors and new modules. The latter results in an energy upgrade to 1.35 GeV allowing to reach sub 4 nm wavelength. In the following 14-month lasting shutdown starting mid 2024 the FLASH1 FEL beamline will be completely rebuild. The design is based on external seeding at MHz repetition rate in burst mode allowing for coherent tuneable FEL radiation in wavelength and polarization by installation new APPLE-III undulators. Post compression of the beam downstream of the radiators will allow for high quality THz generation and together with the new experimental end stations and pump probe lasers provide a unique portfolio for next generation user experiments.

INTRODUCTION

The FLASH facility [1-3], housed at DESY, Hamburg, currently consists of a superconducting linac powering two FEL beamlines (FLASH1 and FLASH2). These beamlines provide extreme ultraviolet to soft x-ray radiation generated via self-amplified spontaneous emission (SASE) to facilitate various kinds of user experiments. In addition, a significant share of the FLASH operation time is committed to research and development, which e.g. led to developments like the gas monitor detector for FEL beam position and intensity diagnostics [4]. The developed components in R&D also contributed significantly to upgrades and improvements the facility has undergone since it was built in 2003/2004, at that time named VUV-FEL at TTF2 [5]. To increase the available parameter range and enable next generation user experiments the current facility upgrade, coordinated in the FLASH2020+ project, has already been started. One of the main goals is to provide coherent and spectro-temporally stable beams while also extending the wavelength range even further into the water window.

The individual updates required to achieve the project milestones are grouped in a two-stage process: During a nine-month shutdown which finished in mid-August 2022 the linac has been in focus with upgrades targeting the beam quality and energy, described in detail in the following. The second stage will target the current FLASH1 FEL beamline, removing all of its components and replacing it by an externally seeded beamline. The latter includes an upgrade of the existing photon diagnostics and photon beam transport to allow for most efficient use of beamtime by users with fully characterised beams for every shot at highest possible intensities.

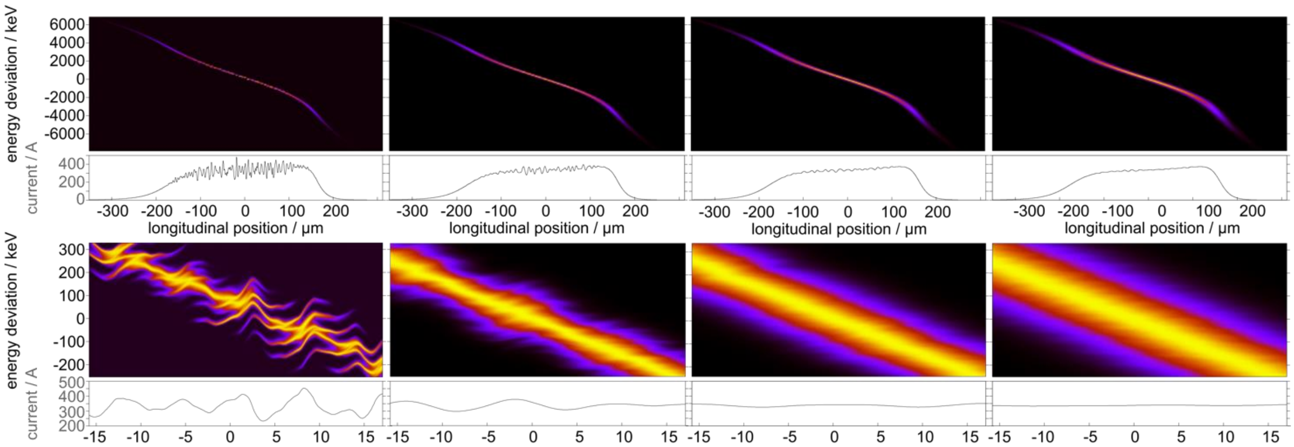

Figure 1: Numerical simulation of the phase space of the full electron beam (top) and the central slice (bottom) together with the current profile at the end of the linac using a recently developed semi-Lagrangian Vlasov simulation code [6]. The images on the left display the situation with the laser heater at zero laser power resulting in an initial sliced energy spread of 3 keV before compression. Towards the right the laser power is increased to reach sliced energy spreads of 5

† lucas.schaper@desy.de

ISBN: 978-3-95450-220-2 ISSN: 2673-5474 doi: 10.18429/JACoW-FEL2022-TUP51

keV, 7 keV and 9 keV respectively. The current profiles visualise how the increased slice energy spread reduces the micro bunching while also increasing the characteristic wavelength of the features

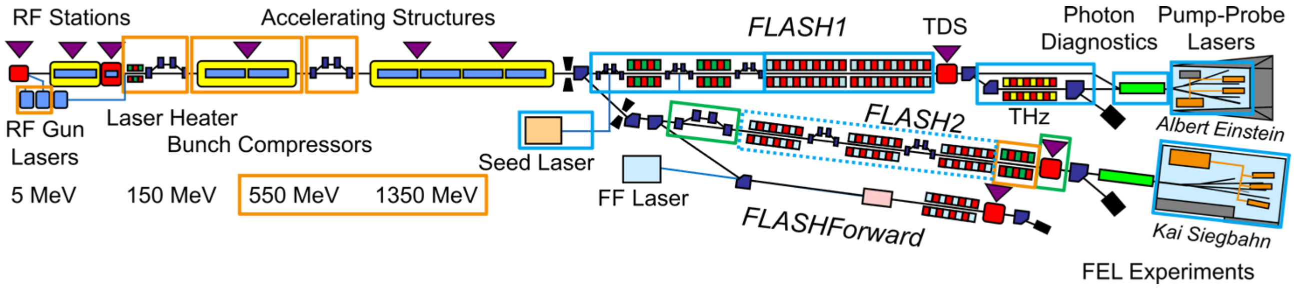

Figure 2: Schematic drawing of the FLASH facility with the accelerator section on the left starting at the gun (red square) the electron is accelerated to 150 MeV in the first modules (ACC1, yellow and ACC39, red) before being overlapped with a laser in the laser heater and then compressed in the first bunch compressor. In the now new modules (ACC2 and ACC3, yellow) the beam is then brought to 550 MeV and further compressed in the second bunch compressor. The final beam energy, currently determining the wavelength of the FEL radiation in FLASH1, is then adjusted using the following modules (ACC4 ,5, 6 and 7, yellow). Downstream of the accelerator the portions of the bunch train beam can be distributed into the FLASH2 or Flash-forward beamline and in parallel to FLASH1. For the FLASH1 beamline the schematic already illustrates the seed beamline while for FLASH2 a future upgrade option for generation of ultrashort pulses is displayed. Upgrades of the FLASH 2020+ project are illustrated in coloured boxes with green already being in operation, orange installed in the current shutdown and blue upgrades to be implemented starting 2024.

FIRST INSTALLAION PHASE 2021-2022

With the FLASH2 FEL beamline being the most recent addition to the FLASH user facility, which already got retrofitted with a dedicated bunch compressor and a transverse deflecting structure, called PolariX [7], to increase diagnostic capabilities and electron beam quality the accelerator was at highest priority for the current upgrade phase. In the nine-month lasting shutdown until August 2022 the linear accelerator has undergone severe modification to enhance the electron beam properties and increase the available parameter range for users, especially towards short wavelengths. Starting with the electron generation at the gun, two new photo injector lasers systems have been installed allowing for more independent control of the bunch train parts being sent to the FEL beamlines. Tweaking of the laser pulse duration and the spot size on the cathode will allow operation with tailored electron beam properties. This will enable for example the generation of THz at highest bunch charges in FLASH1 while providing short pulses with low charge in FLASH2. The old photoinjector lasers, which are approaching the end of their lifetime, will still be used to bring the facility back in operation at the end of the shutdown and serve as a backup after commissioning of the new systems.

Downstream of the superconducting acceleration modules ACC1 and the phase space linearizing module ACC39 the completely redesigned first compression and matching section now also incorporates a laser heater. In contrast to other designs [8], here, the laser heater acts on the non-dispersed electron beam to avoid transverse nonuniformities. Simulations of this system show an effective decrease in the beam substructure induced by micro bunching for mildly increasing the initial sliced energy spread from 3 keV to about 9 keV [9]. While microbunching is a gain process with a stochastic seed originating from noise, the laser heater allows to control the gain and thus flattens the current profile of the resulting electron beam, as can be seen in Fig 1. Since for external seeding a fine controlled substructure will be imprinted on the beam starting from a reproducible and homogenous current profile is crucial to deliver stable FEL output to user experiments. In addition to heating the entire electron bunch more elaborate schemes are also being investigated.

For increasing the maximum electron energy of FLASH, the two acceleration modules downstream of the first bunch compressor called ACC2 and AAC3 have been replaced by new state-of-the-art modules and the RF distribution has been optimised. As a result, the former XFEL prototype modules will allow operation at average gradient close to 30 MeV/m and thus increase the possible electron beam energy by 100 MeV to a total of 1.35 GeV. The higher electron energy in turn allows to generate higher photon energies and provide the users with sub 4nm photon wavelengths in the fundamental, extending the feasible experimental applications. In FLASH2 additionally the installation of a short period afterburner, foreseen for the year 2023, will allow to boost intensity at the third harmonic and thus facilitate experiments at wavelength as low as 1.39 nm. The design of the afterburner follows the APPLE III principle allowing for variable polarisation accessible to experiments for the first time at FLASH.

Although not bound to the times of an accelerator shutdown the occasion is also used to expand and upgrade the installations in the experimental halls in parallel. New beamline components, e.g. for the time-delay

ISBN: 978-3-95450-220-2 ISSN: 2673-5474 doi: 10.18429/JACoW-FEL2022-TUP51

compensating monochromator beamline FL23 in the FLASH2 experimental hall "Kai Siegbahn", have been prepared and put in place while in the FLASH1 hall "Albert Einstein" the existing pump-probe laser hutch undergoes an extensive refurbishment. Here, a new air-condition system will reduce temperature and humidity fluctuations providing an environment for stable operation of the 10 Hz millijoule laser system to be reinstalled. The project is progressing well, and all shutdown-related milestones were reached in time ensuring a smooth transition into the upcoming commissioning phase starting mid-August. With a very dense commissioning schedule ahead the whole FLASH team is looking forward to see the improvements also transferring to successful user campaigns starting in early November 2022. The following period of 2.5 years of user experiments as well as own R&D and preparatory seeding experiments using the new installed hardware will allow to further optimize and tweak the machine, also ensuring a smoother commissioning phase after installation of the seeded beamline.

SECOND INSTALLATION PHASE: FLASH1 - A NEW EXTERNALLY SEEDED BEAMLINE

The second stage of the FLASH2020+ project is focussed on the FLASH1 FEL beamline. In a 14-month shutdown period starting mid 2024 the complete existing beamline will be disassembled and removed from the accelerator tunnel. Once empty the infrastructure of the accelerator tunnel will be modernised and adjusted to host a new externally seeded FEL beamline, of which details are discussed in a separate contribution [10-12]. In short, using the concepts of echo-enabled harmonic generation [13] and high gain harmonic generation [14] and a newly developed 1 MHz burst tuneable seed laser in the range from 297 nm to 317 nm [15,16] coherent FEL radiation from 60nm down to 4nm can be generated. With the experience from the FLASH 2 afterburner the radiators for the new FLASH1 beamline will also follow the APPLE III concept and allow users to scan polarisation during experiments.

Downstream of the new radiators the generated FEL pulses are separated from the electron beam and passed over a new photon diagnostic section before being passed into the FLASH1 experiment hall "Albert Einstein". From the separation point the electron beam is passed via an additional bunch compressor into the THz undulator where radiation between 1 and 300 THz can be generated and also transported into the “Albert Einstein” hall for experiments. The post compression is a necessity of the drastically different bunch properties conducive for seeding with not fully compressed bunches with peak current around 500A and highly compressed bunches with highest possible peak current to allow for generating THz intensities on the 100 microjoule level. bunch properties conducive for seeding with rather long bunches with peak current around 500A and short bunches with highest possible peak current to allow for generating THz intensities on the 100 microjoule level.

On a similar note, the FLASH facility will be unique in operating an externally seeded beamline at FLASH1 and in parallel a SASE beamline at FLASH2 sharing the same linac. Also, here the different bunch properties required by the two mechanisms are challenging to be realised for parallel operation. A first proof-of-principle experiment has been conducted at the FLASH facility already in 2021 demonstrating the feasibility of parallel operation for the first time worldwide. Results are being presented in a separate contribution [17].

To fully exploit the beam properties of the seeded FEL also the Albert Einstein hall will experience further upgrades. Here, new pump-probe lasers with increased repetition rate, higher pulse energy and an increased wavelength portfolio will be made available to all beamlines. For elaborate pump-probe experiments a new beamline called FL11 will be installed which is optimised for highest transmission at short wavelengths and which allows to combine FEL, pump-probe laser and THz radiation at the end station. While using the FEL at other end stations, here experiments combining THz and Pump-probe laser can be performed in parallel.

Additional Upgrades Within the Project

As already indicated in Fig. 2, the upgrade plans within the FLASH2020+ project, e.g. with installations for generation of attosecond pulses at FLASH2, span beyond what can be described here and are subject to availability of additional funding. They will be presented in detail when more robust information is available.

CONCLUSION

With the current accelerator upgrades and the future installation of a 1 MHz repetition rate externally seeded beamline in burst mode the FLASH facility will significantly broaden its parameter set available to users. This creates opportunities for new kinds of user experiments and especially with the planned stability of the seeded FEL will allow for new classes of experiments not possible at FELs before.

ACKNOWLEDGEMENTS

The authors would like to thank all people involved in the FLASH2020+ project as well as in FLASH operation. A special thanks also to the large number of people ensuring timely progress in the installation phases and to Enrico Allaria (Elletra).

REFERENCES

[1] W. Ackermann *et al.*, “Operation of a free-electron laser from the extreme ultraviolet to the water window”, *Nat. Photonics*, vol. 1, pp. 336–342, 2007. doi:10.1038/nphoton.2007.76

[2] B. Faatz *et al.*, “Simultaneous operation of two soft x-ray free-electron lasers driven by one linear accelerator”, *New J. Phys.*, vol. 18, p. 062002, 2016. doi:10.1088/1367-2630/18/6/062002

ISBN: 978-3-95450-220-2 ISSN: 2673-5474 doi: 10.18429/JACoW-FEL2022-TUP51

[3] K. Honkavaara and S. Schreiber, “FLASH: The Pioneering XUV and Soft X-Ray FEL User Facility”, in *Proc. 39th Int. Free Electron Laser Conf. (FEL’19)*, Hamburg, Germany, Aug. 2019, paper THP074, pp. 734–737, 2019. doi:10.18429/JACoW-FEL2019-THP074

[4] M. Richter *et al.*, "Measurement of gigawatt radiation pulses from a vacuum and extreme ultraviolet free-electron laser", *Appl. Phys. Lett.*, vol. 83, p. 2970, 2003. doi:10.1063/1.1614417

[5] K. Honkavaara *et al.*, “Status of the Free-Electron Laser User Facility FLASH”, presented at the 40th Int. Free Electron Laser Conf. (FEL’22), Trieste, Italy, Aug. 2022, paper MOP37, this conference

[6] Simulation code: http://selav.desy.de

[7] F. Christie *et al*. "A PolariX TDS for the FLASH2 Beamline", in *Proc. 39th Int. Free Electron Laser Conf. (FEL’19)*, Hamburg, Germany, Aug. 2019, paper WEP006, pp. 328-331, 2019. doi:10.3204/PUBDB-2019-03833

[8] M. Hamberg, F. Brinker, and M. Scholz, “Commissioning and First Heating with the European XFEL”, in *Proc. 8th Int. Particle Accelerator Conf. (IPAC’17)*, Copenhagen, Denmark, 2017, pp. 2625-2627, paper WEPAB024 doi:10.18429/JACoW-IPAC2017-WEPAB024

[9] Ph. Amstutz and M. Vogt, “Microbunching Studies for the FLASH2020+ Upgrade Using a Semi-Lagrangian Vlasov Solver”, *Proc. 13th Int. Particle Accelerator Conf. (IPAC’22)*, Bangkok, Thailand, Jun. 2022, pp. 2334-2337. doi:10.18429/JACoW-IPAC2022-WEPOMS037

[10] E. Ferrari *et al.*, “Status of the Seeding Upgrade for FLASH2020+ Project”, presented at the 40th Int. FreeElectron Laser Conf. (FEL’22), Trieste, Italy, Aug. 2022, paper TUP42, this conference

[11] M. Beye *et al.* “FLASH2020+, Conceptual Design Report”, DESY, Hamburg, 2020. doi:10.3204/PUBDB-2020-00465

[12] L. Schaper *et al.*, “Flexible and Coherent Soft X-ray Pulses at High Repetition Rate: Current Research and Perspectives”, *Appl. Sci.*, vol. 11, p. 9729, 2021. doi:10.3390/app11209729

[13] G. Stupakov, “Using the Beam-Echo Effect for Generation of Short-Wavelength Radiation”, *Phys. Rev. Lett.*, vol. 102, p. 074801, 2009. doi:10.1103/PhysRevLett.102.074801

[14] L.H. Yu, “Generation of Intense UV Radiation by Subharmonically Seeded Single-Pass Free-Electron Lasers”, *Phys. Rev. A*, vol. 44, pp. 5178–5193, 1991. doi:10.1103/PhysRevA.44.5178

[15] T. Lang *et al.*, “High repetition rate, ultra-low noise andwavelength stable UV seed laser system for tunable twocolorEEHG FEL seeding”, presented at the 40th Int. Free Electron Laser Conf. (FEL’22), Trieste, Italy, Aug. 2022. paper TUP43, this conference

[16] M.M. Kazemi *et al.*, “Towards seeded high repetition rateFEL: Concept of seed laser beam transport and incoupling”, presented at the 40th Int. Free Electron Laser Conf. (FEL’22), Trieste, Italy, Aug. 2022. paper TUP45, this conference

[17] S. Ackermann *et al.*, “First Demonstration of Parallel Operation of a Seeded FEL and a SASE FEL”, presented at the 40th Int. Free Electron Laser Conf. (FEL’22), Trieste, Italy, Aug. 2022, paper TUP41, this conference

ISBN: 978-3-95450-220-2 ISSN: 2673-5474 doi: 10.18429/JACoW-FEL2022-TUP52

THE NEW FLASH1 UNDULATOR BEAMLINE FOR THE FLASH2020+ PROJECT

Johann Zemella, Mathias Vogt*
Deutsches Elektronen-Synchrotron DESY, Hamburg, Germany

Abstract

The 2nd stage of the FLASH2020+ project at DESY will be an upgrade of the FLASH1 beamline to enable HGHG and EEHG seeding with two modulator-chicane stages, and a radiator section with 11 APPLE-III undulators to enable FEL radiation with controllable polarization. A key feature of FLASH, namely the capability of providing several thousand FEL pulses in the extreme UV and soft X-ray must not be compromised. Downstream of the radiator the beamline houses longitudinal diagnostics, a double bend (quasi-) achromat to separate the electrons from the photons and divert the electron beamline from the photon diagnostics, a post-compressor, a THz-Undulator (requires an electron beam that is compressed more strongly than for seeding), and finally the dumpline, capable of safely aborting up to 100 kW electron beam power.

This article describes the conceptional and some technical details of the beamline with emphasis on the upstream part (modulators and radiator) designed for seeding.

INTRODUCTION

FLASH the XUV- and soft X-ray user facility at DESY in Hamburg [1–7] is currently undergoing a substantial upgrade and refurbishment project, FLASH2020+ [8–10]. The FLASH accelerator consists of four functionally distinct sections: the common part (injector, linac), called FLASH0, which is upgraded and refurbished in the current shutdown [3, 5], the two independently operated undulator beamlines FLASH1 & FLASH2 [11, 12], and the experimental beamline FLASH3. The superconducting linac supplies long RF pulses with a flat top usable for beam operation of up to 800 µs). This flat top can be split with a transition time of typically 70 µs, so that both beamlines can be served with sub-trains of up to several hundred bunches at bunch frequencies of up to1 MHz at every RF-pulse. The RF pulse repetition frequency is 10 Hz. FLASH1 will be basically completely rebuilt in 2024/25 which is the topic of this contribution.

Conceptual Overview of the Beamline

In the past both FLASH1/2 were dedicated SASE (Self-Amplified Spontaneous Emission) FELs (Free-Electron Lasers). In the future the new FLASH1 beamline, however will be optimized for high repetition rate HGHG (High Gain Harmonic Generation) and EEHG (Echo-Enabled Harmonic Generation) external seeding [9] within the FLASH2020+ project.

SASE has proven to be an extremely powerful and robust FEL mechanism, but external seeding potentially enhances the control over properties of the produced FEL radiation, i.p. the longitudinal coherence, substantially [9].

The incoming bunch is overlaid in the first undulator (modulator UM1) with the first seed laser beam (L1). Thereby an energy modulation is impregnated on the bunch PSD. Next the energy modulation from L1 and UM1 is strongly oversheared in the first magnetic chicane (**CH1**). Then the bunch is overlaid in the second undulator (modulator UM2) with the second seed laser beam (L2). Finally bunch is moderately sheared in the second magnetic chicane (**CH2**) so that its sinusoidally modulated fine structure generates bunching whose higher order Fourier harmonics will seed the FEL process in the radiator.

Downstream of the radiator the electron beam passes through a longitudinal diagnostic section before it is separated from the FEL beam, post-compressed, sent through an electromagnetic undulator for THz radiation used for highly synchronized pump-probe experiments [13] before it is finally dumped.

Here we give an overview of the FLASH1 beamline with emphasis on the FEL sections, namely the two modulator sections with their chicanes and the radiator section. The other sections of the beamline, collimation, matching, longitudinal diagnostics, horizontal separation from the FEL beam, post-compression, THz undulator and the dump beamline have been described in greater detail in [14].

BEAMLINE DETAILS

The undulator beamline is split into several functional sections as is shown in Fig. 1

A section for diagnostic collimation and matching will be installed upstream of the modulator section immediately following the FLASH1/FLASH2 switch yard.

The modulator sections FL1MOD1/2 contain the 2.5 m long planar modulator undulators UM1 and UM2. The magnetic structure of the undulators is not yet fixed but will soon be finalized. Each modulator is surrounded by two 0.6 m long intersections (see Fig. 2 left) equipped with a beam position monitor (BPM), a quadrupole with x/y-mover, a screen station, 2 beam loss monitors (BLMs) and x/y-steering using air-coils or small ferrite coils. The modulator sections also contain the two vertical C-chicanes **CH1** and **CH2** needed for the EEHG external seeding process as briefly explained in subsection . An additional chicane **InC** (Fig. 3) is needed upstream of modulator UM1 for in-coupling of the first seed laser L1. The seed laser L2 is coupled in through **CH1** (Fig. 4) upstream UM2. The laser beams are coupled out

* vogtm@mail.desy.de

ISBN: 978-3-95450-220-2 ISSN: 2673-5474 doi: 10.18429/JACoW-FEL2022-TUP52

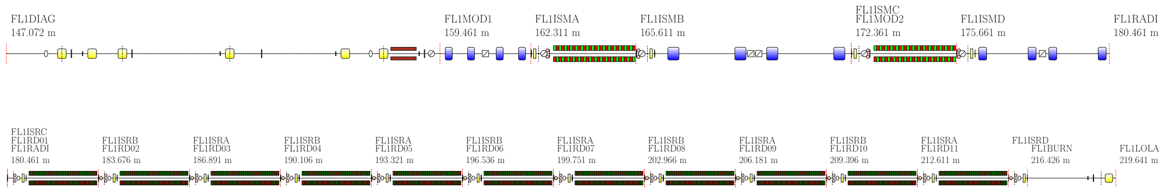

Figure 1: Schematic layout [15] of the seeded FLASH1 undulator beamline: top: FL1DIAG-FL1MOD2 (Δs = 33.43 m), bottom: FL1RADI-FL1BURN (Δs = 39.18 m). Each line is to scale but the two lines vary in overall length.

and diagnosed at the downstream chicanes **CH1** and **CH2** (Fig. 5).

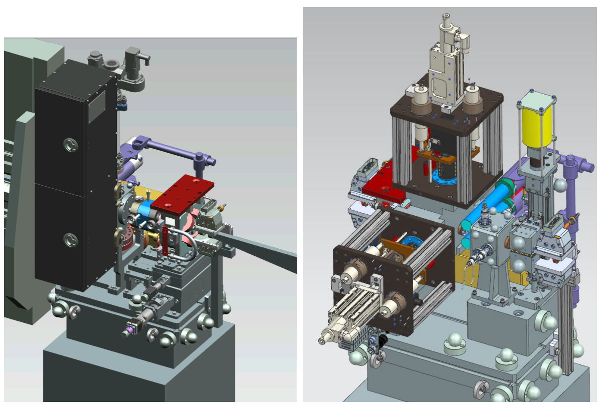

Figure 2: 3D CAD model of the intersection types used (left) with the modulator undulators, and (right) with the radiators and both both wire scanner ports equipped.

The **InC** chicane has only two operational states: active, for inserting the in-coupling mirror, and flat, for retracted mirror. The two seeding chicanes **CH1** and **CH2** need to be fully tunable during set up of the FEL Process. Because of the delicacy of the seeding process this requires almost perfect chicanes in the complete tuning range. All chicanes should guarantee an M_{56}-reproducibility of 1×10^{-3}, spurious dispersion < 1 mm and an orbit-closure under tuning of < 200 µm which is already technically challenging. Table 1 shows the minimum required beam offsets and the M_{56} tuning ranges (for inserted and retracted in/out-coupling mirrors where applicable). The large tuning ranges are challenging because they impose large good-field regions to fully accommodate the beam for various deflection angles, and simultaneously excellent field quality inside these regions, All magnets should comply to $|\delta B\mathrm{d}l/B\mathrm{d}l| < 5 \cdot 10^{-4}$ inside their good-field region. The design constraints on the chicane dipoles in the FLASH1 beamline are described in detail in [14].

Table 1: Chicane specifications

chic.	beam offset	M_{56} m. in	M_{56} m. out
InC	≥ 7.5 mm	—	~ 0 µm
CH1	≥ 20.0 mm	400 µm - 14.5 mm	0-250 µm
CH2	≥ 7.5 mm	40-350 µm	0-300 µm

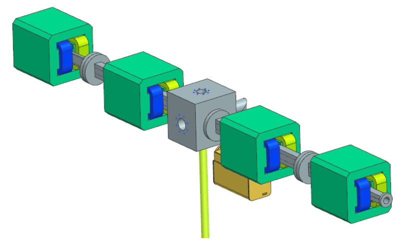

Figure 3: 3D CAD model of the in-coupling chicane **InC**. The yellow pipe is part of the in-coupling system of seed laser L1.

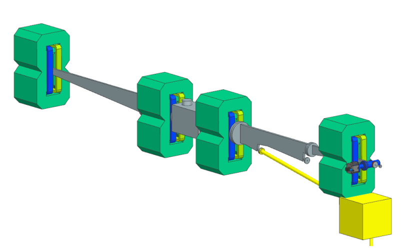

Figure 4: 3D CAD model of the over-folding (EEHG) chicane **CH1**. The yellow pipe and box are part of the in-coupling system of seed laser L2.

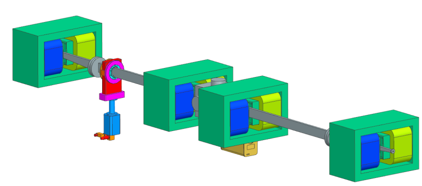

Figure 5: 3D CAD model of the bunching chicane **CH2**.

The radiator undulator section consists of eleven 2.44 m long APPLE-III-type undulator segments (see Fig. 6), surrounded and interleaved by twelve 0.6 m long intersections (see Fig. 2 right) each with a BPM, a phase shifter, a quadrupole with x/y-mover, a wire scanner station (either horizontal or vertical equipped[1]), 2 BLMs, and steering using air-coils or small ferrite coils.

Downstream of the 11 seed radiators space is foreseen for a 3rd harmonic afterburner which will, however, not be installed in the 2024/25 shutdown.

[1] Fig. 2 (right) shows both wire scanners equipped, which is in principle possible as a further upgrade.

ISBN: 978-3-95450-220-2 ISSN: 2673-5474 doi: 10.18429/JACoW-FEL2022-TUP52

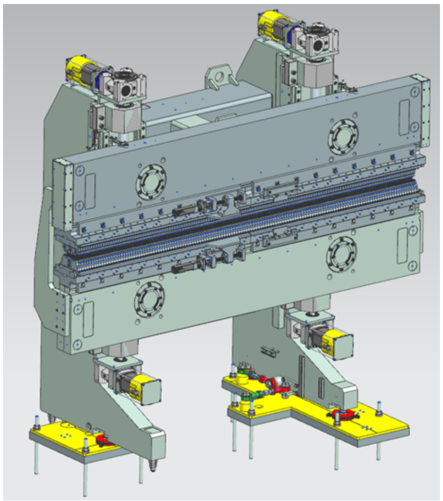

Figure 6: 3D CAD model of the APPLE-III undulator.

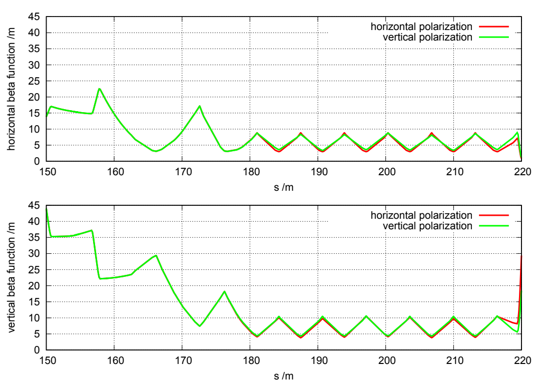

Figure 7: Optics in modulator and radiator section for different polarization settings of the radiator for a beam energy of 1350 MeV. Top: horizontal plane; bottom: vertical plane.

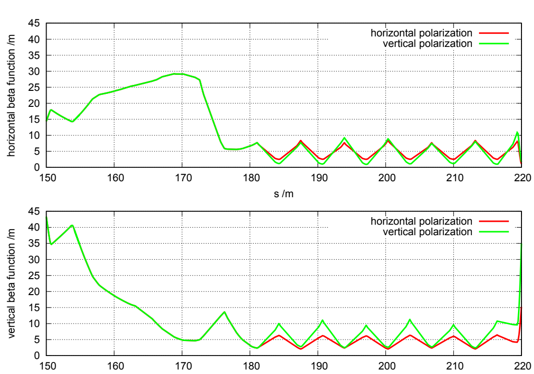

Figure 8: Optics in modulator and radiator section for different polarization settings of the radiator for a beam energy of 750 MeV. Top: horizontal plane; bottom: vertical plane.

Optics

The electron optics for the FLASH1 beamline must meet many requirements to ensure good FEL performance as well as proper operability of the accelerator: (1) Efficient collimation of the electron beam. (2) Capability to measure and adapt electron optics upstream of the modulators without interfering with FLASH2 operation. (3) Electron beam size inside the modulators < 150 µm. (4) Small average beta functions in the radiator to ensure high FEL gain. (5) Optics adaption during Polarization scan should only use quadrupoles downstream of the second modulator. The above requirements must be fulfilled for the three standard energy working points: 1.35 GeV, 0.95 GeV and 0.75 GeV.

The beam optics is calculated using MAD8 [16] with Linac extensions [17, 18]. The wigglers are implemented as a matrix for planar undulator which is tilted for different polarization states.

In the septum dipole for the separation of the FLASH2 beamline, the horizontal beta function has a strong focus that needs to be matched into the FLASH1 diagnostics and collimation section. To ensure an efficient collimation, the phase advance between the two collimators should be between 60° and 120° and the beta functions at the collimators should be large. In addition, the optics must be so that the beam sizes in the modulators fulfill $\beta_{x,y}^{\mathrm{mod1,mod2}} < 30$ m assuming a normalized emittance of 1 µm. There is no additional optics matching section between the last modulator and the radiator section, not only because the beamline is lacking space, but also because we want to keep the deteriorating effects of spurious dispersion and drift-M_{56} on the fine-structured phase space, prepared for seeded FEL operation as small as possible. All changes of the undulator focusing due to changes in the polarization settings and the undulator-Ks of the radiators have to be compensated using only the last quadrupole downstream of the second modulator and the quadrupoles in the radiators section. The currently used design beam optics for the FLASH1 beamline is depicted for horizontal and vertical radiator polarization states for 1350 MeV in Fig. 7 and for 750 MeV in 8. As can be seen, the optics adaption look good but is not completely symmetric. It is obvious that the sensitivity to changes in the undulator settings is largest at small energies.

The beamline designed for FLASH1 is finished and the component design is close to finalization. We are looking forward to installing the new beamline in the 2024/25 shutdown.

ACKNOWLEDGMENTS

We thank all the people involved in the design of the FLASH1 beamline, the seeding concepts, and the FLASH1 hardware.

ISBN: 978-3-95450-220-2 ISSN: 2673-5474 doi: 10.18429/JACoW-FEL2022-TUP52

REFERENCES

[1] W. Ackermann *et al.*, “Operation of a free-electron laser from the extreme ultraviolet to the water window”, *Nat. Photonics*, vol. 1, pp. 336–342, 2007. doi:10.1038/nphoton.2007.76

[2] K. Honkavaara, C. Gerth, M. Kuhlmann, J. Rönsch-Schulenburg, L. Schaper, R. Treusch, M. Vogt, J. Zemella, S. Schreiber, “Status of the Free-Electron Laser User Facility FLASH”, presented at the 40th Int. Free Electron Laser Conf. (FEL’22), Trieste, Italy, Aug. 2022, paper MOP37, this conference.

[3] M. Vogt, Ch. Gerth, K. Honkavaara, M. Kuhlmann, J. Rönsch-Schulenburg, L. Schaper, S. Schreiber, R. Treusch, J. Zemella, “Status of the Superconducting Soft X-ray Free-Electron Laser User Facility”, presented at the 13th Int. Particle Accelerator Conf. (IPAC’22), Bangkok, Thailand, June 2022, paper TUPOPT005.

[4] S. Schreiber, J. Roensch-Schulenburg, F. Christie, K. Honkavaara, M. Kuhlmann, R. Treusch, M. Vogt, and J. Zemella, “Status Report of the Superconducting Free-Electron Laser FLASH at DESY”, presented at the 12th Int. Particle Accelerator Conf. (IPAC’22), Campinas, Brazil, May 2021, paper TUPAB115. doi:10.18429/JACoW-IPAC2021-TUPAB115

[5] J. Rönsch-Schulenburg, K. Honkavaara, S. Schreiber, R. Treusch, M. Vogt “FLASH - Status and Upgrades”, presented at the 39th Int. Free Electron Laser Conf. (FEL’19), Hamburg, Germany, Aug. 2019, paper FRA03. doi:10.18429/JACoW-FEL2019-FRA03

[6] J. Rossbach, J. R. Schneider, and W. Wurth, “10 years of pioneering X-ray science at the free-electron laser FLASH at DESY”, *Phys. Rep.*, vol. 808, pp. 1–74, 2019. doi:10.1016/j.physrep.2019.02.002

[7] K. Honkavaara and S. Schreiber, “FLASH: The Pioneering XUV and Soft X-Ray FEL User Facility”, in *Proc. FEL’19*, Hamburg, Germany, Aug. 2019, pp. 734–737. doi:10.18429/JACoW-FEL2019-THP074

[8] M. Beye, *et al.*, “FLASH2020+, Conceptual Design Report”, DESY, Hamburg, 2020. doi:10.3204/PUBDB-2020-00465

[9] L. Schaper, S. Ackermann, E. Allaria *et al.*, “Flexible and Coherent Soft X-ray Pulses at High Repetition Rate: Current Research and Perspectives”, *Appl.Sci*, vol. 10, 9729, 2021. doi:10.3390/app11209729

[10] L. Schaper *et al.*, “FLASH2020+ Project Progress: Current Installations and Future Plans”, presented at the 40th Int. Free Electron Laser Conf. (FEL’22), Trieste, Italy, Aug. 2022, paper TUP51, this conference.

[11] B .Faatz, *et al.*, “Simultaneous operation of two soft x-ray free-electron lasers driven by one linear accelerator”, *New J. Phys.*, vol. 18, p. 062002, 2016. doi:10.1088/1367-2630/18/6/062002

[12] J. Roensch-Schulenburg, *et al.*, “Experience with Multi-Beam and Multi-Beamline FEL-Operation”, *J. Phys.: Conf. Series*, vol. 874, p. 012023, 2017. doi:10.1088/1742-6596/874/1/012023

[13] R. Pan, *et al.*, “Photon diagnostics at the FLASH THz beamline”, J. Synchrotron Radiat., vol. 26 , pp. 700-707, 2019. doi:10.1107/S1600577519003412

[14] M. Vogt and J. Zemella, “The New FLASH1 Beamline for the FLASH2020+ Project”, in *Proc. IPAC’22*, Bangkok, Thailand, Jun. 2022, pp. 1010–1013. doi:10.18429/JACoW-IPAC2022-TUPOPT006

[15] adapted version of: Jan Schmidt, “tikz-palattice — Draw particle accelerator lattices with TikZ”, (2017). https://ctan.org/pkg/tikz-palattice?lang=en

[16] H. Grote, F.C. Iselin, “The MAD Program (Methodical Accelerator Design) Version 8.15”, CERN/SL/90-13 (AP), 1990.

[17] H. Grote, *et. al.*, H. Grote, E. Keil, T. O. Raubenheimer, and M. Woodley, “Extension of MAD Version 8 to include Beam Acceleration”, in *Proc. EPAC’00*, Vienna, Austria, Jun. 2000, paper TUP3A02, pp. 1390–1392.

[18] J. Zemella, Ph. Amstutz, W. Decking, M. Vogt, “More upgrades ’n’ bug-fixes for linac-mad at DESY”, 2000-2022, unpublished.

ISBN: 978-3-95450-220-2 ISSN: 2673-5474 doi: 10.18429/JACoW-FEL2022-TUP53

FUTURE UPGRADE STRATEGY OF THE FERMI SEEDED FEL FACILITY

E. Allaria, L. Badano, F. Bencivenga, C. Callegari, F. Capotondi, D. Castronovo, P. Cinquegrana, M. Coreno, M. B. Danailov, A. Demidovich, G. De Ninno, P. Del Giusto, S. Di Mitri, B. Diviacco, W. M. Fawley, M. Ferianis, G. Gaio, F. Gelmetti, L. Giannessi, G. Kurdi, M. Lonza, M. Malvestuto, M. Manfredda, C. Masciovecchio, I. Nikolov, G. Penco, K. C. Prince, E. Principi, P. R. Rebernik, C. Scafuri, N. Shafqat, P. Sigalotti, A. Simoncig, S. Spampinati, C. Spezzani, L. Sturari, M. Trovò, M. Veronese, R. Visintini, M. Zangrando, Elettra-Sincrotrone Trieste S.C.p.A, Basovizza, Italy.
T. Tanaka, RIKEN SPring-8 Center, Hyogo, Japan.
G. Penn, Lawrence Berkeley National Laboratory, USA
G. Perosa, F. Sottocorona, Università degli Studi di Trieste, Trieste, Italy

Abstract

FERMI is undergoing a series of upgrades to keep the facility in a world-leading position. The ultimate goal of the development plan consists in extending the facility spectral range to cover the water window and above and to reduce the minimum pulse duration below the characteristic lifetime of core holes electrons of light elements. We present here the main elements of this upgrade strategy.

INTRODUCTION

The upgrade involves deep modifications of the linac and of the two FERMI FELs with the ambition of extending the FEL performances and the control of the light produced to include the K-edges of N and O, and the L_{23}-edges of elements of the first two periods. One of the main requisites of this upgrade is the preservation of the uniqueness of FERMI: the possibility to control the properties of the radiation by seeding the FEL with an external laser system. Through the control of the microbunching formation in the electron beam the seed allows amplification of almost Fourier transform-limited pulses [1–3], to synchronize the FEL pulses with unprecedented precision to an external laser [4] and to control many pulse properties as phase and coherence [5, 6]. The extended photon energy range will allow resonant experiments (XANES, XMCD, SAXS, CDI,…) exploiting several important edges (life-time in the range of few fs), larger wave-vector (non-linear Optics), ultrafast chemistry (conical intersections lifetime 0.5 – 10 fs) [7]. Presently, the spectral range up to 310 eV is covered by the two FELs: FEL-1 and FEL-2; the first provide photons in the range 20 – 65 eV, the second in the range 65 – 310 eV. In view of the upgrade, the photon energy distribution between the two FELs has to be adapted to the upgraded scenario, with FEL-1 still covering the low photon energy range, but extended to reach a photon energy of 100 eV [8], and FEL-2 dedicated to the high energy range, from 100 eV to about 550 eV.

FEL-2 UPGRADE

To extend the FEL-2 spectral range to the oxygen K-edge, two options were considered, either by using EEHG directly, or with a cascade employing both EEHG and HGHG techniques in the “fresh-bunch” injection technique now used on FEL-2. The implementation of EEHG first solution requires a first large dispersion chicane of up to 15 mm for optimized EEHG operation. This makes the scheme prone to a number of effects which may result in a degradation of the FEL spectral purity and of the FEL gain in the final radiator [9, 10]. The large chicane is indeed an amplifier of microbunching instability (MBI). A second issue is the emission of incoherent synchrotron radiation (ISR) and the intra-beam scattering (IBS) along the chicane. These two effects are the source of mixing of the filamented phase space that produces the high harmonic bunching in EEHG after the second chicane, a factor reducing the bunching at the entrance of the amplifier.

All these effects would be mitigated in a scheme where the chicanes have a lower dispersion. This is the reason why we considered the second option, where the EEHG generates a seed that is then used in fresh-bunch to seed a second HGHG stage, similarly to what is done in the present FEL-2 configuration. The present double-stage HGHG with fresh-bunch scheme, can be upgraded by converting the first stage to an EEHG configuration aimed at reaching harmonics of the order of 30. The second stage would then up-convert the output of the first stage to harmonics of the order 120 – 130 as required.

This configuration needs a much lower dispersion, of the order of 4-5 mm, which is only a factor two larger than the one used in the FERMI EEHG experiment. We analysed the four different configurations of seeded FELs shown in Fig. 1 and selected the most promising one with the aim of extending the seed coherence to the highest harmonic orders.

ISBN: 978-3-95450-220-2 ISSN: 2673-5474 doi: 10.18429/JACoW-FEL2022-TUP53

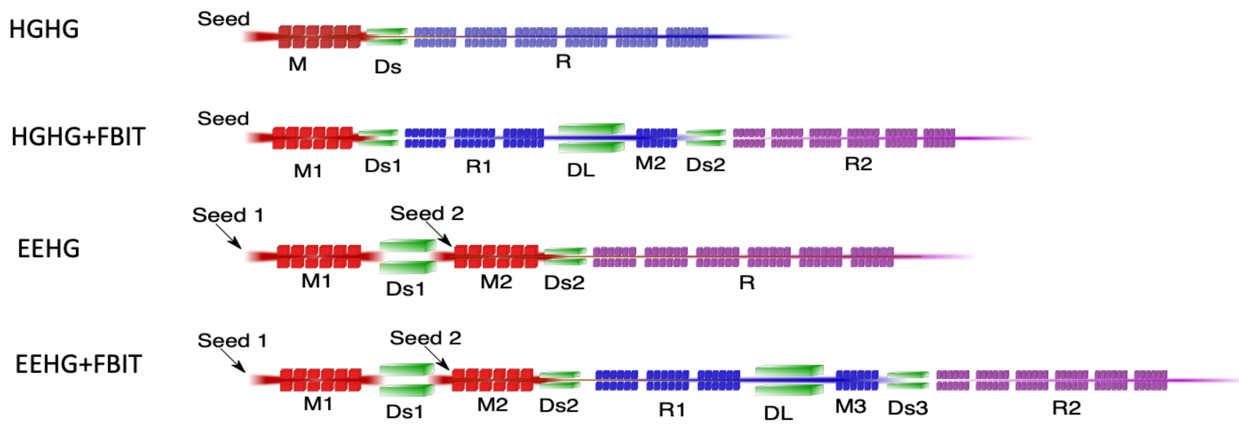

Figure 1: Schematic layout of the four configurations analyzed, in order from top to bottom: High-gain harmonic generation (HGHG as in FEL-1), double stage, high-gain harmonic generation with fresh-bunch injection tech. (HGHG+FBIT as in FEL-2), Echo-enabled harmonic generation (EEHG), Double stage, echo-enabled harmonic generation with fresh-bunch injection tech. (EEHG+FBIT).

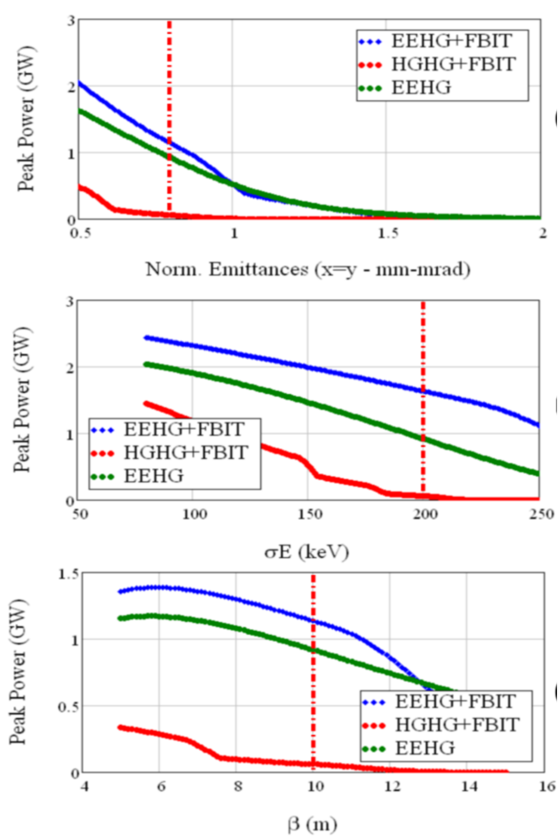

Figure 2: Dependence of the estimated FEL output power on electron beam emittance, energy spread and beta (Twiss) parameter. Assumptions: wavelength of operation 2 nm, linear polarization. Other parameters as listed in Table 1.

The explicit dependence of the pulse peak power on the various parameters and for both the polarizations is shown in the plots represented in Fig. 2. Table 1 lists the parameters used in the calculations.

Any degradation of the beam parameters with respect to the reference values of Table 1 has an effect on the FEL output power. The figures show a higher sensitivity to the beam quality of the HGHG+FBIT configuration, if compared to the one of the EEHG+FBIT and pure EEHG configurations. Pure HGHG cannot reach this wavelength and is excluded from the comparison.

Table: 1 Reference Beam/Seed Parameters

Beam parameter	**Value (unit)**
Energy	1800 (MeV)
Energy spread	200 (keV)
Current	1000 (A)
Emittance	0.8 (mm mrad)
Seed parameters	**Value (unit)**
Seed wavelength range λ_s	240-266 nm
Seed1 time duration	100 fs
FEL parameters	**Value (unit)**
Polarization	linear

HGHG+FBIT shows worse performances in all the conditions because of the large harmonic orders required on both the two stages to reach harmonics of order 130. Pure EEHG scheme was considered with ten undulators in the final amplifier. Its performance is comparable to EEHG+FBIT, but requires a much larger 1st dispersion (12 – 15 mm vs. 5 mm in EEHG+FBIT) and is prone to amplification of microbunching instability. In this pure EEHG scheme a lower bunching factor is available at the amplifier making this configuration sensitive to the gain in the final amplifier. Larger gain requires a longer amplifier and enhances the amplification from “shot-noise”, i.e. the SASE background. Another disadvantage associated too the large chicane required by pure EEHG is the effect on a chirped ebeam where current spikes at the head/tail could further enhance SASE emission. Figure 2 indicates the EEHG+FBIT configuration as the more robust solution to reach the 2 nm target wavelength.

ISBN: 978-3-95450-220-2 ISSN: 2673-5474 doi: 10.18429/JACoW-FEL2022-TUP53

SIMULATIONS

The performance of the pure EEHG and EEHG+FBIT schemes at 2.1 nm was evaluated by running time-dependent GENESIS 1.3 [11]. The parameters optimization was achieved by analytical estimates and by running preliminary steady state simulations. Figure 3 shows the power (left) and spectrum (right) after 8 radiators, in both pure EEHG and EEHG+FBIT configurations, when an intensity close to saturation is reached in the seeded part of the electron-beam. The electron-beam current, energy, and energy spread profiles at the end of the FERMI linac (just before the first modulator) were calculated using the particle tracking ELEGANT [12] simulations. The results were obtained using smoothed electron-beam profiles, corresponding to initial peak bunching (at the radiator entrance) of around 1.5%. The smoothing procedure was calibrated averaging out modulations on the scale shorter than approximately 5 µm, as it could be expected according to the laser heater configuration. These simulations were run with $5*10^6$ particles per slice and include effects in the chicane such intra-beam scattering and wakefields, which significantly affect the output, especially at short wavelengths.

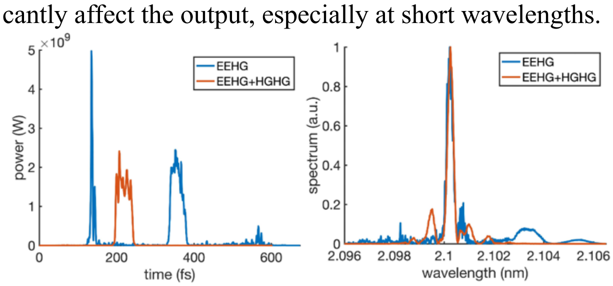

Figure 3: Power (left) and spectrum (right) of the EEHG scheme at 2.1 nm obtained from time-dependent GENESIS 1.3 simulations in EEHG (blue) and EEHG+FBIT (red) configurations.

In Fig. 4 the same simulation was run with Genesis 1.3 ver. 4.4, in one-to-one mode, i.e. one simulated electron per real electron. No smoothing procedure is therefore applied to the beam phase space in this case, but this second simulation does not include collective effects in the chicane.

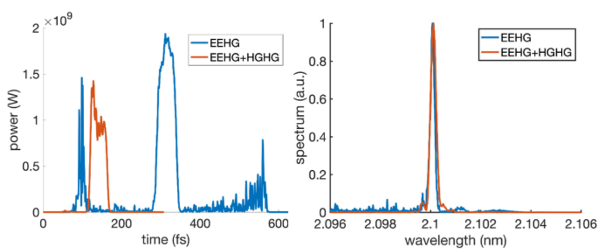

Figure 4: Power temporal profile (left) and spectrum (right) for the HGHG stage at 2.1 nm obtained from time-dependent GENESIS 1.3 (4.4) in one-to-one mode simulation for the pure EEHG (blue) and EEHG+FBIT (red) configurations.

Pulse energy at the GW level is reached in both the configurations, the small differences in peak power between EEHG and EEHG+FBIT are not significative and may be due to small differences in the tuning of the input parameters. Both simulations in Figs. 3 and 4 points out the higher contamination of SASE background in the pure EEHG configuration with respect to the EEHG+FBIT configuration. This SASE signal depends on the number of macro particles used in the simulation and on the smoothing procedure applied, but even the "smoothed" case of Fig. 3 still shows a residual but visible SASE background after eight undulator modules.

The above results show that using a pure EEHG configuration, the FEL output at such short wavelengths is sensitive to the level of microbunching and starts getting affected by SASE emission. The EEHG+FBIT simulation instead is less affected by the ASASE background, and the differences between Fig. 3 and Fig. 4 are probably due to the collective effects in the chicane that were not included in Fig. 4. Comparing the pure EEHG and EEHG+HGHG configurations (c.f., Fig. 3 and Fig. 4), the latter performs significantly better in terms of the spectral quality because of a lower sensitivity to the electron beam properties and a lower contribution from SASE.

We have presented a partial view of the pathway for the upgrade of the FERMI FEL facility over a time span of about nine years. The facility undergoes technological transformations that will allow the extension of the spectral range to the target of the oxygen K-edge. The reader is addressed to [7] for a more comprehensive overview.

REFERENCES

[1] E. Allaria *et al.*, "The FERMI Free-Electron Lasers", *J. Synchrotron Radiat.*, vol. 22, pp. 485-491, May 2015. `doi:10.1107/S1600577515005366`

[2] E. Allaria *et al.*, "Highly Coherent and Stable Pulses from the FERMI Seeded Free-Electron Laser in the Extreme Ultraviolet", *Nat. Photonics*, vol. 6, pp. 699-704, Oct. 2012. `doi:10.1038/nphoton.2012.233`

[3] E. Allaria *et al.*, "Two-Colour Pump-Probe Experiments with a Twin-Pulse-Seed Extreme Ultraviolet Free-Electron Laser", *Nat. Commun.*, vol. 4, pp. 1-7, Sep. 2013. `doi:10.1038/ncomms3476`

[4] M. B. Danailov *et al.*, "Towards Jitter-Free Pump-Probe Measurements at Seeded Free Electron Laser Facilities", *Opt. Express*, vol. 22, pp. 12869-12879, 2014. `doi:10.1364/OE.22.012869`

[5] K. C. Prince *et al.*, "Coherent Control with a Short-Wavelength Free-Electron Laser", *Nat. Photonics*, vol. 10, 176-179, Mar. 2016. `doi:10.1038/nphoton.2016.13`

[6] O. Y. Gorobtsov *et al.*, "Seeded X-Ray Free-Electron Laser Generating Radiation with Laser Statistical Properties", *Nat. Commun.*, vol. 9, pp. 1-6, Oct. 2018. `doi:10.1038/s41467-018-06743-8`

[7] E. Allaria *et al.*, "FERMI 2.0 Conceptual Design Report", `https://www.elettra.eu/images/Documents/FERMI%20Machine/Machine/CDR/FERMI2.0CDR.pdf`

[8] C. Spezzani *et al.*, "FERMI FEL-1 Upgrade to EEHG", presented at the FEL2022, Trieste, Italy, Aug. 2022, paper TUP59, this conference.

[9] E. Hemsing, "Bunching Phase and Constraints on Echo Enabled Harmonic Generation", *Phys. Rev. Accel. Beams*, vol. 21, p. 050702, May 2018. `doi:10.1103/PhysRevAccelBeams.21.050702`

ISBN: 978-3-95450-220-2 ISSN: 2673-5474 doi: 10.18429/JACoW-FEL2022-TUP53

[10] G. Stupakov, "Effect of Coulomb collisions on echo-enabled harmonic generation (EEHG)", in *Proc. FEL'11*, Shanghai, China, Aug. 2011, paper MOPB20, pp. 49–52.

[11] S. Reiche, "GENESIS 1.3: A Fully 3D Time-Dependent FEL Simulation Code", *Nucl. Instrum. Methods Phys. Res., Sect. A*, vol. 429, pp. 243-248, 1999. doi:10.1016/S0168-9002(99)00114-X

[12] M. Borland, "ELEGANT: A Flexible SDDS-Compliant Code for Accelerator Simulation", Argonne National Lab., Illinois, USA, Technical report No. LS-287, Aug. 2000, doi:10.2172/761286

ISBN: 978-3-95450-220-2 ISSN: 2673-5474 doi: 10.18429/JACoW-FEL2022-TUP54

CHIRPED PULSE AMPLIFICATION IN A SEEDED FEL: TOWARDS THE GENERATION OF HIGH-POWER FEW-FEMTOSECOND PULSES BELOW 10 nm

D. Garzella*, G. De Ninno [1], E. Allaria, A. Brynes, C. Callegari, P. Cinquegrana, M. Coreno, I. Cudin, M.B. Danailov, A. Demidovich, S. Di Mitri, B. Diviacco, L. Giannessi, L. Novinec[1], G. Penco, G. Perosa, P. Rebernik, A. Simoncig, F.Sottocorona, L. Sturari, M. Trovò, M. Zangrando, Elettra-Sincrotrone Trieste, Basovizza, Italy
F. Frassetto, L. Poletto, CNR IFN-Padova, Padua, Italy
P. Zeitoun, Laboratoire d'Optique Appliquée, Palaiseau, France
[1]also at University of Nova Gorica, Nova Gorica, Slovenia

Abstract

In this contribution we report the successful implementation of CPA in a seeded XUV FEL. After the first unique result, the FERMI CPA collaboration team (open entity to which interested colleagues from abroad can participate) has set-up a second experiment for demostrating and implementing a two-stage harmonic generation scheme on the FERMI FEL-2 branch, aiming at generating coherent and phase-tailored few-femtosecond FEL pulses, with gigawatt peak power in the sub-10 nm spectral range. The set-up of the second experiment is still udergoing. Here we discuss the work in progress, together with the main scientific and technical bottlenecks and their implications.

INTRODUCTION

In optical conventional lasers, chirped pulse amplification (CPA) revealed to be, in the early 80's, a revolutionary technique, allowing the generation of extremely powerful femtosecond pulses in the infrared and visible spectral ranges, taking advantage of their emission broadband (10's of nm). Nowadays, CPA is the basis for the worldwide operation of laser systems delivering very ultrashort pulses, in the few femtosecond (quasi single cycle) regime, and carrying peak powers up to the Petawatt scale. The experimental implementation of CPA on a seeded FEL in the extreme-ultraviolet, successfully achieved on FERMI in last recent years, has been driven by the following considerations : for any given FEL configuration, a limit presently exists in the generation of ultra-short pulses, as the output pulse energy is limited by the reduced number of electrons participating in the amplification process. Moreover, the pulse shortening is constrained by the FEL gain bandwidth. Eventually, stretching the seed pulse allows one to extract energy from the whole electron bunch, substantially enhancing the FEL pulse energy at saturation. in seeded FELs the bandwidth of the output emission can be significantly larger than that of the seed. This allows at obtaining, after compression, a FEL pulse shorter than the one generated when the FEL is operated in standard (i.e., no-CPA) mode.

* david.garzella@elettra.eu

CHIRPED PULSE AMPLIFICATION

CPA General Setup

CPA lasers [1] show four major stages : the oscillator and preamplifier (also called "the front end"); the stretcher, aiming at dispersing the laser broad spectrum through a dispersive element, like a prism or a diffraction grating ; the main amplifier, where the CPA main feature takes place : to achieve very high energies (with a net gain up to 6 orders of magnitude). Stretching the pulse allows at keeping costant the laser fluence while reducing the intensity, which mitigates the occurrence of phase distortion issues and prevent from damage on optics during the pulse propagation; finally the compressor, another dispersing element similar to the first one, where the previously induced group delay dispersion is fully compensated, and the laser pulse duration is set back to the original value, tipically in the Fourier-Transform limit (TF) regime. In a seeded FEL the setup is quite similar [2]. The seed laser is chirped, stretched and colinearly injected in the undulator. Thanks to the time- energy correlation. the resonance condition is also dispersed on a longer temporal scale, inducing the broadening of the gain bandwidh, thus experiencing a different electron bunching pattern. Higher amplification occurs and the FEL phase pattern reproduces the seed laser, scaled by the harmonic bunch number [3]. Finally, thanks to a XUV compressor, tipically composed of two gratings in classical mount configuration [4], the FEL pulse duration results shorter by a higher factor than the one reckoned by Stupakov's law [3].

Theoretical Background

In order to numerically compare the obtained results and the expected pulse duration under the actual experimental conditions, here is a brief summary and the main outcomes of the CPA FEL theory. In the following the considered seed laser pulse has a gaussian spectral shape . The corresponding electric field in the frequency domain is $\hat{E}(\omega) \sim e^{-\omega^2/(2\sigma_\omega^2)} e^{-i\beta\omega^2/4}$, where σ_ω is the (rms) laser bandwidth and β is the so-called group delay dispersion (GDD) [5]. The Inverse Fourier Transform $E(t)$ of $\hat{E}(\omega)$ is $E(t) \sim e^{-t^2/(2\sigma_t^2)} e^{i\Gamma t^2}$. In presence of strong chirp, for $\beta \gg 2/\sigma_\omega^2$, the coefficient of the quadratic temporal phase,

ISBN: 978-3-95450-220-2 ISSN: 2673-5474 doi: 10.18429/JACoW-FEL2022-TUP54

Γ, and the (rms) laser pulse duration, σ_t, are related to σ_ω and β through the following relations: $\Gamma = \beta/(4/\sigma_\omega^4 + \beta^2)$ and $\sigma_t \simeq 1/2\beta\sigma_\omega$. This regime is the one suitable for CPA. It has been experimentally demonstrated [6] that the latter relation is valid also for non-Gaussian pulse profiles, provided that the spectral and temporal profiles (both in amplitude and phase) be equivalent, in the case of strongly chirped pulses . When dealing with a seeded FEL, in which the seeding pulse has a gaussian laser profile, it is assumed that the FEL is expected to have a quasi-Gaussian pulse profile. In this case, following [3], the duration of the FEL pulse operating in standard conditions , almost at the saturation level (without CPA) is $(\sigma_t)_{\mathrm{FEL}}^{\mathrm{noCPA}} \simeq n^{-1/3}(\sigma_t)_{\mathrm{seed}}$, with $(\sigma_t)_{\mathrm{seed}}$ the seed pulse duration. Furthermore, thanks to the harmonic jump, the phase of the FEL pulse is n times that of the seed. Thus, by assuming an almost flat electron bunch, this high level chirp holds for the FEL pulse too [7]. The amount of GDD to be compensated by the optical compressor, β_{FEL}, is then $\beta_{\mathrm{FEL}} \simeq \beta_{\mathrm{seed}}/n$ with β_{seed} the seed laser GDD. Finally, the resulting relations for the FEL bandwith and duration, respectively , are the following, expressed in terms of the FWHM spectral ($\Delta\omega$) and temporal (Δt) FEL and seed ones.

$$
\begin{aligned}
(\Delta\omega)_{\mathrm{FEL}} &= n^{2/3}(\Delta\omega)_{\mathrm{seed}} \\
(\Delta t)_{\mathrm{FEL}}^{\mathrm{min}} &= \frac{(\Delta t)_{\mathrm{seed}}^{\mathrm{TL}}}{n^{2/3}}
\end{aligned} \tag{1}
$$

FEL-1 Experiment

In the experiments performed on FEL-1 [7], FERMI was set at an electron energy of 1.2 GeV with a peak electron current of about 500 A and an almost costant current profile around the seeding region (i.e., few hundreds of femtosecond). The seeding pulse was a gaussian profile at the third harmonic of a Ti:Sapphire laser (a wavelength of 261nm). When operated without chirping, the seed had a FWHM duration of 170 fs and a FWHM bandwidth of about 0.7 nm. For the CPA operation, a positive linear frequency chirp was introduced by propagating the third-harmonic pulse through a calcium fluoride plate that stretched the pulse duration to 290 fs. The peak power at the entrance of the modulator was about 250 MW, for both the standard and CPA configurations. The FEL resonant wavelength was set at the 7$^{\mathrm{th}}$ harmonic, 37.3 nm.

The FEL pulse duration was measured using a pump-probe cross-correlation scheme, combining the XUV FEL pulse and an IR optical laser ultrashort pulse and detecting the photoionization products after interaction with a He gas sample. The main results for the experiment carried out on FEL-1 are fully reported in [7]. FEL spectra with the PRESTO monochromator [8] and time-of-flight sequences with the VMI set-up installed on the Low Density Matter beamline [9] have been recorded in both no-CPA and CPA configurations. Data for several positions of the XUV compressor have been measured, in order to look at the behaviour of the group delay compensation, thus the variation of the FEL pulse duration. The principal outcome is illustrated in fig. 1.

At its minimum, the FEL spectra exhibited a mean value of 51fs, in fully agreement with theory and exhibiting a Time-Bandwidth Product (TBP) of 1.1, say very close to the Fourier Limit.

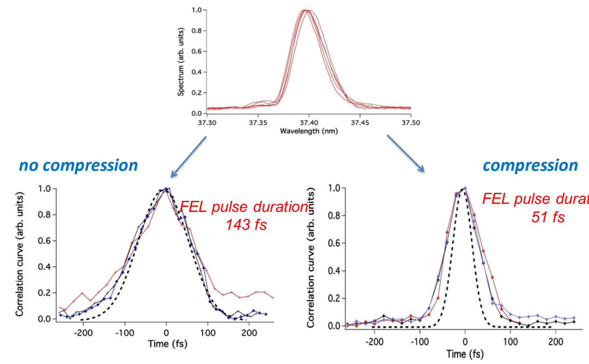

Figure 1: Above : FEL Pulse spectra centered around 37nm, showing the stability both for the central wavelength and the spectral width; Below left : corresponding measured pulse duration in no-CPA mode; Below right : corresponding measured pulse duration in CPA mode [7]

FEL-2 CASCADE EXPERIMENT

Once the feasibility of CPA has been proven, the next step and challenge is given by the quest for the smallest wavelength, thus the highest harmonic number and the shortest FEL pulse. This implies the operation of a seeded FEL in cascade regime, where the phase pattern given by the chirped seed laser is propagated through two HGHG stages. Moreover, dealing with shorter wavelengths, one could have facing with smallest signals levels, which implies to pay more attention with the detection scheme and the observables' choice.

FEL operation Issues In the first attempt with FEL-2, held in fall 2017, the beam energy was setup at 0.95 GeV, the seed set at a wavelength of 265 nm, whereas the FEL wavelength was 16.5 nm , with a harmonic number of 16. The first challenge was keeping the maximum amplification yeld and generate the highest pulse energy level. by using the fresh bunch technique [10, 11]. This generally implies using a longer electron bunch, while keeping other parameters under control. Attention was then payed for producing, transporting and matching a quite long electrons beam ($\approx$ 800 fs) with a quite strong electrons energy chirp (15- 18 MeV/ps); Preventing high-order terms carried by the seed and/or in the electron beam energy distribution, and mitigating their effects; Minimizing stochastic errors, like anomalous coherent microbunching instability, that could affect the FEL operation. Several shifts were dedicated to carry on the electron bunch preparation and the tailoring of the expected features, with satisfying results [12].

Signal Detection Issues The XUV compressor, designed and used for the FEL-1 experiment [4, 7] in the

ISBN: 978-3-95450-220-2 ISSN: 2673-5474 doi: 10.18429/JACoW-FEL2022-TUP54

classical mount configuration, has four optical elements: two gratings and two plane folding mirrors for steering the beam back to the original propagation axis. The two grazing incidence mirrors (incidence angle interval 1- 4 deg) exhibits about 90% efficiency. The gratings pair ensures the group delay compensation, say the quantity related to the optical path variation for each spectral component of the FEL pulse. This quantity depends on the variation of the FEL subtended angle $k = \alpha + \beta$ where α and β are the incident angles respectively on the first and the second grating [4] (see fig. 2). The compressor is hosted in a ultra high-vacuum chamber and moved by external stepper motors. The angular resolution is 65.8 μrad/step in a full step mode; controllers are capable of a 1/8-step resolution, spanning an angle variation in the range between -0.5 deg and 14.5 deg.

Mini-Timer Set-up and Diproi Beamline The experimental set-up, called Mini-Timer [13] was mounted on the DiPROI Beamline [14, 15]. Here the FEL beam is splitted in two pulses balanced in energy, which follow a symetrical path and are then recombined, under a controlled subtended angle, onto a solid sample. The interaction between the two FEL beams and the surface of the sample induces a thermal transient with an interference intensity pattern corresponding to a refractive index transient grating [16]. A third laser beam impinges also onto the surface, with a fixed angle. The beam is then refracted by the transient grating and the outcoming beam (either the transmitted or the reflected one) is collected by an integrating detector, in the present case a CCD camera.

Observables and Temporal Analysis The setup above can be included in the varied class of the four-wave mixing experiments [17]. In its typical configuration, the two FEL beams (the pumps) have always the same mutual delay, and the variable parameter is the pump-probe delay, for investigating the thermal behaviour of the sample through the refractive index dynamics retrieval. However, as such dynamics is very slow compared to the FEL pulse length, the diffraction yeld can be measured as a function of the delay between the two arms [18]. Indeed, Trebino [17] showed that transient grating experiments can be performed in this "self-correlation" mode, which can be analitically treated as a "fourth-order correlation" in beam intensities. Trebino analysis has been reconsidered by Nighan [19], who reformulated the final relation ruling the measured curve, by assuming a gaussian laser pulse, with a pulse duration τ_p, and a coherence time τ_c :

$$\eta(\tau_d) \propto \sqrt{\frac{2\ln 2}{\pi}} \times \left(\frac{\tau_c}{\tau_p}\right) \times e^{-(2\ln 2\frac{\tau_d^2}{\tau_p^2})} + e^{-(\pi\frac{\tau_d^2}{\tau_c^2})} \quad (2)$$

Data Analysis

The experiment underwent several issues, mainly an initial lack of the diffraction signal from the sample, due to unexpected efficiency of the commercial gratings, which was measured to be 0.35 % each, and a failure on the stepper motors of the compressor gratings. Thus, only some datasets were acquired. Results are summarized in fig. 3, where the behaviour of the diffraction yeld vs. the delay between the two FEL arms is reported, for different chirp condition. Discrete amounts of chirp were set by inserting one or two calibrated UV-grade fused silica plates. Furthermore, a fine chirp tuning could be applied by changing the seed laser compressor parameters, mainly the distance between the gratings. Experimental data are interpolated and fitted by means of the eq. 2 showing that both coherence time τ_c and pulse duration τ_p can be retrieved. Examples are given for different macroscopic chirp conditions : no, chirp low positive chirp, high positive chirp and negative one. Beyond the original goals of the experiment, Is has been demonstrated the capability of simultaneously characterising a seeded XUV FELin its temporal and spectral features, whatever be the chirp state, and allowing even at characterizing and controlling phase modulation and second order dispersion behaviour all along the FEL interaction and the beam transport.

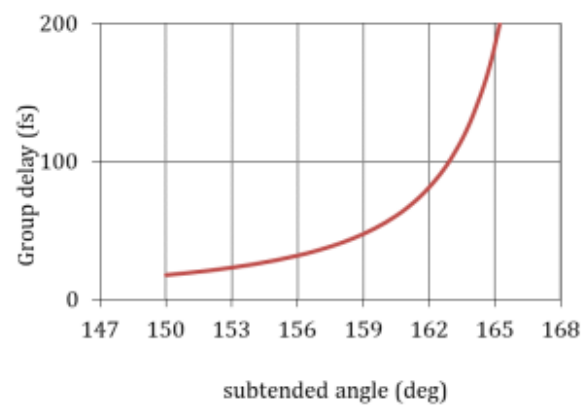

Figure 2: Group Delay Compensation vs. the subtended angle $k = \alpha + \beta$, for a pair of diffraction grating with 2400 grooves/mm.

FEL-2 NEXT EXPERIMENTS AND PERSPECTIVES

Learning from the successful experiment in 2016 and the first attempt on FEL-2 in 2017, we realized that the main technical bottleneck depends on the overall efficiency exhibited by the pulse compressor. Then, our efforts have been concentrated on the quest of gratings with high efficiency on a broad spectral range below 25 nm. Further features, like the maximum delay compensation vs. the subtended angle, are also mandatory for maximizing the gain, thus It is very important to characterize the efficiency spectral response in between the operation limits . Thus, In order to stretch the pulse from the initial duration (and then to compensate in the compression stage) up to 150 fs with a pair of gratings exhibiting 2400 grooves/mm (see fig. 2), the optimum grazing incidence angle should be found in the range 81- 87 deg.

ISBN: 978-3-95450-220-2 ISSN: 2673-5474 doi: 10.18429/JACoW-FEL2022-TUP54

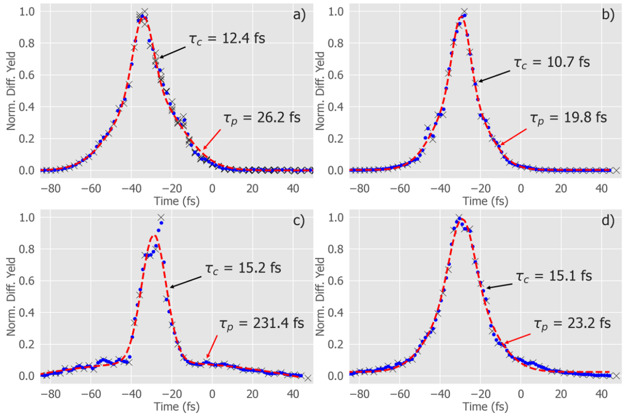

Figure 3: Normalized diffraction yeld vs. delay between the two FEL splitted pulses in the Mini-Timer experiment, illustrating the contribution of τ_c and τ_p. a) with no induced chirp: b) with low positive chirp: c) with high positive chirp: d) with negative chirp. **x** crosses : experimental points; • dots : interpolated points; ▬ straight line : "Nighan-like" fit (eq.2).

Very recently, a pair of XUV gratings has been purchased to [TM]Horiba-Jobin Yvon, The expected spectral performances per grating, as numerically calculated from measurements performed on the fabrication master, are illustrated in fig. 4; Such values, when experimentally confirmed, should allow at achieving an overall total efficiency of 1- 2% range, corresponding to energies on target of the order of few μJ, largely detectable either on VMI detectors or by self-diffraction of a transient grating.

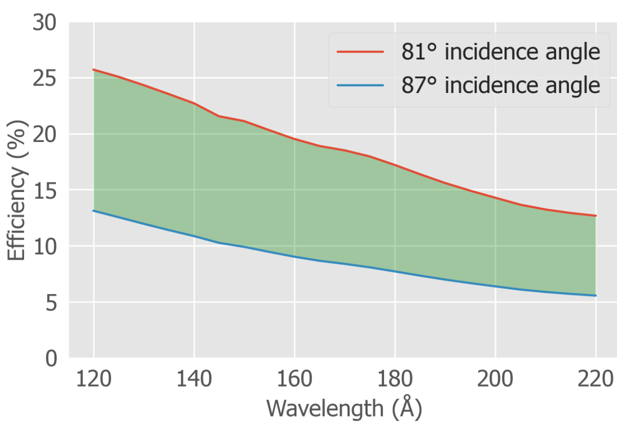

Figure 4: Spectral behaviour of the diffraction gratings, as expected by numerical simulations from the measured parameters of the master. The filled region is the available one for actual compressor operation.

CONCLUSION

We reminded the results that have been uniquely obtained at FERMI on the FEL-1 branch. It has been then shown, though also some preliminary results, that efforts are made to setup a new experiment on the FEL-2 branch for demon-

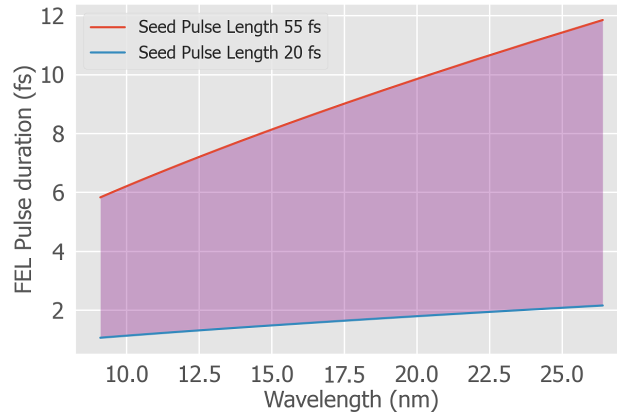

Figure 5: Spectral behaviour of the expected pulse duration, following eq. 1. The FEL operation, the filled one is limited between the present seed pulse duration and the expected upgrades.

strating the capability of transposing the chirp induced in the seed through a two-stage cascade, keeping the phase features even in the electron delay line. Both results and future experiment expectations are supported by theoretical and numerical studies, showing that the long term perspectives call for a program willing to generate coherent and phase-tailored few-femtosecond pulses with gigawatt peak power in the sub-10 nm spectral range. Referring to eq. 1, these pulse durations should already be achievable in the next experiment, as shown by fig. 5. Chirped Pulse Amplification technique, implemented on seeded Free Electron Lasers, still remains a promising way for achieving very short coherent and powerful (thus intense) soft x-ray pulses. Indeed, efforts have to be concentrated on solving technological issues (like the overall compressor efficiciency on a large spectral banwidth), though previous results on FEL1 and the promising experiments foreseen on FEL2 showed that 100 μJ pulses, less than 5 fs long, in the 100 eV energy range

ACKNOWLEDGEMENTS

The authors acknowledge the support of the entire FERMI team during the preparation of the experiments. The research leading to these results has received funding from LASERLAB-EUROPE (grant agreement no. 871124, European Union's Horizon 2020 research and innovation programme).

REFERENCES

[1] D. Strickland and G. Mourou, "Compression of amplified chirped optical pulses," *Optics Communications*, vol. 56, no. 3, pp. 219–221, 1985. doi:10.1016/0030-4018(85)90120-8

[2] L. Yu, E. Johnson, L. D, and D. Umstadter, "Femtosecond free-electron laser by chirped pulse amplification," *Physical Review E*, vol. 49, no. 5, B, pp. 4480–4486, 1994. doi:10.1103/PhysRevE.49.4480

ISBN: 978-3-95450-220-2 ISSN: 2673-5474 doi: 10.18429/JACoW-FEL2022-TUP54

[3] D. Ratner, A. Fry, G. Stupakov, and W. White, "Laser phase errors in seeded free electron lasers," *Physical Review Special Topics-Accelerators and Beams*, vol. 15, no. 3, 2012. doi:10.1103/PhysRevSTAB.15.030702

[4] F. Frassetto and L. Poletto, "Grating configurations to compress extreme-ultraviolet ultrashort pulses," *Applied Optics*, vol. 54, no. 26, pp. 7985–7992, 2015. doi:10.1364/AO.54.007985

[5] I. Walmsley, L. Waxer, and C. Dorrer, "The role of dispersion in ultrafast optics," *Review of Scientific Instruments*, vol. 72, no. 1, 1, pp. 1–29, 2001. doi:10.1063/1.1330575

[6] D. Gauthier, B. Mahieu, and G. De Ninno, "Direct spectrotemporal characterization of femtosecond extreme-ultraviolet pulses," *Physical Review A*, vol. 88, no. 3, 2013. doi:10.1103/PhysRevA.88.033849

[7] D. Gauthier *et al.*, "Chirped pulse amplification in an extreme-ultraviolet free-electron laser," *Nature Communications*, vol. 7, p. 13 688, 2016. doi:10.1038/ncomms13688

[8] E. Allaria *et al.*, "Highly coherent and stable pulses from the fermi seeded free-electron laser in the extreme ultraviolet," *Nature Photonics*, vol. 6, no. 10, pp. 699–704, 2012. doi:10.1038/NPHOTON.2012.233

[9] C. Svetina *et al.*, "The low density matter (ldm) beamline at fermi: Optical layout and first commissioning," *Journal of Synchrotron Radiation*, vol. 22, no. 3, SI, pp. 538–543, 2015. doi:10.1107/S1600577515005743

[10] L. Yu and I. BenZvi, "High-gain harmonic generation of soft x-rays with the ''fresh bunch" technique," *Nuclear Instruments & Methods in Physics Research Section A-Accelerators Spectrometers Detectors and Associated Equipment*, vol. 393, no. 1-3, pp. 96–99, 1997, 18th International Free-Electron-Laser Conference, ROME, ITALY, AUG 26-30, 1996. doi:10.1016/S0168-9002(97)00435-X

[11] E. Allaria *et al.*, "Two-stage seeded soft-x-ray free-electron laser," *Nature Photonics*, vol. 7, no. 11, pp. 913–918, 2013. doi:10.1038/NPHOTON.2013.277

[12] L. Giannessi, "Recent machine physics activities at fermi. a report to the fermi machine advisory committee," Tech. Rep., 2018.

[13] F. Bencivenga *et al.*, "Short-wavelength four wave mixing experiments using single and two-color schemes at fermi," *Journal Of Electron Spectroscopy and Related Phenomena*, vol. 257, 2022. doi:10.1016/j.elspec.2019.146901

[14] L. Foglia *et al.*, "Four-wave-mixing experiments and beyond: The timer/mini-timer setups at fermi," in *Advances in X-Ray Free-Electrons Lasers Instrumentation IV*, SPIE, vol. 10237, 2017. doi:10.1117/12.2268068

[15] F. Capotondi *et al.*, "Multipurpose end-station for coherent diffraction imaging and scattering at fermi@elettra free-electron laser facility," *Journal of Synchrotron Radiation*, vol. 22, no. 3, SI, pp. 544–552, 2015. doi:10.1107/S1600577515004919

[16] R. Mincigrucci *et al.*, "Timing methodologies and studies at the fermi free-electron laser," *Journal of Synchrotron Radiation*, vol. 25, no. 1, pp. 44–51, 2018, Workshop on FEL Photon Diagnostics, Instrumentation and Beamline Design (PhotonDiag), SLAC Natl Accelerator Lab, Stanford, CA, MAY 01-03, 2017. doi:10.1107/S1600577517016368

[17] R. Trebino, E. Gustafson, and A. Siegman, "4th-order partial-coherence effects in the formation of integrated-intensity gratings with pulsed-light sources," *Journal of the Optical Society of America B-Optical Physics*, vol. 3, no. 10, pp. 1295–1304, 1986. doi:10.1364/JOSAB.3.001295

[18] F. Capotondi *et al.*, "Characterization of ultrafast free-electron laser pulses using extreme-ultraviolet transient gratings," *Journal of Synchrotron Radiation*, vol. 25, no. 1, pp. 32–38, 2018, Workshop on FEL Photon Diagnostics, Instrumentation and Beamline Design (PhotonDiag), SLAC Natl Accelerator Lab, Stanford, CA, MAY 01-03, 2017. doi:10.1107/S1600577517015612

[19] N. WL, T. Gong, L. Liou, and P. Fauchet, "Self-diffraction - a new method for characterization of ultrashort laser-pulses," *Optics Communications*, vol. 69, no. 3-4, pp. 339–344, 1989. doi:10.1016/0030-4018(89)90129-6

ISBN: 978-3-95450-220-2 ISSN: 2673-5474 doi: 10.18429/JACoW-FEL2022-TUP56

NON-LINEAR HARMONICS OF A SEEDED FEL AT THE WATER WINDOW AND BEYOND

G. Penco†, E. Allaria, L. Badano, F. Bencivenga, A. Brynes, C. Callegari, F. Capotondi, A. Caretta, P. Cinquegrana, M.B. Danailov, D. De Angelis, A. Demidovich, S. Di Mitri, L. Foglia, G. Gaio, A. Gessini, L. Giannessi, G. Kurdi, M. Manfredda, M. Malvestuto, C. Masciovecchio, R. Mincigrucci, I. Nikolov, E. Pedersoli, S. Pelli Cresi, E. Principi, P. Rebernik, A. Simoncig, S. Spampinati, C. Spezzani, M. Trovò, M. Zangrando, G. De Ninno
Elettra – Sincrotrone Trieste SCpA, Basovizza, Italy
G. Perosa, F. Sottocorona, Università degli Studi di Trieste, Trieste, Italy
S. Dal Zilio, Istituto Officina dei Materiali, Consiglio Nazionale delle Ricerche, Trieste, Italy
V. Chardonnet, M. Hennes, B. Vodungbo, E. Jal, Sorbonne Université, CNRS, Laboratoire de Chimie Physique-Matière et Rayonnement, France
J. Lüning Helmholtz-Zentrum Berlin für Materialien und Energie GmbH, Berlin, Germany
P. Bougiatioti, C. David, B. Roesner, Paul Scherrer Institut, Villigen PSI, Switzerland
M. Sacchi, Institut des NanoSciences de Paris, CNRS, Sorbonne Université, Paris, France and Synchrotron SOLEIL, L'Orme des Merisiers, Saint-Aubin, Gif-sur-Yvette, France
E. Roussel, PhLAM/CERLA, Villeneuve d'Ascq

Abstract

The advent of free electron lasers (FELs) in the soft and hard X-ray spectral region has opened the possibility to probe electronic, magnetic and structural dynamics, in both diluted and condensed matter samples, with femtosecond time resolution. In particular, FELs have strongly enhanced the capabilities of several analytical techniques, which take advantage of the high degree of transverse coherence provided. FELs based on the harmonic up-conversion of an external seed laser are also characterised also by a high degree of longitudinal coherence, since electrons inherit the coherence properties of the seed. At the present state of the art, the shortest wavelength delivered to user experiments by an externally seeded FEL light source is about 4 nm. We show here that pulses with a high longitudinal degree of coherence (first and second order) covering the water window and with photon energy extending up to 790 eV can be generated by exploiting the so-called nonlinear harmonic regime, which allows generation of radiation at harmonics of the resonant FEL wavelength.

Moreover, we report the results of two proof-of-principle experiments: one measuring the oxygen K-edge absorption in water (~ 530 eV), the other analysing the spin dynamics of Fe and Co through magnetic small angle x-ray scattering at their L-edges (707 eV and 780 eV).

INTRODUCTION

The high degree of transverse coherence of the FELs pulses has been exploited by several techniques, including Fourier transform holography, coherent diffraction imaging, and ptychography. In the case of a seeded FEL, the output radiation has been proven to have also a high degree of longitudinal coherence [1-3] that is of crucial importance for techniques such as linear and nonlinear spectroscopies and coherent control, requiring both phase and wavelength manipulation within a given pulse. In a seeded FEL operating in High Gain Harmonic Generation (HGHG) mode [4] an external seed laser imprints an energy modulation on an electron beam passing through an undulator (called modulator). Then, the electrons are sent through a magnetic dispersive section that converts this energy modulation into a density modulation, known as bunching, whose spectral content includes higher harmonics of the seed, with a progressively fading coefficient [5]. The electron beam is then injected into an undulator tuned to be resonant to a given harmonic of the seed: since the process is stimulated by the seed laser, all electrons emit in phase, resulting in the generation of nearly Fourier-transform-limited pulses. The reduction of the bunching with the increase of the harmonic order sets a limit on the shortest wavelength that can be generated. In fact, the bunching level at the desired harmonic has to be substantially larger than the shot noise, in order to avoid the Self Amplified Spontaneous Emission (SASE) process becoming dominant, thereby spoiling the longitudinal coherence of the FEL output.

The HGHG scheme has been implemented at FERMI in a two-stage cascade, using the emission from the first stage to seed the second one. In this configuration the shortest wavelength delivered to users for experiments is about 4nm [6-8], corresponding to the 65^{th} harmonic of an ultraviolet laser. The possibility to reach a similar spectral regime in a single stage FEL by adopting the echo-enabled harmonic generation (EEHG) scheme [9] has been recently proven. Moreover, coherent and stable emission at 2.6 nm (~474 eV) was observed [10], although the parameters used for the experiment allowed only a feeble intensity, comparable to the broadband spontaneous emission coming from the whole electron bunch.

† giuseppe.penco@elettra.eu

ISBN: 978-3-95450-220-2 ISSN: 2673-5474 doi: 10.18429/JACoW-FEL2022-TUP56

In order to extend the FERMI tuning range into the water window and up to the L-edge of the 3d transition metals (up to ~800 eV), we exploit at FERMI the nonlinear harmonic generation (NHG) regime [11,12]. This is based on the fact that the exponential gain leading to the emission at the harmonic λ_n drives the bunching also at its harmonics $\lambda_m = \lambda_n/m$, where m is an integer, with the consequent generation of light at λ_m.

In this paper, we report the generation of the third nonlinear harmonic at about 700-800 eV and at the oxygen K-edge (~530 eV), as well as the characterization of this radiation component in terms of spectral purity, pulse energy and longitudinal coherence [13]. In particular, we show that the high coherence properties of the seed laser are transferred to both the fundamental FEL wavelength and its nonlinear harmonics.

FEL PULSE CHARACTERIZATION AT 530 eV AND AT 700-800 eV

The experiment described below was carried out at the FERMI FEL-2 line, which is based on two HGHG stages, operating in the fresh bunch mode [14]. In the case of circularly polarized light, all nonlinear harmonics are emitted off axis, while in linear polarization only odd harmonics are emitted on axis. We focused on the third nonlinear harmonic emission and we set the fundamental wavelength with a linear horizontal polarization. In the following, we report one of the cases of interest: the third harmonic of 5.3 nm, i.e. 1.77 nm, corresponding to the Co L-edge (~700 eV). Changing the seed laser wavelength from 240 to 260 nm and tuning accordingly the radiator gap, it was also possible to lase in third harmonic also at the Fe L-edge (~780 eV) obtaining a similar performance.

The electron beam energy was set to 1.488 GeV. The bunch charge was 600 pC and the bunch duration (FWHM) about 0.9 ps (corresponding to a peak current of about 800 A). The FEL-2 first stage was tuned to be resonant at 21.2nm (12^{th} harmonic of a 254.4 nm seed laser) and the second stage at 5.3nm (4^{th} harmonic).

To estimate the pulse energy of the output radiation at 700 eV, we used a calibrated photodiode and a set of solid-state filters to minimize contributions from undesired radiation (i.e., the seed laser and the emission from the first stage). Inserting different kinds of solid-state filters with known transmission curves it was possible to estimate a pulse energy of about 19.4 μJ at 233 eV (with a rms uncertainty of 0.1 μJ) and 150 nJ at 700 eV (with a rms uncertainty of 100 nJ). The derived estimation is in good agreement with the typical ratio of 1% documented in literature [15] and expected from simulations. More details are reported in [13].

Two spectrometers were used to characterize simultaneously the FEL emission at the fundamental (5.3 nm, 233 eV) and at the third nonlinear harmonic (1.77 nm, 700 eV) on a shot-to-shot basis: one (called PRESTO) [16] integrated in the common photon transport line of the FERMI experimental hall and one (called WEST) installed downstream of the EIS-TIMEX end station [17]. The FEL gain curves at 233 eV and at 700 eV were measured by progressively detuning the undulator gap of the second stage radiator and taking the shot-to-shot integrated signal of the PRESTO and WEST spectrometers. The obtained results were scaled according to the pulse energy estimation mentioned above, and compared with numerical simulations run with GENESIS 1.3 [18] (see Fig. 1).

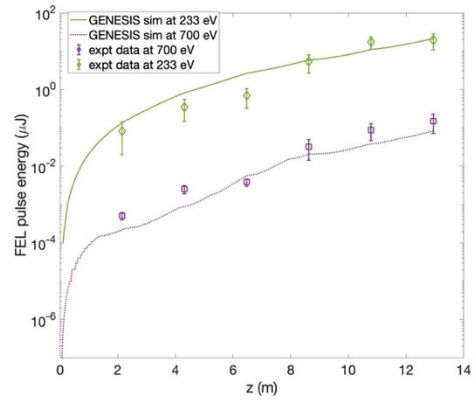

Figure 1: Measured (markers) and GENESIS simulated (lines) FEL gain curves at 233 eV and at 700 eV. Error bars correspond to the standard deviation from the mean value calculated over 50 shots.

Simulations are in good agreement with the measurements. The harmonic growth results in fact from the sum of a linear and a nonlinear contribution; the former dominates in the first part of the radiator, where as a result of the seeding there is a non-negligible bunching also at the harmonic of the resonant wavelength. When the fundamental field grows along the radiator, it contributes to the increase of the electron bunching at its harmonics, entering into a nonlinear regime and sustaining the harmonic gain. The relevant contribution to the harmonic amplification coming from the fundamental growth is confirmed by the GENESIS simulation: if the latter is artificially suppressed, the harmonic field is reduced by about 50%.

The spectral quality of the nonlinear harmonic at 700 eV was studied by acquiring 400 consecutive single-shot spectra (see Fig. 2). The statistics over the FEL bandwidth (see Fig. 2d) reveal that the largest fraction of shots have a relative FWHM bandwidth smaller than 0.1%. However, residual microbunching instabilities can be responsible for a certain broadening of the FEL spectrum and in fact numerical simulations foresee an unstructured FEL pulse with a relative FWHM bandwidth of a few 10^{-4}. Microbunching instabilities are usually damped by the laser-heater (LH) system [19] and in an optimized condition the maximum FEL intensity is obtained with a LH pulse energy of about 1μJ. Increasing the LH power beyond this value causes the larger induced energy spread to lower the FEL gain and consequently to decrease the FEL intensity, but at the same time damping the residual microbunching instabilities. We show in [13] that with a trade-off LH pulse energy of 2.7 μJ, the average FEL bandwidth is reduced, with a significant fraction of shots

ISBN: 978-3-95450-220-2 ISSN: 2673-5474 doi: 10.18429/JACoW-FEL2022-TUP56

(about 20%) exhibiting a relative FWHM bandwidth of 0.05%, approaching the ideal case resulting from the simulations.

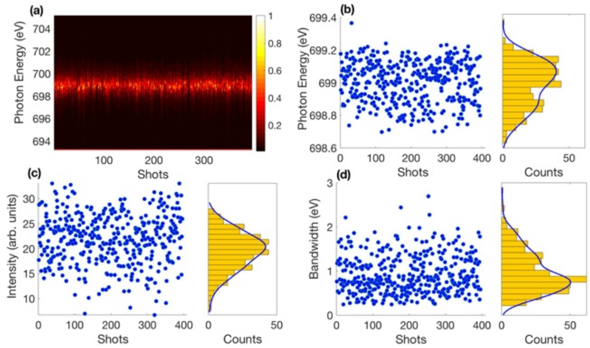

Figure 2: (a) Series of 400 consecutive single-shot spectra at 700 eV acquired with the PRESTO spectrometer. Also shown are the statistics of (b) the central wavelength stability, (c) the spectral intensity, and (d) the FWHM spectral bandwidth.

A similar spectra characterization was performed tuningthe fundamental at 7 nm in linear horizontal polarization and measuring the spectra of the third nonlinear harmonic at 2.33 nm (~530 eV), corresponding to the oxygen K-edge [13].

LONGITUDINAL COHERENCE

The statistical properties of the light emitted by a seeded FEL differ substantially from those of a SASE FEL source: the former resembles those of laser light [20], while SASE has the typical statistics of chaotic light [21]. We used the statistics of the spectra acquired at 530 eV and at 700 eV to calculate the normalized second-order correlation function $g^{(2)}$, defined in [22], as

$$g^{(2)}(\lambda_1, \lambda_2) = \frac{\langle I(\lambda_1) I(\lambda_2)\rangle}{\langle I(\lambda_1)\rangle\langle I(\lambda_2)\rangle}, \quad (1)$$

where $I(\lambda_1)$ and $I(\lambda_2)$ are spectral intensities at different wavelengths measured simultaneously and the angular brackets indicate averaging over a large ensemble of different radiation pulses.

In the literature, it is very common to represent $g^{(2)}$ as a function of $\Delta\lambda = \lambda_1 - \lambda_2$. The value of $g^{(2)}(\Delta\lambda = 0)$, generally indicated as $g^{(2)}(0)$ is 1 for a fully coherent source. FERMI has been proven to provide laser-like output with $g^{(2)}(0)$ close to 1 [20], while SASE FELs are characterized by $g^{(2)}(0) \approx 2$ [23].

We have analysed the spectra acquired at 533 eV and 700 eV and calculated the $g^{(2)}$ function, averaged over a very narrow central bandwidth ($\Delta\lambda = 3 \times 10^{-4}\ nm$) and over a larger interval ($\Delta\lambda = 1.5 \times 10^{-3}\ nm$). The value found was of $g^2(0)$~1.16 and was almost independent of the bandwidth chosen (Fig. 3). In both cases, narrow and broader range, it was very close to the typical performance obtained at FERMI in the nominal spectral range (see [13] for more details). This supports the theory indicating that the high coherence properties of the seed laser are transferred not only to the fundamental FEL wavelength but also to its nonlinear harmonics.

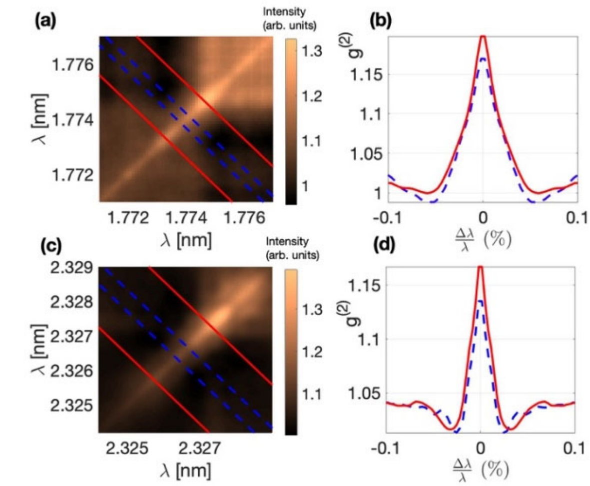

Figure 3: Measurements of the $g^{(2)}$ function for 700 eV (1.77 nm) and 530 eV (2.33 nm) radiation: (a) and (c) the $g^{(2)}$ function calculated as defined in Eq. (1) for the two different photon energies and (b) and (d) the mean values of $g^{(2)}$calculated by averaging over a very narrow central bandwidth (blue dotted line) and over a larger one (red solid line).

PROOF OF PRINCIPLE EXPERIMENTS

To demonstrate that nonlinear harmonics generated by a seeded FEL can find useful applications, we report the results of two proof-of-principle experiments.

X-Ray Absorption Spectroscopy of Water Across the Oxygen K-edge

The x-ray-absorption spectroscopy (XAS) spectrum of steady room-temperature water across the oxygen K edge (~535 eV) has been measured at the EIS-TIMEX beamline in the spectral region 530–545 eV operating in transmission geometry [13].

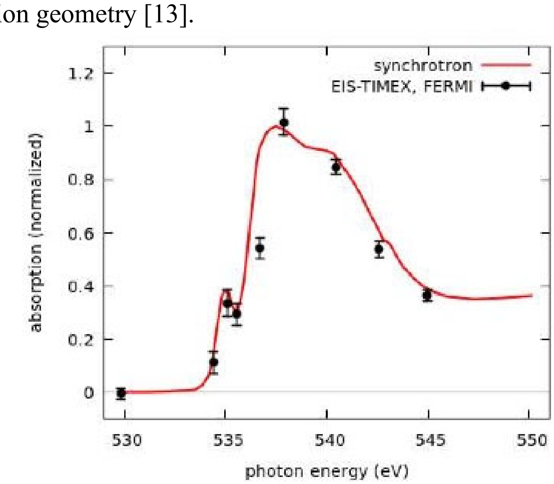

Figure 4: Normalized XAS at the O K-edge measured in transmission geometry with the nonlinear harmonics FEL generated at FERMI (black circles) compared with a similar measurement performed at the SSRL synchrotron (red continuous line).

ISBN: 978-3-95450-220-2 ISSN: 2673-5474 doi: 10.18429/JACoW-FEL2022-TUP56

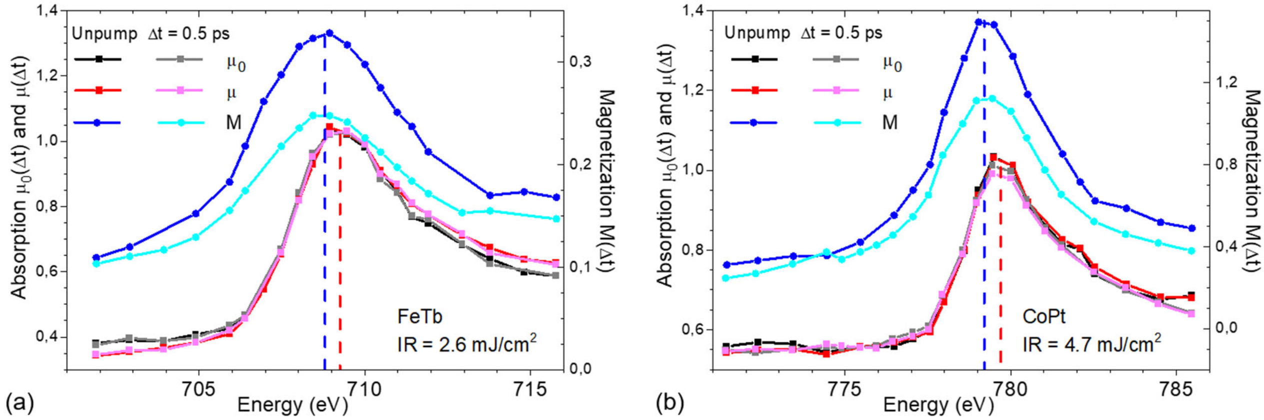

Figure 5: Absorption spectrum at Fe L_3-edge without pumping (red) and after 0.5-ps IR-laser pulse with an average energy density of 2.6 mJ/cm^2 (magenta). Black and grey lines are reference static absorption spectra simultaneously collected in a nearby unpumped area of the sample. The blue and cyan lines show the magnetic scattering efficiency without optical pump and 0.5 ps after pumping, respectively (right scale). (b) same as (a) for CoPt sample at the Co L_3-edge for a pump IR laser average energy density of 4.7 mJ/cm^2. The data show that while the XAS signal is minimally affected by the optical excitation, the magnetic signal is strongly reduced after the optical stimulus.

The water sample was confined in a sealed microfluidic cell, with thin Si3N4 windows (100-nm thickness) transparent to the soft x-ray radiation. For each photon energy, the spectral line was measured by integrating 1500 shots. The results are plotted in Fig. 4: the high wavelength stability of FERMI at 530 eV and the narrow bandwidth has allowed to identify typical features of the water spectrum, such as the pre-peak observable at about 535 eV. In Fig. 4 we report a similar measurement done at the SSRL synchrotron [24] for comparison, and the results are in good agreement.

This proof-of-principle experiment paves the way for light-driven sub-ps dynamic studies in water and other molecules as well as in solid oxides by monitoring the time-resolved x-ray-absorption spectrum at the O K-edge.

Probing Spin Dynamics at Transition Metal L-edge

In a second pilot experiment, the nonlinear harmonics produced by the seeded FEL were used in combination with an external optical pulse to detect the spin dynamics occurring in transition-metal magnetic thin films.

In particular, the FEL was tuned to generate photons across the Fe and Co $L_{2,3}$ edges, corresponding to the 702–716 eV (~1.77 nm) and 771–785 eV (~1.59 nm) ranges, respectively. The measurements have been performed at the DiProI end-station of FERMI [25] and the experimental setup was designed to collect time-dependent absorption and spin dynamics information of the magnetic sample.

The experimental results are plotted in Fig.5 above.

REFERENCES

[1] E. Allaria *et al*., "Two-stage seeded soft-X-ray free-electron laser", *Nat. Photonics, vol.* 7, pp. 913-918, 2013.

[2] G. De Ninno *et al*., "Single-shot spectro-temporal characterization of XUV pulses from a seeded free-electron laser", *Nat. Comm.*, vol. 6, p. 8075, 2015.

[3] K.C. Prince *et al.,* "Coherent control with a short-wavelengthfree-electron laser", *Nat. Photonics*, vol. 10, pp. 176-179, 2016.

[4] L.H. Yu, "Generation of intense uv radiation by subharmonically seeded single-pass free-electron lasers", *Phys. Rev. A*, vol. 44, p. 5178, 1991.

[5] E. Allaria and G. De Ninno, "Soft-X-Ray Coherent Radiation Using a Single-Cascade Free-Electron Laser", *Phys Rev. Lett.*, vol. 99, p. 014801, 2007.

[6] R.K. Lam *et al.,* "Soft X-Ray Second Harmonic Generation as an Interfacial Probe", *Phys Rev. Lett.*, vol. 120, p. 023901, 2018.

[7] H.-Y.Wang *et al.,* "Time-resolved observation of transient precursor state of CO on Ru(0001) using carbon K-edge spectroscopy", *Phys. Chem. Chem. Phys*., vo. 22, p. 2677, 2020.

[8] E. Diesen *et al.,* "Ultrafast Adsorbate Excitation Probed with Subpicosecond-Resolution X-Ray Absorption Spectroscopy", *Phys Rev. Lett*., vol. 127, p. 016802, 2021.

[9] G. Stupakov, "Using the Beam-Echo Effect for Generation of Short-Wavelength Radiation", *Phys Rev. Lett.*, vol. 102, p. 074801, 2009.

[10] P. R. Ribic *et al.,* "Coherent soft X-ray pulses from an echo-enabled harmonic generation free-electron laser", *Nat. Photonics*, vol. 13, p. 555, 2019.

[11] Z. Huang and K.-J. Kim, "Three-dimensional analysis of harmonic generation in high-gain free-electron lasers", *Phys Rev. E*, vol. 62, p. 7295, 2000.

[12] E.L. Saldin, E.A. Schneidmiller, and M. V. Yurkov, "Properties of the third harmonic of the radiation from self-amplified spontaneous emission free electron laser", *Phys Rev. ST Accel. Beams*, vol. 9, p. 030702, 2006.

[13] G. Penco *et al*., "Nonlinear harmonics of a seeded free-electron laser as a coherent and ultrafast probe to investigate matter at the water window and beyond", *Phys Rev A*, vol. 105, p. 053524, 2022.

[14] I. Ben-Zvi, K.M. Yang, and L.H. Yu, "The fresh-bunch tecnique in FELs", *Nucl. Instrum. Methods Phys Res. Sect. A*, vol. 318, p. 726, 1992.

ISBN: 978-3-95450-220-2 ISSN: 2673-5474 doi: 10.18429/JACoW-FEL2022-TUP56

[15] D. Ratner *et al.,* "Second and third harmonic measurements at the linac coherent light source", *Phys Rev. ST Accel. Beams,* vol. 14, p. 060701, 2011.

[16] C. Svetina *et al.,* "PRESTO, the on-line photon energy spectrometer at FERMI: Design, features and commissioning results", *J. Synchrotron Radiat.*, vol. 23, p. 35, 2016.

[17] C. Ferrante *et al.,* "Non-linear self-driven spectral tuning of extreme ultraviolet femtosecond pulses in monoatomic materials", *Light Sci. Appl.*, vol. 10, p. 92, 2021.

[18] S. Reiche, "GENESIS 1.3: a fully 3D time-dependent FEL simulation code", *Nucl. Instrum. Methods Phys. Res. Sect. A* vol. 429, 243, 1999.

[19] S. Spampinati *et al.,* "Laser heater commissioning at an externally seeded free-electron laser", *Phys Rev. ST Accel. Beams*, vol. 17, p. 120705, 2014.

[20] O.Y. Gorobtsov *et al.,* "Seeded X-ray free-electron laser generating radiation with laser statistical properties", *Nat Commun.* vol. 9, p. 4498, 2018.

[21] O.Y. Gorobtsov *et al.,* "Statistical properties of a free-electron laser revealed by Hanbury Brown–Twiss interferometry", *Phys Rev. A*, vol. 95, p. 023843, 2017.

[22] R. Loudon, The Quantum Theory of Light, 3rd ed. (Oxford University Press, Oxford, 2000).

[23] A.A. Lutman *et al.,* "Femtosecond x-ray free electron laser pulse duration measurement from spectral correlation function", *Phys Rev. ST Accel. Beams, vol.* 15, p. 030705, 2012.

[24] L-A. Näslund *et al.,* "X-ray absorption spectroscopy measurements of liquid water", *J. Phys. Chem. B*, vol. 109, pp. 13835-13839, 2005. `doi:10.1021/jp052046q`

[25] F. Capotondi *et al.,* "Multipurpose end-station for coherent diffraction imaging and scattering at FERMI@Elettra free-electron laser facility", *J. Synchrotron Radiat.*, vol. 22, p. 544, 2015.

ISBN: 978-3-95450-220-2 ISSN: 2673-5474 doi: 10.18429/JACoW-FEL2022-TUP57

FREQUENCY PULLING IN A SUPERRADIANT FEL AMPLIFIER

Najmeh S. Mirian, DESY, Hamburg, Germany
Michele Di Fraia, Simone Spampinati, Filippo Sottocorona[1], Enrico Allaria, Laura Badano, Miltcho B. Danailov, Alexander Demidovich, Giovanni De Ninno[2], Simone Di Mitri, Giuseppe Penco, Primož Rebernik Ribič[2], Carlo Spezzani, Giulio Gaio, Mauro Trovó, Nicola Mahne, Michele Manfredda, Lorenzo Raimondi, Marco Zangrando, Oksana Plekan, Kevin C. Prince[3], Carlo Callegari and Luca Giannessi[4], Elettra Sincrotrone Trieste, Basovizza, Italy
Richard J. Squibb, University of Gothenburg, Gothenburg, Sweden
Xi Yang, National Synchrotron Light Source II, Brookhaven National Laboratory, Upton, NY, USA
[1] also at Università degli Studi di Trieste, Trieste
[2] also at Laboratory of Quantum Optics, University of Nova Gorica, Nova Gorica, Slovenia
[3] also at Centre for Translational Atomaterials, Swinburne University of Technology, Melbourne, Victoria, Australia
[4] also at Istituto Nazionale di Fisica Nucleare, Laboratori Nazionali di Frascati, Frascati, Italy

Abstract

A superradiant cascade is a method proposed to shorten the pulse duration in seeded FEL. Pulses shorter than the typical duration supported by the FEL gain bandwidth of the FEL amplifier in the linear regime were measured at FERMI, user FEL facility in Italy. In these conditions we observed a strong frequency pulling phenomenon that will be discussed in this contribution. Finally, we report the most recent measurements carried on FEL-2 set-up in what we label "superradiant mode" of operation.

INTRODUCTION

Ultrashort pulses can probe terahertz-driven dynamics such as coherent phonons or collective excitations in condensed matter, opening the way to the observation of field-dependent, coherently driven phenomena [1-3]. Most pump–probe experiments with FELs must cope with the many complications of poor synchronization and large intensity fluctuations: the need for post-processing, the rejection of outliers reducing the efficiency of data collection, and rogue pulses that may be the cause of premature sample damage. Externally seeded FELs, currently based on high gain harmonic generation (HGHG), are ideal in terms of synchronization (a few femtoseconds (ref. [4]) and control of pulse properties, which are inherited from the seed source [5-7]. The typical pulse duration, in a seeded HGHG FEL, is a function of the seed duration and decreases with harmonic order [8]; at the FERMI machine used in this study, two HGHG FELs cover the range from 100 to 4 nm (refs. [5-9]), with pulses from 90 fs down to 20 fs (for a 70 fs seed). An alternative, which exploits the FEL dynamic process itself to beat the gain bandwidth limit, was proposed in refs. [10-14]: driving the FEL amplifier into saturation and superradiance, along a cascade of undulators resonant at progressively higher harmonics of an initial seed. This is the practical realization of an idealized condition under which a radiation pulse at the onset of saturation in a FEL amplifier propagates and grows as a self-similar solitary wave, undergoing longitudinal compression [15,16]. After saturation, the peak power of an isolated spike moving along a uniform electron beam grows proportionally to the square of the distance covered along the undulator and its duration becomes shorter than the duration supported by the FEL gain bandwidth at the Fourier transform limit (FTL) [17]. A few experiments carried out at visible wavelengths have demonstrated several of the key elements of the scheme [18-20]. In the experiment reported in ref. [1] a few steps forward in the comprehension and characterization of the extreme-ultraviolet (EUV) X-ray superradiant pulses resulting from a cascaded FEL were achieved. A three-stage superradiant cascade (SRC) starting from an ultraviolet (UV) seed pulse and reaching the EUV spectral range was realized at FERMI, according to the scheme proposed in ref. [21].

EXPERIMENT

The experiments were carried out at the FERMI FEL-2 line during three experimental sessions labelled A, B and C.

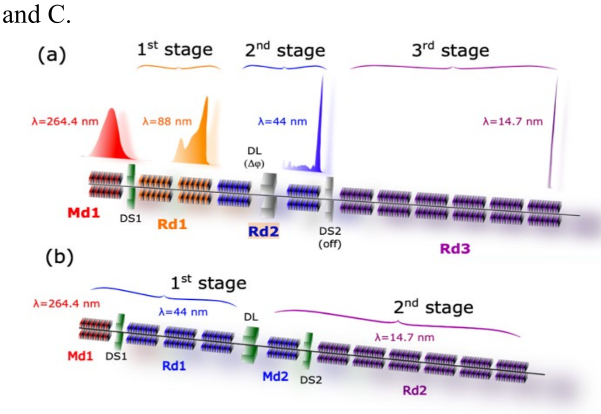

Figure 1: FEL layout (a) FEL-2 in SRC, (b) FEL-2 in HGHG.

ISBN: 978-3-95450-220-2 ISSN: 2673-5474 doi: 10.18429/JACoW-FEL2022-TUP57

The beam/undulator parameters changed slightly from one session to another as listed in Table 1. The beam/undulator parameters changed slightly from one session to another as listed in Table 1. The output wavelength of 14.7 nm was reached as harmonic 18 of the seed (264.4 nm, the third harmonic of a Ti:Sa amplifier). Figure 1 (b) shows the standard two-stage HGHG cascade with fresh-bunch, tuned to reach the final wavelength with a 6 × 3 conversion. Figure 1 (a) shows instead the FEL-2 layout as modified for SRC operation, reaching the same final wavelength with a triple harmonic jump: 3 × 2 × 3. The first two sections were arranged into an additional frequency-conversion stage at 88 nm to initiate the cascade with a shorter gain length and to induce saturation already in the first stage; the dispersive section DS2 was set to zero and the delay line was used as a phase shifter to match the phase between the two second-stage undulators at 44 nm. The switching between the two configurations is done by just tuning the undulator gaps, dispersive sections and seed intensity, while preserving the same electron beam properties and seed duration.

Table 1 Electron Beam, Seed and Undulator Parameters

Beam/seed parameters	**A (SRC/HGHG)**	**B (SRC)**	**C (HGHG)**
Beam energy (MeV)	750 ± 1	900 ± 1	940 ± 1
Peak current (A)	700 ± 30	700 ± 30	700 ± 30
Energy spread (keV)	130 ± 30	<80	<80
Beam size (μm)	90 ± 10	92 ± 10	90 ± 10
Seed wavelength (nm)	264.4 ± 0.1	266.2 ± 0.1	250.0 ± 0.1
Seed energy (μJ)	40 ± 2	44 ± 2	31 ± 2
Seed duration (fs)	55 ± 5	55 ± 5	90 ± 5
Harmonics up-shifts	3 × 2 × 3 / 6 × 3	3 × 2 × 3	7 × 3
Undulator parameters (SRC/HGHG, see Fig. 1)			
Undulator		Period (cm)	Periods
MOD1		10.036	30
RAD1 and RAD2/RAD1 and MOD2		5.52	42
RAD3/RAD2		3.48	66

RESULTS

The reader is addressed to ref. [1] for a detailed description of the obtained results. The main conclusions were the following:

1) It was demonstrated that it is possible to iterate the conversion in a superradiant cascade more than once, reaching harmonic 18 in a three stage conversion process (264 nm -> 88 nm -> 44 nm -> 14.7 nm).
2) In SRC mode pulses can be shorter than those allowed by the gain bandwidth of the corresponding FEL amplifier, while preserving or even exceeding the expected saturation peak power.
3) By measuring the pulse autocorrelation traces in the time domain together with the pulse spectral width, it was shown the possibility of determining the duration of the front peak in the superradiant pulse from the spectral properties, as predicted by the theory in [17].
4) The analysis of the spectra in SRC have shown an unexpected behavior consisting of a substantial ‘frequency-pulling’ effect [22], which is normally barely observed in HGHG mode [23].

Concerning the frequency pulling, the FEL spectral behavior in SRC mode was measured while varying the resonance condition in the final amplifier (Fig. 2a). The seed laser wavelength λ_{seed} and the initial undulator settings were optimized to amplify the harmonic h of the seed laser, $\lambda_s = \lambda_{seed}/h$; the FEL central emission wavelength λ_p differ slightly from λ_s. The undulator gap and K-parameter data were converted to relative wavelength detuning $(\lambda_g - \lambda_s)/\lambda_s$, where λ_g is defined as the resonant wavelength imposed by the undulator setting, using the standard magnetic calibration of the undulators. For comparison, a similar measurement was carried out later, in a typical HGHG mode and is shown in Fig. 2b. Each data point represents a sum of 10^3 shots in superradiance mode and 10^2 shots in HGHG mode. In Fig. 2c we show the correlation between the central emission relative wavelength shift $(\lambda_p - \lambda_s)/\lambda_s$ and the undulator relative detuning, in HGHG (black) and SRC (blue) modes. In HGHG mode (black line) we observe the typical behavior of a modest correlation with a slope

$$\eta = \frac{\lambda_p - \lambda_s}{\lambda_g - \lambda_s} \simeq 0.039 \pm 0.035$$

and with a decaying intensity when the amplifier is detuned. Conversely, in SRC configuration we have $\eta \simeq 0.91 \pm 0.02$, that is, λ_p closely follows the resonant condition set

ISBN: 978-3-95450-220-2 ISSN: 2673-5474 doi: 10.18429/JACoW-FEL2022-TUP57

by the undulator, showing a strong 'frequency-pulling' phenomenon [22]. This strong frequency-pulling seems to be a distinguishing feature of superradiance. In a seeded FEL in HGHG mode, the periodically pre-modulated beam initiating the amplification determines the central emission wavelength λ_p; when the gain is detuned by varying the undulator gap (Fig. 2c, black line), we observe the typical behavior: the radiation spectrum remains almost centered on the integer harmonic of the seed, that is, $\lambda_p \simeq \lambda_s$. Conversely, in SRC mode (Fig. 2c, blue line), the central wavelength of emission closely follows the resonant undulator wavelength. This effect is correlated to the bandwidth of the amplification and to the initial condition initiating the process. Let us assume the amplification in the final amplifier as driven by a "Gaussian equivalent" seed pulse, centered at λ_s and with relative spectral width σ_s, and a Gaussian shaped FEL gain function centered at the wavelength λ_g and relative width σ_g. In a linear amplifier, the relative detuning of the FEL emission central wavelength λ_p, as a function of λ_g would be given by [23],

$$\eta = \frac{\sigma_s^2}{\sigma_g^2 + \sigma_s^2}$$

Inverting this equation, we estimate the equivalent pulse duration that should start the amplification process in order to show a given correlation. To match the measured value of $\eta = 0.91$, we find $\sigma_s \simeq 4.5 \times 10^{-3}$, which corresponds to an FTL equivalent root-mean-square seed duration $\sigma_t \approx 0.86$ fs. In superradiance, the final amplifier behaves as if the amplification was initiated by a pulse as short as a single cycle of the optical seed, a clear difference with the behavior of HGHG where the modest correlation is consistent with the seed duration predicted by the theory.

The cascade configuration of Fig. 1 can be modified to reach different harmonics of the original seed. Other configurations studied include the triple harmonic conversion, 3×2×2 and four harmonic conversions, 3×2×3×2 and 3×2×2×2. In order to set-up a four stage conversion we used the same configuration described in Fig. 1a, where the last six undulators which form the 3rd stage, were split in two stages: the first three radiators tuned at h18 (or h12) and the last three tuned at the second harmonic, i.e. harmonic 36 (or harmonic 24) of the seed laser. These last configurations were studied in a separate session, where the seed was generated as harmonic conversion of a wavelength tunable OPA laser system, delivering λ_{seed}=247.2 nm, for h12 and h24 only. The spectra are shown in Fig. 3.

We acquired 10^3 spectra for configuration. According to the point 3) of the achievements in ref. [1], i.e. the duration of the front peak in the superradiant pulse can be determined from the spectral properties of the pulse, we estimated the expected pulse duration. Harmonics 18 and 12 were also characterized in terms of frequency pulling. In Table 2 a summary of the analysis for the four configurations is reported.

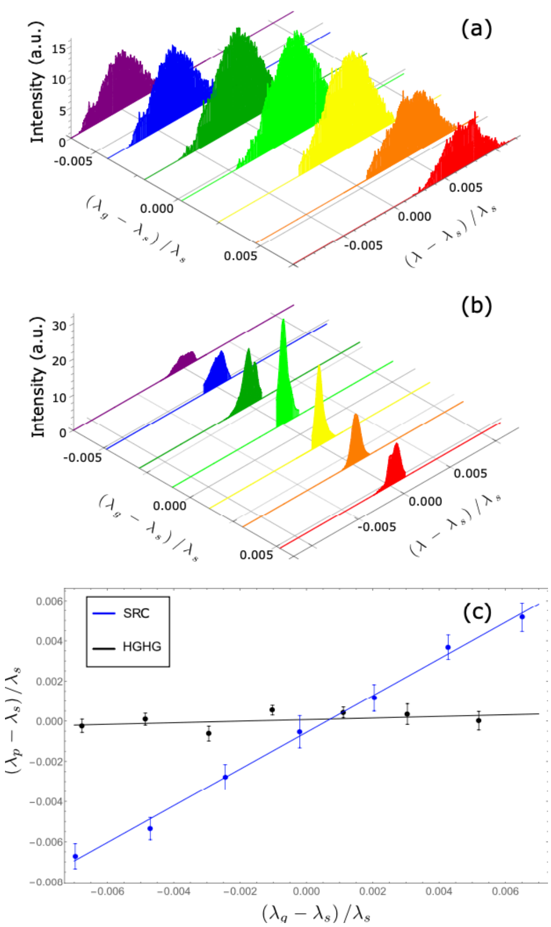

Figure 2: Frequency pulling. (a) FEL spectrum versus the final amplifier resonant frequency in SRC mode of operation. (b) FEL spectrum versus the final amplifier resonant frequency.

The pulling effect was not measured for h24 and h36 due to the low signal to noise ratio available, in the other cases the frequency pulling was observed with correlations above 0.8 (see Figs. 4 and 5). The pulse duration estimate for h18 matches the situation measured with a different seed laser in ref.[1].

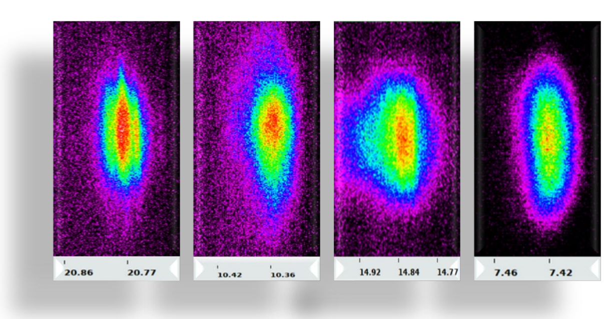

Figure 3: Examples of spectra acquired. From left, at h12, h24, h18 and h36. The spectrum at h24 was integrated at 0.1s.

ISBN: 978-3-95450-220-2 ISSN: 2673-5474 doi: 10.18429/JACoW-FEL2022-TUP57

Table 2: summary of the analysis for the four configurations

Parameter	**h12**	**h24**	**h18**	**h36**
Spectral Width (nm - FWHM)	0.069 ± 0.003	0.033 ± 0.008	0.076 ± 0.007	0.092 ± 0.008
Pulse Duration (fs - FWHM)	8.98 ± 0.11	4.69 ± 0.15	4.54 ± 0.17	1.7 ± 0.44
Energy per pulse (μJ)	38-40	0.5	16.6	0.1
Final Wavelength (nm)	20.6	10.3	14.67	7.3
Seed Laser (nm)	247.2	247.2	264	264
Frequency Pulling	0.847 ± 0.075	N/A	0.801 ± 0.008	N/A

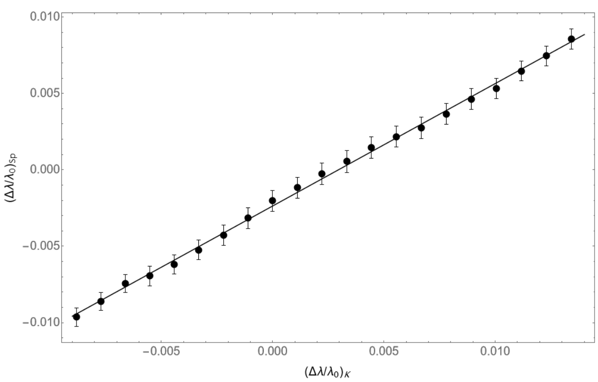

Figure 4: FEL emission wavelength vs resonance wavelength at h18.

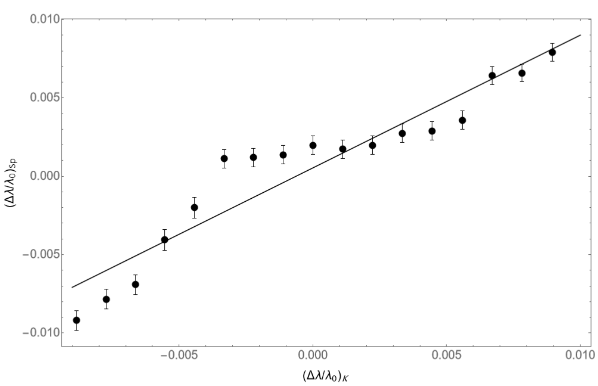

Figure 5: FEL emission wavelength vs resonance wavelength at h12.

CONCLUSION

In conclusion, we confirm the observation of frequency pulling in superradiance in different cascaded configurations at FERMI FEL-2. We also confirm the possibility to set-up superradiant cascaded configurations reaching different harmonic orders, to operate the FEL in this regime using the tunable seed available when the seed laser is based on the OPA scheme. Finally, the reconstruction of the pulse duration based on the spectral analysis foresees the generation of ultrafast pulses in the EUV spectral range. These results support the hypothesis that this regime can be extended to the soft-X ray spectral range when the beam energy of the FERMI linac will be increased in the next future [24-25].

REFERENCES

[1] N.S. Mirian, M. Di Fraia, S. Spampinati, *et al.*, “Generation and measurement of intense few-femtosecond superradiant extreme-ultraviolet free-electron laser pulses”, *Nat. Photon.*, vol. 15, pp. 523–529, 2021. doi: 10.1038/s41566-021-00815-w

[2] F. Bencivenga, F. Capotondi, E. Principi, M. Kiskinova, and C. Masciovecchio, “Coherent and transient states studied with extreme ultraviolet and X-ray free electron lasers: present and future prospects”, *Adv. Phys.*, vol. 63, pp. 327–404, 2015. doi: 10.1080/00018732.2014.1029302

[3] K. C. Prince *et al.*, “Coherent control with a short-wavelength free-electron laser”, *Nat. Photonics,* vol. 10, pp. 176–179, 2016. doi: 10.1038/nphoton.2016.13

[4] M. B. Danailov *et al.*, “Towards jitter-free pump-probe measurements at seeded free electron laser facilities”, *Opt. Express,* vol. 22, pp. 12869–12879 2014. doi:10.1364/OE.22.012869

[5] E. Allaria *et al.*, “Highly coherent and stable pulses from the FERMI seeded free-electron laser in the extreme ultraviolet”, *Nat. Photonics,* vol. 6, pp. 699–704 2012. doi:10.1038/nphoton.2012.233

[6] G. De Ninno *et al.,* “Single-shot spectro-temporal characterization of XUV pulses from a seeded free-electron laser”, *Nat. Commun.,* vol. 6, p. 8075, 2015. doi:10.1038/ncomms9075

[7] O. Y. Gorobtsov *et al.,* “Seeded X-ray free-electron laser generating radiation with laser statistical properties”, *Nat. Commun.,* vol. 9, p. 4498, 2018. doi: 10.1038/s41467-018-06743-8

[8] P. Finetti *et al.*, “Pulse duration of seeded free-electron lasers”, *Phys. Rev. X,* vol. 7, p. 021043, 2017. doi: 10.1103/PhysRevX.7.021043

[9] E. Allaria *et al.*, “Two-colour pump–probe experiments with a twin-pulse-seed extreme ultraviolet free-electron laser”, *Nat. Commun.,* vol. 4, p. 2476, 2013. doi:10.1038/ncomms3476

[10] B. W. J. McNeil, N. R. Thompson, D. J. Dunning, and B. Sheehy, “High harmonic attosecond pulse train amplification in a free electron laser”, *J. Phys. B,* vol. 44, p. 065404, 2011. doi: 10.1088/0953-4075/44/6/065404

ISBN: 978-3-95450-220-2 ISSN: 2673-5474 doi: 10.18429/JACoW-FEL2022-TUP57

[11] D. Gauthier *et al.*, "Chirped pulse amplification in an extreme-ultraviolet free-electron laser", *Nat. Commun.*, vol. 7, p. 13688, 2016. doi: 10.1038/ncomms13688

[12] T. Tanaka and P. Rebernic Ribič, "Shortening the pulse duration in seeded free-electron lasers by chirped microbunching", *Opt. Express,* vol. 27, pp. 30875–30892, 2019. doi:10.1364/OE.27.030875

[13] P. K. Maroju *et al.*, "Attosecond pulse shaping using a seeded free-electron laser", *Nature,* vol. 578, pp. 386–391, 2020. doi:10.1038/s41586-020-2005-6

[14] J. Duris *et al.*, "Tunable isolated attosecond X-ray pulses with gigawatt peak power from a free-electron laser", *Nat. Photonics,* vol. 14, pp. 30–36, 2020. doi: 10.1038/s41566-019-0549-5

[15] R. Bonifacio, L. De Salvo Souza, P. Pierini, and N. Piovella, "The superradiant regime of a FEL: analytical and numerical results", *Nucl. Instrum. Methods Phys. Res. A,* vol. 296, pp. 358–367, 1990. doi: 10.1016/0168-9002(90)91234-3

[16] R. Bonifacio, N. Piovella, and B. W. J. McNeil, "Superradiant evolution of radiation pulses in a free-electron laser", *Phys. Rev. A*, vol. 44, pp. R3441–R3444, 1991. doi: 10.1103/PhysRevA.44.R3441

[17] X. Yang, N. Mirian and L. Giannessi, "Postsaturation dynamics and superluminal propagation of a superradiant spike in a free-electron laser amplifier", *Phys. Rev. Accel. Beams,* vol. 23, p. 010703, 2020. doi: 10.1103/PhysRevAccelBeams.23.010703

[18] T. Watanabe *et al.*, "Experimental characterization of superradiance in a single-pass high-gain laser-seeded free-electron laser amplifier", *Phys. Rev. Lett.,* vol. 98, p. 034802, 2007. doi: 10.1103/PhysRevLett.98.034802

[19] L. Giannessi *et al.*, "High-order-harmonic generation and superradiance in a seeded free-electron laser", *Phys. Rev. Lett.,* vol. 108, p. 164801, 2012. doi: 10.1103/PhysRevLett.108.164801

[20] L. Giannessi *et al.*, "Superradiant cascade in a seeded free-electron laser", *Phys. Rev. Lett.*, vol. 110, p. 044801, 2013. doi:10.1103/PhysRevLett.110.044801

[21] L. Giannessi, P. Musumeci, and S. Spampinati, "Nonlinear pulse evolution in seeded free-electron laser amplifiers and in free-electron laser cascades", *J. Appl. Phys.*, vol. 98, p. 043110, 2005. doi: 10.1063/1.2010624

[22] O. Svelto and D. C. Hanna, *Principles of Lasers*, Springer, 2010.

[23] E. Allaria *et al.*, FERMI 2.0 Conceptual Design Report, https://www.elettra.eu/images/Documents/FERMI%20Machine/Machine/CDR/FERMI2.0CDR.pdf

[24] L. Giannessi *et al*. "Future Upgrade Strategy of the FERMI Seeded FEL Facility", presented at 40th Int. Free Electron Laser Conf. (FEL' 22), Trieste, Italy, Aug. 2022, paper TUP53, this conference.

ISBN: 978-3-95450-220-2 ISSN: 2673-5474 doi: 10.18429/JACoW-FEL2022-TUP58

STUDIES OF WAVELENGTH CONTROL AT FERMI

F. Sottocorona, G. Perosa, Università degli Studi di Trieste, Italy
L. Giannessi[1], E. Allaria, S. Di Mitri, M. B. Danailov., Elettra-Sincrotrone Trieste S.C.p.A, Basovizza, Italy
[1]also at INFN LFN, Frascati, Roma, Italy

Abstract

FEL basic theory indicates that the output wavelength of a seeded FEL operated in the HGHG configuration is determined by the wavelength of the seed laser and light is emitted when undulators are tuned to an exact harmonics of the seed laser. In a realistic case, when taking into account the electron beam imperfections and the finite bandwidths of the seed and of the amplification process, the output wavelength is influenced by these factors and can deviate from the exact harmonic giving some flexibility to control the FEL wavelength without the need to change the seed laser wavelength. In this work, we consider the effects of the dispersive section, the curvature of the electron beam longitudinal phase-space and the frequency pulling as major contributors. We show how these quantities influence the effective final FEL wavelength. Furthermore, we show how one can reconstruct the electron beam longitudinal phase-space from the analysis of the FEL wavelength sensitivity to the seed laser delay with respect to the beam arrival time.

INTRODUCTION

In a Self-Amplified Spontaneous Emission FEL, the output wavelength is governed by the resonance condition in the amplifier [1]. Operations of seeded FEL such as High Gain Harmonic Generation [2] require the resonance condition to be set at one of the higher harmonics of the seed used to modulate the beam, undulator tuning is no longer a free parameter and wavelength is determined by the seed laser. This condition is the result of the interference process of the emission of the density modulated beam and contributes to the superior wavelength stability of the FEL that is not dominated by the beam energy jitter [3]. In practice, there are different phenomena in the HGHG harmonic conversion process that can shift the output wavelength from this condition, such as the effect of the dispersive element in the undulator chain or the frequency pulling phenomenon shifting the wavelength when the undulator resonance does not coincide with the one of density modulation. In order to control the properties of the FEL light and understanding of the various elements of the machine involved in the process is required for an accurate tuning of the FEL.

THEORETICAL BACKGROUND

It is well known from literature that the FEL emission is based on the coherent radiation emitted by a high-brightness, relativistic electron beam passing through the periodic field of an undulator. The interaction between the undulator magnetic field and the transverse motion of the wiggling electrons leads to an energy exchange from the e-beam into the electromagnetic radiation. The output wavelength of this process can be calculated by the relation

$$\lambda_{res} = \frac{\lambda_u}{2\gamma^2}(1 + a_w^2) \tag{1}$$

where λ_u is the undulator period, a_w is equal to the undulator strength parameter K, for circular polarizations, and $K/\sqrt{2}$ for linear polarizations, and γ_0 is the energy of the beam (in mc^2 units). Normally, for small adjustments of the FEL wavelength, the energy of the e-beam can be kept constant, and the parameter a_w is varied by varying the undulator gaps. FEL amplification occurs only within the gain bandwidth that can be estimated from the Pierce parameter ρ [2]. In the case of FERMI ρ is of the order of 10^{-3}. The range of the wavelength tuning, with fixed gap, is therefore pretty small. In terms of beam energy, the corresponding accuracy to stay within the gain bandwidth is of about a MeV, at a beam energy of 1 GeV. In a seeded FEL like FERMI, the generation of coherent FEL pulses is the result of few processes. First, as a result of the interaction between the electrons and the external seed, inside a modulator, the beam is modulated in energy, with the period of the modulation being equal to the wavelength λ of the seed. In a second step, this energy modulation is converted into density modulation by a dispersive chicane. As a result, the electron beam is subdivided into micro-bunches that can emit in phase, producing coherent emission at the fundamental wavelength. Because bunching can have strong harmonic components, coherent emission can also be produced at the harmonics of the resonant wavelength. In the third phase, bunched electrons passes through undulator tuned to a specific harmonic n of the seed and emit coherently. Finally, FEL amplification occurs leading to generation of high power pulses at λ/n.

The dispersive section has the main role of energy-density conversion, but, in combination of an energy chirp into the electron beam has also the effect of compressing (or decompressing) the bunch, because electrons at different energies travel on different paths. Since the seeding process is done before the dispersive element, the wavelength impressed by the seed is also slightly compressed by the dispersive element. This effect is present when the e-beam has not a flat longitudinal phase-space. In particular, linear compression of the beam is determined by the linear chirp. Therefore, the harmonic coherent emission will no longer occur at λ_{seed} /n, but rather at the compressed wavelength. This new wavelength can be calculated by the relation

ISBN: 978-3-95450-220-2 ISSN: 2673-5474 doi: 10.18429/JACoW-FEL2022-TUP58

$$\frac{\lambda_{seed}/n}{\lambda_{HGHG}} = \frac{1}{1 - \frac{R_{56}}{\gamma(z)}\frac{d\gamma}{dz}} \tag{2}$$

where $\gamma(z)$ is the energy profile, as a function of the internal coordinate z, R_{56} is the dispersive section value and λ_{HGHG} is the value of the bunching wavelength after the dispersive section. The Eq. (1) shows that it is possible to finely control the wavelength of the coherent bunching by acting on the R56 or the linear chirp of the electron beam. For an optimized FEL both R56 and linear chirp cannot freely change. The first determine the amount of bunching and large variations will lead or to significant reduction of bunching (low FEL intensity) or overbunching [4]. The second is determined by linac settings, large changes may lead to not optimal beam properties; however, due to the typical quadratic chirp (see Fig. 1) and the use of a seed much shorter than the electron beam, the linear chirp component of the interested electrons can be varied by properly selecting the relative timing between the seed laser and the electron beam. This feature can then be used for fine wavelength adjustments. Furthermore, a third effect can modify the output wavelength and need to be considered. In case the bunching wavelength (λ_{HGHG}) does not match the resonant wavelength (λ_{res}), then a frequency pulling effect [5] will move the final wavelength into slightly different values defined by the relation

$$\lambda_{FEL} = \frac{1}{\frac{1}{\lambda_{\mathrm{HGHG}}} - \left(\frac{1}{\lambda_{\mathrm{HGHG}}} - \frac{1}{\lambda_{\mathrm{res}}}\right)\frac{\sigma_{\mathrm{s}}^2}{\sigma_{\mathrm{s}}^2 + \sigma_{\mathrm{u}}^2}} \tag{3}$$

where the various wavelengths are defined before, λ_{FEL} is the final wavelength, σ_s is the rms of the seed laser bandwidth and σ_u is the rms of the gain process and can be estimated by the Pierce parameter ρ. From the relation above, we can see that, if $\sigma_s \ll \sigma_u$ then the wavelength shift is really small and can be neglected and the final FEL wavelength is uniquely determined by the seeding. Instead, if $\sigma_s \gg \sigma_u$, the wavelength is shifted towards λ_{res}, this corresponds to the case of a SASE FEL.

NUMERICAL ANALYSIS

In addition to the change of the seed laser wavelength, fine control of the output FEL wavelength, is then possible via control the resonance and the longitudinal phase space.

While the resonance and the pulling are determined by the undulator setting and the electron beam energy that are well known, in order to determine the contribution associated to the electron beam phase space, it is required a measurement that in our case can be obtained with a deflecting cavity combined with an electron energy spectrometer. Due to the high impedance cavity, the typical electron energy distribution at FERMI is characterized by high order chirps. In our study, we start considering a generic function for γ(z), up to the third order, expanded around a specific point z_0

$$\gamma(z) = \chi_0 + \chi_1(z - z_0) + \frac{\chi_2}{2}(z - z_0)^2 + \frac{\chi_3}{6}(z - z_0)^3 \tag{4}$$

where the χ_0 is the resonance energy and χ_i, with i>0 , are the linear, quadratic and cubic chirp. The function, that mimic the standard FERMI electron beam is plotted in Fig.1.

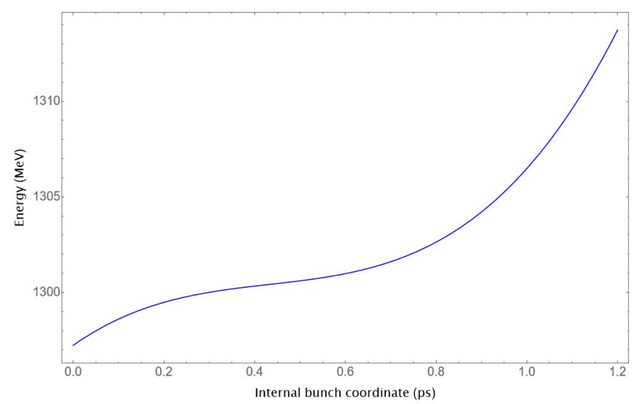

Figure 1: Example of phase-space. Here we have used χ_0 = 1300 MeV, χ_1 = 4 MeV/ps, χ_2 = -20 MeV/ps^2 and χ_3 = 150 MeV/ps^3.

FERMI FEL-1 setup is characterized by an undulator period λ_u = 5.52 cm and, for our studies, used in circular polarization. In order to change the resonance, practically we have to change the gaps of the radiators and this will change the value of the strength parameter a_w. But for every value of a_w, there is a value of the resonance energy χ_0 that gives the same effects. Therefore, numerically, it's easier to change the value of χ_0 and see how the output wavelength changes. In Fig. 2, we have plotted the resonance wavelength for changes of the electron beam energy value

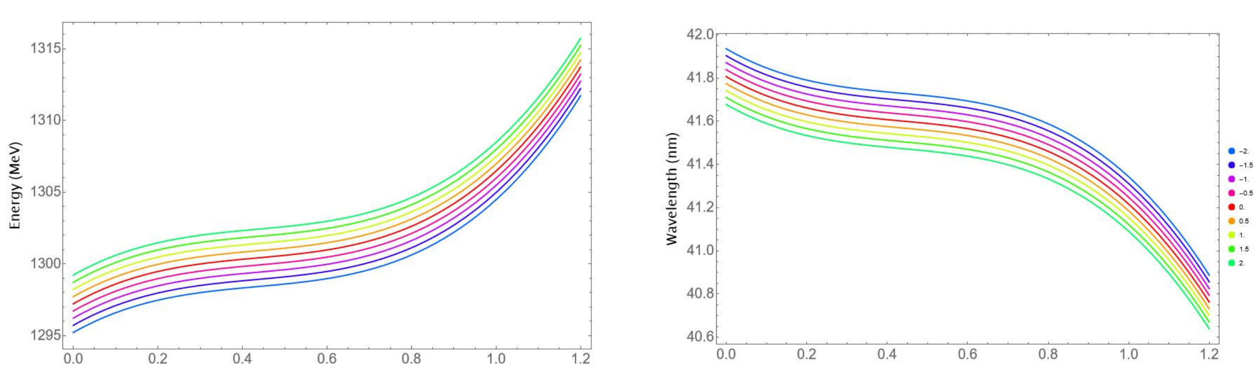

Figure 2: Behaviour of λ_{res} as a function of the resonance energy. In the legends the values are in MeV

ISBN: 978-3-95450-220-2 ISSN: 2673-5474 doi: 10.18429/JACoW-FEL2022-TUP58

by ±2 MeV, with steps of 0.5 MeV. The second analysis reported in Fig. 3 shows the effect of the dispersive section. The resonance relation is used to determine the bunching wavelength for different values of R_{56}. Due to the variation of the linear chirp component in the considered electron beam, the bunching wavelength will change along the electron beam. In both cases, we used a value of $\lambda_{seed} = 250.0$ nm and we consider the 6th harmonic. Figure 3 also shows how, for fixed value of the internal coordinate, a change in R_{56} implies a different change in the output wavelength, and larger is the value of the dispersive section, larger is wavelength change. The last effect that we want to analyse is the resonance when frequency pulling is taken into account. We can see from λ_{FEL} relation, the final wavelength is a superposition of the two wavelengths coming from the resonance relation and from the dispersive section compression.

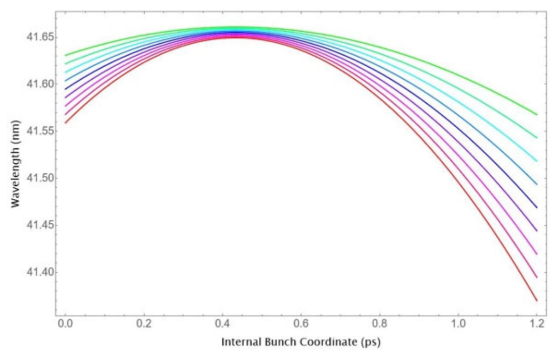

Figure 3: Behaviour of λ_{HGHG} as a function of the value of dispersive section R_{56}. In the legends the values are in ps (in order to match the units of measure)

Assuming a given value for the dispersive section and the undulators strength, and the phase-space profile as before, in Fig. 4 is reported the behaviour of λ_{FEL} as a function of the pulling coefficient $F.P. = \sigma_s^2 / (\sigma_s^2 + \sigma_u^2)$. The plot shows a deformation of the profile, as the coefficient F.P. increases in value. For low values of FP (red line in Fig. 4) the FEL wavelength profile follow the one of λ_{HGHG} (Fig. 3). For large values of FP instead (orange line), the FEL wavelength follow the resonant wavelength (Fig. 2). For an intermediate value of FP, the final wavelength is the result of a combined effect.

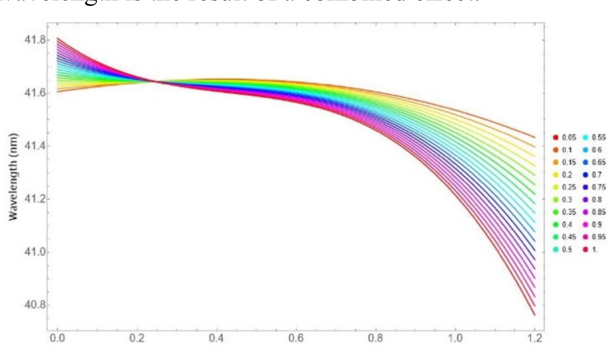

Figure 4: Behaviour of λ_{FEL} as a function of the value of the frequency pulling coefficient.

EXPERIMENTAL ANALYSIS

For the experiment we used a seed laser at 250 nm and the FEL tuned at harmonic 10. As reported in previous section the seed delay scan can be used to finely tune the values of the FEL wavelength by selecting the internal coordinates of the seeded part. For a given longitudinal phase-space, the behaviour of the FEL wavelength vs the seed delay can be determined with equations described above. the dispersive section at a fixed value and acquiring three seed delay scans with the undulators gap set for different resonances. The machine data allow to determine the ρ (from beam energy and undulator setting) and σ_s (from seed laser parameters) parameters. This allows to estimate the contribution of the frequency pulling to the final wavelength. More problematic is the determination of the electron beam chirp. The quadratic and cubic chirp are responsible of the variation of the FEL wavelength vs the seed delay. The linear chirp, however, is only responsible of introducing an offset on the measured FEL wavelength. This offset can be masked by possible uncertainty associated to the calibration of the spectrometer used to acquire the wavelength profile. Therefore, there isn't a simple way to uniquely identify the contribution of the linear chirp simply using the response of the FEL vs the seed delay scan. In Fig. 5 the results of our measurements are reported together with the predictions using equation previously described and a suitable phase space for the electron beam.

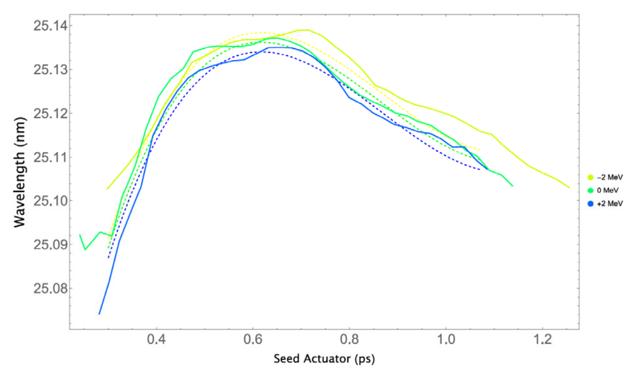

Figure 5: Reconstruction of the wavelength behaviour, coming from a seed scan, from different values of resonance. Solid lines are the wavelength profile of the seed scans, while the dashed lines are coming from the analysis described in the previous section.

As we have seen also the strength of the dispersive section plays a role in the determination of the final FEL wavelength, this has been also verified experimentally with dedicated measurements with the seed laser at 250 nm and the undulators at harmonic 6 we acquired FEL wavelength vs seed delay for different values of R_{56}.

As for the previous measurements Fig. 6 reports the experimental data together with the results of the theoretical analysis. As we can see from the plots, the overall behaviour is reproducible, but there is still some discrepancy, for some values of z. Some explanations for the differences could be: for each case, we have assumed

ISBN: 978-3-95450-220-2 ISSN: 2673-5474 doi: 10.18429/JACoW-FEL2022-TUP58

the fact that the phase-spaces, for each value of the parameter (dispersive section and resonance energy), are the same. There could have been some fluctuation in the phase-space that gives rise to some different behaviour, especially for values of z that are far from z_0. Also we have used just four order in the phase-space definition, maybe high orders are needed to fully reproduce the behaviour of the wavelength.

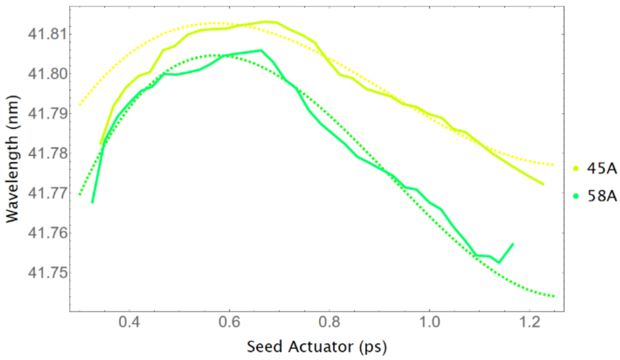

Figure 6: Reconstruction of the wavelength behaviour, coming from a seed scan, for different values of dispersive section. Solid lines are the wavelength profile of the seed scans, while the dashed lines are coming from the analysis described in the previous section.

PHASE-SPACE RECONSTRUCTION

It is possible to exploit the dependence of the FEL wavelength on the seed delay to determine the properties of the electron beam. Interpolating the behaviour of the wavelength vs the internal bunch coordinate (or the seed actuator) we can reconstruct the function $\lambda_{FEL}(z)$. Using the same relations described in the theoretical analysis and combining them, we can use the wavelength function obtained to resolve for $\gamma(z)$, therefore we can obtain a measurement of local longitudinal phase-space. This implies the knowledge of the other effects that play a role in the determination of the FEL wavelength, that may be difficult. In case that the measures of the FEL wavelength and of the seed laser wavelength are subject to an uncertainty due to the calibration of the spectrometers, this simple method cannot uniquely determine the linear chirp component of the phase-space. Nevertheless, from our measurements, we can still observe that the possibility to reconstruct the phase-space is concrete and it is possible to achieve a good estimation of the electron beam phase space at the modulator. Also the main features are correctly reproduced: the plot shown in Fig. 7 refers to the effect of the dispersive section. The two phase-spaces coincide in the measurements and also the discrepancy at the beginning that is also present in the wavelength plot with a known phase-space. Figure 8 report the phase space that is reconstructed from the delay scans done at difference resonance energies. Again, looking at the theory, the reconstruction has a good behaviour and the characteristic separation is well reproduced.

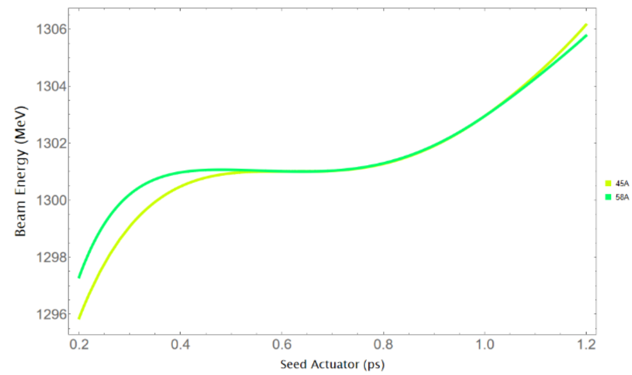

Figure 7: Phase-space reconstructed from the seed scan at different dispersive section values.

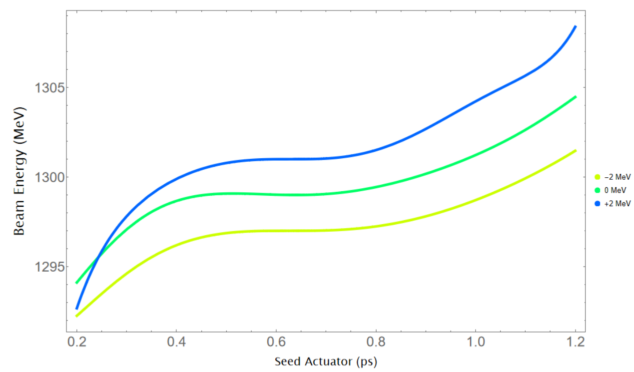

Figure 8: Phase-space reconstructed from the seed scan at different resonance energy values.

REFERENCES

[1] E. Saldin, E. V. Schneidmiller, M. V. Yurkov, "The Physics of Free Electron Lasers", *Springer Book Archive*, 2000. doi:10.1007/978-3-662-04066-9.

[2] L. H. Yu, "Generation of intense UV radiation by subharmonically seeded single-pass free-electron lasers". *Physical Review A*, vol. 44, p. 5178, Oct. 1991. doi:10.1103/PhysRevA.44.5178

[3] E. Allaria, R. Appio, L. Badano, *et al*, "Highly coherent and stable pulses from the FERMI seeded free-electron laser in the extreme ultraviolet". *Nature Photonics*, vol. 6, pp. 699–704, Oct. 2012. doi:10.1038/nphoton.2012.233

[4] D. Gauthier, P. R. Ribič, G. De Ninno, E. Allaria, P. Cinquegrana, *et al*, "Spectrotemporal Shaping of Seeded Free-Electron Laser Pulses". *Phys. Rev. Lett.*, vol. 115, p. 114801, Sep. 2015. doi:10.1103/PhysRevLett.115.114801

[5] E. Allaria, G. De Ninno, and C. Spezzani, "Experimental demonstration of frequency pulling in single-pass free-electron lasers", *Opt. Express*, vol. 19, pp. 10619-10624, 2011. doi:10.48550/arXiv.1105.5536

ISBN: 978-3-95450-220-2 ISSN: 2673-5474 doi: 10.18429/JACoW-FEL2022-TUP62

CONTROL OF THE LONGITUDINAL PHASE AND BENCHMARKING TO HBSASE

Saeid Pirani, Francesca Curbis, Mihai Pop, Sverker Werin*
Department of Physics, Lund University, P.O. Box 118, SE-22100 Lund, Sweden

Abstract

Improvement of the longitudinal coherence in the proposed Soft X-ray FEL, the SXL, for the MAX IV Laboratory is an important design aspect to enhance the user case. One of the main considered methods is HBSASE. However the final compression in the MAX IV acceleratos is done at full energy, and thus leaving an energy chirp in the electron pulse. This chirp in longitudinal phase space has to be removed for an efficient implementation of HBSASE. In this paper we show in simulations how the phase space is improved by first overcompressing the pulse, and then correct it by a two-plate wakefield de-chirper. The resulting pulse is then shown to have qualities such that, by HBSASE, a significant narrowing of the FEL bandwidth is achieved at 1 nm.

INTRODUCTION

Free Electron Lasers (FEL) driven by linear accelerators can provide high power photon pulses with short duration, narrow bandwidth and high brilliance. The transverse coherence is excellent, while the longitudinal coherence in a SASE FEL is limited. To improve the longitudinal coherence, intensity and wavelength stability different seeding techniques can be implemented. While longer wavelength FELs can make use of external lasers for directly seeding, this is not easily achieved in the X-ray range. Thus other techniques have to be used, such as EEHG (Echo Enhanced Harmonic Generation) [1], Self-seeding [2] or HBSASE (High Brightness SASE) [3]. All these techniques put additional requirements on the electron beam quality and provide different enhancement of the fundamental properties.

One critical parameter is the flatness of the longitudinal phase space. The compression of the pulse, wakefields and CSR will influence the energy distribution along the pulse. Wakefields are also commonly used to adjust and correct the longitudinal phase space. A limitation is that the wakefields normally reduce the energy of the tail of the electron pulse, and thus pulses with lower energy in the tail cannot easily be adjusted. This is the situation in the MAX IV linear accelerator using achromat bunch compressors and final compression at full energy.

In this paper we discuss how the sign of the chirp can be flipped through over-compression. The flipped chirp is then removed by standard de-chirper, using parallel metallic plates with a corrugated surface. Finally, by simulations we show a proof of concept of the beam being used in a HBSASE mode at 1 nm with improved spectral properties and reduced jitter.

* sverker.werin@maxiv.lu.se

MAX IV ACCELERATOR AND THE SXL PROJECT

The MAX IV Laboratory is a synchrotron radiation facility operating two storage rings, at 3 and 1.5 GeV respectively, and a full energy linear accelerator injector. Around the facility 16 beamlines (2022) provides a palette of performance including one beamline placed directly on the linear accelerator in the Short Pulse Facility operating with pulses compressed down to 100 fs.

A Soft X-ray FEL (the SXL project) [4] is being designed and consists of a FEL placed on the 3 GeV linac targeting the 1–5 nm wavelength range. The FEL will start in SASE mode with pulses of intermediate, 15 fs, and short, 1 fs, pulse length. Following on SASE operation seeding is requested and suitable methods are studied.

The MAX IV linear accelerator (Fig. 1) is based on normal conducting S-band linac structures. At 256 MeV the first bunch compressor (BC1) is placed. The main linac consists of 36 structures which are followed by another bunch compressor (BC2) at full energy, 3 GeV. This implies that there will be a remaining energy chirp in the electron beam when it enters the FEL. While this is not an issue for ordinary SASE operation, HBSASE operation will be negatively affected.

The longitudinal wakefields in a linac accelerating structure increase the chirp used for compression. Thus a smaller off-crest RF-phase for a specified compression is required.

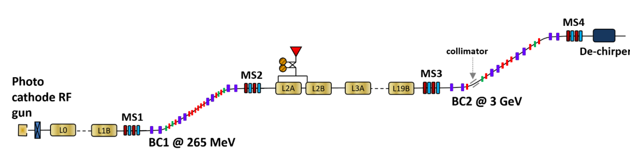

Figure 1: The MAX IV linac.

The linac and SXL has a standard operation mode called high charge long pulse mode [4]. The different modes have been studied by start-to-end simulation using Astra [5], Elegant [6] and Genesis [7], for the FEL. In Fig. 2 the longitudinal phase space and beam current after the second bunch compressor (BC2) is shown. The RF phases in the linacs before and after BC1 are set on 26.3 and zero degree, respectively.

REVERSING THE LONGITUDINAL CHIRP BY OVER COMPRESSION

Since the compression in the MAX IV linac requires a negative chirp in energy, over-compression can be implemented to reverse the chirp. This allow to use a standard de-chirper

ISBN: 978-3-95450-220-2 ISSN: 2673-5474 doi: 10.18429/JACoW-FEL2022-TUP62

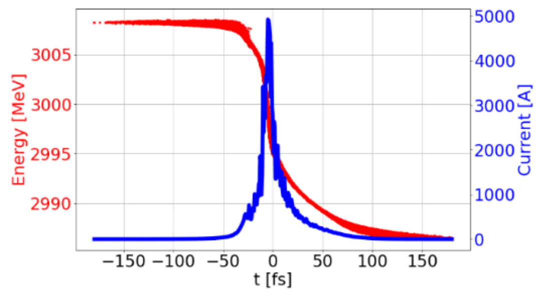

Figure 2: Phase space and e-beam current the FEL entrance in standard mode (charge 100 pC).

and in thurn to get a beam better suited for HBSASE operation. The over-compression is achieved by re-tuning of the RF phase in the linac section (L1) before the first bunch compressor (BC1) from 26.3 deg to 27 deg.

This results in a slightly more compressed pulse after BC1, which then generates more wakefields in the main linac, which in turn further increases the chirp. With an increased chirp the bunch passes full compression inside the second bunch compressor (BC2).

The resulting longitudinal phase space is shown in Fig. 3.

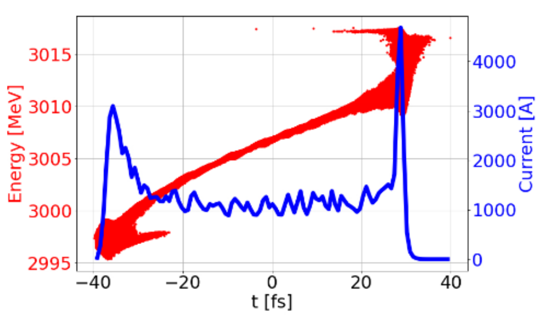

Figure 3: Phase space and e-beam current for the overcompressed beam at the exit of the second bunch compressor (BC2) (without scraper).

Scrapers and Emittance

In order to reduce CSR effects near full compression, the current spikes at the head and the tail of the pulse are removed by a collimator in a high dispersion point of the first acromat of BC2. It results in roughly 31 % loss in the bunch charge (Fig. 4).

The horizontal emittance will be influenced by CSR during over-compression. In Fig. 5 it is shown that the horizontal emittance increases by a factor of two, reaching 0.6 mm mrad.

REMOVING THE RESIDUAL CHIRP

The De-Chirper

The SXL de-chirper (see Fig. 6) is a corrugated structure with p=h=0.5 mm and g=0.25 mm, based on existing de-chirper experience in LCLS [8]. The de-chirper is divided

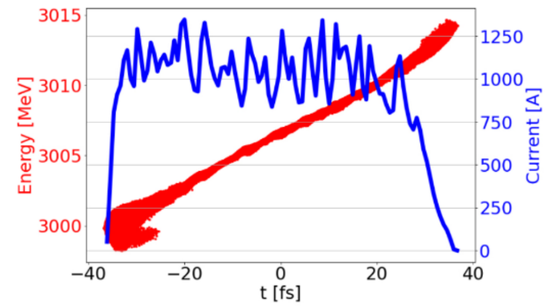

Figure 4: The electron beam after the second bunch compressor (BC2) with a collimator in a high dispersion point.

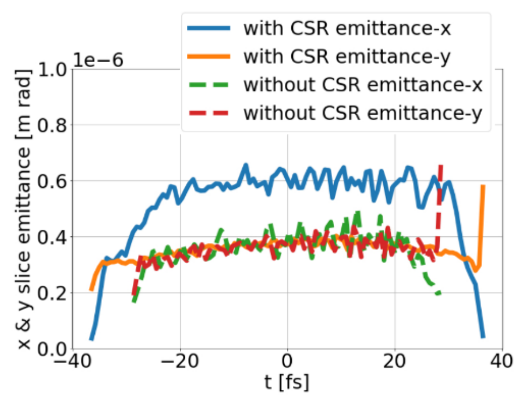

Figure 5: The effect of CSR on the slice emittance after BC2.

into two sections with a total length of 5.9 m and using a half-gap down to 1 mm.

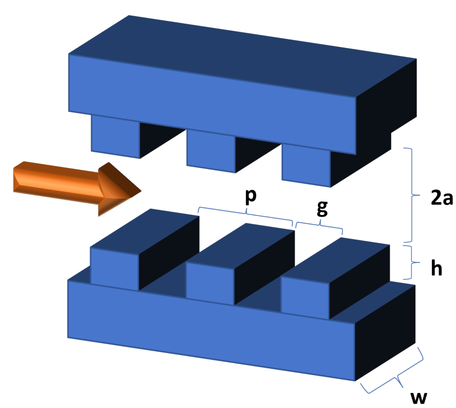

Figure 6: Geometry of the de-chirper (not to scale).

Figure 7 illustrates the longitudinal phase space and the beam current after the de-chirper.

The electron beam parameters at the FEL entrance are: pulse length 75 fs, with 69.2 pC bunch charge, a slice energy spread for the core part of the beam of 100 keV and around 1 kA current.

ISBN: 978-3-95450-220-2 ISSN: 2673-5474 doi: 10.18429/JACoW-FEL2022-TUP62

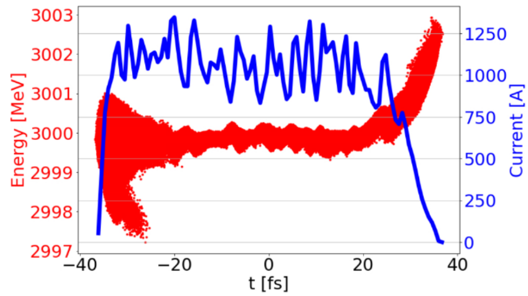

Figure 7: Longitudinal phase space and current after the dechirper.

PERFORMANCE IN HBSASE MODE

HBSASE is a method to narrow the bandwidth, increasing longitudinal coherence and reduce the central wavelength jitter. The method is based on delaying the electron pulse between each undulator to force a coupling of the optical mode over a longer distance in the pulse.

Layout of the FEL line in SXL

The SXL will contain 20 undulator modules with intrasections consisting of a delay chicane/phase shifter, a quadrupole and diagnostics (BPMs and screens). The undulators are 2 m long APPLE-X undulators to allow full polarization control [9]. A schematic view of the FEL line is shown in in Fig. 8.

In the basic SASE mode of operation, the radiation will be generated with 0.5% and 0.8% spectral bandwidth at 1 nm and 5 nm respectively, (for a 3 GeV beam with 3.9 kA peak current, 0.46 MeV energy spread and 100 pC charge [4]).

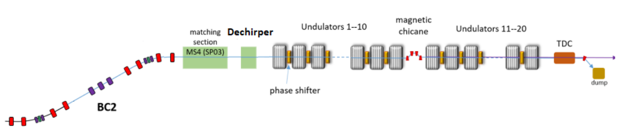

Figure 8: Schematic view of the SXL FEL line.

Optimizing HBSASE and Results

A quick optimisation to reach maximum bandwidth reduction started with a linear descending pattern with prime numbers for the delays between the undulators. The delays were then optimised using prime numbers close to the original choice. To prevent over bunching of the micro bunch structure, the last two delays were kept small. The optimized delay values for the chicanes are presented in Fig. 9.

Figure 10 shows the gain curve and spectral bandwidth comparing HBSASE and SASE, both using the overcompressed electron beam. For each case an average result of 15 simulations with different random seeds for the electrons' shot noise is considered. The spectral bandwidth for HBSASE and SASE modes are 0.48 eV (0.039%) and 2.24 eV (0.18%) respectively which implies a factor of 4.6 in bandwidth reduction. Compared to SASE operation with the standard beam [4] at 1 nm there is a factor of 11.8 reduction in bandwidth.

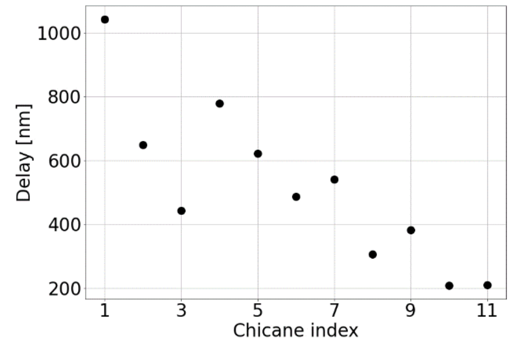

Figure 9: Delay sequence used for HBSASE simulations.

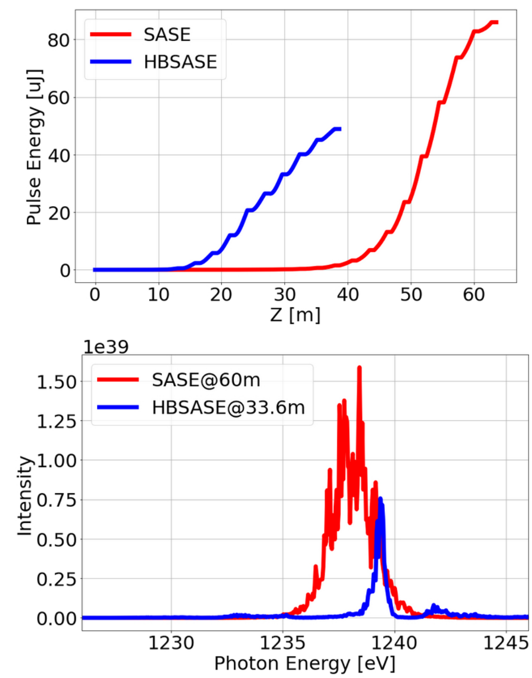

Figure 10: Gain curve (top) and spectral bandwidth (bottom) comparison for SASE and HBSASE (both using the overcompressed pulse).

SUMMARY AND CONCLUSIONS

We have shown that it is possible to over-compress the electron beam in the MAX IV linac without significant loss in electron beam performance. The overcompressed beam can thus be adjusted using a traditional de-chirper resulting in a flat longitudinal phase space. The resulting beam is well suited to drive the SXL FEL in HBSASE mode significantly reducing the radiation bandwith and the saturation length. The resulting electron pulse is also a good candidate for future applications using a fresh-bunch technique.

ISBN: 978-3-95450-220-2 ISSN: 2673-5474 doi: 10.18429/JACoW-FEL2022-TUP62

ACKNOWLEDGEMENTS

The authors would like to thank LUNARC for computer services.

REFERENCES

[1] G. Stupakov, "Using the beam-echo effect for generation of short-wavelength radiation," *Phys. Rev. Lett.*, vol. 102, pp. 1–4, 2009. doi:10.1103/PhysRevLett.102.074801

[2] J. Feldhaus, E. L. Saldin, J. R. Schneider, E. A. Schneidmiller, and M. V. Yurkov, "Possible application of x-ray optical elements for reducing the spectral bandwidth of an x-ray sase fel," *Opt. Commun.*, vol. 140, no. 4-6, pp. 341–352, 1997. doi:10.1016/S0030-4018(97)00163-6

[3] B. W. J. McNeil, N. R. Thompson, and D. J. Dunning, "Transform-limited x-ray pulse generation from a high-brightness self-amplified spontaneous-emission free-electron laser," *Phys. Rev. Lett.*, vol. 110, no. 13, pp. 1–5, 2013. doi:10.1103/PhysRevLett.110.134802

[4] W. Qin *et al.*, "The fel in the sxl project at max iv," *J. Synchrotron Radiat.*, vol. 28, pp. 707–717, 2021. doi:10.1107/S1600577521003465

[5] K. Flöttmann, "Astra: A space charge tracking algorithm," Manual, DESY, Germany, 2017.

[6] M. Borland, "Elegant: A flexible sdds-compliant code for accelerator simulation," *Rep. LS-287*, 2000.

[7] S. Reiche, "Genesis 1.3: A fully 3d time-dependent fel simulation code," *Nucl. Instrum. Methods Phys. Res., Sect. A*, vol. 429, no. 1, pp. 243–248, 1999. doi:10.1016/S0168-9002(99)00114-X

[8] Z. Zhang *et al.*, "Electron beam energy chirp control with a rectangular corrugated structure at the linac coherent light source," *Phys. Rev. Spec. Top. Accel Beamss*, vol. 18, no. 1, p. 010702, 2015. doi:10.1103/PHYSREVSTAB.18.010702

[9] H. Tarawneh, P. N'gotta, L. Roslund, A. Thiel, and K. Åhnberg, "Compact APPLE X for Future SXL FEL and 3 GeV Ring at MAX IV Laboratory," in *Proc. 10th International Particle Accelerator Conference (IPAC'19)*, Melbourne, Australia, 2019, pp. 1833–1835. doi:10.18429/JACoW-IPAC2019-TUPRB072

ISBN: 978-3-95450-220-2 ISSN: 2673-5474 doi: 10.18429/JACoW-FEL2022-TUP64

EEHG SEEDING SCHEME AT SwissFEL ATHOS FEL

R. Ganter†, G. Aeppli[1], C. Arrell, H.-H. Braun, M. Calvi, A. Cavalieri, A. Dax, P. Dijkstal, E. Ferrari[2], N. Hiller, M. Huppert, P. Juranic, C. Kittel, X. Liang, S. Neppl, E. Prat, S. Reiche, A. Trisorio, C. Vicario, D. Voulot,
Paul Scherrer Institut, Villigen, Switzerland
[1]also at ETH, Zürich and EPFL, Lausanne, Switzerland
[2]also at DESY, Hamburg, Germany

Abstract

In order to improve the brightness and coherence of the soft x-ray FEL line of SwissFEL (Athos), components for an Echo Enabled Harmonic Generation (EEHG) scheme are currently being installed. The first components have been installed to allow ESASE operation test in spring 2022. This first stage consists in a 10 mJ class seed laser, a U200 modulator with individual control of each half period gap and a four electromagnet dipole chicane (R_{56} ~ 850 µm). The large magnetic chicane and the second modulator are still in preparation for an installation by the end of 2022. This paper describes the different components as well as preliminary results of the commissioning with beam.

ATHOS MODES OF OPERATION

Athos is the second Free Electron Laser (FEL) of SwissFEL which had its first lasing in December 2019 [2-4]. It covers the soft x-ray wavelength range extending from 0.65 nm to 5 nm. It is complementary to Aramis, the FEL already in operation since 2016, which operates in the hard x-ray wavelength range from 0.1 to 0.7 nm. Both FELs share the same photoinjector and linac in which two electron bunches are accelerated with only 28 ns time separation at a repetition rate of 100 Hz [5]. A series of fast kicker magnets followed by a DC septum magnet situated about 300 m downstream the photocathode are deflecting the second bunch towards Athos as the first bunch continues towards the Aramis FEL (Fig. 1). Being the second FEL of SwissFEL, the design of Athos was more ambitious than Aramis and the choice was made at the very early stage to have a very versatile FEL line with different operation modes to control as many parameters as possible of the generated FEL pulses. The ultimate goal is to offer the users a full control of the main light parameters and to push the performances beyond the state of the art. To achieve these goals a few key technologies and design choices had to be made [3]. From day one, Athos has been equipped with small chicanes (CHIC chicanes) between subsequent undulator segments (Fig. 1, top) speeding up the SASE process by about 20 % (optical klystron mode of operation [6]). The undulator design is a so-called APPLE X design [7] where the four magnet arrays can move radially and independently such that a transverse magnetic field gradient can be obtained [8]. Recently a seed laser has been commissioned and is the main ingredient required to do enhanced SASE (ESASE) [9], mode-locked lasing [10] or Echo Enabled Harmonic Generation (EEHG) [11].

With the introduction of an external seed laser, it becomes possible to manipulate the time structure of the generated FEL pulse. For example in the ESASE scheme, a train of attosecond pulses can be generated. Overlapping the seed laser and the electron bunch in a modulator (U200) introduces an energy modulation in the electron bunch, this energy modulation is converted in a density modulation when the bunch passes through an electromagnetic chicane. The obtained electron density peaks will dominate the lasing and generate a train of sub-femtoseconds pulses with a regular periodicity. These peaks are not phase locked but phase locking can be obtained with the mode locking scheme which requires to use the small chicanes situated between every undulator segment. In fact, when the sum of the chicane delay and the radiation phase slippage after one undulator segment is exactly equal to the seed laser period, then it becomes possible to reduce the bandwidth of individual pulses and to propagate the phase information over many pulses of the train. The pulses are then phase locked.

With the EEHG scheme very high harmonics of the seed laser wavelength can be amplified and the bandwidth of the radiated pulses is further reduced close to the Fourier Transform limit. Also, the shot to shot wavelength jitter is reduced which is a very important parameter for experiments. The produced pulses are then almost fully coherent, both transversally and longitudinally.

EEHG COMPONENTS

Layout

ESASE and mode-locking modes of operation are using half of the components required for EEHG. Logically the project was then split in two phases. In the first phase, a completely new laser room with controlled air temperature, humidity and cleanness has been installed in a building room next to Athos. The seed laser was installed together with an UHV vacuum line to transfer the laser pulses over about 13 m from seed laser room to a laser table near the incoupling electromagnet dipole (Fig. 1-Bottom). This dipole is in fact the last dipole of the SwissFEL dogleg allowing easy incoupling onto Athos axis. About two meters downstream from the in-coupling window, a modulator U200 has been installed where the electron bunches and the seed laser pulses should overlap.

† romain.ganter@psi.ch.

ISBN: 978-3-95450-220-2 ISSN: 2673-5474 doi: 10.18429/JACoW-FEL2022-TUP64

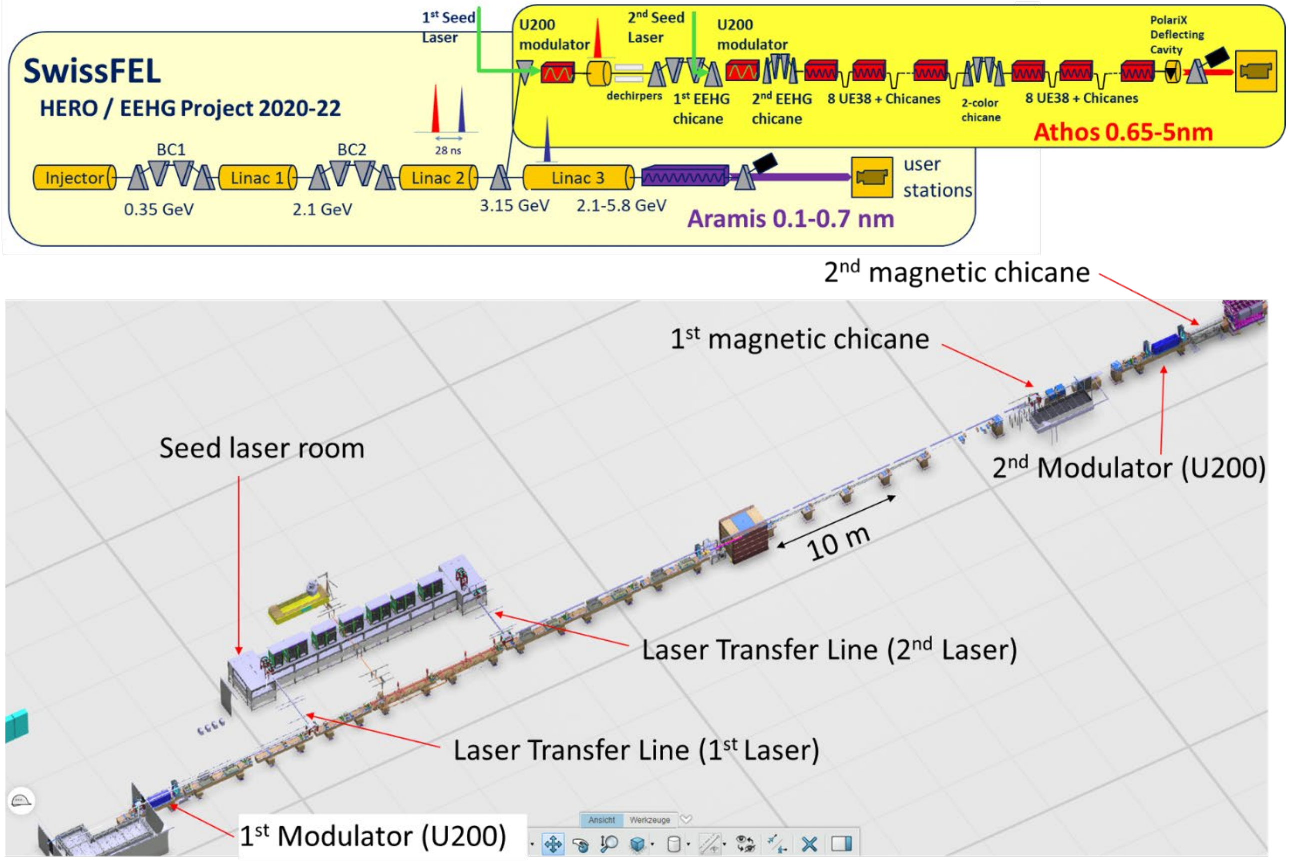

Figure 1: Schematic of SwissFEL with the Athos line and the main components required for EEHG (top). 3D illustration of the Athos areal where the EEHG are installed giving an idea of the scale (bottom).

Sixty meters further downstream in the line a chicane made out of four electromagnets (2nd magnetic chicane in Fig. 1) was recently commissioned. With these elements it became possible to perform first ESASE tests as well as mode locking tests as described below. The rest of the components (the 2nd Laser Transfer Line, the 2nd modulator and the strong magnetic chicane (1st magnetic chicane in Fig. 1)) with laser in coupling are still in preparation.

Seed Laser

Laser pulses of a few mJ at 800 nm (266 nm for EEHG) are focused to a spot size of 400 um rms in the modulator. The detailed description of the seed laser is given in a companion paper [1].

Modulator U200

The modulator design was inspired by the pre-existing permanent magnet CHIC chicanes installed between the undulator segments of Athos and which have a total length of 200 mm with 4 permanent magnets in a row [5]. The U200 consists in fact of a series of 9 such CHIC chicanes placed on a granite girder (Fig. 2). Only the magnetic polarisation configuration of the 4 permanent magnets differs to the chicanes and is here ++/-- as it is +-/-+ in an Athos undulator chicane.

With this ++/-- magnetic arrangement there is the nice feature that every half period of the U200 is independently motorized with two motors per half period for the upper and lower magnets (Fig. 2). As a consequence the undulator shimming can easily be done directly with the motors and the relation between local K and gap for every half period was recorded during a Hall probe measurement campaign. Figure 3 illustrates the beam trajectory within the undulator assuming a beam energy of 3 GeV, the end magnets are set such that the beam enters and exits on axis. This setting of the end magnets can easily be changed with the motors. From Fig. 3, we see that the trajectory horizontal oscillation (x direction) is about 400 μm at maximum for K=36 which corresponds to a gap of 11.5 mm. The vacuum chamber is made out of copper with an elliptical cross section (8 x 16 mm inside dimensions) and 0.5 mm wall thickness allowing an absolute minimum gap of 10.8 mm.

For a laser wavelength around 800 nm, the resonance will be at K=24.6 such that the orbit transverse motion amplitude will be rather 200 um and then smaller than the laser spot size (400 um rms) in the modulator.

During first modulator assembly it was found out that due to the repulsive force of two adjacent magnet blocks of same half period (++ or --), the blocks were not perfectly parallel despite the clamping system. It was then decided to glue together the two magnet blocks of the same half period. In addition, two guiding rails are holding the half period magnet keeper instead of one in the original CHIC

ISBN: 978-3-95450-220-2 ISSN: 2673-5474 doi: 10.18429/JACoW-FEL2022-TUP64

design. This is to avoid any mechanical tilt of the keepers when having different gaps between adjacent half periods.

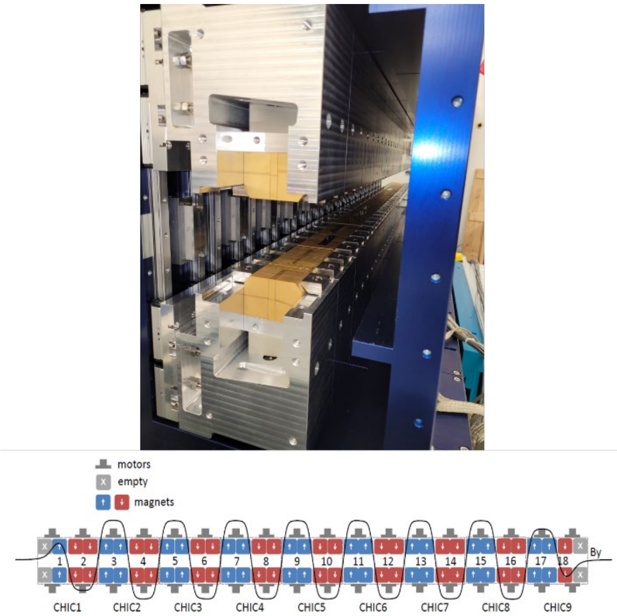

Figure 2: Picture of the U200 gap where every half period can be motorized independently (top) as depicted in the bottom schematic (bottom)

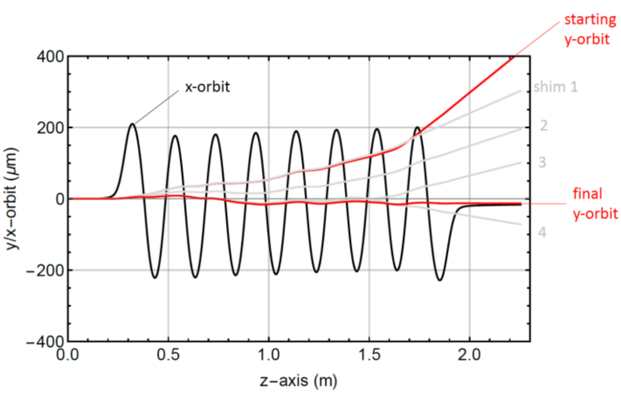

Figure 3: Beam trajectory for K = 36 (minimum gap of 11.5 mm) in horizontal plane (black) and in vertical plane (red). The grey curves show the effect of steel corrections strips.

Finally small steel correction strips have been glued directly on some magnets, within the gap, to correct the vertical orbit (dark strips visible on the magnet surface in Fig. 2 top picture). Indeed, vertical magnet pointing errors of individual blocks were not negligible and had to be compensated to obtain a flat vertical orbit (red and grey curves in Fig. 3).

Overlap Diagnostic

In order to overlap the seed laser pulses with the electron bunches, screens were installed upstream and downstream of the U200 for spatial and temporal overlap. For transversal overlap a Cromox Al_2O_3 or a YAG screen can be inserted depending on seed laser wavelength. The downstream screen feedthrough is also equipped with an OTR screen (50 um Si + 200 nm Al) which will direct the transition radiation of the electron bunches as well as the seed laser pulses on a photodiode or photomultiplier. The diode resolution (rise time of 15 ps) will only allow a coarse overlap of the laser pulses (about 500 fs FWHM) and electron bunches (50 fs rms). The fine tuning has to be done by scanning a seed laser delay stage over typically 50 ps with 0.1ps increment and looking for a decrease in SASE intensity. During the first test the SASE intensity decreased by almost 80%, clearly indicating the temporal overlap. The photomultiplier (500 ps rise time) with a larger acceptance window was finally not used since the photodiode could easily capture some signal.

Compression Chicanes

For the EEHG scheme, two compression chicanes with different R_{56} values are required. Their parameters are summarized in Table 1. The "strong" chicane serves also as in-coupling point for the second (not yet installed) seed laser. It is almost 10 m long and its main particularity is that the vacuum chamber between the 3rd and 4th dipole is movable transversally to the beam propagation by 100 mm (see Fig. 4) such that one can either couple the seed laser onto the Athos axis (Chicane ON and Position IN) or leave the electron beam orbit straight (chicane OFF and Position Out).

Table 1: EEHG Compression Chicane Parameters

EEHG Weak Chicane	**Max.**
Deflecting angle	1.55 deg (27 mrad)
Transverse beam offset at central dipoles	18.4 mm
R_{56}	849 μm
Delay in ps	1.41 ps at 3.15 GeV
Chicane Total length	2.12m
EEHG strong Chicane	
Deflecting angle (at 3.15 GeV)	2.79 deg (48 mrad)
Transverse beam offset at central dipole	193 mm
R_{56}	18 mm
Delay in ps	30 ps
Chicane Total length	9.15 m

FIRST ESASE RESULTS

The detection of time overlap was found by detecting an FEL pulse energy drop by almost 80% while scanning a delay stage. The Athos line is equipped with a transverse deflecting cavity (with variable polarisation) downstream the undulator line [12]. This diagnostic device gives the possibility to streak the bunch horizontally and then in a vertically oriented dispersion section (like the beam dump section) to observe the bunch energy distribution along its length. The electron energy spread gets larger when the seed laser is activated. So far the streaking resolution was not enough to observe a train of sub-fs pulses but the deflecting cavity was not yet conditioned to its full power.

ISBN: 978-3-95450-220-2 ISSN: 2673-5474 doi: 10.18429/JACoW-FEL2022-TUP64

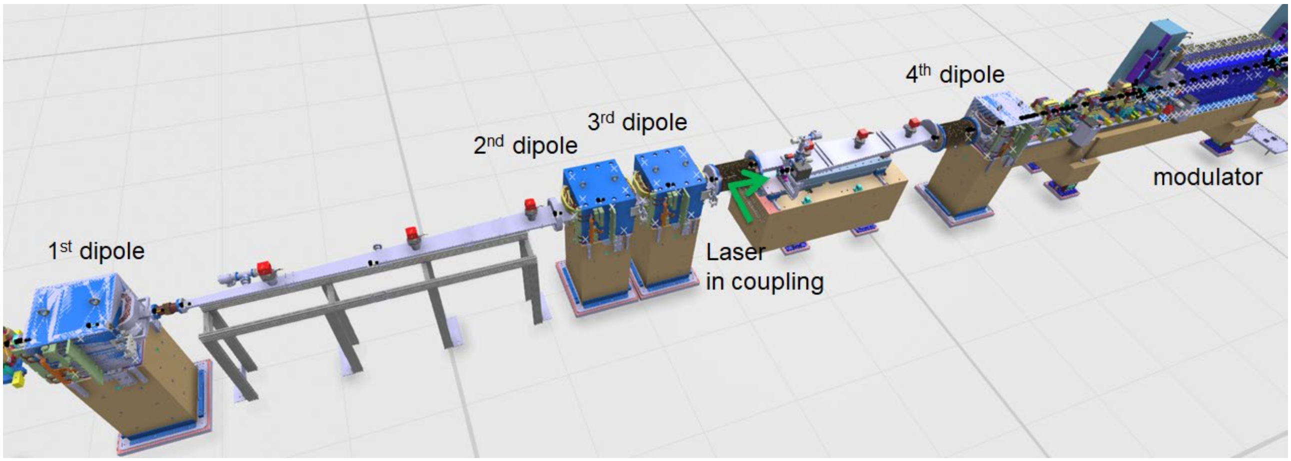

Figure 4 : 3D Layout of the « strong » EEHG chicane with a movable vacuum chamber between the 3rd and 4th dipole to allow laser in coupling.

Once the overlap between the electron bunch and the laser pulses is insured, the ESASE mode of operation is straight forward and best proven by looking at the FEL pulse spectrum. For this purpose, the single shot spectrometer of the Athos line has been used. Up to 100 spectra are acquired and a second order correlation analysis of these spectra revealed side band frequency peaks which are characteristic of a train of short pulses with regular periodicity. This periodicity is exactly equal to the seed laser period (800 nm or 2.7 fs or 1.55 eV). It is more difficult to determine whether mode locking could be reached. To achieve mode locking, the delays induced by the CHIC chicanes between the undulators together with the natural phase slippage of the radiation with respect to the electron bunch in each undulator segment should be equal to the seed laser period. When such a condition is fulfilled the individual pulses of the train should have the same phase and should be below one fs in duration. This would then be a train of sub-femtosecond long, phase locked pulses. Unfortunately, the autocorrelation plot does not exhibit much difference between the ESASE mode and the mode locked operation mode. Most probably this comes from spectral resolution limitations. Further measurements and analysis are planned on mode locking lasing even if an indirect measurement of phase conservation over individual pulses in a train might be difficult.

CONCLUSION

Components required for EEHG at SwissFEL are under preparation. Preliminary studies with the first stage involving only one modulator, a seed laser and a compression chicane showed are consistent with generation of a train of sub-femtosecond pulses. The mode locking scheme where `individual pulses of the train are also phase locked is more difficult to characterize. The installation of the rest of the EEHG components should be completed by April 2023.

ACKNOWLEDGEMENTS

The authors would like to thank all PSI technical staff that participated in designing and building this facility.

This project received funding from the European Research Council under the European Union’s Horizon 2020 research and innovation program, within the Hidden, Entangled and Resonating Order (HERO) project with Grant Agreement 810451.

REFERENCES

[1] A. Trisorio *et al.*, “Laser-Based Seeding of SwissFEL Athos”, presented at the FEL2022, Triest, Italy, Aug. 2022, paper TUP65, this conference.

[2] J. Alex *et al.*, "Athos Conceptual Design Report," Paul Scherrer Institut, PSI Villigen, 17-02, September 2017 2017.

[3] R. Abela *et al.*, "The SwissFEL soft X-ray free-electron laser beamline: AthosThis article will form part of a virtual special issue on X-ray free-electron lasers," *J. of Synchrotron Radiat.,* vol. 26, no. 4, pp. 1073-1084, 2019. doi: 10.1107/S1600577519003928.

[4] M. Yabashi, "Compact design delivers hard X-rays", *Nat. Photonics,* vol. 14, no. 12, pp. 715-716, 2020. doi: 10.1038/s41566-020-00721-7.

[5] R. Ganter *et al.*, "Status of Athos, the soft X-ray FEL line of SwissFEL", in *39th international free-electron laser conference. FEL2019*, Hamburg, H. S. In W. Decking, G. Geloni, S. Schreiber, M. Marx, & V. R. W. Schaa (Eds.), Ed., 2019, vol. 39, pp. 753-756. doi: 10.18429/JACoW-FEL2019-THP085.

[6] E. Prat, E. Ferrari, M. Calvi, R. Ganter, S. Reiche, and T. Schmidt, "Demonstration of a compact x-ray free-electron laser using the optical klystron effect", *Appl. Phys. Lett.,* vol. 119, no. 15, p. 151102, 2021. doi: 10.1063/5.0064934.

[7] T. Schmidt, & Calvi, M. , "APPLE X undulator for the SwissFEL soft X-ray beamline Athos", *Synchrotron Radiat. News,* vol. 31, no.3, pp. 35-40, 2018. doi: 10.1080/08940886.2018.1460174.

ISBN: 978-3-95450-220-2 ISSN: 2673-5474 doi: 10.18429/JACoW-FEL2022-TUP64

[8] E. Prat, M. Calvi, and S. Reiche, "Generation of ultra-large-bandwidth X-ray free-electron-laser pulses with a transverse-gradient undulator", *J. Synchrotron Radiat.,* vol. 23, pp. 874-879, 2016. doi:10.1107/S1600577516007177

[9] A. A. Zholents, "Method of an enhanced self-amplified spontaneous emission for x-ray free electron lasers", *Phys. Rev. ST Accel. Beams,* vol. 8, no. 4, p. 040701, 2005, doi: 10.1103/PhysRevSTAB.8.040701.

[10] N. Thompson and B. McNeil, "Mode Locking in a Free-Electron Laser Amplifier", *Phys. rev. lett.,* vol. 100, p. 203901, 2008. doi:10.1103/PHYSREVLETT.100.203901.

[11] D. Xiang and G. Stupakov, "Echo-enabled harmonic generation free electron laser", *Phys. Rev. Accel. Beams,* vol. 12, no. 3, p. 030702, 2009. doi:10.1103/PhysRevSTAB.12.030702.

[12] P. Craievich *et al.*, "Novel X-band transverse deflection structure with variable polarization," *Phys. Rev. Accel. Beams,* vol. 23, no. 11, p. 112001, 2020. doi:10.1103/PhysRevAccelBeams.23.112001.

ISBN: 978-3-95450-220-2 ISSN: 2673-5474 doi: 10.18429/JACoW-FEL2022-TUP65

LASER-BASED SEEDING OF SwissFEL ATHOS

A. Trisorio, S. Reiche, C. Arrell, A. L. Cavalieri[1], A. Dax, C. M. Deutschendorf, P. Dijkstal, E. Divall, R. Ganter, R. Ischebeck, N. Hiller, M. Huppert, P. Juranic, S. Neppl, E. Prat, C. Sydlo, C. Vicario, D. Voulot, G. Aeppli[2]
Paul Scherrer Institute, Villigen PSI, Switzerland
E. Ferrari, DESY, Hambug, Germany
[1]also at University of Bern, Bern, Switzerland
[2]also at ETH Zürich, Zürich, Switzerland

Abstract

We are implementing a laser-based seeding scheme at the SwissFEL soft X-ray Athos beamline. The project has two phases. In the first phase (funded via the HERO ERC project [1]) trains of attosecond pulses having a phase relation in between will be generated. In the second phase, an Echo Enabled Harmonic Generation (EEHG) scheme will be implemented and allow the generation of fully coherent X-ray Free Electron Laser (FEL) pulses down to 1 nm photon wavelength. In this proceeding, the laser facility for phase 1 as well as its features and performance are presented in details. Finally, some first commissioning results with electron beam and E-SASE FEL mode of operation obtained in June 2022 are also shown.

INTRODUCTION

FELs are the newest generation of large scale research facilities. They have been developed over the last fifteen years, especially in soft and hard X-ray spectral range. Since the lasing process of these machines is based on the self-amplified spontaneous emission (SASE) mechanism, the emitted FEL radiation suffers from large shot-to-shot intensity and photon-energy fluctuations and the limited longitudinal coherence inherent in the SASE mechanism. One possibility to overcome such limitations, is to use another (coherent) source as a trigger for the FEL process. A source of choice is an optical laser system, synchronized with the FEL accelerator and with appropriate pulse duration, wavelength and intensity. In 2012, direct seeding of the Fermi FEL facility demonstrated tunable emission throughout the 65 to 20 nm wavelength range, with unprecedented shot-to-shot wavelength stability, low-intensity fluctuations, close to transform-limited bandwidth, transverse and longitudinal coherence and full control of polarization [2]. As an upgrade of SwissFEL Athos towards fully coherent soft X-ray facility, a laser-based, two stage seeding facility following an Echo Enable Harmonic Generation (EEHG) scheme [3] is being implemented. Taking profit of the unique available CHIC chicane scheme [4], and using the mode locking approach [5], we target to produce trains of phase-locked attosecond pulses and fully coherent radiation down to 1 nm wavelength at Athos using the EEHG scheme.

SEED LASER FACILITY AT SwissFEL ATHOS

As depicted in Figure 1, the SwissFEL Athos beamline is hosting the laser-based seeding facility. A laser laboratory hosts two Ti:Sa laser amplifiers. The first phase of the project (HERO) started in January 2020 and finished in April 2022 with the first commissioning results shown here. The second phase, so-called EEHG started in May 2022 and is supposed to be ready for first commissioning in May 2023. For each phase, the seed laser facility consists of the laser itself, the transport towards the interaction point (modulator) through a vacuum transfer line and launching optics, and as well diagnostics placed before and after the modulator to ensure spatial and temporal overlap between the seed laser pulse and the electron bunch.

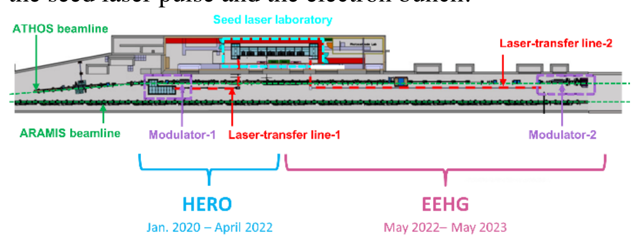

Figure 1: Overview of the project phases and the seed laser facility at the ATHOS beamline. The seed laser laboratory (cyan), the laser transfer lines (red) as well as the launching optical setups into the modulators (violet) where the seed laser pulse interacts with the electron bunch are integrated in the accelerator facility.

Seed Laser System

The seed laser system is a dual output, terawatt-class, femtosecond laser system based on Titanium Sapphire (Ti:Sa) technology with wavelength tuning capability. A detailed layout is shown in Figure 2. As one can see, it consists of two Chirped Pulse Amplifiers (Pulsar - Amplitude) seeded with a common laser oscillator (Gecco – Laser Quantum). The repetition rate of the laser oscillator is locked to the FEL Optical Master Oscillator (OMO). Using a common oscillator to seed both amplifiers reduces drastically the timing jitter between the two compressed outputs of the two amplifier chains. This is crucial to ensure the stability of the overall seeded FEL operation mode.

ISBN: 978-3-95450-220-2 ISSN: 2673-5474 doi: 10.18429/JACoW-FEL2022-TUP65

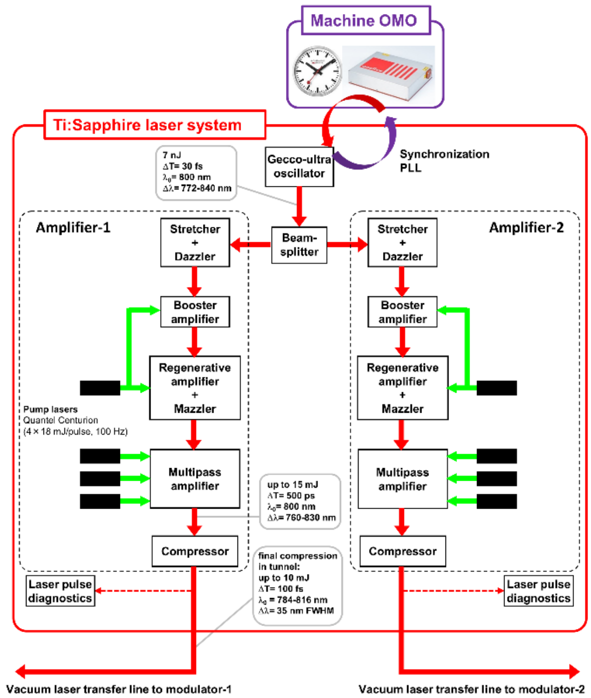

Figure 2: Detailed layout of the seed laser system.

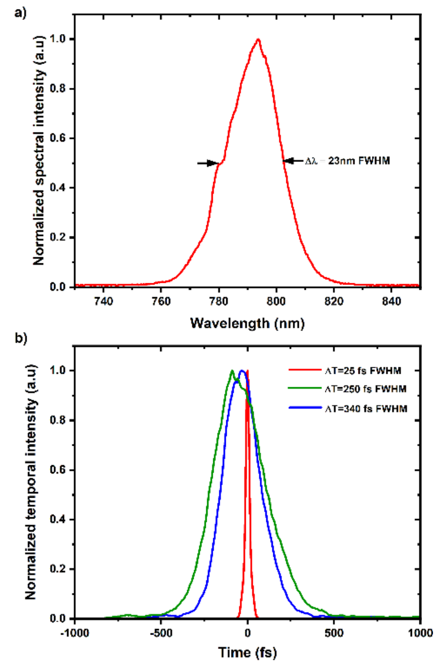

Figure 3: a) Measured spectrum and b) pulse temporal profiles of the compressed 25 fs (red), stretched 250 fs (blue) and 340 fs (green) amplified pulses at 793 nm.

The spectral tunability is achieved using low-loss Acousto-Optic Programmable Gain Control Filter (AOPGCF, Mazzler™) inside the regenerative amplifier together with the use of an Acousto-Optic Programmable Dispersive Filter (AOPDF, Dazzler™) before the amplifier. This technique has been demonstrated and implemented on a similar CPA laser chain and a detailed description of this can be found in [6]. The two systems can deliver up to 10 mJ, 25 fs FWHM (Fourier Limited) pulses at 793 nm (Fig. 3 a) and 3 b) respectively, red lines). Thanks to the Dazzler, one can stretch the pulses to longer pulse durations, for example 250 fs or 340 fs (Fig. 3b), blue and green line respectively) without changing the seed laser pulse arrival time in the modulator. Table 1 summarizes all important laser parameters. As one can see, we achieved an excellent pulse energy stability of <0.37 % rms over 30 min thanks to the multiple pump lasers and active feedback loop. The beam profile on target (the modulator center) is round and the relative pointing stability on target is <1.1% rms over 30 min. We succeeded in locking our seed laser oscillator within 22 fs rms integrated timing jitter (over 10 Hz-10 MHz bandwidth) with respect to the accelerator Optical Master Oscillator (OMO).

Moreover, after the compressor, the amplified laser pulse arrival time is measured and using a balanced optical correlator [7] and is stabilized down to 2.7 fs rms using a feedback loop, thus ensuring that the laser arrival time is kept stable during the experiment.

Table 1: Seed Laser Parameters

Parameter	Measured value
Pulse duration on target (FWHM)	25 fs – 600 fs
Pulse energy on target	≤5 mJ
Pulse energy stability (over 30 min)	0.37 % rms
Beam diameter on target	X=433 µm Y=394 µm
Relative pointing stability on target (over 30 min)	<1.1% rms
Locked oscillator integrated jitter (over 10 Hz-10 MHz bandwidth)	22 fs rms

Seed Laser Facility

In order to host the seed laser systems and launch the two beams into the SwissFEL accelerator, we started to build a dedicated laser facility. While the first phase of the project (Fig. 1-HERO) has been built and will be described below in more details, the second phase (Fig. 1-EEHG) is currently in construction. Figure 4 gives a detailed overview of the HERO seed laser facility with its different sub-systems.

As one can see, the seed laser laboratory hosts an H shaped (eleven meter long) optical table, a laser housing as well as the racks upstairs hosting the laser and controls electronics. The seed laser system was installed on that optical table. The four photos in Fig. 4 (upper left and right) give an overview of these elements after their installation.

ISBN: 978-3-95450-220-2 ISSN: 2673-5474 doi: 10.18429/JACoW-FEL2022-TUP65

From the seed laser laboratory, an ultra-high vacuum laser transfer line (22 m long) allows to transfer the laser beam from the laboratory to the L-shaped optical table that is in the tunnel. In order to preserve the laser pointing stability in the tunnel, a 4-f type imaging system is also included inside the laser transfer line. The L-shaped optical table is equipped with a laser housing to avoid airflow perturbations and for safety reasons. It hosts the launching optical setup. This consists of a variable telescope and focusing optics to achieve a laser beam diameter of 400 µm at $1/e^2$ at the center of the modulator-1 and with a Rayleigh length of 40 cm (almost half of the modulator length) [8]. We also have motorized steering optics coupled to a beam pointing stabilization system. Finally, an online and an offline joule meters are available to measure the laser pulse energy. At the table output, the laser is injected into the accelerator from the side of the accelerator's dogleg through a viewport. Both the laser and the electrons goes through the so-called U200 modulator-1 [8] where the interaction will take place. In order to characterize the seed laser spatial overlap with the electron bunch at the modulator-1 entrance and exit, two diagnostic modules [9] have been installed. Each module host a camera and objective imaging a movable screen. We have two type of screens installed: a high resolution YAG screen (for characterizing the transverse beam profile of the electron bunch) and a Cromox (Al_2O_3:Cr) screen used to visualize both the laser and the electron bunch beams and to overlap them spatially. At the modulator-1 exit, a third diagnostic module including an OTR screen and a fast photodiode is used to achieve the fine temporal overlap of the laser pulse and the electron pulse within ±500 ps.

These diagnostics modules turned out to be very useful and allowed to achieve the necessary overlaps quickly.

FIRST COMMISSIONING WITH BEAM

Aside from purely optical characterization of the seed laser (see section *SEED LASER SYSTEM*), an important parameter to quantify is the time jitter between the seed laser pulse and the electron bunch at the modulator-1. Due to the lack of dedicated diagnostic, we intended to evaluate this time jitter using an indirect measurement shown in Figure 5.

Scanning the delay between the seed laser and the electron bunch (using a piezo driven delay stage with absolute encoder and 1 nm resolution) and recording the 1 keV-FEL photon pulse energy, we obtain the 'cross-correlation' curve shown in Fig. 5 a. As one can see, when the seed laser and the electron bunch fully overlap in time, the FEL effect can be almost supressed (see red circle). This is due to the fact that seeding the electron beam with a high laser power combined with the large R56 set on the chicane, the electron bunch energy spread is blown-up. This leads to a

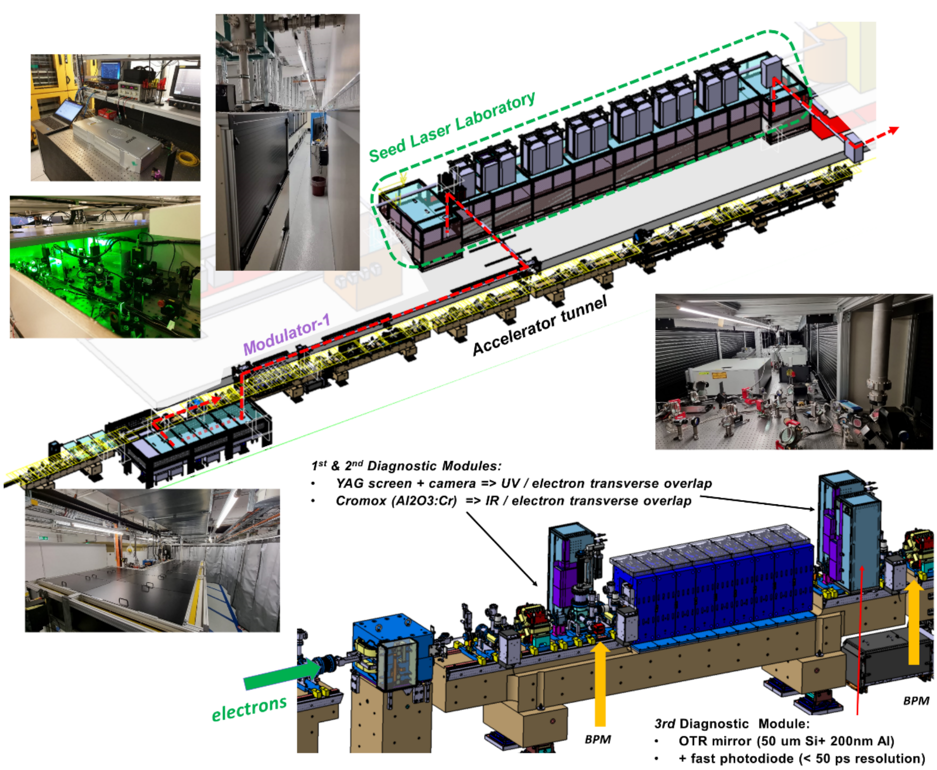

Figure 4: HERO seed laser facility overview. A seed laser laboratory host the laser system, the laser vacuum transfer line allows the transport of the beam from the laboratory towards the L-shaped optical table in the SwissFEL accelerator tunnel. The optical table host the launching optics as well as the necessary diagnostics.

ISBN: 978-3-95450-220-2 ISSN: 2673-5474 doi: 10.18429/JACoW-FEL2022-TUP65

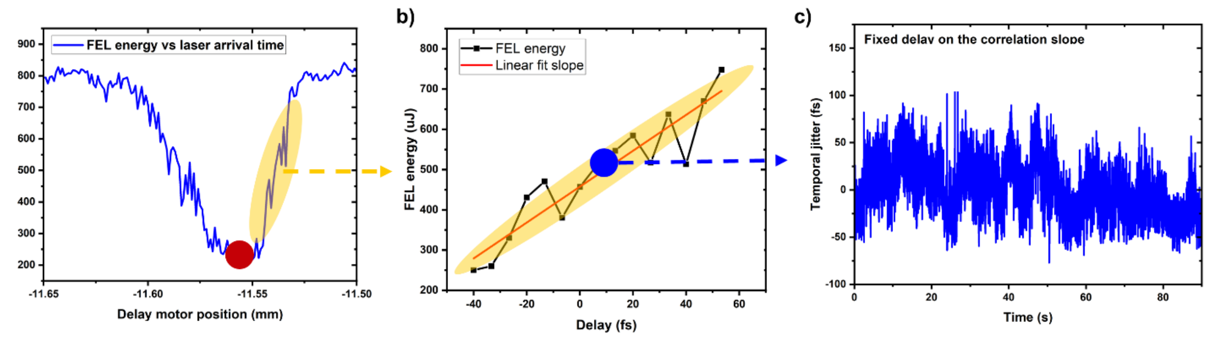

Figure 5: Measurement of the time jitter between the seed laser and electron bunch at the modulator-1. a) Cross-correlation signal obtained by scanning the temporal delay between the seed laser and the electron bunch and monitoring the FEL photon pulse energy. At full overlap (red circle), the FEL emission is strongly supressed. On the slope (orange area), the variation of the FEL photon pulse energy has almost a linear dependence on the delay b). Fitting this dependence allows for a calibration from which, the laser / electron time jitter can be evaluated c) fixing the laser delay at a defined position.

dramatic decrease of the FEL amplification process (similar effect as a laser heater setup). On the slope (Fig. 5 b) - orange area), the variation of the FEL photon pulse energy has almost a linear dependence on the delay. Fitting this dependence allows for a calibration from which, the laser versus electron time jitter can be evaluated fixing the delay at a defined position. The result is shown in Figure 5 c) where the time jitter was measured to be 28 fs rms over 90 s (9 000 shots of the FEL). Measuring the time drift was also attempted, however, we encountered issues with temporal jumps of the laser arrival time and thus could not obtain an accurate measurement. This issue is under investigation and trouble shooting.

To finish with, we wanted to obtain evidence of the manipulation of the phase space of the 3.2 GeV electron bunch with the seed laser. Figure 6 shows the effect of the seed laser on the energy spread along the bunch when the radiator undulators of Athos are disabled. The beam was streaked using a passive streaker cavity [10]. As one can see, the electron bunch energy spread is blown-up when the seed laser is in use. The visible substructure in the longitudinal beam phase space is a combination of the laser interaction and unrelated microbunching effects.

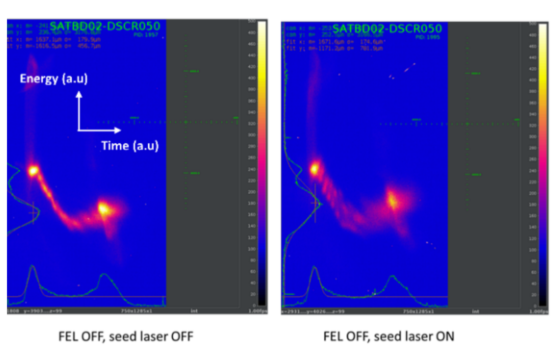

Figure 6: Unseeded (left) and seeded (right) electron bunch energy spread recorded on screen and after passive streaker cavity [10].

With the given configuration we explored the methods of E-SASE [11] and Slicing [12] to produce a periodic pulse trains of attosecond pulses, locked to the phase of the seed laser. In practice, the operation of E-SASE with a mean current of about 2 kA caused too much space charge distortion by the current spikes so that slicing produced the cleaner signal. The indication of the pulse train are side bands in the FEL spectrum. They are more pronounced in the spectral correlation function g_2 [13], as shown in Figure 7 for the nominal slicing configuration. Up to four side bands are visible, limited by the weak signal of the individual spectra beyond 5 eV away from the central photon energy. The sidebands have a spacing of 1.55 eV, corresponding to the 793 nm laser wavelength.

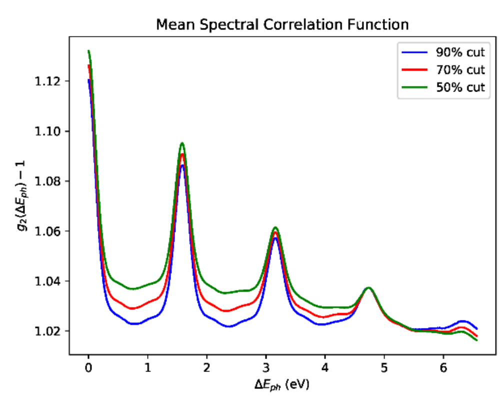

Figure 7: Spectral correlation function of the seeded, FEL operation mode. The presence of pronounced side bands indicates that the E-SASE mode is effectively lasing producing a train of FEL attosecond pulses.

CONCLUSION

In the frame of the HERO project, we designed, built and commissioned a dedicated laser facility, transport, launching optical setup as well as diagnostics, in order to seed the SwissFEL Athos FEL line. The laser system optical feature and stability have been characterized. Moreover, a successful commissioning of the facility was achieved in June 2022, showing a clear evidence of laser-based, electron bunch manipulation as well as slicing FEL operation mode with the photon beam.

ISBN: 978-3-95450-220-2 ISSN: 2673-5474 doi: 10.18429/JACoW-FEL2022-TUP65

REFERENCES

[1] G. Aeppli *et al.,* "Hidden, Entangled and Resonating Order (HERO)", *Nat. Rev. Mater.,* vol. 5, pp. 477-479, 2020. doi:10.1038/s41578-020-0207-z

[2] E. Allaria *et al.,* "Highly coherent and stable pulses from the FERMI seeded free-electron laser in the extreme ultraviolet", *Nat Photonics*, vol. 6, pp. 699–704, 2012. doi:10.1038/nphoton.2012.233

[3] G. Stupakov, "Using the Beam-Echo Effect for Generation of Short-Wavelength Radiation", *Phys. Rev. Lett*., vol. 102, p. 074801, 2009. doi:10.1103/PhysRevLett.102.074801

[4] E. Prat *et al*., "Undulator beamline optimization with integrated chicanes for X-ray free-electron-laser facilities", *J. Synch. Rad.* vol. 23, pp. 861-868, 2016. doi:10.1107/S1600577516007165

[5] E. Kur *et al.,* "A wide bandwidth free-electron laser with mode locking using current modulation", *New J. Phys.,* vol. 13, p. 063012, 2011. doi:10.1088/1367-2630/13/6/063012

[6] A. Trisorio *et al.*, "Ultrabroadband TW-class Ti:sapphire laser system with adjustable central wavelength, bandwidth and multi-color operation", *Optics Express,* vol. 19, pp. 20128, 2011. doi:10.1364/OE.19.020128

[7] A. Dax *et al.*, "Arrival time fluctuation of the SwissFEL photocathode laser: characterization by a single color balanced cross correlator", *Optics Express,* vol. 30, pp. 15495-15511, 2022. doi:10.1364/OE.444679

[8] M. Calvi *et al*., "The HERO Modulator for Echo Enable Harmonic Generation", submitted to *J. Synch. Rad.,* 2022.

[9] R. Ischebeck *et al.,* "Transverse profile imager for ultrabright electron beams", *Phys. Rev. ST Accel. Beams*, vol 18, p. 082802, 2015. doi:10.1103/PhysRevSTAB.18.082802

[10] P. Dijkstal, "Self-synchronized and cost-effective time-resolved measurements at x-ray free-electron lasers with femtosecond resolution", *Phys. Rev. Research*, vol. 4, p. 013017, 2022. doi:10.1103/PhysRevResearch.4.013017

[11] A.A. Zholent "Method of an enhanced self-amplified spontaneous emission for x-ray free electron lasers", *Phys. Rev. ST Accel. Beams*, vol. 8, p. 040701, 2005. doi:10.1103/PhysRevSTAB.8.040701

[12] E.L. Saldin *et al.,* "Self-amplified spontaneous emission FEL with energy-chirped electron beam and its application for generation of attosecond x-ray pulses", *Phys. Rev. ST Accel. Beams*, vol. 9, p. 050702, 2006. doi:10.1103/PhysRevSTAB.9.050702

[13] J.W. Goodman, "Statistical Optics", *Wiley-VCH*, Hoboken, NJ, USA, 2015.

ISBN: 978-3-95450-220-2 ISSN: 2673-5474 doi: 10.18429/JACoW-FEL2022-TUP69

HIGH REPETITION RATE SEEDED FREE-ELECTRON LASER WITH A HARMONIC OPTICAL KLYSTRON IN HIGH-GAIN HARMONIC GENERATION

H. Sun, Shanghai Institute of Applied Physics, Shanghai, China
University of Chinese Academy of Sciences, Beijing, China
G. Paraskaki, DESY, Hamburg, Germany
B. Faatz, C. Feng*, B. Liu†, Shanghai Advanced Research Institute, Shanghai, China

Abstract

External seeding techniques like high-gain harmonic generation (HGHG) and echo-enabled harmonic generation (EEHG) have been proven to be able to generate fully coherent radiation in the EUV and X-ray range. However, towards seeding at a high repetition rate, the repetition rate of current laser systems with sufficient power for seeding is limited to the kilohertz range. One attractive solution to this limitation is to reduce the required seed laser power. In this contribution, we will present a harmonic optical klystron scheme with high gain harmonic generation. With the harmonic optical klystron scheme as the seeding technique, the required seed laser power is decreased, and higher harmonics than in a standard single-stage HGHG can be achieved.

INTRODUCTION

External seeding techniques have been proposed and proven to be able to generate widely tunable, fully temporally and spatially coherent radiation [1, 2]. These seeding schemes are triggered by stable, coherent external lasers, and thus their output radiation can be stable and coherent. However, the repetition rate of current laser systems with sufficient power to modulate the electron beam is limited to the kilohertz range.

To relax the power requirements of external seeding lasers in high repetition rate FELs, some methods, such as self-amplification of coherent energy modulation (Optical Klystron) [3, 4] and direct amplification enabled harmonic generation (DEHG) [5] were proposed. For seeding at a high repetition rate, optical cavity-based FEL schemes [6–10] have been introduced to recirculate the radiation in the modulator to seed the high repetition rate electron bunches. This scheme overcomes the limitation of requiring high repetition rate seed laser systems.

In this contribution, a harmonic optical klystron HGHG (HOK HGHG) configuration is studied for seeding at a high repetition rate. The harmonic optical klystron concept was studied in Ref. [11] to enhance self-amplified spontaneous emission or introduced as a harmonic cascade method in Ref. [12]. Similar to Ref. [12], instead of using a single modulator, the modulator is divided into two parts separated by a chicane as shown in Fig. 1. Here, we present the HOK HGHG simulation results for a single pass. In Ref. [9], more information about the resonator seeding based on HOK HGHG is presented.

SIMULATIONS

Layouts for HOK HGHG configuration is shown in Fig. 1. In this setup, the first modulator is resonant at the fundamental wavelength of the seed laser and the second modulator is tuned to a harmonic of the first modulator. In the first modulator, a small energy modulation of the electron beam is induced and it is transformed into a density modulation after traversing through the first chicane with a longitudinal dispersion $R_{56,1}$. Then the electron beam is modulated at the harmonic of the seed laser wavelength in the second modulator. A density modulation will occur at a harmonic of the seed laser wavelength when the electron beam traverses through the second chicane with a longitudinal dispersion $R_{56,2}$. Finally, the FEL amplification of a harmonic of the seed laser wavelength is taking place in the radiator. In the next simulations, we use the typical parameters of a soft X-ray FEL. The electron beam parameters are summarized in Table 1. The simulations are performed with Genesis 1.3 [13] .

Figure 1: The layouts of the HOK HGHG scheme (top) and the standard single-stage HGHG scheme (bottom).

In our simulations, to generate fully coherent x-rays in the water window range, we use a 50 nm seed laser from the high harmonic generation (HHG) source. In fact, in the current laser system, the repetition rate of an HHG source cannot reach 1 MHz. Our concern is to reduce the required seed laser power as much as possible. It should be noted that the advantages of this scheme in terms of reducing required seed laser power still apply to longer wavelengths. To generate coherent radiation in the water window range, here we tuned the second modulator to the 4th harmonic (m=4) of the seed laser and the radiator is tuned to the 5th (n=5) harmonic of

* fengchao@zjlab.org.cn
† liubo@zjlab.org.cn

ISBN: 978-3-95450-220-2 ISSN: 2673-5474 doi: 10.18429/JACoW-FEL2022-TUP69

this wavelength, which is the 20th harmonic of the seed laser wavelength as shown in Fig. 1. In our simulation, we used a long modulator to decrease the power requirement of seed laser. The length of the first modulator is set to 6 m and the input seed laser power at 50 nm is set to 1.7 MW. In the first modulator of the HOK HGHG scheme, an energy modulation $A_1 = 4.8$ is induced and some additional energy spread is introduced accordingly. The energy spread after the first modulator of the HOK HGHG scheme is 552 keV in the simulation. Then the electron beam passes through the second modulator with a length of 3 m, and the energy spread σ_{E_2} will increase to 917 keV due to the coherent emission generated in the second modulator. For the simulation parameters in Table 1, the FEL pierce parameter ρ_r in the radiator which is resonant at 2.5 nm is 0.001. In the HOK HGHG scheme, $\sigma_{E_2}/E = 3.6 \times 10^{-4} \ll \rho_r$, which is beneficial to the FEL gain.

Table 1: Simulation Parameters

Electron beam	
Energy	2.53 GeV
Uncorrelated energy spread	0.164 MeV
Peak current	800 A
Emittance	0.5 mm·mrad
Charge	100 pC
Bunch length (FWHM)	110 fs
Seed laser	
Wavelength	50 nm
Peak power	1.7 MW
Modulator	
Period	50 mm
K_{rms}	9.80 / 4.75
Segment length	3 m
Number of segments	2+1
Radiator	
Period	20 mm
K_{rms}	3.21
Segment length	4 m
Number of segments	4

The electron beam with a bunching of 6.20% at the 20th harmonic of the seed laser is sent into a radiator for FEL amplification. The gain curve along the radiator is shown in Fig. 2a. It can be seen that the peak power of the radiation grows exponentially and reaches saturation at 15 m with a GW level. The output spectra at the point is shown by the yellow curve in Fig. 2b, where the calculated FWHM bandwidth is 1.78×10^{-4}, which signifies the excellent temporal coherence of the radiation. In addition, the HOK HGHG scheme is compared with the standard single-stage HGHG scheme. For the standard single-stage HGHG scheme, in order to get bunching at 20th harmonic, the required energy modulation amplitude is larger than 10 at least. In the meantime, in order to achieve FEL exponential amplification, the energy spread of the electron beam at the entrance of the radiator has to fulfill the requirment of $\sigma_{E_r}/E \ll \rho_r$, where ρ_r is the FEL pierce parameter. For the simulation parameters in Table 1, the FEL pierce parameter ρ_r in the radiator which is resonant at 2.5 nm is 0.001, therefore the requirement $\sigma_{E_r}/E \ll \rho_r$ leads $\sigma_{E_r} = \sqrt{\sigma_E^2 + \Delta E^2/2} \ll 2.53$ MeV, which is equivalent to $A = \Delta E/\sigma_E \ll 22$. Therefore, we have determined the value range limit of energy modulation amplitude.

We optimized three cases in standard single-stage HGHG mode with energy modulation of 12, 15 and 18 respectively to generate effective bunching at the 20th harmonic of the seed laser. The gain curve along the radiator for the standard single-stage HGHG with energy modulations of 12, 15 and 18 are shown in Fig. 2a. It can be seen that the case with energy modulation of 12 has a small bunching of 3% and a long saturation length of 30 m. For the cases with energy modulation of 15 and 18, even though they have higher initial bunching of 5% and 8% respectively, the FEL performances will be poorer due to the induced larger energy modulation. Taking the standard single-stage HGHG with energy modulation of 15 as an example, the output spectra profiles of FEL radiation at different locations along the radiator are shown in Fig. 2c. The radiation pulse shows highly temporal coherence in the early part of the radiation section, as shown in this figure, but deteriorates in longitudinal coherence from the fifteen meter mark to the saturation point. Due to the long saturation length required, the SASE background becomes non-negligible as it becomes visible in Fig. 2c. In conclusion, the HOK HGHG scheme is more advantageous in generating comparatively high harmonic radiation, such as a shorter saturation length and a higher signal-to-noise ratio of the radiation.

For a linear accelerator, the beam energy profile usually has an energy curvature due to the radio frequency curvature and wakefield effects. The energy chirped electron beam may be helpful in overcoming the sensitivity of the output power to the electron beam energy jitter. However, these energy chirps would possibly degrade the FEL performances like the wavelength shifting and spectral bandwidth broadening. The beam energy offset $\delta = \frac{E-E_0}{E_0}$ at the Linac end can be described mathematically by a Taylor expansion:

$$\delta = \delta_0 + hs_i + h's_i^2 + O\left(s^3\right), \tag{1}$$

where δ_0 is the uncorrelated energy offset, s_i is the particle longitudial coordinate relative to the bunch center, $h = \frac{dE}{ds}\frac{1}{E}$ is a linear energy chirp with dimensions of m^{-1}, and $h' = \frac{d^2E}{ds^2}\frac{1}{E}$ is the quadratic chirp with dimensions of m^{-2}. The simulations were performed using the electron beam parameters summarized in Table 1. The effect of a linear beam energy chirp on the final FEL central wavelength shifting for the HOK HGHG scheme is shown in Fig. 3a. Similar to a standard single-stage HGHG scheme, the FEL

ISBN: 978-3-95450-220-2 ISSN: 2673-5474 doi: 10.18429/JACoW-FEL2022-TUP69

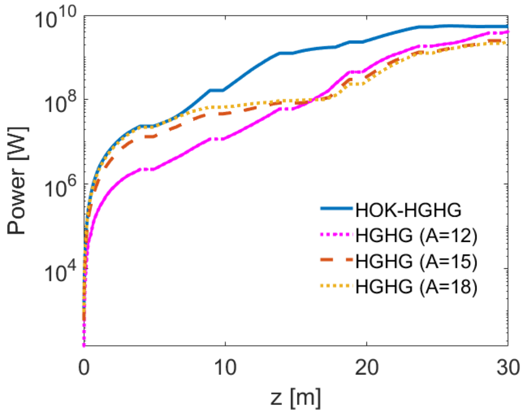

(a)

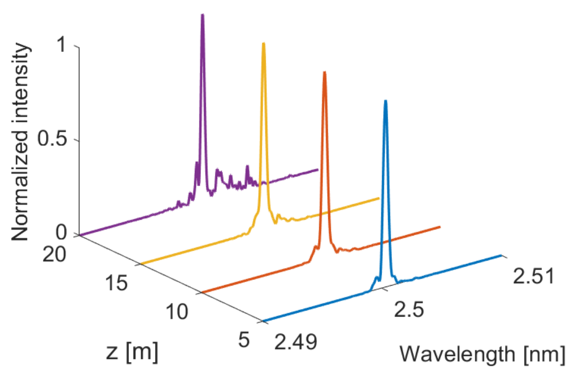

(b)

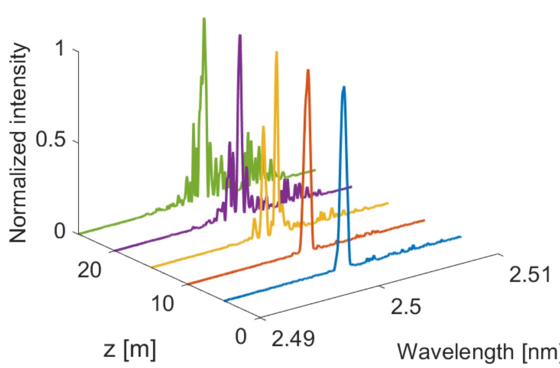

(c)

Figure 2: (a) The gain curves for an FEL output wavelength of 2.5 nm along the radiator for the four cases (HOK HGHG and the standard single-stage HGHG (A=12,15,18).). The output spectra profiles at different locations along the radiator for (b) HOK HGHG scheme and (c) HGHG (A=15).

central wavelength shifts in the HOK HGHG scheme when there is a linear beam energy chirp in the electron beam. In a realistic case, there are still nonlinear energy chirps in the electron beam. In the simulation, we used an electron beam with a quadratic energy chirp ($h' = 500\,000\,\mathrm{m}^{-2}$), as an example to study the nonlinear energy chirp effects on the

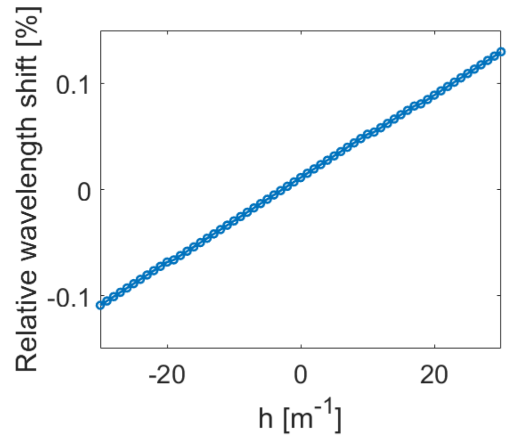

(a)

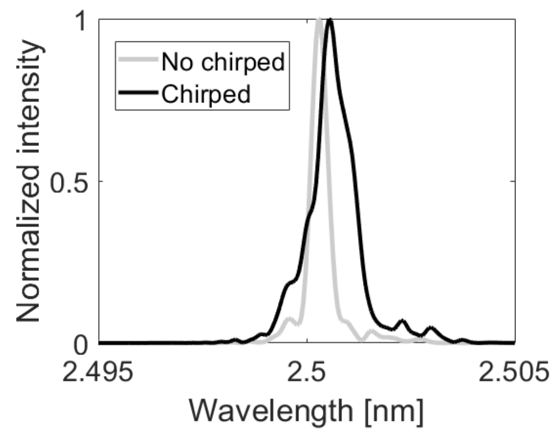

(b)

Figure 3: (a) Impact of a linear energy chirp on the central wavelength relative shift of the final FEL radiation for the HOK HGHG scheme. (b) The output spectra profiles for HOK HGHG scheme at the end of the radiator (Black line represents the case with a quadratic energy chirp and grey line represents the case with no energy chirp.).

HOK HGHG scheme. The effect of nonlinear energy chirp on the FEL bandwidth increase of the HOK HGHG scheme is shown in Fig. 3b. It is found that the spectra bandwidth with a quadratic energy chirp ($h' = 500\,000\,\mathrm{m}^{-2}$) increases by a factor two compared with the case without energy chirp.

SUMMARY AND OUTLOOK

In this contribution, we presented the simulation results of the HOK HGHG scheme for a single pass. With the harmonic optical klystron scheme as the seeding technique, the required seed laser power is decreased, and higher harmonics than in a standard single-stage HGHG can be achieved. In addition, we studied the energy chirp effects on this scheme in this paper. Start-to-end simulations with a more realistic electron beam will be conducted in the future.

ISBN: 978-3-95450-220-2 ISSN: 2673-5474 doi: 10.18429/JACoW-FEL2022-TUP69

ACKNOWLEDGMENT

This work was supported by the National Natural Science Foundation of China (12122514 and 11975300) and Shanghai Science and Technology Committee Rising-Star Program (20QA1410100). G. Paraskaki was supported by the Impuls- und Vernetzungsfond der Helmholtz-Gemeinschaft e.V. within the CAS-Helmholtz International Laboratory on Free-Electron Laser Science and Technology (CHILFEL), Grant No. InterLabs-0002. B. Faatz was Funded by Chinese Academy of Sciences President's International Fellowship Initiative (PIFI), Grant No. 2020FSM0003.

REFERENCES

[1] L. H. Yu and J. Wu, "Theory of high gain harmonic generation: an analytical estimate", *Nucl. Instrum. Methods Phys. Res., Sect. A*, vol. 483, pp. 493-498, 2002. doi:10.1016/S0168-9002(02)00368-6

[2] G. Stupakov, "Using the Beam-Echo Effect for Generation of Short-Wavelength Radiation", *Phys. Rev. Lett.*, vol. 102, p. 074801, Feb. 2009. doi:10.1103/PhysRevLett.102.074801

[3] J. Yan *et al.*, "Self-amplification of Coherent Energy Modulation in Seeded Free-Electron Lasers", *Phys. Rev. Lett.*, vol. 126, p. 084801, 2021. doi:10.1103/PhysRevLett.126.084801

[4] G. Paraskaki, E. Allaria, E. Schneidmiller, and W. Hillert, "High repetition rate seeded free electron laser with an optical klystron in high-gain harmonic generation", *Phys. Rev. Accel. Beams*, vol. 24, p. 120701, Dec. 2021. doi:10.1103/PhysRevAccelBeams.24.120701

[5] X. Wang, C. Feng, B. Faatz, W. Zhang, and Z. Zhao, "High-repetition-rate seeded free-electron laser with direct-amplification of an external coherent laser", *New J. Phys.*, vol. 24, p. 033013, 2022. doi:10.1088/1367-2630/ac5492

[6] S. Ackermann, B. Faatz, V. Grattoni, M.M. Kazemi, T. Lang, C. Lechner, G. Paraskaki, J. Zemella, G. Geloni, S. Serkez, *et al.*, "Novel method for the generation of stable radiation from free-electron lasers at high repetition rates", *Phys. Rev. Accel. Beams*, vol. 23, p. 071302, 2020. doi:10.1103/PhysRevAccelBeams.23.071302

[7] G. Paraskaki, V. Grattoni, T. Lang, J. Zemella, B. Faatz, and W. Hillert, "Optimization and stability of a high-gain harmonic generation seeded oscillator amplifier", *Phys. Rev. Accel. Beams*, vol. 24, p. 034801, 2021. doi:10.1103/PhysRevAccelBeams.24.034801

[8] G. Paraskaki, S. Ackermann, B. Faatz, G. Geloni, T. Lang, F. Pannek, L. Schaper, and J. Zemella, "Advanced Scheme to Generate MHz, Fully Coherent FEL Pulses at nm Wavelength", *Appl. Sci.*, vol. 11, p. 6058, 2021. doi:10.3390/app11136058

[9] H. Sun, C. Feng, B. Faatz, B. Liu, and G. Paraskaki, "Seeding with a harmonic optical klystron resonator configuration in a high repetition rate free electron laser", *Phys. Rev. Accel. Beams*, vol. 25, p. 060701, 2022. doi:10.1103/PhysRevAccelBeams.25.060701

[10] G. Paraskaki, S. Ackermann, G. Geloni, B. Faatz, C. Feng, B. Liu, and H. Sun, "Optical-cavity based seeded FEL schemes toward higher repetition rate and shorter wavelengths", presented at the 40th Int. Free Electron Laser Conf.(FEL'22), Trieste, Italy, Aug. 2022, paper MOP20, this conference.

[11] G. Penco *et al.*, "Optical Klystron Enhancement to Self Amplified Spontaneous Emission at FERMI", *Photonics*, vol. 4, p. 15, 2017. doi:10.3390/photonics4010015

[12] D. J. Dunning, N. R. Thompson, and B. W. J. McNeil, "Design study of an HHG-seeded harmonic cascade free-electron laser", *J. Mod. Opt.*, vol. 58, p. 1362, 2011. doi:10.1080/09500340.2011.586475

[13] S. Reiche, "GENESIS 1.3: a fully 3D Time-Dependent FEL Simulation Code", *Nucl. Instrum. Methods Phys. Res. Sect. A*, vol. 429, p. 243, 1999. doi:10.1016/S0168-9002(99)00114-X

ISBN: 978-3-95450-220-2 ISSN: 2673-5474 doi: 10.18429/JACoW-FEL2022-TUP70

PREPARATORY EXPERIMENTAL INVESTIGATIONS IN VIEW OF EEHG AT THE DELTA STORAGE RING *

B. Büsing †, A. Held, S. Khan, C. Mai, A. Radha Krishnan, Z. Usfoor, V. Vijayan
Zentrum für Synchrotronstrahlung (DELTA), TU Dortmund, 44227 Dortmund, Germany

Abstract

At DELTA, a 1.5-GeV electron storage ring operated by the TU Dortmund University, the seeding scheme CHG (coherent harmonic generation), the counterpart to HGHG (high-gain harmonic generation) without FEL gain, is used to provide ultrashort pulses in the femtosecond regime at harmonics of the seedlaser wavelength. To provide higher harmonics and thus shorter wavelengths, it is planned to upgrade the short-pulse facility to the EEHG (echo-enabled harmonic generation) scheme, which has yet not been implement at any storage ring. To install the needed three undulators and two chicanes, about a quarter of the storage ring needs to be modified. The paper presents the layout of the envisaged EEHG facility and the demo project SPEED (Short-Pulse Emission via Echo at DELTA) where all components are realized in a single undulator.

ECHO-ENABLED HARMONIC GENERATION

The seeding scheme echo-enabled harmonic generation (EEHG) [1, 2] makes use of a two-fold laser-induced modulation of the electron energy to generate a complex density modulation. As shown in Fig. 1, the interaction of an ultrashort laser pulse and an electron bunch in an undulator (modulator) tuned to the laser wavelength results in a sinusoidal energy modulation. A strong first chicane after the first modulation leads to thin stripes in the longitudinal phase space due to the energy-dependent path length. With an additional modulator and a second weaker chicane in front of a third undulator (radiator), a periodic density modulation is generated, so-called microbunches. In the radiator, which is tuned to a harmonic of the laser wavelength, these microbunches lead to coherent emission of radiation.

EEHG was proposed and successfully demonstrated as seeding scheme for free-electron lasers (FELs) [3–5] to trigger the microbunching process. Adopted in storage rings, this seeding scheme is a promising candidate to generate ultrashort synchrotron radiation pulses in the extreme ultraviolet regime.

SEEDING AT DELTA

Since 2011, the short-pulse facility at DELTA, a 1.5-GeV electron storage ring operated by the TU Dortmund University, based on the seeding scheme coherent harmonic generation (CHG) [6, 7] provides ultrashort synchrotron radiation pulses. This seeding scheme is based on a single laser-electron interaction and is limited to low harmonics of the laser wavelength. The seeding experiments take place in a single undulator acting as one modulator, one chicane and the radiator. Seeding is performed by 800-nm pulses of a Ti:sapphire laser system or their second harmonic. In addition, radiation in the terahertz regime is coherently emitted in a subsequent dipole magnet. The present setup is depicted in Fig. 2 (top).

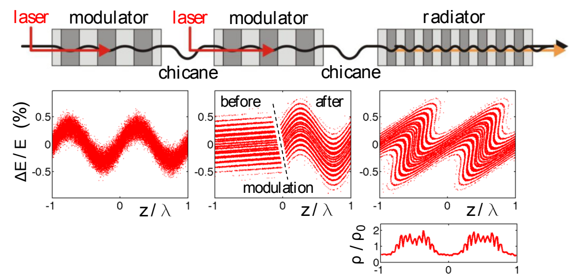

Figure 1: Magnetic setup for EEHG, corresponding longitudinal phase space distributions, and the final longitudinal electron density.

Storage Ring Optics for EEHG

To realize an EEHG-based short-pulse facility at DELTA, it is necessary to remodel a quarter of the storage ring so that all three undulators and the two chicanes can be placed in a single straight section, see Fig. 2 (bottom). The beam optics is optimized using the simulation code *elegant* [8] to fulfill all boundary conditions such as an achromatic straight section to not influence the longitudinal phase space while conserving the optics for the rest of the ring and not changing the source point of the other beamlines [9]. The resulting beta functions are shown in Fig. 3 and the main parameters of the present CHG and the future EEHG optics are listed in Tab. 1.

Table 1: Main Parameters of the DELTA Storage Ring

Parameter	**Present**	**EEHG**
electron beam energy	1.5 GeV	1.5 GeV
circumference	115.20 m	115.21 m
hor. tune	9.19	8.59
vert. tune	3.28	3.55
mom. comp. factor	$4.9 \cdot 10^{-3}$	$4.7 \cdot 10^{-3}$
rel. energy spread	$7 \cdot 10^{-4}$	$7 \cdot 10^{-4}$
hor. emittance	16 nm rad	22 nm rad
max. hor. beta function	45 m	22 m
max. vert. beta function	51 m	25 m

* Work supported by the BMBF under contract 05K16PEB and 05K19PEB, Forschungszentrum Jülich and by the Federal State NRW
† benedikt.buesing@tu-dortmund.de

ISBN: 978-3-95450-220-2 ISSN: 2673-5474 doi: 10.18429/JACoW-FEL2022-TUP70

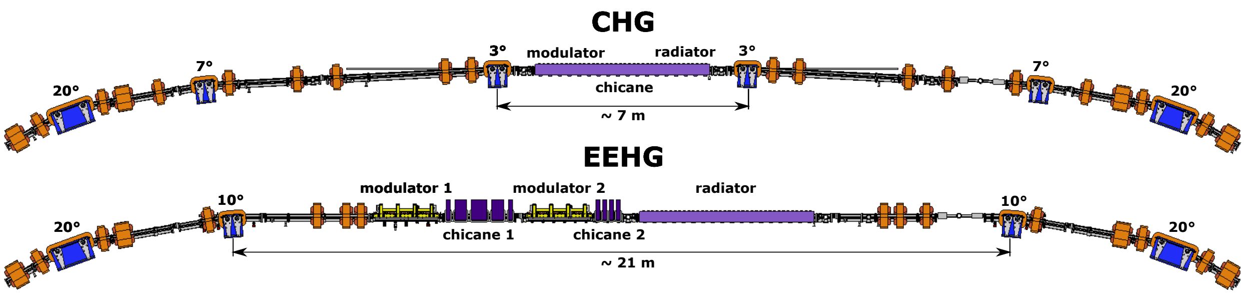

Figure 2: Present (top) northern part of the storage ring with an undulator separated into three parts for CHG and the future modifications to enable a long straight section for EEHG (bottom) with dipoles in blue and quadrupoles in orange.

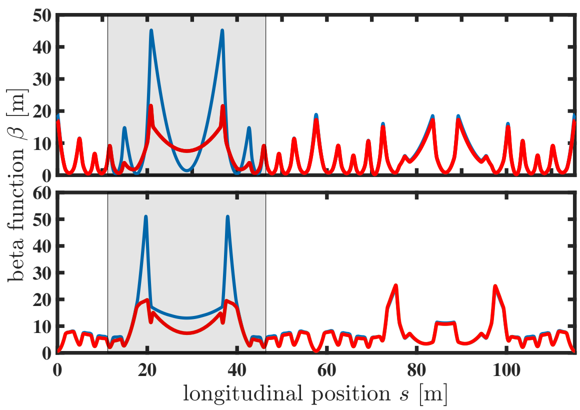

Figure 3: Horizontal (top) and vertical (bottom) beta function versus longitudinal position s of the present (blue) and the future EEHG optics (red). Inside the modified area (gray), the maximum beta function is reduced by more than a factor of two. Outside of the EEHG region, the beta function does not change significantly.

MAGNETS

In the future magnetic setup, the present quadrupole magnets will be reused while the coils of the 7° dipoles will be powered with a higher current as 10° and one pair of dipoles (3°) will be removed. This allows to generate a straight section of about 21 m with nearly the same ring circumference as before. The future setup is shown in Fig. 2 (bottom).

Undulators

Two new electromagnetic undulators U200 with a period length of 200 mm and their girders are in house and will be used as modulators while the present undulator U250 will act as radiator. The main parameters of the undulators are listed in Tab. 2.

Table 2: Parameters of the Undulators U200 and U250

Parameter	**U200**	**U250**
pole gap	40 mm	50 mm
total length	1.85 m	4.85 m
period length	200 mm	250 mm
number of periods	7	17
max. *B*-field	0.62 T	0.76 T

Dispersive Magnetic Chicanes

The requirements for the magnetic chicanes were obtained by simulation of the laser-electron interaction with *elegant* [10]. Modeling of the magnetic field using *CST Microwave Studio* [11] resulted in five magnets for the first strong chicane and a more conventional four-magnet design for the second chicane, see Fig. 4. The main parameters are listed in Table 3.

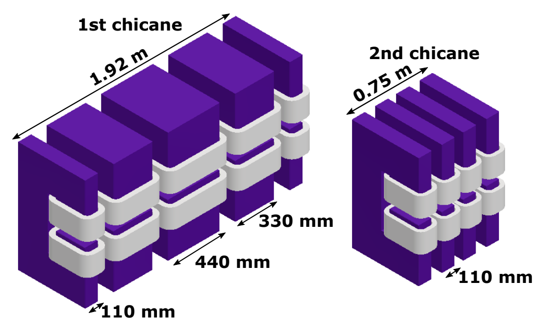

Figure 4: Mechanical design of the strong first chicane (left) and the weaker second chicane (right).

Table 3: Parameters of the Chicanes

Parameter	**1st Chicane**	**2nd Chicane**
total length	1.92 m	0.75 m
No. of magnets	5	4
max. current	500 A	400 A
max. R_{56}	1.73 mm	0.20 mm
max. hor. deflection	11.15 mm	5.38 mm

VACUUM CHAMBERS

For remodeling the short-pulse facility, most of the vacuum chambers will be reused or just slightly modified. For the undulators U200, new vacuum chambers with a reduced

ISBN: 978-3-95450-220-2 ISSN: 2673-5474 doi: 10.18429/JACoW-FEL2022-TUP70

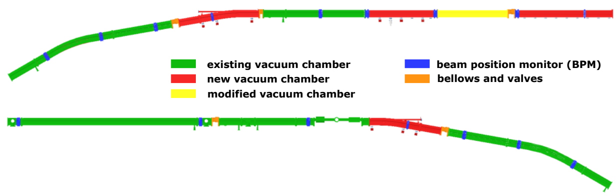

Figure 5: Chamber layout upstream and downstream of the straight section center for the envisaged EEHG-based short-pulse facility, reusing existing chambers (green), modified chambers (yellow) and introducing new chambers (red). Beam position monitors (blue) as well as bellows and valves (orange) are taken into account.

height due to the smaller gap were manufactured, the chamber for the short second chicane is included in one of them. New 10° dipole chambers were designed taking the laser beam size into account. A preliminary arrangement of the chambers including beam position monitors (BPMs), pumping ports for external pumps, bellows and valves was carried out and is shown in Fig. 5.

SPEED: AN EEHG DEMO PROJECT

Before modifying one quarter of the DELTA storage ring, it was decided to realize a fast and less elaborate demonstration experiment to test the feasibily of such a complex seeding scheme for short-pulse generation at a storage ring.

The SPEED project (Short-Pulse Emission with Echo at DELTA) is based on rewiring the present electromagnetic planar undulator U250 to create two sections acting as modulators, two dispersive chicanes, and a radiator. The storage ring remains unchanged and will be operated in single-bunch mode with a typical current of 10 mA. Table 4 summarizes the previous and the new setup and Fig. 6 shows an estimate of the magnetic field as well as the resulting beam position and cumulative R_{56} values as function of the longitudinal position s for both configurations. Note that the usual endpole design of two poles with $1/4$ and $-3/4$ of the magnetic field amplitude, which keeps the electron beam centered to the undulator axis [12], has been abandoned. Instead, a single endpole with $1/2$ of the field amplitude allows to use two more poles while accepting the drawback of a field-dependent horizontal beam shift.

Table 4: U250 in CHG and EEHG Configuration

CHG	modulator	14 poles
	chicane (R_{56})	6 poles (170 μm)
	radiator	14 poles
EEHG	1. modulator	8 poles
	1. chicane (R_{56})	8 poles (471 μm)
	2. modulator	8 poles
	2. chicane (R_{56})	6 poles (72 μm)
	radiator	6 poles

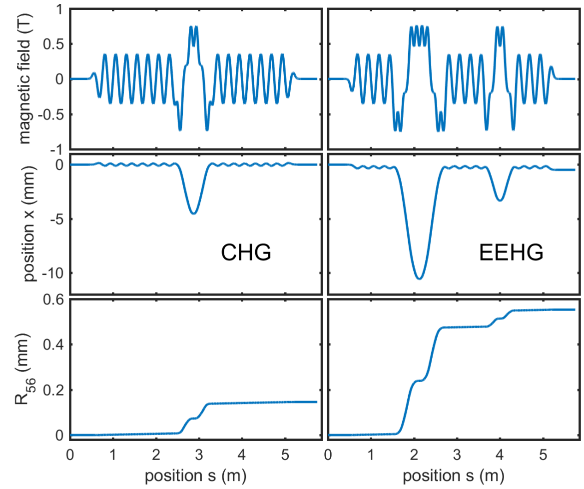

Figure 6: Magnetic field (full current), horizontal beam position, and cumulative R_{56} of the undulator U250 in CHG (left) and EEHG (right) configuration.

The twofold energy modulation is performed using the 400-nm pulses after second-harmonic generation (SHG) of the 800-nm pulses from the present Ti:sapphire laser system plus the residual 800-nm pulses emerging from the SHG process. The temporal overlap between laser pulses and the electron bunches is performed as in CHG operation, i.e., observing laser and spontaneous undulator pulses with a streak camera [13]. The overlap of both laser pulses with the same electrons is established by the methods developed earlier [14, 15]. Due to longitudinal dispersion in the storage ring, each laser pulse causes a dip in the electron density distribution giving rise to coherently emitted THz radiation in a dipole magnet with an intensity given by the interference of radiation from the two dips.

Coherently emitted pulses from the radiator will be detected at and above 200 nm by a Czerny-Turner monochromator combined with an image-intensified gated CCD camera [16]. For smaller wavelengths down to 30 nm, an in-vacuum grating spectrometer will be employed, where a conventional CCD camera images a gated micro-channel plate through a window flange [17].

To our knowledge, the SPEED project at DELTA is the worldwide first implementation of an EEHG scheme at a storage ring. At the time of writing (August 2022), the hardware setup was completed and the correct wiring of all components was checked. Energy modulation with both, 400 and 800-nm pulses, was verified by coherently emitted THz radiation and the spatial as well as temporal overlap was established (see Fig. 7). Values of R_{56} exceeding the conservative estimates in Tab. 4 were found from the interference of radiation from two undulators set to the same wavelength and the chicane between them (“optical klystron”) [18]. The next steps in future dedicated beamtime are to perform CHG with the second chicane only, and then set the first chicane to an R_{56} value, which clearly overbunches the first energy modulation, and search for an EEHG signature.

ISBN: 978-3-95450-220-2 ISSN: 2673-5474 doi: 10.18429/JACoW-FEL2022-TUP70

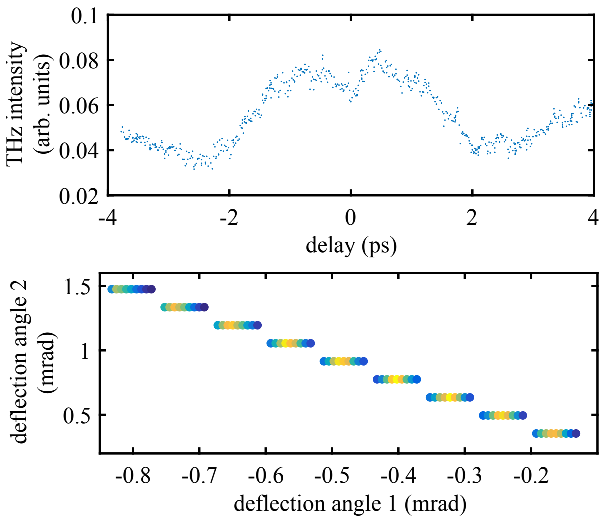

Figure 7: Top: THz signal as function of the delay between two EEHG seed pulses. The dip at zero delay occurs because the number of coherently emitting electrons is reduced when both pulses interact with the same bunch slice. Bottom: Color-coded THz signal as function of deflection angles from the last two laser mirrors optimizing the spatial and angular laser-electron overlap.

In case of success, the project will not only demonstrate EEHG-based short-pulse generation at a storage ring but will prove that this method can be applied within a typical straight section of about 5 m length. Instead of the present undulator with 25 cm period length and only a few magnetic poles for each section, a dedicated setup may be composed of permanent-magnet undulators with tunable gap and period lengths of about 10 cm for both modulators and below 5 cm for the radiator. This way, a compact EEHG device with sufficient intensity for ultrafast-science applications, possibly with all components constructed on a common girder, could be placed in a straight section which is usually occupied by a single undulator.

CONCLUSION

To implement EEHG instead of CHG at the DELTA short-pulse facility, a quarter of the storage ring needs to be remodeled. Towards this upgrade, new optics was developed and most of the necessary hardware like quadrupole and dipole magnets as well as vacuum chambers will be reused or is already procured. Earlier in 2022, it was decided to perform a demo experiment. By rewiring the existing undulator U250, two modulators, two chicanes and a radiator are created in a single device. First tests were performed and we are confident to achieve the first EEHG signal at a storage ring in the near future.

ACKNOWLEDGEMENTS

We are pleased to thank our colleagues at DELTA and other institutes, particularly FZJ in Jülich, HZB in Berlin, DESY in Hamburg and KIT in Karlsruhe, for their continuous support and advice.

REFERENCES

[1] G. Stupakov, “Using the beam-echo effect for generation of short-wavelength radiation”, *Phys. Rev. Lett.*, vol. 102, p. 74801, 2009. doi:10.1103/PhysRevLett.102.074801

[2] D. Xiang and G. Stupakov, “Echo-enabled harmonic generation free electron laser”, *Phys. Rev. Spec. Top. Accel. Beams*, vol. 12, p. 030702, 2009. doi:10.1103/PhysRevSTAB.12.030702

[3] Z. T. Zhao *et al.*, "First lasing of an echo-enabled harmonic generation free-electron laser", *Nat. Photonics*, vol. 6, pp. 360–363, 2012. doi.org/10.1038/nphoton.2012.105

[4] E. Hemsing *et al.*, "Echo-enabled harmonics up to the 75th order from precisely tailored electron beams", *Nat. Photonics*, vol. 10, pp. 507-511, 2016. doi:10.1038/nphoton.2016.101.

[5] P. Rebernik Ribic *et al.*, “Coherent soft X-ray pulses from an echo-enabled harmonic generation free-electron laser”, *Nat. Photonics*, vol. 13, pp. 555—561, 2019. doi:10.1038/s41566-019-0427-1

[6] R. Coisson and F. De Martini, "Free-electron coherent relativistic scatterer for UV-generation", in *Physics of Quantum Electronics*, 9, S. F. Jacobs *et al.*, Addison Wesley, 1982.

[7] S. Khan *et al.*, "Coherent Harmonic Generation at DELTA: A New Facility for Ultrashort Pulses in the VUV and THz Regime", *Sync. Radiat. News*, 24, pp. 18-23, 2011. doi:10.1080/08940886.2011.618092

[8] M. Borland, Advanced Photon Source LS-287, 2000.

[9] R. Molo, “Towards Echo-Enabled Harmonic Generation at FLASH1 and DELTA”, Dissertation, TU Dortmund, Germany, 2017.

[10] A. Held *et al.*, “Status of the Short-Pulse Source at DELTA”, in *Proc. IPAC’21*, Campinas, Brazil, May 2021, pp. 1518–1521. doi:10.18429/JACoW-IPAC2021-TUPAB066

[11] CST STUDIO SUITE ®, https://www.cst.com/products/csts2

[12] J. A. Clarke, *The Science and Technology of Undulators and Wigglers*. Oxford, UK: Oxford Science Publications, 2009.

[13] S. Khan *et al.*, “Diagnostics of and with Laser-Induced Energy Modulation at the DELTA Storage Ring”, in *Proc. IBIC’14*, Monterey, CA, USA, Sep. 2014, paper MOPD24, pp. 202–208.

[14] A. Meyer auf der Heide *et al.*, “Progress Towards an EEHG-Based Short-Pulse Source at DELTA”, in *Proc. IPAC’17*, Copenhagen, Denmark, May 2017, pp. 2582–2585. doi:10.18429/JACoW-IPAC2017-WEPAB010

[15] S. Khan *et al.*, “Seeding of Electron Bunches in Storage Rings”, in *Proc. FEL’17*, Santa Fe, NM, USA, Aug. 2017, pp. 94–97. doi:10.18429/JACoW-FEL2017-MOP027

[16] Andor iStar 334T.

[17] HP Spectroscopy easy LIGHT XUV.

[18] P. Elleaume, “Optical Klystrons”, *Journal de Physique Colloques*, vol. 44, pp.C1-333-C1-352, 1983. doi:10.1051/jphyscol:1983127

ISBN: 978-3-95450-220-2 ISSN: 2673-5474 doi: 10.18429/JACoW-FEL2022-TUP71

SPECTRO-TEMPORAL PROPERTIES OF COHERENTLY EMITTED ULTRASHORT RADIATION PULSES AT DELTA *

A. Radha Krishnan†, B. Büsing, A. Held, S. Khan, C. Mai, Z. Usfoor, V. Vijayan
Center for Synchrotron Radiation (DELTA), TU Dortmund, Dortmund, Germany

Abstract

At the 1.5 GeV synchrotron light source DELTA operated by the TU Dortmund University, the short-pulse facility employs the seeding scheme coherent harmonic generation (CHG) to produce ultrashort pulses in the vacuum ultraviolet and terahertz regime. This is achieved via a laser-induced electron energy modulation and a subsequent microbunching in a dispersive section. The spectro-temporal properties of the CHG pulses as well as the coherently emitted terahertz radiation are influenced by the seed laser parameters and can be manipulated by varying the laser pulse shape and the strength of the dispersive section. CHG spectra for different parameter sets were recorded and compared with the results of numerical simulations to reconstruct the spectra. A convolutional neural network was employed to extract the spectral phase information of the seed laser from the recorded spectra. In addition, the shaping of the coherently emitted THz pulses by controlling the seed pulse spectral phase using a spatial light modulator was also demonstrated.

INTRODUCTION

Synchrotron radiation is proven vital for the study of properties of matter in a variety of experiments due to its characteristics such as high intensity, collimation and tunable wavelength. However, a lower limit to the achievable pulse duration is given by the electron bunch length which is usually in the order of several tens of picoseconds. These pulses lack the temporal resolution to probe the atomic processes taking place on the sub-picosecond scale. On the other hand, conventional mode-locked lasers can produce light pulses in the femtosecond regime but are in the visible and infrared wavelength range. Coherent harmonic generation (CHG) [1] is a technique that combines the advantages of these two radiation sources to produce coherent femtosecond light pulses of short wavelength.

CHG in storage rings is similar to the high-gain harmonic-generation (HGHG) seeding scheme used for free-electron lasers (FEL) but without the FEL gain [2–4]. As depicted in Fig. 1, CHG is based on a laser-electron interaction in an undulator that is tuned to the seed laser wavelength (modulator). The laser-electron interaction induces a sinusoidal modulation of the electron energy, which is then transformed into a density modulation (microbunches) via a dispersive section (chicane). These microbunches results in coherent emission in a subsequent undulator that is tuned to a target harmonic of the seed laser wavelength (radiator). Since the laser pulse only modulates a very thin slice of the electron bunch, the resulting coherently emitted pulse will also have a pulse length comparable to that of the laser pulse.

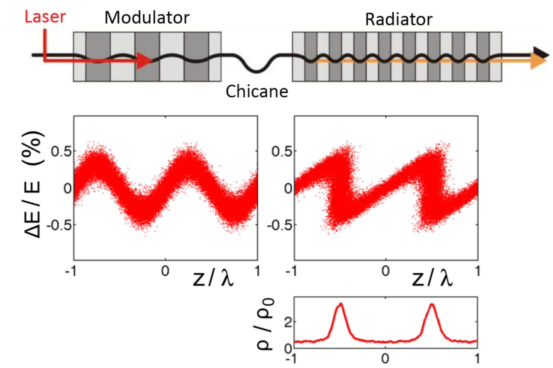

Figure 1: Magnetic setup for CHG, corresponding longitudinal phase space distributions and final longitudinal electron density.

The power of the CHG radiation at the n^{th} harmonic of the laser wavelength λ is given by

$$P(\lambda/n) \sim N_e^2 b_n^2 \tag{1}$$

where b_n is the bunching factor and N_e is the number of modulated electrons. For the CHG scheme, the bunching factor is given by [5],

$$b_n = |J_n(nAB)|e^{-\frac{n^2B^2}{2}} \tag{2}$$

where $A = \Delta E_{\max}/\sigma_E$ is the relative energy modulation amplitude and $B = R_{56}k\sigma_E/E_0$ is the dimensionless chicane parameter. Here, R_{56} is the matrix element of the chicane describing its longitudinal dispersion which quantifies the strength of the chicane, E_0 is the nominal beam energy, σ_E is the rms energy spread and $k = 2\pi/\lambda$. When seeded with a Gaussian laser pulse, the energy modulation amplitude A varies longitudinally following the pulse shape of the laser. Since the amplitude of the energy modulation along the bunch is proportional to the electric field of the laser, the Gaussian distribution of the modulation follows a length larger than that of the seed pulse by a factor of $\sqrt{2}$. Due to this non-uniform energy modulation, the optimum R_{56} required will be different along the longitudinal position of the bunch. This allows one to manipulate the pulse shape of the CHG radiation by controlling the chicane strength. As can be seen in Fig. 2, the CHG radiation will be a single bell-shaped pulse for R_{56} = 50 μm (green line) where

* Work supported by BMBF (05K16PEA, 05K16PEB, 05K19PEB, 05K19PEC), DFG (INST 212/236-1 FUGG) and the federal state of NRW.
† arjun.krishnan@tu-dortmund.de

ISBN: 978-3-95450-220-2 ISSN: 2673-5474 doi: 10.18429/JACoW-FEL2022-TUP71

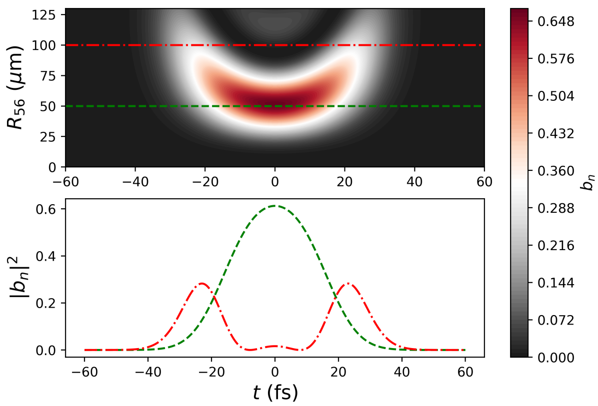

Figure 2: Intensity plot of theoretical bunching factor as a function of longitudinal position and chicane strength R_{56} (top). Bunching factor squared as a function of time along the specified lines in the top figure (bottom).

the bunching is maximized at the centre of the modulated slice. For stronger chicanes, e.g. 100 µm (red line), microbunching occurs for the electrons with a lower energy modulation at the head and tail of the slice, while the electrons at the centre with maximum energy modulation are overbunched. Consequently, this results in separate pulses originating from different longitudinal positions influencing the spectral properties of CHG radiation.

A laser pulse with central frequency ω_0 can be expressed in the frequency domain in terms of spectral amplitude $\tilde{E}(\omega)$ and spectral phase $\varphi(\omega)$

$$\tilde{E}(\omega) = |\tilde{E}_0(\omega)|e^{-i\varphi(\omega)}, \tag{3}$$

where $\varphi(\omega)$ can be expanded into a Taylor series as

$$\varphi(\omega) = D_0 + D_1 \cdot (\omega - \omega_0) + D_2 \cdot (\omega - \omega_0)^2 + D_3 \cdot (\omega - \omega_0)^3 + \dots . \tag{4}$$

Here, D_0 is the central phase advance, D_1 is the group delay, D_2 is the group delay dispersion (GDD), and D_3 is the third order dispersion (TOD). A transform-limited pulse with shortest pulse length corresponds to a GDD of zero, while a non-zero GDD introduces a linear frequency chirp to the laser pulse. If the seed pulse is not chirped, the successive CHG pulses at high R_{56} have the same frequency, which results in interference fringes in the CHG spectra as shown in Fig. 3 (left). Instead, if the seed pulse has strong frequency chirp, the successive maxima of the bunching factor would result in maxima at specific frequencies in the CHG spectra, see Fig. 3 (right). In addition to the effects of GDD, a non-zero TOD in the seed pulse would influence the wavelength distribution of the CHG pulse and also introduces asymmetry in the spectra since it makes the pulse shape of the laser pulse asymmetric.

Studies exploring the spectral and temporal properties of the CHG radiation have been carried out previously at

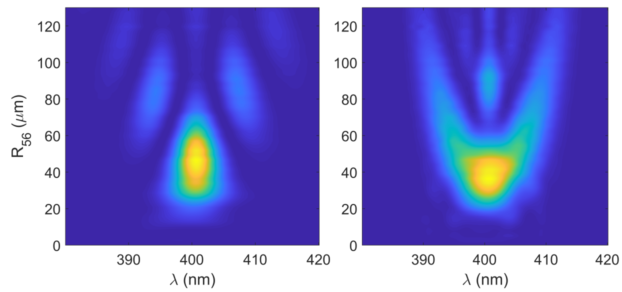

Figure 3: (Left) Simulated CHG spectra for a seed pulse with zero frequency chirp. (Right) Simulated spectra for a seed pulse with strong chirp.

DELTA [6] and similar observations were made at FERMI [7] in the context of HGHG for FELs. In the studies at DELTA, interpreting the CHG spectra was difficult due to the higher-order dispersion present in the seed pulses. In this work, it was attempted to include the effects of higher-order spectral phase on the spectral and temporal properties of the CHG radiation.

THE DELTA SHORT-PULSE SOURCE

At the 1.5 GeV electron storage ring DELTA at TU Dortmund University, a short-pulse facility based on the CHG scheme is being operated to produce ultrashort synchrotron radiation pulses in the vacuum ultraviolet regime [4]. Relevant parameters of the storage ring, the undulators and the laser system are given in Table 1.

Table 1: Parameters of the DELTA Short-Pulse Facility

Storage ring circumference	115.2 m
Electron beam energy	1.5 GeV
Beam current (single-/multibunch)	20/130 mA
Horizontal emittance	15 nm rad
Relative energy spread (rms)	$7{\times}10^{-4}$
Bunch length (FWHM)	80 ps
Modulator/radiator period length	0.25 m
Number of modulator/radiator periods	7
Undulator periods used as chicane	3
Max. modulator/radiator K parameter	10.5
Max. chicane R_{56} (@ 800 A)	~ 170 µm
Laser wavelength	800 nm
Pulse energy @ 800 nm	8 mJ
Min. pulse length	40 fs
Repetition rate	1 kHz

Pulses from a titanium:sapphire laser system are focused directly into the electromagnetic undulator U250 or are frequency-doubled first. The 7 upstream/downstream periods of the U250 act as modulator/radiator for CHG with a chicane between them. A diagnostics beamline is used to observe the spatial and temporal overlap of the laser pulse and the electron bunch with the help of screens and a streak camera. In the dipole magnet downstream, the energy-dependent

ISBN: 978-3-95450-220-2 ISSN: 2673-5474 doi: 10.18429/JACoW-FEL2022-TUP71

path length of the electrons transforms the laser-induced energy modulation to sub-millimeter dip in the longitudinal electron density which results in coherent emission of broadband THz radiation. The laser-electron overlap is then optimized by maximizing the intensity of this THz radiation. On the other hand, laser pulses can be shaped to optimize properties of the THz radiation for experimental purposes, e.g., to produce narrowband radiation to deduce the spectral characteristics of far-infrared detectors [8].

OBSERVATION OF CHG SPECTRA

The spectra of the CHG radiation were recorded using a Czerny-Turner-type spectrometer equipped with an image-intensified CCD (iCCD) camera [9]. With a gating window as short as 2 ns, the iCCD camera allows to capture the CHG spectra without the background of the 2600 spontaneous sychrotron radiation pulses between consecutive CHG pulses. Wavelengths down to 200 nm can be recorded using this method, which covers the 2nd, 3rd and 4th harmonic of the seed wavelength. For observing even shorter wavelengths, an XUV spectrometer was installed recently which can record spectra down to 30 nm [10]. Presently, a MgF window that seperates the beamline from the storage ring vacuum blocks wavelengths below around 130 nm limiting the observation of CHG spectra to the 6th harmonic (133 nm) of the seed wavelength. Shown in Fig. 4 are the observed CHG spectra for the 2nd, 4th and 6th harmonic of the 800 nm seed without (left column) and with (right column) frequency chirp. When seeding with an unchirped laser pulse, pronounced spectral fringes appear at large R_{56}. On the other hand, seeding with a strongly chirped laser pulse results in a parabolic feature similar to the simulations. The asymmetry observed in the spectral features may be attributed to the higher-order dispersion in the seed laser pulse which was not taken into account in Fig. 3.

In order to study the effects of the spectral phase of the seed laser on the CHG radiation, the CHG spectra were simulated for different seed pulse parameters. A convolutional neural network (CNN) [11] was designed using TensorFlow [12] to predict the GDD and TOD from the CHG spectra given as the input. The CNN was trained on a set of over 9000 numerically simulated spectra for different combinations of GDD and TOD. A random noise was added to the simulated spectra in order to account for the noise in the measurements. The spectral phase of the seed pulse was controlled by tuning the separation between the gratings in an optical compressor [13]. The CNN was used to predict the GDD and TOD of the seed pulse from the observed CHG spectra for different grating separations. Figure 5 shows the observed and predicted spectra using the CNN for two different compressor settings.

The trained neural network could reconstruct the spectral features observed for different compressor settings by predicting the GDD and TOD of the seed laser pulse. The mean of the predicted values from 10 trials with the same input and their standard deviation is plotted in Fig. 6. A linear

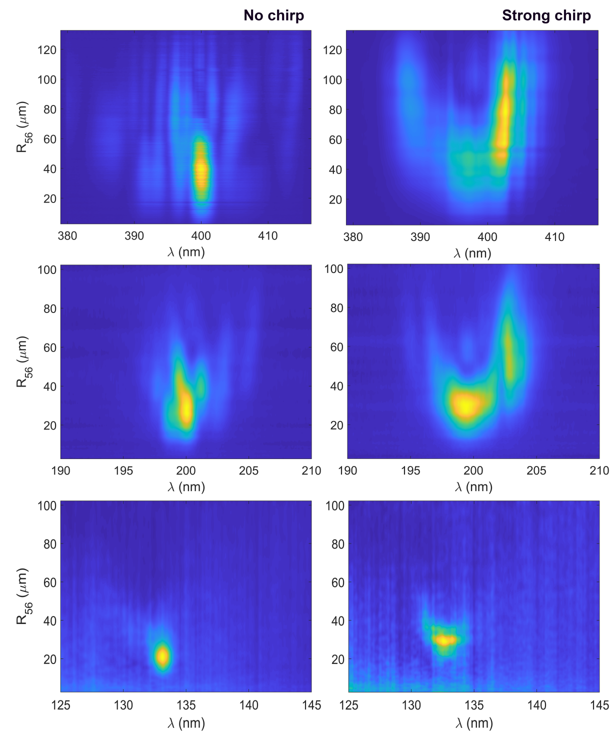

Figure 4: Observed CHG spectra for the 2nd, 4th and 6th harmonic of the seed laser wavelength with unchirped seed pulse (left) and with strong positive chirp (right).

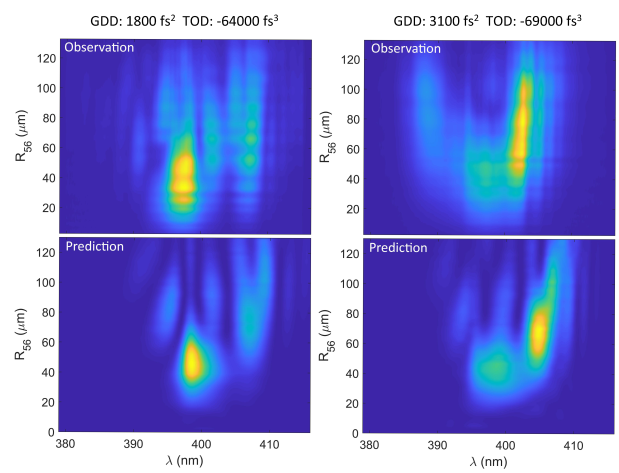

Figure 5: Observed (top) and predicted (bottom) CHG spectra for different settings of the laser compressor at the 2nd harmonic of the seed laser wavelength.

relationship between the grating separation in the compressor and the GDD of the laser pulse was observed (Fig. 6 (top)) while the TOD shows a negative linear relationship to the compressor length (Fig. 6 (bottom)). This behaviour is in agreement with the theory [13]. The results suggest that the asymmetry visible in the spectra could be due to a large negative TOD (> 50000 fs^3) present in the seed laser pulse. The origin of this non-zero TOD could be that the compressor is under-compensating the TOD introduced by

ISBN: 978-3-95450-220-2 ISSN: 2673-5474 doi: 10.18429/JACoW-FEL2022-TUP71

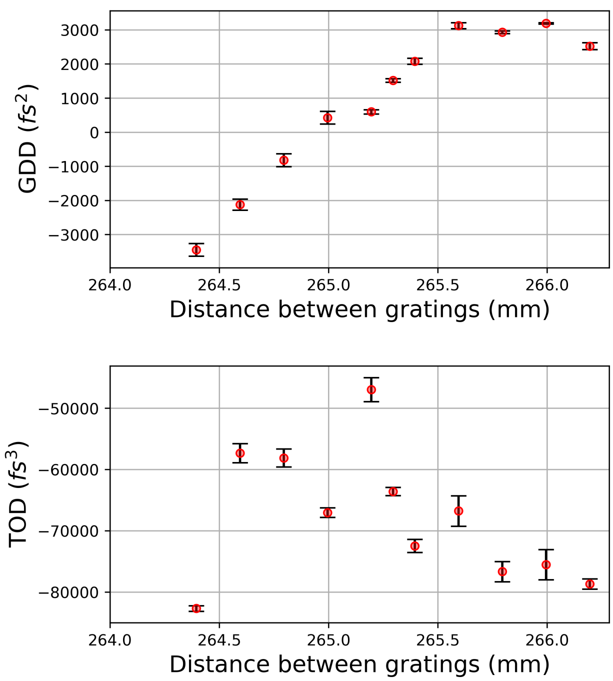

Figure 6: Predicted GDD and TOD values for different compressor settings. The points indicate the mean and the error bars show the standard deviation of predictions from ten individually trained models.

the pulse stretcher in the chirped-pulse amplification scheme. However, it is also to be noted that there are outliers at high GDD which don't fit to the otherwise linear relationship observed. This points to the inefficiency of the model to correctly predict the spectral phase at large GDD values. The CNN model needs to be improved to resolve this. A more detailed study involving direct measurements of the spectral and temporal properties of the seed pulse, such as frequency-resolved optical gating (FROG) [14], is also required to confirm the effects of higher-order dispersion on the CHG spectra. In this study, only the effects of 2nd and 3rd order dispersion on the CHG pulse properties was investigated. Looking into even higher order spectral phase could prove to be helpful in further tailoring the CHG pulses.

CONTROLLING THE SPECTRAL PHASE FOR SHAPING OF THZ PULSES

The control of the spectral phase of the laser pulse was previously implemented using a so-called 4f-pulse shaper setup [15,16] to optimize the coherently emitted THz pulses. Here, a spatial light modulator (SLM) is used to control individual coefficients of Eq. (4) which allows to correct for TOD introduced by the laser pulse compressor by adding the inverse of the third-order term

$$\varphi_{\text{SLM,corr}}(\omega) = -D_3 \cdot (\omega - \omega_0)^3. \tag{5}$$

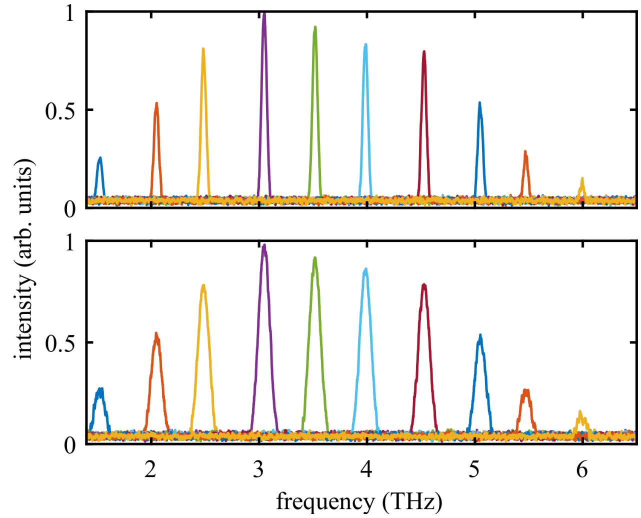

Figure 7: Narrowband THz spectra from a laser-electron interaction with intensity modulation induced by a spatial light modulator. The bandwidth was either set to 80 GHz (top) or 200 GHz (bottom) by changing the phase-shifting pattern.

The correction leads to a linearization of the laser pulse chirp and offers ideal conditions for further control of the pulse shape by a modulation of the spectral phase. Figure 7 shows spectra of coherently emitted, narrowband THz pulses which were generated by adding another modulation of

$$\varphi_{\text{SLM,mod}}(\omega) \propto \cos[\Delta T(\omega - \omega_0)]. \tag{6}$$

The periodic modulation of the spectral phase causes the occurrence of a pulse train with a temporal spacing of ΔT. Due to the periodic structure, the emission spectra are narrowband and the bandwidth can be controlled by the duration of the pulse train. As the SLM acts as a frequency-dependent phase-shifting filter, further pulse shapes and thus more complex spectral shapes like rectangular spectra can be realized [16].

Currently this method is implemented for long laser pulses with ps length and is successfully demonstrated to be a useful tool in shaping the coherently emitted THz pulses. This way of controlling the spectral phase may also be extended to be used for shaping the CHG pulses as well. For a control over the spectro-temporal properties of sub-ps CHG pulses, however, the intensities could exceed the damage threshold of the SLM. Methods to avoid this problem are currently under investigation.

ACKNOWLEDGEMENTS

We are pleased to thank our colleagues at DELTA and the TU Dortmund University. The continuous support from other institutes, particularly from DESY Hamburg, HZB Berlin, and KIT Karlsruhe is gratefully acknowledged.

ISBN: 978-3-95450-220-2 ISSN: 2673-5474 doi: 10.18429/JACoW-FEL2022-TUP71

REFERENCES

[1] R. Coisson and F. De Martini, "Free-electron coherent relativistic scatterer for UV-generation", *Physics of Quantum Electronics*, vol. 9, pp. 939-960, 1982.

[2] M. Labat *et al.*, "Coherent harmonic generation on UVSOR-II storage ring", *Eur. Phys. J. D*, vol. 44, pp. 187-200, 2007. doi:10.1140/epjd/e2007-00177-6

[3] G. De Ninno *et al.*, "Generation of Ultrashort Coherent Vacuum Ultraviolet Pulses Using Electron Storage Rings: A New Bright Light Source for Experiments", *Phys. Rev. Lett.*, vol. 101, p. 053902, 2008. doi:10.1103/PhysRevLett.101.053902

[4] S. Khan *et al.*, "Generation of ultrashort and coherent synchrotron radiation pulses at DELTA", *Sync. Rad. News*, vol. 26, no. 3, p. 25, 2013. doi:10.1080/08940886.2013.791213

[5] G. Stupakov, "Using the beam-echo effect for generation of short-wavelength radiation", *Phys. Rev. Lett.*, vol. 102, p. 074801, 2009. doi:10.1103/PhysRevLett.102.074801

[6] M. Huck *et al.*, "Ultrashort and Coherent Radiation for Pump-probe Experiments at the DELTA Storage Ring", in *Proc. IPAC'14*, Dresden, Germany, Jun. 2014, pp. 1848–1851. doi:10.18429/JACoW-IPAC2014-WEOAA03

[7] D. Gauthier *et al.*, "Spectrotemporal Shaping of Seeded Free-Electron Laser Pulses", *Phys. Rev. Lett.*, vol. 115, p. 114801, 2015. doi:10.1103/PhysRevLett.115.114801

[8] C. Mai, M. Brosi, B. Büsing, F. Frei, C. Gerth, S. Khan, *et al.*, "A Tunable Narrowband Source in the Sub-THz and THz Range at DELTA", in *Proc. IPAC'18*, Vancouver, BC, Canada, Apr. 4, pp. 4534–4537, doi:10.18429/JACoW-IPAC2018-THPMK098

[9] Andor iStar DH334T 18U-E3, https://andor.oxinst.com/products/intensified-camera-series/istar-334t

[10] HP Spectroscopy easyLIGHT XUV, https://www.hp-spectroscopy.com/easylight-xuv

[11] Y. LeCun, Y. Bengio, and G. Hinton, "Deep learning", *Nature*, vol. 521, p. 436, 2015. doi:10.1038/nature14539

[12] M. Abadi *et. al.*, "Tensorflow: A system for large-scale machine learning", *12th USENIX Symposium on Operating Systems Design and Implementation*, 265, 2016.

[13] P. Ungelenk *et. al.*, "Continuously tunable narrowband pulses in the THz gap from laser-modulated electron bunches in a storage ring", *Phys. Rev. ST Accel. Beams*, vol. 20, p. 020706, 2017. doi:10.1103/PhysRevAccelBeams.20.020706

[14] R. Trebino *et. al.*, "Measuring ultrashort laser pulses in the time-frequency domain using frequency-resolved optical gating", *Rev. Sci. Instrum.*, vol. 68, no. 9, p. 3277, 1997. doi:10.1063/1.1148286

[15] A. M. Weiner, "Femtosecond pulse shaping using spatial light modulators", *Rev. Sci. Instrum.*, vol. 71, pp. 1929–1960, 2000. doi:10.1063/1.1150614

[16] C. Mai, "Towards arbitary Pulse Shapes in the Terahertz Domain", C. Mai, B. Büsing, A. Held, S. Khan, and D. Krieg, "Towards Arbitrary Pulse Shapes in the Terahertz Domain", in *Proc. IPAC'21*, Campinas, Brazil, May 2021, pp. 3977–3979. doi:10.18429/JACoW-IPAC2021-THPAB097

ISBN: 978-3-95450-220-2 ISSN: 2673-5474 doi: 10.18429/JACoW-FEL2022-TUP73

SENSITIVITY OF ECHO-ENABLED HARMONIC GENERATION TO SEED POWER VARIATIONS

F. Pannek*, W. Hillert, University of Hamburg, Hamburg, Germany
S. Ackermann, E. Ferrari, L. Schaper, Deutsches Elektronen-Synchrotron DESY, Hamburg, Germany

Abstract

The external seeding technique Echo-Enabled Harmonic Generation consists of two undulators which are used to imprint energy modulations to an electron bunch via interaction with a seed laser. Each of these so-called modulators is followed by a chicane which introduces longitudinal dispersion. Proper adjustment of the amplitudes of the energy modulations and dispersive strengths allows to achieve bunching at high harmonics of the seed laser wavelength. In the near future, this seeding scheme will be utilized in one of the beamlines of the free-electron laser (FEL) user facility FLASH at DESY to provide stable seeded radiation down to the soft X-ray regime at high repetition rate. Dedicated numerical simulations are carried out within the foreseen parameter space to investigate how variations of the energy modulations due to power fluctuations of the two seed lasers affect the bunching properties and the stability of the generated FEL radiation.

INTRODUCTION

Echo-Enabled Harmonic Generation (EEHG) [1, 2] is an external seeding scheme which makes use of two undulators, so-called modulators, each followed by a chicane. In the first modulator the electron bunch interacts with a seed laser and is modulated in energy. The large longitudinal dispersion of the first chicane transfers the energy modulation in multiple energy bands in the longitudinal phase space. By interaction with another seed laser in the subsequent second modulator, an energy modulation is imprinted on these energy bands, which is finally converted to a density modulation with high harmonic content in the second chicane. Since this scheme relies on two seed lasers, it is indispensable to investigate the influence of variations in the seed laser power on the stability of the free-electron laser (FEL) radiation generated in the subsequent undulator radiator. Numerical modeling and simulations are performed within the parameter range of the future FLASH2020+ upgrade [3, 4].

THEORY

The energy modulation amplitudes $\Delta E_{1,2}$ imprinted on the electron bunch in the first and second modulator are proportional to the square root of the peak power $P_{1,2}$ of the first and second seed laser [5]. In EEHG, the energy modulation amplitudes $A_{1,2}$ are commonly described in terms of the rms beam energy spread σ_E, such that

$$A_{1,2} = \frac{\Delta E_{1,2}}{\sigma_E} \propto \sqrt{P_{1,2}}\,. \tag{1}$$

* fabian.pannek@desy.de

The dispersive strengths of the two chicanes are described by the parameters $B_{1,2} = R_{56}^{(1,2)} k_1 \sigma_E / E$, where $R_{56}^{(1,2)}$ is the longitudinal dispersion, k_1 the wavenumber of the first seed laser and E the electron beam energy.

The EEHG bunching around the harmonic wavenumber $k_\mathrm{E} = a_\mathrm{E} k_1$ can be calculated according to [6]

$$\begin{aligned} b(k) = \mathrm{e}^{-\frac{1}{2}\left(\xi_\mathrm{E}+\frac{k-k_\mathrm{E}}{k_1}B\right)^2} \int_{-\infty}^{\infty} J_m\left(-\frac{k}{k_1}B_2 A_2(t)\right) \\ \cdot J_n\left(-\left[\xi_\mathrm{E}+\frac{k-k_\mathrm{E}}{k_1}B\right]A_1(t)\right)\cdot \mathrm{e}^{-\mathrm{i}(k-k_\mathrm{E})ct}\,c\mathrm{d}t\,, \end{aligned} \tag{2}$$

with the EEHG scaling factor $\xi_\mathrm{E} = nB_1 + a_\mathrm{E} B_2$, the harmonic number $a_\mathrm{E} = n + mk_2/k_1$, n and m being two integers, $B = B_1 + B_2$, the Bessel functions $J_{n,m}$ of the first kind of order n and m, respectively, and the speed of light c. In this study, the time-dependent energy modulation amplitudes $A_{1,2}(t)$ are based on Gaussian seed laser envelopes and have the peak values $A_{1,2}$. Applying a Fourier transform to $b(k)$ results in the temporal description $b(t)$ of the bunching.

SEED LASER POWER VARIATIONS

In the following, the effect of power variations of both seed lasers is investigated at the 15th and the 75th harmonic at $n = -1$ working points. For simplicity, the wavelengths of the two seed lasers are set to $\lambda_{1,2} = 300\,\mathrm{nm}$, the full width at half maximum (FWHM) pulse durations of the first and second seed are $\tau_1 = 150\,\mathrm{fs}$ and $\tau_2 = 50\,\mathrm{fs}$. The 15th harmonic corresponds to 20 nm and is achieved with a 950 MeV electron bunch with an rms energy spread of 105 keV, whereas, the 75th harmonic corresponds to 4 nm and is achieved with an electron energy of 1.35 GeV with 150 keV rms energy spread.

First, power variations of the two seed lasers are explored by utilizing Eq. (2) and the proportionality in Eq. (1). The FWHM pulse duration $\Delta\tau$ and bandwidth $\Delta\nu$ are estimated from $|b(t)|^2$ and $|b(k)|^2$, respectively. The time-bandwidth product (TBP) is calculated as TBP = $\Delta\tau \cdot \Delta\nu$.

The results of the bunching equation are finally compared to numerical simulations of the EEHG and radiator beamline with the FEL code GENESIS 1.3, version 4 [7, 8]. Here, a Gaussian electron bunch of $\sigma_z = 100\,\mu\mathrm{m}$ rms length with $I_\mathrm{p} = 500\,\mathrm{A}$ peak current and a normalized emittance of $\varepsilon_\mathrm{n} = 0.6\,\mathrm{mm\,mrad}$ is assumed. The seed lasers are focused at the center of the respective modulator and have a beam waist much larger than the transverse electron beam size. The radiator beamline consists of helical undulator modules with 76 periods of $\lambda_\mathrm{u} = 33\,\mathrm{mm}$ length.

ISBN: 978-3-95450-220-2 ISSN: 2673-5474 doi: 10.18429/JACoW-FEL2022-TUP73

15th Harmonic

At the 15th harmonic, EEHG can provide more than 10 % bunching, however, sufficient amplification in the radiator is already present for lower bunching. In Fig. 1, seed laser power variations are investigated at several working points providing 3 % peak bunching by making use of Eq. (2). In general, a power jitter of the first seed laser has only a small effect on the bunching at the entrance of the radiator (Fig. 1a) compared to the second seed laser (Fig. 1b). Depending on the initial energy modulation amplitudes, power variations of the seed lasers have different large effects on the bunching. It is also apparent that working points with less effect on the bunching value have a larger effect on the spectro-temporal properties and vice versa. Note that working points with different energy modulation amplitudes also differ in their spectral and temporal characteristics, such that only relative changes of the bandwidth and pulse duration are shown here.

The bunching obtained from GENESIS simulations is in good agreement with the one predicted by Eq. (2), as it can be seen in Fig. 2a on the example of the $A_1 = 3$, $A_2 = 2$ working point. The peak power of the second seed laser is changed by ±4 %, which corresponds to the multi bunch stability rms fluctuation of the seed laser foreseen for FLASH2020+.

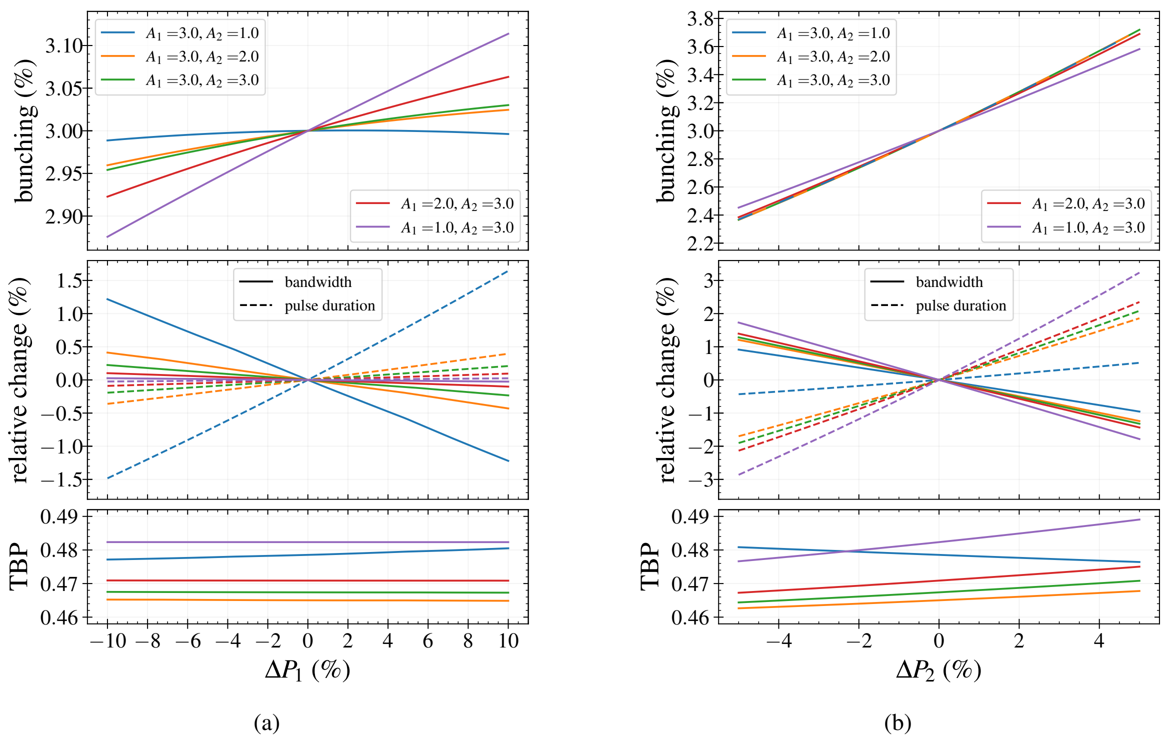

Figure 1: Effect of power variations of (a) the first and (b) the second seed laser on the peak bunching, the FWHM pulse duration and bandwidth as well as the time-bandwidth product of the FEL pulse at the 15th harmonic based on Eq. (2). The legend states the energy modulation amplitudes for no variation in seed laser power.

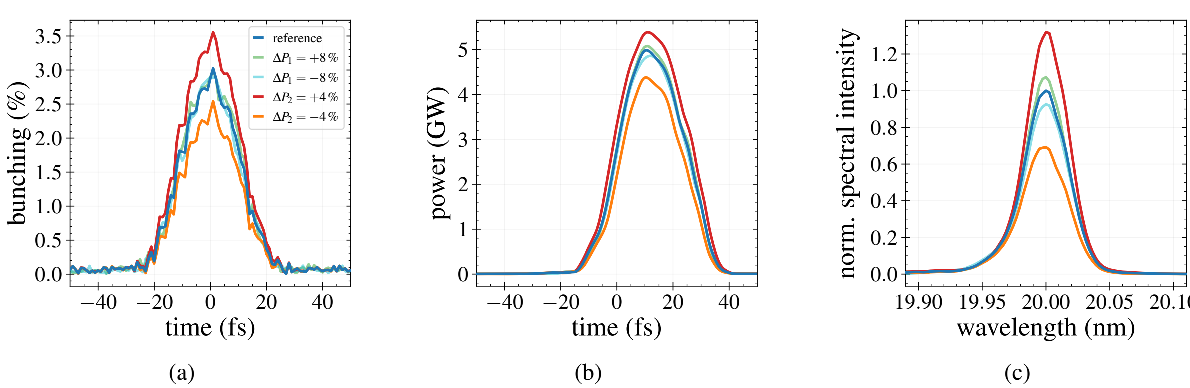

Figure 2: GENESIS simulations with $A_1 = 3$, $A_2 = 2$ and $R_{56}^{(1,2)}$ values optimized for 3 % peak bunching at the 15th harmonic, showing the effect of power variations of the first and second seed on (a) the bunching before entering the radiator, (b) the power profile and (c) the spectral intensity after the 5th radiator module. The radiator undulators are tapered.

ISBN: 978-3-95450-220-2 ISSN: 2673-5474 doi: 10.18429/JACoW-FEL2022-TUP73

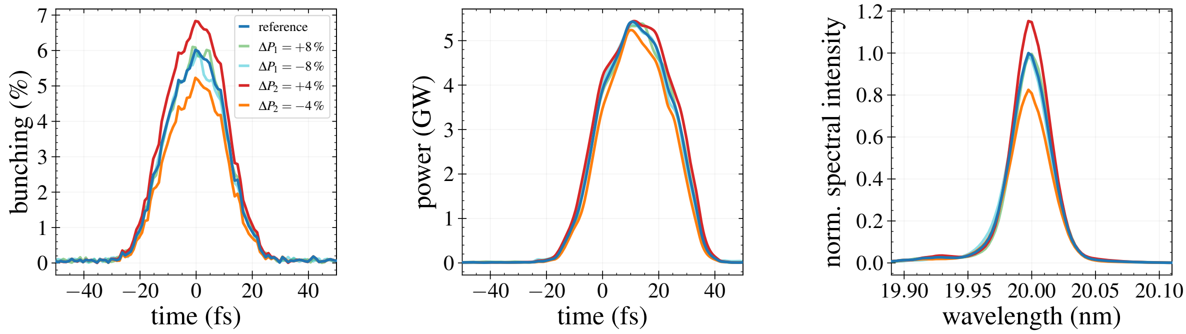

(a) (b) (c)

Figure 3: Same as Fig. 2, but with $R_{56}^{(1,2)}$ values optimized for 6 % peak bunching and accordingly tapered radiator modules.

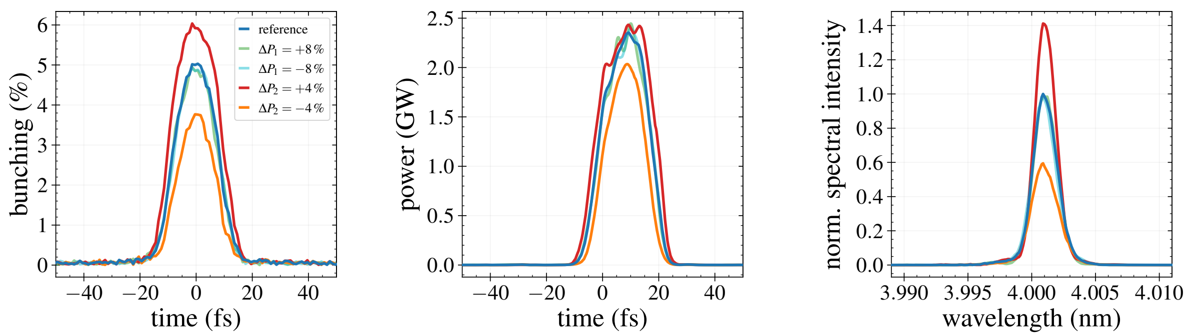

(a) (b) (c)

Figure 4: GENESIS simulations with $A_1 = 3$, $A_2 = 5$ and $R_{56}^{(1,2)}$ values providing about 5 % peak bunching at the 75th harmonic, showing the effect of power variations of the first and second seed laser on (a) the bunching before entering the radiator, (b) the power profile and (c) the spectral intensity after the 11th radiator module. The radiator modules are tapered.

The power of the first seed is varied by ±8 % to highlight the robustness of the EEHG setup to power variations of this laser. Figures 2b and 2c show that the effect of the power variations on the bunching is also reflected in the final power profiles and spectra of the FEL radiation. Here, the radiator beamline is tapered for maximum power after the 5th radiator module. Additional radiator modules result in unwanted features in the spectral and time domain.

As a comparison, simulations based on a working point with 6 % peak bunching at the same energy modulation amplitudes have been carried out, as demonstrated in Fig. 3. Even though the relative changes in bunching properties before entering the radiator are on a similar level as for the 3 % bunching case, the stability of the pulse properties after the 5th radiator module has improved.

75th Harmonic

For higher harmonics, the spacing of the intricate EEHG structures in the longitudinal phase space decreases, making the scheme potentially more sensitive to a power jitter of the seed lasers. Here, the study is limited to GENESIS simulations of one working point at the 75th harmonic with $A_1 = 3$, $A_2 = 5$ providing about 5 % peak bunching. This is close to the maximum achievable bunching in this parameter space and still results in clear spectral and temporal shapes after 11 tapered radiator modules. Figure 4 indicates that the bunching and thus the final FEL radiation is still insensitive to power variations of the first seed, whereas the sensitivity to the laser power of the second seed is slightly increased.

CONCLUSION

The EEHG seeding scheme is very robust to variations in power of the first seed laser even at harmonics as high as the 75th. Results suggest that high bunching working points and tapering of the radiator can reduce the sensitivity of the FEL pulses to power fluctuations of the second seed laser.

ACKNOWLEDGMENTS

This work has been financially supported by BMBF within the project “05K2019-STAR”. The authors gratefully acknowledge the Gauss Centre for Supercomputing e.V. (www.gauss-centre.eu) for funding this project by providing computing time on the GCS Supercomputer JUWELS [9] at Jülich Supercomputing Centre (JSC). This research was supported through the Maxwell computational resources operated at DESY, Hamburg.

ISBN: 978-3-95450-220-2 ISSN: 2673-5474 doi: 10.18429/JACoW-FEL2022-TUP73

REFERENCES

[1] G. Stupakov, "Using the Beam-Echo Effect for Generation of Short-Wavelength Radiation", *Phys. Rev. Lett.*, vol. 102, p. 074801, 2009.
doi:10.1103/PhysRevLett.102.074801

[2] D. Xiang and G. Stupakov, "Echo-enabled harmonic generation free electron laser", *Phys. Rev. ST Accel. Beams*, vol. 12, p. 030702, 2009.
doi:10.1103/PhysRevSTAB.12.030702

[3] M. Beye *et al.*, "FLASH2020+: Making FLASH brighter, faster and more flexible – Conceptual Design Report", Deutsches Elektronen-Synchrotron, 2020.
doi:10.3204/PUBDB-2020-00465

[4] L. Schaper *et al.*, "Flexible and Coherent Soft X-ray Pulses at High Repetition Rate: Current Research and Perspectives", *Appl. Sci.*, vol. 11, no. 20, p. 9729, 2021.
doi:10.3390/app11209729

[5] E. Hemsing *et al.*, "Beam by design: Laser manipulation of electrons in modern accelerators", *Rev. Mod. Phys.*, vol. 86, pp. 897–941, 2014.
doi:10.1103/RevModPhys.86.897

[6] N. Mirian *et al.*, "Spectrotemporal control of soft x-ray laser pulses", *Phys. Rev. Accel. Beams*, vol. 23, p. 060701, 2020.
doi:10.1103/PhysRevAccelBeams.23.060701

[7] S. Reiche, "GENESIS 1.3: a fully 3D time-dependent FEL simulation code", *Nucl. Instrum. Methods A*, vol. 429, p. 248, 1999.
doi:10.1016/S0168-9002(99)00114-X

[8] S. Reiche, "Update on the FEL Code Genesis 1.3", in *Proc. 36th Int. Free Electron Laser Conf. (FEL'14)*, Basel, Switzerland, paper TUP019, pp. 403-407, Aug. 2014.

[9] Damian Alvarez, Jülich Supercomputing Centre, "JUWELS Cluster and Booster: Exascale Pathfinder with Modular Supercomputing Architecture at Juelich Supercomputing Centre", *Journal of large-scale research facilities*, vol. 7, p. A138, 2021.
doi:10.17815/jlsrf-7-183

ISBN: 978-3-95450-220-2 ISSN: 2673-5474 doi: 10.18429/JACoW-FEL2022-TUP74

CALCULATION OF THE CSR EFFECT ON EEHG PERFORMANCE

D. Samoilenko*, W. Hillert
Institute for Experimental Physics University of Hamburg 20148 Hamburg, Germany
N. Mirian†, P. Niknejadi, L. Schaper, Deutsches Elektronen-Synchrotron DESY, Hamburg, Germany
D. Zhou, KEK, Ibaraki, Japan

Abstract

Externally seeded FELs can produce fully coherent short-wavelength pulses with the advantage of higher shot-to-shot stability and spectral intensity than SASE radiation. For the FLASH2020+ project, the Echo-Enabled Harmonic Generation (EEHG) seeding technique achieves seeded FEL radiation in the XUV and soft X-ray range down to wavelengths of 4 nm. The implementation of the EEHG requires precise phase space manipulations in the seeding section of the beamline, which would make the performance of the EEHG sensitive to the collective effects, such as Coherent Synchrotron Radiation (CSR) in some working range. Therefore, it is essential to consider the CSR in EEHG simulations and to understand its impact on the electron beam properties. In this work, we compare different methods for calculating CSR and investigate the mechanism of its effect on the EEHG performance.

INTRODUCTION

Echo-Enabled Harmonic Generation (EEHG) [1] is an external seeding technique for Free Electron Lasers (FEL). Implementation of EEHG gives a number of advantages as compared to Self Amplified Spantaneous Emission (SASE) mode. These advantages include shot-to-shot stability, increased longitudinal coherence and narrow-bandwidth spectrum. The choice of EEHG above other seeding techniques also allows to reach higher harmonics of the seed laser wavelength [2]. Currently FLASH facility is undergoiong a major upgrade to implement EEHG technique in one of the beamlines to allow for FEL radiation at wavelengths down to 4 nm [3]. The challenge here is that EEHG requires creation of fine structures in the electron beam phase space achieve such wavelengths. These structures also have be transported through the seeding section without significant distortions. The distortions can be created, for example, by collective effects. In the strong EEHG chicane the Coherent Synchrotron Radiation (CSR) is particularly concerning. In our previous work we already addressed the effect of CSR in the strong EEHG chicane and showed, that it can have an effect on EEHG performance [4, 5]. In this work we focus on the analytical treatment of EEHG, introduced in [6] to get a better understanding of the mechanism behind this effect. We show how this mechanism connects the EEHG bunching spectrum to the impedance in chicane 1. We also compare different models for the calculation of the impedance to discuss the effect of the chicane chamber. We show how the difference in the impedance for the two models translates into the properties of the electron beam with particle-tracking simulations and find the resluts to be consistent with the analytical consideration.

METHODS

Schematic representation of the EEHG setup is given in Fig. 1. The most relevant parameters are listed in Table 1. The simulations are done by ELEGANT simulation code [7]. For the analytical treatment we follow the method presented

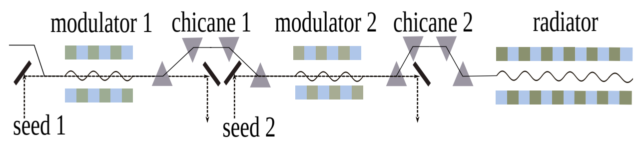

Figure 1: EEHG setup.

Table 1: Simulation Parameters

Initial beam parameters	
Central energy	1350 MeV
Slice energy spread	150 keV
Bunch length rms (σ_z)	96 µm
Peak current	500 A
Normalized emittance	0.6 mm · mrad
Seeding section parameters	
Seed lasers wavelength	300 nm
A_1	3.10
$R_{56}^{(1)}$	7.05 mm
$L_D^{(1)}$	42 cm
A_2	5.18
$R_{56}^{(2)}$	81.25 µm

in [8]. The evolution of the electron beam phase space is described by the set of equations:

$$\begin{aligned} P_1 &= P + A_1(z)\sin(k_1 z) \\ z_1 &= z + B_1 P_1/k_1 \\ P_2 &= P_1 + A_2(z_1)\sin(k_2 z_1) + \Delta p_2(z_1) \\ z_2 &= z_1 + B_2 P_2/k_2, \end{aligned} \tag{1}$$

where $P = \Delta E/\sigma_E$ is the normalized energy, $A_{1,2}(z) = \Delta E_{1,2}(z)/\sigma_E$ is the normalized energy modulation induced in the first and the second modulator respectively, $k_{1,2}$ is the wavenumber of the first and the second seed laser respectively, $B_{1,2} = k_{1,2}R_{56}^{(1,2)}\sigma_e/E$ is the normalized dispersion in

* dmitrii.samoilenko@desy.de
† najmeh.mirian@desy.de

ISBN: 978-3-95450-220-2 ISSN: 2673-5474 doi: 10.18429/JACoW-FEL2022-TUP74

the first and the second chicane respectively, E is the energy and σ_E is the initial slice energy spread. The term $\Delta p_2(z_1)$ in Eq. (1) can represent any energy distortions that occur in between the two chicanes. In our case, it represents the CSR-induced energy kicks and (if the chamber effect is included) resistive wakefields (RW) from the chicane chamber. The kicks can be represented as a superposition of plain wave components at different wavelengths [8]:

$$\Delta p_2 = \sum_{\mu=0}^{\infty} p_2(k_\mu)\sin(k_\mu z + \varphi_{2\mu}). \tag{2}$$

The bunching factor at the exit of the seeding section is calculated as the Fourier transform of the particle distribution. If $\Delta p_2 = 0$ it leads to the well-known result [1]:

$$\bar{b}_{nm}(k_E) = e^{-\xi_E^2/2} J_n(-\xi_E A_1) J_m(-a_E A_2 B_2), \tag{3}$$

where $a_E = n + mk_2/k_1$ is the harmonic number, $k_E = a_e k_1$ is the corresponding wavenumber, $\xi_E = nB_1 + a_E B_2$, n and m are integer numbers. In the presence of energy modulation Δp_2 the bunching factor at a_E harmonic is [8]:

$$b_{nm}(k_E) = \bar{b}_{nm}(k_E) \times \prod_{\mu=0}^{\infty} \sum_{l_1=-\infty}^{\infty} (-1)^{l_1} J_{l_1}(-a_E B_2 p_2(k_\mu)) e^{-il_1\varphi_{2\mu}}, \tag{4}$$

from Eq. (4) we can calculate the properties of CSR-affected bunching spectrum. For example, the corrected value of the bandwidth is given by:

$$\sigma_k^2 = \bar{\sigma}_k^2 + \sum_{\mu=0}^{\infty} \left[\frac{(a_E B_2)^2}{2} \left(p_2(k_\mu) k_\mu \right)^2 \right], \tag{5}$$

where $\bar{\sigma_k}$ is the bandwidth with $\Delta p_2 = 0$. The only missing component is the amplitudes of the energy kicks $p_2(k_\mu)$. We can evaluate the amplitudes by considering the impedance felt by the particles inside chicane 1. If we neglect the chamber effects, the CSR impedance of a single chicane dipole in free space (FS) is given by [9]:

$$Z_{FS}(k) = (-0.94i + 1.63) \frac{Z_0 k_\mu^{1/3}}{4\pi \rho^{2/3}} L_D, \tag{6}$$

where $Z_0 = 377\Omega$ is the impedance of free space, ρ is the bending radius and L_D is the dipole length. To include the effect of the chamber walls we employ parallel plates (PP) model. In case of PP model the CSR impedance is [10]:

$$Z_{PP}(k) = \frac{2\pi Z_0}{h} \left(\frac{2}{k\rho} \right)^{(1/3)} L_D \times \sum_{\nu=0}^{\infty} \Big\{ \mathrm{Ai}'(X_\nu^2) \left[\mathrm{Ai}'(X_\nu^2) - i\mathrm{Bi}'(X_\nu^2) \right] + X_\nu^2 \mathrm{Ai}(X_\nu^2) \left[\mathrm{Ai}(X_\nu^2) - i\mathrm{Bi}(X_\nu^2) \right] \Big\}, \tag{7}$$

where h is the distance between the plates (i.e. chamber height), $\nu = 0, 1, 2..$, Ai and Bi are Airy functions of the first and the second kind, respectively, and

$$X_p = \frac{(2\nu + 1)\pi}{h} \left(\frac{\rho}{2k^2} \right)^{1/3}.$$

To make the discussion of the chamber effect complete, we also calculate the contribution of resistive wakefields. The corresponding impedance can be calculated by [11]:

$$Z_{RW}(k) = \frac{Z_0 c}{4\pi} \frac{2s_0}{ca^2} \int_0^\infty \mathrm{sech}(x) \times \left(\frac{2}{1-i} \frac{1}{\sqrt{ks_0}} \cosh(x) - iks_0 \frac{\sinh(x)}{x} \right)^{-1} dx \quad , \tag{8}$$

where $a = h/2$, $s_0 = (2a^2/Z_0\sigma_c)^{1/3}$ and σ_c is the conductivity of the resistive wall material.
The amplitude of the energy modulation from one dipole is then [12]

$$p_2(k_\mu) = 2 \left| eI_0 b(k_\mu) Z_{FS,PP}(k_\mu) \right| , \tag{9}$$

where I_0 is the peak current, $b(k_\mu)$ is the bunching at the wavelength k_μ, e is the elementary charge, m_e is the electron rest mass and c is the speed of light in vacuum.

RESULTS AND DISCUSSION

In Fig. 2 we see the comparison of the impedance calculated for a single dipole of chicane 1. The first conclusion from this plot is that the CSR-impedance of the PP model is significantly different from that for free space. The difference is evident in the region 0-2 THz (note the typical frequency of the bunch $\frac{c}{2\pi\sigma_z} = 0.5$ THz). For higher frequencies the two models give very similar results. The second conclusion is that the contribution of RW is much smaller than that of CSR. For this reason, in the rest of the paper we will neglect RW and consider CSR wakes only.

Following Eq. (6-9) we calculated the amplitudes $p_2(k_\mu)$ using the parameters from Table 1. The results are illustrated in Fig. 3. From the plot we conclude that the spectral content of Δp_2 changes significantly between FS and PP impedance models. Up to ~ 600 µm the amplitudes are very close, but longer wavelength components get significantly suppressed by PP as compared to FS model. From Eq. (5) we conclude that this difference will play a role in bunching bandwidth broadening.

To verify our predictions we compare results of ELEGANT simulations. The impedance is included in the simulations using `ZLONGIT` element after each dipole of chicane 1. First, we take a look at the energy modulation for FS and PP models. Figure 4 shows the energy centroid of the electron bunch at the exit of chicane 1 in both cases. From the plot we see that the amplitude of the energy modulation for PP model is generally smaller.

ISBN: 978-3-95450-220-2 ISSN: 2673-5474 doi: 10.18429/JACoW-FEL2022-TUP74

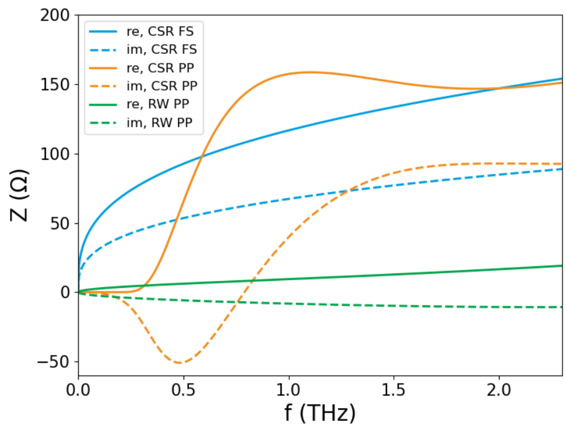

Figure 2: Impedance calculated for a single dipole of chicane 1.

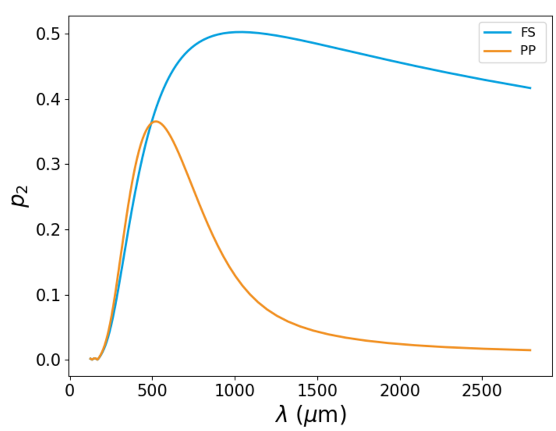

Figure 3: Amplitudes of the energy modulations at different wavelengths, calculated with Eq. (9).

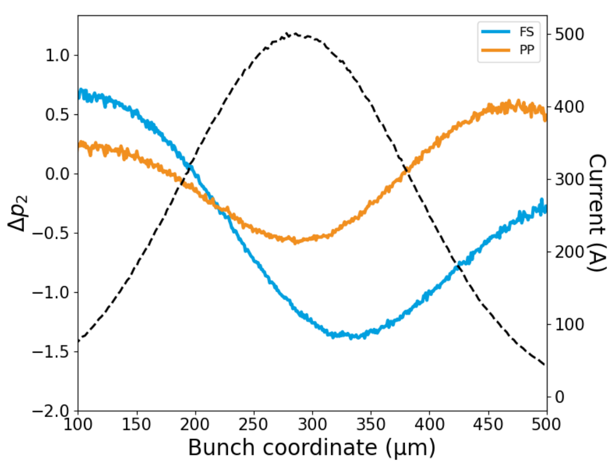

Figure 4: Energy centroid after chicane 1. Black dotted line is the current profile.

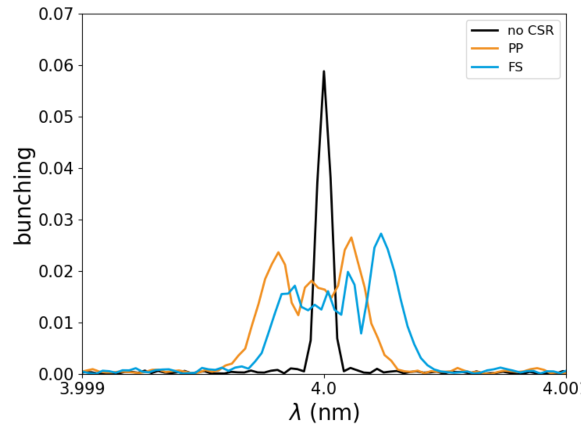

Figure 5: Bunching spectrum after chicane 2.

In Fig. 5 we see that the bunching spectrum for PP model is quite close to that for FS. Numerically calculated RMS bandwidth values are given in Table 2. Such a small difference between the two models can be explained using formulas given above. One can see that the amplitudes p_2 are entering Eq. (2) without any additional factors, while p_2 in Eq. (5) is multiplied by k_μ, which reduces the contribution from long wavelengths. From Fig. 3 one can see that the amplitudes p_2 are different only in the long wavelength range. This can explain why we have a significant difference in Δp_2 but not in the bandwidth.

We can also evaluate the spectral broadening from Eq. (5) with a semi-analytical approach. The shape of PP curve in Fig. 4 allows us to approximate Δp_2 very easily with Eq. (2) using only 1 term with $p_2 \approx 0.25$ and $k_\mu = 2\pi/(400\,\mu\mathrm{m})$. We plug in k_μ and p_2 in Eq. (5) and calculate the modified bunching bandwidth in terms of the wavelength: $\sigma_\lambda = 1.3 \cdot 10^{-4}$ nm. The calculated value is comparable with the simulation.

Table 2: RMS Bandwidths of the Bunching Spectra

No CSR	FS	PP
$8.3 \cdot 10^{-5}$ nm	$1.6 \cdot 10^{-4}$ nm	$1.5 \cdot 10^{-4}$ nm

CONCLUSION

We have employed analytical treatment to study the effect of CSR on EEHG bunching spectrum. We have presented analytical formulas and calculate the impedance inside the strong EEHG chicane and estimate the change in impedance given by the effect of the chicane chamber. We have concluded that RW impedance in our case is much smaller than the CSR impedance. We have also represented that the amplitudes of CSR fields can be affected by the chamber shielding in the long-wavelength range. The latter finding is confirmed by the ELEGANT simulations. The simulations also show that the chamber shielding does not significantly affect the

ISBN: 978-3-95450-220-2 ISSN: 2673-5474 doi: 10.18429/JACoW-FEL2022-TUP74

bunching spectrum. This finding has been explained qualitetively by analytical treatment. Finally, by a semi-analytical calculation of the bandwidth we have demonstrrated the quntitative consistency bentween the analytical treatment and the simnulations.

ACKNOWLEDGEMENTS

The authors gratefully acknowledge the Gauss Centre for Supercomputing e.V. (www.gauss-centre.eu) for funding this project by providing computing time through the John von Neumann Institute for Computing (NIC) on the GCS Supercomputer JUWELS [13] at Jülich Supercomputing Centre (JSC). The work is supported by BMBF within “05K2019-STAR”project.

REFERENCES

[1] G. Stupakov, “Using the Beam-Echo Effect for Generation of Short-Wavelength Radiation”, *Phys. Rev. Lett.*, vol. 102, p. 074801, 2009. doi:10.1103/PhysRevLett.102.074801

[2] E. Hemsing *et al.*, “Echo-enabled harmonics up to the 75th order from precisely tailored electron beams”,’ *Nat. Photonics*, vol. 10, pp. 512–515, 2016. doi:10.1038/nphoton.2016.101

[3] L. Schaper *et al.*, “Flexible and Coherent Soft X-ray Pulses at High Repetition Rate: Current Research and Perspectives”, *Appl. Sci.*, vol. 11, p. 9729, 2021. doi:10.3390/app11209729

[4] D. Samoilenko *et al.*, “Discussion on CSR instability in EEHG Simulation”, in *Proc. IPAC’21*, Campinas, Brazil, May 2021, pp. 1622–1625. doi:10.18429/JACoW-IPAC2021-TUPAB103

[5] D. Samoilenko *et al.*, “Sensitivity of EEHG Simulations to Dynamic Beam Parameters”, in *Proc. IPAC’22*, Bangkok, Thailand, Jun. 2022, pp. 1463–1466. doi:10.18429/JACoW-IPAC2022-TUPOMS024

[6] E. Hemsing, B. Garcia, Z. Huang, T. Raubenheimer, and D. Xiang, “Sensitivity of echo enabled harmonic generation to sinusoidal electron beam energy structure”, *Phys. Rev. Accel. Beams*, vol. 20, p. 060702, 2017. doi:1103/PhysRevAccelBeams.20.060702

[7] M. Borland, “elegant: A Flexible SDDS-Compliant Code for Accelerator Simulation”, in *Proc. 6th International Computational Accelerator Physics Conference (ICAP 2000)*, September 11-14, 2000, Darmstadt, Germany LS-287, doi:10.2172/761286

[8] N. Mirian *et al.*, “Characterization of soft x-ray echo-enabled harmonic generation free-electron laser pulses in the presence of incoherent electron beam energy modulations”, *Phys. Rev. Accel. Beams*, vol.24(8), p.080702, 2021. doi:10.1103/PhysRevAccelBeams.24.080702

[9] S. Di Mitri, S. Spampinati, “Microbunching instability study in a linac-driven free electron laser spreader beam line”, *Phys. Rev. Accel. Beams*, vol.20, p. 120701, 2017. doi:10.1103/PhysRevAccelBeams.20.120701

[10] G. Stupakov, D. Zhou, “Analytical theory of coherent synchrotron radiation wakefield of short bunches shielded by conducting parallel plates”, *Phys. Rev. Accel. Beams*, vol. 19, p.04402, 2016. doi:10.1103/PhysRevAccelBeams.19.044402

[11] K. Bane and G. Stupakov, “Using surface impedance for calculating wakefields in flat geometry”, *Phys. Rev. Accel. Beams*, vol. 18, p. 034401, 2015. doi:

[12] Z. Huang *et al.*, “Measurements of the linac coherent light source laser heater and its impact on the x-ray free-electron laser performance”, *Phys. Rev. ST Accel. Beams*, vol. 13, p.020703, 2010. doi:10.1103/PhysRevSTAB.13.020703

[13] D. Alvarez, “JUWELS Cluster and Booster: Exascale Pathfinder with Modular Supercomputing Architecture at Juelich Supercomputing Centre”, *Journal of large-scale research facilities*, vol. 7, p. A183, 2021. doi:10.17815/jlsrf-7-183

ISBN: 978-3-95450-220-2 ISSN: 2673-5474 doi: 10.18429/JACoW-FEL2022-TUP75

ARIA, A VUV BEAMLINE FOR EUPRAXIA@SPARC_LAB

M. Opromolla*[1], V. Petrillo[1], University of Milan, Milan, Italy
F. Nguyen, A. Petralia, A. Selce, ENEA-Frascati, Frascati, Italy
F. Stellato, University of Rome Tor Vergata and INFN-Rome Tor Vergata, Rome, Italy
M. Coreno[2,3], Z. Ebrahimpour, M. Ferrario, A. Ghigo, L. Giannessi[3], A. Marcelli[2,4], F. Villa, INFN-LNF, Frascati, Italy
[1] also at INFN-Milan, Milan and LASA, Segrate, Italy
[2] also at CNR-ISM, Trieste, Italy
[3] also at Elettra-Sincrotrone Trieste, Trieste, Italy
[4] also at RICMASS-International Centre for Material Science Superstripes, Rome, Italy

Abstract

EuPRAXIA@SPARC_LAB is a new Free Electron Laser (FEL) facility currently under construction at the Laboratori Nazionali di Frascati of the INFN. The electron beam driving the FEL will be delivered by an X-band normal conducting LINAC followed by a plasma wakefield acceleration stage. It will be characterized by a small footprint and include two different plasma-driven photon beamlines. In addition to the soft-X-ray beamline, named AQUA and delivering to the user community ultra-bright photon pulses for experiments in the water window, a second beamline, named ARIA, has been recently proposed and included in the project. ARIA is a seeded FEL beamline in the High Gain Harmonic Generation configuration and generates coherent and tunable photon pulses in the range between 50 and 180 nm. Here we present the potentiality of the FEL radiation source in this low energy range, by illustrating both the layout of the FEL generation scheme and simulations of its performances.

INTRODUCTION

Free Electron Laser (FEL) light sources are capable of generating high quality and tunable pulses in the VUV-X-ray energy range, characterized by a peak brilliance larger than 10^{30} photons s^{-1}mrad^{-2}mm^{-2}, 0.1 % bandwidth and a short pulse duration, of the order of tens of femtoseconds or even less, which are needed for a wide class of experiments [1–7]. Thanks to such output pulse properties, FELs allow ultrafast time-resolved measurements and provide a high signal-to-noise ratio [8–10]. Due to the required space for electron acceleration, undulators and photon beamlines (in the order of many hundreds of meters up to few km), the present X-ray FEL facilities can only be realized in large scale laboratories and few of them are currently in operation.

Plasma Wakefield Acceleration, either laser- or particle-driven, is recognized as one of the most promising techniques for novel high-gradient accelerating structures: very high accelerating gradients beyond 1 GV/m can be achieved [11–17], *i.e.* about one order of magnitude larger than the ones of a normal-conducting LINAC structure, thus leading to an essential footprint and cost reduction for the whole facility. The EuPRAXIA Design Study [18] aims at realizing a new FEL facility driven by plasma acceleration. In this framework, the INFN Frascati National Laboratories, as a part of the EuPRAXIA project, will host EuPRAXIA@SPARC_LAB [19], a compact facility based upon a high brightness X-band LINAC, a particle-driven plasma acceleration stage and a FEL. The layout of its acceleration stage and FEL undulator lines is shown in Fig. 1. Before being matched and injected into the undulator line, the electrons are accelerated in two pairs of eight X-band accelerating cavities, separated by a magnetic bunch compressor (BC in Fig. 1) and followed by the plasma module.

This facility is able to fulfill the 1 GeV beam energy foreseen by EuPRAXIA in a low charge configuration by using particle- or laser- driven plasma acceleration, but it also can achieve the same energy at an higher charge from the X-band RF LINAC without the plasma module. The electron beam parameters at 1 GeV for FEL operation in both beam modes are reported in Table 1.

Table 1: EuPRAXIA@SPARC_LAB Electron Beam Parameters. The Normalized Emittance Is Here Reported

	LINAC	LINAC+PWA
Charge (pC)	200	30
Bunch length (rms, μm)	34	2
Energy (GeV)	1	1
Peak current (kA)	0.7	1.8
Slice energy spread (%)	0.01	0.05
Slice emittance (mm mrad)	0.5	0.8

As required by the EuPRAXIA Design Study, a first FEL beamline called AQUA [20–22], operating in the water window at 3-4 nm, was funded and included in the project baseline. It will use the full undulator length available to the project and requires very high quality electron beams.

A second lower photon energy FEL beamline in the VUV range (around 50-180 nm), called ARIA [23], has been recently considered and included in the project baseline, although not yet fully funded. In comparison with AQUA, such VUV beamline is highly flexible, with a larger input parameter acceptance, and requires a shorter magnetic length to lase.

* michele.opromolla@mi.infn.it

ISBN: 978-3-95450-220-2 ISSN: 2673-5474 doi: 10.18429/JACoW-FEL2022-TUP75

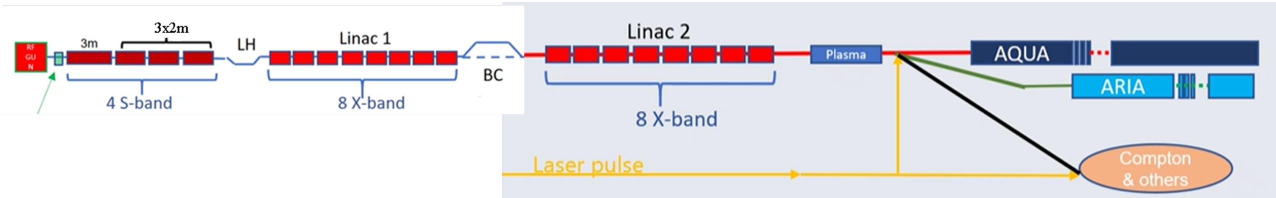

Figure 1: Layout of the EuPRAXIA@SPARC_LAB acceleration and undulator chain.

In this proceeding we will discuss the ARIA FEL line, including its layout, operating modes and performances, and give an overview of its scientific case.

FEL SIMULATIONS

ARIA is a seeded FEL beamline in the standard High-Gain Harmonic Generation (HGHG) configuration, delivering continuously tunable pulses in the VUV wavelength spectrum between 50 and 180 nm [24]. Figure 2 shows its compact layout: the laser seed pulse modulates the electron bunches in a three meter-long modulator, followed by a dispersive section for electron density modulation at higher harmonics of the seed and a final amplification stage made up of four radiators. Table 2 lists the main characteristics of the undulators and the seeding source.

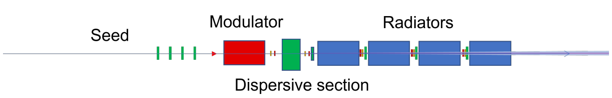

Figure 2: Layout of the ARIA HGHG FEL. The seed pulse is superimposed on the electron bunches at the modulator entrance; the dispersive section is a four-dipole chicane which converts the energy modulation into a density modulation. Its length ~2 m is kept constant and the dispersion strength is tuned by varying the dipoles' magnetic fields. The amplification stage is made up of four radiators.

Table 2: ARIA Line: Undulator (Top) and Seed Laser (Bottom) Specifications

Undulator	**Modulator**	**Radiator**
Length (m)	3	4 x 2.1
Period length (cm)	10	5.5
Type	Apple-II	Apple-II
Seed	**Range**	**Simulated**
Wavelength (nm)	410-560	460
Pulse energy (μJ)	1-30	6-30
FWHM Duration (fs)	150-200	170

The electron bunches entering this line are seeded by a long near-UV/blue laser, which can be realized with commercial OPA amplifiers. The main seed parameters considered in the following simulation results are reported in the third column of Table 2. The choice of a long wavelength seed simplifies the switch between two OPA processes, allowing to cover the full wavelength range (after second harmonic generation) with harmonic orders 3-9, while the use of APPLE-II undulators allows amplification of pulses with variable polarization.

The flexibility associated to the two-fold electron acceleration in the conventional LINAC or through the beam-driven plasma module enables FEL operation in the long and short beam modes. The electron beam parameters for both operating modes are summarized in the third and fourth column of Table 1, respectively. On one hand, long and high-charge electron bunches from the LINAC generate narrow linewidth photon pulses suitable for spectroscopic applications in the first case. On the other hand, short and low-charge electron bunches amplify a single longitudinal mode [25], whose shot-to-shot stability and second-order coherence are ensured by the presence of the seed.

The Xie model [26] gives an estimate of the expected performances in terms of photon pulse energy. Short electron bunches provide pulse energies below 20 μJ in the 50-70 nm range, while up to 60 μJ are obtained at longer wavelengths. The circular polarization may allow to reach slightly larger (>20 μJ) photon energies for intermediate wavelength values around 100 nm. Besides, pulse energy levels of the order of hundreds-μJ are obtained in the long beam mode.

The ARIA line is therefore capable of producing FEL pulses characterized by an energy of 10-100 μJ and very short pulse durations, determined by the short electron bunch length and the large gain bandwidth. The FEL gain bandwidth is proportional to the Pierce parameter ρ_{3D} as well as to the ratio $\sqrt{L_{tot}^{SASE}/L_u}$ between the SASE saturation length and the actual undulator length, when $L_u < L_{tot}^{SASE}$: a large ρ_{3D} parameter (of the order of 10^{-2}) in this long wavelength range and the presence of the seed, especially when driving the FEL with short and high-current electron bunches from the plasma acceleration module, enable the generation of ultra-short femtosecond-class pulses.

Simulations of the ARIA FEL has been carried out by using the 3D FEL code GENESIS 1.3 used in time-dependent mode, with the maximum available precision [27] and considering an ideal electron beam, characterized by a Gaussian current profile and seeded by a FT-limited laser pulse. The main e-beam and seed properties are listed in Tables 1 and 2, respectively. The electron beam is matched to the modulator, with an average Twiss beta function of 8-9 m. The harmonic FEL emission is optimized by finely tuning both the seed intensity and the dispersion strength R_{56}, representing the particle longitudinal displacement per unit momentum error.

ISBN: 978-3-95450-220-2 ISSN: 2673-5474 doi: 10.18429/JACoW-FEL2022-TUP75

Starting from the 460 nm seed pulse, the optimized values of seed energy Es and dispersion strength R_{56} vs harmonic number (HN) are shown in Fig. 3: short electron bunches were considered at first, but these results are valid for both beam modes. The achieved pulse energies and FWHM pulse durations at different harmonics of the seed are reported in Fig. 4: for each case, the considered seed energy and dispersion strength are the ones presented in Fig. 3.

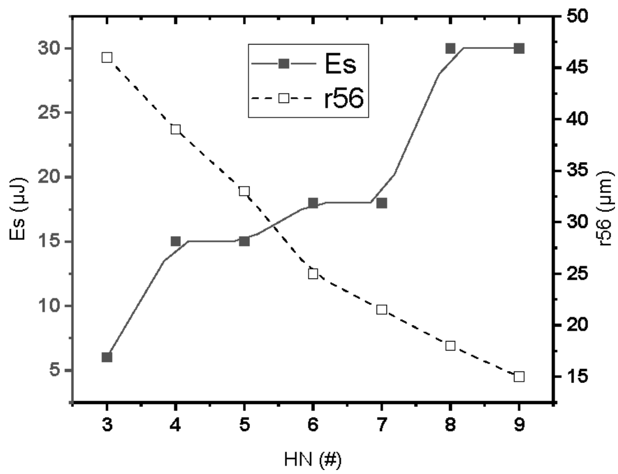

Figure 3: Seed energy Es (solid line, black squares) and dispersion strength R_{56} (dashed line, white circles) vs harmonic number HN of the 460 nm seed.

Two example cases of output pulses at saturation, namely the third (HN=3, ~153 nm) and ninth (HN=9, ~51 nm) harmonics of the seed, are shown in Figure 5. The simulated FEL pulse temporal profiles (HN=3 yellow, HN=9 orange) in the two beam modes (see Table 1) are here presented: the low-charge, short beam operation mode is shown on the left, while the results on the right are obtained by operating with the higher charge and long electron beams. The corresponding spectral amplitudes are also shown. Lower harmonics ($\leq$ 5) in the short beam mode (30 pC case) saturate after two or three radiators only: early saturation deteriorates and stretches the output pulse. Larger seed intensities may help avoiding it, or the radiation can be extracted beforehand, eventually using the last radiator for pulse gymnastics or double pulses' generation [28, 29]. The radiation pulse properties in the short (a) and long (b) beam modes are summarized, for the odd harmonic orders in the range 3-9, in Table 3. The performances in terms of pulse energy agree with the expected ones from the Xie scaling relations. The longitudinal coherence of the FEL radiation is described by the time-bandwidth product reported in Table 3: FEL pulses close to the Fourier-Transform limit are produced in the short beam mode. Stable FEL pulses, characterized by few tens to hundreds-μJ pulse energies and ~15-100 fs pulse durations can be produced in the whole spectral range.

SCIENTIFIC GOALS

Many different experimental opportunities may be provided by the ARIA beamline. Its photon energy range may

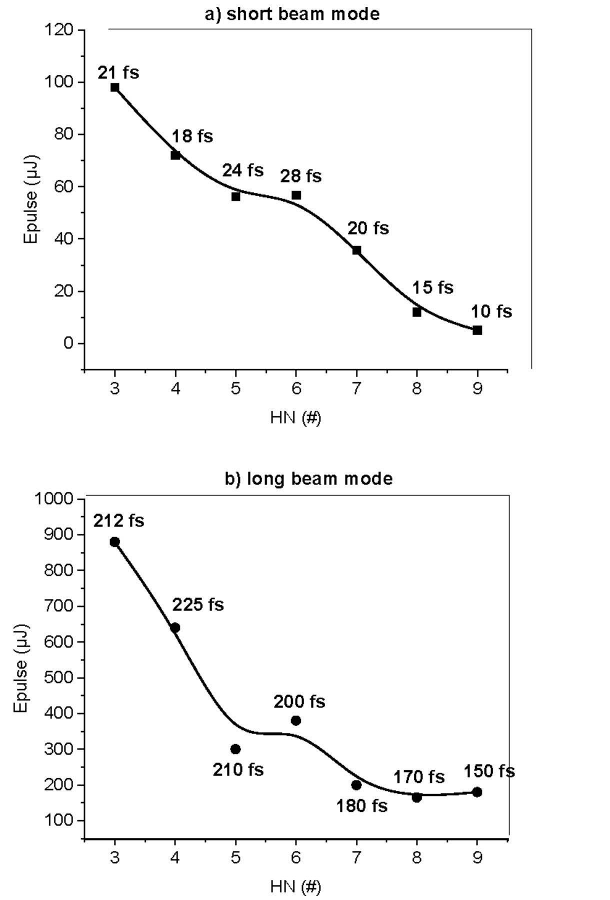

Figure 4: Output pulse energy at saturation vs harmonic number, starting from the 460 nm seed pulse. Top plot a): short beam mode, 30 pC case. Bottom plot b): long beam mode, 200 pC case. The FWHM pulse duration is specified on top of each point.

give access to the photo-ionization thresholds and to the valence ionic states of atmospheric constituents. The ability of the VUV-FEL to shift the wavelength of the scattered light from the visible into the deep UV will allow to probe new electronic transitions within the 7-20 eV range for classes of cluster materials such as nano-carbons and potential gap dielectrics. Its pulsed time structure makes it an ideal source for spectroscopy and studies of the light-induced dynamics in such complex media with state-of-the-art mass spectrometric and electron spectrometry techniques [30]. The possibility of changing the polarization of the FEL light allows to obtain important information, e.g., correlating chirality and natural dichroism in biotic media. The high brightness of this FEL source may enable the first direct analysis of low density systems as well as spectroscopic studies of exotic species. Due to the extremely low number of target particles in cluster experiments, great advances are also expected at a VUV FEL such as the ARIA beamline. The implementation of resonant techniques in the VUV range can enable studies on aggregates of elements with high vaporization temperatures, allowing to look at the formation of free clusters of varied chemical nature [31]. A VUV monochromatic beam-

ISBN: 978-3-95450-220-2 ISSN: 2673-5474 doi: 10.18429/JACoW-FEL2022-TUP75

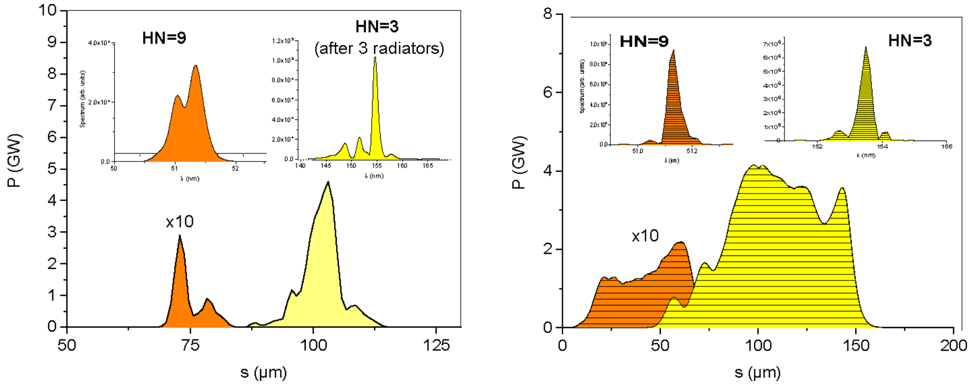

Figure 5: FEL emission at 51 nm (orange), 9^{th} harmonic, and 153 nm (yellow), 3^{rd} harmonic of the 460 nm seed. Output pulses' longitudinal power profile (GW) at saturation vs s(μm). The corresponding spectral amplitudes (arb. units) vs λ(nm) are shown above. Left: short beam mode. Right: long beam mode. The lower wavelength pulse profile (orange) is magnified and shifted with respect to the other one for a better visualization. In the short 30 pC beam mode, the longer wavelength saturates after 3 radiators only.

Table 3: Radiation Properties in the 50–150 nm Spectral Range at Saturation, in the Short (a) and Long (b) Pulse Mode

Radiation properties / HN	3a*	3b	5a	5b	7a	7b	9a	9b
Wavelength (nm)	153	153	92	92	65	65	51	51
Seed energy (μJ)	6	6	15	15	18	18	30	30
Dispersion R56 μm)	46	46	33	33	23	23	15	15
Pulse energy (μJ)	100	880	57	290	36	199	4	13
Photons/shot (10^{13})	7.6	67	2.6	13	1.16	6.47	0.1	3.3
FWHM Duration (fs)	21	212	24	210	20	180	10	150
Bandwidth BW (%)	1.7	0.23	0.7	0.11	0.52	0.08	0.47	0.14
Time-BW Product (#)	1.88	2.57	1.5	2.03	1.3	1.8	0.69	3.33
Pulse size (mm)	0.74	0.85	0.63	0.56	0.51	0.45	0.35	0.43
Pulse divergence (mrad)	0.1	0.26	0.07	0.18	0.05	0.15	0.04	0.11

*saturation after 3 radiators.

line together with photo-emission techniques would allow the study of species of interest in the physics of the upper atmosphere and in combustion phenomena. The electronic structure of these species is not very well known in the region of photo-ionization due to the lack of high-intensity sources at wavelengths below 180 nm. Finally, ARIA represents a perfect source for two-photon photo-emission (2PPE) experiments, a technique that matches the advantages of direct and inverse photo-emission [32].

CONCLUSIONS

The feasibility and expected performances of a compact, flexible and cost-effective FEL facility in the VUV spectral region have been investigated. We presented FEL simulations and some of the possible applications of the emitted radiation. This FEL line is capable of delivering close to Fourier-transform limit pulses [33] and gives the possibility of tuning the pulse duration in two different conditions: ultra-short pulses with a large gain bandwidth are generated by a low-charge, short electron bunches from the plasma wakefield acceleration, or intensity and spectrally stable, ultra-narrow bandwidth pulses by longer bunches

Scientific investigations in atomic, molecular and cluster physics may benefit from this beamline, broadening the possibilities offered by existing FELs or other sources, such as harmonics emitted in gas, in the VUV spectral region.

REFERENCES

[1] C. Bostedt et al., "Linac coherent light source: The first five years", *Rev. Mod. Phys.*, vol. 88, p. 015007, 2016. doi:10.1103/RevModPhys.88.015007

[2] C. Pellegrini, A. Marinelli, and S. Reiche, "The physics of x-ray free-electron lasers",*Rev. Mod. Phys.*, vol. 88, p. 015006, 2016. doi:10.1103/RevModPhys.88.015006

[3] P. Emma et al., "First lasing and operation of an ångstrom-wavelength free-electron laser", *Nat. Photonics*, vol. 4, pp. 641–647, 2010. doi:10.1038/nphoton.2010.176

[4] W. Ackermann et al., "Operation of a free-electron laser from the extreme ultraviolet to the water window", *Nat. Photonics*, vol. 1, pp. 336–342, 2007. doi:10.1038/nphoton.2007.76

[5] Z. Huang and I. Lindau, *SACLA hard-X-ray compact FEL*, *Nat. Photonics*, vol. 6, pp. 505–506, 2012. doi:10.1038/nphoton.2012.184

ISBN: 978-3-95450-220-2 ISSN: 2673-5474 doi: 10.18429/JACoW-FEL2022-TUP75

[6] E. Allaria *et al.*, "The FERMI free-electron lasers", *J. Synchrotron Radiat.* , vol. 22, pp. 485–491, 2015. doi:10.1107/S1600577515005366

[7] I.S. Ko *et al.*, "Construction and commissioning of PAL-XFEL facility", *Applied Sciences*, vol. 7, 2017. doi:10.3390/app7050479

[8] M. Harmand *et al.*, "Achieving few-femtosecond time-sorting at hard X-ray free-electron lasers", *Nat. Photonics*, vol. 7, pp. 215–218, 2013. doi:10.1038/nphoton.2013.11

[9] H.-S. Kang *et al.*, "Hard X-ray free-electron laser with femtosecond-scale timing jitter", *Nat. Photonics*, vol. 11, pp. 708–713, 2017. doi:10.1038/s41566-017-0029-8

[10] S. Schulz *et al.*, "Femtosecond all-optical synchronization of an X-ray free-electron laser", *Nat. Commun.*, vol. 6, no. 5938, 2015. doi:10.1038/ncomms6938

[11] E. Esarey, C.B. Schroeder and W.P. Leemans, "Physics of laser-driven plasma-based electron accelerators", *Rev. Mod. Phys.*, vol. 81, pp. 1229–1285 (2009). doi:10.1103/RevModPhys.81.1229

[12] J.B. Rosenzweig, B. Breizman, T. Katsouleas and J.J. Su, "Acceleration and focusing of electrons in two-dimensional nonlinear plasma wake fields", *Phys. Rev. A*, vol. 44, 1991. doi:10.1103/PhysRevA.44.R6189

[13] W.P. Leemans, B. Nagler, A. Gonsalves J, C.S. Tóth, K. Nakamura, C. Geddes, *et al.*, GeV electron beams from a centimetre-scale accelerator, *Nat. Phys.*, vol. 2, pp. 696–699, 2006. doi:10.1038/nphys418

[14] I. Blumenfeld *et al.*, "Energy doubling of 42 GeV electrons in a metre-scale plasma wakefield accelerator", *Nature*, vol. 445, p. 7129, 2007. doi:10.1038/nature05538

[15] J.B. Rosenzweig, G. Andonian, M. Ferrario, P. Muggli, O. Williams, V. Yakimenko, *et al.*, "Plasma Wakefields in the Quasi-Nonlinear Regime", *AIP Conf. Proceedings*, vol. 1507, 2012. doi:10.1063/1.4773767

[16] M. Litos *et al.*, "High-efficiency acceleration of an electron beam in a plasma wakefield accelerator", *Nature*, vol. 515, pp. 92–95 (2014), doi:10.1038/nature13882

[17] S. Romeo, E. Chiadroni, M. Croia, M. Ferrario, A. Giribono, A. Marocchino, *et al.*, "Simulation design for forthcoming high quality plasma wakefield acceleration experiment in linear regime at SPARC_LAB", *Nucl. Instrum. Methods Phys. Res., Sect.* A, vol. 909, pp. 71–75, 2018. doi:10.1016/j.nima.2018.02.081

[18] R. Assmann *et al.*, "EuPRAXIA conceptual design report", *Eur. Phys. J. Spec. Top.*, vol. 229, pp. 3675–4284, 2020. doi:10.1140/epjst/e2020-000127-8

[19] M. Ferrario *et al.*, "EuPRAXIA@SPARC_LAB Design study towards a compact FEL facility at LNF", *Nucl. Instrum. Methods Phys. Res., Sect.* A, vol. 909, pp. 134–138, 2018. doi:10.1016/j.nima.2018.01.094

[20] F. Villa, A. Cianchi, M. Coreno, S. Dabagov, A. Marcelli, *et al.*, "Design study of a photon beamline for a soft X-ray FEL driven by high gradient acceleration at EuPRAXIA@SPARC_LAB", *Nucl. Instrum. Methods Phys. Res. Sect.* A, vol. 909, pp. 294-–297, 2018. doi:10.1016/j.nima.2018.02.091

[21] F. Villa, A. Balerna, E. Chiadroni, A. Cianchi, M. Coreno, S. Dabagov, *et al.*, "Photon Beam Line of the Water Window FEL for the EuPRAXIA@ SPARC_LAB Project", *J. Phys. Conf. Ser.*, Vol. 1596, p. 012039 2020. doi:10.1088/1742-6596/1596/1/012039

[22] A. Balerna, S. Bartocci, G. Batignani, A. Cianchi, E. Chiadroni, *et al.*, "The Potential of EuPRAXIA@SPARC_LAB for Radiation Based Techniques", *Condens. Matter*, vol. 4, no. 30, 2019. doi:10.3390/condmat4010030

[23] F. Villa, M. Coreno, Z. Ebrahimpour, L. Giannessi, A. Marcelli, M. Opromolla, *et al. ARIA—A VUV Beamline for EuPRAXIA@SPARC_LAB*, Condens. Matter 7, 11 (2022), doi:10.3390/condmat7010011

[24] L.H. Yu *et al.*, "High gain harmonic generation free electron laser", *Science*, vol. 289, pp. 932–934, 2000. doi:10.1126/science.289.5481.932

[25] J.B. Rosenzweig *et al.*, "Generation of ultra short, high brightness electron beams for single spike SASE FEL operation", *Nucl . Instrum . Methods Phys. Res.* A, vol. 593, pp. 39–44, 2008. doi:10.1016/j.nima.2008.04.083

[26] M. Xie, "Design optimization for an X-ray Free Electron Laser driven by SLAC Linac", *Proceedings Particle Accelerator Conference*, vol. 1, pp. 183–185, 1995. doi:10.1109/PAC.1995.504603.

[27] S. Reiche, "GENESIS 1.3: a fully 3D time-dependent FEL simulation code", *Nucl. Instrum. Methods Phys. Res., Sect.* A, vol. 429, pp. 243–248, 1999. doi:10.1016/S0168-9002(99)00114-X

[28] V. Petrillo *et al.*, "Observation of time domain modulation of free electron laser pulses by multipeaked electron-energy spectrum", *Phys. Rev. Lett.*, vol. 111, 2013. doi:10.1103/PhysRevLett.111.114802

[29] A. Petralia *et al.*, "Two color radiation generated in a seeded free electron laser with two electron beams", *Phys. Rev. Lett.*, vol. 115, p. 014801, 2015. doi:10.1103/PhysRevLett.115.014801

[30] S. Pathak, L.M. Ibele, R. Boll, C. Callegari, A. Demidovich, *et al.*, "Tracking the ultraviolet-induced photochemistry of thiophenone during and after ultrafast ring opening", *Nat. Chem.*, vol. 12, pp. 795–800, 2020. doi:10.1038/s41557-020-0507-3

[31] M., Bogana, L. Ravagnan, C.S. Casari, A. Zivelonghi, A. Baserga, *et al.*, "Leaving the fullerene road: presence and stability of sp chains in sp2 carbon clusters and cluster-assembled solids", *New J. Phys.*, vol. 7, p. 81, 2005. doi:10.1088/1367-2630/7/1/081

[32] U. Höfer, I. Shumay, C. Reuß, U. Thomann, W. Wallauer and T. Fauster, "Time-resolved coherent photoelectron spectroscopy of quantized electronic states on metal surfaces", *Science*, vol. 277, pp. 1480-–1482, 1997. doi:10.1126/science.277.5331.1480

[33] E. Allaria, B. Diviacco, C. Callegari, P. Finetti, B. Mahieu, J. Viefhaus, *et al.*, "Control of the Polarization of a Vacuum-Ultraviolet, High-Gain, Free-Electron Laser", *Phys. Rev. X*, vol. 4, p. 041040, 2014. doi:10.1103/PHYSREVX.4.041040

ISBN: 978-3-95450-220-2 ISSN: 2673-5474 doi: 10.18429/JACoW-FEL2022-TUP76

TRANSVERSALLY SEPARATED CROSSED POLARIZED FEL SUBPULSES

G. Perosa*, F. Sottocorona, Università degli Studi di Trieste, Trieste, Italy
E. Allaria, F. Bencivenga, A. Caretta, G. De Ninno[2], L. Foglia, S. Di Mitri, D. Garzella,
L. Giannessi[1], S. Laterza, R. Mincigrucci, G. Penco, C. Spezzani, P. Rebernik Ribic, M. Trovò,
Elettra-Sincrotrone Trieste S.C.p.A., Basovizza, Italy
S. Khan, Center for Synchrotron Radiation, TU Dortmund University, Dortmund, Germany
[1]also at Laboratori Nazionali di Frascati, INFN, Frascati, Italy
[2]also at University of Nova Gorica, Nova Gorica, Slovenia

Abstract

The extension of four-wave mixing (FWM) technique to the extreme ultraviolet and soft X-ray ranges allows to monitor the dynamics of coherent excitations of matter, when realized with the exquisite coherent property of bright FEL pulses. We show for the first time a scheme to provide transversally separated pulses with parallel or crossed linear polarizations, realized at FERMI FEL. This configuration paves the way to explore additional features of pump and probe and FWM techniques, and, in particular, the possibility to excite a transient polarization grating on the sample. For this reason, such a technique is important for the detection of circular dichroism and chiral properties of matter and the characterization of spin waves and magnons. By tailoring the electrons trajectory along the undulator line, we demonstrate the possibility of deliver balanced and stable couple of pulses with an horizontal separation of the order of millimeters at the focusing mirror of the experimental station.

INTRODUCTION

Modern science advancement relies on the possibility to produce short laser-like coherent pulses in the XUV regime and in the X-rays to probe electronic structure in atoms, molecules and solid state matter [1]. In this scenario, free-electron lasers (FELs) are invaluable tools for research. In particular, the versatility of seeded FELs scheme is paving the way towards the tayloring of coherent light and its exploitation in novel experimental schemes [2–4]. One of the most known example of the FEL-based experiment is the four-wave mixing (FWM) technique in the extreme ultraviolet and soft X-ray ranges [5]. It is well established that the interference of two pulses with linear parallel polarizations will result in a modulation of the light intensity, translated into a density grating at the sample position. On the contrary, when the polarizations are crossed, a sinusoidal oscillation of the light chirality is obtained and, consequently, a polarization grating is induced in the sample. Although the principle of this technique has been already demonstrated in the optical regime [6], FEL radiation can provide the proper wavelength range to investigate the chiral features of a sample down to nanometer scale. In this work we demonstrate that FERMI FEL1 [7] can provide the kind of light required for this type of experiment, by delivering spatially separated crossed polarized pulses, preserving the good spectral properties of seeded FELs.

* giovanni.perosa@elettra.eu

EXPERIMENTAL REALIZATION

From now on we are going to refer to the FEL scheme with transversally separated subpulses with crossed or parallel polarizations as TSXPU or TSPPU respectively. As already explained and as the name underlines there are two main ingredients that are crucial. In [8], a possible solution to get crossed polarized beams is proposed and consists of splitting the undulator line into two sections. Following this prescription, the overall setup for FEL1 used for the experiment is shown in Fig. 1.

Table 1: FEL and Electrons Parameters

Parameters	Values
Electron beam energy	1.3 GeV
Seed laser wavelength	249.6 nm
Seed laser energy	26 µJ
FEL harmonic	12
FEL wavelength	20.8 nm
FEL polarization	LV+LH, LV+LV
FEL energy pulse	8 µJ per pulse

The possibility to generate crossed or parallel polarized pulses that are also separated in the horizontal plane is given instead by the careful design of the electrons' trajectory [9, 10]. In fact, the introduction of an angle θ between the directions followed along each section results in a separation d which is proportional approximately to $d \approx \theta L$ (for small θ), where L is the distance from the diagnostic or experimental station. The general idea in shown in Fig. 2.

However, it becomes mandatory to balance the reduction of FEL gain given by the off-axis trajectory, the increase of the separation given by the tilt and the relative energy pulse of the two beams. To do so, we tested a trajectory given by two line segments, one for each three-undulators section, both off-axis with respect to the undulator line. This strategy resulted successful to overcome the aforementioned issues and is summarized in Fig. 3. Another possible origin for the reduction of the signal could be a imperfect microbunches rotation given by the kicks in the trajectory [10]. From the practical point of view, we exploit the correctors along the undulator line, determining an increasing kick to the left for

ISBN: 978-3-95450-220-2 ISSN: 2673-5474 doi: 10.18429/JACoW-FEL2022-TUP76

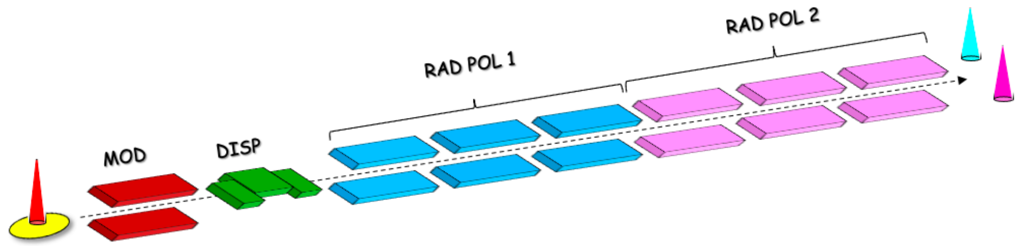

Figure 1: Layout of the scheme realized on FEL1 at FERMI. The undulator line is broken into 2 sections: the first one is lasing along a tilted direction with a specific polarization; in the second one the electron bunch follows a different trajectory, and the pulse is prepared with a polarization that can be parallel or orthogonal to the first.

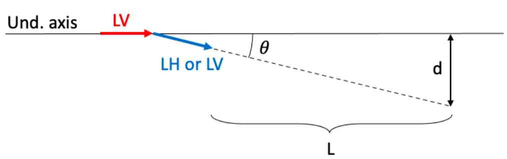

Figure 2: Basic idea of trajectory tilting.

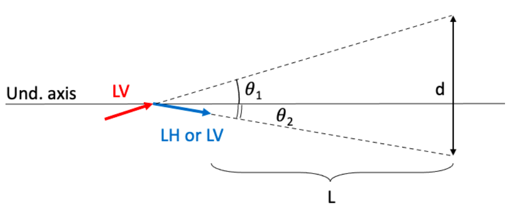

Figure 3: Geometry of the trajectory used for the experiment.

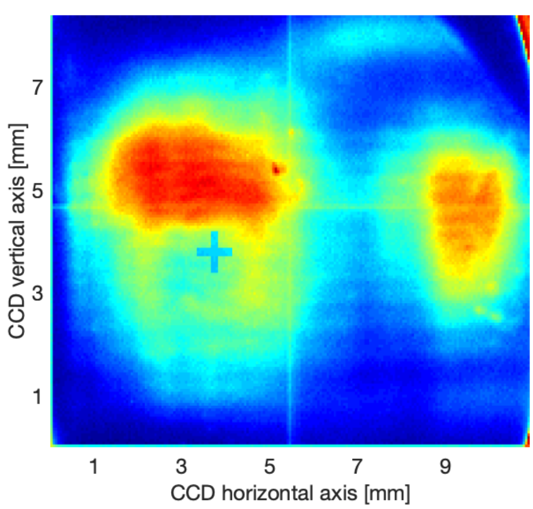

Figure 4: CCD image of the two subpulses. On the right the horizontally polarized pulse; on the left the vertically polarized one.

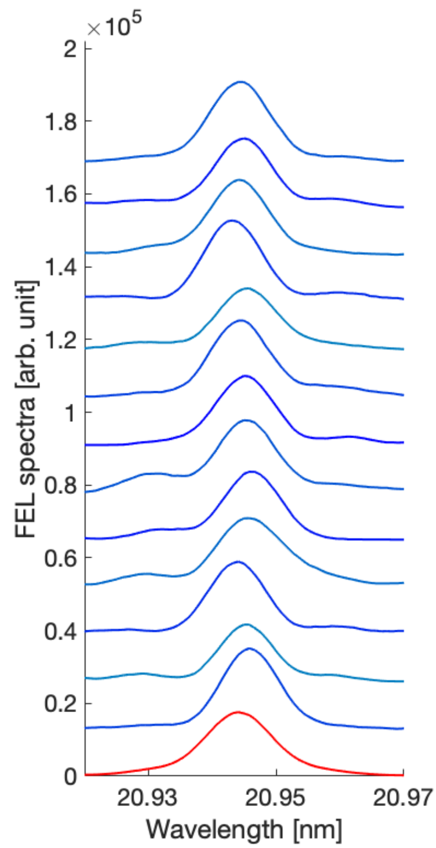

Figure 5: FEl spectra of the TSXPU. Single shot sepctra in blue; averaged spectrum over 500 shots in red.

the first three radiators and to the right for the last three. The machine parameters are summarized in Table 1: a 1.3 GeV electron beam is used, along with a 249.6 nm seed laser to produce light at 20.8 nm, corresponding to harmonic 12. At the experimental station, approximately 70 m after the last undulator, a CCD is used to measure the spatial separation of the two subpulses. A false colours image, averaged over 500 shots is shown in Fig. 4, demonstrating the neat separation of ≈5 mm between the centers of the transverse modes. We

ISBN: 978-3-95450-220-2 ISSN: 2673-5474 doi: 10.18429/JACoW-FEL2022-TUP76

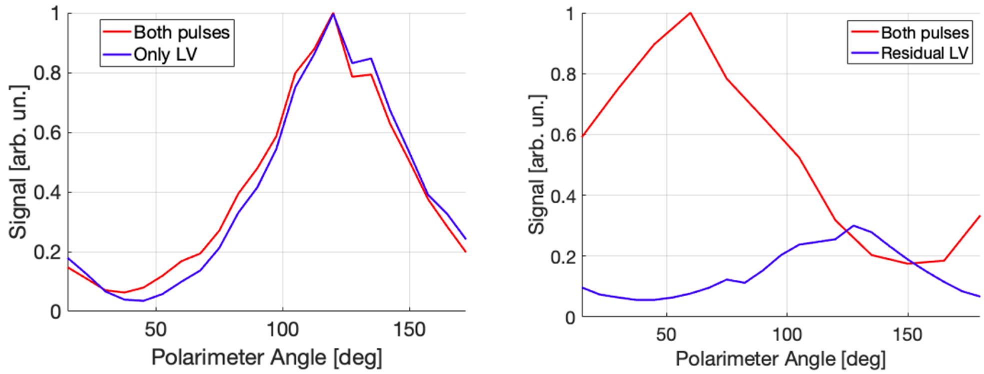

Figure 6: Results of the polarimeter measurement for the two separated pulses: on the left, the comparison of the normalized signal in the case of both pulses (red curve) and only the first one (blue curve) when the LV pulse is centered on the detector; on the right the comparison of the normalized signal in the case of both pulses (red curve) and the residual LV light (blue curve) when the LH pulse is centered on the detector.

recall that the right spot is the one corresponding to the first pulse (LV), while the left is for the second one (LH). Referring to Fig. 3, we estimate the sum $\theta_1 + \theta_2$ to be 100 µrad, which is consistent with the value determined looking at the beam position monitors.

POLARIZATION MEASUREMENT

The degree of polarization of the two subpulses in the TSXPU has been measured separately using a polarimeter and a mirror to move the position of the subpulses. This gives us the possibility to center one of the two spots on the detector. Its geometry was such that the maximum (minimum) reflectivity for the linear horizontal polarization was obtained at 45 degrees (135 degrees). The results are shown in Fig. 6. In the left plot, we compare the normalized signal registered for the linear vertical polarization with and without the second pulse, after centering the first signal on the detector. This second scheme was achieved opening all the undulators after the third to 100 mm gap. From this measurement we were expecting a minimum for 45 degrees, since the second pulse is not impinging on the detector and the light should be purely vertically polarized. The single pulse curve (the blue one) shows the expected minimum at 45 degrees, slightly shifted towards a lower angle when the second pulse is present (red curve). This means that, even if they are significantly separated, there is a small spurious contribution coming from the horizontally polarized pulse. Both plots do not follow Malus' law of intensity, most probably because of the non linear response of the detector. In the right plot instead, we compare the signal registered in the position of the LH pulse in two cases: last three undulators are tuned or open. As before, given the spatial separation between subpulses, a minimum at 135 degrees should be expected in the former case and a flat profile in absence of signal. However, in this case, we see that a non-trivial contribution coming from the LV light (blue curve). This signal is high enough to shift minimum and maximum of ≈15 degrees. This suggests that there is a partial overlapping with the other mode and a more elliptic degree of polarization in the second spot.

CONCLUSION

In conclusion, we have demonstrated and characterized a novel FEL scheme designed to deliver transversally separated crossed or parallel polarized subpulses. This configuration provides a "ready-to-go" option to extend FWM technique and induce polarization gratings on magnetic or dichroic samples or detect chiral properties of matter. This scheme is achieved by tilting the electron trajectory in order to separate in space the emitted light, but still preserving part of the FEL gain along the splitted undulator line. At harmonic 12 of FERMI FEL1, corresponding to 20.8 nm, we were able to obtain balanced light pulses of ≈8 µJ each with a separation of 5 mm. Polarization measurements confirm a nearly perfectly linear degree of polarization for both pulses.

REFERENCES

[1] C. Pellegrini, A. Marinelli, and S. Reiche, "The physics of x-ray free-electron lasers", *Rev. Mod. Phys.*, vol. 88, p. 015006, 2016. doi:10.1103/RevModPhys.88.015006

[2] K. C. Prince *et al.*, "Coherent control with a short-wavelength free-electron laser", *Nat. Photonics*, vol. 10, pp. 176–179, 2016. doi:10.1038/nphoton.2016.13

[3] D. You *et al.*, "New Method for Measuring Angle-Resolved Phases in Photoemission", *Phys. Rev. X*, vol. 10, p. 031070, 2020. doi:10.1103/PhysRevX.10.031070

[4] G. Penco *et al.*, "Nonlinear harmonics of a seeded free-electron laser as a coherent and ultrafast probe to investigate

ISBN: 978-3-95450-220-2 ISSN: 2673-5474 doi: 10.18429/JACoW-FEL2022-TUP76

matter at the water window and beyond", *Phys. Rev. A*, vol. 105, p. 053524 (2022).
doi:10.1103/PhysRevA.105.053524

[5] F. Bencivenga *et al.*, "Four wave mixing experiments with extreme ultraviolet transient gratings", *Nature*, vol. 520, pp. 205-208, 2015.
doi:10.1038/nature14341

[6] M. Terazima, "A New Method for Circular Dichroism Detection Using Cross-Polarized Transient Grating", *J. Phys. Chem.*, vol. 99, pp. 1834-1836, 1995.
doi:10.1021/j100007a007

[7] E. Allaria *et al.*, "Highly coherent and stable pulses from the FERMI seeded free-electron laser in the extreme ultraviolet", *Nat. Photonics*, vol. 6, pp. 699–704, 2012.
10.1038/nphoton.2012.233

[8] E. Ferrari *et al.*, "Free electron laser polarization control with interfering crossed polarized fields", *Phys. Rev. Accel. Beams*, vol. 22, p. 080701, 2019.
10.1103/PhysRevAccelBeams.22.080701

[9] A. A. Lutman *et al.*, "Polarization control in an X-ray free-electron laser", *Nat. Photonics*, vol. 10, pp. 468–472, 2016.
10.1038/nphoton.2016.79

[10] J. P. MacArthur *et al.*, "Microbunch Rotation and Coherent Undulator Radiation from a Kicked Electron Beam", *Phys. Rev. X*, vol. 8, p. 041036, 2018.
10.1103/PhysRevX.8.041036

ISBN: 978-3-95450-220-2 ISSN: 2673-5474 doi: 10.18429/JACoW-FEL2022-WEAI1

REVIEW OF RECENT PHOTOCATHODE ADVANCEMENTS

L.Monaco* and D. Sertore, INFN Milano - LASA, Segrate, Italy

Abstract

Photocathodes are routinely used as a source of electrons in high brightness beam photoinjectors. The properties of the photocathode have a significant influence on the parameters of the electron beams and on the operation of the machines. The choice of photocathode materials is an important step in reaching the challenging requirements of modern accelerators. Recent advancements towards more performing photocathodes are here presented and discussed.

INTRODUCTION

Photocathodes are key components of modern and advanced high brightness electron sources [1]. Illuminated by a laser beam, photocathodes emit electrons at proper phases in a high electric field region, necessary to accelerate the electron bunch to high energy to compensate for space charge forces and optimize beam emittances.

To generate the required electric field, the most common solutions are DC and RF guns. The solution adopted by different labs is mainly related to the kind of application of the specific machine. Indeed, polarized electron sources typically use DC guns due the extreme requirements of vacuum necessary for the operation of these kind of photocathodes (i.e. GaAs/Cs). Nearly the same vacuum conditions are necessary for the operation of alkali antimonide photocathodes due to their sensitiveness to vacuum level and composition. Recently, antimonide photocathodes have been used also in RF guns with limited performances due to dark current and limited operative lifetime. RF guns are instead routinely used with metallic photocathodes and, in case of high QE (Quantum Efficiency) materials, with cesium telluride (Cs_2Te).

Photocathodes properties determine also the minimal electron beam emittance through the so called thermal emittance. This property depends on the electron transverse velocity and hence on many parameters like photocathode surface roughness, distribution of work function on the surface, etc. This has motivated, in the present years, a strong activity based on solid state physics, surface science and material engineering to improve and optimize present photocathodes and explore new materials.

This paper presents the recent photocathode advancements with emphases on semiconductor photocathodes and their application in user dedicated accelerators. These materials are nowadays used in the main FEL user facilities and they are the best candidates for the coming new advanced CW FEL machines (see LCLS-II, SHINE, ..) and very high current electron source for ERLs or for the beam cooling of the Electron Beam Collider (EIC).

* laura.monaco@mi.infn.it

PHOTOCATHODE REQUIREMENTS

Photocathodes requirements are specific to their applications and a simple classification is not easily achievable.

However, it is possible to identify a common set of properties that are a minimal requirement for application of photocathode in modern accelerator machines [2]. They can be summarized in the following points:

- Long operative lifetime. This is important for photocathode operation in user facility based machine. Long operative lifetime implies also stable photocathodes properties in particular for operation in RF guns.
- Low dark current. Activation of components along the accelerators must be avoided and, hence, it is important to limit field emitters both from the photocathode and from the gun. In DC gun operation where the electric field is static, this is even detrimental for the photocathode itself since it generates ion back bombardment that damages the photoemissive film.
- Fast response time. Prompt response of the photocathode material to laser illumination is mandatory to guarantee proper phasing between laser and electric field (in particular for the RF gun operation). Moreover, the emitted electron bunch needs to be as similar as possible to the laser beam profile in order to minimize the effect induced by the space charge on the electron beam emittance.
- High QE. This parameter is extremely important for high repetition rate or CW applications. Lower repetition rate electron sources usually use metal photocathodes with QE in the 1×10^{-6} range.

Besides the previous presented parameters, electron polarization is a very specific requirement that only a family of photocathode is able to satisfy, i.e. III-V materials. This class of photocathodes is the subject of many studies towards improving the polarization ratio and the lifetime. Indeed these are Negative Electron Affinity (NEA) photocathodes and they need usually an atomic layer of Cesium on the surface to preserve the electron polarization. Consequently, the specification for vacuum level and composition are very demanding and require specific vacuum system. It is then clear that polarized photocathode are a class of photocathodes by itself and, given the limited space here available, they will not be addressed it here but recent updates have been presented at the Snowmass2021 Electron Workshop [3].

METAL

Metal photocathodes are widely used in low repetition rate electron sources and where fast response time and very low emittance are required.

The most common material is copper (see LCLS for example) but, recently, magnesium has been used in SRF gun at HZDR Elbe [4–6]. Given the “simplicity” of the mate-

ISBN: 978-3-95450-220-2 ISSN: 2673-5474 doi: 10.18429/JACoW-FEL2022-WEAI1

rial and the possibility to machine and then use it without particular regards about keeping vacuum conditions, there has been many proposal for surface topological engineering to enhance the photocathode performance. Recently, it has been proposed a photocathode with spiral flat microemitters machined on the exposed surface to enhance the emitted electron beam brightness [7].

Being the QE for metal low, several attempts are pursued to increase it. This is typically done by depositing very thin layer of properly selected materials on top of the photocathodes in order to lower the work function of the composite structure. This has been done at STFC by depositing a thin layer of MgO on top of a copper cathode [8], showing a significant improvement of the photocathode QE. Concerning the robustness, at STFC a comparative study of the QE degradation of polycrystalline and single-crystal Ag samples induced by oxygen shows that the effect is more relevant on single-crystal and, that can be partially recovered with the exposition of carbon monoxide. MTE (Mean Transverse Energy) measurements at room and cryogenic temperature reveal that QE decrease is more rapid at low temperature due to the increased sticking probability of the oxygen on the photocathode surface [9].

ALKALI TELLURIDE AND ANTIMONIDE

Alkali telluride and antimonide photocathodes nowadays are the most used materials for delivering high brightness electron beam.

The choice of these materials is mainly based on the need of having high QE photocathodes for high repetition rate and/or high average current applications. While alkali telluride provide reliable and stable performances, they need UV light (4^{th} harmonic of common lasers), a drawback that the alkali antimonide try to solve being sensitive to visible light and hence needing only the second harmonic, so relaxing request on the light sources. Both require a high quality vacuum, more stringent for the antimonide ones that result to be less robust than the telluride ones. The vacuum level required are of the order of 1×10^{-11} hPa and 1×10^{-10} hPa, for alkali antimonide and telluride respectively. Here below, the two families (anitmonide and telluride) of photocathodes will be shortly presented with focus on recent advancements.

Cs_2Te

Cs_2Te is commonly used in high repetition rate accelerator due to its high QE, long operative lifetime, relatively low emittance and fast response time. These performances are the result of more than twenty years of development starting from the production, operation in RF guns and post-operation analysis done at INFN Milano - LASA [10].

These photocathodes are used as electron source in user facilities like FLASH (DESY), European XFEL (Germany), LCLS-II (SLAC, USA) and in many accelerators around the world. The performances of cesium telluride are now taken as reference for the development of new photocathodes. Just to give some number: the QE at the production is in 10 % range and it drops during operation to few percent; operative lifetime is now around 1400 d; response time in the hundredths femtosecond range [11]; thermal emittance below 1 mm/mrad; dark current well below limiting values [12–16].

Recently HDZR-ELBE join the list of laboratories that use cesium telluride photocathodes. They successfully deposited Cs_2Te on copper substrate [17] to improve thermal conductivity with respect to Mo. Since it start operation in May 2020, seven films have been produced and operated in CW condition up to 100 kHz, with an average lifetime between 2 and 3 months. The total extracted charge, from Jun 2020 to Feb 2022, has been 91.3 C for a total of 3064 h of user beam.

Co-evaporation towards production The improvement of thermal emittance is based on the pioneering work of Gaowei [18] that showed how the adoption of a co-deposition process for the film growth reduces significantly the roughness and hence its contribution to the photocathode thermal emittance. Since then, many labs are working towards the implementation of this technique into photocathode growth.

A collaboration between CERN and ASTeC has recently grew four photocathodes by coevaporation on copper substrates at CERN. The samples were transferred to STFC where they were fully characterized by QE, XPS and TESS. These studies showed a large variability in the performance of the six photocathodes. The authors measured also Mean Transverse Energy (MTE) at different temperatures from 178 K to room temperature. The MTE curves change with temperature as expected. Authors measured, on one of the photocathodes, an increased of transverse energy above 400 nm (below photoemission threshold), probably due to surface compounds with a low surface coverage and therefore low effective QE [19].

ASTeC has also started an its own activity dedicated to cesium telluride in the framework of CLARA activities. Interestingly, they have grown two photocathodes on Mo: one with sequential deposition and one with coevaporation. They use ion beam sputtering for Te evaporation. Their XPS analysis shows in both cases mixed phase of Cs_xTe and, in the case of coevaporation, some amount of oxygen probably coming from the Cs source, not yet fully conditioned [20].

Alkali antimonide (Na-K-Cs-Sb)

Cesium telluride, although its good performance, has the drawback of being photo sensitive only to UV light. This has some implications one which is the need of the forth harmonic of the fundamental wavelength of common lasers to operate. Despite the high QE, this make the cesium telluride impractical for very high repetition rate or high average current operations. The natural choice is to move to alkali antimonide that are sensitive to visible light and hence require only a second harmonic to photo emit. Their sensitivity to vacuum conditions however requires at least an order of magnitude better vacuum with respect to telluride photocathode.

ISBN: 978-3-95450-220-2 ISSN: 2673-5474 doi: 10.18429/JACoW-FEL2022-WEAI1

The multi alkali antimonide have gain a new interest in the recent years supported by an intense R&D activity for the improvement of their properties in term of robustness (and lifetime) and thermal emittance. Moreover, they have benefit from the improvement on the vacuum technology that allows their operation not only in DC but also in RF guns.

DC gun operation Electron-Ion Colliders (EIC) ask for unpolarized electron beams with high average current, low emittance and long operative lifetime (I > 100 mA, $\epsilon \approx$ 1.5 mm mrad^{-1}, > 3 days) [1] for producing cold electron beams for hadron cooling. Thanks to their capability to work in visible range providing high QE and their low emittance, antimonide photocathodes are nowadays the best candidates. The operation of K-Cs-Sb in DC guns has been demonstrated [21, 22] and up to 65 mA have been extracted [23]. These experiments show that main limitations come from the QE degradation and the short operative lifetime and these motivate several research activities dedicated to improve the photocathode performances also in view of the new advance CW FEL machines and very high current electron source for ERLs.

Main causes of QE limitation are the thermal heating and the ion back bombardment issue. It has been seen that cathode temperature and laser power shining on the coating can cause the QE drop. Indeed, QE drops above 70 °C as well as if the power of the impinging laser exceeds some W [24] . To address the above thermal limitations, different solutions are being explored that imply cooling of the cathodes (p. es. used in Cornell and SBU-BNL DC guns) [24] or the solution developed for the MIST DC gun (10 mA unpolarized beam current) for the MESA accelerator in Mainz where the heat will be transferred from the puck that hold the cathode towards the boron nitride (BN) stem via a metallic gripper [25].

The ion back bombardment on the cathode surface caused by the beam ionized vacuum gases has been avoided by depositing off center cathodes and adjusting the beam optics to compensate for this.

RF gun operation at high gradient Operating alkali antimonide photocathodes in RF gun benefits from the higher accelerating gradient available but poses new challenges on vacuum level in the RF gun and the photocathode operation in high fields.

In the framework of a INFN Milano LASA - DESY PITZ collaboration, three KCsSb photocathodes have been prepared in a new dedicated deposition system at LASA and shipped to PITZ for testing in the RF gun [26]. The sequential deposition process was developed in the R&D system at LASA and transfer to the deposition system [27]. The three photocathodes, with QE above 5 % at 516 nm, have been successfully transfer to PITZ preserving the high QE. Their operation in the RF gun has been limited to 30–40 MV/m due to vacuum events that degraded significantly the QE. The dark current of these cathodes was higher than the one measured with Cs_2Te photocathodes, mainly due to the lower photoemission threshold. At PITZ, also the response time of a low (0.4 %) QE cathode was measured to be less than 100 fs. Since the QE degradation could indicate possible changes in the surface chemistry of the film, a new measurement on a fresh photocathode must be done to confirm this preliminary results. Finally, thermal emittance and emittance measurements confirm value smaller than the ones obtained for Cs_2Te (at 40 MV/m and 100 pC about 23 % decrease of emittance with a 4D brilliance enhancement of about 60 %), consistent with expectations. Post-usage analysis highlighted the increase of the photoemission threshold and showed the appearance of a shoulder at low energy in the spectral response for one of the cathodes, probably due to oxidation of the film.

A joint project between Cornell and UCLA allowed to test a Na-K-Sb photocathode, produced at Cornell, in the high gradient gun of the PEGASUS facility at UCLA. The QE, after deposition at the Bright Beams Center in Cornell, was about 1.5 % at 532 nm. The photocathode was transported then to UCLA in a dedicated suitecase but, at its arrival, the QE was dropped to about 8×10^{-2} % at 405 nm. Despite this low value, the QE remained stable for multiple weeks of operations. The photocathode QE was measured in the RF gun as 0.5 % at 266 nm, 8×10^{-2} % at 405 nm and they also performed measurement at 800 nm showing a mixing of the 2-photon and 3-photon photoemission. Finally, the thermal emittance measurements scale consistently with the change of photon wavelength [28].

Photocathode development To improve the performance of alkali photocathodes, several researches start aiming to develop more robust alkali antimonide photocathodes (for example Na-K-Sb that can withstand higher temperatures), new protective coatings, different growing procedures to increase the final smoothness of the coating, QE increase to limit the laser power needed.

The research on multi-alkali photocathodes involves many laboratory. Recently, at HZB they have deposited NaKSb co-evaporated (Sb + alkalis coevaporation) and sequential NaKSb photocathodes, aiming of setting up the growing process towards application for their SRF gun. The QE was between 0.3–2.0 % at 515 nm. Also the lifetimes were quite widespread. XPS analysis showed indeed different compositions of the grown films. Further studies are planned to improve the reproducibility of the growing process [29].

The transfer of the growing process to substrate like the plugs compatible with RF guns is a key element for photocahode operations. This activity has been pursued in China where different laboratories have developed their own photocathode deposition system, suitcase and transfer system inspired to the INFN LASA ones [30]. Concerning photocathode deposition, at SARI, for example, they deposit firstly Sb and then they coevaporate K and Cs. During the deposition they monitor not only photocurrent but also the reflectivity to have better control of the growing process.

Brightness improvement As important as the development of robust photocathodes is the R&D activity dedicated

ISBN: 978-3-95450-220-2 ISSN: 2673-5474 doi: 10.18429/JACoW-FEL2022-WEAI1

to improve the brightness of the electron beam generated from the photocathodes. Sources of increase of the thermal emittance are the roughness and the non uniformity of the surface photoemission threshold. Both effects contribute to the electron transverse momentum and hence to the emittance.

To reduce these contribution, we have already mention the development of co-evaporation deposition that guarantees a smoother final surface. A further step in this direction is the result obtained by Parzick et al. [31] that succeeded in growing an epitaxial Cs_3Sb photocathodes on a 3C SiC(100) substrate. Besides already important result of a larger lattice order of the epitaxial growth photocathode, the authors achieved a remarkable QE of 2 % at 532 nm on a film thinner than 10 nm. Moreover, they observed an enhanced QE at 650 nm with respect to the standard spectral response of cesium antimonide. This epitaxial film have allowed also ARPES measurements to unveil the band structure that has been compared with DFT (Density Functional Theory) calculation. The difference between the theoretical expectation and the measured data are attributed to strain and intrinsic instability of the grown Cs_3Sb.

To further improve the smoothness of cesium antimonide photocathodes, recently a substrate of a single crystal strontium titanate (STO), that matches the lattice constant of Cs_3Sb [32], has been used to growth this photocathode. The growth on a matched-lattice has improved the smoothness and also the uniformity of the surface photoemission threshold, opening a new path towards film optimization for improved high brightness beams. STO(100) was chosen from an open-source list of 150 commercially available candidate substrates, 23 which are lattice-matched to Cs_3Sb using the MPInterfaces [33] software package (a machine learning approach).

Graphene protective coating To reduce alkali antimonide sensitivity to vacuum conditions, an interesting approach is based on layers of graphene.

A collaboration between LANL and KEK has developed a process to deposit Cs_2KSb on graphene layers [34, 35]. The authors has shown that the quality of the graphene plays an important role in the final film performances. The CsK_2Sb photocathode deposited on the proper graphene layer show good QE but also the measurement through the graphene layers present a reasonable QE, dependent on the number of graphene layers. During this study, it was observed an unexpected QE enhancement when the graphene was deposited on a metal substrate as well as that the graphene layer can be cleaned by heating above 500 °C and used as a reusable substrate for these bialkali antimonide photocathodes.

A different approach to the use of graphene layers has been presented in [36]. In this work, a 10 nm Sb layer is deposited on a Si substrate. The Sb layer is then cover with graphene multilayers. The advantage of this solution is that is possible to retain the Sb layer on the Si substrate up to 600 °C with a clear improvement on the substrate cleanliness and Sb reusability. The authors then succeeded to deposit cesium on top of this support and grow a Cs_3Sb photocathode as reported from XPS measurements. The future plan of this research is to fully characterize the photoemissive properties of this film.

QE enhancer As a last topic in this overview of new possible ideas to enhance multialkali antimonide, the proposal of using Surface Plasmon Polaritons (SPP) needs to be presented. As already done in metals, proper engineering of the photocathode substrate might be used to enhance the QE. In the approach followed by [37], the complex constituted by substrate and bialkali antimonide are designed to enhance absorption by exciting SPP at the desired photon wavelength. This model is then implemented in a Monte Carlo model and, from their simulations, the authors show a factor at least of 2 on the QE when illuminated with the selected photon energy.

PHOTOCATHODE DIAGNOSTIC IN PRODUCTION SYSTEMS

Diagnostic during the deposition of photocathode film that will be operated in electron sources in accelerator facility is important. Indeed, it allows having many important information: feedback on the deposited cathode with the possibility to improve their reliability; post usage analysis to correlate photocathode performance in operation with the measured properties; continuous improvement and R&D on cathode for accelerator applications that might behave differently from the research films. Many production systems are already equipped with interesting diagnostic and here some of the new improvements are presented.

Recently, INFN LASA [38] is developing a TRAnsverse Momentum Measurement (TRAMM) device that, when completed and fully characterized, will be installed on one of the production system present in the laboratory. This device is supported by INFN-CSN5.

At DESY, a new laboratory dedicated to photocathode is being developed [39]. Blue lab will be a deposition chamber equipped with AES, XPS and, in the future, with a electron momentum spectrometer.

Finally, the Alkali-metal Photocathode Preparation Facility (APPF) [40] has been developed at STFC. This facility has a multiprobe system (for QE and work function measurement), the Transverse Energy Spread Spectrometer (TESS) for MTE measurement and a CMA for AES investigations. A feature of this system is the ability to accept both Omicron sample as INFN type plugs allowing to cross check R&D and production photocathode in the same system.

PHOTOCATHODE TEST FACILITIES

An essential tool for developing new photocathodes and improving the present ones are dedicated test facilities able to make a full characterization of the photoemissive properties of the films as under operation. In fact, the availability of user machines is limited for obvious reasons; moreover test of new photocathodes may require a change of machine parameters to fit the experiment or can imply some risks of pollution or damages that must be avoided.

ISBN: 978-3-95450-220-2 ISSN: 2673-5474 doi: 10.18429/JACoW-FEL2022-WEAI1

Being so important, the most recent photocathode test facilities are here reported.

HERACLES [41] at Cornell is a facility dedicated to study photocathode lifetime while in mA operations. The facility is based on a DC gun capable to reach 200 kV and 10 mA. Photocathodes are transported by a UHV suitcase. The first photocathode tested was a cesium antimonide that delivered 8 mA beam with stable current over a 3 h period.

At INFN LASA, in the framework of the BriXSinO activities, a new laboratory is being setting up for photocathode stress test [42]. This facility is based on a DC gun designed for 100 kV and 5 mA. The photocathode under test will be Cs_2Te operated at 92.857 MHz.

Finally, recently the PITZ facility at DESY has been upgraded to allow test of of visible sensitive photocathodes. This has allowed to measure INFN LASA photocathode in 2021 and new tests are foreseen either at the end of 2022 or beginning 2023.

MODERN APPROACH TO PHOTOCATHODE DEVELOPMENT

The “art” of photocathode deposition in the recent years is moving from an empirical “trial and error” approach to a more coherent and coordinated activity that involves different disciplines. This is well represented by ACERT that aims to develop new techniques and applied to photocathodes motivated by theory and guided by real-time *in-situ x-ray* analysis [43]. The same approach is being followed also by HZB in the context of the Sealab/BerlinPRO where they developed an integrated complex able to combine theoretical investigations, surface science techniques, and deposition dedicated system [29].

Moreover, Machine Learning (ML) is coming to the photocathode selection process through the work reported in [44]. This approach is based on coupling Density Functional Theory with ML. A general photoemission model was developed and used with the ML to predict work functions of photocathodes. Ones the materials were selected, they were further screened to select based on desired criteria such as commercial availability or, for example, air stable visible sensitive photocathodes. The next step will be to experimentally verified these findings.

Not only ML has been used for photocathode selection but also Artificial Intelligence (AI) has been introduced for photocathode growth. In fact in [45] has been developed and implemented an automatic process for growth of Cs_3Sb photocathodes. This has been possible thanks to a proper selection of significant parameters to follow during the growth. This process will be extended to other photocathodes (like Cs_2Te) and the feedback loop used, now implemented, will be replaced by AI process.

CONCLUSION

This paper presents a selection, based on our knowledge, of new advancements on photocathodes. The field of photocathode is expanding very fast and we hope to have given a taste of its complexity but also of its richness and multidisciplinarity that makes it very stimulating and challenging.

ACKNOWLEDGEMENTS

We have selected many works from many authors. We acknowledge all of them for the inspiration that they have given in the preparation of this paper.

REFERENCES

[1] D. Filippetto *et al.*, *Electron sources for accelerators*, 2022. doi:10.48550/ARXIV.2207.08875

[2] D. Dowell *et al.*, “Cathode r&d for future light sources,” *Nucl. Instrum. Methods Phys. Res., Sect. A*, vol. 622, no. 3, pp. 685–697, 2010. doi:10.1016/j.nima.2010.03.104

[3] *Snowmass2021 electron source workshop*.

[4] J. Teichert *et al.*, “Successful user operation of a superconducting radio-frequency photoelectron gun with mg cathodes,” *Phys. Rev. Accel. Beams*, vol. 24, p. 033 401, 3 2021. doi:10.1103/PhysRevAccelBeams.24.033401

[5] R. Xiang, “Recent progress on advanced photocathodes for sc rf guns,” in *Photocathode Physics for Photoinjectors Workshop*, 2021.

[6] R. Xiang and J. Schaber, “Review of recent progress on advanced photocathodes for superconducting rf guns,” *Micromachines*, vol. 13, no. 8, 2022. doi:10.3390/mi13081241

[7] C. Pierce *et al.*, “Generating bright femtosecond electron beams from flat surfaces,” in *Photocathode Physics for Photoinjectors Workshop 2021*, 2021.

[8] C. Benjamin, G. R. Bell, H. M. Churn, L. B. Jones, T. C. Q. Noakes, and T. J. Rehaag, “Photocathode Performance Characterisation of Ultra-Thin MgO Films on Polycrystalline Copper,” in *Proc. IPAC’22*. doi:10.18429/JACoW-IPAC2022-MOPOMS025

[9] L. A. J. Soomary, L. B. Jones, T. C. Q. Noakes, and C. P. Welsch, “Controlled Degradation of a Ag Photocathode by Exposure to Multiple Gases,” in *Proc. IPAC’22*. doi:10.18429/JACoW-IPAC2022-THPOPT034

[10] D. Sertore, “Overview of high qe photocathode r&d in europe,” in *Snowmass 2021 Electron Source Workshop*, 2022.

[11] G. Loisch *et al.*, “Direct measurement of photocathode time response in a high-brightness photoinjector,” *Appl. Phys. Lett.*, vol. 120, no. 10, p. 104 102, 2022. doi:10.1063/5.0078927

[12] F. Sannibale *et al.*, “APEX Phase-II Commissioning Results at the Lawrence Berkeley National Laboratory,” in *Proc. IPAC’16*. doi:10.18429/JACoW-IPAC2016-TUOCA02

[13] S. Schreiber, S. Lederer, D. Juarez-Lopez, F. Brinker, L. Monaco, and D. Sertore, “Photocathodes for the Electron Sources at FLASH and European XFEL,” presented at FEL’22, Trieste, Italy, Aug. 2022, paper TUP07, this conference.

[14] L. Monaco, G. G. Rocco, P. Michelato, C. Pagani, and D. Sertore, “Growing and Characterization of Cs2Te Photocatodes with Different Thicknesses at INFN LASA,” in *Proc. FEL’19*. doi:10.18429/JACoW-FEL2019-WEA04

ISBN: 978-3-95450-220-2 ISSN: 2673-5474 doi: 10.18429/JACoW-FEL2022-WEAI1

[15] P. W. Huang *et al.*, "Test of Cs2Te Thickness on Cathode Performance at PITZ," in *Proc. FEL'19*. doi:10.18429/JACoW-FEL2019-WEP062

[16] D. Sertore *et al.*, "R&D on High QE Photocathodes at INFN LASA," in *Proc. IPAC'22*. doi:10.18429/JACoW-IPAC2022-THPOPT027

[17] R. Xiang *et al.*, "Study on QE Evolution of Cs_2Te Photocathodes in ELBE SRF Gun-II," in *Proc. IPAC'22*. doi:10.18429/JACoW-IPAC2022-THPOPT022

[18] M. Gaowei *et al.*, "Codeposition of ultrasmooth and high quantum efficiency cesium telluride photocathodes," *Phys. Rev. Accel. Beams*, vol. 22, p. 073 401, 2019. doi:10.1103/PhysRevAccelBeams.22.073401

[19] L. A. J. Soomary *et al.*, "Performance Characterisation at Daresbury Laboratory of Cs-Te Photocathodes Grown at CERN," in *Proc. IPAC'22*. doi:10.18429/JACoW-IPAC2022-THPOPT033

[20] R. Valizadeh, V. R. Dhanak, A. N. Hannah, and S. Lederer, "Synthesis of First Caesium Telluride Photocathode at ASTeC Using Sequential and Co-Deposition Method," in *Proc. IPAC'22*. doi:10.18429/JACoW-IPAC2022-MOPOMS027

[21] X. Gu *et al.*, "Stable operation of a high-voltage high-current dc photoemission gun for the bunched beam electron cooler in rhic," *Phys. Rev. Accel. Beams*, vol. 23, p. 013 401, 1 2020. doi:10.1103/PhysRevAccelBeams.23.013401

[22] E. Wang, "Electron source requirements for electron-ion collider," in *Snowmass 2021 Electron Source Workshop*, 2022.

[23] B. Dunham *et al.*, "Record high-average current from a high-brightness photoinjector," *Appl. Phys. Lett.*, vol. 102, no. 3, p. 034 105, 2013. doi:10.1063/1.4789395

[24] L. Cultrera, "Robust cathodes to produce high current electron beams," in *Snowmass 2021 Electron Source Workshop*, 2022.

[25] M. A. Dehn, K. Aulenbacher, and P. S. Plattner, "MIST - The MESA-Injector Source Two," in *Proc. IPAC'22*. doi:10.18429/JACoW-IPAC2022-THPOPT024

[26] D. Sertore *et al.*, "R&D on High QE Photocathodes at INFN LASA," in *Proc. IPAC'22*. doi:10.18429/JACoW-IPAC2022-THPOPT027

[27] S. Mohanty *et al.*, "Development and Test Results of Multi-Alkali Antimonides Photocathodes from the High Gradient RF Gun at PITZ," Triest, Italy, Aug. 2022, presented at FEL2022, Triest, Italy, Aug. 2022, paper TUP04, unpublished.

[28] C. Pennington, "Testing alkali antimonide photocathodes in high gradient injectors," in *Photocathode Physics for Photoinjectors Workshop*, 2021.

[29] S. Mistry, T. Kamps, J. Kühn, and C. Wang, "Multi-Alkali Antimonide Photocathode Development for High Brightness Beams," in *Proc. IPAC'22*. doi:10.18429/JACoW-IPAC2022-THPOPT019

[30] H. Xie, "Overview of the semiconductor photocathode research in china," *Micromachines*, vol. 12, no. 11, 2021. doi:10.3390/mi12111376

[31] C. T. Parzyck *et al.*, "Single-crystal alkali antimonide photocathodes: High efficiency in the ultrathin limit," *Phys. Rev. Lett.*, vol. 128, p. 114 801, 11 2022. doi:10.1103/PhysRevLett.128.114801

[32] P. Saha *et al.*, "Physically and chemically smooth cesium-antimonide photocathodes on single crystal strontium titanate substrates," *Appl. Phys. Lett.*, vol. 120, no. 19, p. 194 102, 2022. doi:10.1063/5.0088306

[33] K. Mathew *et al.*, "Mpinterfaces: A materials project based python tool for high-throughput computational screening of interfacial systems," *Comput. Mater. Sci*, vol. 122, pp. 183–190, 2016. doi:https://doi.org/10.1016/j.commatsci.2016.05.020

[34] H. Yamaghchi, "Towards the use of 2d materials as unique protection layer for bialkali photocathodes," in *Photocathode Physics for Photoinjectors Workshop*, 2021.

[35] L. Guo, K. Goto, Y. Takashima, H. Yamaguchi, and M. Yamamoto, "Dependence of CsK2Sb Photocathode Performance on the Quality of Graphene Substrate Film," in *Proc. IPAC'22*. doi:10.18429/JACoW-IPAC2022-THPOPT028

[36] J. Biswas, "Progress towards long lifetime photocathodes with protective layer," in *Photocathode Physics for Photoinjectors Workshop*, 2021.

[37] Z. Jiang, Q. Gu, X. Li, E. Wang, M. Gaowei, and W. Liu, "Monte carlo simulations of electron photoemission from plasmon-enhanced bialkali photocathode," *Phys. Rev. Accel. Beams*, vol. 24, p. 033 402, 3 2021. doi:10.1103/PhysRevAccelBeams.24.033402

[38] D. Sertore *et al.*, "Assembly and Characterization of Low-Energy Electron Transverse Momentum Measurement Device (TRAMM) at INFN LASA," in *Proc. IPAC'22*. doi:10.18429/JACoW-IPAC2022-THPOPT026

[39] P. Juarez, S. Lederer, S. Schreiber, F. Brinker, L. Monaco, and D. Sertore, "Photocathodes at flash and european xfel," in *Photocathode Physics for Photoinjectors Workshop*, 2021.

[40] H. M. Churn, C. Benjamin, L. B. Jones, and T. C. Q. Noakes, "The Alkali-Metal Photocathode Preparation Facility at Daresbury Laboratory: First Caesium Telluride Deposition Results," in *Proc. IPAC'22*. doi:10.18429/JACoW-IPAC2022-THPOPT044

[41] M. B. Andorf, J. Bae, A. C. Bartnik, I. V. Bazarov, L. Cultrera, and J. M. Maxson, "HERACLES: A High Average Current Electron Beamline for Lifetime Testing of Novel Photocathodes," in *Proc. IPAC'22*. doi:10.18429/JACoW-IPAC2022-THPOMS036

[42] D. Sertore *et al.*, "Photocathode Stress Test Bench at INFN LASA," in *Proc. IPAC'22*. doi:10.18429/JACoW-IPAC2022-THPOPT025

[43] J. Smedley, "Cathode characterization and fabrication," in *Photocathode Physics for Photoinjectors Workshop*, 2021.

[44] E. R. Antoniuk, "Novel ultrabright photocathodes discovered from machine learning and density functional theory driven screening," in *Photocathode Physics for Photoinjectors Workshop*, 2021.

[45] V. Pavlenko, "Automated growth of photocathode films: From the basics of process control towards artificial intelligence," in *Photocathode Physics for Photoinjectors Workshop*, 2021.

ISBN: 978-3-95450-220-2 ISSN: 2673-5474 doi: 10.18429/JACoW-FEL2022-WEAO4

CHIRPED PULSE LASER SHAPING FOR HIGH BRIGHTNESS PHOTOINJECTORS

C. Koschitzki, H. Qian, Z. Aboulbanine, G. Adhikari, N. Aftab, P. Boonpornprasert, G. Georgiev, J.D. Good, M. Gross, A. Hoffmann, M. Krasilnikov, X. Li, O. Lishilin, A. Lueangaramwong, G. Loisch, R. Niemczyk, A. Oppelt, G. Vashchenko, T. Weilbach, F. Stephan, DESY Zeuthen, Germany
I. Hartl, DESY Hamburg, Germany

Abstract

In this publication we show the current status on spectral-spatial shaping at the Photo Injector Test Facility at DESY in Zeuthen (PITZ). The laser pulse shaper presented here is based on spectral amplitude modulation of chirped laser pulses. In this unique approach one can modulate the spatial profile of individual time slices in density and diameter. The photoinjector requires a wavelength of 257.5 nm, but the laser shaping applies at a wavelength at least greater than 400 nm, in this paper, at 1030 nm. Both the shape preservation and fourth harmonic generation efficiency of the chirped laser pulses are discussed.

INTRODUCTION

The free electron laser (FEL) is currently the most powerful source for coherent X-rays. It is typically based on linear electron accelerators, which rely on a low transverse emittance electron source, to allow X-ray lasing in the undulator. As the emittance in modern FELs is limited by the source emittance, it is intuitive to also optimize the photoemission laser shape to control the emittance growth due to nonlinear space charge forces during the low energy transportation. For electron beams, dominated by space charge effects, it was shown that shaping of the extracting laser pulse can reduce the space charge induced emittance growth [1] [2]. Another study shows, that slice mismatch of a triangular driver beam for high efficiency beam based plasma acceleration can be reduced [3], if the extraction laser allows for independent control of slice charge and charge density. A Spatial Light Modulator (SLM) based laser pulse shaper with such a capability has been proposed by Mironov [4] and a variation of such a shaper has been used to shape the output of an infrared (IR) laser amplifier at 1030 nm. The photo injector cathode requires a UV pulse to extract electrons, thus the fourth harmonic was obtained from two consecutive second harmonic generation (SHG) stages. A high quality laser pulse shaping was demonstrated for the IR pulses.

SLM SHAPER

The shaper is an imaging zero compressor or Martinez system as shown in Fig. 1, where a 4f-telescope with two identical lenses images the surface of one grating to another grating and ultimately path length differences of different wavelengths add up to zero. The SLM is then placed at the Fourier plane in between the two lenses, where a collimated

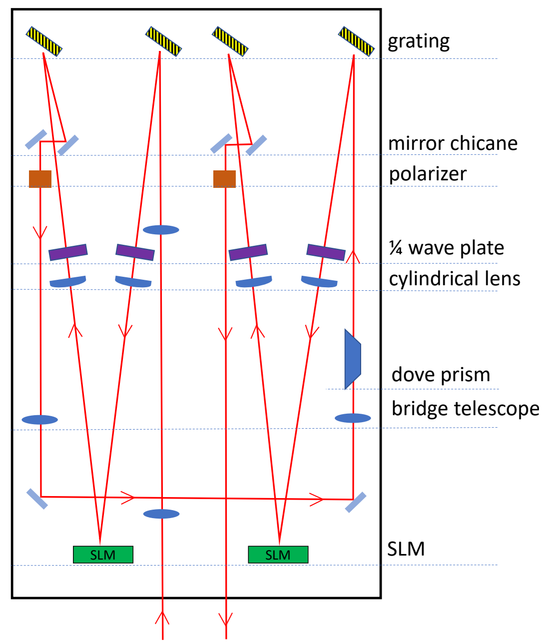

Figure 1: Schematic of a double SLM Shaper.

beam in absence of the gratings would be focused. Due to the grating dispersion the intensity distribution at the SLM plane parallel to the table corresponds to the spectral amplitude distribution. This is still true, if cylindrical lenses are used and the lens rotation is aligned with the grating rotation. But since neither the grating nor the lenses act on the transverse vertical axis, the optical transfer is identical to a free drift for the transverse vertical axis. Thus in the vertical plane an image of the SLM can be transported, if the lens is placed outside the shaper, i.e. after the second grating. Then of the two axis of our two dimensional SLM, one axis corresponds to spectrum, while the other corresponds to a spatial axis like in a typical spectrograph setup. The liquid crystals in an SLM act as polarization dependent phase shifters and a setup like this could be operated as a digital prism. In order to turn it into an attenuator we can use two quarter wave plates at 45 degrees, before and after the SLM. This turns the phase shift into a polarization rotation and thus 180 degrees of phase shift become an attenuation between 0 and 100% after a subsequent polarizer. As only one spatial dimension is accessible in a single shaper, the laser beam is rotated by 90 degree using a Dove Prism and sent through a

ISBN: 978-3-95450-220-2 ISSN: 2673-5474 doi: 10.18429/JACoW-FEL2022-WEAO4

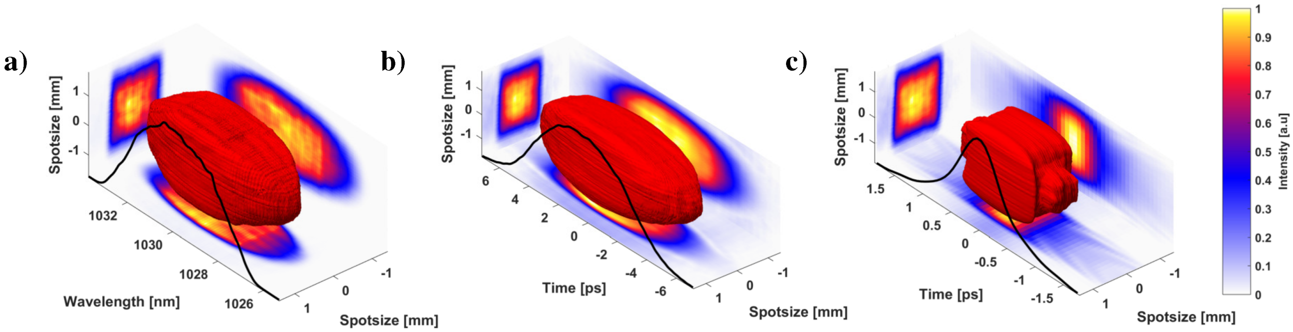

Figure 2: Volume data of spectrograph slitscan with isosurface 25% peak intensity and projections for **a)** the spectrograph data and for Eq. (2) applied to longitudinal axis with group velocity dispersion (GVD) of **b)** 0.8 ps^2 and **c)** 0.1 ps^2 respectively.

second identical shaper setup. The bridge part between the shapers needs to take into account that the image of the first shaper is propagated in the second shaper and the images have separated image planes. Our optical simulations have shown that one solution is to image output grating to input grating with a 4f-telescope with magnification of one and a focal length longer than the focal length of the cylindrical lens inside the shaper. The attenuation of a single shaper is a function of the form $f_a(x,\lambda)$ which can be applied to the initial laser intensity distribution $I(x,y,\lambda)$, typically a 3D gaussian. The final attenuation function can be written as:

$$f_a(x,y,\lambda) = f_{a1}(x,\lambda)\cdot f_{a2}(y,\lambda), \qquad (1)$$

which can not be rotationally symmetric in the x-y plane, because of the missing x-y correlation. A third transverse SLM shaper was added to the setup with $f_{a3}(x,y)$, but has no distinction in the wavelength domain. Thus a 3D radial symmetry around the propagation axis can still not be achieved. Figure 2 shows a measurement of a shaped quasi ellipsoid. It was obtained using a volume slit scan with a spectrograph. The spatial-temporal laser pulse profile can then be obtained by a Fourier transformation including the spectral phase.

$$I(x,y,t) = Fourier(I(x,y,\lambda)\cdot e^{i*GDD^2*\lambda^2})d\lambda. \qquad (2)$$

The GVD is obtained from the geometric parameters of the compressor in our chirped pulse amplifier (CPA) system. Our CPA system provides laser pulses with a 7 nm FWHM spectra and a transform limited pulse duration of 300 fs FWHM. Our target pulse duration is between 10-20 ps with a typical group delay dispersion of 1.5 ps^2. At these large GVD the distributions in Eq. (2) become self similar.

With laser pulses significantly closer to the transform limit, the required spectral distribution for most desired temporal pulse shapes might not be achievable, given the symmetry condition by Eq. (1). Some distributions might theoretically be achievable, but with low shaping efficiency ε_s. It is calculated by the best fit of the desired spectral-spatial distribution under the initial distribution. Also more complex spectral phase distributions are achievable and temporal shapers exist, that rely fully on spectral phase shaping [5].

CONVERSION

The shaped IR pulses have to be converted to UV wavelength and conversion efficiency has to be weighed against pulse preservation considerations. In order to preserve the transverse shape, the nonlinear crystals have to be put in an image plane of our beam transport. Then the transverse output intensity distribution becomes approximately the square of the input distribution. A nonlinear conversion outside an image plane yields the square of the diffracted intensity and subsequently a distorted distribution at the image plane. For the case of conversion at the focal plane, this effect is typically similar to a low pass Fourier filter as high spatial frequencies get suppressed due to their low amplitude. This effect can still cause distortion if the Rayleigh length d_R becomes smaller or equal to the crystal thickness. Furthermore we will refer to it as nonlinear depth of field (NDoF). Another effect concerning the transverse shape is the nonlinear walkoff, as the generated harmonic pulse propagates at an angle θ through the crystal with respect to the fundamental. This leads to a linear smearing or walk-off δ of the generated harmonic distribution by $\delta = \theta \cdot d_c$ with the crystal thickness d_c. The temporal walk-off can be neglected in our case. The phase matching is done by critical phase matching, where the birefringent crystal axis are geometrically aligned to match the index of refraction for the center wavelength of our spectrum. Neighboring wavelength are only quasi phase matched and thus a limited phase matching bandwidth exists, which gets smaller with increasing crystal thickness. For BBO of 1 mm thickness the FWHM phase matching bandwidth is 0.792 THz or 0.7 nm around 515 nm respectively and thus smaller than the initial spectral width of 1.5 THz. For 0.25 mm crystal thickness the bandwidth increases to 3.17 THz and it is tolerable to counteract it with the shaper. Thicker crystals require additional broadband phase matching [6]. For conversion efficiency we can obtain a simple scaling law for two consecutive SHG processes. We assume efficiency is low, neglect saturation, assume perfect broadband phase matching. Thus the output pulse energy E_{VIS} of a single SHG from 1030 nm (IR) to 515 nm (VIS) scales like

$$E_{VIS} \propto E_{IR}^2 \frac{1}{\tau_{IR}} \frac{1}{M^2} d_{LBO}^2 \qquad (3)$$

ISBN: 978-3-95450-220-2 ISSN: 2673-5474 doi: 10.18429/JACoW-FEL2022-WEAO4

and from VIS to UV like

$$E_{UV} \propto E_{VIS}^2 \frac{1}{\tau_{VIS}} \frac{1}{M^2} d_{BBO}^2 \tag{4}$$

thus follows

$$E_{UV} \propto E_{IR}^4 \frac{1}{\tau^3} \frac{1}{M^6} d_{LBO}^4 d_{BBO}^2 \tag{5}$$

The IR pulse duration τ_{IR} may not be identical to the VIS or UV pulse duration due to nonlinear pulse shortening, but they are proportional. In the case of a flattop they are identical. Similarly the transverse size may decrease through conversion steps, but will be proportional to the initial size and thus the magnification M of our variable telescope between shaper and conversion. The image magnification between LBO plane and BBO plane was fixed to $M = 1$ as we used 2 aspheric lenses with 50 mm diameter and 100 mm focal length, to maximize optical resolution. Lastly we approximated the dependency of the crystal thicknesses d_{LBO} and d_{BBO} to $\propto d^2$ for thin crystals. Thus we see that the transverse size has the biggest impact and should be set as low as crystal damage threshold and diffraction limited optical resolution allow, with a given pulse energy and duration. LBO thickness should be chosen to achieve approximately 50% conversion efficiency, which is slightly saturated. If for a given pulse duration and input IR pulse energy the UV pulse energy exceeds the requirements, the most promising trade is to decrease the BBO thickness, as it also has the larger nonlinear walkoff angle (85 mrad) and smaller phase matching bandwidth compared to LBO. Minimum BBO crystal thickness available was 100 µm. In Fig. 3 a transverse mask in the shape of the letter Pi was applied to the laser and the image was taken at each conversion step from IR to VIS to UV and eventually to electrons. The UV image on the PITZ cathode generated an electron distribution, which could be imaged to a fluorescent screen with magneto optical transport. The transverse shape was reasonably preserved in this scenario, but conversion efficiency was very low and only 30 pC of charge were generated at a pulse duration of 1 ps. A typical application requires pulses on the order of 250 pC at 10 ps.

The conversion shown in Fig. 4 represents a typical result at a sufficient conversion efficiency. It can be seen that shape outlines are preserved. However since $E_{UV} \propto E_{IR}^4$ it is practically impossible to preserve the homogeneous filling of the volume. Distortions can then only be corrected if the correction fulfils the condition in Eq. (1).

Thus we have to conclude, that a shape preserving double conversion is impractical and the order has to be switched, such that amplified short IR pulses are first converted to VIS, stretched, shaped and then converted again. A preliminary setup without VIS stretcher and only a single shaper was able to produce significantly more homogeneous results as seen in Fig. 5.

2D + 1D PARABOLOID

For a typical European XFEL working point with a bunch charge of 250 pC, we have compared three different longitudinal electron bunch shapes with and without transverse truncation in simulations. With identical transverse size the longitudinal length has been matched such that the peak current is the same for all distributions.

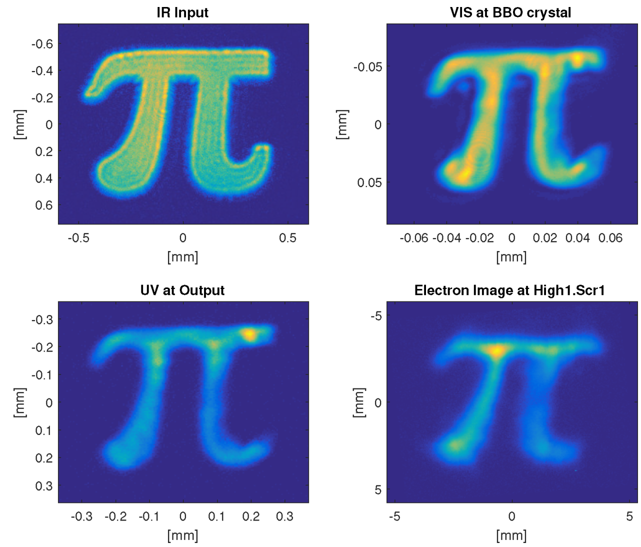

Figure 3: Transverse beam profile in **a)** IR before conversion **b)** VIS at BBO location **c)** UV at conversion section output **d)** electron beam on fluorescent screen

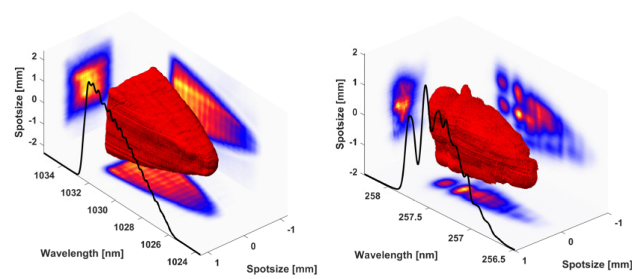

Figure 4: Spectrograph scans for triangle pulses with IR double shaper **a)** IR before conversion and **b)** after 2 consecutive conversions to UV.

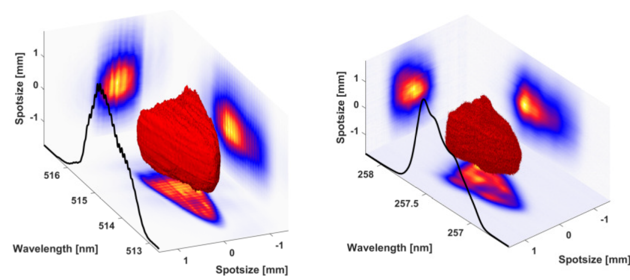

Figure 5: Spectrograph scans for triangle pulses with VIS single shaper **a)** VIS before conversion and **b)** after conversion to UV.

The phase space is plotted in a radial density plot in Fig. 6 as introduced in [7]. First we can note that the core emittance is very similar in all cases and that a worsened emittance is largely due to a small fraction of the charge occupying a large phase space. If this charge was to be truncated, the

ISBN: 978-3-95450-220-2 ISSN: 2673-5474 doi: 10.18429/JACoW-FEL2022-WEAO4

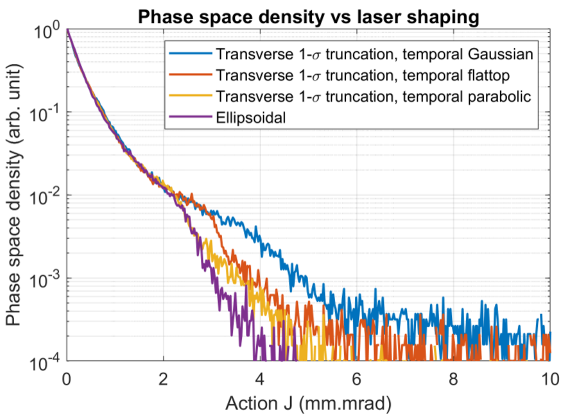

Figure 6: Radial phase space density plot for different pulse shapes and quasi parabolic transverse profiles. Emittances are summarized in Table 1

difference between the cases vanishes quickly. Since the Ellipsoidal case, which yields best performance in all cases, has a transverse parabolic projection, we compared the different longitudinal cases with the ellipsoid using flattop and quasi parabolic transverse shapes. The quasi parabolic shape is a 2D transverse Gaussian, cropped at 1 σ. Improved emittances from transverse cropping has already been experimentally proven by S. Li et. al. [8].

Table 1: Shape comparison

laser shapes	100% emit	95% emit	Action < 2 Emittance	Action < 2 percentage	core emit
Transverse Flattop					
Gauss	0.70	0.42	0.36	92.0%	0.29
Flattop	0.61	0.41	0.37	92.9%	0.28
Parabolic	0.53	0.39	0.37	93.9%	0.28
Transverse Parabolic					
Gauss	0.66	0.37	0.36	94.4%	0.30
Flattop	0.53	0.34	0.36	96.0%	0.30
Parabolic	0.43	0.33	0.37	97.5%	0.30
Ellipsoid	0.40	0.32	0.36	98%	0.29

In particular the longitudinal parabolic shape is close to the ellipsoid performance regarding the radial phase space. Hence we conclude that the most important property of the ellipsoid regarding high brightness are the parabolic projections, which do not require a spatially and temporally correlated approach and could be achieved separately with a temporal and a transverse shaper. The main ability of our 3D shaping approach is the separable control of charge and charge density along the temporal axis, which could allow to control the slice emittance mismatch in distributions like the ones needed for high transformer ratio plasma wake drivers [3]. In this application a triangular integrated charge profile is required. If the triangular profile is created with decreasing charge density, a problematic slice emittance mismatch is created, which could be avoided using transverse tapering as shown in Fig. 4.

SUMMARY

The pulse shaping method using two SLM shapers in Martinez configurations yields convincing results, given the limitations from the condition Eq. (1). The application is however severely limited by the necessity to convert the wavelength in a shape preserving way. The strength of some distortions effects, like nonlinear walkoff and NDoF, can be limited by trading off conversion efficiency. If a conversion to the fourth harmonic of the shaped wavelength is required, the high sensitivity to input intensity poses significant practical problems to preserve the shaped distributions. Ideally the shaped pulses are applied directly to a VIS sensitive photo cathode, but shape preservation could be sufficient for practical applications if only one conversion to the second harmonic is required. In order to achieve high brightness beams the authors want to point out the possibility of parabolic shaped pulses, which have a similar beam quality compared to ellipsoidal shapes. This shape can be produced with a 1D longitudinal shaper and additional 2D transverse shaper. The temporal spatial correlation approach presented, could benefit applications which require time resolved and separable tuning of charge and charge density.

REFERENCES

[1] T. Rublack *et al.*, “Production of quasi ellipsoidal laser pulses for next generation high brightness photoinjector”, *Nucl. Instr. and Meth. Sect. A*, vol. 829, pp. 438–44, 2016. doi:10.1103/PhysRevAccelBeams.20.080704

[2] H. J. Qian, M. Krasilnikov, and F. Stephan, “Beam Brightness Improvement by Ellipsoidal Laser Shaping for CW Photoinjectors”, in *Proc. FEL'17*, Santa Fe, NM, USA, Aug. 2017, pp. 432-435. doi:10.18429/JACoW-FEL2017-WEP008

[3] G. Loisch *et al.*, “Photocathode laser based bunch shaping for high transformer ratio plasma wakefield acceleration”, *Nucl. Instr. and Meth. Sect. A*, vol. 909, pp. 107-110, 2018. doi:10.1016/j.nima.2018.02.043

[4] S. Mironov *et al.*, “Shaping of cylindrical and 3D ellipsoidal beams for electron photoinjector laser drivers”, *Appl. Opt.*, vol. 55, pp. 1630-1635, 2016. doi:10.1364/AO.55.001630

[5] I. Will *et al.*, “Generation of flat-top picosecond pulses by coherent pulse stacking in a multicrystal birefringent filter”, *Opt. Express*, vol. 16, pp. 14922-14937, 2008. doi:10.1364/OE.16.014922

[6] J. P. Torres *et al.*, “Angular dispersion: an enabling tool in nonlinear and quantum optics”, *Adv. Opt. Photonics*, vol. 2, pp. 319–369, 2010. doi:10.1364/AOP.2.000319

[7] C. Richard *et al.*, “Measurements of a 2.1 Mev h-beam with an allison scanner”, *Rev. Sci. Instrum.*, vol. 91, p. 073301, 2020. doi:10.1063/5.0004502

[8] S. Li *et al.*, “Ultraviolet laser transverse profile shaping for improving x-ray free electron laser performance”, *Phys. Rev. Accel. Beams*, vol. 20 p. 080704, 2017. doi:10.1103/PhysRevAccelBeams.20.080704

ISBN: 978-3-95450-220-2 ISSN: 2673-5474 doi: 10.18429/JACoW-FEL2022-WEBI1

COMPARISON OF EULERIAN, LAGRANGIAN AND SEMI-LAGRANGIAN SIMULATIONS OF PHASE-SPACE DENSITY EVOLUTION

Ph. Amstutz*
Deutsches Elektronen-Synchrotron DESY, Hamburg, Germany

Abstract

Good understanding of the underlying beam dynamics is mandatory for the successful design and operation of Free-Electron Lasers. In particular, it is important that all physically relevant collective effects are adequately represented in simulation codes so that their influence on the phase-space evolution of the bunch can be calculated with sufficient accuracy at all relevant length scales. Besides coherent collective effects such as space charge or coherent radiative interaction also incoherent effects such as intra-beam scattering are suspected to have a significant impact on the efficacy of sophisticated lasing techniques.

Most of the well-known and widely-used beam dynamics codes employ the Lagrangian approach, in which the particle bunch is represented by discrete points in phase-space and track the solutions of their equations of motion. In contrast to that, in the Eulerian and semi-Lagrangian approach, the bunch is described by a numerical representation of its phase-space density function.

This contribution discusses the working principles of the three classes of simulation methods Lagrangian, Eulerian, and semi-Lagrangian and highlights their respective advantages and short-comings, when applied to the simulation of collective beam dynamics in FELs.

INTRODUCTION

Many applications of particle accelerators and in particular FELs require a high particle density, so that the number of particles contained in a bunch is typically very large. If the particles can be assumed to be initially independent and identically distributed (IID), then the entire bunch can be represented by a function of one set of single-particle phase-space coordinates, describing the probability of any one particle to occupy a certain position in phase-space — the single-particle phase-space density (PSD). In practice, this PSD can usually be obtained either based on experimental data or from a theoretical model of the generation process. As this macroscopic PSD depends only on one set of phase-space coordinates, instead of the phase-space coordinates of all individual particles, it is more likely tat the evolution of the PSD can actually be simulated numerically. In the following we will present an overview of the various kinetic equations frequently encountered in beam dynamics, which describe the evolution of PSDs and outline the three principle families of methods to solve them numerically: Eulerian, Lagrangian, and Semi-Lagrangian methods.

* philipp.amstutz@desy.de

KINETIC EQUATIONS

In the following we will briefly recap how an evolution equation of a PSD of a non-interacting particles is derived starting from Hamiltonian mechanics and then show how it can be extended to describe interaction between the particles and stochastic motion of the particles, yielding a set of well-known kinetic equations.

Consider a Hamiltonian dynamical system with a non-collective Hamiltonian $H(t, z)$, $\quad H\colon \mathbb{R} \times \mathbb{R}^{2d} \to \mathbb{R}$ and d degrees of freedom, so that the dimension of its phase-space is $2d$. Using the Poisson bracket $\{f, g\} \equiv \nabla_z f^{\mathrm{T}} J \nabla_z g$ the equations of motion (EOM) of the phase-space coordinates $z \equiv (q_1, \dots, q_d, p_1, \dots, p_d)^{\mathrm{T}}$

$$\mathrm{d}_t z = \{z, H\} \equiv J \nabla_z H, \quad J = \begin{pmatrix} 0 & \mathbb{I}_d \\ -\mathbb{I}_d & 0 \end{pmatrix} \tag{1}$$

are solved by the flow $\phi_{t \leftarrow t_0}\colon \mathbb{R}^{2d} \to \mathbb{R}^{2d}$

$$z(t) = \phi_{t \leftarrow t_0}(z(t_0)) \tag{2}$$

where $z(t_0)$ are the known initial conditions [1, 2]. Stochastic terms may be added to the EOM to describe random processes affecting the trajectory of a particle.

For a phase-space density $\Psi(t, z)$, i.e. a function describing the probability of finding any particle in a certain position in phase-space, from the conservation of probability it can be seen that its total time-derivative vanishes

$$\mathrm{d}_t \Psi = \partial_t \Psi + \mathrm{d}_t z^{\mathrm{T}} \nabla_z \Psi = 0, \tag{3}$$

which is known as the *Liouville equation* [3, 4].

Liouville Equation

It can be seen that the Liouville equation is a linear, first-order PDE, taking the form of a continuity or advection equation, with the velocity field $(J \nabla_z H)^{\mathrm{T}}$:

$$\partial_t \Psi - \{H, \Psi\} = \partial_t \Psi + (J \nabla_z H)^{\mathrm{T}} \nabla_z \Psi = 0. \tag{4}$$

Hence the time evolution of a PSD of non-interacting particles in a Hamiltonian system can be interpreted as an incompressible fluid being transported along the vector field of the Hamiltonian. In the next section it will be shown how the *method of characteristics* can be employed to derive an closed-form solution of the Liouville equation, which is known as *Liouville's theorem*.

Boltzmann Equation

While the Liouville equation describes the case of non-interacting particles, it can be extended to also capture interaction between the particles. In many systems of interest, the

ISBN: 978-3-95450-220-2 ISSN: 2673-5474 doi: 10.18429/JACoW-FEL2022-WEBI1

interaction between the particles is driven by a long-range range force such as gravity or the Coulomb force, in case of charged particle beams. While in these systems all particles interact with each other at all times, the interaction potential decreases with increasing distance so that particles interact more strongly with particles in their direct vicinity than with those far away. If multi-particle scattering processes can be neglected the interaction is dominated by binary collisions. This case is described by the *Boltzmann equation*

$$\partial_t \Psi - \{H, \Psi\} = C[\Psi] \tag{5}$$

which introduces a collision term on the right-hand side of the Liouville equation [4]. The collision term is given by a threefold momentum integral

$$\begin{aligned} C[\Psi] = \int_{\mathbb{R}^{3d}} \mathrm{d}^d p''' \, \mathrm{d}^d p'' \, \mathrm{d}^d p' \, W(p''', p'', p', p) \times \\ [\Psi(q, p''')\Psi(q, p'') - \Psi(q, p')\Psi(q, p)], \end{aligned} \tag{6}$$

where $W(p''', p'', p', p)$ is the scattering cross-section, describing the probability of two particles with initial momenta p''' and p'' attaining the momenta p' and p after the collision. Obviously, this collision term on the right hand side is difficult to evaluate. However, often it can be approximated and simplified. If the Boltzmann equation admits an equilibrium Ψ_∞, then often for evolution close to this equilibrium the approximation $C[\Psi] \approx \tau^{-1}[\Psi_\infty - \Psi]$ is valid, where τ is the relaxation time of the system. A typical example of application in accelerator physics is the rigorous treatment of intra-beam scattering. The Boltzmann equation is a first-order, non-linear integro-partial differential equation.

Vlasov Equation

If the interaction is such that the interaction with the many far-away particles cannot be neglected in comparison to the few close-by particles it is often advisable to combine the interaction with all particles in a smooth field. This is the so-called *mean-field approximation*. A kinetic equation including this type of interaction can be obtained by including the interaction potential in form of a collective Hamiltonian $H_{\mathrm{col}}[\Psi]$ which depends on the PSD Ψ itself. This results in the *Vlasov equation* [5,6]

$$\partial_t \Psi - \{H_0 + H_{\mathrm{col}}[\Psi], \Psi\} = 0. \tag{7}$$

Many physically relevant systems can described by a Vlasov equation with an appropriate collective Hamiltonian. In the case of electrostatic interaction the interaction potential is the solution of a Poisson equation with the configuration space density acting as the source term, so that

$$H[\Psi]_{\mathrm{col}} = V[\Psi](q) = \int_{\mathbb{R}^{2d}} G(q', q)\Psi(q', p') \, \mathrm{d}^d q' \, \mathrm{d}^d p', \tag{8}$$

where G is the Green function of the Poisson equation. For general electro magnetic cases the system becomes a Vlasov-Maxwell system, where the configuration space density and configuration space current density act as the source terms. The Vlasov equation is a first-order, non-linear integro-partial differential equation.

Fokker-Planck Equation

In some physical systems the single particle motion is not completely deterministic. If for instance a particle emits a synchrotron radiation photon, the emission causes a change in a particles momentum in a randomly distributed direction. Such a random process can be described by adding an appropriate stochastic term to the single-particle EOM, which then become stochastic differential equations (SDEs). To derive a kinetic equation these stochastic terms can be integrated out using averaging methods, which yields the *Fokker-Planck equation* [7,8]

$$\begin{aligned} \partial_t \Psi - \{H, \Psi\} = \\ \nabla_p[K(z,t)\,\Psi] + \tfrac{1}{2}\nabla_p[Q(z,t)\nabla_p\{Q(z,t)\Psi\}]. \end{aligned} \tag{9}$$

The damping term K and the diffusion term Q can be determined from the SDEs of the single-particle EOM. The Fokker-Planck equation is a linear, second-order PDE.

METHOD OF CHARACTERISTICS

Using the method of characteristics a PDE can be transformed into two ordinary differential equations: one for the so-called *characteristics*, which are particular trajectories through the domain of the PDE, and one for the value of the solution of the PDE along those characteristics [9]. In the particular case of the Liouville equation, this allows an exact analytical solution — a result known as Liouville's theorem. More complicated kinetic equations can also be solved approximately with the method of characteristics by using operator splitting methods. These insights are the groundwork for two of the numerical methods we will introduce in the next section. Consider an initial value problem for $u(t,z), u \colon \mathbb{R} \times \mathbb{R}^{2d} \to \mathbb{R}$ of the form

$$\begin{cases} \partial_t u + A(t,z)^{\mathrm{T}} \nabla_z u = B(t,z) \\ u(t_0, z) = u_0(z) \end{cases}, \tag{10}$$

where u_0 is a known initial condition. Given any path $\xi(t), \xi : \mathbb{R} \to \mathbb{R}^{2d}$ with $\xi(t_0) = z_0$ define $v(t), v : \mathbb{R} \to \mathbb{R}$ as the value of the solution of the PDE along that path $v(t) = u(t, \xi(t))$. The total derivative of $v(t)$ is then given by

$$\mathrm{d}_t v = \partial_t u + \mathrm{d}_t \xi^{\mathrm{T}} \nabla_z u. \tag{11}$$

By comparing terms it can be seen that Eq. (11) is equivalent to Eq. (10) if

$$\begin{cases} \mathrm{d}_t \xi = A(t, \xi), & \xi(t_0) = z_0 \\ \mathrm{d}_t v = B(t, \xi(t)), & v(t_0) = u_0(z_0) \end{cases}, \tag{12}$$

which are two ODEs equivalent to the PDE.

Application to the Liouville Equation

Inspecting the Liouville equation (3) it can be seen that it is of the form Eq. (10) with $A(t,z) = J^{\mathrm{T}} \nabla_z H(t,z)$ and $B(t,z) = 0$. Plugging this into Eq. (12) it follows immediately from

$$\mathrm{d}_t v = 0, \quad v(t_0) = \Psi_0(z_0) \tag{13}$$

ISBN: 978-3-95450-220-2 ISSN: 2673-5474 doi: 10.18429/JACoW-FEL2022-WEBI1

that the value of the solution is constant constant along the characteristics

$$v(t) = u(t, \xi(t)) = \Psi_0(z_0). \tag{14}$$

The ODE for the characteristics is

$$\mathrm{d}_t \xi = J^{\mathrm{T}} \nabla_z H(z,t), \quad \xi(t_0) = z_0, \tag{15}$$

which are exactly Hamilton's EOM. The characteristic $\xi(t)$ starting at $\xi(t_0) = z_0$ is therefore given via the symplectic flow ϕ generated by the Hamiltonian H: $\xi(t) = \phi_{t\leftarrow t_0}(z_0)$ — a fact that is commonly referred to as Liouville's theorem. A remarkable feature of the symplectic flow, is that it injective, so that it is is always invertible, in the sense that for all $t_0, t_1 \in \mathbb{R}$ and $z \in \mathbb{R}^{2d}$: $\phi_{t_0 \leftarrow t_1}(\phi_{t_1 \leftarrow t_0}(z)) = z$. Employing this invertibility, an explicit solution for the PSD can be obtained from Equation (14)

$$\begin{aligned} &\Psi(t, \phi_{t\leftarrow t_0}(z_0)) = \Psi(t_0, z_0) \\ &\iff \Psi(t, z_0) = \Psi(t_0, \phi_{t_0 \leftarrow t}(z_0)). \end{aligned} \tag{16}$$

It is noteworthy that this holds for any symplectic map $M \in \mathrm{Symp}(\mathbb{R}^{2d})$. Going forward we will use the map notation in favor of the flow notation when the specific flow and times are of no importance.

An elegant formulation of the solution of the Liouville equation is via propagation operators commonly referred to as *Perron-Frobenius operators* [6]. For any map M there is an associated Perron-Frobenius operator $\mathscr{M}$ defined by

$$\mathscr{M}\Psi(t_0, \cdot) \equiv \Psi(t_0, M^{-1}(\cdot)) = \Psi(t_1, \cdot). \tag{17}$$

Vlasov-Poisson Equation: Operator Splitting

We have seen that an explicit solution for the Liouville equation can be constructed via the method of characteristics when the solution of the single-particle EOM is known. In case of the Vlasov equation, however, the EOM of the characteristics depend on the collective state of the system via a collective term in the Hamiltonian. Due to this collective dependence it is in general not possible to find explicit solutions for the characteristics, so that the method of characteristics is not directly applicable. Consider the Vlasov-Poisson Eq. (7) with the collective Hamiltonian $V[\Psi](q)$ given by Eq. (8) and a separable single-particle Hamiltonian $H_0 = T(p) + K(q)$. It is apparent that a Poisson-type collective Hamiltonian is invariant under maps that change the momentum coordinates only –so called kick maps– as it depends merely on the configuration-space density. Kick maps are generated by a Hamiltonian that does not depend on the momentum coordinates. Hence, the Hamiltonian $V[\Psi](q) + K(q)$ is invariant under its own induced dynamics. The solution of the Vlasov equation $\partial_t \Psi - \{V[\Psi] + K, \Psi\} = 0$ where the collective Hamiltonian depends on the current PSD is equal to the solution of the Liouville equation $\partial_t \Psi - \{V[\Psi_0] + K, \Psi\} = 0$, in which the collective Hamiltonian is constant and depends only on the initial condition Ψ_0 of the PSD as a parameter. A solution to the full Vlasov-Poisson equation with Hamiltonian $T(p) + V[\Psi](q) + K(q)$ can therefore be approximated for a small time step Δt using Strang-splitting of the exact Perron-Frobenius operator $\mathscr{M}_{\Delta t}$, which is given by

$$\mathscr{M}_{\Delta t} = \mathscr{T}_{\frac{\Delta t}{2}} \mathscr{V}[\Psi^*]_{\Delta t} \mathscr{T}_{\frac{\Delta t}{2}} + O(\Delta t^2), \tag{18}$$

where $\mathscr{T}$ and $\mathscr{V}$ are the Perron-Frobenius operators associated to the autonomous flows generated by the Hamiltonians T and $V[\Psi^*] + K$ respectively, where $\Psi^* \equiv \mathscr{T}_{\Delta t/2} \Psi_0$ and the subscripts denote propagation time [10]. Note that the error term for a separable Hamiltonian is second order in Δt.

NUMERICAL METHODS

In the previous sections we have seen that the kinetic equations are partial differential equations. Apart from certain special cases, analytic solutions cannot be obtained in the majority of cases. Hence, numerical solution methods have to be employed. The numerical solution methods that are useful in the simulation of kinetic equations can be categorised in three broad categories which will be introduced in the following: Lagrangian, Semi-Lagrangian, and Eulerian methods.

Lagrangian Approach

In the Lagrangian approach the PSD is approximated based on macroparticles carrying information about the PSD that are tracked along the characteristics through phase space. The number of macroparticles N in a simulation is typically much smaller than the actual number of particles in the physical system. Reducing the number of macroparticles can reduce the computational costs of this approach enough to make it viable [11,12]. In a typical macroparticle simulation, the initial macroparticle ensemble $\{z_1, \dots, z_n\}$ is generated by sampling a distribution function χ. The actual PSD Ψ can then be approximated by a Klimontovich density

$$\Psi_K(t_0, z) = \sum_{i=1}^{N} w_i\, \delta(z - z_i) \quad \text{with} \quad w_i = \frac{1}{N} \frac{\Psi(t_0, z_i)}{\chi(z_i)}, \tag{19}$$

where the weights w_i in general depend on the PSD and the distribution function of the macroparticles [13]. Employing the method of characteristics it can be seen that the new Klimontovich density $\Psi_K(t_1, z)$ after propagation by a map M is given by

$$\Psi_K(t_1, z) = \Psi_K(t_0, M^{-1}(z)) = \sum_{i=1}^{N} w_i\, \delta(z - M(z_i)). \tag{20}$$

Hence, the new Klimontovich density can be obtained by tracking all macroparticles forward in time while keeping their weights.

Based on the Klimontovich density expected values of the actual PSD in a region $\Omega \subset \mathbb{R}^{2d}$ can be approximated by

$$\int_\Omega f(z)\, \Psi(z)\, \mathrm{d}^{2d}z \approx \int_\Omega f(z)\, \Psi_K(z)\, \mathrm{d}^{2d}z = \sum_{z_i \in \Omega} w_i f(z_i). \tag{21}$$

ISBN: 978-3-95450-220-2 ISSN: 2673-5474 doi: 10.18429/JACoW-FEL2022-WEBI1

The error of this approximation depends on the number of particles $N(\Omega)$ in Ω and typically is $O(1/\sqrt{N(\Omega)})$. Slightly better error behaviour might be achieved by sampling the particle distribution using low-discrepancy sequences. An approximation of the smooth PSD or projections thereof can be reclaimed by binning the macroparticles on a coarse grained grid or via meshless interpolation methods [14].

While the distribution function of the macroparticles can in principle be chosen freely, there are two canonical choices for χ: The most intuitive choice is to use the PSD as the macroparticle distribution function $\chi = \Psi(t_0, \cdot)$. In this case the weights of all particles are equal $w_i = N^{-1}$. The other obvious choice is to distribute the macroparticles uniformly inside a region of phase space $V \subset \mathbb{R}^{2d}$. One way to achieve such a distribution is to randomly sample the uniform density which is constant $\chi = |V|^{-1}$ inside V and 0 else. In this case all particles have a different weight $w_i = |V|\, \Psi(t_0, z_i)\, N^{-1}$, which therefore have to be accounted for explicitly in a numerical implementation. It is however also possible to generate uniformly distributed macroparticles deterministically by placing them on a grid covering V. This has the added benefit that the weights of a quadrature formula can be included in the macroparticle weights, which can aid the accuracy of calculations of expected values [15]. A uniform distribution samples the core of the PSD with the same density of macroparticles as the tail, which is of significant advantage when calculating higher order moments of the PSD. The main advantage of Lagrangian methods is their inherent preservation of probability. In addition they ameliorate the curse of dimensions in the sense that the computational cost grows only linearly with the number of dimensions and number of involved macroparticles. However, the inherent introduction of artificial shot noise is strongly enhanced when going to higher dimensions without adequately resizing the macroparticle ensemble. This becomes particularly troublesome when studying collective instabilities at small length scales, which might be artificially excited by the numerical shot-noise.

Semi-Lagrangian Approach

The hallmark of semi-Lagrangian methods is to directly employ the method of characteristics to update the PSD [16], whose values are stored on the nodes of a $2d$-dimensional grid with coordinates z_i, which for the sake if notational simplicity will be label with a single index. Using the method of characteristics we have seen that the PSD after applying a map M is given by $\Psi(t_1, z) = \Psi(t_0, M^{-1}(z))$. Hence, the new value of the PSD at the node with coordinates z_i can be determined numerically by applying the inverse of the map M to z_i –which corresponds to tracking it backwards in time– and evaluate the previous PSD $\Psi(t_0, \cdot)$ at the resulting coordinates. As $M^{-1}(z_i)$ will in general not coincide with any of the grid nodes, evaluating $\Psi(t_0, \cdot)$ at $M^{-1}(z_i)$ requires an interpolation scheme that approximates $\Psi(t_0, \cdot)$ based on the known values. Local cubic interpolation, based on the nearest neighbors of $M^{-1}(z_i)$ is generally regarded as a reasonable method, which is easy to implement, has acceptable computational costs and does not suffer from the artificial diffusion that occurs when using linear interpolation. If one restricts M to maps that change coordinates in only one dimension, then global interpolation methods such as spline interpolation or trigonometric interpolation can be applied, which can have desirable advantages over local polynomial interpolation [10].

One particular advantage of the semi-Lagrangian approach is that it is numerically unconditionally stable and does not impose an upper limit on the length of a time step, in contrast to the Eulerian method introduced below. Further, it yields a smooth density, which –in contrast to macroparticle methods– does not suffer from artificial shot-noise. The semi-Lagrangian method suffers severely from the curse of dimensions, making it generally viable only for low-dimensional systems. If the support of the PSD cannot be represented efficiently on a homogeneous rectangular grid coordinate transformations [17] or domain decomposition methods [18, 19] can be employed to enable the simulation of these exotic PSDs.

Eulerian Approach

The Eulerian approach is characterized by the solution of the kinetic equation being represented on discrete, fixed points or regions in phase space. Many families of methods fall in this category, for instance finite differences, finite volumes, finite elements methods [20]. For the purpose of illustration, we will briefly outline how a second-order finite difference scheme with a first-order time step can be put into use to simulate a Liouville equation in two dimensions. The finite difference method approximates the solution of the PSD on discrete grid nodes $z_{i,j} = z_0 + i\, h_q + j\, h_p$ and at discrete times $n\,\Delta t$. The local rate of change for the value of $\Psi_{i,j}$ at each grid node is then determined from the kinetic equation, which in case of the Liouville equation is equal to the Poisson bracket $\partial_t \Psi_{i,j} = \{H, \Psi\}(z_{i,j})$. To approximate the occurring derivatives, a finite difference scheme based on the neighboring grid nodes is employed. For instance, the central, backward and forward second-order finite differences operators for the first derivative in the q dimension are given by

$$\mathrm{D}_q^0 \Psi_{i,j} \equiv \tfrac{1}{2h_q}(-\Psi_{i-1,j} + \Psi_{i+1,j}) \tag{22}$$

$$\mathrm{D}_q^- \Psi_{i,j} \equiv \tfrac{1}{2h_q}(\ \ \Psi_{i-2,j} - 4\,\Psi_{i-1,j} + 3\,\Psi_{i,j}) \tag{23}$$

$$\mathrm{D}_q^+ \Psi_{i,j} \equiv \tfrac{1}{2h_q}(-3\,\Psi_{i,j} + 4\,\Psi_{i+1,j} - \Psi_{i+2,j}) \tag{24}$$

which in the limit $h_q \to 0$ approach the $\mathrm{d}_q \Psi(z_{i,j})$. Analogous operators exist for the p-dimension. The finite difference approximation of the Poisson bracket is then given by replacing the derivatives by the finite differences operators. Using the explicit time-forward Euler method $\Psi_{i,j}([n+1]\,\Delta t) = \Psi_{i,j}(n\,\Delta t) + \partial_t \Psi_{i,j}(n\,\Delta t)\,\Delta t + O(\Delta t^2)$ yields a coupled system of linear equations $\Psi^{n+1} \approx S_{\Delta t}\Psi^n$. Any sensible finite difference scheme has to fulfill certain conditions that ensure their numerical stability, consistency

ISBN: 978-3-95450-220-2 ISSN: 2673-5474 doi: 10.18429/JACoW-FEL2022-WEBI1

with the PDE it approximates, and convergence to the exact solution of the PDE for small time steps. In case of an advection equation such as the Liouville equation, the scheme can only be stable if an upper limit for the length of a time step is not exceeded –the CFL criterion [21]– and if the finite difference operators (22)–(24) are selected using an *upwind* scheme, which uses points upstream of the local velocity field. Among the advantages of the finite difference method is the fact that no EOM for characteristics have to be derived and solved to apply it. Due to the PSD being stored on a grid, integrals of the PSD which are needed for the calculation of collective terms can be computed easily. Further, any additional terms occurring in the kinetic equation –such as the Fokker-Planck terms– can be treated directly by simply adding them to the local rate of change, potentially using discretizations of higher order derivatives. Exotic PSDs can be managed with similar techniques as in the semi-Lagrangian approach. The CFL criterion limits the maximum step size severely so that in application many time steps are required to simulate even simple systems where the solution of the EOM is known exactly.

NUMERICAL EXAMPLES

We will investigate two numerical examples in the two-dimensional phase space using each of the methods presented above. For the finite difference (FD) scheme, we chose a second-order upwind scheme using an explicit Euler time step. The solution of the EOM needed in the Lagrangian and semi-Lagrangian methods are approximated by a second-order explicit symplectic integrator. For the semi-Lagrangian (SL) method we implemented linear and cubic local interpolation. Two macroparticle methods are compared: Monte Carlo macroparticle tracking (MCMPT) where the macroparticles are distributed with Ψ and weighted macroparticle tracking (WMPT) with randomly, homogeneously distributed macroparticles.

As a first example we simulate the Liouville equation with Hamiltonian $H = (q^2 + p^2)/2$ and a bivariate Gaussian distribution –cut off at 6σ and offset by 3σ where $\sigma = 1$– as the initial condition, see Fig. 1. The simulation domain is $[-10\sigma, 10\sigma) \times [-10\sigma, 10\sigma)$, the grid size is 256×256, and the number of macroparticles used is 256^2. Among other things, these results highlight: the perfect conservation of probability of Lagrangian schemes, the good performance of WMPT concerning higher-order moments, and the good conservation of energy by FD schemes, as they are not affected by approximation errors in the solution of EOM. The second example is a simulation of the classroom Vlasov-Poisson equation on the domain $[0, 4\pi) \times [-5, 5)$, with a grid size of 256×512 and the initial condition $\Psi_0(q,p) = \frac{1}{\sqrt{2\pi}} \exp(-\frac{p^2}{2}) \times \alpha\, [1 + \sin(k_0\, q)]$ where $\alpha = 0.5$ and $k_0 = 0.5$ are the amplitude and wave number of a monochromatic perturbation, cf. [10]. This system exhibits strong Landau damping as can be seen in Fig. 2a. While the results of the SL and FD simulations agree well for nearly the whole simulation time, the MCMPT simulations conducted

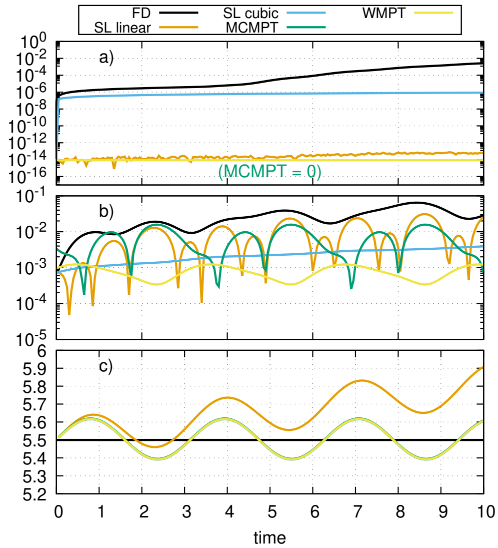

Figure 1: a) deviation of the integral of Ψ from unity; b) excess kurtosis in q of Ψ; c) expected value of H (SL cubic, WMPT and MCMPT coincide graphically).

with 10^4, 10^5, and 10^6 particles, converge only slowly to the same long-time behaviour with increasing number of macroparticles. The same slow convergence can be seen for the Fourier coefficients of the configuration-space density $\rho(q) = \int_{\mathbb{R}} \Psi \mathrm{d}p$, see Fig. 2b. These results indicate that in the macroparticle simulations the artificial modulations induced by numerical shot-noise affect the behaviour of the system measurably, unless a very large number of macroparticles is used.

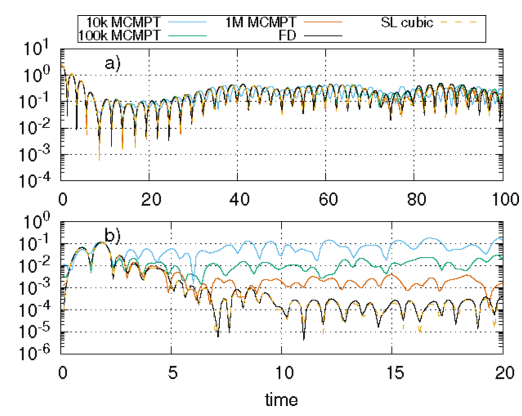

Figure 2: a) L^2 norm of the electric field $\|\partial_q V[\Psi]\|_2$; b) Absolute value of the Fourier coefficient of third harmonic of the configuration-space density $|\tilde{\rho}(3\, k_0)|$.

ACKNOWLEDGEMENTS

The author is deeply indebted to M. Vogt, whose continued support made this contribution possible.

ISBN: 978-3-95450-220-2 ISSN: 2673-5474 doi: 10.18429/JACoW-FEL2022-WEBI1

REFERENCES

[1] L. Perko, *Differential Equations and Dynamical Systems* Springer, 2001.

[2] K. R. Meyer and G. R. Hall, *Introduction to Hamiltonian Dynamical Systems and the N-Body Problem*, Springer, 1992.

[3] J. Liouville, "Note sur la Théorie de la Variation des constantes arbitraires", *J. Math. Pures Appl.* vol. 3, pp. 342–349, 1838.

[4] L. D. Landau and E. M. Lifshitz, *Physical Kinetics*. Oxford : Pergamon, Course of theoretical physics 10, 1980. 10.1016/C2009-0-25523-1

[5] A. A. Vlasov, "The Vibrational Properties of an Electron Gas", *Sov. Phys. Usp.*, vol. 10, 1968. 10.1070/PU1968v010n06ABEH003709

[6] R. L. Warnock and J. A. Ellison, "A General method for propagation of the phase space distribution, with application to the sawtooth instability", in *Proceedings of 2nd ICFA Advanced Accelerator Workshop on the Physics of High Brightness Beams*, US, 2000. pp. 322–348.

[7] C. W. Gardiner, *Handbook of Stochastic Methods*. Springer, 2002.

[8] J. M. Jowett, "Introductory Statistical Mechanics for Electron Storage Rings", *AIP Conf. Proc.*, vol. 153, pp. 864–970, 1987. 10.1063/1.36374

[9] L. C. Evans, *Partial Differential Equations*. Providence, R.I.: American Mathematical Society, 2010.

[10] C. Z. Cheng and G. Knorr, "The Integration of the Vlasov Equation in Configuration Space", *J. Comput. Phys.*, vol. 22, pp. 330–351, 1976. 10.1016/0021-9991(76)90053-X

[11] C. K. Birdsall and A. B. Langdon, *Plasma Pysics via Computer Simulation*. New York: Taylor & Francis, 2005.

[12] R. W. Hockney and J. W. Eastwood , *Computer Simulation Using Particles*. New York: Taylor & Francis, 1988.

[13] A. Y. Aydemir, "A unified Monte Carlo interpretation of particle simulations and applications to non-neutral plasmas", *Phys. Plasmas*, vol. 1, pp. 822–831, 1994. 10.1063/1.870740

[14] R. L. Warnock, J. A. Ellison, K. A. Heinemann, and G. Q. Zhang, "Meshless Solution of the Vlasov Equation Using a Low-discrepancy Sequence", in *Proc. EPAC'08*, Genoa, Italy, Jun. 2008, paper TUPP109, pp. 1776–1778.

[15] M. Vogt, J. A. Ellison, and T. Sen, "Simulations of Three 1-D Limits of the Strong-Strong Beam-Beam Interaction in Hadron Colliders using Weighted Macro-Particle Tracking", *Phys. Rev. ST Accel. Beams*, vol. 5, 2002. doi:10.1103/PhysRevSTAB.5.024401

[16] E. Sonnendrücker *et.al.*, "The Semi-Lagrangian Method for the Numerical Resolution of Vlasov Equations", Research Report RR-3393, INRIA, 1998. Published also as doi:10.1006/jcph.1998.6148

[17] M. Venturini, R. Warnock, and A. Zholents, "Vlasov solver for longitudinal dynamics in beam delivery systems for x-ray free electron lasers", *Phys. Rev. Spec. Top. Accel. Beams* vol. 10, p. 054403, 2007. doi:10.1103/PhysRevSTAB.10.054403

[18] Ph. Amstutz and M. Vogt, "A Time-Discrete Vlasov Approach to LSC Driven Microbunching in FEL-like Beam Lines", in *Nonlinear Dynamics and Collective Effects in Particle Beam Physics*, World Scientific, 1994, pp. 182–191. doi:10.3204/PUBDB-2017-14057

[19] SelaV$_{1D}$, https://selav.desy.de

[20] S. Bartels, *Numerical Approximation of Partial Differential Equations*. Springer, 2016. doi:10.1007/978-3-540-85268-1

[21] R. Courant, K. Friedrichs, and H. Lewy, "Über die partiellen Differenzengleichungen der mathematischen Physik", *Math. Ann.* vol. 100, pp. 32–74, 1928. doi:10.1007/BF01448839

ISBN: 978-3-95450-220-2 ISSN: 2673-5474 doi: 10.18429/JACoW-FEL2022-WEP01

DESIGN OF A NEW BEAMLINE FOR THE ORGAD HYBRID RF-GUN AT ARIEL UNIVERSITY

A. Weinberg*, A. Nause†, Ariel University, Ariel, Israel

Abstract

The ORGAD Hybrid RF-gun was commissioned in Ariel University. The main beamline of the hybrid S-band (2856 MHz) photo injector is currently driving a 150 kW, short pulse THz-FEL. In order to use the RF gun for other applications, a new and independent beam line is required. A secondary beamline is only feasible with the design of a dispersive beam-line dogleg section. High quality beam is crucial for the designated applications such as Ultra-fast Electron Diffraction (UED). The design is based on transfer matrices analytical model followed by simulations. Full 3D GPT (General Particle Tracer) simulations were done on this secondary beamline in which we manipulate and compress the beam to maintain beam emittance and pulse duration. An optimization procedure of the design using realistic field-maps and fringe fields of the quadrupoles was performed to reconstruct the electron beam quality parameters after passing through the dispersive dogleg section. The optimization results demonstrate improved beam quality are presented.

INTRODUCTION

The main beamline of the hybrid S-band (2856 MHz) photo injector [1] ORGAD accelerator is currently used to drive a 150 kW, short-pulse THz-FEL. Using a 90 cm Undulator the THz-FEL is emitting super-radiantly (radiation emitted coherently from all the electrons within the pulse [2]) at 1–3 THz. In order for the electrons to emit coherently in the super-radiant regime, the emitting electron bunch must be shorter than the wavelength of the emitted radiation, in this case less than 100 µm.

A new and independent beam line is required for additional e-beam emission based experiments such as MeV-UED, Compton scattering, noise suppression and enhancement schemes, sub-radiant emission, etc. This secondary beamline is feasible with the design of a dogleg section [3]. A dogleg is constructed of two dipole sections, with higher-order magnetic electron-optics such as quads and sextupoles, added to prevent dispersion. The construction of a dogleg requires a full 3D start-to-end simulations of the entire RF GUN and beamlines. In this work, simulations were carried out using the General Particle Tracer code (GPT), and optimization procedure [4] was performed on these simulations using realistic field-maps. Figure 1 shows the two beamlines and the beam-optics elements. The major challenge in the design was maintaining beam parameters at optimal values for the additional e-beam emission based experiments.

* amirwe@ariel.ac.il

† arieln@ariel.ac.il

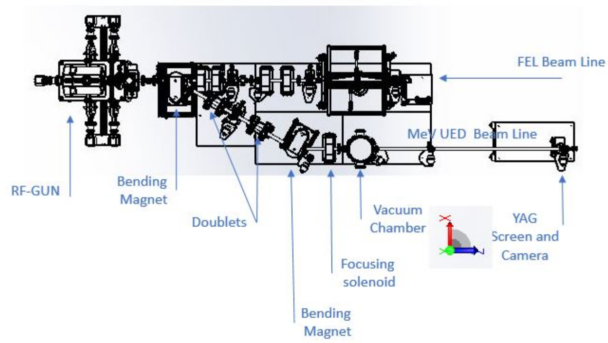

Figure 1: Ariel University's Hybrid Gun. The top beamline is the superradiant THz FEL. The lower beamline is designed for different experiments such as MeV-UED.

DESIGN

The hybrid gun was designed to produce an extremely short pulse in order to emit THz super-radiantly. For this reason, the traveling-wave section of the gun is used to apply a negative chirp on the beam. This is achieved by setting a phase difference of $-\frac{\pi}{2}$ between the standing wave and the traveling-wave sections. However, if required, this phase difference can be varied, resulting with a higher beam energy, or a positive chirp. A dogleg section is designed as a bunch compressor and a positive chirp at the entrance is essential. The planned oblique section of the dogleg design is symmetric around its center and consists of two doublets (focusing and defocusing quadrupoles), with the defocusing quadrupoles facing the center of the section. Sextupole magnets are located on the top of, or next to, the focusing quadrupoles to decrease second order longitudinal dispersion (Fig. 2).

This symmetric configuration of the dogleg electron-optics suggests a preferred beam transport design in which the longitudinal waist is located at the center of the section. Thus, the beam arrives to the center with a positive chirp and emerges with a negative chirp. We begin with an analytical model based on transfer matrices [3] before starting the numerical simulation and optimization procedure. We calculate the transport matrix of the entire dogleg system as the product of the thin lens first order (see Eq. (1)) and second order matrices of the electron optical elements [3].

We find out the value of the longitudinal dispersion parameter at the center of the dogleg, for our given electron optics configuration using the analytical expression (Eq. (2)) to be $R_{56} = -0.0297$ m. The second order matrices were solved analytically using a MATLAB script. The second order dispersion element T_{566} obtained is -0.63 m with no

ISBN: 978-3-95450-220-2 ISSN: 2673-5474 doi: 10.18429/JACoW-FEL2022-WEP01

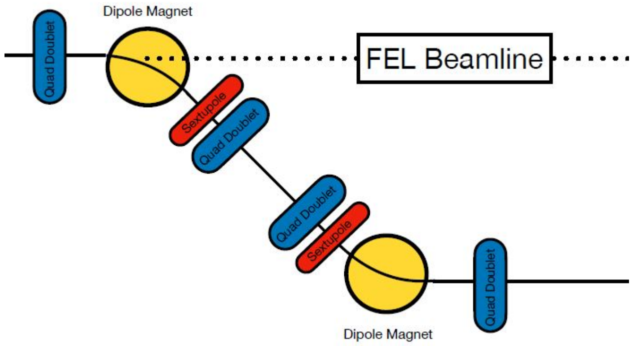

Figure 2: Schematics of the dogleg section with its electron-beam optical elements. Dipole magnets in Yellow, Quadrupoles doublets in Blue and Sextupoles in Red.

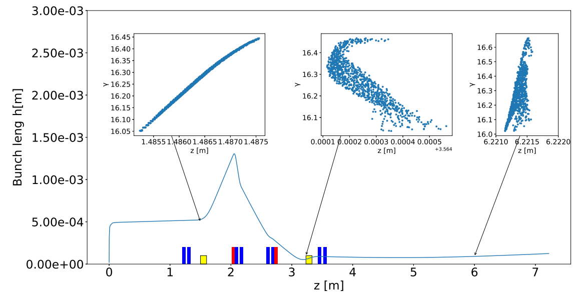

Figure 3: Electron bunch length along the beam trajectory. Longitudinal phase-space at locations before during and downstream the dogleg are presented in frames.

Sextupoles.

$$\begin{bmatrix} x(t) \\ x'(t) \\ y(t) \\ y'(t) \\ l(t) \\ \delta(t) \end{bmatrix} = \begin{bmatrix} R_{11} & R_{12} & 0 & 0 & 0 & \eta_x \\ R_{21} & R_{22} & 0 & 0 & 0 & \eta'_x \\ 0 & 0 & R_{33} & R_{34} & 0 & 0 \\ 0 & 0 & R_{43} & R_{44} & 0 & 0 \\ R_{51} & R_{52} & 0 & 0 & 1 & \eta_z \\ 0 & 0 & 0 & 0 & 0 & 1 \end{bmatrix} \begin{bmatrix} x_0 \\ x'_0 \\ y_0 \\ y'_0 \\ l_0 \\ \delta_0 \end{bmatrix} \tag{1}$$

$$R_{56} = \eta_z = \frac{L}{\beta^2\gamma^2} - \alpha\rho + \frac{\alpha\rho}{\gamma^2} + \rho\sin(\alpha) \quad \text{(center of dogleg)} \tag{2}$$

SIMULATIONS

Full 3D simulations of the hybrid RF-gun and its parallel beamline including full space-charge effects were performed using GPT. The simulations start from the cathode, with randomized normal distribution of particles, using a charge of -30 pC. As mentioned previously the dogleg section is designed as a bunch compressor with a positive chirp at the entrance. The chirp at the end of the dogleg will become negative and a drift section downstream the dogleg will allow us to obtain a waist at a location of our choice Fig. 3. We set the "sweet-spot" of this simulation to be 5 m downstream from the cathode, at the designated vacuum chamber. A significant beam-quality degradation was expected downstream the dogleg and the purpose of this process was to minimize the degradation and obtain optimal parameters for the secondary parallel beam-line.

The simulation goal is optimal emittance and bunch length parameters at this "sweet-spot" location. This procedure was continuously compared to the analytical calculations. The transverse emittance analytical expression includes several first order (R_{16},R_{26}) and second order (T_{166}, T_{266}) dispersion elements. The first order dispersion elements are minimized using the quadrupoles doublets, while the second order dispersion elements values, T_{566}, are both minimized by the sextupoles. Both the first and second longitudinal dispersion corrections minimize the transverse emittance value.

OPTIMIZATION PROCEDURE

We suggested an optimization procedure on the design of the beam-line with the dogleg, aimed to reconstruct the electron beam quality parameters after passing through the dispersive section. The optimization process was performed on a large number of variables as was possible. Typical field maps for quadrupoles in simulation software were based on ideal field maps and included non-fringe field components. The Quadrupoles were modeled using a realistic 3D field map imported from CST. In the first optimization process we iterated through four different parameters:

- L1- The doublet location. The distance from the dogleg dipoles (center of dipole) to the doublet centers.
- L2- The gap in the doublets (between the centers of the focusing and defocusing quadrupoles).
- gf- The focusing quadrupole magnetic field gradient.
- gd- The defocusing quadrupole magnetic field gradient.

The optimization process consisted of iterating through all parameters, exploiting the fact that the dogleg section between the two bends is symmetric, which enables variation of both doublets parameters simultaneously. To find the optimal locations and field strengths of the quadrupoles we define a figure of merit: $A = \epsilon_x \cdot \sigma_z$ for which we search for a minimal value as a function of the desired parameters, Fig. 4.

In the other optimization step, we added two sextupoles on top of the quadrupoles (or positioned next to the doublets). Sextupole field gradients optimization was performed on the ideal GPT sextupole model. Our code scanned the first sextupole field gradient parameter, while the second sextupole field gradient parameter polarity was inverted. Sextupole field values were derived in a similar method such as in the quads optimization, by plotting a contour map for the parameter A. For a charge of -30 pC and beam energy of 7.8 MeV the optimization procedures resulted in recompression of the electron beam to a length of σ_z= 37 µm and an emittance of ϵ_x= 1.48 µm. These results show minor degradation of beam normalized emittance and pulse duration.

ISBN: 978-3-95450-220-2 ISSN: 2673-5474 doi: 10.18429/JACoW-FEL2022-WEP01

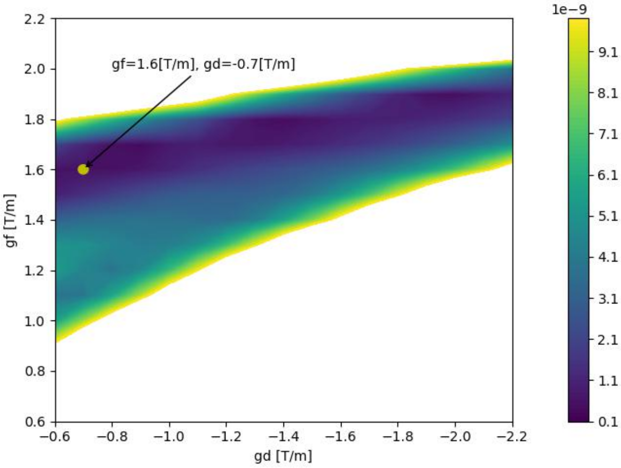

Figure 4: Contour map of beam parameter A. Y axis is beam optics focusing quad gradient and x axis is the defocusing quad gradient strength. Using the selected value (using the minimal value of the parameter A) marked in a yellow dot, we obtain the required magnetic field gradients of the quad doublets.

CONCLUSIONS

We performed an analytical design and full 3D simulations of a dogleg section for a secondary parallel beam-line driven by a hybrid RF photo-injector. Optimization procedure presented here, based on realistic consideration of simulated and measured field maps of quadruples, enables recuperation of beam parameters after a dispersive dog-leg. The optimized recuperated beam parameters attainable for the ORGAD RF-Linac are suitable for operation in high quality beam demanding applications as UED.

REFERENCES

[1] A. Nause *et al.*, ”6 MeV novel hybrid (standing wave - traveling wave) photo-cathode electron gun for a THz superradiant FEL”, *Nucl. Instr. Meth.*, vol. 1010, p. 165547, 2021. doi:10.1016/j.nima.2021.165547

[2] A. Gover *et al.*, ”Superradiant and stimulated-superradiant emission of bunched electron beams”, *Rev. Mod. Phys.*, vol. 91, issue 3, p. 035003, 2019. doi:10.1103/RevModPhys.91.035003

[3] A. Weinberg, A. Nause, ”Dogleg design for an MeV Ultra-fast electron Diffraction beamline for the hybrid Photo-emitted RF GUN at Ariel University”, *Nucl. Instr. Meth.*, vol. 989, 164952, 2021. doi:10.1016/j.nima.2020.164952

[4] A. Weinberg and A. Nause, ”Beam-line optimization based on realistic electron-optics 3D field-maps implementation provides high-quality e-beam via a dogleg section”, *Phys. Plasmas*, vol. 29, p. 063104, 2022. doi:10.1063/5.0087858

ISBN: 978-3-95450-220-2 ISSN: 2673-5474 doi: 10.18429/JACoW-FEL2022-WEP03

DESIGN CONSIDERATIONS FOR A NEW EXTRACTION ARC AT THE EUROPEAN X-RAY FREE ELECTRON LASER

S. D. Walker*
Deutsches Elektronen-Synchrotron DESY, Hamburg, Germany

Abstract

It has been proposed that a new arc, called T20, should be installed for a third fan of undulators at the European X-ray Free Electron Laser (EuXFEL) in the next decade. Due to geometric constraints this arc will need to be at a much larger angle than for the existing arc, called T1. It is expected therefore that coherent synchrotron radiation effects (CSR) in T20 on the bunch emittances will be considerable. To preserve the x-ray beam qualities in any downstream undulators, this effect will need to be understood and ideally mitigated. In this paper the status of the T20 beamline design is discussed, the expected downstream beam properties are shown and possible strategies for improving the beam quality are outlined.

INTRODUCTION

X-ray free electron lasers (XFELs) require ultra-bright electron beams to achieve the desired photon beam characteristics. This means that ultra-short (high peak current) electron bunches with small transverse emittances and energy spread are necessary. However, the impact of coherent synchrotron radiation (CSR), in which radiation from the bunch's tail interacts with its head and subsequently dilutes the bunch's emittance, mandates linear machines. Running counter to this is the desire for multiple undulator beamlines and user experiments. For this reason, XFEL facilities around the world typically branch at relatively small angles (a few degrees with respect to the linac) after acceleration to two or more undulator lines. Still, the effects of CSR on the beam when diverting to these separate lines must be accounted to maintain performance in the downstream undulators.

The EuXFEL [1, 2] splits into three beamlines (T1, T2 and TLD) after the collimation section at the *switchyard*. Directly ahead of the switchyard lies T2, where SASE1 and SASE3 are situated. To the left lies T1 and SASE2, and downwards lies TLD and a beam dump. An additional beamline that branches to the right, called T20, and with it a new set of undulators is planned for the end of the decade. The switchyard and the beam distribution system, including the proposed T20 beamline, were mostly developed during the initial EuXFEL design process [3–5]. The use of CSR mitigation techniques was limited in the T1 arc design due to its small total bending angle (2.3°) rendering them less necessary. Whilst the T20 arc is much larger at 6° to 7°, the T20 design was frozen after considering only the linear optics, without studying collective or non-linear effects. For this reason the impact of CSR on bunches passing through the T20 arc must be investigated, and possible mitigation strategies developed and implemented. In this paper design considerations for transporting ultra-bright bunches in the T20 beamline to new sets of undulators are discussed.

THE T20 BEAMLINE AND COHERENT SYNCHROTRON RADIATION EFFECTS

The T20 arc design mostly developed during the EuXFEL design process outlined in Refs. [3–6] forms a baseline for the performance of subsequent T20 arc designs, as it meets the most fundamental constraints on any such arc—it bends the bunch sufficiently, it matches the upstream optics, and it doesn't overlap with any of the existing magnets, tunnel walls or infrastructure.

To understand the design's performance with regards CSR I tracked 14 GeV, 250 pC Gaussian bunches with initial transverse emittances of 0.6 mm mrad and consisting of two hundred thousand macroparticles with peak currents of 3 kA, 5 kA and 7 kA using OCELOT [7] and its 1D CSR model. I justified the use of the 1D CSR model by evaluating the Derbenev criterion [8] along the entire arc and found that it was satisfied everywhere. The result from this peak current scan is shown in Fig. 1. The local linear dispersion's effect on the emittance at each observation point is accounted for by tracking, without collective effects, each bunch to the end of the arc (where $\eta = \eta' = 0$) before calculating the emittance. The changes in the emittance, $\Delta\varepsilon_x$, are 0.37 mm mrad, 1.3 mm mrad and 3.7 mm mrad at 3 kA, 5 kA and 7 kA, respectively. As expected, this is worse than the simulated impact of CSR on the smaller-angled T1 arc [9], where the simulated projected emittance growth is on order of 1.1 mm mrad in the 7 kA case. The vertical emittances are not discussed here as $\theta_x \gg \theta_y$ for the T20 arc.

The development of the emittance growth can be broadly split into three regions, first the Lambertson kicker-septum scheme up to the 30 m point, the middle six dipoles centred at 50 m and the final three dipoles centred at 70 m (the last two dipoles are vertical). Whilst the emittance growth is clearly dominated by the second two set of dipoles, the impact of the extraction system cannot be neglected, causing the emittance to grow by 0.6 mm mrad to 0.9 mm mrad in the 3 kA to 7 kA range.

The beamline layout, the switchyard, and its position within the tunnel and hall are shown in Fig. 2 and demonstrates the spatial constraints imposed upon the T20 lattice design. The railing at $(z, x) = (2120\,\mathrm{m}, -3.5\,\mathrm{m})$ is 16.3 m from the upstream wall and is angled at 6.6° with respect to the straight ahead (i.e., T2) direction. The angle of this wall

* stuart.walker@desy.de

ISBN: 978-3-95450-220-2 ISSN: 2673-5474 doi: 10.18429/JACoW-FEL2022-WEP03

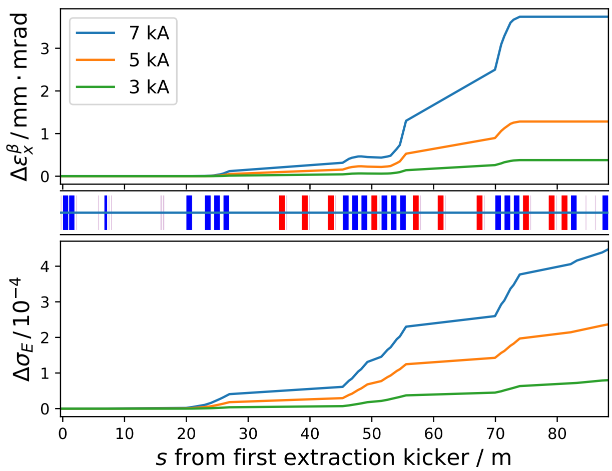

Figure 1: The original T20 design's simulated emittance and energy spread growth along the beamline due to CSR for a range of peak currents. The dispersion-free emittances at the generally dispersive observation points in the beamline were calculated by directly mapping the bunch at each point to the end of the line before calculating the emittance. The Gaussian bunch's initial transverse emittances were 0.6 mm mrad, and the bunch charge used was 250 pC. Dipoles and quadrupoles are shown in blue and red, respectively. Unpowered magnets are shown translucent.sdsa

and the size of the opening into the hall are the immediate fixed constraints on the necessary bending angle. In this design most of the bending is done in the upstream tunnel using relatively weak magnets 0.64 T, meaning much of the space is taken up just by dipoles. For an upgrade of this magnitude, one can reasonably assume new, stronger magnet designs and a maximum field of 1.5 T for a normal-conducting dipole. For the maximum possible future EuXFEL energy of 22 GeV, this corresponds to a minimum bending radius of $\rho = 49$ m, or a maximum curvature of $h = 1.17\,^\circ\,\mathrm{m}^{-1}$.

MITIGATION OF COHERENT SYNCHROTRON RADIATION EFFECTS

There are several approaches to mitigating emittance growth due to CSR. Three possible approaches are outlined in this section, however the list here is not exhaustive and other techniques [10–12] may also need to be considered, although all but the first method following rely on cancelling out a CSR kick in one or more dipoles with one or more additional dipoles further downstream.

Beta Function Waist

The simplest approach involves introducing a waist in the β function in the bending plane of the magnet to minimise the non-linearity of the CSR field and so-called *phase mixing* [13]. Minimising phase mixing preserves slice emittance whereas other methods only prefer its projection. For this reason for any applied CSR mitigation technique, it is generally useful to also have such waists. Additionally, it is useful to consider that when sufficient phase advance is needed between dipoles, a waist in the first dipole will be beneficial as $\delta\varphi \approx \frac{\delta s}{\beta}$, i.e. it will maximise the phase advance going into the downstream section. This approach was applied in the design of the FLASH2 extraction arc [14] as there was insufficient space for other approaches, which tend to require more quadrupoles. To examine the benefits of such a waist, I tracked 250 pC bunches at three different peak currents through a 1 m-long 1.5 T dipole field. The sensitivity to the central β-function is particularly stark at the higher currents, and is shown in Fig. 3.

Point-kick Analysis

The point-kick analysis outlined in [15, 16] describes an approach in which the CSR kick can be cancelled completely in the linear regime over a single double bend achromat (DBA). Perfect cancellation for two identical dipoles, on top of the usual achromatic conditions, additionally requires that

$$\frac{\alpha_1 - \alpha_2}{\beta_1} \cong -\frac{12}{L}, \tag{1}$$

where the subscripted Greek letters refer to the Courant-Snyder parameters in the middle of the dipoles, and L is the dipole length. Figure 4 shows the range of optical parameters that satisfy Eq. (1), and specifically show that satisfying this condition is difficult at such large energies due to the relatively weak quadrupole focusing. Large regions of the space have unrealistic optical parameters either in the first or second dipole.

Optical Balance

This involves balancing the Courant-Snyder parameters and phase advances between consecutive dipoles (either $(2n+1)\pi$ or $2n\pi$) depending on the dipole polarities) so that the CSR kicks cancel each other out in aggregate [17, 18]. This cancellation can occur over several dipoles. This approach is similar to the previous one, in that both schemes rely on a linear proportionality between the magnet length and the CSR-indcued energy spread. For a Gaussian bunch the CSR-induced energy spread is given by

$$\Delta\sigma_E = 0.2459\frac{eQ\mu_0 c^2 L_\mathrm{B}}{4\pi\sigma_z^{4/3}\rho^{2/3}} \tag{2}$$

where the symbols have their usual meanings [8]. More to the point, $\Delta\sigma_E \propto L_\mathrm{B}$.

To ensure that such an approach can be applied, I tracked three different peak currents through various dipole lengths at 1.5 T, shown in Fig. 5. The impact of the nonlinear transient effects is clear for small magnet lengths, but the resulting energy spread is sufficiently small to be neglected. Beyond this there is a linear relationship between the magnet length and the induced energy spread, suggesting the applicability of such cancellation techniques even at such short bunch lengths.

ISBN: 978-3-95450-220-2 ISSN: 2673-5474 doi: 10.18429/JACoW-FEL2022-WEP03

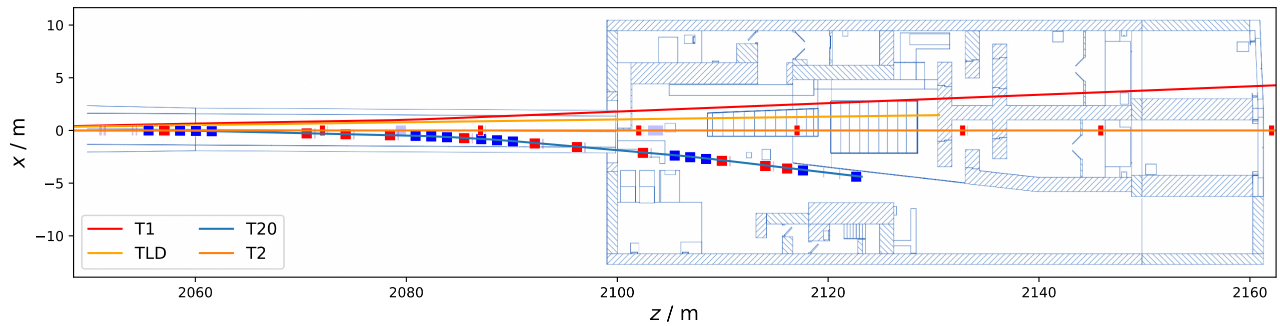

Figure 2: A blueprint for the tunnel and hall in the region of the switchyard at the EuXFEL with the various beamlines superimposed on top. For clarity, only the magnets of the T2 and T20 beamlines are displayed. Dipoles and quadrupoles are shown in blue and red, respectively. Unpowered magnets are shown transparent.

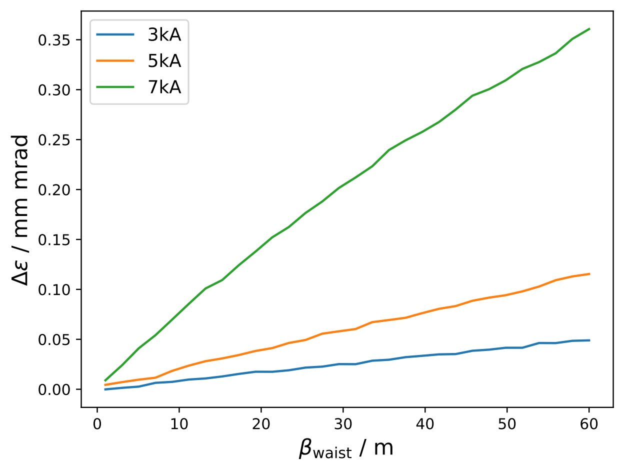

Figure 3: Waist scan at 22GeV for a 250pC bunch for various peak currents, with $L_{\mathrm{B}} = 1.5\,\mathrm{m}$ and $\theta = 1.7°$, which corresponds to a maximum reasonable magnetic field of 1.5 T. The beta waist is in the middle of the dipole and the emittance is sampled 2m past the end of the dipole to account for transient effects.

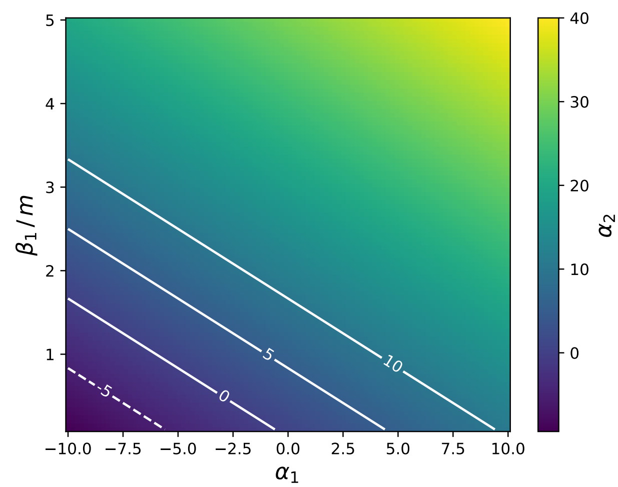

Figure 4: The required Courant-Snyder parameters in a double bend achromat with 1.5 m dipoles to achieve perfect cancellation in the linear regime given the condition in Eq. (1).

CONCLUSION

I described the proposed T20 arc discussed its challenges. The main challenge is the strong CSR effect on bunches in the arc due to the large bending angle, which leads to unacceptable emittance growth at large peak currents. There are several solutions, but they all require strong focussing. This is difficult for two reasons, firstly space is at a premium in the tunnel, and secondly quadrupoles will be effectively quite weak due to the very high beam energy. For these reasons cancelling the CSR kick over two or three achromats may be necessary. Additionally, the EuXFEL is designed for bunch energies up to 1 nC, and the performance of any arc design will need to consider this much higher bunch charge. Finally, a full analysis of chromatic effects will be needed to achieve the required $\pm 1.5\,\%$ energy acceptance.

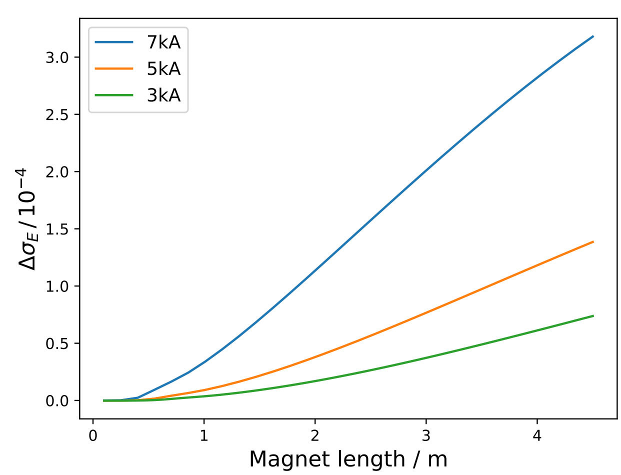

Figure 5: The CSR-induced energy spread in a 250 pC Gaussian bunch for magnets with a range of lengths and $\rho = 48\,\mathrm{m}$, the minimum plausible bending radius at 22 GeV and using normal-conducting magnets.

ISBN: 978-3-95450-220-2 ISSN: 2673-5474 doi: 10.18429/JACoW-FEL2022-WEP03

ACKNOWLEDGEMENTS

I would like to thank Nina Golubeva for helpful discussions regarding optics design. I would like to thank Winni Decking for various useful discussions. I would like to thank Daniel Thoden for help with accessing EuXFEL blueprints.

REFERENCES

[1] M. Altarelli *et al.*, "XFEL: The European X-Ray Free-Electron Laser technical design report", DESY, Hamburg, Germany, Rep. DESY-06-097, Jul. 2007. doi:10.3204/DESY_06-097

[2] W. Decking *et al.*, "A MHz-repetition-rate hard X-ray free-electron laser driven by a superconducting linear accelerator", *Nat. Photonics*, vol. 14, pp. 391–397, 2020. doi:10.1038/s41566-020-0607-z

[3] W. Decking and F. Obier, "Layout of the beam switchyard at the European XFEL" in *Proc. 11th Eur. Particle Accelerator Conf. (EPAC'08)*, Genoa, Italy, Jun. 2008, paper WEPC073, pp. 2163–2165.

[4] V. Balandin, W. Decking, and N. Golubeva, "Tilted sextupoles for correction of chromatic aberrations in beam lines with horizontal and vertical dispersions" in *Proc. 1st Int. Particle Accelerator Conf. (IPAC'10)*, Kyoto, Japan, May 2010, paper THPE062, pp. 4656–4658.

[5] V. Balandin, W. Decking, and N. Golubeva, "Optics for the beam switchyard at the European XFEL" in *Proc. 2nd Int. Particle Accelerator Conf. (IPAC'11)*, San Sebastián, Spain, Sep. 2011, paper WEPC008, pp. 2016–2018.

[6] S. D. Walker and N. Golubeva, "An overview of the T20 beamline for the LUXE Experiment at the European XFEL" in *Proc. 13th Int. Particle Accelerator Conf. (IPAC'22)*, Bangkok, Thailand, Jun. 2022, paper TUPOPT008, pp. 1014–1017. https://accelconf.web.cern.ch/IPAC2022/papers/tupopt008.pdf

[7] I. Agapov, G. Geloni, S. Tomin, and I. Zagorodnov, "OCELOT: A software framework for synchrotron light source and FEL studies", *Nucl. Instrum. Methods Phys. Res., Sect. A*, vol. 768, pp. 151–156, Dec. 2014. doi:10.1016/j.nima.2014.09.057

[8] Y. Derbenev, J. Rossbach, E. Saldin, and V. Shiltsev, "Microbunch Radiative Tail-Head Interaction", DESY, Hamburg, Germany, Rep. TESLA-FEL-95-05, Sep. 1995.

[9] I. Zagorodnov, "Beam Dynamics in SASE2 Arc", https://www.desy.de/fel-beam/s2e/talks/2020_09_29/MAC2019_Zagorodnov.pdf (retrieved 13 Aug. 2022).

[10] M. Venturini, "Design of a triple-bend isochronous achromat with minimum coherent-synchrotron-radiation-induced emittance growth", *Phys. Rev. Accel. Beams*, vol. 19, no. 6, p. 064401, Jun. 2016. doi:10.1103/PhysRevAccelBeams.19.064401

[11] C. Zhang, Y. Jiao, C.-Y. Tsai, "Quasi-isochronous triple-bend achromat with periodic stable optics and negligible coherent-synchrotron-radiation effects", *Phys. Rev. Accel. Beams*, vol. 24, no. 6, p. 060701, Jun. 2021. doi:10.1103/PhysRevAccelBeams.24.060701

[12] R. Hajima, "Emittance compensation in a return arc of an energy-recovery linac", *Nucl. Instrum. Methods Phys. Res., Sect. A*, vol. 528, pp. 335–339, Aug. 2004. doi:10.1016/j.nima.2004.04.063

[13] Dohlus, Martin; Kabel, Andreas; Limberg, Torsten, "Optimal Beam Optics in the TTF-FEL Bunch Compression Sections: Minimizing the Emittance Growth", in *Proc. PAC'99*, New York, NY, USA, Mar. 1999, paper TUP74, pp. 1650–1652. doi:10.1109/PAC.1999.794210

[14] M. Scholz, "Design of the Extraction Arc for the 2nd Beam Line of the Free Electron Laser FLASH", Ph.D. thesis, Phys. Dept., Univ. Hamburg, Hamburg, Germany, 2013.

[15] Y. Jiao, X. Cui, X.Huang, and G. Xu, "Generic conditions for suppressing the coherent synchrotron radiation induced emittance growth in a two-dipole achromat", *Phys. Rev. Accel. Beams*, vol. 17, no. 6, p. 060701, Jun. 2014. doi:10.1103/PhysRevSTAB.17.060701

[16] M. Venturini, "CSR-induced emittance growth in achromats: linear formalism revisited", *Nucl. Instrum. Methods Phys. Res., Sect. A*, vol. 794, pp. 109-112, Sep. 2015. doi:10.1103/PhysRevAccelBeams.19.064401

[17] D. Douglas, "Suggestion and enhancement of CSR-driven emittance degradation in the IR-FEL driver", JLab, Newport News, VA, USA, Rep. JLAB-TN-98-012, Mar. 1998.

[18] S. Di Mitri, M. Cornacchia, and S. Spampinati, "Cancellation of Coherent Synchrotron Radiation Kicks with Optics Balance", *Phys. Rev. Lett.*, vol. 110, no. 1, p. 014801, Jan. 2013. doi:10.1103/PhysRevLett.110.014801

ISBN: 978-3-95450-220-2 ISSN: 2673-5474 doi: 10.18429/JACoW-FEL2022-WEP04

UPGRADE TO THE TRANSVERSE OPTICS MATCHING STRATEGY FOR THE FERMI FEL

A. D. Brynes*, E. Allaria, S. Di Mitri, L. Giannessi, G. Penco, G. Perosa, S. Spampinati, M. Trovò
Elettra-Sincrotrone Trieste S.C.p.A., Trieste, Italy

Abstract

Good control over the transverse distribution of an electron bunch is crucial for optimising the beam transport through a linear accelerator, and for improving the energy transfer of electrons to photons within the undulators of a free-electron laser (FEL). In order to achieve this, it is necessary to match, as closely as possible, the Twiss parameters of the electron bunch to the design values. This is done, in the case of the FERMI FEL, by finding the optimal quadrupole strengths in various matching sections using a particle tracking code. This contribution reports an upgrade to the matching tools in use in the FERMI control room: the functionalities of two existing programs have been merged into a single tool; and some new options are available in order to provide more flexibility when performing transverse optics matching.

INTRODUCTION

Transverse optics matching is a procedure which aims to modify the beam distribution of a particle bunch such that the measured Twiss parameters match the design values [1]. This is an important aspect of accelerator operations and the optimisation of the performance of the machine; in the case of free-electron lasers (FELs), control (and therefore knowledge) of the transverse beam distribution is also important in order to maximise the efficiency of the FEL process and to minimise losses. In general, matching requires a measurement of the Twiss parameters at a dedicated location and an optimisation algorithm which uses a simulation code to take in the measured values and change some elements of the machine, with the goal of minimising the mismatch between the design and measured Twiss parameters.

In the case of the FERMI FEL [2], matching is performed at five locations, consisting of at least one measurement screen and four quadrupole magnets: three along the linac (at the entrance of the laser heater, the exit of the first bunch compressor, and at the end of the linac), and two at the entrance to each of the FEL lines. Matching is routinely done in the FERMI control room using two different programs for the linac and the FEL (refs. [3] and [4] respectively) – this contribution describes an upgrade which combines the functionality of both of these applications into one tool, and includes some new features.

MATCHING PROCEDURE

In order to perform accurate beam matching, a measurement of the transverse beam emittance and Twiss parameters is required. This is typically done at FERMI using the single quad-scan technique [5] at various dedicated matching stations along the machine, and the results of the measurement are written to a dedicated TANGO server [6]. In the process of the upgrade to the matching tools, the program to measure the Twiss parameters has also been updated. The MATLAB-based code that performs the quadrupole scan was migrated to Python in order to make it more robust and faster, and also some new features have been introduced. The previous iteration of the program selected the quadurpole scan range in order to achieve a phase advance variation of $4\pi/3$ during the scan, leaving a certain degree of freedom to the operator. To make the program results less dependent on the operator, the current range of the quadrupole scan and the fitting range can be determined automatically such that it is symmetric with respect to the minimum beam size, and ensuring a phase advance in both planes of $4\pi/3$. The study of an alternative method to measure the transverse beam parameters, based on measurements of the transverse beam size on three or more screens [7], has also recently been started. The method has been tested on the FEL-1 line to derive the beam emittance and the Twiss parameters at matching quadrupole used for the single quadrupole scan method, using measurements of the transverse beam envelope along the undulators. With more measurements (of which seven are, in principle, available along the undulator), the system is overdetermined and a factorization of the matrix [8] or least squares method has to be used to obtain a solution. In a first test, we obtained – in the vertical plane – values of the initial Twiss parameters which were very close to those measured measured with the single quadrupole scan method. The horizontal Twiss parameters derived from this method, however, were larger by around 50 % than those obtained with the standard emittance measurement. The Twiss parameters are then used as an input to the matching algorithm, which runs as follows:

1. Read in the measured Twiss parameters at the quadrupole entrance, measured beam energy and quadrupole strengths upstream of the measurement screen.
2. Reverse the values of $\alpha_{x,y}$ and back-track along the line to a pre-defined location (consisting of at least four quadrupoles).
3. Take the back-tracked Twiss parameters (again reversing the values of $\alpha_{x,y}$) and forward-track using an optimisation procedure in order to reach the design Twiss parameters at the measurement location.
4. The matching procedures then run as follows:

* alexander.brynes@elettra.eu

ISBN: 978-3-95450-220-2 ISSN: 2673-5474 doi: 10.18429/JACoW-FEL2022-WEP04

(a) For linac matching: compare the simulated Twiss parameters at the measurement quadrupole with the nominal values.
(b) For FEL matching: find a set of quadrupole strengths which achieves a periodic FODO cell across two undulators for an average value of $\beta_{x,y}$ or phase advance, and use the matching quadrupoles to match the beam to the FODO channel.

When performing matching in the linac, the figure of merit to minimise is the mismatch parameter [9]:

$$\xi = \frac{1}{2}\left(\beta_d \gamma_m + 2\alpha_d \alpha_m + \beta_m \gamma_d\right), \tag{1}$$

where β, γ and α refer to the beam Twiss parameters, and the subscripts $_d$ and $_m$ refer to the design and measured parameters, respectively. When this parameter is equal to 1, the beam is matched, and the measured parameters at the quadrupole are equal to the design values. In general, a mismatch of less than 5 % is considered an acceptable value. If the mismatch is greater than this, then some options are available to improve it: the matching can be performed again with different initial starting values for the quadrupoles; additional quadrupoles can be included; a different optimisation algorithm can be used; or the number of iterations can be changed. This can also be used as the procedure for matching at the entrance to the undulator line. In practice, it is also sometimes necessary to fine-tune the quadrupoles in between the undulators in order to reduce the beam losses.

TRANSPORT OPTIMISATION

A similar routine has been implementing for transporting the beam from one measurement location to another, with the goal of achieving the design optics parameters throughout the machine. Three different optics settings are produced:

1. The measured initial Twiss parameters are tracked forward using the current machine settings.
2. The beam is matched to the design optics at a specified location based on the measured initial Twiss parameters.
3. The design optics are produced based on ideal Twiss and lattice settings.

By comparing the second and third of these optics settings, it is possible to determine how closely the current machine setup matches the design parameters.

PARTICLE TRACKING

The back- and forward-tracking is performed using the OCELOT simulation toolkit [10, 11], which includes built-in matching functionality, either for single-particle tracking or particle bunches. The tracking lines (both forward and back) are defined, along with all of the accelerator elements, in an ELEGANT [12] lattice file; the actual quadrupole (and undulator) strengths, dipole bend angles, and RF voltages and phases, are read from the control system and written to OCLEOT lattices before tracking. The OCELOT source code had to be modified in order to include the focusing effect in both the horizontal and vertical planes when working with variable-polarisation undulators. The lattice file which is read in by the program is defined in a configuration file. OCELOT includes a matching procedure which uses SciPy [13] minimisation functions. The user can specify the lattice elements to be modified, and the beam parameters to achieve at a given lattice location. A variety of optimisation routines are available by default in OCELOT, although in practice the Nelder-Mead simplex algorithm [14] has been found to be the most effective and fastest in finding a solution. The design Twiss parameters at the various measurement locations are the default matching targets (which are also defined in the configuration file), although the user can customise these values for non-standard configurations. Additional quadrupoles can be included in the matching line if the procedure fails using the standard matching setups.

One further option, not included in the previous tools, is the ability to perform multi-particle matching. This allows for the (optional) inclusion of collective effects such as space-charge and coherent synchrotron radiation, which could have an impact on the beam optics at low beam energy or in dispersive regions (respectively). Operationally, there is not a significant increase in computation time for this option, unless a very large number of particles are tracked, and collective effects are included.

OPERATIONAL EXPERIENCE

The new optics matching tool has been used for matching in the FERMI linac and the undulator line in FEL-1, which consists of a modulator and six radiators in a standard HGHG (high-gain harmonic generation) configuration [2, 15]. Matching in the FEL-2 line is more complicated, since this is composed of a two-stage HGHG line [16, 17] with additional quadrupoles in between the FEL sections, and so this requires more rigorous testing.

A typical output from the matching procedure in the linac is shown in Fig. 1 – in this case, the plot represents the matched β and α functions to reach a waist in the diagnostics section at the end of the FERMI linac. Given that the beam transport was reasonably good before performing the matching, the program managed to converge to a small mismatch value (less than 5 %) within fewer than 100 iterations.

In the case of matching along the undulator line, it has generally been found to be more difficult to match the upstream electron beam optics to that which is required to enter the FODO channel found by the matching algorithm. The algorithm generally requires more iterations to converge, and in some cases has been unable to find a suitable condition. A typical plot produced for the FEL match is shown in Fig. 2. If difficulties are encountered during this procedure, then the user can configure the desired average β function in the FEL FODO; even varying this value by 1 m (from a nominal value of 10 m) can allow the matching procedure to converge more easily.

ISBN: 978-3-95450-220-2 ISSN: 2673-5474 doi: 10.18429/JACoW-FEL2022-WEP04

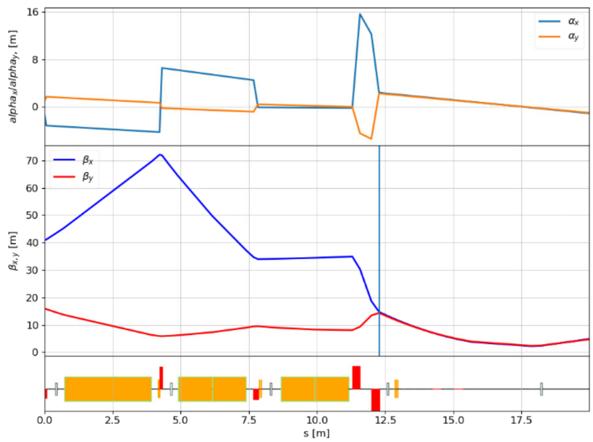

Figure 1: Twiss parameters (top plot: $\alpha_{x,y}$; middle plot: $\beta_{x,y}$) calculated at one of the linac matching stations after performing the optics matching. Quadrupoles, accelerating structures and screens are shown along the bottom in red, green and white respectively.

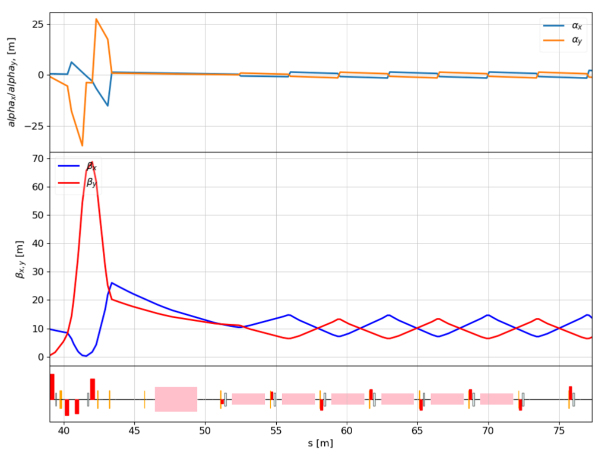

Figure 2: Result of optics matching in the FEL-1 undulator section. The colour scheme for the lattice is the same as that in Fig. 1, with the undulators shown in pink.

During FERMI operation, there have been occasions when the matching procedure (including the previous FEL matching program) has found a theoretical solution, but the losses in the FEL undulators have still remained large. It is possible that this failure to find a good experimental matching condition is the result of errors, either in the measurement of the Twiss parameters, the strengths of the quadrupoles, or some other factor.

Therefore, another program which can visualise these errors has been developed (see Fig. 3). The user can choose to include errors in the Twiss parameters, quadrupole strengths or beam energy, and the β functions are tracked forward from a given measurement point. The shaded areas in Fig. 3 represent the possible range of β functions along the FEL-1 line, given an error in the initial Twiss parameters of 10 %. In this case, the beam losses along the FEL remained large. It can be seen that these sustained losses could be attributed

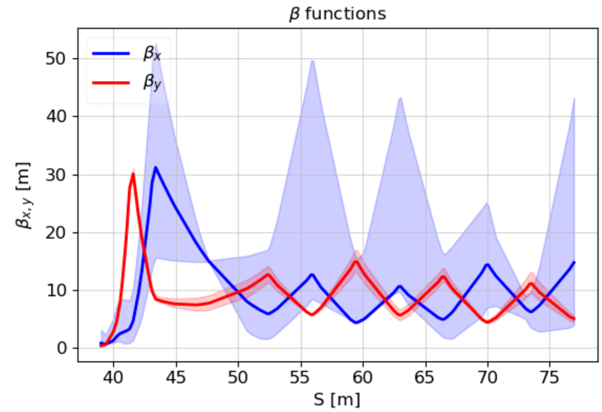

Figure 3: Tracking of the β functions in the FEL-1 line with a 10 % error included in the initial Twiss parameters. The shaded areas represent the possible range of β functions given the full combinatorial range of errors in $\beta_{x,y}$ and $\alpha_{x,y}$.

to an error in the measurement of Twiss functions, since the maximum value of β_x along the line becomes much larger than the nominal (i.e. error-free) value at certain points. As discussed above, it is possible that there are some inaccuracies in the standard method of measuring the beam Twiss parameters. This program also allows the user to tweak the quadrupole settings manually in order to try and find a condition in which the transverse beam parameters are under control.

SUMMARY

The functionalities of two control room applications for performing transverse optics matching in the FERMI FEL have been merged into one tool, with the goal of streamlining the matching process and allowing for greater flexibility in terms of how the matching is done, and to allow for upgrades to the lattice. This work builds on the strong foundation of the matching tools that have been in use during routine FERMI operation, including the integration of the optics and lattice parameters into the control system. As the FERMI lattice is upgraded to accommodate echo-enabled harmonic generation [18] on the FEL-1 line [19], and further upgrades are made to FEL-2, the matching procedure described here will be used to optimise the transverse beam distribution through the FEL in order to optimise its performance. Further developments and commissioning time are required in order to test this procedure on the FEL-2 line.

REFERENCES

[1] M. G. Minty and F. Zimmermann, "Measurement and Control of Charged Particle Beams," *Springer*, 2003.

[2] E. Allaria *et al.*, "Highly coherent and stable pulses from the FERMI seeded free-electron laser in the extreme ultraviolet," *Nat. Photon.*, vol. 6, p. 699, 2012. doi:10.1038/nphoton.2012.233

ISBN: 978-3-95450-220-2 ISSN: 2673-5474 doi: 10.18429/JACoW-FEL2022-WEP04

[3] S. Di Mitri, M. Cornacchia, C. Scafuri, and M. Sjöström, "Electron beam optics and trajectory control in the FERMI free electron laser delivery system," *Phys. Rev. ST Accel. Beams*, vol. 15, p. 012 802, 2012. doi:10.1103/PhysRevSTAB.15.012802

[4] F. Iazzourene and C. Scafuri, "Application Programs of Elettra and FERMI@Elettra," in *Proc. IPAC'14*, Dresden, Germany, Jun. 2014, pp. 3146–3149. doi:10.18429/JACoW-IPAC2014-THPRO107

[5] A. W. Chao, K. H. Mess, M. Tigner, and F. Zimmermann, "Handbook of Accelerator Physics and Engineering," 2013.

[6] T. Controls, 30, 2018. https://tango-controls.org/

[7] H. Wiedemann, *Particle Accelerator Physics*, 4th Ed. Springer, 2015.

[8] W. H. Press, S. A. Teukolsky, W. T. Vetterling, and B. P. Flannery, *Numerical Recipes: The Art of Scientific Computing*, 3rd Ed. Cambridge University Press, 2007.

[9] M. Sands, "A beta mismatch parameter," *SLAC-AP-85*, 1991. https://lib-extopc.kek.jp/preprints/PDF/1991/9105/9105527.pdf

[10] I. Agapov, G. Geloni, S. Tomin, and I. Zagorodnov, "OCELOT: A software framework for synchrotron light source and FEL studies," *Nucl. Instrum. Meth. A*, vol. 768, p. 5, 2014. doi:10.1016/j.nima.2014.09.057

[11] *OCELOT*, 2018. https://github.com/ocelot-collab/ocelot/

[12] M. Borland, "Elegant: A flexible sdds-compliant code for accelerator simulation," 2000. doi:10.2172/761286

[13] *SciPy*, 2018. https://scipy.org/

[14] J. A. Nelder and A. Mead, "A simplex method for function minimization," *Comput. J.*, vol. 7, p. 308, 1965. doi:10.1093/comjnl/7.4.308

[15] L. H. Yu, "Generation of intense uv radiation by subharmonically seeded single-pass free-electron lasers," *Phys. Rev. A*, vol. 44, pp. 5178–5193, 1991. doi:10.1103/PhysRevA.44.5178

[16] L. H. Yu and I. Ben-Zvi, "High-gain harmonic generation of soft x-rays with the 'fresh bunch' technique," *Nucl. Instrum. Meth. A*, vol. 393, no. 2, pp. 96–99, 1997. doi:10.1016/S0168-9002(97)00435-X

[17] E. Allaria *et al.*, "Two-stage seeded soft-x-ray free-electron laser," *Nat. Photon.*, vol. 7, p. 913, 2013. https://www.nature.com/nphoton/journal/v7/n11/pdf/nphoton.2013.277.pdf

[18] G. Stupakov, "Using the beam-echo effect for generation of short-wavelength radiation," *Phys. Rev. Lett.*, vol. 102, p. 074 801, 2009. doi:10.1103/PhysRevLett.102.074801

[19] D. Nölle, "FERMI FEL-1 upgrade to EEHG," presented at the 40th International Free Electron Laser Conference(FEL'22),Trieste, Italy, Aug. 2022, paper TUP59, this conference.

ISBN: 978-3-95450-220-2 ISSN: 2673-5474 doi: 10.18429/JACoW-FEL2022-WEP05

WAKEFIELD CALCULATIONS OF THE UNDULATOR SECTION IN FEL-I AT THE SHINE

H. Liu[1], Shanghai Institute of Applied Physics, Chinese Academy of Sciences, Shanghai, China
J. W. Yan, European XFEL, Schenefeld, Germany
J. J. Guo, Zhangjiang Laboratory, Shanghai, China
T. Liu, H. X. Deng, B. Liu,
Shanghai Advanced Research Institute, Chinese Academy of Sciences,
Shanghai, China
[1]also at University of Chinese Academy of Sciences, Beijing, China

Abstract

The wakefield is an important issue in free electron laser (FEL) facilities. It could be extremely strong when the electron bunch is ultra short. Wakefileds are generated by the electron bunch and affect the electron bunch in turn which possibly destroy the FEL lasing. Wakefield study of the undulator section in FEL-I at the Shanghai high-repetition-rate XFEL and extreme light facility (SHINE) has been carried on in our work before. It shows that the wakefield has a critical impact on lasing performance. In order to diminish the impact of the wakefield, four different pipe schemes were presented. Based on sufficient calculations of resistive wall wakefields and geometry wakefields, we compare the results of these schemes and choose the optimal one for designation of the FEL-I.

INTRODUCTION

In FEL facilities the accumulative effects of wakefields always lead to critical impacts on the electron bunch, resulting in the energy spread and the deviation of transverse position. Thus the lasing performance will be decreased. The SHINE is under construction and the wakefield estimations are required. The SHINE contains three different undulator lines (FEL-I, FEL-II and FEL-III) designed for different functions. The wakefields of FEL-I undulator section have been studied in our work before [1]. However the wakefields of inner segments between undulators were calculated simply. In this paper, we calculate the wakefields of inner segments considering more exquisite structures in FEL-I. We consider gradual changed connections between beam pipes of different diameters and corrugated pipes. We compare wakefields of different schemes of inner segments. In order to estimate the roughness wakefields, we develop the original theory to make it reliable in our cases. Based on the results, we give some suggestions for the designation of the inner segments in FEL-I.

FEL-I PIPE SCHEMES

In our work before, the diameter of the vacuum chamber is 16mm and the corrugated pipes are shielded. The wakefields of the undulator section in FEL-I were studied and showed a critical impact on lasing performance. It is worth noting that the sum of geometry wakefields of the step-outs (discontinuous connections of pipes with different diameters, Figure 1) is one of the main parts of the total wakefield. Thus we consider a new scheme to diminish this part of wakefield through narrowing the aperture variation of step-outs. Since the apertures of the vacuum chambers in undulators and the gap of photon absorbers are fixed, the only changeable pipe is the vacuum chamber in the inner segment. In order to narrow the aperture variation, smaller diameter vacuum chambers should be adopted. However a smaller diameter means a lager resistive wall wakefield [2, 3] and further more, the wakefields of corrugated pipes [4–6] may be introduced because of unshielding. In addition, different materials could lead to different results.

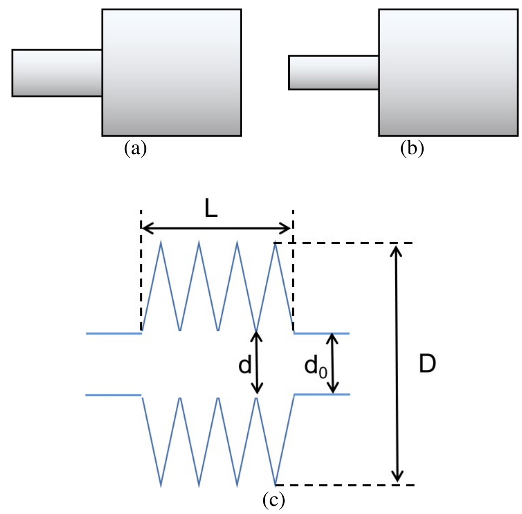

Figure 1: (a) and (b) are the diagram of two kinds of step-outs. (c) shows the geometry of the corrugated pipe.

Table 1: Parameters of Four Pipe Schemes

d_0	d	D
12	shielded	shielded
10	12	23
8	10	20
6	8	18

On the foundation that synthesize the above considerations, we proposed four different pipe schemes with three kinds of materials, copper, aluminum and stainless steel 304. The detailed parameters of the four pipe schemes are shown in Table 1. The differences of these schemes are the diame-

ISBN: 978-3-95450-220-2 ISSN: 2673-5474 doi: 10.18429/JACoW-FEL2022-WEP05

ters of pipes, d_0 is the diameter of the vacuum chambers in inner segments while the minimal diameter and the maximal diameter inside the corrugated pipe are represented by d and D as shown in Figure 1.

WAKEFIELD CALCULATION

We adopted the wakefield simulation code ECHO2D [7], which supports calculations of resistive wall wakefields and geometry wakefields respectively or in the same time. We have compared theoretical results and simulation results of the resistive wall wakefields [8] in our previous work which demonstrated great agreements. In this paper we only perform simulations. We calculate resistive wall wakefields of inner segments including vacuum chambers and photon absorbers (for scheme1 in which the corrugated pipes are shielded by copper pipes, the resistive wall wakefields of copper pipes are counted.) The results are shown in Figure 2. It is obvious that the smaller diameter scheme results in a stronger resistive wall wakefield, which is even more serious when the material is stainless steel 304.

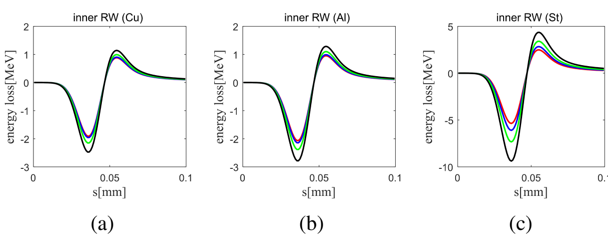

Figure 2: The sum of resistive wall wakefields of inner segments. In all the figures in this section, the results of scheme 1-4 are expressed by red lines, blue lines, green lines and black lines.

The geometry wakefields generated by two kinds of step-outs (connections from undulators and photon absorbers to the vacuum chambers of inner segments) and corrugated pipes. We calculate the geometry wakefield of every single part and the sum of them. Figure 3 shows all the results of geometry wakefields. Actually we calculate the resistive wall wakefield and the geometry wakefield of a corrugated pipe in the same time, although the resistive wall wakefield is unconspicuous. As illustrated in Figure 3, the situation is the exact opposite of the resistive wall wakefields. Reducing the aperture contributes to the decrease of the total geometry wakefields. Although the wakefield of the corrugated pipe in scheme 4 is lager than that in other schemes, geometry wakefields of step-outs constitute the main part of the sum.

In order to choose an optimal scheme, we calculate the total wakefield of the overall undulator section including the wakefields of vacuum chambers in the undulators. The results are illustrated in Figure 4. When the material of the inner segment is copper or aluminum, a smaller aperture means a smaller total wakefield. Nevertheless, when the material is stainless steel 304, the results of these four schemes turn out to be similar, because the resistive wall wakefields

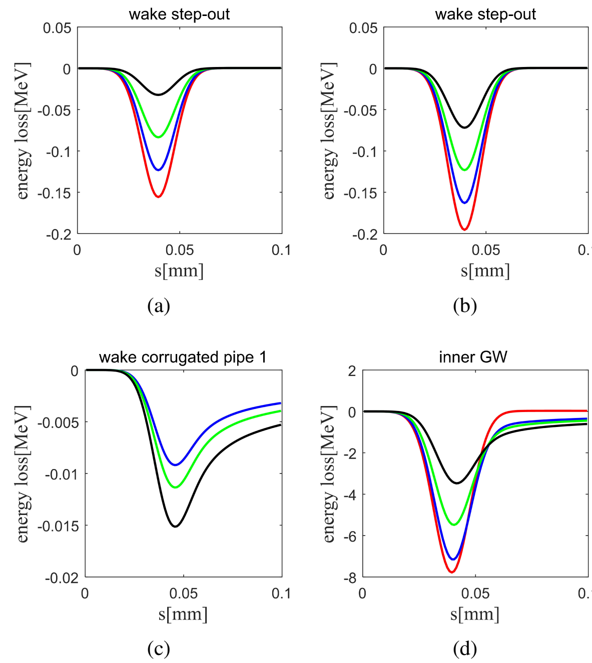

Figure 3: The geometry wakefields of inner segments. (a) and (b) show the geometry wakefields of step-outs while (c) is the result of the corrugated pipe. We calculated the sum of all the geometry wakefields and put the result in (d).

become as important as the geometry wakefileds. The wakefild of the copper inner segment is closed to the aluminum one, while the wakefield of the stainless steel inner segment is obviously too large. In addition, due to price concern we chose aluminum as the material of inner segments. Thus it is obvious that scheme 4 is the best choice. However, considering engineering issues, we chose scheme 3 as the final scheme.

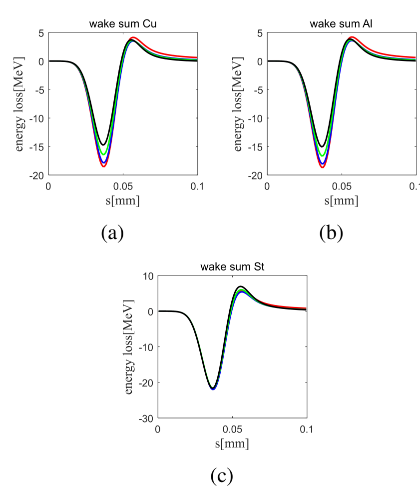

Figure 4: The total wakefield of the overall undulator section.

ISBN: 978-3-95450-220-2 ISSN: 2673-5474 doi: 10.18429/JACoW-FEL2022-WEP05

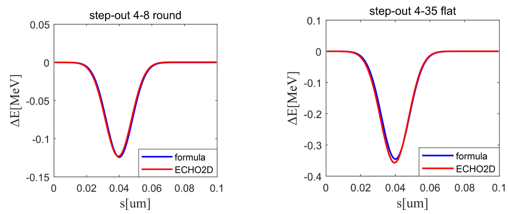

(a) (b)

Figure 5: The simulation results and theoretical results of step-out wakefileds.

DISCUSSION

In the process of finding the optimal scheme, we wondered if a taper step-out (a connection with a slope or an arc between pipes of different apertures) will be helpful in diminishing the wakefield [9]. At first we compared the simulation results with the theoretical results [10] to demonstrate the reliability. The formula we referenced is

$$Z_{||} = \frac{Z_0}{\pi} ln \frac{b}{a} \quad .$$

This formula is applied to round pipes, for flat pipes, the fraction b/a should be replaced by πb/4a.The results are shown in Figure 5. The simulation results and the theoretical results agree well. Then we calculated the wakefileds of taper step-out (both slope mode and arc mode). All the simulation results are almost the same. If we calculate not only the geometry wakefield but also add the resistive wall wakefield in the same time, the taper step-outs will generate smaller wakefields but the difference is not obvious.

In addition, we need an estimation of the roughness wakefield for the designation of FEL-I. Based on the bump mode theory proposed by K.Bane [11] (the diagram of the bump mode is shown in Figure 6), we suggested an upgrade. The original formula is

$$W_{rms} = -\alpha f \frac{cZ_0}{3^{1/4} 2^{3/2} \pi^{3/2}} \frac{r}{b\sigma_z^2} \quad ,$$

where α is a packing factor expressing the relative area on the surface occupied by the bumps.

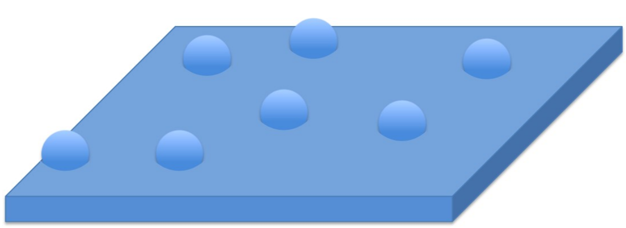

Figure 6: The diagram of the bump mode theory.

In this theory, the slant angle θ is neglected, which is an important parameter of the roughness level of surface. Moreover, the value of α is artificially selected. This leads to an overlarge value in some cases. We supposed that a bump is limited to an equal-height triangle as shown in Figure 7. We hypothesized that the wakefield generated by a bump is similar to an equal-height triangle. This hypothesis is based on our experience that the geometry wakefield mainly depends on the aperture variation. Thus the packing factor α could be expressed by the roughness slant angle θ

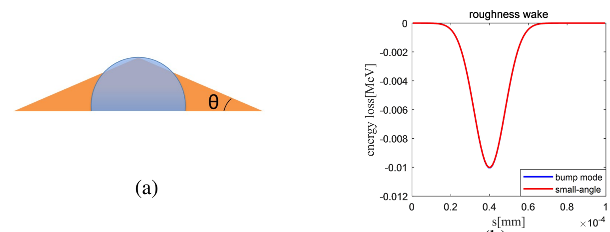

(a) (b)

Figure 7: The schematic diagram of our hypothesis and the roughness wakefields calculated based on our new theory and small-angle approximation.

$$\alpha = \frac{\pi}{4} tan^2\theta \quad .$$

The comparison of roughness wakefield calculated by our new bump mode theory and small-angle approximation [12] is shown in Figure 7. We are gratified by the great agreement, which demonstrates the reliability of our proposal.

CONCLUSION

In order to diminish the wakefields, four different pipe schemes were presented. Vacuum chambers with small diameters generate stronger resistive wall wakefields and lead to the corrugated pipes unshielded. However a smaller diameter of vacuum chamber means a smaller geometry wakefield of the step-out. The taper scheme shows little help for diminishing the wakefield. Thus the choice of optimal scheme should be based on sufficient calculations. Further more the choice of materials was also considered. The results show that the total wakefield decreases when we choose a smaller diameter. Synthetically considering engineering issues, we chose the 8mm diameter pipe scheme and aluminum as the material of vacuum chambers. We also studied the roughness wakefield in FEL-I. Based on the bump mode theory, we suggested an upgrade showing a great agreement with small-angle approximation. Thus this theory could be more reliable.

ACKNOWLEDGMENTS

The authors would like to thank Y. M. Wen and Q. S. Tang for helpful discussions. This work was partially supported by the National Key Research and Development Program of China (Grants No. 2016YFA0401901, No. 2018YFE0103100) and the National Natural Science Foundation of China (Grants No. 11935020, No. 11775293).

ISBN: 978-3-95450-220-2 ISSN: 2673-5474 doi: 10.18429/JACoW-FEL2022-WEP05

REFERENCES

[1] H. Liu *et al.*, "Calculation of undulator section wakefield at the SHINE," in *Proc. SPIE, Eighth Symposium on Novel Photoelectronic Detection Technology and Applications*, vol. 12169, 2022. doi:10.1117/12.2622215

[2] K. Bane and G. Stupakov, "Using surface impedance for calculating wakefields in flat geometry," *Phys. Rev. ST Accel. Beams*, vol. 18, pp. 034401, 2015. doi:10.1103/PhysRevSTAB.18.034401

[3] B. Podobedov, "Resistive wall wakefields in the extreme anomalous skin effect regime," *Phys. Rev. ST Accel Beams*, vol. 12, iss. 4, 2009. doi:10.1103/PhysRevSTAB.12.044401

[4] K. Bane and G. Stupakov, "Impedance of a rectangular beam tube with small corrugations," *Phys. Rev. Accel. Beams*, vol. 6, p. 024401, 2003. doi:10.1103/PhysRevSTAB.6.024401

[5] K. Bane and G. Stupakov, "Corrugated Pipe as a Beam Dechirper," *Nucl. Instrum. Methods Phys. Res., Sect. A*, vol. 690, pp. 106-110, 2012. doi:10.1016/j.nima.2012.07.001

[6] I. Zagorodnov, G. Feng, and T. Limberg, "Corrugated structure insertion for extending the SASE bandwidth up to 3% at the European XFEL," *Nucl. Instrum. Methods Phys. Res., Sect. A*, vol. 837, pp. 69-79, 2016. doi:10.1016/j.nima.2016.09.001

[7] I. Zagorodnov, K. Bane, and G. Stupakov, "Calculation of wakefields in 2D rectangular structures," *Phys. Rev. ST Accel Beams,* vol. 18, p104401, 2015. doi:10.1103/PhysRevSTAB.18.104401

[8] G. Stupakov *et al.*, "Resistive wall wakefields of short bunches at cryogenic temperatures," *Phys. Rev. ST Accel. Beams*, vol. 18, 2015. doi:10.1103/PhysRevSTAB.18.034402

[9] J. Arthur, *et al.*, "Linac Coherent Light Source (LCLS) Conceptual Design Report," SLAC–R–593, Apr. 2002. doi:10.2172/808719

[10] M. Dohlus *et al.*, "Impedances of Collimators in European XFEL," TESLA-FEL Report, Apr. 2010.

[11] K. Bane, and G.V. Stupakov, "Wake of a Rough Beam Wall Surface," in *1998 International Computational Accelerator Physics Conference*, 1998.

[12] M. Song *et al.*, "Wakefield issue and its impact on X-ray photon pulse in the SXFEL test facility," *Nucl. Instrum. Methods Phys. Res., Sect. A*, vol. 822, pp.71-76, 2016. doi:10.1016/j.nima.2016.03.089

ISBN: 978-3-95450-220-2 ISSN: 2673-5474 doi: 10.18429/JACoW-FEL2022-WEP06

LASER PLASMA ACCELERATOR BASED SEEDED FEL COMMISSIONING ON COXINEL AT HZDR

A. Ghaith*, J. P. Couperus, U. Shramm, A. Irman, HZDR, Dresden, Germany
M. Labat, A. Loulergue, M. E. Couprie, Synchrotron SOLEIL, L'Orme des Merisiers, France
E. Roussel, PhLAM–Physique des Lasers Atomes et Molécules, Lille, France

Abstract

The tremendous developments on Laser Plasma Accelerators (LPAs) have significantly improved the electron beam properties and stability making it possible to drive a Free Electron Laser (FEL). We report on the electron beam transport and manipulation using the COXINEL beamline implemented at HZDR that has recently led to the first measurements of an LPA-based seeded FEL in the UV region. Our experiment, cross-checked with Elegant simulations, shows that the beamline enables the handling of the large divergence via high gradient quadrupoles, reducing the slice energy spread with the help of a chicane, controlling the position and dispersion in both transverse planes using beam pointing alignment compensation and implementing the super matching optics. We also show that the beamline properly allows for the spectral tuning and spatial overlap between the electron beam and the seed.

INTRODUCTION

A Free Electron Laser (FEL) consists of a relativistic electron beam traversing a sinusoidal magnetic field generated by an undulator. The electrons interact with the emitted radiation leading to a gain of the FEL wave at the resonant wavelength λ_r [1]:

$$\lambda_r = \frac{\lambda_u}{2\gamma^2}\left(1 + \frac{K_u}{2}\right) \tag{1}$$

where λ_u is the undulator period, γ the relativistic factor, K_u the undulator parameter. The FEL wavelength can be varied by changing the electron beam energy or/and undulator magnetic field. In case of a long undulator, the energy modulation in the electron beam transforms to a density modulation leading to a micro-bunching mechanism. In consequence, a positive feedback is attained between the coherence level and the bunching process, where the FEL wave experiences an exponential gain until saturation. The FEL efficiency can be reinforced by applying an external laser tuned at λ_r to enhance the micro-bunching process. The FEL systems typically operate using conventional Linacs, which are limited to tens to hundreds of MeV/m accelerating gradient, and the pursue for shorter wavelength FEL requires a large accelerator scale and costly infrastructure. Following the advancement on chirped pulse lasers, Laser Plasma Accelerator (LPA) can now generate high energy electron beams within a very short accelerating distance [2–8]. Several experiments have been trying to demonstrate FEL using an LPA the past decade [9–11], and recently amplification has been reported in the self-amplified spontaneous emission configuration at 27 nm wavelength [12].

We report here on the COXINEL beamline design [13, 14] that aims at demonstrating FEL in the seeded configuration at 270 nm. The electron beam transport is discussed along side measurements compared to simulations using Elegant [15].

COXINEL BEAMLINE DESCRIPTION

The COXINEL transport line [16–18], as shown in Fig. 1, starts with a triplet of high gradient permanent magnet based quadrupoles with variable gradient that strongly focuses the LPA electron beam and permits the handling of the divergence. The electron beam is then sent through a four-dipole-magnet chicane enabling to reduce the slice energy spread and lengthening the electron bunch. A second set of quadrupoles placed after the chicane allow for the implementation of the supermatching optics [14]. The commissioned undulator is a hybrid in-vacuum 2 meter long undulator with adjustable magnetic gap. Finally a dipole dummp is placed at the end of the line allowing for photon diagnostics.

QUAPEVAS

In order to achieve FEL amplification, one crucial requirement has to be satisfied $\varepsilon_n < \frac{\gamma\lambda_r}{4\pi}$, where ε_n is the normalized emittance. The typical ε_n of electron beams generated by LPA is around 1 mm.mrad, however the chromatic term, in the following expression,

$$\varepsilon_n^2(s) \approx \varepsilon_{n0}^2 + \gamma^2\sigma_\gamma^2\sigma_{x,z}'^4 s^2$$

increases significantly after a drift s, where σ_γ is the energy spread and $\sigma'_{x,z}$ the divergence. For example, a typical LPA electron beam of 1 mrad divergence, 200 MeV energy and 5% spread: ε_n increases by a factor of 8 after 20 cm drift. Hence the need for high gradient quadrupoles placed very close to the generation source point to mitigate the emittance growth. At COXINEL, a triplet of QUAPEVAs [19, 20] is placed ≈ 4.2 cm from the gas jet (see Fig.2). The QUAPEVA is composed of two concentric quadrupoles, the one at the center has a Halbach hybrid structure, surrounded by the other one that consists of four rotating cylindrical magnets to provide the gradient tunability . It is also mounted on a translation table allowing for horizontal and vertical displacement.

* a.ghaith@hzdr.de

ISBN: 978-3-95450-220-2 ISSN: 2673-5474 doi: 10.18429/JACoW-FEL2022-WEP06

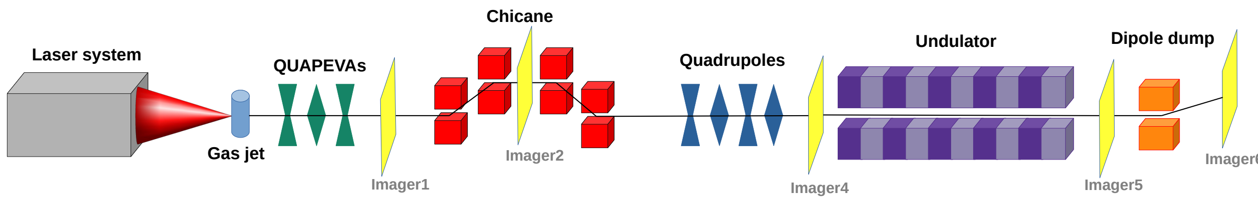

Figure 1: COXINEL beamline schematic view of the magnetic components and the imagers placed along the line.

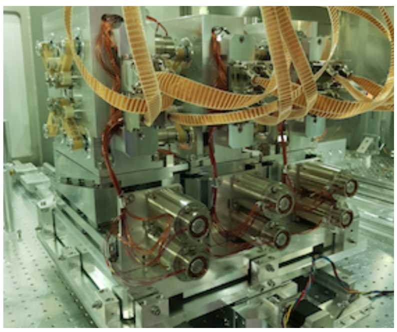

Figure 2: QUAPEVA triplet installed in the vacuum chamber at HZDR and mounted on a translation table.

Chicane

Another FEL requirement concerns the energy spread (RMS) $\sigma_\gamma < \rho$, where ρ is the FEL Pierce parameter that is typically of the orders of 10^{-3}. LPA based electron beams have typically an energy spread of the orders of few percent. A de-mixing chicane can be implemented to disperse the electron beam and sort it in energy to reduce the slice energy spread $\delta\sigma_\gamma$:

$$\sigma_s = \sigma_{s0} + R_{56}\sigma_\gamma \quad , \quad \delta\sigma_\gamma = \frac{\sigma_{s0}}{\sqrt{\sigma_{s0}^2 + R_{56}^2\sigma_\gamma^2}}\sigma_\gamma \qquad (2)$$

where σ_{s0} is the initial bunch length and R_{56} the chicane strength. Furthermore, the decompression of the LPA ultra-short bunch enhances the interaction length of the radiation field with the electron bunch. The chicane used at COXINEL is composed of four electro-magnet dipoles (see Fig. 3) providing a maximum field of 0.55 T.

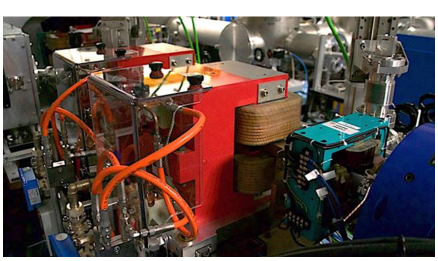

Figure 3: Chicane dipoles installed at COXINEL beamline.

Quadrupoles

After the beam traverses the chicane, energy-position correlation is achieved. By taking advantage of this correlation, another set of quadrupoles is implemented to enable the supermatching optics, in which each energy slice is focused at a different location inside the undulator. This focusing can be synchronized with the FEL wave slippage to acquire better FEL performance [14]. At COXINEL, four electro-magnet based quadrupoles are installed before the undulator as shown in Fig. 4.

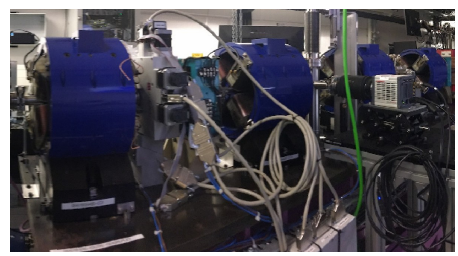

Figure 4: Electro-magnet quadrupoles installed at COXINEL.

Undulator

The photon source is an in-vacuum hybrid-structure planar undulator with NdFeB magnets and Vanadium Premendur poles constructed at synchrotron SOLEIL (see Fig. 5). It consists of 100 number of periods of length 20 mm. In addition, the undulator has an adjustable gap allowing for peak field variation and thus radiation wavelength tunability. The measured peak field B_u versus gap g can be expressed as:

$$B_u = 2.58 \exp\left(-3.37\frac{g}{\lambda_u} + 0.095\frac{g^2}{\lambda_u^2}\right)$$

COXINEL BEAMLINE OPERATION

The electron beam transport rely on beam pointing alignment compensation (BPAC) that is based on the transport matrix to compensate for an initial electron beam pointing or residual misalignment of the QUAPEVAs magnetic center. Accordingly, the electron beam position and dispersion can be independently corrected [21], thanks to a modification of the QUAPEVAs position via the translation tables.

ISBN: 978-3-95450-220-2 ISSN: 2673-5474 doi: 10.18429/JACoW-FEL2022-WEP06

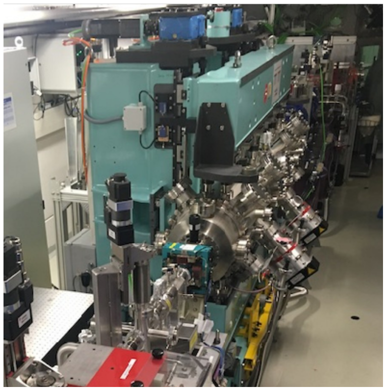

Figure 5: Undulator U20 installed at COXINEL.

Transport

Table 1 shows the electron beam parameters at the source and at the undulator entrance after the transport using Elegant. The *Slice* column corresponds to a 3 µm longitudinal slice of the electron beam for better visualization of the phase space manipulation from source to undulator. The emittance stays more or less the same, as for the slice energy spread, it is reduced by a factor of 30, considering there is no energy chirp on the electron beam at the generation source. The FEL ρ parameter is also calculated, where the sliced bunch at the undulator satisfies the FEL requirements.

Table 1: Electron beam parameters (RMS) at source and undulator entrance

Parameter	**Source**	**Undulator**		**Unit**
	Total	Total	Slice	
Energy	196	196	195.5	MeV
σ_γ	5	4.99	0.16	%
Hor. size	4	450	78	µm
Ver. size	4	90	28	µm
Hor. divergence	0.8	0.035	0.043	mrad
Ver. divergence	0.7	0.55	0.16	mrad
Hor. ε_n	1.2	6.0	1.3	mm.mrad
Ver. ε_n	1.1	18.9	1.7	mm.mrad
Bunch length	3	95	3	µm
Charge	300	300	4.1	pC
Current	30	0.95	0.41	kA
Pierce ρ	1.1	0.2	0.5	%

Figure 6 shows the electron beam phase space at the undulator computed with Elegant. The nominal energy (196 MeV) is well focused in the middle of the undulator, and the lower and higher energies are focused at the entrance and exit, respectively.

Five imaging systems are installed along the beamline as presented in Fig. 2. The transverse distribution of the electron beam measured at COXINEL is shown in Fig. 7 and is compared with simulations using Elegant code [15]: (a,e) in the middle of the chicane; (b,f) before the undulator,

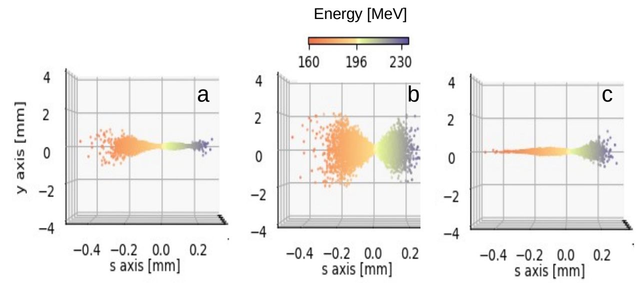

Figure 6: Simulations showing the phase space at the undulator: entrance (a), center (b) and exit (c).

(c,g) after the undulator; (d,h) after the dipole dump. The discrepency of the electron beam shape after the undulator is mainly due to the undulator real magnetic field that is not taken into account in simulations.

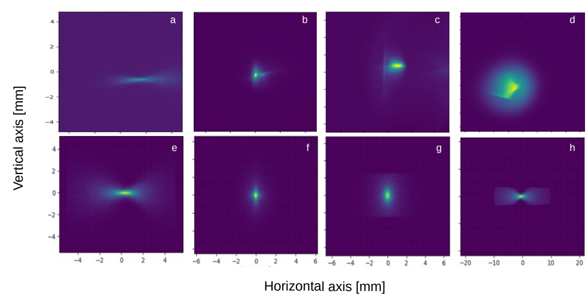

Figure 7: Electron beam transverse profile measured with the imagers along the line (a,b,c,d) and compared with Elegant simulations (e,f,g,h) using the initial parameters of Table 1.

Electron Beam and Seed Alignment

The COXINEL experiment current objective is to demonstrate low gain FEL in a seeded configuration at 269 nm wavelength. A small fraction of the LPA main laser is extracted with a 0.5 inch pick–off mirror to generate the seed by frequency conversion. The seed has a central wavelength of 269 nm with a bandwidth of 3.9 nm–FWHM after spatial filtering. The seed is then injected into the line and propagates with the electron beam inside the undulator. Before FEL measurements, one has to precisely align the seed and the electron beam. The temporal alignment is attained by measuring and observing the seed and undulator radiation on a streak camera with a delay stage added for the seed. The spatial and spectral alignment are achieved by observing the radiation with a UV spectrometer installed at the end of the line. The wavelength can be adjusted by varying the undulator gap. As for the position of the undulator radiation, i.e. position of the electron beam, a corrector located before the undulator can steer and align it spatially with the seed. Figure 8 presents a measurement of the spatio-spectral distribution of both the seed, centered at 269 nm, and undulator radiation exhibiting a broad wavelength range due to the

ISBN: 978-3-95450-220-2 ISSN: 2673-5474 doi: 10.18429/JACoW-FEL2022-WEP06

large energy spread. Low gain FEL signals were indeed observed during the last run [22].

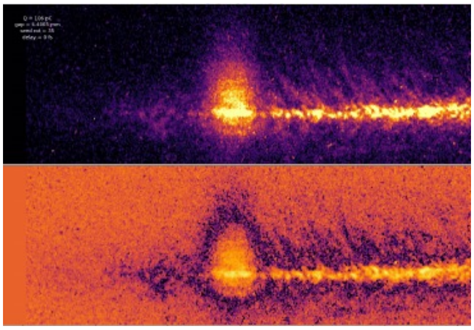

Figure 8: Spatio-spectral distribution measurement of the seed and undulator radiation using the spectrometer. Top (linear scale), bottom (log scale).

CONCLUSION

The COXINEL beamline has been succesively installed and commisioned at HZDR, and an FEL signal has been measured [22]. We have shown here that the LPA electron beam phase space can be manipulated through an adequate transport line to improve its properties. By the use of high gradient quadupoles placed at the vicinity of the generation point, one is able to transport and control the electron beam. A chicane allows to reduce the slice energy spread by almost a factor of 30. The measurements are cross-checked with simulations using Elegant beam optics code.

REFERENCES

[1] J. M. Madey, "Stimulated emission of bremsstrahlung in a periodic magnetic field," *Journal of Applied Physics*, vol. 42, no. 5, pp. 1906–1913, 1971. doi:10.1063/1.1660466

[2] T. Tajima and J. M. Dawson, "Laser electron accelerator," *Physical Review Letters*, vol. 43, no. 4, p. 267, 1979. doi:10.1103/PhysRevLett.43.267

[3] J. Couperus *et al.*, "Demonstration of a beam loaded nanocoulomb-class laser wakefield accelerator," *Nature Communications*, vol. 8, no. 1, pp. 1–7, 2017. doi:10.1038/s41467-017-00592-7

[4] U. Schramm *et al.*, "First results with the novel petawatt laser acceleration facility in dresden," in *Journal of Physics: Conference Series*, IOP Publishing, vol. 874, 2017, p. 012 028. doi:10.1088/1742-6596/874/1/012028

[5] A. Irman *et al.*, "Improved performance of laser wakefield acceleration by tailored self-truncated ionization injection," *Plasma Physics and Controlled Fusion*, vol. 60, no. 4, p. 044 015, 2018. doi:10.1088/1361-6587/aaaef1

[6] X. Wang *et al.*, "Quasi-monoenergetic laser-plasma acceleration of electrons to 2 gev," *Nature communications*, vol. 4, no. 1, pp. 1–9, 2013. doi:10.1038/ncomms2988

[7] W. Leemans *et al.*, "Multi-gev electron beams from capillary-discharge-guided subpetawatt laser pulses in the self-trapping regime," *Physical Review letters*, vol. 113, no. 24, p. 245 002, 2014. doi:10.1103/PhysRevLett.113.245002

[8] E. Esarey, C. Schroeder, and W. Leemans, "Physics of laser-driven plasma-based electron accelerators," *Reviews of modern physics*, vol. 81, no. 3, p. 1229, 2009. doi:10.1103/RevModPhys.81.1229

[9] M. Fuchs *et al.*, "Laser-driven soft-x-ray undulator source," *Nature Physics*, vol. 5, no. 11, pp. 826–829, 2009. doi:10.1038/nphys1404

[10] M. P. Anania *et al.*, "An ultrashort pulse ultra-violet radiation undulator source driven by a laser plasma wakefield accelerator," *Applied Physics Letters*, vol. 104, no. 26, p. 264 102, 2014. doi:10.1063/1.4886997

[11] H.-P. Schlenvoigt *et al.*, "A compact synchrotron radiation source driven by a laser-plasma wakefield accelerator," *Nature Physics*, vol. 4, no. 2, pp. 130–133, 2008. doi:10.1038/nphys811

[12] W. Wang *et al.*, "Free-electron lasing at 27 nanometres based on a laser wakefield accelerator," *Nature*, vol. 595, no. 7868, pp. 516–520, 2021. doi:10.1038/s41586-021-03678-x

[13] M.-E. Couprie *et al.*, "Progress towards laser plasma based free electron laser on coxinel," in *Journal of Physics: Conference Series*, IOP Publishing, vol. 1596, 2020, p. 012 040. doi:10.1088/1742-6596/1596/1/012040

[14] A. Loulergue, M. Labat, C. Evain, C. Benabderrahmane, V. Malka, and M. Couprie, "Beam manipulation for compact laser wakefield accelerator based free-electron lasers," *New Journal of Physics*, vol. 17, no. 2, p. 023 028, 2015. doi:10.1088/1367-2630/17/2/023028

[15] M. Borland, "Elegant: A flexible sdds-compliant code for accelerator simulation," Argonne National Lab., IL (US), Tech. Rep., 2000.

[16] T. André *et al.*, "First Electron Beam Measurements on COXINEL," in *Proc. of International Particle Accelerator Conference (IPAC'16), Busan, Korea, May 8-13, 2016*, Busan, Korea, 2016, pp. 712–715. doi:doi:10.18429/JACoW-IPAC2016-MOPOW005

[17] M.-E. Couprie *et al.*, "Coxinel: Towards free electron laser amplification to qualify laser plasma acceleration," *The Review of Laser Engineering*, vol. 45, no. 2, p. 94, 2017. doi:10.2184/lsj.45.2_94

[18] M. Couprie *et al.*, "Towards a free electron laser using laser plasma acceleration on COXINEL," in *AIP Conference Proceedings*, AIP Publishing LLC, vol. 2054, 2019, p. 030 034.

[19] F. Marteau *et al.*, "Variable high gradient permanent magnet quadrupole (quapeva)," *Applied Physics Letters*, vol. 111, no. 25, p. 253 503, 2017. doi:10.1063/1.4986856

[20] A. Ghaith *et al.*, "Tunable high gradient quadrupoles for a laser plasma acceleration based fel," *Nuclear Instruments and Methods in Physics Research Section A: Accelerators, Spectrometers, Detectors and Associated Equipment*, vol. 909, pp. 290–293, 2018. doi:10.1016/j.nima.2018.02.098

[21] T. André *et al.*, "Control of laser plasma accelerated electrons for light sources," *Nature Communications*, vol. 9, no. 1, pp. 1–11, 2018. doi:10.1038/s41467-018-03776-x

[22] M. Labat *et al.*, "Seeded free-electron laser driven by a compact laser plasma accelerator," 2022.

ISBN: 978-3-95450-220-2 ISSN: 2673-5474 doi: 10.18429/JACoW-FEL2022-WEP08

SIMULATION STUDY OF A DIELECTRIC BEAM ENERGY DECHIRPER FOR THE PROPOSED NSRRC EUV FEL FACILITY

C.K. Liu, S.H. Chen, S.Y. Teng, Department of Physics, NCU, Taoyuan, Taiwan
W.Y. Chiang†, W.K. Lau, NSRRC, Hsinchu, Taiwan

Abstract

In this report, we present a simulation study of dielectric beam energy dechirper designed for the proposed NSRRC EUV FEL (National Synchrotron Radiation Research Center Extreme UltraViolet Free Electron Laser) facility. As revealed from ELEGANT (ELEctron Generation ANd Tracking) [1] simulation of the high brightness driver linac system, a residual correlated energy spread of about 42 keV/μm is left over after bunch compression. To maximize radiation output pulse energy, this energy chirp is removed by a capacitive dechirper structure when the bunch is slightly over-compressed. We successfully used a 1-m long corrugated pipe to remove the residual energy chirp in the simulation study. However, to save space and for a simplified mechanical design, we also consider the usage of two orthogonally oriented planar dielectric-lined waveguide (DLW) structures for removal of residual energy chirp after bunch compression. Both longitudinal and transverse wake fields due to this DLW dechirper at various gap heights, dielectric layer thickness and dielectric constants have been calculated by Computer Simulation Technology (CST) [2] code for evaluation purposes. Longitudinal wake functions can be deduced for ELEGANT simulation.

INTRODUCTION

A 66.5-200 nm FEL facility driven by a 250 MeV high brightness electron beam has been proposed in NSRRC. The baseline design is a 4th harmonic HGHG FEL that utilize 266-800 nm optical parametric amplifier (OPA) as seed [3-4]. The 200-250 pC drive beam is delivered by a high brightness linac system equipped with a 60 MeV photoinjector and a 100 MeV magnetic bunch compression system using nonlinear optics. A pair of 5.2-m constant-gradient traveling-wave rf linac structures energized by a single 35 MW pulsed klystron/SLED system are used to boost the compressed beam to nominal energy in an efficient way. It is worth noting that the photoinjector has now been operational for generation of THz super-radiant spontaneous undulator radiation (THz SSUR) for some pilot experiments. In previous simulation study, a 1-m corrugated pipe had been used to reduce correlated energy spread of the drive beam [5]. The structure parameters of the corrugated pipe used are recalled in the Table 1 and Fig. 1.

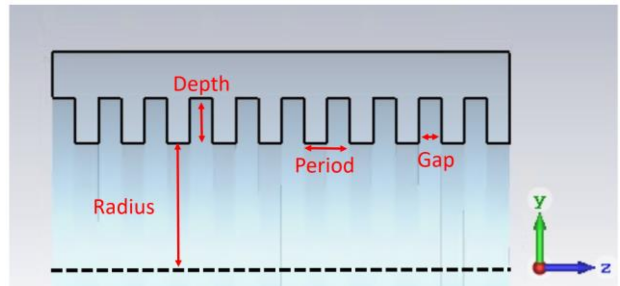

Figure 1: Corrugated beam pipe 2D structure.

Table 1: Dimensions of the Corrugated pipe Dechirper Used in Previous ELEGANT Simulation Study [2].

Parameter	Values
Pipe radius [mm]	1.25
Depth [mm]	0.5
Period [mm]	0.5
Gap [mm]	0.25
Total length [m]	1.0

Figure 2 depicts the electron distribution of the drive beam in longitudinal phase space when the compressed beam passes through such corrugated pipe dechirper. The expected performance of the dechirper has been achieved according to ELEGANT simulation. However, besides relatively large construction cost, the space occupied by the dechirper too long to fit into the 38-m bunker at the NSRRC Accelerator Test Area (ATA). Furthermore, such configuration is not practical because of its unchangeable beam aperture.

In this study, the possibility of using a rectangular dielectric-lined waveguide (DLW) structure for removal of correlated energy spread is under consideration. Longitudinal and transverse wake fields due to this DLW dechirper at various gap heights, dielectric constants and dielectric layer thickness have been calculated by CST code for evaluation purposes. Rectangular DLW structure is considered because it allows a changeable beam gap for wake field amplitude control.

† chiang.wy@nsrrc.org.tw

ISBN: 978-3-95450-220-2 ISSN: 2673-5474 doi: 10.18429/JACoW-FEL2022-WEP08

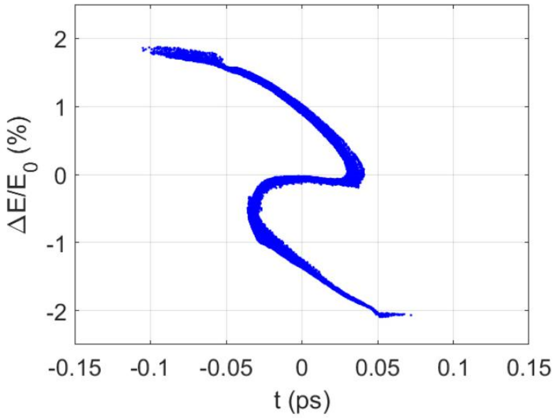

Figure 2: Longitudinal phase space distribution of electrons at driver linac exit. A 1-m corrugated pipe dechirper has been added into the system after the main linac in ELEGANT simulation [3].

DLW DECHIRPER DESIGN

When an electron bunch of charge q traverses along the rectangular DLW structure, longitudinal wake field induced. It is possible to use the longitudinal wake potential to correct the correlated energy spread that remains after bunch compression. Longitudinal wake potential is defined as by the convolution integral of wake function and bunch distribution:

$$\mathrm{W}_{\lambda}(\mathrm{s}) = -\int_{0}^{+\infty} W(s')\lambda(s-s')ds', \tag{1}$$

$\mathrm{W}(\mathrm{s}')$ is longitudinal wake function, $\mathrm{W}_{\lambda}(s)$ is wake potential and $\lambda(s-s')$the longitudinal bunch charge distribution bunch.

We use the wakefield solver of CST software to calculate the wake potentials of the rectangular DLW dechirper. This solver assumed that the drive bunch has a Gaussian line charge distribution. Many previous studies have been done to simulate parallel corrugated plates and DLW structures using CST [6-8]. Good agreement between simulation and experimental results can be obtained. Figure 3 shows the rectangular DLW structure based on the geometry considered in [7]. The reasons of using rectangular DLW structure are its flexibility to tune the gap of waveguide or to trim the thickness of dielectric layers. The dielectric property of the material being used in the simulation is very close to diamond (i.e., dielectric constant is chosen at 5.8). Dimensions of the DLW structure under study are listed in the Table 2: W is the width of rectangular DLW dechirper; $2a$ and b are the gap height of the dechirper and thickness of the dielectric layer respectively, and L the length of DLW structure.

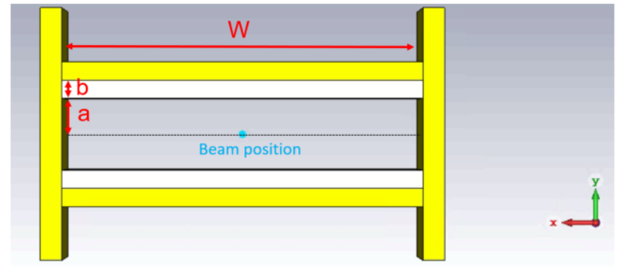

(a)

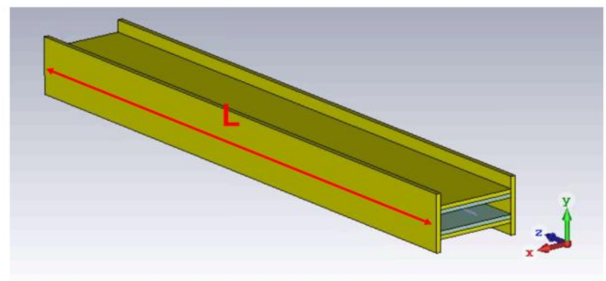

(b)

Figure 3: The rectangular DLW structure geometry.

Table 2: Typical Dimensions of the Rectangular DLW Structure in This Simulation Study.

Parameter	**Values [μm]**
W	100
a	5
b	10
L	750

The RMS length of the Gaussian bunch σ_z is set at about 12.8 μm and the bunch charge Q is 250 pC in this study. Figure 4 shows the calculated longitudinal wake potentials excited by rectangular DLW dechirper at various widths. This study is to estimate the range of rectangular DLW wake field in horizontal direction with the beam parameters as stated above. When W is increased beyond 100 μm, wake potential in limited in a certain extent in horizontal direction. Thus, we choose W at 100 μm in the discussions hereafter.

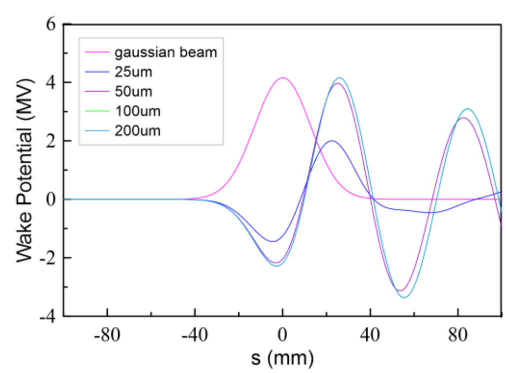

Figure 4: Calculated longitudinal wake potentials of rectangular DLW dechirper at various widths W.

ISBN: 978-3-95450-220-2 ISSN: 2673-5474 doi: 10.18429/JACoW-FEL2022-WEP08

Figure 5 are the calculated longitudinal wake potentials of excited by the bunch in the dechirper at different gap heights. At 10 µm gap height, the first peak of the wake potential reaches 2.29 MV. This value of decreases as dechirper gap height increases. If the gap is increased to 30um, value of the first peak will be reduced to 0.69 MV.

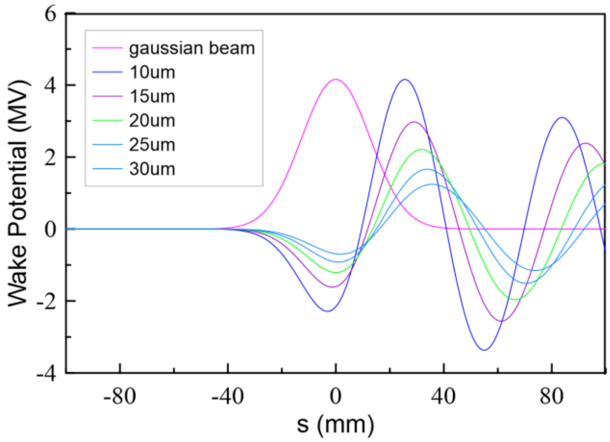

Figure 5: Wake potential for different gap heights of dechirper.

Figure 6 shows the excited longitudinal wake potentials at different thickness of the dielectric layer. Amplitude of the wake potential increases as dielectric layer thickness increases. When the layer thickness of dielectric layer is at 1 µm, value of the first peak of wake potential is 0.46 MV. It is worth noting that it is easier to fabricate thinner dielectric layer.

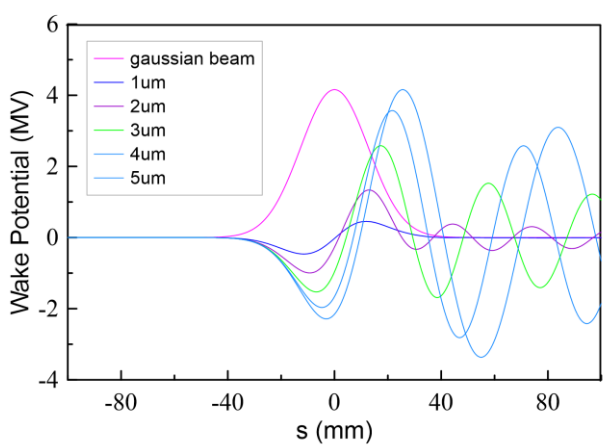

Figure 6: Wake potential on dielectric layers of different thicknesses.

Figure 7 shows the wake potentials at different dielectric constants. These results indicated that higher dielectric constant would have slightly stronger wakes. Thus, we can choose the proper material based on cost or process reason.

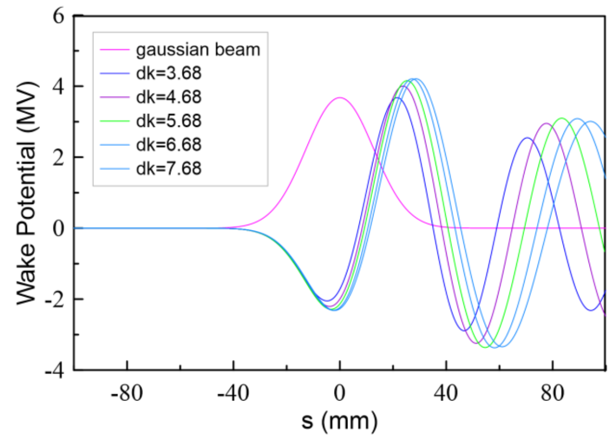

Figure 7: Wake potential for different dielectric constant of dielectric layers.

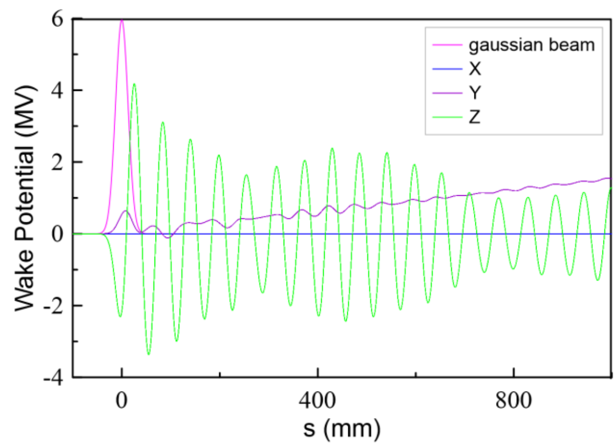

Figure 8: Transverse wake potential for 1 µm beam position offset on y-axis.

Figure 8 is the result of the transverse wake potential when particle beam has a 1 µm vertical offset from the y-axis in Figure 1. Since the gap height of DLW dechirper is 20 µm and the bunch length are about 12.74 µm. Thus, it shown that the transverse displacement of 1 µm has a much impact on the transverse wake potential. The wake potential increases as the tracing distance increases. It will have a greater impact on the bunch tail.

WAKE FUNCTION CAULCULATION

Base on dechirper parameters listed in the Table 2, Wake potential have calculated by CST software and the result shown in Figure 9(a). Here, CST used Gaussian beam charge density function defined as

$$\lambda(s) = \frac{Q}{\sqrt{2\pi}\sigma} e^{(\frac{s^2}{2\sigma^2})}. \qquad (2)$$

According to Eq. (1), wake function can be obtained from wake potential by deconvolution process. Figure 9(b) shown the wake function from the deconvolution process. Analytic wake function will be calculated in next step and compared with this.

ISBN: 978-3-95450-220-2 ISSN: 2673-5474 doi: 10.18429/JACoW-FEL2022-WEP08

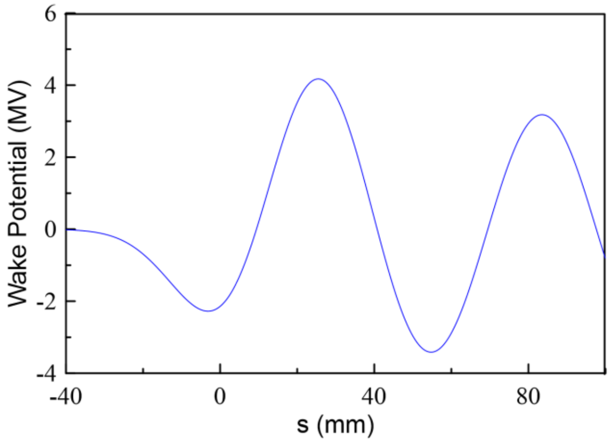

(a)

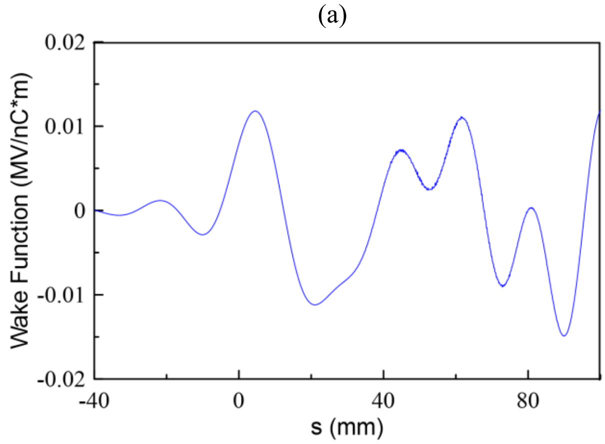

(b)

Figure 9: (a) longitudinal wake potentials excited by DLW dechirper with dimensions listed in Table 2. (b) the corresponding longitudinal wake function obtained by deconvolution.

CONCLUSION

In this paper, CST software is used to simulate the wake potentials of the DLW structures with different dimensions and dielectric constants. This will provide us physical insights in further DLW dechirper design. In the future, CST PIC solver will be used to simulate the effect of the dechirper structure on electron distributions in phase spaces. At the same time, the wake function deduced from the calculated Gaussian bunch excited wake potential by CST can be used to simulate the effect of the dechirper on correlated beam energy dechirper in cooperate with the particle tracking code ELEGANT.

ACKNOWLEDGEMENTS

This work was supported by the Ministry of Science and Technology (MOST), Taiwan, under Grant numbers of MOST- 109-2112-M-213 -013, MOST- 110-2112-M-213 -018, MOST -110-2112-M-008 -022.

REFERENCES

[1] M. Borland, "ELEGANT: A flexible SDDS-compliant code for accelerator simulation", in *Proc. 6th International Computational Accelerator Physics Conference (ICAP'00)*, Darmstad, Germany, Sep. 2000. doi:10.2172/761286

[2] CST Software, https://www.cst.com.

[3] W. K. Lau *et al.*, "An Updated Design of the NSRRC Seeded VUV Free Electron Laser Test Facility", in *Proc. FEL'19*, Hamburg, Germany, Aug. 2019, pp. 651-653. doi:10.18429/JACoW-FEL2019-THP030

[4] S. Y. Teng, C. H. Chen, W. K. Lau, and A. P. Lee, "Start-to-End Simulation of the NSRRC Seeded VUV FEL", in *Proc. FEL'19*, Hamburg, Germany, Aug. 2019, pp. 266-268. doi:10.18429/JACoW-FEL2019-TUP091

[5] W. K. Lau, C. H. Chen, H. P. Hsueh, N. Y. Huang, and J. Wu, "Simulation Study of the NSRRC High Brightness Linac System and Free Electron Laser", in *Proc. IPAC'18*, Vancouver, Canada, Apr.-May 2018, pp. 4329-4331. doi:10.18429/JACoW-IPAC2018-THPMK016

[6] Y. C. Nie *et al.*, "Potential applications of the dielectric accelerators in the SINBAD facility at DESY", *Nucl. Instrum. Methods Phys. Res., Sect. A*, vol. 829, pp. 183-186, 2016. doi:10.1016/j.nima.2016.01.038

[7] Y. Nie *et al.*, "Simulations of an energy dechirper based on dielectric lined waveguides", *Nucl. Instrum. Methods Phys. Res., Sect. A*, vol. 909, pp. 271-275, 2018. doi:10.1016/j.nima.2017.11.050

[8] L. Ficcadenti *et al.*, "Longitudinal and Transverse Wakefields Simulations and Studies in Dielectric-Coated Circular Waveguides", in *Proc. IPAC'18*, Vancouver, Canada, Apr.-May 2018, pp. 4708-4711. doi:10.18429/JACoW-IPAC2018-THPML027

ISBN: 978-3-95450-220-2 ISSN: 2673-5474 doi: 10.18429/JACoW-FEL2022-WEP09

DESIGN CONSIDERATIONS FOR THE EXTRACTION LINE OF THE PROPOSED THIRD BEAMLINE PORTHOS AT SwissFEL

S. Reiche*, P. Craievich, M. Schär, T. Schietinger
Paul Scherrer Institut, Villigen PSI, Switzerland

Abstract

It is planned to extend SwissFEL by a third beamline, named Porthos, operating in the hard X-ray regime. Three bunches will be accelerated within one RF pulse and distributed into the different beamlines with resonant kickers operating at the bunch spacing of a few tens of nanoseconds. While the full extent of Porthos will not be realized before the end of this decade, the extraction line from the main linac will also serve the P^3 (PSI Positron Production) experiment for the demonstration of a possible positron source for the FCC-ee project at CERN. We present the design of the switchyard, which will serve both purposes with only minimal changes.

INTRODUCTION

The free-electron laser (FEL) facility SwissFEL [1] at the Paul Scherrer Institute drives the two independent undulator beamlines Athos and Aramis for the soft and hard X-ray range, respectively. Two electron bunches are generated in the SwissFEL RF photogun within the same RF pulse, accelerated up to the GeV range and compressed in two stages. At 3.2 GeV the second bunch is extracted from the main linac and transported to the Athos undulator, while the other bunch is accelerated further to reach beam energies of up to 6 GeV. Since SwissFEL has demonstrated that multiple beamlines can be operated at the same repetition rate as the RF system, it is planned to extend the facility by a third beamline, called Porthos. Its extraction shares many similarities with the Athos extraction but is placed at the end of the existing linac, putting the operation range of Porthos into the hard X-ray regime. A schematic layout of SwissFEL with the planned third beamline is shown in Fig. 1.

In this contribution we describe the design strategies for the extraction line and its synergy with a planned experiment, named P^3 for “PSI Positron Production” [2], to demonstrate the positron yield for a possible positron source for the FCC project [3].

EXPERIENCE FROM THE ATHOS EXTRACTION LINE

Since the extraction lines for Porthos and Athos share the same purpose they follow the same design guideline. Since we already gained some experience with the operation of the Athos line, we may apply this knowledge to improve upon the design and to eliminate potential bottlenecks in performance and operation.

* sven.reiche@psi.ch

Design Principle

In SwissFEL two electron bunches are generated and accelerated within a single RF pulse. At an energy of about 3.2 GeV and after two stages of bunch compression a resonant kicker system operating at 17.8 MHz [4] extracts the second bunch from the main linac and sends it into the Athos extraction line. Since the time separation between the two bunches is only 28 ns the combination of a kick in the vertical direction for an offset of 10 mm and a Lambertson septum [5], which steers the beam horizontally, offers optimal performance. The other bunch travels on a straight path, passing through a hole in the lower yoke of the septum magnet.

The extraction line provides an offset of 3.75 m for the Athos beamline with respect to the main linac and Aramis beamline. The transport consists of two sections with a total bending angle of 5° and −5°, respectively, and a straight middle section with its length matched to the overall offset. The dispersion function should be closed in the middle section for reducing constraints on the Twiss function between the two bending sections.

The design [6] solves three problems to preserve the beam quality needed to drive the soft X-ray beamline Athos. The first problem is the closure of the vertical dispersion, originating at the resonant kicker. Since it is impractical to generate an offset without dispersion in a short distance before the Lambertson septum, the vertical dispersion leaks through the first bending section and is then caught by a downward dogleg. Two quadrupoles within the dogleg close the vertical dispersion function after the second dogleg dipole. The tunability is limited and requires values for the dispersion functions η_y and η'_y close to those at the Lambertson septum entrance.

The second problem is the residual R_{56} for the simplest solution of a double-bend system—two bending dipoles and a center quadrupole with a focal length half the distance between the bending magnets. It decompresses any bunch with a residual energy chirp from the last compression stage. Without compensating this intrinsic R_{56} of the double-bend system, the electron bunch needs to be compressed stronger to compensate for the elongation by the extraction line. The coherent synchrotron radiation (CSR) [7] effects are unnecessarily stronger and the risk of electron beam quality degradation is high. The Athos extraction design compensates it by a weak center dipole and a total bending of 2° by the Lambertson magnet, 1° by the center dipole and again 2° by the last bending magnet of the first section. The beam transport ensures that the sign of the dispersion function η_x changes for the center dipole and is inverted back for a

ISBN: 978-3-95450-220-2 ISSN: 2673-5474 doi: 10.18429/JACoW-FEL2022-WEP09

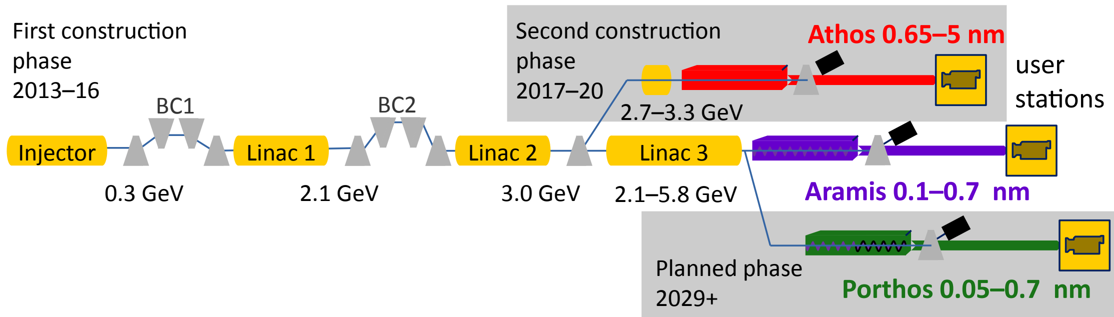

Figure 1: Schematic layout of the SwissFEL Facility.

complete closure after the last dipole. Thus the focusing strength of the quadrupole defines the net R_{56} value while the dipoles are operated at fixed deflection angles.

The third problem is the compensation and mitigation of the transverse kicks of the CSR in each horizontal bending dipole. The angle for the vertical dogleg is small and the effect on the beam negligible. The general guideline calls for minimizing the betatron function β_x in each bending magnet to a value of around 1 to 2 m. In addition, the betatron phase advance between the two bending sections is tuned so that the opposite signs of the kicks cancel each other.

Experience

The main drawback in the Athos extraction line is the limited flexibility in the beam transport due to the center dipole. In a simple bend-quadrupole-bend system only a betatron phase advance of 180° is needed if the betatron-function values β_x are small at the entrance and exit of the bending section due to the mitigation of the transverse CSR kicks. It resembles a simple point-to-point imaging system. An additional benefit is that with the CSR acting in the same direction the 180° phase advance already compensates the kick in first order. In a triple-bend system, such as in Athos, the flip in the dispersion function for the center dipole requires much more than 360° betatron phase advance. Thus the intrinsic kick compensation is lost. However, the beam transport in the vertical plane is even more problematic, since it should provide a similar phase advance in the vertical plane. It is difficult to place defocusing quadrupoles in the bending section without reducing the phase advance in the horizontal plane. The outcome are very large betatron function values at the quadrupole location while operating in a nearly unstable beam transport lattice. Small errors in the quadrupole strengths have a large impact on the betatron function along the extraction line and the matching at the undulator entrance can be lost easily.

These days we follow a different configuration where we do not flip the sign of the dispersion function η_x anymore. The enhanced decompression by the center dipole is compensated by leaking out dispersion from the first bending section through the straight section and closing it only after the second bending section. This gives us a larger flexibility on tuning the net R_{56} while keeping the maximum values of the betatron function below 80 m.

PORTHOS EXTRACTION LINE DESIGN

Figure 2 shows the principal components, such as quadrupoles and dipoles, for the proposed extraction line of Porthos. The design addresses the major restriction of the Athos design, which is the control of the overall R_{56} without large optics function values and an unstable beam transport. There are two possible solutions: First, a reverse bend for the center dipole. This eliminates the need to flip the sign of the dispersion function η_x. However the overall deflecting strengths of the outer dipoles are larger. Instead of the Athos configuration with deflections of $(2°, 1°, 2°)$, a possible solution with a reverse bend would be $(2.7°, -0.4°, 2.7°)$, but there remains a strong coupling between optics and net compression. The second solution, which is the one favored for Porthos, is to use a fixed double-bend system with net decompression and to compensate with a normal four-dipole chicane. Since the natural focusing of the chicane is very small, we have a 'knob' to control the R_{56} independently from the optics function.

With the R_{56} control removed from the bending sections, the required number of quadrupoles is four per section. The optical functions—both betatron and dispersion—have a mirror symmetry at the center point of the section. The first two quadrupoles enforce the matching condition $\eta'_x = \eta'_y = 0$, while the matching quadrupoles upstream of the Lambertson septum do the same for the optical function ($\alpha_x = \alpha_y = 0$). The positions have been roughly optimized to provide balanced focusing for both planes. The betatron function β_x has a value of about 1 m at the location of the septum and the last dipole. The last bending section has the same layout and uses the same quadrupole strengths as the first, although the already closed vertical dispersion would allow for a more compact solution in principle. In between the two bending sections there is the downward dogleg closing the vertical dispersion and compensating the 10 mm offset from the resonant kick upstream of the extraction line. Figure 3 shows the betatron and dispersion functions along the extraction line. The Lambertson septum is placed at the orbit coordinate $s = 429$ m.

ISBN: 978-3-95450-220-2 ISSN: 2673-5474 doi: 10.18429/JACoW-FEL2022-WEP09

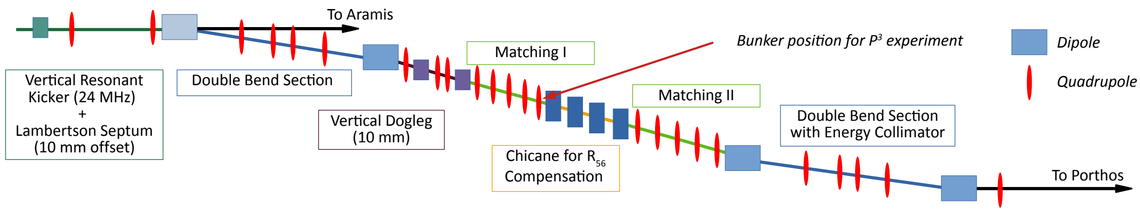

Figure 2: Components in the Porthos extraction line.

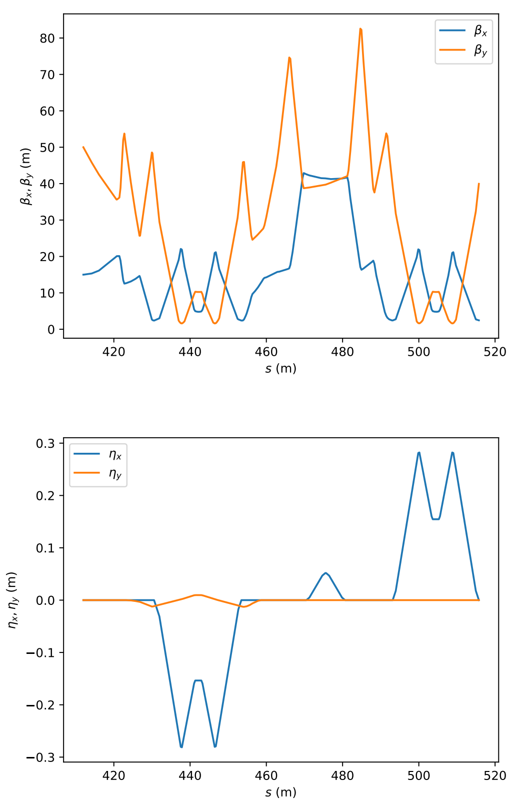

Figure 3: Betatron and dispersion functions along the Porthos extraction line (upper and lower plot, respectively).

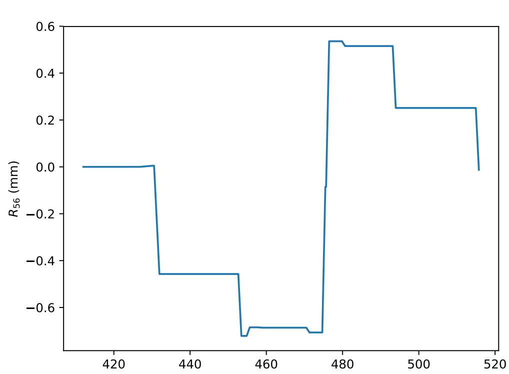

Figure 4: R_{56} value for isochronous operation.

The main dipoles have a deflection angle of 2.55°, which is driven by the available space in the SwissFEL tunnel while providing the longest possible space between the exit of the extraction line and the position of the Porthos beam dump. The downward dogleg features an angle of 0.2° while the chicane in the middle has an angle of 0.71° for isochronous operation (Fig. 4). The location also favors the mitigation of the microbunching instability [8]. Any accumulated energy modulation by the induced microbunching from the first bending section is reversed since the chicane enforces a bunching at the opposite phase. Thus the second half of the extraction line removes the energy modulation from the first half. The R_{56} can be fine-tuned to minimize the microbunching content in general.

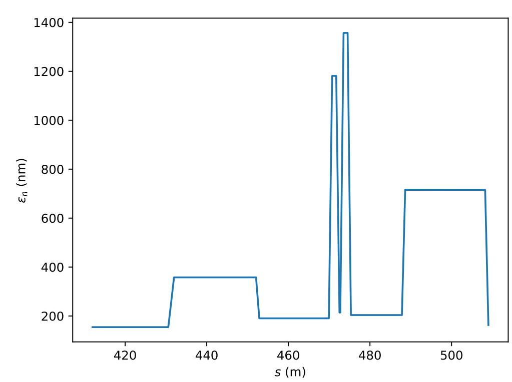

Figure 5: Normalized emittance in x along the extraction line.

We performed Elegant simulations [9] to estimate the impact of CSR by tracking a 200 pC bunch with a Gaussian current distribution and an rms duration of 40 fs, cut at ±40 fs. In general, small beta functions in the main dipole help to mitigate the emittance increase by the kicks but an effect is still noticeable. For the chicane a large betatron function value is chosen with little phase advance so that the net CSR kick is small. The effect on the normalized emittance is shown in Fig. 5. The growth is about 5% for an initial projected emittance of 180 nm. The efficiency in this compensation is shown in Fig. 6 where the phase space distributions in the t-x and t-x' planes are shown in the last bending section (left plots) and the exit (right plots). At the energy collimator position (left plots) there is a strong variation in x visible along the bunch, much larger than the

ISBN: 978-3-95450-220-2 ISSN: 2673-5474 doi: 10.18429/JACoW-FEL2022-WEP09

intrinsic beam size. It increases the projected emittance up to 700 nm (see Fig. 5 at s = 500 m). With the last CSR kick added in the last dipole of the switchyard (right plots) this variation along the bunch is removed and the initial projected emittance is mostly recovered. The emittance growth for a 20 fs bunch is about 20% but can be further optimized with the phase advance in the bending section and in between them.

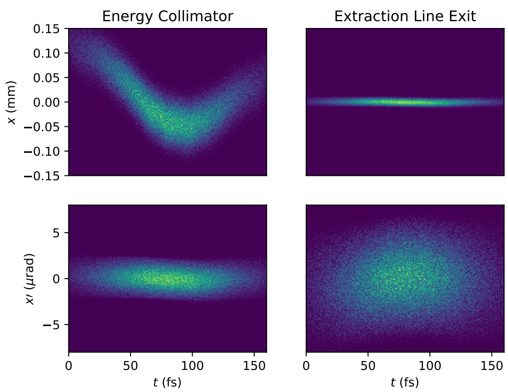

Figure 6: Time-resolved electron beam distributions in x and x' in the center of the last bending section (energy collimator) and at the exit of the transport line (left and right plot, respectively).

The energy loss by CSR cannot be compensated and adds up for each dipole. For the truncated Gaussian distribution of 40 fs rms length the variation in energy loss is about 4 MeV. The effective loss potential depends on the current profile [10] and flatter profiles, such as at SwissFEL with the leading and trailing horn cut away in the first bunch compressor, the variation is significantly reduced.

The final layout has sufficient space, about 20 m, for placing accelerating cavities. This would increase the operating beam energy of Porthos enabling higher photon energies, without sacrificing space in the beamline between extraction end and beam dump.

POSITRON PRODUCTION EXPERIMENT P^3 AT SwissFEL

Since the Porthos beamline will not be implemented until the period 2029 to 2032, an early realization of the extraction line is required to drive the P^3 experiment. The positron source will be set up in a bunker with a footprint of roughly 10 × 4 m near the center of the new beam line. The energy of 6 GeV of the SwissFEL electron beam corresponds to the drive beam energy in the baseline design of the FCC-ee injector complex and makes it the natural candidate to drive a positron source demonstrator. Recent advances in high-temperature superconductors (HTS) allow for a highly efficient matching of the extremely large positron emittance at the exit of the production target through an on-axis solenoidal field of more than 10 T. In addition to this device, the P^3 experiment envisages the use of two S-band standing-wave RF cavities with a large radial aperture of 20 mm surrounded by a multi-Tesla field generated by conventional superconducting solenoids. Simulations show that these key devices can increase the positron capture efficiency at the end of the experiment by up to 75%. This corresponds to an estimated positron yield of 8 positrons per electron at the damping ring of the FCC-ee injector complex, an improvement of about an order of magnitude compared to the state-of-the-art at SuperKEKB.

Based on the final layout of the extraction line the realization for the P^3 experiment should be consistent without any major changes in the type and position of its components. Since the experiment has dedicated beam development shifts, there is no need for a resonant kicker and the Lambertson extraction. Thus the Lambertson is replaced temporarily with a spare dipole, which deflects the beam by 2.55°. Also, the beam elevation by 10 mm due to the resonant kicker up to the downward dogleg is excluded in the initial realization. Since the experiment will operate with an uncompressed bunch with a few ps rms pulse duration, there is no need for corrector magnets for CSR kick compensation either. Five quadrupoles after the bending section will control the beam size at the target location of the experiment in a range between 20 and 1000 µm. Therefore the initial implementation of the extraction line consists of two dipole magnets, about nine quadrupole magnets, steerer magnets and some basic instrumentation like beam position monitors and screens, up to the point where the beam enters the experimental chamber.

CONCLUSION

The proposed P^3 experiment to demonstrate the positron yield for a future FCC position source benefits from an early realization of the extraction line for the third FEL beamline Porthos at SwissFEL, scheduled for construction between 2029 and 2032. Therefore, initial design studies for the Porthos layout have been done to extract an electron bunch while preserving its brightness. The design benefits also from the experience at the existing extraction line for the soft X-ray beamline Athos, avoiding any strong coupling between dispersion and optics function. The implementation of the extraction line will start in 2023 with only selected components, sufficient to transport a 6 GeV electron beam to the experimental target of the P^3 experiment.

REFERENCES

[1] E. Prat *et al.*, "A compact and cost-effective hard X-ray free-electron laser driven by a high-brightness and low-energy electron beam," *Nat. Photonics*, vol. 14, no. 12, pp. 748–754, 2020. doi:10.1038/s41566-020-00712-8

[2] P. Craievich, M. Schaer, N. Vallis, and R. Zennaro, "FCC-ee Injector Study and the P3 Project at PSI," *CHART Scientific Report 2021*, pp. 1–47, 2021. https://chart.ch/wp-content/uploads/2022/05/Chart-Scientific-Report-2021-FCCee-Injector.pdf

[3] I. Chaikovska *et al.*, "Positron Source for FCC-ee," in *Proc. IPAC'19*, Melbourne, Australia, May 2019, pp. 424–427. doi:10.18429/JACoW-IPAC2019-MOPMP003

ISBN: 978-3-95450-220-2 ISSN: 2673-5474 doi: 10.18429/JACoW-FEL2022-WEP09

[4] M. Paraliev and C. H. Gough, "Resonant Kicker System With Sub-part-per-million Amplitude Stability," in *Proc. IPAC'17*, Copenhagen, Denmark, May 2017, pp. 3174–3177. doi:10.18429/JACoW-IPAC2017-WEPIK098

[5] G. R. Lambertson, "Charged particle extracting magnet for an accelerator," US3323088A, 1967. https://patents.google.com/patent/US3323088/en

[6] N. Milas and S. Reiche, "Switchyard Design: Athos," in *Proc. FEL'12*, Nara, Japan, Aug. 2012, pp. 109–112. https://jacow.org/FEL2012/papers/MOPD37.pdf

[7] E. L. Saldin, E. A. Schneidmiller, and M. V. Yurkov, "On the coherent radiation of an electron bunch moving in an arc of a circle," *Nucl. Instrum. Methods Phys. Res., Sect. A*, vol. 398, no. 2, pp. 373–394, 1997. doi:10.1016/S0168-9002(97)00822-X

[8] J. Qiang *et al.*, "Design Optimization of Compensation Chicanes in the LCLS-II Transport Lines," in *Proc. IPAC'16*, Busan, Korea, May 2016, pp. 1695–1698. doi:10.18429/JACoW-IPAC2016-TUPOR018

[9] M. Borland, "ELEGANT: A flexible SDDS-compliant code for accelerator simulation," Argonne National Lab., IL (US), Tech. Rep. LS-287, 2000. doi:10.2172/761286

[10] C. Mitchell, J. Qiang, and P. Emma, "Longitudinal pulse shaping for the suppression of coherent synchrotron radiation-induced emittance growth," *Phys. Rev. ST Accel. Beams*, vol. 16, no. 6, p. 060 703, 2013. doi:10.1103/PhysRevSTAB.16.060703

ISBN: 978-3-95450-220-2 ISSN: 2673-5474 doi: 10.18429/JACoW-FEL2022-WEP10

ORBIT JITTER ANALYSIS AT SwissFEL

S. Reiche*, Paul Scherrer Institut, Villigen PSI, Switzerland
E. Ferrari, Deutsches Elektronen-Synchrotron DESY, Hamburg, Germany

Abstract

We use the beam-synchronous readout of the beam position measurement at the hard X-ray FEL beamline Aramis at SwissFEL to analyze the intrinsic orbit jitter, applying a classification algorithm and principal component analysis (PCA). The method sorts the jitter in a set of eigenvectors and -values. With the magnitude of the eigenvalues the impact of the different jitter sources can be estimated. From the purely stochastic results we derive also a physical interpretation by matching the linear transport functions to the eigenvectors, reconstructing the orbit jitter in terms of the center of mass jitter of the electron bunch in the transverse positions, momenta, and the mean energy. Any deviation from the theoretical prediction indicates possible wrong set values of the transport magnets or errors in the BPM calibration (sign flip or faulty amplitude calibration). We present the results and give an outlook on extending the analysis to additional channels such as charge, compression and arrival time monitors as well as the FEL output signal.

INTRODUCTION

SwissFEL [1] is an X-ray free-electron laser (FEL) facility at the Paul Scherrer Institute, where the energy of an relativistic electron beam is transferred to an intense, transversely coherent X-ray pulse with femtosecond pulse durations and gigawatt peak powers. For the optimum performance of the hard X-ray branch Aramis with a tuning range between 1 to 7 Å, the orbit within the periodic magnetic field of the undulator [2] needs to be straight within a few microns. Unfortunately, machine jitters add shot-to-shot variations in beam parameters, for instance orbit but also beam charge and bunch length, among many others, which affect the FEL operation. To quantify these jitter sources and their source locations a statistical analysis of the machine data can give valuable insight. We present such an analysis for the hard X-ray branch Aramis at SwissFEL.

PRINCIPAL COMPONENT ANALYSIS

While many of the SwissFEL sensor readings exhibit fluctuations on a shot-to-shot basis, they are typically strongly correlated among each other. The number of actual independent sources is significantly smaller. The process of finding collective jitter sources from the sensor readings is called principal component analysis (PCA) [3]. Its application to the orbit jitter in the hard X-ray beamline Aramis at SwissFEL is described in the following sections.

* sven.reiche@psi.ch

Data Preparation

The data are taken from the beam position monitors (BPMs) [4] along the hard X-ray beamline Aramis. The beamline starts at the exit of the linear accelerator and takes all BPMs up to the beam dump after the undulator. There are in total 39 BPMs with two channels each for the position in x- and y. The data acquisition uses the beam-synchronous stream [5], ensuring that a single record of all channels belongs to the same shot in the machine. The acquisition rate is 100 Hz. During the data acquisition the orbit feedback system remains enabled.

The rms orbit jitters are overall small, with the largest jitter occurring in the dispersive section of the energy collimator and reaching about 30 µm. Within the undulator beamline it is less than 5 µm. Therefore we assume that the observed jitter is a linear superposition of different jitter sources such as energy deviation or jitter in the transverse position. The former will manifest itself only in BPM readings of dispersive sections of the beamline.

The BPM readings represent the absolute orbit position but since we are analyzing the relative orbit jitter, we subtract a reference orbit to convert the data. For the sake of simplicity this is the first record of the acquired data records. The observed relative orbit can be described by a general transport matrix $\tilde{\mathbf{R}}$ and an input vector $\tilde{\vec{r}}$. The naming reflects a generalizing approach of the linear transport matrix in beam optics with $\vec{r}(s_1) = \mathbf{R}(s_0 \rightarrow s_1)\vec{r}(s_0)$. The six components of $\vec{r}$ consist of the two transverse positions x and y, two transverse momenta x' and y', longitudinal position t and relative energy deviation $\delta = \Delta E/E$. The analogy to the PCA becomes obvious, since a jitter in one of the input parameters (e.g., in x) can be regarded as the jitter source. The response of the transport matrix to a change in x describes the principal component of this jitter source. In practice there might be other jitter sources (e.g., coherent synchrotron radiation kicks from a jitter in the bunch charge or length). The model for the linear transport is a subset of the more general description by PCA.

The PCA becomes simpler in the linear regime and can be expressed by a set of eigenvectors. Figure 1 illustrates the case for two observed BPM readings. Note that the eigenvectors are evaluated from the 'center of mass' position of the distribution and not from the origin. Therefore we prepare our records by subtracting as a second step the mean value for each channel. Since the mean orbit is a superposition of valid orbits, the subtraction preserves the validity of the measured orbit as part of a linear transport system. It turns out that the first step of subtracting the first measured orbit from all others is actually not needed and that the subtraction of the mean BPM readings can be applied directly.

ISBN: 978-3-95450-220-2 ISSN: 2673-5474 doi: 10.18429/JACoW-FEL2022-WEP10

The analysis includes $N = 78$ BPM channels. A given measurement of all channels can be represented by a single point in a 78 dimensional space. In other words, the number of possible observed jitter sources is limited to 78. With a total of M independent orbit measurements the dataset contains $N \times M$ data values. In our case of a linear system this is identical to linear combinations of N eigenvectors. The corresponding eigenvalues indicate the amplitude in these eigenvectors to cover all jitters with the correct amplitude. In a compact form the dataset is the matrix multiplication of a $N \times K$ eigenvector matrix and a $K \times M$ amplitude matrix, where the inner dimension K remains undefined for the moment. The process to factorize the 'data matrix' into these two matrices is the Singe Value Decomposition (SVD) of a matrix and thus identical with a PCA in the linear regime. Due to the nature of the SVD the inner dimension K is the minimum of either M or N. For datasets with many measured records the eigenvector matrix settles to a size of $N \times N$ as discussed qualitatively above.

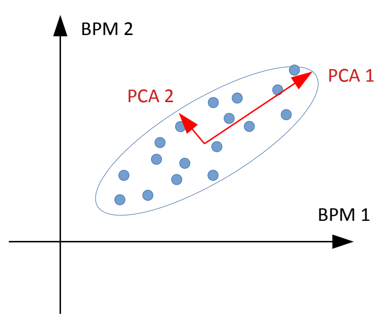

Figure 1: Illustration of PCA for the parameter space of two BPM readings.

A python program for a single thread analysis, using the Numpy library [6], analyzes up to 60 000 measurements. For sample sets above 1000 shots the execution times scales quadratically with the number of samples. To optimize the needed number of samples, we iterate the analysis, starting with 100 samples and then doubling the size for each iteration. The convergence parameter is the length difference between the current and previous eigenvector for the two dominant modes, which should converge ideally towards zero. With 4000 samples the difference drops below 0.1%, which is smaller than the expected calibration error of an individual BPMs. Thus a linear PCA of the BPM readings takes 40 seconds to acquire the data at 100 Hz and about one second to derive the eigenvectors with sufficient numerical stability in the analysis.

Stochastic Analysis

Applying SVD to the measured BPM data gives a list of eigenvectors $\vec{p}$ and eigenvalues λ. Each eigenvector/-value can be regarded as a single mode of the machine jitter. The relative magnitude of the jth jitter source is given by $|\lambda_j|^2 / \sum_i |\lambda_i|^2$ since the errors are independent from each other. The dominant mode describes about 87% of the total measured jitter with a rapid drop in the amplitude for the following values: 6.9%, 2.6%, 1.3% The contribution of the remaining modes after the 4th account is less 2%.

Since the eigenvectors are orthonormal it is straightforward to subtract the contribution of a given jitter source from the measured data with $\vec{r} \to \vec{r} - (\vec{r} \cdot \vec{p}_j)\vec{p}_j$. Starting with the largest jitter source we correct the data iteratively for each jitter source to see the location of the drop in jitter. Figure 2 shows the results. The strongest reduction for the first mode occurs in the range between $z = 0$ m and 60 m. This corresponds mostly to the dispersive part of the Aramis energy collimator (between $z = 30$ m to 60 m) but also before. Thus we conclude that the dominant jitter source is in energy. The correlation with the BPMs before the dispersive section suggests also a strong correlation with the position in x. This can happen when the dispersion in the upstream bunch compressor is not closed due to some tilt correction of the electron beam [7]. The second component is present mostly in x within the FODO lattice of the undulator (from $z = 75$ m to 160 m). The following two components describe dominantly the jitter in the y-direction, while the fifth and sixth are hard to associate with any specific location. With these six components removed, the residual fluctuation at all BPMs is around 500 nm or smaller. At this point the individual error in the processing of the BPM raw signal is dominant and can no longer be associated with a collective jitter source any. Thus we restrict the following discussion to the top six modes.

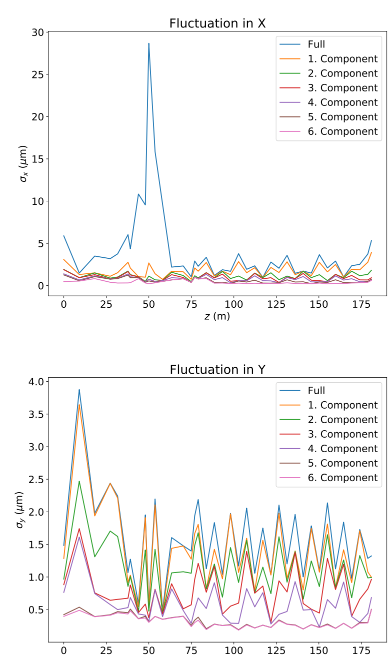

Figure 2: Stepwise removal of dominant jitter sources.

It is not surprising that the dominant component strongly correlates with the point of largest fluctuation, namely the position with the largest dispersion in the machine. This is a form of biasing the data, since the dominant eigenvector

ISBN: 978-3-95450-220-2 ISSN: 2673-5474 doi: 10.18429/JACoW-FEL2022-WEP10

tends to include these sensors with largest jitters. This is not a problem for homogeneous data, such as only BPM readings in our case. For inhomogeneous data (e.g., when bunch charge readings are included) all sensor data should be normalized by the observed rms jitter. Nevertheless an explicit biasing allows assessing the impact of a given parameter. In our case it is the energy fluctuation and its impact on the rest of the orbit. It gives a measure of how well the dispersion function is closed after the energy collimator.

Physics Interpretation

As the set of eigenvectors from the PCA describes the propagation of perturbations through the beamline, it encodes the linear transport in that part of the machine. Therefore it should be possible to express any eigenvector by a linear combination of the orbit response in the beam transport model. If this assumption is valid then any orbit jitter can be expressed as the jitter in the initial 'center-of-mass' values of the electron distribution in the six-dimensional phase space. In reality this is not the case for two reasons. The first is that some jitters are not observable. As long as there are neither elements in the beam transport that depend explicitly on the arrival time of the bunch (for instance an RF deflecting structure) nor sensors entering the analysis recording it (beam arrival-time monitors, BAM), any jitter in the arrival time will not exhibit any observable jitter. To include time-arrival jitter in the analysis the sensor list can be expanded by the BAM signals. The situation is similar for a fully non-dispersive section. Here any energy jitter occurs only as a second-order effect in the orbit. Nevertheless, this information is known and can be taken out of the model accordingly. The second reason of possible unknown jitter sources has more severe implications. We encounter it in our data when we calculate the transport matrix by our online model and match the amplitudes of the model transport vector to the eigenvectors. For the Aramis beamline this approach does not work when applied to the full beamline. We may, however, consider short subsections where we can assume that there are no hidden jitter sources. Then there is quite a good agreement between the eigenvector and the linear combination of the model transport vector. In Fig. 3 the result for restricting the fitting only to the first ten BPM readings indicates a significant deviation at the exit of the energy collimator in the x-direction. The reason is not fully understood but we suspect the effect of a transverse kick by the coherent synchrotron radiation in the energy collimator dipoles. Since it depends on the bunch length and charge this effect is not included in the linear transport model. Another possible source can be that the running feedback system converts one jitter source into another, e.g., incoming orbit jitter can be mistaken as an energy jitter, when a given BPM in the dispersive section of the energy collimator is used as a measure for the energy deviation. This can happen on a timescale slower than the bunch spacing of 100 ms, but is still visible in the data acquisition over 4000 shots.

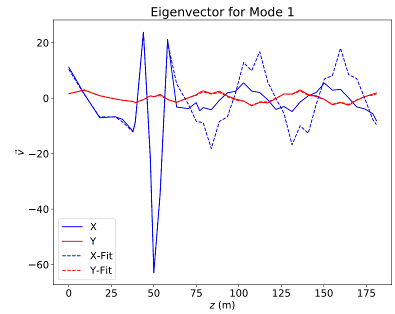

Figure 3: Reconstruction of the dominant eigenvector from the beamline model.

Nevertheless the fit to the first part of the beamline allows a reconstruction of the initial condition for each shot with

$$(x \quad x' \quad y \quad y' \quad \delta)^{\mathrm{T}} = \mathbf{F} \cdot \mathbf{N} \cdot \vec{r} \quad , \tag{1}$$

$\vec{r}$ a single measurement of all BPM channels, $\mathbf{N}$ the largest eigenvectors of the PCA, ordered in rows, and $\mathbf{F}$ the fitting constants to the model transport functions. We cross-checked this approach by reconstructing the jitter in x and y at any BPM where we can directly compare with the raw data of the sensors. This gives excellent agreement with deviations of less than 500 nm for each point. The analysis of the orbit jitter and the possibility to project those onto jitters in the initial condition gives us a robust way to differentiate between jitters in energy and orbit and thus to invoke the corresponding feedbacks to counteract. The required calculation is fast since it involves the matrix multiplication of two matrices and a vector (see Eq. (1)) of moderate size.

With the ever-present jitter in the machine and the reconstruction of the model-based transport functions, the settings can be checked for consistency. One example is the dispersion function for the Aramis lattice without excluding any incoming dispersion from the machine. The knowledge of this function is valuable for checking if the magnets in the energy collimator are scaled correctly with the beam energy to preserve the isochronous set-up of the energy collimator. The approach is to find the orbit jitter which correlates exclusively with a pure energy jitter. This excludes the correlated jitter in position and energy due to leaked dispersion upstream, corresponding to the initial condition of $\eta_x = \eta_y = 0$ m and $\eta'_x = \eta'_y = 0$ rad. In other words, any jitter of BPMs upstream of the energy collimator should not correlate with the energy dependent jitter we are looking for. Therefore, we calculate the correlation strength between all BPM channels with the BPM readings of the first two BPMS in x and y and then subtract these correlations from them. We then take the orbit jitter at the location of the largest dispersion, namely at the center BPM of the energy collimator, and correlate it with all BPM readings. The result of this correlation vector, scaled to the expected dispersion within the collimator, is shown in Fig. 4. In this case, some dispersion is leaked out of the energy collimator due to errors in the quadrupole strengths. From the amplitude

ISBN: 978-3-95450-220-2 ISSN: 2673-5474 doi: 10.18429/JACoW-FEL2022-WEP10

and the periodicity of the dispersion in the FODO lattice of the undulator the correction can be calculated to close the dispersion. This measurement is typically invasive by actively changing the electron beam energy, but the precision in the BPM readings and the correlation among the BPMs is sufficient to get the same information without interrupting the photon delivery to the users. This can be the foundation of an adaptive feedback system to close the dispersion after each change in the electron energy set-point.

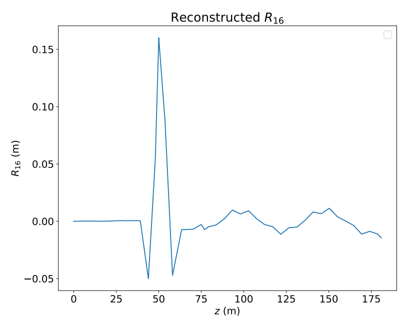

Figure 4: Dispersion function with non isochronous configuration of energy collimator.

CLASSIFICATION ANALYSIS

An alternative approach to the PCA analysis just described is to use a classification algorithm. In our case, we explored the data using K-means [8], one of the most basic clustering algorithms in unsupervised learning. The K-means algorithm divides the sample set into N disjoint clusters, each of them characterized by their sample mean, also known as centroid. The aim of the algorithm is to choose centroids that minimize the inertia of the data, by iteratively assigning each of the data points to the nearest centroid, and then recompute the new centroids for each cluster. (A data point consists of the collection of machine trajectories, compression, charge, etc.) Convergence is achieved, and the classification is completed, when the old and new centroid values differ by less than a threshold value. Note that, as we chose an unsupervised algorithm, we do not introduce labels for the data and let the algorithm classify the trajectories and other machine parameters of interest (e.g., FEL pulse energy, bunch charge, compression signals, etc.).

We used the K-means implementation of the python package `scikit-learn` [9], with the sole input parameter the number of different clusters that we would like to obtain. In our case, we chose to keep the default of eight clusters. By looking at the clustered data, one can immediately recognize that the algorithm identifies different ranges in pulse energy for the machine, both in terms of overall intensity, as well as jitter amplitude. Considering the trajectories corresponding to each cluster, one can observe clear trends in the betatron oscillations along the undulator FODO-line, as well as a clear indication for the correct energy setting, for instance by looking at the trajectory in the dispersive BPM in the energy collimator or in the dump area. In our example, the electron beam energy was shifted and the best performances were observed when the energy was retuned to the correct value predicted by the algorithm.

The clustered data can be further explored with regard to correlation with any machine parameter of interest. In our case, for simplicity, we chose the FEL pulse energy. While considering the correlation coefficients between the BPM readings and the FEL pulse energy, for example, using the full data set one can exploit general trends and dependences among the parameters. However, by looking at the correlations of single clusters one can clearly identify, for example, the different impact of machine jitters on the performance, depending on which cluster is considered. This result can help in identifying more stable working points, as well as to help identify possible underlying issues. In our case, the clustered trajectories exposed a non-negligible second-order dispersion term that was leaked into the undulator line. This was due to the non-optimal placement of the sextupole magnets in the energy collimator section. When these magnets were shifted to their optimal position, the corresponding second-order dispersion term vanished.

OUTLOOK

The analysis of the Aramis orbit jitter demonstrates the wealth of information that can be obtained by a PCA, identifying the primary jitter sources, their amplitudes and their possible locations. Furthermore the results can be compared to a machine model, pointing out any significant deviations, such as leaked dispersion, inconsistent BPM calibration (including polarity flips) or wrong set values of quadrupoles or dipoles. Since the PCA can obtain this information non-invasively during user operation, they can serve as adaptive feedback or fault-check algorithm towards more reliable operation of SwissFEL.

Using a clustering algorithm, one can identify the best operating parameters, in terms of compression, trajectory, charge, etc., for best FEL performance, only using the jitter of the machine instead of using exploratory algorithms. We chose an unsupervised learning algorithm in order not to bias our exploration of the data only towards best performance of the machine in terms of pulse energy, but to really explore the behavior of the machine itself.

The next step will extend the analysis to the entire machine, including also non-BPM data, such as charge readings, compression signals or FEL pulse energy. In particular the last is interesting since the emitted FEL pulse energy should correlate with the BPM reading in the FEL dump, providing a consistency check of the pulse detector or possibly an estimate of the pulse energy on a shot-to-shot basis even without the photon detector.

REFERENCES

[1] E. Prat *et al.*, “A compact and cost-effective hard X-ray free-electron laser driven by a high-brightness and low-energy electron beam,” *Nat. Photonics*, vol. 14, no. 12, pp. 748–754,

ISBN: 978-3-95450-220-2 ISSN: 2673-5474 doi: 10.18429/JACoW-FEL2022-WEP10

2020. doi:10.1038/s41566-020-00712-8

[2] M. Calvi, C. Camenzuli, R. Ganter, N. Sammut, and T. Schmidt, "Magnetic assessment and modelling of the Aramis undulator beamline," *J. Synchrotron Radiat.*, vol. 25, no. Pt 3, pp. 686–705, 2018. doi:10.1107/S1600577518002205

[3] K. Pearson, "LIII. On lines and planes of closest fit to systems of points in space," *Lond. Edinb. Dubl. Phil. Mag*, vol. 2, no. 11, pp. 559–572, 1901. doi:10.1080/14786440109462720

[4] B. Keil *et al.*, "Design of the SwissFEL BPM System," in *Proc. IBIC'13*, Oxford, UK, Sep. 2013, pp. 427–430. https://jacow.org/IBIC2013/papers/TUPC25.pdf

[5] S. G. Ebner *et al.*, "SwissFEL - Beam Synchronous Data Acquisition - The First Year," in *Proc. ICALEPCS'17*, Barcelona, Spain, Oct. 2017, pp. 276–279. doi:10.18429/JACoW-ICALEPCS2017-TUCPA06

[6] C. R. Harris *et al.*, "Array programming with NumPy," *Nature*, vol. 585, no. 7825, pp. 357–362, 2020. doi:10.1038/s41586-020-2649-2

[7] M. W. Guetg, B. Beutner, E. Prat, and S. Reiche, "Optimization of free electron laser performance by dispersion-based beam-tilt correction," *Phys. Rev. ST Accel Beams*, vol. 18, no. 3, p. 030 701, 2015. doi:10.1103/PhysRevSTAB.18.030701

[8] S. Lloyd, "Least squares quantization in PCM," *IEEE Trans. Inf. Theory*, vol. 28, no. 2, pp. 129–137, 1982. doi:10.1109/TIT.1982.1056489

[9] *Scikit-learn: Machine learning in Python — scikit-learn 1.1.2 documentation*. https://scikit-learn.org/stable/

ISBN: 978-3-95450-220-2 ISSN: 2673-5474 doi: 10.18429/JACoW-FEL2022-WEP11

MEASUREMENT OF ORBIT COUPLING BY THE APPLE-X UNDULATOR MODULES IN THE SOFT X-RAY BEAMLINE ATHOS AT SwissFEL

S. Reiche*, M. Calvi, R. Ganter, Paul Scherrer Institut, Villigen PSI, Switzerland
E. Ferrari, DESY, Hamburg, Germany

Abstract

Orbit response measurements in the soft X-ray beamline of Athos have shown coupling of the beam transport between the transverse planes, which is influenced by the on-axis field strength of the APPLE-X undulator modules. A model reproduces this observation if a coupling term is included in the transport matrix of the undulator module. The presentation shows the estimate of the coupling strength as a function of beam energy, undulator field strength and orbit excitation.

INTRODUCTION

SwissFEL [1] is a free-electron laser (FEL) facility delivering coherent hard and soft X-rays to users from Switzerland and worldwide. The soft X-ray beamline Athos [2] uses the novel APPLE-X undulator type [3] to allow for an independent control on polarization and field strength without the broken symmetry of a APPLE-II or III configuration. The chosen undulator type has proven its high effectiveness during commissioning and user operation of Athos, but we observed a strong coupling between the orbits of the x- and y-plane. In this paper we describe the investigation on the possible sources and their quantification. While the effect is undesired, it can be accounted for (e.g., in the orbit feedback system) by means of an improved model of the beam transport.

POSSIBLE SOURCES FOR COUPLING

We observed early during the commissioning of the Athos undulator beamline that the orbits in both planes were coupled. Given the symmetry of the involved magnets (undulator, phase shifters and quadrupole magnets) this was unexpected. We explored possible sources and checked them systematically.

Coupling can be generated by quadrupoles that have a non-zero roll angle, effectively converting parts of the field to that of a skew quadrupole. Since the coupling strength is roughly at the percent level of the normal quadrupole field, the roll would be on the order of 10 mrad. However, to explain the observed resonant growth in the betatron amplitude, the roll angles need to have the same signs as the quadrupole field gradient in the FODO lattice of the Athos beamline. This is highly unlikely if the effect is caused by a systematic misalignment. Neither did field measurements for the quadrupole type indicate a skew quadrupole component nor can a systematic tilt in the support structure reproduce an alternation in the roll angle. Similar exclusion applies to the delaying chicanes between the undulator modules. They are planar by design and the coupling is not influenced by the strength of the chicanes.

We also tested for possible transverse wakefields, e.g., when the beam passes close to the vacuum chamber wall. In the case where the chamber is slanted at that position (e.g., in the upper left region of a round vacuum chamber), a steering in one plane causes a kick in the perpendicular plane. However this effect is highly asymmetric and nonlinear, contrary to our observation. Alternative trajectories through the undulator vacuum chamber didn't change the coupling either.

On the other hand changing the magnetic field of the undulator field itself has an impact on the coupling strength. Thus we conclude that the primary reason for the coupling lies in the magnetic field of the APPLE-X undulators. Our studies of this effect are described in the following section.

MODELING OF COUPLING TERMS

For the analysis of the orbit response in the Athos undulator beamline we developed a simple model for a possible coupling of the undulator field. For the helical configuration the magnetic field is symmetric against swapping the x and y coordinate. Thus the transport matrix should also be symmetric. Instead of an explicit solution for the transport matrix, we approximate each undulator module with a series of thin lenses and drifts. We express the effective quadrupole strength of the natural focusing with k_n, which occurs in the matrix element R_{21} and R_{43} of the thin-length approximation. In analogy we define the skew quadrupole strength with k_s for the R_{23} and R_{41} coefficient. We allow for different values of k_n and k_s.

The complete expression for the transport matrix is then

$$M = \left[\begin{pmatrix} 1 & 0 & 0 & 0 \\ -k_n \frac{L_u}{m} & 1 & -k_s \frac{L_u}{m} & 0 \\ 0 & 0 & 1 & 0 \\ -k_s \frac{L_u}{m} & 0 & -k_n \frac{L_u}{m} & 1 \end{pmatrix} \cdot \begin{pmatrix} 1 & \frac{L_u}{m} & 0 & 0 \\ 0 & 1 & 0 & 0 \\ 0 & 0 & 1 & \frac{L_u}{m} \\ 0 & 0 & 0 & 1 \end{pmatrix}\right]^m , \tag{1}$$

with the value m as the number of subdivisions to be chosen sufficiently large. For the fitting of the orbit response we use $m = 100$.

The total transport channel is quasi a FODO lattice, transporting the beam from the first beam position monitor (BPM) stepwise to the succeeding BPMs. After each BPM there is a quadrupole and—for most of the sections—an undulator module, except for the first five sections, which are reserved

* sven.reiche@psi.ch

ISBN: 978-3-95450-220-2 ISSN: 2673-5474 doi: 10.18429/JACoW-FEL2022-WEP11

for a possible upgrade of Athos, and the 14th section, which hosts the delaying chicane for two-color operation. The quadrupoles alternate in polarity, forming the basis of the FODO lattice.

For the symmetric helical configuration of the APPLE-X undulator module the natural focusing term should be:

$$k_n = \frac{1}{4}\left(\frac{k_u K}{\gamma}\right)^2 \tag{2}$$

with k_u the undulator wavenumber, K the undulator parameter, and γ the electron energy in units of the electron rest mass. Breaking the symmetry (e.g. APPLE-II/III type undulator) affects also the natural focusing, with different values for the x- and y-plane, resulting in a less stringent condition,

$$k_{n,x} + k_{n,y} = \frac{1}{2}\left(\frac{k_u K}{\gamma}\right)^2 \quad , \tag{3}$$

which arises from Maxwell's equations and the available total magnetic flux, to be considered constant as long as the value of K is kept constant.

For the analysis of the coupling in the beam orbit, we postulate that analogous to redistributing the quadrupole strengths in the x and y plane, a similar redistribution can be made between the normal and skew quadrupole components. This results in a further generalized relation for the available field strengths:

$$k_{n,x} + k_{n,y} + k_{s,x} + k_{s,y} = \frac{1}{2}\left(\frac{k_u K}{\gamma}\right)^2 \quad . \tag{4}$$

With the measurements at the Athos beamline, we will check if this proposed relation is valid or not, as discussed in the following.

MEASUREMENTS AT SwissFEL

The orbit response for an electron beam energy of 3.17 GeV is shown in Fig. 1. For the measurement we took 100 shots as the reference orbit and repeated it with a change of the corrector current at the entrance of the beamline section by 1 A, separately in the x- and y-direction. The resulting kick corresponds to an angle of 50 µrad in the orbit.

Both excitations lead to a growing betatron oscillation in the perpendicular plane. The growth rate scales with the undulator field strength, confirming again that the reason for the coupling lies in the undulator field. We checked if the coupling strength depends on the excited betatron amplitude and repeated the orbit response for various corrector strengths. The correlation of the last BPM reading to the 4th BPM in the perpendicular plane is shown in Fig. 2. The dependence is linear and therefore we can exclude an octupole field component as the driving coupling source. This linear response validates the orbit response measurement of Fig. 1, since the excited betatron amplitude is different for kicks in x and y. The asymmetry arises from the focusing properties of the first quadrupole, which enhances the kick in the defocusing plane but reduces it in the focusing plane.

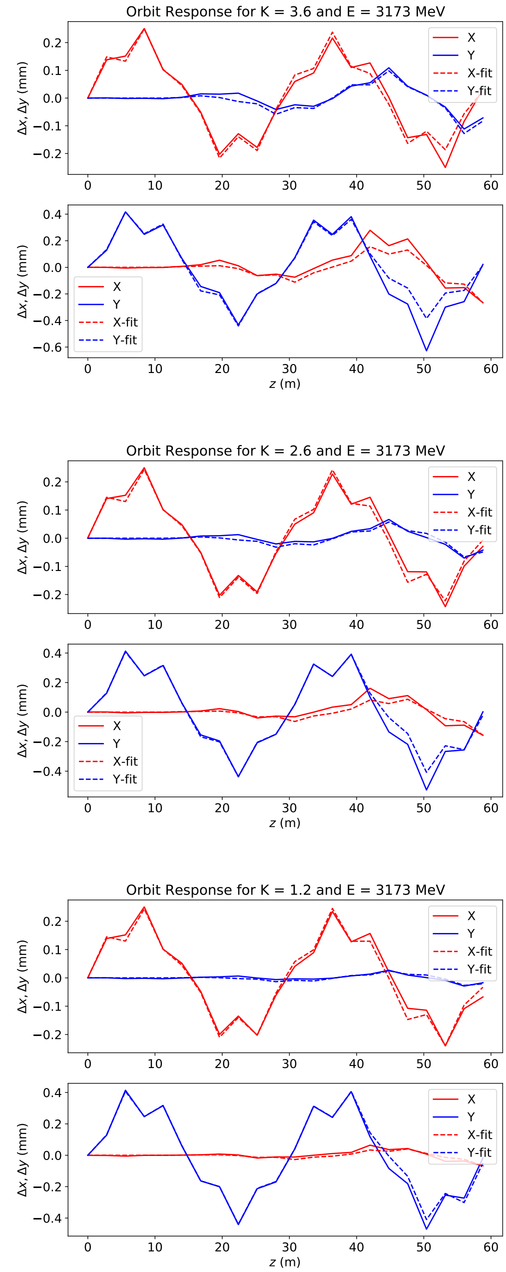

Figure 1: Orbit response for steering in the x- and y-direction for $K = 3.6$ (top), $K = 2.6$ (middle), and $K = 1.2$ (bottom).

We observe for the direction of the coupling that a positive amplitude in one plane kicks the electron beam in the positive direction of the other plane. Our model reflects this by using the same sign for k_s in Eq. (1). This is in stark contrast to the transport matrix of a real skewed quadrupole magnet. However any kind of natural focusing of the undulator field is a second-order effect from the transverse dependence of the magnetic field. As a result even the natural focusing differs from a normal quadrupole field, since it can provide focusing in both planes simultaneously. Nevertheless, the pure existence of an effective skew quadrupole

ISBN: 978-3-95450-220-2 ISSN: 2673-5474 doi: 10.18429/JACoW-FEL2022-WEP11

field breaks the theoretical rotation symmetry of the undulator field. Instead it only has a mirror symmetry along the direction $x = y$. A possible explanation might be the field at the entrance and exit of the undulator, since two banks of the permanent magnet arrays, opposite to each other, stick out for a given helical polarization. By changing the helicity the symmetry plane should change from $x = y$ to $x = -y$. However measurements with different polarization do not confirm this.

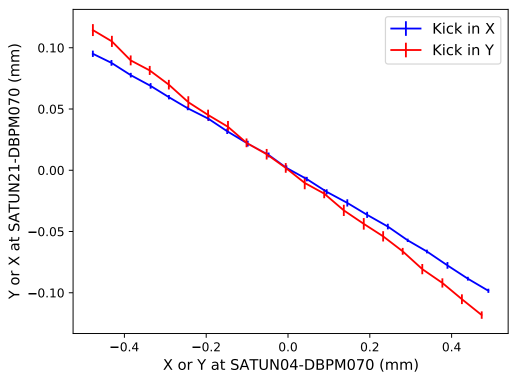

Figure 2: Linearity of the coupling for different excitation amplitudes

Figure 3 shows the fitted values for the natural focusing and the skew quadrupole component. For large values of K they follow in good agreement the scaling with K^2. Only for small values the measured strengths are larger than expected by the scaling. The effective strengths from the normal and skew quadrupole effect have opposite signs. Note that the sum of both components agrees in magnitude with the expected focal strength, thus hinting at the postulated sum rule of Eq. (4). However the sum of the natural focusing and the skew quadrupole component is negative, which is a strong counter argument against the second order focusing effects of the undulator (namely the natural focusing), which is always positive in its combined effect of both planes.

We repeated the orbit response measurements at a lower energy of 2.77 GeV and compared to the previous ones at 3.17 GeV. The obtained ratios in the skew quadrupole component are 0.92 and 0.87 for K-values of 3.6 and 2.6, respectively. Comparison to the beam energy ratio (0.87) suggests a rather linear scaling with that parameter. Natural focusing scales with the square of the energy change. The measurements of the focusing quadrupole component k_n have too large errors to extract any quantitative information from them, except that they decrease even less with energy when compared to the skew quadrupole component.

CONCLUSION

Orbit response measurements have shown a coupling of the electron motion in the soft X-ray FEL beamline Athos. Since it depends on the undulator field strength, the origin of the coupling lies in the undulator field. The strength scales

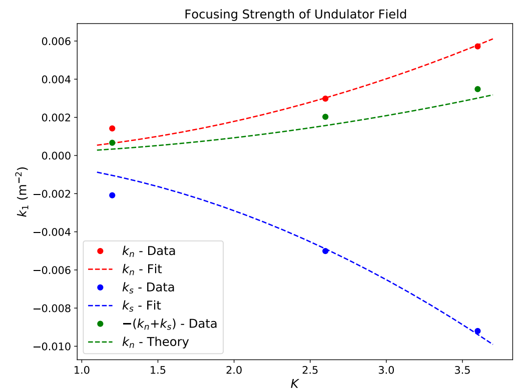

Figure 3: Focal strength of the normal and skew quadrupole component for different undulator field strengths.

with the undulator field and the beam energy. Due to the symmetry of the APPLE-X undulator type an effective skew quadrupole component is not expected. The coupling breaks the symmetry to a mirror symmetry of a plane, lying at a 45° angle with respect to the horizontal plane. The amount of measured field strength is larger than predicted by theory, even for natural focusing.

For the regular operation of Athos the coupling is manageable but requires an updated beam transport model to include the coupling terms in the precalculation of the response matrices of the orbit feedback and in the matching to the undulator lattice.

REFERENCES

[1] E. Prat *et al.*, "A compact and cost-effective hard X-ray free-electron laser driven by a high-brightness and low-energy electron beam," *Nat. Photonics*, vol. 14, pp. 748–754, 2020. doi:10.1038/s41566-020-00712-8

[2] R. Abela *et al.*, "The SwissFEL soft X-ray free-electron laser beamline: Athos," *J. Synchrotron Radiat.*, vol. 26, no. 4, pp. 1073–1084, 2019. doi:10.1107/S1600577519003928

[3] T. Schmidt and M. Calvi, "APPLE X Undulator for the SwissFEL Soft X-ray Beamline Athos," *Synchrotron Radiat. News*, vol. 31, no. 3, pp. 35–40, 2018. doi:10.1080/08940886.2018.1460174

ISBN: 978-3-95450-220-2 ISSN: 2673-5474 doi: 10.18429/JACoW-FEL2022-WEP12

APPLICATION OF MACHINE LEARNING IN LONGITUDINAL PHASE SPACE PREDICTION AT THE EUROPEAN XFEL

Z. H. Zhu[1,2]*
Shanghai Institute of Applied Physics, Chinese Academy of Sciences, Shanghai, China
[1]also at University of Chinese Academy of Sciences, Beijing, China
[2]also at Deutsches Elektronen-Synchrotron DESY, Hamburg, Germany
S. Tomin, J. Kaiser
Deutsches Elektronen-Synchrotron DESY, Hamburg, Germany

Abstract

Beam longitudinal phase space (LPS) distribution is the crucial property to driving the high-brightness free-electron laser. However, the beam LPS diagnostics is often destructive and the relevant physical simulation is too time-consuming to be involved in the control room. Therefore, we explored applying the machine learning models to facilitate the virtual diagnostic of the LPS distribution at European XFEL. Two different model designs are proposed and the performance demonstrates its feasibility based on the simulations. This work lays the further investigation of the real-time virtual diagnostics in the operational machine.

INTRODUCTION

In the past decade, The X-ray free-electron laser (XFEL) facilities around the world provide coherent and ultra-short X-ray radiation with tunable wavelength and high-brightness [1], facilitating the ultra-fast scientific research and discovery with atomic spatial resolution [2–4]. In the daily operation of the facility, the electron beam with high quality is indispensable to the desirable lasing performance in the undulator sections, especially the beam longitudinal properties, such as the charge distribution and slice energy spread distribution along the beam. The acquirement of these essential beam properties requires the measurement of the entire beam longitudinal phase space (LPS) with a diagnostic instrument such as transverse deflecting structure (TDS). However, this measurement is conducted in an interceptive manner, which makes it impossible to be taken during the photon delivery to the experimental stations unless it is implemented downstream of the undulator section. In addition to that, the LPS measurement is subject to the resolution limitations from the TDS. One potential approach is beam physical simulation in which the collective effects are modeled and the beam dynamics results are well matched with experimental measurement [5]. Unfortunately, it is too computationally expensive to be applicable in the control room.

To overcome these difficulties, machine learning (ML), especially the deep neural network, has the potential to cope with system modeling in the accelerator community as a result of the rapid development of computer science. Based on it, we are enabled to construct the surrogate model with the fast-execution speed with ML, which has demonstrated its data processing capabilities in many industrial fields. With this powerful tool introduced, some ML applications in accelerators have been explored and studied in the past few years. Based on the built surrogate model with fast execution and reliable accuracy, some beam dynamics optimization projects can benefit from the orders of magnitude increase in speed [6, 7].In addition to that, it can also facilitate the automatic online tuning and beam phase space control in FEL facility [8, 9].

Because of the powerful capability of interpreting images, there has been some recent research about neural network-based virtual diagnostic of 2D beam LPS distribution in the accelerator community [10–13]. In this paper, we propose an alternative manner to predict the beam LPS distribution. This surrogate model is built to provide the prediction of the slice beam properties distributions and its corresponding LPS is reconstructed based on them. Furthermore, Convolutional neural networks (CNN) have been implemented as the second method. We compare the results from these two approaches and the preliminary study paves the path for further investigation on the online virtual diagnostic in the operational machine.

METHODOLOGY AND RESULTS

Here we demonstrate the feasibility of the machine learning-based beam LPS reconstruction with beam dynamics simulations from European X-ray Free-Electron Laser [14]. The schematic layout of the European XFEL accelerator is shown in Fig. 1. In the main linac section, the beam experiences the longitudinal density modulations at three bunch compressor chicanes with the nominated beam energy of 130 MeV, 700 MeV, and 2.4 GeV respectively. The initial beam distribution at the end of the gun cavity is simulated with ASTRA [15]. The remaining physical tracking, which simulates the beam dynamics from the gun cavity exit to the collimator section at the entrance of the undulator, is conducted with OCELOT code [16].

In the simulations, the momentum compaction factor in each dispersive section is kept as their initial values. We tune the upstream RF parameters to adjust the energy chirp at the entrance of each dispersive section to change the com-

* zihan.zhu@desy.de

ISBN: 978-3-95450-220-2 ISSN: 2673-5474 doi: 10.18429/JACoW-FEL2022-WEP12

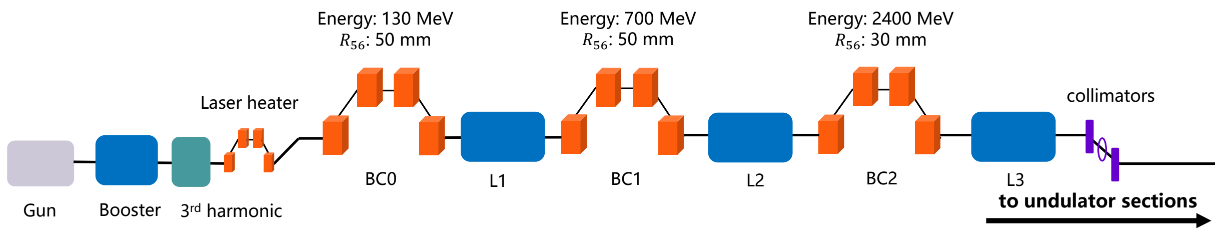

Figure 1: Schematic layout of EuXFEL linear accelerator from the gun cavity exit to the entrance of the undulator.

pression scenarios. The first three parameters are the first-, second-, and third-order coefficient in energy distribution at the injector (I1) exit, which define the detailed compression scenario in the first bunch compressor. The other two parameters control the compression strengths in the second and third chicane sections. In this preliminary study, we adjust the RF settings with relatively small variations based on the nominal design of beam dynamics. The scanning range of each parameter can be found in Table 1.

Table 1: The Five Input Features and these Values Ranges for Simulation

Parameters	Range
I1 chirp (1/m)	[-8.2, -8]
I1 curvaure (1/m^2)	[260, 280]
I1 skewness (1/m^3)	[45000, 47000]
L1 chirp (1/m)	[-13.7, -12.6]
L2 chirp (1/m)	[0, 2]

The total sample number is 40,000, 70% of which is used for model training and the rest 30% for validation. The open-source machine learning library Pytorch [17] is applied here to build the architecture for all the neural networks presented in this paper.

Slice Parameters-based LPS Prediction

The first method of the LPS distribution prediction is based on the three slice beam property distributions: current, mean energy, and slice energy spread.For each simulation in the sample set, these three distributions are generated with longitudinal beam dynamics analysis with 300 slices. The beam current profile indicates the density distribution along the beam, and the beam energy distribution can be predicted based on the Gaussian distribution assumption in each longitudinal slice.

Additionally, the bin width in the longitudinal position for each sample is collected as the scaling parameter, which describes the bunch longitudinal extent. The constructed fully-connected neural network contains the architecture of four hidden layers. In each of them, the neuron number is 256, and Rectified Linear Unit (ReLU) [18] is selected as the activation function.

After the model construction, we test its performance using examples of different compression scenarios, from

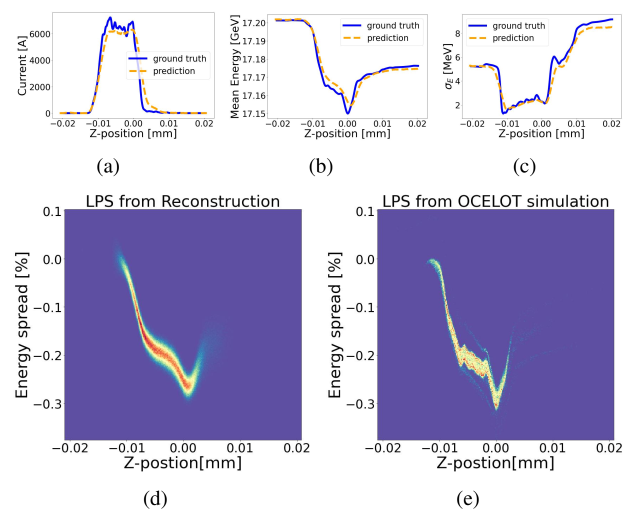

Figure 2: One example to illustrate the reconstruction according to the three property distribution (a-c). (d) The reconstructed LPS distribution based on the NN prediction. (e) The groud truth from OCELOT simulation. The head of the bunch is on the left of the coordinate.

which a good agreement can be found between the model prediction and the corresponding simulation result. Fig. 2 shows the beam property distributions from one validation case of normal compression intensity. In Fig. 2(d), the reconstructed LPS distribution matches well with the one from the simulation that is shown in Fig. 2(e).

Based on this model, the immediate beam LPS distribution can be obtained and this tool is eligible for being introduced in the control room to provide real-time online virtual diagnostic. Furthermore, it is noteworthy that the training process during the model construction is fast, which means it is feasible to introduce the model in the control room and retrain it based on the existing one with updated measurement samples. Consequently, its accuracy will be enhanced as well as its robustness. One potential issue for this method is some information in the LPS distribution is lost during the reconstruction, which is illustrated in Fig. 3. This problem results from the outliers in the LPS distribution, which can be observed in Fig. 3(e). This distribution leads to a larger slice energy spread, resulting in inaccuracy in the prediction based on the Gaussian distribution assumption.

ISBN: 978-3-95450-220-2 ISSN: 2673-5474 doi: 10.18429/JACoW-FEL2022-WEP12

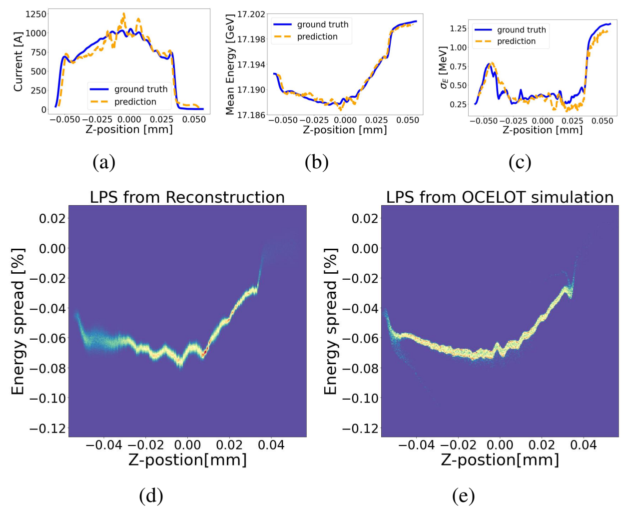

Figure 3: Another example from the validation set in which the distribution in the bunch head and tail is spoiled.

Image-based LPS Prediction

Other than the method presented above, we also give an attempt on treating the entire LPS distribution as an image and conduct image processing. The power of convolutional encoder-decoder network, which is introduced to this image regression project, has been demonstrated with applications from numerous industrial fields including facial recognition, image classification, speech recognition, etc. For each sample, its 2D LPS image is generated after binning the beam distribution in phase space with a 2D histogram of the same shape. Here we construct the convolutional encoder-decoder network to power the virtual diagnostics of LPS distribution after multi-stage longitudinal density modulation and compare its performance of it with the previous method.

The architecture of the network is shown in Fig. 4. Its output is an image of 300×300 pixels that displays the 2D distribution in the phase space. The other fully connected neural network is deployed to provide the resolution prediction based on the same input features. Due to the different bunch lengths between the samples, the pixel resolutions in the two coordinates vary between the samples as well. For a nearly full compression case, the time resolution for the LPS image can be as high as 0.3 fs/pixel.

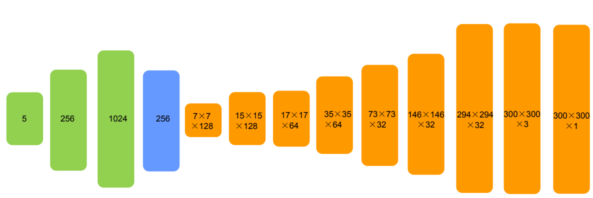

Figure 4: The contains one input layer, which is followed by three fully connected layers (green). The latent layer is highlighted in blue. Downstream it, the eight transposed convolutional layers (orange) are built as the decoder.

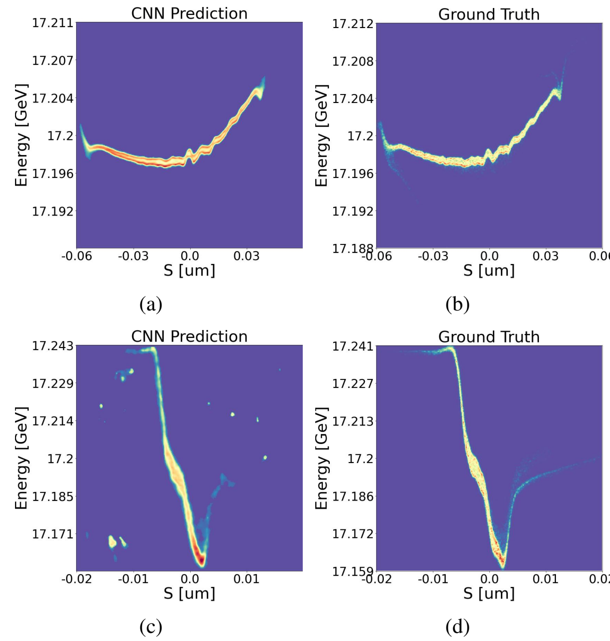

Figure 5: Two examples as the performance of the CNN model. The top row shows the LPS from a long bunch case (under compression), and the bottom one shows the short bunch case (full compression).

As evidenced in Fig. 5, there is a good agreement between the prediction from the model and the ground truth. Compared with the first method whose neural network is designed to predict the slice beam property distributions, the most obvious advantage of this method is the predicted 2D image can reproduce the detail in the beam distribution in LPS, such as the microbunching structure and the outliers around the bunch head. Concerning the training duration, it takes nearly 20h on one Graphics Processing Unit node, which is much more computationally-intense than the previous method in which the model training is easily conducted in a single CPU within 5 minutes.

CONCLUSION

In this paper, the machine learning-based prediction of the beam longitudinal phase space distribution is presented. Two different strategies are validated with simulation samples and the pros and cons of each are discussed. According to performance in the validation set, both of them achieve good and fast prediction of the beam LPS distribution after multi-stage longitudinal charge modulations. With its fast execution and reliable prediction, the online virtual diagnostic and optimization of beam longitudinal properties can be achievable. The performance test of the constructed model on the operational machine is in the following schedule and it lays the foundation for further exploration of machine learning applications in the accelerator operation.

ISBN: 978-3-95450-220-2 ISSN: 2673-5474 doi: 10.18429/JACoW-FEL2022-WEP12

ACKNOWLEDGEMENTS

This work was supported by the Youth Innovation Promotion Association CAS (2021282) and CAS-DAAD Program for Promotion of Outstanding Young Scholars, 2021 (57575641).

REFERENCES

[1] C. Pellegrini, A. Marinelli, and S. Reiche, "The physics of x-ray free-electron lasers," *Rev. Mod. Phys.*, vol. 88, p. 015 006, 1 2016. doi:10.1103/RevModPhys.88.015006

[2] H. Öström *et al.*, "Probing the transition state region in catalytic co oxidation on ru," *Science*, vol. 347, no. 6225, pp. 978–982, 2015. doi:10.1126/science.1261747

[3] C. Dejoie *et al.*, "Serial snapshot crystallography for materials science with swissfel," *IUCrJ*, vol. 2, no. 3, pp. 361–370, 2015. doi:10.1107/S2052252515006740

[4] J. M. Martin-Garcia, C. E. Conrad, J. Coe, S. Roy-Chowdhury, and P. Fromme, "Serial femtosecond crystallography: A revolution in structural biology," *Arch. Biochem. Biophys.*, vol. 602, pp. 32–47, 2016, Protein Crystallography. doi:10.1016/j.abb.2016.03.036

[5] I. Zagorodnov, S. Tomin, Y. Chen, and F. Brinker, "Experimental validation of collective effects modeling at injector section of x-ray free-electron laser," *Nucl. Instrum. Methods Phys. Res., Sect. A*, vol. 995, p. 165 111, 2021. doi:https://doi.org/10.1016/j.nima.2021.165111

[6] J. Wan, P. Chu, and Y. Jiao, "Neural network-based multiobjective optimization algorithm for nonlinear beam dynamics," *Phys. Rev. Accel. Beams*, vol. 23, no. 8, p. 081 601, 2020. doi:10.1103/PhysRevAccelBeams.23.081601

[7] A. Edelen, N. Neveu, M. Frey, Y. Huber, C. Mayes, and A. Adelmann, "Machine learning for orders of magnitude speedup in multiobjective optimization of particle accelerator systems," *Phys. Rev. Accel. Beams*, vol. 23, no. 4, p. 044 601, 2020. doi:10.1103/PhysRevAccelBeams.23.044601

[8] Z. Zhu, Y. Chen, W. Qin, M. Scholz, and S. Tomin, "Machine Learning Based Surrogate Model Construction for Optics Matching at the European XFEL," in *Proc. IPAC'22*, Bangkok, Thailand, 2022, paper MOPOTK013, pp. 461–464. doi:10.18429/JACoW-IPAC2022-MOPOTK013

[9] A. Scheinker, A. Edelen, D. Bohler, C. Emma, and A. Lutman, "Demonstration of model-independent control of the longitudinal phase space of electron beams in the linac-coherent light source with femtosecond resolution," *Phys. Rev. Lett.*, vol. 121, p. 044 801, 4 2018. doi:10.1103/PhysRevLett.121.044801

[10] C. Emma, A. Edelen, M. J. Hogan, B. O'Shea, G. White, and V. Yakimenko, "Machine learning-based longitudinal phase space prediction of particle accelerators," *Phys. Rev. Accel. Beams*, vol. 21, p. 112 802, 2018. doi:10.1103/PhysRevAccelBeams.21.112802

[11] A. Hanuka *et al.*, "Accurate and confident prediction of electron beam longitudinal properties using spectral virtual diagnostics," *Sci. Rep.*, vol. 11, no. 1, pp. 1–10, 2021. doi:10.1038/s41598-021-82473-0

[12] J. Zhu, Y. Chen, F. Brinker, W. Decking, S. Tomin, and H. Schlarb, "High-fidelity prediction of megapixel longitudinal phase-space images of electron beams using encoder-decoder neural networks," *Phys. Rev. Appl.*, vol. 16, p. 024 005, 2021. doi:10.1103/PhysRevApplied.16.024005

[13] A. E. Pollard, D. J. Dunning, and M. Maheshwari, "Learning to Lase: Machine Learning Prediction of FEL Beam Properties," Shanghai, China, Oct. 2021, presented at ICALEPCS'21, Shanghai, China, Oct. 2021, paper WEPV020, unpublished.

[14] W. Decking *et al.*, "A MHz-repetition-rate hard x-ray free-electron laser driven by a superconducting linear accelerator," *Nat. Photonics*, vol. 14, no. 6, pp. 391–397, 2020. doi:10.1038/s41566-020-0607-z

[15] K. Flöttmann *et al.*, *ASTRA: A space charge tracking algorithm*, 2011.

[16] S. I. Tomin, I. V. Agapov, M. Dohlus, and I. Zagorodnov, "OCELOT as a Framework for Beam Dynamics Simulations of X-Ray Sources," in *Proc. IPAC'17*, Copenhagen, Denmark, May 2017, pp. 2642–2645. doi:10.18429/JACoW-IPAC2017-WEPAB031

[17] A. Paszke *et al.*, "Pytorch: An imperative style, high-performance deep learning library," *Adv. Neural Inf. Process Syst.*, vol. 32, 2019.

[18] A. F. Agarap, "Deep learning using rectified linear units (relu)," *CoRR*, vol. abs/1803.08375, 2018. http://arxiv.org/abs/1803.08375

ISBN: 978-3-95450-220-2 ISSN: 2673-5474 doi: 10.18429/JACoW-FEL2022-WEP13

DEMONSTRATION OF HARD X-RAY MULTIPLEXING USING MICROBUNCH ROTATION THROUGH AN ACHROMATIC BEND *

R. A. Margraf†[1], J. P. MacArthur, G. Marcus, H.-D. Nuhn, A. Lutman, A. Halavanau, Z. Huang[1]
SLAC National Accelerator Laboratory, Menlo Park, USA
[1]also at Stanford University, Stanford, USA

Abstract

Electrons in a X-ray free electron laser (XFEL) develop periodic density fluctuations, known as microbunches, which enable the exponential gain of X-ray power in an XFEL. When an electron beam microbunched at a hard X-ray wavelength is kicked, microbunches are often washed out due to the dispersion and R_{56} of the bend. An achromatic (dispersion-free) bend with small R_{56}, however, can preserve microbunches, which rotate to follow the new trajectory of the electron bunch. Rotated microbunches can subsequently be lased in a repointed undulator to produce a new beam of off-axis X-rays. In this work, we demonstrate hard X-ray multiplexing in the Linac Coherent Light Source (LCLS) Hard X-ray Undulator Line (HXU) using microbunch rotation through a 10 µrad first-order-achromatic bend created by transversely offsetting quadrupole magnets in the FODO lattice. Quadrupole offsets are determined analytically from beam-matrix theory. We also discuss the application of microbunch rotation to out-coupling a cavity-based XFEL (CBXFEL) [1].

INTRODUCTION

Microbunch rotation using achromatic bends has long been known as an option for for out-coupling infrared FEL oscillators [2], and MacArthur et al. demonstrated a 5 µrad rotation with a single offset quadrupole for soft x-ray microbunches [3]. However, microbunch rotation with hard X-rays has proved more challenging. Shorter microbunches, separated at the radiation wavelength, λ_r, are more sensitive to bunching factor ($\theta \approx (\frac{2\pi}{\lambda_r} + \frac{2\pi}{\lambda_u})z$) degradation due to changes in the z position of the particles relative to the center of the microbunch.

Cavity-based XFELs, such as the X-ray Regenerative Amplifier FEL (XRAFEL) [4, 5] and X-ray FEL Oscillator (XFELO) [6] typically operate Bragg-reflecting cavities at hard X-ray wavelengths. To extend microbunch rotation as an out-coupling mechanism for these cavities, we need to extend it to hard X-rays, such as the 9.832 keV X-ray energy used by the CBXFEL project [1].

MICROBUNCH ROTATION FROM AN OFFSET QUADRUPOLE TRIPLET

MacArthur et al. [3] proposed a triplet of three offset quadrupoles to perform microbunch rotation at hard X-ray wavelengths. Such a scheme is illustrated in Fig. 1, where α is the microbunch rotation angle, f_1, f_2, and f_3 are the quadrupole focal lengths, and L_1, and L_2, are the distances between the quadrupoles.

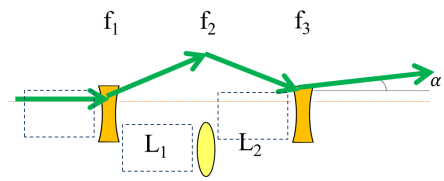

Figure 1: Offset quadrupole triplet for microbunch rotation.

Later work [7, 8] identified microbunch rotation through this triplet is optimized when the kicks from the three quadrupoles form a first-order achromatic bend. To preserve microbunching through a bend, one has to prevent the energy spread of the electron beam from coupling to the longitudinal and transverse dimensions of the beam. In transfer matrix formalism, for a kick in x, these are the R_{16} (Dispersion), R_{26} (Dispersion') and R_{56} elements. An achromatic bend sets the Dispersion and Dispersion' elements to zero. The quadrupole offsets which achieve this can be analytically found. In the thin quadrupole limit, these are [7, 8]:

$$\begin{aligned} o_1 &= \frac{\alpha f_1 f_2}{L_1} \\ o_2 &= \frac{-\alpha f_2 (f_2 L_1 + f_2 L_2 - 2 L_1 L_2)}{L_1 L_2} \\ o_3 &= \frac{\alpha (L_2^2 + f_2 f_3)}{L_2}. \end{aligned} \tag{1}$$

If we implement microbunch rotation in a FODO lattice where $f_1 = f_3 = -f_2$, and $L_1 = L_2 = L$, these simplify to:

$$\begin{aligned} o_1 &= \frac{-\alpha f_1^2}{L} \\ o_2 &= -2\alpha f_1 \left(1 + \frac{f_1}{L}\right) \\ o_3 &= \frac{-\alpha (f_1^2 - L^2)}{L}. \end{aligned} \tag{2}$$

A more lengthy analytical solution also exists in the thick quadrupole limit [7], and this was used to determine the quadrupole offsets for this experiment, which differed by a few µrad from the thin quadrupole values.

To preserve microbunching, we must also keep R_{56} small. An expression for R_{56} through the offset quadrupole triplet

* This work was supported by the Department of Energy, Laboratory Directed Research and Development program at SLAC National Accelerator Laboratory, under contract DE-AC02-76SF00515.
† rmargraf@stanford.edu

ISBN: 978-3-95450-220-2 ISSN: 2673-5474 doi: 10.18429/JACoW-FEL2022-WEP13

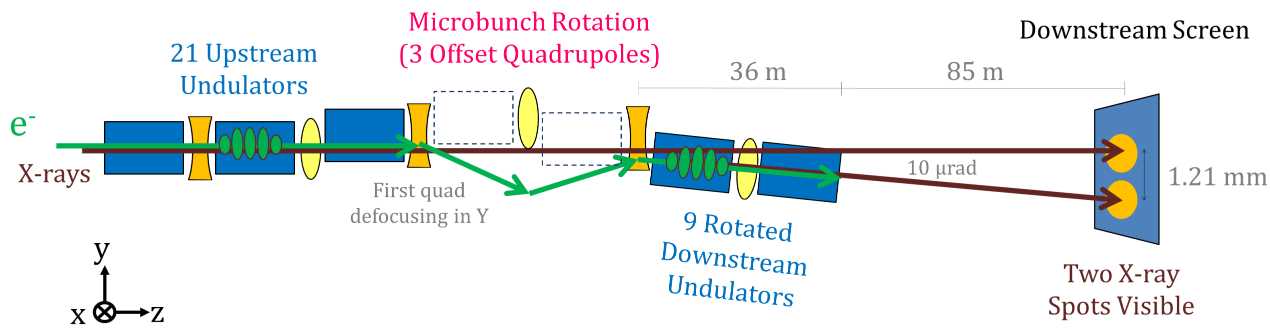

Figure 2: Side view of experimental set-up in LCLS-II Hard X-ray Undulator Hall.

in a FODO lattice is given in Eq. (3) [8]. A smaller R_{56} can be achieved by picking the first quadrupole in the triplet to be defocusing in the dimension of the kick (eg. $f_1 < 1$).

$$R_{56} = \alpha^2 f_1 \left(1 + \frac{2f_1}{L}\right) + \frac{2L}{\gamma^2} \tag{3}$$

To lase the rotated microbunches, one must then align undulators to the new repointed trajectory. One important detail to note is that the electron beam does not fully return on-axis in the third quadrupole. Propagating an on-axis beam through the beam matrices defined in [7] in the thin quadrupole limit for a FODO lattice, one can show the trajectory in the third quadrupole is equal to αL_1. Our entire repointed undulator line is thus offset by this amount.

EXPERIMENTAL DEMONSTRATION

Set-up

A schematic of the experimental set-up, performed using the LCLS-II Hard X-ray Undulator line (HXU) with the 120 Hz Cu linac, is given in Fig. 2. We offset three undulator girders and their associated quadrupoles in Y using the analytically calculated offsets. We chose to kick vertically instead of horizontally because the LCLS-II HXU undulators are horizontal gap, and a vertical shift allowed us to continue to lase in the undulator immediately before the quadrupole triplet, even though that undulator was offset vertically with its attached quadrupole. We repointed the undulators downstream of the offset quadrupoles to the new electron beam trajectory. No scanning of the triplet quadrupole offsets was needed. To maximize power in the repointed spot, we used corrector dipoles to flatten the orbit in the repointed section, and scanned the K of the repointed undulators.

Experimental parameters are given in Table 1. B'_1, B'_3, B'_2 are the quadrupole gradients, L_{Quad} is the effective quadrupole length, L_{Und} is the length of the undulator in each segment, and λ_u is the undulator period. E_{e^-} and E_{λ_r} define the energy of the electron and X-ray beams. $\epsilon_{x,norm}$ is a typical LCLS Cu Linac normalized emittance in the undulator hall. Δt_{FWHM}, I_{core} and $\Delta E_{slice,core}$ define the electron beam pulse duration and the average current and average slice emittance within the central FWHM pulse duration. These last three quantities were calculated from measured time-resolved energy distribution of the electron bunch downstream of the undulator line, without undulator lasing. Time dependent horizontal streaking is provided by an X-ray transverse deflecting cavity (XTCAV).

Table 1: Experimental Parameters

f_1=f_3, f_2	(−12.0, 12.0) m	L_1=L_2	4.013 m
B'_1=B'_3, B'_2	(−35.7, 35.7)T/m	L_{Quad}	8.4 cm
λ_u	2.6 cm	L_{Und}	3.4 m
E_{e^-}	10.79 GeV	E_{λ_r}	10.14 keV
$\epsilon_{x,norm}$ [1]	0.4×10^{-6} m*rad	I_{core}	4.38 kA
Δt_{FWHM}	32.7 fs	$\Delta E_{slice,core}$	12.3 MeV

Triplet Quadrupole Offsets: 10 µrad

o_1	366 µm	o_2	489 µm	o_3	323 µm

Triplet Quadrupole Offsets: 20 µrad

o_1	733 µm	o_2	978 µm	o_3	646 µm

The final table section defines the quadrupole offsets. Microbunch rotation was demonstrated at 10 µrad and 20 µrad.

Example Images

Figure 3 shows example single-shot images on the downstream screen. Screen coordinates have been converted into the angular separation between the two beams to clearly show multiplexing at 10 µrad and 20 µrad. The mean angular separations between the two rotated spots were (9.9 ± 0.1) µrad and (20.1 ± 0.1) µrad respectively. Both spot separations agree with the theoretical value within the precision of the screen calibration. To accommodate large quadrupole offsets within the range of the undulator girder movers, the on-axis beam was repointed between the 10 µrad and 20 µrad datasets. Without additional tuning, this caused lower power in the on-axis spot in the 20 µrad case. This repointing was additionally important to allow the 20 µrad repointed spot to pass through the aperture on the gas detector. Further repointing could have prevented the rotated spot in B) from being clipped by this aperture.

[1] Typical LCLS Value

ISBN: 978-3-95450-220-2 ISSN: 2673-5474 doi: 10.18429/JACoW-FEL2022-WEP13

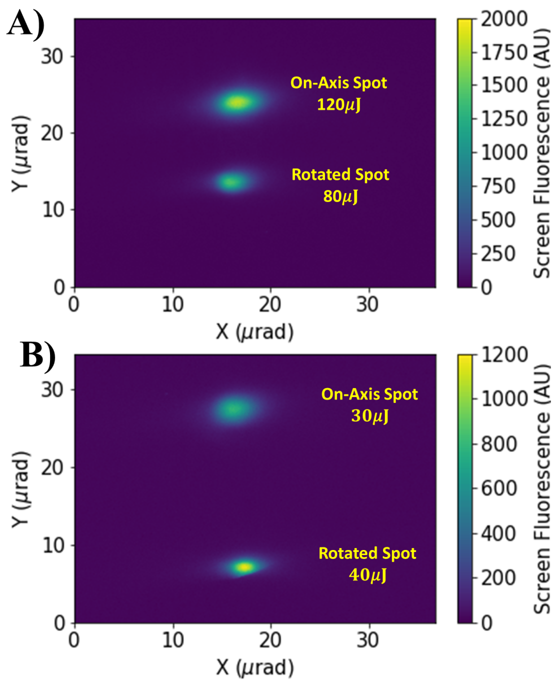

Figure 3: Example single shot microbunch rotation images with average X-ray pulse energies. A) 10 μrad and B) 20 μrad.

K Optimization

We maximized X-ray power by scanning K in the rotated undulator section, as shown in Fig. 4. Our upstream undulators had a linear taper of $\Delta K = -0.0002$ per undulator to compensate for wakefield energy losses in the undulator line. If the average K in the undulator directly upstream of the microbunch rotation triplet was 2.5439, the K following the linear taper for the first repointed undulator would be 2.5435. However, when we scan the repointed undulator section, while keeping the linear taper, we find the optimal K of the first repointed undulator is 2.5396, a detune of -0.15%. Our current simulation efforts, not shown here, suggest the magnitude of this detune is highly dependant on the saturation of the electron beam entering the microbunch rotation triplet. A more highly saturated beam has lost more energy during lasing than a fresh electron beam. We speculate that when the electron beam is separated from the on-axis X-ray beam, the optimal K decreases due to the energy loss from the lasing in the upstream section.

After performing this scan, we added a quadratic taper to the repointed undulator section to further increase power. This quadratic taper is present in the following scans.

Gain in Repointed Undulator Section

We examined the gain in the repointed undulator section by inserting a kick after each repointed undulator, as shown in Fig. 5, with a polynomial fit. We predicted the gain would be quadratic, consistent with superradiant emission [9]. The gain here appears to be primarily linear, with a quadratic component. Perhaps with further taper optimization, quadratic gain might be possible in future studies.

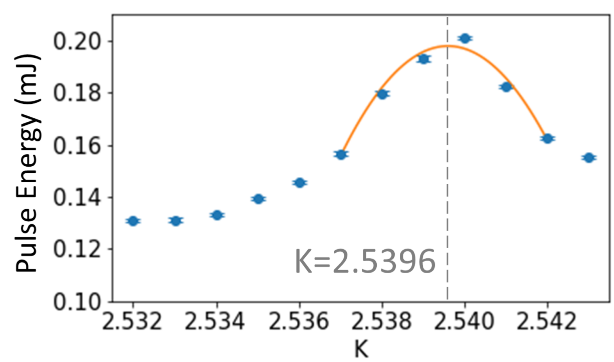

Figure 4: Undulator K scan for the 10 μrad case. The combined pulse energy of the on-axis and rotated X-ray beams was measured on a gas detector as the K of the repointed undulator section was scanned. The gain in the repointed undulator segment varied considerably with K. We optimized K to maximize pulse energy. Error bars give the standard error of the mean.

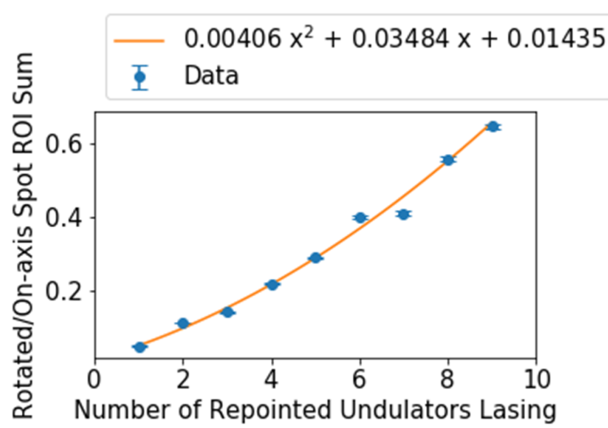

Figure 5: Gain in rotated undulator section for the 10 μrad case. In this run, the power in the on-axis spot was 120 μJ. Error bars give the standard error of the mean.

Phaseshifter Scan

To demonstrate that the gain in the repointed undulator section comes from the microbunching in the electron beam, and not from interaction with the on-axis X-ray seed, we performed a phaseshifter scan, shown in Fig. 6. In a typical on-axis undulator, as in Fig. 6A, using a phaseshifter to delay the electron bunch by 180° relative to the X-ray pulse supresses lasing. However, we find that in the microbunch rotation case, as in Fig. 6B, the power in the repointed undulator section does not change. This suggests there is negligible interaction between the on-axis X-ray beam and the repointed electron beam.

ISBN: 978-3-95450-220-2 ISSN: 2673-5474 doi: 10.18429/JACoW-FEL2022-WEP13

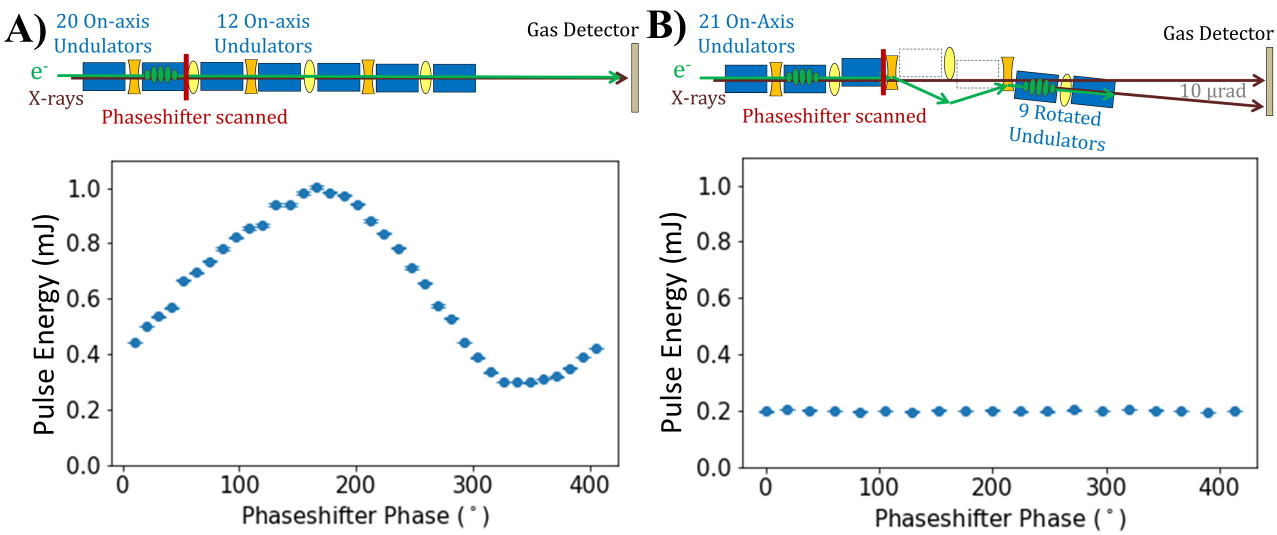

Figure 6: Phaseshifter Scan Demonstration for the 10 μrad case. A) All 32 undulators were aligned on axis, and a phaseshifter was scanned. B) With the microbunch rotation triplet and repointed undulator line installed, the phaseshifter just upstream of the microbunch rotation triplet was scanned. Error bars give the standard error of the mean.

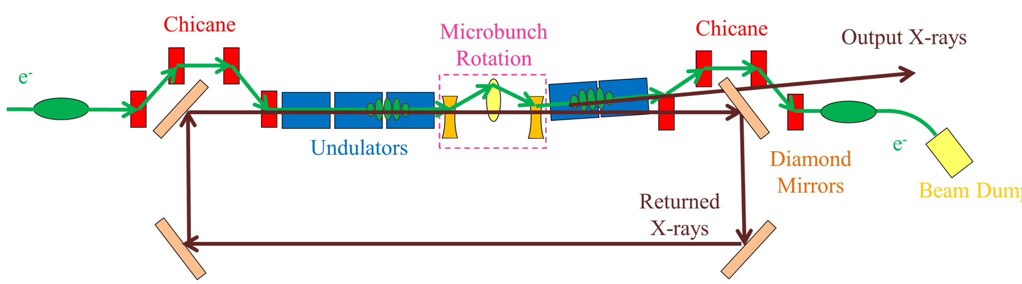

Figure 7: Microbunch rotation as an out-coupling scheme for a cavity-based XFEL.

CONCLUSIONS AND APPLICATIONS TO A CAVITY-BASED XFEL

These results demonstrate microbunch rotation is possible with hard X-ray wavelengths. To our knowledge, this is the first time microbunch rotation has been demonstrated with hard X-rays in the literature. Furthermore, demonstrating microbunch rotation with hard X-ray wavelengths at >10 μrad is significant for the application of microbunch rotation to a cavity-based XFEL.

Proposed cavity-based XFELs [1, 10, 11] use Bragg-reflecting mirrors to circulate X-ray pulses which interact with a series of electron bunches. The CBXFEL project [10] will test a rectangular cavity of diamond (400) Bragg-reflecting mirrors at 9.832 keV, which have an angular reflectivity bandwidth (FWHM) of 8.8 μrad.

A microbunch rotation out-coupling scheme for a cavity-based XFEL is depicted in Fig. 7. X-rays produced by on-axis undulators remain inside the cavity, while re-pointed X-rays miss the rocking curve of the Bragg reflection and are transmitted out of the cavity.

A 10 μrad microbunch rotation is sufficient to miss the Bragg rocking curve of the diamond 400 reflection used by the CBXFEL project. Thus, our demonstration of 10 μrad and 20 μrad rotation of 10.14 keV microbunches supports the feasibility of microbunch rotation for out-coupling a hard X-ray cavity.

In future publications, we will support these experimental results with simulations. Comparing the K detune and gain curve observed here with simulation should provide insight into how to quickly optimize microbunch rotation schemes in the future. We will also continue to consider the applicability of microbunch rotation in upcoming cavity-based FEL projects.

REFERENCES

[1] G. Marcus *et al.*, “Cavity-Based Free-Electron Laser Research and Development: A Joint Argonne National Laboratory and SLAC National Laboratory Collaboration”, in *Proc. FEL’19*, Hamburg, Germany, Aug. 2019, pp. 282–287. doi:10.18429/JACoW-FEL2019-TUD04

[2] N.G. Gavrilov, G.N. Kulipanov, V.N. Litvinenko, A.S. Sokolov, and N.A. Vinokurov, “On Mutual Coherency of Spontaneous Radiation from Two Undulators Separated by Achromatic Bend”, *IEEE J. Quantum Electron.*, vol. 27, no. 12, pp. 2566–2568, 1991. doi:10.1109/3.104134

[3] J. P. MacArthur, A. A. Lutman, J. Krzywinski, and Z. Huang, “Microbunch Rotation and Coherent Undulator Radiation

ISBN: 978-3-95450-220-2 ISSN: 2673-5474 doi: 10.18429/JACoW-FEL2022-WEP13

from a Kicked Electron Beam," *Phys. Rev. X*, vol. 8, no. 4, p. 041036, 2018. doi:10.1103/PhysRevX.8.041036

[4] Z. Huang and R.D. Ruth, "Fully coherent x-ray pulses from a regenerative-amplifier free-electron laser", *Phys. Rev. Lett.*, vol. 96, pp. 144801, 2006. doi:10.1103/PhysRevLett.96.144801

[5] G. Marcus *et al.*, "Refractive Guide Switching a Regenerative Amplifier Free-Electron Laser for High Peak and Average Power Hard X Rays", *Phys. Rev. Lett.*, vol. 125, no. 25, p. 254801, Dec. 2020. doi:10.1103/PhysRevLett.125.254801

[6] K.-J. Kim, Y. Shvyd'ko, and Sven Reiche, "A proposal for an x-ray free-electron laser oscillator with an energy-recovery linac", *Phys. Rev. Lett.*, vol. 100, p. 244802, 2008. doi:10.1103/PhysRevLett.100.244802

[7] R. A. Margraf, X. J. Deng, Z. Huang, J. P. MacArthur, and G. Marcus, "Microbunch Rotation for Hard X-Ray Beam Multiplexing", in *Proc. FEL'19*, Hamburg, Germany, Aug. 2019, pp. 665–668. doi:10.18429/JACoW-FEL2019-THP036

[8] R. A. Margraf, J. P. MacArthur, G. Marcus, and Z. Huang, "Microbunch Rotation as an Outcoupling Mechanism for Cavity-based X-Ray Free Electron Lasers", in *Proc. IPAC'20*, Caen, France, May 2020, pp. 35. doi:10.18429/JACoW-IPAC2020-WEVIR03

[9] Q. Jia, "Analysis of emissions from prebunched electron beams", *Phys. Rev. Accel. Beams*, vol. 20, no. 7, p. 070702, 2017. doi:10.1103/PhysRevAccelBeams.20.070702

[10] K.-J. Kim *et al.*, "Test of an X-ray Cavity using Double-Bunches from the LCLS Cu-Linac", in *Proc. IPAC'19*, Melbourne, Australia, May 2019, pp. 1887–1890. doi:10.18429/JACoW-IPAC2019-TUPRB096

[11] P. Rauer, "A Proof-Of-Principle Cavity-Based X-Ray Free-Electron-Laser Demonstrator at the European XFEL", Ph.D dissertation, Department of Physics, University of Hamburg, Hamburg, 2022. doi:10.3204/PUBDB-2022-02800

ISBN: 978-3-95450-220-2 ISSN: 2673-5474 doi: 10.18429/JACoW-FEL2022-WEP14

INTRABEAM SCATTERING EFFECTS IN THE ELECTRON INJECTOR OF THE EUROPEAN XFEL

E. Gjonaj*, H. De Gersem, Technische Universität Darmstadt, TEMF, Darmstadt, Germany
T. Limberg, DESY, Hamburg, Germany

Abstract

A numerical procedure for beam dynamics simulations including IBS effects is presented. The method is implemented in the tracking code Reptil and, furthermore, it is applied in the simulation of the injector section of the E-XFEL. This allows to identify precisely the amount by which IBS contributes to the uncorrelated energy spread growth in the injector. It is found that IBS is responsible for nearly doubling the slice energy spread of the bunch at the central slice. Various aspects related to the IBS-induced growth of the slice energy spread in the injector compared to space-charge related effects are discussed.

INTRODUCTION

The main limitation in the operation of X-Ray Free Electron Lasers (XFEL) is posed by the microbunching instability (MBI) [1,2]. This is a space-charge induced amplification in the longitudinal phase-space that grows from shot noise. In the European XFEL (E-XFEL), MBI is partially mitigated by means of a laser heater which is placed right after the injector section. The laser heater introduces a small amount of uncorrelated energy spread to the beam, thus, attempting to suppress MBI by the Landau damping mechanism. This process, however, is critical since excessive heating may affect the FEL process. This is why, an accurate estimation of the intrinsic slice energy spread (SES) of the beam in the injector, before laser heating is applied, is crucial for an optimal operation of the facility [2].

In the case of the E-XFEL, tracking simulations for a bunch of 250 pC predict a SES of about 1 keV at the exit of the injector section. However, recent measurements using a transverse deflecting structure indicate that this figure is as high as 6 keV [3]. In the case of SwissFEL, an even higher SES of 15 keV was reported [4], although the operation modes of both machines are quite similar.

These discrepancies are hard to explain. At least partially, they are attributed to intrabeam scattering (IBS) effects [3]. Unfortunately, such measurements do not provide sufficient insight on the cause of SES growth. This could be related to the emission process, wakefields in the gun, IBS or a combination of all. This motivates the present study, where the specific contribution of IBS to the SES growth in the E-XFEL injector is investigated by numerical simulations. A novel IBS modeling approach is introduced that includes in particle tracking simulations the combined effects of the collective, space-charge interaction on the one hand and Coulomb collisions on the other.

* gjonaj@temf.tu-darmstadt.de

The E-XFEL injector section considered in the simulations (see Fig. 1) has a total length of 40 m, it includes the electron gun, a booster module (A1) and a third-harmonic module (AH1). The main injector and beam parameters used in the simulations are summarized in Table 1.

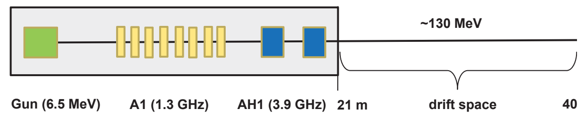

Figure 1: Schematics of the E-XFEL injector beam line.

Table 1: Main Injector Parameters Used in the Simulations

Component	Parameter	Value
Gun (1.3 GHz)	Field gradient	56.3 MV/m
A1 (1.3 GHz)	Field gradient	34.4 MV/m
AH1 (3.9 GHz)	Field gradient	17.3 MV/m
Bunch	Charge	250 pC
Bunch	Duration on cathode	3 ps
Bunch	Spot size on cathode	0.25 mm

SIMULATION METHOD

For the IBS simulations, the tracking code Reptil is extended such that it includes collisional effects in addition to collective interactions. For the IBS modeling, two different Monte-Carlo collision models are considered. These are the Takizuka & Abe's [5] and the Nanbu's [6] models as described below.

The Reptil Code

The **Re**lativistic **P**article **T**racker for **I**njectors and **L**inacs (Reptil) is a particle tracking code developed at the TU Darmstadt. The code employs a modified, 4$^{\text{th}}$-order-accurate Adams-Moulton scheme for the integration of particle's equations with an adaptive time step. Various space-charge solvers are implemented in Reptil. These include particle-particle solvers based on the Barnes-Hut and the FMM methods [7], as well as 3D particle-mesh solvers using the integrated Green's function approach [8]. Due to the specifics of IBS modeling, only the particle-mesh approach is used in the following. In addition, Reptil supports various types of accelerating cavities, multipole magnets, and external wakefields. All computations are highly parallelized for shared as well as for distributed memory platforms.

ISBN: 978-3-95450-220-2 ISSN: 2673-5474 doi: 10.18429/JACoW-FEL2022-WEP14

IBS Modeling

The simplest Monte-Carlo binary collision model was proposed by Takizuka & Abe in 1977 [5]. In this method, the particles are first grouped into cells. Then, for each randomly chosen pair within a cell, an effective collision event is applied. Assuming that a large number of small-angle collisions occurs within a given time interval, the scattering angle distribution for a single collision is Gaussian. Therefore, the total scattering angle Θ in the center-of-mass frame after N independent collision events follows a normal distribution with with zero mean and variance [9]

$$< \delta^2 >= \frac{e^4 N_e \log \Lambda}{8\pi \varepsilon_0^2 \mu_e^2 |u|^3} \Delta\tau, \tag{1}$$

where e is the elementary charge, N_e the electron density, $u = v_\alpha - v_\beta$ is the relative velocity, μ_e the reduced electron mass and $\Delta\tau$ the time step. Furthermore, $\log \Lambda$ denotes the Coulomb logarithm (to be discussed later). The scattering angle Θ is then obtained from a random sample of the distribution given by Eq. (1) using $\delta = \tan(\Theta/2)$. This defines the rotation of the relative velocity as

$$\begin{aligned}
\Delta u_x &= \frac{u_x u_z \sin\Theta\cos\Phi}{u_\perp} - \frac{u_y u \sin\Theta\sin\Phi}{u_\perp} - u_x(1-\cos\Theta),\\
\Delta u_y &= \frac{u_y u_z \sin\Theta\cos\Phi}{u_\perp} + \frac{u_x u \sin\Theta\sin\Phi}{u_\perp} - u_y(1-\cos\Theta),\\
\Delta u_z &= -u_\perp \sin\Theta\cos\Phi - u_z(1-\cos\Theta),
\end{aligned}$$

where $u = |u|$, $u_\perp = \sqrt{u_x^2 + u_y^2}$ and the azimuthal angle Φ represents rotations out of the scattering plane. The latter is a uniformly distributed random angle in the interval $[0, 2\pi]$. The post-collisional velocities of the two particles are

$$\begin{aligned}
v'_\alpha &= v_\alpha + \Delta u/2,\\
v'_\beta &= v_\beta - \Delta u/2.
\end{aligned} \tag{2}$$

Note that the particle momenta are strictly conserved. However, this does not apply to the kinetic energy which, consequently, gives rise to the IBS effect.

The above basic method is essentially non-relativistic. In the case of accelerator beams, two major modifications are needed. The first consists in transferring all scattering angle calculations to the rest frame of the bunch. The non-relativistic particle velocities in the rest frame are computed by the transformations,

$$\begin{aligned}
v_x &= c\beta_x,\\
v_y &= c\beta_y,\\
v_z &= c\gamma_0\gamma(\beta_z - \beta_0),
\end{aligned} \tag{3}$$

where c is the speed of light, β and γ are the relativistic β- and γ-factors of the particle in the laboratory frame, respectively. Furthermore, β_0 and γ_0 denote the relativistic factors of the average frame for an electron bunch moving in the z-direction. Once the scattered velocities in the rest frame are computed, the inverse transformations to Eq. (3) are applied to determine the particle momenta in the laboratory frame. Note also that the local particle density N_e and the collision interval $\Delta\tau$ in the rest frame are scaled accordingly. This procedure is repeated in every time step of the simulation in addition to the standard space-charge field and particle tracking calculations. Thus, the momentum changes due to Coulomb collisions are added on top of the collective particle dynamics that is due to electromagnetic cavity fields and the space-charge interaction.

The second modification concerns the calculation of the local Coulomb logarithm. The latter is defined as $\log \Lambda \approx \log(b_{max}/b_{min})$, where b_{max} and b_{min} are the maximum and minimum impact parameters of the collision process, respectively [10]. The minimum impact parameter for classical collisions is given by the Landau parameter, $b_{min} = e^2/\mu|u|^2$ corresponding to the minimum inter-particle distance for an electron pair with given kinetic energy. The choice of b_{max} is ambiguous in the literature. However, in the context of particle-mesh simulations, the collision model needs to be applied only over a small region corresponding to the mesh cell containing the particle pair. This is because the long range Coulomb interaction is properly resolved by the space-charge field calculation on the mesh. Thus, restricting the maximum impact parameter to the size of a mesh cell allows to separate collective effects from collisional ones. In the Reptil implementation, $b_{max} = \max(\Delta_x, \Delta_y)$ is used, where $\Delta_{x,y}$ are the mesh sizes along the transverse directions.

The second collision model considered is Nanbu's approach [6]. The main observation is that for large intervals $\Delta\tau$, the single collision events can no longer considered to be independent. Therefore, the distribution of the cumulative scattering angle resulting from a large number of successive collisions is no longer Gaussian. Nanbu used direct particle-particle simulations to identify this distribution. Specifically, a model parameter, A, is defined by the solution of

$$\coth(A) - A^{-1} = \exp(-2 < \delta^2 >), \tag{4}$$

where $< \delta^2 >$ is defined as in Eq. (1). Then, the scattering angle is found from the empirical distribution function

$$\Theta(u) = \cos^{-1}\left(A^{-1}\log\left[\exp(-A) + 2u\sinh(A)\right]\right), \tag{5}$$

where u is a random variable uniformly distributed in $[0, 1]$. Nanbu's method, essentially allows to use a larger time step in the simulation. The remaining procedure and implementation for relativistic beams is identical with the Takizuka & Abe's model.

RESULTS

The investigation consists of three parts. First, the simulations without IBS (but including space-charge) are validated against an established tracking code such as Astra [11]. Then, IBS simulations are performed for the complete injector line shown in Fig. 1. Lastly, the effect is analyzed by comparing the simulation results with an analytical model in the drift-space of the injector only.

ISBN: 978-3-95450-220-2 ISSN: 2673-5474 doi: 10.18429/JACoW-FEL2022-WEP14

Validation

The validation results are shown in Figs. 2 and Fig. 3. In the Reptil case, a series of mesh resolutions (denoted in the Figures as nx × ny × nz) and number of particles varying between 1-5 millions are used. The SES and transverse emittance of the bunch at the exit of the injector show a perfect agreement with Astra. In particular, the computed SES is quite robust being nearly insensitive to numerical parameters. Note that in Astra, the space-charge field is assumed to be 2D-rotational symmetric, whereas in Reptil a fully 3D-field solver is employed.

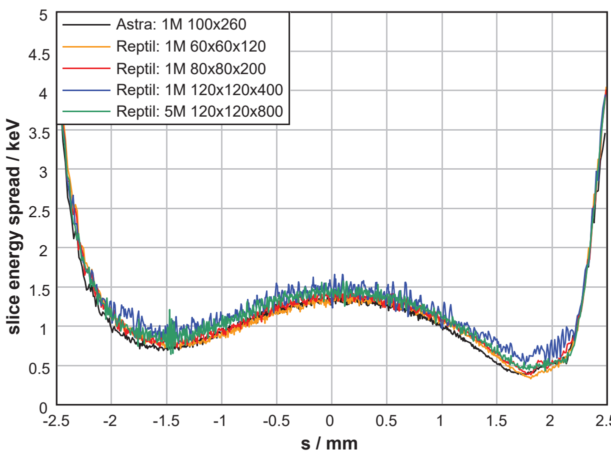

Figure 2: Computed SES at the end of the injector line not including the IBS effect: comparison with Astra.

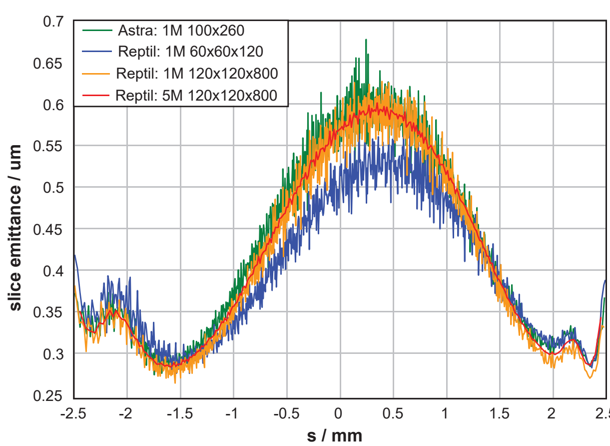

Figure 3: Computed slice emittance at the end of the injector line not including IBS: comparison with Astra.

IBS Simulations

The impact of IBS is demonstrated in Fig. 4 and 5. The average SES is substantially increased by about 1 keV at the exit of the injector section. In addition, the IBS effect contributes to a ”flattening” of the longitudinal phase-space resulting in a more uniform SES distribution among the slices. Both, the Takizuka & Abe’s and the Nanbu’s models yield identical results indicating that the results are numerically robust. It should be noted that the slice emittance of the bunch (not shown in the paper) is nearly unaffected by IBS as is expected from theory [1].

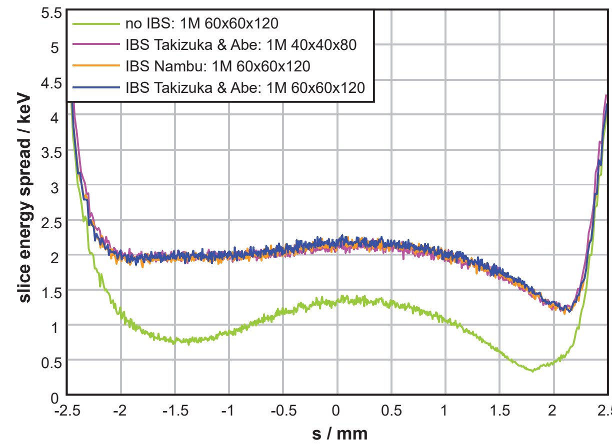

Figure 4: Computed SES at the end of the injector line including IBS: comparison with the non-IBS case.

In Fig. 5, the longitudinal phase-space broadening caused by IBS is clearly observed. This is manifested by the appearance of a longer tail of the distribution in the IBS case towards smaller longitudinal momenta. This reveals that the IBS interaction results in a net momentum transfer from the longitudinal degrees of freedom to the transverse ones rather than the other way round.

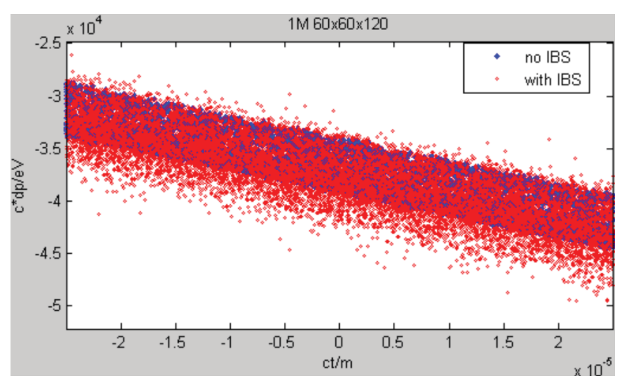

Figure 5: Longitudinal phase-space occupation at the end of the injector line: comparison with the non-IBS case.

Analysis

For a better understanding the process, one can restrict the investigation within the drift space behind the AH1-module (cf. Fig. 1) where the bunch is not subject to acceleration and space-charge forces become less relevant. Starting with an initial bunch distribution obtained by Astra simulations at 21 m, the final SES computed with and without IBS effects are shown in Fig. 6. Obviously, the SES grows even in the absence of IBS. This related to the drop of the space-charge field energy in the drift space that results from the fact that the beam is slightly diverging (see Stupakov el al. [12] for

ISBN: 978-3-95450-220-2 ISSN: 2673-5474 doi: 10.18429/JACoW-FEL2022-WEP14

a discussion). However, IBS still provides the dominant contribution to the total SES.

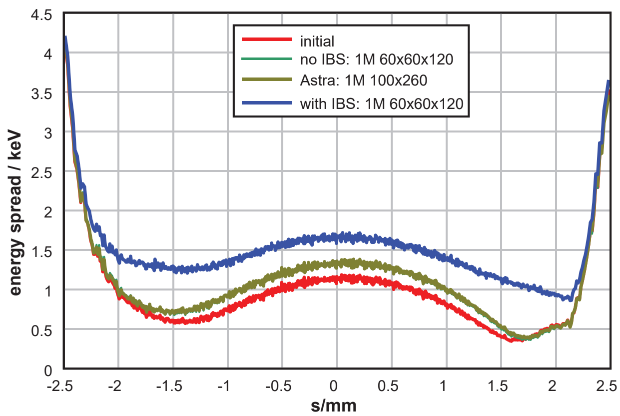

Figure 6: Various SES contributions in the drift space. The Astra and the "no IBS"curves lie on top of each other.

A comparison of the SES growth (for the central slice) in the drift space is shown in Fig. 7. In the addition to the simulations, SES curves obtained by the analytical model of Bane [13] are shown. In this model, the Coulomb logarithm is a free parameter. Therefore, two SES curves corresponding to typical values $\Lambda_c = 7.5$ and $\Lambda_c = 10$, respectively, are shown. Obviously, the analytical model strongly underestimates the effect. Even when the IBS-induced SES computed analytically is added to the intrinsic bunch SES without IBS, the total values are substantially smaller than the simulated SES. This indicates a limited applicability of the analytical model for IBS estimations, at least in the injector case. This is due to the many assumptions involved in this model, notably the high-energy approximation and the assumption of a perfectly Gaussian bunch distribution.

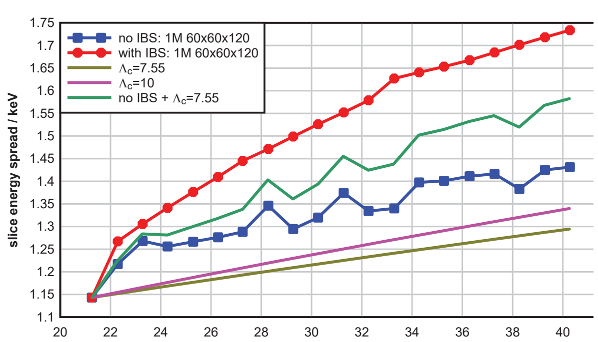

Figure 7: Growth of the slice energy spread in the drift space: comparison with the theoretical model [13].

CONCLUSION

IBS simulations for the E-XFEL injector allow to draw a number of conclusions. The simulations show that the impact of IBS is substantial leading to a nearly doubling of the SES. Theoretical IBS models may not properly describe the SES growth in the injector. The variation of SES in this section depends strongly on space-charge effects. Thus, care must be taken in experimental studies, since SES is not a conserved quantity but rather it depends on where and how it is measured. The simulations including IBS effects predict a (central slice) SES of roughly 2 keV for the E-XFEL injector. This figure is still smaller than the measured value of nearly 6 keV reported in [3]. This indicates that other important factors may contribute to SES growth. These include the emission process and the wakefields in the electron gun. Last but not least, it has been demonstrated that IBS effects can be consistently incorporated in space-charge tracking simulations of the injector. The application of this approach for start-to-end simulations of a complete FEL beam line is closely within reach.

REFERENCES

[1] S. Di Mitri *et al.*, "Experimental evidence of intrabeam scattering in a free-electron laser driver", *New J. Phys.*, vol. 22, p. 083053, 2020. doi:10.1088/1367-2630/aba572

[2] D. Bazyl, Y. Chen, M. Dohlus, and T. Limberg, "CW Operation of the European XFEL: SC-Gun Injector Optimization, S2E Calculations and SASE Performance", DESY Report DESY-21-138, doi:10.48550/arXiv.2111.01756

[3] S. Tomin, I. Zagorodnov, W. Decking, N. Golubeva, and M. Scholz, "Accurate measurement of uncorrelated energy spread in electron beam", *Phys. Rev. Accel. Beams*, vol. 24, p. 064201, 2021. doi:10.1103/PhysRevAccelBeams.24.064201

[4] E. Prat, E. Ferrari, S. Reiche, and T. Schietinger, "High resolution dispersion-based measurement of the electron beam energy spread", *Phys. Rev. Accel. Beams*, vol. 23, p. 090701, 2020. doi:10.1103/PhysRevAccelBeams.23.090701

[5] T. Takizuka and H. Abe, "A binary collision model for plasma simulation with a particle code", *J. Comput. Phys.*, vol. 25, pp. 205-219, 1977. doi:10.1016/0021-9991(77)90099-7

[6] K. Nanbu, "Theory of cumulative small-angle collisions in plasmas", *Phys. Rev. E* vol. 55, p. 4642, 1997. doi:10.1103/PhysRevE.55.4642

[7] S. A. Schmid, H. De Gersem, M. Dohlus, and E. Gjonaj, "Simulating Space Charge Dominated Beam Dynamics Using FMM", in *Proc. NAPAC'19*, Lansing, MI, USA, Sep. 2019, pp. 909–911. doi:10.18429/JACoW-NAPAC2019-WEPLE10

[8] D. T. Abell, P. J. Mullowney, K. Paul, J. Qiang, V. H. Ranjbar, and R. D. Ryne, "Three-Dimensional Integrated Green Functions for the Poisson Equation", in *Proc. PAC'07*, Albuquerque, NM, USA, Jun. 2007, paper THPAS015, pp. 3546–3548.

[9] J.D. Jackson, Classical electrodynamics, Wiley, New York, NY, 3rd edition, 1999.

[10] G. J. Pert, "Inverse bremsstrahlung in strong radiation fields at low temperatures", *Phys. Rev. E*, vol. 51, p. 4778, 2008. doi:10.1103/PhysRevE.51.4778

[11] K. Floettmann, https://www.desy.de/~mpyflo/Astra_manual/Astra-Manual_V3.2.pdf.

ISBN: 978-3-95450-220-2 ISSN: 2673-5474 doi: 10.18429/JACoW-FEL2022-WEP14

[12] G. Stupakov, and Z. Huang, "Space charge effect in an accelerated beam", *Phys. Rev. Accel. Beams*, vol. 11, p. 014401, 2008. `doi:10.1103/PhysRevSTAB.11.014401`

[13] K. Bane, "An Accurate, Simplified Model of Intrabeam Scattering", SLAC Report SLAC-AP-141, May 2002, `doi:10.48550/arXiv.physics/0205058`.

ISBN: 978-3-95450-220-2 ISSN: 2673-5474 doi: 10.18429/JACoW-FEL2022-WEP15

PROTECTION OF THE EUROPEAN XFEL UNDULATORS FROM THE ADDITIONAL BEAM LOSSES CAUSED BY THE INSERTION OF A SLOTTED FOIL

A. Potter, A. Wolski, University of Liverpool, Liverpool, UK
F. Jackson, STFC/ASTeC, Daresbury Laboratory, Daresbury, UK
S. Liu, DESY, Hamburg, Germany

Abstract

The European XFEL undulators are made of permanent magnets that need to be protected from beam losses that could cause demagnetisation. Under current operating conditions, beam losses in the undulators are prevented by a collimation section downstream of the main linac. In the future, a slotted foil may be installed in the European XFEL to reduce the X-ray pulse length; however, particles scattered by the foil could lead to significant radiation dose rates in the undulators. In this paper, we report a study to assess the level of the beam losses in the European XFEL undulators that would be caused by a slotted foil, and to determine the optimal apertures to use in the collimators to minimise the losses. We also assess whether shielding or an additional collimator in front of the undulator could help to reduce the losses.

INTRODUCTION

A potential way of reducing the X-ray pulse length at the European XFEL is to insert a slotted foil in a bunch compressor [1] to scatter electrons at the head and tail of each bunch so that they are either lost downstream of the foil or do not contribute to the lasing process in the SASE sections. Simulations of the electron transport from the slotted foil to the SASE section showed that particles scattered by the slotted foil would cause some radiation dose in the undulator magnets [2].

Beam loss in the undulators at the European XFEL is a problem that has been observed previously. The beamline contains a diagnostic undulator that allows monitoring of radiation dose rates, which can be correlated with demagnetisation of the undulator. To prevent the demagnetisation of the undulators in the SASE section, a total dose limit of 55 Gy over the 10-year lifetime of the undulators was set [3].

An estimate of the dose rates from simulations suggested that if a slotted foil was used to reduce the X-ray pulse length, the 55 Gy dose limit would be quickly exceeded [2]. The simulations showed that some particles scattered by the slotted foil would interact with the collimators downstream of the linac. Particles scraping the surface of a collimator could be further scattered rather than absorbed, and could then perform large betatron oscillations as they continued along the beamline. These particles would generally be lost at a section of the beamline close to the entrance of the SASE section where there is a reduction in the beam-pipe aperture. Particles lost in this way would create a shower of secondary

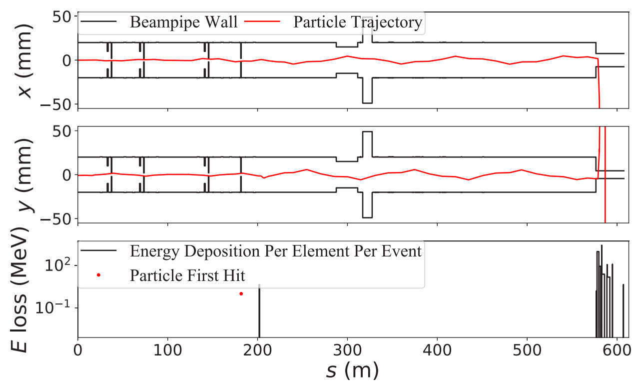

Figure 1: Top and middle plots: trajectory of a particle scattered by a collimator. The particle travels along the following beamline section at large betatron amplitude, before being lost at an aperture reduction near the undulators. Bottom plot: energy deposition by the primary (scattered) particle and by the secondary particles created by the loss of the primary particle.

particles travelling outside the beam-pipe that could be absorbed by the diagnostic undulator and by the first sections of the SASE undulator [2]. Figure 1 shows (in simulation) the trajectory of a primary particle that demonstrates this behaviour. Also shown in the figure is the energy deposited at different locations by this particle or by the secondary particles that it generates. It can be seen that the initial interaction of the primary particle with a beamline component is at the end of the collimation section, and that this results in the loss of the particle at the beam-pipe aperture reduction. The loss of the particle is followed by further energy deposition from a shower of secondary particles.

The study reported here aims to explore ways to reduce the dose caused by a slotted foil to an acceptable level. Two options have been considered. The first is to add shielding after the vacuum chamber transition (where there is a significant reduction in beampipe aperture) to absorb secondary particles generated by the loss of primary beam particles. The second option is to install a collimator upstream of the vacuum chamber transition to absorb primary beam particles that have a high betatron amplitude (as in the example in Fig. 1). Different options and configurations need careful study, because with any components installed to absorb particles there is the risk of creating further particle showers which could increase, rather than reduce the absorbed dose.

ISBN: 978-3-95450-220-2 ISSN: 2673-5474 doi: 10.18429/JACoW-FEL2022-WEP15

SIMULATIONS

Simulations were carried out with BDSIM [4]. In addition to particle tracking, BDSIM can model the interaction, including generation of secondaries, between particles and components along the beamline. For this study, particles were tracked from just upstream of the slotted foil to a point part way through the undulator (including several undulator modules). In each tracking run, 200,000 electrons were tracked, with initial 6D phase space coordinates provided from start to end simulations using XTrack [5]. The European XFEL has a designated collimation section containing four main collimators to intercept primary particles, and three supplementary collimators to absorb secondary particles. Each of the main collimators has four available fixed circular apertures (of 4, 6, 8 and 20 mm diameter) [6]. In previous simulations of the slotted foil scheme [2], it was found that beam losses in the undulator did not simply decrease as collimator apertures were reduced: losses are caused by particles "grazing" the edges of the apertures, and smaller apertures approach nearer the core of the beam, where the particle density is higher and such grazing interactions are more likely. Thus, intermediate diameter apertures give the lowest undulator losses.

For studies of beam losses in the undulators, each undulator module is split into many volume elements. The total energy deposited by all particles (primary and secondary) in each volume element is recorded, and the results then used to estimate the dose rate in each undulator module. Scattering and generation of secondaries are modelled using Monte Carlo techniques. Due to the limited number of particles in the initial phase space distribution (200,000) and the fact that events that can cause losses in the undulator are rather rare, tracking runs are performed 100 times for each configuration that needs to be considered. Results are then aggregated to allow some statistical analysis.

The additional shielding considered for this study was placed between the diagnostic undulator and the first SASE module. Some preliminary simulations were performed with the shielding in other locations, and although there was a large variation in the results, it was found that the shielding was not effective for protecting the SASE modules if it was installed upstream of the diagnostic undulator. As the diagnostic undulator does not contribute to the SASE output of the machine, it was decided to place the shielding after this undulator, so that modules contributing to the SASE process would be protected. The shielding (made of lead) had a length of 500 mm, and had the same transverse dimensions as the undulators it was intended to protect.

Since the charge tracked in the simulation was much lower than the charge of a single bunch at the European XFEL, a scaling factor was used to convert the energy deposited in the undulators in the simulation into an estimate of the energy that would be deposited in a corresponding configuration in actual operation. Depending on the random seed, in a single tracking run there may be no energy deposited in the undulator at all, or the energy may be deposited in different volume elements. Therefore, it would not be appropriate simply to apply a linear scaling of the total energy deposited in an entire undulator module from one simulation up to the charge of the European XFEL. Instead, the mean energy deposition over 100 random seeds was calculated for each volume element; the mean energy deposition (for each volume element) was then scaled to match the XFEL bunch charge. Projections (onto different cross-sections of an undulator module) of the average energy deposition over 100 random seeds are shown in Fig. 2.

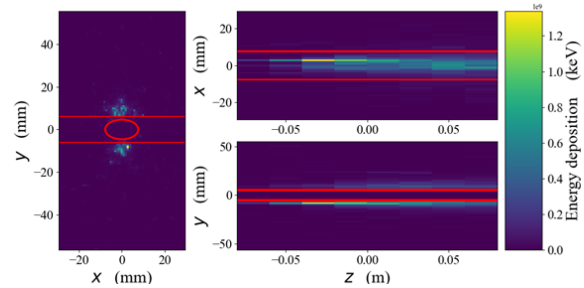

Figure 2: Projections of the mean energy deposition in volume elements in an undulator module over 100 simulations. The collimator aperture in this example was 4 mm; no shielding or additional collimation was included. Left: projection onto the transverse plane. Right: projections onto the x–z (top) and y–z (bottom) planes, with z the longitudinal coordinate.

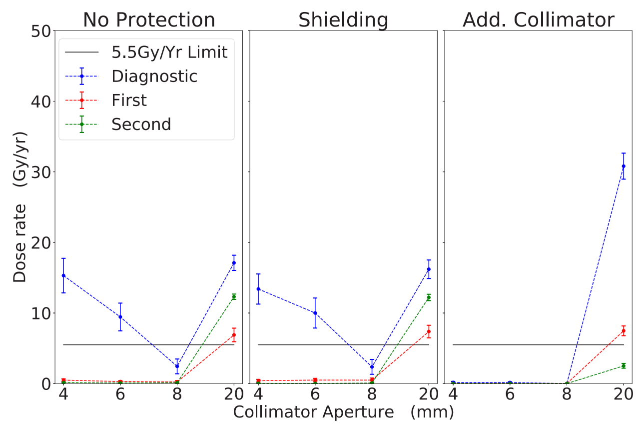

Figure 3: Dose rates in the diagnostic undulator (blue points and lines), and first and second modules (red and green points and lines, respectively) of the SASE undulator without additional protection (left), with shielding (middle) or with additional collimation (right).

RESULTS AND DISCUSSION

Dose rates found from simulations with different collimator apertures and shielding/collimation configurations are shown in Table 1. Values given for the dose rate refer to the volume element that received the largest dose over 100 simulations. The results are also shown in Fig. 3.

ISBN: 978-3-95450-220-2 ISSN: 2673-5474 doi: 10.18429/JACoW-FEL2022-WEP15

Table 1: Dose rates in the volume element with maximum energy deposition in the diagnostic undulator, and in the first and second SASE undulator modules, without protection, with shielding, and with an additional collimator. Also shown is the fraction of random seeds in each configuration for which there was no energy deposition in the undulators. Values are obtained by combining the results from 100 tracking runs, scaled to the European XFEL beam intensity (27,000 bunches per second, with 250 pC bunch charge).

		Diagnostic undulator		First SASE module		Second SASE module	
Collimator aperture	**Protection method**	**Dose rate (Gy/Yr)**	**% seeds with (no dose)**	**Dose rate (Gy/Yr)**	**% seeds with (no dose)**	**Dose rate (Gy/Yr)**	**% seeds with (no dose)**
4mm	No Protection	15.3	45	0.490	78	0.134	85
	Shielding	13.4	44	0.402	85	0.0339	95
	Add. Collimator	0.155	98	0.00	100	0.000213	99
6mm	No Protection	9.44	63	0.284	89	0.0792	95
	Shielding	10.0	63	0.498	88	0.0141	96
	Add. Collimator	0.149	98	0.00	100	0.00375	99
8mm	No Protection	2.44	88	0.232	94	0.119	95
	Shielding	2.36	88	0.493	95	0.0746	98
	Add. Collimator	0.00	100	0.00	100	0.00	100
20mm	No Protection	17.1	0	6.89	1	0.119	0
	Shielding	16.2	0	7.38	4	12.2	0
	Add. Collimator	30.8	0	7.48	0	2.51	3

Note that the dose in a single tracking run is caused by just a small number of macroparticles, even in cases with a relatively large energy deposition. This leads to large fluctuations in the energy deposition in individual volume elements between different runs, and to a significant number of seeds in many configurations, in which there is no energy deposition at all. For this reason the values in Table 1 are based on combining results from 100 tracking runs in each case.

It is also worth noting that uncertainties in the simulation results arise for a number of different reasons. For example, the simulations do not include a fully complete and detailed model of the beamline geometry and components in all sections, which could impact the dose received by the undulators in different configurations. Also, machine errors, such as steering and focusing errors, have not been included, but could affect particle losses. Finally, it should be mentioned that comparisons of simulated radiation loads along the machine using a screen in place of the foil show some differences with measurements under corresponding conditions [7], although the results of the simulations have been shown to be a good indication of the dose rates that may be expected.

The lowest dose in the diagnostic undulator is achieved using a main collimator aperture of 8 mm: this is in agreement with previous simulation results [2]. Without any additional protection, the dose rate in the SASE undulator modules in some cases comes close to or exceeds the specified limit of 5.5 Gy/yr. Use of an additional collimator appears to be more effective than the inclusion of extra shielding in reducing the dose in the undulators. The additional collimator used in the simulations has already been proposed as additional protection in connection with the installation of a dechirper (wakefield structure), as part of an alternative method for producing short X-ray pulses at the European XFEL [8]: thus, this solution has the additional benefit of not requiring extra cost or effort. In some cases for the main collimator aperture, the shielding actually increases the undulator dose: this may be because of the location of the shielding within the undulator section, which could result in scattering and production of secondary particles close to the undulators. Taking into account some level of uncertainty in the simulation results, installation of shielding close to the undulators appears inadvisable.

With a main collimator aperture of 20 mm, the undulator dose rates are still high, even with the extra protection of an additional collimator. This emphasises the importance of the main (existing) collimation section in the European XFEL. The main collimators make a major contribution to the protection of the undulators in the slotted foil scheme, and although the extra protection from an additional collimator is important, it cannot substitute on its own for the main collimators.

In addition to the main collimation section downstream of the main linac, the European XFEL currently has collimators installed in the bunch compressors. In this study, the collimators in the bunch compressors were not used (i.e. were left fully open); however, the collimator in BC2 downstream of the slotted foil could potentially be used to provide some additional protection, and this could be investigated in the future.

REFERENCES

[1] P. Emma *et al.*, "Femtosecond and Subfemtosecond X-Ray Pulses from a Self-Amplified Spontaneous-Emission–Based

ISBN: 978-3-95450-220-2 ISSN: 2673-5474 doi: 10.18429/JACoW-FEL2022-WEP15

Free-Electron Laser," *Phys. Rev. Lett.*, vol. 92, p. 074 801, 2004. doi:10.1103/PhysRevLett.92.074801

[2] A. Potter, A. Wolski, *et al.*, "Studies of particle losses from the beam in the EU-XFEL following scattering by a slotted foil," *Energy*, vol. 10, no. 2, p. 100, 2021.

[3] F. Wolff-Fabris, J. Pflueger, F. Schmidt-Föhre, and F. Hellberg, "Status of radiation damage on the European XFEL undulator systems," *J. Phys.: Conf. Ser.*, vol. 1067, no. 3, p. 032 025, 2018. doi:10.1088/1742-6596/1067/3/032025

[4] L. Nevay *et al.*, "BDSIM: An accelerator tracking code with particle–matter interactions," *Comput. Phys. Commun.*, vol. 252, p. 107 200, 2020. doi:10.1016/j.cpc.2020.107200

[5] M. Dohlus, *Xtrack*, 2015. https://www.desy.de/xfel-beam/s2e/talks/2015_05_18/about_Xtrack.pdf

[6] V. Balandin, R. Brinkmann, W. Decking, and N. Golubeva, "Optics Solution for the XFEL Post-Linac Collimation Section," DESY, Hamburg, Germany, TESLA-FEL Report 2007-05, Tech. Rep., 2007.

[7] A. Potter *et al.*, "Investigation of the beam losses and radiation loads for the implementation of a slotted foil in the European XFEL," presented at the 40th International Free Electron Laser Conference (FEL'22), Trieste, Italy, Aug. 2022, paper WEP16, this conference.

[8] J. Guo *et al.*, "Beam loss study for the implementation of corrugated structure at the European XFEL," *Nucl. Instrum. Methods Phys. Res., Sect. A*, vol. 1034, p. 166 780, 2022. doi:10.1016/j.nima.2022.166780

ISBN: 978-3-95450-220-2 ISSN: 2673-5474 doi: 10.18429/JACoW-FEL2022-WEP16

INVESTIGATION OF BEAM LOSSES AND RADIATION LOADS FOR THE IMPLEMENTATION OF A SLOTTED FOIL AT THE EUROPEAN XFEL

A. Potter, A. Wolski, University of Liverpool, Liverpool, UK
F. Jackson, STFC/ASTeC, Daresbury Laboratory, Daresbury, UK
B. Beutner, J. Branlard, A. Dehne, S. Liu, N. Walker, DESY, Hamburg, Germany

Abstract

Ultra-short X-ray pulses in an X-ray FEL can be generated by means of a slotted foil inserted into a bunch compressor. There is an ongoing study into whether such a technique could be used at the European XFEL. One important factor that must be considered is whether the additional beam losses and radiation loads caused by the foil are acceptable with a normal operating beam power up to 500 kW. As there is currently no foil installed at the European XFEL, experimental investigations were carried out by inserting a screen in the bunch compressor at the location where a foil would be inserted. Neutron radiation measurements have been compared with simulations using BDSIM to provide validation and calibration of simulations for the case of a slotted foil and also to provide an approximate limit of the number of bunches that should be allowed through the foil to avoid radiation damage.

INTRODUCTION

One of the techniques currently being investigated for producing ultra-short X-ray pulses at the European XFEL is based on the use of a silicon slotted foil in a bunch compressor [1]. The correlation between the transverse and longitudinal position of particles in a bunch in the compressor leads to the scattering of particles by the foil and consequent degradation of the emittance at the head and tail of the bunch. Particles at the centre of the bunch pass through a slot in the foil, and are not scattered. The short section of the bunch where the emittance is preserved will lase as normal in the undulator sections, while the scattered particles will either be lost along the beamline, or will not contribute to lasing.

This study focuses on the particles that are lost along the beamline as a result of use of a slotted foil. Losses can be a problem at the European XFEL because of the high beam power. Previous studies have estimated the effect of a slotted foil for short-pulse generation on heat loads in the collimators [2], and on radiation loads in the undulators [3]. However, radiation resulting from beam losses can affect various accelerator systems and components over the length of the machine, including electronics in the control systems and diagnostics. Losses in European XFEL are routinely monitored using fixed beam loss monitors (BLMs), but losses can also be measured using MARWIN [4], a robot that can move along the beamline tunnel parallel to the machine. MARWIN is equipped with a radiation monitor (LB6419 [5]), and can provide neutron and gamma radiation dose rate as a function of longitudinal position along the accelerator. At the European XFEL, the BLMs are not calibrated, and they are set to different gains empirically [6]. Also, the insertion of a foil would cause many losses meaning that many of the BLM reading are saturated. For these reasons, the data from MARWIN is better suited for this study.

Currently, there is no slotted foil installed at the European XFEL, so direct measurements of losses caused by the foil cannot be made. It is planned to install the foil at a screen station in the second of three bunch compressors. To reproduce as closely as possible the scattering effects of the foil, we can insert the screen at this location into the beam. Simulations have been performed of the losses caused by the screen and the losses from a slotted foil. Results of simulations in the case of the screen can be compared with the experimental measurements made using MARWIN, to validate and calibrate the simulations. The simulations in the case of the foil can then be used to determine parameter regimes that will allow beam losses and radiation loads to be maintained within safe limits during short-pulse operation.

SIMULATIONS

Simulations were performed using BDSIM [7], a tracking code with the capability to model a range of interactions between beam particles and the beamline components, including the production of secondary particles. For this study, simulations included all electromagnetic and hadronic interactions. A model of the beamline was constructed starting from the first dipole in the bunch compressor (BC1) where the foil would be inserted, through a collimation section (CL) where many losses are expected to occur, and ending at the entrance of one of the undulator beamlines (SASE1). The layout is shown in Fig. 1.

In the first simulation, the beam was tracked with a slotted foil inserted in BC1. The energy deposited per metre of beamline was recorded, and the simulation repeated 10 times. Although the same initial distribution of particles was used for the beam, the random nature of the scattering processes leads to some variation in the energy deposited in the beamline. The mean energy deposition per metre was calculated. The full simulation was repeated with a screen inserted instead of the foil.

The mean energy deposition per tracking run was scaled up to match the bunch charge (250 pC) normally used in operation and converted to a radiation power load by multiplying by the bunch repetition rate. The bunch repetition rate is variable, but for the experimental measurements of the effects of the screen on the dose rates, a bunch rate of 10 Hz was used (limited by the setup of the machine protection system with a screen inserted in the beamline). The simulation

ISBN: 978-3-95450-220-2 ISSN: 2673-5474 doi: 10.18429/JACoW-FEL2022-WEP16

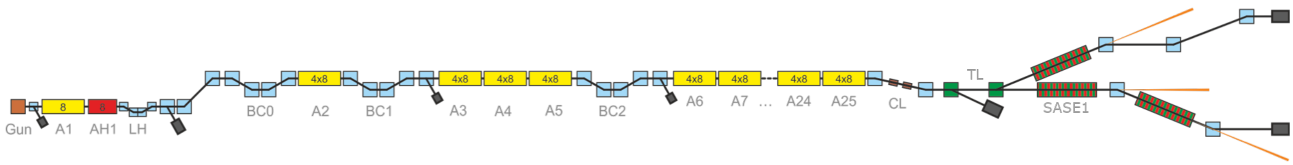

Figure 1: Layout of the European XFEL. In simulations, particles were tracked from the start of BC1 to the start of SASE1. The screen station (where the slotted foil will also be located) is in bunch compressor 1.

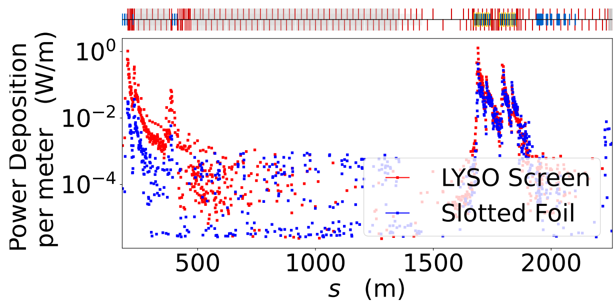

Figure 2: The power deposition per meter caused by the insertion of a slotted foil (blue) and a LYSO screen (red) from BC1 (at s =181 m) to the SASE1 undulator entrance.

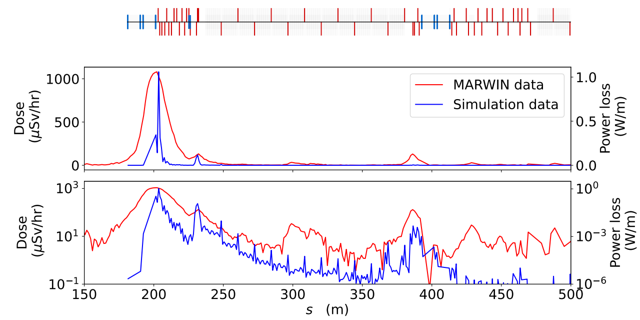

Figure 3: Comparison between the simulation of the energy deposition and measurements of the neutron flux from BC1 to L3 at the European XFEL when a screen is inserted in BC1 on a linear axis (top) and a logarithmic axis (bottom).

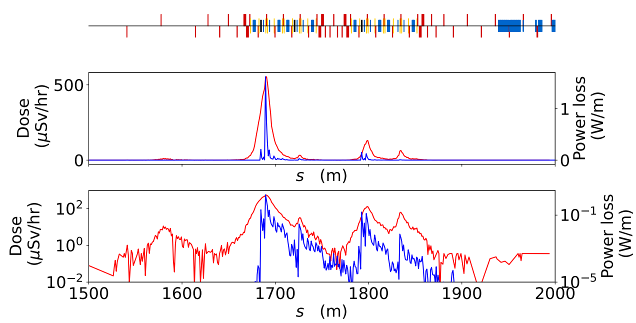

Figure 4: Comparison between the simulation of the energy deposition and measurements of the neutron flux from CL to TL at the European XFEL when a screen is inserted in BC1 on a linear axis (top) and a logarithmic axis (bottom).

results, scaled to match the operational parameters during the experiments, are shown in Fig. 2.

The simulation results show significant losses directly after the foil/screen location and in the collimation section, both for the case of the foil and for the screen. Although the losses in BC1 are much lower for the foil than for the screen, in the collimation section the losses are comparable. This is a result of the different thicknesses of the foil and the screen: the screen is much thicker than the foil so particles are scattered more strongly, leading to higher losses in BC1. By the time the beam reaches the collimation section, many of the particles scattered by the screen have already been lost, whereas many of the particles scattered by the foil reach the collimators.

RADIATION MEASUREMENTS

Four measurement runs were made using MARWIN: with and without the screen, from BC1 to L3 and from CL to the transfer line between the collimator section and the switchyard (TL). Measurements in the different sections were made on separate days because of the limited time available for experimental studies. The radiation readings without the screen were subtracted from those made with the screen, in order to remove background radiation, and to leave just the contribution from the screen.

COMPARISONS

It is worth mentioning that the simulation models the energy deposited into beamline components, whereas the measurements recorded the number of neutrons detected some distance from the components. As a result, it is not possible to compare the simulation results directly with the measurements. The same simulation was used to count the number of neutrons produced in each meter of beamline. The results show variation in neutron dose rate with a similar variation along the beamline as the power deposition shown in Fig. 2; however, the simulations produce very low statistics, and consequently large uncertainties, so the neutron dose rates found from simulation are not presented here. Instead, we compare the simulated energy deposition with the dose measurements: it is expected that peaks in the radiation dose measurements will occur at the same longitudinal positions as peaks in the simulated energy deposition, and that the largest peaks in the measurements will occur where the simulated energy deposition is highest because neutrons are generated by high energy electron/gamma rays.

It can be seen in Figs. 3 and 4 that the major peaks in both the simulations and the measurements occur at the same

ISBN: 978-3-95450-220-2 ISSN: 2673-5474 doi: 10.18429/JACoW-FEL2022-WEP16

longitudinal positions. Also, the relative sizes of the peaks are the same. However, there is some variation in the ratio of the size of each peak in the measurement to the size of the corresponding peak in the simulation. The peaks in the neutron dose rate measurements by MARWIN are wider than the peaks in the power deposition in the simulations. This is due to the direction that a neutron travels between its production (caused by some energy deposition) and it being detected by MARWIN.

The two largest peaks are the ones that need to be considered when deciding operational limits for operation with the slotted foil. The peak in the first bunch compressor (just after the foil/screen at $s = 204$ m) we refer to as Peak 1; the other, at the first main collimator in the collimation section (at $s = 1690$ m) we refer to as Peak 2.

Since the experimental measurements were made with a screen rather than a slotted foil, the results need to be scaled to provide estimates of the dose rate that would result from insertion of a foil. The scaling factor can be determined from the simulations of the two cases (screen inserted, and slotted foil inserted). More specifically, for each of the peaks mentioned above (Peak 1 and Peak 2) we divide the peak power deposition from simulation with the slotted foil, by the peak power deposition from simulation with the screen. The dose measured at these locations with MARWIN is multiplied by the resulting scaling factor, to give the dose that would be measured with the slotted foil inserted in place of the screen, with the same beam conditions. Finally, the dose can be scaled by a chosen bunch rate to predict the dose that would be seen with the slotted foil under different operational beam conditions.

At Peak 1, the simulation predicted that the foil would produce 0.0881% of the radiation that would be produced with the screen. At this same peak, MARWIN measured a dose rate of 1080 µSv/h; therefore, we expect a dose rate at this location with the slotted foil of 0.951 µSv/h at a bunch rate of 10 Hz. The same calculation for Peak 2 suggests a dose rate at this location of 61 µSv/h at the same bunch rate. The dose rate expected at Peak 2 is much higher than that expected at Peak 1; therefore, this peak should be used to determine a limit on the bunch rate when operating the machine with a slotted foil.

Note that the prediction of the dose rate with the slotted foil, depends on two assumptions: first, that the dose measured by MARWIN is proportional to the power deposited in the beamline; and second, that the power deposited in the beamline is proportional to the bunch rate.

It was mentioned when discussing the radiation measurements (above) that a background measurement was taken with the beam running with bunch rate 10 Hz, but without the screen inserted. It was observed that under these conditions, the neutron dose rate (D_{BG}) at the collimator at 1690 m was 40 µSv/h. The additional dose (D_{foil}) expected from insertion of the foil is 61 µSv/h when running at the same bunch rate. Under normal operating conditions, the radiation dose in the collimator section is acceptable even when running at a maximum bunch rate (N_{max}) of 2700 bunches per bunch train, with 10 bunch trains per second. The number of bunches, N_{foil}, that would result in the same dose rate when operating with the foil is given by:

$$N_{\mathrm{foil}} = \frac{D_{\mathrm{BG}}}{D_{\mathrm{BG}} + D_{\mathrm{foil}}} \times N_{\mathrm{max}} \approx 1000\,\text{bunches/train} \qquad (1)$$

This method of calculating the maximum bunch rate when the foil is inserted assumes that the background measurement of 40 µSv/hr can be scaled with the bunch rate. However, this may not be the case if there is some contribution from dark current to this value. The maximum bunch rate with the foil inserted would be lower if there is a significant contribution from dark current to the background measurement.

CONCLUSION

The purpose of the first part of this study was to measure the radiation dose rates found using a neutron detector (MARWIN) when a screen was inserted in the beamline of European XFEL, and to use the measured data to validate simulations of the power deposition under similar conditions. Simulations were then used in combination with the data from MARWIN to calculate a limit on the bunch rate that could be achieved when operating with a slotted foil, before reaching the same radiation dose rates as under current operations with the maximum bunch rate.

With a screen inserted in the beamline, the dose rate measured by MARWIN and power deposition found from simulations showed peaks at the same longitudinal positions. It was concluded that the simulations can be used to predict the locations of peak radiation dose when a slotted foil is inserted, and to predict the size of these peaks.

With the slotted foil, the highest radiation dose rate is expected in the collimator section. With appropriate scaling of the simulation results and use of the MARWIN measurements, it is expected that the dose rate in this section can be kept within current limits by limiting the bunch rate to 1000 bunches/train, with 10 bunch trains per second.

REFERENCES

[1] P. Emma *et al.*, "Femtosecond and subfemtosecond x-ray pulses from a self-amplified spontaneous-emission–based free-electron laser," *Phys. Rev. Lett.*, vol. 92, p. 074 801, 7 2004. doi:10.1103/PhysRevLett.92.074801

[2] A. Potter, A. Wolski, S. Liu, and F. Jackson, "Heat load on the european xfel collimators from beam particles scattered by a slotted foil," Beschleunigerphysik, Tech. Rep., 2021. doi:10.3204/PUBDB-2021-05595

[3] A. Potter, W. Decking, F. Jackson, S. Liu, and A. Wolski, "Studies of Particle Losses From the Beam in the EU-XFEL Following Scattering by a Slotted Foil," in *Proc. IPAC'21*, Campinas, SP, Brazil, 2021, paper TUPAB125, pp. 1681–1684. doi:10.18429/JACoW-IPAC2021-TUPAB125

[4] A. Dehne, N. Moller, and T. Hermes, "Marwin: A mobile autonomous robot for maintenance and inspection in a 4d environment," in *2017 International Conference on Research and Education in Mechatronics (REM)*, 2017, pp. 1–5. doi:10.1109/REM.2017.8075228

ISBN: 978-3-95450-220-2 ISSN: 2673-5474 doi: 10.18429/JACoW-FEL2022-WEP16

[5] *Berthold technologies*, https://www.berthold.com/.

[6] T. Wamsat, T. Lensch, and P. Smirnov, "Status and Commissioning of the European XFEL Beam Loss Monitor System," in *Proc. 9th International Particle Accelerator Conference (IPAC'18)*, Vancouver, BC, Canada, April 29-May 4, 2018, pp. 1940–1943. doi:10.18429/JACoW-IPAC2018-WEPAF053

[7] L. Nevay *et al.*, "Bdsim: An accelerator tracking code with particle–matter interactions", *Comput. Phys. Commun.*, vol. 252, p. 107 200, 2020. doi:10.1016/j.cpc.2020.107200

ISBN: 978-3-95450-220-2 ISSN: 2673-5474 doi: 10.18429/JACoW-FEL2022-WEP17

FEASIBILITY OF SINGLE-SHOT MICROBUNCHING DIAGNOSTICS FOR A PRE-BUNCHED BEAM FOR TESSA AT 515 nm*

A. H. Lumpkin[1]†, Argonne Associate, Argonne National Laboratory, Lemont IL, USA
D.W. Rule, Silver Spring, Maryland, USA
P. Musumeci, UCLA, Los Angeles, USA
A. Murokh, RadiaBeam Technologies, Santa Monica, USA
[1]also affiliated at Fermi National Accelerator Laboratory, Batavia, USA

Abstract

The feasibility for microbunching diagnostics of the electron beam after co-propagating it and a high-power laser pulse through a short undulator (modulator) is discussed. This provides an energy modulation that can be converted to a periodic longitudinal density modulation (or microbunching) via the R_{56} term of a chicane. Coherent optical transition radiation (COTR) imaging techniques can be used for beam size, divergence, energy, spectral, alignment, and temporal characterizations on a single shot of this pre-bunched beam for a TESSA experiment at 515 nm.

INTRODUCTION

Co-propagating a relativistic electron beam and a high-power laser pulse through a short undulator (modulator) provides an energy modulation which can be converted to a periodic longitudinal density modulation (or microbunching) via the R_{56} term of a chicane. Such prebunching of a beam at the resonant wavelength and the harmonics of a subsequent free-electron laser (FEL) amplifier seeds the process and results in improved gain in a Tapering Enhanced Super-Radiant Stimulated Amplification (TESSA) experiment [1,2]. We describe potential characterizations of the resulting microbunched electron beams after the modulator using coherent optical transition radiation (COTR) imaging techniques for transverse size (50 µm), divergence (sub-mrad), trajectory angle (0.1 mrad), coherence factor, spectrum (few nm), and pulse length (ps). The transverse spatial alignment is provided with near-field imaging and the angular alignment is done with far-field imaging and two-foil COTR interferometry (COTRI). Analytical model results for a 515 nm wavelength COTRI case with a 10% microbunching fraction will be presented. COTR gains of 22 million were calculated for an initial charge of 1000 pC which enables splitting the optical signal for single-shot measurements of all the cited parameters.

EXPERIMENTAL ASPECTS

The TESSA-515 experiments are being staged at the Fermilab Accelerator Science and Technology (FAST) facility where the superconducting TESLA-type linac [3] will generate the driving beam for the FEL experiments. A schematic of the linac is shown in Fig. 1. Also shown are the photocathode rf gun, the two TESLA capture cavities operating at about 20 MV/m gradient, the chicane for bunch compression, the cryomodule (with eight, 9-cell cavities) and the high-energy transport line to the location of the FEL experiment. The nominal electron beam properties are given in Table 1, and the final energy of 220 MeV results in the generation of 515 nm radiation in the tapered undulator at the laser seed wavelength. An Amplitude Magma seed laser generating 5 mJ per pulse at 1030 nm will be used as a seed [4]. We will use the frequency-doubled component from the 10-mm thick beta-BBO crystal.

Past experiments on wakefield effects [5-7] in the cavities, which are correlated with their higher-order mode strength, motivated our instrumenting HOM detectors for all 10 cavities. In the single-bunch phase for the TESSA test, the short-range wakefields would be a concern so proper on-axis steering of the beam through the 10 cavities is warranted. In the oscillator configuration, the submacropulse centroid-slewing effects will also be critical to minimize.

Table 1: Electron Beam Parameters.

Parameter	Unit	Value
Charge	nC	0.5-1.0
Emittance	mm mrad	2-5
Gun energy	MeV	4.5
Beam energy	MeV	220

COTR FORMALISM

Microbunching of an electron beam, or a z-dependent density modulation with a period λ, can be generated by several mechanisms [8]. The laser-induced microbunching (LIM) occurs at the modulator resonant wavelength (and harmonics) as the e-beam micropulse co-propagates through the modulator with the seed laser beam. The energy modulation is converted to a longitudinal modulation by the chicane's small R_{56} term. This is a narrow-band effect. The modulator is a helical undulator with 10 periods 3.2-cm period length.

A microbunched beam will radiate coherently as an FEL or by interaction at a vacuum to metal screen interface as COTR. The first microbunching diagnostics station is located after the chicane as schematically shown in Fig. 2. A thin blocking foil for the seed laser also serves as the source of forward COTR, and this is followed 6.3 cm downstream

* Work supported by the U.S. Department of Energy, Office of Sci-ence, Office of Basic Energy Sciences, under Contract No. DE-AC02-06CH11357.
† lumpkin@anl.gov

ISBN: 978-3-95450-220-2 ISSN: 2673-5474 doi: 10.18429/JACoW-FEL2022-WEP17

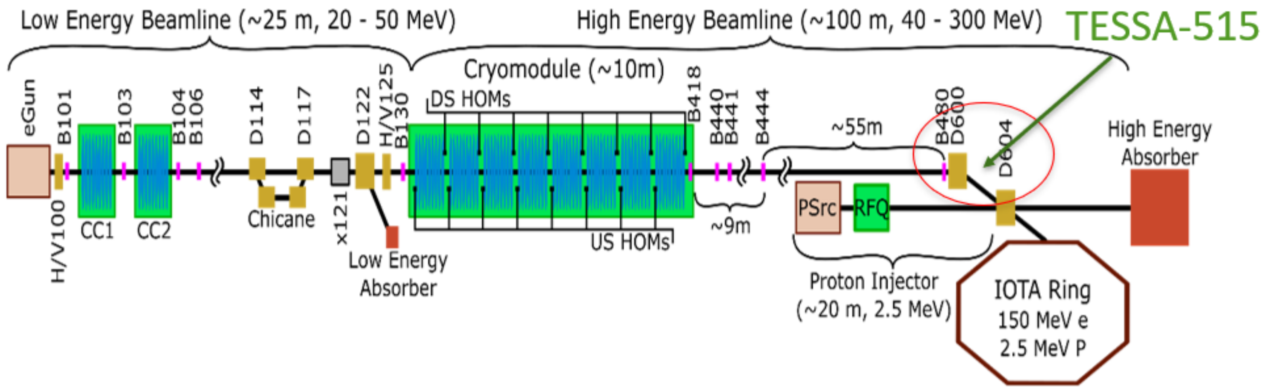

Figure 1: A schematic of the FAST linac with gun, capture cavities (CC1 and CC2), the chicane, cryomodule, high energy transport, and location of the proposed TESSA-515 nm experiment (see Fig. 2).

by a second foil at 45 degrees for backward COTR. The pair form a COTR interferometer.

Some background on the incoherent OTR and COTR methods is warranted. When a charged-particle beam enters and exits a foil, the induced currents generate backward and forward OTR, respectively, in cones of half-angle 1/γ around the specular reflection or beam direction [9-11]. Thus, the configuration after the dispersive section in Fig. 2 generates OTR at 90º to the beam direction, enabling minimally invasive OTR characterization. The number W_1 of OTR photons that a single electron generates per unit frequency ω per unit solid angle Ω in a single foil is

$$\frac{d^2W_1}{d\omega d\Omega} = \frac{e^2}{\hbar c}\frac{1}{\pi^2\omega}\frac{\left(\theta_x^2+\theta_y^2\right)}{\left(\gamma^{-2}+\theta_x^2+\theta_y^2\right)^2} \qquad (1)$$

where $\hbar$ is Planck's constant/2π, e is electron charge, c is the speed of light, and θ_x and θ_y are radiation angles [12].

This angular distribution pattern has both energy and divergence information. After convolving Eq. (1) with Gaussian distributions representing beam divergences, the solid black curve in Fig. 3 shows the angular distribution of OTR at λ = 515 ± 5 nm that a 220 MeV, N-electron bunch with divergence $\sigma_{x\prime} = \sigma_{y\prime} \equiv \pi r^2\sigma_\theta = 0.1$ mrad generates in one foil. There is one peak at divergence $\theta \equiv \theta_x = \theta_y = 1/\gamma \sim 2.2$ mrad. When N_B of the N particles are microbunched, a coherence function $\boldsymbol{J(k)}$ becomes involved, and for two foils an interference function $\boldsymbol{I(k)}$. The spectral angular distribution function then becomes:

$$\frac{d^2W}{d\omega d\Omega} = |r_{\parallel,\perp}|^2\,\frac{d^2W_1}{d\omega d\Omega}\left[N\,\boldsymbol{I}(\boldsymbol{k}) + N_B(N_B-1)\boldsymbol{J}(\boldsymbol{k})\right] \qquad (2)$$

where $|r_{\parallel,\perp}|^2$ is the reflectance of the second (Al) foil for parallel, perpendicular polarization components, respectively. I(k) is [13]

$$\boldsymbol{I}(\boldsymbol{k}) = 4\sin^2[\tfrac{kL}{4}\left(\gamma^{-2}+\theta_x^2+\theta_y^2\right)] \qquad (3)$$

where $k = |\boldsymbol{k}| = 2\pi/\lambda$, using a small-angle approximation. Peaks of $\boldsymbol{I(k)}$ occur at angles $\theta_x^2 + \theta_y^2 = (2\lambda/L)(p - p_0)$, where p = 1/2, 3/2, ..., and $p_0 = L/(2\lambda\gamma^2)$. Adjacent peaks are separated by $\Delta(\theta_x^2 + \theta_y^2) = 2\lambda/L$. Choosing L = 6.3 cm results in p_0 = 0.3 which allows for significant fringe sensitivity to beam energy and divergence. The dashed red curve in Fig. 3 shows the two-foil OTR angular distribution for L = 6.3 cm, with λ, γ, and σ_θ as for the black curve. Now there are multiple fringes.

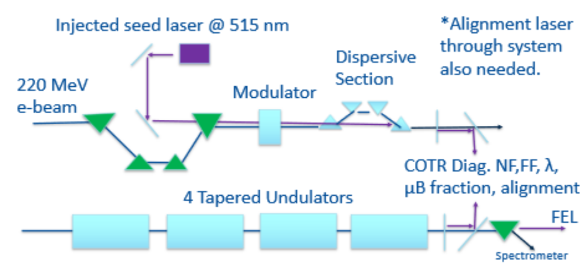

Figure 2: Schematic of the prebuncher, microbunching diagnostics locations, and the TESSA amplifier undulators.

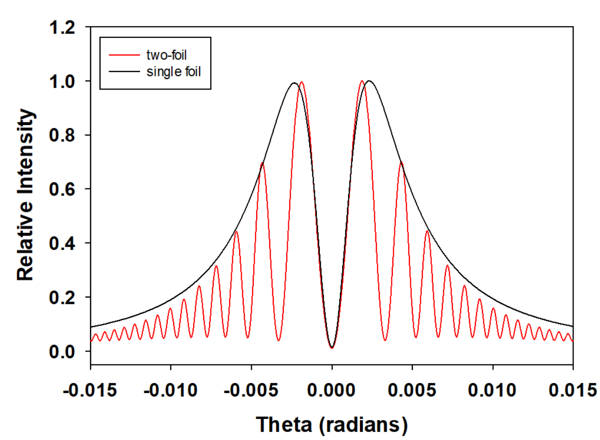

Figure 3: Calculated angular distribution patterns for incoherent OTR from a single foil (black) and a two-foil configuration (red) with L= 6.3 cm, λ=515 nm, and a 220 MeV electron beam energy.

The coherence function was defined previously for the beam sizes assuming Gaussian spatial distributions at each source point with a drift between them [14]. At the larger

40th International Free Electron Laser Conference,Trieste JACoW Publishing
ISBN: 978-3-95450-220-2 ISSN: 2673-5474 doi: 10.18429/JACoW-FEL2022-WEP17

beam sizes and small divergences, the potential transverse size growth in the drift is a negligible effect in the present case. However, for completeness we present this aspect. The coherence function can be defined as

$$\boldsymbol{J}(\boldsymbol{k}) = \left[H_1(\boldsymbol{k}) - H_2(\boldsymbol{k})\right]^2 + H_1(\boldsymbol{k})H_2(\boldsymbol{k})\boldsymbol{I}(\boldsymbol{k}) \quad (4)$$

where $H_j(\boldsymbol{k}) = \rho_j(\boldsymbol{k})/Q = g_j(k_x)g_j(k_y)F(k_z)$ for an *e*-bunch of charge distribution $\rho_j(\boldsymbol{x})$ and total charge Q, with j = 1, 2. Here we have introduced two microbunch form factors, H_1 and H_2, to account for the increase in bunch radius from the first to the second interferometer foil due to beam divergence. Each $H_j(\boldsymbol{k})$ is a product of Fourier transforms $g_j(k_i)=exp(-\sigma_i^2k_i^2/2)$ of transverse ($i=x,y$) charge form factors (with $k_i \approx k\theta_i$), and of longitudinal form factor $F_z(k_z) = \exp(-\sigma_z^2k_z^2/2)$, with $k_z \sim k$ and $\theta << 1$, assuming the Fourier transform $\rho_j(\boldsymbol{k})$ of $\rho_j(\boldsymbol{x})$ is separable. If $\boldsymbol{J}(\boldsymbol{k}) << 1$ or $N_B \to 0$, only the incoherent OTR term (~N) remains in Eq. (2).

COTRI MODEL RESULTS

An example of the COTRI model results is shown in Fig. 4. For an initial beam size of 5 µm at foil 1, the sensitivity to beam divergence for 3 steps from 0.1 mrad to 0.7 mrad is clear in the variation in the modulation of the fringes. The lowest divergence has the deepest minimum.

The transverse beam size also directly determines the coherence factor as a function of theta [15]. In this case, beam sizes from 5 to 100 µm are considered in Fig. 5. The maximum gain of 22 million is calculated for the 5-µm case at small angles and 1000 pC with a 10% microbunching fraction. The roll off of the COTR gain with increasing theta is particularly severe for the 50- and 100-µm cases. Only the first lobes near ± 1/γ are enhanced as seen in Fig. 6 for the green and dashed black curves, respectively, and their peak positions and shapes are altered compared to the others.

Due to the high gains seen in Fig. 5, the splitting of the COTR to acquire in a single-shot the near-field imaging, far-field imaging, optical spectral content, pulse length, and energy is feasible as shown in Fig. 7.

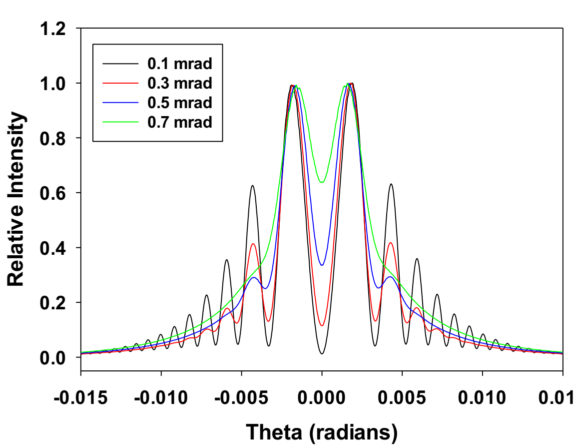

Figure 4: Calculated COTRI profiles for four divergences for a beam size of 5 µm at foil 1 and λ=515 nm.

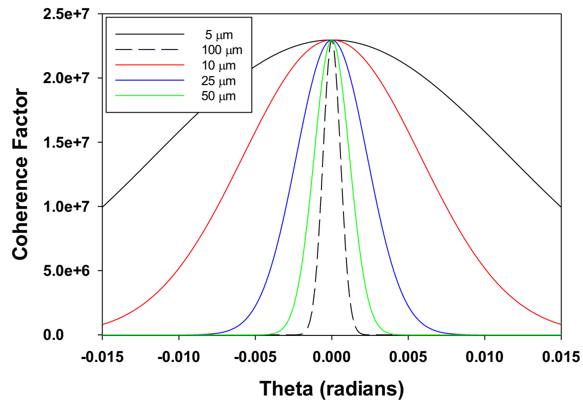

Figure 5: Calculations of the effect of beam size on the coherence function for 10% microbunching and a charge of 1000 pC.

The determination of the COTR gain versus OTR from the images can provide the bunching fraction estimates. The NF and FF COTR images also provide critical information about the alignment of the seed laser pulse and the electron beam in x, θ_x, y, θ_y, and z where image symmetry and overall COTR intensity are key tuning aids.

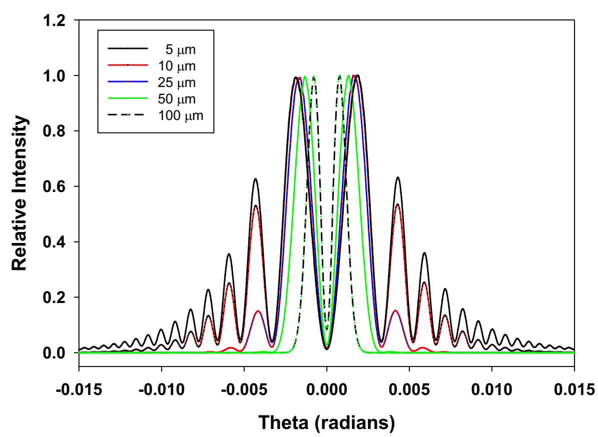

Figure 6: Calculations of the effect of beam size on the number of strongly enhanced COTRI fringes (I_{tot}) using a divergence of 0.1 mrad with L= 6.3 cm, λ=515 nm, and a 220-MeV electron beam energy.

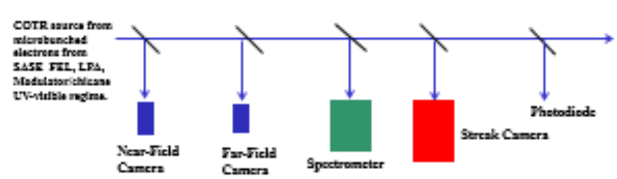

Figure 7: Schematic of single-shot COTR diagnostics for beam size, divergence, spectrum, bunch length, and radiated energy.

ISBN: 978-3-95450-220-2 ISSN: 2673-5474 doi: 10.18429/JACoW-FEL2022-WEP17

SUMMARY

In summary, the microbunching of the electron beam in the prebuncher (modulator plus dispersive element) will result in strong emissions at the 515 nm wavelength of the seed laser and the modulator at resonance. The COTR signal enhancement will enable co-alignment of the two beams and the single-shot characterization of several key parameters of the microbunched beam. These values will be input for the simulations of the subsequent TESSA experiment.

ACKNOWLEDGEMENTS

The first author acknowledges the support of N. Sereno and J. Byrd of the Accelerator Systems Division, ANL and for the loan of the microbunching diagnostics chamber for this experiment.

The submitted manuscript has been created by UChicago Argonne, LLC, Operator of Argonne National Laboratory ("Argonne"). Argonne, a U.S. Department of Energy Office of Science Laboratory, is operated under Contract No.DE-AC02-06CH11357. The U.S. Government retains for itself, and others acting on its behalf, a paid-up nonexclusive, irrevocable worldwide license in said article to reproduce, prepare derivative works, distribute copies to the public, and perform publicly and display publicly, by or on behalf of the Government. The Department of Energy will provide public access to these results of federally sponsored research in accordance with the DOE Public Access Plan. http://energy.gov/downloads/doe-public-access-plan. This work has been partially funded by DOE grants DE-SC0017102 and DE-SC0018559.

REFERENCES

[1] J. Duris, A. Murokh, and P. Musumeci. "Tapering enhanced stimulated superradiant amplification.", *New J. Phys.*, vol. 17, p. 063036, 2015. doi:10.1088/1367-2630/1719/063036

[2] Y. Park *et al.*, "Tapered helical undulator system for high efficiency energy extraction from a high brightness electron beam.", *Nucl. Instrum. Methods Phys. Res., Sect. A*, vol. 1028, p. 166370, 2022. doi:10.1016/jnima.2022.166370

[3] D. Broemmelsiek *et al.*, "Record High-gradient SRF Beam Acceleration at Fermilab", *New J. Phys.*, vol. 20, p. 110318, 2018. doi:10.1088/1367-2630/aacc57

[4] P. Musumeci and A. Murokh, "FAST-GREENS: A High-Efficiency FEL Driven by a Superconducting rf Accelerator", presented at FEL'22, Trieste, Italy, Aug. 2022, paper TUP33, this conference.

[5] A. H. Lumpkin et al., "Submacropulse electron-beam dynamics correlated with higher-order modes in Tesla-type Super-conducting rf cavities", Phys. Rev. Accel. Beams, vol. 21, p. 064401, 2018. doi:10.1103/PhysRevAccelBeams.21064401.

[6] A. H. Lumpkin et al.,"Submicropulse electron-beam dynamics correlated with short-range wakefields in Tesla-type superconducting rf cavities", *Phys. Rev. Accel. and Beams*, vol. 23, p. 054401, 2020. doi:10.1103/PhysRevAccelBeams.21064402

[7] A. H. Lumpkin et al., "Submacropulse electron-beam dynamics correlated with higher-order modes in a Tesla-type Cryomodule", *Phys. Rev. Accel. and Beams*, vol. 25, p. 064402, 2022. doi:10.1103/PhysRevAccelBeams.21064402

[8] A. H. Lumpkin, "Microbunching in Relativistic Electron Beams", presented at FEL'22, Trieste, Italy, Aug. 2022, paper MOBI03, this conference.

[9] V. L. Ginzburg and I. M. Frank, "Radiation from uniformly moving sources (Vavilov-Cherenkov effect, transition radiation and some other phenomena)", *Sov. Phys. JETP* 16, p.15, 1946

[10] D. W. Rule,"Transition radiation diagnostics for intense charged particles beams", *Nucl. Instrum. Meth. Phys. Res. B,* vol. 24, pp. 901-904, 1987. doi:10.1016/S0168-583X(87)80275-6

[11] A. H. Lumpkin, "Advanced, time-resolved imaging techniques for electron-beam characterisation" in *Proc. Accelerator Instrumentation Workshop* 1990, Batavia, IL, 1991, AIP conference proceedings, vol. 229, pp. 151-179 doi:10.1063/1.40746

[12] D. W. Rule and A.H. Lumpkin, "Analysis of Coherent Optical Transition Radiation Interference Patterns Produced by SASE-Induced Microbunches", in *Proc. IPAC'01*, Chicago, IL, USA, Jun. 2001, paper TPAH029, pp. 1288-1290.

[13] L. Wartski, S. Roland, J. Lasalle, M. Bolore, and G. Fillippi, "Interference phenomenon in optical transition and its application to particle beam diagnostics and multiple-scattering measurements", *J. Appl. Phys.,* vol. 46, p. 3644, 1975. doi:10.1063/1.322092

[14] A. H. lumpkin, M. LaBerge, D.W. Rule *et al.*, "Coherent Optical Signatures of Electron Microbunching in Laser-Driven Plasma Accelerators", *Phys. Rev. Lett.*, vol. 125, p. 014801, 2020. doi:10.1103/PhysRevLett.125.014801

[15] A. H. Lumpkin, R. J. Dejus, and D. W. Rule, "First Direct Comparisons of a COTRI Analytical Model to Data from a SASE FEL at 540, 265, and 157 nm", in Proc. FEL'04, Trieste, Italy, Aug.-Sep. 2004, paper TUPOS49, pp. 519-522

ISBN: 978-3-95450-220-2 ISSN: 2673-5474 doi: 10.18429/JACoW-FEL2022-WEP18

CONSIDERATIONS ON WAKEFIELD EFFECTS IN A VUV FELO DRIVEN BY A SUPERCONDUCTING TESLA-TYPE LINAC*

Alex H. Lumpkin†, Fermi National Accelerator Laboratory, Batavia, IL USA
Henry P. Freund[1], University of New Mexico, Albuquerque, NM, USA
Peter Van der Slot, University of Twente, Enschede, the Netherlands
[1]also at University of Maryland, College Park, MD, USA

Abstract

The effects on beam dynamics from long-range and short-range wakefields from TESLA-type cavities are considered in regard to a proposed FEL oscillator (FELO) operating at 120 nm. This would be driven by the Fermilab Accelerator Science and Technology (FAST) linac at 300 MeV with a 3-MHz micropulse repetition rate. Our wakefield studies showed measurable effects on submacropulse centroid stability and on submicropulse head-tail kicks that can lead to emittance degradation. In the case of the former, we use MINERVA/OPC to simulate the ~100-µm centroid slew effects on the saturated output power levels of the FELO.

INTRODUCTION

The electron-beam properties needed for successful implementation of a free-electron-laser oscillator (FELO) on a superconducting TESLA-type linac at the Fermilab Accelerator Science and Technology (FAST) facility include the intrinsic normalized emittance and the submacropulse centroid stability [1]. We have demonstrated that short-range wakefields (SRWs) and long-range wakefields (LRWs) including higher-order modes (HOMs) are generated for off-axis beams in the two, 9-cell capture cavities and eight, 9-cell cavities of a cryomodule in the FAST linac [2-4]. The resulting degradation of the emittance and centroid stability would impact the FELO performance. At 300 MeV and with the 4.5-m long, 5-cm period undulator, the saturation of a vacuum ultraviolet (VUV) FELO operating at 120 nm has previously been simulated with GINGER and MEDUSA-OPC using the non-degraded beam parameters [1]. The measured electron-beam dynamics due to the SRWs (submicropulse, 100-micron head-tail kicks) and HOMs (submacropulse centroid slew of up to 100s of microns) will be presented [2-4]. These are mitigated by steering on axis as guided by the minimization of the HOM signals and beam dynamics effects. Simulations using MINERVA/OPC [5-7] of the effects of a submacropulse centroid slew on FELO performance will also be reported for the first time.

EXPERIMENTAL ASPECTS

The Fermilab Accelerator Science and Technology (FAST) facility includes the superconducting TESLA-type linac [8] which could generate the driving beam at 300 MeV. This would enable an FELO operating at 120 nm. A schematic of the linac is shown in Fig. 1, and the photocathode rf gun. the two TESLA capture cavities operating at about 20 MV/m gradient, the first chicane for bunch compression, the cryomodule (with eight, 9-cell cavities) and the high energy transport line to the location of the FEL experiment are shown. The nominal electron beam properties are given in Table 1. The FELO experiments would be based on the U5.0 planar undulator [9,10] in hand with a 5.0-cm period, tunable magnetic gap, and 4.55-m length as summarized in Table 2. A schematic of the resonator cavity positioned in the high energy transport end of the beamline is shown in Fig. 2. In practice, the second 4-magnet chicane could provide e-beam bunch compression as well as access for the upstream mirror and be placed closer to the D600 dipole with the undulator downstream of this dipole. There is a second dipole, D603 (not shown), that would direct the electron beam off the optical axis and to the high-energy absorber. The 50-m optical cavity round-trip time matches the 3-MHz micropulse repetition rate. The downstream mirror was assumed to have about 80% reflectance at 120 nm, and we would use a 1-mm radius hole outcoupling.

Table 1: FAST Electron Beam Parameters

Parameter	Unit	Value
Charge	nC	0.5-1.0
Emittance norm.	mm mrad	2-5
Gun energy	MeV	4.5
Beam energy	MeV	300

Table 2: Summary of the U5.0 Undulator Parameters [7]

Parameter	Unit	Value
Period	cm	5.0
K value	…..	0.45-3.9
Length	m	4.55
Tunable gap	cm	1.4-2.17
Maximum field at 1.4 cm	T	0.89

Past experiments on wakefield effects in the cavities which are correlated with their HOM signal strength motivated our instrumenting detectors on the HOM couplers for

* Work supported by the U.S. Department of Energy, Office of Science, under Contract No. DE-AC02-06CH11359.
† lumpkin@fnal.gov

ISBN: 978-3-95450-220-2 ISSN: 2673-5474 doi: 10.18429/JACoW-FEL2022-WEP18

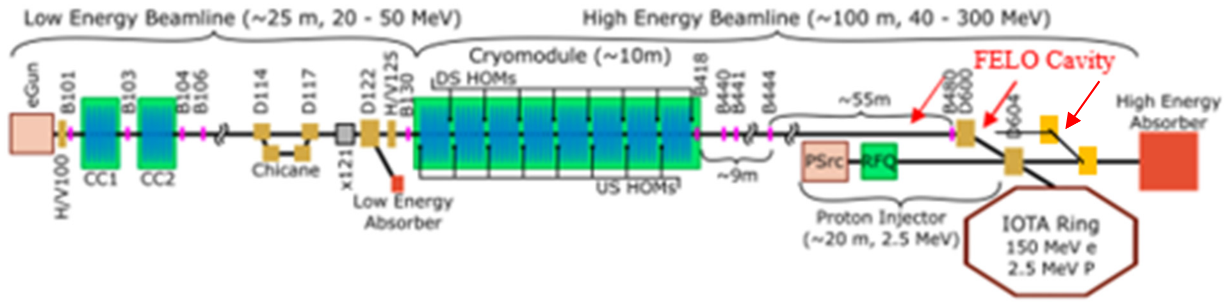

Figure 1: A schematic of the FAST linac showing the gun, capture cavities CC1 and CC2, the chicane, the cryomodule with US and DS HOM coupler locations, and the high energy transport to the FELO (see Fig. 2).

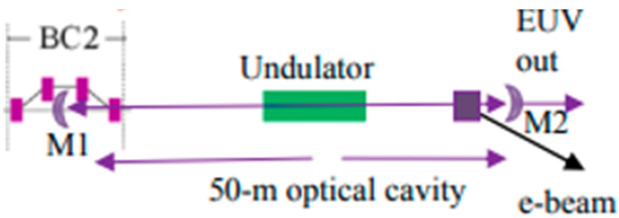

Figure 2: Schematic of a potential configuration for the FELO in the high energy transport area. A chicane would be added to provide access for the upstream mirror of the resonator.

all 10 cavities. The HOM detectors are based on passband filtering on the first two HOM dipole bands from 1.6 -1.9 GHz and Schottky detectors as described elsewhere [2,4].

BEAM DYNAMICS FROM WAKEFIELDS

Long-range Wakefields and HOMs

In the oscillator configuration, the submacropulse centroid slewing effects due to near-resonances of an HOM with a beam harmonic should be mitigated by careful, on-axis steering through the cavities. Examples of our observations after the cryomodule at 100 MeV energy are shown in Fig. 3. In the 50-b pulse train over 16.6 µs we see noticeable submacropulse centroid slewing in the bunch-by-bunch rf beam-position-monitor (BPM) data, particularly in B441 data with 300-µm total slew for -1 A (-2 mrad) steering [4]. We see the direction of the slew was correlated with the beam steering of the corrector V125 located 4 m before the CM. The corrector strength is 2 mrad/A. We also observed correlated centroid slew at location B480 located 64 m downstream of the cold BPM and just before the D600 dipole. The charge per micropulse was only 125 pC, and the kick effect goes directly with charge and inversely with beam energy. The higher charge in the FEL experiments and the 3x higher beam energy would roughly cancel these scaling effects so we ran our simulations initially at 100 µm total in 100 passes as reported in the next section.

Short-range Wakefields

The short-range wakefields also could be a concern so proper on-axis steering of the beam through the 10 cavities is warranted to avoid head-tail centroid shifts within each micropulse. An example of the SRW kick from the capture cavity CC2 at about 35 MeV is shown in Fig. 4 where corrector V103 was used to steer the beam into CC2 [3,11]. The data were taken at the OTR screen at the down-stream location X121 as shown in Fig. 1. The magnitudes of the observed head-tail kicks versus charge and different angular steering up to ± 4 mrad are shown. At 1.5 nC of charge, head-tail kicks up to 300 µm were seen. The corresponding projected profiles from the y-t data increased up to 650 µm from 400 µm [11]. This would directly correspond to an emittance-dilution effect.

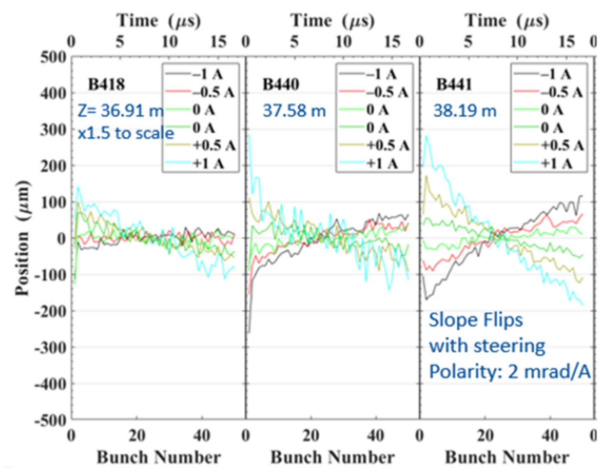

Figure 3: Submacropulse vertical centroid motion in the cold BPM and first two BPMs just after the CM due to HOMs excited by off-axis beam steering.

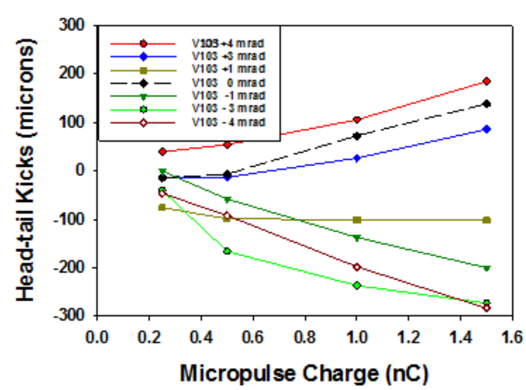

Figure 4: Submicropulse vertical centroid effect as the y-t head-tail kick for the streak camera images obtained at OTR screen X121 versus charge and V103 steering angle.

ISBN: 978-3-95450-220-2 ISSN: 2673-5474 doi: 10.18429/JACoW-FEL2022-WEP18

MINERVA/OPC SIMULATIONS

The simulations were done in the steady-state regime with only a single temporal slice so there is no issue with the cavity detuning. The MINERVA simulations start with shot noise so that no initial seed is provided [5-7]. The basic parameters of the simulations are listed in Table 3 below for the FELO at 120 nm using the 5.0-cm period undulator.

Table 3: Parameters used in the Simulation

Electron Beam	
Kinetic Energy	301.25 MeV
Peak Current	100 A
rms Energy Spread	0.0005
Normalized Emittance	2.0 mm-mrad
Beam Size *x* (rms)	122 µm
Beam Size *y* (rms)	120 µm
Twiss a_x	1.0
Twiss a_y	1.0
Repetition Rate	3.0 MHz
Undulator (flat pole face)	wiggle plane in *x*
Period	5.0 cm
Magnitude	2.4614 kG
Length (1 period entry/exit taper)	90 λ_w
Resonator & Optics	concentric, hole out-coupling
Wavelength	120 nm
Cavity Length	50 m
Mirror Curvature	25.32 m
Hole Radius (downstream mirror)	1.0 mm

In order to study the effect of a slew on the oscillator performance, we have added the possibility of including a slew in the beam centroid at the initialization of MINERVA. In order to engage this option, we specify (1) the slew direction, (2) the number of bunches (one bunch for each pass) over which the slew will be applied, and the maximum slew displacement over the number of bunches, and (4) the displacement (from the axis of symmetry) at the start of the simulation. Note that the default setting is that the initial displacement is zero. Therefore, if we specify that there will be 100 bunches and that the maximum displacement will be 100 µm, then the displacement will increase by 1 µm on each pass. If it is required that the simulation goes beyond 100 passes, then this increase in the slew will continue at this rate for each additional pass.

Figure 3 shows the out-coupled power vs pass assuming that there is no initial slew on the electron beam. A steady state is reached after about 60 passes at a power level of about 7.5 MW, while the power incident on the downstream mirror is about 154 MW for an out-coupling of about 5%. The single pass gain in the steady state is about 65%. Also shown in the inset are the case of no slew (blue) and 100 µm slew (red) plotted with a linear vertical axis. The output power sags to 5.5 MW at the end of 100 passes under these conditions with initial displacement of zero in the x plane.

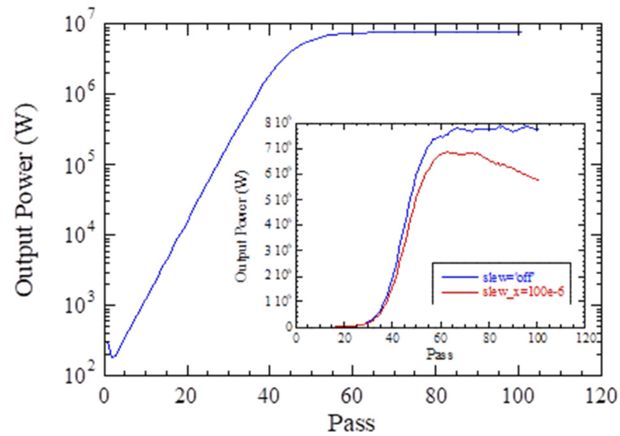

Figure 3: Plot of output power vs pass number at 120 nm with no slew with the inset showing on a linear vertical scale the power loss for a 100-µm slew (red curve).

Figure 4 shows the effect of displacements in the x-direction which corresponds to the wiggler plane, and in the y-direction. It is clear from the figure that the effect of the slew is greater if it is in the wiggle plane. This is probably because there is no focusing in that direction in a planar undulator so the beam will remain off axis in that direction. While it might still excite radiation, the mode is probably also off axis and may not exit the resonator through the hole. It is also important to note that the degradation is only about 30% as the slew increases to 100 µm for a beam whose extent is about 120 µm. The fact that there is virtually no degradation in the performance when the slew is in the y-direction is probably due to the fact that there is focusing in that direction, and the beam will oscillate about the axis of symmetry. A mitigation effect occurs if the beam can be steered so it starts off axis at -1/2 the total slew in the x plane.

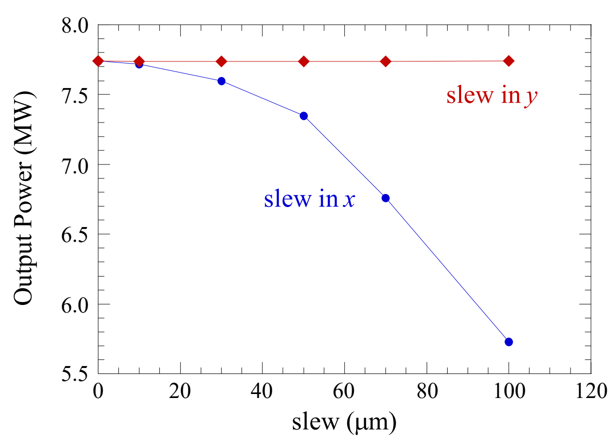

Figure 4: A comparison of the effects of slew in the x (or wiggle) plane (blue) and the y plane (red). The vertical focusing effects of the planar undulator mitigate the power loss for vertical slew.

ISBN: 978-3-95450-220-2 ISSN: 2673-5474 doi: 10.18429/JACoW-FEL2022-WEP18

SUMMARY

In summary, we have considered for the first time the effects on the FELO performance at 120 nm should sub-macropulse centroid slews occur as may be driven by the HOMs in the TESLA-type cavities. Proper steering into the cavities to minimize the HOMs and at the undulator to make the slew symmetric in x should preserve FELO performance. These considerations would also apply to the recently proposed Tapering Enhanced Super-Radiant Stimulated Amplification (TESSA) based oscillator experiment at FAST at 515 nm [12].

ACKNOWLEDGEMENTS

The first author acknowledges the support of C. Drennan and M. Lindgren of the Accelerator Division at FNAL.

REFERENCES

[1] A.H. Lumpkin, H. P. Freund, and M. Reinsch, "Feasibility of an XUV FEL Oscillator at ASTA", in *Proc. FEL'13*, New York, NY, USA, Aug. 2013, paper MOPSO51, pp. 88-91.

[2] A.H. Lumpkin *et al*., "Submacropulse electron-beam dynamics correlated with higher-order modes in Tesla-type superconducting rf cavities*, Phys. Rev. Accel. and Beams*, vol. 21, p. 064401, 2018.

[3] A.H. Lumpkin, R.M. Thurman-Keup, D. Edstrom. J. Ruan, "Submicropulse electron-beam dynamics correlated with short-range wakefields in Tesla-type superconducting rf cavities", *Phys. Rev. Accel. Beam*s, vol. 23, p. 054401, 2020.

[4] A.H. Lumpkin *et al*., "Submacropulse electron-beam dynamics correlated with higher-order modes in a Tesla-type Cryomodule*", Phys. Rev. Accel. Beams*, vol. 25, p. 064402, 2022.

[5] H.P. Freund, P.J.M. van der Slot, D.A.G. Grimminck, I.D. Setya, and P. Falgari, "Three-Dimensional, Time-Dependent Simulation of Free-Electron Lasers with Planar, Helical, and Elliptical Undulators", *New J. Phys.* vol. 19, 023020, 2017.

[6] H.P. Freund, P.J.M. van der Slot, and Yu. Shvyd'ko, "An X-Ray Regenerative Amplifier Free-Electron Laser Using Diamond Pinhole Mirrors", *New J. Phys.,* vol. 21, p. 093028, 2019.

[7] P.J.M. van der Slot and H.P. Freund, "Three-Dimensional, Time-Dependent Ana lysis of High- and Low-Q Free-Electron Laser Oscillators," *Appl. Sci.*, vol. 11, p. 4978, 2021.

[8] D. Broemmelsiek *et al*., "Record High-*gradient SRF Beam Acceleration at Fermilab", New J. Phys.,* vol. 20, p. 113018, 2018.

[9] E. Hoyer *et al*., "The U5.0 Undulator for the Advanced Light Source", *Rev, Sci. Instrum.*, vol. 63 (1), p. 359, 1992.

[10] P. Heimann *et al*., "Experimental characterization of ALS undulator radiation", *Rev. Sci. Instrum.,* vol. 66 (2), p. 1885, 1995.

[11] A.H. Lumpkin *et al.*, "Direct Observations of Submicropulse Electron-Beam Effects from Short-range Wakefields in TESLA-Type Superconducting rf Cavities" in *Proc. IBIC'20*, Santos, Brazil, Sep. 2020, pp. 56-60. `doi:10.18429/JACoW-IBIC2020-TUPP17`

[12] Alex Murokh and Pietro Musumeci, "FAST-GREENS: A High-Efficiency FEL Driven by a Superconducting RFAccelerator", presented at FEL'22, Trieste, Italy, August 2022, paper TUP33.

ISBN: 978-3-95450-220-2 ISSN: 2673-5474 doi: 10.18429/JACoW-FEL2022-WEP20

ACHIEVEMENTS AND CHALLENGES FOR SUB-10 fs LONG-TERM ARRIVAL TIME STABILITY AT LARGE-SCALE SASE FEL FACILITIES

B. Lautenschlager*, M. K. Czwalinna, J. Kral, J. Müller, S. Pfeiffer,
H. Schlarb, C. Schmidt, S. Schulz, M. Schütte, B. Steffen
Deutsches Elektronen-Synchrotron DESY, Notkestr. 85, 22607 Hamburg, Germany

Abstract

A high temporal stability of produced photon pulses is a key parameter for some classes of experiments, e.g., those using a pump-probe scheme. A longitudinal intra bunch-train feedback system, that reduces the intra bunch-train and the train-to-train arrival time fluctuations down to the sub-10 fs level was implemented at the European X-ray free electron laser (EuXFEL). The low arrival time jitter of the electron beam is preserved in the generated photon pulses. However, over long measurement periods, additional environmental factors acting on different time scales have to be considered. These factors include the temperature, relative humidity and in case of the European XFEL ground motions due to ocean activities. Mitigation of the residual timing drifts between pump laser and FEL pulses requires additional measures to disentangle the overlaid effects. The latest results and future challenges for the long-term arrival time stabilization will be presented.

INTRODUCTION

The European XFEL (EuXFEL) is a free electron laser facility with a 2 km long superconducting electron accelerator and a total length of 3.4 km. The facility operates in a 10 Hz burst mode with an RF pulse length of 600 µs. Each RF pulse can accelerate up to 2700 bunches with the maximum repetition rate of 4.5 MHz. The superconducting radio frequency (SRF) cavities accelerate the electron bunch-trains up to an electron beam energy of 17.5 GeV. Three undulator beamlines can be used to provide photon pulses to the different experiments.

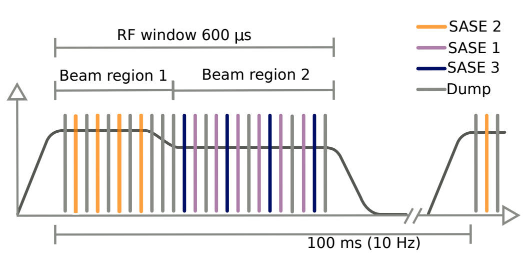

Figure 1: Schematic of the electron bunch distribution to the different SASE beamlines and the dump [1].

A system of slow and fast kickers distributes the electron bunches into the three different undulator beamlines and a dump, see Fig. 1. Photon energies in the range from 0.25 to 25 keV can be provided, using different linac energies and variable gap undulators. A three stage compression scheme, with the three magnetic chicanes, BC1, BC2, and BC3 can be used to influence the longitudinal parameters, like the compression and arrival time. The RF pulse can be separated into different beam regions, with different RF parameters in amplitude and phase, in order to provide individual compression schemes for the beamlines [2].

A longitudinal intra bunch-train feedback (L-IBFB) adjusts the electron bunch energies in front of a magnetic bunch compression chicane by actuating the preceding accelerator's module amplitude and phase. This introduces an energy dependent path length of the electron bunches through the chicane and thus a change of the arrival time. The bunch arrival time monitors (BAMs) measure the relative arrival time of the electron bunches, with a resolution down to 3 fs [1], against a femtosecond stable optical reference system [3]. The laser based synchronization system is also used to synchronize the lasers in the experimental hutches. An overview of optical reference system can be found in [4].

The low-level radio frequency (LLRF) system controls the 1.3 GHz RF field of the SRF cavities in phase and amplitude. An optical reference module (REFM-OPT) is used to resynchronize the RF phase with respect to the laser pulses, coming from the optical synchronization system, to compensate for drifts in the 1.3 GHz RF reference distribution chain, due to humidity and temperature variations [5]. Different controllers are combined in the LLRF system to achieve the typical RF field stability in amplitude of $\Delta A/A \approx 0.008$ % and in phase of $\Delta\Phi \approx 0.007$ deg [6, 7]. A second order multiple-input multiple-output controller is used to react within a bunch-train. To minimize repetitive errors from bunch-train to bunch-train a learning feedforward control algorithm is applied. A combination of the measured field information in amplitude and phase and beam-based measurements, e.g., the arrival time, is included in the LLRF control strategy and introduced in [8, 9]. This combination is used by the L-IBFB to stabilize the the electron bunch arrival time below 10 fs (rms) [1].

ARRIVAL TIME MEASUREMENT AND STABILIZATION AT THE EUROPEAN XFEL

A schematic of the EuXFEL facility is shown in Fig. 2. The bunch arrival time monitors provide the arrival time bunch-by-bunch using an electro-optical detection scheme. The electromagnetic field of the electron bunches is captured by four broadband (40 GHz) RF pickups. The induced RF signal is sampled by an ≈ 200 fs laser pulse of the optical ref-

* bjoern.lautenschlager@desy.de

ISBN: 978-3-95450-220-2 ISSN: 2673-5474 doi: 10.18429/JACoW-FEL2022-WEP20

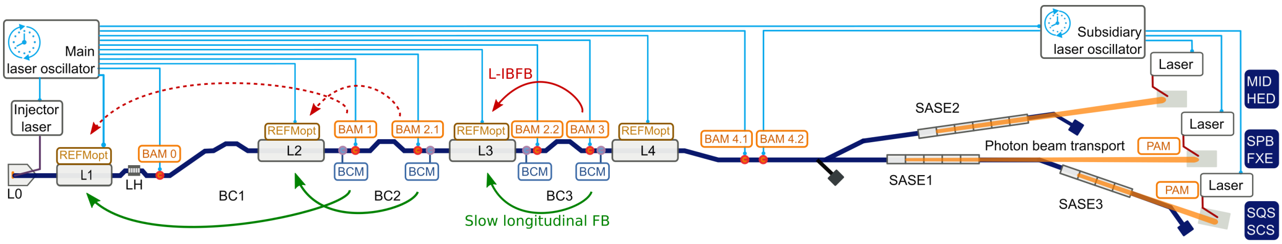

Figure 2: Schematic of the EuXFEL facility with the diagnostic units, like the bunch arrival time monitor (BAM) and bunch compression monitor (BCM), the distribution of the optical reference system (blue lines), the feedback loops (red and green lines) and the the different accelerator parts L1, L2, L3 and L4, which are including the SRF modules and the LLRF system [1].

erence system, within a Mach-Zehnder type electro-optical modulator. The passing light amplitude is modulated by the RF field, such that the strength of the modulation is proportional to the arrival time variations of the single electron bunches [10–12]. Further developments and optimizations of the past years of the BAMs and the optical synchronization system has led to relative electron bunch arrival time measurements with a resolution down to 3 fs [1].

The arrival time of the generated FEL pulses is measured by photon arrival time monitors (PAMs), which are however exclusive to some user experiments. A detailed description can be found in [13]. It has been verified by correlations between BAM and PAM measurements, that the electron bunch arrival time jitter is preserved for the FEL pulses during the SASE process [1].

The BAM measurements are used in feedback loops to reduce the arrival time jitter to the sub-10 fs level. At locations in the accelerator with a significant longitudinal dispersion, any change in beam energy gain upstream of such a dispersive section results in an arrival time change downstream of it. This effect is exploited in the combination of two longitudinal feedbacks, an intra-train loop for correcting fast fluctuations, and a slow loop for compensation of drifts to keep to L-IBFB in its dynamic operation range. At EuXFEL, those feedback combinations are implemented for the RF stations directly upstream of the three bunch compression chicanes, BC1, BC2 and BC3.

The LLRF controller uses a combined and weighted error signal of the RF field measurements together with the beam-based measurements, e.g. the arrival time, to control the amplitude and phase of the RF station and thus the energy prior to a chicane in order to stabilize the arrival time [9]. The longitudinal feedback for slow drift compensation uses the compression and energy or arrival time as monitor signal and the sum-voltage and chirp of one accelerator section as actuator. For timing critical experiments at the EuXFEL the combination of the L-IBFB at L3 (red solid line, Fig. 2) and the slow feedbacks at all locations (green solid lines, Fig. 2) are permanently activated and used in standard operation.

After BC3, the accelerator part L4 increases the beam energy without influencing the arrival time, such that the two monitors, BAM4.1 and BAM 4.2, located 1.5 km apart from BAM3 can be used as out-of-loop monitors. The two monitors BAM3 and BAM4.1 show an excellent correlation (0.99 Pearson's coefficient over 1 minute of data) for the bunch-train mean values with a correlation width of 1.15 fs [1].

RESULTS

This section presents the results of the short term arrival time measurements with activated L-IBFB , as well as, long term comparison between the BAM3 and BAM4.1 over days. The presented data were acquired with an electron bunch repetition of 2.25 MHz and a typical charge of 250 pC. Each bunch train included over 800 bunches. Figure 3 shows the

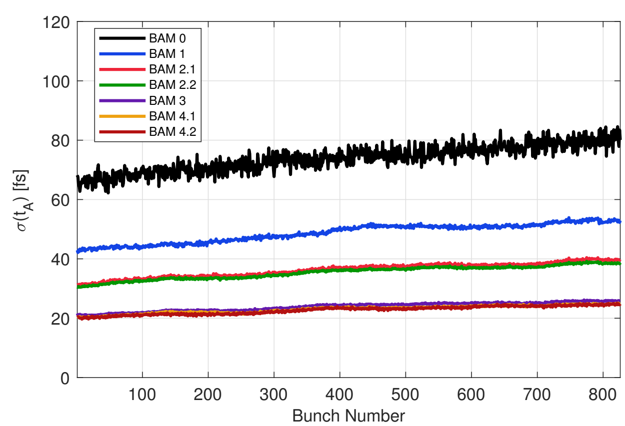

Figure 3: Arrival time jitter $\sigma(t_A)$ with the L-IBFB disabled at different BAM locations, starting with the BAM0 in the injector section and ends with the BAM4.2 at the end of the acceleration part. Each line represents the standard deviation of 600 consecutive bunch-trains with a bunch-to-bunch repetition rate of 2.25 MHz.

evolution of the measured arrival time jitter $\sigma(t_A)$ along the accelerator, starting with an incoming arrival time jitter of ≈ 70 fs (rms, mean of the bunch-train) measured with the BAM0 (black solid line) in the injector section. The jitter is reduced with each compression stage to the final value of $\approx$22 fs (rms, mean of the bunch-train) measured consistently with the three equivalent monitors BAM3, BAM4.1 and BAM4.2. The arrival time jitter (standard deviation) is

ISBN: 978-3-95450-220-2 ISSN: 2673-5474 doi: 10.18429/JACoW-FEL2022-WEP20

calculated from 600 consecutive bunch-trains, which corresponds to one minute of data.

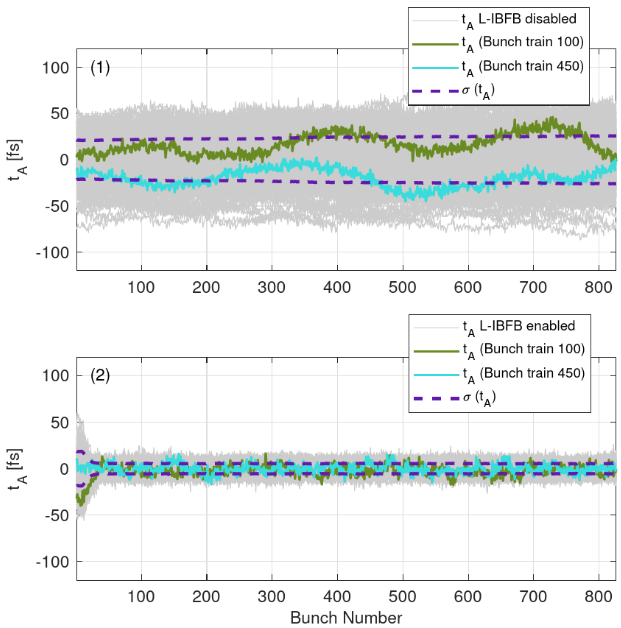

Figure 4: Comparison of the arrival time data of 600 bunch-trains, where the mean arrival time had been subtracted from each bunch train, with the L-IBFB disabled (first plot) and with the L-IBFB activated (second plot). The gray lines are the arrival time of the individual bunch-trains with two highlighted bunch-trains (100 and 450, colored lines) and the purple dashed lines are the standard deviation of the 600 bunch-trains and represents the arrival time jitter $\sigma(t_A)$.

Figure 4 shows the mean free arrival time measured with the BAM3 after the third chicane BC3. The first plot shows the situation with the L-IBFB disabled, and in comparison to that, the second plot shows the measured arrival time and standard deviation with the L-IBFB activated at L3. The comparison of the two plots shows how the L-IBFB acts from bunch-to-bunch at the beginning of the bunch-train. The peak-to-peak value is reduced significantly within the first few bunches until the final stabilized arrival time is reached. Figure 5 shows the same effect by comparing the arrival time jitter directly. The black line represents the arrival time jitter with the L-IBFB disabled and a mean jitter value of above 20 fs (rms). That value is pushed down by the longitudinal intra bunch-train feedback below 6 fs (rms, purple line), which corresponds to a tremendous improvement of the arrival time stability by a factor of 4. The steady state arrival time jitter is reached after an adaption time of ≈15 µs (30–40 bunches with a repetition rate of 2.25 MHz). The kicker distribution system diverts the first few bunches from the transient region into the dump, such that only the highly stabilized bunches are used for the SASE process (compare Fig. 1).

The L-IBFB operates together with the slow longitudinal feedback over days in order to achieve a highly stabilized arrival time, which is shown in the first plot of Fig. 6.

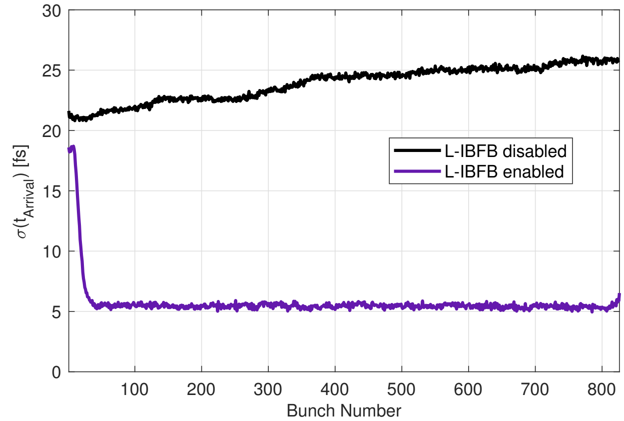

Figure 5: Comparison of the arrival time jitter, with the L-IBFB disabled and enabled, measured with the in-loop BAM3 after the third chicane BC3. The standard deviation is computed over the same 600 consecutive bunch-trains as before.

The comparison to the measurement with the out-of-loop BAM4.1 (second plot, Fig. 6), in 1.5 km distance, shows a long range baseline fluctuation over days. Although, there is no section with a significant longitudinal dispersion in between the BAM3 and BAM4.1. The out-of-loop arrival time measurement shows a clear oscillation with a period of ≈ 12 h and a variation of roughly ±150 fs.

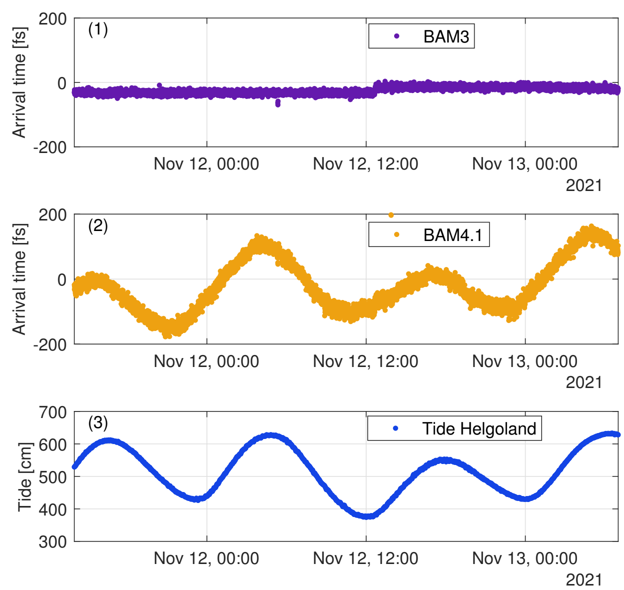

Figure 6: Comparison of long term arrival time measurements. The first plot shows the arrival time measured with the in-loop BAM3. The second plot shows the arrival time measured with the out-of-loop BAM4.1. The third plot shows the tide at the North Sea, *Source of the tidal data: www.pegelonline.wsv.de*.

The proximity to the North Sea, the 12 h period and the comparison to the measured tide, shown in the third plot of Fig. 6, suggests that these arrival time drifts could be

ISBN: 978-3-95450-220-2 ISSN: 2673-5474 doi: 10.18429/JACoW-FEL2022-WEP20

correlated to physical length changes of the accelerator, due to ground motions induced by the tidal range. The observed timing drifts are manifest, as well as, fluctuations between the photon pulses arrival time and the stabilized optical synchronization timing that drives the user experiment.

CONCLUSION

The presented results show that the arrival time stability is improved significantly, by a factor of 4, down to the 6 fs (rms) level, when using the longitudinal intra bunch-train feedback. Long term fluctuations, with a period of ≈12 h were observed in between two distant arrival time measurement stations 1.5 km apart from each other. These fluctuations closely resemble the local tide in the main parameters, like the 12 h period. The induced timing variation in the order of hundreds of femtoseconds is detrimental to long-term averaging timing sensitive experiments. Investigations of the exact magnitude and its mitigation is ongoing.

OUTLOOK

To investigate and compensate for the long term arrival time instabilities several upgrades and developments are ongoing. A new laser pulse arrival time monitor (LAM) is under development. The LAM could be used to measure the arrival time of the probe laser pulses in the experimental hutches, to detect and compensate for arrival time drifts, due to temperature or humidity changes. The last arrival time measurement is 1.5 km apart from the experimental hutches and the propagation of the arrival time drifts are unknown at the moment. Three new BAMs will be installed directly after each undulator section. These SASE BAMs will be used to investigate and evaluate the arrival time drifts further and could be used to compensate for the observed arrival time drifts. Other effects recently observed in the arrival time difference between two BAMs 1.5 km apart from each other, with a frequency of 0.2 Hz are under investigation and could be linked to ground motions induced by ocean waves.

REFERENCES

[1] M. K. Czwalinna *et al.*, "Beam Arrival Stability at the European XFEL", *Proc. IPAC2021*, Campinas, SP, Brazil, 2021. `doi:10.18429/JACoW-IPAC2021-THXB02`

[2] W. Decking *et al.*, "A MHz-repetition-rate hard X-ray free-electron laser driven by a superconducting linear accelerator", *Nat. Photonics*, vol. 14, pp. 391-397, 2020. `doi:10.1038/s41566-020-0607-z`

[3] F. Löhl *et al.*, "Electron Bunch Timing with Femtosecond Precision in a Superconducting Free-Electron Laser", *Physical Review Letters*, vol. 104, no. 14, p. 144 801, 2010. `doi:10.1103/PhysRevLett.104.144801`

[4] S. Schulz *et al.*, "Femtosecond all-optical synchronization of an x-ray free-electron laser", *Nature Communications*, vol. 6, pp. 5938–5949, 2015. `doi:10.1038/ncomms6938`

[5] T. Lamp *et al.*, "Femtosecond Laser-to-RF Synchronization and RF Reference Distribution at the European XFEL", in *Proc. FEL2019*, Hamburg, Germany, 2019, pp. 343-345. `doi:10.18429/JACoW-FEL2019-WEP010`.

[6] C. Schmidt *et al.*, "Recent Developments of the European XFEL LLRF System", in *Proc. IPAC'13*, Shanghai, China, 2013, paper WEPME009, pp. 2941–2943.

[7] M. Omet *et al.*, "LLRF Operation and Performance at the European XFEL", in *Proc. IPAC2018*, Vancouver, BC, Canada, 2018, pp. 1934–1936. `doi:10.18429/JACoW-IPAC2018-WEPAF051`.

[8] S. Pfeiffer,"Symmetric grey box identification and distributed beam-based controller design for free-electron lasers", Ph.D. thesis, TUHH, Hamburg, Germany, 2014.

[9] S. Pfeiffer *et al.*, "Fast Feedback Strategies for Longitudinal Beam Stabilization", in *Proc. IPAC'12*, 2012, paper MOOAA03, pp. 26–28.

[10] M. Viti *et al.*,"The Bunch Arrival Time Monitor at FLASH and European XFEL", in *Proc. ICALEPCS'17*, Barcelona, Spain, 2017, pp. 701–705. `doi:10.18429/JACoW-ICALEPCS2017-TUPHA125`

[11] A. Angelovski *et al.*, "Evaluation of the cone-shaped pickup performance for low charge sub-10 fs arrival-time measurements at free electron laser facilities", *Phys. Rev. ST Accel. Beams*, vol. 18, no. 1, p. 012 801, 2015. `doi:10.1103/PhysRevSTAB.18.012801`

[12] M. K. Czwalinna *et al.*, "New design of the 40 GHz bunch arrival time monitor using MTCA.4 electronics at FLASH and for the European XFEL", in *Proc. IBIC'13*, Oxford, United Kingdom, 2013, paper WEPC31, pp. 749–752.

[13] H. J. Kirkwood *et al.*, "Initial observations of the femtosecond timing jitter at the European XFEL", in *Optics Letters*, vol. 44, pp. 1650-1653, 2019. `doi:10.1364/OL.44.001650`

ISBN: 978-3-95450-220-2 ISSN: 2673-5474 doi: 10.18429/JACoW-FEL2022-WEP21

OPTIMIZATION IN THE STRUCTURE OF KLYSTRON DRIVE SIGNAL TO EXTEND RF PULSE FLATTOP LENGTH AT THE EUROPEAN XFEL

V. Vogel, V. Ayvazyan, M. Bousonville, J. Branlard, L. Butkowski, A. Cherepenko, S. Choroba, J. Hartung, S. Goeller, N. Walker and S. Wiesenberg,
Deutsches Elektronen-Synchrotron DESY, Hamburg, Germany

Abstract

Currently 26 RF stations are in operation at the European X-ray Free Electron Laser (XFEL) and all RF stations can deliver sufficient power to reach maximum gradients in the accelerating modules, limited only by cavity and coupler properties. It was demonstrated that by activating a dynamic frequency shift (DFS) of the RF drive signal, the requested klystron power can be reduced by up to 20%, keeping the gradient levels unchanged. Currently, the RF pulse starts when the level of klystron HV reaches 99% of the nominal voltage. If one allows the RF pulse to start at 80% level of the nominal voltage, then the RF pulse length can be increased. The first demonstration of the proposed procedure with the 10MW multi-beam klystrons (MBK) at the klystron test stand and at the XFEL RF stations A10.L3 and A23.L3 will be presented as well. The described procedure can be used both to increase the duration of the RF flat top as well as to shorten the duration of the HV, which could lead to energy savings. In this article we will present a proposal for increasing the XFEL RF pulse flattop length using phase and amplitude compensation during the rise and fall of the HV, as well as applying DFS when filling the cavities of the accelerator.

INTRODUCTION

Currently, XFEL has three laser lines, each of which requires a specific electron beam parameter set for better lasing [1]. The transition between different beam region cannot be done instantly, as it needs some time to change energy and phase in several accelerator modules. At the moment the high voltage (HV) pulse has a length of 1.7 ms and the RF pulse a length of 1.4 ms, out of which only 0.6 ms can be used for the beam acceleration. The level of klystron output power is 15% below the saturated power to provide margin for feedback regulation. The optimization of the klystron drive signal can help increase the length of beam time without touching other accelerator parameters. Keeping the design klystron power level and using DFS can reduce the filling time up to 10%. We can get another 20% if the RF pulse starts at the 80% level and stops at 70% of nominal HV. The phase change and lower power during the rise and fall of the HV need to be compensated. The result is a longer RF pulse flattop which can be used to accelerate a longer beam pulse.

KLYSTRON DYNAMIC FREQUENCY SHIFT

When a cavity is filled with electromagnetic field the cavity surfaces are under pressures known as Lorentz forces. These pressures in the case of standing wave are proportional to the square of the surface electric and magnetic fields as in [2]:

$$P_{sw} = 0.25\,(\varepsilon_0 E^2 - \mu_o H^2). \tag{1}$$

The resulting cavity detuning is therefore proportional to the accelerating field squared:

$$\Delta f = -K E_{acc}^2. \tag{2}$$

For the TESLA type superconducting cavities (SC), the typical Lorentz force detuning constant K is about 0.9 Hz/(MV/m)^2. To keep the phase and amplitude stable during RF flattop, piezoelectric actuators are used [3][4]. The piezoelectric actuators induce mechanical cavity deformations that compensate the effect of Lorentz detuning during RF flattop. In [5] and [6], a procedure for changing of the klystron frequency during filling time was proposed. This procedure was later named DFS and tested at FLASH. The main idea of DFS is to keep the klystron frequency during filling time matched to the cavity frequency, by modulating the klystron phase:

$$\varphi(t) = \Delta\varphi(G)\left(1 - e^{-\frac{t}{\tau(G)}}\right). \tag{3}$$

where $\Delta\varphi$ is the initial phase offset that depends on cavity gradient, τ is the mechanical time constant that also depends on cavity gradient, and G is cavity gradient.

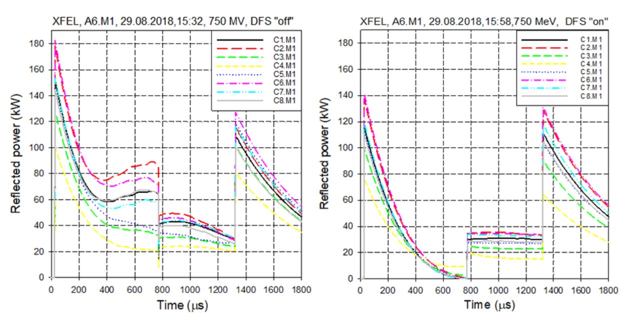

Figure 1: Effect of DFS on reflected power from cavities.

The formula Eq. (3) is not an exact solution for the single cavity, but it gives enough good results for the sum of 32 different cavities fed by one klystron. For the XFEL TESLA type of cavities with filling time of 750 µs and gradient about 20 MV/m, Δφ = -55 degrees, and the time constant is about 230 – 320 µs. With the optimization of the cavity filling procedure, the reflected power was reduced significantly, allowing the cavity gradient to be increased or the cavity filling time shortened, with the same level of forward RF power. Figure 1 shows the impact of DFS on the reflected power from the cavities.

ISBN: 978-3-95450-220-2 ISSN: 2673-5474 doi: 10.18429/JACoW-FEL2022-WEP21

MAX USE OF FULL HV PULSE LENGTH

The high voltage pulse of the XFEL klystron cathodes has a rise time of about 265 µs. Part of this rise time can be used to fill SC with energy [7]. The fall time is about 120 µs and part of this time can be used to extend the RF pulse. The klystron RF output power during the rise and fall times will be lower than at the flat top of the HV pulse. The methods of amplitude compensation for the rise and fall times are different, because during the rise time the klystron works close to saturation, while during the fall time it must work in both a linear mode and a mode close to saturation, with a reserve for the beam loading compensation and RF control.

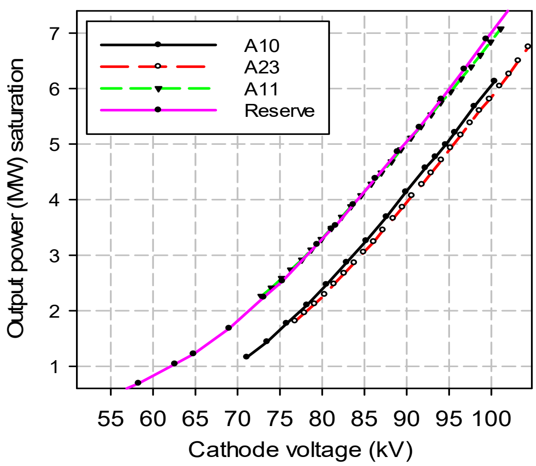

Figure 2: Saturated output power as a function of cathode voltage for klystrons type A (A10, A23) and klystrons type B (A11, reserve).

The RF phase shift due to the change of klystron voltage and power should also need to be compensated. Figure 2 shows the saturated output power for different klystrons as a function of cathode voltage. Usually these kinds of data are not provided by klystron manufactures and should be collected during klystron acceptance tests. Figure 3 shows the input power at which the output power saturated for the different klystrons. It is very important during the HV rise time to keep the klystron output power very close to the saturation level up to the moment when a measured cavity gradient will be equal to the theoretical value. Figure 4 shows this procedure for a HV shift of 170 µs. In this case, about 300 µs in needed to full compensation of the power drop during the rise time.

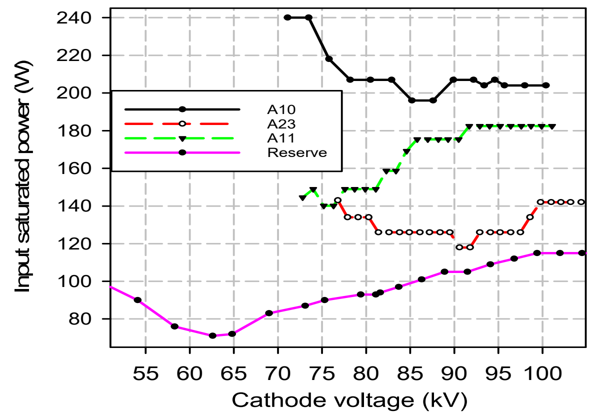

Figure 3: Saturated input power for different klystrons as a function of cathode voltage.

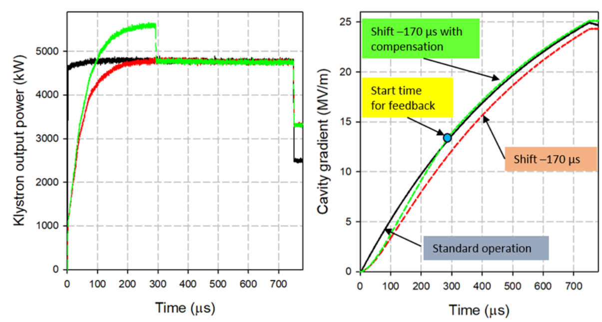

Figure 4: (Left) Klystron output power, black: normal operation, red: with 170 µs HV shift, green: 170 µs shift with compensation. (Right) Cavity filling curves.

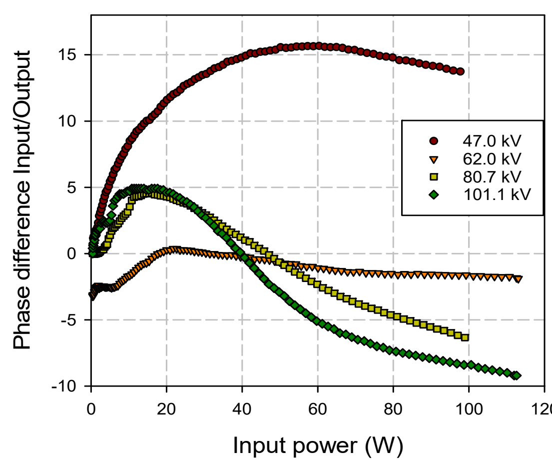

Figure 5: Klystron output phase change as a function of input power for different cathode voltages.

During amplitude compensation the input power changes from a level that is close to saturation to linear regime, which produces an additional phase shift. Figure 5 shows the phase shift for different cathode voltage.

EXPERIMENTAL RESULTS

The experimental tests of increasing the flattop length were done first at the klystrons test stand [8], [9] and then at several XFEL RF stations.

ISBN: 978-3-95450-220-2 ISSN: 2673-5474 doi: 10.18429/JACoW-FEL2022-WEP21

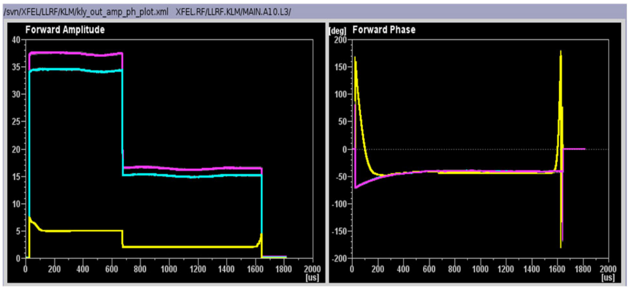

Figure 6: Klystron amplitude shapes (left), and the corresponding phases (right) during compensation of the rise and fall times plus DFS for XFEL RF station A10.L3. The achieved flattop was 950 µs (cf nominal 650 µs). Yellow: input amplitude and phase; cyan and magenta: output amplitudes and phases, for both arms of the klystron.

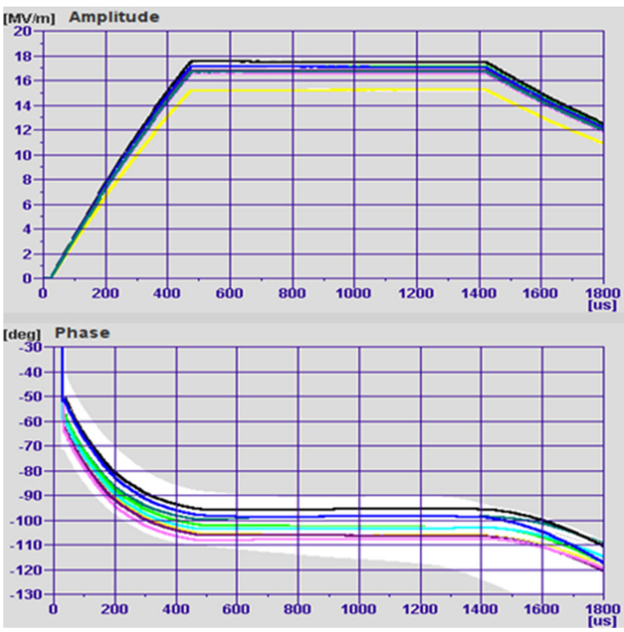

Figure 7: A23.L3, cavities gradients and phases during test of 970 µs flattop. All feedbacks regulations are active.

During the tests at the XFEL stations, special care was needed before the application of the compensation and DFS: First, the station energy was reduced by a factor of two; then HV and RF start trigger pulses were set and RF pulse length fixed. It was very important to reduce station energy, since during the fall time the klystron output phase can become inverted with respect to the cavity phases, and the cavities then work as power multipliers. Under these conditions the reflected power from the cavities can increase by up to a factor of four, possibly causing serious damage to the cold couplers and/or circulators. After the first step of phase compensation the station energy was returned to the nominal value and amplitude compensation was done. After the second step of phase compensation all compensation parameters were stored in the user feedforward correction table and all feedback regulations were activated. Figure 6 shows the final achieved klystron output power and phase during the test of station A10.L3. It can be seen that a large phase change at the klystron input is required to achieve flat phase on the klystron output at the end of the pulse. Figure 7 shows the gradients and phases in the cavities for the long-pulse test at station A23.L3. In additional to a short test (~10 hours), a long test for more than 120 hours for flattop length of 750 µs and station energy of 665 MeV was performed. During this test the temperatures of cold and warm parts of high-power couplers, the helium levels inside cryomodules and radiation level were recorded. All changes were at the expected levels.

CONCLUSION

Using the DFS feature together with an amplitude and phase compensation during the HV rise and fall time, a flattop length of 970 µs compared to the nominal 650 µs and at a station energy of 665 MeV (14 GeV run) with nominal Q_{load} was demonstrated. No limitations from the high-power RF couplers and the cryogenic system were observed for over 120 hours of operation with an extended RF flattop of 750 µs (cf nominal 650 µs). During the studies, the physical limits for the klystron had not yet been reached. A high-energy run configuration (17.5 GeV) requires future investigations along with low-level RF control.

REFERENCES

[1] W. Decking *et al.*, "A MHz-repetition-rate hard X-ray free-electron laser driven by a superconducting linear accelerator", in *Nat. Photonics*, vol. 14, pp. 391–397, 2020. doi:10.1038/s41566-020-0607-z

[2] E. Haebel and J. Tückmantel, "Electromagnetic Surface Forces in RF Cavities", CERN, Geneva, Switzerland, Rep. CERN AT-RF-91-99, Dec. 11, 1991

[3] S. N. Simrock, "Lorentz Force Compensation of Pulsed SRF Cavities" in *Proc. LINAC'02*, Gyeongju, Korea, Aug. 2002, paper WE204.

[4] M. Grecki, V. Ayvazyan, J. Branlard, *et al.*, "On-line RF amplitude and phase calibration", in *Proc. IPAC'17*, Copenhagen, Denmark, May 2017, pp. 3957-3959. `doi:10.18429/JACoW-IPAC2017-THPAB103`

[5] V. Vogel, V. Ayvazyan, Z. Geng, *et al.*, "Optimization of cavities filling procedure", FLASH seminar, Mar. 2009, DESY, Hamburg, Germany.

[6] V. Ayvazyan *et al.*, "Optimization of filling procedure for TESLA-type cavities for klystron RF power minimization for European XFEL", in *Proc. IPAC'10,* Kyoto, Japan, May. 2010, paper TUPEA039, pp. 1416-1418

[7] TESLA Technical Design Report, DESY Hamburg, 2001.

[8] V. Vogel *et al.*, "Summary of the test and installation of 10 MW MBKs for the XFEL", in *Proc. LINAC'16*, East Lansing, MI, USA, Sep. 2016, pp. 506-508 `doi:10.18429/JACoW-LINAC2016-TUPLR017`

[9] V. Vogel *et al.*, "Status of the 10 MW MBKs during Commissioning of the European XFEL in DESY", in *Proc. LINAC'18*, Beijing, China, Sep. 2018, pp. 102-104 `doi:10.18429/JACoW-LINAC2018-MOPO036`

ISBN: 978-3-95450-220-2 ISSN: 2673-5474 doi: 10.18429/JACoW-FEL2022-WEP22

RF COMMISSIONING AND FIRST BEAM OPERATION OF THE POLARIX TRANSVERSE DEFLECTING STRUCTURES IN THE FLASH2 BEAMLINE

M. Vogt*, J. Rönsch-Schulenburg, S. Schreiber, and F. Christie[1]
Deutsches Elektronen-Synchrotron DESY, Hamburg, Germany
[1]now at TNG Technology Consulting GmbH, Unterföhring, Germany

Abstract

In January 2021 two X-band (12 GHz) PolariX Transverse Deflecting Structures with variable streak polarization were installed into the FLASH2 beamline at FLASH. Since none of the RF components for the FLASH2-PolariX RF-distribution system nor the two PolariX structures could be pre-conditioned, RF-conditioning was and is quite tedious. Nevertheless, after 6 weeks of conditioning, we have already been able to streak the electron beam enough to start commissioning of the PolariX controls and the software. After 4 months of conditioning in parallel to FLASH2 user operation, we achieved a stable 5.5 MW flat top of 400 ns operation. Next step will be to include RF pulse compression to achieve the design power of 22 MW.

INTRODUCTION

FLASH [1–5] at DESY (Hamburg, Germany) is a free-electron laser (FEL) user facility. FLASH consists of a normal-conducting photo-injector, and a superconducting linac. The superconducting LINAC can accelerate several thousand electron bunches per second in 10 Hz bursts of up to 800 µs length. The long bunch trains are split in two parts and are shared between two undulator beamlines. FEL radiation can be generated with the SASE (Self Amplified Spontaneous Emission) process and fundamental wavelengths ranging from 4 nm to 90 nm. In addition, FLASH hosts a seeding experiment Xseed [6], and a plasma wakefield acceleration experiment FLASHForward [7]. In order to keep FLASH a state-of-the-art FEL user facility, an upgrade project “FLASH2020+” is on-going [8–10], which includes an upgrade of the longitudinal diagnostics. Optimizing the performance of an FEL requires a precise knowledge of the longitudinal phase space distribution of the bunch. Transverse deflecting structures (TDSs) enable high resolution, direct measurement methods to determine the longitudinal properties of the bunch and allow to measure transverse-to-longitudinal correlations (centroid shift, mismatch, emittance, etc.) in the plane perpendicular to the streaking plane. The RF structures support an Eigenmode with a transverse electric field component, thereby deflecting electrons within the bunch transversely depending on the arrival time in respect to the RF wave. High amplitudes of the electric field and high RF frequency both improve the resolution. A collaboration between CERN, PSI and DESY has been established to develop and build an advanced modular X-band TDS [11, 12]. The PolariX is an X-band (12 GHz) TDS with the new feature that the polarization of the transverse electric field can be varied by tuning the phase difference between two perpendicular in-coupling ports of the structure. This allows the measurement of the longitudinal distribution of emittance and mismatch in both transverse planes and even, to some extent, phase space tomography [13].

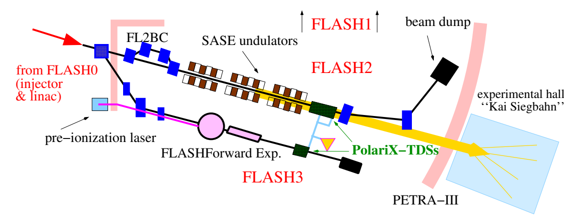

Figure 1: Schematical view of the FLASH2/3 beamlines with the 2+1 PolariXes and the shared X-band RF transmitter. Not to scale.

The prototype PolariX structure was installed in an optimized diagnostic section of the FLASHForward experiment in 2020 [14]. The prototype was pre-conditioned at CERN and some RF equipment could be pre-conditioned at a test assembly of klystron and modulator at DESY. In the winter shutdown 2020/2021 a system of two short (0.8 m long) PolariX-structures was installed in FLASH2 [15, 16]. Figure 1 gives a schematic overview of the layout of the FLASH2/3 beamlines and the installed PolariX system. In FLASH2 the RF structures were installed 2.0 m downstream of the end of the last SASE undulator and 2.40 m upstream, of the 3.5°-dipole separating the electron beam from FEL beam[1]. Any single bunch in the standard 1 µs timing pattern can be kicked onto a screen located 5.5 m downstream of the separator dipole. Immediately downstream of the PolariX section the beam of potentially several thousand bunches per second and a maximum beam power of 100 kW has to be prepared to be safely dumped. This set up is not optimal since there is not enough space for many quadrupoles *and* sufficient phase advance between them to achieve the wanted high temporal and energy- resolution with the streak from only one standard PolariX structure. However, with two PolariXes and a carefully designed beam optics this set up allows to measure the shape of the complete longitudinal bunch phase space distribution with temporal resolutions in the sub-10 fs range and supplies sufficient energy resolution

* vogtm@mail.desy.de

[1] Positions refer to *center* positions unless otherwise noted.

ISBN: 978-3-95450-220-2 ISSN: 2673-5474 doi: 10.18429/JACoW-FEL2022-WEP22

to determine the fraction of the bunch that participated in the FEL process.

FLASH2 and FLASHforward share the same tunnel, and the corresponding PolariXes were located close to each other. Thus, it was decided to use a common RF driver system for both PolariX diagnostic stations. The structures are driven by a 6 MW Toshiba klystron E37113A operated at a frequency of 11.988 GHz. The klystron is located in the tunnel in between the PolariX sections of FLASH2 and FLASHForward. The required HV pulses are generated by an Ampegon Type-μ M-class modulator which is located in a service isle outside the tunnel. To generate more streaking voltage for FLASH2, an RF pulse compressor (X-BOC, X-band barrel open cavity [17]) was installed at the output port of the klystron during the winter shutdown 2020/2021.

A remote-controlled waveguide switch is used to switch the RF power between the FLASHForward PolariX and the two FLASH2 PolariXes. Ceramic windows isolate the vacuum in the waveguide distribution system from the beam vacuum systems in FLASH2 and FLASHForward. The FLASH2 system first splits the power between the two PolariX units. A phase shifter with a range of 0° to 200° is placed before one of the PolariXes to compensate unavoidable phase differences between the two structures.

RF CONDITIONING

Conditioning of the FLASH2 PolariX TDS system started quickly after the installation in the FLASH2 beamline. The two structures, the X-BOC, the phase shifters, and all the new waveguide components could not be pre-conditioned prior to the installation. Since the RF controls for generating a well-behaved RF pulse at the output of the X-BOC were not fully functional, we started conditioning with the X-BOC thermally detuned by about 25 25 K. So far, stable operation has been achieved at a power level of 6 MW for 400 ns, equivalent to what has been achieved at the FLASHForward PolariX. We did not reach the design performance, but achieved sufficient power to perform phase space mappings with an already very good resolution below 10 fs with a moderate optics suitable for multi-bunch mode (see below). The conditioning will resume after restarting FLASH from the 9 month 2021/22 shutdown [5]. In particular we plan to quickly move to condition the system with activated X-BOC.

PolariX COMMISSIONING

The complex transverse (time-independent) field-amplitudes, streaking ($\hat{E}_s := E_{x,s} + iE_{y,s}$), and kicking ($\hat{E}_k := E_{x,k} + iE_{y,k}$) the bunch which traverses the compound system of two PolariXes can be parameterized as follows.

$$\begin{aligned}\hat{E}_s &= \ A\left(\exp(i\psi_1) + \exp(i\psi_2)\cos(\psi_{12})\right)\cos(\phi_{\mathrm{RF}})\\ \hat{E}_k &= -A\left(\exp(i\psi_1) + \exp(i\psi_2)\sin(\psi_{12})\right)\sin(\phi_{\mathrm{RF}})\ ,\end{aligned}$$

where $A := \sqrt{R_s P_{\mathrm{fwd}}/4}$ is the (real) amplitude due to the forward power after twice splitting with 3 dB per arm, ψ_1 and ψ_2 are the phase differences between the horizontal and the vertical port of structure 1 and structure 2 respectively, ψ_{12} is the phase difference of beam-to-RF between structure 1 and 2, and ϕ_{RF} is the common RF phase from the klystron input drive amplifier and controller. The phases depend on the position of the corresponding three phase shifters (control knobs) as well as on path differences of the waveguide distribution system between the corresponding ports — and thus *all* have to be adjusted empirically. The problem is that the two PolariXes cannot be operated alternatively but only in parallel (behind the 1st 3 dB splitter). The set-up is such that one may expect that ψ_1 and ψ_2 come out similar for parallel streak amplitude in both structures. Under the assumption that interference of the phase shifters is weak, one may maximize the streak (minimize the kick), and fix the polarization direction, by iteration of tuning the various knobs one-by-one. In fact, tuning and calibrating the phase shifters took about one shift(8 h).

When setting up a TDS for a measurement, its effective streak, i.e. the mapping of longitudinal distance inside the bunch to observed transverse distance on the screen must be calibrated. This is usually done by varying ϕ_{RF} and correlate it with the bunch centroid position on the screen. The RF-coupling of the PolariX system to the FLASH master timing was initially done in a way that included a lot of ambient jitter and phase drifts. Thus that the above phase scans had to be optimized for scanning time rather than sample size. However, we have developed a suite of tools that perform the streak calibration, take and evaluate calibrated picture. Furthermore the RF-coupling of the system will be improved in the next long shutdown 2024/25. The default streak orientation is vertical, since the dispersion from the electron/photon separation which is used for the energy measurement is in the horizontal plane. Since the complete FLASH sub-train always has to pass this dispersion section, we are able to perform online bunch length measurements *and* can map the complete longitudinal phase space on an off-axis screen for an arbitrarily kicked bunch out of the sub-train. The energy resolution can unfortunately not be well calibrated in non-destructive mode due to aperture limitation for the off-axis screen. In destructive (single bunch) mode the energy resolution can be calibrated with improved accuracy. First preliminary scans of the vertical slice emittance have been successfully performed using a horizontal streak and a vertical quadrupole scan on the screen. We have developed a technique to compensate the unavoidable horizontal dispersion in a horizontal quadrupole scan, but could not yet spend enough time on this method to obtain useful results before the machine went into the ongoing shutdown last November.

USER OPERATION

Since mid-2021 we routinely use PolariX for tuning compression for FLASH2 i.p. for user experiments requesting short FEL pulses. In addition, we offer dedicated PolariX measurements to users who need pulse length estimates for evaluating their experiment. So far, we did not offer continuous PolariX bunch length monitoring because of

ISBN: 978-3-95450-220-2 ISSN: 2673-5474 doi: 10.18429/JACoW-FEL2022-WEP22

electromagnetic interference between the PolariX system (RF, and/or kicker) and certain photon diagnostics and because of insufficient radiation shielding between the PolariX screen and certain photon diagnostics. This last problem is under survey and we are planning to improve the shielding on one or the other side. Figure 2 shows two bunches which

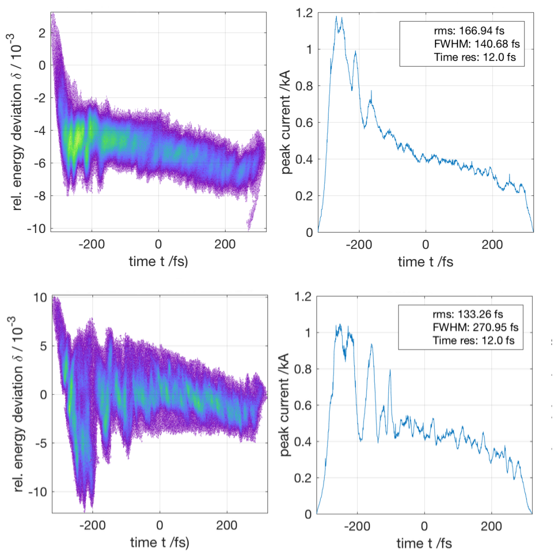

Figure 2: Two bunches of the same beam set up: Top row with open undulators. Bottom row with closed undulators.

have been set up almost identically except that one (top row) was measured with open undulators while the other (bottom row) was measured with closed undulators and a single pulse SASE energy of 250 µJ at 21 nm. One observes the enhanced energy spread and the reduced centroid energy in the head of the bunch (to the left). This indicates the region of active FEL lasing and therefore gives an estimate on the photon pulse length. Figure 3 shows a bunch prepared

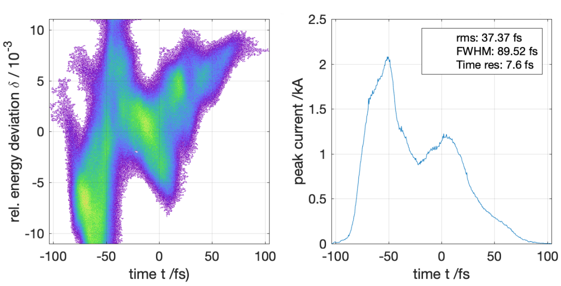

Figure 3: Bunch prepared for short pulse operation for a user experiment.

for user operation with short pulses. Note the very good temporal resolution below 8 fs.

MACHINE STUDIES

Since PolariX at FLASH is operational (with reduced power), many FEL and accelerator studies included dedicated and "service"- PolariX measurements. In particular we had a campaign on studying micro bunch effects with several lattice and compression variants in FLASH1 (with LOLA [18]), and in FLASH2 (with PolariX). This study is still being evaluated and will be reported elsewhere. Figure 4 is an exotic example of a heavily micro-bunched bunch observed during the dedicated micro-bunching studies. In

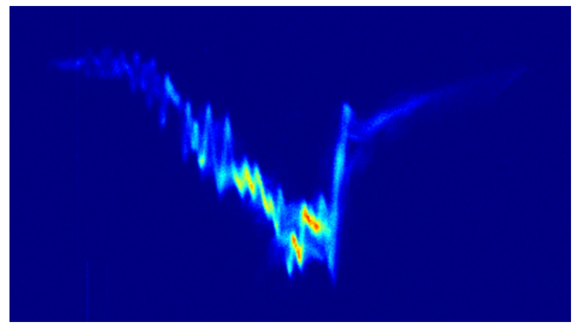

Figure 4: Heavily micro-bunched bunch prepared for accelerator studies.

addition we have complemented the THz photon pulse streaking studies [19] with PolariX measurements with closed and opened FLASH2 undulators. The evaluation of the lasing bunch region using PolariX images with open and closed undulators still needs a lot of manual, intervention, i.e. by-eye interpretation of PolariX phase space mappings with and without FEL process. Nota bene: one can *never* compare images of the *same* bunch with and without lasing! A project has been started [20] to employ machine learning to evaluate the images.

CONCLUSION & OUTLOOK

Two PolariX TDSes have been installed in FLASH2. The initial RF conditioning and the PolariX commissioning was very successful. We routinely use PolariX at FLASH2 for tuning for users and machine studies. We are looking forward to continuing our efforts after recommissioning FLASH after the 1st long FLASH2020+ shutdown in September.

ACKNOWLEDGMENTS

The authors thank all members of the PolariX collaboration for designing, manufacturing and providing the PolariX structures. We particularly thank the members of the DESY technical groups that installed and operate and maintain the PolariX system with all its subsystems.

REFERENCES

[1] W. Ackermann *et al.*, "Operation of a free-electron laser from the extreme ultraviolet to the water window", *Nat. Photonics*, vol. 1, pp. 336–342, 2007. `doi:10.1038/nphoton.2007.76`

[2] B. Faatz *et al.*, "Simultaneous operation of two soft x-ray free-electron lasers driven by one linear accelerator", *New J. Phys.*, vol. 18, p. 062002, 2016. `doi:10.1088/1367-2630/18/6/062002`

ISBN: 978-3-95450-220-2 ISSN: 2673-5474 doi: 10.18429/JACoW-FEL2022-WEP22

[3] J. Rossbach, J. R. Schneider, and W. Wurth, "10 years of pioneering X-ray science at the free-electron laser FLASH at DESY", *Phys. Rep.*, vol. 808, pp. 1–74, 2019. doi:10.1016/j.physrep.2019.02.002

[4] K. Honkavaara and S. Schreiber, "FLASH: The Pioneering XUV and Soft X-Ray FEL User Facility ", presented at the 39th Int. Free Electron Laser Conf. (FEL'19), Hamburg, Germany, Aug. 2019, paper THP074, pp. 734–737. doi:10.18429/JACoW-FEL2019-THP074

[5] K. Honkavaara, C. Gerth, M. Kuhlmann, J. Rönsch-Schulenburg, L. Schaper, R. Treusch, M. Vogt, J. Zemella, and S. Schreiber, "Status of the Free-Electron Laser User Facility FLASH", presented at the 40th Int. Free Electron Laser Conf. (FEL'22), Trieste, Italy, Aug. 2022, paper MOP37, this conference.

[6] S. Ackermann *et al.*, "First Demonstration of Parallel Operation of a Seeded FEL and a SASE FEL", presented at the 40th Int. Free Electron Laser Conf. (FEL'22), Trieste, Italy, Aug. 2022, paper TUP41, this conference.

[7] R. D'Arcy *et al.*, "FLASHForward: plasma wakefield accelerator science for high-average-power applications", *Phil. Trans. R. Soc. A*, vol. 377, p. 20180392, 2019. doi:10.1098/rsta.2018.0392

[8] M. Beye *et al.*, "FLASH2020+, Conceptual Design Report", DESY, Hamburg, 2020. doi:10.3204/PUBDB-2020-00465

[9] L. Schaper, S. Ackermann, E. Allaria *et al.*, "Flexible and Coherent Soft X-ray Pulses at High Repetition Rate: Current Research and Perspectives", *Appl. Sci.*, vol. 10, p. 9729, 2021. doi:10.3390/app11209729

[10] L. Schaper *et al.*, "FLASH2020+ Project Progress: Current Installations and Future Plans", presented at the 40th Int. Free Electron Laser Conf. (FEL'22), Trieste, Italy, Aug. 2022, paper TUP51, this conference.

[11] P. Craievich, *et al.*, "Novel X-band transverse deflection structure with variable polarization", *Phys. Rev. Accel. Beams*, vol. 23, p. 112001, 2020. doi:10.1103/PhysRevAccelBeams.23.112001

[12] B. Marchetti, *et al.*, "Experimental demonstration of novel beam characterization using a polarizable X-band transverse deflection structure", *Sci. Rep.*, vol. 11, p. 3560, 2021. doi:10.1038/s41598-021-82687-2

[13] D. Marx, *et all*, "Characterization of Ultrashort Electron Bunches at the SINBAD-ARES Linac", DESY-THESIS-2019-026, Dissertation, Hamburg University, 2019. doi:10.3204/PUBDB-2019-04190

[14] R. T. P. D'Arcy, A. Aschikhin, P. González Caminal, V. Libov, and J. Osterhoff, "Longitudinal Phase Space Reconstruction at FLASHForward Using a Novel Transverse Deflection Cavity, PolariX-TDS", in *Proc. IPAC'18*, Vancouver, Canada, Apr.-May 2018, pp. 1567–1570. doi:10.18429/JACoW-IPAC2018-TUPML017

[15] F. Christie, J. Rönsch-Schulenburg, and M. Vogt, "A PolariX TDS for the FLASH2 Beamline", in *Proc. FEL'19*, Hamburg, Germany, Aug. 2019, pp. 328–331. doi:10.18429/JACoW-FEL2019-WEP006

[16] F. Christie, J. Rönsch-Schulenburg, S. Schreiber, M. Vogt, and J. Zemella, "Redesign of the FLASH2 Post-SASE Undulator Beamline", in *Proc. IPAC'21*, Campinas, Brazil, May 2021, pp. 1626–1629. doi:10.18429/JACoW-IPAC2021-TUPAB104

[17] R. Zennaro, M. Bopp, A. Citterio, R. Reiser, and T. Stapf, "C-band RF Pulse Compressor for SwissFEL", in *Proc. IPAC'13*, Shanghai, China, May 2013, paper WEPFI059, pp. 2827–2829.

[18] M. Yan *et al.*, "First Realization and Performance Study of a Single-Shot Longitudinal Bunch Profile Monitor Utilizing a Transverse Deflecting Structure", in *Proc. IBIC'13*, Oxford, UK, Sep. 2013, paper TUPC36, pp. 456–459.

[19] S. Duesterer *et al.*, "Single-shot temporal characterization of XUV FEL Pulses", presented at the 40th Int. Free Electron Laser Conf. (FEL'22), Trieste, Italy, Aug. 2022, poster WEP35, this conference.

[20] G. Goetzke *et al.*, "AI Methods for an improved evaluation of FEL diagnosic data", presented at the 40th Int. Free Electron Laser Conf. (FEL'22), Trieste, Italy, Aug. 2022, poster WEP36, this conference.

ISBN: 978-3-95450-220-2 ISSN: 2673-5474 doi: 10.18429/JACoW-FEL2022-WEP23

OPTIMIZATION AND FINE TUNING OF MACHINE PARAMETERS WITH MODEL-LESS ALGORITHM

F. Tripaldi, F. Galassi and G. Gaio, Elettra Sincrotrone Trieste, Trieste, Italy

Abstract

Despite the use in machine physics of high-performance software for calculating and predicting machine parameters, when these are applied to the real world, additional operating point search is often necessary to obtain the desired performance.

Furthermore, small configuration changes required by FEL users during running experiments, lead to search new optimal working points in a short time.

Use of tools based on model-less algorithms such as Nelder-Mead and 1D or 2D scans allow the automatic and online search for the best fine setup of machine and FEL parameters in short times.

The development of MIMOFB (Multi Input Multi Output Feedback) software used as optimizer with model-less algorithms has provided a versatile tool that can be applied in many situations.

The ability to concatenate optimizations with pre-programmed batch executions allows to develop complex optimization strategies and iterate them by refining algorithm's parameters.

At FERMI MIMOFB optimizers are currently used with good results for fine-tuning the electron beam magnetic optics and trajectory, by acting on the current of quadrupoles and correctors magnets for FEL signal optimization and terahertz parasitic signal maximization.

INTRODUCTION

A high-level software allowing to control the spatial and temporal overlap of the laser seed and electron beams in the undulator chain is currently in use at FERMI [1]. A good strategy to maintain the long-term stability of the FEL signal consists in minimizing the correlation between the FEL intensity itself and several machine parameters, acquired on the shot-to-shot basis [2, 3].

At the same time, stochastic optimization algorithms (SO) are strictly integrated into the trajectory feedback loops; they change at each shot the feedback set points, acquires sensors and actuators and couples them with the objective function [2, 3].

Until now, no optimization strategy had been implemented for the optimization of the electron transport and confinement magnetic optics.

The ultimate goal is to apply algorithms to optimize the FEL performance by tuning the electron-beam trajectory and the machine optics along the undulator chain. The optimization algorithms implemented in the tool developed at FERMI (called MIMOFB), were initially tested on a simpler case, regarding the optimization of the THz signal generated by the exhausted electrons after the FEL line and transported to the TeraFERMI beamline [4]. After a brief introduction about the MIMOFB, we show the successful optimization of the TeraFERMI signal acting on the quadrupoles and steerers placed in the FERMI's main beam dump line. In the second part, we show how the MIMOFB can be used to improve the FEL intensity acting on the quadrupoles along the FEL undulator chain.

The optics matching procedure, which imposes the design values of the Twiss functions to the electron beam, is performed with dedicated tools that were developed during the FERMI commissioning and improved over time [5, 6].

However, although the emittance and Twiss parameter calculation tools are increasingly advanced and precise, their results depend significantly on the quality of the input data. These are represented in FERMI by electron beam sizes measured through the scan of quadrupole currents, from the analysis of CCD cameras images at various machine points. This kind of measurement is affected by many variables which are affected by systematic errors, non-standard procedures and settings that can compromise the reproducibility and the reliability of the measurement itself.

Similarly, small but significant last-minute changes to the machine configuration, for example due to changed required by the beamline running the experiment, require to optimize the new setup as quickly as possible.

MIMOFB AS OPTIMIZER

Starting from the aforementioned requirements and exploiting the experience gained on the Elettra synchrotron [7], we implemented the MIMOFB on FERMI, as optimizer based on mode-less algorithms (Nelder-Mead) [8]. In particular, we focused on the optimization of the electron beam optics in the spreader common line (SFEL1) and along the undulators (IUFEL1) to maximize the FEL intensity, and in the main beam dump (MBD) line to maximize the TeraFERMI signal.

Differently from the Elettra, MIMOFB optimization in FERMI has been configured adding some constraints. This is done by introducing another set of dedicated sensors with a very low weighting coefficients (1e-6) such as they do not impact significantly final objective function [7], but act as thresholds during optimization process.

This implementation was necessary for example because the control of the charge losses before the end of the elec-

ISBN: 978-3-95450-220-2 ISSN: 2673-5474 doi: 10.18429/JACoW-FEL2022-WEP23

trons path (MBD Current Monitor) is monitored by the Machine Protection System (MPS), which inhibits the transport of electrons when limits are exceeded.

The Nelder-Mead algorithm used by MIMOFB [7] provides variable intensity kicks to the actuators to search for the best region in the multiparameter space. The application of these kicks often brings the system to areas where the beam charge losses and/or radiation losses overcome the allowed thresholds.

To prevent MPS intervention, safety limit values are set for these sensors that must not be exceeded. When this happens, the MIMOFB discards the values of the actuators obtained and passes to the next optimization step to continue the configured optimization strategy.

Kick Factor

The maximum kick value of the actuators is set by the operator and is chosen according to the effects it produces on the target and constraint sensors. It has to be sufficiently large to explore different regions out of the local maximum for the target signals, but it should not allow the constraint sensors going outside the limits imposed.

A global scaling factor, called *limit kick factor* in MIMOFB configuration, allows simultaneous kick amplitude control on all actuators that is applied by the optimization algorithm. In this way, it is possible to reshape the impact of optimization on different sensors by acting on only one parameter.

Batch Programming

Another important aspect for optimization success is given by the actuators sequence, the so-called "batch programming". Knowing the system model to be optimized allows one to choose the best strategy. For example, in a FODO machine section, it is possible to choose to preserve this configuration by optimizing first the focusing quadrupoles and then the defocusing ones. In a more complex strategy, after optimizing the quadrupoles, it is possible to insert some optimization steps acting on the trajectory, using the steering correctors.

The batch programming reported here are results of many empirical tests and chosen among those that have led to the best results both in terms of targets reached and in terms of time needed to obtain them.

In the future, further improvements in MIMOFB tool will lead to the development of automatic strategy evaluation systems.

OPTIMIZATION FOR THE TERAFERMI SIGNAL

The TeraFERMI beamline provides THz pulses to be used for non-linear spectroscopy and pump-probe studies. The mechanism for the THz emission is called Coherent Transition Radiation, and is based on the interaction of a relativistic electron bunch with a metallic screen [4]. The optimization of the electron beam optics after FEL emission is crucial to guarantee the best performance.

The MIMOFB optimizer searches for the highest THz radiation signal, which strongly depends on focusing and compression of the electron bunches, by acting on MBD quadrupoles and correctors.

The peculiarity of this beamline is that it is parasitic to the operation of the FEL, and therefore any optimization operation has to work on the machine section not interfering with it. For this reason, the electron beam transport optics is modified only in the final section, downstream of the undulators chain, the MBD.

Configuration

Sensors The optimization algorithm main target is represented by the signal of a pyroelectric detector available on TeraFERMI beamline. However, such a maximization must be done without forgetting machine protection. Additional sensors are, indeed, taken into account. These are beam loss monitor and Cherenkov detector fibers, each of them with the appropriate weight; it's just the correct choice of weights (usually small, 1e-6) that ensures these sensor references works effectively as constrains.

Actuators and Batch Programming The actuators in this configuration are represented by the magnetic optic quadrupoles and the trajectory correctors of the final section of the FERMI accelerator, i.e., MBD FEL1 and MBD common to FEL1 and FEL2 [9].

The maximum applicable kicks were chosen by trying values that could achieve an appreciable response on the pyro signal without tripping the protection system.

As described in the introduction, the effectiveness of optimization also depends on the batch programming of operations.

In the reported case it was chosen to optimize in parallel two different groups of machine elements: first the quadrupoles (magnetic optics) and then the steering magnets (trajectory).

The operations on the optics were divided into groups of overlapping actuators while maintaining the order of installation of the machine layout. Starting first with the last quadrupoles of the FEL1 section divided into groups of three overlapping by one element and continuing with the quadrupoles of the MBD section common to FEL2. The same choice was made on the last two steps of batch programming, deputed to optimize the trajectory using steering correctors.

Limit Kick Factor The possibility of applying a high limit kick factor, and thus exploring large areas of the system input space, is conditioned by whether or not the FEL needs to be kept on. In fact, in this case there is a concrete possibility that a too large kick could produce losses at a level that the MPS stops operations. For this reason, during operations with FEL ON it is necessary to limit kick strength and settle a less fast optimization, but this increases the risk of not getting out of the local maximum.

On the other hand, the use of high kick factors, when even allowed, hinders the convergence of the optimization by not allowing the algorithm to correctly evaluate the surroundings of a local maximum.

ISBN: 978-3-95450-220-2 ISSN: 2673-5474 doi: 10.18429/JACoW-FEL2022-WEP23

Results

Figures 1 and 2 shows the behavior of quadrupoles strength and steering correctors kick during the automatic optimization procedure. The pyro signal and the BLM trends are shown in Figs. 3 and 4 respectively. The starting point of the optimization is at around 350k counts.

Some actuators, like the psq_mbd_fel.01, .02 and .04, results more involved than others. However, also correctors play a relevant role. Their contribution occurs for the first time in seconds 350 to 450: despite the modest improvement in the THz intensity associated to them (see Fig. 3), their manipulation allows the system to move to a different working point. In this way, a second iteration leads to a very large improvement. This occurs at second 450, when the pyro signal jumps abruptly from about 800k counts to 1.2 million.

Important improvements in losses control (see Fig. 4) can be associated to trajectory optimization and quadrupoles fine tuning. The correctors contribution occurs at seconds 350 and 750. From the second 500 onward there is no further increase in signal, however, there is an overall improvement in losses reduction.

OPTIMIZATION IN FEL OPTIC – SFEL1 AND IUFEL1

Configuration

Similarly to what was done on TeraFERMI, MIMOFB was used to maximize FEL intensity by performing optics-only optimization in the SFEL1 and IUFEL1 sections [9]. During this experiment, the FEL was operated at 20.8nm (harmonic 12 of 249.6nm).

Sensors In both optimizations, the main target to be maximized was the intensity measured by the POS2 CCD, with a region of interest plotted around the central core of the spot.

As a secondary sensor, the beam losses measured by the Cherenkov fibers installed along the undulators was included. This sensor was assigned a weight of 0.2 in the contribution to the objective function.

Charge measured in CM MBD was configured as the working limit, with a minimum set at 485pC and a negligible weight (1e-6).

For logging purposes, Ionization Monitor 1 of FEL1 was also included in the sensors to allow a posteriori analysis and comparison of the response of the two methods of FEL intensity assessment (Figs. 5 and 7).

Actuators and Batch Programming This optimization involves only the optics; therefore, the transport quadrupoles SFEL1 and IUFEL1 were configured. They started from strength values worked out with optics software.

Because of the limited number of quadrupoles in SFEL1, the choice was to optimize them in parallel in one step. By contrast, the nine quadrupoles of IUFEL1 were grouped into four steps following the FODO structure: a partial superposition between the first and third, and between the second and fourth, respectively, has been preserved.

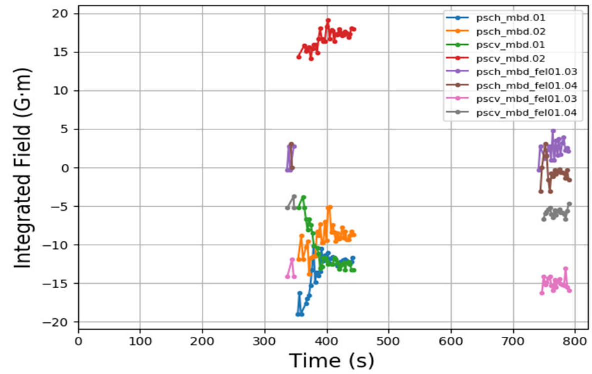

Figure 1: TF Opt. – Steering magnets kicks

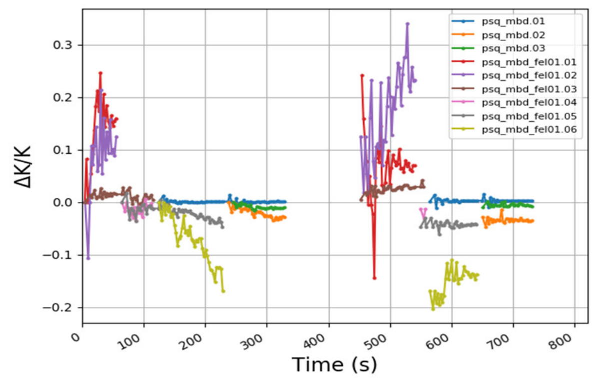

Figure 2: TF Opt. - MBD Quadrupoles kicks

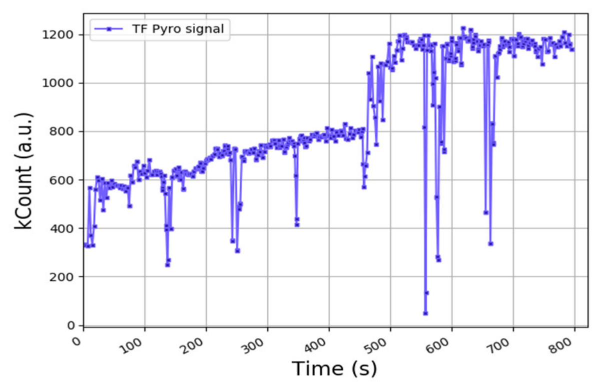

Figure 3: TF Opt. - Pyro signal

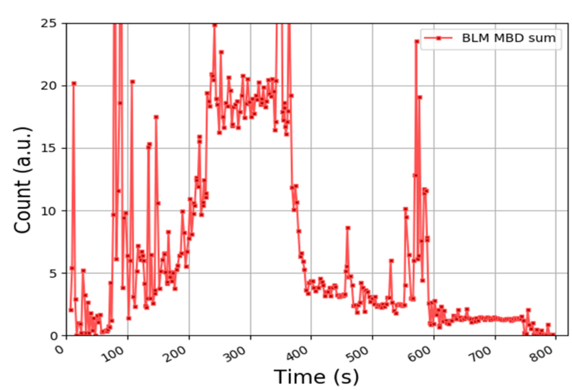

Figure 4: TF Opt. - Beam Losses Monitor counts

ISBN: 978-3-95450-220-2 ISSN: 2673-5474 doi: 10.18429/JACoW-FEL2022-WEP23

Results

Figures 6 and 8 shows the behavior of quadrupoles strength in SFEL1 and IUFEL1 sections respectively, during the optimization procedure.

The sensors trends (POS2 CCD and I0M1) are shown in figs. 5 and 7. Optimizations of SFEL1 and IUFEL1 resulted in an increase in FEL intensity read on IOM1 from 170 µJ to 180 µJ and from 180 µJ to 200 µJ, respectively.

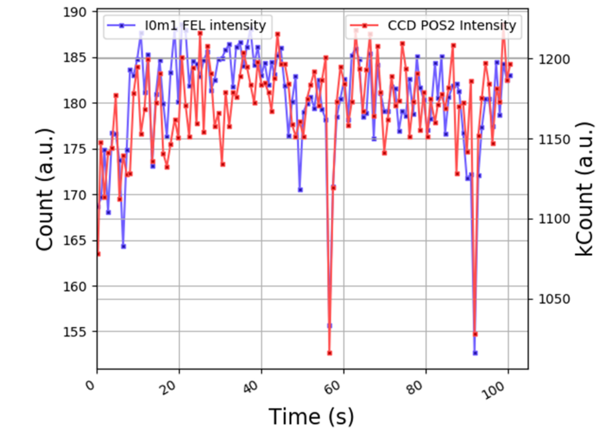

Figure 5: SFEL1 Opt. - FEL Intensity (POS2 CCD, I0M1)

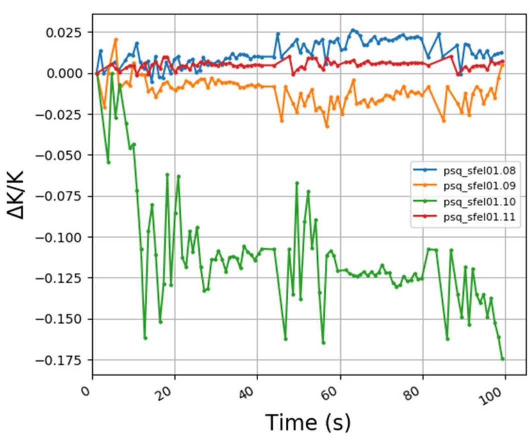

Figure 6: SFEL1 Opt. - Quadrupoles kicks

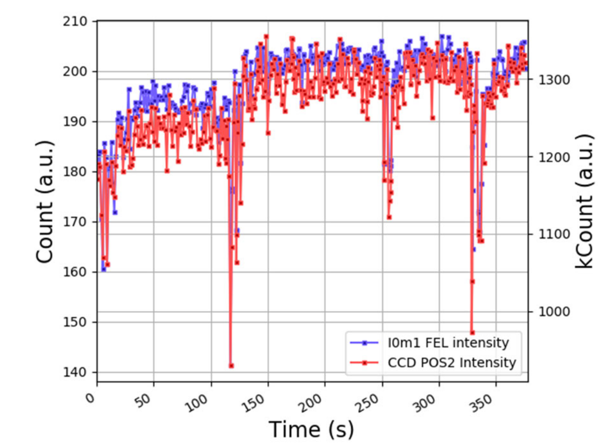

Figure 7: IUFEL1 Opt. - FEL Intensity (POS2 CCD, I0M1)

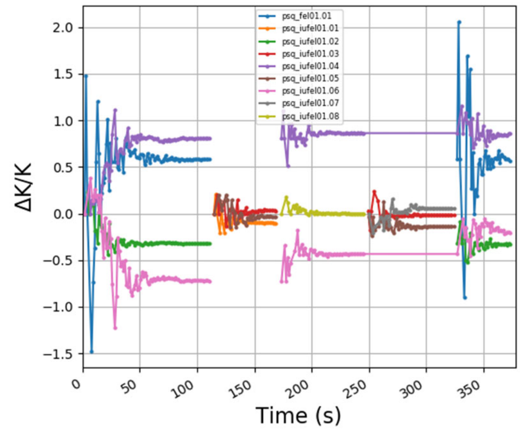

Figure 8: IUFEL1 Opt. - Quadrupoles kicks

CONCLCUSION

This tool achieved excellent results when applied starting from an electron beam optics computed by machine preparation software that drew on theoretical physical models.

Thanks to the use of this tool it has been possible to achieve values of usable radiation from the source that were hardly achieved by manual optimization operations (> 1e6 counts on the TF pyro).

It proved to be very useful in cases of configuration changes during user runs served by the FEL and allowing TeraFERMI to conduct experiments under previously prohibitive conditions, again considering the parasitic character of this beamline.

ACKNOWLEDGEMENTS

We are grateful to the whole FERMI team for the dedicated work and support during the experiment.

REFERENCES

[1] E.Allaria, et al., "The FERMI free-electron lasers", *J. Synchrotron Rad.* vol. 22, pp. 485-491, 2015. `doi:10.1107/S1600577515005366`

[2] G. Gaio, et al., "Automatic FEL Optimization at FERMI", in *Proc. ICALEPCS'15*, Melbourne, Australia, Oct. 2015, pp. 26-29. `doi:10.18429/JACoW-ICALEPCS2015-MOC3O03`

[3] G. Gaio, et al., "Advances in automatic performance optimization at FERMI", in *Proc. ICALEPCS'17*, Barcelona, Spain, Oct. 2017, pp. 352-356. `doi:10.18429/JACoW-ICALEPCS2017-TUMPA07`

[4] S. Di Mitri, et al., "Coherent THz Emission Enhanced by Coherent Synchrotron Radiation Wakefield", *Sci. Rep.*, vol. 8, p. 11661, 2018. `doi:10.1038/s41598-018-30125-1`

[5] S. Di Mitri et al., "Electron beam optics and trajectory control in the FERMI free electron laser delivery system", *Phys. Rev. ST Accel. Beams*, vol. 15, p. 012802, 2012. `doi:10.1103/PhysRevSTAB.15.012802`

[6] A. D. Bryne et al., "Upgrade to the transverse optics matching strategy for the FERMI FEL", presented at FEL'22, Trieste, August 2022, paper WEP04, this conference

ISBN: 978-3-95450-220-2 ISSN: 2673-5474 doi: 10.18429/JACoW-FEL2022-WEP23

[7] G. Gaio, S. Krecic, F. Tripaldi, "Online automatic performance optimization for the Elettra synchrotron", in *ICALEPCS'21*, Shanghai, China, 2022. doi:10.18429/JACoW-ICALEPCS2021-WEPV008

[8] J. Nelder and R. Mead, "A Simplex Method for Function Minimization", *Comput J.*, vol. 7, pp. 308-313, Jan. 1965.. doi:10.1093/COMJNL/7.4.308, corrections in doi:10.1093/comjnl/8.1.27

[9] C.J. Bocchetta *et al*. "FERMI@Elettra Conceptual Design Report", Sincrotrone Trieste, Trieste, Italy, Technical Report ST/F-TN-07/12, 2007

ISBN: 978-3-95450-220-2 ISSN: 2673-5474 doi: 10.18429/JACoW-FEL2022-WEP25

VIRTUAL DIAGNOSTIC FOR LONGITUDINAL PHASE SPACE IMAGING FOR THE MAX IV SXL PROJECT

J. S. Lundquist*, S. Werin, F. Curbis, Department of Physics, Lund University, Lund, Sweden

Abstract

Accurate and high resolution detection of the Longitudinal Phase Space (LPS) of the electron beam is a great advantage for operating and setting up a FEL. In the case of the soft X-ray FEL being proposed at the MAX IV synchrotron facility in Lund, this information will mainly be supplied by a Transverse Deflecting Cavity (TDC) which is currently being installed and scheduled for commissioning in the autumn (2022). Performing the LPS measurement with the future TDC is limited in two regards: it is destructive and may be low in resolution as compared to the maximum compression possible in the MAX IV linac. In this project we propose using machine learning tools to implement a virtual diagnostic to retrieve the LPS information non-destructively using fast, non-invasive measurements and critical set-points in the linac as inputs for a neural network. In this paper we summarize the current progress of this project which thus far has focused on simulation studies of the TDC and the training of a virtual diagnostic using the TDC's simulated output.

INTRODUCTION

The Soft X-ray Laser (SXL) is a free electron laser currently being proposed as an expansion to the existing synchrotron light facility MAX IV in Lund, Sweden. The SXL is designed as a extension to the operating linac, currently used to drive two electron storage rings as well as a Short Pulse Facility (SPF). The SPF currently hosts only one end-station (FemtoMAX), but two more beamlines are currently planned as new branches at the end of the linac. One is the SXL, where the beam will pass through a 156 m long undulator hall before reaching two experimental end-stations; the other line is reserved for a Transverse Deflecting Cavity (TDC). This is a diagnostic beamline, meant to produce new information of the state of beam, useful for operating the SXL. Figure 1 shows a detailed layout of the MAX IV linac with these proposed beamlines present. The TDC line operates by allowing the beam to pass through a particular accelerating structure which kicks the beam transversely, in order to turn it, in this case horizontally. This allows for a longitudinal image of the beam as it impacts on a screen further down the beamline. One can also pass the beam through a dipole magnetic field before the screen to retrieve information of the energy distribution of the beam. With these two techniques used in tandem one can get a full image of the Longitudinal Phase Space (LPS) of the beam, crucial information for operating the SXL optimally [1].

As the TDC requires the beam to impact on a screen this measurement is destructive and can not be performed in parallel with studies at the SXL beamlines. A non-destructive tool for extracting the same diagnostic information is thus highly attractive. For this project, the possibility of using Machine Learning (ML) methods to develop a virtual diagnostic monitoring this information is being investigated. The virtual diagnostic in this case would interpret non-destructive signals from the entire linac and then produce predictions of the TDC image without interacting with the beam. If this can be achieved with high reliability and accuracy, the operations of the current linac and the future SXL could be significantly improved. Similar projects have shown promising results [2, 3].

In this paper, the early strides of this project are summarized. This includes two main results: predictions of the TDC output based on simulation data and predictions of the beam's transverse image in a dispersive section of the linac based on real data collected during study time on the accelerator. These are referred to as the *simulated* and *experimental* case respectively. The following two sections will go into more detail on the simulation and experiment performed to generate the data used in training the constructed virtual diagnostics, followed by a section covering the machine learning methods used in the virtual diagnostic itself.

DATA COLLECTION

A crucial early step is finding the input channels one could possibly use for training the ML structures. For this project, we require non-destructive, fast measurements which are also correlated to the result of the destructive measurement of the TDC, i.e., they should have a strong dependence or influence on the energy and temporal distribution of the final beam. Below in Table 1 a summary of the different input channels selected, both for the simulation and experimental case, can be seen. Here, L01 refers to a specific early accelerating structure separated from the remainder of the linac by a bunch compressor, L02-19 are then referring to the rest of the 18 accelerating structures which have synchronized setpoints for phase and voltage.

These setpoints were then used as input to different ML structures, either outputting images, or scalar values for the position of the beam centroid. The following two subsections summarize the methods for procuring the data through simulation and experiment.

Simulation

The accelerator simulation code elegant was used for the simulations of the TDC output. Scans were performed of the RF parameters summarized in Table 1, at first systematically to find the limits in each channel, then using 1000 random setpoints from the tested range to produce the final dataset.

* johan.lundquist@maxiv.lu.se

ISBN: 978-3-95450-220-2 ISSN: 2673-5474 doi: 10.18429/JACoW-FEL2022-WEP25

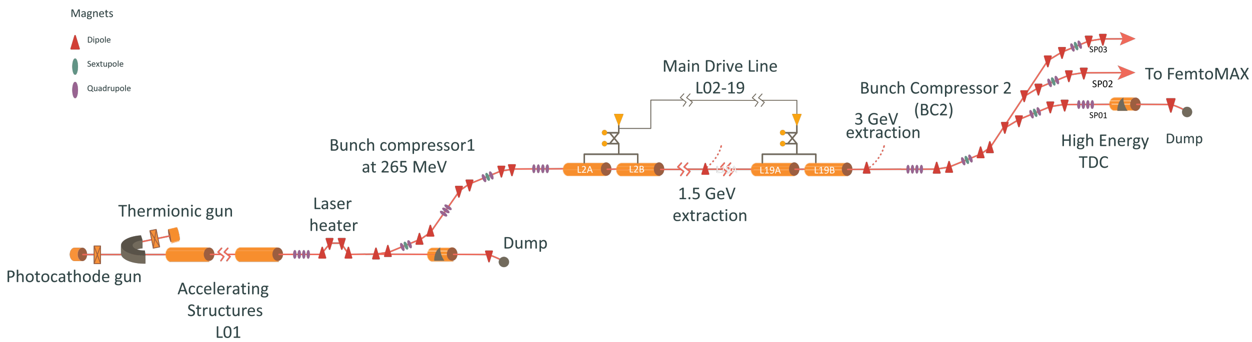

Figure 1: Detailed layout of the MAX IV linac with the currently proposed components of two TDCs and a laser heater, as well as the proposed beamline SP03, going to the SXL.

Table 1: Input Channels from Simulation and Experiment

Input	Range
Simulation	
Input	**Range**
L01 Phase	±20°
L02-19 Phase	±20°
L01 Voltage	±2.5 MV
L02-19 Voltage	±2.5 MV
21 BPMs, X and Y	
Experiment	
Input	**Range**
L01 Phase	170.5-181.5°
L02-19 Phase	2.0-16.0°
L02-19 RF Filltime	2.75-3.15 μs
21 BPMs, X and Y	

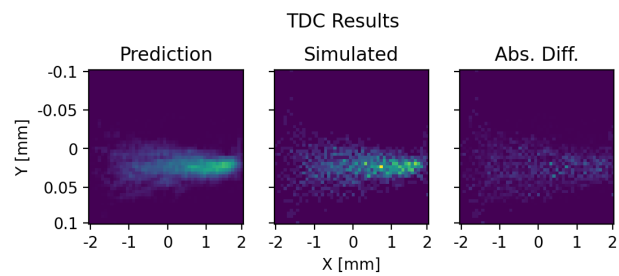

Figure 2: Example of prediction on simulation data for the TDC screen. Leftmost image shows the prediction of the virtual diagnostic, center image shows the corresponding result from the simulation, and the rightmost image shows the absolute difference between the other two.

For each setpoint, 2000 particles were simulated passing through the linac and into the TDC line. Here, the TDC structure itself was on, but the dipole extracting the energy information was deactivated in order to construct a simpler case for the networks to handle. Each setpoint resulted in a change to the temporal distribution of the beam, and thus changing the shape of the beam on the image.

Elegant outputs the transverse position for each of the 2000 particles. This information was reformatted into a 2D histogram of 50 × 50 bins, as to imitate the output of a CCD camera, as will be used in the real TDC beamline. The simulations were set to keep the beam within a 4×0.2 mm^2 area, adjusting the strength of dipole magnets as to retain the central position of the entire beam. An example of the results of this simulation can be seen in the central image of Fig. 2.

Experiment

Beamtime with the MAX IV linac was scheduled to allow the collection of images recorded on a YAG screen in a dispersive section of the second bunch compressor. Such images show the temporal profile of the beam, similar to the process in the TDC beamline. Initial scans of the L01 and main linac phases were performed in steps of 0.5°, then the SLED cavity fill-time of the main linac was stepped through the range indicated in Table 1 in steps of 0.1 μs, with a main linac phase scan performed at each step. For each scan step, 5-10 images were recorded from the YAG screen. In total 1150 images were collected for use in the virtual diagnostic.

The full images were 1200 × 1080 pixels in size, far larger than the simulated 2D histograms. In order to limit the required information contained in the predictions by the networks, these images were sliced down to 200 × 50 pixels. Slicing was done about the point of maximum intensity after the application of a background subtraction and median filtering. In most cases this resulted in a clear image of the entire beam profile, such as the center image in Fig. 4.

VIRTUAL DIAGNOSTIC

The term *virtual diagnostic* in this case refers to an artificial neural network (ANN) mapping the different non-destructive signals from the main linac to the desired images from the TDC, or the screen in the dispersive section of the bunch compressor in the experimental case. An ANN consists of many layered nodes with weighted connections between them. By updating the weights associated with these connections using a defined loss and optimization function, a network can extract the complex mapping between inputs and outputs [5]. For this project, this type of structure will be used to map the connection between specific BPM sig-

ISBN: 978-3-95450-220-2 ISSN: 2673-5474 doi: 10.18429/JACoW-FEL2022-WEP25

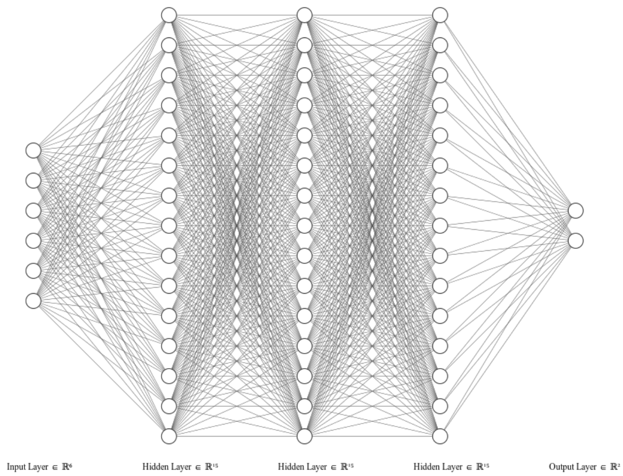

Figure 3: Simplified example of the ANN structure, the circles representing nodes and the lines showing the trainable connections between them. The two output nodes would in this case be the X and Y beam centroid positions. Image constructed using NN-SVG tool [4].

nals and linac setpoints to the outcome of a simulated TDC measurement or to the output of a measured YAG screen image in a bunch compressor.

Two types of networks were constructed for the results in this paper: one type consisting solely of these densely connected nodes for use in predicting the location of the beam centroid on the screen, a simplified example of which can be seen in Fig. 3. The second type of network was constructed with the first few layers being of this same type, densely connected nodes, but with the final layers utilizing a convolutional neural network (CNN) structure. A CNN type of network applies weights to inputs as a matrix of weights moving as a filter across a larger input matrix. The input vector was reshaped into many smaller matrices, which were then put through the convolutional layers. The output matrix from these CNN layers was the final image prediction.

For the simulated results, only the type of network using CNN layers was necessary, as the beam was always centered within the same $4 \times 0.2\ \mathrm{mm}^2$ area, and thus no prediction of the beam centroid was necessary. Here, we utilized a network structure and training parameters as summarized in Table 2.

For the experimental results, the beam was not centered on the intercepting screen, but rather moved across the screen while changing the energy. When the 1200×1080 pixel images were sliced down to 200×50 pixels, the information of where on the screen the beam landed was lost. This is where the simpler ANN structure was utilized, to predict the location of the beam centroid on the screen, while the convolutional type network was used for the image predictions, just as in the simulated case, with a structure and training parameters similar to those summarized in Table 2.

Table 2: Network Structure and Training Parameters

Structure	200 Dense Nodes 200 Dense Nodes 2500 Dense Nodes $100 \cdot 2 \times 2$ CNN Kernels $4 \cdot 4 \times 4$ CNN Kernels $1 \cdot 5 \times 5$ CNN Kernels
Data Sets	1000 Total Images 900 For Training 100 For Predictions
Activation Function	ReLU
Loss Function	Mean Absolute Error
Optimization Algorithm	ADAM
Learning Rate	10^{-3}
Training Epochs	1200
Batch Size	50

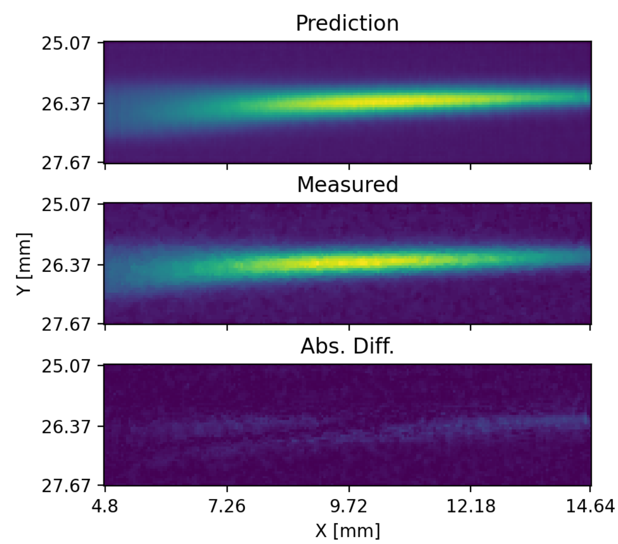

Figure 4: Example of prediction on measured data for the bunch compressor screen. Top image shows the prediction of the virtual diagnostic, center image shows the corresponding measured result, and the bottom image shows the absolute difference between the other two.

RESULTS

Figure 2 shows an example of the results of the *elegant* simulations and the virtual diagnostics' predictions of the TDC output. The leftmost image shows a prediction from the ML model, the center image shows the corresponding result from the simulation, and the rightmost image shows the absolute difference between the other two images. In total, across the 100 images used for predictions, the predictions of the virtual diagnostic reached an RMS error of 12.5 %. The size of the data set could undoubtedly be expanded here, but during simulation the variation in input data was prioritized over volume of images or simulated particles. Furthermore, the particle distributions are simplified by the deactivation of the final dipole magnet extracting the energy distribution.

ISBN: 978-3-95450-220-2 ISSN: 2673-5474 doi: 10.18429/JACoW-FEL2022-WEP25

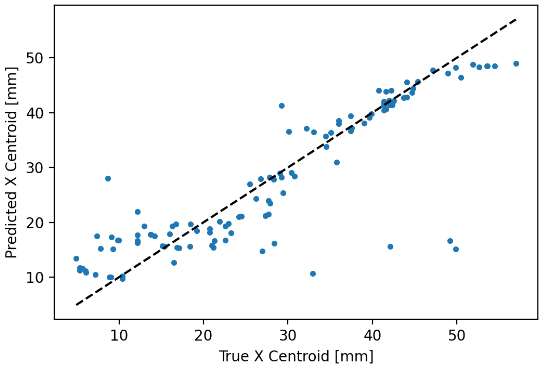

Figure 5: Centroid predictions on real data for bunch compressor screen. The dashed slope one line represents ideal predictions.

For a more complete image of the LPS, the dipole should be activated in future simulations. However, within these limitations we see promising results.

Figure 4 shows an example of the image results of the beamtime and data processing of the experimental results for one set-point, along with an example of the virtual diagnostics' predictions. The top image shows the prediction of the virtual diagnostic for this specific set-point, the center image shows the corresponding measured image on the YAG screen, and the bottom image shows the absolute difference between the other two images. In total, on the 115 measured images saved for predictions, the image predictions of the virtual diagnostic reached an RMS error of 17.3 %. The axes of the prediction image were set using the separate neural network configured to predict the beam centroid on the screen.

Figure 5 shows these centroid predictions, plotted against each prediction's corresponding true value. Thus the ideal virtual diagnostic would form a slope one line, which is also shown in Fig. 5 as the dashed line. Specifically, this figure shows the predictions for the horizontal position of the beam centroid, the axis along which the beam primarily moved with different set-points, as it is the plane of bending for the dipole magnet involved. In total on the 115 centroid positions saved for prediction, the network reached a RMS error of 0.63 mm in the horizontal plane and a RMS error of 1.06 mm in the vertical plane.

OUTLOOK

Virtual diagnostics have been constructed and trained to predict images, both measured and simulated, dependent on the energy and temporal profile of the beam. These predictions have reached a promising level of accuracy with limited time for data collection and training the networks, showing the possibility for the project to develop further in the future. A clear direction is to introduce the energy distribution to the TDC simulations and produce good predictions on such a dataset. Further in the future, the MAX IV TDC should be operational and real measurements can be performed to construct all new datasets for training networks, which could then be used in normal operation of the linac.

REFERENCES

[1] D. Olsson *et al.*, "A Transverse Deflecting Cavity Prototype for the MAX IV LINAC," in *Proc. IBIC'19*, Malmö, Sweden, Sep. 2019, pp. 575–577. doi:10.18429/JACoW-IBIC2019-WEPP025

[2] C. Emma, A. Edelen, M. J. Hogan, B. O'Shea, G. White, and V. Yakimenko, "Machine learning-based longitudinal phase space prediction of particle accelerators," *Phys. Rev. Accel. Beams*, vol. 21, p. 112 802, 2018. doi:10.1103/PhysRevAccelBeams.21.112802

[3] C. Emma, A. Edelen, A. Hanuka, B. O'Shea, and A. Scheinker, "Virtual diagnostic suite for electron beam prediction and control at facet-ii," *Information*, vol. 12, no. 2, 2021. doi:10.3390/info12020061

[4] A. LeNail, "Nn-svg: Publication-ready neural network architecture schematics," *J. Open Source Softw.*, vol. 4, no. 33, p. 747, 2019. doi:10.21105/joss.00747

[5] I. Goodfellow, Y. Bengio, and A. Courville, *Deep Learning*. MIT Press, 2016, http://www.deeplearningbook.org.

ISBN: 978-3-95450-220-2 ISSN: 2673-5474 doi: 10.18429/JACoW-FEL2022-WEP27

DEVELOPMENT OF THE RF SYSTEMS FOR THE PolFEL ACCELERATOR*

J. Szewiński†, P. Bartoszek, K. Chmielewski, K. Kostrzewa, T. Kowalski, P. Krawczyk, R. Nietubyć, D. Rybka, Z. Wojciechowski, National Centre for Nuclear Research, Otwock-Świerk, Poland

Abstract

PolFEL stands for Polish Free Electron Laser, the first FEL research infrastructure in Poland. This facility is under development, and it will operate in three wavelength ranges: IR, THz and VUV, using different types of undulators. Machine will be driven by 200 MeV linear superconducting accelerator, which will operate in both, pulsed wave (PW) and continous wave (CW) modes. This contribution will describe the concept, current status and the first results of the RF systems development.

INTRODUCTION

PolFEL will be a 4-th generation light source, based on the 200 MeV superconducting linear accelerator [1]. It will generate coherent light in 3 ranges: THz, IR and VUV.

To deliver proper beam conditions, a stable RF field is required in the accelerator cavities, and to achieve this, a high-power and low-level RF systems are required. PolFEL accelerator will be driven by a solid state amplifiers, in the single cavity regulation mode where one cavity will be driven by one amplifier. For such control mode, vector sum calculation is not needed, which simplifies the the RF control system in comparison to such Free Electron Lasers such as X-FEL or FLASH.

To simplify the LLRF system even more, a direct sampling technique is planned to be implemented in PolFEL [2]. This technique reduces the need for the separate devices such as downconverters and LO generation modules. The key part of the direct sampling LLRF system will be the clocking solution for the ADCs, but since the whole clock tree will be integrated into the ADC board, it can be optimized for this particular application.

HIGH POWER RF SYSTEM OVERVIEW

The aim of the RF system is to deliver power to accelerating modules which is needed to accelerate the electron beam. The accelerating modules of in PolFEL accelerator will be made of TESLA-type, 9-cell RF Structures. Each criomodule will have two such RF structures, but each structure will be driven and controlled individually. RF power from solid state amplifiers to the criomodules will be delivered using WR650 waveguides. Solid state amplifiers will be placed in the hall next to the accelerator tunnel. Because construction of PolFEL accelerator will utilize existing buildings, the design of the waveguides distribution system is not straight-forward and requires significant effort.

* Work supported by National Information Processing Institute, https://opi.org.pl/

† J.Szewinski@ncbj.gov.pl

Table 1: SSA Key Parameters

Parameter	Value
Lower frequncy range (-3dB)	≤ 1270 MHz
Upper frequecy range (-3dB)	≥ 1310 MHz
Output power in pulsed mode	≥ 7kW
Maximal pulse duration	≥ 1 ms
Output power in continous mode	≥ 5kW
Maximal power of input signal	≥ 10 dBm
Amplifier gain	≥ 60 dB
Max. required power supply level	≤ 20 kW
Operational temerature range	5 °C - 40 °C

One of the features that helps in the wageguide design is single cavity regulation mode. Because of this, there is no need for splitting the RF power withing the waveguide distribution system. Each waveguide will deliver RF power directly from the solid state RF amplifier to the RF structure. In such configuration, circulators and loads does not have to be placed close to the criomodules and can be placed next to the RF amplifiers out of radiation impact area, which also helps in the design.

Solid State Amplifier

The RF power in the PolFEL accelerator will be generated by solid state amplifiers (SSA). Because of PolFEL will operate in continuous mode a dedicated RF power source is needed. Dedicated RF amplifier for PolFEL will be designed and delivered by the Kubara Lamina S.A. company [3]. The requirements for the RF amplifier are following show in Table 1.

By the time of writing this paper, the prototype of the SSA amplifier was under development (Fig. 1).

LOW-LEVEL RF SYSTEM OVERVIEW

High speed and high bandwidth ADCs makes possible to sample directly the RF signal of the frequency 1.3 GHz. Well known and also evaluated [4,5] for this purpose is Texas Instruments ADS5474, which input bandwidth covers range up to 1.4 GHz. Possibility of direct RF sampling allows to significantly simplify the LLRF hardware.

The components of the PolFEL LLRF system are similar to the ones used at X-FEL [6] because of the same fundamental frequency 1.3 GHz, but the layout of the system is more like the one used at ESS [7], because ESS operates also in single cavity regulation mode.

LLRF system scheme in the Fig. 2 show the configuration used at ESS. Configuration used at ESS for controlling

ISBN: 978-3-95450-220-2 ISSN: 2673-5474 doi: 10.18429/JACoW-FEL2022-WEP27


Figure 1: Prototype of the solid state amplifier for PolFEL under development.

single cavity occupies 3 slots in the MTCA chassis, and results in total number of 6 devices (3xAMC + 3xRTM) for single cavity (Fig. 2). One slot is occupied by the main LLRF Controller, which uses both boards: AMC with FPGA and data converters, and RTM with the downconverters and vector modulator. Other two slots are occupied by the piezo controller, and LO clock signal generator.

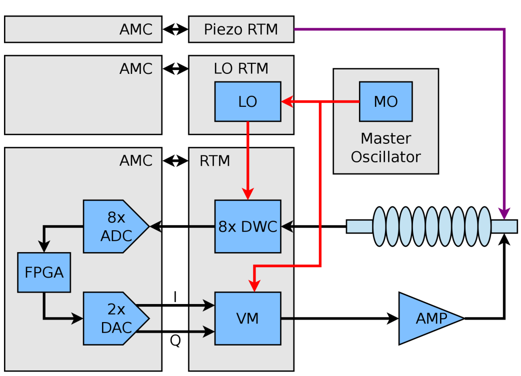

Figure 2: ESS LLRF System architecture.

The concept of the PolFEL LLRF controller (Fig. 3) is much simpler, for single cavity control single MTCA chassis slot is occupied. From the rear side of the slot the Piezo RTM will be placed, and from the front side an AMC FMC Carrier will be used. All LLRF specific infrastructure will be placed on the custom dual FMC board. With respect to the amount of connected I/O pins in the FMC connectors, any MTCA.4 FMC carrier can be used. This configuration does not require down-converters, so separate LO generation device is not required as well.

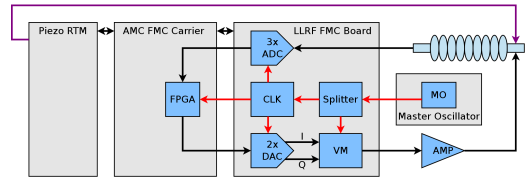

Figure 3: PolFEL LLRF System architecture.

The function of the LO generation is performed by proper circuitry integrated in the FMC board along with the ADCs and DACs. The ADC sampling clock is generated directly from the 1.3 RF signal, and the distance from RF input to the ADC or vector modulator is less than 10 cm. All clock distribution for a single LLRF system will be made on the single PCB.

Initial Tests of LLRF with the Copper Cavity

To evaluate described concept, a test setup has been assembled. To make tests as much similar to the final application, a 1.3 GHz, 3-cell, copper cavity has been used.

As a first step, the cavity has been measured and couplers tuned using Vector-Network Analyzer (Fig. 4). In the next step, the field in the cavity has been excited using the RF generator on one side, while the signal from the other coupler was connected to FPGA based system (Xilinx KC705 evaluation board) with ADS5474 ADC attached on the Curtiss-Wright ADC511 FMC mezzanine. Using digital I/Q detection, it was possible in the FPGA to restore the amplitude and phase of the cavity field.

In order to close the feedback loop, vector modulator was needed. For the purpose the FMC board with dual-channel DAC and vector-modulator has been designed, and manufactured (Fig. 5).

Having all components available, the complete setup has been assembled (Fig. 6). Signal from the RF generator has been split and delivered to vector modulator as source RF signal to be modulated, and to clock synthesizer, which generates frequencies suitable for ADCs and DACs. Clock synthesizer can additionally provide clock signal to the FPGA

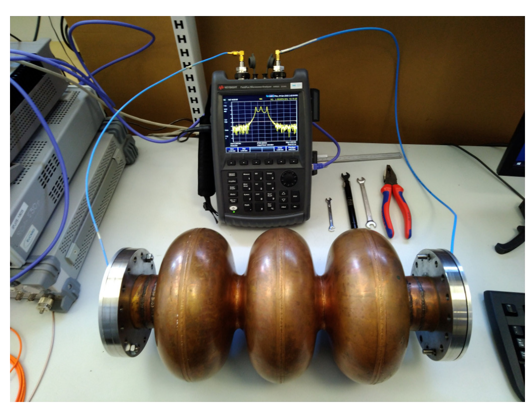
Figure 4: Cavity characterized using VNA.

ISBN: 978-3-95450-220-2 ISSN: 2673-5474 doi: 10.18429/JACoW-FEL2022-WEP27

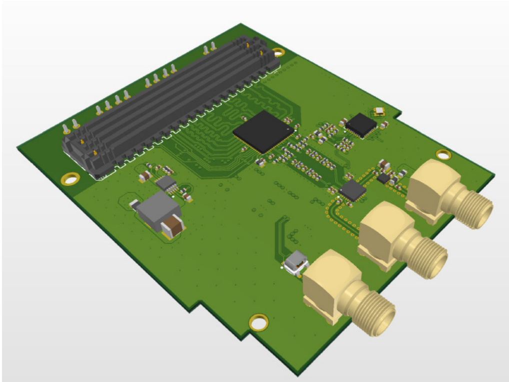

Figure 5: Vector modulator FMC board.

device using FMC_M2C signals, but this was not necessary because ADCs and DACs provides clock synchronized with their data.

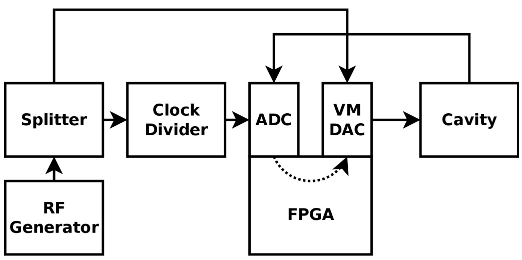

Figure 6: The scheme of the test setup.

Finally, using presented test setup, feedback loop on the copper cavity has been closed. Images below (Figs. 7, 8, 9) shows the single pulse of the input and output of the controller.

Figure 7 shows amplitude and phase the output signal from the controller on top of the feed-forward value (the ideal drive signal). The difference between feed-forward and output signal is caused by working closed loop feedback.

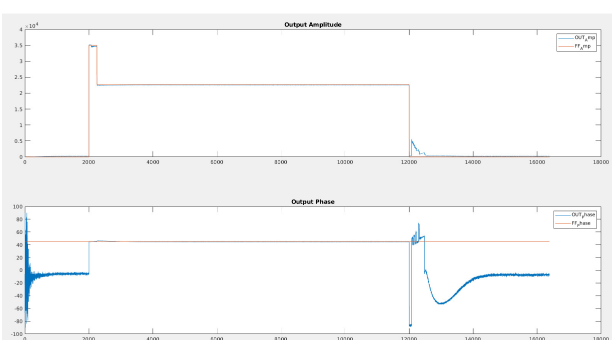

Figure 7: Controller output.

Figure 8 shows similar image like Fig. 7, but it shows the amplitude and phase of the controller input signal on top of the set-point value (expected cavity field).

To show better the input signal on top of the set-point Fig. 9 shows magnified amplitude and phase regions of the RF pulse.

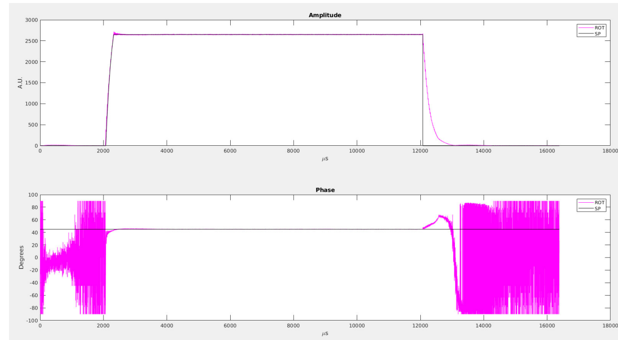

Figure 8: Controller input.

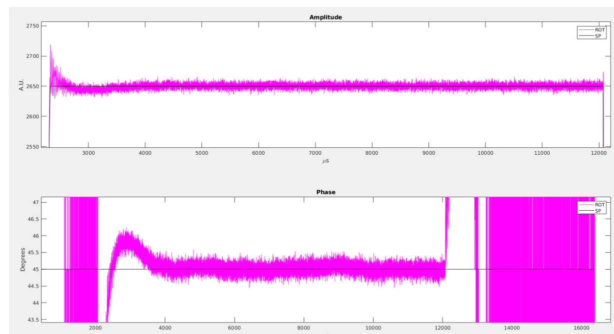

Figure 9: Controller input (magnified).

REFERENCES

[1] G. Wrochna *et al.*, “On the PolFEL free electron laser projec”, *Synchrotron Radiation in Natural Science*, vol. 8, pp. 1-7, 2009.

[2] T. Kowalski *et al.*, “Experimental Evaluation of Sub-Sampling IQ Detection for Low-Level RF Control in Particle Accelerator Systems”, *Sensors*, vol. 22, pp. 1-17, 2021. doi:10.3390/s22010038

[3] KUBARA LAMINA S.A., https://kubaralamina.com/

[4] Z. Geng and S. Simrock, “Evaluation of Fast ADCs for Direct Sampling RF Field Detection for the European XFEL and ILC”, in *Proc. LINAC’08*, Victoria, Canada, Sep.-Oct. 2008, paper THP102, pp. 1030–1032.

[5] Y. Okada *et al.*, “Direct Sampling of RF Signal for 1.3 GHz Cavity”, in *Proc. PAC’09*, Vancouver, Canada, May 2009, paper WE5PFP088, pp. 2216–2218.

[6] J. Branlard *et al.*, “The European XFEL LLRF System”, in *Proc. IPAC’12*, New Orleans, LA, USA, May 2012, paper MOOAC01, pp. 55–57.

[7] A. J. Johansson, F. Kristensen, A. M. Svensson, and R. Zeng, “LLRF System for the ESS Proton Accelerator”, in *Proc. IPAC’14*, Dresden, Germany, Jun. 2014, pp. 2465–2467. doi:10.18429/JACoW-IPAC2014-WEPME079

ISBN: 978-3-95450-220-2 ISSN: 2673-5474 doi: 10.18429/JACoW-FEL2022-WEP28

RF CONDITIONING AND FIRST EXPERIENCES WITH THE PolariX TDS AT PSI

P. Craievich*, J. Alex, C. Beard, H.-H. Braun, M. D'Amico, R. Fortunati, R. Ganter, Z. Geng, R. Kalt, T. Kleeb, T. G. Lucas, F. Marcellini, R. Menzel, M. Pedrozzi, E. Prat, S. Reiche, W. Tron, R. Zennaro
Paul Scherrer Institut, Villigen-PSI, Switzerland

Abstract

In 2017, a collaboration between DESY, PSI and CERN was established with the aim of developing and building seven advanced X-Band Transverse Deflection Structures (TDS) with the novel feature of a variable polarization of the deflecting force. Seven deflectors were produced by PSI, of which, five were installed in three experiments at DESY while the remaining two were installed in the ATHOS soft X-ray beamline in SwissFEL. The ultimate goal of this project was to provide sub-fs resolution for soft X-ray pulse profiles. In early 2022, the X-band power source of the TDS for SwissFEL was completed and system commissioning began. This contribution summarizes the first deflection experiments performed.

INTRODUCTION

Several experiments at DESY (FLASH II, FLASHForward, SINBAD) and PSI (ATHOS at SwissFEL) were interested in the utilization of high gradient X-band Transverse Deflection Structure (TDS) systems for high resolution longitudinal diagnostics. In this context, a collaboration between DESY, PSI and CERN was established to develop and build an advanced modular X-Band TDS system which included the novel feature of providing variable polarization of the deflecting force. This structure was aptly named the Polarizable X-band (PolariX) TDS [1, 2]. In recent years, seven deflectors were built in total and installed at the various facilities. Currently, the two deflectors in FLASH II and the one FLASHForward are routinely used in operation while the two installed in SINBAD are ready for commissioning as soon as the RF system will be available. The remaining two were installed in the post-undulator diagnostic section in the ATHOS soft X-ray beamline at SwissFEL [3, 4], with the aim of providing sub-fs resolution for soft X-ray pulse profiles. In early 2022, the X-band power source for the TDS in ATHOS was completed and commissioning of the whole TDS system has begun. This contribution summarizes the progress of the project at PSI, including the results from the first month of RF conditioning and the first set of experiments performed with variable polarization.

THE PolariX TDS SYSTEM

The SwissFEL project at PSI consists of a 6 GeV accelerator facility feeding two undulator beamlines, Aramis [5]

Table 1: RF parameters for two PolariX TDSs installed in ATHOS. The frequency corresponds to operational temperatures of 33.3° and 32.5° for the TDS1 and TDS2, respectively.

Cell parameter			**Unit**
Frequency	11995.2		MHz
Phase advance/cell	120		°
Iris radius	4		mm
Iris thickness	2.6		mm
Group velocity	-2.666		%c
Quality factor	6490		
Shunt impedance	50		MΩ/m
1x TDS parameter			**Unit**
n. cells	120		
Filling time	129.5		ns
Total length	1160		mm
Power-to-voltage	6.1		MV/(MW)$^{1/2}$
2x TDS + BOC			**Unit**
BOC Q_0	157800		
BOC β	7.88		
RF pulse width	1.5	1.0	µs
Power-to-voltage	19.1	17.7	MV/(MW)$^{1/2}$

and Athos [3, 4], operating in parallel at 100 Hz. The Athos line consists of a fast-kicker magnet placed at a beam energy of 3.2 GeV, a dog-leg transfer line, a small linac, and 16 APPLE X undulators [6]. It is designed to operate in advanced modes of operation slightly different from standard SASE operation and produce soft X-ray FEL radiation with pulse durations ranging from a few to several tens of femtoseconds [7]. Electron beam diagnostics based on a TDS system placed downstream of the undulators (post-undulator TDS) in conjunction with an electron beam energy spectrometer can indirectly measure the pulse length of these ultra-short photon pulses by analysing the induced energy spread on the electron bunch due to the FEL process.

Figure 1 shows a schematic layout of the ATHOS post-undulator diagnostic section. Beam slice emittance in both transverse planes are investigated by a multi-quadrupole scan technique combined with the TDS. By means of the TDS, the beam is vertically and horizontally streaked and a multi-quadrupole scan is performed in the horizontal and vertical direction, respectively, with the constraint of keeping the vertical/horizontal beam size constant over the whole scan. For this purpose, five quadrupoles were foreseen to be placed downstream of the TDS. Reconstruction of the longitudinal

* paolo.craievich@psi.ch

ISBN: 978-3-95450-220-2 ISSN: 2673-5474 doi: 10.18429/JACoW-FEL2022-WEP28

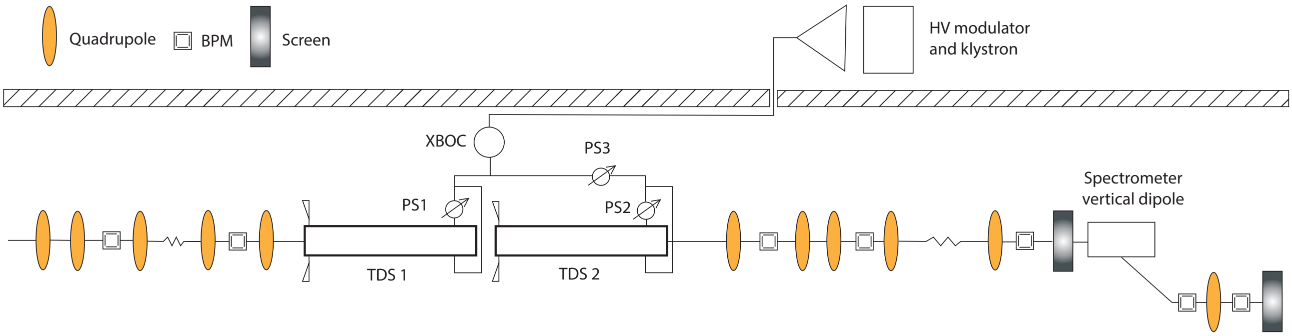

Figure 1: Schematic layout of the diagnostic section after the ATHOS undulators. The overall length is approx. 35 m while the waveguide lengths from the klystron output to the TDS inputs are approx. 11 m and approx. 12 m for TDS1 and TDS2, respectively.

phase-space is performed by means of the spectrometer line. The β-function, β_d, at the deflector is determined by five quadrupoles placed upstream of the TDS with the aim of having the same β_d for different polarizations. The time resolution is on sub-fs scale if the integrated deflecting voltage is more than 50 MV with a β_d=50 m and a normalized emittance of 300 nm. Further details on the specifications and expected performance can be found in [8].

Figure 1 also shows a schematic of the RF system and the position of the klystron with its High-Voltage (HV) modulator. The RF system consists of the two deflectors, the waveguide network with the X-band BOC pulse compressor (XBOC), and three phase shifters. All waveguide RF components including the XBOC and phase shifters were designed and built at PSI. An initial estimate of the total attenuation of the power distribution system, including waveguide attenuation and insertion losses, found a value of -1.25 dB corresponding to a power loss of 25%. Figure 2 shows a picture with the two TDSs installed in the bunker. The TDSs are constant impedance, backward travelling wave structures. Table 1 lists the RF parameters for the base cell, a single TDS and for the whole system consisting of two TDSs with the XBOC. Figure 3 shows a picture of the HV modulator and the CPI VKK-8311 50 MW X-band klystron installed in the technical gallery. The HV modulator was also developed and built in-house and is capable of delivering a pulsed voltage of up to 400 kV with a pulse length of 3.0 µs (fwhm).

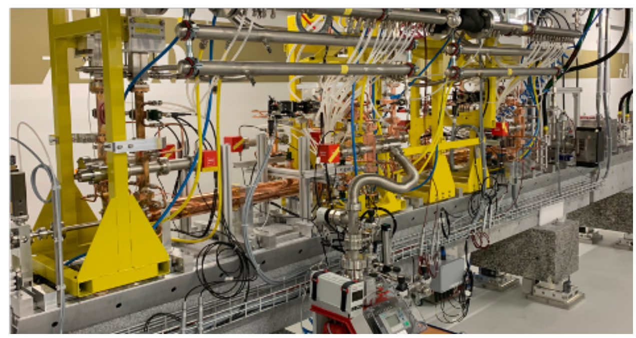

Figure 2: Picture of the two PolariX TDS installed in the post-undulator diagnostic section in ATHOS.

Figure 3: Picture of the 50 MW X-band klystron and of the its PSI HV modulator.

RF CONDITIONING

In the first weeks of RF conditioning the power available from the RF source was limited to 10 MW due to a problem with the power supply control of the vacuum pump installed in the klystron. Once the problem was resolved, conditioning continued with RF power from the klystron being increased up to 30 MW. The conditioning strategy involved keeping a constant pulse length for the compressed RF pulse into the TDSs while increasing the total RF pulse length from the klystron to increase the compression factor of the XBOC. The compressed RF pulse length in the TDS was 150 ns, a value close to the filling time of the TDSs. Figure 4 shows the RF power and pulse length at the klystron output as a function of the number of pulses during operation at an RF pulse repetition rate of 100 Hz. After about three weeks of integrated conditioning time, a peak power from the klystron of 30 MW with a total RF pulse length of 1 µs was achieved. Assuming a flat klystron voltage pulse, this corresponds to a peak power at the TDS inputs of 67 MW and thus an inte-

ISBN: 978-3-95450-220-2 ISSN: 2673-5474 doi: 10.18429/JACoW-FEL2022-WEP28

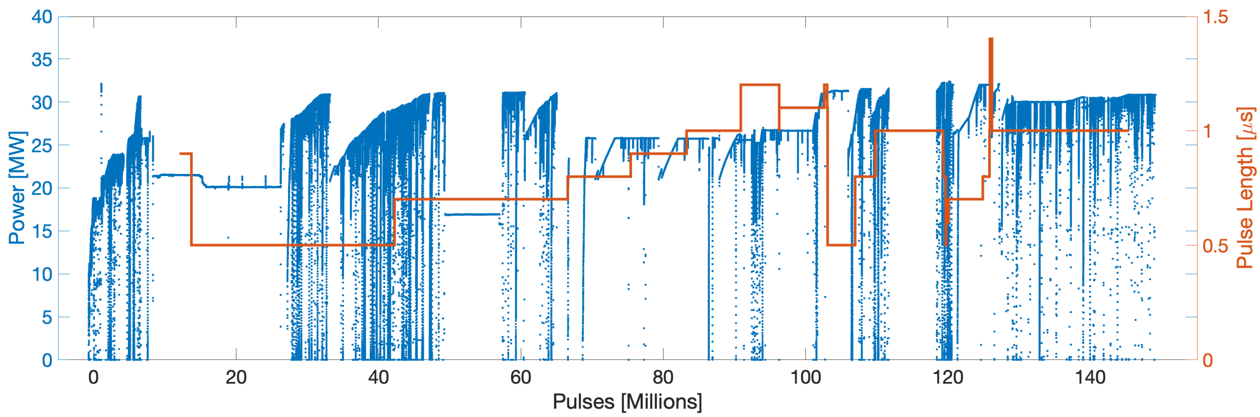

Figure 4: Conditioning curve of the PolariX TDSs illustrated as the klystron drive power (blue) and total RF pulse length (red).

grated deflection voltage of approximately 84 MV, including the attenuation of the power distribution system. The simulations carried out during the design phase [1] showed that the electric and magnetic field maxima are located in the input matching cell and that at this power level they should be around 172 MV/m and 615 kA/m respectively. The value of the modified Poynting vector, on the other hand, is localised in the regular deflector cells and should be about 5.4 MW/mm^2. For now, the conditioning at these power levels has only been carried out for the horizontal polarisation, and will continue in the coming weeks with the other polarizations starting with the vertical polarization.

To understand the structures' high power performance, the breakdown location can be determined using a time-of-propagation difference, t_d, for the transmitted and reflected RF signals during a breakdown event [9]. This difference is expressed in nanoseconds where the zero nanoseconds represents the RF input of the structure and the filling time (130 ns) represent the RF output of the structure. Given the structure is constant impedance there's a linear mapping of the time-of-propagation to the physical location of the breakdown. Figure 5 illustrates the number of breakdown events for both TDSs as a function of t_d. It can be observed that the total number of breakdowns decreases along the structures. This corresponds to the exponential attenuation of the surface electric field along the structure itself and is expected in a constant impedance structure.

FIRST STREAKING AND VARIABLE POLARIZATION

The phasing of the three phase shifters, PS1, PS2 and PS3 in Fig. 1, was the first task performed with the electron beam. This was carried out at low RF power from the klystron (300 kW), while measuring the position of the beam centroid on the BPMs placed downstream of the TDSs. Once the reference phases were defined, two of the phase shifters, PS1 and PS2, were used simultaneously to change the polarization of the deflecting force while the third phase shifter, PS3, ensured synchronism between the two TDSs.

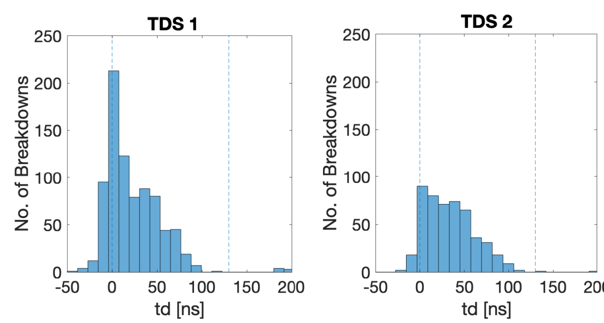

Figure 5: Number of breakdown events in the two TDSs as a function of the time-of-propagation difference, t_d, for the transmitted and reflected RF signals during a breakdown event.

The global RF phase (phase of klystron driver), on the other hand, was used to change the synchronization phase between the electron bunch and electromagnetic field once the polarization of the deflecting force had been defined. Figure 6 shows the position of the bunch centroid on a BPM placed downstream of the TDSs as a function of the global RF phase (circles). This was performed for different polarizations of the deflecting field where each color represents a polarisation variation of 5°.

Furthermore, with the aim of verifying the functionality of the whole system, a preliminary measurement campaign was carried out to measure the bunch length, temporal profile and longitudinal phase-space at the spectrometer. Figures 7, 8 and 9 show the results of the first streaking when the RF power from the klystron was limited at 10 MW. The duration and time profile of the electron bunch were measured in the so-called zero-crossings, which are separated by 180-degree in phase. Taking the average of the two measurements, the pulse duration was found to be 21 fs (rms) with a resolution of 2.36 fs, and a calibration factor of 33.89 µm/fs. Another important piece of information that came out from the measurements was the jitter of the arrival time, which was estimated to be 9 fs (rms). This last value confirms

ISBN: 978-3-95450-220-2 ISSN: 2673-5474 doi: 10.18429/JACoW-FEL2022-WEP28

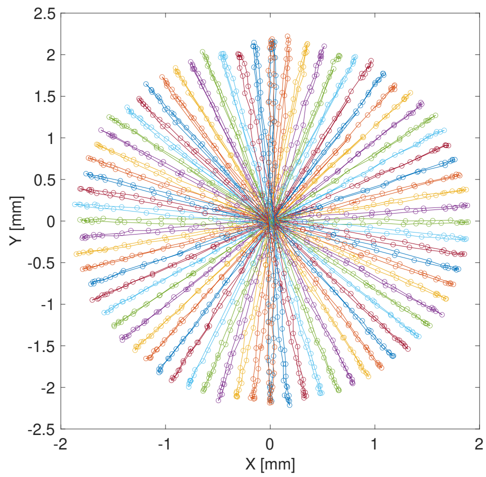

Figure 6: Variable streaking at low deflecting voltage.

the outstanding stability of SwissFEL's linac also for the ATHOS beamline.

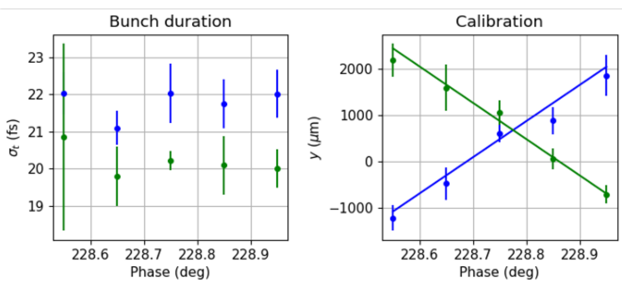

Figure 7: Calibration factor and bunch duration measurements. Blue: first zero-crossing, Green: second zero-crossing. Calibration factor 33.89 µm/fs, bunch duration 21.0 fs (rms), time resolution 2.36 fs (rms), arrival time jitter 9.0 fs (rms).

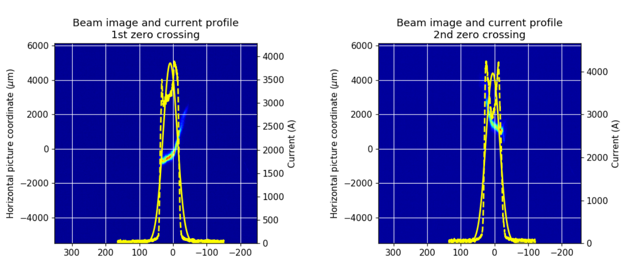

Figure 8: Bunch temporal profile measurements. Left: first zero-crossing, Right: second zero-crossing.

The last measurement performed in this measurement campaign was the reconstruction of the longitudinal phase-space. Figure 9 shows the image taken in the spectrometer with the TDSs switched off (left) and TDSs switched on (right). As can be clearly observed from this figure when the TDSs are turned on, a clear correlation between the horizontal position and the time duration of the bunch is introduced.

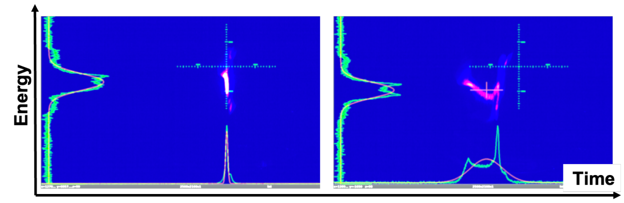

Figure 9: Reconstruction of the longitudinal phase-space at the spectrometer. Left: TDSs in OFF, Right: TDSs in ON.

CONCLUSION

This paper presented the project status of PolariX TDSs at PSI. These structures are used in the diagnostic section of the ATHOS beamline in SwissFEL and a brief description of their integration in the whole system was presented. The RF system includes the two TDSs, an X-band BOC pulse compressor, and an X-band klystron and a HV modulator. Except for the klystron, all waveguide components, the XBOC and the HV modulator were designed and manufactured at PSI. The analysis of the RF conditioning and breakdown events of the first phase of conditioning was presented. Assuming a flat klystron voltage pulse, an integrated deflecting voltage of 80 MV has been obtained so far, corresponding to a surface electric field of 250 MV/m. However, this conditioning activity is in its initial stage and will continue in the coming months including for different polarizations. A first set of measurements with variable polarization was also described together with the first results of bunch length, profile and longitudinal phase-space. The next measurement campaign, scheduled for September, will focus on achieving the target resolution by optimizing the RF system, diagnostic line optics and emittance.

ACKNOWLEDGEMENTS

We thank all the technical groups involved in the installation and commissioning of this complex system. Thanks also go to our colleagues at CERN and DESY involved in this collaboration for the useful discussions.

REFERENCES

[1] P. Craievich, A. Grudiev, B. Marchetti, *et al.*, "Novel X-band transverse deflection structure with variable polarization", *Phys. Rev. Accel. Beams*, vol. 23, p.112001, 2015. `doi.org/10.1103/PhysRevAccelBeams.23.112001`

[2] B. Marchetti, A. Grudiev, P. Craievich, *et al.*, "Experimental demonstration of novel beam characterization using a polarizable X-band transverse deflection structure", *Sci. Rep.*, vol. 11, p. 3560, 2021. `doi.org/10.1038/s41598-021-82687-2`

[3] R. Abela *et al.*, "Athos Conceptual Design Report", Report No. PSI Bericht Nr. 17-02, ISSN 1019-0643, 2017.

[4] R. Ganter *et al.*, "Status of Athos, the Soft X-Ray FEL Line of SwissFEL", in *Proc. FEL'19*, Hamburg, Germany, Aug. 2019, pp. 753–756. `doi:10.18429/JACoW-FEL2019-THP085`

ISBN: 978-3-95450-220-2 ISSN: 2673-5474 doi: 10.18429/JACoW-FEL2022-WEP28

[5] E. Prat, R. Abela, M. Aiba, *et al.*, "A compact and cost-effective hard X-ray free-electron laser driven by a high-brightness and low-energy electron beam", *Nat. Photonics*, vol. 14, pp. 748–754 ,2020. `doi.org/10.1038/s41566-020-00712-8`

[6] T. Schmidt and M. Calvi, "APPLE X Undulator for the SwissFEL Soft X-ray Beamline Athos", *Synchrotron Radiat. News*, vol. 31, no.3, p. 35-40, 2018. `doi.org/10.1080/08940886.2018.1460174`

[7] E. Prat *et al.*, "First lasing of Athos, the soft X-ray FEL beamline of SwissFEL", presented at FEL'22, Trieste, Italy, Aug. 2022, paper MOA02, this conference.

[8] P. Craievich *et al.*, "Sub-Femtosecond Time-Resolved Measurements Based on a Variable Polarization X-Band Transverse Deflecting Structures for SwissFEL", in *Proc. FEL'17*, Santa Fe, NM, USA, Aug. 2017, pp. 499–502. `doi:10.18429/JACoW-FEL2017-WEP040`

[9] T.G. Lucas, "High Field Phenomenology in Linear Accelerators for the Compact Linear Collider", PhD Thesis, University of Melbourne (2018).

ISBN: 978-3-95450-220-2 ISSN: 2673-5474 doi: 10.18429/JACoW-FEL2022-WEP31

MACHINE LEARNING DEVELOPMENTS FOR CLARA

D. J. Dunning*, A. E. Pollard, M. Maheshwari, A. J. Gilfellon, W. Okell, E. W. Snedden
STFC Daresbury Laboratory and the Cockcroft Institute, Warrrington, UK

Abstract

CLARA is an electron beam test facility being developed in phases at STFC Daresbury Laboratory. The first phase, with up to 35 MeV electron beam energy, has been operated since 2018 for a wide range of accelerator applications. The second phase, presently being installed, will expand the range of applications by taking the beam to 250 MeV energy and via a dog-leg to an experimental station that will feature a new high-power laser. Machine learning will play an important role in the future development of the facility, with aims to rapidly deliver bespoke beam properties, to detect and diagnose anomalies, and to provide virtual diagnostics. This paper summarises machine learning developments to date, in the areas of RF breakdown detection, photo-injector laser pulse shaping, and longitudinal phase space shaping. Studies to date have largely been offline or using simulated data but steps towards deployment are also reported.

INTRODUCTION

At the CLARA facility [1] we aim to use machine learning (ML) to deliver an efficient, automated accelerator with rapidly customisable beam properties. CLARA is an electron beam test facility being developed in phases at STFC Daresbury Laboratory. The first phase, with up to 35 MeV electron beam energy, has been operated since 2018 for a wide range of accelerator applications. The second phase, presently being installed, will expand the range of applications by taking the beam to 250 MeV energy and via a dog-leg to an experimental station that will feature a new high-power laser. A third phase utilising the 250 MeV beam in the straight-ahead line is also envisaged - originally planned to test FEL concepts for a UK XFEL, its use will now be defined in the next stage of this project [2, 3]. The layout of CLARA is shown in Fig. 1.

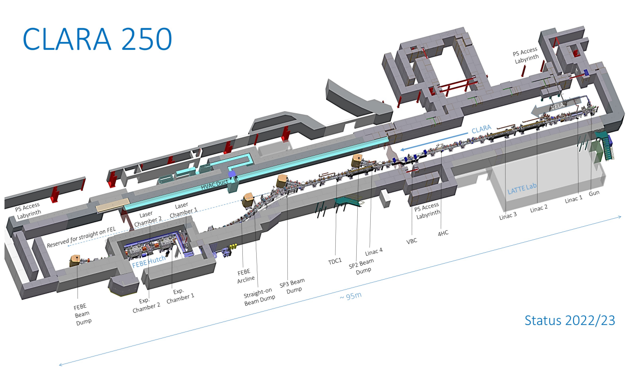

Figure 1: Schematic layout of CLARA.

This paper summarises ML developments for CLARA to date, in the areas of customisable bunch properties (longitudinal phase space shaping [4, 5] and photo-injector laser pulse temporal profile shaping [6]) and anomaly detection, specifically for RF breakdown detection [7]. ML-based work on diagnostics is also in progress [8]. Studies to date have largely been offline or using simulated data but steps towards deployment are being taken and are also reported.

CUSTOMISABLE BUNCH PROPERTIES

Both for CLARA itself, and as a demonstrator for future projects, it is highly desirable to rapidly reconfigure and optimise different setups to meet user needs. For example, shaping the temporal profile of the electron bunch is of critical importance for applications such as free-electron lasers, where it strongly influences efficiency and the profile of the photon pulse generated, and in novel acceleration techniques where it can e.g. contribute to enhanced interaction of a witness beam with the driving electric field. We have carried out two projects with this aim, described in this section.

Longitudinal Phase Space Shaping

Our first project on customisable bunch shaping was simulation-based, to demonstrate the idea of bespoke shaping of the longitudinal phase space (LPS). Work in this area of incorporating image recognition into particle accelerator control using convolutional neural networks is well established, starting with Edelen et al. [9] and developed further, often focusing on LPS, in [10–15]. Our work on this topic to date is detailed in [4, 5] and is summarised here.

Dataset We used a dataset of LPS images and associated parameters, as described in [4] and briefly outlined here. It was generated from the results of previous work, using a Multi-Objective Genetic Algorithm [16] to find optimal beam characteristics for a potential CLARA upgrade [17]. Approximately 10,000 start-to-end simulations of the accelerator were generated using the simulation code ASTRA [18] (up to the linac 1 exit) and Elegant [19] for the remainder, with Genesis [20] for FEL simulations. Images were generated showing the LPS upon entry to the FEL line by binning the particles in a 2D histogram defined by the region of interest (ROI) for each bunch to create 100×100 pixel images. Each example in the dataset therefore consisted of an LPS image, 4 real values describing the bounds of the ROI, 17 accelerator parameters describing the phase and amplitude of the linacs, the laser heater factor, the dechirper factor, and the bunch compression. Though not referred to here, FEL output data and non-ROI images were also generated [4].

Model Following the approach taken in previous studies [11], we began by developing a fully connected parameter to image generative model [4]. We then developed a

* david.dunning@stfc.ac.uk

ISBN: 978-3-95450-220-2 ISSN: 2673-5474 doi: 10.18429/JACoW-FEL2022-WEP31

conditional variational autoencoder (CVAE) model and experimented with CNN and DNN based generators. However, as seen in previous works, the generator showed a tendency to produce a great many artifacts and fine details were lost. We therefore created a deep neural network which utilised a convolutional CVAE, with the addition of a discriminator, resulting in a model known as a CVAE-GAN [21]. A discriminator endeavours to identify real and generated images. When this is affixed to the generative model (the CVAE), the weights of the discriminator are frozen and the generated images are intentionally mislabelled as being real images. The resulting error is then backpropagated through the generative network to train the generator to produce images that would 'fool' the discriminator. This error is combined with an absolute difference error metric between the input and output images, as well as the Kullback-Liebler divergence constraint on the latent space of the CVAE.

LPS Shaping Given that the forward pass of neural networks can be run in linear time, this allows for the rapid sampling of LPS graphs from the space. In combination with Bayesian Optimisation, we can therefore perform a guided search for image similarity with an LPS graph drawn by an operator, as shown in the example in Fig. 2, yielding a set of machine parameters to produce the desired shape.

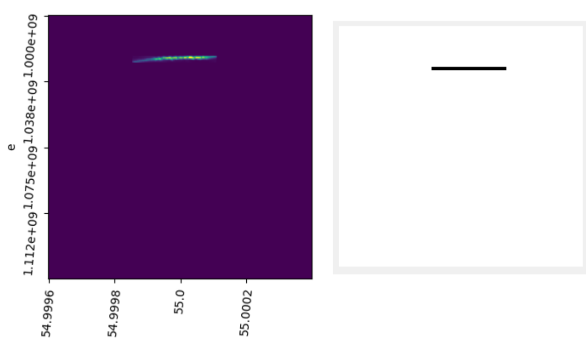

Figure 2: An example of the drawing interface with target drawn by operator (right) and the resulting LPS graph (left) which most closely matched the operator's drawing. On a mid-range laptop, this search took approximately 20 seconds.

Photoinjector Laser Temporal Profile Shaping

Our second project on customisable bunch shaping focuses on shaping the temporal profile of the photo-injector laser pulses. This offers a direct route to deployment by focusing on part of the facility available during the Phase 2 installation, leading towards control over the longitudinal properties of the electron bunch (e.g. [22]). Details of our work are given in [6] and are summarised here.

Apparatus Following the temporal shaping concept presented in [23], we have developed an apparatus for temporally shaping the photoinjector laser pulses at CLARA, shown schematically in Fig. 3. The input laser pulse is spectrally dispersed by a transmission grating. A concave mirror one focal length away from the grating collimates the spectrum and focuses the laser pulse to a line focus, along which the laser wavelength varies approximately linearly. A fused-silica acousto-optic modulator (AOM) is placed at the position of the focus, and a transducer driven with an RF waveform at 200 MHz central frequency generates an acoustic wave in the AOM, which propagates along the line focus of the laser. The laser pulses are diffracted from the induced refractive index modulation, and the spectral components are recombined using a second concave mirror and transmission grating.

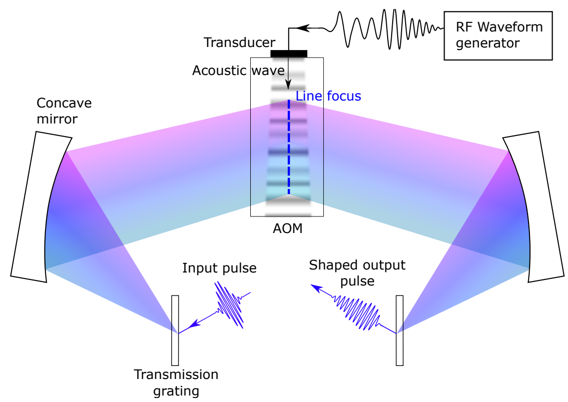

Figure 3: Schematic of the temporal pulse shaper at CLARA.

To shape the laser pulse temporally, the spectral phase can be adjusted by varying the temporal phase of the acoustic wave via the temporal phase of the RF drive wave. The laser pulses can also be shaped temporally by varying the temporal amplitude of the acoustic wave; however, as this approach is lossy, it is necessary to carry out all shaping using only the phase. In order to produce a particular target pulse temporal intensity profile, we need to find a suitable spectral phase mask to apply to the shaper. This is non-trivial for arbitrary shapes, as we require both the phase and amplitude in either the spectral or temporal domain to fully define the pulse. However we know only the temporal intensity and the spectral intensity, leaving the temporal and spectral phase as unknowns with many potential solutions.

Dataset Initially we used simulated data to train and test a ML model to find the required phase mask to achieve a particular target pulse temporal profile. The simulated laser pulses have a spectral intensity with Gaussian shape in wavelength, central wavelength of 266 nm, and FWHM bandwidth of 1.5 nm. As pulses in the CLARA photoinjector laser system are temporally stretched before entering the shaper, our simulated unshaped pulses have 8×10^4 fs^2 of spectral phase applied. For our training set, we generate 10^5 pairs of spectral phase profiles and corresponding temporal intensity profiles, with a further 10^5 pairs generated for the test set. Each pair consists of a spectral phase profile consisting of 2642 samples over 5.78 nm and a temporal intensity profile of 294 samples over 12 ps.

Encoding physical constraints Recent research has explored encoding physical laws into ML models with partial

ISBN: 978-3-95450-220-2 ISSN: 2673-5474 doi: 10.18429/JACoW-FEL2022-WEP31

differential equations as priors [24] to reduce the data requirements of these otherwise data-intensive approaches. This approach has come to be known as Physically Informed Neural Networks (PINNs) and can be used to constrain the outputs of deep neural networks within physical reality, by encoding properties such as conservation of energy *a priori*. To encode the physical limitation of the AOM bandwidth into the network, we developed a regulariser which acts to limit the gradient of the spectral phase profile to a physical limit of $\pi/0.015$ rad/nm, corresponding to a maximum phase change per wavelength step of $\delta\varphi \approx 0.153\pi$ rad/step.

Model The architecture for the network is a simple deep neural network with three hidden layers using the ReLu [25] activation function, with batch normalisation between the layers. The final output layer uses a linear activation function. We use the Adam optimiser [26] with a learning rate schedule decaying from 0.001 at a rate of $e^{0.001}$ per epoch after the first 100 epochs. Without the limitations of the AOM it is possible to achieve very high quality matches to the target patterns, however these are not physically achievable since they require spectral phase transitions well beyond what is physically possible. However, with the physical limitations imposed by the PINN, we achieve high quality matches to arbitrary temporal phase profiles which are physically realisable, as shown in Fig. 4.

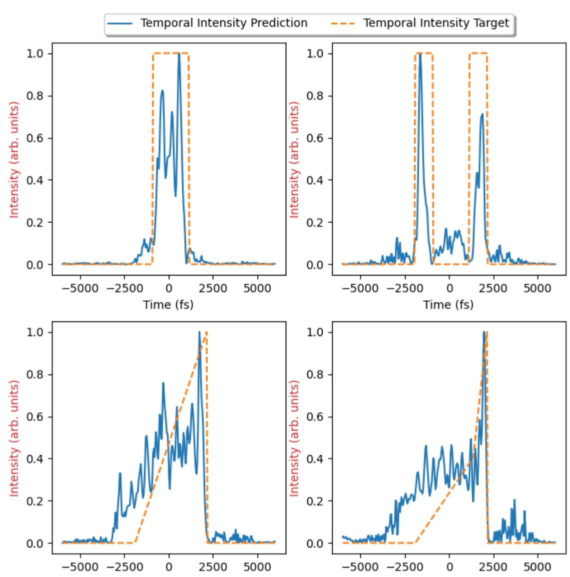

Figure 4: Demonstration of solutions found for arbitrary pulse shapes (physically realisable via gradient constraint).

Deployment Deployment of the ML system for control of the laser pulse shape has begun, with users able to specify arbitrary pulse shapes for which the ML system produces an appropriate spectral phase profile. This generated profile is then sent to the laser control system and applied to the AOM, with a total time between user request and laser activation at less than 100 ms. In an effort to further improve results, this live system is being used to further train the model to account for minor deviations between simulation and reality.

RF BREAKDOWN DETECTION

Another main area of our ML programme is anomaly detection, specifically for RF breakdown detection. Our work on this topic is detailed in [7] and summarised here.

Motivation

RF structures, for example the CLARA high repetition rate gun [1], must undergo a conditioning process before operational use, in which the gradient is gradually increased up to the operating value. Breakdowns (vacuum arcing) during this process can cause damage that limits the ultimate operating accelerating gradient - a critical factor for accelerator performance and cost-effectiveness. There are two main aims with this project. Firstly, we aim to assemble a ML based system that could be used to replace the mask method of RF breakdown (BD) detection currently used. Secondly, we aim to ensure that the mid-process features of the same mechanism could be used as inputs for an ML algorithm to predict whether or not the next RF pulse would lead to a BD.

Related work includes Solopova et al.'s [27] application of a decision tree model to classify RF cavity faults at CEBAF. This work was then continued in [28] with a random forest model and a larger dataset of breakdown events. Obermair et al. [29] took the first step towards ML based detection and prediction of breakdowns, through applying deep learning on two available data types (event and trend data) to predict breakdowns 20 ms in advance with good accuracy.

Approach for CLARA

In our work [7], ML techniques are applied to detect breakdown events in RF pulse traces by approaching the problem as anomaly detection. Offline data from various sources has been used to develop the techniques, which we aim to test at CLARA, which could then be applied generally. To this end, we constructed a β convolutional variational autoencoder (βCVAE) [30] with RF conditioning data as inputs. After being trained as an anomaly detector this acted as a live BD detector, in conjunction with a dense neural network (NN), which would act with the capacity to replace the current non-ML based BD detection system. In addition to this, the βCVAE's latent space could act as a viable input for a long short-term memory (LSTM) recurrent neural network (RNN) that could be used to predict BDs, based on the methodology set out by Kates-Harbeck et al.[31] who had success in predicting disruptive instabilities in controlled fusion plasmas.

Dataset We used data gathered during the RF conditioning of CLARA's 10 Hz photoinjector (Gun-10), which includes both the RF pulse traces themselves and other non-RF data, such as temperature and pressure. The data was gathered before ML was taken into consideration and was therefore not ideal for our purposes, but it was deemed to be sufficient for progress to be made. The trace data was only recorded when the RF breakdown detector was activated and a BD identified, then the conditioning script would

ISBN: 978-3-95450-220-2 ISSN: 2673-5474 doi: 10.18429/JACoW-FEL2022-WEP31

record the pulse associated with the BD, as well as the two previous and two subsequent pulses. Altogether, there were 40 traces recorded per breakdown event (8 traces for each of the 5 pulses). Specifically the traces were forward and reverse power and phase for both the klystron and cavity.

In order to provide the ground truth and label each recorded trace as either, noise, healthy, BD or anomaly, the traces were first grouped together by using sklearn's t-SNE [32] and DBSCAN functions. The traces from each delivered cluster were then over-plotted and inspected by eye with any pure groups receiving the appropriate label and composite clusters undergoing further t-SNE/DBSCAN analysis until only pure groups remained. Figure 5 shows an example of the clustering that was returned for this data set.

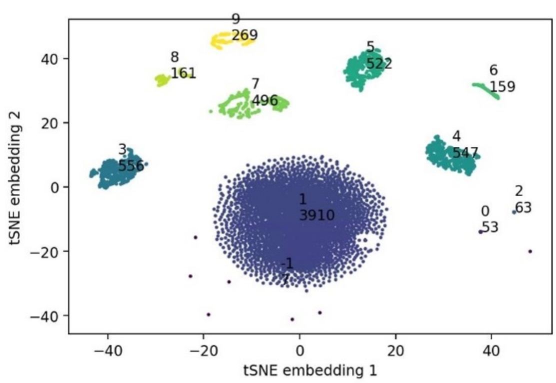

Figure 5: Results of applying the t-SNE/DBSCAN method to label the CLARA Gun-10 data set. Each cluster is indexed with its population displayed below, i.e. the cluster in the top right has an index of 6 and a population of 159. As examples of the principal trace types, the large central cluster indexed as 1 represents noise traces, cluster 4 contains only healthy traces, 8 breakdown traces, and 7 is composite (healthy/BD).

Model It was found that the most effective input for the βCVAE was a 2D array comprised of the four normalised power traces, with dimensions of 4×1017. The most optimal structure of the found for βCVAE is displayed in Fig. 6. The βCVAE was trained on 4659 healthy traces in order to create the anomaly detector, which was then validated using another 1164 healthy traces. For both training and validation the Adam optimiser and categorical cross entropy loss function were used. Testing the βCVAE involved exposing the algorithm to 706 healthy and 706 BD traces (1412 traces in total) and subtracting the reconstructed traces from the original traces to produce 1D reconstruction error traces. These were then used as an input for a simple dense neural network classifier with one ReLU activated hidden layer with the same dimensions as the input layer and a binary (healthy/BD) softmax activated output layer. Again the Adam optimiser and categorical cross entropy loss function were used.

Results A confusion matrix was constructed by comparing the class assigned by the model to the ground truth in order to check for the accuracy and recall of the BD row for the system, as in Table 1. The key statistic is the recall of the

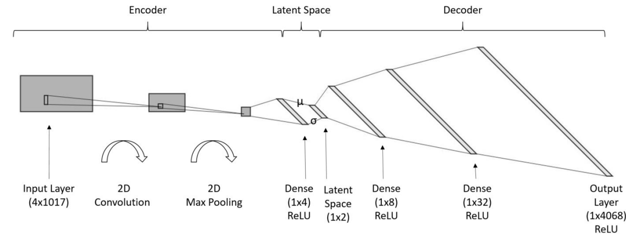

Figure 6: The final structure of the βCVAE.

BD row, since the accelerator not reacting to a false negative could be damaging to the accelerating structure, whereas reacting to a false positive merely results in a slight reduction in the time efficiency of the conditioning. An accuracy of 96.9% and a BD row recall of 98.0% was achieved. Further inspection revealed that the model was in fact doing even better since about half the false negatives were actually those mislabelled by our largely unsupervised method.

Table 1: Results of β CVAE Breakdown Classification

	Positive	Negative
True	95.8%	98.0%
False	4.2%	2.0%

Deployment Work is now underway at CLARA to deploy this ML system, operating at 400Hz, using a Xilinx Alveo U200 FPGA card. In order to facilitate further work in prediction of RF breakdowns, a full duty cycle recording system is being developed in parallel to capture all RF traces at 400Hz. Following testing of this system against the mask method, integration into the safety interlocks is intended.

REFERENCES

[1] D. Angal-Kalinin *et al.*, "Design, specifications, and first beam measurements of the compact linear accelerator for research and applications front end," *Phys. Rev. Accel. Beams*, vol. 23, no. 4, p. 044 801, 2020. doi:10.1103/PhysRevAccelBeams.23.044801

[2] J. Marangos *et al.*, "UK XFEL Science Case," UK Research, Innovation, Science, and Technology Facilities Council (United Kingdom), Tech. Rep., 2020.

[3] D. J. Dunning *et al.*, "Facility Concept Outlines for a UK XFEL," presented at the 40th International Free Electron Laser Conference (FEL'22), Trieste, Italy, Aug. 2022, paper TUP32, this conference.

[4] M. Maheshwari, D. Dunning, J. Jones, M. King, H. Kockelbergh, and A. Pollard, "Prediction and Clustering of Longitudinal Phase Space Images and Machine Parameters Using Neural Networks and K-Means Algorithm," in *Proc. IPAC'21*, Campinas, SP, Brazil, 2021, pp. 3417–3420. doi:10.18429/JACoW-IPAC2021-WEPAB318

[5] A. Pollard, D. Dunning, and M. Maheshwari, "Learning to Lase: Machine Learning Prediction of FEL Beam Properties," in *Proc. ICALEPCS'21*, Shanghai, China, 2022, pp. 677–680. doi:10.18429/JACoW-ICALEPCS2021-WEPV020

ISBN: 978-3-95450-220-2 ISSN: 2673-5474 doi: 10.18429/JACoW-FEL2022-WEP31

[6] A. Pollard, D. Dunning, W. Okell, and E. Snedden, "Machine Learning Approach to Temporal Pulse Shaping for the Photoinjector Laser at CLARA," in *Proc. IPAC'22*, Bangkok, Thailand, 2022, pp. 2917–2920. doi:10.18429/JACoW-IPAC2022-THPOTK061

[7] A. Pollard, D. Dunning, and A. Gilfellon, "Machine Learning for RF Breakdown Detection at CLARA," in *Proc. ICALEPCS'21*, Shanghai, China, 2022, pp. 681–685. doi:10.18429/JACoW-ICALEPCS2021-WEPV021

[8] J. Wolfenden *et al.*, "Broadband Imaging of Coherent Radiation as a Single-Shot Bunch Length Monitor with Femtosecond Resolution," in *Proc. IPAC'21*, Campinas, SP, Brazil, 2021, pp. 2147–2150. doi:10.18429/JACoW-IPAC2021-TUPAB285

[9] A. Edelen, S. Biedron, J. Edelen, and S. Milton, "First Steps Toward Incorporating Image Based Diagnostics into Particle Accelerator Control Systems Using Convolutional Neural Networks," in *Proc. NAPAC'16*, Chicago, IL, USA, Oct. 2016, pp. 390–393. doi:10.18429/JACoW-NAPAC2016-TUPOA51

[10] A. Scheinker, A. Edelen, D. Bohler, C. Emma, and A. Lutman, "Demonstration of Model-Independent Control of the Longitudinal Phase Space of Electron Beams in the Linac-Coherent Light Source with Femtosecond Resolution," *Phys. Rev. Lett.*, vol. 121, no. 4, p. 044 801, 2018. doi:10.1103/PhysRevLett.121.044801

[11] C. Emma, A. Edelen, M. Hogan, B. O'Shea, G. White, and V. Yakimenko, "Machine learning-based longitudinal phase space prediction of particle accelerators," *Phys. Rev. Accel. Beams*, vol. 21, no. 11, p. 112 802, 2018. doi:10.1103/PhysRevAccelBeams.21.112802

[12] C. Emma *et al.*, "Machine Learning-Based Longitudinal Phase Space Prediction of Two-Bunch Operation at FACET-II," in *Proc. IBIC'19*, Malmö, Sweden, 2019, pp. 679–683. doi:10.18429/JACoW-IBIC2019-THBO01

[13] A. Edelen, N. Neveu, C. Emma, D. Ratner, and C. Mayes, "Machine learning models for optimization and control of x-ray free electron lasers," in *Proc. NeurIPS Machine Learning for the Physical Sciences Workshop (NeurlPS2019)*, Vancouver, Canada, 2019.

[14] A. Hanuka *et al.*, "Accurate and confident prediction of electron beam longitudinal properties using spectral virtual diagnostics," *Sci. Rep.*, vol. 11, no. 1, pp. 1–10, 2021. doi:10.1038/s41598-021-82473-0

[15] J. Zhu, Y. Chen, F. Brinker, W. Decking, S. Tomin, and H. Schlarb, "High-fidelity prediction of megapixel longitudinal phase-space images of electron beams using encoder-decoder neural networks," *Phys. Rev. Applied*, vol. 16, no. 2, p. 024 005, 2021. doi:10.1103/PhysRevApplied.16.024005

[16] D. Dunning, H. C. Cortés, J. Jones, and N. Thompson, "Multi-Objective FEL Design Optimisation Using Genetic Algorithms," in *Proc. FEL'19*, Hamburg, Germany, 2019, pp. 711–714. doi:10.18429/JACoW-FEL2019-THP065

[17] D. Dunning, L. Cowie, J. Jones, *et al.*, "XARA: X-Band Accelerator for Research and Applications," in *Proc. FEL'19*, Hamburg, Germany, Aug. 2019, pp. 715–718. doi:10.18429/JACoW-FEL2019-THP066

[18] K. Floettmann, "ASTRA - A Space Charge Tracking Algorithm," Tech. Rep. http://www.desy.de/~mpyflo

[19] M. Borland, "Elegant: A flexible SDDS-compliant code for accelerator simulation," Argonne National Lab., IL (US), Tech. Rep., 2000.

[20] S. Reiche, "GENESIS 1.3: a fully 3D time-dependent FEL simulation code," *Nucl. Instrum. Methods Phys. Res., Sect. A*, vol. 429, p. 243, 1999. doi:10.1016/S0168-9002(99)00114-X

[21] J. Bao, D. Chen, F. Wen, H. Li, and G. Hua, "CVAE-GAN: Fine-Grained Image Generation through Asymmetric Training," in *Proceedings of the IEEE international conference on computer vision*, 2017, pp. 2745–2754.

[22] G. Penco *et al.*, "Experimental demonstration of electron longitudinal-phase-space linearization by shaping the photoinjector laser pulse," *Phys. Rev. Lett.*, vol. 112, p. 044 801, 2014. doi:10.1103/PhysRevLett.112.044801

[23] C. W. Hillegas, J. X. Tull, D. Goswami, D. Strickland, and W. S. Warren, "Femtosecond laser pulse shaping by use of microsecond radio-frequency pulses," *Opt. Lett.*, vol. 19, no. 10, pp. 737–739, 1994. doi:10.1364/ol.19.000737

[24] M. Raissi, P. Perdikaris, and G. E. Karniadakis, "Physics Informed Deep Learning (Part I): Data-driven Solutions of Nonlinear Partial Differential Equations," *arXiv*, doi:10.48550/arXiv.1711.10561

[25] A. F. Agarap, "Deep Learning using Rectified Linear Units (ReLU)," *arXiv*, 2018. doi:10.48550/arXiv.1803.08375

[26] D. Kingma and J. Ba, "Adam: A Method for Stochastic Optimization," in *Int. Conf. on Learn. Represent., (ICLR2015)*, San Diego, CA, USA, May, 2015. doi:10.48550/arXiv.1412.6980

[27] A. Solopova *et al.*, "SRF Cavity Fault Classification Using Machine Learning at CEBAF," in *Proc. IPAC'19*, Melbourne, Australia, 2019, pp. 1167–1170. doi:10.18429/JACoW-IPAC2019-TUXXPLM2

[28] C. Tennant, A. Carpenter, T. Powers, A. Shabalina Solopova, L. Vidyaratne, and K. Iftekharuddin, "Superconducting radio-frequency cavity fault classification using machine learning at Jefferson Laboratory," *Phys. Rev. Accel. Beams*, vol. 23, no. 11, 2020. doi:10.1103/physrevaccelbeams.23.114601

[29] C. Obermair *et al.*, "Machine Learning Models for Breakdown Prediction in RF Cavities for Accelerators," in *Proc. IPAC'21*, Campinas, SP, Brazil, 2021, pp. 1068–1071. doi:10.18429/JACoW-IPAC2021-MOPAB344

[30] I. Higgins *et al.*, "beta-VAE: Learning Basic Visual Concepts with a Constrained Variational Framework," in *Int. Conf. on Learn. Represent., (ICLR2017)*, Toulon, France, 2017. https://openreview.net/forum?id=Sy2fzU9gl

[31] J. Kates-Harbeck, A. Svyatkovskiy, and W. Tang, "Predicting disruptive instabilities in controlled fusion plasmas through deep learning," *Nature*, vol. 568, no. 7753, pp. 526–531, 2019. doi:10.1038/s41586-019-1116-4

[32] L. Van der Maaten and G. Hinton, "Visualizing Data using t-SNE," *Journal of Machine Learning Research*, vol. 9, pp. 2579–2605, 2008. http://jmlr.org/papers/v9/vandermaaten08a.html

ISBN: 978-3-95450-220-2 ISSN: 2673-5474 doi: 10.18429/JACoW-FEL2022-WEP38

SHORT PERIOD APPLE-X UNDULATOR MODELING FOR THE AQUA LINE OF THE FUTURE EuPRAXIA@SPARC_LAB FACILITY

A. Petralia[1*], M. Carpanese[1], M. Del Franco[2], A. Doria[1], F. Nguyen[1], L. Giannessi[2], A. Selce[1]
[1]ENEA Fusion and Technology for Nuclear Safety and Security Department, R.C. Frascati, Frascati, Italy
[2]INFN Laboratori Nazionali di Frascati, Frascati, Italy

Abstract

The study for a short period Apple-X variable polarizing undulator is presented, with small gap of operation and high magnetic field. This will be the base module for the AQUA line of the EuPRAXIA@SPARC_LAB FEL facility, of next realization at the INFN Laboratory of Frascati. The undulator allows to achieve radiation between 3.5 and 6 nm with a 1 GeV electron beam energy, lower than other FELs operating in the world, so giving the possibility to have a Soft X-ray source with a full polarization control in a more cost effective way and with less required space than the state of the art devices. An overview of the magnetic design is given with the main parameters and performances in terms of the field properties, tuning capabilities and the effects on the electron beam motion.

INTRODUCTION

In the recent years some efforts have been done on research and experimentation on the possibility of using plasma accelerators to pilot Free Electron Lasers (FELs) [1]. The possibility to accelerate electron beams over short distances using plasma-based technology has the potential for a revolution in the field of particle accelerators. The much more compact nature of plasma-based accelerators would allow the construction of much smaller and therefore much less expensive machines capable of operating a FEL. Recently, some first experimental demonstrations have been obtained that encourage to continue on this path [2,3] (see also M. Galletti and M. Labat talks, these proceedings). In this direction the European project EuPRAXIA goes, aiming at the realization of the first user FEL machine driven by plasma accelerator [4]. In this context, a study and design work is in progress at the INFN National Laboratories of Frascati (INFN LNF), with the participation of the ENEA undulator experts, for a compact FEL piloted by an X-band RF accelerator but which also provides for the presence of a plasma acceleration stage, for a final maximum beam energy of 1 GeV. This machine, namely EuPRAXIA@SPARC_LAB [5], will be a user facility and two FEL lines are foreseen. The first one is a SASE FEL line, called AQUA, and will produce radiation at λ = 4 nm in the spectral region of the so called "water window" (see F.Nguyen poster, these proceedings). The second, called ARIA, will be a seeded FEL line operating in the wavelengths range 50-180 nm (see M. Opromolla poster, these proceedings). Regarding the AQUA line, the vaue of the beam energy (E = 1 GeV) and the desired resonance require to have an undulator with short period λ_u and a magnetic peak field B that gives a value $K_{\mathrm{rms}} \approx 1$ for the undulator deflection parameter, according to the FEL resonance formula

$$\lambda = \frac{\lambda_u}{2\gamma^2}(1 + K_{\mathrm{rms}}^2) \tag{1}$$

being m_o and c respectively the rest mass of an electron and the speed of light and $\gamma = E/m_o c^2$ is the Lorentz factor. Furthermore the polarization control of the emitted radiation is desired, varying from Linear (LP) to Circular (CP) passing through all intermediate levels. For these reasons, the best choice is the use of an Apple-X type undulator. Starting from the initial scheme proposed in [6], in the last few years some Apple-X undulators have been made or are under construction [6–8]. Thanks to its geometry, the Apple-X allows to fit the required parameters for the EuPRAXIA@SPARC_LAB FEL operation. In addition, the characteristics of this type of undulator are such that the resonance wavelength and the tuning range are the same for all polarization setting.

UNDULATOR DESIGN

The undulator under development for AQUA has a much shorter period than other Apple-X built so far. The choice of the period is determined by the desired resonance wavelength with an energy beam equal to 1 GeV but also to have a good compromise between the tuning range and the value of the saturation length which has to be less than 30 meters (including beam optics), being this the maximum available space for the undulator line. For these reasons, the value λ_u = 18 mm is chosen for the undulator period. The value K_{rms} = 0.8 for the undulator parameter is hence required for the operation at 4 nm, according with Eq. (1).

The undulator structure is made of four Neodymium-Iron-Boron (NdFeB) permanent magnet blocks with octagonal shape with a magnetization at 45° and a remanent field Br=1.35 T, with a locking thoot to fix the block magnets to the holder. The magnets are disposed radially at equal distance around the electron beam axis. The resultant square hole in the centre of the structure allows the installation of a 5 mm external diameter vacuum pipe for the propagation of the electrons. Longitudinally we have four blocks per period arranged according to the Halbach configuration. The minimum achievable gap is settled as 1.5 mm, being this a good compromise between the maximum wanted magnetic field value (and hence the maximum K), and some constructive

* alberto.petralia@enea.it

ISBN: 978-3-95450-220-2 ISSN: 2673-5474 doi: 10.18429/JACoW-FEL2022-WEP38

constraints due to the mounting tolerances of the magnets, the movement of the girders and the holders for the vacuum pipe (see Fig. 1).

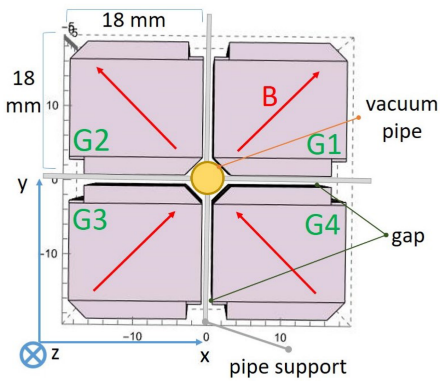

Figure 1: Structure of the AQUA Apple-X undulator, transverse view.

The wavelength tuning is obtained by moving the four magnets radially in order to adjust the magnetic gap, while the polarization control is realized by shifting longitudinally (namely a "phase" shift) two diagonally opposite girders with the magnets arrays respect to the other two. The general expression for the undulator parameter K_{rms} in a variable polarization undulator is

$$K_{\mathrm{rms}} = \sqrt{\frac{K_x^2}{2} + \frac{K_y^2}{2}} \tag{2}$$

where K_x and K_y are the undulator deflection parameter associated to the peak magnetic field for respectively the two radial and vertical components B_x and B_y. The symmetrical geometry of the Apple-X gives the same K_{rms}, and hence the same tuning range, for all polarization modes (Fig. 2). The maximum achievable K is limited by the longitudinal dimension of the blocks magnet (one quarter of the undulator period), for this reason we do not have a large tuning range but the parameters have been optimized to increase it as much as possible. Simulations have been performed by means of the RADIA code [9]. The modelling parameters and the resulting capabilities are summarized in Table. 1 and shown in Fig3.

The end magnets design is given by three magnets at both end and begin of the girders with longitudinal size respectively 1/4,1/2 and 3/4 of the standard block (Fig. 4). This gives a standard symmetric configuration for a zero-displacement orbit [10]. Considering the ideal model and including the effects of the NdFeB susceptibility, this configuration ensure values of the first and second field integrals which are respectively $|I1_{x,y}| < 0.05\,G\,m$ and $|I2_{x,y}| < 0.05\,G\,m^2$ for any polarization setting.

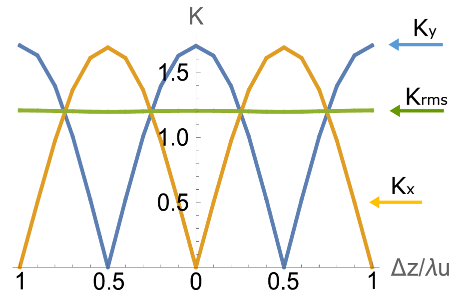

Figure 2: Undulator K parameter variation with different polarization setting given by a girders shift Δz in unit of λ_u, at the minimum gap=1.5 mm.

Table 1: Undulator Basic Parameters

Parameter	Value
Magnetic Material	NdFeB
Remanent field B_r	1.35
Period Length λ_u	18 mm
Blocks per period	4
Block magnet x,y size	18 mm x 18 mm
Central hole diameter	5.5 mm
Magnetic gap range	1.5-4 mm
K_{rms} range	1.2 - 0.6
Resonance tuning range	3.5 - 5.8 nm
Module length	2 m

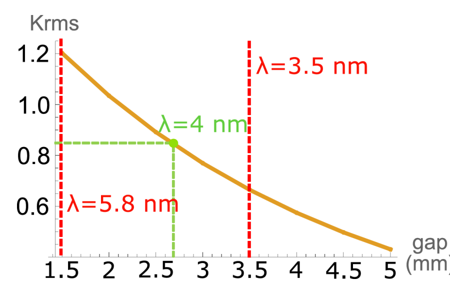

Figure 3: K_{rms} variation vs gap and tuning range.

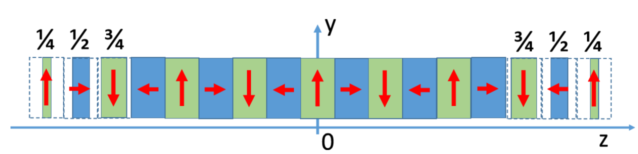

Figure 4: End magnets design scheme.

UNDULATOR PERFORMANCES

Field Profile

The estimation of the field profile gives a perfect symmetry between the horizontal (x) and vertical (y) direction when the device works in circular polarization mode. This reflects both on field gradients and the focusing properties of the undulator.

The transverse field gradients show a parabolic profile but with a strong variation, especially for the cross components $\Delta B_y/\Delta x$ and $\Delta B_x/\Delta y$, due to both small gap and

ISBN: 978-3-95450-220-2 ISSN: 2673-5474 doi: 10.18429/JACoW-FEL2022-WEP38

aperture of the central hole which causes a loss of homogeneity. The homogeneity map shows the good field region for the operation of the undulator. The transverse field (and so the K) variation affects the bandwidth of the produced radiation since the off axis injected electrons feels a different K and so they oscillate at a different frequency respect to the ones moving on axis. The effect can be normally neglected if the K variation is under few per mill. For the undulator under study this happens if $x, y < 200\,\mu\text{m}$ from axis, where the maximum B variation is <0.3%. Considering a distance of $x, y = 150\,\mu\text{m}$, the field variation goes down to less than 0.15%. The transverse field variations within 200 µm from axis in both x and y are listed in Table. 2 for Linear end Circular mode. This fixes the homogeneity region of the AQUA Apple-X undulator. According to the EuPRAXIA@SPARC_LAB electron beam parameters, the transverse rms size of the beam is of the order of 100 µm which is four times less than the field homogeneity range. Anyway this gives constraints on the precision of the beam alignment tool. The possibility of enhancing this parameter with different shape of the magnets will be further explored.

Table 2: Undulator field homogeneity at a distance $x, y = 200\,\mu\text{m}$ from axis, for Linear (LP) and Circular (CP) polarization mode.

	LP	**CP**
$\Delta B_y/\Delta y$	-0.05%	-0.03%
$\Delta B_y/\Delta x$	0.27%	0.29%
$\Delta B_x/\Delta x$	—	-0.03%
$\Delta B_x/\Delta y$	—	0.3%

Focusing Properties

A first step to investigate the effect of the undulator on the electron beam optics is done by calculating the trajectory for an electron moving on the magnetic axis which is plotted in Fig. 5 for the Linear and Circular polarization mode. The magnetic design of the undulator is optimized to have a zero offset and angle at the end of the device when we operate in LP, to do this the size of the ending magnets have been slightly optimized. When we shift to CP some differences occur between the two directions. At the exit we have a non-zero offset and angle for both horizontal and vertical trajectory, this is due to the anisotropy on magnetization properties of NdFeB. Anyway, since the deviations are very small over a 2 meter module length, this effect can be neglected or eventually managed by correction coils mounted directly on the undulator or by beam correctors installed in the line between the undulator modules.

The effects on the off-axis moving electrons has been also estimated, limiting the study to the homogeneity region within 200 µm from axis. The qualitative results shows that, within this range, the undulator has a focusing effect in the x direction and weakly defocusing on the y direction in Linear polarization mode. When we shift to Circular mode we have a focusing effect in both direction with very

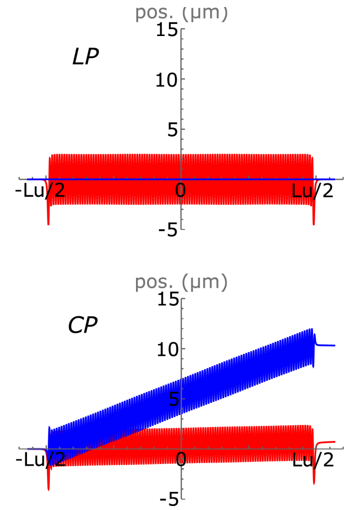

Figure 5: Trajectory of an on-axis moving electron over 110 undulator periods (2 m module length), in LP and CP operation mode. Blue and red lines refers to respectively vertical and horizontal trajectory.

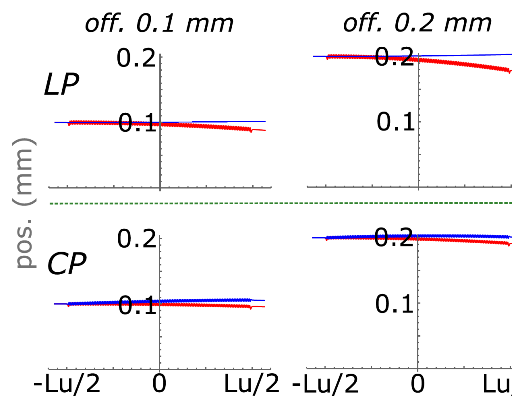

Figure 6: Trajectory of an off-axis moving electron with entrance at 100 µm and 200 µm, in LP and CP operation mode. the blue and red lines are respectively the vertical and horizontal trajectory.

similar behaviour (Fig. 6). A quantitative numerical calculation is done by means of the focusing potential (Fig. 7) and kick maps to be used in the tracking studies [11]. As expected because of the transverse field profile, the focusing strength grows with the distance from axis; as a consequence, the average deflection angle in the trajectory of an electron at the exit of the device increases with the offset entrance. The kick angle values are of the order of few mrad and are given from the intensity scale with multiplying by the factor $\frac{e_o^2}{(\gamma^2-1)\, m_o^2\, c^2}$.The angle variation is linear up to a distance of 800 µm where the transverse variation of the field becomes no longer parabolic.

MECHANICAL CONSIDERATION

A prototyping of the AQUA Apple-X undulator is foreseen in the next years. A starting point to manage the mechanical design is given by another Apple-X undulator in way of realization by Kyma s.r.l. in the framework of the SABINA

ISBN: 978-3-95450-220-2 ISSN: 2673-5474 doi: 10.18429/JACoW-FEL2022-WEP38

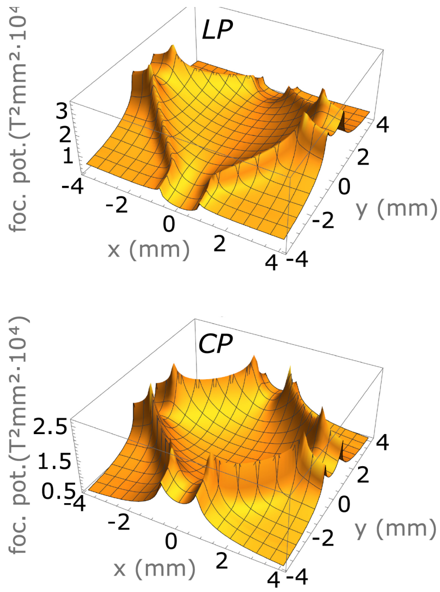

Figure 7: Apple-X undulator focusing potential map for horizontal and circular polarization modes at minimum gap of 1.5 mm, in the whole square aperture.

project [12, 13] at INFN LNF for a THz FEL line (see also S. Macis and Kyma poster on SABINA, this proceedings). Even the SABINA undulator has larger period and field, the mechanical structure can be rescaled to a shorter period undulator. Some preliminary calculations on the AQUA undulator show that the magnetic forces acting on the girders are comparable to the SABINA case and they are less than 600 kg/m. This values can be managed by opportune conventional motors and for this reason no compensating structure with additional magnets have been foreseen. A more detailed tolerance study for the mechanical issues will be done in the next months.

CONCLUSION

The magnetic modeling for a compact short period Apple-X undulator is presented for the operation at a 4 nm resonance wavelength with a 1 GeV energy beam. The magnetic structure and geometry has been defined together with the main performance in terms of tuning capabilities and the effects on the electron beam motion. The mechanical design is in progress and the mechanical tolerance study will be performed soon. A first step of the prototyping will be the realization of the SABINA Apple-X undulator which will allow to understand criticism and lead the study for the opportune mechanical structure for the AQUA undulator. Several challenges need to be addressed especially about the homogeneity region but also on the magnetic measurement tools wich are under study together with other experts in the field. The present study is an encouraging step toward the construction of a compact soft X-ray FEL and the undulator characteristics fit well the needs of the AQUA soft X-ray line at the EuPRAXIA@SPARC_LAB facility on next realization at INFN LNF, Italy.

ACKNOWLEDGEMENTS

The Authors express their sincere thanks and appreciation to Dr. Bruno Diviacco (Elettra) and Dr. Thomas Schmidt (PSI) for interesting and very usefull discussions and suggestions.

REFERENCES

[1] C. Emma *et al.*, “Free electron lasers driven by plasma accelerators: status and near-term prospects”, *High Power Laser Sci. Eng.*, vol. 9, p. E57, 2021. doi:10.1017/hpl.2021.39

[2] R. Pompili *et al.*, “Free-electron lasing with compact beam-driven plasma wakefield accelerator”, *Nature*, vol. 605, pp. 659-662, 2022. doi:10.1038/s41586-022-04589-1

[3] W. Wang *et al.*, ”Free-electron lasing at 27 nanometres based on a laser wakefield accelerator”, *Nature*, vol. 595, pp. 516–520, 2021. doi:10.1038/s41586-021-03678-x

[4] R. W. Assmann *et al.*, “Eupraxia conceptual design report”, *Eur. Phys. J. Spec. Top.*, vol. 229, pp. 3675–4284, 2020. doi:10.1140/epjst/e2020-000127-8

[5] M. Ferrario *et al.*, “EuPRAXIA@ SPARC_LAB Design study towards a compact FEL facility at LNF”, *Nucl. Instrum. Methods Phys. Res., Sect. A*, vol. 909, pp. 134-138, 2018. doi:10.1016/j.nima.2018.01.094

[6] T. Schmidt and M. Calvi, "APPLE X undulator for the SwissFEL soft X-ray beamline Athos", Synchrotron Radiat. News, vol. 31, no. 3, pp. 35-40, 2018. doi:10.1080/08940886.2018.1460174

[7] P. Li, T. Wei, Y. Li, and J. Pflueger, “Magnetic design of an Apple-X afterburner for the SASE3 undulator of the European XFEL”, *Nucl. Instrum. Methods Phys. Res., Sect. A*, vol. 870, pp. 103-109, 2017. doi:10.1016/j.nima.2017.07.023

[8] H. Tarawneh, P. N’gotta, L. K. Roslund, A. Thiel, and K. Åhnberg, “Compact APPLE X for Future SXL FEL and 3 GeV Ring at MAX IV Laboratory”, in *Proc. IPAC’19*, Melbourne, Australia, May 2019, pp. 1833–1835. doi:10.18429/JACoW-IPAC2019-TUPRB072

[9] Radia – 3D Magnetostatics Computation Software, https://www.esrf.fr/Accelerators/Groups/InsertionDevices/Software/Radia

[10] B. Diviacco and R. P. Walker, “Pure permanent magnet end-configurations”, Sincrotrone Trieste Internal Report, ST/M-TN-92/5, 1992.

[11] P. Elleaume, “A New Approach to the Electron Beam Dynamics in Undulators and Wigglers”, in *Proc. EPAC’92*, Berlin, Germany, paper EPAC1992_0661, pp. 661-664. https://jacow.org/e92/PDF/EPAC1992_0661.PDF

[12] L. Sabbatini *et al.*, “SABINA: A Research Infrastructure at LNF”, in *Proc. IPAC’21*, Campinas, Brazil, May 2021, pp. 4505–4507. doi:10.18429/JACoW-IPAC2021-THPAB372

[13] F. Dipace *et al.*, “FEL Design Elements of SABINA: A Free Electron Laser For THz-MIR Polarized Radiation Emission”, in *Proc. IPAC’21*, Campinas, Brazil, May 2021, pp. 1612–1614. doi:10.18429/JACoW-IPAC2021-TUPAB100

ISBN: 978-3-95450-220-2 ISSN: 2673-5474 doi: 10.18429/JACoW-FEL2022-WEP39

DESIGN OF THE SUPERCONDUCTING UNDULATOR FOR EUPRAXIA@SPARC_LAB*

C. Boffo†, M. Turenne, Fermi National Accelerator Laboratory, Batavia, IL, USA
F.Nguyen, A. Petralia, ENEA-Frascati, Frascati, Italy
L. Giannessi, INFN-Laboratori Nazionali di Frascati, Frascati, Italy

Abstract

EuPRAXIA@SPARC_LAB is a new Free Electron Laser (FEL) facility that is currently under construction at the Laboratori Nazionali di Frascati of the INFN. Fermilab is contributing to the project with the design, manufacturing and qualification of a prototype conduction cooled superconducting undulator (SCU) that, if successful, could be integrated in the final machine.

The design of the SCU capitalizes on the extensive experience present at Fermilab on cryomodules. Specifically, the system is based on the warm strongback concept developed for the PIP-II project which enables a modular design with multiple undulator coils integrated in a single vacuum vessel. Here we focus on the overall design concept of the magnet system, its modularity, cost reduction potential and industrialization strategy.

INTRODUCTION

The INFN-LNF Laboratory is developing EuPRAXIA@SPARC_LAB [1], a 1 GeV compact light source facility directly driven by a plasma accelerator, which represents the first phase of the EuPRAXIA European project [2].

According to the present design, the machine will include two Free Electron Laser (FEL) beamlines, AQUA and ARIA. AQUA is a Self-Amplified Stimulated Emission (SASE) line with a 4 nm target wavelength. While the baseline for AQUA foresees the use of Apple-X permanent magnet undulators, superconducting undulators (SCU) could provide an advantage in terms of tunability and flexibility during machine operation. Fermilab is designing EuSCU16, a 16 mm period length SCU, aiming to demonstrate that this technology is mature for integration in a FEL user facility.

UNDULATOR SPECIFICATIONS

The main specifications for EuSCU16 requited to meet the operating parameters of the AQUA beamline are summarized in Table 1. At present, SCUs installed in user facilities are stand-alone units cooled by means of cryocoolers, either utilizing a thermosiphon or a conduction cooling cryogenic scheme [3]. While this prototype includes only a single magnet array, its modular design allows for future expansions and installation of multiple units in a single vacuum vessel as it is typically performed in cryomodules for both superconducting RF and accelerator magnets.

Table 1: EuSCU16 Specifications

Parameter	Value	Units
Period	16	mm
Beam stay clear	5	mm
FEL wavelength	4	nm
Peak field on axis at 5 mm beam stay clear	1.5	T
Cooling medium	Cryocoolers	-
Magnet length	1.2	m
Vacuum vessel length	< 1.5	m
Cooldown time	< 7	days
Operating temperature	≤ 4.2	K

In addition, the cryogenic scheme can be adapted to include liquid helium piping to support operation of multiple vacuum vessels in series connected to a cryogenic plant.

ELECTROMAGNETIC DESIGN

The geometry of the period and the choice of superconductor are the core SCU design elements with impact on performance. EuSCU16 uses a commercially available 0.5 mm by 0.7 mm (bare) NbTi rectangular enamel-insulated strand that is continuously wound without joints throughout each array. The rectangular shape was chosen to maximize the engineering current density within the winding packages.

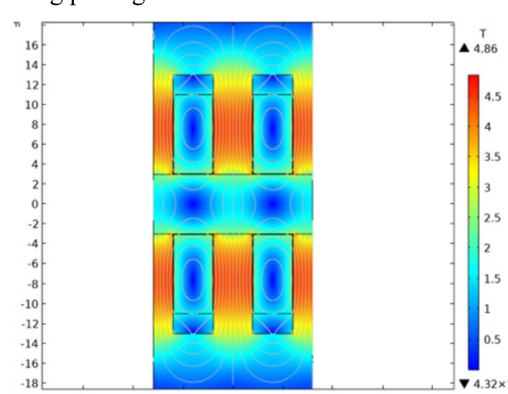

Figure 1: Electromagnetic design of the one period of EuSCU16. A peak field of 4.86 T is reached in the soft iron former at operating current of 500 A. Peak field on axis is 1.5 T.

* This work was produced by Fermi Research Alliance, LLC under Contract No. DE-AC02-07CH11359 with the U.S. Department of Energy.
† crboffo@fnal.gov

ISBN: 978-3-95450-220-2 ISSN: 2673-5474 doi: 10.18429/JACoW-FEL2022-WEP39

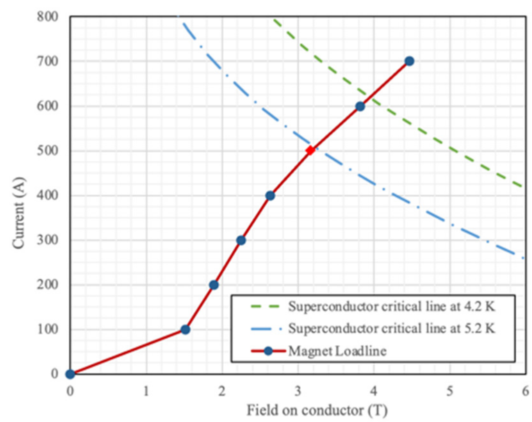

Figure 2: Loadline of EuSCU16 showing the temperature margin of the system; the red diamond indicates the operating point.

The period geometry, shown in Fig. 1 was optimized using COMSOL [4]. Each winding package includes 13 layers with 7 turns per layer. Winding technique optimization and technician training are underway to mitigate the risk of inter-strand electrical shorts, a typical risk for rectangular shaped conductor tight windings.

Figure 2 shows the loadline of the EuSCU16 magnet. The system operates at 500 A with a temperature margin of 1 K with respect to 4.2 K; however, being a cryocooled system it is expected to operate below 4 K.

CRYOGENIC DESIGN

The magnet system is kept at operating temperature via two GM cryocoolers, each providing a cooling power of 1.8 W at 4.2 K. The cryocoolers are positioned at each end of the vacuum vessel and connect to the magnet arrays and the beam pipe. Table 2 summarizes the calculated heat loads at the first and second stages of the two cryocoolers. The radiation contribution is minimized by means of a 30 layer multi-layer insulation (MLI) blanket wrapped around the thermal shield. The conductive load is optimized by using glass fiber reinforced (G11) supports for the cold mass similar in design to those used in PIP-II, FRIB and LHC [5].

Each magnet current leads is connected to one cryocooler and comprised of two sections: phosphor bronze resistive rods bridge the room temperature cryostat to the first stage of the cryocoolers, while commercial HTS leads rated to 1000 A bridge the two stages of the cryocoolers.

Heat is extracted from the cold mass by means of conduction using local OHFC copper foils that connect each single winding package to a large bus bar that connects to the second stages of the cryocoolers This is an optimal approach for a stand-alone system because it does not require the presence of a cryogenic plant and reduces efforts during installation. Furthermore, the absence of liquid cryogens simplifies the safety requirements connected to the implementation of pressure vessel norms. However, the amount of cryocoolers required becomes economically impractical for a large number of devices.

Table 2: System Heat Loads

Heat loads [W]	**Stage 1 40 K**	**Stage 2 4.2 K**
Radiation	4.6	0.20
Conduction	9.6	0.28
Current leads	50.0	0.21
Instrumentation	1.0	0.02
Dynamic losses	-	0.47
Total	**65.2 W**	**1.18 K**

When several SCUs are connected in series in a long FEL line, a solution like that used in SRF cryomodules becomes appealing. The present SCU design allows to swap the existing high purity copper bus bars with 2-phase helium pipes while maintaining the same magnet configuration. The thermal shield can also be adapted to integrate cooling piping at 50 K.

MECHANICAL DESIGN

The mechanical design of the system, shown in Fig. 3 and Fig. 4, focuses on cost reduction and modularization. The vessel is manufactured out of carbon steel, with flanges close to the beam made from stainless steel. While the prototype device integrates a single magnet array, its design allows to integrate more than one magnet unit in a single vessel, thus minimizing the inactive length of the system. This is achieved by implementing the warm strongback concept developed for the PIP-II cryomodules [6]. The cold mass, which includes the magnet array, the beampipe and the thermal shield, is supported by two G11 posts. The cold mass is mounted on the posts, assembled, and aligned on rails; the fully assembly is then slid inside the vacuum vessel. The strongback remains at room temperature, thus one of the posts is fixed in position while the other is allowed to slide on the rails to compensate for thermal shrinking.

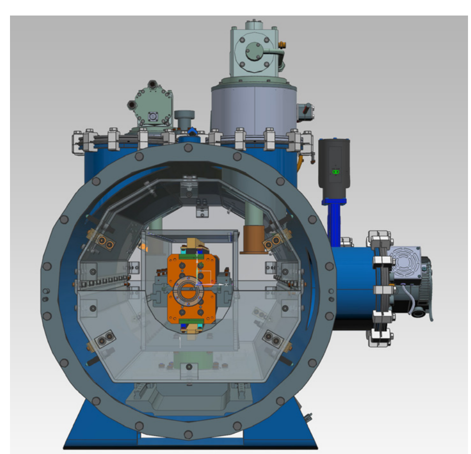

Figure 3: View of the magnet system without end flanges.

ISBN: 978-3-95450-220-2 ISSN: 2673-5474 doi: 10.18429/JACoW-FEL2022-WEP39

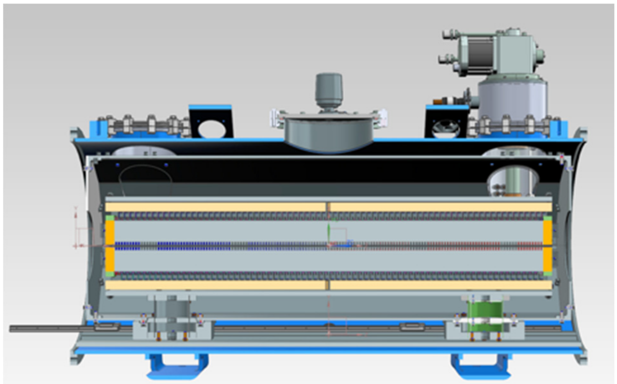

Figure 4: Cross section of EuSCU16 showing the cold mass support posts installed on rail.

The vertical shrinking of the cold mass can be predicted through finite element simulations and compensated for during assembly. Minimizing the difference between the active length of the magnet arrays and the vacuum vessel is also critical. At present the 1.5 m long vessel integrates a 1.2 m long magnet. The inactive space is used to minimize thermal loads to the cold mass and is populated with corrector coils.

The cryocoolers are mounted on domes that also include the current leads assembly and the thermal shield. They are pre-assembled in advance, outside the vacuum vessel to ease operations. The thermal shield is divided in a lower half that is supported by the two G11 posts, while the top half is assembled as the last element of the cold mass before MLI installation and insertion in the vacuum vessel.

PROTOTYPING

While the design of the overall system is being completed, prototyping of critical components has started. Magnet formers 300 mm long have been manufactured by local industry with the goal of verifying the ability to meet the stringent accuracies required by undulators. As shown in Fig. 5 an absolute positioning of the poles along the beam direction with an accuracy of ±10 µm was achieved.

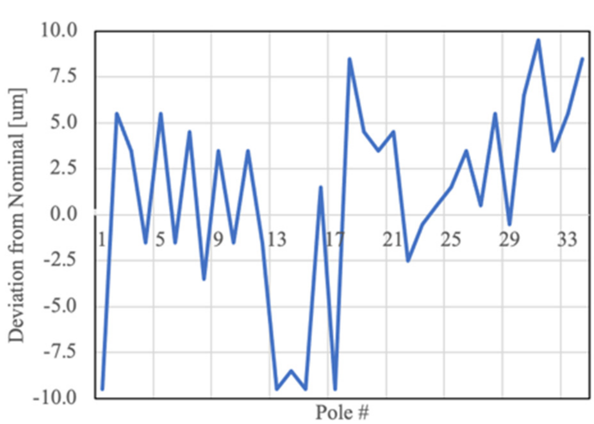

Figure 5: Deviation from the absolute position of each pole along the beam axis of a 300 mm long magnet former.

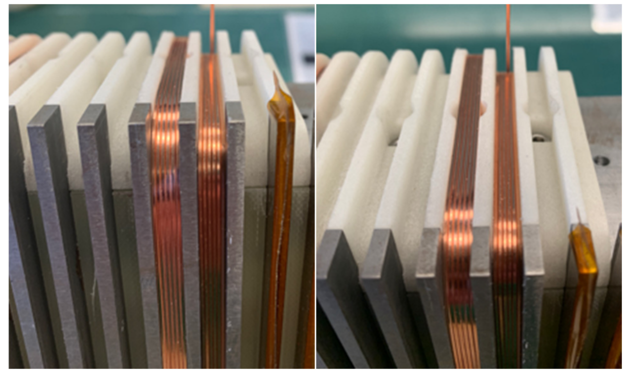

Figure 6: Testing of the winding process.

The developed manufacturing process can be extended up to formers 2 m in length. A flatness of 40 µm for the pole surface measured with a coordinate measuring machine was also achieved. Figure 6 shows the ongoing testing of the winding process.

CONCLUSION

While the EUPRAXIA@SPARC_LAB baseline foresees the use of Apple X undulators for the AQUA FEL beamline, SCUs offer tunability and flexibility during operation. A prototype superconducting device with 16 mm period length is being designed, manufactured, and tested at Fermilab aiming to demonstrate its technology maturity. Ultimately the prototype will be delivered to INFN-LNF and potentially installed in the machine. The device is being specifically designed for FEL applications, thus departing from the stand-alone configuration developed for synchrotron light sources. It embraces the cryomodule topology adopted in large accelerator facilities where multiple devices are installed in series.

REFERENCES

[1] M.Ferrario *et al.*,"EuPRAXIA@SPARC_LAB Design study towards a compact FEL facility at LNF", *Nucl. Instrum. Methods Phys. Res., Sect. A*, vol. 909, p. 134, 2018.

[2] R.W.Aßmann *et al.*,"EuPRAXIA Conceptual Design Report" *Eur. Phys. J. Spec. Top.*, vol. 229, no.24, p. 3675, 2020 [erratum: *Eur. Phys. J. Spec. Top.*, vol. 229, p. 11, 2020.]

[3] J. Bahrdt, E. Gluskin, "Cryogenic permanent magnet and superconducting undulators" *Nuclear Instrum. Methods in Phys. Res., Sect. A*, vol. 907, pp. 149-168, 2018.

[4] Commercial finite element software

[5] T. Nicol *et al.*, "SSR1 cryolodule design for PXIE", in *Proc. IPAC'12*, New Orleans, LA, USA, May 2012, paper WEPPD005, pp. 2504-2506.

[6] V. Roger, S. Cheban, T. H. Nicol, Y. O. Orlov, D. Passarelli, and P. Vecchiolla, "Design Update of the SSR1 Cryomodule for PIP-II Project", in *Proc. IPAC'18*, Vancouver, Canada, Apr.-May 2018, pp. 2721-2723. `doi:10.18429/JACoW-IPAC2018-WEPML019`

ISBN: 978-3-95450-220-2 ISSN: 2673-5474 doi: 10.18429/JACoW-FEL2022-WEP40

BEAM BASED ALIGNMENT OF A SEEDED FEL

E. Allaria†, A. Brynes, B. Diviacco, L. Giannessi[1] and C. Spezzani
Elettra-Sincrotrone Trieste S.C.p.A. Trieste, Italy
[1]also at INFN LFN, Frascati, Roma, Italy

Abstract

Optimal FEL gain in a seeded FEL requires the careful alignment of different components. As for SASE FELs, the gain is optimized when the electron bunch travels in a straight line along the axis of each undulator in the radiator section. We have recently developed an alignment strategy for the optimization of the FERMI FELs which combines the beam-based alignment of the magnetic elements (undulators and quadrupoles) with the collinear alignment of spontaneous emission from each undulator. The method is divided into 3 steps. In the first step, we measure the undulator spontaneous emission with a spectrometer to fine-tune each undulator gap and set the best electron beam trajectory for collinear emission of each module. In the second step, the alignment of the undulator axis on the electron trajectory previously defined is achieved by looking at the undulator focusing effect. Finally, the seed laser is superposed on the electrons and aligned to maximize the bunching along the defined direction. This procedure can lead to an improvement in the control over the electron beam trajectory and results in a more efficient FEL process characterized by more stable and larger energy per pulse and a cleaner optical mode. A description of the method with the obtained results are reported in this work.

INTRODUCTION

High gain single pass Free Electron Lasers such as FERMI [1] rely on the energy exchange between the electron beam and the FEL radiation occurring along a long radiator (~ 100 m) composed of several undulators. To optimally couple the electrons to the radiation several conditions need to be satisfied:

1. Electron trajectory should be straight;
2. Resonance condition to the FEL wavelength should be met in each undulator;
3. Undulator need to be aligned to the electron beam axis.

In case of seeded FEL such as FERMI it is also required that:

4. the seed laser is aligned to the same electron beam axis.

Due to the strong interplay between these conditions, it is required to establish a procedure that allows to individually adjust each of them. It has been observed that the emission mode of a seeded FEL is strongly affected by the pointing of the seed laser [2]. With the procedure recently implemented at FERMI the first 3 points are cured before the seed laser is aligned.

† enrico.allaria@elettra.eu

DEFINING THE BEAM TRAJECTORY

FEL pulses produced by both FEL lines at FERMI can be characterized using the PADReS setup [3,4] accounting various optical elements and diagnostic including a spectrometer and various FEL profiles relying on YAG screens and CCD (Figure 1).

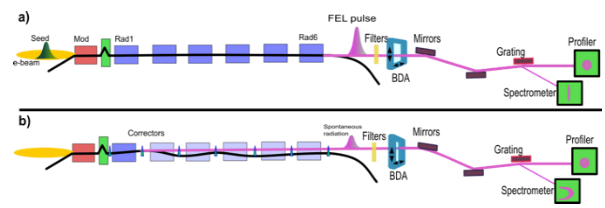

Figure 1: FEL-1 line and the used devices for the characterization of the FEL (top) and for the trajectory alignment procedure (bottom).

To define the straight trajectory on the long radiator, we use PADReS diagnostic on the spontaneous emission produced by the electron beam on a single undulator tuned at the desired wavelength while other undulators are open.

The PRESTO spectrometer collects the light dispersed in the horizontal plane by means of a diffraction grating onto a 2D detector, providing simultaneously the spectral distribution of the source (horizontal projection) and its intensity profile (vertical projection).

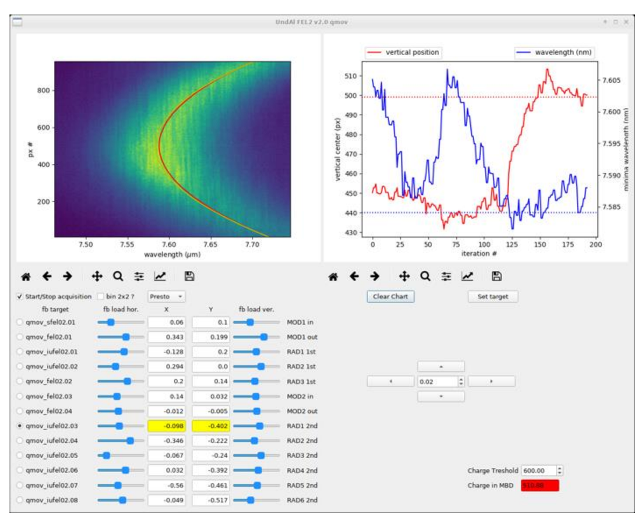

Figure 2: GUI used to monitor the evolution of the spontaneous emission mode while changing the trajectory in the resonant undulator.

ISBN: 978-3-95450-220-2 ISSN: 2673-5474 doi: 10.18429/JACoW-FEL2022-WEP40

The spontaneous emission appears in a typical C-shape (as show in Fig. 2) corresponding to a vertical cut of the undulator emission cone integrated over the beam defining aperture (BDA). This shape reflects the quadratic relationship between wavelength and angle of deviation from the axis contained in the resonant condition equation for the emission from an undulator. The minimum of the parabola identifies the emission axis. In order to improve the accuracy, we set the BDA to a very small horizontal opening.

In these conditions a wavelength shift of the transmitted radiation is measured in PRESTO as the horizontal pointing of the electron beam is varied in the resonant undulators (blue line in Fig. 2 right panel). The shortest wavelength corresponds to the radiation mode centred to the BDA. In the vertical direction BDA are left open and changes of the electron beam trajectory will lead to vertical movements of the measured spectrum (red line in Fig. 2 right panel).

The procedure starts with the first radiator. The radiation wavelength is minimized with horizontal kicks to the electron trajectory and vertical trajectory is optimized to centre the radiation mode into the detector. The radiation mode (position and wavelength) is then taken as a reference.

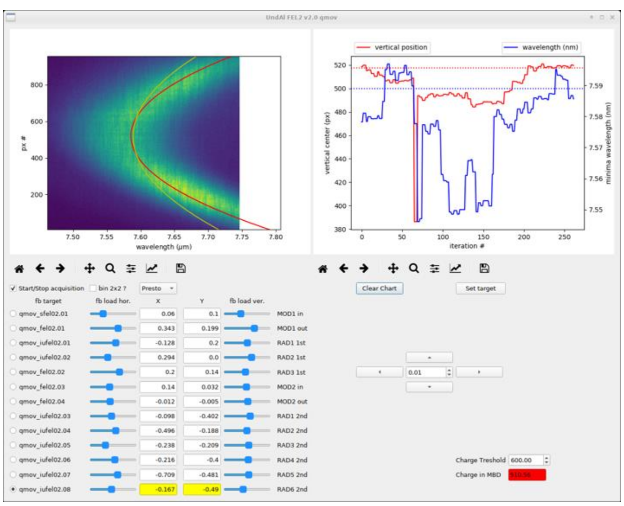

Figure 3: Alignment of the radiation mode of last undulator to the mode from one upstream.

The first undulator is then open and second one is put on resonance. Again, trajectory on rad 2 is adjusted (without changing trajectory on radiators upstream) to find minimal wavelength (horizontal) and nominal pointing (vertical).

Trajectory is moved by changing the target position on the beam position monitors (BPM) downstream the interested undulators, the trajectory feedback adjust the correctors to keep trajectory unchanged everywhere except the desired BPM. If after the optimization a wavelength shifts exists between the two undulators, an offset to the undulator gap is used to have the same resonant wavelength. Accuracy of the procedure is of the order of 10 µm for the trajectory and 5 µm for the undulator gap.

One after the other, the trajectory of the electron beam in all undulators is optimized.

A successful alignment of the electron beam trajectory leads to an improved FEL performance with larger stability and a nicer transverse mode of the FEL spot as measured in the profiles (Fig. 4).

A typical side effect of a well-defined straight trajectory is that most of the correctors used by the feedback are relaxed.

Current Limitations of the Procedure

Due to the need to work with spontaneous emission that from single undulator is very weak the method requires the availability of a very sensitive detector in the spectrometer. The method can only be done using an in vacuum EUV camera. Moreover, due to the need to have the full “c” shape measured by the detector the method only works for relatively short wavelength (<15 nm).

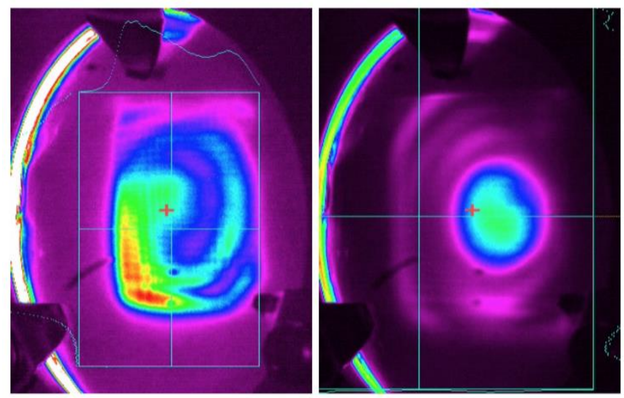

Figure 4: FEL spot profile before (left) and after (right) a successful alignment procedure. To be noted that the CCD gain has been reduced.

For FEL-1 it has been possible to apply the method looking at the emission mode of the third harmonic of the resonant wavelength with the undulator set in horizontal polarization.

Given the need to work at short wavelength the method also requires the undulators to work at relatively large gap. As a result, the method may not take into consideration the undulator focusing that may occur in case of an undulator not aligned with the electron beam axis and operated a smaller gap.

In order to verify and possible solve this a second procedure has recently been implemented.

UNDULATOR ALIGNEMENT

The relative alignment of the undulators to the defined nominal electron beam trajectory is estimated by measuring the kick produced by the undulators to the electron beam when closing the gap.

ISBN: 978-3-95450-220-2 ISSN: 2673-5474 doi: 10.18429/JACoW-FEL2022-WEP40

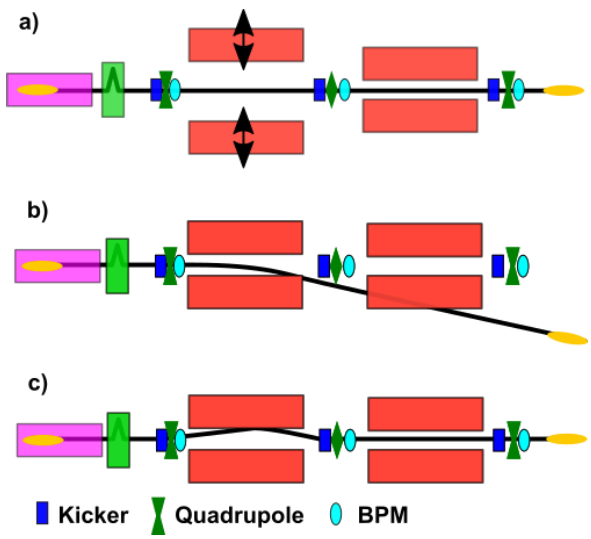

Figure 5: Scheme used to measure the undulator offset with respect to the electron beam trajectory. a) straight trajectory with undulator open. b) Undulator induced kick on the trajectory. c) Kick compensated by the feedback.

Instead of estimating the undulator induced kick by measuring the induced beam offset in the two downstream BPMs (Fig. 5b) the procedure implemented at FERMI uses the measured strength of the correctors (upstream and downstream of the undulator) required to keep the trajectory at 0 in all BPMs (Fig. 5c). The strength of the corrects is measured as a function of the undulator gap (Fig. 6).

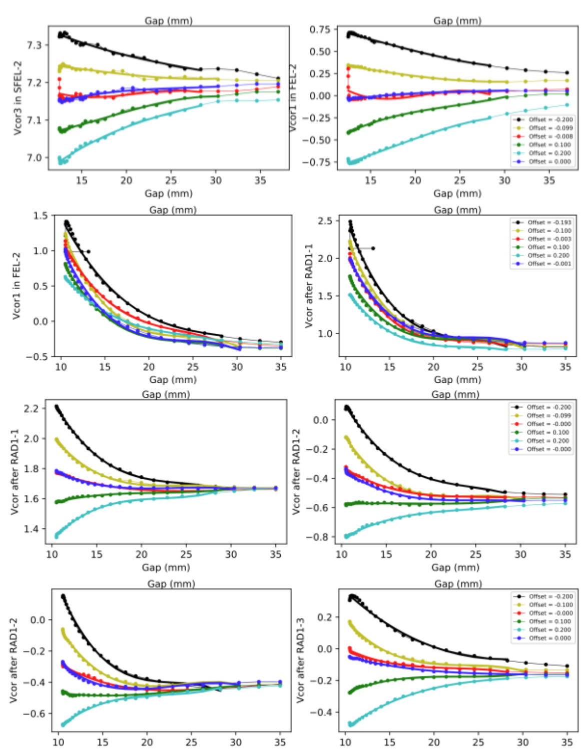

Figure 6: Measurements done on the modulator and first 3 radiators of FEL-2 for five different values of the undulator vertical offset.

The measured undulator kick is the result of a combination of residual field integral and undulator focusing. An accurate discrimination between the two effects in not straightforward and not yet implemented, nevertheless looking at the decay of the corrector strength occurring over the range of ~10 mm gap it is possible to estimate the effect of undulator focusing. Repeating the measurement with different values for the undulator axis it is possible to identify which axis has a minimum impact on the electron beam. The procedure is repeated for each undulator.

FERMI undulator design allows to change the undulator axis in the vertical direction adding an offset of up to 500 µm. The same measurement can be done also by moving the electron beam axis in the whole undulator area, this is done using the quadrupole movers that move both the BPM and the quadrupoles so that the beam is always passing at the centre of the quadrupoles and no extra kick from the quadrupoles is added. By using this second option it has been possible to measure both the vertical and the horizontal alignment of the undulators with respect to a nominal trajectory.

For the APPLE-II radiators of FERMI measurements can be repeated for different polarizations, this could allow an easier discrimination between the residual field integral and the undulator focusing due to the misalignment.

Recently the method has been tested on both FEL-1 and FEL-2. Measurements on FEL-1 show small residual offsets of the radiators with respect to the nominal trajectory, typically one or two undulator can have a maximum offset of less than 100 µm. Correction of the offsets has not shown a significant improvement of the FEL, but more systematic studies need to be performed.

Measurements on FEL-2 instead showed a large offset of one of the radiators of the first stage (Fig. 6 second panel), while downstream undulator appears to be aligned within 50 – 100 µm. Results from rad1-1 suggests that the undulator has an offset of about 500 µm. The large offset between the rad1-1 axis and the closest undulator has been confirmed by laser tracker measurements.

ACKNOWLEDGEMENTS

We are grateful to the FERMI team and operators and to the alignment group for the precious support provided during the machine preparation and data acquisition.

REFERENCES

[1] E. Allaria *et al.*, "The FERMI free-electron lasers", J. Synchrotron Radiat., vol. 22, pp. 485–491, 2015. doi:10.1107/S1600577515005366

[2] S. Khan *et al.*, "Characterization and Optimization of Ultrashort and Coherent VUV Pulses at the DELTA Storage Ring", in *Proc. IPAC'15*, Richmond, VA, USA, May 2015, pp. 1452-1455. doi:10.18429/JACoW-IPAC2015-TUPWA022

[3] M. Zangrando *et al.*, "The photon analysis, delivery, and reduction system at the FERMI@Elettra free electron laser user facility", *Rev. Sc. Instrum.*, vol. 80, p.113110, 2009. doi: 10.1063/1.3262502

ISBN: 978-3-95450-220-2 ISSN: 2673-5474 doi: 10.18429/JACoW-FEL2022-WEP40

[4] C. Svetina *et al.* "PRESTO, the on-line photon energy spectrometer at FERMI: design, features and commissioning results", *J. Synchrotron Rad.*, vol. 23, pp. 35-42, 2016. doi: 10.1107/S1600577515021116

ISBN: 978-3-95450-220-2 ISSN: 2673-5474 doi: 10.18429/JACoW-FEL2022-WEP42

DEVELOPMENT OF A PHOTOELECTRON SPECTROMETER FOR HARD X-RAY PHOTON DIAGNOSTICS AT THE EUROPEAN XFEL

J. Laksman*, F. Dietrich, J. Liu, Th. Maltezopoulos, M. Planas, W. Freund, R. Gautam,
N. Kujala, S. Francoual[1], J. Grünert
European XFEL, Schenefeld, Germany
[1]also Deutsches Elektronen-Synchrotron DESY, Hamburg, Germany

Abstract

We developed an angle-resolved photoelectron spectrometer, based on the electron time-of-flight concept, for hard X-ray photon diagnostics at the European Free-Electron Laser. The instrument shall provide users and operators with pulse-resolved, non-invasive spectral distribution diagnostics, which in the hard X-ray regime is a challenge due to the poor cross-section and high kinetic energy of photoelectrons for the available target gases. We report on the performance of this instrument as obtained using hard X-rays at the PETRA III synchrotron at DESY. We demonstrate a resolving power of 10 eV at incident photon energies up to 20 keV.

INTRODUCTION

The unique properties of X-ray Free-Electron Laser (XFEL) radiation offering high-intensity and coherent X-ray pulses at Ångström wavelengths have found applications where the ability to take snapshots of samples at unprecedented molecular length and time scales provides new scientific insights. However, the stochastic nature of Self-Amplification of Spontaneous Emission (SASE) has the consequence that every photon pulse displays individual characteristics in terms of spectral distribution and intensity. At the European XFEL (EuXFEL) facility in Schenefeld, Germany, the X-ray photon diagnostics group (XPD) utilizes a variety of dedicated techniques for providing beam parameters [1]. For soft X-rays, the angle-resolved Photo-Electron Spectrometer (PES) with 16 electron Time-Of-Flight (eTOF) flight-tubes as dispersive elements provides pulse resolved photon energy and polarization diagnostics [2]. Electron spectrometers based on the eTOF principle have flight-tubes with applied voltages that decelerate the electrons. Fast electronics register the time difference from ionization to detection which is related to the kinetic energy of the photoelectrons. The PES, in Fig.1, which uses gas targets is non-invasive and has found applications for soft X-ray photon diagnostics and experiments [3, 4]. Adapting the PES concept to the hard X-ray range is not straightforward due to the poor ionization cross-section and very high kinetic energies of photoelectrons in that regime. This contribution describes the development of the new PES dedicated to photon diagnostics at hard X-rays and presents results from measurements at the beamline P09 at PETRA III [5].

* joakim.laksman@xfel.eu

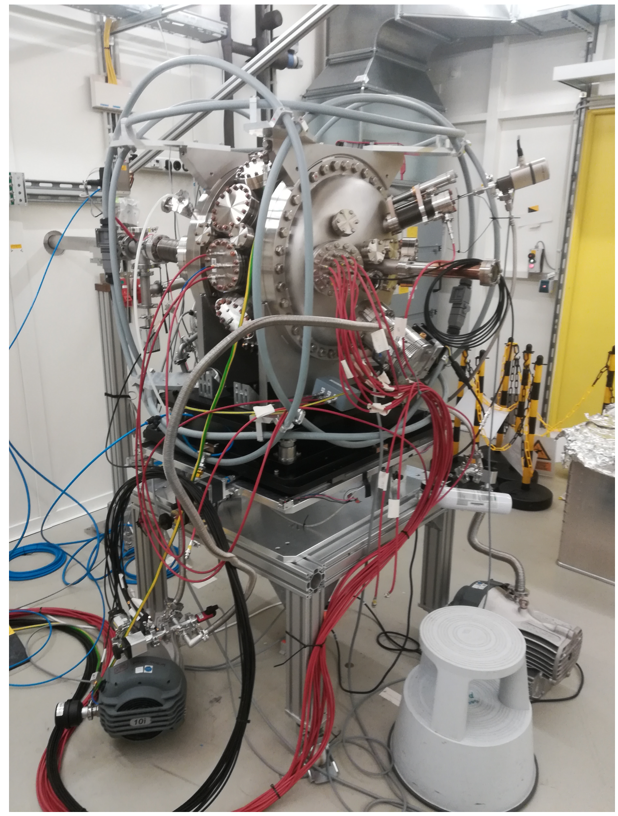

Figure 1: The hard X-ray PES installed at the P09 beamline at PETRA III. A target gas is injected into the center. Emitted photoelectrons are decelerated and focused through the electron optics of the flight-tubes before they reach the detector. Helmholtz coils encapsulate the device to cancel external magnetic fields, which otherwise influence the electron trajectories.

INSTRUMENT

A picture of the device installed at the P09 beamline is presented in Fig. 1. The spectrometer consists of 12 eTOF flight-tubes oriented perpendicular to the X-ray beam at angles of $0°, 30°, \ldots, 330°$. In order to maximize the flight-tubes performance as dispersive elements, while simultaneously focussing the photo-emitted electrons to the detector, we chose a design where the flight-tubes are divided in *retardation region* and *Einzel lens*, separated with a high transmission gold mesh to prevent field penetration between the two regions. An effusive gas jet is injected via a capillary in the interaction region where it interacts with the X-ray beam

ISBN: 978-3-95450-220-2 ISSN: 2673-5474 doi: 10.18429/JACoW-FEL2022-WEP42

and photoelectrons are emitted. The interaction region has a ∅35 mm inner cylindrical diameter and encapsulates the source region to make it field-free. Following the IR are nine 2 mm thick electrodes where gradually higher potentials are applied. These 10 first electrodes are serially connected via 100 MΩ resistors to work as voltage dividers, thus within a short distance, a steep retardation is imposed capable of decelerating electrons from many keV to only a few 10 eV. Following the strong deceleration, electrons must be guided to the detector which is achieved by a three-element electrostatic Einzel lens. For a robust monolithic design, flight-tubes were machined out of aluminum so that each electrode segment is a round block with 12 conical holes that work as parts of the flight-tube. Electrodes are separated 1 mm from each other with PEEK spacers. To avoid oxidation, aluminum parts were chromatized with the surface treatment *SurTec 650* that ensures the preservation of the electrical conductivity. On both faces of the nested concentric flight-tube electrode cylinders, we have aluminum disks that work as shields. The vacuum vessel is made of non-magnetic stainless steel and care has been taken that all parts are non-magnetic. A 3D Helmholtz coil structure comprised of three mutually orthogonal pairs of coils surrounds the chamber and is used to compensate for the background magnetic field which otherwise would influence the electron trajectories. A fluxgate-type magnetometer (*Bartington Mag-03*) to monitor the magnetic field is mounted in a pocket flange to be as close as possible to the source region. The detectors are *Hamamatsu F9892-31* Micro Channel Plates (MCP) with 42 mm active area and 0.7 ns pulse width. For alignment of the instrument to the beam, the setup is supported by decoupled transverse and vertical translation motion stages controlled by stepper motors.

A target gas that is typically a noble gas is injected as an effusive jet in the interaction region via a ∅100 µm inner-diameter capillary. Target gas criteria are high cross section (σ) and low natural line-width (Γ) In the case of polarization studies also an anisotropy parameter (β) far from 0 becomes relevant. Furthermore the presence of Auger lines can be valuable for kinetic energy calibration of the spectrum.

Before installation in the EuXFEL SASE1 tunnel, the device was tested at the hard X-ray beamline P09 at PETRA III, DESY that offers high energy tuneability from 2.7 keV to 24 keV, full polarization control, high energy resolution and flux [5]. The Si(111) crystal monochromator with the energy bandwidth 1.3×10^{-4} was selected. The beam was uncollimated of size ~2.1 mm × 1.5 mm (V×H) FWHM and mirrors were used to suppress higher harmonics. Measurements were carried out when the machine was operating in timing mode at 5.2 MHz (192 ns pulse separation). For data acquisition a programmable four channel *Lecroy WavePro 725Zi* oscilloscope 2.5 GHz and 40 GS/s was used.

The CAD model was imported into the commercial software *SIMION 8.0* for electron trajectory simulations in order to quantify the performance and improve the design prior to manufacturing. The simulated spectra enables us to define a calibration function that transforms TOF to electron kinetic energy and further on to spectral distribution regardless of the target gas. The kinetic energy scale of the electron spectra were in addition calibrated by measuring the well-established Kr LMM Auger lines, thus confirming the simulations reliability for TOF to E_K calibration.

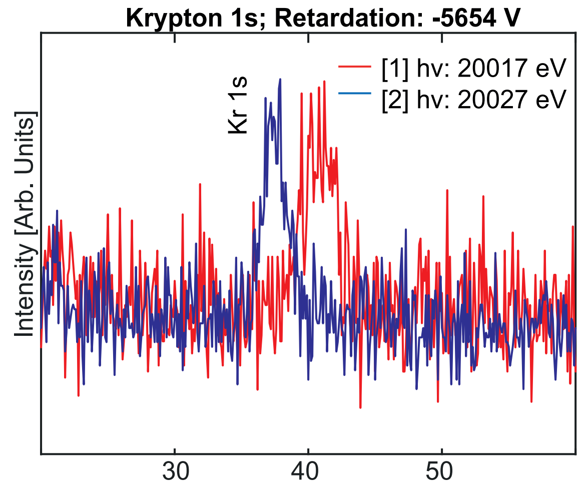

Figure 2: Kr 1s spectra collected at 20 017 eV (red) and 20 027 eV (blue) photon energy with fixed retardation voltage at −5654 V. Peaks are clearly shifted from which we estimate a resolving power of 10 eV.

Table 1: Photoelectron binding energy (E_B) and Lorentzian natural line broadening (Γ) in eV for the typical target gases: Xenon and Krypton.

Orbital	**Xenon**		**Krypton**	
	E_B **[eV]**	Γ **[eV]**	E_B **[eV]**	Γ **[eV]**
1s	34 565.13	9.6	14 327	2.65
2s	5452.57	2.76	1921.4	4.28
$2p_{1/2}$	5106.72	2.79	1730.90	1.31
$2p_{3/2}$	4786.47	2.60	1679.07	1.17

RESULTS AND ANALYSIS

For photon energies above 14 keV, Kr 1s is the most suitable choice. The binding energy is 14 327 eV and the natural line broadening is 2.65 eV (Table 1). Figure 2 presents Kr 1s TOF spectra for photon energies 20 017 eV (red) and 20 027 eV (blue). Here we have $\sigma = 0.008$ Mb. Retardation voltage is fixed at −5654 V. Peaks are clearly shifted from which we estimate a resolving power of 10 eV.

For the spectrometer to be valuable as a photon diagnostics device at EuXFEL it is important that it can perform single pulse diagnostics. In the 40 bunches mode, at 100 mA, P09 beamline at PETRA III provides $\sim 10^5$ photons per pulse. SASE1 beamline at EuXFEL provides $\sim 10^{12}$ photons per pulse. We estimate that at P09 we must collect data from $10^{12}/10^5 = 10^7$ pulses in order to reach comparable statistics as at the EuXFEL. Our spectrum corresponds to $\sim 10^7$ pulses. The integrated number of collected photoelectrons in the

ISBN: 978-3-95450-220-2 ISSN: 2673-5474 doi: 10.18429/JACoW-FEL2022-WEP42

peak is ~200 which is sufficient to calculate the mean-value and standard deviation of the spectral distribution.

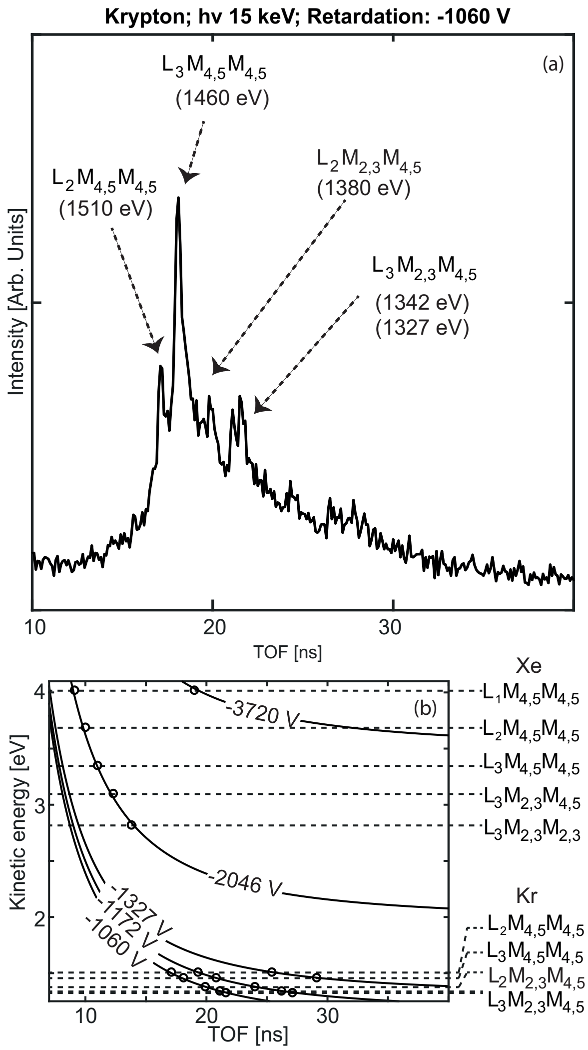

Figure 3: (a) Kr LMM Auger spectrum collected at 15 keV photon energy with target gas Krypton. (b) Comparison of simulated TOF to E_K calibration for different voltage settings and measured data from Kr LMM Auger lines and Xe LMM Auger lines.

Figure 3(a) presents an Auger spectrum at retardation voltage (−1060 V) where LMM line groups corresponding to transitions from vacancies in the L_2 and L_3 subshell can be resolved. The presence of Auger lines that are photon energy independent provides us with an intrinsic TOF to kinetic energy calibration. Furthermore, their polarization independence makes Auger lines suitable for the normalization of detector signals for polarimetry. Most dominating are $L_{2,3}M_{4,5}M_{4,5}$ but also $L_{2,3}M_{2,3}M_{4,5}$ have sufficient signal to noise ratio to be detected. Lower E_K leads to better resolution. Indeed, for the $L_3M_{2,3}M_{4,5}$ line group, two bands can be resolved, each corresponds to transitions to several different final states, dominated by $^1F_3$ and $^3D_3$. Figure 3(b) shows simulated TOF to E_K calibration curves for five different voltage settings compared with measured data from Kr LMM and Xe LMM auger lines. The agreement is excellent, thus we use Auger lines to confirm that our calibration procedure is correct.

CONCLUSION

We have created a novel design for an angular photoelectron spectrometer for the hard X-ray regime. We built and tested this device which is based on the well-known eTOF concept but allows for much higher photon energies thanks to a fundamentally new layout of the flight tubes. A resolving power of ~10 eV for up to 8.7 keV electron kinetic energy has been demonstrated and we have shown that the instrument is suitable for hard X-ray photon diagnostics for both spectral distribution and polarization. By comparing Auger lines with simulated spectra we have confirmed that simulations are reliable for kinetic energy calibration.

ACKNOWLEDGEMENTS

We thank the following EuXFEL scientific support groups: Project Management (PM), Vacuum (VAC), Electronic and Electrical Engineering (EEE), Information Technology and Data Management (ITDM), Data Analysis (DA), and Control Software (CTRL). We appreciate the dedicated support by the P09 beamline group at the PETRA III facility of DESY and helpful discussions with Jens Viefhaus and our colleagues Michael Meyer and Adrian Mancuso from the EuXFEL experimental endstations. We acknowledge DESY (Hamburg, Germany), a member of the Helmholtz Association HGF, for the provision of experimental facilities. Parts of this research were carried out at beamline P09 at PETRA III. Beamtime was allocated for proposals 11008253 and 11009265.

REFERENCES

[1] J. Grünert *et al.*, ”X-ray photon diagnostics at the European XFEL”, *J. Synchrotron Radiat.*, vol. 26, pp. 1422-1431, 2019. `doi:10.1107/S1600577519006611`

[2] J. Laksman *et al.*, ”Commissioning of a photoelectron spectrometer for soft X-ray photon diagnostics at the European XFEL”, *J. Synchrotron Radiat.*, vol. 26, pp. 1010-1016, 2019. `doi:10.1107/S1600577519003552`

[3] S. Serkez *et al.*, ”Opportunities for Two-Color Experiments in the Soft X-ray Regime at the European XFEL”, *Appl. Sci.*, vol. 10, 2020. `doi:10.3390/app10082728`

[4] K. Li, J. Laksman, T. Mazza, G. Doumy, D. Koulentianos, A. Picchiotti, S. Serkez, N. Rohringer, M. Ilchen, M. Meyer, and L. Young, ”Ghost-imaging-enhanced noninvasive spectral characterization of stochastic X-ray free-electron-laser pulses”, *Commun. Phys.*, vol. 5, no. 191, 2022. `doi:10.1038/s42005-022-00962-8`

[5] J. Strempfer, S. Francoual, D. Reuther, D. Shukla, A. Skaugen, H. Schulte-Schrepping, T. Kracht, and H. Franz, ”Resonant scattering and diffraction beamline P09 at PETRA III”, *J. Synchrotron Radiat.*, vol. 20, pp. 541-549, 2013. `doi:0.1107/S0909049513009011`

ISBN: 978-3-95450-220-2 ISSN: 2673-5474 doi: 10.18429/JACoW-FEL2022-WEP44

CHARACTERISATION OF A DIAMOND CHANNEL CUT MONOCHROMATOR DESIGNED FOR HIGH REPETITION RATE OPERATION AT THE EuXFEL*

K. R. Tasca†, L. Samoylova‡, A. Madsen, I. Petrov, A. Rodriguez-Fernandez, R. Shayduk, M. Vannoni, A. Zozulya, European XFEL GmbH, 22986 Schenefeld, Germany
R. Barrett, T. N. Tran Thi, European Synchrotron Radiation Facility, 38000 Grenoble, France

Abstract

The European X-ray Free-Electron Laser (EuXFEL) is a unique FEL facility that provides X-ray pulses of high spectral brilliance and high photon flux at MHz repetition rate. However, the high peak power, produced in trains of up 2700 fs pulses at a rate of 10 Hz, induces a periodic temperature increase of the hard X-ray monochromators, thereby reducing their transmitted intensity. To address this limitation, a diamond channel cut monochromator (DCCM) was proposed as an alternative to the currently used silicon monochromators. The heat load effect of typical EuXFEL pulses at 300 K and 100 K was simulated by finite element analysis (FEA) and indicates that the significant reduction of the transmitted intensity occurs after a higher number of pulses when compared to silicon. The DCCM first prototype was manufactured from an HPHT type IIa diamond single block and characterised by rocking curve imaging (RCI). The RCI results demonstrated the high crystalline quality of the DCCM with rocking curve widths of the same order as the width predicted by the dynamical theory and a uniformly reflected intensity over the surface. The performance as a monochromator was demonstrated by measuring the double bounce reflection. The resulting images after two successive reflections showed a diffracted beam of the same size and parallel to the incident beam and confirmed its applicability.

INTRODUCTION

The EuXFEL provides X-ray pulses of high spectral brilliance and high photon flux at MHz-repetition rate [1]. However, the high peak power of the EuXFEL beam imposes a high dynamical heat load on the optical elements, such as mirrors and monochromators. Currently, in the hard X-ray regime, cryo-cooled silicon (1 1 1) monochromators are used to reduce the spectral bandwidth of the beam generated by self-amplified spontaneous emission or as spectral purification elements in seeded operation mode [2–4]. Yet, the use of a silicon monochromator introduces some limitations on the instrument operation, since the transmission of the Si monochromator at MHz repetition rates is affected by the heat load, thus reducing the intensity of the transmitted pulses by a factor of two after around 150 pulses [5]. To address these challenges imposed by the MHz repetition rate photon beams to the hard X-ray monochromator, we proposed a cryo-cooled diamond channel cut monochromator (DCCM) as an alternative to silicon. The monolithic design of the channel-cut ensures high mechanical stability and for hard X-rays, the diamond absorption cross section is one order lower than that of silicon, so the volumetric heat load effect is significantly reduced. In addition, diamond has a smaller thermal expansion coefficient and higher thermal conductivity compared to silicon, as well as high reflectivity and narrow Darwin widths [6–9].

The heat load from the EuXFEL high-energy pulses increases the temperature of the crystal and induces deformations in the crystal lattice with 10 Hz periodicity. This strongly affects the monochromator reflectivity properties and results in a decrease of the transmitted intensity through the monochromator with the accumulation of the absorbed energy in the first crystal [5]. Deformations of the lattice resulting from accumulated heat on the crystal affect the reflectivity curve. As a result of the lattice deformation with a change in d-spacing, the centre of the rocking curve is shifted, the width is broadened and the maximum intensity decreases. These variations of the diffraction profile result in a performance decrease of the monochromator, reducing the transmitted intensity and slightly increasing the bandwidth. The maximum acceptable shift of the peak position of the diffraction profile from the first crystal with respect to the second one is determined by the relative bandwidth that gives an estimation of the amount of heat that leads to the detuning of the monochromator and therefore the maximum acceptable temperature difference (ΔT) between the two crystals of the monochromator. Estimates of the acceptable ΔT between the two crystals of a diamond monochromator show that this temperature threshold is reached after a six to ten times higher number of pulses in comparison with a silicon monochromator in the same conditions, suggesting that diamond can be a suitable alternative to silicon [10, 11].

Due to the recent technological developments in the high pressure and high temperature (HPHT) crystal growth technique, diamond single crystals of type IIa with suitable size and high crystal quality suitable for X-ray optics applications are now available [8, 12, 13].

As mentioned above, an X-ray monochromator requires a high-quality perfect single-crystal. The most common techniques used to determine crystalline perfection are the measurement of X-ray diffraction profile and X-ray topography [9]. In this work, we present the X-ray characterisation results of the DCCM by the rocking curve imaging (RCI) method [14, 15], which combines rocking curve analysis and

* Work supported the R&D program of EuXFEL
† kelin.tasca@xfel.eu
‡ liubov.samoylova@xfel.eu

ISBN: 978-3-95450-220-2 ISSN: 2673-5474 doi: 10.18429/JACoW-FEL2022-WEP44

topography. The performance of the DCCM as a double-crystal monochromator was demonstrated by recording an image of the double-bounce reflection and measuring its diffraction profile.

X-RAY DIFFRACTION CHARACTERISATION OF THE DCCM

The DCCM, shown in Fig. 1, was cut from a single crystal diamond block of high-quality HPHT IIa type diamond of $4 \times 4 \times 5$ mm^3 with [1 1 0], [1 -1 0] and [0 0 1] crystallographic orientations. The two diffracting surfaces are oriented in the [1 1 0] direction, with 2.5 mm length (along to the beam direction), 2 mm width, 1 mm thickness and the gap between them is 2 mm. The channel was made by laser cutting and the surfaces were not polished.

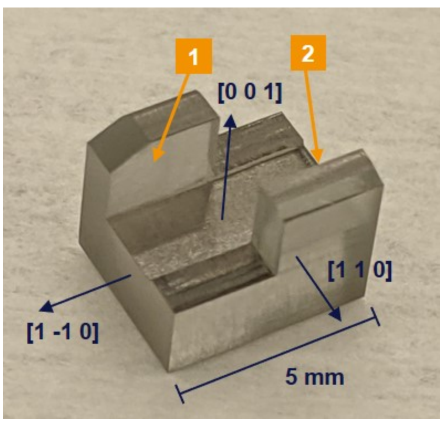

Figure 1: The diamond channel cut monochromator and its crystallographic orientations.

The crystal quality of the DCCM was investigated by the RCI technique [14]. The RCI is a combination of rocking curve evaluation and X-ray diffraction topography. The crystal is illuminated by a narrow bandpass monochromatic X-ray beam and rotated in a small angular range through its Bragg angle (θ_B). For each angular step of the rocking curve, a high-resolution X-ray camera takes a topography image resulting in a sequence of detector frames. The sequence of images is then analysed to produce calculated maps of the full width at half maximum (FWHM), integrated intensity and peak position from the curve fitting of each pixel.

The RCI measurement was performed at the beamline BM05 of the European Synchrotron Radiation Facility (ESRF) [16] with a monochromatic X-ray beam defined by a double-crystal Si(3 3 3) monochromator in vertical scattering geometry. The pco.gold detector was placed perpendicular to the diffracted beam at a distance of 200 mm from the sample. The detector is coupled to a microscope objective which images a scintillator screen resulting in a pixel size of 6.5 µm × 6.5 µm. The X-ray beam was limited by slits to a size of 0.6 mm × 1.3 mm (H×V) to illuminate the entire surface of the first blade.

First, to characterise one of the blades of DCCM, we choose the C(2 2 0) reflection and photon energy of 18 keV. The (2 2 0) planes diffract at $\theta_B = 15.849\,°$ with Darwin width, calculated by the dynamical theory of X-ray diffraction [9], of 1.1″. A set of 201 images in ω steps of 0.035″ in a range of 7.2″ was recorded and analysed with a python script to fit the curves and generate the maps [17, 18].

An X-ray image taken at the centre of the C(2 2 0) diffraction is shown in Fig. 2. This image shows an almost regular bright and dark pattern of vertical grooves and some intensity contrast, indicated by black arrows in Fig. 2, indicating the presence of defects on the surface. The vertical grooves were observed in the microscopy image of Fig. 3 and can be associated with the laser cutting process [11]. The fitting of the rocking curves of the three pixels indicated as px1, px2 and px3 in Fig. 2 is shown in Fig. 4. The analysis of the rocking curves demonstrates the effect of the grooves on the diffraction profile, which is characterised by slightly narrower FWHM and peak displacement to larger angles of the curves of more intense stripes relative to the curves of the dark stripes. The FWHM of the local rocking curves is of the same order as the Darwin width. The indicated defects in Fig. 2 are located in the dark stripes and present broader rocking curves, decrease in maximum intensity and peak displacement.

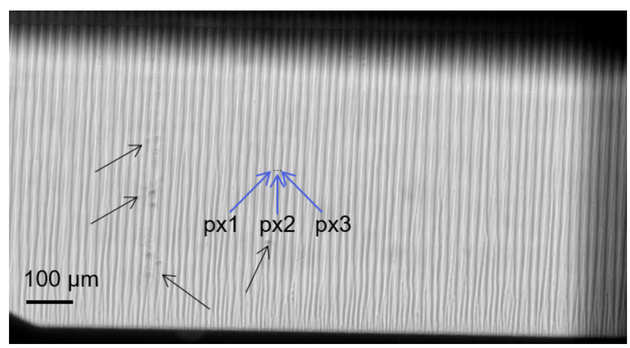

Figure 2: Topography of DCCM C(2 2 0) single reflection at 18 keV taken at the centre of the rocking curve. The black arrows indicate some surface defects and the blue arrows the analysed pixels px1, px2 and px3.

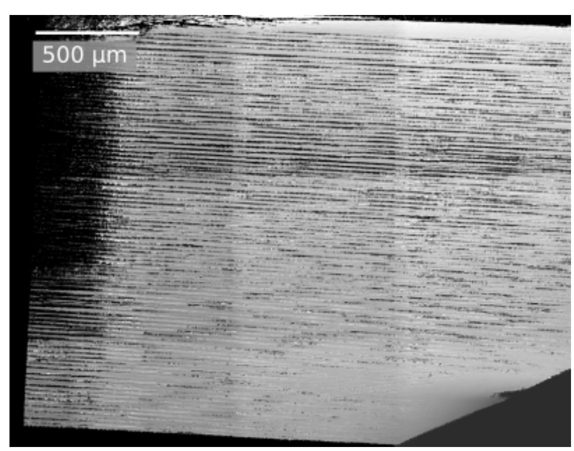

Figure 3: Confocal microscopy image of blade 1 of DCCM.

ISBN: 978-3-95450-220-2 ISSN: 2673-5474 doi: 10.18429/JACoW-FEL2022-WEP44

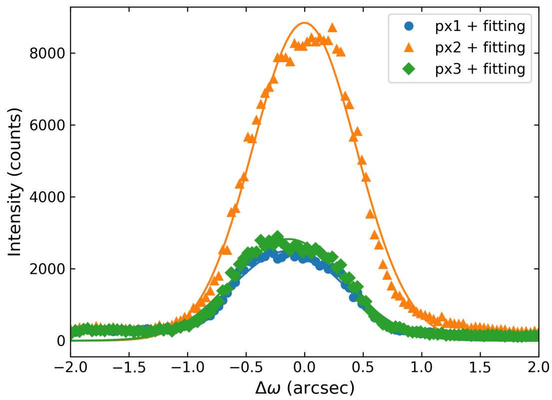

Figure 4: C(2 2 0) rocking curve at 18 keV of three pixels located at the centre of the image. px1 and px3 are located in dark stripes and have a width of 1.1 " and px2 is from a bright stripe and 1.0″ width. The dots are experimental data and the lines are the curve fitting.

Figure 5 shows the distribution map of the FWHM over the entire sample.

The map of Fig. 6 shows the relative peak displacement with respect to a rocking curve taken at the centre of the image. In this map, it is observed a pattern of displacement to low/high angles that correspond to the differences in contrast observed in the topographies associated with the grooves in the microscopy images and a shift to lower angles in the defect regions indicated by the black arrows in the topography of Fig. 2 and an overall displacement to low angles in the bottom and to high angles in top of the sample, with a displacement of ~0.5″ from the bottom to the top, which is smaller than the Darwin width.

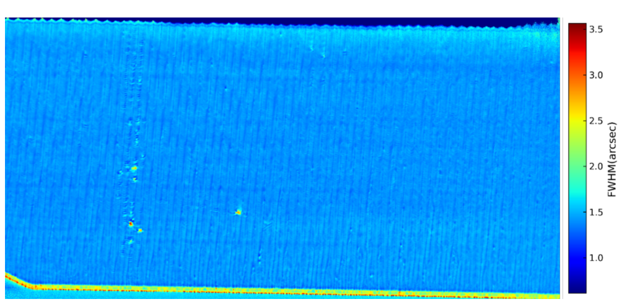

Figure 5: FWHM distribution map of blade 1 of DCCM.

The X-ray topography and the RCI maps in Figs. 2, 5 and 6 reveal the good crystalline quality of the DCCM blade. No apparent areas of intrinsic defects originating from the crystal growth are observed on the topography and the rocking curve width in almost the entire sample is of the same order of magnitude as for a perfect crystal. However, contrast features related to surface imperfection, with estimated profile characteristics in the µm range [11], are clear and might hide the presence of bulk defects.

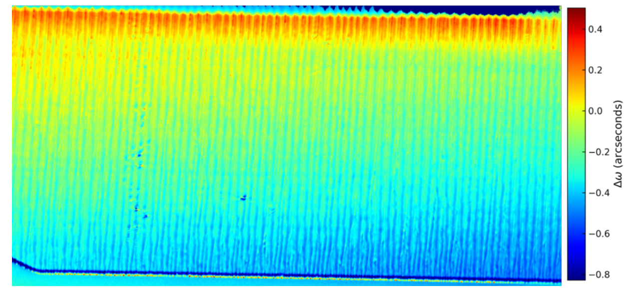

Figure 6: RCI map of the peak displacement with respect to the centre of blade 1 of DCCM.

DOUBLE-BOUNCE REFLECTION

After the characterisation of a single blade, the energy was changed to 21 keV and the crystal rotated to diffract the (4 4 0) planes in order to observe the diffracted beam after two successive reflections of DCCM. The DCCM was rotated through its θ_B of 27.92° in an angular range of 2.88″ and steps of 0.14″ and a set of 21 images were recorded. The beam was observed horizontally aligned and with the same size as the incident beam. The resulting diffraction image acquired at the peak of the diffraction profile is shown in Fig. 7. This image shows the surface's bright/dark striped contrast pattern and additional points of intensity contrast. These intensity contrasts arise from the convolution of defects on both blades of the channel cut. The combined (4 4 0) rocking curve, shown in Fig. 8, features a width of 1″ which is broader than the expected 0.6″ convoluted curve width. The broadening may be attributed to crystal defects, the mismatch between Bragg angles of Si(3 3 3) (θ_B = 16.41°) and C(4 4 0) (θ_B = 27.92°) and the monochromator bandwidth.

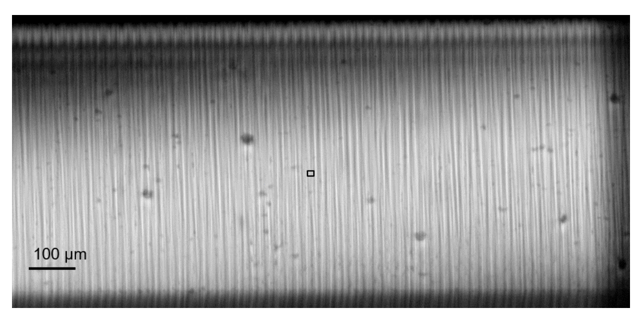

Figure 7: Topography of DCCM (4 4 0) double-bounce reflection at 21 keV taken at the centre of the rocking curve.

CONCLUSION

We have presented the X-ray characterisation results of a HPHT IIa type diamond channel cut monochromator designed to operate at hard X-rays at the EuXFEL and demonstrated its working principle as a double-bounce monochromator. With the RCI technique, which allows characterising with high-resolution both the individual crystal blades and the double-bounce reflection, we measured the crystalline quality of a single blade and the double-bounce diffraction. The images showed periodic structures that correspond to

ISBN: 978-3-95450-220-2 ISSN: 2673-5474 doi: 10.18429/JACoW-FEL2022-WEP44

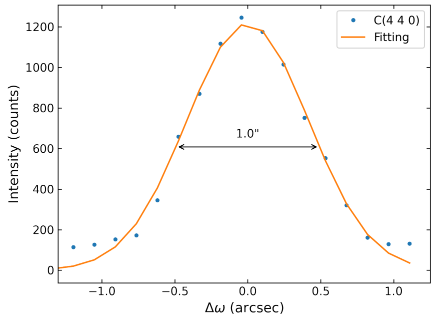

Figure 8: C(4 4 0) double-bounce rocking curve at 21 keV.

the manufacturing process and exhibited a high crystalline quality close to the expected for a perfect crystal. Further polishing of the surfaces should improve the surface quality. The diffraction after two successive reflections was observed and we demonstrated the capability of the DCCM to operate as a monochromator for a beam size of 500 µm in the energy range from 6-20 keV [11]. A proof of principle experiment at EuXFEL is scheduled to confirm the performance.

ACKNOWLEDGEMENTS

We would like to thank S. Terentyev, S. Martyushov, S. Polyakov and S. Zholudev from Technological Institute for Superhard and Novel Carbon Materials (Moscow, Russia) for growing and manufacturing the DCCM, performing the initial characterisation and for helpful comments. We thank C. Deiter (EuXFEL, Germany) for the microscopy image.

REFERENCES

[1] W. Decking *et al.*, "A MHz-repetition-rate hard X-ray free-electron laser driven by a superconducting linear accelerator", *Nat. Photonics*, vol. 14, pp. 391-397, Jun. 2020. doi:10.1038/s41566-020-0607-z.

[2] X. Dong *et al.*, "Design of a cryo-cooled artificial channel-cut crystal monochromator for the European XFEL", *AIP Conf. Proc*, vol. 1741, p. 040027, Jul. 2016. doi:10.1063/1.4952899.

[3] A. Madsen *et al.*, "Materials Imaging and Dynamics (MID) instrument at the European X-ray Free-Electron Laser Facility", *J. Synchrotron Radiat.*, vol. 28, pp. 637–649, Mar. 2021. doi:10.1107/S1600577521001302.

[4] U. Zastrau *et al.*, "The High Energy Density Scientific Instrument at the European XFEL", *J. Synchrotron Radiat.*, vol. 28, pp. 1393-1416, Sep. 2021. doi:10.1107/S1600577521007335

[5] I. Petrov *et al.*, "Performance of a cryo-cooled crystal monochromator illuminated by hard X-rays with MHz repetition rate at the European X-ray Free-Electron Laser" *Opt. Express.* vol. 30 no. 4 pp. 4978-87, 2022. doi:10.1364/OE.451110

[6] C. Giles *et al.*, "Diamond thermal expansion measurement using transmitted X-ray back-diffraction", *J. Synchrotron Radiat.*, vol. 12, pp. 349-353, 2004. doi:10.1107/S0909049505003432

[7] A. V. Inyushkin *et al.*, "Thermal conductivity of high purity synthetic single crystal diamonds", *Phys. Rev. B*, vol. 97, pp. 144305, 2018. doi:10.1103/PhysRevB.97.144305

[8] R. C. Burns *et al.*, "HPHT growth and x-ray characterization of high-quality type IIa diamond", *J. Phys.: Condens. Matter*, vol. 21, pp. 364224, 2009. doi:10.1088/0953-8984/21/36/364224

[9] A. Authier, "Dynamical Theory of X-ray Diffraction", Oxford: Oxford University Press, 2003

[10] H. Sinn *et al.*, "CDR X-Ray Optics and Beam Transport", XFEL, Rep. XFEL.EU TR-2011-002, 2011

[11] K. R. Tasca, *et al.*, "Study of a diamond channel cut monochromator for high repetition rate operation at the EuXFEL: FEA thermal load simulations and first experimental results", presented at the 14th International Conference on Synchrotron Radiation Instrumentation (SRI2021), Hamburg, Germany, Mar. 2022.

[12] S. N. Polyakov *et al.*, "Characterization of top-quality type IIa synthetic diamonds for new X-ray optics", *Diamond Relat. Mater.*, vol.20, pp. 726-728, 2011. doi:10.1016/j.diamond.2011.03.012

[13] S. Terentyev *et al.*, "Curved diamond-crystal spectrographs for x-ray free-electron laser noninvasive diagnostics", *Rev. Sci. Instrum.*, vol. 87, no. 12, p. 125117, 2016. doi:10.1063/1.4973326

[14] D. Lübbert *et al.*, "µm-resolved high resolution X-ray diffraction imaging for semiconductor quality control", *Nucl. Instrum. Methods Phys. Res. Sect. B*, vol. 160, no. 4, pp. 521-27, Apr. 2000. doi:10.1016/S0168-583X(99)00619-9

[15] T. N. T. Thi *et al.*, "Synchrotron Bragg diffraction imaging characterization of synthetic diamond crystals for optical and electronic power device applications", *J. Appl. Cryst*, vol. 50, pp. 561–569, 2017. doi:10.1107/S1600576717003831

[16] E. Ziegler *et al.*, "The ESRF BM05 Metrology Beamline: Instrumentation And Performance Upgrade", *AIP Conference Proceedings*, vol. 705, pp. 436-439, Jun. 2004. doi:10.1063/1.1757827

[17] T. N. T. Caliste *et al.*, "Rocking Curve Imaging Investigation of the Long-Range Distortion Field between Parallel Dislocations with Opposite Burgers Vectors", *Appl. Sci.*, vol. 11, pp. 9054, 2021. doi:10.3390/app11199054

[18] T. N. T. Caliste, "RCIA software", https://gitlab.com/l_sim/scripts/rcia, accessed on 16 Aug. 2022

ISBN: 978-3-95450-220-2 ISSN: 2673-5474 doi: 10.18429/JACoW-FEL2022-WEP45

MAGNETIC FIELD INVESTIGATION IN A COMPACT SUPERCONDUCTING UNDULATOR WITH HTS TAPE

D. Astapovych*, N. Glamann, A. W. Grau, B. Krasch, D. Saez de Jauregui,
Karlsruhe Institute of Technology (KIT), Karlsruhe, Germany

Abstract

The superconducting undulator (SCU) based on the second-generation high-temperature superconducting (HTS) tapes is a promising application for building tabletop free-electron laser (FELs). The short period < 10 mm undulators with a narrow magnetic gap < 4 mm are especially relevant. The advantage of the HTS tape is that it shows both high critical current density and high critical magnetic field. Each tape has 50 µm thickness and 12 mm width and is further scribed by a laser to achieve a meander structure, hence, providing the desired magnetic field pattern.

Thus, a new approach to a superconducting undulator has been presented in the past and is further developed at KIT: each coil is wound with a single 15 m structured HTS tape. As a result, 30 layers of scribed sections lay above each other, and therefore, provide the required magnetic field. The results of the magnetic field measurements together with the results of the numerical investigation will be presented and discussed.

INTRODUCTION

An idea of the undulator using the meander-structured HTS tapes was proposed by Prestemon [1,2]. Figure 1 shows a photo of a second-generation HTS tape with a meander structure, which has been made in-house at KIT using the pulsed YAG laser system at the Institute of Technical Physics (ITeP). The main parameters of the laser-scribed tapes are presented in Table 1 and used later in the computations.

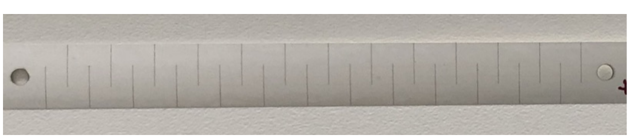

Figure 1: Segment of laser-scribed HTS tape.

Table 1: Main parameters of laser-scribed HTS tapes

Parameter	Value
HTS tape thickness (μm)	55
Period length (mm)	8.05
Period number	12.5
HTS tape groove section (μm mm)	25 4

A concept of a jointless undulator using the structured HTS tapes has been proposed by T. Holubek [3]. The design is the following: a 15 m single-piece of structured HTS tape is folded in half, resulting in the opposing current direction between two layers. Further, two non-magnetic stainless steel yokes are used to wind coils with such tapes, hence, 30 layers of scribed sections lay above each other and provide the needed magnetic field. Figure 2 shows the photo of the undulator prototype based on this winding concept.

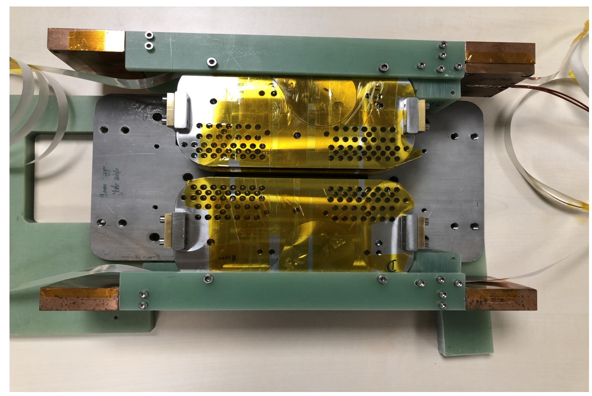

Figure 2: Undulator prototype: structured HTS tape wounded around non-magnetic stainless steel core.

Setup for Magnetic Field Measurements

The magnetic field measurements station CASPER (**C**h**A**racterization **S**et-u**P** for Field **E**rror **R**eduction), which was built and installed at our institute and is operated at KARA [4], is shown in Fig. 3. In principle, CASPER is a

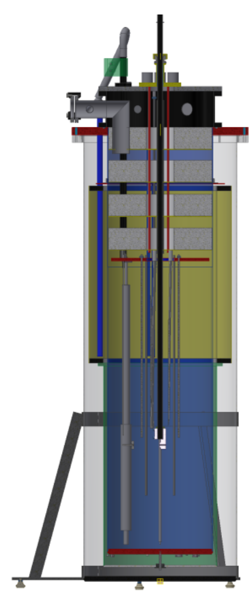

Figure 3: Magnetic field measurements station CASPER I.

* daria.astapovych@kit.edu

ISBN: 978-3-95450-220-2 ISSN: 2673-5474 doi: 10.18429/JACoW-FEL2022-WEP45

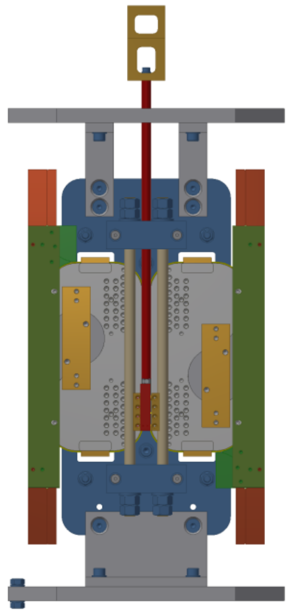

Figure 4: Magnetic field measurement system.

liquid helium bath cryostat that allows to perform magnetic field measurements at 4 K. The maximum current of 1500 A can be achieved through a pair of vapor cooled current leads. In addition, the power supply is provided with a quench detection system. More information on this system can be found in Ref. [4].

In order to place the undulator prototypes inside of the cryostat, a complete new measurement system was designed and fabricated, and is shown in Fig. 4. The magnetic field is measured with an array of ten Hall probes in-house calibrated at KIT at 4.2 K and attached to a sledge. The sledge is later moved by a computer controlled stepper motor.

MAGNETIC FIELD

Measurements

During the experiment, the undulator with the wound structured HTS tapes is vertically submerged into the CASPER I. As previously mentioned, the measurements are conducted at 4 K in liquid helium. The magnetic field generated by the HTS tapes is measured by the array of Hall probes.

Figure 5 shows the mean values of the peaks of the measured magnetic field generated at different current values. As one can notice, the Hall probes at the ends of the array are less affected by the magnetic field. Therefore, in further computations, the Hall probes number 5 – 7 have been used to compare the results as ones, which are (located) in the center of the array.

It is important to mention that these measurements have been conducted with a slightly larger gap between the HTS tapes stacks: 5.6 mm instead of 4 mm. The reason is to protect the Hall probes' array from any possible damage due to the possible shrinking of surrounding parts at 4 K.

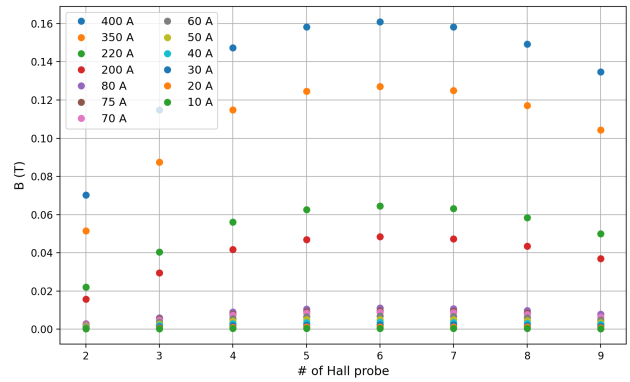

Figure 5: Mean values of peaks of measured magnetic field generated at different current.

Simulations

The magnetic field was simulated using the software Opera 3d (TOSCA solver) [5] and using a Biot-Savart solver written in Python language. Figure 6 shows the model used in the Opera simulations. The magneto-static TOSCA Solver

Figure 6: Model of the structured HTS tapes used in Opera 3d (TOSCA).

allows to use the so-called Biot-Savart conductors, which do not require meshing, hence, saving time on computations. The model considered the racetrack current path through all the 60 layers of the structured HTS tapes.

Another tool to compute the magnetic field is a Biot-Savart solver written in Python [6]. This code also considers a simplified model of line currents, which assumes that line currents are sinusoidal. Figure 7 shows the magnetic field along the axis calculated for different current flowing through the tapes. For example, at nominal operating current $I = 500$ A, a peak magnetic field is estimated to be 170 mT.

Figure 8 shows the comparison of the measured and computed magnetic field. As one can notice, the results are in a good agreement. While the Biot-Savart Solver in Python has a straightforward computation of the magnetic field through

ISBN: 978-3-95450-220-2 ISSN: 2673-5474 doi: 10.18429/JACoW-FEL2022-WEP45

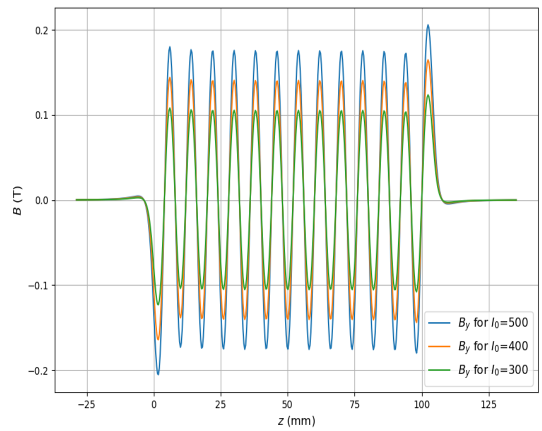

Figure 7: Magnetic field for different applied current, computed with the Biot-Savart Solver written in Python.

the applied current, the Opera computation considers the current density and very dependant on a small change in the model dimensions. The magnetic field at 400 A obtained in the measurements is about 160 mT in comparison to Biot-Savart Solver's ≈140 mT and Opera's ≈170 mT. Here, the results for the middle Hall probe are presented.

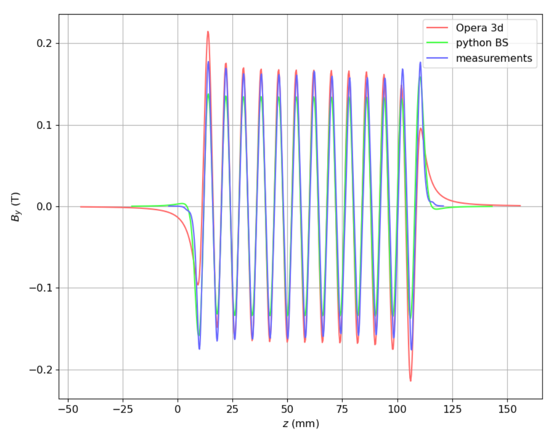

Figure 8: Comparison of the measured and computed magnetic field.

SUMMARY AND OUTLOOK

For the first time, the measurements have been conducted with all the 30 layers of the HTS tapes in each of two stacks in a long run. The first results confirm the principle of such a superconducting undulator using HTS tapes. The critical current at this stage is slightly higher than 400 A, which might be improved. One has to take into account that the HTS tapes are very sensitive to stretching, folding etc.. Also, they are not perfectly homogeneous in terms of carrying critical current [7].

The small differences between the measurements and computations can be explained by both the measurement uncertainties and the numerical errors. In order to converge the results from Opera simulations, the model based on meshing might be used together with the properties of each layer in the HTS tape.

Even though further measurements with the current prototype are planned, the next approach is foreseen - the design with individually structured HTS tape pieces, which are stacked and soldered alternating at the tape ends. For more details see Ref. [6].

ACKNOWLEDGEMENTS

The authors would like to thank R. Nast (ITeP, KIT) for his help with producing the laser-scribed structure on the HTS tapes.

This work is supported by the German federal ministry of education and research (BMBF) under grant No.05K19VK1.

REFERENCES

[1] S. Prestemon, D. R. Dietderich, A. Madur, S. Marks, and D. Schlueter, "High Performance Short-Period Undulators Using High Temperature Superconductor Tapes", in *Proc. PAC'09*, Vancouver, Canada, May 2009, paper WE5RFP075, pp. 2438–2440.

[2] S. Prestemon *et al.*, "Development and analysis of HTS-undulator components for FEL applications", *IEEE transactions on applied superconductivity*, vol. 21, no 3, pp. 1880-1883, 2013. `doi:10.1109/TASC.2010.2098014`

[3] T. Holubek *et al.*, "A novel concept of high temperature superconducting undulator", *Superconductor Science and Technology*, vol. 30, no 11, p. 115002, 2017. `doi:10.1088/1361-6668/aa87f1`

[4] E. Mashkina *et al.*, "CASPER-A magnetic measurement facility for superconducting undulators", *Journal of Physics: Conference Series*, vol. 97, p. 012020, 2008. `doi:10.1088/1742-6596/97/1/012020`

[5] Dassault Systèmes, 78946 Vélizy-Villacoublay Cedex, France. Available: `https://www.3ds.com/fr/produits-et-services/simulia/produits/opera/`

[6] A. Will *et al.*, "Design and Fabrication Concepts of a Compact Undulator with Laser-Structured 2g-HTS Tapes", presented at the 12th Int. Particle Accelerator Conf. (IPAC'21), Campinas, Brazil, May 2021, paper THPAB048, this conference.

[7] SuperPower, Inc., `http://www.superpower-inc.com/`.

ISBN: 978-3-95450-220-2 ISSN: 2673-5474 doi: 10.18429/JACoW-FEL2022-WEP47

DESIGN OF THE INNOVATIVE APPLE-X AX-55 FOR SABINA PROJECT, INFN - LABORATORI NAZIONALI DI FRASCATI

J. Počkar, M. Kokole, T. Milharčič, U. Primožič, Kyma Tehnologija d.o.o., Sežana, Slovenia
M. Del Franco, G. Di Pirro, A. Selce, A. Ghigo, INFN Laboratori Nazionali di Frascati, Rome, Italy
A. Pertalia, ENEA, Rome, Italy
R. Geometrante, Kyma S.p.A., Trieste, Italy
L. Giannessi[1], Elettra Sincrotrone Trieste, Trieste, Italy
[1]also at INFN Laboratori Nazionali di Frascati, Rome, Italy

Abstract

Kyma S.p.A. was awarded the design and production of the APPLE-X undulator for SABINA project at INFN - Laboratori Nazionali di Frascati. SABINA (Source of Advanced Beam Imaging for Novel Applications) is a project aimed at the enhancement of the SPARC_LAB research facility. The two user lines that are going to be implemented are; a power laser target area and a THz radiation line.

Here we present the magnetic design and a novel mechanical implementation of this APPLE-X undulator for the THz/MIR radiation line. Undulator is made from three 1.35 m long sections. Each section consists of an APPLE-X magnetic array with 55 mm undulator period, a minimum bore diameter of 14.85 mm and a mechanical frame. The undulator design is both compact and lightweight. This is achieved by novel mechanical design and implementation of the multiple dynamic corrections through the motion control system.

SABINA PROJECT

SABINA (Source of Advanced Beam Imaging for Novel Applications) is a project aimed at the enhancement of the SPARC_LAB research facility with the final goal to shape it into a facility opened for external users. A reduction of the number and extent of faults and consequential increase of the uptime is the first main objective of the project. The second objective is the improvement of the accelerator performances. Both objectives will be achieved through the consolidation of technological systems and updates of replacement of critical equipment [1].

THz/MIR Line

SABINA will implement a self-amplified spontaneous emission Free Electron Laser (SASE FEL) providing a wide spectral range of intense, short and variable polarization pulses for investigation in physics, chemistry, biology, cultural heritage, and material science.

This new THz/MIR radiation line will produce pulses covering a broad spectral region from 3 THz to 30 THz, obtained by tuning the electron beam produced at the SPARC photo-injector to an energy between 30 and 100 MeV. The high brightness electron beam will be transported up to an APPLE-X undulator where photon pulses in the picosecond range and energy of tens of μJ, with linear, circular and elliptical polarization will be produced.

UNDULATOR

In order to reach required photon wavelength, low beam energy and long undulator period are required. Since beam energy is restricted to the range 30-100 MeV as previously mentioned and because of physical constraints for which the total undulator length must be less than 4.5 meters, an undulator with a period length of 55 mm has been proposed [2].

The undulator is divided in three modules of ~1.3 meters each, separated by about 20 cm of drift space to allow the installation of holders for the vacuum pipe and beam position diagnostics. Magnetic correctors to handle the electron beam orbit will be placed externally, outside the undulator modules.

An additional constraint on the radiation properties required by the SABINA project is the generation of switchable left-right circular polarization. In order to accomplish this request an APPLE2-type undulator was initially proposed. Such device allows to produce vertically/horizontally linear polarized radiation and left/right-handed elliptical polarized radiation [3].

The magnetic configuration that was finally chosen is an APPLE-X that has also the property of focusing the beam on both the horizontal and vertical planes. This feature is not common to other variable polarization undulators based on permanent magnets such as the APPLE II [4].

Tender

The INFN National Laboratory of Frascati has put the supply of the APPLE-X undulator described above to tender on March 2021. Offerors with suitable technical credentials and experience in the field of Insertion Device (ID) fabrication have been asked to bid for the design, engineering, manufacturing, assembly, testing, and final delivery of three devices that where referred as AX-55. AX-55 will be the first APPLE-X device in the world designed and build by industry.

ISBN: 978-3-95450-220-2 ISSN: 2673-5474 doi: 10.18429/JACoW-FEL2022-WEP47

Figure 1: AX-55 General Layout.

Kyma has applied for the tender and was awarded the contract for the procurement of the AX-55 in November 2021. The final design of the magnetic, mechanical and control systems was approved on June 2022. At the time of writing of this paper most of the mechanical parts have been fabricated and the project is in the phase of assembly of the main undulator body and the magnetic sub-system.

Figure 1 shows the general layout of the AX-55. The magnetic design and the design of a novel concept of mechanical structure for APPLE-X devices is presented in the following chapters.

MAGNETIC DESIGN

The study of a magnetic circuit model for the AX-55 undulator was conducted mainly on the basis of the reference design provided in the technical specification [5], part of the tender documentation. The requested parameters for the device and electron beam are presented in the following table.

Table 1: Requested Parameters

Parameter	Value
Electron beam energy	30 - 100 MeV
Beam current	250 - 400 mA
K max at horizontal polarization	4.803
K max at circular polarization	3.396
Peak field at horizontal polarization	0.935 T
Peak field at circular polarization	0.66 T
Period length	55.0 mm
Number of periods	24
Vacuum chamber diameter	10.0 mm

The magnetic circuit is made of four Halbach arrays in four adjacent quadrants (QN, QX, QZ, QS). Quadrant N (normal) is the base quadrant (Figure 2).

Four permanent magnet blocks in series form one undulator period. The period length λu = 55.0 mm. Magnetization of pole (type A) blocks is at 45° to the vertical axis (see Figure 3). This provides additional on axis field strength. The full-size magnet block has a 28 mm x 28 mm profile and is 13.65 mm thick. The spacing between adjacent magnets in the central region is 0.1 mm. Horizontal and vertical gap between arrays is 5.0 mm. There are 5.5 x 5.5 mm chamfers in two diagonal corners of the block and 5 x 5 mm square cuts on other corners (see Figure 3).

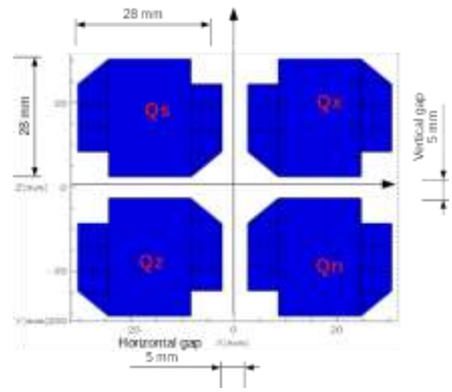

Figure 2: Quadrants with Adjacent Magnetic Arrays.

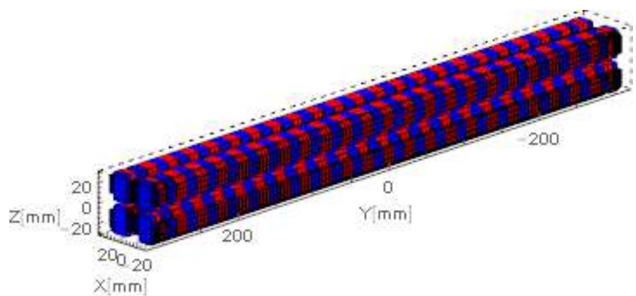

Figure 3: Short 3D View of the RADIA Model.

Full length of the magnetic core is 1331.85 mm including magic fingers and excluding girder movement. There are 22 periods in the magnet core. 1386.85 mm of longitudinal space is needed for the undulator operation. This includes space for movement for girders.

This undulator has a displacement-free and steering-free termination. There are two different types of terminations. Termination 1 is used in quadrants QN and QS, Termination 2 is used in quadrants QX and QZ. Both termination types are composed of one vertically magnetized full block, two vertically magnetized half blocks and four horizontally magnetized half blocks (see Figure 4, Table 2).

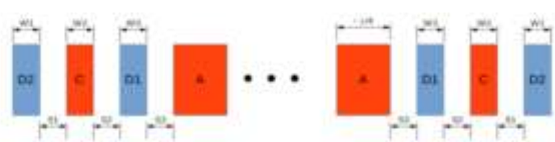

Figure 4: End Section Configuration Blocks.

Table 2: Longitudinal Spacing between Magnetic Blocks and Block Widths in Terminating Sections

Spacing	[mm]	Block Width	[mm]
S1	1.0	W1 (D2)	4.7
S2	5.2	W2 (C)	6.8
S3	2.0	W3 (D1)	8.5

The magnetic structure is modularized, meaning that magnetic blocks are first arranged in sequences of three and five blocks. An M5 and an M3 module form a double period that is repeated 11 times through the central region

ISBN: 978-3-95450-220-2 ISSN: 2673-5474 doi: 10.18429/JACoW-FEL2022-WEP47

of all four magnetic arrays. Added to these modules are four termination modules discussed above.

Magnetic Modelling

All the calculations and parameters below have been obtained from a RADIA/Mathematica model taking into account 3D effects (actual shape of the magnetic blocks) and non-unit and anisotropic permeability (μ_{par} = 1.05, μ_{per} = 1.15). The remanence of magnet blocks was assumed to be B_r = 1.26 T, (H_{cj} > 1990 kA/m). RADIA version 4.31 and Mathematica 10.1 was used.

Table 3 shows photon energies at different polarization modes and different gaps with reference to the required parameters (see Table 1).

Table 3: Photon Energies at Different Polarization Modes

Phase (Shift)	**Effec. Mag. Field**	**K_{max}**
0.0 mm	Bz = 0.942 T Bx = 0.000 T	4.84
$\lambda_u/4$	Bz = 0.672 T Bx = 0.671 T	3.45
$\lambda_u/2$	Bz = 0.000 T Bx = 0.942 T	4.84
circ. polarization (13.7854 mm)	Bz = 0.673 T Bx = 0.669 T	3.44

All parameters required by the tender specifications are met by the presented magnetic design (see Table 3).

MECHANICAL DESIGN

As for most IDs, AX-55 is a tightly coupled mechanical system, but it can be nonetheless logically partitioned in the following sub-systems: main frame, phase and gap kinematics, magnetic structure and the alignment platform.

The general layout of the AX-55 undulator is presented on Figure 1. The overall dimensions of the undulator at phase 0 mm are 1925 mm in height, 1323 mm in length and 1500 mm wide. The overall weight of the undulator is approx. 3800 kg.

Main Frame

The main frame is rigidly fixed to the alignment platform. The bottom plate is fixed to the floor, possibly on pre-set grouted plates (see Figure 1).

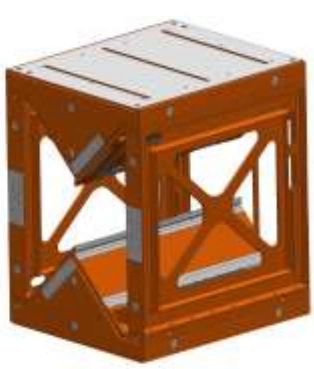

Figure 5: Main Frame.

The undulator main frame is composed of four major welded steel parts (see Figure 5). The whole system is designed symmetrically, so that the top and bottom beams as well as both frame sides are identical. This closed mechanical structure is compact and lightweight and jet very rigid. The structure features precision assembly pins so that it can be opened during final installation around the vacuum chamber.

Beams and Girders

Top and bottom beams (see Figure 6) feature a phase displacement mechanism that moves one of the two quadrants longitudinally. The mechanism is composed of two guide rails and a ball screw spindle (actuated by a servo motor) mounted on precisely machined slots on the corresponding beam. An aluminium plate mounted on top of the rail carriages is the interface to the gap drive mechanism.

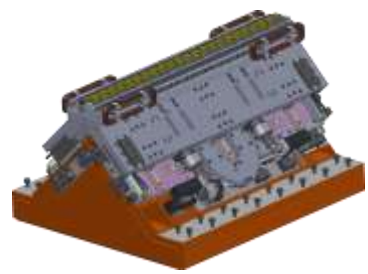

Figure 6: Main Frame and Beam.

The gap drive mechanism moves both quadrants radially. It is composed of three guide rails and two ball screw spindles (actuated by servo motors) per quadrant. One set is mounted directly to the beam, while the other is mounted on the interface plate of the corresponding phase mechanism.

Girders and Magnetic Arrays

Each undulator has four identical girders. Each girder is precisely machined from a single aluminium piece. The girders are fixed on guide rail carriages of the gap drive mechanism. A set of base plates that are the basis for assembly of magnet holders are screwed on top of every girder.

Each undulator consists of four magnetic arrays. All four arrays can be moved radially at the same time. This action opens or closes the gap between arrays. Two diagonally positioned arrays can be moved also longitudinally. This action introduces a phase displacement. Gap and phase movements are driven independently by the control system that enforces synchronous action of eight gap and two-phase axes.

Figure 7: Girders with Magnetic Structure.

ISBN: 978-3-95450-220-2 ISSN: 2673-5474 doi: 10.18429/JACoW-FEL2022-WEP47

The magnetic array is a periodic magnetic structure that is built with M3 and M5 magnetic modules. A single [M3, M5] pair corresponds to two magnetic periods of eight magnet blocks. The periodic structure starts and ends with a magnetic termination, which is composed of specially sized magnet blocks. Magic finger holders are positioned at the beginning and at the end of the array (see Figure 8).

Figure 8: M3 and M5 Modules and Magic Finger Holder.

FEM Analyses

FEM analysis has been performed on the girder, frame and holder to evaluate the expected deformation and stress. The dimensioning of pieces has been adjusted so that the deflections are minimized (see Figure 9). Consequentially the predicted stress levels in the material are very low.

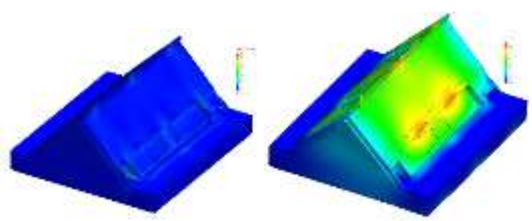

Figure 9: Von Mises Stress and URES Resultant Displacement of the Beam.

Of particular importance is the relative displacement under dynamic stress of the top surface of the girder assembly since these offsets along the magnetic structure have a direct negative effect on field quality and beam trajectory. It was observed that all the values of surface displacement are in the worst-case scenario contained in 3 µm (see Figure 10) which is very good result (considerably better than our previous APPLE-II projects).

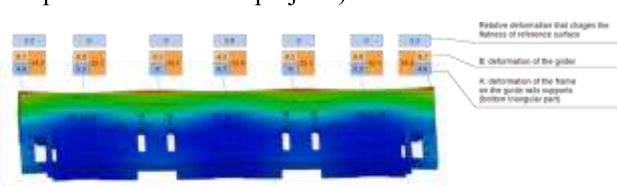

Figure 10: Relative Displacement of the Reference Surface for the Magnets.

There are some border points on the holder with higher stress levels, which have been expected and are in the range of what was observed on several APPLE-II designs in the past. The predicted overall displacement of the magnet is in the range of 25 µm (see Figure 10). This value is better compared to our previous APPLE-II projects.

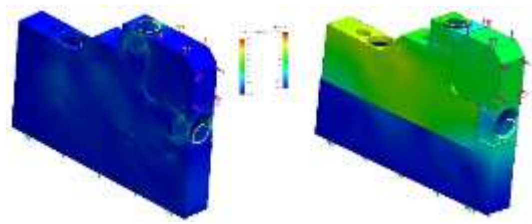

Figure 11: Von Mises Stress and URES Resultant Displacement of the Magnet Holder.

CONCLUSION

The magnetic and mechanical design of a novel APPLE-X device was carried out observing the requirements defined in the technical specification [5] of the tender for the procurement of the AX-55 undulator for the SABINA project at INFN. The magnetic design confirmed that the objectives set in the tender can be met and good magnetic performance of the APPLE-X magnetic structure can be expected. The design of the structural mechanics and kinematic sub-systems had to be engineered from ground up. No previous implementations of such devices exist in the industry and little experience was acquired by laboratories as well. We believe that we found a good functional solution to the requirements and the thorough structural analysis that was performed on all critical elements shows very good performance with small deformations even with a lightweight design that was proposed. This make us conclude that the AX-55 design is a very good option to be considered for future applications of this kind.

ACKNOWLEDGEMENTS

SABINA is a project co-funded by Regione Lazio with the “Research infrastructures” public call within PORFESR 2014-2020.

REFERENCES

[1] L. Sabbatini *et al.*, “SABINA: A Research Infrastructure at LNF”, in proceedings of *12th Int. Particle Accelerator Conf. (IPAC'21)*, Campinas, Brazil, May 2021. doi:10.18429/JACoW-IPAC2021-THPAB372

[2] F. Dipace *et al.*, “FEL Design Elements of SABINA: A Free Electron Laser for THz-MIR Polarized Radiation Emission”, in proceedings of *12th Int. Particle Accelerator Conf. (IPAC'21)*, Campinas, Brazil, May 2021. doi:10.18429/JACoW-IPAC2021-TUPAB100

[3] M. Calvi, C. Camenzuli, E. Prat, and Th. Schmidt, “Transverse gradient in Apple-type undulators”, *J. Synchrotron Rad.*, vol. 24, pp. 600–608, 2017. doi:10.1107/s1600577517004726

[4] S. Sasaki, “Analyses for a planar variably-polarizing undulator”, *Nucl. Instrum. Methods Phys. Res. A*, vol. 347, pp. doi:10.1016/0168-9002(94)91859-7

[5] A. Ghigo, L. Giannessi, A. Petralia, L. Pellegrino, G. Di Pirro, L. Sabbatini, M. Bellaveglia, “SPECIFICHE TECNICHE per l'ondulatore AX-55 del progetto SABINA”, *INFN-LNF*, December 2020

ISBN: 978-3-95450-220-2 ISSN: 2673-5474 doi: 10.18429/JACoW-FEL2022-WEP49

CONCEPTUAL DESIGN OF THE THz UNDULATOR FOR THE PolFEL PROJECT

J. Wiechecki†, National Synchrotron Radiation Centre SOLARIS, Kraków, Poland
P. Krawczyk, R. Nietubyć, National Centre for Nuclear Research, Otwock-Świerk, Poland
P. Romanowicz, D. Ziemiański, Cracow University of Technology, Kraków, Poland

Abstract

PolFEL will be the first free-electron laser facility in Poland. It will be driven with RF continuous-wave superconducting linac including an SRF injector furnished with a lead film superconducting photocathode. PolFEL will provide a wide wavelength range of electromagnetic radiation from 0.6 mm down to 60 nm. The linac will be split into three branches. Two of them will feed undulators chains dedicated for VUV, and IR radiation emission, respectively, and a single THz undulator will be settled in the third branch. The design of the THz undulator has been recently accomplished. It consists of a 1560 mm long permanent magnet structure ordered as a Halbach array of 8 periods. Large block dimensions, gap flux zeroing at full opening and 0.5 THz – 5 THz wavelengths range imposed on the undulator significantly influenced the final shape of the device, including block holders, girders and frame robustness unto magnetic forces, and hindered manufacturing and assembling processes. The following publication presents the challenges and solutions that were accompanying the conceptual phase.

PolFEL FACILITY

PolFEL Superconducting Free electron laser is an ongoing project led by NCBJ with 9 contortions members onboard. Superconducting Electron Gun based on the submicrometre Pb film deposited onto a head of Nb dismountable plug, impinging by 257 nm light laser beam used to liberate electrons to the linear accelerator. The linear accelerator will consist of 5 Rossendorf-RI-type cryomodules (CM), two energy branches up to 187 MeV (High Energy) and a second up to 72 MeV (Low Energy). This configuration will guide the electron beam through succeeding three CMs, boosts their energy and supply the VUV undulators chain (HE) and IR undulator chain or pass it by, on the way towards the THz undulator (LE, respectively).

DESIGN CHALLENGES

The boundary conditions given for both the THz branch and the THz undulator are very demanding. They must be considered simultaneously with all two other types of undulators embedded into the PolFEL project. The device consists of 100 x 100 x 40 mm size NdFeB magnet blocks, ordered in 8 periods 1560 mm long Halbach array. The electron beam high is 1400 mm above the floor level.

† jaroslaw.wiechecki@uj.edu.pl

The required gap range is 100 – 600 mm. These typical parameters must be compiled with imposed tolerances (see Table 1).

Table 1: Selected Tolerances Required for the Undulator

Parameter	Value
Undulator period length variation $\Delta\lambda u$ (RMS)	<160 µm
Magnet block centre straightness (RMS) in the horizontal plane	<400 µm
The relative angle between the corresponding block surface in the upper and lower girder	$<1\cdot10^{-2}$ rad
Maximum change of the gap width Δg along the undulator	<30 µm
The maximum deflection of the undulator beam	<15 µm
Absolute accuracy of undulator beam vertical positioning	<2 µm
First integral IB1 of the transverse magnetic field along the undulator	$< 3\cdot10^{-6}$ T·m
Second integral IB2 of the transverse magnetic field along the undulator	$< 3\cdot10^{-6}$ T·m^2
Beam parallelism tolerance: relative beam twist angle along the magnetic z-axis (roll)	$< 1\cdot10^{-2}$ rad
Beam parallelism tolerance: relative beam twist angle along the undulation x-axis (pitch)	$\pm30\cdot10^{-6}$ rad
Beam parallelism tolerance: relative beam twist angle along the vertical y-axis (yaw)	$\pm0,5\cdot10^{-3}$ rad
Tolerance of the undulator magnetic axis vertical positioning concerning the electron beam Δy	< 150 µm
Tolerance of the undulator magnetic axis horizontal positioning concerning the electron beam Δx	< 1000 µm

These requirements force the following considerations:

- Wide range of gap requires more space (from 100 mm to 600 mm)
- Three different types of undulators require a unified design
- Wide range of adjustment pulleys for magnet blocks (up to 1.5 mm)

ISBN: 978-3-95450-220-2 ISSN: 2673-5474 doi: 10.18429/JACoW-FEL2022-WEP49

- The size of the magnets and the magnitude of the forces between them must be taken into consideration while designing the girders and keepers
- High demands towards the tolerances vs. manufacturing capabilities (highly accurate compensation of the manufacturing inaccuracies for mechanical components)
- Low weight
- Ease of transportation
- Development of a simple assembly method for both main construction and the magnetic blocks (considering the safety of people and machine)

CONSTRUCTION

The THz undulator is based on the standard device solution where an L-shaped frame is used as a support for two movable girders (see Fig.1).

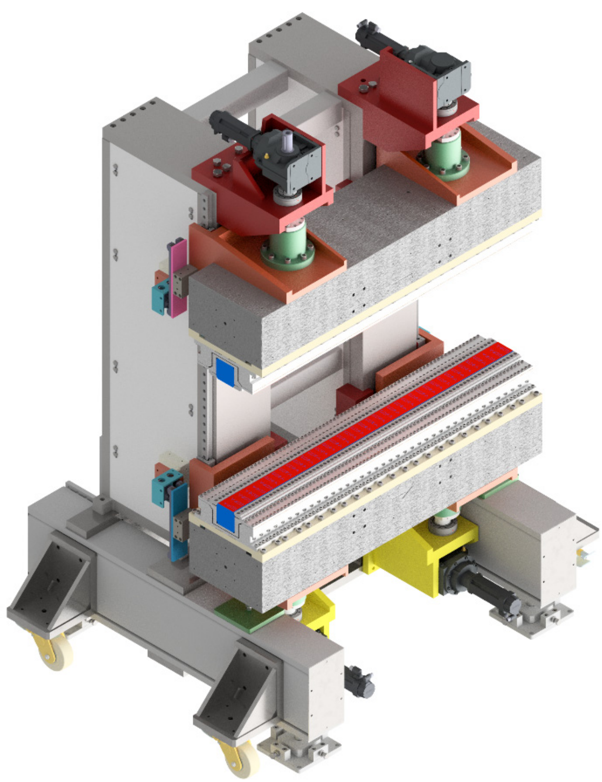

Figure 1: Prototype of the THz undulator.

Main Frame

Due to the boundary conditions, the main frame of an undulator is designed as a universal solution for all three types of undulators: THz, VUV and IR. The project is calculated for the most demanding case, in which the forces of interaction from the magnetic blocks are the highest. It concerns the IR undulator, in which the value of this force equals ~19 kN. At the same time, efforts were made to keep the structure relatively light.

Drive System

Each undulator's girder is driven by two SIEMENS motors which, through a drive system consisting of a 100:1 worm gear and a ball screw can independently raise or lower the undulator jaw. In addition, the entire system moves relative to the frame on rails and carriages from the Schneeberger company. The design uses carriages with integrated absolute encoders. There are two carriages and one encoder for each of the four axes.

Magnetic Array

The girders of the undulator are solid aluminium blocks with dimensions of 410x260x1560 mm, on which neodymium magnets will be in special holders arranged in the form of a Halbach structure. The magnets are grouped in 6 packages of 5 pieces and 3 packages of 3 pieces for each girder to simplify the assembly and calibration procedure. Additionally, it is assumed to use linear bearings screwed directly to the inner plane of the undulator jaws, on which the above-mentioned groups of magnets will move precisely.

Magnet Keeper

The heart of the undulator is neodymium magnets made of NdFeB alloy, which are mounted in special holders (see Fig. 2) enabling their movement in axes perpendicular to the axis of the electron beam. Due to the imposed adjustment ranges, the magnet mounting elements allow the magnets to shift in the vertical axis within the +/- 0.75 mm range and rotate about the beam axis. Such a large range and the forces that occur are impossible to compensate in the single screw adjustment system. Accordingly, a lever system is used for which the handle is either tightened or loosened. This is done in the range of up to 400 µm. The missing range is compensated by additional washers that raise or lower the magnet relative to the main bracket.

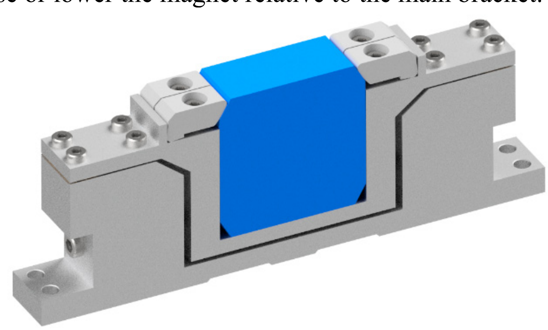

Figure 2: Prototype of the magnet keeper.

FEA

The required magnetic field and its distribution were determined during theoretical calculations and then verified in the FEA program FEMM. The conducted analysis gave an idea of the field distribution for extreme values of the gap.

Alignment

The design provides the possibility of precise adjustment of the device with an accuracy of 100 µm on adjustment supports.

ISBN: 978-3-95450-220-2 ISSN: 2673-5474 doi: 10.18429/JACoW-FEL2022-WEP49

Manufacturing

Due to the inability to obtain high-class manufacturing accuracy of individual subassemblies of the undulator, an additional possibility of calibrating critical elements of the structure has been foreseen. This applies to the orientation of the supporting pillars and the position of the undulator girders with adapters for the drive system. It is assumed that at each stage of assembly, the construction will be additionally verified with precise measuring devices such as a laser tracker, measuring arm or other measuring systems, appropriate to the installed fragments of the device.

MIRO POSITIONING SYSTEM

According to the boundary conditions, the undulator requires an additional possibility of controlling the offset within the range of up to 100 μm using the movement of the undulator's jaws, without having to enter the accelerator tunnel. The final position of the undulator girders depends on the position of the electron beam, measured by adjacent detectors (pinhole) located upstream and downstream of the undulator.

The coupling between the position of the girders and the position of the detectors is realized using confocal sensors, which measure the deviation from the new position of the beam within the measurement range defined by the sensor parameters. When a change in the beam position in the vertical plane is detected, the operator closes the jaws of the undulator and reads the ranges that need to be calibrated. Then, by forcing new offsets for each end of the undulator upper girder, it results in automatic adjustment of the jaws about the new beam trajectory. If the offset range is too large to compensate, a standard alignment procedure is required using traditional measurement techniques such as Laser Tracker.

CONCLUSION

The THz undulator is in the final design phase. All requirements have been taken into consideration. In the final FEA, the stability of the entire construction will be checked to verify the boundary conditions.

ACKNOWLEDGEMENTS

The authors would like to thank the undulator groups from Daresbury Laboratory and Paul Scherer Institute, for their support and constructive discussions.

ISBN: 978-3-95450-220-2 ISSN: 2673-5474 doi: 10.18429/JACoW-FEL2022-WEP50

CONTROLLING BEAM TRAJECTORY AND BEAM TRANSPORT IN A TAPERED HELICAL UNDULATOR

A. Fisher*, J. Jin, P. Musumeci
Department of Physics and Astronomy, University of California Los Angeles, CA, USA

Abstract

A helical undulator provides a stronger FEL coupling than common planar geometries as the beam transverse velocity never vanishes. However, a significant challenge lies in tuning and measuring the fields with limited access to the beam axis along the undulator. Confirming the good field region off axis is difficult given the limited space available for 3D hall probe scans, and is important for low energy beams used to create THz radiation which have large amplitude oscillations. We present our tuning procedures developed for the meter-long THESEUS undulators, consisting of two orthogonal permanent magnet Halbach arrays shifted by a quarter period relative to one another. The Hall probe and pulsed wire measurements are guided by the general field expansion of helical undulators to correctly tune fields on and near the axis.

INTRODUCTION

The helical geometry of the THESEUS undulators allows for stronger FEL coupling at the cost of increased engineering complexity and limited tuning access to the beam axis in the undulator [1]. Accurate tuning of the tapered undulator fields is necessary to provide straight trajectories with the correct slippage. In addition to Hall probe measurements, pulsed-wire measurements can provide an independent measurement of the electron beam tranverse velocity and trajectory in tight arrangements. We also investigate using 3D pulse-wire measurements to ensure the electrons sample accurate fields far off-axis in the THz waveguide FEL [2].

In this paper, we present the tuning procedures developed for the THESEUS undulators at UCLA and organize as follows. First we derive the form of the undulator field expansion and fit the free parameters to a numerical simulation for the magnetic fields. Next we describe our Hall probe tuning procedure, including corrections to probe angle and transverse offset. Finally we present a pulsed-wire measurement setup developed at UCLA and discuss corrections, fiducialization, and our 3D pulse-wire measurements.

UNDULATOR FIELD EXPANSION

The tuning procedure for the THESEUS undulators utilizes a theoretical expansion for fields off-axis. For static fields with no current sources, $\nabla \times \vec{B} = 0$ implies the existence of a scalar magnetic potential $\vec{B} = -\nabla\phi$ that satisfies Laplace's equation.

$$\nabla \cdot \vec{B} = \nabla^2 \phi = 0 \tag{1}$$

Considering first a planar undulator with period $\lambda_u = \frac{2\pi}{k_u}$ and peak field $B_y = B_0$ at the origin, we assume a separation of variables solution with constant ϕ_0, such that $\phi = \phi_0 X(x) Y(y) \cos(k_u z)$.

Dividing Eq. (1) by ϕ constrains

$$\frac{1}{X}\frac{\partial^2 X}{\partial x^2} + \frac{1}{Y}\frac{\partial^2 Y}{\partial y^2} - k_u^2 = 0. \tag{2}$$

To hold for all space, $X(x)$ and $Y(y)$ must be trigonometric or hyperbolic trigonometric functions. Physically, we expect B_y to be an even function with positive concavity and so identify $Y(y) = \sinh(\alpha k_u y)$ where α is a real parameter. Therefore, $X(x) = \cos(\beta k_u x)$ with $\beta^2 = \alpha^2 - 1$ and $\phi_0 = -\frac{B_0}{\alpha k_u}$ such that

$$\phi = \frac{-B_0}{\alpha k_u}\cos(\beta k_u x)\sinh(\alpha k_u y)\cos(k_u z). \tag{3}$$

The potential for an undulator with flat faces (infinite in x) is given by $\alpha = 1$, $\beta = 0$ whereas an undulator with equal focusing due to parabolic-pole shaped faces is given by $\alpha = 1/\sqrt{2}$, $\beta = i/\sqrt{2}$.

The THESEUS undulators are a helical geometry composed of two permanent magnet Halbach arrays shifted by a quarter period relative to each other. The full potential is given by

$$\phi = \frac{B_0}{\alpha k_u}\sinh(\alpha k_u x)\cos(\beta k_u y)\sin(k_u z) - \frac{B_0}{\alpha k_u}\cos(\beta k_u x)\sinh(\alpha k_u y)\cos(k_u z) \tag{4}$$

The undulators were designed with the magnetic code RADIA [3]. By fitting α in Eq. (4) to the design fields (for $\sqrt{x^2 + y^2} < 1$ mm), we find $\alpha = 1.53$ and $\beta = \sqrt{\alpha^2 - 1} = 1.16$. We emphasize that the THESEUS undulator differs from common textbook definitions as the strength of the peak magnetic fields forms a saddlefunction in the transverse dimension[4, 5].

HALL PROBE

The enclosed geometry of a helical undulator increases the difficulty of Hall probe tuning. Our design uses a flat metal piece that slides along a notched, hollowed out rod. The rod fits snugly in the tensioned vacuum pipe and is held fixed relative to the undulator with set screws at both ends. A 3-axis hall probe is glued to the flat piece and pulled along the undulator with a 1-m translation stage.

Errors in the probe roll angle and transverse offset can be inferred from measurements as seen in Fig. 1. A roll angle

* afisher000@g.ucla.edu

ISBN: 978-3-95450-220-2 ISSN: 2673-5474 doi: 10.18429/JACoW-FEL2022-WEP50

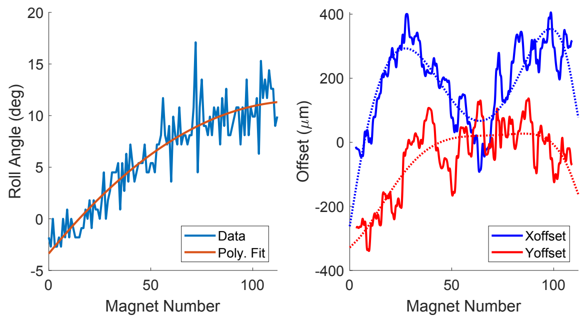

Figure 1: Measurements and polynomial fits for roll angle and offset errors. The roll angle is from the machining process and was independently confirmed with laser measurements. The effect of gravity ($+\hat{y}$) can be seen in the yoffset error.

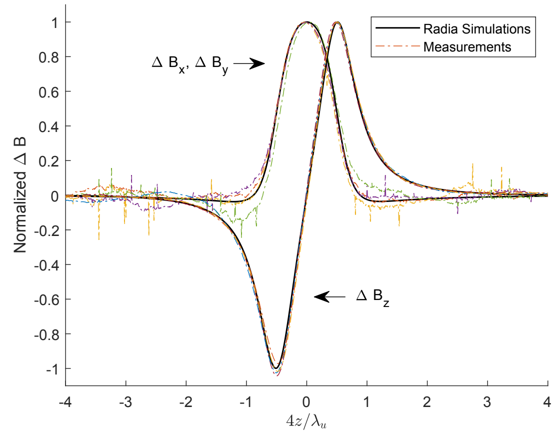

Figure 2: Magnet Eigenfunctions.

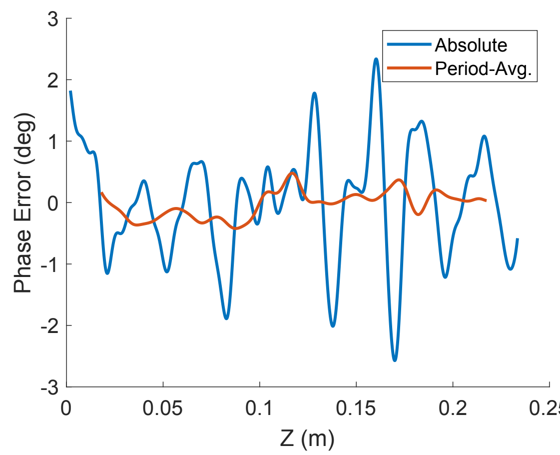

Figure 3: Tuning Phase Error.

mixes the B_x and B_y fields such that the measured period is shortened or lengthened relative to the actual undulator period, providing an accurate estimate of the angle along the undulator. Transverse offset of the probe from the magnetic axis is manifest through the appearance of non-zero B_z fields and can be calculated by expanding the B_z field to first order in x,y:

$$B_z = -B_0 k_u \left(x\cos(k_u z) + y\sin(k_u z) \right) \tag{5}$$

$$x(z) = \frac{-1}{B_0 \pi} \int_{z-\lambda_u/2}^{z+\lambda_u/2} B_z \cos(k_u z) \tag{6}$$

$$y(z) = \frac{-1}{B_0 \pi} \int_{z-\lambda_u/2}^{z+\lambda_u/2} B_z \sin(k_u z). \tag{7}$$

From a raw field measurement, the ideal undulator field expansion is used to transform the fields from the probe axis to the magnetic axis of the undulator. A Matlab script uses superposition of magnet eigenfunctions (known changes in field due to individual magnet movement) to optimize the adjustments needed to achieve a desired undulator field. An example of magnet eigenfunctions is given in Fig. 2. The number of optimization parameters can be halved by grouping the adjustments of opposite magnet pairs. Transverse and longitudinal fields are optimized by changing the gap or offset of a magnet pair, respectively.

Initially, the fields are coarsely tuned to match the design fields. Afterwards, we fine tune to minimize the slippage error between electrons and the radiation as well as straighten the trajectory inside the undulator.

The distance that radiation slips ahead of electrons in the undulator is given by

$$S(z) = \frac{1}{2} \int_{-\infty}^{z} \frac{1}{\gamma^2} + x'^2 + y'^2 dz \tag{8}$$

where x', y' are the transverse trajectory angles [6]. For ideal fields in a helical undulator, $x'^2 + y'^2 = \frac{K^2}{\gamma^2}$ where K is the undulator strength parameter. In practice, it is more instructive to present the slippage error in terms of the radiation phase.

$$\phi_{\mathrm{error}}(z) = \left(\frac{2\pi}{\lambda} \right) \frac{1}{2} \int_{z_0}^{z} x'^2 + y'^2 - \frac{K^2}{\gamma^2} dz. \tag{9}$$

Figure 3 shows the phase error for a 9-period prebuncher. As the entrance fields are tuned later with the pulsed-wire (probe angle and offset cannot be accurately measured in entrance period), x' and y' are computed by numerically integrating fields and then subtracting the linear component of the trajectories.

PULSED WIRE

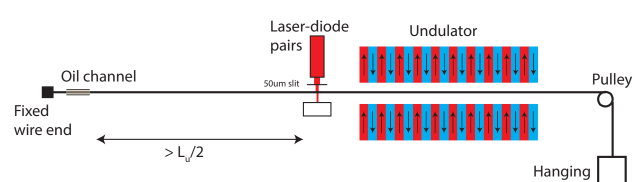

Figure 4: Cartoon of Pulsed-wire Measurement.

ISBN: 978-3-95450-220-2 ISSN: 2673-5474 doi: 10.18429/JACoW-FEL2022-WEP50

Pulsed-wire setups can measure undulator fields along a given axis with very little clearance. A cartoon of our setup is shown in Fig. 4. A 50 µm diameter CuBe wire is strung through the undulator and tensioned with a hanging weight over a pulley. Wire vibrations from air currents and previous measurements are damped with an oil channel. Square-wave current pulses provided from a function generator excite forces on the wire due to the undulator magnetic fields and generate traveling waves. The wire's displacement (in both transverse dimensions) is measured with laser-photodiode pairs as the amount of blocked laser light is proportional to the wire position. The separation between the lasers and oil channel must be greater than half the undulator length so that a single waveform is measured without any interference from reflections.

The setup can be used to measure the transverse velocity or trajectory of an electron beam by using short ($v_0\Delta t \ll \lambda_u$) or long ($v_0\Delta t > N_u\lambda_u$) current pulses where v_0 is the traveling wave velocity on the wire, Δt is the current pulse length, λ_u is the undulator period and N_u is the number of periods in the undulator [7, 8].

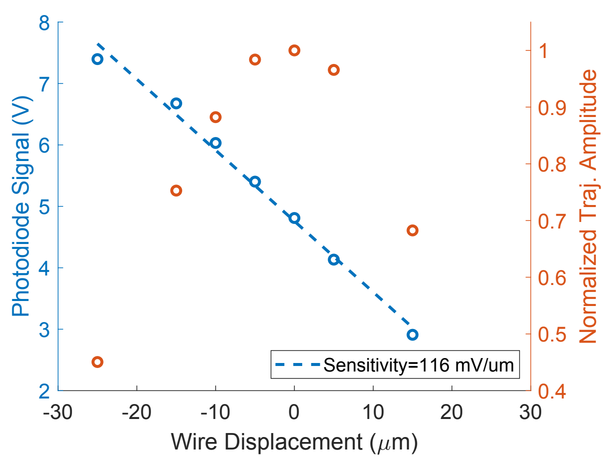

Figure 5: Pulsed-wire Calibration.

The sensitivity of the measurement depends on the relative change in photodiode signal and can be improved by adding a 50 µm slit to block excess laser light. However, laser diffraction will limit the range of the linear relationship between photodiode voltage and wire displacement. Figure 5 shows that even when the measured data appears linear, the instantaneous slope (proportional to amplitude of trajectory measurement) changes by 10% for displacements greater than ≈10 µm.

Wire dispersion causes the waveform to deform as it propagates. The dispersion can be computed by comparing frequency shifts between measurements of the waveform at two locations using Fourier transforms. Algorithms can be used to reconstruct the shape of the original pulse [9]. Additionally, differences in earth magnetic fields between the tuning room and beamline should be considered.

Figure 6 compares the trajectories measured with pulsed-wire and hall probe pulsed-wire trajectory with the integrated

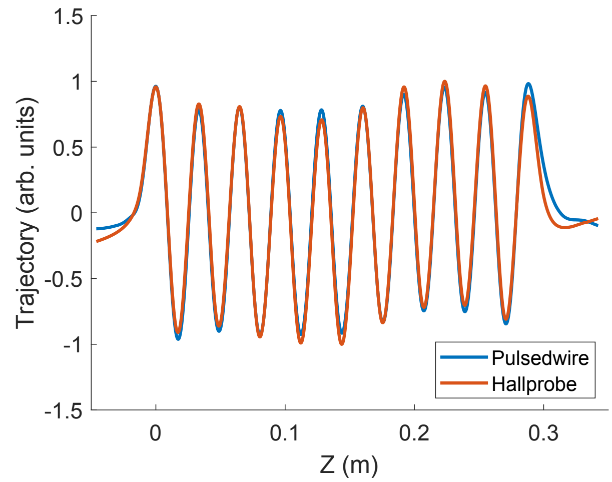

Figure 6: Measured E-beam Trajectories.

hall probe fields by scaling the horizontal and vertical dimensions to fit the position of the peaks. The least squares linear fit will correct for linear errors which is necessary as the entrance field is not assumed to be tuned correctly for the hall probe measurements.

For the THz waveguide FEL experiment at UCLA, the electron beam samples fields far (1 mm) off axis, introducing possibly significant field errors. As a 3D hall probe scan is impossible due to the enclosed undulator geometry, we investigated ways to tune the off axis fields using pulsed-wire scans. For ideal undulator fields, the pulsed wire measurements should show the same mean trajectory path (except for negligible field focusing effects). However, net quadrupole and sextupole field moments can be introduced by localized magnet errors when the gap or centering of a magnet pair is off. By measuring the pulsed wire trajectory at several offsets, we can identify locations with significant higher order moments and tune the magnets accordingly. The constraint that the trajectory remains straight does limit the ability to correct all moments completely, but the effect of higher order moments can be significantly reduced.

FIDUCIALIZATION

We also perform trajectory measurements at different transverse offsets to determine the magnetic axis of the undulator and align the wire. The trajectory amplitudes along the undulator are proportional to the strength of the measured magnetic fields and reveal the concavity of the fields as a function of offset. For each trajectory measurement, the signal extrema are found using polynomial fits of the peaks. The amplitudes are computed using the average of the neighboring extrema, along with a correction to account for large angles in the trajectory. Quadratic fits of amplitude versus wire offset data at each peak reveal the locations of the magnetic axis along the undulator. Figure 7 shows the good agreement between data (from a single undulator peak) with the theoretical field concavity.

ISBN: 978-3-95450-220-2 ISSN: 2673-5474 doi: 10.18429/JACoW-FEL2022-WEP50

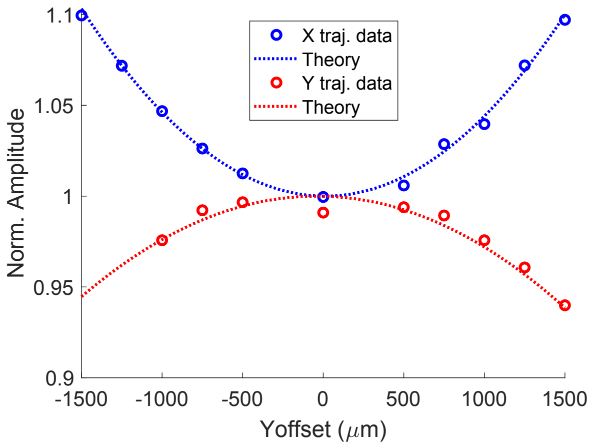

Figure 7: Wire Alignment from measured field concavity.

Once the wire has been positioned on the magnetic axis, it can be referenced to the undulator using fiducial cups. The positions of cups on the undulator and wire holders are measured with a laser tracking system, defining the wire axis (magnetic axis) with respect to the undulator to an accuracy of less than 30 µm.

CONCLUSION

Tuning procedures for hall probe and pulsed-wire measurements have been developed at UCLA for the THESEUS undulators, made specifically to target high efficiencies with strong undulator field tapering. Errors in the probe angle and tranverse offset can be accurately estimated from the period length and B_z field of a raw measurement. The fields can then be transformed to the magnetic axis using the theoretical field expansion. After tuning to minimize phase (or slippage) errors, pulsed-wire measurements are used to confirm the probe measurements and straighten the trajectory through the entrance and exit periods. We align the wire to the magnetic axis and explore quadrupole and sextupole field moment errors using wire scans at different offsets.

ACKNOWLEDGMENTS

This work was supported by DOE grant No. DE-SC0009914 and a fellowship from the Julian Schwinger Foundation for physics research.

REFERENCES

[1] Y. Park *et al.*, “Tapered helical undulator system for high efficiency energy extraction from a high brightness electron beam,” *Nucl. Instrum. Methods Phys. Res., Sect. A*, vol. 1028, p. 166 370, 2022. `doi:10.1016/j.nima.2022.166370`

[2] A. Fisher *et al.*, “Single-pass high-efficiency terahertz free-electron laser,” *Nat. Photonics*, pp. 1–7, 2022. `doi:10.1038/s41566-022-00995-z`

[3] O. Chubar, P. Elleaume, and J. Chavanne, “A three-dimensional magnetostatics computer code for insertion devices,” *J. Synchrotron Radiat.*, vol. 5, no. 3, pp. 481–484, 1998. `doi:10.1107/S0909049597013502`

[4] J. A. Clarke, *The science and technology of undulators and wigglers*. OUP Oxford, 2004, vol. 4.

[5] F. Ciocci, G. Dattoli, L. Giannessi, C. Mari, and A. Torre, “Optical properties of helical undulators,” *Nucl. Instrum. Methods Phys. Res., Sect. A*, vol. 63, no. 3, pp. 319–325, 1992.

[6] Z. Wolf, “Introduction to lcls undulator tuning,” SLAC National Accelerator Lab., Menlo Park, CA (United States), Tech. Rep., 2018.

[7] R. Warren, “Limitations on the use of the pulsed-wire field measuring technique,” *Nucl. Instrum. Methods Phys. Res., Sect. A*, vol. 272, no. 1-2, pp. 257–263, 1988. `doi:10.1016/0168-9002(88)90233-1`

[8] A. D’Audney, “Ultra-high resolution pulsed-wire magnet measurement system, an,” Ph.D. dissertation, Colorado State University, 2016.

[9] D. Arbelaez, T. Wilks, A. Madur, S. Prestemon, S. Marks, and R. Schlueter, “A dispersion and pulse width correction algorithm for the pulsed wire method,” *Nucl. Instrum. Methods Phys. Res., Sect. A*, vol. 716, pp. 62–70, 2013. `doi:10.1016/j.nima.2013.02.042`

ISBN: 978-3-95450-220-2 ISSN: 2673-5474 doi: 10.18429/JACoW-FEL2022-WEP55

DEVELOPMENT OF DIAMOND-BASED PASS-THROUGH DIAGNOSTICS FOR NEXT-GENERATION XFELs

R. Padilla†, E. Gonzalez, S. Kachiguine, F. Martinez-Mckinney, S. Mazza, M. Nizam, N. Norvell, E. Potter, E. Ryan, B. Schumm, M. Tarka, M. Wilder, Santa Cruz Institute for Particle Physics and the University of California at Santa Cruz, Santa Cruz, CA, USA

B. Jacobson, J. MacArthur, I. Silva Torrecilla, D. Zhu, SLAC National Accelerator Laboratory, Menlo Park, CA, USA

J. Bohon, D. Kim, J. Smedley, Los Alamos National Laboratory, Los Alamos, NM, USA

C. Grace, T. Prakashc, Lawrence Berkeley National Laboratory, Berkeley, CA, USA

C. T. Harris, Sandia National Laboratory, Albuquerque, NM, USA

D. Stuart, University of California, Santa Barbara, CA, USA

E. Prebys, University of California, Davis, CA, USA

Abstract

FELs deliver intense pulses on the femtosecond scale, with peak intensities and positions that fluctuate strongly on a pulse-to-pulse basis. The fast drift velocity and high radiation tolerance properties of chemical vapor deposition (CVD) diamonds make these crystals a good candidate material for developing a high frame rate pass-through diagnostic for the next generation of X-ray Free Electron Lasers (XFELs). We report on two diamond based diagnostic systems being developed by a collaboration of a UC campuses and National Laboratories supported by the University of California and the SLAC National Laboratory.

For the first of these diagnostic systems, we have developed a new approach to the readout of diamond diagnostic sensors designed to facilitate operation as a pass-through detection system for high frame rate XFEL diagnostics. Making use of the X-ray Pump Probe (XPP) beam at the Linac Coherent Light Source (LCLS), the performance of this new diamond sensor system has been characterized. Limits in the magnitude and speed of signal charge collection are explored as a function of the generated electron-hole plasma density.

A leading proposal for improving the efficiency of producing longitudinally coherent FEL pulses is the cavity-based X-ray free electron laser (CBFEL). In this configuration, the FEL pulses are recirculated within an X-ray cavity in such a way that the fresh electron bunches interact with the FEL pulses stored in the cavity over multiple passes. This creates a need for diagnostics that can measure the intensity and centroid of the X-ray beam on every pass around the recirculatory path. For the second of these diagnostic systems, we have created a four-channel, position-sensitive pass-through diagnostic system that can measure the intensity and centroid of the circulating beam with a repetition rate up to 50 MHz. The diagnostic makes use of a planar diamond sensor thinned to 43 μm to allow for minimal absorption and wave-front distortion of the circulating beam. A single-pulse resolution of 3 μm was achieved for nJ scale pulses.

† remopadi@ucsc.edu

INTRODUCTION

Advanced X-ray Free Electron Lasers (XFELs) will provide high-intensity, high repetition rate (up to 10 GHz) pulses of coherent X-rays. However, the unstable nature of XFELs causes fluctuations in the intensity as well as in its centroid position of each pulse. Developing a pass-through diagnostic capable of measuring the intensity and centroid location pulse-by-pulse over a large dynamic range can be beneficial as a diagnostic for accelerator operations and experiments making use of XFEL beams.

Monocrystalline diamond presents specific characteristics that can be taken advantage of in sensor applications. Diamond shows a fast saturated drift velocity of approximately 200 μm/ns [1] and an exceptional thermal conductivity of about 2200 W/m·K. As an example of diamond performance: for a 30 μm diamond sensor the expected charge collection time with saturated drift velocity is about 150 ps. Additionally, diamond has a large band gap of 5.5 eV leading to an electron/hole pair creation energy of 13.3 eV [2], which limits the amount of signal charge generated inside the diamond. These characteristics differentiates diamond form other semiconductor materials and makes it a good candidate for a high-intensity, multi-GHz X-ray beam pass-through diagnostic.

In this proceeding we report on two studies making use of pass-through diamond sensors. In the first, making use of a specially designed fast readout scheme, we investigated the intrinsic charge collection efficiency and speed of diamond sensors. In the second, we characterized the performance of a position and intensity monitor designed to operate at repetition rates up to 50 MHz. These diagnostics made use of 4x4 mm^2 electronic-grade diamonds from the Element 6 corporation, thinned to 37 μm and 43 μm, respectively, and with the surface electrode divided into four equal quadrants for the position monitor. The studies were done on April 5-6, 2021, and April 16, 2022, in the X-ray Pump Probe (XPP) beamline of the Linac Coherent Light Source (LCLS) at the SLAC National Accelerator Laboratory (SLAC). During both runs, we made use of a monochromatic X-ray beam of 11.9 keV with single pulse intensities varying from 0.2 μJ to 80 μJ. In the first case,

ISBN: 978-3-95450-220-2 ISSN: 2673-5474 doi: 10.18429/JACoW-FEL2022-WEP55

the charge collection efficiency and time performance were described as a function of the density of signal charge generated by the passing beam. In the second case, the X-ray pulse position and uncertainty were characterized as a function of the asymmetry between two channels.

GHz-RATE XFEL PASS-THROUGH DIAGNOSTIC USING DIAMOND

For this study, a low-impedance signal path assembly for reading out fast diamond sensors was developed at the Santa Cruz Institute of Particle Physics (SCIPP). The circuit includes a bank of 44 parallel 22 µF capacitors (adding to 1 mF) that provides a signal return path that bypasses the high voltage supply. Also, two resistors of values 1 Ω and 10 mΩ were included to shunt the current signal to ground (Fig. 1). The SCIPP board was designed to allow high-bandwidth signals to circulate across the assembly with limited impedance. In order to reduce inductance effects, an indium band was used instead of bond wires to connect the 37 µm diamond sensor to the 1 Ω resistor completing the signal path (Fig. 2). The diamond sensor signals passing through the shunt resistance were picked off through 50 Ω traces connected to a SMA connector. The signal from the 1 Ω pick-off is reported here.

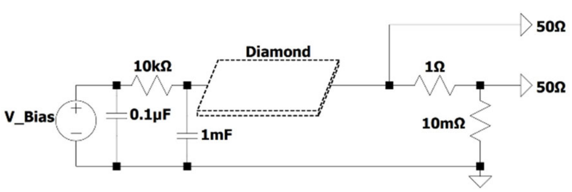

Figure 1: Schematic of the SCIPP readout signal path.

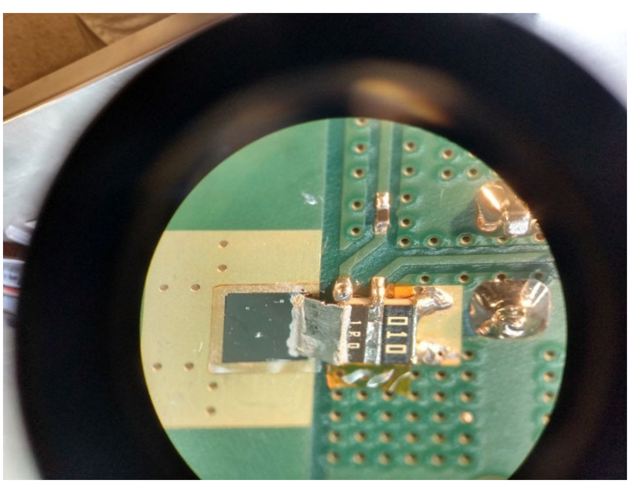

Figure 2: SCIPP Readout PCB signal path displaying the 37 µm diamond sensor, 1 Ω and 10 mΩ resistors, low-impedance indium band, and 50 Ω traces.

During the beam test on April 5-6, 2021, the X-ray beam was used in two modes – unfocused (FWHM of 350 µm) and focused (FWHM of 43 µm) beam. We performed studies at 100 V, 60 V, and 20 V bias voltage. Figure 3 shows the temporal average traces with an unfocused beam and 100 V bias voltage. Additionally, the unfocused beam was run both at full strength and attenuated to 10%, giving us the opportunity to study a larger dynamic range.

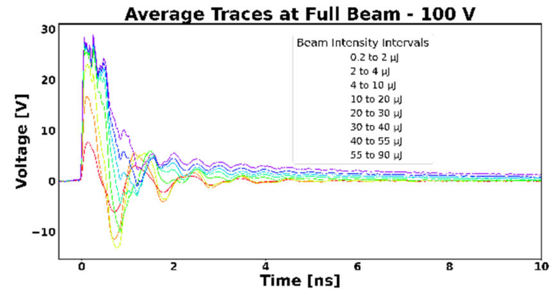

Figure 3: Average signal pulses over the first 10 ns.

The corresponding collected charge, Q_{coll}, was measured by finding the integral of the average traces for the different intensity and dividing by the effective signal-path resistance of 0.98 Ω. The deposited charge Q_{dep} was estimated from the mean intensity value for each interval, scaled to match the deposited charge for low-intensity pulses where the charge collection efficiency was known to be complete. By using the ration between Q_{coll} and Q_{dep}, we obtained the charge collected efficiency for higher pulse intensity. In addition, we defined a plasma density, ρ_p, in terms of deposited charge and the volume occupied by the electron-hole plasma according to:

$$\rho_p = \frac{1}{2}\frac{Q_{dep}}{V_{dep}} \tag{1}$$

where the factor ½ represents the fraction of a two-dimensional gaussian beam included within its FWHM. Figure 4 shows a plot of the resulting charge collection efficiency as a function of plasma density for a sensor bias of 100 V. The charge collection efficiency is observed to decrease from full charge collection for plasma densities above 10^{16} charge/cm^3.

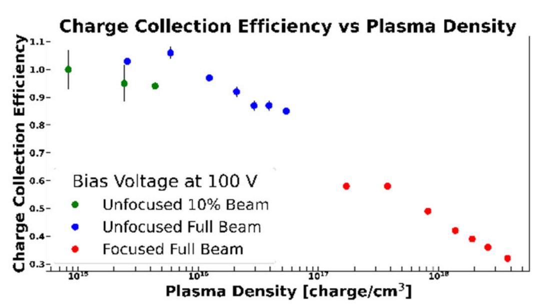

Figure 4: Estimated charge collection efficiency as a function of plasma density for 100 V (corresponding to a bias field of 2.7 V/µm).

By making use of the charge collection values found when $Q_{coll}(t\rightarrow\infty)$ for 100 V, 60 V, and 20 V, we were able to estimate the time to reach a fraction of the collected charge. Figure 5 shows the time it takes for 95% of the charge to be collected as a function of plasma density. Here, we observed that the charge collection time depends on both the applied field and the plasma density, approaching 100 ns even for the highest applied field of 2.7 V/µm.

ISBN: 978-3-95450-220-2 ISSN: 2673-5474 doi: 10.18429/JACoW-FEL2022-WEP55

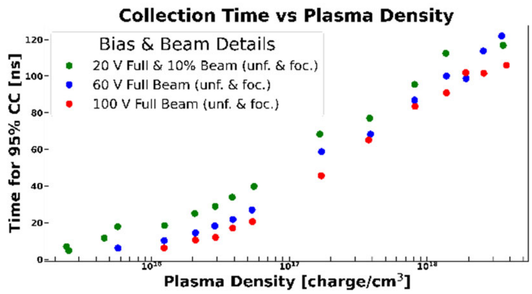

Figure 5: Estimated time to collect 95% of $Q_{coll}(t\rightarrow\infty)$ as a function of plasma density for different bias voltage.

50-MHz POSITION & INTENSITY PASS-THROUGH DIAGNOSTIC

The next part of the study has been motivated by the cavity-based X-ray free electron laser (CBFEL) under development by the Argonne National Laboratory (ANL) and SLAC [3]. In this project, a recirculatory longitudinal coherent X-ray beam will interact with fresh electron bunches over multiple passes inside a rectangular cavity. The CBFEL project requires a pass-through diagnostic that measures intensity and position of the circulating beam at every pass.

A new readout system capable of achieving repetition rates up to 50 MHz was built at SCIPP. The system makes use of a planar diamond sensor thinned to 43 µm that reduces the beam absorption and wave-front distortion. A bank of 8 parallel 0.2 µF capacitors is included to provide signal return path that bypasses the voltage supply. Signals from the diamond sensor pass through a passive RC network that shapes the signal into a form easily acquired by commercial digitizers. After shaping the output signal, it has a risetime of 1.5 ns and returns to baseline within 20 ns. Figure 6 shows the 4-channel readout board designed to measure the intensity and centroid position of the recirculating FEL beam.

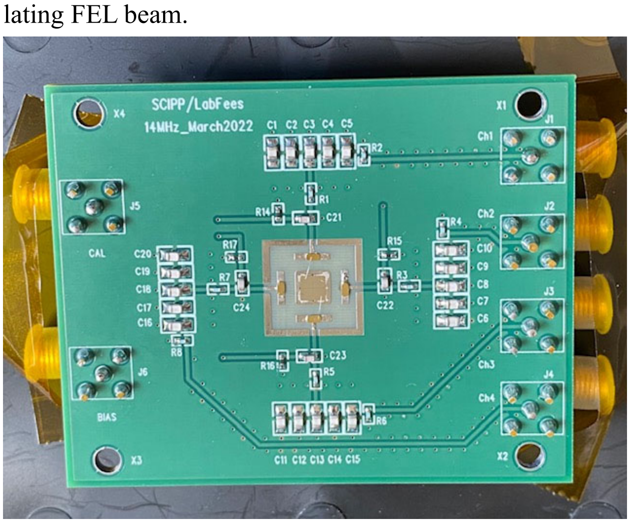

Figure 6: 4-channel readout board picture with a 4-quadrant 43 µm diamond sensor.

The new PCB board was taken on April 16, 2022, to the XPP beam line at SLAC and it was tested under an attenuated (1000x attenuation) monochromatic high-intensity X-ray beam and with a 50 V bias voltage. Figure 7 shows a typical trace read out form one of the quadrants during the run. In this study a sweep across two quadrants of the diamond sensor is presented.

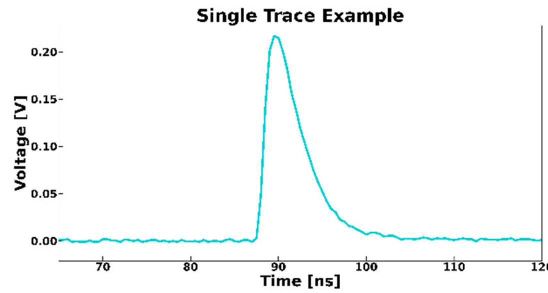

Figure 7: Example of a single pulse extracted from a single quadrant. All quadrants exhibit similar pulse shapes.

The corresponding collected charge at quadrant 3 and 4 was measured by integrating the average traces and dividing it by the effective path resistance of 240 Ω; this was done only for an intensity interval of 3.1 nJ to 4.7 nJ. Figure 8 shows the average collected charge measured as the XPP beam was moved in intervals of 50 µm across quadrant 3 and 4. Moreover, the combined collected charge from Q_4 and Q_3 was characterized as a function of delivered beam intensity. Figure 9 displays the linear correlation between these two parameters, showing that a pass-through diagnostic is achievable for repetition rate as large as 50 MHz.

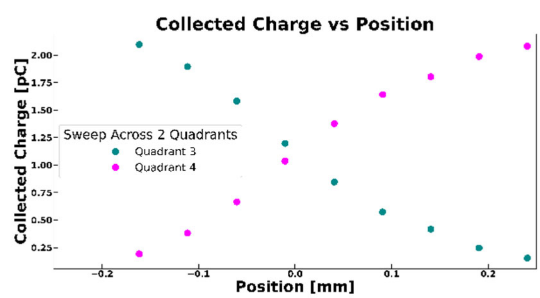

Figure 8: Fraction of the measured collected charge (Q_3 and Q_4) at each quadrant as a function of position.

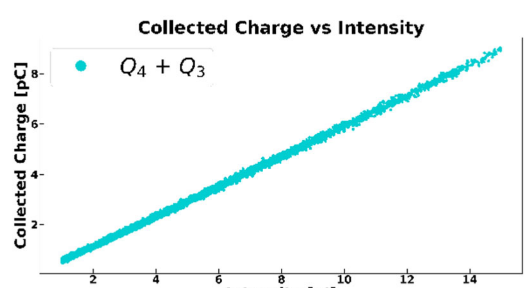

Figure 9: Linear correlation between the sum of Q_4 and Q_3 and the beam intensity.

The one-dimensional position resolution of the quadrant diagnostic was studied as follows. First, the asymmetry A of the Q_4 and Q_3 signals was formed according to:

ISBN: 978-3-95450-220-2 ISSN: 2673-5474 doi: 10.18429/JACoW-FEL2022-WEP55

$$A = \frac{Q_4 - Q_3}{Q_4 + Q_3} \quad (2)$$

where Q_4 and Q_3 are the charge collected from each of the two quadrants for each position of the XPP beam. An advantage of using the asymmetry is that it takes only the range between -1 and 1; instead of the ratio Q_4/Q_3 which can take value from $-\infty$ to $+\infty$.

Once the asymmetry is obtained, the position resolution σ_P can be calculated according to:

$$\sigma_P = \frac{dP}{dA}\sigma_A \quad (3)$$

where dP/dA is the derivative of the position in terms of the asymmetry and σ_A is the asymmetry uncertainty, which also can be calculated by:

$$\sigma_A = \frac{\sigma_Q}{Q}\sqrt{1 + A^2} \quad (4)$$

where σ_Q is the uncertainty in the measured collected charge at any given quadrant and Q is the average collected charge from the sum $Q_4 + Q_3$. In order to find a value for dP/dA and σ_A, a polynomial fit was performed using the asymmetry values across the different positions of the beam. Figure 10 shows the polynomial function describing the position as a function of the asymmetry P(A). By making use of this polynomial, we estimated dP/dA ~ 0.142 for the case when A ~ 0. According to Eq. (4), the square root factor becomes 1 when the beam is exactly half-way between the two quadrants and A ~ 0; as a result, the asymmetry uncertainty can be obtained by measuring σ_Q/Q. By comparing, for each pulse, the total observed collected charge to the value expected for the given pulse energy, an upper limit on the relative charge measurement error σ_Q/Q could be determined. For our case of a mean collected charge of 2.23 pC, the relative error was measured to be ~ 2.5%. Using this result with the already know calculated dP/dA ~ 0.142, we measured the position resolution to be approximately 3 µm for a 4 nJ pulse.

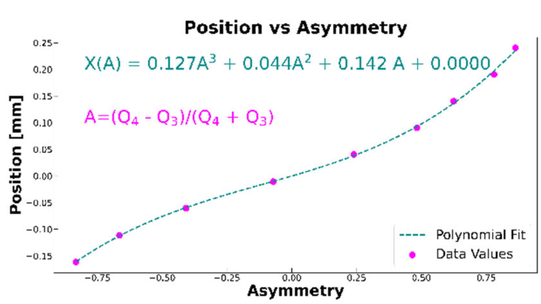

Figure 10: Polynomial fit to the asymmetry values measured from Q_4 and Q_3.

The position of each pulse was computed using the polynomial function P(A) found above in Fig. 10. Figure 11 shows a plot of the position of each pulse in a narrow intensity interval. This provides a direct measurement of the pulse-by-pulse beam jitter of the XPP beam.

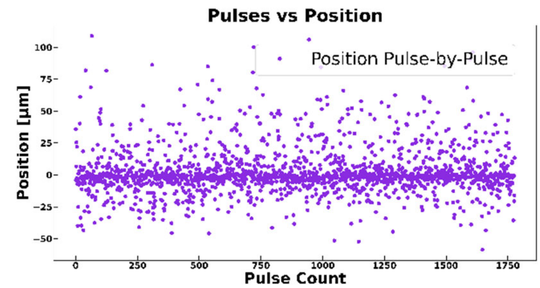

Figure 11: Measured XPP beam jitter with a 3 µm position resolution.

CONCLUSION

We report of the characteristics of charge collection in diamond for large, fast signals, making use of a specially designed readout assembly exposed to intense X-ray pulses at the SLAC LCLS. For highest bias voltage, charge collection efficiency was found to be maintained for plasma densities as high as 10^{16} charge/cm^3. The charge collection efficiency improved monotonically with increasing applied bias voltage. Charge collection time, characterized by the amount of time required to accumulate 95% of the asymptotic value of collected charge, was also found to depend strongly on plasma density and detector bias voltage.

In addition, we characterized the performance of the diamond-based intensity and position monitor for XFEL beams. The 4-quadrant system provides a pass-through diagnostic for frequencies as high as 50 MHz repetition rate. The pulse-by-pulse position resolution was measured to be approximately 3 µm.

ACKNOWLEDGMENT

This work was supported by the UC-National Laboratory Fees Research Program grant ID #LFR-20-653232, and by the U.S. Department of Energy, grant number DE-SC0010107. We also acknowledge the generous support of the SLAC National Accelerator Laboratory, through its provision of LCLS beam time and staff support.

REFERENCES

[1] M. Pomorski *et al*. "Development of single-crystal CVD-diamond detectors for spectroscopy and timing", *Phys. Status Solidi. A,* vol. 203, pp. 3152-3160, Sep. 2006. doi: 10.1002/pssa.200671127

[2] J.W. Keister and J. Smedley, "Single crystal diamond photodiode for soft X-ray radiometry", *Nucl. Instr. Methods Phys. Res., Sect. A,* vol. 606, pp. 774-779, Jul. 2009. doi:10.1016/j.nima.2009.04.044

[3] G. Marcus and F.-J.Decker, "Cavity-Based Free-Electron Laser Research and Development: A Joint Argonne National Laboratory and SLAC National Laboratory Collaboration", in *Proc. 39th Free Electron Laser Conf. (FEL'19),* Hamburg, Germany, Aug. 2019, pp. 282-287. doi:10.18429/JACoW-FEL2019-TUD04

ISBN: 978-3-95450-220-2 ISSN: 2673-5474 doi: 10.18429/JACoW-FEL2022-WEP58

INVESTIGATION OF HIGH ABSORBED DOSES IN THE INTERSECTIONS OF THE EUROPEAN XFEL UNDULATOR SYSTEMS

O. Falowska–Pietrzak†, A. Hedqvist, F. Hellberg, Stockholm University, Stockholm, Sweden
G. Lopez Basurco, Autonomous University of Madrid, Madrid, Spain
F. Wolff-Fabris, European XFEL GmbH, Schenefeld, Germany

Abstract

This work presents measurements of the absorbed doses in the vicinity of phase shifter (PS) installed in intersections of the Undulator Systems at the European X-Ray Free Electron Laser (XFEL). In addition, Geant4 Monte Carlo simulations were performed to further investigate the radiation field present in these intersections. Measurements in the downstream undulator cell in SASE3 showed similar doses for the films placed at the PS entrance and near PS motors. Both measurements and simulations indicate that the radiation field near PS motors is not caused by the high-energy electron interactions with the beam pipe close to the PS. The measurements of the absorbed doses at the PS entrance in the upstream undulator cells are also presented.

INTRODUCTION

The European XFEL GmbH is a free-electron laser facility located in Schenefeld, Germany. It operates three undulator systems called SASE1, SASE2 and SASE3 since 2017, and the radiation damage to the undulators is the matter of concern [1]. In each of these systems, electron bunches of GeV energies that propagate along the undulators in the vacuum beam pipe generate high brilliance X-ray pulses. Each system consists of numerous undulator segments (5 m long) separated by intersections (1.1 m long). The intersection together with the undulator segment is called the undulator cell. There are 35 undulator cells in SASE1 and SASE2, while SASE3 consists of 21 cells. Each intersection contains vacuum systems and correction and diagnostic equipment such as beam position monitor (BPM), beam loss monitor (BLM) and quadrupole magnet (QM). Downstream of the QM a PS is located. It has a movable gap and is composed by permanent magnets from the same type as employed in the undulator segments. It matches the phase of electrons and photons produced through the Self-Amplification Spontaneous Emission (SASE) process [2].

At the entrance of each undulator segment, Radfet dosimeters continuously measure the absorbed doses and are online readable [3]. The radiation field close to the beam pipe can arise from several factors, such as spontaneous undulator radiation and electron interaction with gas molecules. In addition, electrons may hit the beam pipe which results in emission of stray radiation. However, no dosimetry system is installed in the intersections. Recently, it was noticed that the movement of gaps in some PS in SASE3 could not be performed due to PS motor or encoder damage. It might be caused by the radiation present between undulator segments.

In this work, we present the results of gafchromic film measurements at the PS entrance and near PS motors. The measurements are presented together with the Monte Carlo simulations of electron beam losses to better understand the radiation field in the intersections.

METHODS

Gafchromic films

The absorbed doses in the intersections were measured with gafchromic film dosimeters. Film dosimetry is mostly used for medical radiation purposes, but they are also useful for measurements in the high-energy radiation fields. They can be cut in various shapes without changing their properties. Therefore, they can be placed in areas that are difficult to access with other detectors. In addition, film dosimeters give information on 2D dose distributions.

The films undergo polymerization during exposure to ionizing radiation. The subsequent colour change is proportional to the absorbed dose, which can be evaluated through Red (R), Green (G) and Blue (B) values of scanned films through multichannel analysis [4].

In this work, the GAFCHROMIC™ EBT3 films were placed at the PS entrance, perpendicularly to the beam pipe (referred later as PS films) in different SASE1 and SASE3 undulator cells. Films were removed from SASE1 and SASE3 after approximately five and two months, respectively. In addition, in SASE3 the absorbed doses were measured next to the PS motors, located approximately 10 cm above the PS and 40 cm above the beam pipe. The PS and position of the PS motor are shown in Fig. 1.

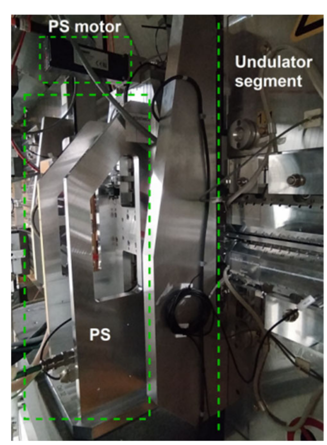

Figure 1: PS and PS motor seen from the downstream side of the undulator system.

† olga.falowskapietrzak@fysik.su.se

ISBN: 978-3-95450-220-2 ISSN: 2673-5474 doi: 10.18429/JACoW-FEL2022-WEP58

Monte Carlo Simulations

Electrons interactions with the beam pipe were simulated using Monte Carlo code Geant4 [5]. The code consists of 2 undulator segments, each 5 m long, separated by 1.1 m long intersections. The aluminum beam pipe along undulator segments is rectangular (70 mm x 10 mm), with an elliptical aperture (15 mm x 9 mm). In the intersection, the beam pipe is circular, with a diameter of 9 mm and 0.5 mm aluminum wall. Intersection components such as absorber, vacuum pump, BMP, BLM, QM and PS were included in the code with simplified geometry. The simulation geometry is schematically presented in Fig. 2. In the simulations 10 000 electrons with energy of 14 GeV hit the beam pipe at two fixed positions along the beam pipe, which were the end of the 1st undulator segment and the middle of the quadrupole magnet. Therefore, it was possible to investigate the effect that all the components in the intersection have on the absorbed dose at the PS entrance. At this stage, no magnetic field was included in the code.

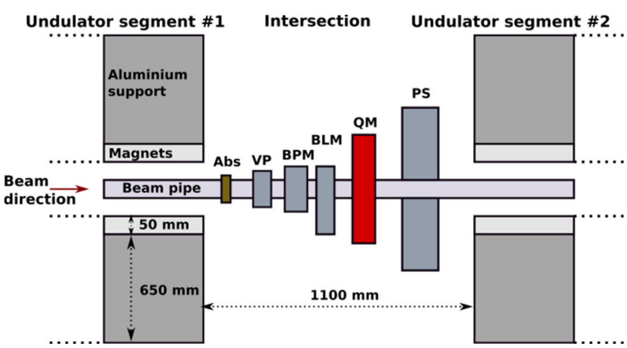

Figure 2: Schematic presentation of the Geant4 code geometry.

RESULTS

The absorbed dose measurements near PS motor in cell #12 in SASE3 is shown in Fig. 3. The measurements show that the radiation near the PS motor after 2 months of irradiation varies between 2 Gy and 3 Gy. The dose is distributed almost homogeneously over the whole film area. Additional measurements near the PS motor in cell #15 in SASE3 showed similar dose distribution pattern. However, the absorbed doses were higher for the same irradiation time and varied between 6 Gy and 8 Gy.

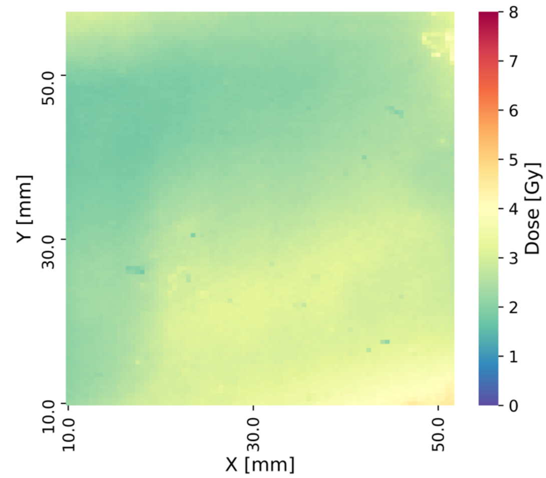

Figure 3: Absorbed dose distribution measured near PS motor in cell #12 in SASE3.

Figures 4 and 5 show dose distributions for the PS film placed in undulator cell #12 in SASE3, above and below the vacuum pipe, respectively. The maximum absorbed dose is almost 8 Gy for the top PS film and 7 Gy for the bottom PS film. The region with the maximum dose is concentrated in a small area near the beam pipe. However, in both cases there is an area with increased dose propagating in the vertical direction of the film. Its shape indicates that this is an effect of the QM, which is located directly upstream of the PS and shields part of the radiation. It suggests that the radiation contributing to the absorbed dose comes from the upstream of the closest QM.

Figure 6 shows the dose distribution at the undulator segment entrance in cell #12 in SASE3. As it can be seen, the maximum absorbed dose is concentrated in a small area near the film's edge. The dose decreases to 0.2 Gy after approximately 10 mm in the vertical direction.

As can be seen from Fig. 4, the absorbed dose measured for the part unshielded by the QM is around 2 Gy. It is comparable to the absorbed dose measured near the PS motor in the same undulator cell.

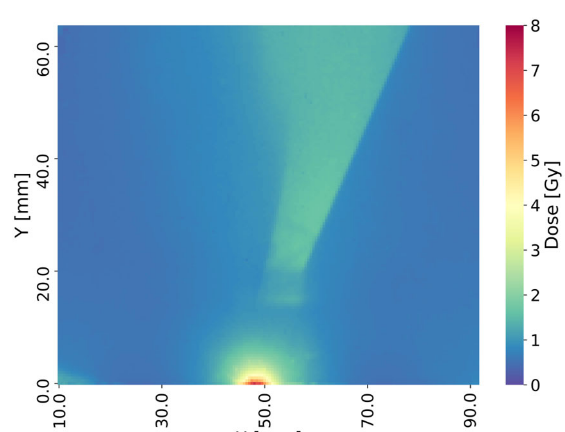

Figure 4: Absorbed dose distribution for the PS film in cell #12 located above the beam pipe in SASE3.

ISBN: 978-3-95450-220-2 ISSN: 2673-5474 doi: 10.18429/JACoW-FEL2022-WEP58

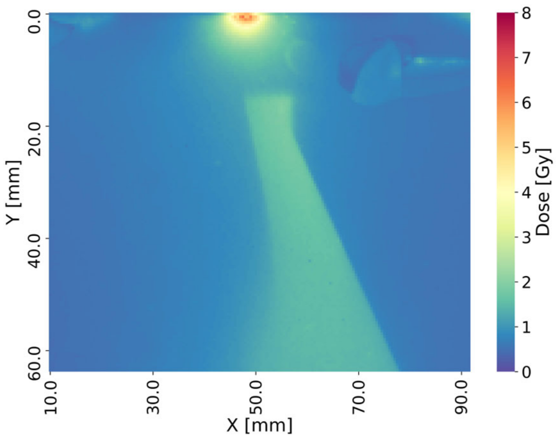

Figure 5: Absorbed dose distribution for the PS film in cell #12 located below the beam pipe in SASE3.

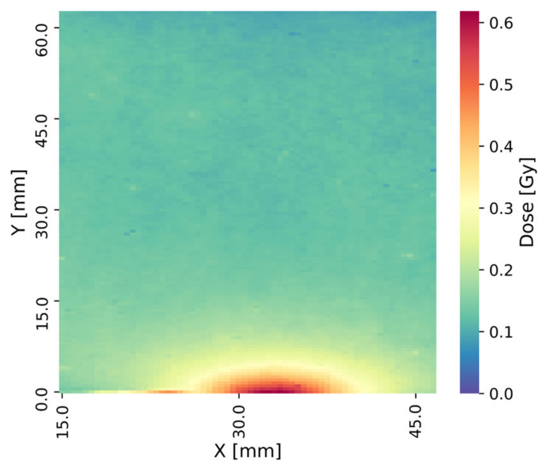

Figure 6: Absorbed dose distribution for the film placed at the undulator segment entrance #12 in SASE3, above the beam pipe.

In order to determine if the interactions of the high-energy electrons with the beam pipe are responsible for the absorbed doses at the PS entrance and near the PS motors in the downstream undulator cells, Geant4 simulations were performed. Figs. 7 and 8 show Geant4 simulations of dose distributions at the PS entrance for electrons hitting the wall at the end of the 1st undulator segment and at the QM, respectively. In this case only electron losses were simulated. In these simulations, electrons hit the beam pipe over its whole aperture at 15° intervals.

The maximum absorbed dose is more than two times higher for electrons interacting with the beam pipe at the end of the upstream segments. It is most likely caused by the fact that the emitted stray radiation interacts with various components along the intersections, creating secondary particles which contribute to the dose. The triangular shape of the dose distribution seen in Fig. 7 is a result of the QM implemented in the code, which shields part of the radiation. However, the shielding effect is not as prominent as in Figs. 4 and 5, and the dose decreases significantly after approximately 20 mm in the vertical direction. As mentioned, the doses measured near the PS motor in cell #12 in SASE3 were similar to the doses measured at the part of the PS not shielded by QM. As only electron losses were simulated, it indicates that they do not contribute to the doses measured near the PS motors in the downstream undulator cells. Therefore, the radiation field in the vicinity of PS motors comes most likely from further upstream of the intersection, e.g. low-energy radiation associated with the SASE process or secondary radiation from the electron interactions with the beam pipe in the upstream undulator cells further away from the PS motors.

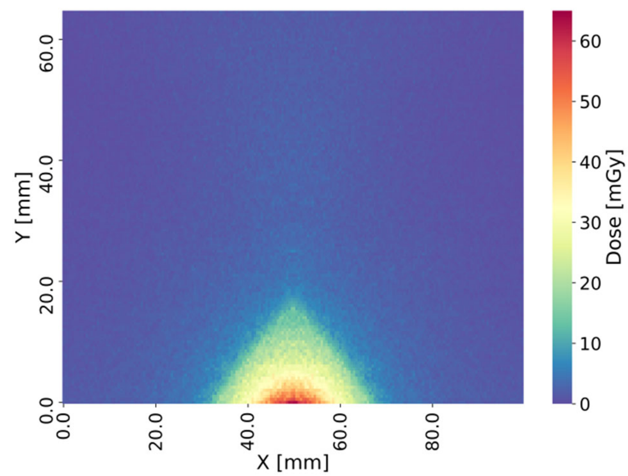

Figure 7: Simulations of the dose distribution at the PS surface for electrons hitting the beam pipe at the end of the 1st undulator segment.

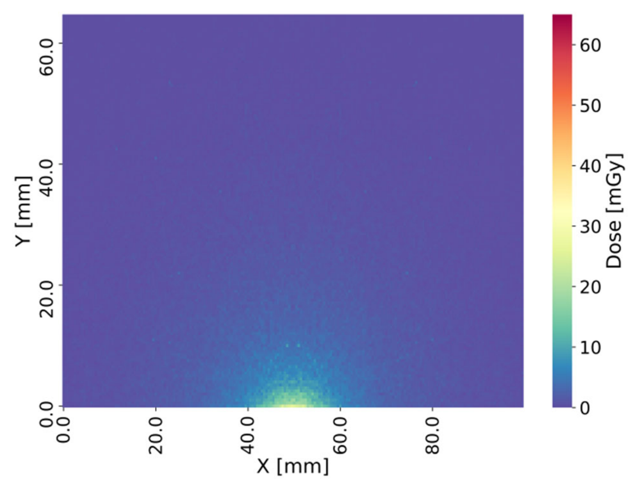

Figure 8: Simulations of the dose distribution at the PS surface for electrons hitting the beam pipe at the QM.

In order to determine if the QM shielding effect is visible in the upstream undulator cells, the films were placed also at the PS entrance in undulator cells #4 – #10 in SASE1, above (top films) and below (bottom films) the vacuum pipe. The measurements showed the highest doses closest to the beam pipe. The maximum absorbed doses were determined as a mean over the area 5 mm in the horizontal direction and 2.5 in the vertical direction around the maximum. The maximum absorbed doses for PS films are presented in Fig. 9. The measurements in cell

ISBN: 978-3-95450-220-2 ISSN: 2673-5474 doi: 10.18429/JACoW-FEL2022-WEP58

#8 showed significant absorbed doses which exceed 20 Gy both for top and bottom films, and they were not included in Fig. 9.

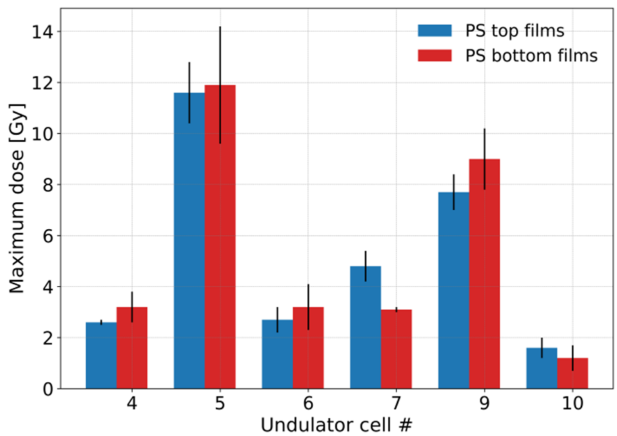

Figure 9: Maximum absorbed doses measured at the PS entrance in different intersections of upstream undulator cells in SASE1.

As seen in Fig. 9, the absorbed doses measured at the entrance of the PS in intersections of upstream cells in SASE1 vary between almost 2 Gy and 12 Gy. However, the QM shielding effect seen in Figs. 4 and 5 was not observed for any of the PS films. As shown in [6], low-energy synchrotron radiation doesn't contribute to the absorbed doses upstream of the undulator cell #13. It suggests that the radiation field in the upstream cells may be a result of high-energy electron interactions with the beam pipe, which creates secondary radiation contributing to the absorbed doses.

CONCLUSION

In this work, gafchromic film measurements were performed in the intersections of the undulator systems at EuXFEL. The measurements in SASE3 showed absorbed doses around 2 Gy and 7 Gy near PS motors in intersections of the undulator cells #12 and #15, respectively. Additional measurements in cell #12 at the PS entrance showed that for the large area of the film propagating in the vertical direction, the absorbed dose is comparable to the dose at the PS motor. The shape of this area indicates that the radiation contributing to the absorbed dose comes from the upstream of the QM.

Geant4 simulations of electron losses were performed in order to determine the source of the radiation field present in the intersections of the downstream undulator cells. The shielding effect of QM is visible in Fig. 7. However it is not as prominent as for film measurements in Figs. 4 and 5. The simulations indicate that the absorbed doses measured near PS motors are not caused by electrons losses, but rather low-energy radiation associated with the SASE process or secondary radiation from the upstream undulator cells further away from the PS motors.

The film measurements at the PS entrance in multiple intersections in SASE1 showed that the radiation field is also present in the intersections of the upstream undulator cells. It is most likely caused by other factors than low-energy synchrotron radiation, e.g. electrons interactions with the beam pipe, which create secondary particles contributing to the dose.

The presented results are preliminary, and a more detailed analysis should be performed in the future to further characterize the radiation field in the undulator system intersections. Additional measurements near PS motors in different undulator cells should be performed in the future in order to identify the source of radiation in this area.

REFERENCES

[1] F. Wolff-Fabris, J. Pflueger, F. Schmidt-Foehre, and F. Hellberg, "Status of the Radiation damage on the European XFEL Undulator Systems", in *Proc. 9th Int. Particle Accelerator Conf. (IPAC'18),* Vancouver, Canada, Apr.-May 2018, pp. 1776-1779, `doi:10.1088/1742-6596/1067/3/032025`

[2] H. H. Lu, Y. Li, and J. Pflueger., "The Permanent Magnet Phase Shifter for the European X-Ray Free Electron Laser", in *Nucl. Instrum. Methods Phys. Res. A,* vol. 605, no. 3, pp. 399-408, Jul. 2009, `doi:10.1016/j.nima.2009.03.217`

[3] F. Schmidt-Foehre, D. Noelle, R. Susen, and K. Wittenburg, "Tests and Measurements with the Embedded Radiation-monitor-system Prototype for Dosimetry at the European XFEL", in *Proc. 3rd Int. Particle Accelerator Conf. (IPAC'12),* New Orleans, LA, USA, May 2018, paper THPPR033, pp. 4041-4043

[4] A. Micke, D. F. Lewis, and X. Yu, "Multichannel film dosimetry with nonuniformity correction", in *Med Phys.,* vol. 38, no. 5, pp. 2523-34, May 2011, `doi:10.1118/1.3576105`

[5] S. Agostinelli, *et al.*, "GEANT4 – a simulation toolkit", *Nucl. Instrum. Meth. A*, vol. 506, no 3, pp. 250-303, Jul. 2003.

[6] S. Liu, Y. Li, and F. Wolff-Fabris, "Undulator Radiation Dose Caused by Synchrotron Radiation at the European XFEL", in *Proc. 10th Int. Particle Accelerator Conf. (IPAC'19),* Melbourne, Australia, May 2019, pp. 1724-1727, `doi:10.18429/JACoW-IPAC2019-TUPRB021`

ISBN: 978-3-95450-220-2 ISSN: 2673-5474 doi: 10.18429/JACoW-FEL2022-WEP60

MILLIMETER-WAVE UNDULATORS FOR COMPACT X-RAY FREE-ELECTRON LASERS*

L. Zhang†[1], J. Easton, C. Donaldson[1], C. Whyte, A. Cross[1], University of Strathclyde, Glasgow, UK
Jim Clarke[1], ASTeC, STFC Daresbury Laboratory, Sci-Tech Daresbury, Daresbury, UK
[1]also at Cockcroft Institute, Daresbury, UK

Abstract

Electromagnetic wave undulators have the advantage of a shorter period compared with the permanent magnet undulators when operating at high frequency, therefore producing FEL radiation at the same wavelength with less electron energy. This paper presents the design of a Ka-band microwave undulator. The ongoing research is to prototype a millimeter-wave undulator operating at ~100 GHz, which will have an undulator period of about 1/10 of the state-of-the-art permanent magnet undulators. The millimeter-wave undulator will allow the generation of soft X-ray radiation at much lower beam energy, such as hundreds of MeV, enabling a reduction in the cost of a compact XFEL facility.

INTRODUCTION

Free-electron lasers (FELs) [1, 2] are capable to produce high-power ultrashort-wavelength, and spatially coherent radiation. The coherent radiation at X-ray wavelength opens various applications and allows the exploration of new studies in biophysical and materials science, surface studies, chemical technology, medical applications, solid-state physics, and others. The FEL radiation is produced in an undulator which is traditionally made of periodic permanent magnets. The radiation wavelength produced by such a permanent magnet undulator (PMU) is

$$\lambda = \frac{\lambda_u}{2\gamma^2}\left(1+\frac{K^2}{2}+\gamma^2\theta^2\right) \quad (1)$$

where λ_u is the undulator period determined by the period of the magnet, γ is the relativistic factor governed by the electron beam energy. θ is the observation angle, which is normally set as 0. K is the undulator strength parameter. It is defined by the peak transverse magnetic field strength of the undulator and the undulator period, as

$$K = 0.0931 B_u[\mathrm{T}]\lambda_u[\mathrm{mm}] \quad (2)$$

Table 1 lists the parameters of PMUs used in Swiss XFEL and Europe XFEL [3, 4]. They show the scale of the periods of the state-of-the-art PMUs. The production of FEL radiation at X-ray wavelength requires high electron beam energy with a few GeV.

Table 1: Examples of the PMU parameters

	Swiss XFEL (Aramis)	Europe XFEL
Structure	Planar hybrid	Planar hybrid
Material	NdFeB	NdFeB
K	1.2	3.0
Period	15 mm	26 mm
Peak field	0.85 T	1.24 T
Gap type	Variable	Variable
Gap	4.7 mm	6.0 mm

The periodic transverse magnetic field in the undulator can also be created from the electromagnetic (EM) waves. The EM undulators [5-7] have the advantage of a shorter period compared with the permanent magnet undulators when operating at high frequency, therefore producing FEL radiation at the same wavelength with less electron energy. Early research on the microwave undulator was hampered by the limited power of the drive source. In 2014, SLAC demonstrated the FEL radiation with an X-band microwave undulator driven by a 50 MW klystron in the experiment [8-10]. It achieved an equivalent B_u of 0.65 T and a period of 13.9 mm. The experiment also demonstrated tuneable radiation at 400-600 nm using an electron bunch with an energy of 50 MeV to 70 MeV and seeded coherent harmonic generation (SCHG) at 160-240 nm using a 120 MeV electron bunch.

Microwave undulators operating at higher frequency allow shorter periods, therefore, achieving shorter FEL radiation wavelength at the same energy of the electron bunch energy. In this paper, the properties of a Ka-band microwave undulator operating at 36 GHz are presented.

MICROWAVE UNDULATOR

The main body of the undulator cavity was composed of a corrugated waveguide that supports the low-loss HE_{11} modes, as shown in Fig. 1. The field pattern satisfies the requirements of an undulator, including the low loss to increase the equivalent magnetic field strength at the same driving power, a maximum field strength at the waveguide center in which the beam propagates to maximize the interaction between the EM wave and the electron bunch, a TE-like mode to maximize the transverse magnetic field and avoid the axial electric field modulating the electron beam, and an overmoded structure to reduce the effect of the forward wave components in the cavity structure.

* Work supported by Science and Technology Facilities Council (STFC) U.K., Cockcroft Phase 4 grant ST/V001612/1.
† liang.zhang@strath.ac.uk

ISBN: 978-3-95450-220-2 ISSN: 2673-5474 doi: 10.18429/JACoW-FEL2022-WEP60

The microwave undulator cavity structure is composed of the corrugated waveguide and the coupler structure. The corrugated waveguide was designed based on the surface impedance approach. The coupler structure was designed based on the near field radiation pattern, and then further optimized to match the operating frequency and to achieve a flat field in the corrugated section [11-13]. The prototype contains 72 regular periods, and its mode pattern is shown in Fig. 2.

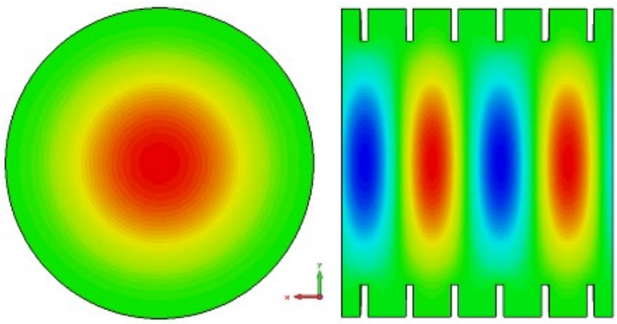

Figure 1: The HE_{11} mode pattern and the corrugated waveguide.

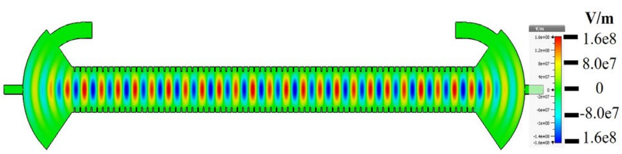

Figure 2: Microwave undulator operating at 36 GHz.

The undulator period was 4.34 mm and the equivalent magnetic field would be 1.27 T when a 1-meter structure is driven by 50 MW of input power. The potential high-power microwave sources to drive the microwave undulator can be gyroklystrons, free-electron masers (FEMs) based on the 2D periodic surface lattice (PSL) interaction region or a Cyclotron Autoresonance Maser (CARM). The dynamic of the electrons in the microwave undulator was also simulated. The drift distance reduces as the increment of electron bunch energy, and a high-power microwave oscillator is feasible as the drive source [14].

Different manufacturing methods were used to prototype the microwave undulator, including the direct machining of the short section of corrugation and then joining together, the electroforming of the whole corrugated waveguide on an aluminum mandrel. Fig. 3 shows the undulator structure made by direct machining, and the measurement results using a vector network analyzer (VNA). Both methods have a close resonance frequency compared with the designed value. Direct machining has a better surface quality and therefore a high Q factor compared with the electroforming method.

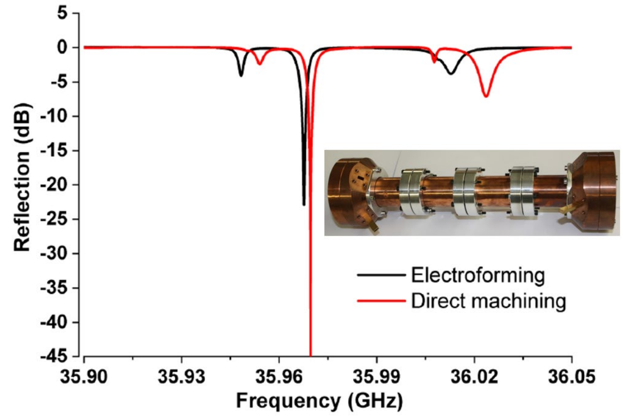

Figure 3: Measured results from CNC machined undulator.

MILLIMETER WAVE UNDULATOR

The long-term goal is to prototype a millimeter-wave undulator operating at ~100GHz, which will have an undulator period of about 1/10 of the state-of-the-art permanent magnet undulators. It will allow the generation of soft X-ray radiation at much lower beam energy, such as hundreds of MeV, enabling a reduction in the cost of a compact XFEL facility.

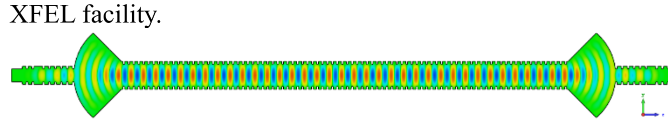

Figure 4: The electric field distribution of the final designed millimeter-wave undulator.

A millimeter wave undulator operating at 94 GHz has been designed and is currently under construction. To maintain a large beam aperture at 94 GHz at a high-Q factor of the undulator cavity, a special design of the coupler structure is therefore required to reduce the leakage power of the EM-wave. An over-moded Bragg reflector was therefore designed to achieve an ultra-high reflection (higher than -0.15 dB) and to maintain a large waveguide radius. Fig. 4 shows the field pattern of the millimeter wave undulator with the Bragg reflector.

ACKNOWLEDGMENTS

This work is supported by Technology Facilities Council (STFC) U.K., Cockcroft Phase 4 under grant ST/V001612/1.

REFERENCES

[1] D. A. G. Deacon, L. R. Elias, J. M. J. Madey, G. J. Ramian, H. A. Schwettman, and T. I. Smith, "First Operation of a Free-Electron Laser," *Phys. Rev. Lett.,* vol. 38, no. 16, pp. 892-894, April 1977. doi: 10.1103/PhysRevLett.38.892.

[2] P. G. Shea and H. P. Freund, "Free-Electron Lasers: Status and Applications," *Science,* vol. 292, no. 5523, p. 1853, 2001. doi: 10.1126/science.1055718.

[3] V. Paul Scherrer Institute, "SwissFEL - Conceptual design report," Switzerland, 2010.

ISBN: 978-3-95450-220-2 ISSN: 2673-5474 doi: 10.18429/JACoW-FEL2022-WEP60

[4] A. Madsen, J. Hallmann, T. Roth, and G. Ansaldi, "Technical Design Report: Scientific Instrument MID," in "XFEL.EU Technical Report," 2013. [Online]. Available: https://bib-pubdb1.desy.de/record/154260

[5] T. Shintake, K. Huke, J. Tanaka, I. Sato, and I. Kumabe, "Microwave Undulator," *Jpn. J. Appl. Phys.,* vol. 21, no. 10A, pp. L601-L603, 1982, doi: 10.1143/JJAP.21.L601.

[6] T. Shintake, K. Huke, J. Tanaka, I. Sato, and I. Kumabe, "Development of Microwave Undulator," *Jpn. J. Appl. Phys.,* vol. 22, no. 5R, pp. 844-851, May 1983. doi: 10.1143/JJAP.22.844.

[7] S. V. Kuzikov, Y. Jiang, T. C. Marshall, G. V. Sotnikov, and J. L. Hirshfield, "Configurations for short period rf undulators," *Phys. Rev. ST Accel. Beams,* vol. 16, no. 7, p. 070701, 2013. doi: 10.1103/PhysRevSTAB.16.070701.

[8] F. Toufexis and S. G. Tantawi, "Development of a millimeter-period rf undulator," *Phys. Rev. ST Accel. Beams,* vol. 22, no. 12, p. 120701, 2019. doi: 10.1103/PhysRevAccelBeams.22.120701.

[9] S. Tantawi *et al.*, "Experimental Demonstration of a Tunable Microwave Undulator," *Phys. Rev. Lett.,* vol. 112, no. 16, p. 164802, 2014. doi: 10.1103/PhysRevLett.112.164802.

[10] M. Shumail, "Theory, design, and demonstration of a new microwave-based undulator," PhD, Department of Electrical Engineering, Stanford University, 2014. [Online]. Available: https://purl.stanford.edu/hm994ym4473

[11] L. Zhang, W. He, J. Clarke, K. Ronald, A. D. R. Phelps, and A. Cross, "Systematic study of a corrugated waveguide as a microwave undulator," *J. Synchrotron Radiat.,* vol. 26, p. 11-17, 2019. doi:10.1107/S1600577518014297.

[12] L. Zhang, W. He, J. Clarke, K. Ronald, A. D. R. Phelps, and A. W. Cross, "Microwave Undulator Using a Helically Corrugated Waveguide," *IEEE Trans. Electron Devices,* vol. 65, no. 12, pp. 5499-5504, 2018. doi: 10.1109/TED.2018.2873726.

[13] L. Zhang *et al.*, "Coupling Structure for a High-Q Corrugated Cavity as a Microwave Undulator," *IEEE Trans. Electron Devices,* vol. 66, no. 10, pp. 4392-4397, 2019. doi: 10.1109/TED.2019.2933557.

[14] L. Zhang *et al.*, "Beam dynamic study of a Ka-band microwave undulator and its potential drive sources," *Sci. Rep.,* vol. 12, no. 1, p. 7071, 2022/04/29 2022. doi: 10.1038/s41598-022-11101-2.

ISBN: 978-3-95450-220-2 ISSN: 2673-5474 doi: 10.18429/JACoW-FEL2022-WEP62

STUDY OF AN ERL-BASED X-RAY FEL*

F. Lin†, V.S. Morozov, Oak Ridge National Laboratory, Oak Ridge, TN, USA
J. Guo, Y. Zhang, Thomas Jefferson National Accelerator Facility, Newport News, VA, USA

Abstract

We propose to develop an energy-recovery-linac (ERL)-based X-ray free-electron laser (FEL). Taking advantage of the demonstrated high-efficiency energy recovery of the beam power in the ERL, the proposed concept offers the following benefits: i) recirculating the electron beam through high-gradient SRF cavities shortens the linac, ii) energy recovery in the SRF linac saves the klystron power and reduces the beam dump power, iii) the high average beam power produces a high average photon brightness. In addition, such a concept has the capability of optimized high-brightness CW X-ray FEL performance at different energies with simultaneous multipole sources. In this paper, we will present the preliminary results on the study of optics design and beam dynamics.

INTRODUCTION

A Free-Electron Laser (FEL) that has been invented and experimentally demonstrated in the 1970s [1, 2] holds a great potential to serve as a high-power and coherent source. FEL performance extends beyond the limitations of fully coherent laser light sources by covering a broad range of wavelength from infrared down to X-ray with a stable and well-characterized temporal structure in the femtosecond time domain. Particularly, XFEL allows scientists to probe the structure of various molecules in detail, and simultaneously explore the dynamics of atomic and molecular processes on their own time scales. XFEL allows for the exploration of new areas in physics, chemistry, biology, medicine and materials.

Techniques have been developed and improved to amplify the spontaneous radiation to provide intense quasi-coherent radiation [3 - 6]. The FEL process strongly depends on the local electron beam properties: current, energy, emittance and energy spread. Therefore, all existing XFELs [7 - 15] are driven by linear accelerators to ensure preservation of the electron beam quality from the source for achieving a high peak brightness. Normal conducting RF cavities, with very high accelerating gradients of up to 60 MV/m, are used to keep the linac length as short as possible. This limits the bunch repetition rate up to about 100Hz in a pulsed beam operation mode, resulting in average photon brightness of as much as 10 orders of magnitude lower than the peak one. Therefore, several XFEL facilities [9, 13] have started considering a CW beam operation mode that is made possible by the high-gradient SRF technology. There were two ERL-based concepts [16, 17] explored to produce FELs in the UV and/or soft X-ray regions.

CONCEPT

We propose an ERL-based compact XFEL facility, schematically illustrated in Fig. 1. Note that the energy gain of 2 GeV from the SRF is chosen for this study only, considering relatively realistic SRF gradient, magnet fields, and geometric footprint of such a facility. Optimization of these parameters can be carried out in each individual case. We leverage the ongoing world-wide efforts on the further improvement of injector and XFEL techniques and focus on the feasibility study of the accelerator system.

Electron beams are generated from the source and accelerated to 250 MeV before the first bunch compression (BC). Then the beams are accelerated in the ERL by SRF cavities with the desired energy gain of 2 GeV. Since space charge effects are significantly suppressed at the GeV electron beam energy, one can utilize the first arc to compress the beam for the second time if needed. The electron beams are either directed into different undulators that can be designed and optimized for particular XFEL radiations parameters or bypass the undulator sections. Electron beams that have been used to produce XFEL can be energy recovered in the ERL after the second arc and dumped downstream. The bypassed electron beams will double energy up to ~ 4 GeV after the ERL and propagate through the third arc. Same as in the first ~ 2 GeV energy loop, the ~ 4 GeV electron beams will either be directed into different undulator sections or bypass the undulators. Again, the electron beams that have produced XFEL will be energy recovered and dumped, and the bypassed electron beams will be further accelerated to ~ 6 GeV for XFEL production and energy-recovered in the ERL before the final dump.

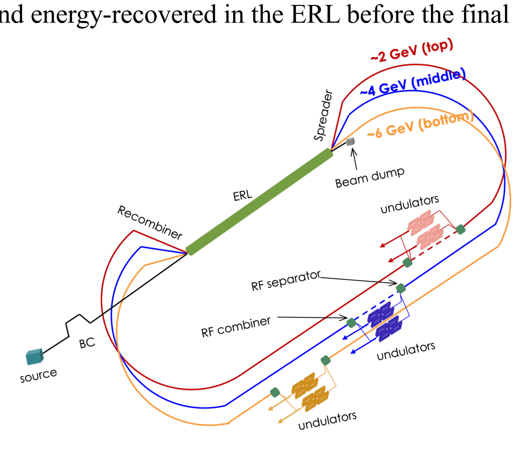

Figure 1: Schematic drawing of the proposed ERL-based XFEL facility.

* Work supported by UT-Battelle, LLC, under contract DE-AC05-00OR22725, and by Jefferson Science Associates, LLC, under contract DE-AC05-06OR23177
† Email: linf@ornl.gov

ISBN: 978-3-95450-220-2 ISSN: 2673-5474 doi: 10.18429/JACoW-FEL2022-WEP62

When a practical working limit of 1 MW dump beam power is considered, the first ERL injection beam energy of 250 MeV results in an average electron beam current of 4 mA. Comparing to the pulsed beam operation mode with the average beam current at the level of a few tens of nA, the CW beam operation mode will boost the average photon brightness significantly. A high bunch repetition rate of several to tens of MHz can produce a mA average beam current with a modest bunch charge. Small charge per bunch allows a short bunch length and a small transverse emittance. For this reason, it is easier to stabilize the beam energy and minimize the energy spread in a CW SRF system than a pulsed normal RF system that may have a reproducibility issue.

In addition to the improving the XFEL performance, this concept minimizes the power consumption by returning the energy back to the SRF cavities and then reusing it to accelerate the subsequent low energy beams. An energy recovery efficiency of up to 99% can be reached according to current development of SRF technology. Besides, the operating cost of the SRF cavities with nearly zero resistive wall losses is much lower than that of the normal conducting RF cavities in the CW mode.

OPTICS

Synchrotron radiation (SR) occurs when electrons propagate through dipoles in an accelerator. Incoherent synchrotron radiation (ISR) refers to the SR power emitted in a fully incoherent region in a dipole magnet. Particle's motion experiences diffusion and excitation from the ISR, resulting in a growth of emittance $\Delta\epsilon_u$ and energy spread $\Delta(\sigma_E^2)$ along the path of length L:

$$\Delta(\sigma_E^2) = \frac{55\alpha(\hbar c)^2}{48\sqrt{3}}\gamma^7 \int_0^L \left(\frac{1}{|\rho_x^3|} + \frac{1}{|\rho_y^3|}\right) ds, \tag{1}$$

$$\Delta\epsilon_u = \frac{55 r_c \hbar c}{48\sqrt{3}mc^2}\gamma^5 \int_0^L \frac{H_u}{|\rho^3|} ds. \tag{2}$$

Here γ is the Lorentz factor and ρ is the dipole magnet bending radius in any $u = x\ or\ y$ plane. Growth of electron beam emittance and energy spread is proportional to the 5th and 7th power of energy, respectively, and inversely proportional to the bending radius. In addition, the change of emittance also depends on the accelerator optics design, characterized by the H function with $H_u = \beta_u D'^2_u + 2\alpha_u D_u D'_u + \gamma_u D_u^2$.

As the FEL process strongly depends on the local electron beam properties, an optimum accelerator design should have minimal growth of the electron beam emittance and energy spread during its propagation from the source to the undulators. Once the electron beam energy is chosen, only the dipole bending radius and optics design are left to be optimized to control the beam properties. From the optics design point of view to reduce the growth of emittance, the horizontal beta function and dispersion need to be suppressed in dipoles, assuming horizontally bending dipole magnets. A large dipole bending radius ensures a small growth in emittance and energy spread of electron beams. However, this results in an increased circumference of an accelerator and its footprint. Therefore, an ultimate design goal of the proposed ERL-based XFEL facility will be preservation of the electron beam quality while making the accelerator facility as compact as possible.

Several arc cell optics designs have been explored extensively. Figure 2 (left) shows the preliminary arc cell lattice. This cell has phase advances of $(\phi_x, \phi_y) = (\frac{5\pi}{2}, \frac{3\pi}{2})$ for better control of sextupole-induced nonlinear resonances and the isochronous condition of $M_{56} = 0$ for better control of CSR-induced emittance growth. To simplify the front-to-end optics for studying electron beam dynamics, the following assumptions are made: i) the same arc cell optics is applied to construct all six arcs at three different electron beam energies of 2.25, 4.25 and 6.25 GeV, ii) straights for ERL and undulators are filled with FODO cells as space holders, iii) cavities are treated as zero-length elements with appropriate phases for acceleration or deceleration of the beams, iv) path length adjustment, spreader/recombiner sections are not implemented but have been demonstrated in existing accelerator facilities. All these detailed features will be added to design later, however, they should not have a significant impact on the beam dynamics. A complete lattice optics and its footprint are plotted in Fig. 2 as well. Table 1 list several high-level optics and beam parameters.

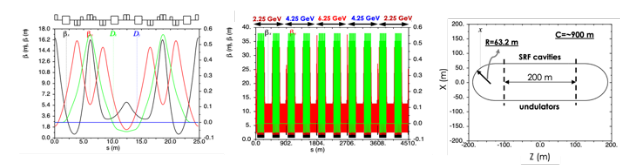

Figure 2: (Left) Arc cell optics. (Middle) Complete lattice optics. (Right) Footprint of the design.

Table 1: Preliminary Design Optics and Beam Parameters

Energy	GeV	2.25	4.25	6.25
Circumference per energy	m		~ 900	
Revolution time per energy	µs		~ 3	
Average current	mA		4	
Energy loss per turn	MeV	0.18	2.26	10.56
SR power	kW	0.7	9.1	42.2
Hor. & Ver. damping time	µm	76.1	11.3	3.6
Long. damping time	ms	38.1	5.7	1.8
Nor. equilibrium emittance	µm	38	254	809
Equilibrium energy spread	10^{-3}	0.54	1.0	1.5

ISBN: 978-3-95450-220-2 ISSN: 2673-5474 doi: 10.18429/JACoW-FEL2022-WEP62

BEAM DYNAMICS

Incoherent Synchrotron Radiation (ISR)

Table 1 shows that the electron beam will not reach to an equilibrium condition since the circulating time of micro-seconds is much shorter than the damping times of milli-seconds. Tracking simulations are carried out to study the degradation of electron beam quality due to ISR. Particles are generated at 2.25 GeV with normalized horizontal emittance $\epsilon_x^N = 0.25\,\mu\text{m}$ and energy spread $\Delta E = 0.1$ MeV. Figure 3 illustrates the locations, in terms of the beam energy, where the particle phase space distributions are plotted in Figs. 4 and 5. Note that all particles survive during the tracking simulation under the condition of no compensation of the energy loss due to the synchrotron radiation. This results in the center momentum of the beam being shifted as shown in Fig. 5 and chirping effect from RF cavities occurring and being enhanced in the energy recovery loops.

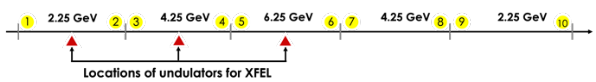

Figure 3: Locations in the unfolded beamline where the particle distributions are plotted in Figs. 4 and 5.

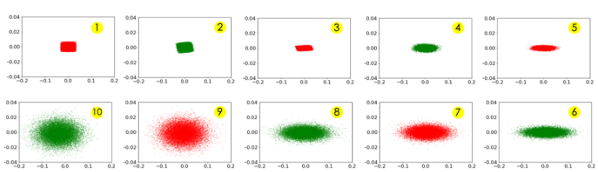

Figure 4: Evolution of the particle distribution in the (x, x') phase space. (x in mm, x' in mrad).

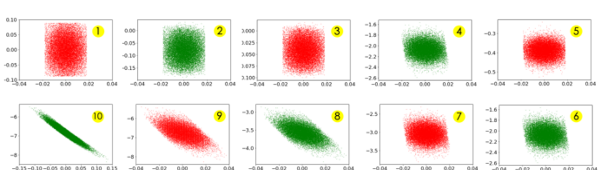

Figure 5: Evolution of the particle distribution in the (z, δ) phase space. (z in mm, $\delta = \delta \times 10^{-3}$).

Table 2 lists the unnormalized horizontal emittance ϵ_x and the relative energy spread $\delta = \Delta E/E$ at several energies of interest. Both the emittance and energy spread are well preserved at 2.25 and 4.25 GeV at the locations of the undulators with help of damping due to increase in the electron beam energy. Because of their strong energy dependence, these two quantities degrade significantly at the proposed highest energy of 6.25 GeV. However, the degradation can be suppressed in by optics optimization using a relatively large dipole bending radius while keeping the footprint compact.

Table 2: Unnormalized horizontal emittance ϵ_x and relative energy spread δ at several energies of interest

Energy (GeV)	**Location**	**δ (10^{-5})**	**ϵ_x (10^{-12} m)**
2.25	Initial	3.91	43.7
2.25	Undulators	3.97	44.1
4.25	Undulators	3.92	31.4
6.25	Undulators	9.30	81.3

Coherent Synchrotron Radiation (CSR)

CSR poses a significant challenge for FEL-driven accelerators with high brightness beams. Rather than the more conventional head-tail instabilities where the tail is affected by the actions of the head, CSR is a tail-head instability. The tail of the beam loses energy while the head gains energy, leading to an undesirable redistribution of the particles in the bunch. With a short bunch length desired in FELs to increase the electron bunch peak current and the peak brightness of photons, CSR has a serious impact on the beam quality that may be critical for the success of FELs. Three sets of parameters, listed in Table 3, are used to explore the CSR effect on the beam quality at the lowest energy of 2.25 GeV. The parameters in the “SASE” case are similar to those in the LCLS-II design [9]. The “SASE-like” case is similar to “SASE” but provides an extended bunch length. The “XFELO” case parameters are from K.J. Kim [18].

Table 3: Beam parameters for studying the CSR effect at the lowest energy of 2.25 GeV

Cases	**Unit**	**SASE**	**SASE-like**	**XFELO**
Energy	GeV		2.25	
Initial rms ϵ_x^N	μm		0.3	
Initial rms δ	10^{-5}		4.4	
Charge per bunch	pC	30	30	100
Bunch length rms	μm	9	30	120

Figures 6 shows the particle horizontal and longitudinal phase space distributions resulting from tracking simulations at the end of the 2.25 GeV arc. Due to its extremely short bunch length of 9 μm (30 fs) rms, the “SASE” case has the horizontal emittance and energy spread increased by a factor of up to several orders of magtitude. With the same bunch charge but a longer rms bunch length of 30 μm (100 fs), the “SASE-like” case has no emittance growth in the horizontal plane and about ten times emittance growth in the longitudinal plane. The “XFELO” case has the least CSR effect on the beam quality among these three cases. There is no horizontal and only modest longitudinal emittance growth. The CSR effect can be further reduced through the same optics

ISBN: 978-3-95450-220-2 ISSN: 2673-5474 doi: 10.18429/JACoW-FEL2022-WEP62

optimiztion that wsa used to suppress the ISR effect on the beam quality.

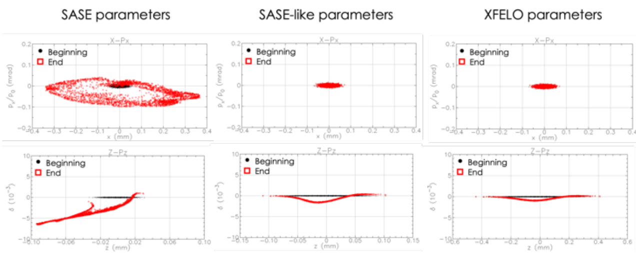

Figure 6: Particle phase space distributions in the horizontal and longitudinal planes.

CONCLUSION

We explore the design feasibility of an ERL-based XFEL. Several arc cell optics are explored to optimize the beam quality and the facility footprint. Complete preliminary linear optics is established, and beam dynamics study is performed. Growth of the beam horizontal emittance and energy spread, due to both incoherent and coherent synchrotron radiation is modest. Further optics and parameter optimization will be carried out to suppress degradation of the beam quality. Potential R&D aspects will be identified as well.

ACKNOWLEDGEMENTS

Authors would like to thank Sarah Cousineau, Fulvia Pilat and Andrei Shishlo for their support and encouragement, thank Steven Benson, Andrew Hutton, Geoffery Krafft, Gunn Tae Park, Robert Rimmer, Chris Tennant and He Zhang for their valuable comments and instructive suggestions and thank David Sagan and Henry Lovelace III for their help in their help in BMAD tracking simulations.

REFERENCES

[1] J. Madey, "Stimulated Emission of Bremsstrahlung in a Periodic Magnetic Field", *J. Appl. Phys*, vol. 42, p 1906, 1971. doi: 10.1063/1.1660466

[2] D.A.G. Deacon, L.R. Elias, J.M.J. Madey, G.J. Ramian, H.A. Schwettman, and T.I. Smith, "First Operation of a Free-Electron Laser", *Phys. Rev. Lett. 38,* p. 892, 1977. doi: 10.1103/PhysRevLett.38.892

[3] A.M. Kondratenko, and E.L. Saldin, "Generation of coherent radiation by a relativistic electron beam in an undulator", *Particle Accelerators*, vol. 10, pp. 207–216, 1980.

[4] L.-H. Yu *et al.,* "High-Gain Harmonic-Generation Free-Electron Laser", *Science,* vol. 289, no. 5481, pp. 932-934 (2000). doi: 10.1126/science.289.5481.932

[5] M. Ferray *et al.,* "Multiple-harmonic Conversion of 1064 nm Radiation in Rare Gases", *J. Phys. B: At. Mol. Opt. Phys.*, 21, L31, 1988. doi: 10.1088/0953-4075/21/3/001

[6] K-J. Kim *et al.,* "A Proposal for an X-Ray Free-Electron Laser Oscillator with an Energy-Recovery Linac", *Phys. Rev. Lett 100,* 2008. doi: 10.1103/PhysRevLett.100.244802

[7] G. Geloni, Z. Huang, and C. Pellegrini, "The Physics and Status of X-ray Free-electron Lasers" in "X-Ray Free Electron Lasers: Applications in Materials, Chemistry and Biology" edited by U. Bergmann, V.K. Yachandra and J. Yano, published by the *Royal Society of Chemistry*, 2017. doi: 10.1039/9781782624097-00001

[8] "Linac Coherent Light Source (LCLS) Conceptual Design Report", *SLAC*, 2002.

[9] "Linac Coherent Light Source (LCLS-II) Conceptual Design Report", *SLAC*, 2011.

[10] M. Yabashi, "Status and future of SACLA: the Japan's X-ray Free-Electron Laser", *Res. in Opt. Sc.*, 2012. doi: 10.1364/ICUSD.2012.IW1D.1

[11] T.-Y. Lee *et al*., "Overview of PAL-XFEL", *AIP Conference Proceedings*, vol. 879, p.252, 2007.

[12] E. Prat *et al.,* "A Compact and Cost-effective Hard X-ray Free-Electron Laser Driven by a High-brightness and Low-energy Electron Beam", *Nat. Photonics*, vol. 14, pp. 748-754, 2020. doi: 10.1038/s41566-020-00712-8

[13] European XFEL, https://www.xfel.eu/facility/overview/index_eng.html

[14] Free-Electron Laser FLASH, https://flash.desy.de/

[15] FERMI lightsource, https://www.elettra.trieste.it/lightsources/fermi.html

[16] "The JLAMP VUV/Sorft X-ray User Facility", http://www.jlab.org/FEL/jlamp/JLAMP_Proposal.pdf

[17] M. W. Poole, J. A. Clarke, and E. A. Seddon, "4GLS: An Advanced Multi-Source Low Energy Photon Facility for the UK", in *Proc. EPAC'02*, Paris, France, Jun. 2002, paper TUPLE001, pp. 733-735.

[18] K.J. Kim, "X-Ray FEL Oscillator", *CERN Accelerator School,* Hamburg, Germany, 2016.

ISBN: 978-3-95450-220-2 ISSN: 2673-5474 doi: 10.18429/JACoW-FEL2022-THAI2

COHERENT 3D MICROSTRUCTURE OF LASER-WAKEFIELD-ACCELERATED ELECTRON BUNCHES*

M. LaBerge[1], A. Hannasch, B. Bowers, R. Zgadzaj, M. C. Downer
University of Texas – Austin, Austin, USA
O. Zarini, A. Debus, J. Couperus Cabadağ, P. Ufer, S. Schöbel, Y.Y. Chang, A. Koehler, R. Pausch, U. Schramm, A. Irman
Helmholtz-Zentrum Dresden-Rossendorf, Dresden, Germany
A. H. Lumpkin, Fermi National Accelerator Laboratory, Batavia, USA
[1]also at Helmholtz-Zentrum Dresden-Rossendorf

Abstract

We present experimental results across three different laser wakefield accelerator (LWFA) injection regimes demonstrating extreme visible microbunching (up to 10%). In each regime we examine the near field (NF) coherent optical transition radiation (COTR) at eight different wavelengths from a foil directly after the end of the accelerator. Depending on the LWFA operating regime, we observe different levels of bunch substructure. How this structure evolves across optical wavelengths is also LWFA-regime dependent. Utilizing multi-wavelength images of the foil, we observe features in the 3D beam that are unresolvable using other techniques. Moreover, with the aid of physically reasonable assumptions about the bunch profile, we present a candidate reconstruction of a 3D electron bunch.

INTRODUCTION

The micron-scale size of electron bunches from laser wakefield accelerators [1] make them ideal short, coherent radiation sources. They are inherently coherent in the terahertz and infrared [2], and with seeding, or through self-amplification, they can be microbunched into the ultraviolet spectrum [3, 4]. However, even without seeding LWFA electron beams have inherent visible microbunching due to LWFA processes [5, 6]. These pre-bunched portions of the beam can be used to jump start the self-amplification process in a free electron laser (FEL) [7]. LWFA electron bunches have also been proposed for use in electron-position colliders [8]. A low transverse beam emittance is of interest for the FEL, staged accelerator, and collider applications. However, measuring the transverse bunch size at the beam waist is particularly difficult in LWFAs. NF incoherent optical transition radiation (IOTR) has traditionally been used in conventional accelerators to monitor small transverse beam sizes [9]. Recently, NF COTR has been used to measure the transverse size of microbunches as well as put a sub-micron upper limit on their normalized emittance [6, 10]. It has been shown that the beam emittance from a LWFA is dependent on the injection regime [11]. We observe that the structure of the visibly microbunched portion of the beam also varies with injection regime. Using models from particle in cell (PIC) simulations or electron spectrum data in tandem with multi-spectral NF COTR imaging, we glean 3D information about LWFA electron bunches, culminating in a candidate 3D reconstruction of the microbunched portion of the beam.

* U. Texas authors acknowledge support from DOE Grant No. DE-SC0011617, and M. C. D. from the Alexander von Humboldt Foundation.

COTR CALCULATIONS

The transverse radiated field produced by a single highly relativistic particle transiting a foil and imaged by a single ideal lens can be described as

$$\frac{d^2\mathbf{E}_\perp(\mathbf{r}_\perp)}{d\omega d\boldsymbol{r}_\perp} \propto \int_0^{\theta_m} d\theta \frac{\theta^2}{\gamma^{-2}+\theta^2} J_1\left(\theta k|\mathbf{r}_\perp|\right)\hat{\boldsymbol{r}}_\perp, \quad (1)$$

where $\mathbf{E}_\perp$ is the transverse field, $\mathbf{r}_\perp$ is the transverse radial coordinate, ω is the angular frequency of the radiation, θ_m is the angular acceptance of the lens, γ is the Lorentz factor, J_1 is the first Bessel function of the first kind, and k is $2\pi/\lambda$ with λ being the imaged wavelength [12]. The magnitude squared this equation is known as the OTR point spread function (PSF) [9]. For NF incoherent OTR, the radiated energy (W_{IOTR}) from a normalized charge density $\rho(\mathbf{r}_\perp, z)$ can be written as

$$\frac{d^2W_{\mathrm{IOTR}}}{d\omega d\boldsymbol{r}_\perp} \propto N_e \int d\boldsymbol{r}' \left|\frac{d^2\boldsymbol{E}_\perp(\boldsymbol{r}_\perp-\boldsymbol{r}')}{d\omega d\boldsymbol{r}_\perp}\right|^2 \int dz \rho(\boldsymbol{r}', z), \quad (2)$$

which is simply a convolution of the PSF and the longitudinally integrated charge density. N_e is the total electron count in the bunch. On the other hand, radiated energy from coherent OTR (W_{COTR}) can be expressed as

$$\frac{d^2W_{\mathrm{COTR}}}{d\omega d\boldsymbol{r}_\perp} \propto N_e^2 \left|\int dz \int d\boldsymbol{r}' \frac{d^2\boldsymbol{E}(\boldsymbol{r}_\perp-\boldsymbol{r}')}{d\omega d\boldsymbol{r}_\perp} e^{ikz} \rho(\boldsymbol{r}', z)\right|^2 \quad (3)$$

The subtle differences in these formulas lead to several significant consequences. First, IOTR scales as N_e where COTR scales as N_e^2. If a portion of the beam is radiating coherently, it is likely that the COTR will dominate the IOTR. However, the portion of the bunch that is coherent depends on the longitudinal Fourier transform of the beam density distribution. If the beam is neither shorter than nor microbunched at the desired wavelength, there will be no COTR. Finally, for COTR, the transverse field is convolved with the charge distribution before taking the magnitude squared. This allows fields from transversely separated electrons to interfere.

ISBN: 978-3-95450-220-2 ISSN: 2673-5474 doi: 10.18429/JACoW-FEL2022-THAI2

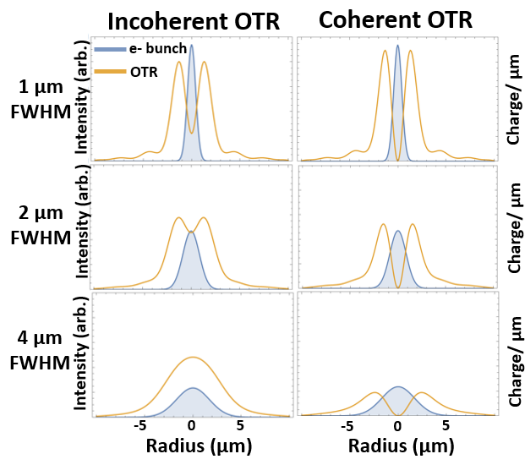

Figure 1: IOTR (left column) and COTR (right column) are compared for transverse beam sizes of 1 (top), 2 (middle), and 4 (bottom) µm FWHM. The transverse beam profile is shown in blue and the resulting NF COTR intensity pattern in yellow. The total charge in each plot is identical and the intensity scale is consistent across all images. The beam energy corresponds to a Lorentz factor of $\gamma = 500$ and the acceptance of the imaging system is $\theta_m = 0.28$.

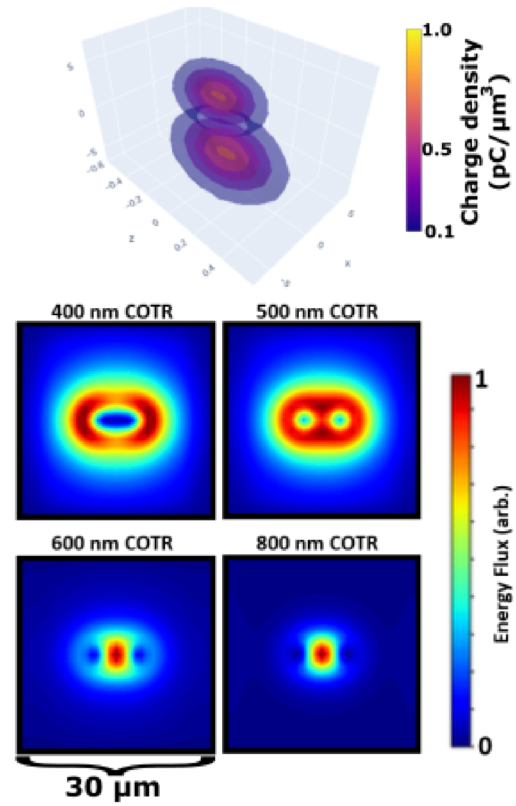

Figure 2: Top: a 3D density plot of two Gaussian beamlets separated both transversely and longitudinally. Bottom: NF COTR images at four different wavelengths produced by the charge distribution above. The amplitudes are normalized on each image such that the maximum pixel value is 1.

This interference is demonstrated in Fig. 1. For narrow beams, the IOTR and COTR patterns appear similar – two lobes with a deep central minimum. However, as the beam gets wider we observe a few key differences. The central minimum washes out in IOTR, whereas in COTR the central minimum remains zero. Also, as the beam widens the total IOTR remain the same, whereas the area under the COTR curve decreases. This is due to destructive interference between transversely separated electrons.

Constructive interference between transversely separated electron populations can occur when there are transverse-longitudinal correlations in the beam. Figure 2 shows one such example. On the top panel is a 3D plot of a synthetic electron density distribution consisting of two Gaussian beamlets, each with a transverse size of 4 µm FWHM, a longitudinal size of 400 nm FWHM and Lorentz factor of $\gamma = 560$. The beamlet centers are separated transversely (x) by 6 µm and longitudinally (z) by 400 nm. The bottom half of Fig. 2 shows four COTR patterns at different wavelengths calculated using this beam and Eq. 3 with $\theta_m = 0.28$. For imaged 400-nm COTR, the two beamlets are in phase with this longitudinal separation. The radial polarization of the transverse COTR electric fields leads to destructive interference between the beamlets, resulting in a broader central minimum. On the other hand, at 800 nm the beamlets are π out of phase, leading to strong constructive interference in the middle. The images at 500 and 600 nm show COTR where the relative phase is between these two extremes.

Figure 2 demonstrates that COTR images encode both transverse and longitudinal beam information. The longitudinal information, however, is encoded spectrally. One consequence of this is when there are longitudinal-transverse correlations in a beam, COTR patterns at different wavelengths have distinct forms. By NF imaging multiple COTR wavelengths, we obtain more transverse-longitudinal beam information.

EXPERIMENTAL BACKGROUND

The experimental results presented here were achieved using the 100 TW arm of the Draco laser at Helmholtz-Zentrum Dresden-Rossendorf [13]. As is shown in Fig. 3, Draco delivers a 800 nm, 30 fs pulse of up to 3 J focused to a 20 micron spot inside a 3 mm long gas jet, driving a blown-out plasma wake. Electron populations enter the tens of micron scale "bubble" accelerating structure through down-ramp [14], ionization [15] or self [16] injection. By the end of the 3 mm jet, these electron bunches have achieved energies greater than 250 MeV. After the exit of the jet, we placed a 65 µm Al foil, followed by a 35 µm Kapton aluminized foil. The first foil reflects the laser while the second foil emits COTR. This radiation is reflected off-axis by a polished silicon wafer, collected by a long working distance microscope objective with a 0.28 numerical aperture, and

ISBN: 978-3-95450-220-2 ISSN: 2673-5474 doi: 10.18429/JACoW-FEL2022-THAI2

sent to an array of cameras to be NF imaged. The electron beam passes through the wafer, is spectrally dispersed in a dipole, and imaged on LANEX scintillating screens [17].

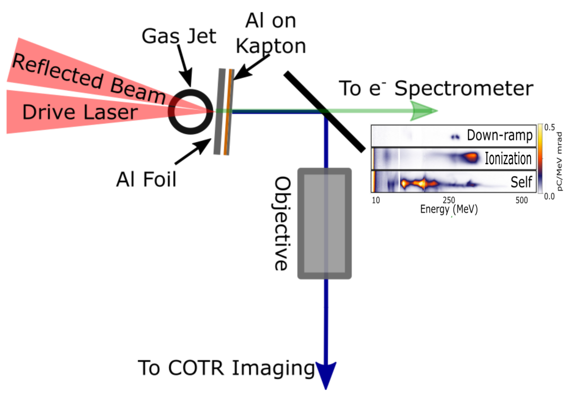

Figure 3: Experiential setup for COTR imaging of LWFA accelerated electron bunches. Two foils are placed at the exit of the gas jet. When LWFA accelerated electrons pass through the second foil, they emit COTR, which is reflected off beam axis by a 200 µm thick polished silicon wafer and collected by a long working distance microscope objective. The electrons pass through the silicon wafer and into the electron spectrometer. Representative electron spectra for down-ramp, ionization, and self injected beams are below the electron trajectory. The COTR is split between eight NF imaging cameras measuring different optical wavelengths.

Figure 3 shows a representative electron spectrum for each injection regime. These spectral images show the bunch divergence in the laser polarization axis on the vertical axis and the energy on the horizontal. The divergence appears high in these plots because these beams were scattered passing through the Si wafer before entering the dipole. Down-ramp injected beams typically produce a low charge (tens of pC), ~250 MeV beam consisting of up to a few, ~5% energy spread beamlets. Our ionization injected beams are typically a couple hundred pC and slightly higher energy (300 MeV), with little observable substructure in the electron spectrum. Finally, self injected beams are several hundred pC and polyenergetic.

The COTR signal is split to eight imaging cameras with bandpass filters centered on 400, 450, 500, 630, 680, 700, 750, and 800 nm. Each bandpass filter has a 10 nm FWHM acceptance. The imaging quality was calibrated using a resolution target, showing a sub 2 µm resolution and a magnification of ~10 pixels/µm. The camera responses were calibrated using a laser source at or near the relevant wavelength in both S and P polarizations. The laser intensity was first measured at the COTR foil location and then the cameras were exposed for a known time window, allowing us to determine the counts per radiated energy at the foil for each camera.

RESULTS

With our energy calibrated detectors, and calibrated electron spectrometer, we measure the microbunching fraction of the beam at each wavelength. We arrive at this figure by taking the square root of the total measured energy on our detector divided by the total counts we would expect if the measured charge was perfectly coherent. The measured charge used here is the total observed charge over 100 MeV. The microbunching fraction at each wavelength is plotted in figure 4 for each of the three regimes. For self and down-ramp injection beams, the microbunching fraction is consistently greater than one percent across the measured spectrum and ionization injected beams hover around one percent.

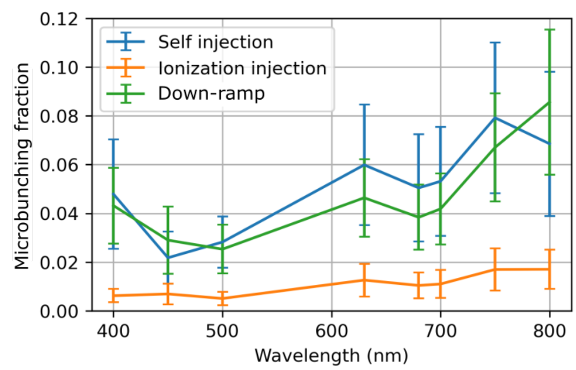

Figure 4: Microbunching fraction is plotted for at each measured wavelength for all three injection regimes. The error bars represent the statistical standard deviation across many shots.

The high levels of microbunching imply that either these beams are sub-micron in length or they have natural deep modulations in this frequency range. It is, however, clear that the microbunching fraction is sensitive to the injection regime. One potential source of microbunching in the accelerator is the drive laser pulse. When accelerating in the bubble, the front of the electron beam can overlap with the back of the laser pulse leading to modulations near the laser frequency along the polarization axis. The extent of this overlap is determined by the laser compression and the longitudinal location of the electron beam inside the bubble. We have seen evidence of this laser induced modulation in particle in cell (PIC) simulations of ionization injected beams. In these simulations the trailing end of the laser pulse only overlaps with the leading ~20% of the beam, resulting in a longitudinal-transverse modulation as seen in Fig. 5. In this figure we examine two cases. The first is where there are many oscillation cycles (Fig. 5a). In this case, we would expect a 750 nm NF COTR pattern that looks like Fig. 5b. Occasionally we see such patterns, as demonstrated by the experimentally measured COTR pattern in Fig. 5c. Typically we see COTR patterns that do not have this level of symmetry around the two annuli. Such asymmetry can be

ISBN: 978-3-95450-220-2 ISSN: 2673-5474 doi: 10.18429/JACoW-FEL2022-THAI2

explained by a modulation that is less than a single cycle (Fig. 5d). This could occur when the laser overlaps with only the very front of the beam. The corresponding asymmetric synthetic (Fig. 5e) and experimentally observed (Fig. 5f) COTR patterns show once more two annuli, but, unlike in b and c, the area around the upper minimum is much brighter than that around the lower minimum.

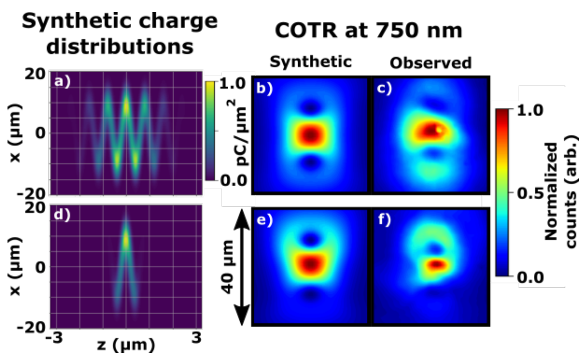

Figure 5: a,d) A projection of a electron bunch modulated at 800 nm. This bunch is propagating in the z direction. b,e) Synthetic 750 nm NF COTR patterns generated by the corresponding bunches in (a,d). c,f) Experimentally measured COTR patterns that are similar to those shown in (b,e).

Unlike ionization injection, down-ramp injected beams typically produce NF COTR patterns that resemble a small (~ 5 μm), single annulus across all imaged wavelengths. This spectral consistency implies that the radiation is likely a result of a single or few temporally short features in the beam. As demonstrated in Fig. 4, these features are also very coherent (few percent), meaning that the imaged COTR is encapsulating much of the spatial beam information. However, to do a 3D reconstruction of the beam, we need more information about the longitudinal beam extent. This could be in the form of infra-red COTR measurements out to wavelengths twice as long as the bunch extent, or a longitudinal profile generated by coherent transition radiation spectroscopy [18, 19]. Here we use the fact that in our down-ramp injection regime the electron bunches are chirped by the linear accelerating field in the bubble. This chirp can be modeled as a function of the electron density in the gas jet and the acceleration length. Using the down-ramp spectrum shown in Fig. 3, we estimated the longitudinal extent of the bunch to be on the scale of a single micron. Employing a differential evolution algorithm with the eight COTR images and this longitudinal extent as inputs, we are able to produce the 3D candidate reconstruction of the bunch shown in Fig. 6.

As we only have information on the coherent portion of the beam, there are electron populations that this diagnostic does not observe – specifically, low spatial frequency charge that makes up the envelope of the bunch. With this in mind, the reconstruction presented here only represents 70% of the total measured charge. Nevertheless, this reconstruction reproduces experimental observations: the measured and reconstructed COTR images shown in the bottom panels of

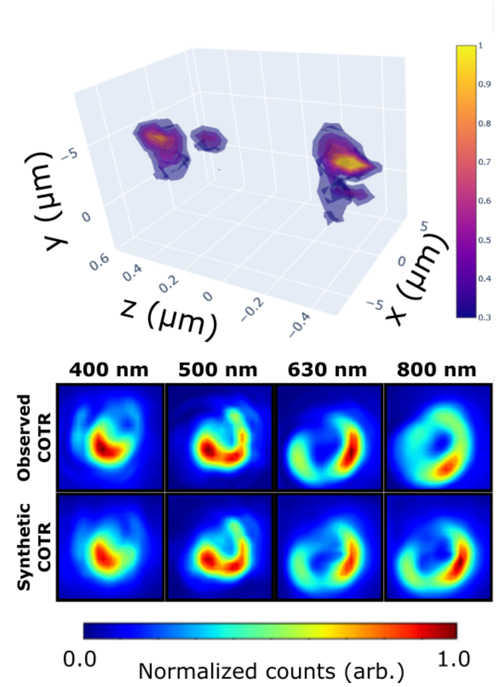

Figure 6: Top: a 3D reconstruction of the electron beam. Bottom: in the top row are experimentally observed COTR images and the bottom row shows COTR images calculated using the electron bunch in the top panel. Each image is normalized such that the maximum count is 1.0.

Fig. 6 show good correspondence, as do those not included in the figure and, as one would expect from the electron-energy spectrum in Fig. 3, the reconstruction shows two main beamlets separated longitudinally (z).

CONCLUSION

In summary, NF COTR captures transverse and longitudinal information about microbunched portions of electron beams. The beams we witness from LWFAs show an injection-method-dependent 1-10% microbunching fraction in the 400-800 nm range. We also use COTR to observe signatures of structures predicted by PIC simulations. Finally, with reasonable estimates limiting the longitudinal size of the bunch, and multi-spectral COTR imaging, we produced a candidate 3D reconstruction of the microbunched portion of a beam.

REFERENCES

[1] J. M. Dawson and T. Tajima, "Laser Electron Accelerator", *Phys. Rev. Lett.*, vol. 43, no. 4, pp. 267–270, 1979. doi:10.1103/PhysRevLett.43.267

[2] C. B. Schroeder *et al.*, "Theory of coherent transition radiation generated at a plasma-vacuum interface", *Phys.l Rev. E*, vol. 69, no. 1, pp. 016501, 2004. doi:10.1103/PhysRevE.69.016501

[3] W. Wang *et al.*, "Free-electron lasing at 27 nanometres based on a laser wakefield accelerator", *Nature*, vol. 595, pp. 516-

ISBN: 978-3-95450-220-2 ISSN: 2673-5474 doi: 10.18429/JACoW-FEL2022-THAI2

520, 2021.
doi:10.1038/s41586-021-03678-x

[4] M. Labat *et al.*, "Seeded free-electron laser driven by a compact laser plasma accelerator", submitted for publication. doi:10.21203/rs-1692828/v1

[5] Y. Glinec *et al.*, "Observation of fine structures in laser-driven electron beams using coherent transition radiation", *Phys. Rev. Lett.*, vol. 98, pp. 98–101, 2007. doi:1103/PhysRevLett.98.194801

[6] A. H. Lumpkin *et al.*, "Coherent Optical Signatures of Electron Microbunching in Laser-Driven Plasma Accelerators", *Phys. Rev. Lett.*, vol. 125, pp. 014801, 2020. doi:10.1103/PhysRevLett.125.014801

[7] A. H. Lumpkin *et al.*, "Evidence for Microbunching "Sidebands" in a Saturated Free-Electron Laser Using Coherent Optical Transition Radiation", *Phys. Rev. Lett.*, vol. 88, pp. 234801, 2002. doi:10.1103/PhysRevLett.88.234801

[8] F. Albert *et al.*, "2020 roadmap on plasma accelerators", *New J. Phys.*, vol. 23, pp. 031101, 2021. doi:10.1088/1367-2630/abcc62

[9] P. Karataev *et al.*, "First Observation of the Point Spread Function of Optical Transition Radiation", *Phys. Rev. Lett.*, vol. 107, pp. 174801, 2011. doi:10.1103/PhysRevLett.107.174801

[10] M. LaBerge *et al.*, "Coherent-transition-radiation-based reconstruction of laser plasma accelerated electron bunches", in *Laser Acceleration of Electrons, Protons, and Ions VI*, International Society for Optics and Photonics, 18 April 2021, pp.117790E. doi:10.1117/12.2592306

[11] S. K. Barber *et al.*, "Measured emittance dependence on the injection method in laser plasma accelerators", *Phys. Rev. Lett.*, vol. 119, pp. 104801, 2017. doi:10.1103/PhysRevLett.119.104801

[12] M. Castellano and V. A. Verzilov, "Spatial resolution in optical transition radiation beam diagnostics", *Phys. Rev. ST Accel. Beams*, vol. 1, pp. 062801, 1998. doi:10.1103/PhysRevSTAB.1.062801

[13] U. Schramm *et al.*, "First results with the novel petawatt laser acceleration facility in Dresden", *J. Phys. Conf. Ser.*, vol. 874, pp. 012028, 2017. doi:10.1088/1742-6596/874/1/012028

[14] K. Schmid *et al.*, "Density-transition based electron injector for laser driven wakefield accelerators", *Phys. Rev. ST Accel. Beams*, vol. 13, pp. 091301, 2010. doi:10.1103/PhysRevSTAB.13.091301

[15] M. Mirzaie *et al.*, "Demonstration of self-truncated ionization injection for GeV electron beams", *Sci. Rep.*, vol. 5, pp. 14659, 2014. doi:10.1038/srep14659

[16] W. Lu *et al.*, "Generating multi-GeV electron bunches using single stage laser wakefield acceleration in a 3D nonlinear regime", *Phys. Rev. ST Accel. Beams*, vol. 10, pp. 061301, 2007. doi:10.1103/PhysRevSTAB.10.061301

[17] T. Kurz *et al.*, "Calibration and cross-laboratory implementation of scintillating screens for electron bunch charge determination", *Rev. Sci. Instrum.*, vol. 89, pp. 093303, 2018. doi:10.1063/1.5041755

[18] S. Bajlekov *et al.*, "Longitudinal electron bunch profile reconstruction by performing phase retrieval on coherent transition radiation spectra", *Phys. Rev. ST Accel. Beams*, vol. 16, pp. 040701, 2013. doi:10.1103/PhysRevSTAB.16.040701

[19] O. Zariri *et al.*, "Multioctave high-dynamic range optical spectrometer for single-pulse, longitudinal characterization of ultrashort electron bunches", *Phys. Rev. Accel. Beams*, vol. 10, pp. 061301, 2022. doi:10.1103/PhysRevAccelBeams.25.012801

ISBN: 978-3-95450-220-2 ISSN: 2673-5474 doi: 10.18429/JACoW-FEL2022-THBO4

AC/DC: THE FERMI FEL SPLIT AND DELAY OPTICAL DEVICE FOR ULTRAFAST X-RAYS SCIENCE

A. Simoncig†, M. Manfredda, G. Gaio, L. Raimondi, C. Fava, S. Gerusina, R. Gobessi, A. Abrami, F. Capotondi, D. De Angelis, R. H. Menk[1,2], M. Pancaldi, E. Pedersoli and M. Zangrando[3], Elettra Sincrotrone Trieste S.C.p.A., Area Science Park, Basovizza, Italy
N. Mahne, Istituto Officina dei Materiali, CNR, Area Science Park, Basovizza, Italy
[1]also at Istituto Nazionale di Fisica Nucleare section of Trieste, Trieste, Italy
[2] also at Department of Medical Imaging, University of Saskatchewan, Saskatoon, Canada
[3] also at Istituto Officina dei Materiali, CNR, Area Science Park, Basovizza, Italy

Abstract

Free-electron lasers (FELs) are the most advanced class of light sources, thanks to their unique capability to lase high-brightness and ultrashort pulses marked by wavelengths spanning the Extreme-Ultraviolet (EUV), the Soft (SXR) and Hard (HXR) X-Ray spectral domains, alongside with temporal duration lying in the femtosecond (fs) timescale. Particularly, the FERMI FEL, located at the Elettra Sincrotrone Trieste campus (Italy), and based on the external laser seeding scheme, has recently set new standards in terms of EUV/SXR pulses emission. FERMI is a single-pass FEL able to lase nearly transform-limited and fully coherent pulses between 100 nm and 4 nm (in first harmonic), alongside the full control of the radiation polarization state, too. Thanks to these almost unique features, FERMI has recently allowed to extend, in a time-resolved approach, both established spectroscopies, daily implemented at synchrotron light sources, and novel non-linear optical methods, combining FELs and laser pulses. Nonetheless, the next step to push the ultrafast X-Ray science standards is widely recognized to the capability to perform experiments engaging exclusively EUV, SXR and HXR pulses. Indeed, exciting (and probing) matter at its (or nearby) electronic resonances, is largely speculated to be the key for disclosing the microscopic mechanisms hiding behind some of the most exotic phases of physical, chemical, and biological systems. Such a goal calls the design of optical devices capable to both split and delay (in time) FEL pulses, without impacting on their unique coherence properties, and required to be fully user-friendly in terms of preserving the perfect overlap of the resulting focal spots, even in the tightest focusing conditions achievable on the sample (few microns).

INTRODUCTION

At FERMI, such a goal is addressed by an optical device installed along the Photon Analysis Delivery and Reduction System (PADReS) and known as AC/DC, which stands for the Auto Correlator/Delay Creator [1-3]. AC/DC is designed to split the incoming FEL photons beam by inserting a grazing incidence flat mirror to create two exact half-spots. These resulting two pulse replicas are free to travel along separate optical paths, being the first one marked by a fixed-length, while the second optical path is characterized by a mobile-length, which can be tuned by moving the relative longitudinal positions of two grazing incidence mirrors mounted onto two specular mechanical rails. In this way, it is possible to introduce a controlled temporal delay between these two EUV/SXR pulses and address the challenge to perform time-resolved experiments within a FEL-FEL configuration. Moreover, AC/DC is designed to exploit multi-colour time-resolved experiments characterized by non-degenerate (in wavelength) pump and the probe pulses to perform multidimensional spectroscopy studies, too. Indeed, thanks to its double cascade scheme, FERMI can deliver two (or more) FEL pulses marked by different wavelengths [4-6]. AC/DC can both a) isolate these FEL pulses, by means of the insertion of free-standing solid-state filters, separately intercepting the beams travelling along the mobile or the fixed-length optical branches, and b) delaying (in time) one respect to the other.

OPTICAL DESIGN

AC/DC can be easily described as composed of four different units (see Fig. 1), which are a) the first grazing incidence mirror (M1), in charge to split the incoming FEL photons beam in two exact half-spots, b) the two, fixed- and mobile-length optical branches (see blue and red lines in Fig. 1), c) the grazing incidence mirror (M4) recombining the two half-spots in the far-field, and d) the (laser) pointing feedback system (see black line in Fig.1), implemented to preserve the spots overlap at the focal plane of the experimental end-station. M1 is mounted onto a vertical actuator to intercept the incoming FEL photons beam along the optical transport trajectory and to split its quasi TEM_{00} gaussian transverse intensity distribution into two exact half-spots. Several Ce:YAG screens, positioned downstream of M1, are used for checking in real-time the proper splitting. The radiation reflected by M1 is steered into the fixed-length optical branch (see blue line in Fig. 1). The grazing incidence angle for this first set of mirrors (M1 and M4) is 2 degrees. M4 is also mounted onto a vertical actuator, which allows its complete extraction during ordinary FEL operations. The pulses propagated after M1 (not reflected) intercept the second set of mirrors (M5 and

† alberto.simoncig@elettra.eu

ISBN: 978-3-95450-220-2 ISSN: 2673-5474 doi: 10.18429/JACoW-FEL2022-THBO4

M8) installed at a grazing incidence angle of 3 degrees. M5 and M8 are mounted on vertical actuators to be easily removed for ordinary FEL operations, too.

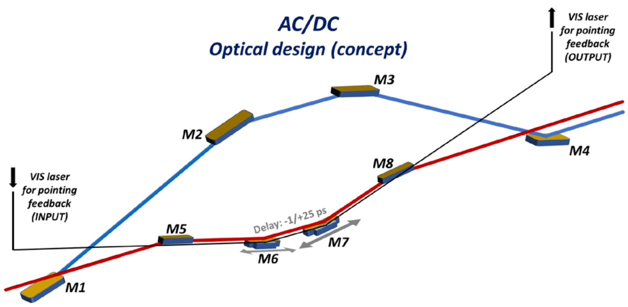

Figure 1: Sketch of AC/DC. Distances, dimensions, and mirrors incidence angles are reported out of scale for the sake of clearness. The incoming beam is split by M1 into two exact half-spots. The pulses reflected by M1 are steered into the (upper) fixed-length optical branch (blue line) and act as probe radiation. Instead, the ones propagating after M1, enter the (lower) mobile-length optical branch (red line), and become the pump beam. M6 and M7 can travel, in a synchronous way, along a couple of specular mechanical rails to insert the desired temporal delay. The black line refers to the optical laser used to implement the feedback signal.

Once reflected by M5 the beam is steered towards M6 and M7, which can travel along a couple of specular mechanical rails to insert the desired amount of temporal delay (see red line in Fig. 1). M8 is designed to intercept the beam emerging from the fixed-length optical branch and to steer it towards the experimental end-station. The routine exact synchronization between the optical branches, can be easily performed by steering and overlapping the two FEL beams onto one of the Ce:YAG screens installed (approximately 20 m) downstream of AC/DC, and scanning the temporal delay in the proximity of the expected value until the interference fringes signal appear, setting the time-zero at the maximum fringes visibility. This is done by acting on the angular degree of freedom of the M4 and M8, while the temporal delay is controlled by means of the longitudinal positions of M6 and M7 (see Fig. 1). The accessible temporal delay varies between -1 ps and approximately +26 ps. Since the mechanical resolution of the M6/M7 longitudinal actuators is approximately 100 microns, the corresponding intrinsic AC/DC temporal resolution is approximately 360 as.

POINTING-FEEDBACK SYSTEM

Preserving a proper spatial overlap at the focal plane of the experimental end-station, which is located approximately 25 meters downstream of AC/DC, is absolutely mandatory to perform time-resolved spectroscopies in the best experimental conditions, suppressing potential systematic sources and increasing the signal to noise ratio. Users at FERMI can routinely perform time-resolved experiments engaging sub-10 microns EUV/SXR focal spots. This means that a pointing stability of the order of approximately 1 μm must be preserved during the whole AC/DC temporal scan. This is strongly required when AC/DC is operating over the whole accessible temporal delay range, which requires to synchronously move the M6/M7 pair along the whole accessible length of the rails, which are approximately 800 mm long each. Indeed, the pointing could be affected by several factors such as a) insufficient mechanical tolerance, b) vibrations of the mirror holders, and c) thermal expansion. The entity of such effects is such that the overlap is typically disrupted over a temporal delay of $\approx$ 10 ps. Such an issue would greatly reduce the performance of AC/DC, so it has been addressed by developing a hybrid opto-numerical laser feedback system.

First, a visible (VIS) laser is injected inside the ultra-high vacuum chamber enclosing AC/DC, to share with the FEL beam the same optical path along the mobile-length optical branch. This is possible since both M6/M7 hold (on their sides) two coplanar Ag-coated laser mirrors to steer the VIS beam. This means that any systematic distortion affecting the photon transport modifies the position of the VIS laser beam, too. The VIS laser is extracted from the ultra-high vacuum chamber (after interacting with the mobile-length optical branch), steered and focused onto a CCD camera. In order to counteract any displacement due to mechanics of AC/DC a real-time feedback, integrated in the FERMI control system, estimates the position of the centroid of the VIS laser beam spot on the CCD camera and keeps it fixed by changing the pitch and roll positions of the M7 through piezo actuators. Nonetheless, the laser-based optical feedback is not sufficient to fully compensate the position errors in the FEL pointing for the entire accessible temporal delay range. Although the coplanarity between the M6/M7 pair and their corresponding laser mirrors has been checked ex-situ, any mechanical and thermal vibrations affecting these holders during the installation inside the ultra-high vacuum chamber, as well as the first pumping operation, can cause a not negligible paraxial error. The result of this error, that cannot be compensated by the optical feedback system, is a residual offset between the two FEL spots, which is more evident when the temporal delay becomes much larger than several (approximately 10) ps and the focusing inside the experimental end-station is extremely tight (few μm sizes). To overcome this limitation, the laser-based feedback operates in synergy with an ad-hoc opto-numerical algorithm, which replaces the raw estimation of the VIS laser beam spot position found on the CCD with a virtual spot position. This is the sum of the effective VIS laser beam spot plus a correction factor that (linearly) depends on the temporal duration. To calibrate the required correction factor at several temporal delays, the CCD camera measures, keeping the optical feedback into an active state, the displacement of the FEL focal spot compared to the one coming from the fixed-length optical branch (used as reference target point). For each of these temporal delay values an optimization algorithm automatically modifies the linear coefficients of the correction factor valid for that delay till the feedback, reacting to the new correction factor applied to the real spot position, brings back the FEL spot to the reference target, so preserving the ideal FEL-FEL pointing. Once this

40th International Free Electron Laser Conference,Trieste JACoW Publishing
ISBN: 978-3-95450-220-2 ISSN: 2673-5474 doi: 10.18429/JACoW-FEL2022-THBO4

procedure is completed, the position returned by the opto-numerical algorithm the overall range is a simple linear interpolation between these calibrated positions.

RESULTS

AC/DC is now currently fully opened to users' activities. Up to now, few time-resolved experiments have been performed. Specifically, in terms of EUV/SXR pulses metrology, AC/DC provides an user-friendly way to study one of the still-debated quantities in the FEL community, that is the FEL pulses longitudinal coherence length. This, in principle, can be done looking at the fringes in the experimental chambers. By measuring the visibility of fringes as a function of the temporal delay it is possible to retrieve this observable (see Fig. 2). These data refer to two different FEL wavelengths, where dots refer to the experimental points (each point is the average over 5 seconds, i.e., 250 shots) and solid lines represent the gaussian fit. It turns out that the coherence length, computed as the full width half maxima (FWHM) of the gaussian fit, divided by $\sqrt{2}$ to consider the autocorrelation effect, is $\tau_C = 66.5$ fs for a dispersive current of 50 A at the FEL wavelength set at 41.6 nm, and $\tau_C = 47.5$ fs for a dispersive current of 60 A, with the machine tuned at 17.8 nm, respectively. The coherence length provides a lower limit to the estimation of the longitudinal pulse length τ_P, i.e., $\tau_c \leq \tau_P$, where the equality holds for Fourier-transformed pulses.

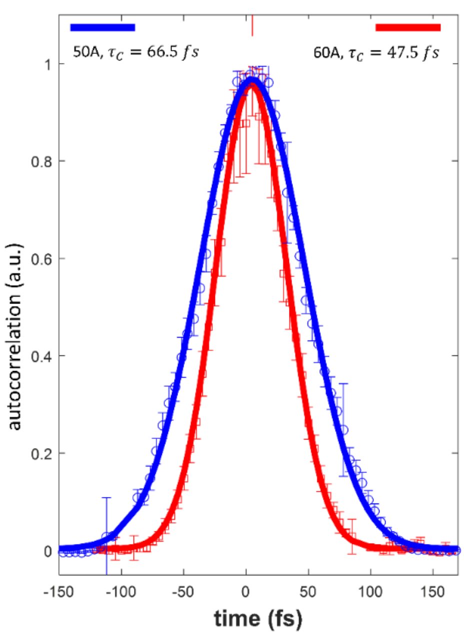

Figure 2: Measurements of the FEL pulse coherence length at FERMI, performed using AC/DC. The data refer to two different settings of the machine (dispersive current values) resulting into two different coherence length values.

CONCLUSION

We presented the optical device to split and delay (in a controlled way) the FEL pulses at FERMI, which is known as AC/DC, and fully opened to users. It is designed to perform time-resolved spectroscopies engaging exclusively EUV/SXR pulses as pump and probe, with an intrinsic temporal resolution of approximately 360 as. We presented its opto-mechanical design, as well as the feedback pointing system, which combines the physical signal acquired by monitoring the position of the laser beam, that mimics the FEL beam trajectory traveling in the mobile-length optical branch, and a dedicated algorithm to correct any residual paraxial errors. To conclude, we presented a brief overview of some preliminary results which emphasize the possibilities that AC/DC offers to the users to implement novel spectroscopical layouts.

ACKNOWLEDGEMENTS

The authors acknowledge the entire FERMI machine physics team for the FEL tuning operations and the FERMI laser team.

REFERENCES

[1] M. Zangrando *et al.*,"First Results from the Commissioning of the FERMI@Elettra Free Electron Laser by means of the Photon Analysis Delivery and Reduction System (PADReS)", in *Proc. SPIE* vol. 8078, p. 80780I, May 2011. `doi.org/10.1117/12.886459`

[2] M. Manfredda *et al.*, "The evolution of KAOS, a multipurpose active optics system for EUV/Soft X-rays", *Syn. Radiat. News*, 35, pp. 29-36, May 2022. `doi.org/10.1080/08940886.2022.2066432`

[3] A. Simoncig *et al.*," AC/DC: the FERMI FEL split and delay optical device for ultrafast X-Rays science", *Photonics*, vol. 9, no. 5, p. 314, May 2022. `doi.org/10.3390/photonics9050314`

[4] C. Pellegrini, A. Marinelli, and S. Reiche, "The physics of x-ray free electron lasers", *Rev. Mod. Phys.* vol. 88, no. 1, p. 015006, Mar. 2016. `doi.org/10.1103/RevModPhys.88.015006`

[5] E. Allaria *et al.*, "Highly coherent and stable pulses from the FERMI seeded free-electron laser in the extreme ultraviolet", *Nat. Photonics*, vol. 6 10, pp. 699-704, Sep. 2012. `doi.org/10.1038/nphoton.2012.233`

[6] E. Allaria *et al.*," Tunability experiments at the FERMI@Elettra free-electron laser", *New J. Phys.*, vol. 14, p. 113009, Nov. 2012. `doi:10.1088/1367-2630/14/11/113009`

ISBN: 978-3-95450-220-2 ISSN: 2673-5474 doi: 10.18429/JACoW-FEL2022-FRAI1

PROBING TRANSIENT STRUCTURES OF NANOPARTICLES BY SINGLE-PARTICLE X-RAY DIFFRACTION

A. Niozu*, Hiroshima University, Higashi-Hiroshima, Japan
Y. Kumagai, Tokyo University of Agriculture and Technology, Tokyo, Japan
T. N. Hiraki, K. Asa, Y. Sato, N. Yokono, K. Nagaya, Kyoto University, Kyoto, Japan
K. Matsuda, Kumamoto University, Kumamoto, Japan
H. Fukuzawa, K. Motomura, Y. Ito, D. You, T. Ono, Y. Li,
S. Saito, Y. Luo, K. Ueda, Tohoku University, Sendai, Japan
M. Bucher, L. Young, Argonne National Laboratory, Argonne, USA
E. Kukk, University of Turku, Turku, Finland
C. Cirelli, C. Bostedt, PSI, Villigen PSI, Switzerland
C. Miron, Universite Paris-Saclay, Paris, France
L. Neagu, National Institute for Lasers, Plasma and Radiation Physics, Bucharest, Romania
C. Callegari, M. Di Fraia, Elettra - Sincrotrone Trieste S.C.p.A., Trieste, Italy
G. Rossi, D. E. Galli, T. Pincelli, Università degli Studi di Milano, Milano, Italy
A. Colombo, Department of Physics, ETH Zürich, Zürich, Switzerland
J. Rist, I. Vela-Pérez, Johann Wolfgang Goethe-Universität, Frankfurt, Germany
M. Yabashi, RIKEN SPring-8 Center, Hyogo, Japan
S. Owada, T. Kameshima, Y. Joti, T. Katayama, T. Togashi, K. Tono, JASRI, Hyogo, Japan

Abstract

We report on our recent experimental results of single-shot and single-particle X-ray diffraction of rare-gas nanoparticles at SACLA. The single-shot diffraction data provided insights into the crystallization kinetics of Xe nanoparticles, where the nanoparticles initially crystallize in the metastable stacking-disordered phase and then transform into the stable face-centered cubic phase. In addition, we investigated the ultrafast structural dynamics of nanoplasma induced by an intense near-infrared laser pulse. We found a relation between the timescale of structural disordering and the speed of ejected ions from nanoplasma. We demonstrate the effectiveness of single-particle diffraction for investigating non-equilibrium structural dynamics at the nanoscale.

INTRODUCTION

The availability of ultrashort and intense X-ray pulses from free-electron lasers (FELs) [1, 2] has opened novel opportunities for probing transient states of matter with unprecedented temporal resolutions. Particularly, single-particle X-ray diffraction is a promising technique for investigating structural dynamics of nanoparticles. Rare-gas nanoparticles have been employed as a model system in several FEL experiments due to their size tunability and simple interatomic interaction.

In this contribution, we report on applications of single-particle X-ray diffraction of rare-gas nanoparticles for the investigations of crystallization dynamics [3, 4] and ultrafast dynamics of laser-induced nanoplasma [5]. The experiments were carried out at SACLA BL3 [6, 7]. Please refer to the references [3–5] for the detailed results and discussions and the reference [8] for the experimental setup.

* niozu@hiroshima-u.ac.jp

CRYSTRALLIZATION KINETICS OF XENON NANOPARTICLES

Crystallization is one of the most ubiquitous physical phenomena in nature; nevertheless, the atomic-scale structural dynamics upon crystallization is still a subject of controversy. The classical theory of nucleation assumes that crystallization starts from a small spherical nucleus having the structure of the stable phase in bulk. On the other hand, more than a hundred years ago, Ostwald proposed his step rule [9], stating that phase transition can proceed via intermediate metastable phases. Recent computational studies have provided novel insights into the microscopic structural pathway of crystallization [10]. In contrast, owing to several technical challenges to observe the atomic-scale dynamics, experimental observations have been so far mostly restricted to slow dynamics, such as crystallization of colloidal systems [11].

We investigated the structure of single Xe nanoparticles crystallized in a supercooled Xe gas jet. Our experiment realized an ideal condition for crystallization, i.e. in the absence of interaction with the surroundings and impurities. The single-particle structures of Xe nanoparticles were probed by FEL pulses ($h\nu$ = 11 keV) several hundreds of microseconds after the growth. The diffraction signals were recorded on a shot-by-shot basis with the multiport CCD sensor detector [12].

The accumulated virtual powder X-ray diffraction pattern of the Xe nanoparticles showed peaks corresponding to the face-centered cubic (fcc) structure (the bulk stable phase of Xe) but also peaks from a structure composed of randomly

ISBN: 978-3-95450-220-2 ISSN: 2673-5474 doi: 10.18429/JACoW-FEL2022-FRAI1

stacked close-packed layers, called the random hexagonal close-packed (rhcp) structure. The existence of the rhcp structure was further supported by a newly developed analysis method for single-particle diffraction patterns [3]. In the analysis, three-dimensional scattering intensity was deduced from positional correlations of two Bragg spots that appeared in single-shot diffraction patterns. The angular correlations of the Bragg spots suggested the emergence of rod-like intensity distributions (called Bragg scattering rods) in reciprocal space, which reflects the lack of crystal periodicity along the stacking axis in rhcp crsytal.

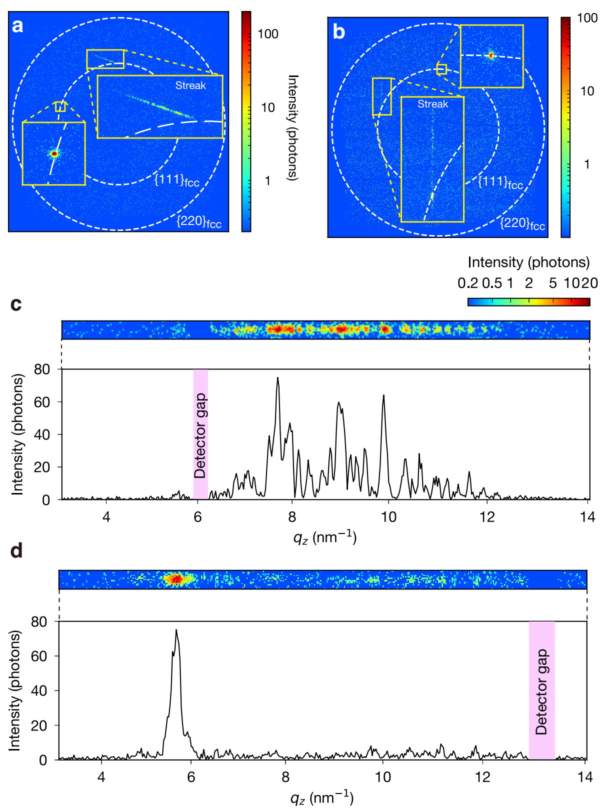

Figure 1: Single-particle diffraction patterns of Xe nanoparticles. c and d are zoomed images of the streak patterns in a and b and their projections of the intensities. Reproduced from [4].

Further structural details of the Xe nanoparticles were obtained through an analysis of the single-particle diffraction patterns. Figure 1 shows representative single-particle diffraction patterns of the Xe nanoparticles. The single particle diffraction patterns show characteristic streaks with speckle intensity distributions. The streaks correspond to the Bragg scattering rods in the reciprocal space originating from the rhcp structure. More interestingly, the diffraction pattern in Fig. 1b shows a streak pattern accompanying a sharp fcc Bragg spot. The diffraction pattern suggests the coexistence of the fcc and rhcp structures in single Xe nanoparticles [13]. From a comparison with simulation results of the streak patterns, we concluded that the Xe nanoparticle consists of comparably sized fcc and rhcp crystals.

The experimental observations are fully explained by the scenario of structure aging previously proposed in studies on crystallization of colloidal particles [11]. In the scenario, crystallization initially occurs at the metastable rhcp phase, and the structure later transforms into the stable fcc structure. This is a manifestation of the Ostwald's step rule, which states that phase transition proceeds via intermediate phases. The emergence of the stacking-disordered phase at the initial step of crystallization was explained by a general consideration on the free energy landscape and is therefore potentially applicable to crystallization of a wide variety of materials.

ULTRAFAST STRUCTUAL EVOLUTION OF INTENSE LASER-HEATED NANOPARTICLES

Understanding the fundamental interaction between intense lasers and matter is essential for their applications. Irradiation of a nanoparticle with an intense laser pulse leads to the formation of non-equilibrium nanoplasma, which expands and disintegrates within the picosecond timescale. The nanoplasma dynamics is crucially relevant to structure determination of matter with FELs based diffraction-before-destruction scheme [14], where the X-ray pulses are diffracted well before serious sample damage emerges.

Pump-probe measurements combining an FEL and synchronized optical laser have realized the real-time observation of the ultrafast structural dynamics induced by the laser pulses. A few pioneering experiments [15, 16] of laser-heated nanoparticles have reported on the ultrafast evolution of the density profiles.

We investigated the crystalline order of laser-heated Xe nanoparticles by time-resolved X-ray diffraction [5, 17]. Xe nanoparticles were first irradiated by an intense near-infrared (NIR) laser pulse, and the crystalline order was probed with a delayed FEL pulse ($h\nu = 10$ keV) by recording the wide-angle X-ray diffraction pattern. The shot-to-shot time delay between the FEL and NIR laser pulses was determined with an arrival timing monitor tool [18], and the temporal resolution was improved to ~ 20 fs.

Figure 2 shows the delay-dependence of Bragg diffraction intensities of NIR laser-irradiated Xe nanoparticles at different NIR excitation intensities. After the laser irradiation, the diffraction intensities exhibited rapid decay within 1 ps, indicating the loss of crystalline order in the produced nanoplasmas. The results suggest that the nanoplasma retain the inner crystalline order a few hundreds of femtoseconds after the laser pulse [17], despite huge energy absorption in the electron system upon the laser excitation. Moreover, significant laser intensity dependence was observed in the time scale of the decay of the diffraction intensities.

To understand the laser intensity dependence in terms of the plasma parameters, we carried out ion time-of-flight measurements of NIR irradiated Xe nanoparticles. We found that the time scale of the decay was roughly proportional to the inverse of the speed of ejected ions, which is equivalent to the plasma sound speed except for a factor of order unity.

ISBN: 978-3-95450-220-2 ISSN: 2673-5474 doi: 10.18429/JACoW-FEL2022-FRAI1

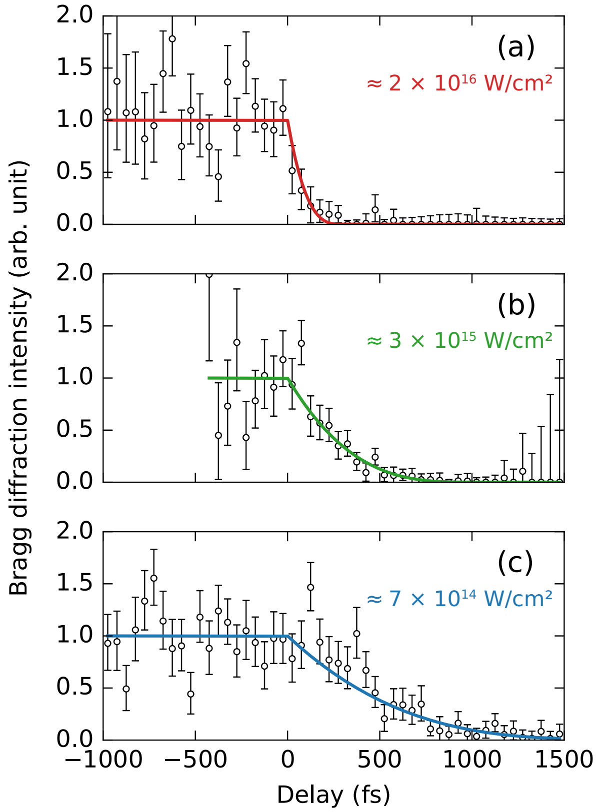

Figure 2: Delay dependence of Bragg diffraction intensities of Xe nanoparticles at different NIR laser intensities. Reproduced from [5].

The observations are consistent with the recently proposed scenario for nanoplasma dynamics [17], in which crystalline disorder is caused by a rarefaction propagating toward the inner crystalline core at the sound speed of plasma. Our results provide fundamental insights into the structural dynamics of laser-induced nanoplasmas, contributing to future applications of intense lasers including FELs.

ACKNOWLEDGEMENTS

The experiments were performed at SACLA with the approval of JASRI (Nos. 2016A8057, 2016B8077 and 2018B8063). This study was supported by the X-ray Free Electron Laser Utilization Research Project and the X-ray Free Electron Laser Priority Strategy Program of the Ministry of Education, Culture, Sports, Science and Technology of Japan (MEXT), by the Proposal Program of SACLA Experimental Instruments of RIKEN, by the Japan Society for the Promotion of Science (JSPS) KAKENHI Grant No. JP15K17487, JP16K05016, by JSPS Grant-in-Aid for JSPS Fellows No. JP19J14969, by CNR under the Japan-Italy Research Cooperative Program, and by the IMRAM project.

REFERENCES

[1] W. Ackermann *et al.*, "Operation of a free-electron laser from the extreme ultraviolet to the water window," *Nat. Photonics*, vol. 1, no. 6, pp. 336–342, Jun. 2007. doi:10.1038/nphoton.2007.76

[2] P. Emma *et al.*, "First lasing and operation of an ångstrom-wavelength free-electron laser," *Nat. Photonics*, vol. 4, no. 9, pp. 641–647, Sep. 2010. doi:10.1038/nphoton.2010.176

[3] A. Niozu *et al.*, "Characterizing crystalline defects in single nanoparticles from angular correlations of single-shot diffracted X-rays," *IUCrJ*, vol. 7, no. 2, pp. 276–286, Mar. 2020. doi:10.1107/S205225252000144X

[4] A. Niozu *et al.*, "Crystallization kinetics of atomic crystals revealed by a single-shot and single-particle X-ray diffraction experiment," *Proc. Natl. Acad. Sci.*, vol. 118, no. 51, p. e2111747118, Dec. 2021. doi:10.1073/pnas.2111747118

[5] A. Niozu *et al.*, "Relation between Inner Structural Dynamics and Ion Dynamics of Laser-Heated Nanoparticles," *Phys. Rev. X*, vol. 11, no. 3, p. 031046, Aug. 2021. doi:10.1103/PhysRevX.11.031046

[6] T. Ishikawa *et al.*, "A compact X-ray free-electron laser emitting in the sub-ångström region," *Nat. Photonics*, vol. 6, no. 8, pp. 540–544, 2012. doi:10.1038/nphoton.2012.141

[7] K. Tono *et al.*, "Beamline, experimental stations and photon beam diagnostics for the hard x-ray free electron laser of SACLA," *New J. Phys.*, vol. 15, no. 8, p. 083035, Aug. 2013. doi:10.1088/1367-2630/15/8/083035

[8] H. Fukuzawa, K. Nagaya, and K. Ueda, "Advances in instrumentation for gas-phase spectroscopy and diffraction with short-wavelength free electron lasers," *Nucl. Instruments Methods Phys. Res. Sect. A Accel. Spectrometers, Detect. Assoc. Equip.*, vol. 907, no. March, pp. 116–131, Nov. 2018. doi:10.1016/j.nima.2018.03.017

[9] W. Ostwald, "Studien über die Bildung und Umwandlung fester Körper," *Zeitschrift für Phys. Chemie*, vol. 22U, no. 1, pp. 289–330, Jan. 1897. doi:10.1016/j.nima.2018.03.017

[10] L. Lupi *et al.*, "Role of stacking disorder in ice nucleation," *Nature*, vol. 551, no. 7679, pp. 218–222, 2017. doi:10.1038/nature24279

[11] P. N. Pusey, W. van Megen, P. Bartlett, B. J. Ackerson, J. G. Rarity, and S. M. Underwood, "Structure of crystals of hard colloidal spheres," *Phys. Rev. Lett.*, vol. 63, no. 25, pp. 2753–2756, Dec. 1989. doi:10.1103/PhysRevLett.63.2753

[12] T. Kameshima *et al.*, "Development of an X-ray pixel detector with multi-port charge-coupled device for X-ray free-electron laser experiments," *Rev. Sci. Instrum.*, vol. 85, no. 3, p. 033110, Mar. 2014. doi:10.1063/1.4867668

[13] I. P. Dolbnya, A. V. Petukhov, D. G. A. L. Aarts, G. J. Vroege, and H. N. W. Lekkerkerker, "Coexistence of rhcp and fcc phases in hard-sphere colloidal crystals," *Europhys. Lett.*, vol. 72, no. 6, pp. 962–968, Dec. 2005. doi:10.1209/epl/i2005-10325-6

[14] R. Neutze, R. Wouts, D. van der Spoel, E. Weckert, and J. Hajdu, "Potential for biomolecular imaging with femtosecond X-ray pulses," *Nature*, vol. 406, no. 6797, pp. 752–757, Aug. 2000. doi:10.1038/35021099

ISBN: 978-3-95450-220-2 ISSN: 2673-5474 doi: 10.18429/JACoW-FEL2022-FRAI1

[15] T. Gorkhover *et al.*, "Femtosecond and nanometre visualization of structural dynamics in superheated nanoparticles," *Nat. Photonics*, vol. 10, no. 2, pp. 93–97, Feb. 2016. doi:10.1038/s41566-018-0110-y

[16] L. Flückiger *et al.*, "Time-resolved x-ray imaging of a laser-induced nanoplasma and its neutral residuals," *New J. Phys.*, vol. 18, no. 4, pp. 1–11, 2016. doi:10.1088/1367-2630/18/4/043017

[17] T. Nishiyama *et al.*, "Ultrafast Structural Dynamics of Nanoparticles in Intense Laser Fields," *Phys. Rev. Lett.*, vol. 123, no. 12, p. 123201, Sep. 2019. doi:10.1103/PhysRevLett.123.123201

[18] T. Katayama *et al.*, "A beam branching method for timing and spectral characterization of hard X-ray free-electron lasers," *Struct. Dyn.*, vol. 3, no. 3, p. 034301, May 2016. doi:10.1063/1.4939655

ISBN: 978-3-95450-220-2 ISSN: 2673-5474 doi: 10.18429/JACoW-FEL2022-FRAI2

NOVEL LATTICE INSTABILITY IN ULTRAFAST PHOTOEXCITED SNSE *

Y. Huang, S. Teitelbaum, G. De la Peña, D. A. Reis, M. Trigo,
SIMES, SLAC National Accelerator Laboratory, Menlo Park, California, USA
S. Yang, J. L. Niedziela, D. Bansal, O.Delaire,
Department of Mechanical Engineering and Materials Science,
Duke University, Durham, North Carolina, USA
T. Sato, M. Chollet, D. Zhu,
LCLS, SLAC National Accelerator Laboratory, Menlo Park, California, USA

Abstract

We use ultrafast X-ray scattering to study SnSe, a resonantly bonded material, with an emphasis on its non-equilibrium states. The work presented advances the methodology of ultrafast X-ray scattering enabled by the free-electron lasers (FELs), and shows how these novel methodologies help us understand how electrons and phonons interact in their natural length scale and time scale, and how new non-equilibrium states of matter, possibly related to new functionalities, are created.

INTRODUCTION

We use ultrafast X-ray scattering to study SnSe, a resonantly bonded material. Resonantly bonded materials have various functional properties directly associated with the structures, including ferroelectricity, high thermoelectric figure of merit, and large change of optical constants upon crystallization and amorphization (or phase change materials). They host a number of structural phases that are sensitive to external parameters (e.g., temperature, pressure, and chemical doping) and are expected to exhibit tunability by the light field. The large polarizability in resonantly bonded materials means pronounced coupling between phonons and electronic states, which yields large responses of the X-ray probe. We show that using a combination of ultrafast optical and X-ray lasers, we can understand materials on the natural time and length scales of their chemical bonding, which is not achievable with purely optical probes. The knowledge of the microscopic interactions in the non-equilibrium states will ultimately help us explore possible new functionalities in the non-equilibrium phases.

In particular, we use time-resolved X-ray diffraction to obtain amplitude as well as the phase of atomic motion, which allows us to reconstruct the lattice structure of SnSe. The structural distortions and the related new phase are unexpected, and cannot be correctly concluded from a purely optical (e.g., Raman scattering) measurement. We also use time-resolved X-ray diffuse scattering to access the excited-state dispersion of SnSe, which elucidates how photoexcitation alters the strength of specific bonds leading to this the novel lattice instability observed in diffraction.

* huangyj@stanford.edu

PROBING PHOTOINDUCED LATTICE INSTABILITY IN SNSE

Using time-resolved X-ray diffraction, we demonstrate that SnSe, one of the IV-VI resonantly bonded compounds, hosts a novel photoinduced lattice instability associated with an orthorhombic distortion of the rock-salt structure. This lattice instability is distinct from the one associated with the high-temperature phase, providing a counterexample of the conventional wisdom that laser pump pulse serves as a heat dump. See Fig. 1.

The new lattice instability is accompanied by a drastic softening of the lowest frequency A_g phonon. This mode was previously identified as the soft mode in the thermally driven phase transition to a Cmcm structure. Time-resolved X-ray diffraction directly reveals the phase of motion of the lowest frequency A_g phonon ($A_g^{(1)}$), which is opposite to a motion towards Cmcm. The identification of the distorted structure is made possible by summing up the contributions of several phonon modes. The amplitude, as well as the phase of the motion of each mode, are calculated by fitting the time-resolved X-ray scattering intensity. The findings highlight the importance of diffraction technique, which reveals the phase and amplitude of motion instead of just frequencies compared to conventional optical ultrafast spectroscopies.

We show that the driving mechanism for this new lattice instability is related to the removal of valence electrons from the lone pair orbital. Lone pair electrons tend to locally distort a symmetric structure, in the case of SnSe, the octahedral environment shown in Fig. 1. The Se 4*p*- and Sn 5*s*-derived bands that largely constitute that lone pair, are about 0.7 eV below the top of valence bands, which can be reached with the pump photons of 1.55 eV but not the thermal excitations. Density functional theory (DFT) calculations from our collaborators at Duke University confirm the origin of photoinduced Immm lattice instability.

Our findings have implications in other rocksalt distorted IV-VI semiconductors, several of which have topological states protected by lattice symmetry in the cubic or tetragonal phases. More generally, our work suggests that pump wavelength could provide additional control of structural distortions through orbitally-selective above-gap excitation. This could be exploited to direct a particular structural distortion to desirable outcomes with particular functionality beyond those accessible in thermal equilibrium.

ISBN: 978-3-95450-220-2 ISSN: 2673-5474 doi: 10.18429/JACoW-FEL2022-FRAI2

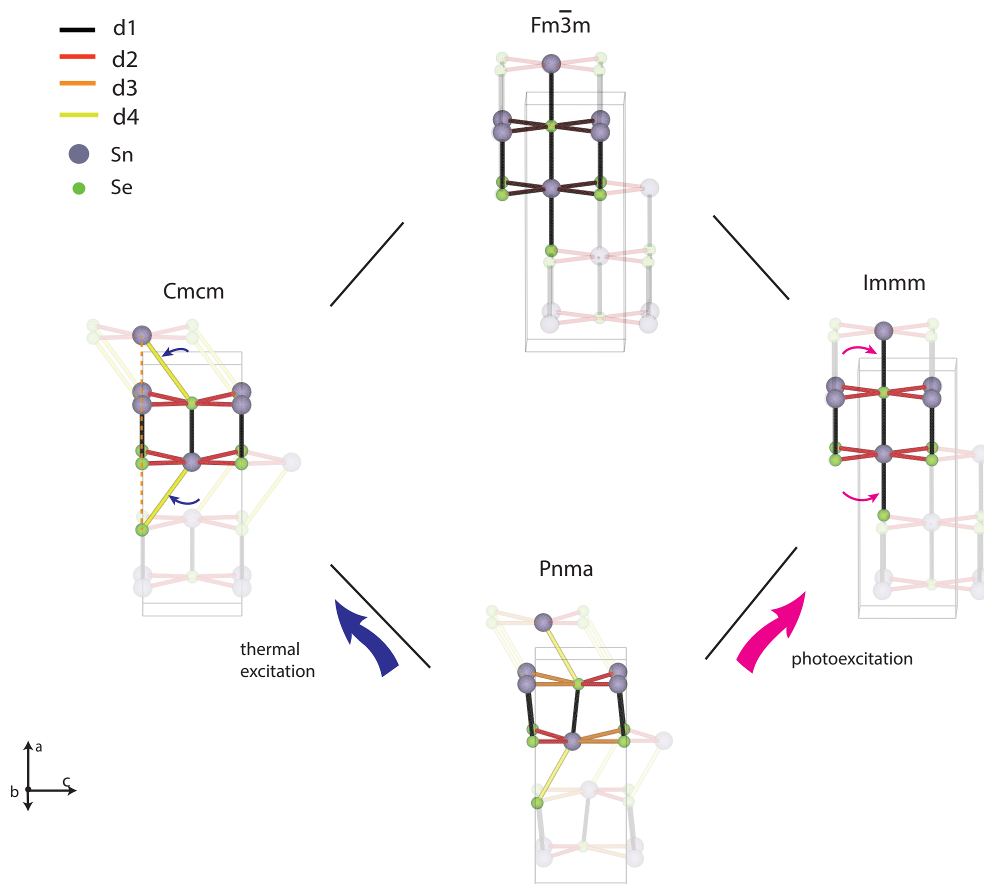

Figure 1: Relations between local coordination and atomic positions for different SnSe structures. At ambient conditions, the Pnma structure has the Sn and Se atoms off-center in the **b** − **c** plane, and is heavily distorted from the symmetric parent cubic structure Fm$\bar{3}$m ($d_1 = d_4 = d_2 = d_3$). Bonds of the same color are equivalent under the symmetry of the given lattice. Above 807 K, SnSe stabilizes in Cmcm ($d_1 \neq d_2 = d_3 \neq d_4$) where d_4 bonds rotate further away from the parent rocksalt structure compared to Pnma. Orange broken lines in the Cmcm structure highlight the atoms located in the same **a** − **b** plane. Under photoexcitation, the atoms move towards the Immm structure, which is the highest symmetry orthorhombic distortion of the rocksalt structure ($d_1 = d_4 \neq d_2 = d_3$). The figure is reproduced from [1] with permission from the American Physical Society.

ISBN: 978-3-95450-220-2 ISSN: 2673-5474 doi: 10.18429/JACoW-FEL2022-FRAI2

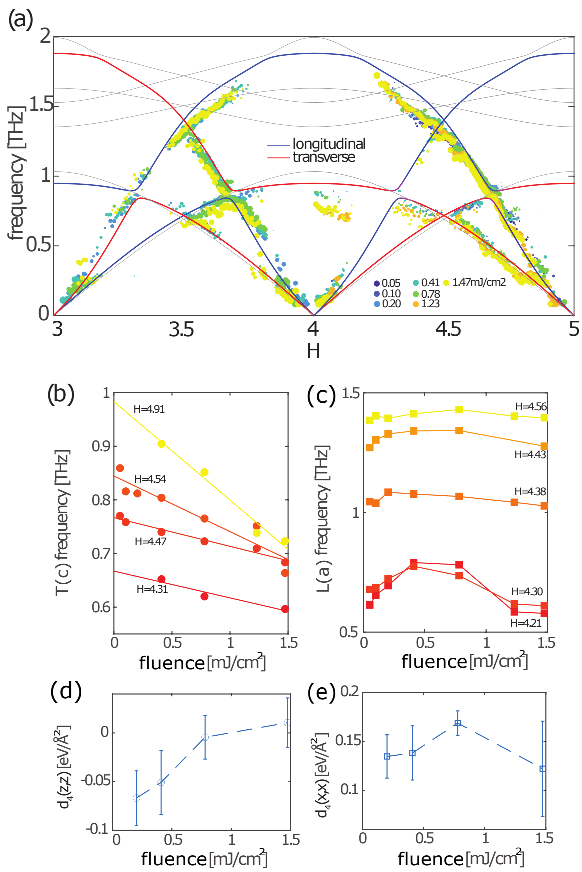

Figure 2: (a) The dispersion of the excitations mapped out along the reciprocal space path from (31-1) to (51-1). The black lines are the ground state phonon dispersion predicted from DFT. (b) Monotonic fluence of T(c) phonons along Γ-*X*-Γ. (d) Non-monotonic fluence of L(a) phonons along Γ-*X*-Γ. (e) The d_{4zz} forces as fitted from the experimental data. The force constant d_{4zz} correlates well with T(c) phonon and is approximately monotonic. (f) The d_{4xx} forces as fitted from the experimental data. The force constant d_{4xx} correlates well with L(a) phonon and is approximately monotonic.

PROBING INTERATOMIC FORCES OF SNSE UNDER PHOTOEXCITATION

Using non-zone-center measurements of time-resolved X-ray scattering [2], we obtain the photoexcited state phonon dispersion and investigate the microscopic details of the photoinduced lattice instability from the perspective of interatomic interactions. In Fig. 2 (a,b) we show the phonon dispersions measured on different portions of the reciprocal space. We infer the photoexcited interatomic forces from the phonon dispersion and identify a certain bond that is largely overlapped with the lone pair orbital as responsible for the observed photoinduced lattice instability. The conclusion is contrary to the consensus that in thermal equilibrium, the resonant bonding network of chalcogen *p* orbitals is the main origin of lattice instability.

The photoexcited state phonon dispersions are obtained mainly for branches T(c), transverse *c*-polarized phonon, and L(a), longitudinal *a*-polarized phonon. T(c) has a monotonic and significant fluence dependence, which eventually lead to the TO ($A_g^{(1)}$) condensation at high q or the folded zone center. L(a) has a non-monotonic fluence dependence, which is unexpected. See Fig. 2 (b,c).

We do least-square fitting of a model of photoexcited forces to the phonon dispersions measured along $\Gamma - X$, taking the DFT forces as the initial starting point and restricting the fit parameters to a physics-informed subset of bonds. We focus on pinning down the interatomic force changes that produce the most prominent features of TA and LA and phonons. We find robust correlation between two fitted force constants of the d_4 bond ($d_{4,zz}$ and $d_{4,xx}$) and the data feature (of T(c) and L(a) respectively), see Fig 2 (e,f). The robustness manifest in various fit settings, including different experimental geometries, slightly different initial fit parameters, and different sets of bond selections.

The fit results suggest that the increase of $d_{4,zz}$ force constants upon increased fluence (see Fig. 2 (d)) is well correlated to the T(c) softening under photoexcitation. We recognize $d_{4,zz}$ as the most relevant for the T(c) and the zone folded TO mode ($A_g^{(1)}$) softening under photoexcitation. The results are not entirely expected, as usually in the equilibrium, the in-plane resonant bonds in SnSe and similar materials are most relevant for controlling the softening of low-lying TO phonons and the lattice instability. On the other hand, we infer that the unusual nonmonotonic fluence dependence of $d_{4,xx}$ is related to the hole relaxation dynamics from Sn_{5s} - Se_{4px}) derived lone pair orbitals. A high excitation density can lead to an increase in carrier relaxation time in semiconductors due to hot phonon bottleneck and screening of the LO polar phonon scattering. Here in the photoexcited SnSe, the holes relax quickly from lone pair orbitals to the band edge at lower fluence and make a thermal-like carrier distribution near the band edge. At higher fluences, the carrier relaxation process is bottle-necked, and holes doped in the Sn_{5s} - Se_{4px}) orbitals lead to the lattice instability.

Time-resolved diffuse scattering reveals the microscopic origin of the photoinduced lattice instability from the perspective of interatomic interactions. In particular, the d_4 bond is identified as closely related to the excited state phonon dynamics. The result is consistent with the diffraction measurement, where we observed that d_4 bond experiences much more significant changes in angles and lengths compared to other near-neighbor derived bonds.

The methodology adopted in this work is the only known way to directly reconstruct interatomic interactions under photoexcitation, and has only been previously applied in a structurally much simpler semimetal [3]. The non-monotonic fluence dependence behavior is unusual, and motivates for sub-ps-scale spectroscopic study or orbital imaging techniques for the non-equilibrium states, which will also benefit from FEL capabilities.

ISBN: 978-3-95450-220-2 ISSN: 2673-5474 doi: 10.18429/JACoW-FEL2022-FRAI2

CONCLUSION

In summary, we show that photoinduced lattice instability does not necessarily coincide with the lattice instability in thermal equilibrium. The findings highlight the importance of time resolved X-ray scattering techniques based on FELs, which reveals the details of interplay between electron orbitals, atomic bonds, and structural instability. The microscopic information of electron phonon coupling obtained from our method, can rationalize certain ways to control materials and to design their functional properties.

ACKNOWLEDGEMENTS

The research results presented here are based on the Linac Coherent Light Source, an FEL operating at SLAC National Laboratory. The authors were supported by the U.S. Department of Energy, Office of Science, Office of Basic Energy Sciences through the Division of Materials Sciences and Engineering.

REFERENCES

[1] Y. Huang *et al.*, "Observation of a Novel Lattice Instability in Ultrafast Photoexcited SnSe," *Phys. Rev. X*, vol. 12, p. 011029, 2022.
`doi:10.1103/PhysRevX.12.011029`

[2] T. Mariano, *et al.*, "Fourier-transform inelastic X-ray scattering from time-and momentum-dependent phonon–phonon correlations," *Nat. Phys.*, vol. 9, no. 12, pp. 790-794, 2013.
`doi:10.1038/nphys2788`

[3] S. Teitelbaum *et al.*, "Measurements of non-equilibrium interatomic forces using time-domain x-ray scattering," *Phys. Rev. B: Condens. Matter*, vol. 103, no. 18, p. L180101, 2021.
`doi:10.1103/PhysRevB.103.L180101`

ISBN: 978-3-95450-220-2 ISSN: 2673-5474 doi: 10.18429/JACoW-FEL2022-FRAO4

FLASH2020+ PUMP-PROBE LASER UPGRADE: CONCEPT AND CURRENT STATUS

S. Ališauskas†, A.-L. Viotti[1], M. Seidel, A. Tajalli, B. Manschwetus, H. Cankaya, and I. Hartl
Deutsches Elektronen-Synchrotron DESY, Hamburg, Germany
[1]also at Department of Physics, Lund University, Lund, Sweden

Abstract

Time-resolved experiments are increasingly relevant in modern FEL user facilities. With the FLASH2020+ upgrade project, the pump-probe capabilities of FLASH will be extended. Besides offering high power fixed wavelengths (1030 nm fundamental and its harmonics), tunable wavelengths are under development: sub-150 fs 2-5 µm mid-infrared pulses for the condensed matter community and sub-40 fs long 200-500 nm UV-Visible pulses for the general chemistry, atomic molecular and optical physics (AMO) communities. Here, we present our pump-probe laser concept.

CONCEPT OF PUMP-PROBE LASER

By 2025, two new pump-probe laser systems will be operational in both the FLASH1 and FLASH2 FEL beamlines, allowing users to perform femtosecond pump-probe experiments [1]. Pump-probe lasers will be placed for both FEL beamlines in laser hutches in the FLASH experimental halls to provide temperature and humidity-stabilized environments, which are essential for laser stability. Both the FLASH1 and FLASH2 pump-probe lasers are of similar construction, see Fig. 1. The primary requirement for user experiments is that the pump-probe laser must be synchronized with the FEL radiation, and should therefore operate in bursts at 10 Hz (with an intra-burst repetition rate up to 1 MHz and a burst duration >600 µs) with a precisely controllable time delay. Utilizing Yb amplifiers based on fiber, thin disk, Innoslab, or cryogenic technology can accomplish this [2-5]. The Yb:YAG Innoslab technology is our preference because it has proven to be the most cost-effective solution and has already been implemented in a few FEL facilities, including European XFEL and LCLS II [6,7]. Due to the gain bandwidth limitations, a high-power Yb:YAG laser generates relatively long pulses (~1 ps FWHM). Frequently, lasers of this type are used to drive a broadband optical parametric amplifier (OPA) to generate the short pulses required for FEL pump-probe experiments [6,7]. Unfortunately, OPCPA has quite a low efficiency, and the final laser system power drops by one order of magnitude.

In our upgrade scheme, we plan to use external pulse post-compression: the pulse will be spectrally broadened by self-phase modulation in multi-pass cells (MPCs). MPCs offer large compression ratios (up to 40 times for one cell) and efficiency levels higher than 90%, while being still very compact and supporting excellent pulse-to-pulse stability [8]. We have been successfully testing the nonlinear compression technique in the recent years [9-12]. We will install gas-filled MPCs in the FLASH1 as well as FLASH2 laser hutches. By tuning the gas pressure, we can control the bandwidth of the output pulses (see Fig. 2 for more details), and subsequently, adjust the laser pulse durations to the experimental needs. A vacuum beamline system will then transport the uncompressed, spectrally broadened pulses with a Fourier limit of as small as 35 fs from the laser hutch to several modular optical delivery stations (MODs) within reach of the instruments, where pulse compressor, frequency conversion, and user controls will be installed. Afterward, the beam is coupled to the instrument and focused onto the interaction point. A single colour laser transport beamline with a modest spectral bandwidth becomes rather simple and will allow us to use high-quality AR and HR optics resulting in very high transmission (close to 99%).

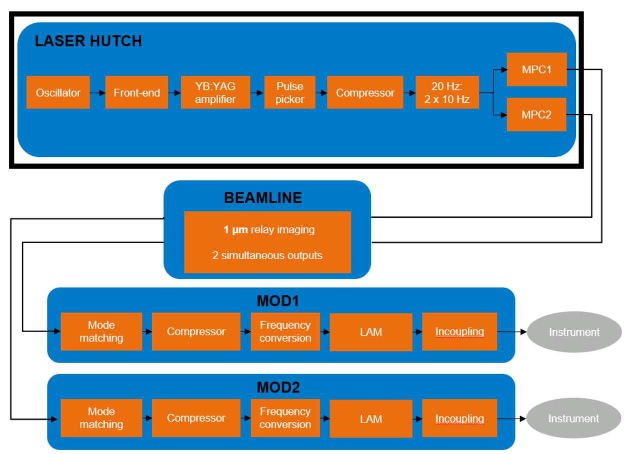

Figure 1: An illustration of the pump-probe laser and its delivery to the experiment.

FLASH's pump-probe laser's will run at 20 Hz and split the output into two 10 Hz pulse trains, one synchronized with the FEL and another shifted by 50 ms. This splitting will be achieved with a fast rotating waveplate and a polarizer. Simultaneously, these two outputs will be sent to MPCs for spectral broadening and afterward send to two MODs: one MOD where users will run the experiment and another MOD where we will prepare for the next user experiment. We are targeting to deliver 1030 nm few millijoule level pulses at the MODs. Currently, the Yb:YAG amplifier intraburst repetition rate is limited to 100 kHz, and in the future, we are considering increasing the intraburst rate to 1 MHz by keeping the same pulse energy. The pulse picker will adjust the burst length after the amplifier. The

† skirmantas.alisauskas@desy.de

ISBN: 978-3-95450-220-2 ISSN: 2673-5474 doi: 10.18429/JACoW-FEL2022-FRAO4

same pulse picker can be used for down-picking the pulses if lower rep-rates will be requested by the users.

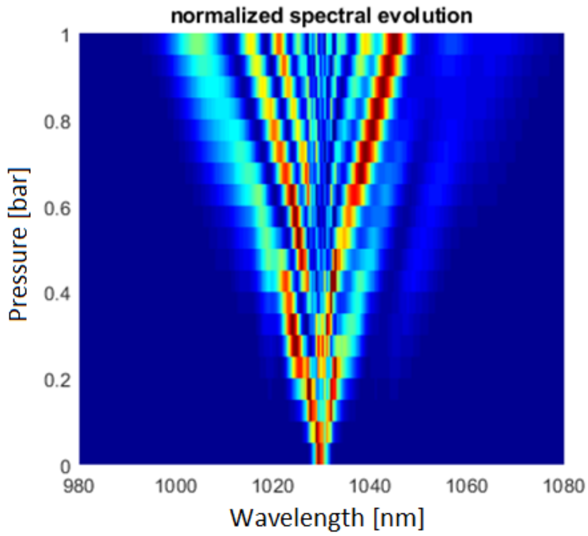

Figure 2: MPC output spectrum evolution as a function of gas pressure inside the MPC. 2.5 mJ input pulse energy is used in this specific case, and krypton is used as a gas medium. Simulations are made with the SISYFOS code [13].

A essential part of FLASH2020+ pump-probe laser upgrade is to provide users with ultra-broadband wavelength tunability in addition to fixed wavelengths. We conducted user survey on the most interesting laser parameters. The ranked list of priorities is as follows:

1. Tunable short-wave mid-IR (SWMIR) with 2-5 µm radiation, pulse duration <150 fs (more details in *Test results of SWMIR OPA*);
2. Tunable UV/VIS 200-500 nm radiation, pulse duration 25-100 fs;
3. High time resolution (cross-correlation) < 20 fs FWHM pump-probe laser source.

Given the multiple options that need to be provided to the users at the experimental stations, a flexible delivery concept is necessary. As the MODs need to squeeze in between the FEL beamlines, long and narrow optical tables can be used. The optical setups must be very flexible and ideally reconfigurable in less than one day. As a solution, we aim for optical setups consisting of several exchangeable breadboards of standard size. The optical setup on the MOD optical table is arranged in several modules which can be swapped easily depending on user needs and are installed on three-point repositioning elements. All combined modules at the MODs should form one complete optical setup. The different modules have the following functions:

- Input and diagnostics module: it contains a beam pointing measurement and active beam pointing stabilization setup, a mode-matching telescope to prepare the beam size for the rest of the modules, and diagnostics (energy, burst, spectrum).
- Pulse compression and diagnostics module: it includes a spectrometer, a four-pass transmission grating compressor for compressing spectrally broadened pulses, and a pulse duration diagnostic unit.
- Frequency conversion module: this module provides the short pulse generation of second, third, and fourth harmonics of the post-compressed 50 fs, 1030 nm pulses or can be swapped for SWMIR OPA (see *Test results of SWMIR OPA* section) or UV/VIS OPA modules with required diagnostics.
- Laser arrival time monitor (LAM) which can in real-time measure timing jitter between FEL main oscillator and pump-probe laser and allow post-correction measurement data.
- Incoupling module with user controls units. This breadboard includes a shutter and energy attenuator, polarization controls (if applicable), and the optics used to couple and focus the pump-probe laser beam into the instrument and to focus it on the target. It also includes beam stabilization and diagnostics of the beam in a virtual focus plane.

TEST RESULTS OF SWMIR OPA

Besides 1030 nm and its harmonics, we also want to offer FLASH users ultra-broadband wavelength tunability. As a first step, we are targeting the SWMIR (2-5 µm) region. A UV/VIS option (200-500 nm) is scheduled for the later upgrade phase and is not presented in this abstract. The majority of commercial OPA's typically use few hundred femtosecond pump sources, which fit very well with our new pump-probe laser concept. Our MPC allows fine-tuning pulse duration in the range from 1 ps down to 50 fs. For our test, we choose Orpheus-ONE-HE OPA (*Light Conversion*) [14] a very compact OPA that can be driven with a 2 mJ pump. For optimized compactness, Orpheus-ONE-HE has limited parameters and no dispersion control.

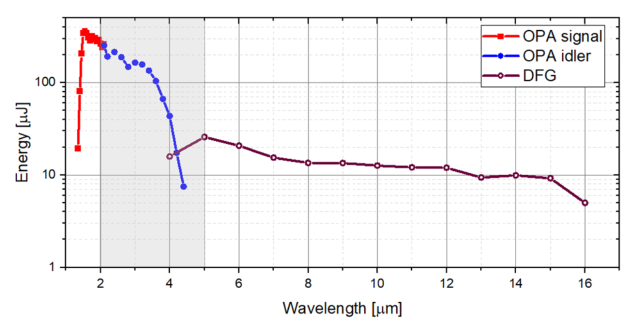

Figure 3: Orpheus ONE-HE (*Light Conversion*) commercial OPA tuning curve pumped with spectrally broadened 2 mJ 130 fs pulses. Grey area marking a region of interest 2-5 µm.

Because our aim is to generate <150 fs pulses, the tests were performed with 130 fs in a time-gated way: OPA occurs when pulses overlap in time, and therefore generated pulses cannot be much longer than the input pump pulse. The Orpheus-ONE-HE consists of three OPA stages covering the tuning range 1.3-4.3 µm (range limited by the OPA crystal idler wave absorption) and additional tuning between 4-16 µm is achieved by generating different

ISBN: 978-3-95450-220-2 ISSN: 2673-5474 doi: 10.18429/JACoW-FEL2022-FRAO4

frequency (DFG) between the OPA signal and the OPA idler waves. Using a 2 mJ input pump, the generated pulses in the 2-5 µm region (OPA idler, and small part of DFG) exceed 10 µJ (see the grey area in Fig. 3). For this entire range, the Fourier limits of the spectra measured are all below 100 fs, and the center wavelength stability was <0.2%.

A standard deviation of <3 % of energy stability was measured for both signal and idler over 12 hours. We conducted the tests at our R&D laboratory, which has a very stable environment. However, at the MOD's we are expecting that the changes in the environment will increase energy instabilities.

CONCLUSION

By 2025, two new pump-probe laser systems will be operational in FLASH1 and FLASH2, allowing users to perform femtosecond pump-probe experiments. In our upgrade scheme, we plan to use an external pulse post-compression of a 1 ps high average power Yb:YAG Innoslab amplifier in gas-filled multi-pass cells allowing us to reach sub-50 fs with a single cell. In contrast to OPA technology (currently used in high repetition rate FEL facilities), this allows us to increase the overall system efficiency and consequently, deliver kW level pump-probe laser to the FEL users. We are also going to offer users ultra-broadband wavelength tuning in two spectral ranges: tunable SWMIR 2-5 µm radiation with pulses <150 fs, and tunable UV/VIS 200-500 nm radiation with pulses <50 fs (in the later FLASH upgrade stage). Eventually, we are also working on the improvement of the time resolution of the pump-probe experiment, with an aim of <20 fs after data processing.

ACKNOWLEDGEMENTS

We acknowledge DESY (Hamburg, Germany), a member of the Helmholtz Association HGF, for the provision of experimental facilities. Parts of this research were carried out with the ULGAN R&D pump-probe laser for FLASH and we would like to thank members of the DESY FS-LA group for assistance. We acknowledge Gunnar Arisholm for providing the SISYFOS code and developing nonlinear pulse propagation simulations in MPCs. A.-L. Viotti also acknowledges support from the Swedish Research Council (Vetenskapsrådet grant No. 2019-06275).

REFERENCES

[1] M. Beye *et al.*, “FLASH2020+ Upgrade of FLASH Conceptual Design Report”, Hamburg, Germany, Mar. 2020. doi:10.3204/PUBDB-2020-00465

[2] M. Müller *et al.*, “3.5 kW coherently combined ultrafast fiber laser”, *Opt. Lett.*, vol. 43, p. 6037, Nov. 2018. doi.org/10.1364/OL.43.006037

[3] B. A. Reagan *et al.*, “Scaling diode-pumped, high energy picosecond lasers to kilowatt average powers”, *High Power Laser Sci. Eng.*, vol. 6, p. E11, Mar. 2018. doi:10.1017/hpl.2018.3

[4] K.-Z. Han *et al.*, “High power single-frequency Innoslab amplifier”, *Appl. Opt.*, vol. 55, p. 5341, Jul. 2016. doi.org/10.1364/AO.55.005341

[5] D. Rand *et al.*, “Cryogenic Yb^{3+}-doped materials for pulsed solid-state laser applications [Invited]”, *Opt. Mater. Express*, vol. 1, p. 434, Jul. 2011.

doi:10.1364/OME.1.000434

[6] G. Palmer *et al.*, “Pump-probe laser system at the FXE and SPB/SFX instruments of the European X-ray Free-Electron Laser Facility”, *J. Synchroton Radiat.*, vol. 26, p. 328, Mar. 2019. doi:10.1107/S160057751900095X

[7] LCLS-I Lasers, https://lcls.slac.stanford.edu/lasers/lcls-ii

[8] A.-L. Viotti *et al.*, “Multi-pass cells for post-compression of ultrashort laser pulses”, *Optica*, vol. 9, p. 197, Feb. 2022. doi:10.1364/OPTICA.449225

[9] P. Balla *et al.*, “Postcompression of picosecond pulses into the few-cycle regime”, *Opt. Lett.*, vol. 45, p. 2572, March 2020. doi:org/10.1364/OL.388665

[10] A.-L. Viotti *et al.*, “60 fs, 1030 nm FEL pump–probe laser based on a multi-pass post-compressed Yb:YAG source”, *J. Synchrotron Radiat.*, vol. 28, p. 36, Jan. 2021. doi:10.1107/S1600577520015052

[11] A.-L. Viotti *et al.*, “Temporal pulse quality of a Yb:YAG burst-mode laser post-compressed in a multi-pass cell”, *Opt. Lett.*, vol. 46, p. 4686, Aug. 2021.

doi:10.1364/OL.435073

[12] M. Seidel *et al.*, “Ultrafast MHz-Rate Burst-Mode Pump-Probe Laser for the FLASH FEL Facility Based on Nonlinear Compression of ps-Level Pulses from an Yb-Amplifier Chain”, *Laser Photonics Rev.*, vol. 202, p. 2100268, Jan. 2022. doi:10.1002/lpor.202100268

[13] G. Arisholm and H. Fonnum, “Simulation system for optical science (SISYFOS) - tutorial, version 2”, Rep. Norwegian Defense Research Establishment, 2021.

[14] Orpheus ONE-HE optical parametric amplifier, https://lightcon.com/product/orpheus-mid-ir-opa/